

CODEN: JASI

The Journal of the Acoustical Society of America

0001-4966

Vol. 108, No. 6

DECEMBER 2000

ACOUSTICAL NEWS—USA	2685
USA Meetings Calendar	2687
ACOUSTICAL NEWS—INTERNATIONAL	2691
International Meetings Calendar	2692
OBITUARIES	2693
BOOK REVIEWS	2695
REVIEWS OF ACOUSTICAL PATENTS	2699

GENERAL LINEAR ACOUSTICS [20]

Effects of the speed of moving noise sources on the sound visualization by means of moving frame acoustic holography	Soon-Hong Park, Yang-Hann Kim	2719
Two- and three-dimensional complex-transducer-point analysis of beam reflection from anisotropic plates	Han Zhang, D. E. Chimenti	2729
A unified boundary element method for the analysis of sound and shell-like structure interactions. II. Efficient solution techniques	Shaohai Chen, Yijun Liu, Xinyu Dou	2738
A variational method for identification of viscoelastic parameters from experimental data	Alberto Di Meglio, Lian Sheng Wang	2746

NONLINEAR ACOUSTICS [25]

Measurement of the acoustic nonlinearity parameter B/A in solvents: Dependence on chain length and sound velocity	J. Banchet, J. D. N. Cheeke	2754
A simplified algorithm for the second-order sound fields	Desheng Ding	2759
Numerical analysis for nonlinear resonant oscillations of gas in axisymmetric closed tubes	Young-Doo Chun, Yang-Hann Kim	2765

AEROACOUSTICS, ATMOSPHERIC SOUND [28]

A new boundary-element method for predicting outdoor sound propagation and application to the case of a sound barrier in the presence of downward refraction	Eric Premat, Yannick Gabillet	2775
--	-------------------------------	------

(Continued)

CONTENTS—Continued from preceding page

UNDERWATER SOUND [30]

Complex Padé approximants for wide-angle acoustic propagators	David Yevick, David J. Thomson	2784
Complex-image approximations to the half-space acousto-elastic Green's function	John A. Fawcett	2791
Wave propagation, stress relaxation, and grain-to-grain shearing in saturated, unconsolidated marine sediments	Michael J. Buckingham	2796
Physical limitations of travel-time-based shallow water tomography	Orlando C. Rodríguez, Sérgio M. Jesus	2816
On a novel application of the Helmholtz integral in the development of a virtual sonar	Anthony J. Romano, Joseph A. Bucaro, Brian H. Houston, Earl G. Williams	2823

ULTRASONICS, QUANTUM ACOUSTICS, AND PHYSICAL EFFECTS OF SOUND [35]

Mode-selective resonance ultrasound spectroscopy of a layered parallelepiped	Hirotsugu Ogi, Paul Heyliger, Hassel Ledbetter, Sudook Kim	2829
Experiments with a flow-through thermoacoustic refrigerator	R. S. Reid, G. W. Swift	2835

STRUCTURAL ACOUSTICS AND VIBRATION [40]

Modeling piezoceramic transducer hysteresis in the structural vibration control problem	S.-H. Lee, T. J. Royston	2843
An illustration of analytical/numerical matching with finite-element analysis for structural vibration problems	Linda P. Franzoni, Christopher D. Park	2856

NOISE: ITS EFFECTS AND CONTROL [50]

A numerical model for the low frequency diffuse field sound transmission loss of double-wall sound barriers with elastic porous linings	F. C. Sgard, N. Atalla, J. Nicolas	2865
---	------------------------------------	------

ACOUSTICAL MEASUREMENTS AND INSTRUMENTATION [58]

Three-dimensional optical measurement of instantaneous pressure	Todd A. Pitts, James F. Greenleaf	2873
---	-----------------------------------	------

ACOUSTIC SIGNAL PROCESSING [60]

Two-dimensional noise source imaging with a T-shaped microphone cross array	Marinus M. Boone, Niels Kinneging, Teun van den Dool	2884
Target parameter estimation using resonance scattering analysis applied to air-filled, cylindrical shells in water	A. Tesei, W. L. J. Fox, A. Maguer, A. Lóvik	2891
Resolution of front-back confusion in virtual acoustic imaging systems	P. A. Hill, P. A. Nelson, O. Kirkeby, H. Hamada	2901

PHYSIOLOGICAL ACOUSTICS [64]

Modeling the combined effects of basilar membrane nonlinearity and roughness on stimulus frequency otoacoustic emission fine structure	Carrick L. Talmadge, Arnold Tubis, Glenis R. Long, Christopher Tong	2911
Interrelations among distortion-product phase-gradient delays: Their connection to scaling symmetry and its breaking	Christopher A. Shera, Carrick L. Talmadge, Arnold Tubis	2933

CONTENTS—Continued from preceding page

APPLIED ACOUSTICS PAPER: PSYCHOLOGICAL ACOUSTICS [66]

- A concept for a research tool for experiments with cochlear implant users** Luc Geurts, Jan Wouters 2949

PSYCHOLOGICAL ACOUSTICS [66]

- Independence of frequency channels in auditory temporal gap detection** Dennis P. Phillips, Susan E. Hall 2957
- Specificity of perceptual learning in a frequency discrimination task** Dexter R. F. Irvine, Russell L. Martin, Ester Klimkeit, Rachel Smith 2964
- Generalization of tactile perceptual skills to new context following tactile-alone word recognition training with the Tickle Talker™** Karyn L. Galvin, Peter J. Blamey, Robert S. C. Cowan, Michael Oerlemans, Graeme M. Clark 2969

SPEECH PRODUCTION [70]

- Simultaneous effects on vowel duration in American English: A covariance structure modeling approach** Molly L. Erickson 2980
- Irregular vocal-fold vibration—High-speed observation and modeling** Patrick Mergell, Hanspeter Herzel, Ingo R. Titze 2996
- A finite-element model of vocal-fold vibration** Fariborz Alipour, David A. Berry, Ingo R. Titze 3003

SPEECH PERCEPTION [71]

- Some effects of duration on vowel recognition** James M. Hillenbrand, Michael J. Clark, Robert A. Houde 3013
- Children's perception of speech in multitalker babble** Marianne Fallon, Sandra E. Trehub, Bruce A. Schneider 3023
- Relationship between *N1* evoked potential morphology and the perception of voicing** Anu Sharma, Catherine M. Marsh, Michael F. Dorman 3030

SPEECH PROCESSING AND COMMUNICATION SYSTEMS [72]

- Spontaneous speech recognition using a statistical coarticulatory model for the vocal-tract-resonance dynamics** Li Deng, Jeff Ma 3036

BIOACOUSTICS [80]

- Time evolution of enhanced ultrasonic reflection using a fibrin-targeted nanoparticulate contrast agent** Christopher S. Hall, Jon N. Marsh, Michael J. Scott, Patrick J. Gaffney, Samuel A. Wickline, Gregory M. Lanza 3049
- Analysis of the axial transmission technique for the assessment of skeletal status** Estelle Camus, Maryline Talmant, Geneviève Berger, Pascal Laugier 3058
- Seismic properties of Asian elephant (*Elephas maximus*) vocalizations and locomotion** C. E. O'Connell-Rodwell, B. T. Arnason, L. A. Hart 3066
- Japanese monkeys perceive sensory consonance of chords** Akihiro Izumi 3073

CONTENTS—Continued from preceding page

LETTERS TO THE EDITOR

Conical radiating waves from immersed wedges [20]	Anne-Christine Hladky-Hennion, Philippe Langlet, Michel de Billy	3079
Seismic-like scaling regime in impulse reflection from underwater sediment [30]	Eric Smith	3084
Psychophysical customization of directional transfer functions for virtual sound localization [66]	John C. Middlebrooks, Ewan A. Macpherson, Zekiye A. Onsan	3088
Minimum audible angles in the horizontal and vertical planes: Effects of stimulus onset asynchrony and burst duration [66]	Thomas Z. Strybel, Ken Fujimoto	3092
INDEX TO VOLUME 108		3096
SUBJECT INDEX TO VOLUME 108		3101
AUTHOR INDEX TO VOLUME 108		3126

NOTES CONCERNING ARTICLE ABSTRACTS

1. The number following the abstract copyright notice is a Publisher Item Identifier (PII) code that provides a unique and concise identification of each individual published document. This PII number should be included in all document delivery requests for copies of the article.
2. PACS numbers are for subject classification and indexing. See June and December issues for detailed listing of acoustical classes and subclasses.
3. The initials in brackets following the PACS numbers are the initials of the JASA Associate Editor who accepted the paper for publication.

Document Delivery: Copies of journal articles can be ordered from the new *Articles in Physics* online document delivery service (URL: <http://www.aip.org/articles.html>).

ACOUSTICAL NEWS—USA

Elaine Moran

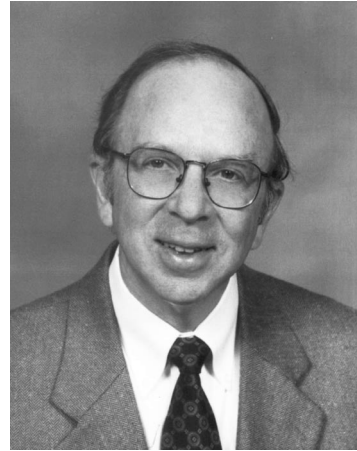
Acoustical Society of America, Suite 1N01, 2 Huntington Quadrangle, Melville, NY 11747-4502

Editor's Note: Readers of this Journal are encouraged to submit news items on awards, appointments, and other activities about themselves or their colleagues. Deadline dates for news items and notices are 2 months prior to publication.

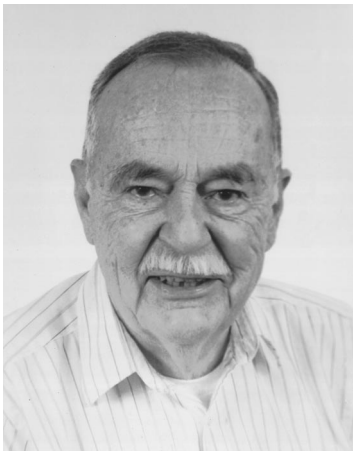
New Fellows of the Acoustical Society of America



Søren Bech—For contributions to architectural and physiological acoustics.



Donald E. Bray—For contributions to ultrasonic nondestructive evaluation.



Gordon R. Hamilton—For contributions to underwater acoustics.



Richard H. Love—For contributions in fisheries acoustics.

Logan Hargrove receives Superior Civilian Service Award

Logan E. Hargrove was awarded the Navy Superior Civilian Service award on 26 July at the Office of Naval Research. The award citation is: "For his superior performance and contributions while serving as Program Officer at the Office of Naval Research from October 1997 to May 2000. Dr. Hargrove's guidance of the S&T Program in Physical Acoustics resulted in the substantial enhancement, focus, and expansion of the National Center for Physical Acoustics (NCPA) at the University of Mississippi. Due to such remarkable improvements, NCPA is well on the way to becoming a nationally known center of activity in acoustics and a potentially strong contributor to the S&T communities supporting Naval and DOD interests. Dr. Hargrove's leadership, professionalism and total dedication to duty, reflect great credit upon himself and the Office of Naval Research and are in keeping with the highest traditions of the Naval Service."

Logan Hargrove is a Fellow of the Acoustical Society of America and was awarded the Biennial Award (now the R. Bruce Lindsay Award) in 1970.

Stetson Scholarship awarded to Elizabeth K. Johnson



The 2000 Raymond H. Stetson Scholarship in Phonetics and Speech Production was awarded to Elizabeth K. Johnson of the Johns Hopkins University.

Ms. Johnson received a B.A. degree at the University of Rochester in 1998 and is working toward a Ph.D. in Psychology at Johns Hopkins. Her current research interests are in the area of bio-developmental factors in speech and phonetics.

The Stetson Scholarship is awarded annually by the Acoustical Society of America to a member of the Acoustical Society for graduate study in scientific areas related to the field of phonetics and speech production. The award consists of a cash stipend (\$3000 in 2000) for one academic year. The scholarship is funded by the Raymond H. Stetson Fund of the Acoustical Society Foundation.

The next scholarship will be awarded in July 2001. Applications are available from the Acoustical Society of America, Suite 1N01, 2 Huntington Quadrangle, Melville, NY 11747-4502, Tel.: 516-576-2360; Fax: 516-576-2377; E-mail: asa@aip.org. The deadline for submitting applications is 15 March 2001.

The next scholarship will be awarded in July 2001. Applications are available from the Acoustical Society of America, Suite 1N01, 2 Huntington Quadrangle, Melville, NY 11747-4502, Tel.: 516-576-2360; Fax: 516-576-2377; E-mail: asa@aip.org. The deadline for submitting applications is 15 March 2001.

The 139th meeting of the Acoustical Society of America held in Atlanta, Georgia

The 139th meeting of the Acoustical Society of America was held 30 May–3 June 2000 at the Westin Peachtree Plaza Hotel in Atlanta, Georgia. This was the second time the Society has met in Atlanta, the first meeting being held in 1980.

The meeting drew a total of 984 registrants. There were 116 nonmembers and 262 students in attendance. Attesting to the international ties of our organization, 101 of the registrants (about 10%) were from outside North America; the United States, Canada, and Mexico accounted for 844, 24, and 4, respectively. There were 20 registrants from the United Kingdom, 13 from Japan, 11 from Korea, 9 from France, 5 from Taiwan, 4 each from Australia, Germany, People's Republic of China, and Sweden, 3 each from Israel, Italy, and The Netherlands, 2 each from Brazil, Hong Kong, New Zealand, and Singapore, and 1 each from Chile, Denmark, Egypt, Finland, Luxembourg, Poland, Russia, South Africa, Turkey and Venezuela. We have truly become an international Society.



FIG. 1. Robin O. Cleveland, recipient of the R. Bruce Lindsay Award with ASA President Patricia Kuhl.

A total of 658 papers were organized into 72 sessions, which covered the areas of interest of all 12 Technical Committees and 1 Technical Group. The meeting also included 8 different sessions dealing with standards.

The local meeting committee arranged technical tours of the Fox Theatre, the Acoustical Laboratories of the Woodruff School of Mechanical Engineering at Georgia Tech, and the Aeroacoustics Laboratories of the Georgia Tech Research Institute.

The ASA sponsored a Workshop on "Finding a Job in Acoustics" which was attended by 20 participants including students, recent graduates, and professors who wished to gain useful information for their students. The workshop included a presentation by a speaker followed by a panel discussion.

The newly-established ASA Student Council met for the first time at the Atlanta meeting. Students representing each of the Technical Committees/Group met with President Pat Kuhl and Executive Council member Jan Weisenberger to discuss topics of interest to students and ways in which student participation in the Society can be increased. Suggestions made at the Student Council meeting included a student section on the ASA Home Page that provided information of special interest to students, a student page in Echoes, an ASA Mentoring Award, an All-Student Social, and a permanent Student Council. Many of these will be implemented before the Newport Beach ASA meeting (4–8 Dec. 2000).

The first ASA Book Fair was held at the meeting. Five publishers and about 10 individual authors participated in the fair which included displays of over 100 titles.

Other special events included four receptions for students in various areas of acoustics which allowed students to meet informally with others working in the technical areas sponsoring the receptions. The Fellows Luncheon was held and included a presentation by Dr. Steven L. Garrett of the



FIG. 2. Lawrence A. Crum, recipient of the Helmholtz-Rayleigh Interdisciplinary Silver Medal with ASA President Patricia Kuhl.



FIG. 3. Murray Strasberg, recipient of the ASA Gold Medal with ASA President Patricia Kuhl.

Pennsylvania State University titled "Thermoacoustics." During the meeting, the President and other ASA leaders met with the leaders of INCE-USA to discuss the long-term future of the relationship between the ASA and INCE. The discussion centered on ways in which the two organizations might collaborate to achieve mutual goals in the future, and was deemed a success.

The plenary session included a Business Meeting, the presentation of awards, announcement of newly elected Fellows of the Society, recognition of the meeting organizers and presentation of the President's tuning fork.

The Business Meeting included a vote on an amendment to the ASA Bylaws to add the immediate Past Vice President as a voting member of the Executive Council and a nonvoting member of the Technical Council. The amendment was passed by the membership.

The President presented three Society awards (see Figs. 1 through 3) and announced the election of 16 new Fellows. The R. Bruce Lindsay Award was presented to Robin O. Cleveland of Boston University "for contributions to nonlinear acoustics, particularly to shock wave lithotripsy." The Helmholtz-Rayleigh Interdisciplinary Silver Medal was presented to Lawrence A. Crum of the University of Washington "for advancing the understanding of the physical, chemical, and biological effects of acoustic cavitation and of high-intensity ultrasound." The Gold Medal was presented to Murray Strasberg of the Carderock Division of the Naval Surface Warfare Center (formerly the David Taylor Model Basin) "for contributions to hydroacoustics, acoustic cavitation and turbulence noise, and for dedicated service to the Society."



FIG. 4. Newly-elected Fellows of the Acoustical Society of America receive their certificates from ASA Vice President Mauro Pierucci and President Patricia Kuhl. (left to right) ASA Vice President Mauro Pierucci, Mendel Kleiner, James M. Hillenbrand, W. Kendall Melville, Charles R. Greene, F. Michael Pestorius, Judith C. Brown, Stephen E. McAdams, Lynne E. Bernstein, Robin S. Langley, Mohsen Badiey, ASA President Patricia K. Kuhl.



FIG. 5. President-Elect Katherine Harris presents the President's Tuning Fork to Patricia Kuhl, outgoing ASA President.

Election of the following persons to Fellow grade was announced: Mohsen Badiey, Lynne E. Bernstein, Judith C. Brown, Brian G. Ferguson, Charles R. Greene, James M. Hillenbrand, Avraham Hirschberg, Mendel Kleiner, Robin S. Langley, Stephen E. McAdams, W. Kendall Melville, Shigeo Ohtsuki, F. Michael Pestorius, Paul O. Thompson, Peter Tyack and Paul Vidmar (see Fig. 4).

The President expressed the Society's thanks to the Local Committee for the excellent execution of the meeting, which clearly required meticulous planning. She introduced the Chair of the Meeting, Yves H. Berthelot, who acknowledged the contributions of the members of her committee including: Jerry H. Ginsberg, Technical Program Chair; George McCall and Jacek Jarzynski, Audio-Visual; Marshall Leach, Registration; Kenneth A. Cunefare, Paper Copying Service and E-mail; Laurence Jacobs, Signs; David Trivett, Technical Tours; Peter H. Rogers, Plenary Session/Fellows Luncheon; Stephanie Cunefare, Rona Ginsberg, Alice Rogers, and Nancy Trivett, Accompanying Persons Program.

The President also extended thanks to the members of the Technical Program Organizing Committee: Jerry H. Ginsberg, Technical Program Chair; David R. Palmer and James F. Lynch, Acoustical Oceanography; Peter H. Rogers, Animal Bioacoustics; Scott D. Pfeiffer, Architectural Acoustics; Ibrahim M. Hallaj, Biomedical Ultrasound/Bioresponse to Vibration; P. K. Raju and Allan D. Pierce, Education in Acoustics; Thomas R. Howarth and Kim C. Benjamin, Engineering Acoustics; James W. Beauchamp, Musical Acoustics; Mary Prince, Noise; James P. Chambers, Richard Raspet, and Yves H. Berthelot, Physical Acoustics; Marjorie R. Leek, Psychological and Physiological Acoustics; Charles Gaumont, Signal Processing in Acoustics; Lynne C. Nygaard, Speech Communication; Joseph W. Dickey, Alison B. Flatau, and David Feit, Structural Acoustics and Vibration; and James C. Presig and William M. Carey, Underwater Acoustics.

The Plenary Session ended with the presentation of the President's Tuning Fork by President-Elect Katherine Harris to Patricia Kuhl, whose term ended at the close of the meeting (see Fig. 5).

PATRICIA K. KUHL
President 1999–2000

USA Meetings Calendar

Listed below is a summary of meetings related to acoustics to be held in the U.S. in the near future. The month/year notation refers to the issue in which a complete meeting announcement appeared.

2001

4–8 February Midwinter Meeting, Association for Research in Otolaryngology, St. Petersburg, FL [ARO Office, 19 Mantua Rd., Mt. Royal, NJ 08061, Tel.: 856-423-7222; Fax: 856-423-3420; E-mail: meetings@aro.org; WWW:www.aro.org/mwm/mwm.html].

- 22–25 March “New Frontiers in the Amelioration of Hearing Loss,” St. Louis, MO [Sarah Uffman, CID Department of Research, 4560 Clayton Ave., St. Louis, MO 63110, Tel.: 314-977-0278; Fax: 314-977-0030; E-mail: suffman@cid.wustl.edu].
- 30 April–3 May 2001 SAE Noise & Vibration Conference & Exposition, Traverse City, MI [Patti Kreh, SAE Int’l., 755 W. Big Beaver Rd., Suite 1600, Troy, MI 48084, Tel.: 248-273-2474; Fax: 248-273-2494; E-mail: pkreh@sae.org].
- 4–8 June 141st Meeting of the Acoustical Society of America, Chicago, IL [Acoustical Society of America, Suite 1NO1, 2 Huntington Quadrangle, Melville, NY 11747-4502, Tel.: 516-576-2360; Fax: 516-576-2377; E-mail: asa@aip.org; WWW: asa.aip.org].
- 9–13 July 2001 SIAM Annual Meeting, San Diego, CA [Society for Industrial and Applied Mathematics (SIAM), Tel.: 215-382-9800; Fax: 215-386-7999; E-mail: meetings@siam.org; WWW: www.siam.org/meetings/an01/].
- 15–19 August ClarinetFest 2001, New Orleans, LA [Dr. Keith Koons, ICA Research Presentation Committee Chair, Music Dept., Univ. of Central Florida, P.O. Box 161354, Orlando, FL 32816-1354, Tel.: 407-823-5116; E-mail: kkoons@pegasus.cc.ucf.edu]. Deadline for receipt of abstracts: 15 January 2001.
- 7–10 October 2001 IEEE International Ultrasonics Symposium Joint with World Congress on Ultrasonics, Atlanta, GA [W. O’Brien, Electrical and Computer Engineering, Univ. of Illinois, 405 N. Mathews, Urbana, IL 61801; Fax: 217-244-0105; WWW: www.ieee-uffc.org/2001].
- 3–7 December 142nd Meeting of the Acoustical Society of America, Ft. Lauderdale, FL [Acoustical Society of America, Suite 1NO1, 2 Huntington Quadrangle, Melville, NY 11747-4502, Tel.: 516-576-2360; Fax: 516-576-2377; E-mail: asa@aip.org; WWW: asa.aip.org].
- 2002**
- 3–7 June 143rd Meeting of the Acoustical Society of America, Pittsburgh, PA [Acoustical Society of America, Suite 1NO1, 2 Huntington Quadrangle, Melville, NY 11747-4502, Tel.: 516-576-2360; Fax: 516-576-2377; E-mail: asa@aip.org; WWW: asa.aip.org].
- 2–6 December Joint Meeting: 144th Meeting of the Acoustical Society of America, 3rd Iberoamerican Congress of Acoustics and 9th Mexican Congress on Acoustics, Cancun Mexico [Acoustical Society of America, Suite 1NO1, 2 Huntington Quadrangle, Melville, NY 11747-4502, Tel.: 516-576-2360; Fax: 516-576-2377; E-mail: asa@aip.org; WWW: asa.aip.org/cancun.html].

ACOUSTICAL NEWS—INTERNATIONAL

Walter G. Mayer

Physics Department, Georgetown University, Washington, DC 20057

17th International Congress on Acoustics, Rome—Further details

The 17th ICA in Rome, 2–7 September 2001, is organized by the Italian Acoustical Society and will take place at the campus of Rome University “La Sapienza.” The campus is located next to San Pietro in Vincoli, a few hundred meters from the Colosseum and the Forum in the archeological part of Rome. The Congress venue is within walking distance from the main railway station; it is also served by subway and various bus lines.

Discounted hotel rates (deadline for early booking 15 February, deadline for hotel confirmation 30 May) appear to be 80–190 euros for two and three star hotels, and 190 euros and up for four and five star hotels. Participants are advised to make hotel reservations early since September is high season for tourists. Assistance with hotel reservations will be offered by the Congress Secretariat through the Congress Web site in due time. The Congress URL is www.ica2001.it; the other coordinates are e-mail: ica2001@uniroma1.it; fax: +39 06 4976 6932; mail: A. Alippi, Dipartimento di Energetica, University of Rome “La Sapienza,” Via A. Scarpa 14, 00161 Rome, Italy.

The registration fee has been set at 350 euros, 400 euros after 30 May 2001. Registration fees for students will be reduced by 50%. The secretariat will help in providing low-cost accommodations or last-minute service.

All aspects of acoustics will be covered at the Congress. The technical program will be organized on the basis of structured sessions. There will be plenary lectures, invited and contributed papers as well as poster sessions. The Congress Proceedings on CD will be distributed free of charge to registered participants. Printed copies will be available and will be mailed upon request.

A number of social events, partner programs, and pre- or post-Congress tours of 2 or 3 days duration are also planned with details to be announced at a later date. The Home Page will be updated periodically to announce further details.

Papers published in JASJ(E)

A listing of Invited Papers and Regular Papers appearing in the latest issue of the English language version of the *Journal of the Acoustical Society of Japan*, JASJ(E), was published for the first time in the January 1995 issue of the Journal. This listing is continued below.

The September 2000 issue of JASJ(E), Vol. 21, No. 5, contains the following contributions:

- V. Makarova, “Acoustic cues of surprise in Russian questions”
 M. Mizumachi and M. Akagi, “The auditory-oriented spectral distortion for evaluating speech signals distorted by additive noises”
 H. Suzuki, S. Oguro, and T. Ono, “A sensitivity correction method for a three-dimensional sound intensity probe”

International Meetings Calendar

Below are announcements of meetings to be held abroad. Entries preceded by an * are new or updated listings with full contact addresses given in parentheses. *Month/year* listings following other entries refer to meeting announcements, with full contact addresses, which were published in previous issues of the *Journal*.

December 2000

4–7

8th Australian International Conference on Speech, Science, and Technology, Canberra, Australia. (Web: www.cs.adfa.edu.au/ssst2000) 10/00

January 2001

14–17

4th European Conference on Noise Control (euro-noise 2001), Patras, Greece. (e-mail: euronoise2001@upatras.gr) 10/00

March 2001

26–29

German Acoustical Society Meeting (DAGA 2001), Hamburg-Harburg, Germany. (e-mail: dega@aku.physik.uni-oldenburg.de) 10/00

April 2001

9–11

Acoustical Oceanography, Southampton, UK. (Fax: +44 1727 850553; Web: www.ioa.org.uk) 8/00

23–25

***1st International Workshop on Thermoacoustics**, s’Hertogenbosch, The Netherlands. (C. Schmid, Acoustical Society of America, Suite 1N01, 2 Huntington Quadrangle, Melville, NY 11747-4502, USA; Web: www.phys.tue.nl/index.html)

May 2001

21–25

***5th International Conference on Theoretical and Computational Acoustics (ICTCA2001)**, Beijing, China. (E. C. Shang, CIRES, University of Colorado, NOAA/ETL, Boulder, CO, USA; Fax: +1 303 497 3577; Web: www.etl.noaa.gov/ictca01)

28–31

***3rd EAA International Symposium on Hydroacoustics**, Jurata, Poland. (G. Grelowska, Polish Naval Academy, Smidowicza 69, 81-103 Gdynia, Poland; Fax: +48 58 625 4846; Web: www.amw.gdynia.pl/pta/sha2001.html)

July 2001

2–5

***Ultrasonics International Conference (UI01)**, Delft, The Netherlands. (W. Sachse, T&AM, 212 Kimball Hall, Cornell University, Ithaca, NY 14853-1503, USA; Fax: +1 607 255 9179; Web: www.ccmr.cornell.edu/~ui01/)

2–6

8th International Congress on Sound and Vibration, Kowloon, Hong Kong. (Fax: +852 2365 4703; Web: www.iiav.org) 8/00

August 2001

28–30

INTER-NOISE 2001, The Hague. (Web: internoise2001.tudelft.nl) 6/99

September 2001

2–7

*(new contacts) **17th International Congress on Acoustics (ICA)**, Rome. (Fax: +39 6 4976 6932; Web: www.ica2001.it) 10/98

10–13

International Symposium on Musical Acoustics (ISMA 2001), Perugia. (Fax: +39 75 577 2255; e-mail: perusia@classico.it) 10/99

October 2001

17–19

32nd Meeting of the Spanish Acoustical Society, La Rioja. (Fax: +34 91 411 76 51; Web: www.ia.csic.es/sea/index.html) 10/99

March 2002

4–8

German Acoustical Society Meeting (DAGA 2002), Bochum, Germany. (Web: www.ika.ruhr-uni-bochum.de) 10/00

June 2002

10–14

***Acoustics in Fisheries and Aquatic Ecology**, Montpellier, France. (D. V. Holliday, BAE SYSTEMS, 4669 Murphy Canyon Road, Suite 102, San Diego, CA 92123-4333, USA; Web: www.ices.dk/symposia/)

August 2002

19–23

***16th International Symposium on Nonlinear Acoustics (ISNA16)**, Moscow, Russia. (O. Rudenko, Physics Department, Moscow State University, 119899 Moscow, Russia; e-mail: isna@acs366b.phys.msu.su)

September 2002

16–21

Forum Acusticum 2002 (Joint EAA-SEA-ASJ Meeting), Sevilla. (Fax: +34 91 411 7651; Web: www.cica.es/aliens/forum2002) 2/00

December 2002

2–6

Joint Meeting: 9th Mexican Congress on Acoustics, 144th Meeting of the Acoustical Society of America, and 3rd Iberoamerican Congress on Acoustics. (e-mail: sberista@maya.esimez.ipn.mx or Web: asa.aip.org) 10/00

OBITUARIES

Alvin M. Liberman • 1917–2000



Alvin M. Liberman, a Fellow of this Society, died on 13 January 2000, from complications of open heart surgery. He was past president of Haskins Laboratories (1975–1986) and professor emeritus in the Department of Psychology at the University of Connecticut and the Department of Linguistics at Yale University. His pioneering work in the field of speech perception set a research agenda that is still being followed today. Al was active in the field for more than 50 years, and was working on revisions to a major paper while he was in the hospital where he spent his last days.

Born in St. Joseph, Missouri, Al stayed close to home for his bachelor's and master's degrees, both from the University of Missouri. He moved to Yale for his Ph.D., in psychology, awarded in 1942. After a stint of aeromedical research for the Army during World War II (still at Yale), he came to Haskins Laboratories in New York to work with Franklin S. Cooper on the development of a reading machine for the blind, work sponsored by the Veterans Administration. Despite years of effort, he and his colleagues never succeeded in devising an acoustic transformation of the letters that listeners could follow faster than Morse code, roughly $\frac{1}{10}$ of a normal speaking rate, and intolerably slow for extended use. This failure raised the question to which he devoted much of the rest of his research career: Why is speech so much more efficient as a carrier of linguistic information than other sounds? The answer gradually emerged from dozens of experiments in the 1950s and 1960s.

Al realized that speech is not an arbitrary signal that just happened to be available as language evolved; rather, speech is an integral part of language. Consonants and vowels, the discrete phonemic elements essential for a sizeable lexicon, do not combine like beads on a string, but are overlapped, or encoded, into syllables; speed is thus purchased at the price of

acoustic complexity. Human listeners are biologically adapted to decode the continuously variable signal of running speech, and to recover its discrete phonemic components. In the course of developing this theoretical view, Al and his colleagues at Haskins Laboratories discovered the main acoustic cues to the consonants and vowels of English. These cues later served to guide the development of speech synthesis by rule, now widely used for man/machine interaction.

Al's provocative work was largely responsible for drawing speech research into the mainstream of experimental cognitive psychology, where his "nativist" views were not to everyone's liking. But he thrived on controversy, and up until the last months of his life he designed a steady stream of ingenious and telling experiments to support what he liked to call his "unconventional view" against the "conventional view" of most other experimental psychologists.

During the 1970s and 1980s, Al increasingly collaborated with his wife, the late Isabelle Yoffe Liberman, and other Haskins Laboratories scientists on reading. A central discovery of this work was that children who have difficulty in learning to read almost always lack what Isabelle termed "phoneme awareness": they cannot easily learn to break a word into its component consonants and vowels. The critical requirement of phoneme awareness in learning to read alphabetic print is now internationally recognized, in large part due to the two Libermans' passionate advocacy of the "alphabetic principle" against the "whole word" or "sight reading" method of instruction. Al was a member of the National Academy of Sciences and of the American Academy of Arts and Sciences, and received the Distinguished Scientific Contribution Award, the highest honor of the American Psychological Association. He also received many other awards, including the Warren Medal from the Society of Experimental Psychologists; honorary doctoral degrees from the State University of New York and from the Université Libre de Bruxelles, a medal from the Collège de France, Paris, and the Wilbur Cross Medal from the Graduate School of Yale University.

He is survived by two sons, Mark of Philadelphia, and Charles of Milton, MA; by a daughter, Sarah Ash, of Raleigh, NC, and by nine grandchildren.

DOUG H. WHALEN

BOOK REVIEWS

P. L. Marston

Physics Department, Washington State University, Pullman, Washington 99164

These reviews of books and other forms of information express the opinions of the individual reviewers and are not necessarily endorsed by the Editorial Board of this Journal.

Editorial Policy: *If there is a negative review, the author of the book will be given a chance to respond to the review in this section of the Journal and the reviewer will be allowed to respond to the author's comments. [See "Book Reviews Editor's Note," J. Acoust. Soc. Am. 81, 1651 (May 1987).]*

PHONETICS—The Science of Speech

M. J. Ball and J. Rahilly

Oxford University Press, New York, 2000.

vii +239 pp. Price: \$65.00 (hardcover) and \$19.95 (paperback).

How many textbooks are current for an introductory course on phonetics? Answer: ten, half by Americans and half by British. "Britain and America, two great nations separated by a common language." What is it that separates them? The British focus on the phonetic alphabet and how to use it; Americans focus on speech acoustic analysis and speech perception by humans and/or machines. So the Americans are more concerned with speech science. British instruction is easily applicable to many languages; American texts use primarily English examples.

This British book relates well to the broader discipline of linguistics. It is an admirable tutor for learning how to make a phonetic transcription of any language. It is well organized, starting with general descriptions of vocal anatomy and sound production, progressing through consonant and vowel articulation and suprasegmentals (prosodics), and skill-building in phonetic transcription listing training programs that are available, then passing at last to methods of acoustic analysis and speech perception. Acoustics and perception are treated only cursorily. An effective supplement to transcription training is Catford's 1988 book which instructs how to recognize the details of your own articulation via 125 exercises in silent articulations!

Ladefoged's *A Course in Phonetics* (3rd ed.) connects both linguistics and speech science very well, at the cost of the range of languages covered in the linguistics parts.

If you use Ball and Rahilly for linguistic transcription then you could use one of the speech science tutorial books in addition, for example, Johnson's *Acoustic and Auditory Phonetics* (1997), which would be suitable for students needing acoustical and engineering connections to phonology, or Denes and Pinson's *The Speech Chain* (1993).

Catford, J. C. (1988). *A Practical Introduction to Phonetics* (Oxford U. P., Oxford, UK).

Denes, P. B., and Pinson, E. N. (1993). *The Speech Chain*, 2nd ed. (Freeman, New York).

Johnson, K. (1997). *Acoustic and Auditory Phonetics* (Blackwell, Oxford, UK).

Ladefoged, P. (1993). *A Course in Phonetics*, 3rd ed. (Harcourt Brace Jovanovich, New York).

J. M. PICKETT

Windy Hill Lab

P.O. Box 198

Surry, Maine 04684

BOOKS RECEIVED

Fundamentals of Physical Acoustics. David T. Blackstock. John Wiley & Sons, 2000. 560 pp. \$90.00 *hc*. ISBN 0471319791.

Acoustic and Electromagnetic Scattering Analysis Using Discrete Sources. Adrian Doicu, Yuri Eremin, and Thomas Wriedt. Academic Press, 2000. 317 pp. \$79.95 *hc*. ISBN 0122197402.

Nonlinear Acoustics at the Turn of the Millennium: ISNA 15, 15th International Symposium (AIP Conference Proceedings, 524). Werner Lauterborn and Thomas Kurz, editors. Springer Verlag, 2000. 569 pp. \$185.00 *hc*. ISBN 1563969459.

Physical Acoustics: Cumulative Subject and Author Index Including Tables and Contents (Physical Acoustics, Vol. 25). R. N. Thurston and Allan D. Pierce, editors. Academic Press, 1999. 307 pp. \$160.00 *hc*. ISBN 124779247.

Structural Acoustics and Vibration. R. Ohayou and C. Soize. Academic Press, 1998. 242 pp. \$74.00 *hc*. ISBN 0125249454.

Vibrations of Shells and Rods. K. C. Le. Springer Verlag, 1999. 423 pp. \$112.00 *hc*. ISBN 3540645160.

Ultrasonic Instruments and Devices. E. P. Papadakis, editor. Academic Press, 1999. 809 pp. \$99.95 *pb*. ISBN 0125319517.

Sonics: Techniques for the Use of Sound and Ultrasound in Engineering and Science. Theodor R. Hueter and Richard H. Bolt. ASA, 2000. 456 pp. \$45.00 (ASA members \$30.00) *hc*. ISBN 1563969556.

Rarefied Gas Dynamics: From Basic Concepts to Actual Calculations. C. Cercignani. Cambridge University Press, 2000. 338 pp. \$74.95 *hc* (\$29.95 *pb*). ISBN 0521650089 *hc*. (0521659922 *pb*).

Adaptive Structures: Dynamics and Control. Robert L. Clark, William

R. Saunders, and Gary P. Gibbs. John Wiley & Sons, 1997. 464 pp. \$125.00 *hc*. ISBN 0471122629.

Signal Processing for Intelligent Sensor Systems. David C. Swanson. Marcel Dekker, 2000. 632 pp. \$195.00 *hc*. ISBN 0824799429.

Designing for Product Sound Quality. Richard H. Lyon. Marcel Dekker, 2000. 215 pp. \$125.00 *hc*. ISBN 0824704002.

Ruido: Fundamentos Y Control. Samir N. Y. Gerges. Spanish Edition. (Florianopolis-SC-Brasil, 1998, contact gerges@mbox1.ufsc.br.) 555 pp. ISBN 8590004601x *pb*.

Marine Mammals and Low-Frequency Sound. National Research Council. National Academy Press, Washington DC, 2000. 160 pp. \$35.00 *pb*. ISBN 030906886-X.

Acoustic Phonetics (Current Studies in Linguistics Series, No. 30). Kenneth N. Stevens. MIT Press, 2000. 607 pp. \$60.00 *hc* (\$35.00 *pb*). ISBN 026219404X *hc* (026269250-3 *pb*).

Coarticulation: Theory, Data, and Techniques (Cambridge Studies in Speech Science and Communication). William J. Hardcastle and Nigel Hewlett, editors. Cambridge University Press, 2000. 400 pp. \$64.95 *hc*. ISBN 0521440270.

Hearing: Its Physiology and Pathophysiology. Aager R. Moller. Academic Press, 2000. 515 pp. \$79.95 *hc*. ISBN 0125042558.

Fundamentals of Hearing. William A. Yost. Academic Press, 2000. 4th edition. 349 pp. \$44.95 *hc*. ISBN 0127756957.

Rhythm Perception and Production. Peter Desain and Luke Windsor, editors. Swets & Zeitlinger Publishers, The Netherlands, 2000. 106 pp. \$85.00 *hc*. ISBN 9026516363.

Songs, Roars, and Rituals: Communication in Birds, Mammals, and other Animals. Lesley J. Rogers and Gisela Kaplan. Harvard University Press, 2000. 207 pp. \$29.95 *hc*. ISBN 0674000587.

Principles of Optimal Design. Panos Y. Papalambros and Douglas J. Wilde. Cambridge University Press, 2000. 390 pp. \$120.00 *hc* (\$44.95 *pb*) ISBN 0521622158 *hc*. (0521627273 *pb*).

Flow Measurement Handbook: Industrial Designs, Operating Principles, Performance, and Applications. Roger C. Baker. Cambridge University Press, 2000. 524 pp. \$110.00 *hc*. ISBN 0521480108.

An Introduction to Turbulent Flow. Jean Mathieu and Julian Scott. Cambridge University Press, 2000. 374 pp. \$90.00 *hc* (\$39.95 *pb*). ISBN 0521570662 (0521775388 *pb*).

REVIEWS OF ACOUSTICAL PATENTS

Lloyd Rice

11222 Flatiron Drive, Lafayette, Colorado 80026

The purpose of these acoustical patent reviews is to provide enough information for a Journal reader to decide whether to seek more information from the patent itself. Any opinions expressed here are those of reviewers as individuals and are not legal opinions. Printed copies of United States Patents may be ordered at \$3.00 each from the Commissioner of Patents and Trademarks, Washington, DC 20231.

Reviewers for this issue:

GEORGE L. AUGSPURGER, *Perception, Incorporated, Box 39536, Los Angeles, California 90039*

DAVID PREVES, *Songbird Medical, Inc., 5 Cedar Brook Drive, Cranbury, New Jersey 08512*

CARL J. ROSENBERG, *Acentech, Incorporated, 33 Moulton Street, Cambridge, Massachusetts 02138*

KEVIN P. SHEPHERD, *M.S. 463, NASA Langley Research Center, Hampton, Virginia 23681*

5,805,726

43.38.Fx PIEZOELECTRIC FULL-RANGE LOUDSPEAKER

Chih-Ming Yang and Jyi-Tyan Yeh, assignors to Industrial Technology Research Institute
8 September 1998 (Class 381/190); filed 11 August 1995

Simple piezoelectric wafers are sometimes used as full-range loudspeakers. They are small (say, 5 cm in diameter), very thin, lightweight, inexpensive, and generate no electromagnetic interference. On the other hand, distortion is high, response is peaky, and the term "full-range" is an overstatement. The invention is a thin sandwich including two piezo wafers affixed to metal disks and at least one damping layer. Response is reasonably smooth from 300 Hz to beyond 20 kHz.—GLA

6,041,127

43.38.Hz STEERABLE AND VARIABLE FIRST-ORDER DIFFERENTIAL MICROPHONE ARRAY

Gary Wayne Elko, assignor to Lucent Technologies, Incorporated
21 March 2000 (Class 381/92); filed 3 April 1997

Six miniature pressure-sensitive microphone elements are flush-mounted on the surface of a small, rigid sphere. Microphone signals are processed in pairs. Sum and difference signals from the three pairs are combined, then filtered and summed to form a single output signal. By employing proper filtering, weighting, and delay, a cardioid pickup pattern is generated which can be electronically steered to any axis. The patent document is quite technical, but clearly written and informative.—GLA

5,991,425

43.38.Ja LOW REFLECTION/LOW DIFFRACTION TREATMENT FOR LOUDSPEAKER TRANSDUCER DIAPHRAGM

Daniel P. Anagnos, assignor to Sony Corporation; Sony Electronics, Incorporated
23 November 1999 (Class 381/423); filed 13 December 1996

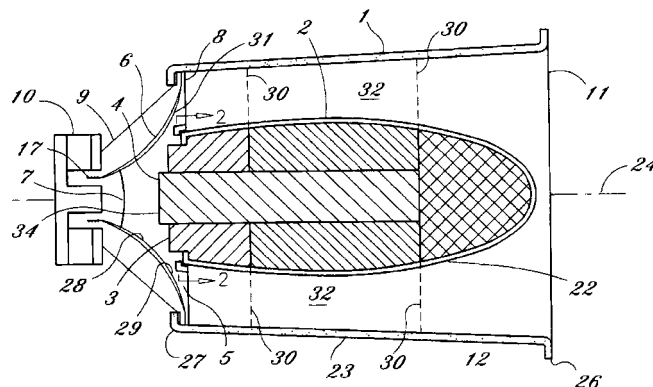
In the 1960s Arthur Janszen marketed a woofer having a plug of absorptive foam filling most of the cone cavity. It was intended to function as a low-pass filter, attenuating unwanted high-frequency energy. The patent describes a much thinner layer of absorptive foam which is said to provide low-pass filtering and also minimize reflection and diffraction of sound waves from adjacent transducers.—GLA

6,026,928

43.38.Ja APPARATUS AND METHOD FOR REDUCED DISTORTION LOUDSPEAKERS

Ashok A. Maharaj, Maracaibo, Venezuela
22 February 2000 (Class 181/152); filed 6 April 1999

Any loudspeaker will produce unpleasant distortion when driven to very high sound levels. The inventor has observed that most of the unwanted noise emanates from the central part of the cone. If the loudspeaker is used as a horn driver, then a special phasing plug can include "...a sound absorb-



ing inner portion adjacent the central portion of the diaphragm for absorbing the noise generated by the central portion at high power." This sounds terribly unscientific, but in practice it probably works fairly well.—GLA

6,031,921

43.38.Ja LOUDSPEAKER UNIT

Akiyo Mizoguchi, assignor to Aiwa Company, Limited
29 February 2000 (Class 381/182); filed in Japan 25 March 1997

A reverse-phase pair of point sound sources forms a gradient system. With appropriate signal processing the coverage pattern can be varied from cardioid to hypercardioid to figure eight, and any pattern can be further shifted toward omnidirectional by varying the relative levels of the two sources. A 1973 paper by Olson explained how this principle could be applied to practical loudspeaker systems. Since then a number of patents have described gradient loudspeaker variations intended for improved home stereo reproduction. This Aiwa patent is about as basic as you can get: two loudspeakers are mounted on two surfaces of a box, connected in reverse-phase, and driven at different levels.—GLA

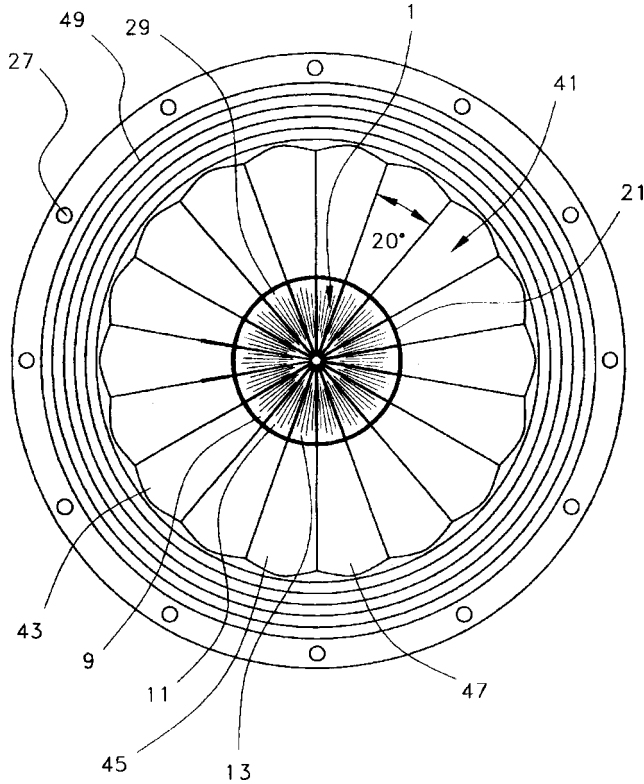
6,026,929

43.38.Ja HIGH FREQUENCY RADIALLY ARCTUATED CENTER SPEAKER CONE WITH VARIABLE THICKNESS

Alexander Faraone, assignor to Single Source Technology and Development, Incorporated

22 February 2000 (Class 181/173); filed 12 November 1997

A small, edge-driven, folded-plate cone **1** is placed at the center of the inventor's earlier loudspeaker design **41** (United States Patent 4,881,617). He informs us that the present invention has unique and unobvious characteristics, including smoother response extending to 20 kHz. Since no performance tests are shown, we will just have to take his word for it.—GLA



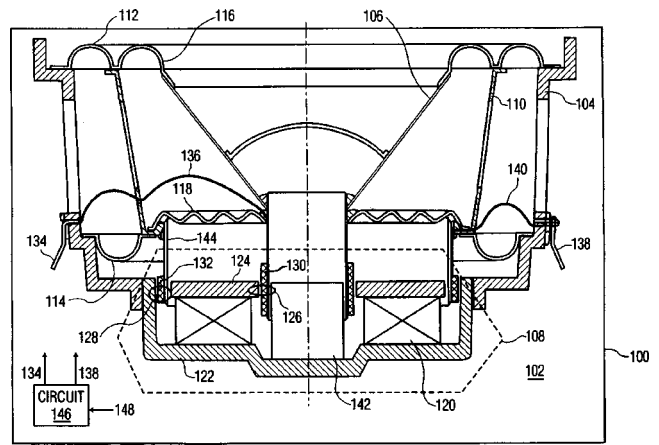
teristics, including smoother response extending to 20 kHz. Since no performance tests are shown, we will just have to take his word for it.—GLA

6,031,925

43.38.Ja TELESCOPING LOUDSPEAKER HAS MULTIPLE VOICE COILS

Yevgeniy Eugene Shteyn, assignor to U.S. Philips Corporation
29 February 2000 (Class 381/401); filed 25 June 1998

Speaker cone **106**, frame **110**, centering spider **118**, and voice coil **126** make up a floating assembly which is driven in turn by outer voice coil **128**. The arrangement is interesting and unusual, but it is difficult to understand why "...a large displacement volume can be obtained with a cone of relatively small diameter, owing to the accumulation of the individual amplitudes of one or more subframes and of the cone." It appears that the maxi-



imum displacement of cone **106** and inner voice coil **126** would be exactly the same if the subframe and the outer voice coil were simply omitted.—GLA

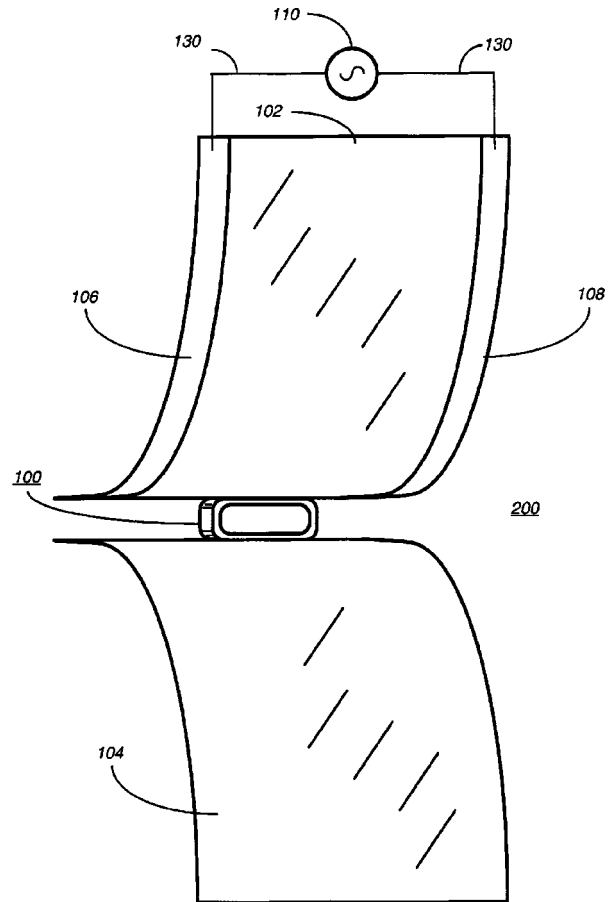
6,044,159

43.38.Ja PLANAR FILM SPEAKER WITH INERTIAL DRIVER

Neil Johan Schmertmann, Boynton Beach, Florida and John Michael McKee, Hillsboro Beach, Florida

28 March 2000 (Class 381/186); filed 17 December 1997

A small inertial transducer **100** is coupled to two rectangular sheets of flexible plastic **104** and **106**. The assembly is suspended from wires **130**



which also provide the electrical signal. The signal is carried from the wires to the transducer through conductive strips **106** and **108**.—GLA

6,044,161

43.38.Ja PILLOW SPEAKER APPARATUS AND METHOD

Keith Lee, Tacoma, Washington
28 March 2000 (Class 381/301); filed 18 November 1998

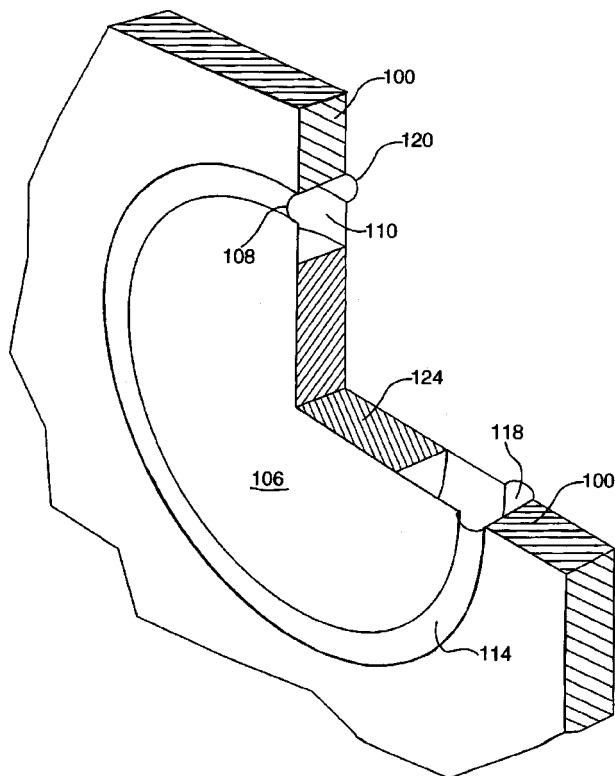
Does anyone remember the pillow speaker? Apparently it is time for an improved version. Two small speakers are recessed into a block of open-cell foam. The rear surface of the block is sculpted into multiple voids—the kind of coffered pattern often found in packing foam. Sound energy from the rear of each speaker finds its way down into the voids “...through which sound waves from the loud speakers can travel, through out the lower body, and upwardly through the upper surface thereby reaching the listener from many directions.”—GLA

6,044,925

43.38.Ja PASSIVE SPEAKER

Joseph Yaacoub Sahyoun, Redwood City, California
4 April 2000 (Class 381/157); filed 30 November 1998

Substituting a passive radiator (drone cone) for a conventional vent in a bass reflex loudspeaker system can achieve similar performance, along with practical advantages and disadvantages. The passive radiator is usually built from a loudspeaker cone and basket, less voice coil and magnet. The



invention is a disk-shaped passive radiator **106** suspended from two peripheral half-rolls **114** and **118**. The goal is to provide a more linear suspension. It would also seem to be more heavily damped and less resistant to wobble. Somehow, this simple idea has been expanded to 31 patent claims.—GLA

6,070,694

43.38.Ja LOUDSPEAKER ASSEMBLY

Albert Burdett *et al.*, assignors to Niles Audio Corporation, Incorporated
6 June 2000 (Class 181/150); filed 4 September 1998

In an earlier patent (United States Patent 6,026,927, not reviewed) the inventors mounted high-frequency loudspeakers on a sort of adjustable lazy susan. The present invention is a swiveling tweeter mount that operates like a recessed ceiling spotlight, allowing a practical range of adjustment while maintaining relatively uniform baffling.—GLA

5,978,490

43.38.Kb DIRECTIVITY CONTROLLING APPARATUS

Hyun-Woo Choi and Jin-Sung Lee, assignors to LG Electronics, Incorporated
2 November 1999 (Class 381/92); filed in Republic of Korea 27 December 1996

The invention automatically sets the directivities of microphones used in an audio-video surveillance system. Although the patent is clearly written in good, technical English, it is not all that easy to understand exactly how the system works. “A certain microphone in the system is selected to have directivity according to a result of comparing levels of input signals supplied into plural partial microphones in a supervisory mode by categorizing directional microphones into a directional mode and the supervisory mode.”—GLA

5,983,191

43.38.Lc METHOD AND APPARATUS FOR AUTOMATICALLY COMPENSATING TONE COLOR

Yeong Ho Ha *et al.*, assignors to LG Electronics, Incorporated
9 November 1999 (Class 704/500); filed in Republic of Korea 11 June 1997

The audio circuitry of a TV receiver includes a computer-controlled, multi-band equalizer. If the user changes channels or adjusts equalization, the computer analyzes the spectral content of the signal, decides what general category it belongs to, looks up the appropriate “tone color,” and adjusts equalization accordingly.—GLA

6,016,182

43.38.Ne MOTION PICTURE FILM AND A TECHNIQUE FOR RECORDING AND/OR REPRODUCING DATA FROM SUCH MOTION PICTURE FILM

Masakazu Ohashi *et al.*, assignors to Sony Cinema Products Corporation
18 January 2000 (Class 352/37); filed in Japan 7 December 1993

Digital information is optically recorded longitudinally bit by bit, supplemented by transverse recordings of each byte. The resulting compression processing blocks also include parity data. Additional tricks are employed to create a robust system that allows error-free playback even when longitudinal or transverse scratches are present.—GLA

5,949,896

43.38.Si EARPHONE

Koji Nageno *et al.*, assignors to Sony Corporation
7 September 1999 (Class 381/328); filed in Japan 19 August 1996

A small, in-the-ear earphone improves on an earlier Sony design by incorporating an acoustical low-cut filter. The result is essentially flat response from about 100 Hz to 5 kHz.—GLA

6,041,130

43.38.Si HEADSET WITH MULTIPLE CONNECTIONS

Raymond G. Goss, assignor to MCI Communications Corporation
21 March 2000 (Class 381/374); filed 23 June 1998

The invention is intended for use in telecommunications call centers but might find other applications as well. Suppose you need to maintain simultaneous voice communications over two completely different systems—say, a conventional telephone network and the Internet. Rather than designing a fancy audio hybrid circuit, the inventor suggests a relatively simple headset. Each earphone contains two transducers, allowing independent stereo reception from each network. Similarly, the microphone boom contains two microphone elements. Possible refinements and controls are also discussed in the patent document.—GLA

5,784,477

43.38.Vk SYSTEM FOR THE FRONTAL LOCALIZATION OF AUDITORY EVENTS PRODUCED BY STEREO HEADPHONES

Florian Meinhard Konig, Germering, Germany
21 July 1998 (Class 381/25); filed in Germany 25 July 1989

To avoid “inside the head” localization, a number of stereo headphone designs locate transducers forward from ear canal openings. The inventor argues that natural localization requires not only a forward shift but an even greater downward shift in placement.—GLA

5,796,844

43.38.Vk MULTICHANNEL ACTIVE MATRIX SOUND REPRODUCTION WITH MAXIMUM LATERAL SEPARATION

David H. Griesinger, assignor to Lexicon
18 August 1998 (Class 381/18); filed 19 July 1996

More than a dozen earlier patents (four issued to Griesinger) deal with the process of expanding left and right stereo signals into various surround sound formats. The present invention is an improved active matrix that redistributes left and right signals, including directionally encoded and non-directional components, into multiple output channels for surround sound playback. The patent includes a succinct analysis of general decoding schemes and should be of interest to anyone working in this field.—GLA

5,959,597

43.38.Vk IMAGE/AUDIO REPRODUCING SYSTEM

Yuji Yamada and Kiyofumi Inanaga, assignors to Sony Corporation
28 September 1999 (Class 345/8); filed in Japan 28 September 1995

The invention is a virtual reality system which sets the video image in a preset orientation and controls sound source localization, both in response to the user’s head movements. According to the patent, this is a compara-

tively simple system which can provide realistic sound and picture orientation without requiring massive computer processing power.—GLA

6,021,205

43.38.Vk HEADPHONE DEVICE

Yuji Yamada and Kiyofumi Inanaga, assignors to Sony Corporation
1 February 2000 (Class 381/310); filed in Japan 31 August 1995

A practical virtual reality presentation must be able to control sound and vision in response to movements of the user’s head. For spatial sound reproduction, enormous computer power may be required to continuously update digital filter coefficients. The invention is a simplified system which requires relatively little processing volume, yet which allows a sound image to be localized simultaneously in forward and backward directions.—GLA

6,021,386

43.38.Vk CODING METHOD AND APPARATUS FOR MULTIPLE CHANNELS OF AUDIO INFORMATION REPRESENTING THREE-DIMENSIONAL SOUND FIELDS

Mark Franklin Davis and Craig Campbell Todd, assignors to Dolby Laboratories Licensing Corporation
1 February 2000 (Class 704/229); filed 8 January 1991

The history of this patent goes back to 1991. It is a continuation of a continuation of a division of a continuation-in-part of a continuation-in-part. It describes an efficient, flexible surround sound coding scheme which is said to be audibly superior to known matrix systems, yet requires less transmission bandwidth. The inventors postulate a kind of spatial masking phenomenon, which is combined with known critical band masking in two embodiments of generalized subband encoding. The patent is clearly written and contains a great deal of interesting information.—GLA

6,023,512

43.38.Vk THREE-DIMENSIONAL ACOUSTIC PROCESSOR WHICH USES LINEAR PREDICTIVE COEFFICIENTS

Naoshi Matsuo and Kaori Suzuki, assignors to Fujitsu Limited
8 February 2000 (Class 381/17); filed in Japan 8 September 1995

To produce a convincing synthetic environment for sound reproduction, the acoustical characteristics of the desired sound field must be added to the signal and the acoustical characteristics of the actual listening environment must be subtracted from the signal. Easier said than done. The invention uses linear predictive analysis within critical bands to minimize the number of digital filter taps required and to simplify processing.—GLA

6,052,470

43.38.Vk SYSTEM FOR PROCESSING AUDIO SURROUND SIGNAL

Tomohiro Mouri, assignor to Victor Company of Japan, Limited
18 April 2000 (Class 381/18); filed in Japan 4 September 1996

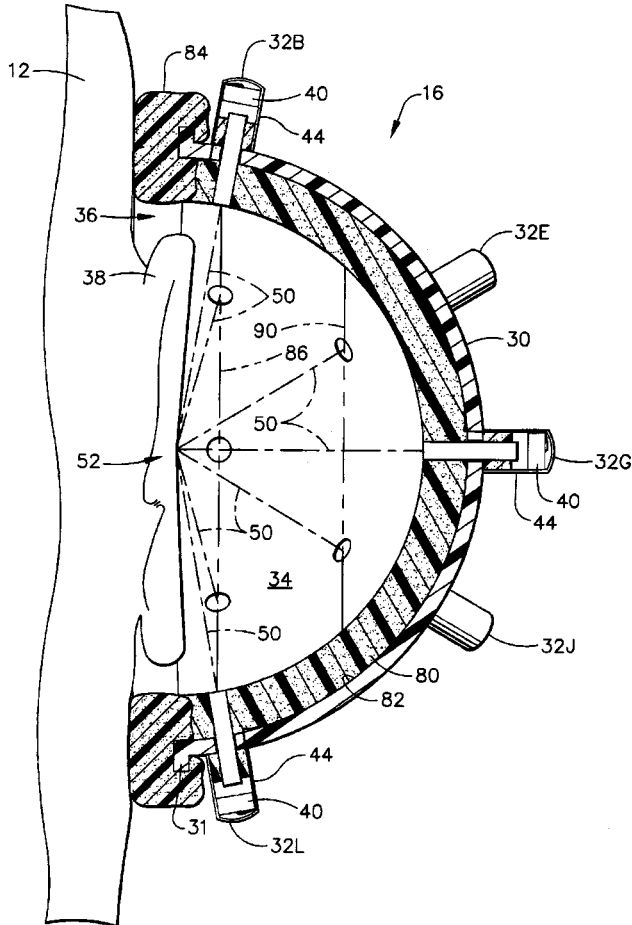
The patent describes a record-reproduce system in which the multi-channel recording includes a surround signal and also a program to process the surround signal. The derived left and right surround channels can then be transformed into virtual sound sources when rear loudspeakers are absent and only front loudspeakers are used.—GLA

6,038,330

43.38.Vk VIRTUAL SOUND HEADSET AND METHOD FOR SIMULATING SPATIAL SOUND

Robert James Meucci, Jr., Senatobia, Mississippi
14 March 2000 (Class 381/371); filed 20 February 1998

A number of prior patents deal with the problem of reproducing multi-channel surround sound via headsets. Mr. Meucci takes the direct approach. Embedded around the hemispherical surface of each ear cup are a plurality



of miniature transducers 40 which squirt energy through "sound focussing" tubes, "...so as to simulate the directional orientation of the sound as perceived by the listener.—GLA

6,021,612

43.50.Gf SOUND ABSORPTIVE HOLLOW CORE STRUCTURAL PANEL

Stanley E. Dunn and Joseph M. Cuschieri, assignors to C&D Technologies, Incorporated
8 February 2000 (Class 52/144); filed 8 September 1995

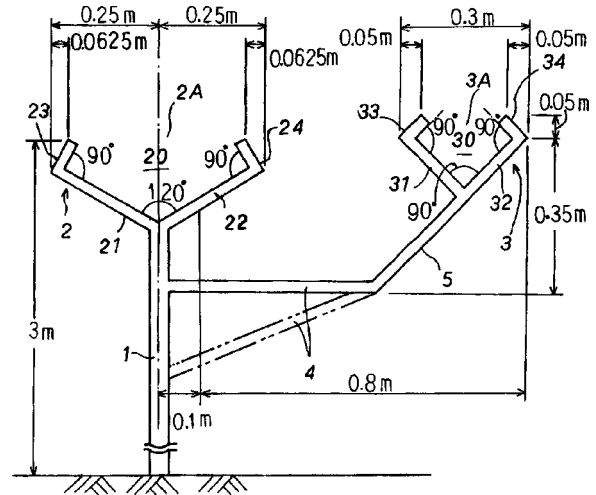
This hollow core metal panel has two exterior skins that envelope and create interior cavities. These cavities serve as Helmholtz resonators through penetrations of the surface and thus provide some sound absorption properties for the panels.—CJR

6,019,189

43.50.Gf NOISE BARRIER WALL

Hiroshi Shima *et al.*, assignors to Bridgestone Corporation; Nihon Doro Kodan
1 February 2000 (Class 181/210); filed in Japan 19 February 1997

This patent describes an extension to a highway noise barrier wall that is meant to improve the noise attenuation of the barrier without increasing the barrier height. The main body of the noise barrier is vertical, but there is



attached on the side opposite to the noise source (i.e., away from the highway) an overhanging extension arm.—CJR

6,029,282

43.50.Gf CYCLIST'S WIND NOISE LIMITING DEVICE

Thomas W. Buschman, Kirtland, Ohio
29 February 2000 (Class 2/422); filed 14 April 1998

The sound-permeable outer body of the device fits over the ear. The body of the device has an open weave porous plastic mesh, and fibers are attached to the mesh. All these reduce the turbulence of the wind noise without impairing the transfer of desired sound.—CJR

6,040,266

43.50.Gf FOAM CATALYST SUPPORT FOR EXHAUST PURIFICATION

Thomas F. Fay III *et al.*, assignors to Ultramet
21 March 2000 (Class 502/439); filed 22 February 1994

A method of manufacturing a material system which functions as both an acoustic absorber and a catalytic converter for application in small two- and four-cycle engine exhaust ducts is described. An open cell carbon foam is formed from polyurethane foam and then coated with an appropriate catalyst.—KPS

6,041,893

43.50.Gf BRAKE JAW

Ludwig Ervens *et al.*, assignors to Textar GmbH
28 March 2000 (Class 188/1.11 W); filed in Germany 19 December 1996

A brake pad for use with disc brakes is described in which an intermediate layer is placed between the friction layer and the lining support. The intermediate layer fulfills two functions; damping of vibration (brake squeal) and generating an acoustic alarm signal when the friction layer reaches its wear limit.—KPS

6,047,790

43.50.Gf SOUND DAMPING DEVICE FOR OSCILLATORY COMPONENTS OF A MOTOR VEHICLE HYDRAULIC SYSTEM

Michael Seidel-Peschmann and Thomas Fritz, assignors to Aeroquip Vickers International GmbH
11 April 2000 (Class 181/200); filed in Germany 23 January 1997

A method to reduce noise radiated from the fluid reservoir of a hydraulic system in an automobile is described. In particular, noise generated by fluid vibration induced by the hydraulic pump is addressed. A vibration absorber is tuned by selection of an appropriate material, shape, and position of attachment to the sidewall of the reservoir. An alternative, double-wall arrangement is also described.—KPS

6,078,671

43.50.Gf SILENCER FOR ATTENUATING A SOUND OR NOISE TRANSMITTED THROUGH AN AIR PASSAGE OF A DUCT

Takashi Kawanishi and Masayoshi Ikeda, assignors to Ebara Corporation
20 June 2000 (Class 381/71.5); filed in Japan 5 September 1996

This is an active noise cancellation silencer adapted to be mounted on an air duct. The silencer includes a noise detecting microphone and a loudspeaker for delivering a noise cancellation signal and a vibration shield between the microphone and the wall of the duct, to reduce transmission of vibration through the duct wall to the microphone.—CJR

6,047,794

43.50.Ki VIBRATION DAMPER FOR USE IN WHEEL BRAKE

Yukio Nishizawa, assignor to Sumitomo Electric Industries, Limited
11 April 2000 (Class 188/73.36); filed in Japan 19 December 1996

This represents an addition to United States Patent 5,960,912 in which automobile brake squeal is suppressed using an active vibration control system. A piezoelectric sensor is used to detect the vibration and a piezoelectric actuator is used to reduce the vibration using a feedback controller. As the brake pads wear, the relationship between the signal applied to the actuator and the resultant vibration changes. It is proposed that this relationship be measured on a periodic basis by applying a known signal to the actuator and examining the response of the sensor. This transfer function is then incorporated into the control system.—KPS

6,039,139

43.50.Lj METHOD AND SYSTEM FOR OPTIMIZING COMFORT OF AN OCCUPANT

David S. Breed *et al.*, assignors to Automotive Technologies International, Incorporated
21 March 2000 (Class 180/271); filed 5 May 1992

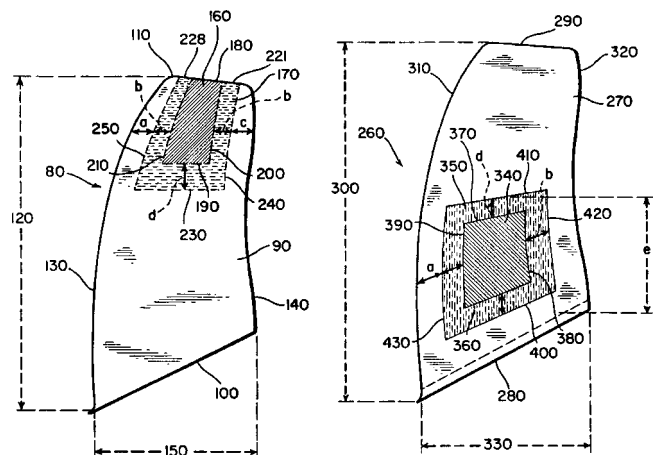
This far-reaching patent describes a system for determining the presence and position of a vehicle occupant. Ultrasonic and laser systems are proposed for this purpose. This information would be used for numerous applications, including optimization of the vehicle's stereo system, as a component of an active noise control system (localized control at the occupants ears), control of headlight glare from other vehicles, and control of air bag deployment.—KPS

6,042,338

43.50.Lj DETUNED FAN BLADE APPARATUS AND METHOD

Perry W. Brafford *et al.*, assignors to AlliedSignal, Incorporated
28 March 2000 (Class 416/203); filed 8 April 1998

This patent describes a method of detuning fan blades of the type found in turbofan engines. In order to minimize stall flutter the mistuned blades are installed in the blade row so that each blade alternates with



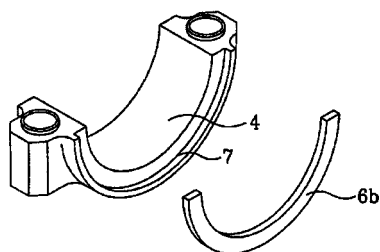
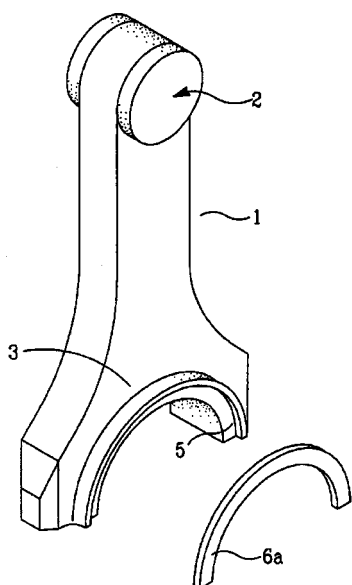
another blade having a slightly different resonant frequency. The tuning is accomplished through the creation of recessed areas 160 and 170 and 340 and 350, yielding a difference in resonant frequencies of about 0.5%.—KPS

6,044,818

43.50.Lj VIBRATION DAMPER FOR INTERNAL COMBUSTION ENGINES

Julian A. Decuir, assignor to Almarv LLC
4 April 2000 (Class 123/192.1); filed 26 August 1998

To suppress vibration between the connecting rod and crankshaft of an internal combustion engine a vibration absorber, consisting of two pieces 6a



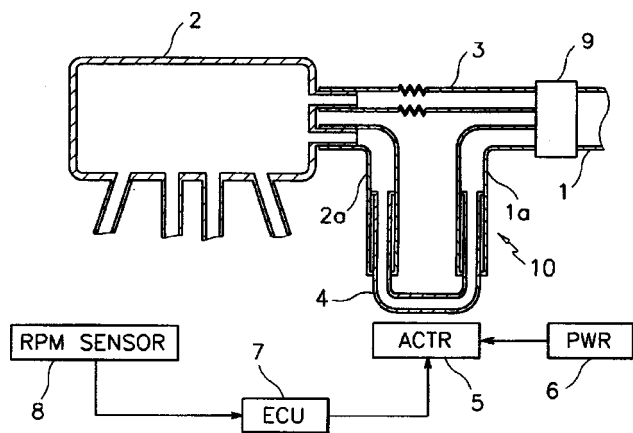
and **6b**, is positioned in a recessed annulus. Arrangements are described for both in-line and V-type engines.—KPS

6,047,677

43.50.Lj INTAKE SYSTEM WITH NOISE REDUCTION STRUCTURE

Tae-joung Kim, assignor to Hyundai Motor Company
11 April 2000 (Class 123/184.55); filed 14 December 1998

An air intake system for an automobile engine which is designed to reduce the propagation of combustion noise back through the air inlet is described. The air inlet **1** is connected to the surge tank **2** via a straight tube



3 and a tube of variable length **4**. The length of this tube is adjusted according to the speed of the engine. Sound propagating towards the inlet thus follows two paths, one of which is adjusted so that phase cancellation occurs at the inlet. Exactly how this occurs over a bandwidth from 100 Hz to 1.6 kHz is not clear.—KPS

6,056,611

43.50.Lj INTEGRATED INDUCTION NOISE SILENCER AND OIL RESERVOIR

Ian G. House *et al.*, assignors to Brunswick Corporation
2 May 2000 (Class 440/88); filed 13 May 1999

The oil reservoir for an outboard engine is shaped and positioned so that it acts as an acoustic barrier to noise emanating from the engine's throttle bodies.—KPS

6,039,009

43.55.Dt ENGINE-OPERATED GENERATOR

Tadafumi Hirose, assignor to Honda Giken Kogyo Kabushiki Kaisha
21 March 2000 (Class 123/2); filed in Japan 24 July 1997

An acoustic enclosure intended for use with a portable gas-powered electrical generator consists of multiple compartments which are arranged to allow for efficient cooling as well as noise reduction. The heat-generating components are within one compartment which is ventilated for cooling. Other components are in another compartment to enable noise reduction and protection from the heat sources.—KPS

5,992,561

43.55.Ev SOUND ABSORBER, ROOM AND METHOD OF MAKING

Larry B. Holben and Daniel M. Beam, assignors to Kinetics Noise Control
30 November 1999 (Class 181/295); filed 6 January 1998

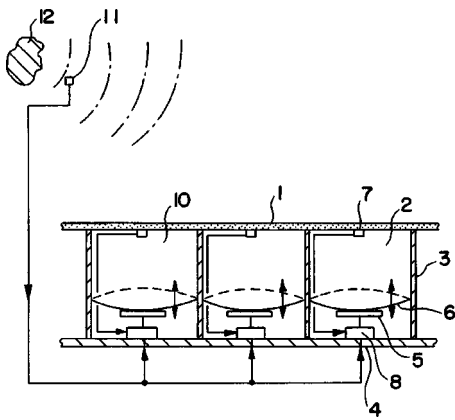
This sound absorber is a triangular panel of glass fiber that is designed and fabricated to hang in the corner of a room. This creates an airspace behind the panel at an efficient location for absorbing sound, especially low-frequency energy.—CJR

6,041,125

43.55.Ev ACTIVE ACOUSTIC WALL

Masaharu Nishimura *et al.*, assignors to Mitsubishi Jukogyo Kabushiki Kaisha; United Technologies Corporation
21 March 2000 (Class 381/71.4); filed in Japan 15 August 1996

The wall has sound pressure detectors provided within respective cells so that a detected signal acts to vibrate an oscillation plate in the cell. The surface of the active wall is a porous material and, due to the oscillations of an oscillator in each cell, the sound pressure on the surface of the porous



material is minimized at all frequencies. The proposed application of this device is for sound-absorbing nacelles or casings for jet aircraft engines, fans or compressors, or even for ordinary sound-absorbing room walls.—CJR

6,057,254

43.55.Ev PROCESS FOR MANUFACTURE OF AN ACOUSTIC PANEL AND ACOUSTIC PANEL WITH SANDWICH CONSTRUCTION

Klaus Bender *et al.*, assignors to Wilhelmi Werke AG
2 May 2000 (Class 442/374); filed in Germany 10 January 1996

The patent describes a dimensionally stable and fireproof acoustic panel with an underlying structural panel covered on one side or both sides by an absorptive cover panel. The acoustic panel in this sandwich construction can be a structural element for sound absorbing ceilings.—CJR

6,073,722

43.55.Pe ANECHOIC ROOM FOR THE ENTIRE AUDITORY RANGE

Gerhard Babuke *et al.*, assignors to Fraunhofer Gesellschaft zur Foerderung der angewandten Forschung E.v.
13 June 2000 (Class 181/30); filed in Germany 4 September 1997

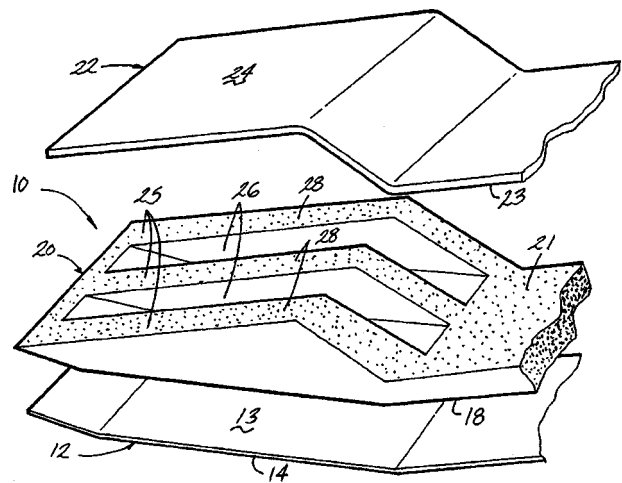
This anechoic room uses low-frequency composite plate resonators that are designed to absorb sound, in particular, below 100 Hz. The absorbers are provided with inside plates made of metal or heavy foil. The treatment has a constant depth of less than 0.25 m, and the resulting surface of the room is planar. Resonators with thicker plates are tuned to lower frequencies, and these are located toward the corners of the room.—CJR

6,024,190

43.55.Ti ACOUSTICAL BARRIER WITH RIBBED DECOUPLER

Kenneth T. Ritzema, assignor to Cascade Engineering, Incorporated
15 February 2000 (Class 181/286); filed 7 January 1998

For a motor vehicle firewall between the engine compartment and passenger area, the special ribbed inner core allows greater separation and decoupling between the opposite plates, more void space between the plates,



and fewer points of contact. It is claimed that these features give greater isolation performance.—CJR

6,065,717

43.55.Ti NOISE ATTENUATING WALL ELEMENT

Klaus Boock, assignor to DaimlerChrysler Aerospace Airbus GmbH
23 May 2000 (Class 244/1N); filed in Germany 21 December 1996

This is a wall element with noise-attenuating characteristics that is suitable for use as an aircraft cabin interior panel element to be mounted directly on the aircraft fuselage structure. The wall panel includes a rigid lightweight composite core between two cover layers, and an outer layer spaced away from one of the covers. The core and the two outer cover layers are air permeable in a direction through the thickness of the panel but the outer layer is not. This outer layer is attached to the fuselage.—CJR

6,077,613

43.55.Ti SOUND INSULATING MEMBRANE

Walter J. Gaffigan, assignor to The Noble Company
20 June 2000 (Class 428/442); filed 12 November 1993

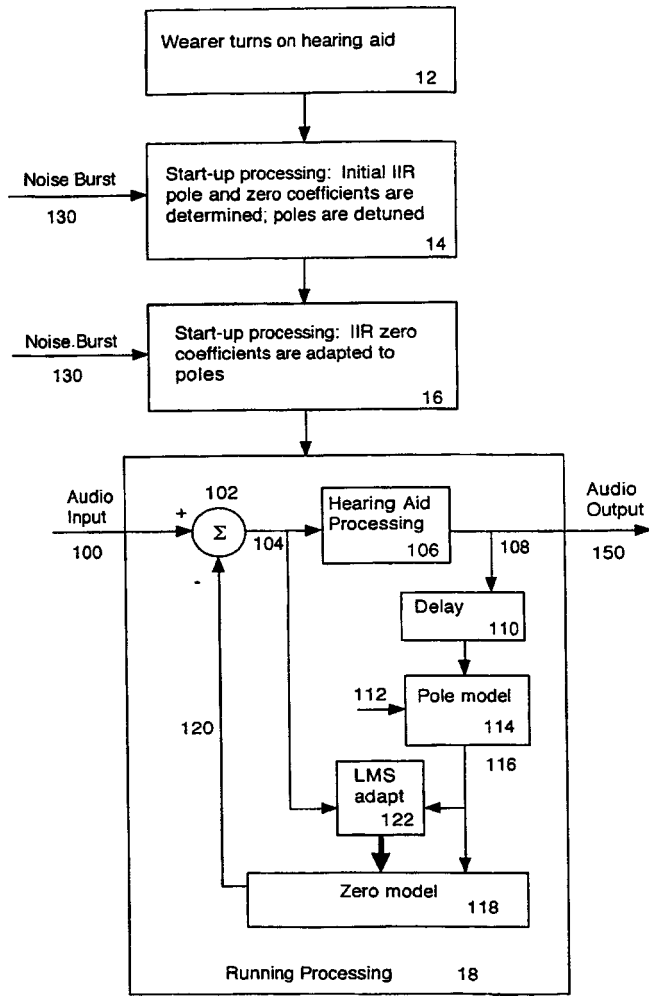
This patent describes a sound-insulating membrane and the process for forming it. The membrane comprises at least two layers: a backing layer and a layer of nonfoam polymeric material. The membrane is intended for use primarily as an underlayment for ceramic tile floors to provide a separation for impact noise. The membrane has a thickness of less than about 0.150 in. It is thought that the membrane assists in improving isolation because the sound energy is dissipated laterally in the polymeric matrix, which is relatively flexible and elastic, at least at a microscopic level.—CJR

6,072,884

43.66.Ts FEEDBACK CANCELLATION APPARATUS AND METHODS

James Mitchell Kates, assignor to AudioLogic Hearing Systems LP
6 June 2000 (Class 381/318); filed 18 November 1997

The system described is said to produce, without introducing audible artifacts, an additional 10 dB of stable gain relative to a hearing aid not



having feedback cancellation. When the hearing aid is turned on, the coefficients of a first adaptive filter are designed using a white noise probe signal to model the components of the hearing aid feedback path that are assumed to stay relatively constant during use. When the hearing aid becomes unstable due to sudden changes, the parameters of a second adaptive filter are varied rapidly without a probe signal to provide instantaneous corrections to the feedback path model. The feedback model signal is subtracted from the hearing aid output signal to form a compensated audio output. The two filters are shown cascaded in various configurations with a short fixed delay.—DAP

6,068,589

43.66.Ts BIOCOMPATIBLE FULLY IMPLANTABLE HEARING AID TRANSDUCERS

Armand P. Neukermans, Palo Alto, California
30 May 2000 (Class 600/25); filed 14 February 1997

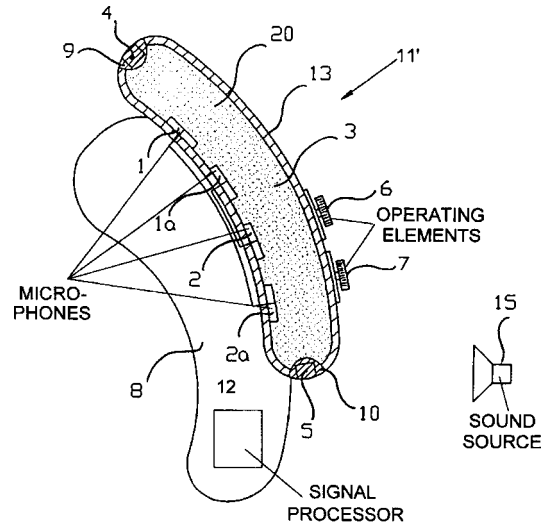
A phased array of at least two microphones, intended to reduce environmental noise, is implanted with a signal processor subcutaneously. The mechanical vibrations of a microactuator stimulate the inner ear fluid directly with a displacement in response to the applied electrical signal.—DAP

6,069,963

43.66.Ts HEARING AID WHEREIN THE DIRECTION OF INCOMING SOUND IS DETERMINED BY DIFFERENT TRANSIT TIMES TO MULTIPLE MICROPHONES IN A SOUND CHANNEL

Raimund Martin and Joseph Sauer, assignors to Siemens Audiologische Technik GmbH
30 May 2000 (Class 381/313); filed in Germany 30 August 1996

A directional hearing aid having at least two microphones in a sound channel is said to provide effective shielding from electromagnetic noise fields and improved protection against contaminants entering the sound in-



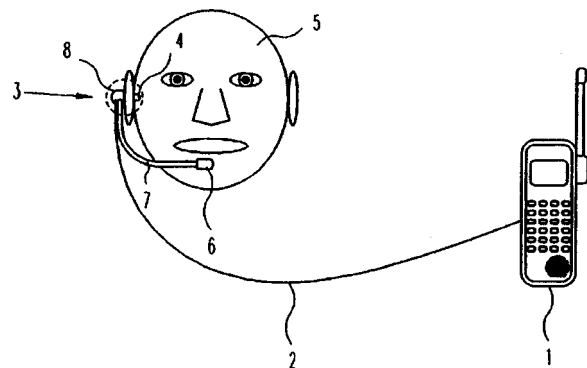
lets. To form a variable directional characteristic, the microphones may be interconnected in pairs, each of which operate over a selected portion of the audio frequency range.—DAP

6,078,675

43.66.Ts COMMUNICATION SYSTEM FOR USERS OF HEARING AIDS

Jan Bowen-Nielsen and Ole Winberg, assignors to GN Netcom A/S
20 June 2000 (Class 381/331); filed in Denmark 18 May 1995

A system is described for a hearing aid wearer to communicate with a mobile telephone located at a distance from the hearing aid. A headset with a microphone is coupled via a cable to a mobile telephone. The headset, which may have an added induction coil, is in close proximity to the hearing



aid for inductive coupling via tele-coil. Alternatively, a direct electrical coupling connection may be used between the hearing aid and headset. Both environmental noise and electromagnetic interference produced in the hearing aid are said to be reduced.—DAP

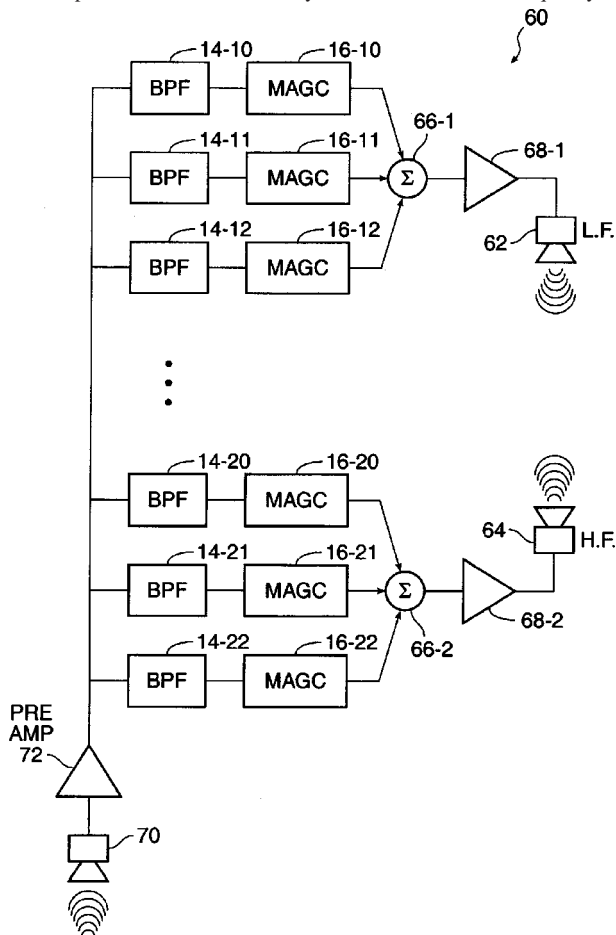
6,072,885

43.66.Ts HEARING AID DEVICE INCORPORATING SIGNAL PROCESSING TECHNIQUES

Thomas G. Stockham, Jr. *et al.*, assignors to Sonic Innovations, Incorporated

6 June 2000 (Class 381/321); filed 8 July 1994

A hearing aid signal processor is comprised of a bank of 12 to 15 bandpass filters, each associated with a separate AGC function. The AGC circuit outputs are summed and may be divided into low-frequency and



high-frequency processing channels. In one implementation, the output of the two summers drive two hearing aid receivers designed to have maximum efficiency at low and high frequencies, respectively.—DAP

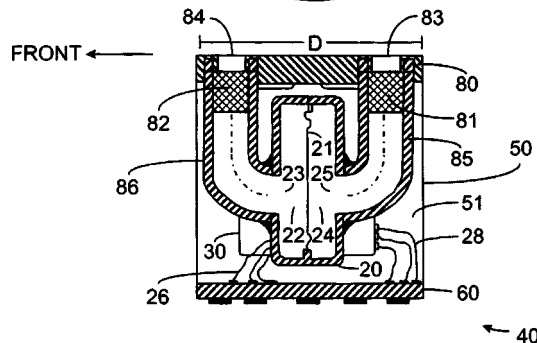
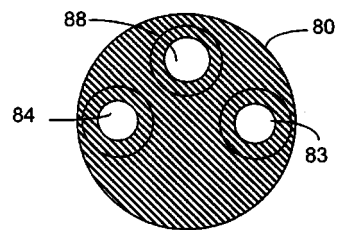
6,075,869

43.66.Ts DIRECTIONAL MICROPHONE ASSEMBLY

Mead C. Killion *et al.*, assignors to Etymotic Research, Incorporated

13 June 2000 (Class 381/313); filed 31 December 1996

A small microphone capsule for use in an in-the-ear hearing aid has two openings to form a directional system. The module contains both an omni-directional and a directional microphone element and has electronics and acoustical damping to provide omni-directional and directional operat-



ing modes in conjunction with a wearer-operated switch. An equalization network within the capsule produces the same sensitivity/frequency response from the microphone system in both operating modes.—DAP

6,038,533

43.72.Ar SYSTEM AND METHOD FOR SELECTING TRAINING TEXT

Adam Louis Buchsbaum and Jan Pieter VanSanten, assignors to Lucent Technologies, Incorporated

14 March 2000 (Class 704/260); filed 7 July 1995

The patent describes a technique for selecting specific utterances from a large database which meet chosen criteria for training a recognition system. A training feature system is, in the preferred embodiment, geared mainly for selecting utterances by prosodic characteristics. Other features can also be used. The system creates factor matrices which represent the makeup of the utterance database in a compressed format. A full-rank submatrix is formed from the union of factor matrices for the chosen divisions of the database. This allows a small number of utterances to be located which meet the desired training criteria.—DLR

6,041,296

43.72.Ar METHOD OF DERIVING CHARACTERISTICS VALUES FROM A SPEECH SIGNAL

Lutz Welling and Hermann Ney, assignors to U.S. Philips Corporation

21 March 2000 (Class 704/209); filed in Germany 23 April 1996

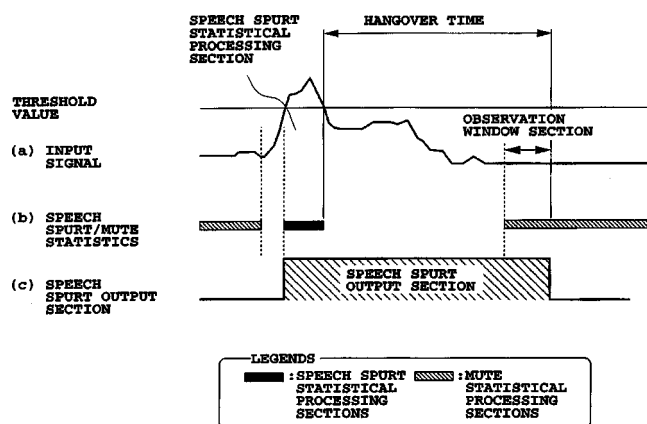
This is an automatic method of extracting formant frequency information from a database of speech segments. The resulting formant data could be used by either a recognition system or a formant synthesizer. Formants are extracted by segmenting in frequency a linear prediction spectrum, and then computing the first three autocorrelation coefficients from each spectral segment. Dynamic programming is used to find both the spectral segmentation and the time boundaries of speech segments suitable for synthesis.—DLR

6,044,342

43.72.Ar SPEECH SPURT DETECTING APPARATUS AND METHOD WITH THRESHOLD ADAPTED BY NOISE AND SPEECH STATISTICS

Nobuki Sato *et al.*, assignors to Logic Corporation
28 March 2000 (Class 704/233); filed in Japan 20 January 1997

This speech/nonspeech discriminator seems to use a fairly typical approach based on measurement of the energy variance during the detected speech and nonspeech intervals. A typical holdover time is allowed after a



speech interval, before the discriminator switches to a nonspeech determination.—DLR

6,044,345

43.72.Ar METHOD AND SYSTEM FOR CODING HUMAN SPEECH FOR SUBSEQUENT REPRODUCTION THEREOF

Raymond N. J. Veldhuis, assignor to U.S. Phillips Corporation
28 March 2000 (Class 704/261); filed in European Patent Office 18 April 1997

This speech coding system begins by extracting formant poles from a typical all-pole analysis. The residue remaining after formant extraction and lip radiation correction is used to fit to a Rosenberg or Liliancrats-Fant glottal pulse model, using a phase continuity constraint. The patent describes an efficient method of computing the fit to the glottal pulse model.—DLR

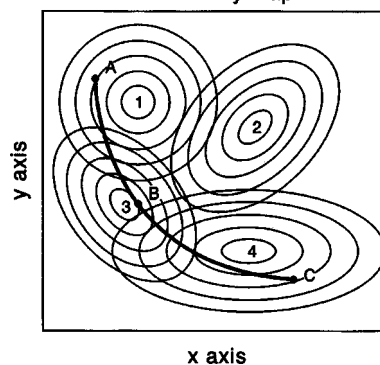
6,052,662

43.72.Ar SPEECH PROCESSING USING MAXIMUM LIKELIHOOD CONTINUITY MAPPING

John E. Hogden, assignor to Regents of the University of California
18 April 2000 (Class 704/256); filed 30 January 1997

The relationship between speech sounds and articulator (vocal tract) shapes is known to be a one-to-many mapping and, as such, has not been useful in recognition or other applications which could benefit from the

Continuity Map



articulator descriptions. This patent describes a method of generating sequences of pseudo-tract shapes based on a probabilistic model constrained by shape continuity measures. The figure shows a continuity map consisting of equiprobability ellipses around each of several symbols in an abstract n -dimensional pseudo-articulator space. The curve is a maximum-likelihood pathway from point A, through point B, to point C.—DLR

6,047,254

43.72.Ar SYSTEM AND METHOD FOR DETERMINING A FIRST FORMANT ANALYSIS FILTER AND PREFILTERING A SPEECH SIGNAL FOR IMPROVED PITCH ESTIMATION

Mark A. Ireton and John G. Bartkowiak, assignors to Advanced Micro Devices, Incorporated
4 April 2000 (Class 704/209); filed 15 May 1996

This voice pitch analyzer performs an initial order-2 linear prediction (LPC) analysis to determine an effective first formant frequency. Multiple short-window order-2 LPC analyses are performed within each speech frame. An F1 center frequency is chosen which minimizes the remaining frame energy. Following removal of that formant, an autocorrelation is done for selected delays to determine the pitch estimate value for the frame.—DLR

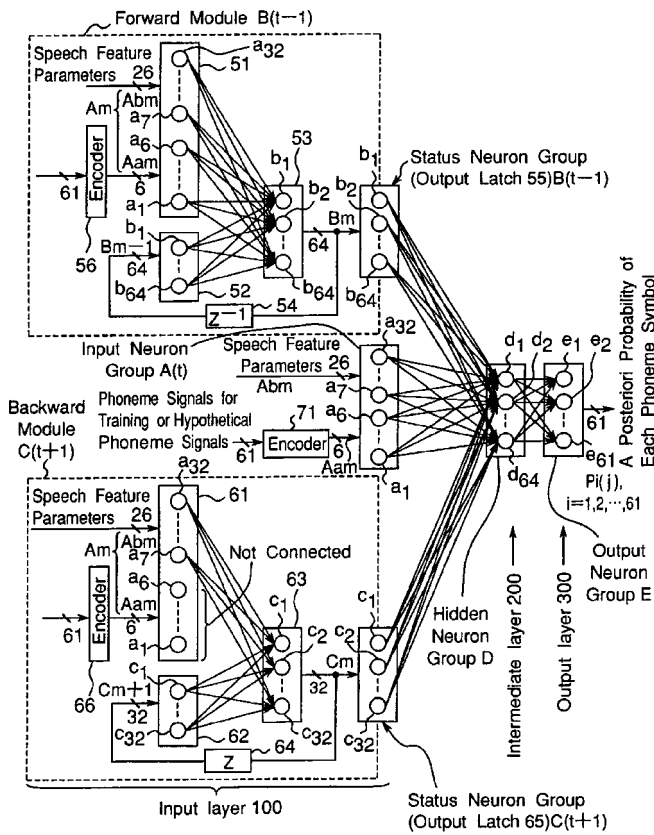
6,041,299

43.72.Bs APPARATUS FOR CALCULATING A POSTERIOR PROBABILITY OF PHONEME SYMBOL, AND SPEECH RECOGNITION APPARATUS

Mike Schuster and Toshiaki Fukada, assignors to ATR Interpreting Telecommunications Research Laboratories
21 March 2000 (Class 704/232); filed in Japan 11 March 1997

This speech recognizer training system accepts three sequential frames of mel cepstral feature data and a training phonemic code symbol corresponding to the middle feature vector. Each of the forward and backward feature vectors are applied to a recurrent neural network, which has extra input nodes fed by the previous state of the hidden layer. The outputs of the forward and backward networks, along with the middle frame vector data

First Preferred Embodiment
Phoneme-Symbol A Posteriori Probability
Calculating Neural Network 11



and the training phoneme symbol, are applied to the inputs of another neural network, a standard feedforward NN with a single hidden layer. The output is a set of *a posteriori* probability values, one for each of the phoneme symbols, given a particular set of three feature vectors.—DLR

5,828,755

43.72.Ew METHOD AND DEVICE FOR PROCESSING SIGNALS

Eric Edmond Feremans of Kortrijk, Belgium and Francis De Smet of Brugge, Belgium
27 October 1998 (Class 381/61); filed 28 March 1995

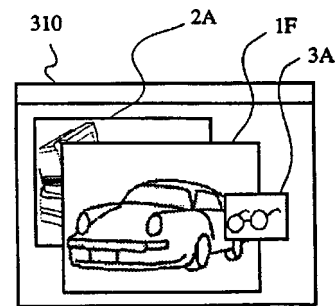
This device is described as a signal enhancer or noise reducer. The incoming signal is bandpass filtered to a range of roughly 3500 to 7000 Hz. A harmonic generator, which is not described, operates in some manner on the input signal and produces high-frequency harmonics above 7000 Hz. These are mixed back into the filtered signal. It is not clear what type of signals the device is intended for. The frequency pass band is clearly too high to be of interest for speech.—DLR

6,040,831

43.72.Ew APPARATUS FOR SPATIALLY CHANGING SOUND WITH DISPLAY LOCATION AND WINDOW SIZE

Shinsuke Nishida, assignor to Fourie, Incorporated
21 March 2000 (Class 345/340); filed in Japan 13 July 1995

This procedure offers a way to combine multiple sound tracks, each describing a particular object or image, such as in an Internet window presentation. An audio volume control is provided for each track so that each



component is mixed according to the current size of the display window and whether that window is on top of the display sequence or partially covered by another window. As the display is changed, the accompanying audio changes dynamically.—DLR

6,041,290

43.72.Ew METHOD OF ADAPTIVELY ADJUSTING THE COEFFICIENTS OF A DIGITAL FILTER IN AN ECHO CANCELLER

Hans Juergen Matt *et al.*, assignors to Alcatel
21 March 2000 (Class 702/191); filed in Germany 15 November 1996

The patent describes a fairly typical arrangement of an adaptive finite impulse response filter to the task of echo cancellation in a telephone system. Two such adaptive FIR filters are provided, one computing a compensating signal which is added to the outgoing line signal, the second compensates an internal feedback term which alters the microphone signal before it is presented to the first FIR filter.—DLR

6,044,147

43.72.Ew TELECOMMUNICATIONS SYSTEM

Michael Peter Hollier, assignor to British Telecommunications public limited company
28 March 2000 (Class 379/338); filed 16 May 1996

This voice processor for use in a communications system cleans up the signal by recognizing it as a speech signal and resynthesizing the recognized voice. The recognizer is a known hidden Markov model decoder, used as a large-vocabulary word recognizer. As each word is recognized, "a generic original-sound waveform can then be selected from memory." In a preferred embodiment, the recognizer is based on a vocal tract model, such that only valid vocal tract configurations are recognized. All other sounds are ignored by the system.—DLR

6,044,340

43.72.Ew ACCELERATED CONVOLUTION NOISE ELIMINATION

Hugo Van Hamme, assignor to Lernout & Hauspie Speech Products N.V.
28 March 2000 (Class 704/226); filed 21 February 1997

Additive noise components, such as background sounds, are relatively easy to remove from a speech signal using well-known methods such as adaptive filters or spectral subtraction. Convolution noise components, such as a microphone characteristic, are not removed by such methods. This

patent describes a method based on log-spectral filtering, which can remove such convolution noise components. The log power spectrum is smoothed according to convexity and cepstral band constraints, leaving a residue which represents the noise component in the log-power domain.—DLR

6,044,341

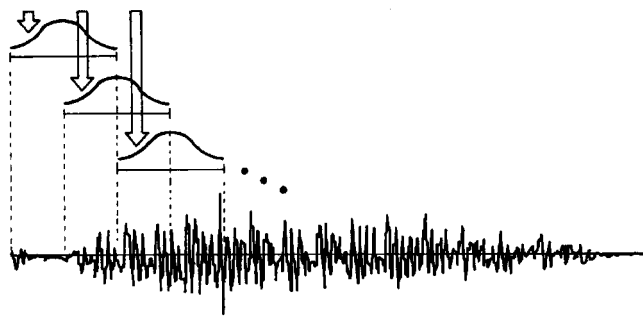
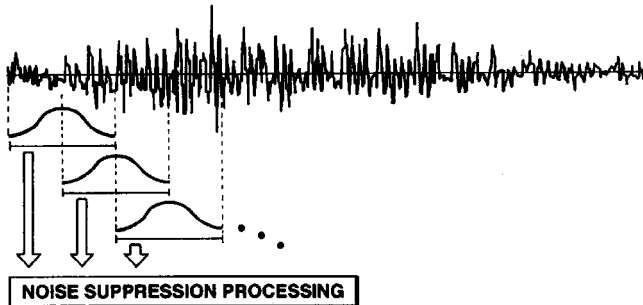
43.72.Ew NOISE SUPPRESSION APPARATUS AND RECORDING MEDIUM RECORDING PROCESSING PROGRAM FOR PERFORMING NOISE REMOVAL FROM VOICE

Hidetaka Takahashi, assignor to Olympus Optical Company Limited

28 March 2000 (Class 704/226); filed in Japan 16 July 1997

This speech noise reduction system performs a spectral subtraction based on an estimation of the noise component following a voicing determination of the input signal. The frame classification is described as

PROCESSING OBJECT SIGNAL



OUTPUT SIGNAL

“voice” versus “non-voice,” with the average of several non-voice frames being used to estimate the background noise. It is not clear how unvoiced speech frames are treated.—DLR

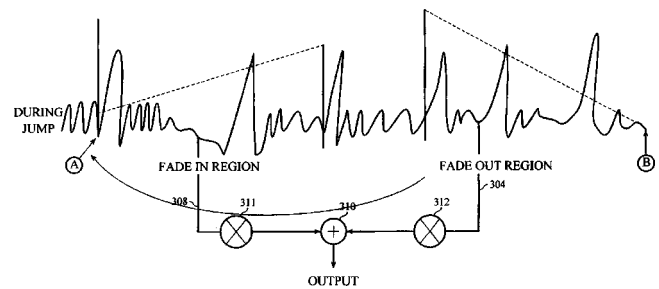
6,049,766

43.72.Ew TIME-DOMAIN TIME/PITCH SCALING OF SPEECH OR AUDIO SIGNALS WITH TRANSIENT HANDLING

Jean Laroche, assignor to Creative Technology Limited

11 April 2000 (Class 704/216); filed 7 November 1996

This speech rate/pitch modification system fragments the incoming speech signal and computes cross-correlations over certain limited ranges of delay values. A set of recombination heuristics takes into account the cur-



rent time discrepancy between the actual playback and the desired change, together with several measures of suitability for rejoining the fragments, including minimizing transients of periodicity or signal amplitude.—DLR

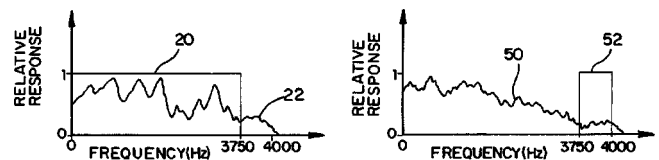
6,052,462

43.72.Gy DOUBLE TALK DETECTION AND ECHO CONTROL CIRCUIT

Youhong Lu, assignor to Tellabs Operations, Incorporated

18 April 2000 (Class 379/410); filed 10 July 1997

This is a typical echo canceller using an adaptive FIR error correction filter, with the novelty being in the method by which the adaptation is restricted to the incoming signal. Well-known methods typically involve detecting silent intervals in the near-end speech, during which the adaptor



may be run. In this device, the incoming line signal is filtered to remove the low band on which the outgoing signal is transmitted. This effectively isolates incoming and outgoing signals, allowing the adaptor to run continuously, but still see only the incoming signal.—DLR

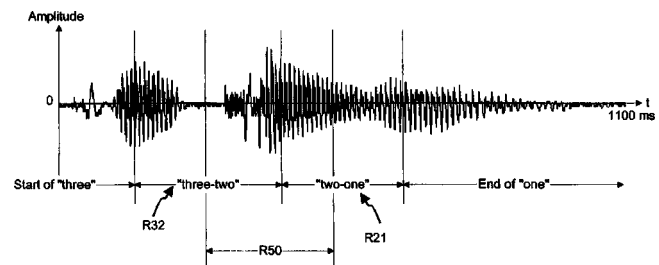
6,047,255

43.72.Ja METHOD AND SYSTEM FOR PRODUCING SPEECH SIGNALS

Robert Alan Williamson, assignor to Nortel Networks Corporation

4 April 2000 (Class 704/212); filed 4 December 1997

This voice response system, suitable for reproducing a small vocabulary, uses what might be called a “di-word” method. For each defined word, a central fragment is stored, along with a matrix of begin/end frag-



ments for each stored word pair. An utterance is constructed by rejoining word and begin/end fragments as required, resulting in a smooth, high-quality output signal.—DLR

6,049,604

43.72.Ja TELEPHONE DIALER HAVING AT LEAST ONE SPEECH SYNTHESIZER PROCESSOR

James Lin, assignor to Winbond Electronics Corporation
 11 April 2000 (Class 379/355); filed 23 June 1997

The device described here is a small, hand-held dialer unit, suitable for placement over a telephone mouthpiece and used to initiate a phone connection to one or more specific parties. Because some called parties may require a combination of DTMF tone pulses and specific spoken messages, the dialed unit integrates the two, and can reproduce any sequence of either DTMF tones or any audio signal, such as a voice message or a background music selection.—DLR

6,052,367

43.72.Ja CLIENT-SERVER SYSTEM

Ronald John Bowater et al., assignors to International Business Machines Corporation
 18 April 2000 (Class 370/352); filed in the United Kingdom 29 December 1995

This patent describes a voice response system (VRS) which may be attached to a world-wide web server in order to convert selected messages from visual display to voice message generation. A VRS database provides synthesis controls and vocabulary information as required for the synthesis. Generated voice packets are formatted in a way suitable for transmission to the web client system, where the voice messages will be played back by the client system.—DLR

6,038,535

43.72.Ne SPEECH CLASSIFIER AND METHOD USING DELAY ELEMENTS

William Michael Campbell, assignor to Motorola, Incorporated
 14 March 2000 (Class 704/275); filed 23 March 1998

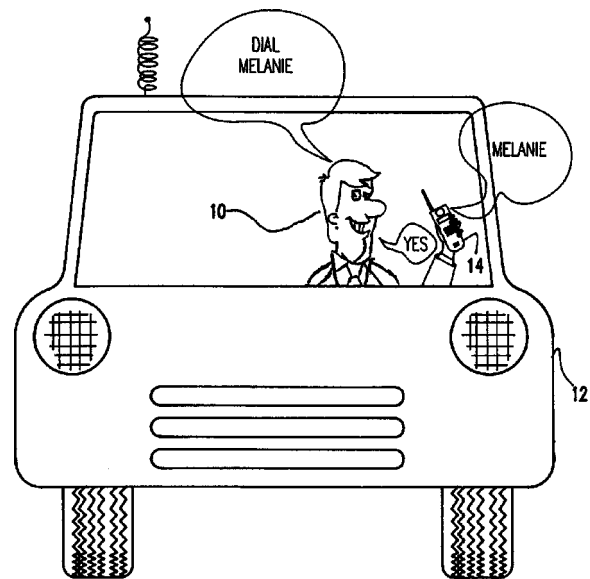
The introductory sections of this patent argue that, for most recognition systems, the training data is not adequately ordered. It is not clear whether the units to be ordered are feature vectors or utterances or some combination of these. It does not help that some terms are redefined. For example, a "class structure" is defined to mean a vector. The discussion then uses both terms, "vector" and "class structure." A series of delay elements is provided to help rearrange the order in which training items are processed. Acoustic feature elements are expanded using a polynomial expansion of up to fourth order.—DLR

6,041,300

43.72.Ne SYSTEM AND METHOD OF USING PRE-ENROLLED SPEECH SUB-UNITS FOR EFFICIENT SPEECH SYNTHESIS

Abraham Poovakunnel Ittycheriah and Stephane Herman Maes, assignors to International Business Machines Corporation
 21 March 2000 (Class 704/255); filed 21 March 1997

This hands-free voice dialer uses a well-known hidden-Markov-model-based Viterbi decoder arrangement to recognize input words as sequences of phonetic unit codes (here called "lefemes"). The lefeme string is compared to a small set of trained words corresponding to commands and names of parties to be dialed. The word database provides the ideal lefeme



string for the best-matching word, a lefeme time alignment value, and pitch, duration, and energy values. The lefeme database provides a speech waveform segment from which the recognized word may be resynthesized.—DLR

6,044,337

43.72.Ne SELECTION OF SUPERWORDS BASED ON CRITERIA RELEVANT TO BOTH SPEECH RECOGNITION AND UNDERSTANDING

Allen Louis Gorin et al., assignors to AT&T Corporation
 28 March 2000 (Class 704/1); filed 29 October 1997

The performance of this large-vocabulary speech recognizer is improved by scanning the training utterances for repeated word sequences, or phrases, referred to as "superwords." The superwords are then treated as separate vocabulary items. Overall recognition rate improves because overall vocabulary size is reduced, and the use of superwords essentially increases the overall constraints of sequential word probabilities.—DLR

6,044,343

43.72.Ne ADAPTIVE SPEECH RECOGNITION WITH SELECTIVE INPUT DATA TO A SPEECH CLASSIFIER

Lin Cong and Safdar M. Asghar, assignors to Advanced Micro Devices, Incorporated
 28 March 2000 (Class 704/236); filed 27 June 1997

This isolated-word speech recognition system begins with a typical linear prediction analysis, followed by extraction of line spectral pairs (LSPs). LSP coefficients are grouped by signal-to-noise ratio values and by time-sequential frames into a feature matrix. The feature matrices are quantized using a fuzzy classifier to assign weights to the matrix elements. The resulting matrix of weights is known as a fuzzy matrix quantizer (FMQ), and is used to drive a typical HMM-based Viterbi decoder.—DLR

6,047,256

43.72.Ne DEVICE FOR GENERATING A REFERENCE PATTERN WITH A CONTINUOUS PROBABILITY DENSITY FUNCTION DERIVED FROM FEATURE CODE OCCURRENCE PROBABILITY DISTRIBUTION

**Shinji Koga *et al.*, assignors to NEC Corporation
4 April 2000 (Class 704/256); filed in Japan 9 February 1988**

This speech recognizer training system seems to be a sort of brute-force hidden Markov model (HMM) generator. There is no specific mention of HMM techniques. What is described is a method for constructing a state transition network of probability distributions, where each distribution is represented by a Gaussian density function. Such a state transition model is generated for each word to be stored in the recognizer memory.—DLR

6,049,768

43.72.Ne SPEECH RECOGNITION SYSTEM WITH IMPLICIT CHECKSUM

**Randy G. Goldberg and John Bruce Harlow, assignors to AT&T Corporation
11 April 2000 (Class 704/273); filed 3 November 1997**

Access to customer information, such as banking records, has progressed from the efforts of a human operator, through DTMF tone entry, to current systems which allow voice entry of the account number or other such sequence. However, the accuracy of voice recognition leaves something to be desired. To solve this problem, the method described in this patent adds a checksum to the customer's spoken account number. When a possible account number has been identified, the checksum for that account is tested against the recognized checksum to verify correct access.—DLR

Effects of the speed of moving noise sources on the sound visualization by means of moving frame acoustic holography

Soon-Hong Park and Yang-Hann Kim^{a)}

Center for Noise and Vibration Control (NOVIC), Department of Mechanical Engineering,
Korea Advanced Institute of Science and Technology (KAIST), Science Town, Taejeon 305-701, Korea

(Received 18 May 1999; revised 25 August 2000; accepted 9 September 2000)

The moving frame acoustic holography (MFAH) method [H.-S. Kwon and Y.-H. Kim, J. Acoust. Soc. Am. **103**, 1734–1742 (1998)] enables the visualization of noise generated by moving noise sources, e.g., moving vehicles, by using a line array of microphones affixed to the ground. However, the sound field of a moving noise source has a *moving effect*, which produces the wavefront distribution different from what would be generated by the source if it were not moving. The moving effect causes errors on the reconstructed hologram by means of MFAH. This paper studies this effect with regard to the speed of noise sources. A formula, which can show the effect, was derived. This enables the analysis of the effect not only on the hologram plane but also on a prediction plane. It was shown that the phase error is more undesirable than that of magnitude. The phase error, which is proportional to the speed of a noise source, shifts the position of noise sources and distorts radiation pattern. A theoretical investigation explicitly showed that the error is negligible for low Mach number ($M < 0.1$). Furthermore, the phase error can be reduced by introducing a *correction factor*. Several numerical examples illustrate the feasibility of the proposed correction method for low Mach number. © 2000 Acoustical Society of America. [S0001-4966(00)02412-7]

PACS numbers: 43.20.-f, 43.35.Sx, 43.60.Sx [ANN]

I. INTRODUCTION

Acoustic holography provides all acoustic variables including sound pressure, particle velocity, acoustic intensity, and power. However, if we try to apply acoustic holography to the noise generated by moving noise sources, we must be able to measure the pressure on the moving plane affixed to the noise sources. This requires a very complex measurement system, e.g., a plane array of microphones, and therefore limits the practical applicability of acoustic holography to the case of moving noise sources. A line array of microphones standing on the ground is obviously more practical than a plane array of microphones affixed to moving noise sources.

References 1–10 are examples that use a line array of microphones standing on the ground. The main objective of these examples is to localize the noise sources of high-speed trains. However, these cannot provide practically valuable acoustic variables such as pressure and intensity distribution of the train noise under investigation. This is simply because they estimate a beamforming power on an assumed source plane. Recently proposed moving frame acoustic holography (MFAH)^{11,12} can overcome this drawback. The method uses a line array of microphones, which continuously sweeps a sound field and produces the hologram of the scanned plane. A practical implementation can be done by simply installing a line array of microphones on the ground. This method has enabled us to visualize the noise generated by moving sources based on acoustic holography.

The movement of a noise source induces a change of wavefront distribution of the radiated sound field. This can be readily understood by comparing the sound field of a

moving monopole and that of a stationary monopole. It is straightforward to realize that the wavefronts are closer together in the forward direction than they would be if the source were stationary. Therefore, the measured sound field by the microphone on the ground has an inherent error. The original radiation pattern and the position of the noise sources cannot be observed. We attempt to study this error and the way to reduce the error. The previous studies^{12–14} have not considered this kind of error explicitly.

A theoretical investigation is based on the assumption that we can express the sound field due to moving surface sources as a superposition of simple waves.^{15,16} This enables us to express the magnitude and the phase errors due to the *moving effect* on the hologram and the prediction plane explicitly. The analysis shows that the errors are mainly dependent on the speed of a noise source. It also assures the practical value of MFAH by showing that the errors are negligible if the speed of moving noise sources is much smaller than the speed of sound ($M < 0.1$). This paper also explains a way of reducing the phase error on a hologram and a predicted sound field. Several numerical examples demonstrate the feasibility of a proposed *correction method* with regard to the speed of noise sources.

II. EFFECTS OF MOVING NOISE SOURCES ON THE HOLOGRAM

A. Sound field generated by a moving surface source in terms of moving monopole distribution^{15,16}

We assume that the sound field generated by a moving surface satisfies the homogeneous wave equation since acoustic holography deals only with sound propagation. The moving surface source is assumed to be in rectilinear motion with low speed [$\mathbf{u}_h = (u, 0, 0)$], which is much less than the

^{a)}Electronic mail: yhkim@mail.kaist.ac.kr

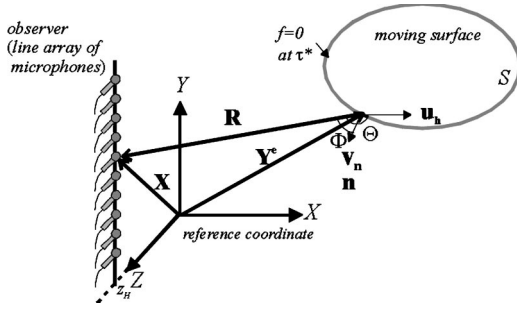


FIG. 1. Position vectors indicating source distribution on the surface S and an observer (a line array of microphones) in the reference coordinate. Note that the reference coordinate is affixed to the ground.

speed of sound. This assumption is reasonable because the major application field of MFAH is low-speed moving sources. We also assume that a line array of microphones (an observer) measures the acoustic pressure due to the moving surface source in the far field. Notice that, in most cases, the hologram of moving source by means of MFAH is allowed to be measured in the far field. Then, the sound field of a moving surface source can be modeled by the distribution of monopoles on the moving surface,^{15,16} that is

$$p(\mathbf{X}; t) = \int_S \frac{1}{4\pi R} \frac{q'(\mathbf{Y}^e; \tau)}{A^e} \Bigg|_{\tau=\tau^*} dS, \quad (1)$$

where $q'(\mathbf{Y}^e; \tau)$ denotes source strength on the surface S , τ represents the emission time (when a source emits sound), and t is the observation time (when an observer receives the sound). \mathbf{X} and \mathbf{Y}^e are the position vectors in the reference coordinate $[(X, Y, Z)]$ affixed to the ground, where superscript e means a variable at the emission time (see Fig. 1). $R \equiv |\mathbf{R}| = |\mathbf{X} - \mathbf{Y}^e|$ is the distance between the observer and the source at the emission time. Notice that S denotes the virtual radiating moving surface,¹⁵ which is described by $f(\mathbf{Y}^e; \tau^*) = 0$ ($\tau^* = t - R/c$) (Fig. 1). f is a function that describes the moving surface. $A^e = \sqrt{1 + M_n^2 - 2M_n \cos \Phi}$ is the amplitude modification factor due to the movement of the surface, where $M_n \equiv |\mathbf{v}_n|/c$ (\mathbf{v}_n is the surface normal velocity) is the local Mach number. Notice that \mathbf{v}_n is sum of velocities due to surface vibration and surface translation; Φ is the angle between \mathbf{R} and surface normal vector \mathbf{n} (Fig. 1). It is noteworthy that A^e modifies the strength of monopole on the surface so that the surface shape can be considered. For example, when the direction of propagation (\mathbf{R}) coincides with that of the surface normal vector (\mathbf{n}) ($\Phi = 0$), $1/A^e$ has a maximum value. When the direction of \mathbf{R} is opposite to \mathbf{n} ($\Phi = \pi$), $1/A^e$ has a minimum value. See Refs. 15 and 16 for the detailed derivation of Eq. (1).

A discrete form of Eq. (1) clearly expresses the distribution of monopoles on the moving surface S . If one discretizes Eq. (1), then one can obtain

$$p(X=0, Y, Z=z_H; t) = \sum_l \frac{1}{4\pi R_l} \frac{q_l(\tau)}{A_l^e} \Bigg|_{\tau=\tau^*}, \quad (2)$$

where $q_l(\tau) \equiv q'(\mathbf{Y}_l^e, \tau) dS$ denotes the strength of monopole on the surface. Subscript l is introduced to denote infinite monopoles on the surface

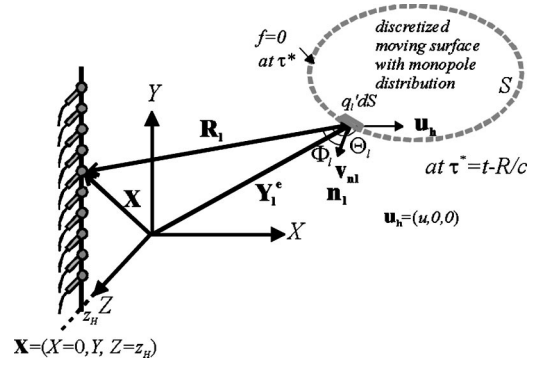


FIG. 2. Source distribution on the surface S can be regarded as the infinite number of distributed moving monopoles. The figure shows position vectors of distributed monopole sources and a line array of microphones in the reference coordinate at the emission time. The monopole sources move along with positive X axis with $\mathbf{u}_h = (u, 0, 0)$. Note that the line array of microphones standing at $X=0, Z=z_H$.

$$\left(\sum_l \equiv \sum_{l=0}^{\infty} \right).$$

In Eq. (2), we assume that a stationary line array of microphones at $\mathbf{X} = (X=0, Y, Z=z_H)$ measures the sound. $R_l \equiv |\mathbf{R}_l| = |\mathbf{X} - \mathbf{Y}_l^e|$ and $A_l^e = \sqrt{1 + M_{nl}^2 - 2M_{nl} \cos \Phi_l}$, where M_{nl} is the local Mach number at the position of the l th monopole and Φ_l is the angle between \mathbf{R}_l and surface normal vector \mathbf{n}_l at the position of the l th monopole (see Fig. 2). When the velocity due to the surface vibration is much smaller than that due to the surface translation, $M_{nl} = M \cos(\Theta_l - \Phi_l)$ can be assumed, where $M = u/c$ and Θ_l is the angle between \mathbf{u}_h and \mathbf{R}_l (Fig. 2).

In practice, when the source emits sound, the relative position between the noise source and the line array cannot be observed. It must be observed when the line array receives the emitted sound (at the observation time). Therefore, it is reasonable to rewrite the measured pressure [Eq. (3)] in terms of variables at the observation time (see Fig. 3); that is

$$p(X=0, Y, Z=z_H; t) = \sum_l \frac{1}{4\pi r_l A_l^o} q_l \left(t - \frac{r_l \{M \cos \theta_l + \sqrt{1 - M^2 \sin^2 \theta_l}\}}{c(1 - M^2)} \right). \quad (3)$$

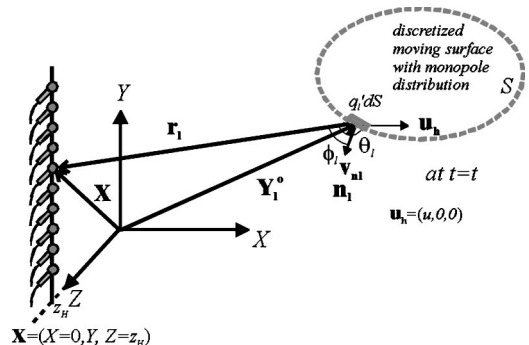


FIG. 3. Position vectors of distributed monopole sources and a line array of microphones in the reference coordinate at the observation time.

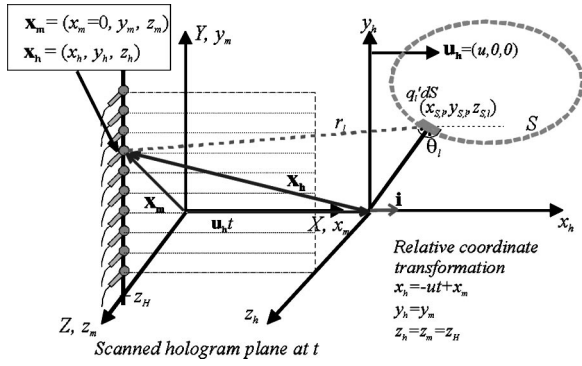


FIG. 4. Three coordinate systems used in MFAH (reference coordinate, hologram coordinate that moves with the noise source, and measurement coordinate that is fixed to the line array of microphone). Relative coordinate transformation enables us to transform the pressure on the measurement coordinate [at $(x_m=0, y_m, z_m=z_H)$] into the pressure on the hologram coordinate [at $(x_h=-ut+x_m, y_h=y_m, z_h=z_H)$]. Position vectors on the obtained hologram are also shown.

Since the speed of noise source is much smaller than the speed of sound ($M \ll 1$), Eq. (3) can be approximated as

$$p(X=0, Y, Z=z_H; t) = \sum_l \frac{1}{4\pi r_l A_l^o} q_l \left(t - \frac{r_l}{c} (1 + M \cos \theta_l) \right) \quad (M \ll 1). \quad (4)$$

The detailed derivation of the argument q_l can be found in Appendix A. Note that $r_l \equiv |\mathbf{r}_l| = |\mathbf{X} - \mathbf{Y}_l^o|$ denotes the distance between a microphone of the line array and the l th monopole on the source surface at the observation time (Fig. 3). The superscript o denotes a variable at the observation time (Fig. 3). θ_l denotes the angle between the velocity vector (\mathbf{u}_h) and \mathbf{r}_l (Fig. 3). Amplitude modification factor can be written as

$$A_l^o \cong 1 + M(\cos \theta_l - \alpha_l \cos \phi_l) \quad (M \ll 1), \quad (5)$$

where ϕ_l is the angle between \mathbf{r}_l and surface normal vector \mathbf{n}_l at the position of the l th monopole and $\alpha_l \equiv \cos(\theta_l - \phi_l)$. (See Appendix B for the detailed derivation of A_l^o for $M \ll 1$.)

If the noise source emits a sound field of frequency f_{h0} [this means $q_l(t) = q_l e^{-i2\pi f_{h0}t}$], Eq. (4) can be further simplified as

$$p(X=0, Y, Z=z_H; t) = \sum_l \frac{q_l}{4\pi r_l A_l^o} \cdot e^{-i2\pi f_{h0}t + ikr_l(1+M \cos \theta_l)} \quad (M \ll 1), \quad (6)$$

where $k = 2\pi f_{h0}/c$.

B. Hologram by means of MFAH

MFAH uses three coordinate systems to describe the relative motion between a noise source and a line array of microphones,^{11,12} (see Fig. 4): The reference coordinate $[(X, Y, Z)]$ is always fixed to the ground. The measurement coordinate $[(x_m, y_m, z_m)]$ is fixed to a line array of microphones and moves with the velocity \mathbf{u}_m . The hologram co-

ordinate $[(x_h, y_h, z_h)]$, fixed to a noise source, moves with the velocity \mathbf{u}_h . The two coordinates move in parallel and their relative velocity is $\mathbf{u}_{m/h} = \mathbf{u}_m - \mathbf{u}_h$.

If we make a line array of microphones fixed to the ground, then this is the case in which the measurement coordinate does not move. This means that the velocity of the measurement coordinate, \mathbf{u}_m , is $(0, 0, 0)$. Without the loss of generality, we can assume that the measurement coordinate coincides with the reference coordinate. When a noise source moves, the hologram coordinate $[(x_h, y_h, z_h)]$ also moves with the velocity \mathbf{u}_h , which is $(u, 0, 0)$. Note that origins of the hologram coordinate and the two fixed coordinates coincide at $t=0$. Since the reference coordinate $[(X, Y, Z)]$ always coincides with the measurement coordinate $[(x_m, y_m, z_m)]$, we can denote $p(X, Y, Z; t) = p_m(x_m, y_m, z_m; t)$, where p_m is the pressure on the measurement coordinate. Then, Eq. (6) can be expressed in the measurement coordinate as

$$p(x_m=0, y_m, z_m=z_H; t) = \sum_l \frac{q_l}{4\pi r_l A_l^o} \cdot e^{ikr_l(1+M \cos \theta_l)} e^{-i2\pi f_{h0}t} \quad (M \ll 1). \quad (7)$$

MFAH enables us to obtain the sound field on the hologram coordinate $[p_h(x_h, y_h, z_h; t)]$, where p_h means the pressure on the hologram coordinate] by using the relative coordinate transformation,^{11,12} that is

$$x_h = u_{m/h}t + x_m, \quad y_h = y_m, \quad z_h = z_m, \quad (8)$$

where $u_{m/h} = u_m - u_h = -u$. Then, the sound pressure measured by a microphone whose location is $(x_m=0, y_m, z_m=z_H)$ can be transformed into the sound pressure observed on the hologram coordinate. The location is $(x_h = u_{m/h}t, y_h = y_m, z_h = z_H)$ (see Fig. 4). If we perform this procedure for all microphones of the line array, the sound field on the hologram coordinate can be obtained by^{11,12}

$$p_h(u_{m/h}t, y_h, z_H; t) = p_m(0, y_m, z_H; t). \quad (9)$$

Then, Eqs. (7) and (9) lead us to

$$p_h(u_{m/h}t, y_h, z_H; t) = \sum_l \frac{q_l}{4\pi r_l A_l^o} \cdot e^{ikr_l(1+M \cos \theta_l)} e^{-i2\pi f_{h0}t} = P_h(x_h, y_h, z_H; f_{h0}) e^{-i2\pi f_{h0}t} \quad (M \ll 1), \quad (10)$$

where

$$P_h(x_h, y_h, z_H; f_{h0}) = \sum_l \frac{q_l}{4\pi r_l A_l^o} \cdot e^{ikr_l(1+M \cos \theta_l)} \quad (11)$$

is the hologram of the moving source. Notice that this can be readily obtained from the complex envelope of the measured signal¹² as well (see Appendix C for the detailed explanation). $r_l = [(x_h - x_{s,l})^2 + (y_h - y_{s,l})^2 + (z_H - z_{s,l})^2]^{1/2}$ represents the distance between the location of the l th monopole source $[(x_{s,l}, y_{s,l}, z_{s,l})]$ and a point on the hologram $[(x_h, y_h, z_H)]$, where $x_h = u_{m/h}t$. θ_l denotes the angle between r_l and the x_h axis (see Fig. 4).

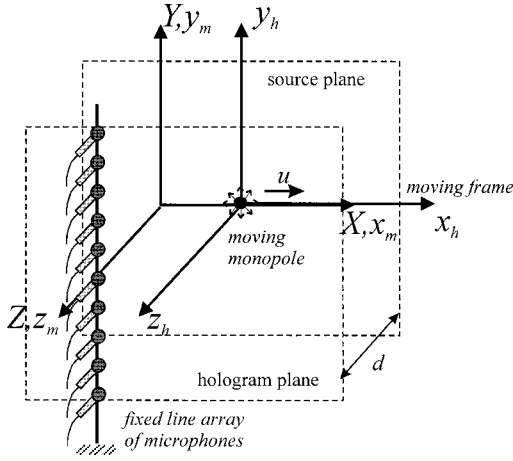


FIG. 5. Simulation configuration for Figs. 6, 7, and 8. We assumed a line array of microphones affixed to the ground. We used a moving monopole (Figs. 6 and 7) and an x -directional moving dipole (Fig. 8). The velocities of the moving monopole and the x -directional moving dipole are 0.1 and 0.2 in Mach number, respectively.

The errors on the hologram [Eq. (11)] can be readily interpreted if the true hologram of the noise source is introduced. We define the true hologram as a sound-pressure distribution that will be radiated from the nonmoving noise source. If we denote the true hologram by $P_h^{\text{true}}(x_h, y_h, z_h; f_{h0})$, it can then be expressed as

$$P_h^{\text{true}}(x_h, y_h, z_H; f_{h0}) = \sum_l \frac{q_l}{4\pi r_l} e^{ikr_l} = \sum_l P_{h,l}^{\text{true}}(x_h, y_h, z_H; f_{h0}) \quad (12)$$

on the hologram coordinate, where $P_{h,l}^{\text{true}}(x_h, y_h, z_H; f_{h0}) = q_l e^{ikr_l}/4\pi r_l$ (for $l=0,1,2,\dots$) denotes the true hologram of l th monopole. It is noteworthy that Eq. (11) at $M=0$ reduces to the true hologram.

Equations (11) and (12) show the effect of a moving noise source on a hologram explicitly,

$$P_h(x_h, y_h, z_H; f_{h0}) = \sum_l \frac{1}{A_l^o} \cdot e^{iMkr_l \cos \theta_l} P_{h,l}^{\text{true}}(x_h, y_h, z_H; f_{h0}) = \sum_l (1 + ME_l^o(x_h, y_h, z_H)) \cdot e^{iMk(x_h - x_{S,l})} P_{h,l}^{\text{true}}(x_h, y_h, z_H; f_{h0}) = \sum_l [1 + M(-ikx_{S,l} + E_l^o(x_h, y_h, z_H))] \times e^{iMkx_h} P_{h,l}^{\text{true}}(x_h, y_h, z_H; f_{h0}) \quad (M \ll 1), \quad (13)$$

where $1/A_l^o \cong 1 + M(\cos(\theta_l - \phi_l)\cos\phi_l - \cos\theta_l) \cong 1 + ME_l^o(x_h, y_h, z_H)$ [see Appendix D for a detailed explanation of $E_l^o(x_h, y_h, z_H)$] and $\cos\theta_l = \mathbf{i} \cdot \mathbf{r}_l / |\mathbf{i}| |\mathbf{r}_l| = (x_h - x_{S,l})/r_l$. Recall that $x_{S,l}$ denotes the location of the l th monopole on the hologram coordinate (see Fig. 4 again) and $e^{-iMkx_{S,l}}$ is a constant. A Taylor series expansion of $e^{-iMkx_{S,l}} = 1 - iMkx_{S,l} + \dots$

$-iMkx_{S,l} + \dots$ is used to derive the third equality of Eq. (13). This equation states that the resulting errors on the hologram can be obtained by the superposition of errors of each monopole. The magnitude and the phase error of each monopole can be represented by $ME_l^o(x_h, y_h, z_H)$ and $e^{iMkx_h} \times e^{-iMkx_{S,l}}$ terms [see the second equality of Eq. (13)]. This clearly states that errors are proportional to Mach number.

The errors on the hologram can be determined exactly if distribution of the moving monopoles and the shape of the surface can be specified. In this paper, we do not deal with the way to distribute the monopoles to duplicate the sound field of a moving source. Recall that our objective is to investigate the order of the errors on both a hologram and a predicted plane in order to justify the use of MFAH for low-speed moving sources. The influence of the errors on a predicted sound field is discussed in the next section.

III. EFFECTS ON A PREDICTED SOUND FIELD AND A METHOD OF REDUCTION OF THE PHASE ERROR

The errors expressed in the wave number domain could provide an easier way to understand. The two-dimensional spatial Fourier transform of Eq. (13) leads us to

$$F_{XY}\{P_h(x_h, y_h, z_H; f_{h0})\} = \sum_l F_{XY}\{1 + M(-ikx_{S,l} + E_l^o(x_h, y_h, z_H))\} ** F_{XY}\{e^{iMkx_h} P_{h,l}^{\text{true}}(x_h, y_h, z_H; f_{h0})\} \quad (M \ll 1), \quad (14)$$

where F_{XY} and $**$ denote the two-dimensional spatial Fourier transform and two dimensional convolution (see Appendix E for the definition of the spatial Fourier transform). If we denote a wave number spectrum by \hat{P} , Eq. (14) can be written as

$$\hat{P}_h(k_x, k_y, z_H; f_{h0}) = \sum_l \hat{P}_{h,l}^{\text{true}}(k_x - Mk, k_y, z_H; f_{h0}) + M \sum_l \{-ikx_{S,l} + \hat{E}_l^o(k_x, k_y, z_H)\} ** \hat{P}_{h,l}^{\text{true}}(k_x - Mk, k_y, z_H; f_{h0}), \quad (15)$$

by using the shifting property of the Fourier transform. This equation expresses the relation between the wave number spectrum due to the moving noise source (\hat{P}_h) and the true wave number spectrum of each monopole ($\hat{P}_{h,l}^{\text{true}}$). Equation (15) has two terms: the first term, which has order of 1, is more significant than the second term, which has order of M . The second term is small enough to be neglected when $M \ll 1$. However, it is noteworthy that all true wave number spectra of the monopole ($\hat{P}_{h,l}^{\text{true}}, l=0,1,2,\dots$) of the first term of Eq. (15) are shifted by the x -directional wave number, Mk , simultaneously. This is due to the phase error e^{iMkx_h} on the hologram.

We can estimate the wave number spectrum on a prediction plane by multiplying Eq. (15) by the kernel (or propagator) $\hat{g}(k_x, k_y, z - z_H) = e^{ik_z(z - z_H)}$ (where $k_z = \sqrt{k^2 - k_x^2 - k_y^2}$); that is,

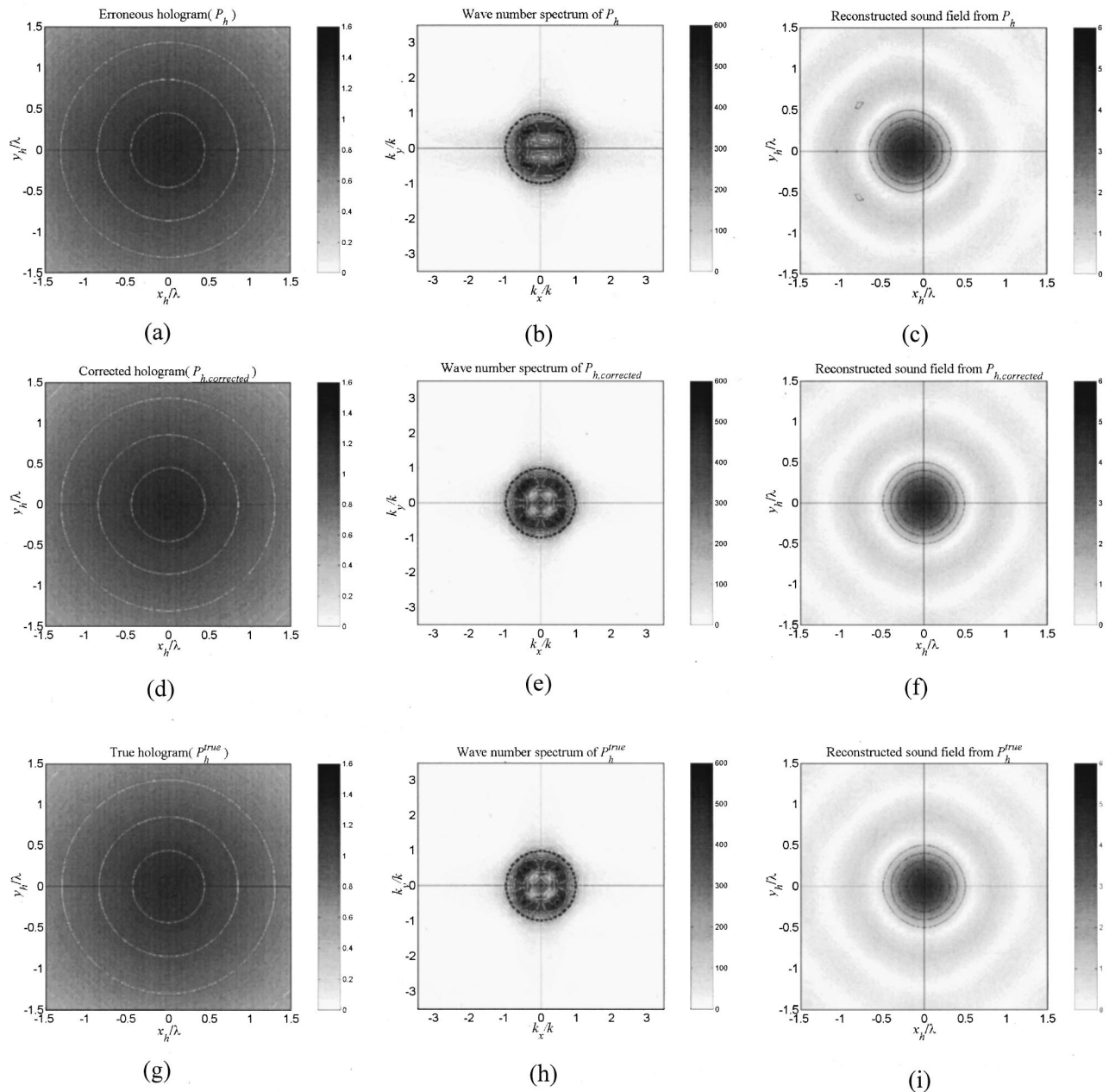


FIG. 6. The reconstructed sound fields of a moving monopole by means of MFAH and their comparison with corrected and true ones. The distance between the hologram and source plane was λ . Note that all figures are magnitude plots. (a) Erroneous hologram. (b) Wave number spectrum of the erroneous hologram. (c) Reconstructed sound field on the source plane from the erroneous hologram. (d) Corrected hologram. (e) Wave number spectrum of the corrected hologram. (f) Reconstructed sound field on the source plane from the corrected hologram. (g) True hologram. (h) Wave number spectrum of the true hologram. (i) True sound field on the source plane.

$$\begin{aligned}
 \hat{P}_h(k_x, k_y, z_p; f_{h0}) &= \hat{P}_h(k_x, k_y, z_H; f_{h0}) e^{ik_z(z_p - z_H)} \\
 &= \sum_l \hat{P}_{h,l}^{\text{true}}(k_x - Mk, k_y, z_H; f_{h0}) e^{ik_z(z_p - z_H)} \\
 &\quad + M \sum_l \{ [-ik_{x,l} + \hat{E}_l^o(k_x, k_y, z_H)] \\
 &\quad * \hat{P}_{h,l}^{\text{true}}(k_x - Mk, k_y, z_H; f_{h0}) \} \\
 &\quad \times e^{ik_z(z_p - z_H)} \quad (M \ll 1), \quad (16)
 \end{aligned}$$

where $z = z_p$ denotes the prediction plane. The two-dimensional inverse spatial Fourier transform of Eq. (16)

leads us to the sound field on the prediction plane. It is noteworthy that the error tends to be zero when $M \rightarrow 0$. Equation (16) enables us to identify the effect of moving noise sources on the predicted sound field. The phase error on the hologram gives more undesirable effects than the magnitude error on the predicted sound field. It comes from the shift of wave number spectrum $[\hat{P}_{h,l}^{\text{true}}(k_x - Mk, k_y, z_H; f_{h0})]$. Recall that a wave number spectrum expresses the distribution of plane waves that makes the sound field. The shifted wave number spectrum means the change of the distribution of plane waves. Thus, this will produce a distorted image that is different from what would be obtained if the source were sta-

tionary. Notice that a change of the wave number inside the radiation circle (propagating waves) normalized by its own one (Mk/k_x) is larger than that outside the radiation circle (evanescent waves). This means that the far-field measurement will produce more erroneous results than the near-field one. Only propagating wave components can be measured in the far field.

However, the error due to the shifted wave number spectrum can be corrected by introducing a correction factor e^{-iMkx_h} . This can be readily obtained in practice if the speed of noise source can be measured. The correction can be done by simply multiplying e^{-iMkx_h} to the obtained hologram [Eq. (13)]. The corrected wave number spectrum on the prediction plane can be written as [compare this with Eq. (16)]

$$\begin{aligned} \hat{P}_{h,\text{corrected}}(k_x, k_y, z_p; f_{h0}) &= \sum_l \hat{P}_{h,l}^{\text{true}}(k_x, k_y, z_H; f_{h0}) e^{ik_z(z_p - z_H)} \\ &\quad + M \sum_l [\{-ikx_{S,l} + \hat{E}_l^o(k_x, k_y, z_H)\} \\ &\quad * * \hat{P}_{h,l}^{\text{true}}(k_x, k_y, z_H; f_{h0})] e^{ik_z(z_p - z_H)} \quad (M \ll 1). \end{aligned} \quad (17)$$

Notice that we can recover the true wave number spectrum. Then, the corrected sound field on the prediction plane can be obtained by taking the two-dimensional inverse spatial Fourier transform; that is,

$$\begin{aligned} P_{h,\text{corrected}}(x_h, y_h, z_p; f_{h0}) &= P_h^{\text{true}}(x_h, y_h, z_p; f_{h0}) + M \sum_l \int_{-\infty}^{\infty} \int_{-\infty}^{\infty} [\{-ikx_{S,l} \\ &\quad + \hat{E}_l^o(k_x, k_y, z_H)\} * * \hat{P}_{h,l}^{\text{true}}(k_x, k_y, z_H; f_{h0})] e^{ik_z(z_p - z_H)} \\ &\quad \times e^{i(k_x x_h + k_y y_h)} dk_x dk_y \quad (M \ll 1) \end{aligned} \quad (18)$$

where

$$\begin{aligned} P_h^{\text{true}}(x_h, y_h, z_p; f_{h0}) &= \sum_l P_{h,l}^{\text{true}}(x_h, y_h, z_p; f_{h0}) \\ &= \sum_l \int_{-\infty}^{\infty} \int_{-\infty}^{\infty} \hat{P}_{h,l}^{\text{true}}(k_x, k_y, z_H; f_{h0}) \\ &\quad \times e^{ik_z(z_p - z_H)} e^{i(k_x x_h + k_y y_h)} dk_x dk_y \end{aligned} \quad (19)$$

denotes the true sound field on the prediction plane. Equation (18) clearly expresses that the errors on the prediction plane are proportional to the speed of the moving noise source. Notice that the errors can be neglected when $M \ll 1$. This justifies the use of MFAH to the low-speed moving noise sources.

IV. NUMERICAL EXAMPLES

Next, we illustrate the effect of simple moving noise sources on a hologram and a prediction plane by means of a numerical simulation. We assumed that a monopole source, which is located at the origin of the hologram coordinate, moves along with the positive X direction (see Fig. 5). Although a moving monopole is the simplest of moving noise

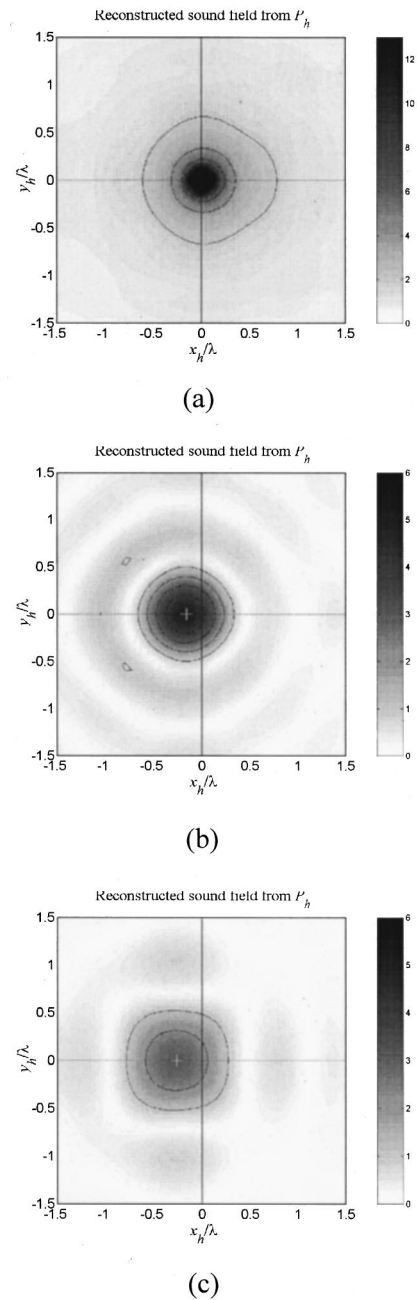


FIG. 7. The effect of distance between the source plane and the hologram plane (d) on the reconstructed sound field on the source plane. All figures are magnitude plots. Layout is the same as Fig. 6. “+” denotes the reconstructed source location. The further away from the source we measure the hologram, the greater the error. (a) $d=0.1 \lambda$. (b) $d=\lambda$. (c) $d=2 \lambda$.

sources, this demonstrates well the effect of the speed of moving sources. Remember that the distribution of moving monopoles expresses a general moving surface source. Note that in the case of moving monopole, the magnitude modification factor is $A_l^o = \sqrt{1 - M^2 \sin^2 \theta_l}$ ($l=0$),¹⁷ therefore, $E_l^o(x_h, y_h, z_H) = M \sin^2 \theta_l / 2$, which can be neglected for $M \ll 1$. The speed of monopole (u) is 123 km/h ($M=0.1$) and its frequency is 450 Hz. We assumed that a fixed line array of microphones measured the radiated sound field (see Fig. 5).

The shortest distance between the line array of microphones and the monopole (d , see Fig. 5) was λ (far-field

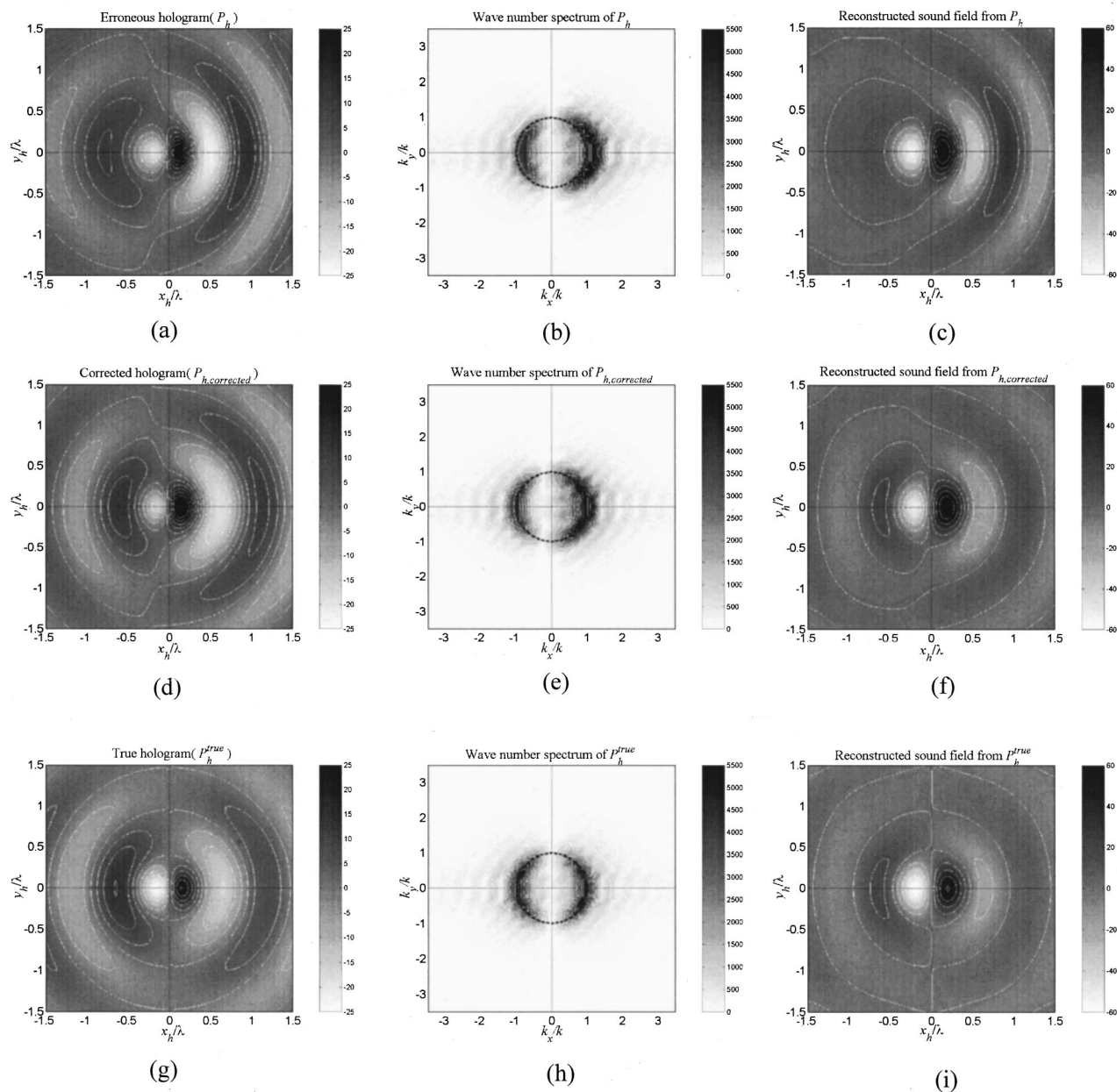


FIG. 8. The reconstructed sound fields of an x -directional dipole by means of MFAH and their comparison with corrected and true ones. The distance between the hologram and source plane was 0.2λ (near-field measurement). (a) Real part of erroneous hologram (magnitude). (b) Wave number spectrum of the erroneous hologram. (c) Real part of reconstructed sound field on the source plane from the erroneous hologram. (d) Real part of corrected hologram. (e) Wave number spectrum of the corrected hologram (magnitude). (f) Real part of reconstructed sound field on the source plane from the corrected hologram. (g) Real part of true hologram. (h) Wave number spectrum of the true hologram (magnitude). (i) Real part of true sound field on the source plane.

measurement). Figures 6(a), (b), and (c) illustrate the magnitudes of the erroneous hologram, corresponding wave number spectrum, and the magnitude of the predicted sound field on the source plane ($z_h=0$). Figure 6(b) shows that the positive shift of the wave number (Mk) increases the intensity of the negative x -directional wave number (k_x) components inside the radiation circle (dotted circle). This makes the radiation pattern of the predicted sound field different from what it would be if $M=0$. Notice that this is the reason why we observe the delay of the source location (about 0.1λ) [Fig. 6(c)]. The corrected ones [Figs. 6(d), (e), and (f)] can be obtained by multiplying e^{-iMkx_h} to the erroneous hologram. Recall that this is possible in practice whenever we can measure the velocity of noise sources. Figure 6(e) demonstrates

that the correction method recovers the true wave number spectrum well [Fig. 6(h)]. The predicted sound field [Fig. 6(f)] also shows a good agreement with the true one [Fig. 6(i)].

As previously discussed, if one measures the pressure away from the source then it produces more erroneous results. The further away from the source, the greater the error. Figure 7 illustrates this. We assumed that the distance between the hologram and the noise source (d) is 0.1λ (near-field measurement), λ (far-field measurement), and 2λ (far-field measurement). The measurement configuration is the same as that of Fig. 6. The results show the predicted sound fields when we do not apply the phase correction method.

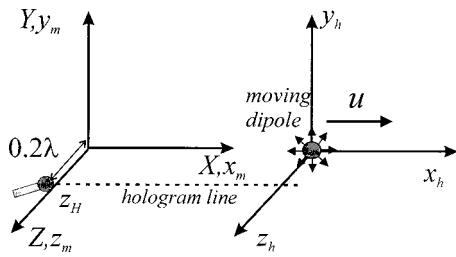


FIG. 9. Simulation configuration for Fig. 10. We used an x -directional dipole moving along with positive X direction. A microphone reconstructs a pressure field on the swept line, which we call the line hologram. The distance between the line hologram and the noise source was 0.2λ (near-field measurement).

Notice that the further away from the source we measure the hologram, the greater the error.

A moving dipole field case would also be of interest to study. We used an x -directional moving dipole located at the origin of the hologram coordinate. The distance between the hologram and the noise source (d) is 0.2λ (the near-field measurement). We assumed the speed of dipole (u) to be 246 km/h ($M=0.2$) to see the effect of speed higher than the previous examples. Remember that the error can be ignored when the speed is $M=0.1$ (Fig. 6). Instead of plotting the magnitude of the sound field, we plot the real part of the sound field to observe the radiation pattern of the dipole. Figures 8(a), (b), and (c) demonstrate that the effect of source motion cannot be neglected. The pressure in the forward direction is much higher than in the backward direction due to the source motion. The proposed phase correction method improves the results [see Figs. 8(d), (e), and (f)].

Compare these with the true ones [Figs. 8(g), (h), and (i)].

We also investigate the errors according to the velocity of a noise source. We use an x -directional dipole source. We assumed that the dipole moves along with the positive X direction and a microphone measures the sound pressure (Fig. 9). Figures 10(a), (b), and (c) show erroneous results according to velocities. The velocities are 0.05, 0.1, 0.2, and 0.3 in Mach number, respectively. Figure 10(a) shows the real parts of sound fields on a hologram line. Figure 10(b) shows the corresponding wave number spectra. The faster noise the sources, the more wave number spectra shift. The real parts of pressure in the prediction line are shown in Fig. 10(c). These illustrate that the errors on the hologram become significant as the velocity of the noise source increases. Notice that the error cannot be ignored when $M \geq 0.2$. However, Figs. 10(d), (e), and (f) demonstrate that the error can be reduced by introducing the proposed correction method. The correction method improves the hologram and the predicted sound field. The shift of wave number spectra [Fig. 10(e)] is reduced, so that desirable results in the source line [Fig. 10(f)] can be obtained. Figure 10(f) shows the correction method improves the erroneous result very well for $M \leq 0.1$.

V. CONCLUSIONS

The effects of moving noise sources on sound visualization by means of MFAH were investigated. Several new findings were obtained. First, we found that the errors due to source motion on a hologram are only dependent on the velocity of noise sources. Second, the phase error is more sig-

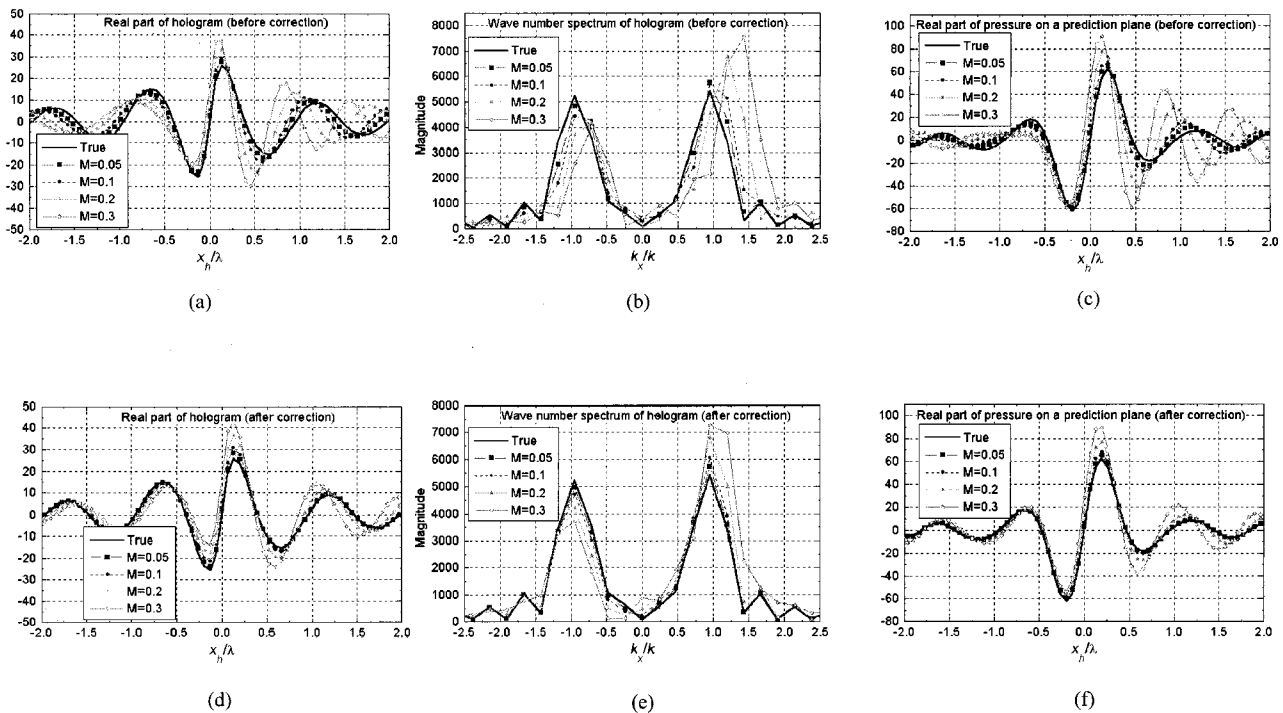


FIG. 10. Erroneous and corrected pressures on hologram line and a source line according to the velocity of noise sources. The velocities are 0.05, 0.1, 0.2, and 0.3 in Mach number. (a) Real part of erroneous line holograms. (b) Wave number spectrum of erroneous line holograms. (c) Real part of pressure on a source line predicted from erroneous line holograms. (d) Real part of corrected line holograms. (e) Wave number spectrum of corrected line holograms. (f) Real part of pressure on a source line predicted from corrected line holograms.

nificant than the magnitude error. We also found that the errors on a predicted sound field are dependent not only on the speed of noise sources but also on the measurement position of hologram (near field or far field). A correction method, which introduces the phase correction factor, was proposed. Several numerical examples illustrated that these errors are not significant when $M \leq 0.1$. The feasibility of the proposed phase correction method was also demonstrated. The results explicitly demonstrate that MFAH can be well applied to the visualization of sound generated by low-speed moving sources.

ACKNOWLEDGMENTS

This work was supported by the Korea Institute of Science and Technology Evaluation and Planning (KISTEP, ‘National Research Laboratory’ Project), and the Ministry of Education (‘Brain Korea 21’ Project).

APPENDIX A: DERIVATION OF THE ARGUMENT OF q_l IN EQ. (4)

In order to derive the argument of q_l in terms of variables with regard to the observation time, R_l must be expressed in terms of r_l and θ_l . From the triangle of Fig. A1 we can write

$$R_l^2 = (MR_l)^2 + r_l^2 - 2MR_l r_l \cos(\pi - \theta_l), \quad (\text{A1a})$$

$$(1 - M^2)R_l^2 - 2Mr_l \cos \theta_l R_l - r_l^2 = 0. \quad (\text{A1b})$$

If we solve Eq. (A1b) for R_l and take a plus sign, then

$$R_l = \frac{r_l \{M \cos \theta_l + \sqrt{1 - M^2 \sin^2 \theta_l}\}}{1 - M^2}. \quad (\text{A2})$$

Therefore, we can obtain the following relationship:

$$\tau^* = t - \frac{R_l}{c} = t - \frac{r_l \{M \cos \theta_l + \sqrt{1 - M^2 \sin^2 \theta_l}\}}{c(1 - M^2)}. \quad (\text{A3})$$

This can be simplified if $M \ll 1$ is satisfied; that is

$$\tau^* \cong t - \frac{r_l(1 + M \cos \theta_l)}{c}. \quad (\text{A4})$$

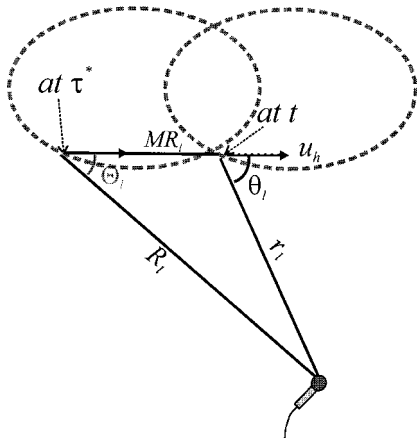


FIG. A1. Law of cosine for Eq. (A1a).

APPENDIX B: DERIVATION OF AMPLITUDE MODIFICATION FACTOR [EQ. (5)]

The amplitude modification factor at the observation time can be written as

$$\begin{aligned} A_l^o &= A_l^e \times \frac{M \cos \theta_l + \sqrt{1 - M^2 \sin^2 \theta_l}}{1 - M^2} \\ &= \sqrt{1 + M_{nl}^2 - 2M_{nl} \cos \Phi_l} \Big|_{\tau = \tau^*} \\ &\quad \times \frac{M \cos \theta_l + \sqrt{1 - M^2 \sin^2 \theta_l}}{1 - M^2}. \end{aligned} \quad (\text{B1})$$

We assume that the velocity due to the surface vibration is much smaller than that due to surface translation and the surface deformation is negligible during the measurement. Then, $M_{nl} = M \cos(\Phi_l - \Theta_l) = M \cos(\phi_l - \theta_l)$ can be assumed. In addition, when the translation velocity of the source is much smaller than the speed of sound, the relation $\cos \Phi_l \cong \cos \phi_l$ can also be assumed. If we express Eq. (B1) by means of a Taylor series expansion and ignore the higher-order terms than order of Mach number, then Eq. (B1) can be simplified as

$$\begin{aligned} A_l^o &\cong (1 - M \cos(\theta_l - \phi_l) \cos \phi_l)(1 + M \cos \theta_l) \\ &\cong 1 + M(\cos \theta_l - \alpha_l \cos \phi_l), \end{aligned} \quad (\text{B2})$$

where $\alpha_l \equiv \cos(\theta_l - \phi_l)$ is constant.

APPENDIX C: MOVING FRAME ACOUSTIC HOLOGRAPHY IN TERMS OF COMPLEX ENVELOPE¹²

Temporal Fourier transform of Eq. (9) leads us to the basic equation of the MFAH¹⁸ for single frequency f_{h0}

$$\begin{aligned} F_T \{p_h(u_{m/h}t, y_h, z_H; t)\} \\ = \frac{1}{u_{m/h}} \hat{P}_h \left(\frac{2\pi(f_{h0} - f)}{u_{m/h}}, y_h, z_H; f_{h0} \right), \end{aligned} \quad (\text{C1})$$

where F_T denotes the temporal Fourier transform, and \hat{P}_h denotes an x -directional wave number spectrum. We denote frequencies in the measurement coordinate and in the hologram coordinate as f and f_{h0} , respectively. Notice that this equation is valid only when the relative velocity ($u_{m/h}$) between the measurement and hologram coordinates is $0 < u_{m/h} < c/2$.¹⁸ The temporal inverse Fourier transform of Eq. (C1) gives us

$$\begin{aligned} p_h(u_{m/h}t, y_h, z_H; t) \\ = \frac{1}{u_{m/h}} \int_{-\infty}^{\infty} \hat{P}_h \left(\frac{2\pi(f_{h0} - f)}{u_{m/h}}, y_h, z_H; f_{h0} \right) e^{-i2\pi ft} df \\ = \frac{1}{u_{m/h}} \int_{-\infty}^{\infty} \hat{P}_h \left(-\frac{2\pi f}{u_{m/h}}, y_h, z_H; f_{h0} \right) e^{-i2\pi ft} df \\ \quad \times e^{-i2\pi f_{h0}t}. \end{aligned} \quad (\text{C2})$$

The first part of the right-hand side of Eq. (C2) can be simplified as

$$\begin{aligned}
& \frac{1}{u_{m/h}} \int_{-\infty}^{\infty} \hat{P}_h \left(-\frac{2\pi f}{u_{m/h}}, y_h, z_H; f_{h0} \right) e^{-i2\pi f t} df \\
&= \frac{1}{u_{m/h}} \int_{-\infty}^{\infty} \hat{P}_h(k_x, y_h, z_H; f_{h0}) \\
&\quad \times e^{-i2\pi[-(u_{m/h}/2\pi)k_x](x_h/u_{m/h})} d\left(\frac{-u_{m/h}}{2\pi}k_x\right) \\
&= \frac{1}{2\pi} \int_{-\infty}^{\infty} \hat{P}_h(k_x, y_h, z_H; f_{h0}) e^{ik_x x_h} dk_x \\
&= P_h(x_h, y_h, z_H; f_{h0}), \tag{C3}
\end{aligned}$$

where $k_x = -2\pi f/u_{m/h}$ and $x_h = u_{m/h}t$ are employed. Therefore, Eq. (C2) can be written as

$$P_h(u_{m/h}t, y_h, z_H; t) = P_h(x_h, y_h, z_H; f_{h0}) e^{-i2\pi f_{h0}t}. \tag{C4}$$

Remember that the complex envelope of a signal $s(t) = C(t)e^{-i2\pi f_{h0}t}$ is defined $C(t)$. Equation (C4) states that the hologram $P_h(x_h, y_h, z_H; f_{h0})$ can be obtained by using the complex envelope of the measured signal.

APPENDIX D: EXPLANATION OF E_l^o TERMS

The magnitude modification factor can be approximated as

$$1/A_l^o \cong 1 + M(\alpha_l \cos \phi_l - \cos \theta_l), \tag{D1}$$

when $M \ll 1$. The magnitude error due to the moving surface can be identified as $\alpha_l \cos \phi_l - \cos \theta_l$ term, which is proportional to the speed of moving surface. We denote this term by E_l^o . Notice that E_l^o is a function of (x_h, y_h, z_H) , since

$$\begin{aligned}
\cos \phi_l &= \mathbf{n}_l \cdot \mathbf{r}_l / |\mathbf{n}_l| |\mathbf{r}_l| \\
&= \{n_{lx}(x_h - x_{S,l}) + n_{ly}(y_h - y_{S,l}) \\
&\quad + n_{lz}(z_H - z_{S,l})\} / r_l, \tag{D2a}
\end{aligned}$$

$$\cos \theta_l = \mathbf{i} \cdot \mathbf{r}_l / |\mathbf{i}| |\mathbf{r}_l| = (x_h - x_{S,l}) / r_l, \tag{D2b}$$

where $\mathbf{n}_l = (n_{lx}, n_{ly}, n_{lz})$, $|\mathbf{n}_l| = 1$ is the unit vector that is normal to the surface at the l th monopole location. The maximum and minimum value of $E_l^o(x_h, y_h, z_H)$ is

$$-2 < E_l^o(x_h, y_h, z_H) < 2, \tag{D3}$$

because $-1 \leq \cos \theta_l \leq 1$ and $-1 \leq \alpha_l \cos \phi_l \leq 1$. This means that the maximum magnitude error is $2M$ multiplied by the true hologram.

APPENDIX E: DEFINITION OF THE TWO-DIMENSIONAL SPATIAL FOURIER TRANSFORM

$$\begin{aligned}
\hat{P}(k_x, k_y, z; f) &= F_{XY}^{-1}\{P(x, y, z; f)\} \\
&= \int_{-\infty}^{\infty} \int_{-\infty}^{\infty} P(x, y, z; f) e^{-i(k_x x + k_y y)} dx dy. \tag{E1}
\end{aligned}$$

$$\begin{aligned}
P(x, y, z; f) &= F_{XY}^{-1}\{\hat{P}(k_x, k_y, z; f)\} \\
&= \frac{1}{(2\pi)^2} \int_{-\infty}^{\infty} \int_{-\infty}^{\infty} \hat{P}(k_x, k_y, z; f) \\
&\quad \times e^{i(k_x x + k_y y)} dk_x dk_y. \tag{E2}
\end{aligned}$$

¹B. Barsikow, W. F. King III, and E. Pfizenmaier, "Wheel/rail noise generated by a high-speed train investigated with a line array of microphones," *J. Sound Vib.* **118**(1), 99–122 (1987).

²B. Barsikow and W. F. King III, "On removing the Doppler frequency shift from array measurements of railway noise," *J. Sound Vib.* **120**(1), 190–196 (1988).

³T. Tanaka, I. Sakamoto, T. Murakami, S. Mori, and S. Ogata, "Measurement of tire/road noise of a running vehicle by acoustical holography," in *Proceedings of Inter Noise 91* (Sydney, Australia, 1991), pp. 1081–1084.

⁴A. Torri, Y. Takano, K. Terada, M. Sebata, A. Iida, K. Horihata, and H. Fujita, "Shinkansens' sound source measurements using microphone arrays," in *Proceedings of Inter Noise 92* (Toronto, Canada, 1992), pp. 1171–1174.

⁵Y. Takano, K. Terada, E. Aizawa, A. Iida, and H. Fujita, "Development of a 2-dimensional microphone array measurement system for noise sources of fast moving vehicles," in *Proceedings of Inter Noise 92* (Toronto, Canada, 1992), pp. 1175–1178.

⁶S. Brühl and K.-P. Schmitz, "Noise source localization on high-speed trains using different array types," in *Proceedings of Inter Noise 93* (Leuven, Belgium, 1993), pp. 1311–1314.

⁷J. F. Hamet, M. A. Pallas, and K.-P. Schmitz, "Deufrako-1: Microphone array techniques used to locate acoustic sources on ICE, TGV-V and TRANSRAPID 07," in *Proceedings of Inter Noise 94* (Yokohama, Japan, 1994), pp. 187–192.

⁸G. Hölzl, P. Fodiman, K.-P. Schmitz, M. A. Pallas, and B. Barsikow, "Deufrako-2: Localized sound sources on the high-speed vehicles on ICE, TGV-V and TRANSRAPID 07," in *Proceedings of Inter Noise 94* (Yokohama, Japan, 1994), pp. 193–198.

⁹H. Nakagawa, T. Tsuru, T. Tanaka, and I. Sakamoto, "Detection and visualization of moving sound source through acoustic holography," in *Proceedings of ASVA 97* (Tokyo, Japan, 1997), pp. 591–594.

¹⁰F. Poisson, J. C. Valiere, and P. Herzog, "High speed sound sources localization using bilinear time-frequency transformation," *Appl. Acoust.* **53**, 1–13 (1998).

¹¹H.-S. Kwon and Y.-H. Kim, "Moving frame technique for planar acoustic holography," *J. Acoust. Soc. Am.* **103**, 1734–1742 (1998).

¹²S.-H. Park and Y.-H. Kim, "An improved moving frame acoustic holography for coherent bandlimited noise," *J. Acoust. Soc. Am.* **104**, 3179–3189 (1998).

¹³S.-H. Park, H.-S. Kwon, and Y.-H. Kim, "Visualization of noise generated by moving vehicles," in *Proceedings of Noise-Con 97* (The Pennsylvania State University, Pennsylvania, 1997), pp. 383–386.

¹⁴Y.-H. Kim and S.-H. Park, "Moving frame acoustic holography for the visualization of pass-by noise," in *Proceedings of Noise-Con 98* (Ypsilanti, Michigan, 1998), pp. 655–660.

¹⁵F. Farassat, "Discontinuity in aerodynamics and aeroacoustics: The concept and applications of generalized derivatives," *J. Sound Vib.* **55**, 165–193 (1977).

¹⁶R. P. Kanwal, *Generalized Functions—Theory and Technique*, 2nd ed. (Birkhauser, Boston, 1998), Chap. 10, pp. 274–286.

¹⁷A. P. Dowling and J. E. Ffowcs Williams, *Sound and Sources of Sound* (Horwood Limited, London, 1983), Chap. 9, pp. 199–204.

¹⁸Reference 11.

Two- and three-dimensional complex-transducer-point analysis of beam reflection from anisotropic plates

Han Zhang^{a)} and D. E. Chimenti

Department of Aerospace Engineering & Engineering Mechanics and Center for NDE,
Iowa State University, Ames, Iowa 50011

(Received 24 March 2000; revised 25 July 2000; accepted 9 September 2000)

In this paper a frequency-domain analysis of the fluid-immersed plate reflection spectrum in which the transmitter and receiver acoustic beams are modeled with complex transducer points is presented. Lamb wave dispersion in the plate forms the major structural features of the reflection spectra. By assuming a linear dependence of the Fresnel length on the frequency for a flat piston transducer, the complex transducer point technique can be employed over a wide frequency range. With the aid of the reciprocity theorem for electroacoustic transducers, a rigorous three-dimensional (3D) expression for the receiver voltage in a pitch-catch transducer arrangement has been derived by using a pair of transmitting and receiving complex transducer points. The calculations are supported by the results of numerous experiments on both isotropic and anisotropic materials in various measurement geometries. The conditions under which a 3D calculation is important are demonstrated, and comparison with a simpler 2D calculation is made. The model calculation is also applied to illuminate several issues related to materials characterization. © 2000 Acoustical Society of America. [S0001-4966(00)02612-6]

PACS numbers: 43.20.Ef, 43.20.Gp [ANN]

I. INTRODUCTION

Since its introduction by Deschamps¹ in 1973, the complex source point (CSP) technique has been widely used to study the behavior of Gaussian beams under various conditions. In acoustics the CSP technique has found wide application in the theoretical study of nonspecular reflection,²⁻⁵ and these calculations have been successfully compared to experiments.⁶⁻⁹ In all these studies the reflected field or receiver voltage is calculated or measured at a single frequency, as a function of various parameters, when the incident angle is close to the Rayleigh or Lamb wave phase-match angle. In such cases a 2D reflected field or receiver voltage calculation in the incident plane is very close to a 3D calculation with some discernible difference in the leaky wave, as we will show in this paper.

As demonstrated in Ref. 10, the voltage measured at the receiver of a pair of *piston* transducers can be accurately approximated by the measured voltage of a pair of transducers apodized to radiate *Gaussian beams*. The reason for this similarity lies in the averaging effect on the signal phase of the second transducer. Therefore, the receiver voltage is relatively insensitive to rapid phase variations in the near field or to the sidelobe variations in the far field of the piston transmitter. This averaging effect is not present, for instance, when a receiving point probe scans the field of a transmitting piston transducer.

The first theoretical studies of the wave physics of the nonspecular reflection for Rayleigh waves were undertaken by Bertoni and Tamir.¹¹ Later, Pitts *et al.*^{12,13} in subsequent work treated the transducer fields using a 2D beam represen-

tations. In these formulations, the incident sheet beams are considered to have no dependence in a direction x_2 normal to the incident plane, say the x_1x_3 plane. Only more recently have calculations appeared using a full 3D formulation.²⁻⁵ In other recent studies^{10,14} computations have been further extended to include the effect of the finite aperture of the receiver. In none of these studies, however, has a careful comparison between the 2D and 3D analyses been made.

A major objective of this work is to perform such a detailed comparison. The results we have obtained show that the 2D calculation is sufficient for the study of the spatial distribution of the receiver voltage, although there exist some minor differences in the leaky wave due to the additional leakage in 3D case. The plate reflection or transmission coefficient calculated as a function of frequency, however, is widely used to model the receiver voltage and to infer indirectly the plate material parameters.¹⁵⁻¹⁸ Such an experiment can be performed easily and efficiently. It is worthwhile to verify the validity of the theoretical model so that its use in the signal analysis and extraction of material properties is fully justified.

In this paper we extend the complex transducer point (CTP) technique to the widely used ultrasonic Lamb wave geometry. As mentioned earlier, most of the previous work on CTP in acoustics has been carried out at a single frequency, with the exception of Zeroug *et al.*¹⁴ We take advantage of the CTP technique, which provides a convenient and mathematically simple model of a 2D or rotationally symmetric 3D Gaussian beam, to make comparisons between Lamb wave spectral behavior calculated with the two different approximations.

We show that, unlike the results for narrow-band operation, in which the 2D and 3D calculations are nearly identical, with subtle differences in the leaky wave region, the

^{a)}Current address: Herzog Services, Inc., 600 South Riverside Road, St. Joseph, MO 64507.

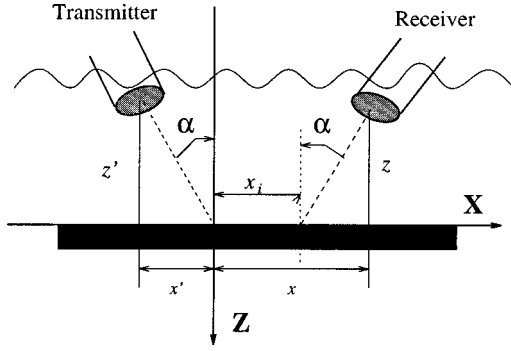


FIG. 1. Geometric configuration used in the experiment and calculation.

reflected frequency spectrum requires a full 3D voltage calculation to achieve the desired accuracy under most conditions. A 2D voltage calculation will not yield accurate results, either for the reflected voltage amplitude or for the positions of reflected voltage minima. The 3D receiver voltage frequency spectra calculated here are compared with extensive experimental results on several materials and in different experimental configurations. The results show that the 3D voltage spectrum calculation must be used under some conditions to deduce precise material parameters. In this paper we focus on the effects of 2D and 3D beam modeling. In dealing with this question, however, we ignore effects that arise from material anisotropy. A recently published paper¹⁹ provides a detailed discussion of this equally important case.

II. THEORY

The experimental geometry that we analyze here is shown in Fig. 1. The transmitter and receiver central axes are set to the same incident angle α , and the surface of the plate lies in the xy plane. The beam central axes and the plate normal lie in the xz plane, which we denote as the “incident plane.” The separation of the beam central axes on the plate surface is denoted by x_i , which will be an important parameter in the analysis presented below.

We first construct the complex Gaussian receiver and complex Gaussian transmitter by displacing the real coordinates of a real point source (x', y', z') and a real point receiver (x, y, z) into the complex plane. According to the geometry shown in Fig. 1

$$\tilde{x} = x - ib \sin \alpha, \quad \tilde{y} = y, \quad \tilde{z} = z + ib \cos \alpha, \quad (1)$$

$$\tilde{x}' = x' + ib \sin \alpha, \quad \tilde{y}' = y', \quad \tilde{z}' = z' + ib \cos \alpha, \quad (2)$$

where α is the transmitter and receiver angle, and b is the so-called Fresnel length of the transmitter and receiver Gaussian beams taken to be identical and given by $b = k_f W_0^2 / 2$. $k_f (= \omega / c_f)$ is the fluid wave number, c_f is the fluid velocity, W_0 is the e^{-1} beamwidth at its waist, and ω is the circular frequency. A good estimate for the beam waist is given by $W_0 = 0.75 r_0$,²⁰ where r_0 is the radius of the piston transducer. The receiver voltage can then be synthesized from the spectral decomposition of the complex Green’s function for a pair of CTPs interacting with a plane layered medium¹⁴

$$V_{\mathcal{R}}(\alpha, x, f) = \frac{-1}{8\pi^2} \gamma(\omega) \omega \rho_f \int_{-\infty}^{\infty} \int_{-\infty}^{\infty} R(k_x, k_y) \times \frac{\exp\{ik_x(\tilde{x} - \tilde{x}') + ik_y(\tilde{y} - \tilde{y}') - i\kappa_f(\tilde{z} + \tilde{z}')\}}{\kappa_f} \times dk_x dk_y, \quad (3)$$

where $\kappa_f = \sqrt{k_f^2 - k_x^2 - k_y^2}$ is the incident wave vector projection onto the z axis, ρ_f is the fluid density, and $\gamma(\omega)$ represents the frequency-dependent transfer function of the transmitter, receiver, and system electronics. It is typically obtained through a calibration procedure.²¹ $R(k_x, k_y)$ is a spectral reflection coefficient that accounts for the interaction of the transducer beams with the plate. The derivation of receiver voltage as a function of frequency is similar to the development of the receiver voltage as a function of scan coordinate,⁸ except that the Fresnel length b is not fixed, but is instead a function of frequency. As mentioned earlier, the calculated frequency spectrum is different for a 3D beam and a 2D beam. We separate our theoretical exposition into two parts: one for the 2D beam, and the other for the 3D beam.

A. 2D calculation

For the 2D case the voltage has no dependence on y , so we let $k_y = 0$, and the z projection of the fluid wave number is $\kappa_f = \sqrt{k_f^2 - k_x^2}$. The voltage calculation Eq. (3) becomes

$$V_{\mathcal{R}}(\alpha, x, f) = \frac{-1}{4\pi} \gamma(\omega) \omega \rho_f \int_{-\infty}^{\infty} R(k) \times \frac{\exp\{ik(\tilde{x} - \tilde{x}') - i\kappa_f(\tilde{z} + \tilde{z}')\}}{\kappa_f} dk. \quad (4)$$

The above integral can be evaluated directly by numerical integration or can be estimated asymptotically. The asymptotic derivation and arguments leading to it are detailed in Ref. 4. However, there exists a numerical integration algorithm that is well suited for oscillating integrands as we have in Eq. (4). To compute the integral in Eq. (4), we use the QUADPACK routine QAG²² in the NAG FORTRAN library, which is an adaptive routine that employs Gauss 30-point and Kronrod 61-point rules.

B. 3D calculation

For the 3D voltage calculation, as suggested in Eq. (3), spherical coordinates would be more convenient; these are used also by Brekhovskikh in his discussion on reflection and refraction of spherical waves.²³ We therefore identify

$$k_x = k_f \sin \theta \cos \phi, \quad k_y = k_f \sin \theta \sin \phi, \quad (5)$$

$$k_z = \kappa_f = k_f \cos \theta,$$

and

$$\frac{dk_x dk_y}{\kappa_f} = k_f \sin \theta d\theta d\phi. \quad (6)$$

The above transformation assigns θ to wave vector variations in the incident xz plane and assigns ϕ to angular varia-

tions in the xy plane. Also, we limit our study to transducers whose aperture centers are located in the incident plane, so $\tilde{y} = \tilde{y}' = 0$. Then Eq. (3) becomes

$$V_{\mathcal{R}}(\alpha, x) = \frac{-1}{8\pi^2} \gamma(\omega) \omega \rho_f \int_0^{2\pi} d\phi \int_0^{\pi/2 - i\infty} d\theta R(\theta, \phi) \times \exp\{ik_f(\sin \theta \cos \phi(\tilde{x} - \tilde{x}') - \cos \theta(\tilde{z} + \tilde{z}'))\} k_f \sin \theta. \quad (7)$$

For isotropic plates, there is complete symmetry in the xy plane and thus the reflection coefficient is independent of ϕ , permitting us to evaluate the integral over ϕ asymptotically using the saddle-point method applied in the ϕ plane. We find that the phase function in Eq. (7) (argument of the exponential) has two saddle points for ϕ . One is $\phi_s = 0$, representing a forward-propagating wave, and the other is $\phi_s = \pi$, representing a backward propagating wave. Ignoring the negligible backward wave, we therefore take $\phi_s = 0$, and the above integral reduces to

$$V_{\mathcal{R}}(\alpha, x) = \frac{\gamma(\omega) \omega \rho_f \exp(-i\pi/4) \sqrt{k_f}}{4\pi \sqrt{2\pi} \sqrt{\tilde{x} - \tilde{x}'}} \int_0^{\pi/2 - i\infty} R(\theta) \times \exp\{ik_f(\sin \theta(\tilde{x} - \tilde{x}') - \cos \theta(\tilde{z} + \tilde{z}'))\} \times \sqrt{\sin \theta} d\theta. \quad (8)$$

The remaining integral in Eq. (8) can again be evaluated asymptotically by changing the integration contour to a steepest descent path, where particular attention must be given to the poles of $R(\theta)$ that may be crossed during the path deformation. The contribution of the poles must be properly accounted for especially when located close to the saddle point. This problem has been solved by Felsen and Marcuvitz,²⁴ and their solution has been widely used to treat both acoustic and electromagnetic wave problems.^{4,5,10} In the present case, the strong phase matching of the incident beam with the leaky Lamb wave means the saddle point is in the vicinity of the pole singularity of $R(\theta)$, which requires a uniform asymptotic treatment as developed in Ref. 4. The steepest descent path calculation yields the specular reflection, whereas the contribution of the residue of each captured or noncaptured, but closely located, pole yields a leaky Lamb wave. The above mathematical decomposition procedure physically corresponds to decomposing the total receiver voltage into a specular reflection and leaky waves. The uniform asymptotic evaluation enters via an error function that regulates the interaction between the saddle-point contribution and the pole contribution.

This same approach is applied here. First, the saddle point can be obtained by setting the first derivative with respect to θ of the phase function

$$p(\theta) = k_f(\sin \theta(\tilde{x} - \tilde{x}') - \cos \theta(\tilde{z} + \tilde{z}')) \quad (9)$$

equal to zero, and we find

$$\theta_s = \arctan \frac{\tilde{x} - \tilde{x}'}{\tilde{z} + \tilde{z}'} (\sin \theta_s > 0). \quad (10)$$

Then, we calculate the contributions of the saddle point and pole, whose sum forms the total receiver voltage

$$V_{\mathcal{R}}(\alpha, x) = \frac{\gamma(\omega) \omega \rho_f \exp(-i\pi/4) \sqrt{k_f}}{4\pi \sqrt{\pi} \sqrt{\tilde{x} - \tilde{x}'}} \exp(ip(\theta_s)) \times \left\{ R(\theta_s) \sqrt{\frac{-2\pi \sin \theta_s}{ik_f \tilde{L}}} + \sum_{j=1}^M 2\pi i \sqrt{\sin \theta_{p_j}} \text{Res}\{R(\theta_{p_j})\} \times \left[\frac{1}{2\sqrt{\pi i \tilde{S}(\theta_{p_j})}} + \frac{1}{2} \exp(-\tilde{S}(\theta_{p_j})^2) \times \text{erfc}(-i\tilde{S}(\theta_{p_j})) \right] \right\}, \quad (11)$$

where all the values of all the square roots are chosen so their real parts are greater than zero and $\tilde{L} = \sqrt{(\tilde{x} - \tilde{x}')^2 + (\tilde{z} + \tilde{z}')^2}$ ($\text{Re}(\sqrt{\cdot}) > 0$) is the complex ‘‘distance’’ from the source to the receiver via the reflection path of the plate upper surface, and $p(\theta_s)$ is the phase function Eq. (9) evaluated at the saddle point $\theta = \theta_s$. Here, $\tilde{S}(\theta_{p_j})$ is the so-called ‘‘numerical distance’’ between the saddle point θ_s and j th pole of the reflection coefficient θ_{p_j} . The numerical distance is given by

$$\tilde{S}(\theta_{p_j}) = \sqrt{ip(\theta_s) - ip(\theta_{p_j})} (\text{Re}(\sqrt{\cdot}) > 0), \quad (12)$$

θ_{p_j} is chosen so that $\text{Im}(\sin \theta_{p_j}) < 0$. In Eq. (11) erfc is the complex complementary error function, given by

$$\text{erfc}(\tau) = \frac{2}{\sqrt{\pi}} \int_{\tau}^{\infty} \exp(-t^2) dt. \quad (13)$$

In the above derivation we ignore the effect of the ϕ dependence of the reflection coefficient, as mentioned above. For anisotropic materials the above formula is still valid under some cases, such as when the sound is propagating along the symmetry axis of an anisotropic plate and the receiver is within the specular reflection region. This case is analyzed in detail in Ref. 19. All experimental data and theoretical calculations on anisotropic media reported in the current paper fall within the range of validity of the general treatment in Ref. 19.

III. EXPERIMENTAL TECHNIQUE

In this section we describe the materials, apparatus, and procedures used in the experiments performed here, and we discuss data acquisition and processing. We have performed experiments on both isotropic and anisotropic materials. For the isotropic samples we have used a 3-mm-thick stainless-steel plate, with a longitudinal wave speed $c_l = 5.64$ km/s, shear wavespeed $c_t = 3.07$ km/s, and density $\rho = 7.9$ kg/m⁻³. Two anisotropic plates have been used in our experiments;

TABLE I. Geometry and acoustic properties of composite plate.

Composite layup	C_{11} GPa	C_{12} GPa	C_{22} GPa	C_{23} GPa	C_{55} GPa	d mm	ρ g/cm ³
Unidirectional	143.0	3.7	16.5	7.6	8.3	0.92	1.60
Biaxial	133.0	3.7	15.5	7.6	6.3	1.52	1.62

these are a uniaxial graphite epoxy plate and a $[0,90]_{3S}$ biaxial graphite epoxy plate. Their material properties can be found in Refs. 17 and 25 and will not be repeated here. Instead, we list the elastic constants in Table I obtained by fitting data from extensive experiments performed in the current paper to the calculations reported here.

Two identical Ultra LS-375-5 piezoelectric transducers with a center frequency of 5 MHz and an effective diameter of 4.95 mm are employed to perform all measurements reported here. The two transducers are attached to a rotation stage that establishes the incident angle with a resolution of 0.01° in a pitch-catch setup. The positioning of the transducer normal to the plate surface is identified ultrasonically by carefully observing the largest reflection, and it is checked geometrically with precision calipers. The experiment itself is performed in one of two ways.

The transmitting transducer is excited with radio-frequency (rf) tone bursts of 50–80 μ s duration. To acquire the reflected frequency spectrum, a frequency sweep of the tone burst is performed under computer control with a step size of 20 kHz in the range of 0.5–12 MHz. After interaction with the elastic plate, the reflected acoustic beam is detected by a receiver. The received signal is amplified from 20 to 40 dB in a low-noise, wideband amplifier and is video detected to reveal the rf envelope of the tone burst. The amplitude of the video signal is synchronously measured using a gated, integrating amplifier, further improving the signal/noise ratio. The resulting dc amplitude is then sampled by a 13-bit A/D converter and sent over a IEEE-488 bus line to a DEC workstation for further offline processing. A more detail description of this frequency sweep instrumentation and data acquisition procedure can be found in Ref. 26.

We have also employed a pulse compression technique via a chirp signal to speed the data acquisition and processing. An arbitrary function generator DS345 (Stanford Research Systems) is used to generate the computer-designed chirp signal and excite the transmitting transducer. The DS345 function generator allows us to download arbitrary digital waveforms and has a maximum digitization rate of 40 MSamples/s. It can, therefore, accurately reproduce signals with frequencies in the range of 0.5–12.5 MHz. The 100- μ s chirp signal is sampled by a Lecroy digitizing oscilloscope and sent to a workstation after reflection from the plate and detection by the receiver. We then perform a fast Fourier transform (FFT) on the digitized chirp signal and plot its frequency spectrum. We can also single out a particular frequency and plot the receiver voltage as a function of spatial coordinate scan.

IV. RESULTS AND DISCUSSION

The accuracy of our theoretical calculation of acoustic beam interaction with elastic structures depends, among

other factors, on how accurately the complex transducer point can model real transducers. Because we study the reflected frequency spectrum, we must verify that the CTP can model the corresponding beam variation as the frequency varies. We first discuss some transducer characteristics and then present the experimental results and theoretical calculations on beam interaction with elastic plates.

A. Transducer characteristics

It is well-known that a piston transducer beam narrows as the frequency increases. This diffraction effect is accurately modeled by the CTP, as seen in Fig. 2, showing the amplitude of the receiver voltage as a function of the scan coordinates at several frequencies. The experiment is performed on a thick aluminum block at an incident angle of 20° , and the transducer is excited with a tone burst of 2, 5, and 8 MHz. After a Fourier transform is performed on the received rf signal, 1.9-, 4.9-, and 7.9-MHz components are extracted and plotted as a function of scan distance in Fig. 2. Because 20° is far from the critical angle of aluminum, the reflection at this angle is largely specular, and so coupling to the leaky Rayleigh wave is avoided. Being specular, the reflection process nearly duplicates the transducer characterization step where the receiver would scan the field of the transmitter in free field (i.e., without the presence of the plate). The experimental results show that a pair of CTPs can account well for the spatial characteristics of the transducers as the frequency varies. This additional result complements the points made earlier concerning the close comparison between the combined piston directivity function and that for combined Gaussian beams, as generated by the CTP formalism. No sidelobes are observed, as expected for Gaussian beams. The beam diffraction effects of the transducers, that is their divergence properties, are well reproduced by the CTP.

B. Beam interaction with plates

Our confidence in using the complex transducer point technique to model the reflected frequency spectrum is enhanced by the excellent agreement seen above in Fig. 2. Now, we proceed to calculate the frequency spectrum of the reflected beam from an elastic plate. Before we present any experimental results, however, we show a comparison of the 2D voltage calculation using Eq. (4) and 3D voltage calculation using Eq. (8) in Fig. 3. The calculation is performed on a 3-mm-thick steel plate at an incident angle 20° . The distance from the transducer surface to the plate along the beam axis is 120 mm. We see substantial differences in the depth of the minima, although the minima locations have not changed appreciably. The 2D Gaussian beam may be regarded as a 3D Gaussian sheet beam. The difference in the results of Fig. 3 is caused by the different frequency-dependent diffraction effects of the two beams: a complex line source and a complex point source. Intuitively, as the frequency increases, we can imagine that on a transverse cut to their axes the Gaussian sheet beam will narrow in one dimension, whereas the 3D rotationally symmetric Gaussian beam will narrow in two dimensions. The stronger narrowing (or collimation) of the 3D reflected beam yields a stronger

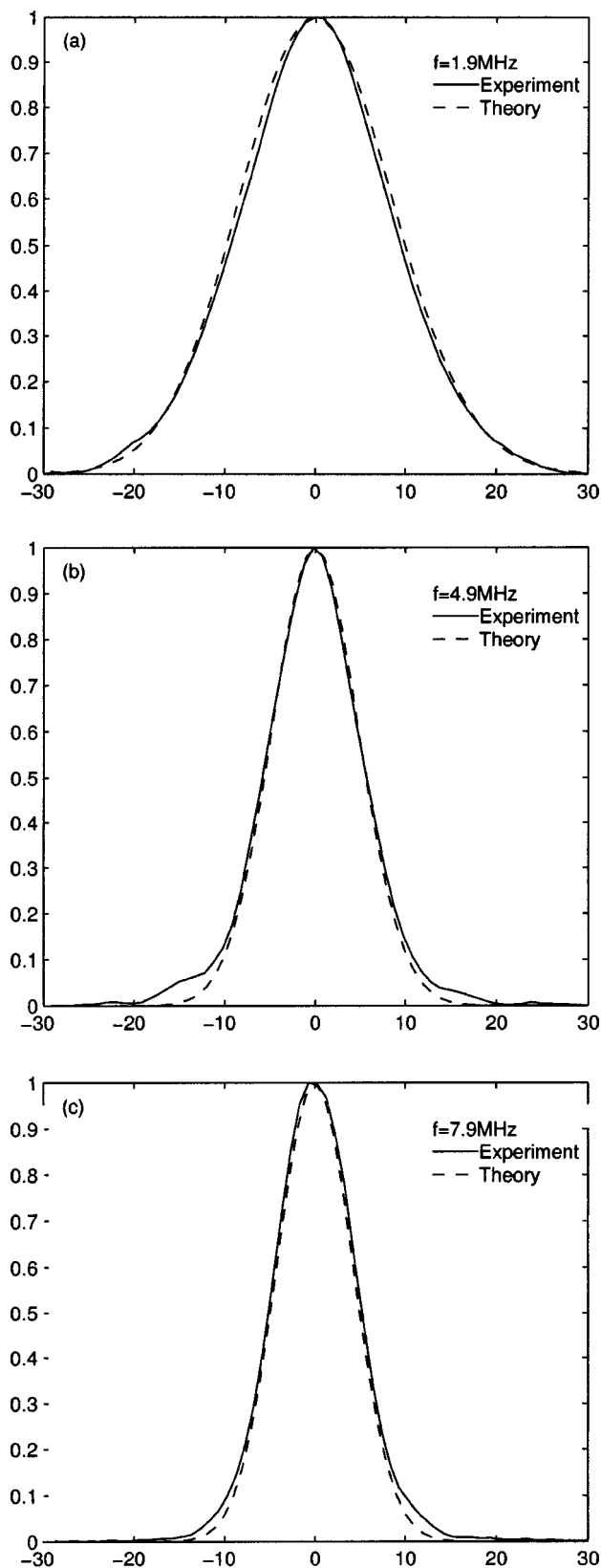


FIG. 2. Spatial characterization of piston transducers with frequency from (a) 1.9 MHz; (b) 4.9 MHz; to (c) 7.9 MHz. All experimental data are fitted by one pair of CTPs with a beamwidth of $w_0=3.56$ mm at the beam waist.

voltage amplitude at the receiver aperture. This explains why the voltage decays as a function of frequency are slower for the 3D case when compared to the 2D case as Fig. 3 shows.

The difference between 2D and 3D results in a simple

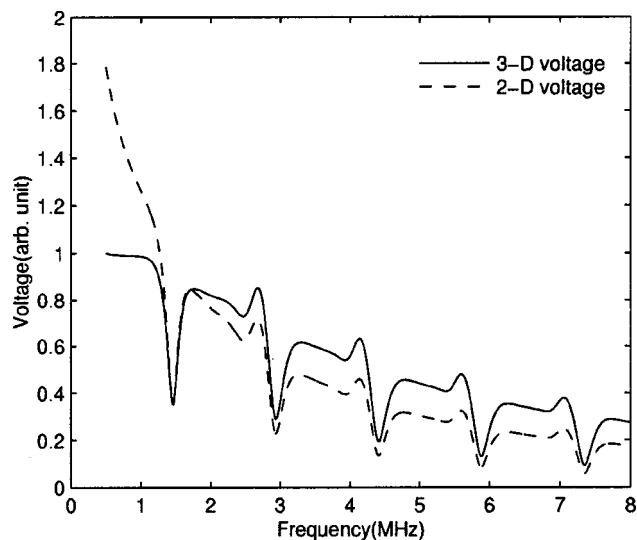


FIG. 3. Comparison of 2D and 3D calculated receiver voltage frequency spectra. Calculations are performed on a 1.5-mm steel plate at 20° incident angle and x coordinate offset of $x_i=5$ mm. The distance from the transducer surface to the plate surface is 120 mm.

x -scan, however, manifests itself in a different manner. In Fig. 4(a) the same expressions [Eq. (4) and Eq. (8)] are used to calculate the receiver voltage as a function of scan distance at 20° and $f=3$ MHz. After normalization by their maximum value, we see some difference in the leaky region ($x>20$ mm). To further explore the difference, we plot the voltage amplitude of Fig. 4(a) on a log scale and the results are shown in Fig. 4(b). The 2D curve is linear in the leaky region ($x>20$ mm) because of the exponential leakage of the leaky wave. The 3D curve appears linear, but really is not because there is an additional decay due to lateral beam spreading. This decay is represented by the $(\tilde{x}-\tilde{x}')^{-1/2}$ in Eq. (8) which is not present in Eq. (4) for the 2D case. Physically, in addition to differences in diffraction between 2D and 3D mentioned before, there is a further physical difference between these cases related to the leaky guided waves. Plane wave components in the 3D beam propagating out of the incident plane can have projections along the plate-mode propagation axis direction in the incident plane with values that reinforce one or more of the leaky guided plate modes. This effect is especially pronounced near normal incidence.¹⁹

We begin the presentation of experimental results with isotropic materials. Shown in Fig. 5(a) is the receiver voltage spectrum from a 3.00-mm steel plate at 10° incidence with x offset of $x_i=6$ mm. The overall features are well predicted by the theory, both the spectral minima positions and the general shape. The depths of the minima are also well fitted by the theory. The amplitude difference at high- and low-frequency results from noise introduced by the transducer response normalization. The receiver voltage spectrum shows periodic transverse resonances characteristic of guided plate waves, but also many other small variations. Nonetheless, all small features are still well modeled by the theory. In fact, all these small variations can be attributed to leaky waves, as confirmed by the separate leaky wave calculations in frame (b). Physically, at 10° the poles associated with the

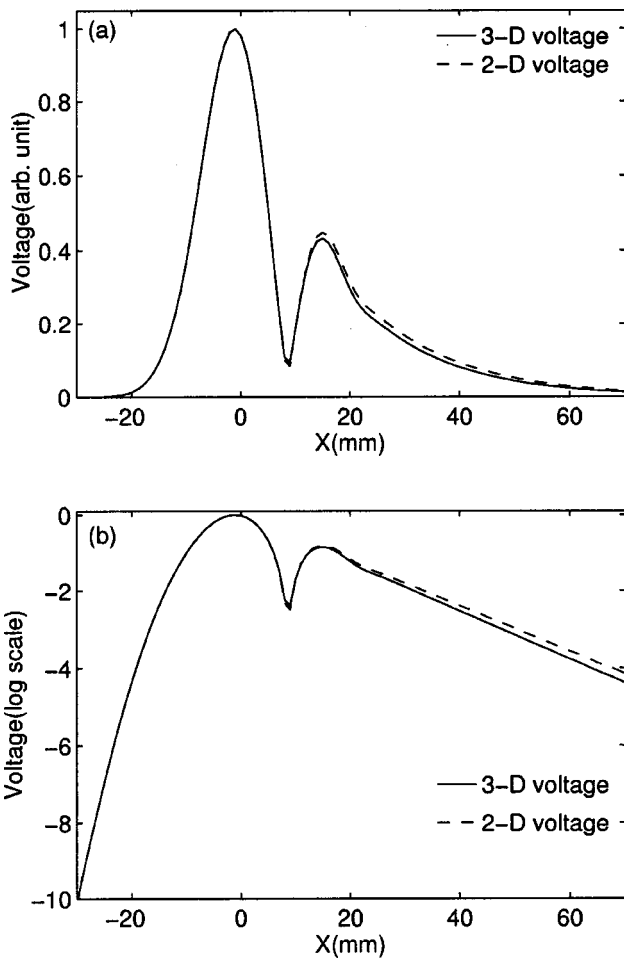


FIG. 4. Comparison of a 2D and 3D x -scan voltage calculation. The calculation is performed on a 1.5-mm steel plate at 20° incident angle and $f = 3$ MHz. The distance from the transducer surface to the plate surface is 120 mm. (a) Voltage amplitude on a linear scale; (b) voltage amplitude on a log scale.

reflection coefficient are closer, and they give the same order of contribution to the total receiver voltage, so their interference produces the small variations. Again, in frame (b) we observe that the sharp peak at the upper right of each cycle of the total receiver voltage spectrum results from interference of the specular reflection and leaky wave. Since 10° is less than the longitudinal critical angle associated with a water-steel interface, the receiver voltage spectrum is sensitive to both shear velocity and longitudinal velocity.

The characteristics in Fig. 5(a) can be computed with numerical integration. This approach, however, does not provide us with as much physical insight as the asymptotic analysis described in Sec. II B. A second point that provides additional motivation to use the asymptotic solution is its computational efficiency as compared to the numerical integration solution. The asymptotic expression given in Eq. (11) indicates that the total receiver voltage consists of a specular reflection and a leaky wave. The asymptotic analysis is performed here to explain the frequency spectrum characteristics shown in Fig. 5(a). The validity of the above analysis is established by the comparison with the direct numerical integration results, as shown in Fig. 6(a) for an incident angle of 20° . The two curves overlap over almost the entire spec-

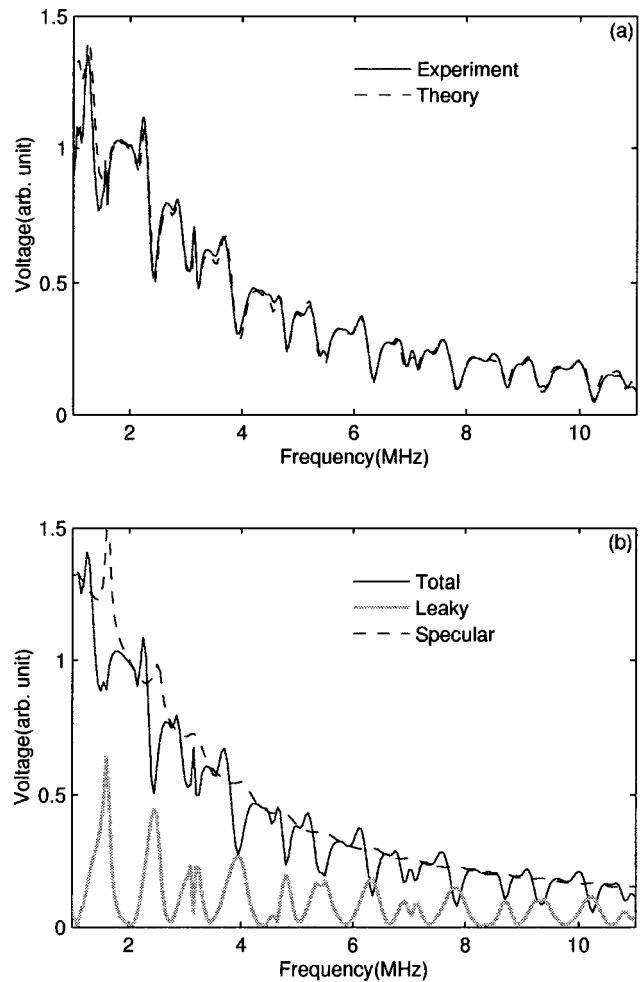


FIG. 5. (a) Receiver voltage spectrum of a steel plate at 10° incidence and at a coordinate offset $x_i = 6$ mm; (b) separate contributions of leaky wave and specular reflection in the total receiver voltage spectrum.

trum. The small discrepancies at low frequency can be attributed to the numerical instability of the algorithm which arises because of the vanishingly small numerical distance \tilde{S}_{p_j} between the saddle point and the pole. When the saddle point and the pole are very close, both the specular reflection and the leaky wave are very large. Their sum, however, remains bounded because of their different phases. In the numerical calculation truncation errors may result, causing the two parts to be not well matched, resulting in anomalous data points. The most difficult part in performing the asymptotic calculation in the present case, however, concerns the presence of multiple poles, and that their positions vary with frequency.

We have developed an algorithm that keeps track of the poles that are within $\pm 7.5^\circ$ of the incident angles. In a 15° range on either side of the central ray we have two or three poles at low frequency and ten or 11 poles at high frequency. The poles lying outside this angular range have negligible effects on the leaky wave contribution. Shown in Fig. 6(b) are the separate contributions of the leaky waves and the specular reflection of such a calculation. The sum of all contributors is also plotted as a solid curve. The total receiver voltage level is influenced by the specular reflection, because the receiver is located within the specular reflection region.

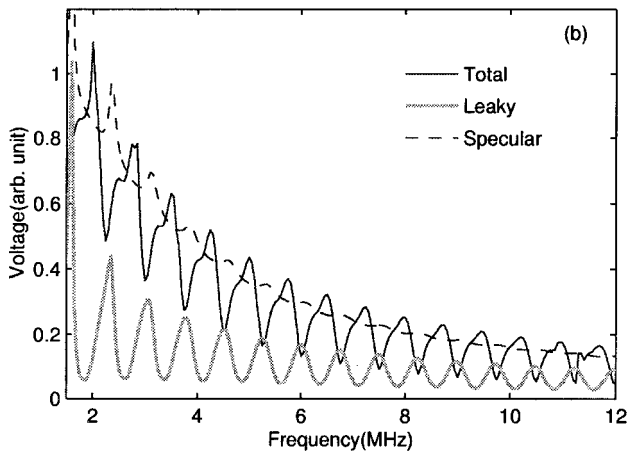
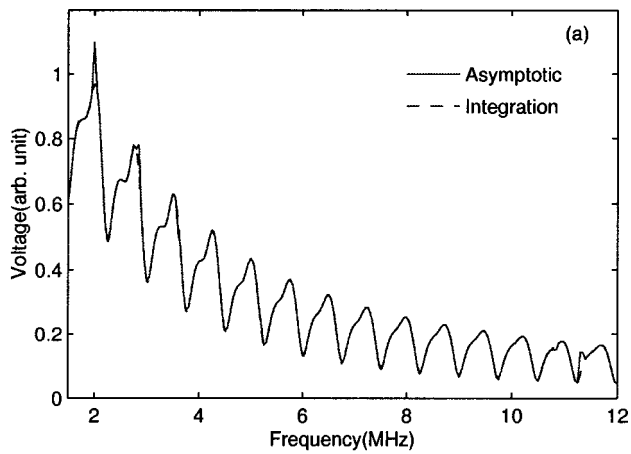


FIG. 6. (a) Comparison of an asymptotic receiver voltage spectrum and a direct numerical integration calculation; (b) separate contributions of the leaky wave and specular reflection in the total receiver voltage spectrum.

The phase difference between the specular reflection and leaky wave is shown by the fact that the total receiver voltage minima occur at the maximum of the leaky waves. The reinforcement of the leaky wave minima and the specular reflection results in a sharp peak on the top of every cycle of the receiver voltage. The sharp peak becomes less obvious because of the decrease in the strength of the specular reflection as frequency increases. The decrease is due to beam diffraction effects shown in Fig. 2.

If the transducer is moved outside of the specular reflection region, we will observe different characteristics. Such a case is shown in Fig. 7(a), where the receiver voltage spectrum is recorded at an incident angle of 20° but with a coordinate offset of $x_r = 11$ mm and is compared with the theoretical prediction. The theoretical modeling and experimental results agree well in a very broad frequency range, except at very low frequencies, where poor transducer response incurs the noise and the corresponding normalization variations. Again, the spectrum observed in frame (a) can be well explained by the asymptotic analysis shown in frame (b). Although the receiver offset is larger than the transducer diameter in this case, the specular reflection still dominates the receiver voltage at low frequency. Because of the beam diffraction effects at low frequency, the leaky wave maximum results in a minimum in the total receiver voltage.

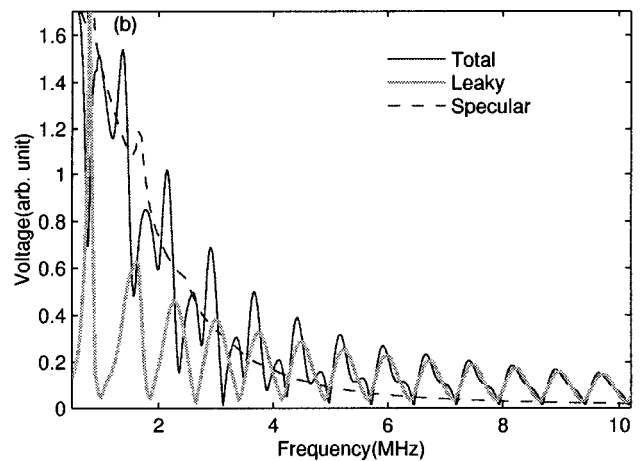
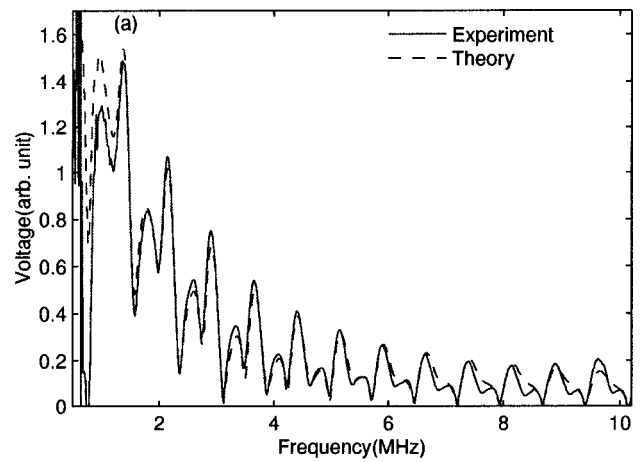


FIG. 7. (a) Comparison of experimental receiver voltage spectrum of a steel plate at 20° incidence and coordinate offset of 11 mm with the theoretical prediction; (b) separate contributions of leaky wave and specular reflection in the total receiver voltage.

The total receiver voltage spectrum shows a periodic small peak followed by a large peak. The small peak aligns with the minimum of the leaky wave at first, and gradually degenerates. Finally, the receiver voltage spectrum minima align with the minima of the leaky wave. Above 7 MHz the leaky wave is almost the sole contribution to the total receiver voltage.

The voltage spectrum calculation can be extended to anisotropic media and employed to characterize composite materials. In the following experimental measurement (and theoretical calculations) the sound is propagating along the symmetry axis of the plate and the receiver is within the specular region. As demonstrated earlier¹⁹ under such cases, the effects of ignoring the ϕ dependency of the voltage is negligible, while ensuring rapid calculation. We report first on a unidirectional graphite-epoxy laminate, whose calculated reflection coefficient is well documented.^{25,27-29} A unidirectional laminate can be grossly regarded as transversely isotropic, so five elastic constants C_{11} , C_{12} , C_{22} , C_{23} , C_{44} , C_{55} determine the elastic behavior of the composite plate, where $C_{44} = (C_{22} - C_{23})/2$. The choice of incident angle is critical to the determination of certain elastic constants.³⁰

At a 20° incident angle the receiver voltage spectrum is strongly influenced by C_{33} , and this fact is verified by the

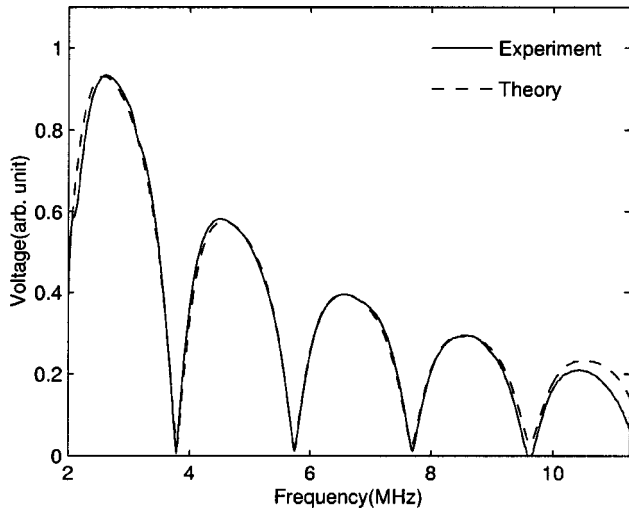


FIG. 8. Receiver voltage spectrum from a unidirectional graphite-epoxy plate at 20° incidence and at an offset of $x_i = 6$ mm with the fiber direction in the incident plane.

experimental results shown in Fig. 8. Here, the offset is also 6 mm and the fiber direction is in the incident plane. The positions of the minima and the amplitude of the maxima of the receiver voltage spectrum are nearly perfectly modeled by the theory. Some minor discrepancy above 10 MHz may result from the transducer response normalization. The elastic constant C_{23} has no significant influence on the receiver voltage when the fiber direction is in the incident plane, but has pronounced effects on it when the fiber direction is normal to the incident plane. An example of this behavior is shown in Fig. 9, where the incident angle is 20° and the offset is 6 mm, but the fiber direction is normal to the incident plane. Although the receiver voltage spectrum is a bit complicated here, all features are well fitted by the theoretical calculation, even the fine variations.

A more complicated composite sample is represented by a 12-ply biaxial graphite epoxy plate. The ply configuration of this sample is $[0,90]_{3s}$. The elastic behavior of such a

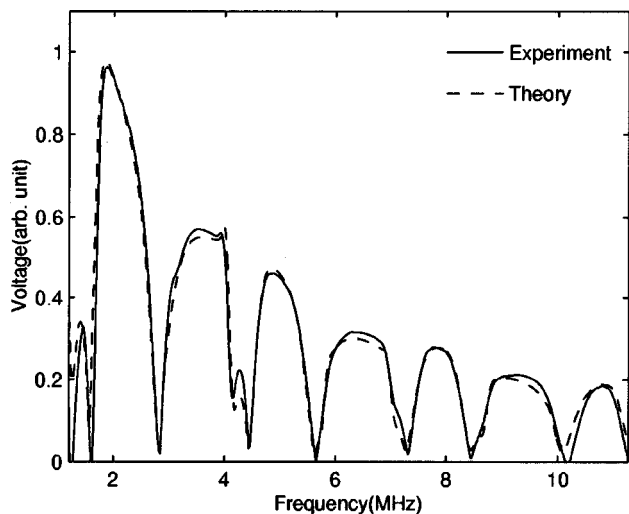


FIG. 9. Receiver voltage spectrum from a unidirectional graphite-epoxy plate at 20° incidence and at an offset of $x_i = 6$ mm with the fiber direction normal to the incident plane.

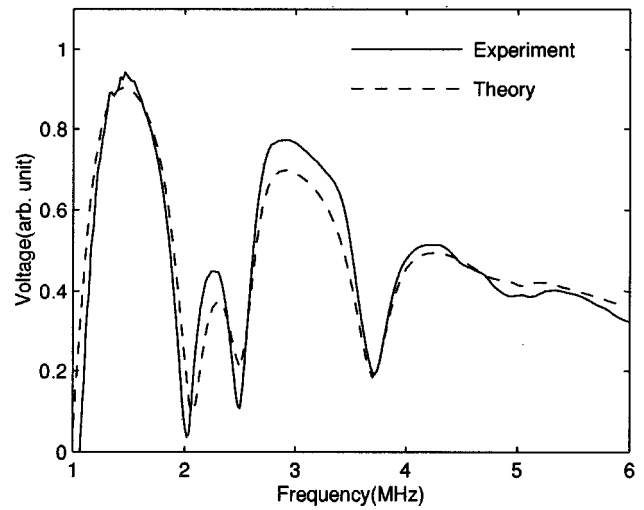


FIG. 10. Receiver voltage spectrum from a biaxial graphite-epoxy plate at 20° incidence and at an offset of $x_i = 6$ mm with the fiber direction in the top layer lying in the incident plane.

laminate cannot be regarded as an orthotropic plate, especially at higher ultrasonic frequencies.¹⁷ The stacking sequence of the lamina is important for the ultrasonic behavior, so the simple reflection coefficient of a unidirectional graphite-epoxy plate cannot be applied here. Instead, a reflection coefficient¹⁷ derived using the transfer matrix is incorporated into our voltage spectrum calculation. Shown in Fig. 10 is the receiver voltage spectrum from the $[0,90]_{3s}$ biaxial composite laminate at 20° incidence and offset of 6 mm. The fiber direction in the top layer lies in the incident plane. The unusual characteristics seen here demonstrate the complexity resulting from the multilayer media. Even so, the results are also in good agreement with the theoretical receiver voltage spectrum calculation, which accounts both for the complex material behavior and the diffraction effects of the transducer beams.

The effect of the stacking sequence is seen in Fig. 11, where the experimental setup is the same as in Fig. 10, except that the top-layer fiber direction is normal to the inci-

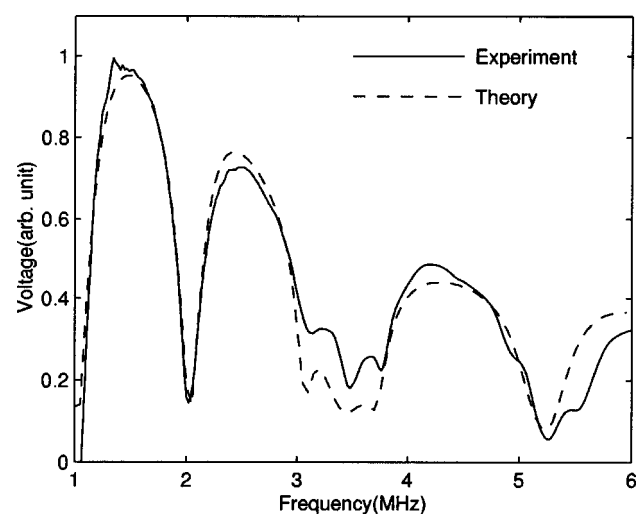


FIG. 11. Receiver voltage spectrum from a biaxial graphite-epoxy plate at 20° incidence and at an offset of $x_i = 6$ mm with the top-layer fiber direction lying normal to the incident plane.

dent plane. The spectral difference below 2 MHz between Figs. 11 and 10 is not significant, indicating that the laminate behaves as a homogeneous orthotropic plate at low frequency. Completely different behavior, however, exists above 2 MHz.

V. CONCLUSION

In this paper we have extended the complex transducer point (CTP) technique to model the Lamb wave spectrum of the receiver voltage. We have shown that the model provides a very powerful tool to analyze the detailed characteristics of the Lamb wave spectrum, as we have verified in extensive experiments. We have found that a 3D beam calculation is generally necessary for the spectral integration, because a 2D beam is not accurate enough to model all features of the measured receiver voltage. The 3D beam calculation can model the reflection spectrum measurement in all experimental configurations for isotropic materials, and it is valid for anisotropic materials under some cases when the angular dependence of the reflection coefficient outside the incident plane can be ignored. We have discussed various materials characterization issues, using the model calculation as a potential application. In most cases the spectrum is sensitive to one or more elastic constants, and this fact permits precise materials characterization. We have also developed an algorithm for the asymptotic analysis of the reflection spectrum.

ACKNOWLEDGMENTS

The authors would like to thank Dr. Smaine Zeroug of Schlumberger-Doll Research for a careful reading of the manuscript. One of the authors, H. Z., would also like to acknowledge the support from Herzog Services, Inc. during the preparation of this paper.

- ¹G. A. Deschamps, "Gaussian beam as a bundle of complex rays," *Electron. Lett.* **7**, 684–685 (1971).
- ²J. Pott and J. G. Harris, "Scattering of an acoustic Gaussian beam from a fluid-solid interface," *J. Acoust. Soc. Am.* **76**, 1829–1838 (1984).
- ³J. G. Harris and J. Pott, "Further studies of the scattering of an acoustic Gaussian beam from a fluid-solid interface," *J. Acoust. Soc. Am.* **78**, 1072–1080 (1985).
- ⁴S. Zeroug and L. B. Felsen, "Nonspecular reflection of two- and three-dimensional acoustic beams from fluid-immersed plane-layered elastic structures," *J. Acoust. Soc. Am.* **95**, 3075–3098 (1994).
- ⁵S. Zeroug and L. B. Felsen, "Nonspecular reflection of two- and three-dimensional acoustic beams from fluid-immersed cylindrically layered elastic structures," *J. Acoust. Soc. Am.* **98**, 584–598 (1995).
- ⁶D. E. Chimenti, J. Zhang, S. Zeroug, and L. B. Felsen, "Interaction of acoustic beams with fluid-loaded elastic structures," *J. Acoust. Soc. Am.* **95**, 45–59 (1994).
- ⁷T. J. Cloutier, A. Safaeinili, D. E. Chimenti, S. Zeroug, and L. B. Felsen, "Ultrasonic beam reflection from fluids loaded cylindrical shells," *J. Appl. Phys.* **83**, 2408–2419 (1998).

- ⁸H. Zhang, D. E. Chimenti, and S. Zeroug, "Transducer misalignment effects in beam reflection from elastic structures," *J. Acoust. Soc. Am.* **104**, 1982–1991 (1998).
- ⁹H. Zhang and D. E. Chimenti, "Ultrasonic beam reflection from lossy layered cylindrical shells," *Ultrasonics* **35**, 441–450 (1997).
- ¹⁰O. I. Lobkis, A. Safaeinili, and D. E. Chimenti, "Precision ultrasonic reflection studies in fluid-coupled plates," *J. Acoust. Soc. Am.* **99**, 2727–2736 (1996).
- ¹¹H. L. Bertoni and T. Tamir, "Unified theory of Rayleigh-angle phenomena for acoustic beams at liquid-solid interfaces," *Appl. Phys.* **2**, 157–172 (1973).
- ¹²L. E. Pitts, T. J. Plona, and W. G. Mayer, "Theory of nonspecular reflection effects for an ultrasonic beam incident on a solid plate in a liquid," *IEEE Trans. Sonics Ultrason.* **SU-24**, 101–109 (1977).
- ¹³T. J. Plona, L. E. Pitts, and W. G. Mayer, "Ultrasonic bounded beam reflection and transmission effects at liquid/solid-plate/liquid interface," *J. Acoust. Soc. Am.* **6**, 1324–1328 (1976).
- ¹⁴S. Zeroug, F. E. Stanke, and R. Burridge, "A complex-transducer-point model for emitting and receiving ultrasonic transducers," *Wave Motion* **24**, 21–40 (1996).
- ¹⁵D. E. Chimenti and A. H. Nayfeh, "Leaky Lamb waves in fibrous composite laminates," *J. Appl. Phys.* **58**, 4531–4538 (1985).
- ¹⁶A. H. Nayfeh and D. E. Chimenti, "Propagation of guided waves in fluid-coupled plates of fiber-reinforced composite," *J. Acoust. Soc. Am.* **83**, 1736–1743 (1988).
- ¹⁷D. E. Chimenti and A. H. Nayfeh, "Ultrasonic reflection and guided wave propagation in biaxially laminated composite plates," *J. Acoust. Soc. Am.* **87**, 1409–1415 (1990).
- ¹⁸S. Zeroug, "Analytical modeling for fast simulation of ultrasonic measurement on fluid-loaded layered elastic structures," *IEEE Trans. Ultrason. Ferroelectr. Freq. Control* **47**, 565–574 (2000).
- ¹⁹O. I. Lobkis and D. E. Chimenti, "3D transducer voltage in anisotropic materials characterization," *J. Acoust. Soc. Am.* **106**, 36–45 (1999).
- ²⁰R. B. Thompson and E. F. Lopes, "The effects of focusing and refraction on Gaussian ultrasonic beams," *J. Nondestruct. Eval.* **4**, 107–123 (1984).
- ²¹R. B. Thompson, D. O. Thompson, and L. W. Schmerr, "Strategies for characterizing transducers and measurement systems," *Review of Progress in Quantitative NDE*, edited by D. O. Thompson and D. E. Chimenti (Plenum, New York, 1996), Vol. 15, pp. 931–937.
- ²²R. Piessens, E. De Doncker-Kapenga, C. Uberhuber and D. Kahaner, *Quadpack, A Subroutine Package for Automatic Integration* (Springer, Berlin, 1983).
- ²³L. M. Brekhovskikh, *Waves in Layered Media* (Academic, New York, 1960), Chap 4.
- ²⁴L. B. Felsen and N. Marcuvitz, *Radiation and Scattering of Waves* (Prentice Hall, Englewood Cliffs, NJ, 1973).
- ²⁵D. E. Chimenti and A. H. Nayfeh, "Ultrasonic reflection and guided waves in fluid-coupled composite laminates," *J. Nondestruct. Eval.* **9**, 51–69 (1990).
- ²⁶A. H. Nayfeh and D. E. Chimenti, "Ultrasonic wave reflection from fluid-coupled orthotropic plates with application to fibrous composite," *J. Appl. Mech.* **55**, 863–870 (1988).
- ²⁷T. Kundu and A. K. Mal, "Acoustic material signature of a layered plate," *Int. J. Eng. Sci.* **24**, 1819–1829 (1986).
- ²⁸M. J. Lowe, "Ultrasonics in multilayered media," *IEEE Trans. Ultrason. Ferroelectr. Freq. Control* **42**, 525–542 (1995).
- ²⁹M. A. Awal and T. Kundu, "V(z) curve synthesis using two ultrasonic transducers," *ASME J. Appl. Mech.* **62**, 517–522 (1995).
- ³⁰S. I. Rokhlin and D. E. Chimenti, "Reconstruction of elastic constants from ultrasonic reflectivity data in a fluid coupled composite plate," *Review of Progress in Quantitative NDE*, edited by D. O. Thompson and D. E. Chimenti (Plenum, New York, 1990), Vol. 9, pp. 1411–1418.

A unified boundary element method for the analysis of sound and shell-like structure interactions.

II. Efficient solution techniques

Shaohai Chen and Yijun Liu^{a)}

Department of Mechanical Engineering, P.O. Box 210072, University of Cincinnati, Cincinnati, Ohio 45221-0072

Xinyu Dou

Acoustics Technology Center, Motorola, Inc., Schaumburg, Illinois 60196

(Received 23 March 2000; revised 15 September 2000; accepted 16 September 2000)

Efficient solution methods are investigated in this paper for solving the linear system of equations resulting from the recently developed boundary element method (BEM) for the coupled structural acoustic analysis [S. H. Chen and Y. J. Liu, *J. Acoust. Soc. Am.* **106**, Pt. 1, 1247–1254 (1999)]. An iterative solver, namely, the quasiminimal residual method (QMR), is selected among others and found to be very favorable over the direct solver for solving the linear systems of equations with complex coefficients generated by the structural acoustic BEM. Four problem-dependent preconditioning schemes are developed to facilitate or accelerate the convergence of the iterative solver. A new effective preconditioner specially designed for frequency-sweep analysis is also presented in this paper. With this preconditioner, the iterative solver has been found to be stable in a frequency-sweep analysis and can converge much faster than the direct solver. The double-precision arithmetic is also found very useful in improving the convergence rate of the iterative solver for structural acoustic problems. © 2000 Acoustical Society of America.

[S0001-4966(00)04512-4]

PACS numbers: 43.20.Fn, 43.20.Rz, 43.40.Rj [CBB]

I. INTRODUCTION

Recently, a unified boundary element method (BEM) was developed for the coupled analysis of acoustic waves interacting with thin, elastic, shell-like structures.¹ Numerical examples demonstrated that the unified BEM developed is very effective and accurate for the analysis of sound and shell-like structure interactions in both scattering and radiation problems. The method is valid for shell-like structures with arbitrarily small or nonuniform thickness, and does not suffer from the thin-shape breakdown and fictitious eigenfrequency difficulty in the exterior acoustic domain. It is the objective of this paper to improve the efficiency of the unified BEM developed by reducing the solution time of solving the linear system of equations generated. An iterative solver of the Krylov subspace type, that is, the quasiminimal residual (QMR) iterative method, is investigated, among others, and found to be very efficient in this type of application. Preconditioning techniques to improve the convergence are developed which include reordering of the mesh, scaling of the submatrices, and other special treatments designed for improving the characteristics of the matrix of the system. Besides these problem-dependent preconditioning techniques, a preconditioner specially designed for frequency-sweep analysis is also presented in this paper.

The iterative methods currently available for solving a linear system of equations $[A]\{x\}=\{b\}$ can be characterized

into two groups, namely, stationary and nonstationary iterative methods. The stationary iterative methods refer to iterative methods such as Jacobi, Gauss–Seidel, successive over-relaxation (SOR), and symmetric successive over-relaxation (SSOR). In general, the stationary iterative methods, if they converge, converge much slower than nonstationary methods.² The nonstationary methods include conjugate gradient (CG), conjugate gradient on the normal equations (CGNE), generalized minimal residual (GMRES), biconjugate gradient (BiCG), quasiminimal residual (QMR), conjugate gradient squared (CGS), biconjugate gradient stabilized (Bi-CGSTAB), Chebyshev iteration, and so on. All nonstationary iterative methods listed above except Chebyshev iteration are of the Krylov subspace type. The differences among them depend on how the basis for spanning the Krylov space is found and how the linear system is enforced in this space. A variety of convergence behaviors for these iterative solvers is therefore observed, although they are all closely related to the characteristics of the left-hand-side matrix $[A]$ and the right-hand-side vector $\{b\}$. CG is derived for symmetric positive definite linear systems, with its convergence rate depending on the condition number of $[A]$. BiCG is applicable to nonsymmetric systems and requires two matrix–vector multiplications (involving $[A]$ or its transpose $[A^T]$). The convergence behavior of BiCG is quite irregular and may suffer breakdowns. CGS is similar to BiCG and has no matrix–vector multiplication with $[A^T]$. It can converge faster than BiCG, although the convergence is still irregular and may be subject to the breakdown problem. BiCGSTAB

^{a)} Author to whom correspondence should be addressed. Electronic mail: Yijun.Liu@uc.edu

is an improved version of CGS designed to avoid the breakdown that often occurred in CGS while preserving the fast convergence rate. GMRES works on nonsymmetric systems directly and generates orthogonal vectors that form the basis spanning the Krylov subspace. Only one matrix–vector multiplication is required at each iteration. It minimizes the residual norm with exact arithmetic in each iteration and guarantees the convergence in less than n steps without restart (where n is the number of equations). Because the orthogonal vectors at each iteration have to be generated by using all the previously computed vectors, the storage requirement and computational effort tend to increase proportionally. In order to control the storage requirement, restarts after a certain number of iterations are often needed. QMR is applicable to both symmetric and unsymmetric matrices with real or complex elements. It requires two matrix-vector multiplications per iteration, both with $[A]$ and $[A^T]$. Instead of forming the exact orthogonal vectors as in GMRES, it generates a biorthogonal basis for the Krylov subspace by using the Lanczos process with short recurrences. Two recurrence schemes, three-term and coupled two-term, have been developed. A look-ahead Lanczos algorithm has been employed to extend QMR to general non-Hermitian matrices and avoid the possible breakdowns in some cases. Smooth convergence behavior can be observed for QMR in general. A FORTRAN package, QMRPACK,³ has been developed, which contains all the QMR algorithms. It should be noted that a transpose-free version of the QMR, TFQMR, has also been developed and added to the QMRPACK. For a complete review on solving linear system with iterative solvers, please refer to Refs. 2 and 4 and the references therein.

The convergence behavior of iterative solvers varies for different types of applications. For a particular type of problem, an iterative solver may or may not converge, or converge more slowly than direct solvers. A suitable preconditioning scheme can greatly improve the situation. Intensive research efforts have been directed to address the suitable iterative solvers for all the existing applications and the corresponding preconditioning schemes. As long as a competitive iterative solver and a suitable preconditioning scheme can be identified for a particular problem, high efficiencies in solving the linear system of equations can be expected over direct solvers.

Generic preconditioning involves finding an economically invertible matrix (often referred to in the literature as a *preconditioner*), and applying the inverse of that matrix through multiplication to the original linear system for a new linear system which has a coefficient matrix with more favorable characteristics. Clearly, it is desirable that the preconditioner resembles $[A]$, as the new coefficient matrix would be close to an identity matrix. The matrix–matrix multiplication is never computed explicitly but integrated into the iterative process, where the factorization of the preconditioning matrix is formed once, and only forward and backward substitution processes are needed for all iterations. The existing generic preconditioning schemes include diagonal preconditioning, block diagonal preconditioning, SSOR preconditioning, incomplete LU decomposition (ILUD), and so on. Diagonal preconditioning employs only the diagonal

terms of $[A]$ to form the preconditioner. It is the simplest, but often quite effective for some applications. The block preconditioner is similar to the diagonal preconditioner but formed by the small blocks on the diagonal direction of $[A]$. The SSOR preconditioner is formulated from the diagonal, lower, and upper triangular parts of $[A]$. A special case of the SSOR preconditioner is the diagonal preconditioner. Although applying the SSOR preconditioner is relatively inexpensive, it is unlikely to obtain a preconditioner closely resembling $[A]$, which is the key feature of a good preconditioner. The ILUD preconditioner is formed by dropping off the nonzero elements in the factorization of $[A]$ in positions where $[A]$ has zeros. This preconditioning scheme is often very effective. The drawback, besides the memory consumption, is the long computing time needed even when $[A]$ is sparse. As a BEM formulation usually generates a fully populated matrix, this preconditioning scheme is not feasible. Preconditioning can also be performed in the process of forming the linear system, which is problem dependent. This is often more effective and economical than generic preconditioning. Some preconditioning schemes of this kind are presented in this paper and shown to be effective for the coupled sound thin-shell interaction problems considered, although with all the preconditioning schemes ever developed, the iterative solution methods in general are considered to be less stable than direct solution methods. This situation may have been changed with a preconditioning scheme developed in this paper for problems requiring frequency-sweep analysis.

To the authors' best knowledge, no applications of iterative solvers for frequency-dependent problems, using the BEM have been reported in the literature. For static problems, such as elastostatic and potential problems, the performance of the iterative solvers in solving linear system of equations generated by the BEM have been reported.^{5–8} In Ref. 5, CGN and GMRES were applied to 2D elastostatic problems with the use of diagonal, block diagonal, and ILUD preconditioners. Example problems with degrees of freedom up to 488 were tested using double-precision arithmetic with residual norm of 10^{-6} as the stopping criterion. The preconditioned GMRES was found to be faster than the direct solver in general, while CGN was found not as fast with or without preconditioners. In Ref. 6, GMRES, CGS, BiCGSTAB, and CGN with diagonal and block diagonal preconditioners were tested on small thermal and elastic problems with 2D and 3D geometries. The largest 3D model used for the elastostatic analysis contains 541 nodes. Stopping criterion in the form of residual norm was set as 10^{-6} (10^{-7} in some cases) and 10^{-4} for elastic and thermal problems, respectively. GMRES with diagonal preconditioning was shown to be significantly faster than the direct solver and was the most effective solver among other iterative solvers tested. CGS and BiCGSTAB were also found faster than the direct solver when used with diagonal preconditioning. In Ref. 7, the comparison of a number of iterative solvers was performed using two linear systems (with 250 and 1000 equations) generated by the BEM for a 2D potential problem. Four different types of matrices, two from the conventional boundary integral equation (BIE) and the other two

from the hypersingular BIE, were considered. GMRES with no restart, BiCG, and QMR outperformed other iterative schemes such as CG, CGS, CGN, and BiCGSTAB, when no preconditioning schemes were considered for all the algorithms. All the iterative algorithms were in general faster than direct methods, even with very stringent stopping criterion (10^{-10}). In Ref. 8, a reorthogonalization scheme with double-precision arithmetic was adopted to generate more accurate basis vectors for GMRES, which was then used to solve a relatively large linear system (up to 4902 equations) resulting from the BEM for 3D elastostatic problems. The solution time in the case of 4902 equations was more than five times faster than that of a direct solver, even with a stringent stopping criterion (10^{-7}). The non-restart version of GMRES was used in Ref. 8.

For dynamic analyses formulated in the BEM, QMR is a very good candidate among all the iterative solvers as it is applicable to unsymmetrical matrices with complex elements and less prone to numerical breakdowns. In this paper, the feasibility and efficiency of the iterative solver QMR in solving the linear system resulting from a BEM formulation of a frequency-dependent coupled structural acoustic problem are demonstrated. In the following, the stopping criterion used in QMR for BEM applications is justified first. The performance of QMR is then demonstrated by a pure acoustic application formulated in the BEM. The preconditioning schemes developed in this paper are then described in detail and tested. Finally, the comparison of the direct solver (LAPACK) and the iterative solver QMR for solving the linear system resulting from the BEM formulation for a coupled sound–structure interaction problem is presented using the testing cases.

II. THE ITERATIVE SOLVER FOR THE STRUCTURAL ACOUSTIC BEM

The detailed formulation of the unified boundary element method for analyzing the coupled sound–structure interaction problem has been presented in Ref. 1. The two sets of ordinary differential equations corresponding to the acoustic field and the elastic field in the frequency domain are recast into two sets of boundary integral equations (BIEs), which are coupled by the interface conditions defined on the wet surface of the elastic structure. After the discretization of the two BIEs on the surfaces of the structure, a linear system of equations $[A]\{x\}=\{b\}$ is obtained, which has the following structure:

$$\begin{bmatrix} H & D & 0 \\ E_a & T_{aa} & T_{ab} \\ E_b & T_{ba} & T_{bb} \end{bmatrix} \begin{Bmatrix} \Phi \\ u_a \\ u_b \end{Bmatrix} = \begin{Bmatrix} \Phi' \\ -U_{ab}t_b \\ -U_{bb}t_b \end{Bmatrix}, \quad (1)$$

where $\{\Phi\}$ and $\{u\}$ are vectors that account for the total disturbed acoustic pressure and displacement at the nodes, respectively; $[H]$ and $[T]$ are square submatrices resulting from the singular kernel of the BIE for acoustic field and elastodynamic field, respectively; $[D]$ and $[E]$ are rectangular submatrices obtained after applying the interface conditions; the subscripts a and b denote the outer (wet) surface and the inner (dry) surface, respectively; $\{\Phi'\}$ and $\{t_b\}$ are known

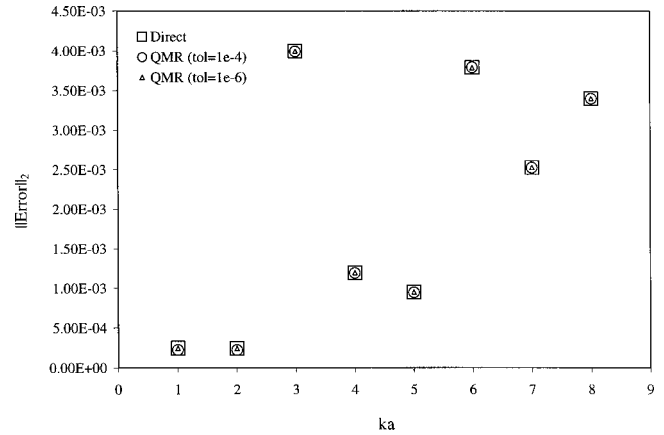


FIG. 1. Error level for the radiation analysis of a pulsating sphere (DOF = 290).

vectors resulting from the incident wave and traction on the inner surface, respectively. Please refer to Ref. 1 for the derivation of (1).

In this paper, the performance of the iterative solver QMR in solving linear systems of complex equations resulting from the BEM, as shown in Eq. (1), is investigated. The QMR algorithm based on the coupled two-term variant of the look-ahead Lanczos process³ is used. The iterative solver is considered converged when the relative residual norm is less than a preset value (often referred to as tolerance). The relative residual norm is defined as

$$\frac{\|r_n\|_2}{\|r_0\|_2} = \frac{\|Ax_n - b\|_2}{\|Ax_0 - b\|_2}, \quad (2)$$

where $\{x_n\}$ is the solution vector at the end of the n th iteration, $\{x_0\}$ the initial guess (usually set as a zero vector), $\{r_n\}$ the residual vector and $\|\cdot\|_2$ the Euclidean norm. The preset tolerance has to be small enough so that reliable results can be obtained, but not so small that computation efforts are wasted.

The proper value of the tolerance was studied numerically using the radiation problem of a pulsating sphere (no coupling with elastic structure), for which the analytical solution is available. A mesh consisting of quadratic elements with 290 nodes was generated over the surface of a unit sphere for this purpose. The corresponding linear systems formed after the discretization of the BIEs were solved using both direct solver and iterative solver. The error with respect to the analytical solution was calculated in the Euclidean norm

$$\|\text{Error}\|_2 = \frac{\|x - X\|_2}{\|X\|_2}, \quad (3)$$

where $\{X\}$ represents the analytical solution, $\{x\}$ the solution resulting from the BEM using direct solver or iterative solver. The error levels at eight frequencies from using direct solver and QMR with two stopping tolerances (10^{-4} and 10^{-6}) are shown in Fig. 1. It can be seen that the direct solver and QMR achieved virtually the same level of accuracy over all eight frequencies. The error level is in general increasing toward higher frequencies, due to the fact that there are fewer elements within one wavelength. Higher er-

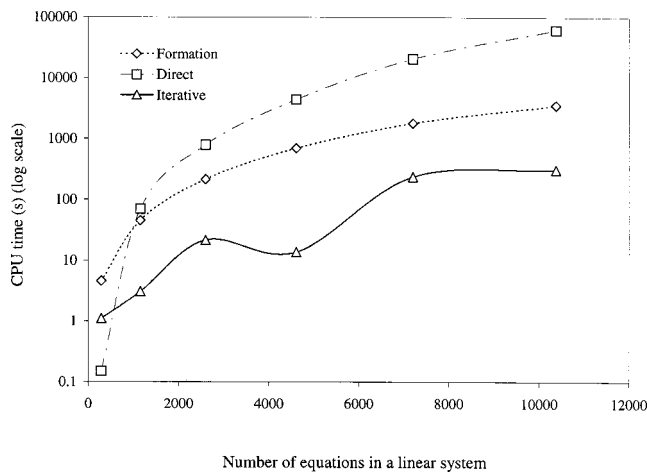


FIG. 2. CPU time consumption for the radiation analysis of a pulsating sphere.

ror levels are observed at $ka=3$ and 6 , which are in the vicinity of the fictitious eigenfrequencies π and 2π , due to the adverse matrix characteristics although unique solutions have been guaranteed by Burton and Miller's formulation (which employs the hypersingular BIE). Since the round-off error (on the order of 10^{-4}) is small relative to the discretization error (on the order of 10^{-3}), solving the linear system more exactly (reducing round-off error) cannot render a more accurate result as compared to the analytical solution (reducing the discretization error). This fact is also supported by the results from the iterative solver. With the stopping criterion set as 10^{-4} , the iterative solver achieved the same level of accuracy as the direct solver (compared to the analytical solution). The solution resulting from using 10^{-6} as the tolerance gave trivial improvement in the accuracy with respect to the analytical solution (Fig. 1), while consuming three times more solution time. The stopping criterion is therefore set as 10^{-4} for all the following test cases, since errors in the 10^{-4} level are acceptable for most engineering purposes. Higher levels of accuracy can only be achieved by using finer meshes to reduce the discretization errors. It was observed that QMR is not free of breakdowns. In fact, when the tolerance was set as 10^{-6} , the iterative solver suffered abnormal termination before it reached the stopping tolerance at $ka=3$. This breakdown was not encountered when double precision was used (Fig. 1), as the direction vectors can be further refined in double-precision arithmetic.

III. PURE ACOUSTICS ANALYSIS—TEST RESULT

The iterative solver was first tested with pure acoustic problems, i.e., without the coupling with structures. The conventional BIE for the same pulsating sphere problem described in the previous section was discretized using six different meshes with the total number of nodes as: 290, 1154, 2594, 4610, 7202, and 10370. The highest frequency feasible for each mesh ($ka=8, 16, 24, 32, 40$, and 48 , respectively) was employed in obtaining the corresponding CPU time consumption. Single-precision arithmetic was used for all six cases. The saving in CPU time by using the iterative solver over direct solver is illustrated in Fig. 2. All data were

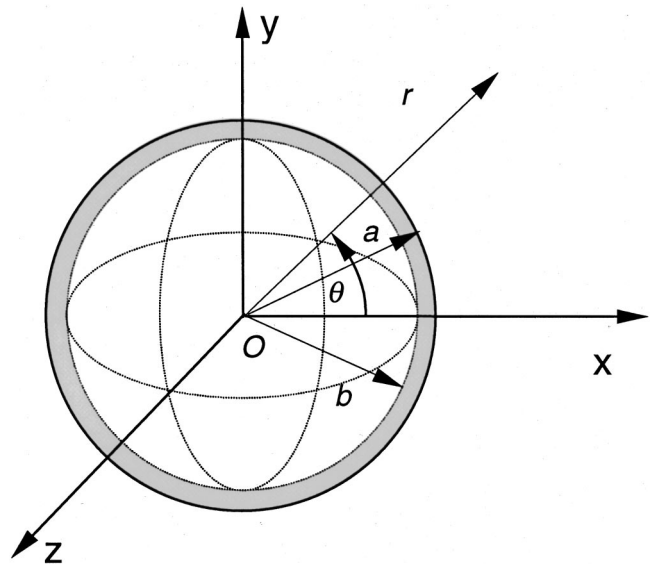


FIG. 3. A spherical shell with uniform thickness (outer radius= a , inner radius= b , thickness= $h=a-b$).

obtained on a Pentium II PC (400 MHz, 256 MB RAM) with WINDOWS NT operating system. An estimated value of the CPU time consumption of the direct solver for the case with the largest mesh was used since the CPU time was too long (estimated over 10 days of clock time) for the direct solver. The ratio between the time consumed by direct solver and that by iterative solver increases as the problem size increases. For the case with 7202 nodes, the iterative solver was 86 times faster than the direct solver. It should be noted that the CPU time consumption of the iterative solver is less for 4610 degrees of freedom than for 2594 degrees of freedom, as the iterative solver is sensitive to the conditioning of the system. The iterative solver was applied without using any preconditioning schemes in this pure acoustic case. From this test, the CPU time savings in solving the acoustic BEM equations using the iterative solver QMR are evident.

IV. COUPLED STRUCTURAL ACOUSTICS ANALYSIS—FIVE PRECONDITIONING SCHEMES

For the coupled problem, the linear system of equations (1) has very high condition numbers in general due to the mismatch of the materials (structure and fluid). A special partitioning scheme has to be used for the direct solver to obtain reliable solutions. The solution time can also be dramatically reduced by using the iterative solver, but not without the help of preconditioning. The three existing preconditioners available in the literature (the diagonal, the block-diagonal, and the SSOR preconditioners) were tested and found not working for the applications considered. Therefore, five new preconditioning schemes are developed in this study. They will be referred to as scheme 1, 2, 3, 4, and 5 in the following sections. A steel spherical shell (Fig. 3) immersed in water will be used as the test case for the first four preconditioning schemes. The dimension of the shell is $a = 1\text{ m}$, $h/a=0.01$, where a is the outer radius and h is the thickness.

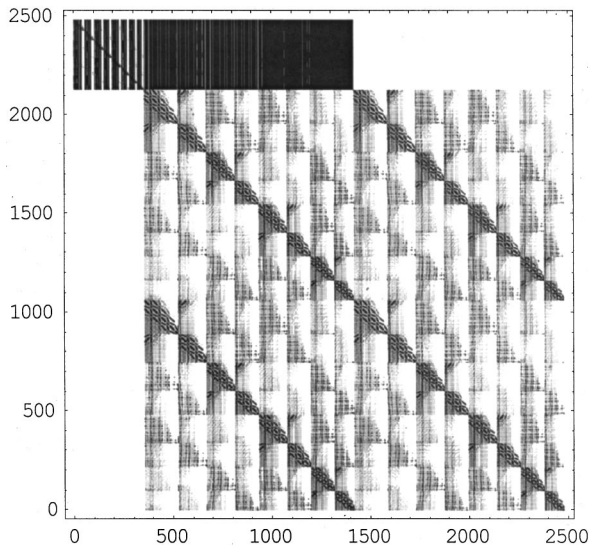


FIG. 4. Image of matrix $[A]$ before applying any of the four preconditioning schemes.

Scheme 1 reorders the nodes on the outer (wet) surface of the structure, which are used for the discretization of the acoustic BIE. This scheme is aimed at providing a suitable numbering of the nodes in the mesh to place all the dominant entries (i.e., with larger absolute values) of the matrix as close as possible to the main diagonal. Specifically, the nodes in the vicinity of every single node in the mesh will be assigned node numbers close to the node number of that node by an algorithm calculating and comparing the distance between nodes. Figures 4 and 5 show the image of the coefficient matrix $[A]$ resulting from the spherical shell model before and after applying scheme 1, respectively. The larger the absolute value of an entry, the darker the dot shown in the image. It can be seen in Fig. 4 that the $[H]$ and $[D]$ submatrices dominate matrix $[A]$ with very large entries distributed all over these submatrices. The $[E_a]$ and $[E_b]$ submatrices consist of very small entries (shown as a nearly white area in the image). The $[T_{aa}]$, $[T_{ab}]$, $[T_{ba}]$, and $[T_{bb}]$ submatrices in $[A]$ result from the singular integral operator

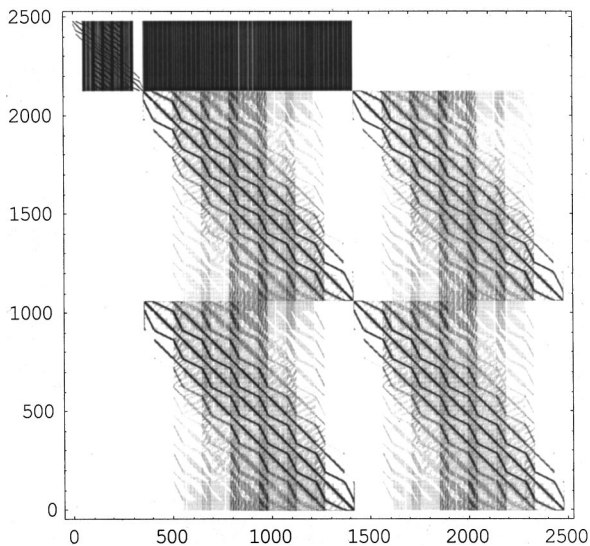


FIG. 5. Image of matrix $[A]$ after applying preconditioning scheme 1.

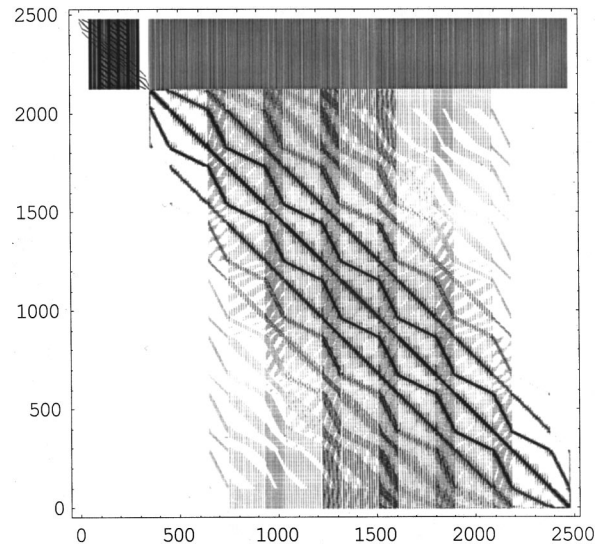


FIG. 6. Image of matrix $[A]$ after applying preconditioning schemes 1 and 2.

for the elastic domain. The diagonal dominant phenomenon is evident in each of the four submatrices, although $[T_{ab}]$ and $[T_{ba}]$ can't contribute to the overall diagonal dominance of $[A]$. Figure 5 shows the image of the same coefficient matrix after applying scheme 1. Significant changes can be observed in submatrices $[H]$, $[T_{aa}]$, $[T_{ab}]$, $[T_{ba}]$, and $[T_{bb}]$.

Scheme 2 involves reordering of all the nodes on the two structure surfaces for the discretization of the elastodynamic BIE. This reordering scheme is motivated by the fact that when the thickness of the shell gets smaller, the matrix entries with contributions from the nearly singular integrals become larger. It is therefore desirable to place these entries closer to the main diagonal by reordering the nodes. Figure 6 shows the coefficient matrix after applying schemes 1 and 2. The entries of the zero block of the primitive matrix are now mixed with the entries of the $[D]$ submatrix. It is evident that the $[T_{aa}]$, $[T_{ab}]$, $[T_{ba}]$, and $[T_{bb}]$ submatrices are now contributing toward the overall diagonal dominance of $[A]$. Because of the coupling process of the two domains, the matrix is again extremely unbalanced with $[D]$ featuring very large entries, while $[E_a]$ and $[E_b]$ consist of very small entries.

Scheme 3 is designed to render a better scaling of the coefficient matrix $[A]$. Because of the mismatch of the two domains with quite different material properties, the entities in $[D]$ are much larger than those in $[E]$. This kind of unbalance among entities in a system matrix results in a very high condition number. A scaling factor related to material properties is used to provide a better scaling. Figure 7 shows the resulting matrix after applying schemes 1, 2, and 3. The matrix is now evidently diagonally dominant with a very clear pattern except for the $[H]$ submatrix.

Scheme 4 is designed to further improve the characteristics of $[A]$ by utilizing the inverse of $[H]$, which is obtained by the direct method. This preconditioning scheme is more expensive than the previous three. However, the resulting coefficient matrix $[A]$ (Fig. 8) has better characteristics that often reduce the total solution time (including the time used for obtaining the inverse of $[H]$). This is due to the further

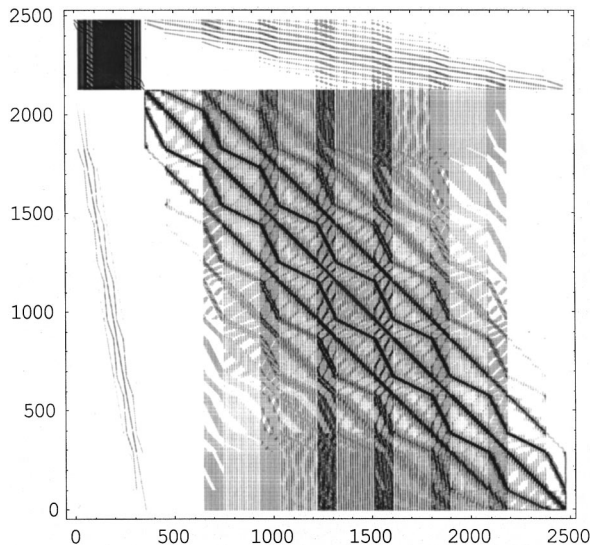


FIG. 7. Image of matrix $[A]$ after applying preconditioning schemes 1, 2, and 3.

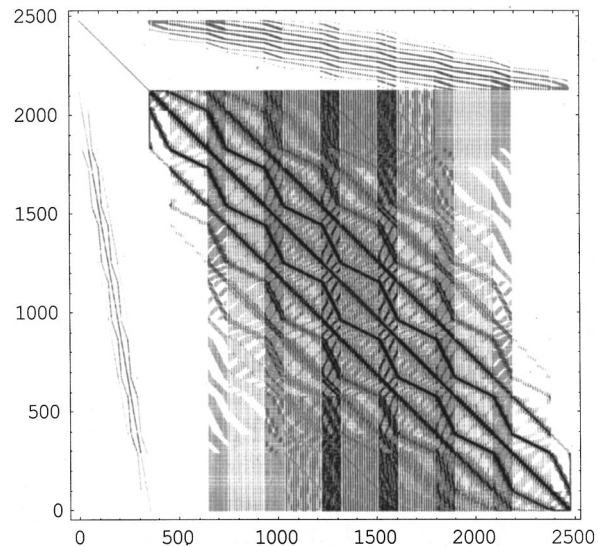


FIG. 8. Image of matrix $[A]$ after applying preconditioning schemes 1, 2, 3, and 4.

reduction in the condition number of $[A]$, as demonstrated in the following test cases.

In practice, a dynamic problem often needs to be solved for many frequencies. Scheme 5 is specially designed for this kind of application. It is found that the coefficient matrix $[A]$ at the first frequency in a frequency sweep can serve as a perfect preconditioner for all the subsequent frequencies. As all the system matrices for different frequency cases result from the same geometry and boundary conditions, they resemble each other. Any one of them can be used as a preconditioner for all the other cases. With the help of this preconditioner, a frequency sweep for a dynamic problem can be performed very efficiently using the iterative solver. The inverse of this preconditioner is never computed explicitly. Instead, a more economical process, the LU factorization, is performed and the result is stored. The matrix–vector multiplication involving the preconditioner in each iteration step is then obtained by one forward and one backward substitution, which consume the same amount of computation effort as that of a direct matrix–vector multiplication. The matrix–vector multiplication involving the transpose of the preconditioner presents no extra computing effort. As the time consumed by each of the consecutive frequency cases can be dramatically reduced by using the iterative solver, the overall time consumption for the frequency sweep can be much less than that by using the direct solver for every frequency. The

more frequencies are involved in a frequency sweep, the more saving in CPU time can be expected. The significance of this scheme is that the iterative solver can converge much faster than the direct solver and provide the efficiency in frequency-sweep analyses.

V. COUPLED STRUCTURAL ACOUSTICS ANALYSIS—TEST RESULTS

The effectiveness of the first four preconditioning schemes in accelerating the convergence of the iterative solver was tested first. Three different meshes for the spherical shell (Fig. 3) with 64, 256, and 576 quadratic elements, which yield 574, 2478, and 5726 equations in the final linear system, respectively, were used. Ten test cases representing all the interesting scenarios were performed using the mesh with 256 elements on the Pentium II PC. Results from five of the ten cases (case 1 with no preconditioning; case 2 with preconditioning scheme 1; case 3 with preconditioning schemes 1 and 2; case 4 with preconditioning schemes 1, 2, and 3; and case 5 with preconditioning schemes 1, 2, 3, and 4) are shown in Table I. It was found that with the application of all the four preconditioning schemes (case 5), the iterative solver converged at the fastest rate among all the test cases. The condition number of the original matrix dropped from the order of 10^8 to the order of 10^4 . The corresponding CPU time consumption of the iterative solver is

TABLE I. The effectiveness of the preconditioning schemes. Note: o—not applied; \checkmark —applied; SP—single precision; DP—double precision.

	Scheme 1	Scheme 2	Scheme 3	Scheme 4	Number of iterations		CPU time (s)	
					SP	DP	SP	DP
Case 1	o	o	o	o	>1000	>1000
Case 2	\checkmark	o	o	o	>1000	932
Case 3	\checkmark	\checkmark	o	o	>1000	933
Case 4	\checkmark	\checkmark	\checkmark	o	355	58
Case 5	\checkmark	\checkmark	\checkmark	\checkmark	190	47	425.83	196.15

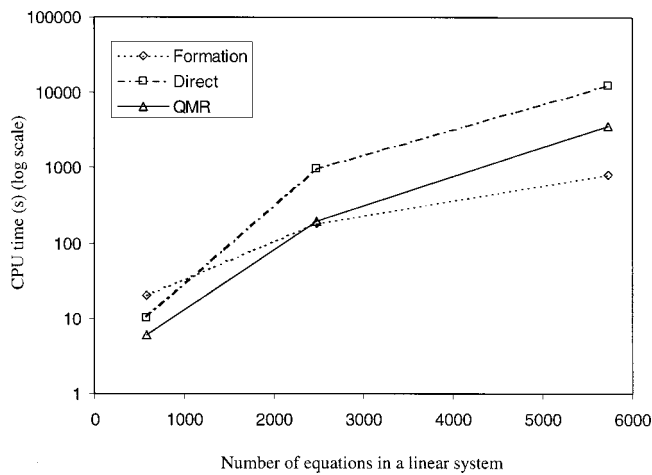


FIG. 9. CPU time consumption for the coupled radiation analysis of a steel spherical shell ($h/a=0.01$).

425.83 s and 196.15 s, compared to 581.38 s and 972.62 s consumed by the direct solver, for single-precision and double-precision arithmetic, respectively. The saving in solution effort rendered by the iterative solver over the direct solver is clearly demonstrated in this coupled analysis, especially in the case of double precision (about five times faster than the direct solver). To show the consistency of this approach, two additional tests were performed on the same spherical shell with the other two meshes using the four preconditioning schemes with double-precision arithmetic. The comparison of CPU time consumption of direct solver and QMR for all the three meshes are shown in Fig. 9. The formation time is also plotted as a reference. The effectiveness of the first four preconditioning schemes is evident.

To demonstrate the effectiveness of scheme 5 for the frequency-sweep analysis, a submarine-like model (Fig. 10) was studied next. The length of the submarine-like model is 7 m, main radius 0.5 m, and the thickness of the shell 0.01 m. The result from the iterative solver with the first four preconditioning schemes could not render fast convergence for this slender submarine-like model in the coupled analysis. With scheme 5, however, a stable result was obtained for the frequency-sweep analysis. The BEM model used in this

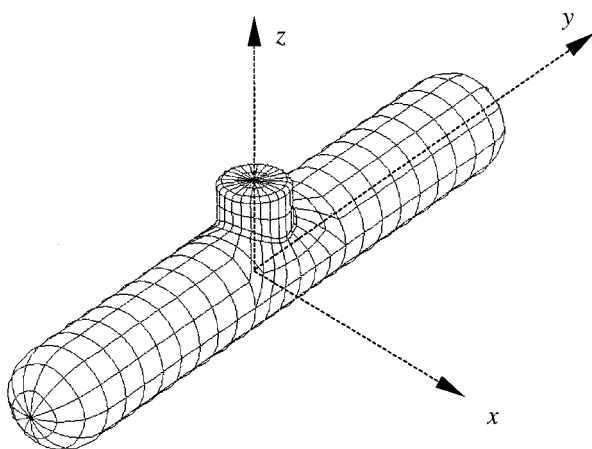


FIG. 10. A submarine-like model (main radius=0.5 m, total length=7 m, and thickness=0.01 m).

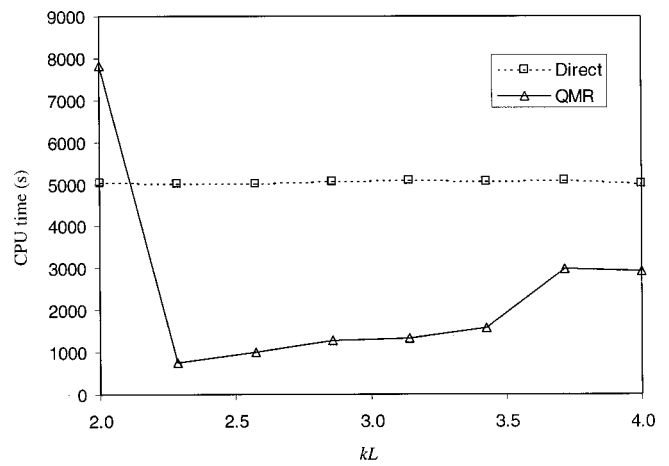


FIG. 11. Comparison of CPU time consumption at each frequency for a scattering problem on the submarine-like model using QMR and direct solver.

study consists of 416 quadratic elements and 1188 nodes. The structure is immersed in seawater and impinged upon by a plane incident wave in the positive x direction. With the use of all the first four preconditioning schemes, the iterative solver could not even come close to convergence in 600 iterations, twice as much time as the direct solver would consume. This extremely slow convergence rate was dramatically changed by using the preconditioner in scheme 5. A frequency sweep over 8 frequencies from $kL=2$ to $kL=4$ was performed for demonstration purpose (L is the total length of the model).

Figure 11 shows the CPU time consumption by using QMR for each frequency case in the frequency sweep, as compared to the direct solver. The preconditioning schemes 1, 2, 3, and 5 were used. Besides the first frequency case, where the LU factorization of the preconditioner was performed, a great deal of savings in CPU time was achieved for all the subsequent cases. It can be seen in Fig. 11 that the preconditioner performed better when the frequency at which the calculation was conducted was closer to the frequency at which the preconditioner was generated. The reason is quite obvious, as the system matrix obtained after preconditioning would be closer to the identity matrix, when the two frequencies are closer to each other. In light of this fact, better performance can be expected when the preconditioner is generated at the middle frequency of a frequency span. The condition number of the resulting linear system (with 4158 unknowns) after applying schemes 1, 2, and 3 is on the order of 10^6 . Scheme 4, which is the most costly one among the first four schemes, is found unnecessary when the preconditioner provided by scheme 5 is used. Since fast convergence is ensured by the preconditioning schemes, the CPU time consumption at each frequency can be much less than that of a direct solver. The more frequency steps in the frequency-sweep analysis, the more savings in CPU time can be achieved in the solution process. The forward-scattering and back-scattering results of the coupled analysis using QMR and the direct solver are compared in Figs. 12 and 13, respectively. The results from pure acoustic analysis (considering the structure as rigid and stationary) are also plotted as

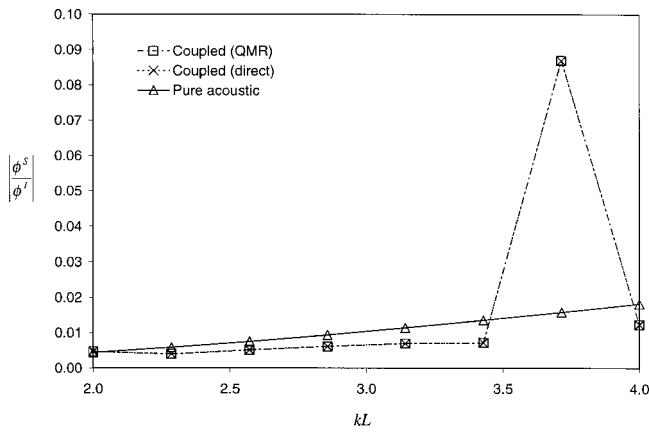


FIG. 12. Forward-scattering result at point (35, 0, 0).

a reference. The consistency between the results from QMR and the direct solver again demonstrates the efficiency and reliability of the iterative solver, and the sufficiency of using 10^{-4} as the stopping tolerance for the QMR solver.

More sophisticated numerical tests, for example those involving nonuniformly applied loads, at higher frequencies or larger models, need to be studied to further fine-tune the iterative solver for the analysis of coupled structural acoustic problems using the BEM.

VI. CONCLUSION

Effective solution schemes for the applications of the unified BEM to coupled sound and thin-shell structure interaction problems have been studied. An iterative solver, namely, the quasiminimal residual method (QMR), was se-

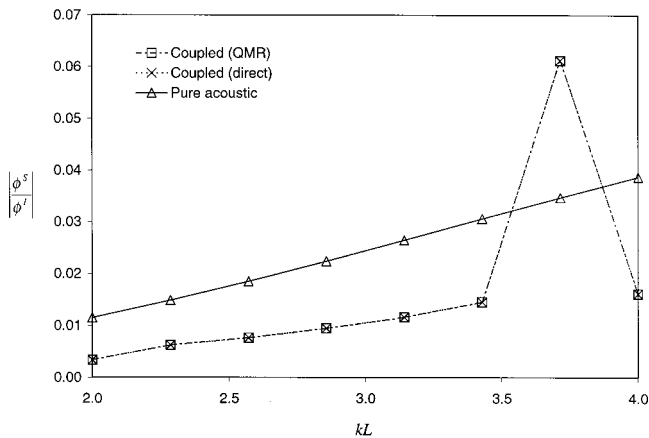


FIG. 13. Backward-scattering result at point (-35, 0, 0).

lected among others and found to be much more efficient compared to the direct solver in solving the linear systems of equations with complex coefficients generated by the structural acoustic BEM. Four problem-dependent preconditioning schemes are developed to accelerate the convergence of the iterative solver. Double-precision arithmetic is also very useful in improving the convergence rate.

In addition, an effective preconditioner (scheme 5) specially designed for frequency-sweep analysis is presented. With this preconditioner, the iterative solver has been found to be stable in a frequency-sweep analysis. The scheme ensures convergence, and the CPU time consumption is much less than that of the direct solver in the case studied in this paper.

To further improve the efficiency of the developed BEM in analyzing even larger structural acoustic problems, methods to reduce the CPU time in the formation of the coefficient matrices should be explored. The formation time has been shown to become dominant in the whole BEM process with the use of the iterative solver (see, e.g., Fig. 2). This reduction can be achieved by using, for example, the multipole expansion method (see, e.g., Ref. 9) emerging recently in the BIE/BEM.

ACKNOWLEDGMENTS

The first two authors (S.H.C. and Y.J.L.) would like to acknowledge the partial support to the University of Cincinnati from Motorola, Inc. for this project. The authors thank the reviewers of this paper for their helpful comments.

- ¹S. H. Chen and Y. J. Liu, "A unified boundary element method for the analysis of sound and shell-like structure interactions: I. Formulation and verification," *J. Acoust. Soc. Am.* **106**, 1247–1254 (1999).
- ²R. Barrett, M. Berry, T. F. Chan, J. Demmel *et al.*, *Templates for the Solution of Linear Systems: Building Blocks for Iterative Methods*, 2nd ed. (SIAM, Philadelphia, 1994).
- ³R. W. Freund and N. M. Nachtigal, "QMRPACK: a package of QMR algorithms," *ACM Trans. Math. Softw.* **22**, 46–77 (1996).
- ⁴G. H. Golub and C. F. V. Loan, *Matrix Computations* (Johns Hopkins University Press, Baltimore, 1983).
- ⁵J. H. Kane, D. E. Keyes, and K. G. Prasad, "Iterative solution techniques in boundary element analysis," *Int. J. Numer. Methods Eng.* **31**, 1511–1536 (1991).
- ⁶K. G. Prasad, J. H. Kane, D. E. Keyes, and C. Balakrishna, "Preconditioned Krylov solvers for BEA," *Int. J. Numer. Methods Eng.* **37**, 1651–1672 (1994).
- ⁷J. E. Romate, "On the use of conjugate gradient-type methods for boundary integral equations," *Comput. Mech.* **12**, 214–232 (1993).
- ⁸C. Y. Leung and S. P. Walker, "Iterative solution of large three-dimensional BEM elastostatic analyses using the GMRES technique," *Int. J. Numer. Methods Eng.* **40**, 2227–2236 (1997).
- ⁹V. Rokhlin, "Rapid solution of integral equations of scattering theory in two dimensions," *J. Comput. Phys.* **86**, 414–539 (1990).

A variational method for identification of viscoelastic parameters from experimental data

Alberto Di Meglio^{a)}

European Organization for Nuclear Research (CERN), Route de Meyrin, 1211 Geneva 23, Switzerland

Lian Sheng Wang^{b)}

School of Electronic & Electrical Engineering, The University of Birmingham, Edgbaston, Birmingham B15 2TT, United Kingdom

(Received 23 December 1999; revised 20 August 2000; accepted 9 September 2000)

An identification method based on a variational algorithm is proposed for the determination of the viscoelastic properties of plates from a set of experimental data. A pulse-transmission configuration with parametric sources is used for the experimental measurements, whereby two electrically mixed high-frequency pulses are combined to generate a low-frequency, narrow-beam signal to minimize the edge-diffraction effect from a finite-sized panel. The variational method is based on an optimization technique adapted from an approach normally used in dynamics for the identification of motion parameters. The fluid–panel–fluid system is initially represented by a transmission matrix model. The model and the known experimental data are then used to build an optimization functional to be minimized by means of a collocation method based on the Hamilton principle analogy. The plate viscoelastic parameters are then calculated by application of well-established numerical procedures to the resulting set of integral-differential equations. © 2000 Acoustical Society of America. [S0001-4966(00)02312-2]

PACS numbers: 43.20.Ye, 43.30.Ky, 43.35.Mr [ANN]

I. INTRODUCTION

Amplitude and phase of the scattered acoustic field vary considerably at different frequencies with the material properties of a scatterer. These properties include the geometry and the physical constitutive parameters of the material.

In order to characterize completely the mechanical properties of viscoelastic materials, 36 frequency-dependent, complex parameters are necessary in the most general case, although the number of parameters can be reduced by using the appropriate hypothesis on the materials such as isotropy and homogeneity and other constitutive relationships such as the relation among bulk modulus, shear modulus, and Poisson ratio.

Determination of these parameters is often performed by means of inversion methods from laboratory measurements of scattered acoustic field. Applications of this method can be found, for example, in the works of Piquette¹ for the complex dynamic bulk modulus of elastomers; Simmonds and Humprey² for the dynamic plate modulus by measurements in the impedance tube; W. F. Zong *et al.*³ for elastic wave and Lamé parameters reconstruction. The inversion problem, however, can become intractable in the presence of too many unknowns or imprecisely known quantities.

A different approach to the problem is given by “curve fitting” experimental data and model data to obtain a compatible set of material properties.

One of the best-known methods based on this principle has been presented by Piquette.⁴ The method, called ONION,

is based on the simultaneous least-square fitting of reflected and transmitted wave data and produces excellent results for thick panels. A minor inconvenience of the method is that it is noncausal, since the model used to fit the data treats the loss as frequency dependent, but assumes that the sound speed is frequency independent.

The purpose of this paper is to describe a different approach to the determination of viscoelastic parameters from best fitting of experimental data. The identification problem is reduced to an optimization problem that can be solved in a best-fit sense. All the parameters are treated as frequency dependent, which render the method consistent with the causality principle.

The method is based on the so-called Hamilton principle analogy used in mechanics to determine the optimal motion of continuous systems in the presence of noise and unknown parameters.⁵ An optimization functional with unknown parameters is built in the form of a pseudo-Hamiltonian function and is solved by collocation in the proper integration interval. The pseudo-Hamiltonian function has the form of a Hamiltonian function, but not necessarily the same physical meaning as in mechanics. The method allows building a set of integral equations in the desired number of unknowns that can then be solved numerically.

In this paper, a set of panels made of loaded butyl rubber is analyzed. The acoustic properties of the panels, namely echo reduction and insertion loss, are measured as varying functions of frequency and angle of incidence. The proposed identification method is then applied and the viscoelastic response functions are determined in the given frequency range.

Readers not familiar with numerical collocation techniques can consult the references for more detailed explanations.⁶

^{a)}Electronic mail: alberto.di.meglio@cern.ch

^{b)}Present address: SACLANT Undersea Research Center, Viale S. Bartolomeo, 400, 19138 La Spezia, Italy. Electronic mail: wang@saclantc.nato.int

TABLE I. Chemical formulation of uncured butyl rubber base (phr).

Unvulcanized butyl rubber	ISO 2302 ASTM D 3188
Butyl	100
IRB 6	50
Zinc oxide (NBS 370)	3
Stearic acid (NBS 372)	1
Sulphur (NBS 371)	1.75
TMTDS (IRM 1)	1

II. THE VISCOELASTIC MATERIAL

The viscoelastic material used for the experimental tests is a loaded butyl rubber compound. The base butyl rubber was supplied by Exxon Chemicals Ltd. as a white, uncured rubber bale. The rubber was compounded in a low-speed milling machine, adding fillers to modify its mechanical properties.¹ It was then calendered and vulcanized to form a set of black plane panels of density ranging from 1000 to 2200 kg m⁻³. The chemical formulations can be found in Tables I and II.⁷

III. THE EXPERIMENT CONFIGURATION

A pulse, single-transmission configuration has been used for the experiments.

One limitation of this type of ultrasonic immersion methods is that high-frequency sources must be used to limit the beamwidth of the source and avoid edge-diffraction effects from limited size panels. In addition, a large number of transducers must be employed if a useful frequency range has to be covered. A method of overcoming both this limitations is the use of a parametric source.

As first proposed by Westervelt,⁸ two high-frequency primary sound waves are used to produce a low-frequency secondary sound wave as an effect of nonlinearity in the propagation. The low-frequency secondary source is the difference between the two main primaries and its -3-dB beamwidth is of the same order of magnitude as the -3-dB beamwidth of the high-frequency primary sources.⁹ In addition, by varying the two primary sources inside the range of useful bandwidth of the transducer, a large frequency bandwidth can be produced as a difference without the need to use a complete set of different transducers.¹⁰

TABLE II. Chemical formulation of vulcanized butyl rubber sheets (phr).

Vulcanized butyl rubber	
Butyl 365	100.00
Stearic acid	0.50
Silica (Hard clay)	variable proportion to obtain desired density
Calcium carbonate	40.00
Zinc oxide	5.00
Polyethylene	6.00
Paraffin wax	4.00
S-315 carbon black	10.00
DMF	6.00
(p. quinanedioxime)	
Red lead (Pb3O4)	9.00
Sulphur	0.80

TABLE III. Electroacoustic transducer parameters.

Transducer parameters	Value
Resonance frequency	1.08 MHz
Q-factor	3.6
Efficiency	36%

The two primary frequencies are mixed electrically in the transmitting apparatus before the transducer. The pressure source level of the secondary source increases as the total primary power increases and as the square of the difference frequency itself increases. In addition, it increases with a decreasing primary frequency.⁷ Consequently, the transducer used as the primary source must have resonance frequency between 0.8 to 3 MHz and low Q factor to have a useful bandwidth, usually less than 6. It must be capable of delivering sufficient power in the water, which typically means efficiency of 30%–40% or more with peak output electrical power of the order of 200 W.⁸ Efficient setup of a material testing environment has been discussed in details by Humphrey¹¹ and Humphrey and Berkta.¹² The characteristics of the transducer used in the present experiment are given in Table III.

The parametric source was truncated by interposition of an acoustic filter placed at 0.5 m in front of the transducer. The filter, made of a 10-mm panel of silica-filled butyl rubber, attenuated the high-frequency components of the signal in order to reduce the effect of additional nonlinearities in water or in the tested panels.

The configuration of the experimental setup and the measurement apparatus are shown in Fig. 1.

IV. THE EXPERIMENTAL MEASUREMENTS

After calibration with a standard aluminum reflector, a set of measurements has been carried out on a set of 600 × 600 × 10-mm butyl rubber panels of density varying from 1000 to 2200 kg m⁻³ in 200 kg m⁻³ increments. Measurements of the reflected and transmitted signal have been obtained for both normal and oblique incidence in the frequency range 30 to 130 kHz in 2-kHz steps. Measurements of the reflected and transmitted pulses have been carried out using a B&K model 8103 hydrophone calibrated over the frequency range of interest was used. The source signal was

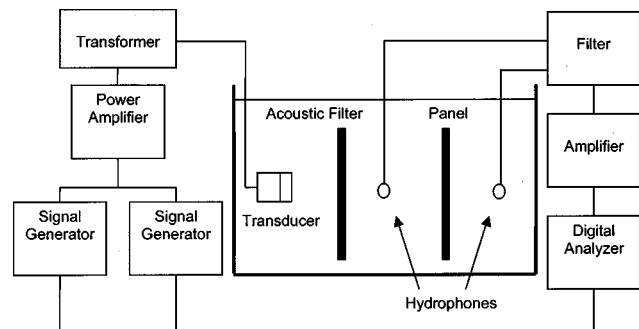


FIG. 1. Experiment setup and measurement equipment.

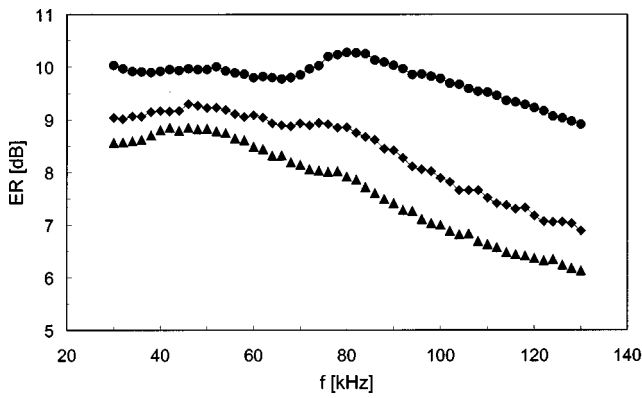


FIG. 2. Power echo reduction ER as a function of frequency f for a 10-mm-thick butyl rubber panel at three different density values at normal incidence (● 1200 kg m^{-3} ; ◆ 1800 kg m^{-3} ; ▲ 2200 kg m^{-3}).

given by a series of pulsed waves with a number of cycles per pulse set to 200 and a 20-ms repetition rate between pulses.

The experimental curves of echo reduction and insertion loss are shown in Figs. 2–7. The plots have been constructed by averaging each measurement up to 1000 times using a Lecroy digital oscilloscope. The reflection and transmission coefficients at fixed angle of incidence θ , $R(\omega)$, and $T(\omega)$, have been defined in terms of the measured fast Fourier transform (FFT) spectra as follows:

$$T(\omega) = \frac{\Phi_t(\omega)}{\Phi_{\text{ref}}(\omega)},$$

$$R(\omega) = \frac{\Phi_r(\omega)}{\Phi_{\text{ref}}(\omega)} = \frac{\Phi_{tr}(\omega) - \Phi_0(\omega)}{\Phi_{\text{ref}}(\omega)}. \quad (1)$$

The spectra in the first case were obtained by recording the transmitted signal $\Phi_t(\omega)$ in the presence of the test panel and then removing the test panel to measure the reference signal $\Phi_{\text{ref}}(\omega)$. In the second case, the net reflected spectrum $\Phi_r(\omega)$ was obtained by recording the total reflected signal $\Phi_{tr}(\omega)$ in the presence of the test panel and then subtracting the incoming signal $\Phi_0(\omega)$ measured after removing the test panel with the hydrophone left in the same position. The reference position in the second case is symmetrical to the measurement position with respect to the panel.¹¹

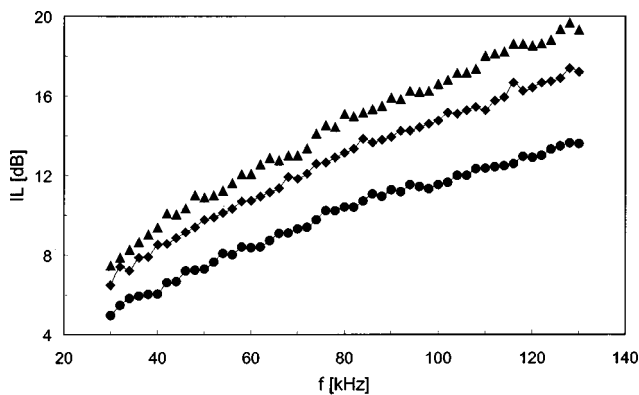


FIG. 3. Power insertion loss IL as a function of frequency f for a 10-mm-thick butyl rubber panel at three different density values at normal incidence (● 1200 kg m^{-3} ; ◆ 1800 kg m^{-3} ; ▲ 2200 kg m^{-3}).

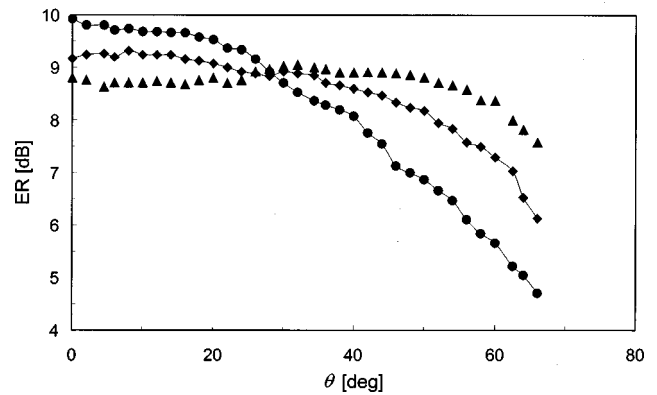


FIG. 4. Power echo reduction ER as a function of angle of incidence θ for a 10-mm-thick butyl rubber panel at 40 kHz for three different density values (● 1200 kg m^{-3} ; ◆ 1800 kg m^{-3} ; ▲ 2200 kg m^{-3}).

It is possible to see from Fig. 2 that the echo reduction curve has two local maxima in the plotted range around 45 and 80 kHz. The maxima are more evident at lower density levels. They tend to disappear, as the material becomes more rigid because of the higher content of heavy hard clay. This behavior, which is typical of viscoelastic materials, is normally due to mechanical resonance phenomena in the molecular chains, triggered by different levels of energy in the forcing signal.

As the frequency of the signal increases, the behavior of the material moves towards the elastic region and the curves show a more decidedly decreasing trend, which means increasing reflection from the panels.

The insertion loss curves follow an increasing trend, whose shape doesn't depend on the density. However, higher density produces higher insertion loss as more sound power is reflected back and less power passed through.

The echo reduction and insertion loss as a function of angle of incidence are shown at three different frequency values in Figs. 4–7. The chosen frequency sample values are 40 and 80 kHz, which are in the range of interest for the analysis to be carried out.

There are marked differences in the echo reduction as a function of the incident angle from the three panels. The low-density panel exhibits the highest echo reduction at the normal incidence. The echo reduction decreases with the in-

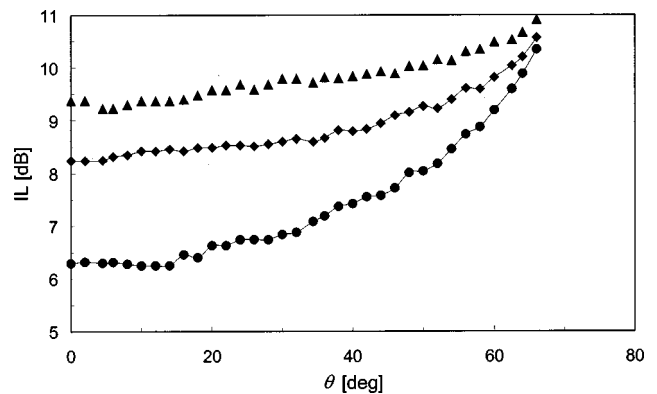


FIG. 5. Power insertion loss IL as a function of angle of incidence θ for a 10-mm-thick butyl rubber panel at 40 kHz for three different density values (● 1200 kg m^{-3} ; ◆ 1800 kg m^{-3} ; ▲ 2200 kg m^{-3}).

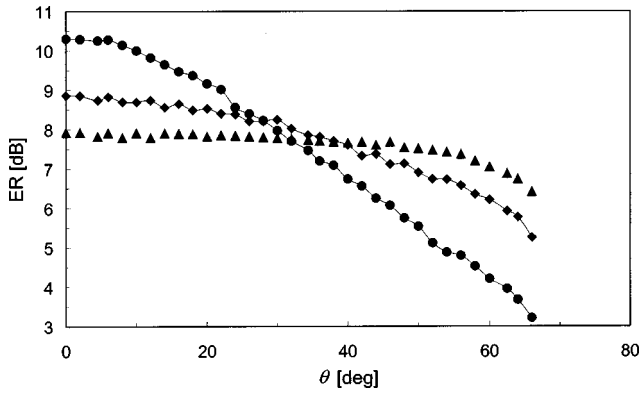


FIG. 6. Power echo reduction ER as a function of angle of incidence θ for a 10-mm-thick butyl rubber panel at 80 kHz for three different density values (● 1200 kg m⁻³; ◆ 1800 kg m⁻³; ▲ 2200 kg m⁻³).

cident angle rapidly from about 10 dB at normal to only 3–4 dB at 66°. The insertion loss of the panel increases with the incident angle in the same range. The high-density panel is less sensitive to variations of the angle of incidence from normal incidence up to about 50°. The medium density panel has echo reduction and insertion loss with lower variation than the low-density panel but higher variation than the high-density panel.

V. THE VARIATIONAL IDENTIFICATION METHOD

The method used to reconstruct the physical properties of the loaded butyl rubber is an optimization method based on the Hamilton principle analogy. The method was developed by one of the authors (Di Meglio) and originally applied to the optimization of the dynamics of a flexible continuous system subject to an optimization goal.⁵

In the present case, the optimization goal is seeking a suitable set of functional complex parameters. These parameters must be such that they minimize the difference between the measured echo reduction and insertion loss and the analytical values calculated from a transmission matrix schema.¹³

We assume the properties of water, the thickness of the panel, and the geometry of the experiment to be known with enough precision to be considered noiseless quantities.

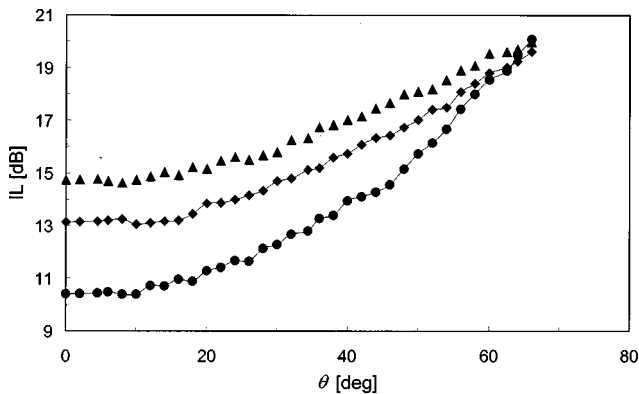


FIG. 7. Power insertion loss IL as a function of angle of incidence θ for a 10-mm-thick butyl rubber panel at 80 kHz for three different density values (● 1200 kg m⁻³; ◆ 1800 kg m⁻³; ▲ 2200 kg m⁻³).

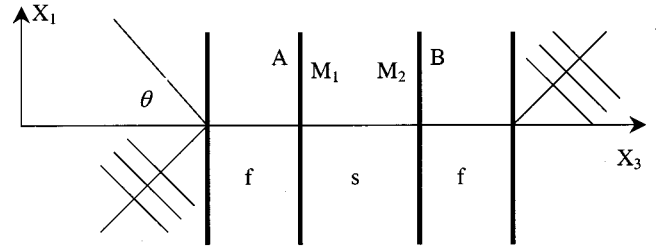


FIG. 8. The fluid–panel–fluid layered model. The points A, M_1 , M_2 , and B refer to the values of the stress and state variables on the two sides of each interface between the fluid layers (f) and the solid layer (s). θ is the angle of incidence of the incoming signal.

The function to be minimized can be derived by the propagation equation expressed in terms of the transmission matrix. Consider the complex-valued equation

$$V_A = \mathbf{T}V_B, \quad (2)$$

where (Fig. 8) V is a vector whose elements are the fluid particle normal velocity v_3 and pressure p and the suffixes A and B represent two points in the fluid surrounding the test panel, respectively, in front of and behind the panel along the line of sight between the acoustic source and a reference point on the panel. The panel is tilted at an arbitrary angle θ . The total transmission matrix \mathbf{T} is given by a transformation of the solid-layer transmission matrix by application of two interface matrices (fluid–panel and panel–fluid)

$$\mathbf{T} = \mathbf{J}_{f,s} \mathbf{T}_s \mathbf{J}_{s,f}, \quad (3)$$

where the index f refers to a fluid layer and the index s refers to a solid layer. The complete form of the transmission matrix \mathbf{T}_s and the interface matrices \mathbf{J} are given in the Appendix.

The vectors V_A and V_B are expressed in terms of the reflection and transmission coefficients R and T as

$$V_A = \begin{pmatrix} 1 + R_A \\ (1 - R_A) \frac{\cos \theta}{Z_c} \end{pmatrix}, \quad V_B = \begin{pmatrix} T_B \\ T_B \frac{\cos \theta}{Z_c} \end{pmatrix}, \quad (4)$$

where $Z_c = \rho_0 c_0$ is the fluid impedance and ρ_0 and c_0 are, respectively, the fluid density and sound speed. The matrix \mathbf{T}_s and therefore the matrix \mathbf{T} can be expressed as a function of the circular frequency ω , the angle of incidence θ , and the complex viscoelastic moduli $\mathbf{G}_1^*(\omega)$ (shear modulus) and $\mathbf{G}_2^*(\omega)$ (bulk modulus):

$$\mathbf{T} = \mathbf{T}(\mathbf{G}_1^*(\omega), \mathbf{G}_2^*(\omega), \omega, \theta), \quad (5)$$

where the $*$ notation implies the complex form

$$\text{Re}(\mathbf{G}(\omega)) = \mathbf{C} + \text{Re} \int_0^\infty \dot{\mathbf{C}}(\tau) e^{-i\omega\tau} d\tau, \quad (6a)$$

$$\text{Im}(\mathbf{G}(\omega)) = \text{Im} \int_0^\infty \dot{\mathbf{C}}(\tau) e^{-i\omega\tau} d\tau, \quad (6b)$$

where $\mathbf{C}(t)$ is a generic viscoelastic response function, the dot notation stands for the time derivative, and \mathbf{C} is the asymptotic value of the function for $t \rightarrow 0$.

Equation (3) can be rewritten in a more compact form by forming the column vector (see Fig. 8 for the meaning of the index M_2)

$$V = \begin{Bmatrix} V_A \\ V_{M_2} \\ V_B \end{Bmatrix}, \quad (7)$$

where V_{M_2} is the vector whose elements are the solid-layer longitudinal and tangential stress components, σ_{33} and τ_{13} , and the longitudinal and tangential velocity components, ν_3 and ν_1 , in the point M_2 . Rearranging the elements of the matrix \mathbf{T} accordingly to form the augmented 8×8 matrix \mathbf{T}_a , we obtain

$$\mathbf{T}_a V = 0. \quad (8)$$

Equation (8) cannot be directly inverted to find the viscoelastic parameters from the knowledge of the reflection and transmission coefficients only. In fact, even in the simplest one-dimensional model there are four complex unknowns, the two stress components σ_{13} (the shear modulus) and σ_{33} (the longitudinal bulk modulus), and the two velocity components ν_1 and ν_3 . There are therefore four complex unknowns, since the relationships between the panel material properties and the surrounding medium, expressed by the transmission matrix \mathbf{T} , are included as part of the system. The number of measured complex values for each frequency sample in this case is only two, namely the measured complex reflection and transmission coefficients.

We can overcome this problem by applying the proposed optimization method to find a best-fit solution.

If we substitute in Eq. (8) the experimental values of the reflection and transmission coefficients, we have the approximate residual form

$$\mathbf{T}_a(\mathbf{G}_1^*(\omega), \mathbf{G}_2^*(\omega), \omega, \theta) V_e(\omega, \theta) = R, \quad (9)$$

where R would be zero if $\mathbf{G}_1^*(\omega)$ and $\mathbf{G}_2^*(\omega)$ were the exact pair of functions for the material and the given experimental values of the reflection and transmission coefficients were exact noiseless quantities.

The set of optimization parameters can be provided directly by the two response functions $\mathbf{G}_1^*(\omega)$ and $\mathbf{G}_2^*(\omega)$. Alternatively, it's more convenient to use a set of functions of the frequency ω that can be directly used in the expression of the elements of \mathbf{T} , such as the mechanical shear modulus $\mathbf{G}^* = [\mathbf{G}_1^*(\omega)]/2$ and the longitudinal bulk modulus $\mathbf{L}^* = \frac{1}{3}(\mathbf{G}_2^*(\omega) + 2\mathbf{G}_1^*(\omega))$

$$\lambda_L^*(\omega) = \frac{\rho\omega^2}{k_L^{*2}} = \frac{1}{3}(\mathbf{G}_2^*(\omega) + 2\mathbf{G}_1^*(\omega)) = \mathbf{L}^*, \quad (10a)$$

$$\lambda_G^*(\omega) = \frac{\rho\omega^2}{k_G^{*2}} = \frac{\mathbf{G}_1^*(\omega)}{2} = \mathbf{G}^*, \quad (10b)$$

where k_L^* and k_G^* are the longitudinal and tangential wave numbers in the solid layer, respectively.

For a given angle of incidence, we can write

$$\mathbf{L}(\lambda^*, \omega) = \mathbf{T}_a(\lambda^*(\omega), \omega) V(\omega), \quad (11)$$

where λ^* is the vector whose elements are λ_L^* and λ_G^* .

In order to minimize the value of Eq. (11), we can now build a scalar performance functional for the optimization process in the given frequency range as (the superscript* is understood)

$$\mathbf{J}(\lambda) = \mathbf{F}(V(\omega_b)) + \int_{\Omega} q^T L(\lambda, \omega) d\omega, \quad (12)$$

where q is an unknown vector of weighing coefficients and $\mathbf{F}(V(\omega_b))$ is a scalar function of boundary conditions

$$\mathbf{F}(V(\omega_b)) = V(\omega_f) - V_f + V(\omega_i) - V_i. \quad (13)$$

If we now define a new set of complex-valued Lagrange multipliers p , we can introduce the experimental values as an explicit constraint in the minimization process. We have

$$p^T [V(\omega) - V_e(\omega)] = 0, \quad (14)$$

where $V_e(\omega)$ is an interpolated vector function built using the value of $V(\omega)$ in each interval between any two sample points (in the case presented here a cubic spline interpolation has been used).

Finally, we define the Hamilton optimization function, \mathbf{H} , as

$$\mathbf{H}(\lambda, p, q, \omega) = q^T L(\lambda, \omega) + p^T V(\omega). \quad (15)$$

If we introduce the Hamilton function (15) in the performance functional and take Eq. (14) into account, we obtain

$$\mathbf{J}(\lambda) = \mathbf{F}(V(\omega_b)) + \int_{\Omega} [\mathbf{H}(\lambda, p, q, \omega) - p^T \bar{V}(\omega)] d\omega. \quad (16)$$

The optimization problem then becomes one of finding the optimization functions $\bar{\lambda}$ that minimize the performance functional $\mathbf{J}(\lambda)$ over a class Λ of admissible functions

$$\mathbf{J}(\bar{\lambda}) = \min_{\lambda \in \Lambda} \mathbf{J}(\lambda), \quad (17)$$

where the class Λ of admissible functions for the minimization problem is equivalent to the class of strong response functions for Boltzmann laws.¹⁴

We consider now the virtual variation of the optimization functions

$$\lambda(\omega) = \bar{\lambda}(\omega) + \delta\lambda(\omega), \quad (18)$$

and the corresponding variations of the propagation vectors and the performance functional

$$V(\omega) = \bar{V}(\omega) + \delta V(\omega), \quad (19)$$

and

$$\mathbf{J}(\lambda) = \mathbf{J}(\bar{\lambda} + \delta\lambda). \quad (20)$$

The necessary condition for $\bar{\lambda}$ to be the desired optimal functions is that the first-order variation $\delta\mathbf{J}(\bar{\lambda})$ of the difference $\Delta\mathbf{J}(\bar{\lambda}) = \mathbf{J}(\bar{\lambda} + \delta\lambda) - \mathbf{J}(\bar{\lambda})$ be zero. We can therefore write the following optimization condition for the residual Eq. (11) (the functional dependence on the variables inside the round brackets has been dropped for brevity and is implicitly understood):

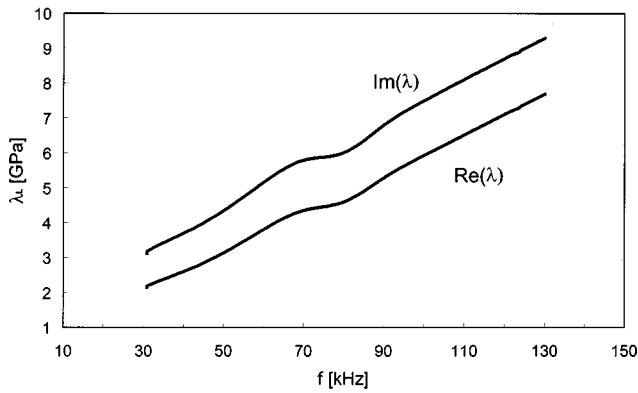


FIG. 9. Longitudinal bulk modulus $\lambda_L^*(\omega) = L^*$ of the loaded butyl rubber compound.

$$\begin{aligned} \delta J(\lambda) &= \int_{\Omega} \left\{ \left[\frac{\partial \mathbf{H}}{\partial V} \right]^T \delta V + \left[\frac{\partial \mathbf{H}}{\partial p} \right]^T \delta p + \left[\frac{\partial \mathbf{H}}{\partial q} \right]^T \delta q \right. \\ &\quad \left. + \left[\frac{\partial \mathbf{H}}{\partial \lambda} \right]^T \delta \lambda - V_e^T \delta p \right\} d\omega \\ &= \int_{\Omega} \left\{ [q^T \mathbf{T}_a + p^T] \delta V + V^T \delta p + \mathbf{T}_a V \delta q \right. \\ &\quad \left. + \left[q^T \frac{\partial L}{\partial \lambda} V \right] \delta \lambda - V_e^T \delta p \right\} d\omega, \end{aligned} \quad (21)$$

where we have taken into account that the virtual variation $\delta \omega$ is zero, since the experiment configuration is fixed.

Since the virtual variations of the independent variables are by definition independent and different from zero, condition (20) represents a system of four vector equations in the four unknown vectors V (system state), the Lagrange multipliers p , q , and λ (optimization parameters). The final system is given in Eq. (22). The multipliers p and q are formally equivalent to kinetic moments, but it is not yet clear if they can be given a specific physical meaning in the present context.

The system of equations (22) can now be solved numerically in the given frequency range. In this case, the system has been solved by applying an algorithm written using the MATLAB macro language based on the nonlinear Newton-

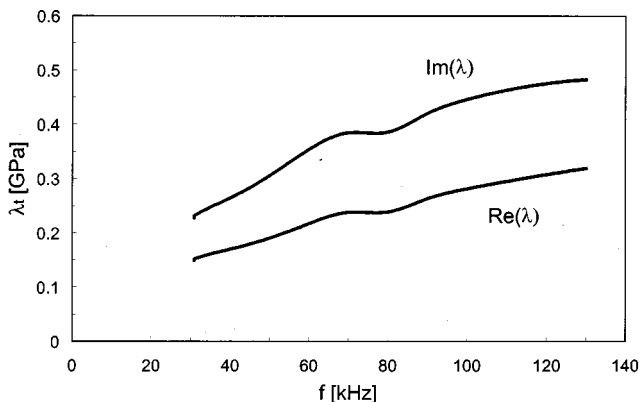


FIG. 10. Shear modulus $\lambda_G^*(\omega) = G^*$ for the loaded butyl rubber compound.

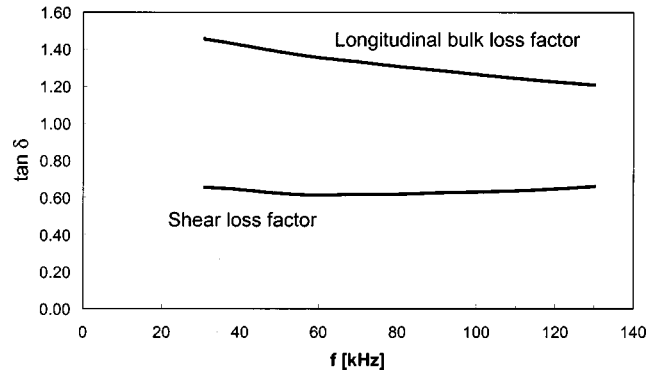


FIG. 11. Longitudinal bulk and shear loss factors δL and δG for the loaded butyl rubber compound.

Raphson method combined with a singular value decomposition (SVD) of the resulting nonlinear algebraic system matrix

$$\begin{aligned} \int_{\Omega} [\mathbf{T}_a q + p] d\omega &= 0, \\ \int_{\Omega} [V - V_e] d\omega &= 0, \\ \int_{\Omega} \mathbf{T}_a V d\omega &= 0, \\ \int_{\Omega} \left[q^T \frac{\partial \mathbf{T}_a}{\partial \lambda} V \right] d\omega &= 0. \end{aligned} \quad (22)$$

VI. DETERMINATION OF THE VISCOELASTIC RESPONSE FUNCTIONS

The viscoelastic parameters obtained from the optimization process for the panel of density $\rho = 1800 \text{ kg m}^{-3}$ are given in Figs. 9–12, where the longitudinal bulk modulus $L = \lambda_L$, the shear modulus $G = \lambda_G$; the loss factors δ_L and δ_G and the Poisson ratio ν are plotted as functions of frequency. As could be expected on physical grounds, the viscoelastic moduli appear to be independent from the angle of incidence, since the material is isotropic. As an example, the curves of longitudinal bulk modulus as a function of the angles of incidence at 40, 80, and 120 kHz are shown in Fig. 13. It can be seen that the values are substantially constant for angles of incidence up to about 55° – 60° , where a more

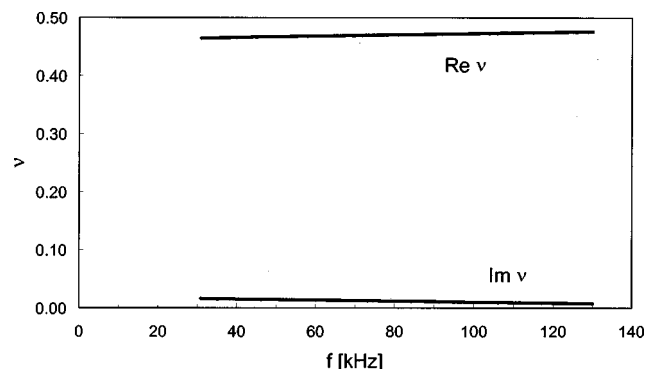


FIG. 12. Viscoelastic Poisson ratio ν for loaded butyl rubber compound.

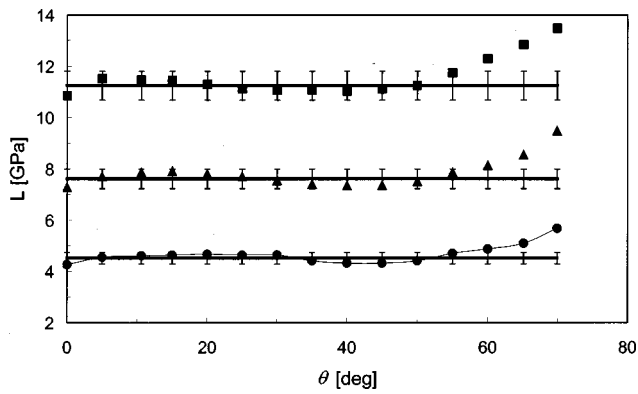


FIG. 13. Longitudinal bulk modulus $\lambda_L^*(\omega) = L^*$ amplitude as a function of the angle of incidence θ for three frequency values (● 40 kHz; ▲ 80 kHz; ■ 120 kHz). The vertical error bars are $\pm 5\%$ of the constant reference value.

pronounced deviation is observed. This angular dependence is thought to be the consequence of the increasing influence of edge diffraction on the experimental data. The reference values of the moduli are taken to be the average of the calculated values up to 55° .

It is finally possible to compute the viscoelastic response functions G_2^* and G_1^* from the knowledge of the viscoelastic moduli L and G using Eqs. (10a) and (10b).

VII. RESULTS COMPARISONS

The results obtained by the method have been compared with experimental and theoretical data published in the literature. Exact agreement should not be expected, however, since the unavoidable differences in rubber formulations lead necessarily to differences in the material properties and behavior.

Experimental curves of butyl rubber Young modulus and loss factor have been reported by Capps¹⁵ and are compared in Figs. 14 and 15 with the results obtained by the proposed variational method. The agreement within the common frequency range is good.

The bulk modulus can be compared with results presented in the already-mentioned paper by Piquette¹ and obtained by inverse scattering analysis. Although the frequency ranges are different, the curves can be qualitatively compared by extrapolation. The bulk modulus and loss factor in

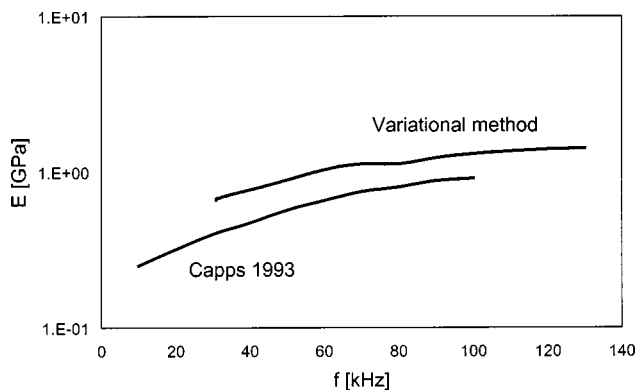


FIG. 14. Storage Young modulus, E . Comparison with experimental data from Capps (Ref. 15) for butyl 70821.

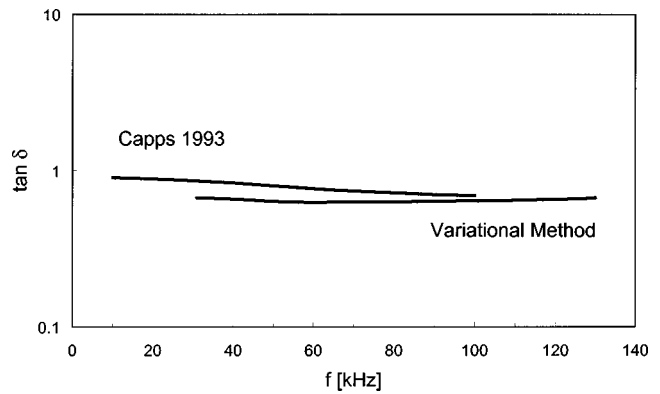


FIG. 15. Young modulus loss factor δE . Comparison with experimental data from Capps (Ref. 15) for butyl 70821.

the two cases are compared in Figs. 16 and 17. From this comparison it can be inferred that the curves of the real and imaginary parts of the bulk modulus cross somewhere around 25 kHz, where the loss factor is $\tan \delta = 1$.

VIII. CONCLUSIONS

In this paper, a novel algorithm has been introduced to derive the viscoelastic properties of viscoelastic plates from experimental data. The complex viscoelastic response functions of the loaded butyl rubber panel have been computed using the algorithm with the measured reflection and transmission coefficients within the frequency range of interest.

This method can be applied even when standard inverse scattering methods would provide an intractable problem. Since no assumptions are made on the mechanical interdependence of the viscoelastic moduli, the method allows the independent calculation of the real and imaginary part of the parameters and the determination of quantities such as the viscoelastic Poisson ratio, which is difficult to predict otherwise.

Further investigation is underway to extend the method to configurations where isotropy or homogeneity conditions cannot be invoked.

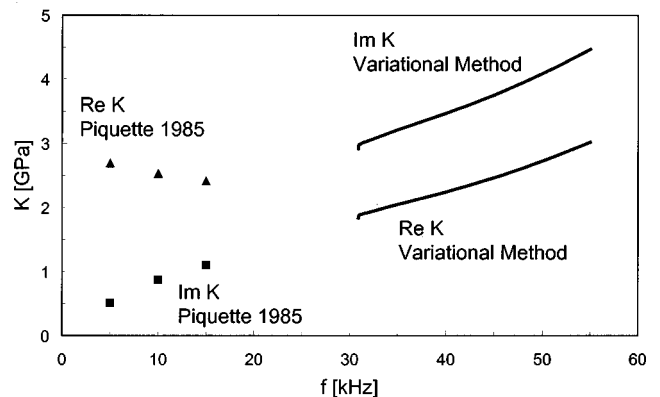


FIG. 16. Bulk modulus, K . Comparison with analytical data from Piquette (Ref. 1).

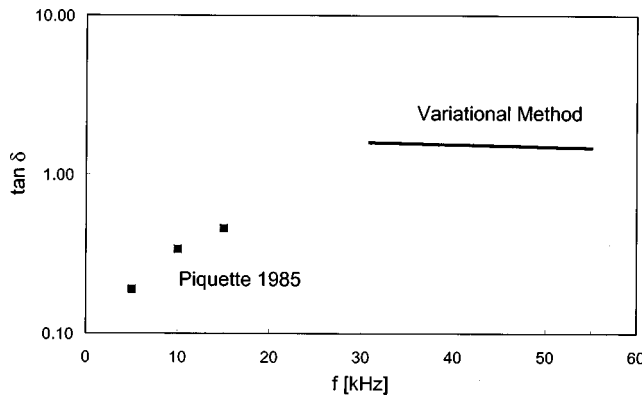


FIG. 17. Bulk modulus loss factor, δK . Comparison with analytical data from Piquette (Ref. 1).

ACKNOWLEDGMENTS

We would like to acknowledge the assistance and guidance of a great number of people who have made this research possible. We would also like to thank friends and colleagues at Birmingham University and at Whitehead ALENIA Sistemi Subacquei who have helped and assisted in this project in so many ways. This work was funded by the European Communities under Contract No. MAS2-CT94-0079.

APPENDIX: THE TRANSMISSION AND INTERFACE MATRICES

The transmission matrix \mathbf{T}_s for the case of an isotropic, homogeneous solid layer assumes the form (d is the thickness of the layer)¹⁶

$$\mathbf{T}_s = |a_{ij}| \quad i, j = 1, \dots, 4, \quad (\text{A1})$$

with

$$a_{11} = C_L + (1 - F)[C_G - C_L],$$

$$a_{12} = jk_1 \left[\frac{FS_L}{k_{L,3}} - \frac{2k_{G,3}S_G}{k_G^2} \right],$$

$$a_{13} = 2k_1 \rho c_G \frac{F}{k_G} [C_L - C_G],$$

$$a_{14} = j\rho c_G \left[\frac{k_G F^2}{k_{L,3}} S_L + \frac{4k_1^2 k_{G,3}}{k_G^3} S_G \right],$$

$$a_{21} = jk_1 \left[\frac{2k_{L,3}}{k_G^2} S_L - \frac{F}{k_{G,3}} S_G \right],$$

$$a_{22} = C_G + 2 \frac{k_1^2}{k_G^2} [C_L - C_G],$$

$$a_{23} = j\rho c_G \left[4 \frac{k_1^2 k_{L,2}}{k_G^3} S_L + \frac{k_1^2 k_G F^2}{k_{G,3} k_1^2} S_G \right],$$

$$a_{24} = a_{13},$$

$$a_{31} = \frac{k_1}{\rho c_G k_G} [C_L - C_G],$$

$$a_{32} = j \frac{1}{\rho c_G} \left[\frac{k_1^2}{k_{L,3} k_G} S_L + \frac{k_{G,3}}{k_G} S_G \right],$$

$$a_{33} = a_{22}, \quad a_{34} = a_{12},$$

$$a_{41} = j \frac{1}{\rho c_G} \left[\frac{k_{L,3}}{k_G} S_L + \frac{k_1^2}{k_{G,3} k_G} S_G \right],$$

$$a_{42} = a_{31}, \quad a_{43} = a_{21}, \quad a_{44} = a_{11},$$

where

$$F = 1 - 2 \frac{k_1^2}{k_G^2}, \quad C_L = \cos(k_{L,3}d),$$

$$S_L = \sin(k_{L,3}d), \quad C_G = \cos(k_{G,3}d),$$

$$S_G = \sin(k_{G,3}d), \quad k_{L,3} = (k_L^2 - k_1^2)^{1/2},$$

$$k_{G,3} = (k_G^2 - k_1^2)^{1/2}, \quad c_L = \left(\frac{L}{\rho} \right)^{1/2}, \quad c_G = \left(\frac{G}{\rho} \right)^{1/2},$$

and k_1 , k_L , and k_G are, respectively, the wave numbers along the direction x_1 and along the longitudinal and shear wave propagation direction.

Finally, the interface matrix can be derived by enforcing the proper boundary conditions on the state variables between layers. \mathbf{J}_{fs} and \mathbf{J}_{sf} therefore have the form

$$\mathbf{J}_{fs} = \mathbf{J}_{sf}^T = \begin{bmatrix} 0 & 1 & 0 & 0 \\ 0 & 0 & 0 & -1 \end{bmatrix}. \quad (\text{A2})$$

¹J. C. Piquette, "Determination of the complex dynamic bulk modulus of elastomers by inverse scattering," *J. Acoust. Soc. Am.* **77**, 1665–1673 (1985).

²D. J. Simmonds and V. F. Humphrey, "Estimation of the dynamic plate modulus of viscoelastic materials by inversion of the impedance tube measurements," *Proc. Inst. Acoust.* **15**(6), 104–114 (1993).

³W. F. Zhong, S. B. Tang, and B. H. Chen, "The multi-parameter inversion of elastic wave in half-space," *Acta Mech. Sin.* **12**(2), 129–135 (1999).

⁴J. C. Piquette, "Transmission coefficient measurement and improved sublayer material property determination for thick underwater acoustic panels: A generalization and improvement of the ONION method," *J. Acoust. Soc. Am.* **92**, 468–477 (1992).

⁵A. Di Meglio and A. E. Finzi, "Minimum time control of flexible spacecraft by Hamilton's principle," *Meccanica* **32**(6), 555–565 (1997).

⁶L. Meirovitch, *Computational Methods in Structural Dynamics* (Sijthoff & Noordhoff, Amsterdam, 1980).

⁷Exxon Chemical Ltd., Technical sheet, 1996.

⁸P. J. Westervelt, "Parametric acoustic array," *J. Acoust. Soc. Am.* **35**, 535–537 (1963).

⁹B. V. Smith, "Introduction to non-linear acoustics and the parametric array," *Proc. Inst. Acoust.* **14**(3), 1–25 (1992).

¹⁰V. F. Humphrey, "Non-linear acoustic as a laboratory tool," *Proc. Inst. Acoust.* **14**(3), 99–113 (1992).

¹¹V. F. Humphrey, "The measurement of acoustic properties of limited size panels by use of a parametric source," *J. Sound Vib.* **98**(1), 67–81 (1985).

¹²V. F. Humphrey and H. O. Berkta, "The transmission coefficient of a panel measured with a parametric source," *J. Sound Vib.* **101**(1), 85–106 (1985).

¹³J. F. Allard, Y. Champoux, and C. Depollier, "Modelization of layered sound absorbing materials with transfer matrices," *J. Acoust. Soc. Am.* **82**, 1792–1796 (1987).

¹⁴M. J. Leitman and G. M. C. Fisher, "The linear theory of viscoelasticity," in *Mechanics of Solids*, edited by C. Truesdell (Springer, New York, 1984), Vol. III.

¹⁵R. N. Capps, *Elastomeric Materials for Acoustical Applications* (NRL, Orlando, FL, 1992).

¹⁶J. S. Sastry and M. L. Munial, "A transfer matrix approach for evaluation of the response of a multi-layer infinite plate to a two-dimensional pressure excitation," *J. Sound Vib.* **182**(1), 109–128 (1995).

Measurement of the acoustic nonlinearity parameter B/A in solvents: Dependence on chain length and sound velocity

J. Banchet and J. D. N. Cheeke

Physics Department, Concordia University, 1455 De Maisonneuve West, Montreal, Quebec H3G 1M8, Canada

(Received 10 January 2000; revised 8 May 2000; accepted 17 August 2000)

This work consists of a systematic study of the acoustic nonlinearity parameter (B/A) in 1-alkanols from methanol to 1-decanol, ketones from acetone to methyl hexyl ketone, and alkyl acetates from ethyl to octyl acetate. By focusing a 14-MHz tone burst through a spherical quartz lens in each solvent, the second harmonic is generated and measured by a 28-MHz transducer at various distances from the focus. This provides the point of maximum second harmonic power, and enables the computation of the nonlinear parameter using a simple model. The B/A values thus obtained are in reasonable agreement with these available in the literature. The B/A values are found to increase with chain length and sound velocity, this increase being in contradiction with Ballou's rule. Moreover, a hybrid model based on Schaaffs' formula for sound velocity fits the experimental results, questioning the validity of Ballou's rule for solvents within a single chemical family. © 2000 Acoustical Society of America. [S0001-4966(00)04211-9]

PACS numbers: 43.25.Ba [MFH]

I. INTRODUCTION

The nonlinearity parameter B/A has been the subject of many previous publications. Measured by the thermodynamic method¹ and later the isentropic phase method,²⁻⁴ or the finite amplitude method,⁵⁻⁹ many materials and especially liquids were characterized to form a wide database of values. Although wide, this list does not cover a large number of organic liquids, especially those having a relatively high molecular weight. Besides, owing to the diversity of experimental techniques, B/A is generally established more through a range than a fixed value for each liquid. Despite some studies comparing the thermodynamic and finite amplitude techniques,^{10,11} it has been quite difficult to exclude one of these methods and at the same time fix a definitive value for B/A for each liquid. Moreover, the recent success of the

isentropic phase method,⁴ with a better accuracy than the other two, has not yet been applied to a wide range of liquids to help obtain definitive values of B/A .

Theoretically, there have been some attempts to predict the value of the nonlinear parameter in different liquids.¹²⁻¹⁵ These models were based on the nature of intermolecular potentials and for most of them the liquid was considered as a system of hard spheres.¹³⁻¹⁵ Although the values found earlier were not that close to the correct values, Sharma¹⁶ recently used thermoacoustic data and obtained a good agreement between experimental results and his predictions. Aside from these theoretical predictions, Ballou¹⁷ found a linear relation between B/A and reciprocal sound speed. Although some theoretical foundation has been mentioned,¹² this law remains uncertain, given the huge scattering of data

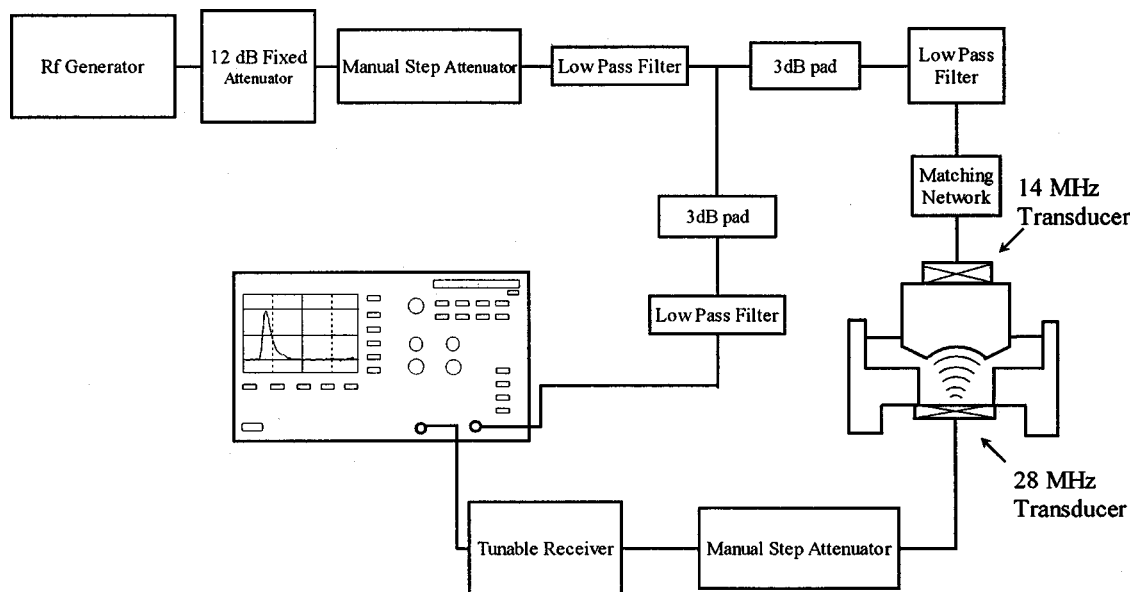


FIG. 1. Experimental setup.

TABLE I. Values of the different parameters used in the calculation of B/A .

Solvents	Density (kg/m ³)	Sound velocity (m/s)	Attenuation coefficient $\times 10^{15}$ (s ² /m)
Methanol	791	1144	30.2
Ethanol	790	1209	48.0
Propanol	804	1229	64.5
Butanol	810	1262	74.3
Pentanol	811	1296	110.0
Hexanol	820	1330	122.0
Heptanol	822	1363	135.0
Octanol	825	1379	183.0
Nonanol	827	1396	210.0
Decanol	829	1410	230.0
Acetone	804	1199	26.1
Methyl ethyl ketone	805	1220	25.6
Methyl propyl ketone	812	1237	24.8
Methyl butyl ketone	812	1265	26.2
Methyl pentyl ketone	821	1287	26.8
Methyl hexyl ketone	819	1309	74.2
Ethyl acetate	900	1170	60.0
Propyl acetate	889	1200	62.0
Butyl acetate	878	1235	63.0
Pentyl acetate	871	1257	64.6
Hexyl acetate	864	1291	63.0
Octyl acetate	870	1301	63.0

Radius of curvature of the lens: 1.622 mm. Diameter of the spherical cavity: 2.200 mm. Sound velocity for the quartz lens: 5596 m/s. Acoustic impedance for the quartz lens: 12.10 Mrayl. Acoustic impedance for Lithium niobate: 34.20 Mrayl.

points. It has already been suggested¹⁸ that a nonlinear relation seemed more appropriate between these two variables and that each family of chemicals should have its own rule.

In this paper, we intend to make an experimental systematic study of the nonlinearity parameter in 1-alkanols, ketones, and esters, and study the variation of this parameter

with chain length and reciprocal sound velocity. We will also calculate this parameter using a model from Tong,¹⁹ that we modify by substituting experimental data into an analytical formula.

II. EXPERIMENTAL SETUP AND THEORETICAL CORRECTIONS

The setup shown in Fig. 1 and described in more detail in Ref. 20, consists of a 14-MHz LiNbO₃ transducer wax bonded to a quartz acoustic lens mounted on a three-dimensional (3-D) displacement system driven by a LABVIEW program. Before being sent to the transducer plus lens system, the 1- μ s pulse produced by a pulse generator is attenuated and filtered by 15-MHz low-pass filters, to prevent any possible electronic harmonics from polluting the signal. The signal is then focused by the lens into the test liquid which is contained in a measurement cell. The transmitted signal is received by a 28-MHz LiNbO₃ transducer glued to the rear end of that cell. The received signal is then sent to a manual step attenuator, amplified by a receiver tuned at 28 MHz and seen on the oscilloscope screen.

The experiment objective is to measure the attenuation needed to keep the harmonic signal constant when the lens is displaced axially. The reading of the manual step allows us to plot an attenuation versus distance graph for each liquid. The point where attenuation is maximum, or in other words the attenuation at the focal point, is then extracted from the tested liquid curve and subtracted from the maximum attenuation value from the water curve; this difference is called Att. With the model of Germain *et al.*,⁷ using a constant power at the focal point instead of a constant power at the input to the transducer, we then compute the ratio of the coefficient of nonlinearity $\beta_{2\text{liq}}$ of the liquid with respect to water β_{2w} using

$$\frac{\beta_{2\text{liq}}}{\beta_{2w}} = \left(10^{\text{Att}/10} \frac{F_w^2 \rho_{\text{liq}} c_{\text{liq}}^5}{F_{\text{liq}}^2 \rho_w c_w^5 \exp[(-7.1/\Phi)(c_{\text{liq}} F_{\text{liq}}^2 (2\alpha_{1\text{liq}} + \alpha_{2\text{liq}}) - c_w F_w^2 (2\alpha_{1w} + \alpha_{2w}))]} \right)^{1/2}. \quad (1)$$

TABLE II. Comparison of experimental B/A values with those reported in the literature.

Liquid	B/A	B/A from other work	Liquid	B/A	B/A from other work	Liquid	B/A	B/A from other work
Methanol	8.6	6.6 ^a , 9.6 ^b , 10.0 ^c	Acetone	8.0	9.2 ^b	Ethyl Acetate	8.7	
Ethanol	9.3	7.5 ^a , 10.5 ^b	Methyl Ethyl Ketone	8.8		Propyl Acetate	9.0	
1-Propanol	9.5	10.7 ^b , 11.1 ^d	Methyl Propyl	8.8		Butyl Acetate	9.2	
1-Butanol	9.8	8.2 ^a , 10.7 ^b	Ketone	9.0		Pentyl Acetate	9.6	
1-Pentanol	10.0	11.6 ^e	Methyl Butyl Ketone	9.0		Hexyl Acetate	9.9	
1-Hexanol	10.2		Methyl Pentyl Ketone	9.1		Octyl Acetate	9.8	
1-Heptanol	10.6		Methyl Hexyl Ketone					
1-Octanol	10.7							
1-Nonanol	10.8							
1-Decanol	10.7							

^aSee Ref. 15.

^bSee Ref. 1.

^cSee Ref. 8.

^dSee Ref. 9.

^eSee Ref. 24.

In this expression, F is the F -number of the lens, ρ the density, c the velocity, α_1 and α_2 the absorption coefficients at fundamental and second harmonic frequencies, and Φ the fundamental frequency. The B/A of the tested liquid is then computed, knowing that $\beta_2 = 1 + B/2A$. Though the lens parameters and sound velocities were measured, the other parameters including the absorption coefficients were taken from the literature²¹⁻²³ (cf. Table I).

III. RESULTS

Experiments were conducted on three chemical families: (1) 1-alkanols including methanol, ethanol, 1-propanol, 1-butanol, 1-pentanol, 1-hexanol, 1-heptanol, 1-octanol, 1-nonanol, and 1-decanol, (2) the ketones covering acetone, methyl ethyl ketone, methyl butyl ketone, methyl propyl ketone, methyl pentyl ketone, and methyl hexyl ketone, and (3) the esters including ethyl acetate, butyl acetate, propyl acetate, pentyl acetate, hexyl acetate, and octyl acetate.

As mentioned earlier, sound velocities for the different liquids were measured using the experimental setup described above except for the attenuators. To perform these measurements, the lens was axially moved by steps of 500 μm on a total distance of 3 mm and a pulse sent through the liquid. The time of flight between the pulse and the received signal was measured, a signal that was time averaged 256 times. In order to obtain an average time of flight for each step, five runs were conducted on each liquid, allowing the speed of sound to be evaluated from the slope of a time versus distance graph. The results were found to match the values listed in the literature²¹ with a maximum error of 2%. Considering the accuracies of our displacement system and of the oscilloscope, the uncertainty on the displacement was maximized by using 1 μm per step and 0.01 μs out of a minimum time of 1 μs , leading to a 1.2% experimental uncertainty on the sound velocity. Using these measured values, we computed the nonlinear parameter for each of the liquids mentioned above. For the sound velocity, published errors were used, whereas uncertainties relative to the other data taken from the literature (attenuation coefficients or densities) had been considered as equal to the variation by one unit of the last significant figure. Moreover, knowing that four attenuation versus distance curves have been obtained for each liquid, and that the maximum deviation of the maximum attenuation value never differed by more than 0.3 dB,

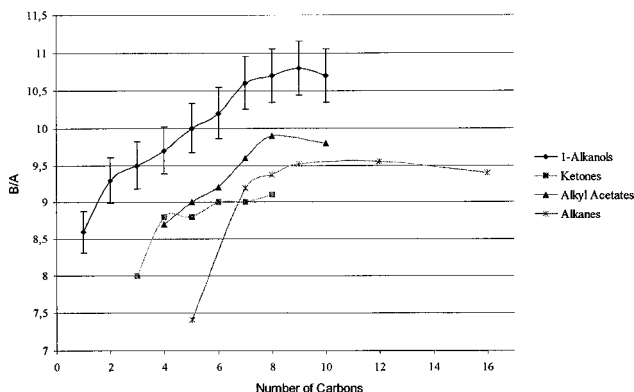


FIG. 2. Dependence of B/A on chain length for different families of liquids.

the uncertainty on Att. has been fixed to 0.1 dB. With these numbers, and the fact that the uncertainties retained on the other factors of Eq. (1) have been the biggest among all the liquids, the error on B/A has been estimated as 8%. Our B/A values, measured at room temperature, are listed in Table II, along with values from the literature for common solvents, used in order to evaluate the validity of our technique. Our results appear to be in good agreement with those found by other researchers, allowing us to obtain the B/A values for the liquids that were not characterized so far.

We were then able to study the dependence of the nonlinear parameter with chain length. Within a specific chemical family, as the same CH_2 group is added, we decided to use the number of carbons as a parameter for evaluating chain length. B/A vs number of carbons present in the liquids is shown in Fig. 2. Finally, we investigated the relation between B/A and reciprocal sound velocity, shown in Fig. 3. In this graph, the straight line represents Ballou's rule, plotted with the original Ballou expression.¹⁷ It is to be noted that we used our experimentally measured sound velocity values to compute the abscissa in this figure. On that graph also appears another family of chemicals, the 1-alkanes, whose values for B/A are taken from Refs. 25 and 26.

IV. DISCUSSION

We chose our chemicals so that they would belong to the same chemical family, but moreover, we paid attention to the fact that adding a CH_2 group in the chain from a chemical to the next one would increase the chain length as linearly as possible. As seen in Fig. 2, we can then conclude that, as the nonlinearity parameter clearly increases with the number of carbons present in the chain, it also increases with chain length.

Moreover, looking closely at the graph, we notice that the B/A values for the longest chains tend to drop or at least to saturate. This remark is especially true for alkanes, and may be valid for the other chemical families.

These two phenomena could be explained using the same argument. It is well known that the longer the molecule, the more sound propagates within the molecule.¹⁴ This means that the longer the molecule, the more the impinging acoustic wave interrogates the skeleton of the molecule. We suggest that, if one nonlinearity parameter exists for the liquid as a whole and a higher one for the carbon chain of the

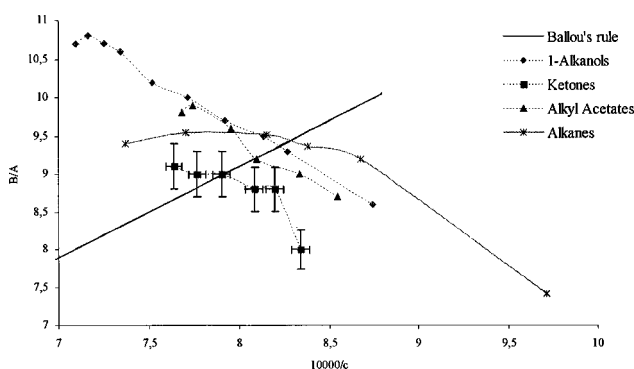


FIG. 3. Dependence of B/A on reciprocal sound velocity for different families of liquids.

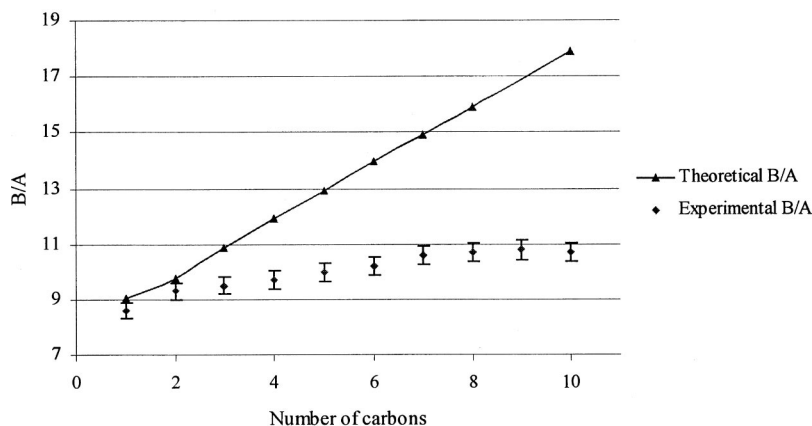


FIG. 4. Comparison between calculated and experimental values of B/A for 1-alkanols using Tong *et al.*'s model.

molecule, then B/A could increase and then saturate through a simple mixture rule, comparable to some already mentioned in the literature.²⁷

Figure 3 shows a general trend for these different organic products: B/A increases with sound velocity. In Fig. 3 is also plotted Ballou's rule, whose goal is to describe a universal relation between B/A and reciprocal sound velocity. This law was first empirically calculated to fit the nonlinear parameter behavior of liquid metals, and then was considered to be applicable to all liquids and solids. It implies that an increase in B/A corresponds to a decrease in sound velocity. Our results actually show the opposite variation.

It has been already stated¹⁸ that Ballou's rule would be more appropriate if it were applied to each family of materials. Indeed, because of the variety of structural, chemical, and dynamical properties among materials, it would seem improbable that a single rule would manage to describe the relation between B/A and sound velocity for liquid metals as well as for organic liquids or polymers. We can then conclude that Ballou's rule represents a rough way to estimate the mean nonlinearity parameter of a whole family, but neither provides any precise information about the value of B/A for a specific member of that family, nor a description of the behavior of B/A with sound velocity for that family.

Finally, we propose a way to predict the nonlinearity parameter, resulting from Tong *et al.*'s model,¹⁹ that we modify in substituting experimental data found in the literature to an analytical expression. In this model, Tong *et al.* derive an expression for the nonlinearity parameter, starting from Schaaff's formula²⁸ for sound velocity. From this formula, Tong *et al.* derive the following expression for B/A :

$$\frac{B}{A} = (\gamma - 1) \frac{1}{T\beta} + J(x), \quad (2)$$

where γ is the specific heat ratio, β the isobaric expansibility, and $J(x)$ a polynomial function depending on the molar volume and the excluded volume b present in the Van der Waals equation. Further, to evaluate x , Tong *et al.* consider the liquid as a system of hard balls, and express b as a function of the molecular radius of the chosen liquid.

The results of B/A calculated with Tong *et al.*'s model are shown in Fig. 4. Although the results present a relatively

good agreement with experimental data for small molecules, it completely fails in predicting B/A for longer molecules. This problem could be related to an overestimation of the molecular radii based on the hypothesis of spherical molecules, symmetry that is far from being adapted to higher order alkanols.

As an alternative, we propose to calculate $J(x)$ by using Eq. (14) in Tong *et al.*'s paper, given by

$$\left(\frac{\partial c}{\partial T}\right)_p = \frac{c\beta}{2} \left(\frac{1}{T\beta} - J(x)\right), \quad (3)$$

where c is the sound velocity of the liquid considered. As values of the partial derivative can be found in the literature,²¹ along with the isobaric expansivity²⁹⁻³² (cf. Table III), we can calculate $J(x)$ and substitute it in Eq. (2) to give B/A . Unfortunately, due to the lack of data in the literature, we were only able to calculate B/A for the complete series of 1-alkanols, whose plot is shown in Fig. 5. Contrary to the previous model, the hybrid one fits our results very well, except for the first four points whose maximum error is 7%. This can be due to the fact that the values for the partial derivative were found in the literature as an average over a wide temperature range (between 10 and 30 °C), rather than at one specific temperature. Exact values should then be measured in order to be more accurate for the evaluation of the nonlinearity parameter through that model.

TABLE III. Values used in the calculation of B/A using Tong *et al.*'s and the hybrid model.

1-Alkanols	Isobaric expansibility $\times 10^3$ (K ⁻¹)	Heat capacity (cal. deg ⁻¹)	$\left(\frac{\partial c}{\partial T}\right)_p$ (m.s. ⁻¹ deg ⁻¹)
Methanol	1.259	10.49	-3.3
Ethanol	1.100	15.64	-4.0
Propanol	0.956	20.82	-3.7
Butanol	0.950	26.29	-4.0
Pentanol	0.902	31.57	-3.5
Hexanol	0.880	37.20	-3.5
Heptanol	0.845	42.70	-3.7
Octanol	0.827	48.20	-3.6
Decanol	0.812	59.11	-3.7

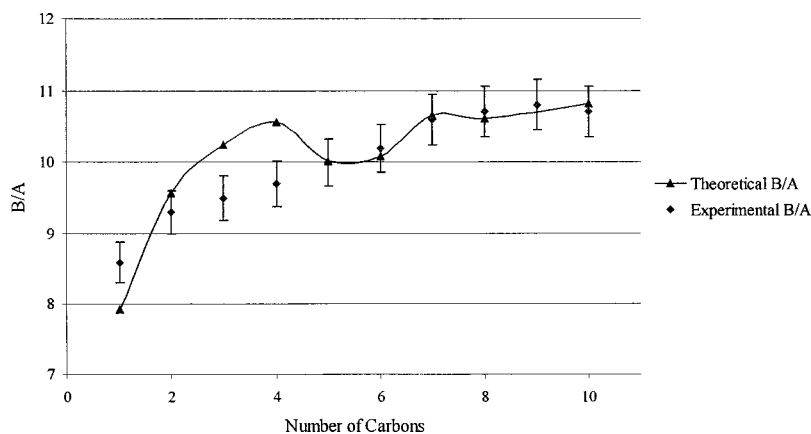


FIG. 5. Comparison between calculated and experimental values of B/A for 1-alkanols using modified Tong *et al.*'s model.

V. CONCLUSIONS

In this study we characterized the nonlinearity parameter of three chemical families and found that our measurements were in reasonable agreement with the values found in the literature, at least for the common liquids. We showed that for alkanols, ketones, and alkyl esters, B/A increases with chain length up to a saturation region for higher order elements. We also showed that these solvents do not obey Ballou's rule, exhibiting an opposite variation, leading to its inadequacy to predict B/A and its dependence with sound velocity. Finally, B/A and chain length dependence could be predicted for 1-alkanols, using a modified model based on Tong *et al.*'s one, achieving better accuracy than with the original model. Nevertheless, more experiments need to be performed, especially on higher order chemicals, to confirm the saturation of the nonlinear parameter with chain length.

ACKNOWLEDGMENT

This work was supported by the Natural Sciences and Engineering Research Council of Canada.

- ¹A. B. Coppens, R. T. Beyer, M. B. Seiden, J. Donohue, F. Guepin, R. H. Hodson, and C. Townsend, "Parameter of nonlinearity in fluids," *J. Acoust. Soc. Am.* **38**, 797–804 (1965).
- ²C. M. Seghal, R. C. Bahn, and J. F. Greenleaf, "Measurement of the acoustic nonlinearity B/A in human tissues by a thermodynamic method," *J. Acoust. Soc. Am.* **76**(4), 1023–1029 (1984).
- ³Z. Zhu, M. S. Roos, W. N. Cobb, and K. Jensen, "Determination of the acoustic nonlinearity parameter B/A from phase measurements," *J. Acoust. Soc. Am.* **74**(5), 1518–1521 (1983).
- ⁴E. Carr Everbach and R. E. Apfel, "An interferometric technique for B/A measurement," *J. Acoust. Soc. Am.* **98**(6), 3428–3438 (1995).
- ⁵W. Cobb, "Finite amplitude method for the determination of the acoustic nonlinearity parameter B/A ," *J. Acoust. Soc. Am.* **73**(5), 1525–1531 (1983).
- ⁶F. Dunn, W. K. Law, and L. A. Frizzel, "Nonlinear ultrasonic wave propagation in biological materials," 1981 IEEE Ultrasonic Symposium, pp. 527–532 (1981).
- ⁷L. Germain, R. Jacques, and J. D. N. Cheeke, "Acoustic microscopy applied to nonlinear characterization of biological media," *J. Acoust. Soc. Am.* **86**(4), 1560–1565 (1989).
- ⁸S. Saito, "Measurement of the acoustic nonlinearity parameter in liquid media using focused ultrasound," *J. Acoust. Soc. Am.* **93**(1), 162–172 (1993).
- ⁹S. Saito, "Measurement of acoustic nonlinearity parameter using focused ultrasound by a concave receiver," *J. Acoust. Soc. Jpn. (E)* **16**(4), 239–246 (1995).
- ¹⁰W. K. Law, L. A. Frizzel, and F. Dunn, "Comparison of thermodynamic and finite amplitude methods of B/A measurement in biological materi-

- als," *J. Acoust. Soc. Am.* **74**(4), 1295–1297 (1983).
- ¹¹H. A. Kashkooli, P. J. Dolan, Jr., and C. W. Smith, "Measurement of the acoustic nonlinearity parameter in water, methanol, liquid nitrogen, and liquid helium-II by two different methods: A comparison," *J. Acoust. Soc. Am.* **82**(6), 2086–2089 (1987).
- ¹²B. Hartmann, "Potential effects on the sound speed in liquids," *J. Acoust. Soc. Am.* **65**(6), 1392–1396 (1979).
- ¹³G. N. Sarsikov and D. A. Tikhonov, "Determination of the nonlinearity parameter B/A in the theory of liquids," *Acoust. Phys.* **39**(3), 283–286 (1993).
- ¹⁴W. M. Madigosky, I. Rosenbaum, and R. Lucas, "Sound velocities and B/A in fluorocarbon fluids and in several low density solids," *J. Acoust. Soc. Am.* **69**(6), 1639–1643 (1981).
- ¹⁵H. Endo, "Prediction of the nonlinearity parameter of a liquid from the Percus-Yevick equation," *J. Acoust. Soc. Am.* **83**(6), 2043–2046 (1988).
- ¹⁶B. K. Sharma, "Relationship between molecular constant, Grüneisen and nonlinearity parameters and intermolecular volume expansivity of liquids using thermo-acoustic data," *Phys. Status Solidi A* **149**, 567–574 (1995).
- ¹⁷R. T. Beyer, *Nonlinear Acoustics* (U.S. G.P.O., Washington, DC, 1974).
- ¹⁸B. Frank and J. D. N. Cheeke, "On the Mie potential and the acoustic nonlinear parameter B/A ," *J. Acoust. Soc. Am.* **101**(2), 1184–1186 (1997).
- ¹⁹J. Tong, Y. Dong, and T. Tong, "Expressions of acoustic parameters in organic liquid derived from Schaaf's theory," *J. Acoust. Soc. Am.* **93**(1), 291–194 (1993).
- ²⁰J. Banchet, J. Cancian, and J. D. N. Cheeke, "Measurement of the acoustic nonlinearity parameter in 1-alkanols," *Ultrasonics* **38**, 301–304 (2000).
- ²¹Landolt-Bornstein, *Zahlenwerte und Funktionen aus Naturwissenschaften und Technik, Gruppe II: Atom und Molekularphysik, Band 5 Molekularkustik* (Springer-Verlag, Berlin, 1967).
- ²²I. A. Mamedov, "Absorption of sound in acetic esters," *Russ. J. Phys. Chem.* **46**(10), 1448–1450 (1972).
- ²³V. A. Atoyan, "Thermodynamic properties of some ketones at temperatures from 273 to 473 K and pressures from 0.1 to 156.8 MPa," *Russ. J. Phys. Chem.* **67**(11), 2062–2065 (1993).
- ²⁴K. L. Narayana and K. M. Swamy, "Nonlinear acoustical properties in *n*-Amyl alcohol," *Acustica* **47**, 51–52 (1980).
- ²⁵K. L. Narayana and K. M. Swamy, "Acoustic nonlinearity parameter (B/A) in *N*-pentane," *Acustica* **49**, 336–339 (1981).
- ²⁶S. Prakash, S. K. Kor, and C. L. Singh, "Nonlinearity acoustic parameter in higher alkanes," *Acustica* **27**, 28–30 (1972).
- ²⁷E. Everbach, Z. Zhu, J. Jiang, Z. Chu, and R. E. Apfel, "A corrected mixture law for B/A ," *J. Acoust. Soc. Am.* **89**(1), 446–447 (1991).
- ²⁸W. Schaaffs, "Zur Bestimmung von Molekularradien organischer Flüssigkeiten aus Schallgeschwindigkeit und Dichte," *Z. Phys.* **114**, 110–115 (1939).
- ²⁹B. Garcia, F. J. Francisco, R. Alcalde, and J. P. Leal, "Molar excess volume of binary mixtures: 2-pyrrolidinone with C_6 - C_{10} *n*-alkanols," *Can. J. Chem.* **74**, 121–128 (1996).
- ³⁰J. A. Riddick, *Organic Solvents: Physical Properties and Methods of Purification* (Wiley, New York, 1986), p. 1325.
- ³¹R. C. Wilhoit, "Physical and thermodynamic properties of aliphatic alcohols," *J. Phys. Chem. Ref. Data Suppl.* **2**, 420 (1973).
- ³²N. A. Lange, *Lange's Handbook of Chemistry*, 13th ed. (McGraw-Hill, New York, 1985).

A simplified algorithm for the second-order sound fields

Desheng Ding

Department of Electronic Engineering, Southeast University, Nanjing 210096, People's Republic of China

(Received 10 June 2000; accepted for publication 26 August 2000)

An analytical description for the second-order field of the sum-, difference-frequency and second harmonic components is derived. This treatment is based on the fact that an arbitrary axially symmetric beam can be expressed as the linear superposition of a set of Gaussian beams [J. J. Wen and M. A. Breazeale, *J. Acoust. Soc. Am.* **83**, 1752–1756 (1988)], so that the three-dimensional integral for the second-order components is typically expressed as a combination of a set of interaction terms of the Gaussian beams. Correspondingly, the evaluation of the field distribution is reduced to the summation of exponential integral functions. From some examples, the present approach provides the results for the second-order field, which are in good agreement with those obtained directly by numerical integration. © 2000 Acoustical Society of America.

[S0001-4966(00)00212-5]

PACS numbers: 43.25.Cb [MAB]

I. INTRODUCTION

As a modification of the Burgers equation, the Khokhlov–Zabolotskaya–Kuznetsov (KZK) equation^{1,2} plays a significant role in analysis of the nonlinear propagation of finite-amplitude sound beams.^{1–9} This equation provides an excellent model for the sound field from a plane source of arbitrary shape, phase and/or amplitude shading when the source dimension to wavelength ratio is large and observation takes place away from the sound source and boundaries. It also can be applied to predict the acoustic field from a focused source. Various computer algorithms have been developed to solve numerically the KZK equation, showing that the computational predictions agree well with the relevant experimental data.^{3–9} Among these algorithms, a universal treatment is the Fourier expansion method (also referred to as the fully nonlinear theory) that expands the sound pressure in a Fourier series with respect to retarded time. Accordingly, the harmonics (and the parametrically generated spectral components by different frequency waves) are governed by an infinite set of coupled differential equations in the amplitudes, which are truncated and solved by numerical approximations, such as the finite difference method. A main disadvantage of this algorithm as well as a variety of its improved versions is time consumption, however.

When the sound pressure level is moderate and all the harmonics (or parametrically generated spectral components) that are higher than the second order are assumed to be negligible; that is, under the so-called quasilinear approximation, an analytical description of the field of nonlinearly generated second harmonic, difference-, and sum-frequency waves has been presented by many investigators.^{10–19} For an arbitrary axially symmetric source, the complex pressure amplitude of the various second-order field components is generally expressed in terms of three-dimensional integrals which have to be evaluated numerically. Correspondingly, the linearized solution for the fundamental (primary) sound field is described by a single-dimensional integral, i.e., the Fresnel diffraction integral. This formulation affords an accurate de-

scription of both far field and near field, except in the near vicinity of the source. The experimental results are in good agreement with the theoretical predictions by numerical integration.

As one may have seen, even though in the linear approximation, an onerous numerical calculation is necessary to describe the fundamental field distribution of an arbitrary source, because the field integrals are in terms of the Bessel function and the exponential function with imaginary arguments, and therefore strongly oscillatory. Fortunately, this problem has been partly overcome by a series of papers.^{20–23} A key ideal is based on the assumption that the beam function may be expanded into a set of basis functions, such as Gaussian, and Gaussian–Laguerre functions. The property of the basic beams represented by these basis functions has been well established, resulting in an analytical expression of the sound field in a relatively simple way.

In the present paper, we consider an excellent work of Wen and Breazeale²¹ as a known result that an arbitrary axially symmetric sound beam can be expanded into an approximate sum of complex Gaussian beams. By this result, we express the nonlinearly generated sum and difference sound fields in terms of the exponential integral function, a special function that has been tabulated. Some numerical examples are presented in comparison with the calculated results directly from the three-dimensional integral. A good agreement is demonstrated. This paper includes the study of the second harmonic field in the companion paper as a special case.²⁰

II. THEORY

A. Field integral

The derivation procedure of the linearized and quasilinear solutions to the KZK equation (or the equivalent of this equation) has been given substantially in many references.^{11–17} Here what we shall do further is to express these field integrals in terms of nondimensional variables. Suppose that two axially symmetric sources (or one source excited by different frequency components) oscillate har-

monically at two different angular frequencies ω_j ($j=1,2$ and $\omega_1 > \omega_2$ without loss of generality) and the sound absorption of the medium is ignored. Formally, the linearized solution of the sound field of the primary (fundamental) waves is expressed as¹¹⁻¹⁷

$$p_1^{(j)}(\xi_j, \eta_j, \tau_j) = \text{Re}[p_{0j} e^{-i\tau_j} \bar{q}_1^{(j)}(\xi_j, \eta_j)], \quad (1a)$$

where

$$\begin{aligned} \bar{q}_1^{(j)}(\xi_j, \eta_j) &= \frac{2}{i\eta_j} \int_0^\infty \exp\left(i \frac{\xi_j^2 + \xi_j'^2}{\eta_j}\right) J_0\left(\frac{2\xi_j \xi_j'}{\eta_j}\right) \\ &\times \bar{q}_1^{(j)}(\xi_j', \eta_j') d\xi_j'. \end{aligned} \quad (1b)$$

The quasilinear solution for the second harmonic, difference-, and sum-frequency waves, entirely named as the second-order sound field, has a universal form of

$$\begin{aligned} p_{lm}(\xi, \eta, \tau) \\ = \text{Re} \left\{ -(l+m)^2 p_{0l} p_{0m} \left[\frac{\beta(ka)^2}{\rho c^2} \right] e^{-i(l+m)\tau} \bar{q}_{lm}(\xi, \eta) \right\}, \end{aligned} \quad (2a)$$

where

$$\begin{aligned} \bar{q}_{lm}(\xi, \eta) &= \frac{1}{2} \int_{\eta'=0}^\eta \int_{\xi'=0}^\infty \frac{\xi'}{\eta - \eta'} \exp\left(\frac{i(l+m)(\xi^2 + \xi'^2)}{\eta - \eta'}\right) \\ &\times J_0\left(\frac{2(l+m)\xi\xi'}{\eta - \eta'}\right) \bar{q}_1^{(1)}(\xi_1', \eta_1') \\ &\times \bar{q}_1^{(2)}(\xi_2', \eta_2') d\xi' d\eta'. \end{aligned} \quad (2b)$$

With the exception for the second harmonic, Eq. (2a) should be multiplied by the factor 1/2. In these equations, $\tau_j = \omega_j t - k_j z$, $p_{0j} = \rho u_{0j} c$ is the characteristic pressure amplitude of primary waves, and u_{0j} is the amplitude of vibration velocity on the source. $k_j = \omega_j / c$ ($k_1 > k_2$) denotes the wave number of primaries. ρ , c , and β are the density, sound speed, and acoustic nonlinear parameter of the medium, respectively. As usual, r and z represent the radial and axial coordinates. Correspondingly, $\xi_j = r/a$ and $\eta_j = 2z/k_j a^2$ are radially and axially dimensionless coordinates, or more properly as auxiliary variables, and the notation a characterizes the size of the sources. Generally, we may take a as the radius of an alternative of the two sources. $\bar{q}_1^{(1)}(\xi_1')$ and $\bar{q}_1^{(2)}(\xi_2')$ defined as the source distribution functions and unnecessarily identical. We shall explain this definition from a typical example in Appendix B. In Eq. (2), the other notations are defined in such a way: $\eta = 2z/ka^2$, $k = (k_1 + k_2)/2$, $l = k_1/k$, and $m = k_2/k$. Additionally, $\tau = \omega t - kz$ with $\omega = kc$. Obviously, when $k_1 = k_2$, Eq. (2b) is just the expression for the second harmonic field. If we simply take $m = -k_2/k$, a negative value, Eq. (2) indeed describes the difference-frequency generation of sound beams.

B. Gaussian expansion

In one paper of Wen and Breazeale,²¹ they expressed the distribution function of an axially symmetric source as a linear superposition of complex Gaussian functions and reduced the sound field distribution to the calculation of

Gaussian functions.²¹ Mathematically, this expansion implies that a class of functions can be expressed approximately by a sum of a set of Gaussian functions, namely,

$$f(\xi) = \sum_{k=1}^N A_k \exp(-B_k \xi^2), \quad (3)$$

where the expansion and Gaussian coefficients, A_k and B_k , can be found out by computer optimization.²¹ Wen and Breazeale obtained one of the coefficient sets, containing only 10 terms of coefficients ($N=10$), to match the circ function; moreover, they calculated the sound field distribution of a uniform piston source. It is found that an excellent agreement between a 10-term Gaussian beam solution and the results of numerical integration is obtained throughout the beam field, and discrepancies exist only in the extreme near field (<0.12 times the Fresnel distance).²¹ In what follows we take Eq. (3) as a *known result, an approximation to the source distribution functions*, and parallel to the second harmonic case,²⁰ we present an efficient approach to calculating the integral (2) for the sum- and difference-frequency fields.

C. Interaction terms of Gaussian beams

From the result above, we may expand the source distribution function $\bar{q}_1^{(j)}(\xi_j)$ into the right-hand-side form of Eq. (3). Accordingly, the fundamental sound beam is given by the linear combination of a series of Gaussian beams,

$$\bar{q}_1^{(j)}(\xi_j, \eta_j) = \sum_{k=1}^{N_j} \bar{q}_{1k}^{(j)}(\xi_j, \eta_j). \quad (4)$$

With substitution of Eq. (4) into Eq. (2b), we have

$$\begin{aligned} \bar{q}_{lm}(\xi, \eta) &= \sum_{k=1}^{N_1} \sum_{k'=1}^{N_2} \frac{1}{2} \int_{\eta'=0}^\eta \int_{\xi'=0}^\infty \frac{\xi'}{\eta - \eta'} \\ &\times \exp\left(\frac{i(l+m)(\xi^2 + \xi'^2)}{\eta - \eta'}\right) J_0\left(\frac{2(l+m)\xi\xi'}{\eta - \eta'}\right) \\ &\times [\bar{q}_{1k}^{(1)}(\xi_1', \eta_1') \bar{q}_{1k'}^{(2)}(\xi_2', \eta_2')] d\xi' d\eta'. \end{aligned} \quad (5)$$

Intuitively, the second-order sound field may be understood, from Eq. (5), as the linear summation of the interactions of all the Gaussian beam components under the quasilinear approximation.

Now we consider a relatively general case in which the two axially symmetric sources are focused spherically. The sound field of a plane source may be viewed as a special case when the focal length goes into infinity. The action of focusing is (approximately) equivalent to a spatial modulation of the plane source distribution.¹¹ By Eq. (3), we may write the distribution function of any focused source into

$$\begin{aligned} \bar{q}_1^{(j)}(\xi_j) &= \left[\sum_{k=1}^{N_j} A_k^{(j)} \exp(-B_k^{(j)} \xi_j^2) \right] \exp(-i \xi_j^2 / \delta_j') \\ &= \sum_{k=1}^{N_j} A_k^{(j)} \exp(-B_k^{(j)} \xi_j^2) \end{aligned} \quad (6)$$

with the Gaussian coefficients $B_k^{(j)} = B_k^{(j)} + i/\delta_j' \cdot D_j$ is the geometric focal length and $\delta_j' = 2D_j/k_j a^2 = \delta_j/(k_j/k)$ the

nondimensional form of this parameter. In most practical uses, we may set $D_1=D_2$ and therefore have $\delta_1=\delta_2=\delta$. This corresponds to the case that two sound beams are focused by the same lens. It is well known that the fundamental field of a Gaussian source $\exp(-B_k^{(j)}\xi_j^2)$ is²¹

$$\hat{q}_{1k}^{(j)}(\xi_j, \eta_j) = \frac{1}{1 + iB_k^{(j)}\eta_j} \exp\left(-\frac{B_k^{(j)}}{1 + iB_k^{(j)}\eta_j} \xi_j^2\right). \quad (7)$$

Thus the sound field with the source distribution of Eq. (6) is expanded into

$$\begin{aligned} \bar{q}_1^{(j)}(\xi_j, \eta_j) &= \sum_{k=1}^{N_j} \frac{A_k^{(j)}}{1 + iB_k^{(j)}\eta_j} \exp\left(-\frac{B_k^{(j)}}{1 + iB_k^{(j)}\eta_j} \xi_j^2\right) \\ &= \sum_{k=1}^{N_j} A_k^{(j)} \hat{q}_{1k}^{(j)}(\xi_j, \eta_j). \end{aligned} \quad (8)$$

The remaining problem is to simplify the integral in Eq. (5). With substitution of Eq. (8) into Eq. (5), we denote by $\bar{q}_{lm}(\xi, \eta; k, j)$ the nonlinear interaction term of any two Gaussian beams $\hat{q}_{1k}^{(1)}(\xi_1, \eta_1)$ and $\hat{q}_{1j}^{(2)}(\xi_2, \eta_2)$. Making some transforms of variables from η'_1 and η'_2 to η' , and letting

$$B_{lk} = \frac{B_k^{(1)}}{l} + \frac{i}{\delta}, \quad B_{mj} = \frac{B_j^{(2)}}{m} + \frac{i}{\delta} \quad (9)$$

finally we have, after a series of complicated computations,

$$\begin{aligned} \bar{q}_{lm}(\xi, \eta; k, j) &= \frac{1}{4r_1} \exp\left(-\frac{s_1}{r_1} \xi^2\right) \\ &\times \left[E_1\left(\frac{s_2}{r_1(r_1\eta + r_2)} \xi^2\right) - E_1\left(\frac{s_2}{r_1 r_2} \xi^2\right) \right], \end{aligned} \quad (10)$$

where

$$r_1 = (lB_{mj} + mB_{lk}) + i(l+m)\eta B_{lk}B_{mj}, \quad (11a)$$

$$r_2 = (lB_{lk} + mB_{mj})\eta - i(l+m), \quad (11b)$$

$$s_1 = (l+m)^2 B_{lk}B_{mj}, \quad (11c)$$

$$s_2 = -i(l+m)lm(B_{lk} - B_{mj})^2 \quad (11d)$$

and $E_1(z)$ is the exponential integral function.²⁴ Therefore, the sum- and difference-frequency sound beams can be expressed by

$$\bar{q}_{lm}(\xi, \eta) = \sum_{k=1}^{N_1} \sum_{j=1}^{N_2} A_k^{(1)} A_j^{(2)} \bar{q}_{lm}(\xi, \eta; k, j). \quad (12)$$

In the particular case of $\xi=0$, i.e., on the acoustic axis, Eq. (10) is further reduced to

$$\bar{q}_{lm}(0, \eta; k, j) = \frac{1}{4r_1} \ln\left(1 + \frac{r_1}{r_2}\right) \quad (13)$$

by using the series expansion of exponential integral functions and letting ξ approach zero in Eq. (10). In this case, the estimation of the second-order sound field is involved in only the logarithm functions.²⁰

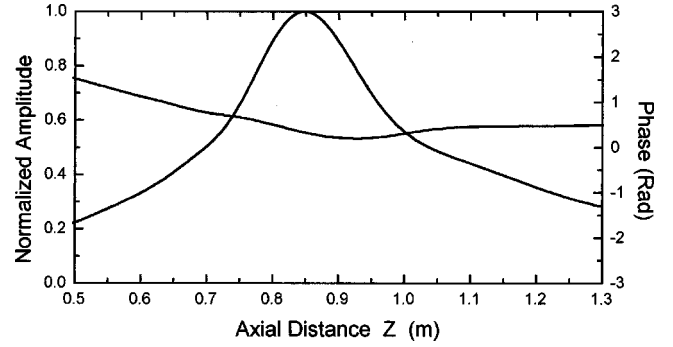


FIG. 1. The field distribution of difference-frequency generation of a focused piston source ($f_1=403$ kHz, $f_2=373$ kHz, $a=20$ cm, $D=85$ cm, $c=1451$ m/s). The present results correspond to Fig. 1 in Ref. 18.

III. NUMERICAL RESULTS

To show the applicability of this method, as an example, we compute the amplitude and phase distributions on the acoustic axis of the difference-frequency pressure by a focused piston source, as shown in Fig. 1. For comparison, the parameters in the calculation are taken from Refs. 13 or 18: $f_1=403$ kHz and $f_2=373$ kHz for the primary frequencies, $a=0.2$ m for the radius of the source, $D=0.85$ m for the focal length, and $c=1451$ m/s for the sound speed in water. It can be seen that our results are in excellent agreement with those calculated using directly numerical integration [see Fig. 1 of Ref. 18, which shows the slow phase and amplitude of the difference-frequency pressure, also see Figs. 2(a) and (b) of Ref. 13].

As our second example, we consider the sum- and difference-frequency sound fields nonlinearly generated by the uniform planar piston sources. All parameter values in the calculation are taken from Refs. 15 and 17. Figures 2(a) and (b) show the results for the pressure amplitude and phase variation on the beam axis. Furthermore, Figs. 2(c)–(f) illustrate the radial distribution of the pressure and phase at the various cross planes normal to the acoustic axis. Again, we see from these figures that a good agreement is obtained (see Figs. 13, 14, and 10 of Ref. 17, and see Fig. 11 of Ref. 15). As one can see from Fig. 1, there is a phase shift of π radians on the phase curves. Similar phenomena appear also in Fig. 2. However, this difference is only due to the different assumptions of the time dependence for the fundamental pressure of Eq. (1) in this paper and the different referenced phase. The Gaussian and expansion coefficients used in our calculation are from Table I of Ref. 21.

In principle, the present calculation method is applicable to the other circumstances under which the distribution of sources is the uniform piston given by the examples above, provided the Gaussian and expansion coefficients for the source function are known. Some further discussions of our method are given in the Appendixes.

IV. CONCLUSION

We have obtained an analytical description for the nonlinear sound fields of the sum (inclusive of the second harmonic as a special case) and difference frequency under the quasilinear approximation. A key to this analysis is based on

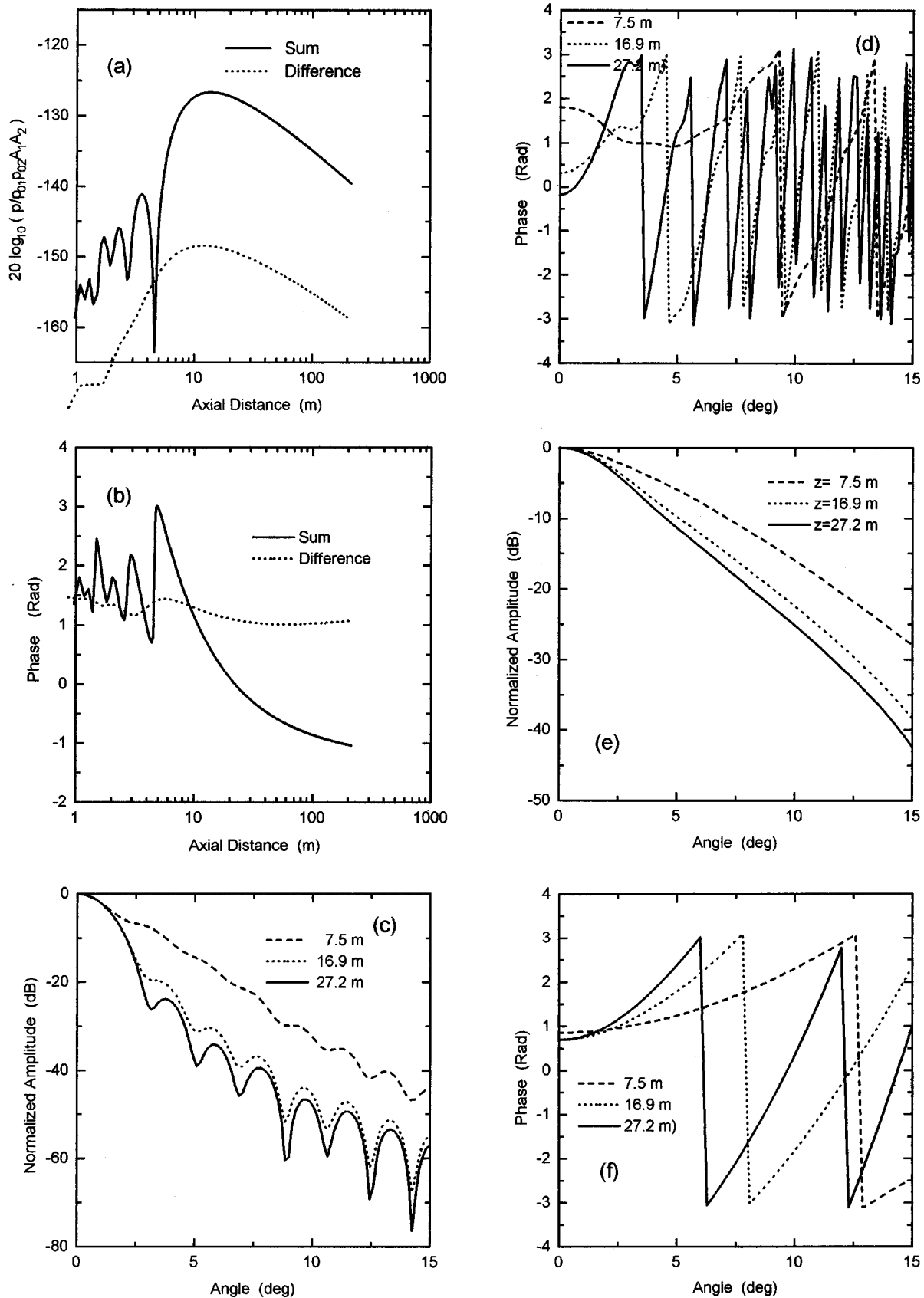


FIG. 2. The second-order sound field distribution ($\rho=995.8 \text{ kg/m}^3$, $c=1497.7 \text{ m/s}$, $\beta=3.59$, $a_1=0.87 \text{ m}$, $a_2=0.83 \text{ m}$, $f_1=16 \text{ kHz}$, $f_2=11 \text{ kHz}$, and here $A_i=\pi a_i^2$ is the surface area of the source). (a) The pressure amplitude of the difference- and sum-frequency components, on the acoustic axis (cf. Fig. 13 of Ref. 17). (b) The phase of the difference- and sum-frequency components, on the acoustic axis (cf. Fig. 14 of Ref. 17). (c) The normalized pressure amplitude of the sum-frequency component, at various plane cross the axis (cf. Fig. 10 of Ref. 17). (d) The phase of the sum-frequency component, at various plane cross the axis (cf. Fig. 11 of Ref. 15). (e) The normalized pressure amplitude of the difference-frequency component, at various plane cross the axis (cf. Fig. 11 of Ref. 15). (f) The phase of the difference-frequency component, at various plane cross the axis (cf. Fig. 11 of Ref. 15). In (e) and (f), $f_1=15 \text{ kHz}$, $f_2=12 \text{ kHz}$.

a known result that the source function can be expanded into a sum of Gaussian functions. Then, the three-dimensional integral governing these second-order fields is generally expressed in terms of exponential integral functions. The numerical examples, have demonstrated that the approach in this paper permits for the second-order field distribution an excellent agreement with the results found in the references. An obvious advantage of this method is an extreme reduction of the computation time for the second-order field distribution.

ACKNOWLEDGMENTS

This work was supported by the National Natural Science Foundation of China via Research Grant No. C-AD40502-19904003.

APPENDIX A

The derivation of the result of Eq. (10) in the text is based on an integral formula of Bessel functions with Gaussian (exponential) functions. It is²⁴

$$\int_0^\infty e^{-a^2 t^2} t^{\mu+1} J_\mu(bt) dt = \frac{b^\mu}{(2a^2)^{\mu+1}} e^{-(b^2/4a^2)} \quad (\text{A1})$$

with $\text{Re}(\mu) > -1$ and $\text{Re}(a^2) > 0$. A brief outline of the derivation process is given here. With the notation (9), Eq. (7) may be written as

$$\hat{q}_{1k}^{(1)}(\xi, \eta) = \frac{1}{1 + iB_{lk}\eta} \exp\left(-\frac{lB_{lk}}{1 + iB_{lk}\eta} \xi^2\right) \quad (\text{A2})$$

and

$$\hat{q}_{1j}^{(2)}(\xi, \eta) = \frac{1}{1 + iB_{mj}\eta} \exp\left(-\frac{mB_{mj}}{1 + iB_{mj}\eta} \xi^2\right). \quad (\text{A3})$$

According to Eq. (2b), we have

$$\begin{aligned} \bar{q}_{lm}(\xi, \eta; k, j) &= \frac{1}{2} \int_{\eta'=0}^{\eta} \int_{\xi'=0}^{\infty} \frac{\xi'}{\eta - \eta'} \\ &\times \exp\left(\frac{i(l+m)(\xi^2 + \xi'^2)}{\eta - \eta'}\right) \\ &\times J_0\left(\frac{2(l+m)\xi\xi'}{\eta - \eta'}\right) \\ &\times \frac{1}{(1 + iB_{lk}\eta')(1 + iB_{mj}\eta')} \\ &\times \exp\left(-\frac{lB_{lk}\xi'^2}{1 + iB_{lk}\eta'} - \frac{mB_{mj}\xi'^2}{1 + iB_{mj}\eta'}\right) d\xi' d\eta'. \end{aligned} \quad (\text{A4})$$

By integrating with respect to ξ' and making some arrangements, we get

$$\begin{aligned} \bar{q}_{lm}(\xi, \eta; k, j) &= \frac{1}{4} \exp\left(-\frac{s_1}{r_1} \xi^2\right) \int_{\eta'=0}^{\eta} \frac{1}{r_1 \eta' + r_2} \\ &\times \exp\left(-\frac{s_2 \xi^2}{r_1(r_1 \eta' + r_2)}\right) d\eta'. \end{aligned} \quad (\text{A5})$$

Thus Eq. (A5) may be expressed as Eq. (10) in the text, from the definition of exponential integral functions.

We want to point out that the present approach is applicable to the calculation of the second-order field distribution when the acoustic absorption of the medium is accounted for. In this case, Eq. (10), replaced by a one-dimensional integral, is of the form $\int x^{-1} e^{-ax-b/x} dx$. The numerical performance of this integral is easy. As expected, a great reduction of computation amount is therefore obtainable in calculation of the sound field distribution.

APPENDIX B

We demonstrate how to evaluate the distribution of the second-order sound fields by using a set of Gaussian and expansion coefficients given in Ref. 21. In this example, the sound sources consist of two parts. One is an annulus with the external radius a_2 and the internal a_1 , uniformly excited at the frequency f_1 , and the other is a circle with the radius a_3 at the frequency f_2 . The other geometry of the sources is the same as that of the first example in the text. The two source distribution functions are

$$\bar{q}_1^{(1)}(r') = \begin{cases} 0, & 0 \leq r' < a_1, \\ 1, & a_1 \leq r' < a_2, \\ 0, & r > a_2 \end{cases} \quad (\text{B1})$$

and

$$\bar{q}_1^{(2)}(r') = \begin{cases} 1, & 0 \leq r' < a_3, \\ 0, & r > a_3. \end{cases} \quad (\text{B2})$$

Put $a = a_2$, $\mu_1 = a_1/a$, and $\mu_3 = a_3/a$. With dimensionless variables, we write

$$\bar{q}_1^{(1)}(\xi') = \begin{cases} 0, & 0 \leq \xi' < \mu_1, \\ 1, & \mu_1 \leq \xi' < 1, \\ 0, & \xi' > 1 \end{cases} \quad (\text{B3})$$

and

$$\bar{q}_1^{(2)}(\xi') = \begin{cases} 1, & 0 \leq \xi' < \mu_3, \\ 0, & \xi' > \mu_3. \end{cases} \quad (\text{B4})$$

The coefficients in Table I of Ref. 21 are given for the circ function of the form

$$\text{circ}(\xi') = \begin{cases} 1, & 0 \leq \xi' < 1, \\ 0, & \xi' > 1. \end{cases} \quad (\text{B5})$$

We observe that Eqs. (B3) and (B4) are always written as the combination of the circ function (B5), so that the coefficients of these two functions may be obtained from the known Table I of Ref. 21. For example, Eq. (B3) is expressed in the form

$$\begin{aligned} \bar{q}_1^{(1)}(\xi') &= \text{circ}(\xi') - \text{circ}(\xi'/\mu_1) \\ &= \sum_{k=1}^N A_k \exp(-B_k \xi'^2) - \sum_{k=1}^N A_k \exp(-B_k / \mu_1^2 \xi'^2) \\ &= \sum_{k=1}^{N_1} A_k^{(1)} \exp(-B_k^{(1)} \xi'^2). \end{aligned} \quad (\text{B6})$$

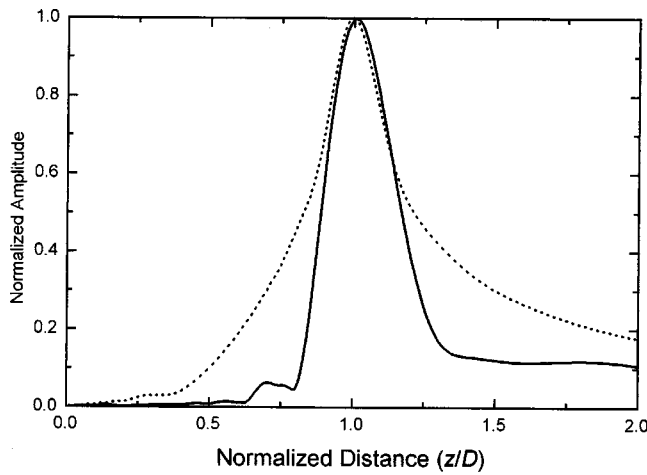


FIG. B1. The normalized amplitude of difference-frequency pressure of a focused source with different excited elements. The amplitude curve in Fig. 1 is also shown here for comparison. Interestingly, the difference-frequency generation of the parametric sound source with such a geometry is sharply focused at the focal region.

Hence the Gaussian and expansion coefficients, $B_k^{(1)}$ and $A_k^{(1)}$, of this function are also known. A similar process is suitable for determination of the coefficients of Eq. (B4). A numerical result for the difference-frequency generation at the beam axis is presented in Fig. B1, where the parameter values are $a_2 = a = 20$ cm, $a_1 = a_3 = 14$ cm ($a/\sqrt{2}$) and the others are the same as those in Fig. 1.

It must be remarked that in the all calculation the exponential integral functions in Eq. (10) should take the principal value. More exactly speaking, Eq. (10) should be calculated according to the following rule. The “principle value” of the difference of two exponential integral functions $E_1(z_1)$ and $E_1(z_2)$ is defined as

$$f(z_1, z_2) = E_1(z_1) - E_1(z_2) - i2\pi \cdot I(z_1, z_2), \quad (\text{B7})$$

where $I(z_1, z_2)$ is equal to -1 and 1 according as the value of $\arg(z_1) - \arg(z_2)$ is equal to or less than $-\pi$, and greater than π ; else $I(z_1, z_2) = 0$.

We wish to point out that other extensions to the work of Wen and Breazeale have been made in separate papers.

¹E. A. Zabolotskaya and R. V. Khokhlov, “Quasi-plane waves in the nonlinear acoustics of confined beams,” *Sov. Phys. Acoust.* **15**, 35–40 (1969).

²V. P. Kuznetsov, “Equation of nonlinear acoustics,” *Sov. Phys. Acoust.* **16**, 467–470 (1971).

³J. Naze Tójtta and S. Tójtta, “Nonlinear equations of acoustics, with

application to parametric acoustic arrays,” *J. Acoust. Soc. Am.* **69**, 1644–1652 (1984).

⁴S. I. Aanonsen, T. Barkve, J. Naze Tójtta, and S. Tójtta, “Distortion and harmonic generation in the nearfield of a finite amplitude sound beam,” *J. Acoust. Soc. Am.* **75**, 749–768 (1984).

⁵M. F. Hamilton, J. Naze Tójtta, and S. Tójtta, “Nonlinear effects in the farfield of a directive sound source,” *J. Acoust. Soc. Am.* **78**, 202–216 (1985).

⁶J. Naze Tójtta, S. Tójtta, and E. H. Vefring, “Propagation and interaction of two collimated finite amplitude sound beams,” *J. Acoust. Soc. Am.* **88**, 2859–2870 (1990).

⁷E. H. Vefring, J. Naze Tójtta, and S. Tójtta, “Effects of focusing on the nonlinear interaction between two collinear finite amplitude sound beams,” *J. Acoust. Soc. Am.* **89**, 1017–1027 (1991).

⁸T. S. Hart and M. F. Hamilton, “Nonlinear effects in focused sound fields,” *J. Acoust. Soc. Am.* **84**, 1488–1496 (1988).

⁹T. Kamakura, N. Hamada, K. Aoki, and Y. Kumamoto, “Nonlinearly generated spectral components in the nearfield of a directive sound source,” *J. Acoust. Soc. Am.* **85**, 2331–2337 (1989).

¹⁰F. H. Fenlon and F. S. McKendree, “Axisymmetric parametric radiation-A weak interaction model,” *J. Acoust. Soc. Am.* **66**, 534–547 (1979).

¹¹B. G. Lucas and T. G. Muir, “The field of a focusing source,” *J. Acoust. Soc. Am.* **72**, 1289–1296 (1982).

¹²B. G. Lucas and T. G. Muir, “Field of a finite-amplitude focusing source,” *J. Acoust. Soc. Am.* **74**, 1522–1528 (1983).

¹³B. G. Lucas, J. Naze Tójtta, and S. Tójtta, “Field of a parametric focusing source,” *J. Acoust. Soc. Am.* **73**, 1966–1971 (1983).

¹⁴G. S. Garrett, J. Naze Tójtta, and S. Tójtta, “Nearfield of a large acoustic transducer. Part. I: Linear radiation,” *J. Acoust. Soc. Am.* **72**, 1056–1061 (1982).

¹⁵G. S. Garrett, J. Naze Tójtta, and S. Tójtta, “Nearfield of a large acoustic transducer. Part. II: Parametric radiation,” *J. Acoust. Soc. Am.* **74**, 1013–1020 (1983).

¹⁶G. S. Garrett, J. Naze Tójtta, and S. Tójtta, “Nearfield of a large acoustic transducer. Part. III: General results,” *J. Acoust. Soc. Am.* **75**, 769–779 (1984).

¹⁷J. B. Berntsen, J. Naze Tójtta, and S. Tójtta, “Nearfield of a large acoustic transducer. Part. IV: Second harmonic and sum frequency radiation,” *J. Acoust. Soc. Am.* **75**, 1383–1391 (1984).

¹⁸J. Naze Tójtta and S. Tójtta, “Sound field of a parametric focusing source,” *J. Acoust. Soc. Am.* **75**, 1392–1394 (1984).

¹⁹S. Saito, “Measurement of the acoustic nonlinearity parameter in liquid media using focusing ultrasound,” *J. Acoust. Soc. Am.* **93**, 162–172 (1993).

²⁰D. Ding, Y. Shui, J. Lin, and D. Zhang, “A simple calculation approach for the second harmonic sound field generated by an arbitrary axial-symmetric source,” *J. Acoust. Soc. Am.* **100**, 727–733 (1996).

²¹J. J. Wen and M. A. Breazeale, “A diffraction beam field expressed as the superposition of Gaussian beams,” *J. Acoust. Soc. Am.* **83**, 1752–1756 (1988).

²²E. Cavanagh and B. D. Cook, “Gaussian-Laguerre description of ultrasonic fields-Numerical example: Circular piston,” *J. Acoust. Soc. Am.* **67**, 1136–1140 (1980).

²³D. Ding, J. Lin, Y. Shui, G. Du, and D. Zhang, “An analytical description of ultrasonic field produced by circular piston transducer,” *Acta Acust. (China)* **18**, 249–255 (1993).

²⁴M. Abramowitz and I. A. Stegun, *Handbook of Mathematical Functions* (Dover, New York, 1964).

Numerical analysis for nonlinear resonant oscillations of gas in axisymmetric closed tubes

Young-Doo Chun^{a)} and Yang-Hann Kim^{b)}

Center for Noise and Vibration Control (NOVIC), Department of Mechanical Engineering,
Korea Advanced Institute of Science and Technology (KAIST), Science Town, Taejeon 305-701, Korea

(Received 13 March 2000; revised 21 July 2000; accepted 27 July 2000)

A numerical investigation on nonlinear oscillations of gas in an axisymmetric closed tube is presented. When the tube is oscillated at a resonant frequency of the interior acoustic field, it is well known that acoustic variables such as density, velocity, and pressure undergo very large perturbation, often described as nonlinear oscillation. One-dimensional nonlinear governing equations, which explicitly include attenuation terms related to viscosity, were derived. Then, the equations were solved numerically by using the higher-order finite difference scheme, which divided into two parts of spatial differentiation and time evolution. Numerical simulations were accomplished to study the effect of the tube shape on the maximum pressure we can obtain. The tubes of cylindrical, conical, and cosine shape, which have the same volume and length, were investigated. Results show that the resonant frequency and patterns of pressure waves strongly depend on not only the tube shape but also the amplitude of driving acceleration. The degree of nonlinearity of wave patterns was also measured by the newly defined *nonlinear energy ratio* of the pressure signals. It was found that the $\frac{1}{2}$ cosine-shape tube is more suitable to induce high compression ratio than other shapes. © 2000 Acoustical Society of America.

[S0001-4966(00)01511-3]

PACS numbers: 43.25.Gf, 43.25.Cb [MFH]

I. INTRODUCTION

It is well known that shocks are often generated and propagate periodically back and forth in a closed cylindrical tube if interior gas is excited with its resonant frequency. This nonlinear phenomenon has been extensively investigated in many works theoretically and experimentally. Betchov¹ introduced a simple theoretical analysis of the inviscid gas motion, based on discontinuous linearized solutions and secular equation. Saenger and Hudson² also developed a theory to understand the steady state motion of the gas, which includes the dissipative effects of wall friction and heat conduction to the tube wall. They tried to describe shock waves under the assumption that the solution consisted of a continuous and discontinuous component. Chester,³ however, elegantly explained the nonlinear phenomena at near-resonant frequency without any assumption on solution form. Lee and Wang⁴ numerically analyzed the nonlinear resonance of a closed rigid tube, in which gas was assumed to be excited by an external body force. The results were very similar to those in a piston-driven resonant tube. All of these works dealt with cylindrical tubes.

Gaitan and Atchley⁵ studied nonlinear standing waves in harmonic and anharmonic tubes driven by a piston at one end at resonance. They found that anharmonic tubes effectively suppressed the generation of higher harmonic components. Recent studies^{6,7} performed at MacroSonix Corp. focused attention on inducing high acoustic pressure without

shock formation in an oscillating axisymmetric tube, and confirmed the feasibility of a sonic compressor as a commercial pump or compressor. The results revealed that the waveform of acoustic pressure is strongly related to the shape of the tube. However, while acoustic losses were considered by allowing viscous damping, governing equations were simplified by using an assumption of isentropic process and velocity potential function, which are usually applied to the motion of inviscid gas. This contrary proposition could, in some degree, mislead physical process occurring in the tube.

In this article, we investigate the nonlinear acoustic phenomena such as harmonics generation, shock formation, resonant frequency shift, etc., which are caused by the oscillation of an entire tube at resonance. First, we derive a nonlinear governing equation including viscous effects. We apply characteristic boundary conditions to this problem, and solve it numerically by using a higher-order finite difference scheme. In order to quantify the degree of nonlinearity of pressure patterns, we propose the *nonlinear energy ratio* of the pressure signals. Furthermore, we estimate pressurizing performance of various tubes such as cylindrical, conical, and cosine tubes, which have the same volume and length, and also check the nonlinear energy ratio of pressure patterns for each tube. From these results, we verify the feasibility of a sonic compressor and suggest the suitable tube shape for obtaining good compression performance. The ultimate objective of this study is to have an outline of designing the tube shape for a sonic compressor with high efficiency.

II. GENERAL GOVERNING EQUATIONS

If a wavelength is much larger than the maximum diameter of a tube, then plane waves, along the longitudinal axis,

^{a)}Electronic mail: chyd@cais.kaist.ac.kr

^{b)}Electronic mail: yhkim@sorak.kaist.ac.kr

dominate the acoustic field in the tube. When the plane waves propagate in an arbitrary axisymmetric tube, the interior acoustic field can be expressed in terms of the longitudinal axis only. In order to derive a governing equation, which describes the motion of gas in the tube, it is convenient to consider an infinitesimal control volume moving with the tube together. It is well known that, in general, the motion of a gas can be perfectly described by using five kinds of equations: three kinds of conservation equations of mass, momentum, and energy and two kinds of state equations.⁸

A. One-dimensional model

First, conservation of mass can be written as

$$\frac{\partial(\rho S)}{\partial t} + \frac{\partial(\rho S u)}{\partial x} = 0, \quad (1)$$

where S is the cross-sectional area, ρ is the gas density, and u is the relative particle velocity to the tube. At both end walls of the tube, the velocity u has to be zero, otherwise a continuum assumption is violated.

Second, conservation of momentum is expressed as

$$\begin{aligned} \frac{\partial(\rho S u)}{\partial t} + \frac{\partial(\rho S u^2)}{\partial x} \\ = -\rho S a_{\text{tube}} + S \frac{\partial}{\partial x} \left(-p + \mu_{\text{eff}} \left(\frac{1}{S} \frac{\partial(uS)}{\partial x} \right) \right), \end{aligned} \quad (2)$$

where p is the absolute pressure, a_{tube} is the driving acceleration of the tube, and μ_{eff} is the effective viscosity including bulk and shear viscosity. Therefore, we can control the input effort by changing the driving acceleration.

Conservation of energy is written in the form

$$\begin{aligned} \frac{\partial(\rho S e)}{\partial t} + \frac{\partial(\rho S e u)}{\partial x} \\ = -\rho S a_{\text{tube}} u + \frac{\partial}{\partial x} \left(-p S u + S u \mu_{\text{eff}} \left(\frac{1}{S} \frac{\partial(uS)}{\partial x} \right) \right) - \dot{q}, \end{aligned} \quad (3)$$

where e is the total energy composed of internal and kinetic energy and \dot{q} is the heat flux through the tube surface. In this study, we ignored the heat transfer between the elements of gas, but considered the conversion of mechanical energy into thermal energy due to viscosity.

For perfect ideal gas, the total energy e can be expressed as

$$e = u^2/2 + C_v T, \quad (4)$$

where C_v is the specific heat at constant volume of interior gas and T is the absolute temperature. In addition, the state equation for ideal gas is

$$p = \rho R T, \quad (5)$$

where R is the gas constant.

Equations (1)–(5) correspond to the general governing equations, so that they can well describe the gas oscillation in the tube. However, there exist some difficulties to directly apply the boundary conditions at both ends of the tube. These are because the equations are expressed in terms of

conservative variables such as ρS , $\rho S u$, and $\rho S e$. In order to conveniently consider boundary conditions, we need to transform these governing equations to those of which are presented with conventional acoustic variables such as ρ , u , and p . It is noteworthy that we can assume the coefficients μ_{eff} and C_v are constant during all processes, without loss of generality. The different form of the governing equations can be easily obtained by expanding Eqs. (1)–(3) and substituting Eqs. (4) and (5) into Eq. (3):

continuity equation

$$\frac{\partial \rho}{\partial t} + u \frac{\partial \rho}{\partial x} + \rho \frac{\partial u}{\partial x} = -\rho u \frac{1}{S} \frac{dS}{dx}, \quad (6)$$

momentum equation

$$\frac{\partial u}{\partial t} + u \frac{\partial u}{\partial x} + \frac{1}{\rho} \frac{\partial p}{\partial x} = -a_{\text{tube}} + \frac{\mu_{\text{eff}}}{\rho} \frac{\partial}{\partial x} \left(\frac{1}{S} \frac{\partial(uS)}{\partial x} \right), \quad (7)$$

energy equation

$$\begin{aligned} \frac{\partial p}{\partial t} + \gamma p \frac{\partial u}{\partial x} + u \frac{\partial p}{\partial x} = -\gamma p u \frac{1}{S} \frac{dS}{dx} + \mu_{\text{eff}} (\gamma - 1) \\ \times \left(\frac{1}{S} \frac{\partial(uS)}{\partial x} \right)^2 - \frac{(\gamma - 1)}{S} \dot{q}, \end{aligned} \quad (8)$$

where γ is the specific heat ratio defined as C_p/C_v and C_p is the specific heat at constant pressure of interior gas. Equations (6)–(8), also, can describe the motion of gas in a tube well.

However, we did not yet discuss the heat flux \dot{q} . Previous studies^{6,7} showed that the assumption of an isentropic process was valid for common refrigerant gases under our analysis conditions. The results⁷ of numerical simulations using the assumption of isentropic process were consistent with experimental results.⁶ This means that the nonreversible effects in Eq. (8) do not appear strongly, and they are relatively small enough to be ignored. In addition, a long time after beginning to excite the tube, the interior acoustic field may reach steady state in the physical sense. At steady state, the heat flux has to be balanced with the heat generation caused by viscous damping in a sense of time average. The second term on the right-hand side in Eq. (8) represents thermal energy converted from mechanical energy through viscosity. This energy transformation is a nonreversible process. Thus, the time-averaged heat flux can be estimated as follows,

$$\langle \dot{q} \rangle_{T_0} = \left\langle S \mu_{\text{eff}} \left(\frac{1}{S} \frac{\partial(uS)}{\partial x} \right)^2 \right\rangle_{T_0}, \quad (9)$$

where $\langle \cdot \rangle_{T_0}$ describes the time-averaged value during the period T_0 . In order to simplify the governing equation without considerable errors, let us replace the heat flux \dot{q} with the *effective outgoing heat flux* \dot{q}_{out} approximately using the relation of Eq. (9) as follows,

$$\dot{q}_{\text{out}} = S \mu_{\text{eff}} \left(\frac{1}{S} \frac{\partial(uS)}{\partial x} \right)^2. \quad (10)$$

Although \dot{q}_{out} does not correspond to the real heat flux at any time, it can quantitatively account for the heat generation and heat flux in a sense of time average. Hence, the energy equation (8) can be simplified as

$$\frac{\partial p}{\partial t} + \gamma p \frac{\partial u}{\partial x} + u \frac{\partial p}{\partial x} = -\gamma p u \frac{1}{S} \frac{dS}{dx}. \quad (11)$$

This simplification, however, does not introduce serious errors in the results because the two terms are very small enough to be ignored. Therefore, the acoustic field in a moving closed tube can be simply described by three governing equations (6), (7), and (11).

One can also find that Eqs. (6), (7), and (11) can be written as a simple vector form

$$\frac{\partial \mathbf{V}}{\partial t} + \mathbf{A} \frac{\partial \mathbf{V}}{\partial x} = \mathbf{H}, \quad (12)$$

where

$$\mathbf{V} = \begin{Bmatrix} \rho \\ u \\ p \end{Bmatrix}, \quad \mathbf{A} = \begin{bmatrix} u & \rho & 0 \\ 0 & u & 1/\rho \\ 0 & \gamma p & u \end{bmatrix},$$

$$\mathbf{H} = \left\{ \begin{array}{c} -\rho u \frac{1}{S} \frac{dS}{dx} \\ -a_{\text{tube}} + \frac{\mu_{\text{eff}}}{\rho} \frac{\partial}{\partial x} \left(\frac{1}{S} \frac{\partial(uS)}{\partial x} \right) \\ -\gamma p u \frac{1}{S} \frac{dS}{dx} \end{array} \right\}.$$

In Eq. (12), the vector \mathbf{V} denotes acoustic variables, \mathbf{A} corresponds to the system matrix, and vector \mathbf{H} represents source terms. As we can see in Eq. (12), time derivatives of the acoustic variables at any time step are related to the combination of spatial derivatives and source terms. Therefore, we can estimate the acoustic variables at the next time step by integrating the time derivatives of acoustic variables in Eq. (12).

However, in order to obtain correct solution of Eq. (12), initial gas properties and specific boundary conditions have to be exactly assigned at each position in the tube. Usually, it is easy to choose initial conditions appropriately because they are gas properties at the initial state, but it is not simple to determine boundary conditions correctly because they are system characteristics. In this study, unfortunately, only a velocity condition can be implemented directly at both ends of a tube. Because of the continuum assumption, the relative particle velocity has to be zero all the time, i.e., $(\partial u / \partial t)_{x=0,l} = 0$, where l is the length of a tube. Therefore, in order to solve Eq. (12) correctly, the information of density and pressure at both ends of a tube have to be related with the known condition of velocity or other interior gas properties.

B. Boundary treatment: Characteristic boundary conditions

In this article, we used characteristic boundary conditions to supplement a lack of boundary conditions. Because this technique is well explained in the references,⁹⁻¹¹ we do not deal with the theory of characteristic boundary condition technique in detail. For the system matrix \mathbf{A} , let us consider the eigenvalue matrix and its left eigenvectors at both ends of a tube. Since the relative particle velocity u is zero at the boundaries,

$$\mathbf{LAL}^{-1} = \Lambda,$$

$$\text{where } \Lambda = \begin{bmatrix} 0 & 0 & 0 \\ 0 & c & 0 \\ 0 & 0 & -c \end{bmatrix}, \quad \mathbf{L} = \begin{bmatrix} 1 & 0 & -1/c^2 \\ 0 & 1 & 1/\rho c \\ 0 & -1 & 1/\rho c \end{bmatrix}. \quad (13)$$

The i th row of matrix \mathbf{L} corresponds to the left eigenvector of \mathbf{A} for the i th eigenvalue ($i=1,2,3$), and Λ is the diagonal matrix constructed with eigenvalues. Hence, the wave speed c can be defined as $c = \sqrt{\gamma p / \rho}$. Because the relative particle velocity is zero at both ends of the tube, the three eigenvalues become 0 and $\pm c$. By multiplication of Eq. (12) by \mathbf{L} , Eq. (12) can be transformed to a characteristic form as follows:

$$\frac{\partial \mathbf{W}}{\partial t} + \Lambda \frac{\partial \mathbf{W}}{\partial x} = \hat{\mathbf{H}}, \quad (14)$$

where the vector of characteristic variables \mathbf{W} is defined by a variational form such as $\partial \mathbf{W} = \mathbf{L} \delta \mathbf{V}$ because \mathbf{L} is not a constant matrix, and the source term is rearranged as $\hat{\mathbf{H}} = \mathbf{LH}$. Therefore, Eq. (14) becomes an uncoupled equation form since Λ is a diagonal matrix. It is usually called the characteristic equation form. Equation (14) says the characteristic information of $(\mathbf{W})_i$ propagates along the characteristic line with the specific speed of $(\Lambda)_{i,i}$, which corresponds to i th eigenvalue. Thus, there are only two kinds of waves at both boundaries. One wave of $(\mathbf{W})_2$ propagates in the positive x direction with speed c , and the other wave of $(\mathbf{W})_3$ propagates in the negative x direction with speed $-c$. At the boundary of $x=0$, the wave of $(\mathbf{W})_2$ corresponds to an incoming wave from the exterior region of the tube to the interior region, but the wave of $(\mathbf{W})_3$ represents an outgoing wave. At the boundary $x=l$, on the other hand, the wave of $(\mathbf{W})_2$ corresponds to an outgoing wave from the interior region to the exterior region, but the wave of $(\mathbf{W})_3$ represents an incoming wave.

In the physical sense, the characteristics of the outgoing waves can be perfectly determined by interior field variables. However, it is not easy to determine the characteristics of incoming waves because, in general, we do not know any

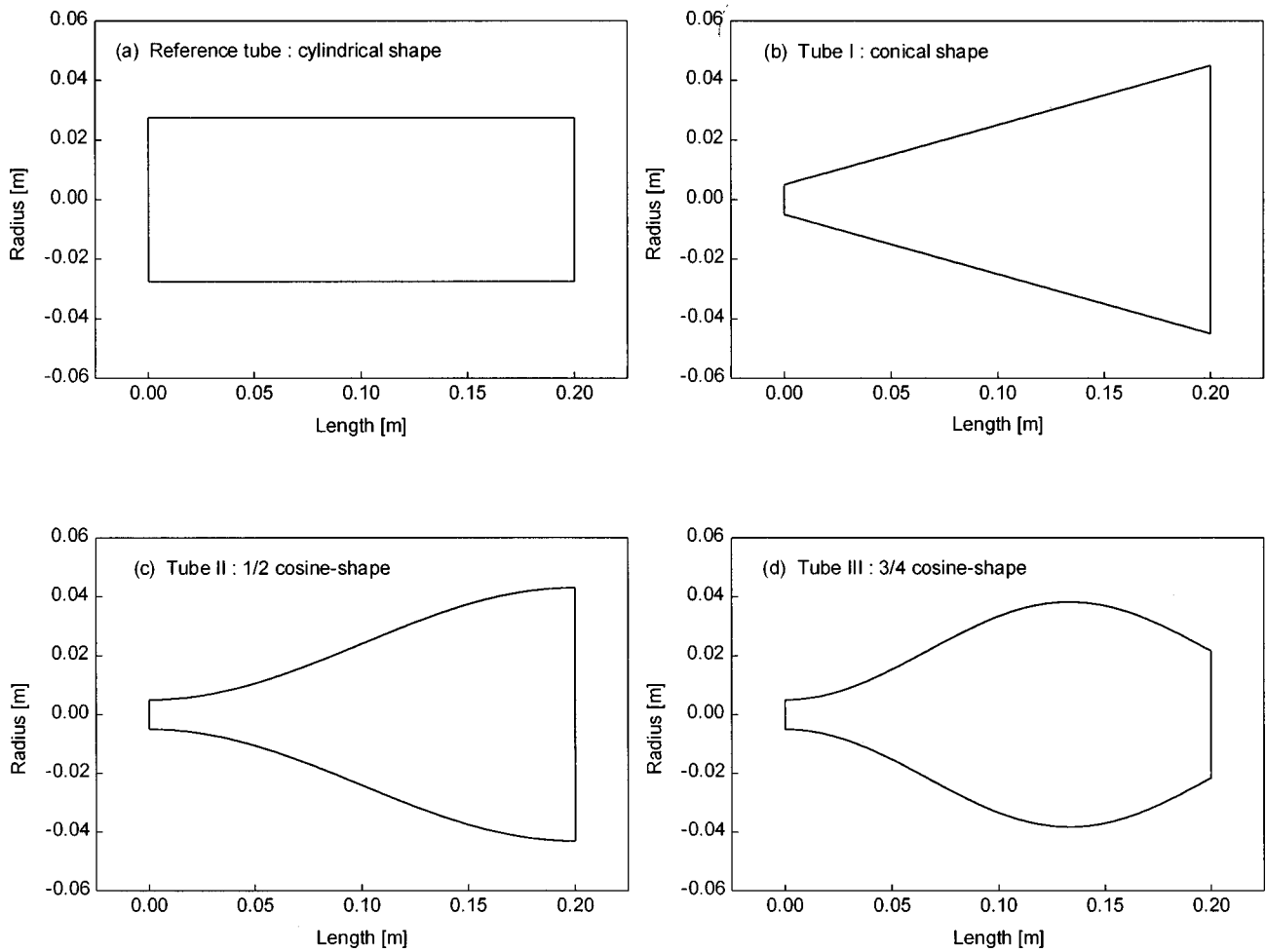


FIG. 1. Geometries of test tubes: (a) reference tube (cylindrical shape), (b) tube I (conical shape), (c) tube II ($\frac{1}{2}$ cosine shape), and (d) tube III ($\frac{3}{4}$ cosine-shape).

information about the variables external to the tube. In order to obtain the correct solutions, we have to describe the behavior of the variables for the incoming wave by using known conditions. If we define a vector $\mathbf{T} \equiv -\Lambda(\partial \mathbf{W} / \partial x)$, then Eq. (14) is rewritten as

$$\left\{ \begin{array}{l} \frac{\partial p}{\partial t} - \frac{1}{c^2} \frac{\partial p}{\partial t} \\ \frac{1}{\rho c} \frac{\partial p}{\partial t} \\ \frac{1}{\rho c} \frac{\partial p}{\partial t} \end{array} \right\} = \mathbf{T} + \hat{\mathbf{H}}. \quad (15)$$

Here, $(\mathbf{T})_1$ and $(\hat{\mathbf{H}})_1$ at both boundaries are zero because of $(\Lambda)_{1,1} = u = 0$, so that the first equation in Eq. (15) corresponding to the entropy wave behaves like an isentropic process. Therefore, for the first equation, it is not necessary to consider the characteristic boundary condition for the heat flux at $x=0$ and $x=1$. This result comes from the assumption that the effective outgoing heat flux \dot{q}_{out} has to be balanced with the heat generation as Eq. (10). However, the other equations in Eq. (15) have to be corrected by using the compatibility relation at both boundaries.⁹⁻¹¹

First, let us consider the characteristic boundary condition at $x=0$. Since the properties of outgoing wave of $(\mathbf{W})_3$ can be estimated by using the interior field variables of $(\mathbf{T} + \hat{\mathbf{H}})_3$, the time derivatives of density, velocity, and pressure can be determined as follows:

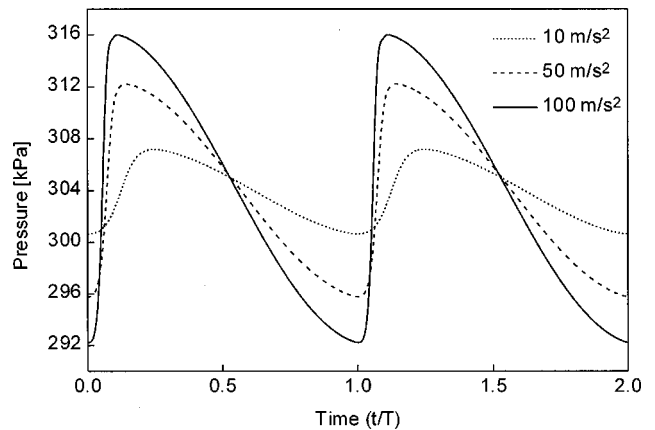


FIG. 2. Pressure patterns predicted at one end of the reference tube at resonance during two cycles when the amplitudes of driving acceleration are 10, 50, and 100 m/s^2 .

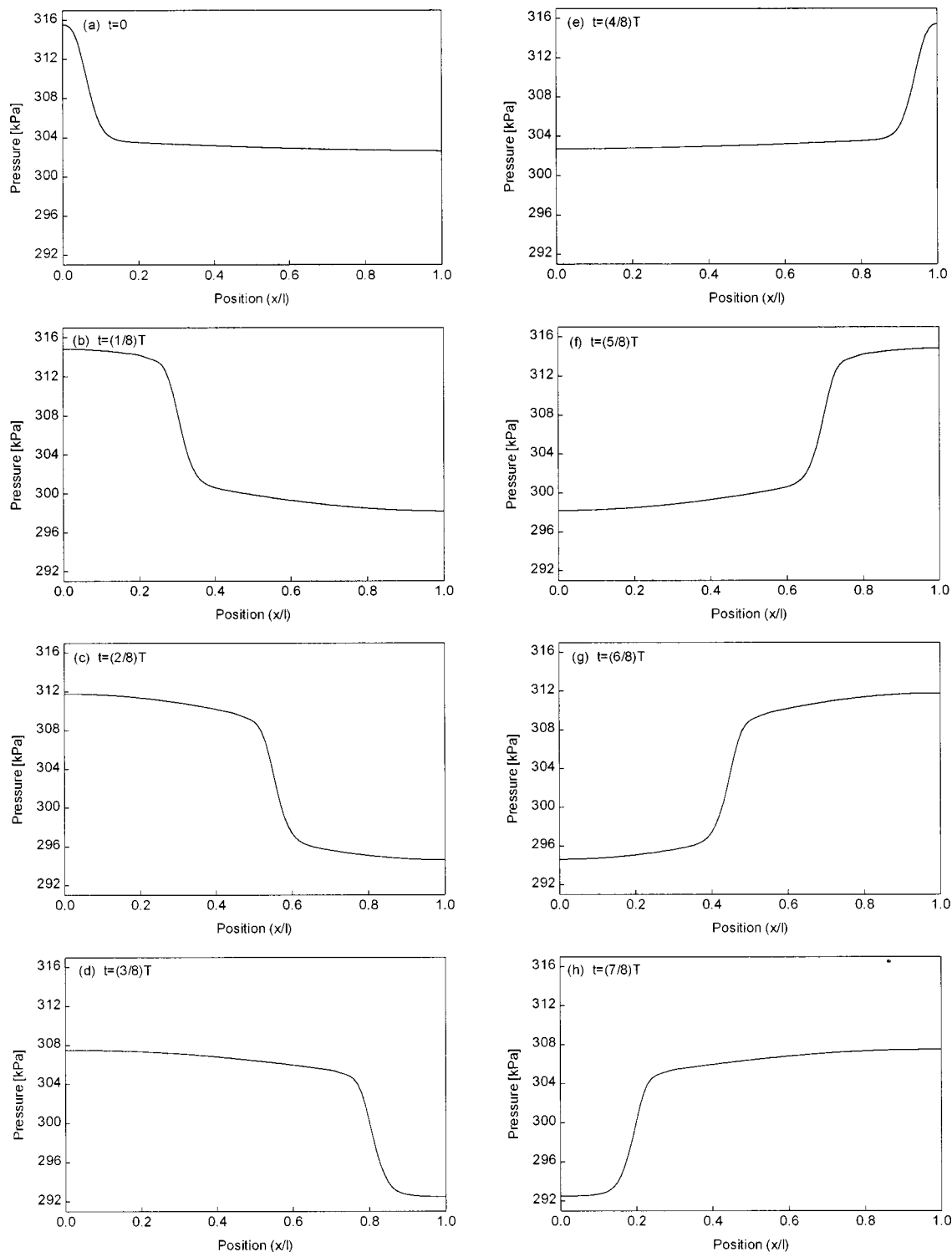


FIG. 3. Pressure profiles in the reference tube for the acceleration of 100 m/s^2 during one cycle. The figures are obtained at every time step of $\frac{1}{8}$ cycle.

$$\left. \frac{\partial u}{\partial t} \right|_{x=0} = 0, \quad \left. \frac{\partial p}{\partial t} \right|_{x=0} = \rho c (\mathbf{T} + \hat{\mathbf{H}})_3, \quad (16)$$

$$\left. \frac{\partial \rho}{\partial t} \right|_{x=0} = \frac{1}{c^2} \left. \frac{\partial p}{\partial t} \right|_{x=0} = \frac{\rho}{c} (\mathbf{T} + \hat{\mathbf{H}})_3.$$

Similarly, let us consider the characteristic boundary condition at $x=l$. Because the property of outgoing wave $(\mathbf{W})_2$

can be estimated through the interior field variables $(\mathbf{T} + \hat{\mathbf{H}})_2$, the time derivatives of density, velocity, and pressure can be determined as follows:

$$\left. \frac{\partial u}{\partial t} \right|_{x=l} = 0, \quad \left. \frac{\partial p}{\partial t} \right|_{x=l} = \rho c (\mathbf{T} + \hat{\mathbf{H}})_2, \quad (17)$$

$$\left. \frac{\partial \rho}{\partial t} \right|_{x=l} = \frac{1}{c^2} \left. \frac{\partial p}{\partial x} \right|_{x=l} = \frac{\rho}{c} (\mathbf{T} + \hat{\mathbf{H}})_2.$$

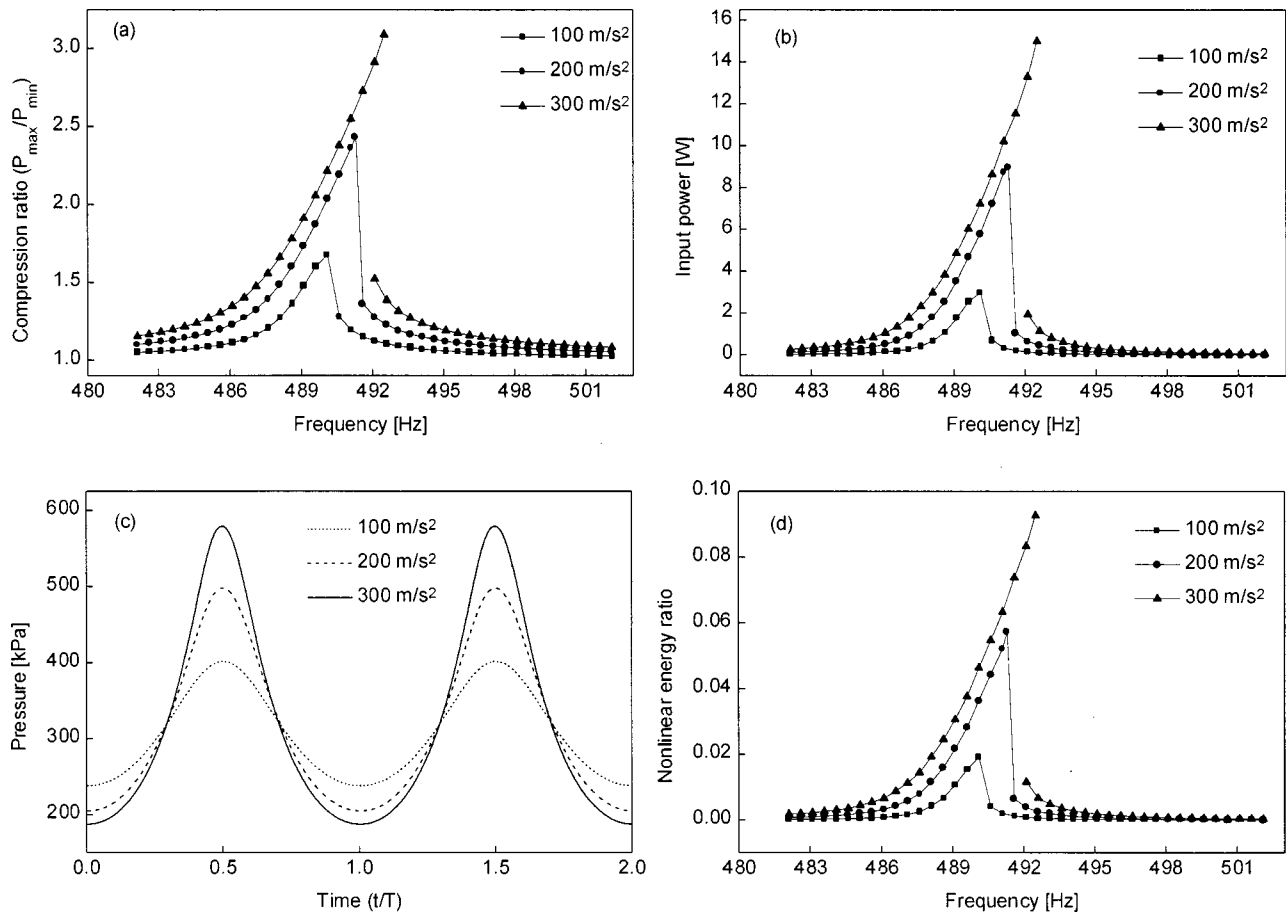


FIG. 4. Simulation results of tube I (conical shape) for different amplitudes of the driving acceleration: 100, 200, and 300 m/s². The results are obtained by harmonically exciting the tube with sweeping frequency up and down: (a) compression ratio at the small end, (b) input power, (c) pressure patterns at the small end at resonance, and (d) nonlinear energy ratio of pressure signal at the small end.

Thus, we can simply describe the motion of the interior gas using the governing equation (14) and the characteristic boundary conditions of Eqs. (16) and (17).

C. Work done and pressurizing performance

Because of viscosity, the energy conversion from mechanical energy to heat flux occurs in an oscillating tube. Therefore, energy input is required to maintain the gas oscillations at steady state. We can give the energy to the interior gas by means of external work. The external force needed to excite the tube is determined by the interior pressure as

$$F_{\text{ext}}(t) = S(0)p(0,t) - S(l)p(l,t) + \int_0^l p(x,t) \frac{dS(x)}{dx} dx. \quad (18)$$

In Eq. (18), the inertia force related to the tube is excluded because it does not affect the mean input power at steady state when the tube oscillates harmonically. Thus, at the steady state, the mean input power can be directly estimated as

$$\langle \dot{W} \rangle_{T_p} = \frac{1}{T_p} \int_{t_0}^{t_0+T_p} F_{\text{ext}} v_{\text{tube}} dt, \quad (19)$$

where v_{tube} is the tube velocity calculated by $v(t) = \int_0^t a_{\text{tube}} dt$ and T_p corresponds to one period. As mentioned previously, at the steady state, the input power for exciting

the tube has to be balanced with the outgoing heat flux through the wall.

In order to estimate the efficiency for compressing interior gas, it is needed to evaluate a pressurizing performance as well as input power. The performance of a commercial compressor is often evaluated by compression ratio, which is defined by the ratio of maximum pressure value to minimum value as follows,

$$\text{compression ratio} = \frac{P_{\max}}{P_{\min}}. \quad (20)$$

In this study, we evaluated the pressurizing performance of a tube by the compression ratio at the small end of the tube because the maximum pressure and minimum pressure always occur at the small end.

III. NUMERICAL RESULTS

Because the motion of the interior gas is determined by the nonlinear governing equation (12), it is not easy to obtain a general solution analytically. In this study, we solve the equation numerically by using a higher-order finite difference scheme. In order to get an accurate numerical solution, we developed a numerical code with a fourth-order compact scheme for spatial differentiation and a fourth-order Adams method for time evolution.¹² Numerical simulations are ac-

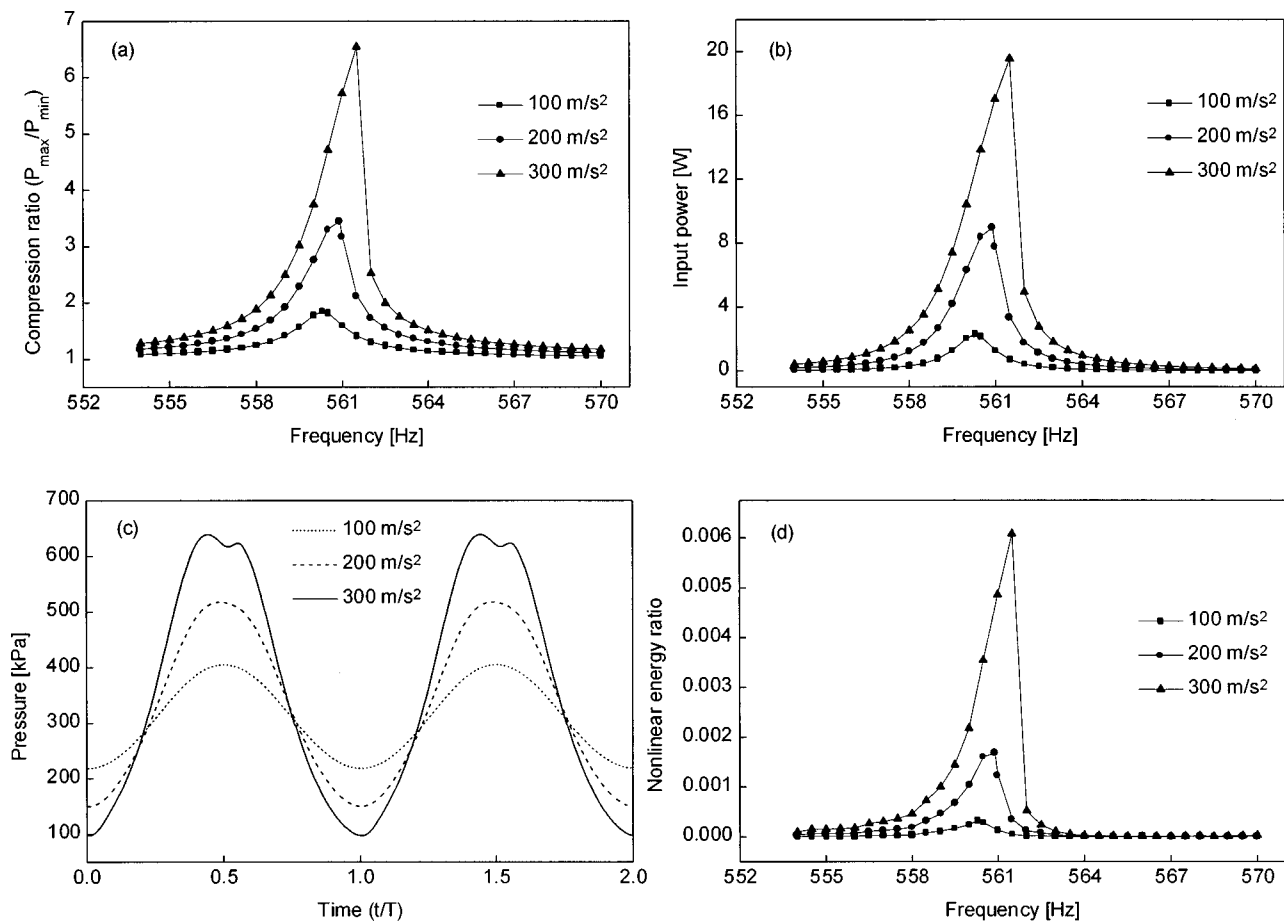


FIG. 5. Simulation results of tube II ($\frac{1}{2}$ cosine shape) for different amplitudes of the driving acceleration: 100, 200, and 300 m/s². The results are obtained by harmonically exciting the tube with sweeping frequency up and down: (a) compression ratio at the small end, (b) input power, (c) pressure patterns at the small end at resonance, and (d) nonlinear energy ratio of pressure signal at the small end.

completed for various tubes such as cylindrical, conical, and cosine-shape tubes, which are shown in Fig. 1. For these tubes, the patterns of area change along the axis may be simply classified as follows:

- (i) reference tube: no area change;
- (ii) tube I: area increases only;
- (iii) tube II: area increases and converges; and
- (iv) tube III: area increases and converges, then decreases.

Although there exist an infinite number of candidate tubes with different shapes, the four kinds of tube shape we selected may roughly represent all possible shape-patterns of simple tubes, which can be expressed by using simple mathematical functions.

The performance evaluation of each tube has to be done under the identical condition. For this purpose, we assume the tubes have same length of $l=0.2$ m and same volume of 4.765×10^{-4} m³ as the reference tube in Fig. 1(a). In addition, we restrict a radius at $x=0$ to be 0.005 m except the reference tube. It is also assumed that the tube is filled with 306 kPa of *Refrigerant-12* at temperature of 27 °C and the entire tube is excited harmonically. The density and specific heat ratio correspond to 14.74 kg/m³ and 1.129, respectively. The effective viscosity μ_{eff} is determined by using the experimental data in Refs. 6 and 7, so that $\mu_{\text{eff}}=0.2$ kg/m·s. Note that the viscosity used in this study is much larger than

others in the literature. The tube is divided with fine mesh of $dx=0.4 \times 10^{-3}$ m to resolve discontinuous waves like shocks. A time step is determined by using the relation of $dt=CFL \cdot dx/c_0$. In this study, we use the *CFL* number of 0.49 to get a stable solution.

A. Reference tube (cylindrical shape)

We chose a cylindrical tube as a reference tube of which the geometry is described by the radius as

$$r(x)=0.0275 \quad \text{for } 0 \leq x \leq 0.2, \quad (21)$$

where the unit is a meter (m).

Figure 2 shows pressure signals predicted at one end of the tube at resonant frequency (381.5 Hz) for different amplitudes of the driving acceleration: 10, 50, and 100 m/s². In spite of the small amplitude of driving acceleration of 10 m/s², the pressure waveform is already distorted and beginning to evolve into shocks. When the tube is excited with the acceleration of 100 m/s², we can see clearly a shock wave which has an abrupt pressure jump. Because acoustic saturation, which limits the maximum possible pressure, occurs in the cylindrical tube, we cannot obtain high enough pressures although we increase the amplitude of driving acceleration.

Furthermore, these nonlinear pressure signals contain not only the exciting frequency component but also its higher

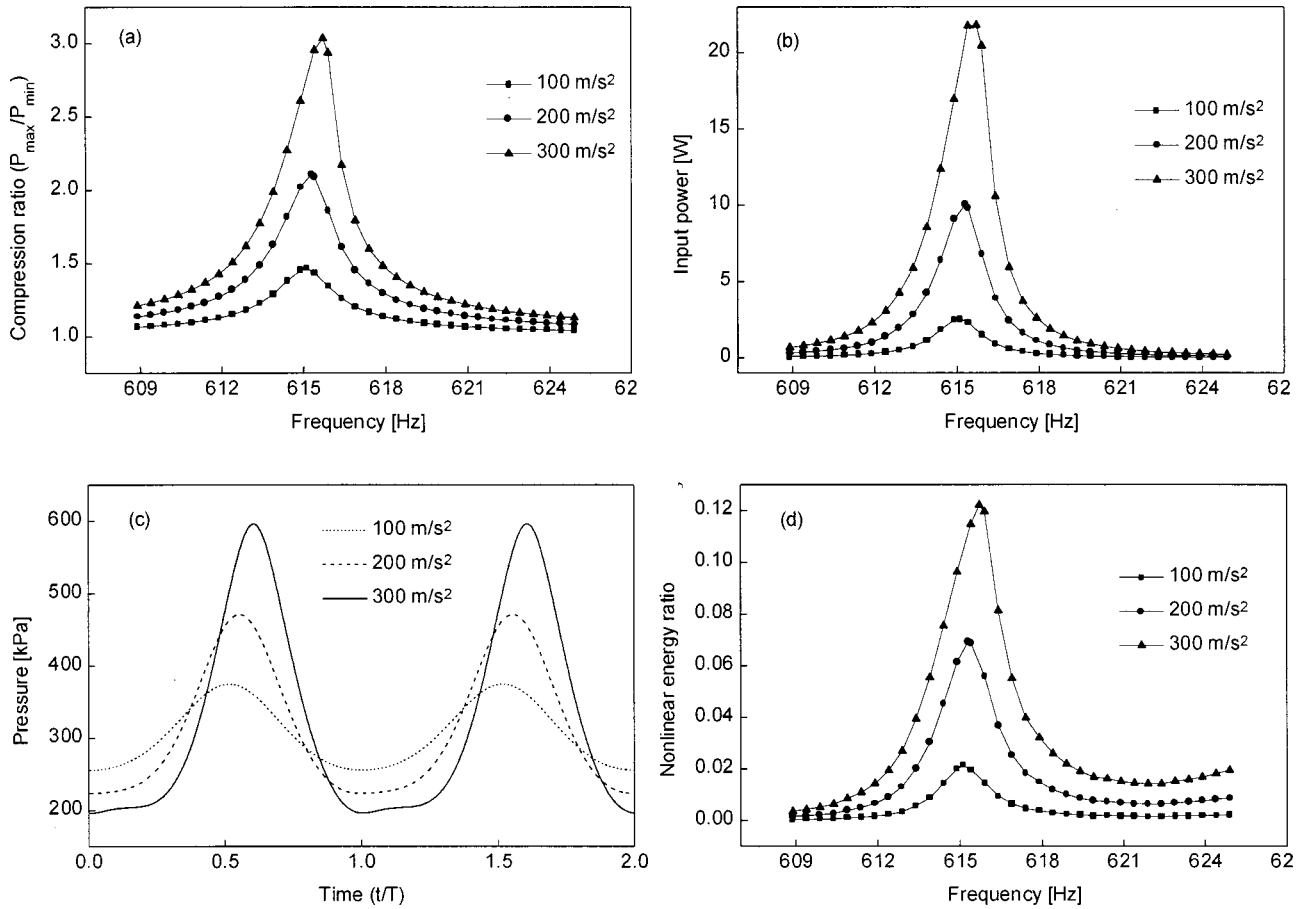


FIG. 6. Simulation results of tube III ($\frac{3}{4}$ cosine shape) for different amplitudes of the driving acceleration: 100, 200, and 300 m/s². The results are obtained by harmonically exciting the tube with sweeping frequency up and down: (a) compression ratio at the small end, (b) input power, (c) pressure patterns at the small end at resonance, and (d) nonlinear energy ratio of pressure signal at the small end.

harmonics. This means that input energy is not concentrated on the exciting frequency component and distributed to the higher harmonics. In order to quantify the degree of nonlinearity of these pressure patterns, we used a *nonlinear energy ratio* defined as a ratio of the energy of higher harmonics to the total signal energy. That is,

$$\text{nonlinear energy ratio} = 1 - \frac{G_{pp}(\omega_0)}{R_{pp}(0) - \mu_p^2}, \quad (22)$$

where $R_{pp}(0)$ is the autocorrelation of pressure signals with zero time delay, μ_p is the mean value of the pressure signals, and $G_{pp}(\omega_0)$ is the autospectrum of the pressure signals with the exciting frequency ω_0 . The denominator of Eq. (22) represents the total signal energy except the static signal component. Hence, the nonlinear energy ratio is bounded between zero and one. If pressure signals contain only the exciting frequency component, the nonlinear energy ratio becomes zero.

The nonlinear energy ratio of pressure signals for the acceleration of 100 m/s² in Fig. 2 is about 0.227. It means a large portion of the input effort spreads over the higher harmonics. In this case, the compression ratio of the reference tube is about 1.081, and the estimated input power for exciting the tube is 1.023 W.

Figure 3 shows the pressure profiles in the reference tube for the acceleration of 100 m/s² during one cycle at steady state. We can clearly observe the propagation of the shock wave in the tube. At the half cycle, the shock propagates in the opposite direction.

B. Tube I (conical shape)

The geometry of tube I in Fig. 1(b) is described as

$$r(x) = r_0 + A_1(x/l) \quad \text{for } 0 \leq x \leq l, \quad (23)$$

where r_0 is 0.005 m, l is 0.2 m, and A_1 is 0.04 m.

Simulation results of tube I are shown in Fig. 4. These results were obtained by harmonically exciting the tube with a frequency of interest. We accomplished the simulations for different amplitudes of the driving acceleration: 100, 200, and 300 m/s². Figure 4(a) shows the compression ratio, defined as the ratio of maximum pressure (P_{\max}) to minimum pressure (P_{\min}), of tube I. It is noteworthy that the ultimate objective is to obtain the highest possible compression ratio. In this case, much higher values of compression ratio were induced than those of the cylindrical tube. The maximum compression ratio is about 3.1 for the acceleration of 300 m/s². Note, as the amplitude of the driving acceleration increases, the resonant frequency also increases and the curves

are skewed toward the upper frequency. When the acceleration is 200 m/s^2 , an abrupt discontinuity of the response curve occurs at the resonant frequency. Specifically for the acceleration of 300 m/s^2 , the response curve has multi-values in the overlapped frequency region; these phenomena were similarly remarked as *hysteresis* in Refs. 6 and 7. Therefore, in order to get the maximum compression ratio effectively, we have to excite the tube by sweeping frequency up to the resonant frequency. Figure 4(b) corresponds to the input power needed to excite the tube. Similar to Fig. 4(a), as the acceleration increases, the curves abruptly jump at resonant frequency and, especially, show a hysteresis pattern for the acceleration of 300 m/s^2 . In this case, the input power of 15 W is consumed to produce the compression ratio of 3.1. Pressure signals at the small end of the tube at each resonance are shown in Fig. 4(c). In contrast to the cylindrical tube, shock waves are not generated in spite of the very large amplitude of the acoustic pressures. Note, as the input efforts increase, the nonlinear pressure pattern has the narrower peak and the broader trough. Figure 4(d) shows the nonlinear energy ratio of tube I, and the curve patterns are very similar to Figs. 4(a) and (b). The maximum nonlinear energy ratio is about 0.092 for the acceleration of 300 m/s^2 and it is smaller than that of the cylindrical tube.

C. Tube II ($\frac{1}{2}$ cosine shape)

The geometry of tube II in Fig. 1(c) is described as

$$r(x) = r_0 + A_2 \left(1 - \cos \left(\pi \frac{x}{l} \right) \right) \quad \text{for } 0 \leq x \leq l, \quad (24)$$

where r_0 is 0.005 m, l is 0.2 m, and A_2 is 0.019 m.

Figure 5(a) shows the compression ratio of tube II. As the acceleration increases, the resonance frequency slightly moved toward the upper frequency although the change is smaller than that of tube I. An abrupt discontinuity of the response curve was also observed at the resonance frequency. However, unlike tube I, the hysteresis pattern did not appear when the tube was excited with acceleration of 300 m/s^2 . In this case, the compression ratio increases up to 6.5, which corresponds to that of a commercial air compressor. In addition, Fig. 5(a) says this tube shape is more effective to compress a gas than tube I when the tubes are oscillated with the same amplitude of driving acceleration. The input power needed to excite the tube is shown in Fig. 5(b). In order to get the compression ratio of 6.5, the input power of 19.5 W is required when acceleration is 300 m/s^2 . Figure 5(c) displays pressure patterns predicted at the small end of the tube at resonance. As the acceleration increases, pressure patterns have a broader peak and lower trough than the results of tube I in Fig. 4(c). Especially, notice that small ripples appear in the peak when acceleration is 300 m/s^2 . Figure 5(d) presents the nonlinear energy ratio. The values are very small in spite of very high pressures. In other words, the shape of tube II may effectively suppress the energy transfer to other higher frequency components, so that most of the input effort can be concentrated into the component of exciting frequency.

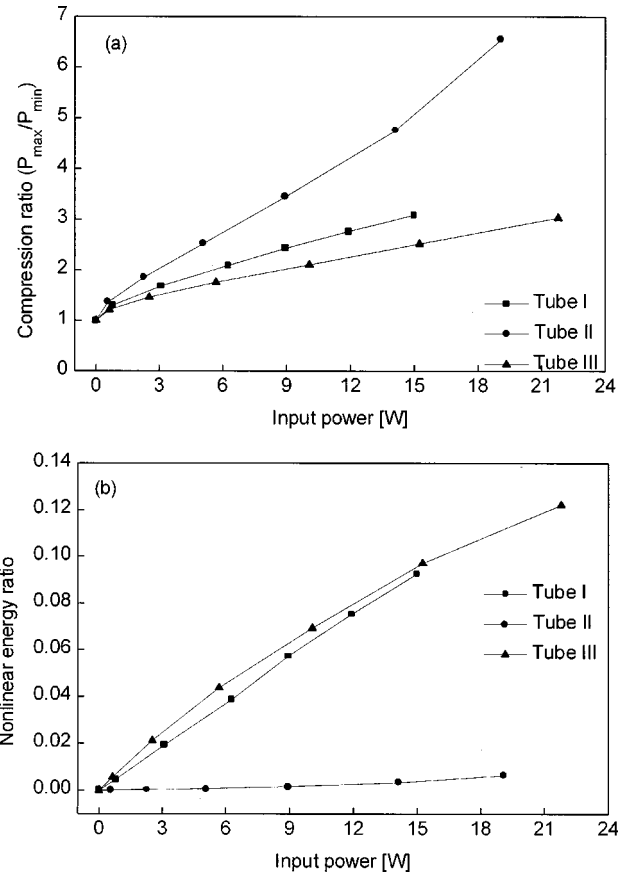


FIG. 7. Simulation results for tubes I, II, and III. The tubes are excited with their resonance frequencies with varying input power: (a) compression ratio at the small end versus input power, and (b) nonlinear energy ratio of pressure signal at the small end versus input power.

D. Tube III ($\frac{3}{4}$ cosine shape)

The geometry of tube III in Fig. 1(d) is described as

$$r(x) = r_0 + A_3 \left(1 - \cos \left(\frac{3\pi}{2} \cdot \frac{x}{l} \right) \right) \quad \text{for } 0 \leq x \leq l, \quad (25)$$

where r_0 is 0.005 m, l is 0.2 m, and A_3 is 0.0166 m.

Compression ratio for tube III is shown in Fig. 6(a). In this case, the resonant frequency is rarely affected by the pressure level. In contrast to tubes I and II, the curves in Fig. 6(a) are not skewed and keep the continuous pattern although driving acceleration increases. However, as seen in Fig. 6(a), the shape of tube III is not so good to induce high compression ratio. Figure 6(b) corresponds to the input power for exciting the tube. It says much more energy consumed than other tubes. The pressure pattern in Fig. 6(c) shows the narrower peak and the broader trough, but a ripple appears. The nonlinear energy ratio is higher than other tubes [see Fig. 6(d)].

Compression efficiencies of the three tubes are compared in Fig. 7(a). It shows tube II is much more efficient than the other tubes. In other words, the shape of tube II is the best among the selected candidates for a sonic compressor. In Fig. 7(b), the nonlinear energy ratio of tube II is remarkably smaller than the other tubes. It means the energy transfer to higher harmonics is greatly suppressed in tube II, so that the input efforts can be effectively concentrated on

the component of exciting frequency. The results imply that the nonlinear energy ratio may be used as a good basis parameter for designing the tube shape of the sonic compressor.

IV. CONCLUSIONS

For a closed axisymmetric tube oscillating harmonically, one-dimensional nonlinear governing equations have been derived and solved numerically. Characteristic boundary conditions were applied to supplement the lacks of boundary conditions. Simulations were accomplished for various tubes such as cylindrical, conical, and cosine-shape tubes with same volume and length.

Shock waves are easily generated in the cylinder tube, but much higher acoustic pressures are induced without shock formation in the conical and cosine tubes. The results show that the nonlinear patterns of acoustic pressures are strongly related to the shape of tube as well as the amplitude of driving acceleration. We evaluated the pressurizing performance of these tubes and calculated the nonlinear energy ratio of pressure pattern. The nonlinear energy ratio well describes not only the energy transfer to higher harmonics but also the compression efficiency. We propose it to be a good measure for designing the good tube shape of sonic compressor. In addition, it was found that the $\frac{1}{2}$ cosine-shape

tube was much more efficient than the other tubes, i.e., it is more suitable for a sonic compressor.

- ¹R. Betchov, "Nonlinear oscillations of a column of gas," *Phys. Fluids* **1**, 205–227 (1958).
- ²R. A. Saenger and G. E. Hudson, "Periodic shock waves in resonating gas columns," *J. Acoust. Soc. Am.* **32**, 961–970 (1960).
- ³W. Chester, "Resonant oscillations in closed tubes," *J. Fluid Mech.* **18**, 44–64 (1964).
- ⁴C. P. Lee and T. G. Wang, "Nonlinear resonance and viscous dissipation in an acoustic chamber," *J. Acoust. Soc. Am.* **92**, 2195–2206 (1992).
- ⁵D. F. Gaitan and A. A. Atchley, "Finite amplitude standing waves in harmonic and anharmonic tubes," *J. Acoust. Soc. Am.* **93**, 2489–2495 (1993).
- ⁶C. C. Lawrenson, B. Lipkens, T. S. Lucas, D. K. Perkins, and T. W. Van Doren, "Measurements of macrosonic standing waves in oscillating closed cavities," *J. Acoust. Soc. Am.* **104**, 623–636 (1998).
- ⁷Y. A. Ilinskii, B. Lipkens, T. S. Lucas, T. W. Van Doren, and E. A. Zabolotskaya, "Nonlinear standing waves in an acoustical resonator," *J. Acoust. Soc. Am.* **104**, 2664–2674 (1998).
- ⁸I. G. Currie, *Fundamental Mechanics of Fluids*, 2nd ed. (McGraw-Hill, New York, 1993).
- ⁹K. W. Thompson, "Time dependent boundary conditions for hyperbolic system," *J. Comput. Phys.* **68**, 1–24 (1987).
- ¹⁰K. W. Thompson, "Time dependent boundary conditions for hyperbolic system, II," *J. Comput. Phys.* **68**, 439–461 (1990).
- ¹¹T. J. Poinso and S. K. Lele, "Boundary conditions for direct simulations of compressible viscous flows," *J. Comput. Phys.* **101**, 104–129 (1992).
- ¹²S. C. Chapra and R. P. Canale, *Numerical Methods for Engineers*, 2nd ed. (McGraw-Hill, New York, 1990).

A new boundary-element method for predicting outdoor sound propagation and application to the case of a sound barrier in the presence of downward refraction

Eric Premat^{a)}

Ecole Nationale des Travaux Publics de l'Etat, DGCB CNRS URA 1652, 2 rue Maurice Audin, 69518 Vaulx-en-Velin Cedex, France

Yannick Gabillet^{b)}

Centre Scientifique et Technique du Bâtiment, 24 rue Joseph Fourier, 38400 Saint-Martin d'Hères, France

(Received 18 December 1998; revised 11 July 2000; accepted 12 July 2000)

A new boundary-element method for predicting outdoor sound propagation over uneven ground is presented. This allows the sound field around complex boundaries (various absorptive properties and shapes) and in the presence of refraction to be calculated accurately. The total sound pressure is expressed as the sum of the incident pressure and the pressure scattered by the obstacles in the propagation medium, involving layer potentials. The Green's function used in this formulation takes meteorological and ground effects into account and relies on recent models for propagation in inhomogeneous media, such as normal modes, residue series, the parabolic equation, or the fast-field program. In this paper, this new method, called Meteo-BEM, is derived, based on both boundary-element methods (BEM) in a quiescent medium, and propagation models in inhomogeneous media. The hypothetical case of a rigid, thin noise barrier on a flat ground, under a known sound-speed gradient condition, is studied. Comparison of numerical simulations with experimental results shows that this new method is a powerful tool for outdoor sound propagation prediction, which gives rise to many applications and developments. © 2000 Acoustical Society of America. [S0001-4966(00)03810-8]

PACS numbers: 43.28.Fp, 43.20.Bi, 43.50.Vt [LCS]

I. INTRODUCTION

Many national regulations concerning traffic noise are becoming more and more demanding, leading to specification of lower and lower maximum acceptable sound levels. Consequently, there is now a need for models to predict noise from traffic and other major environmental noise sources on the ground, at long range. Moreover, noise barriers are nowadays widely used as traffic-noise control devices; it is found that the insertion loss of barriers measured outdoors at long range is often much lower than predicted. This appears to be due to the influence of meteorological conditions: wind and temperature gradients and turbulence. Thus, there is a need to investigate meteorological influences on the performance of noise barriers.

To predict noise barrier efficiency, several empirical and numerical methods have been developed, based on different approaches [empirical model,¹ semiempirical model,² geometrical theory,³⁻⁶ and boundary-element methods (BEM)^{7,8}]. Among these tools, valid in homogeneous media, the BEM has the advantage of allowing the assessment of any kind of shape and absorption of the propagation-domain boundaries—in particular, uneven terrains, various shapes of sound barriers, or impedance discontinuities. In the formulation presented in this paper, the problem is recast in terms of a boundary integral representation, using a Green's function which directly satisfies the sound radiation condition at in-

finity. Furthermore, if the ground is assumed infinite, flat, and of constant admittance, the Green's function can include reflection by the ground^{9,10} and it leads to the discretization of the surfaces of the obstacles only. Therefore, the computation time and computer memory size become small enough to make complex outdoor-noise diffraction problems tractable with the boundary-element method, using desktop computers.

On the other hand, a few models¹¹ have recently been developed which describe the sound propagation in inhomogeneous media using normal-mode solution, residue series solution, fast-field program (FFP), parabolic equation (PE), or Gaussian beams. Among them, the Gaussian beam¹² and the parabolic equation¹³ methods permit the analysis of diffraction in inhomogeneous media. However, the first approach is an asymptotic solution which does not work when one of the dimensions of the problem is less than a wavelength. The second approach, which is a powerful computational method for sound propagation in inhomogeneous media, ignores the backscattered field and, therefore, does not accurately describe a large class of diffraction problems where multiple diffraction and multiple reflection exist—for example, in the case of railway-noise control by screens.

This paper presents a new BEM, called Meteo-BEM, including meteorological effects in the Green's function of the formulation. The key point is that this Green's function is an exact solution of the problem of sound propagation in an inhomogeneous medium; the calculation of its first and second derivatives can be made with good accuracy and involves a reasonable computational cost. In the present paper,

^{a)}Electronic mail: e.premat@cstb.fr

^{b)}Yannick Gabillet, who was born in Auray, France, in 1952, passed away in Grenoble, France, on 19 January 2000.

a Green's function based upon normal modes has been used. Instead of using a numerical method like FFP, or PE which may be unstable in the numerical evaluation of its derivatives, the normal-mode approach offers the advantage of being analytic and easily derivable, and provides a good illustration of the methodology. The choice of this particular Green's function allows only media with a positive constant sound-speed gradient to be studied,¹¹ but it has been shown elsewhere¹⁴ that, in many cases, real sound-speed profiles can be approximated by linear ones, which leads to sufficiently accurate estimations of sound-pressure levels. Other situations require the choice of another appropriate Green's function, such as the residue series in the case of upward refraction. It has been noted that, in the study of wind effects on sound propagation, the medium is not isotropic and the Green's function depends on the relative directions of the sound propagation and the wind. Therefore, if the source and the receiver are both in front of a reflecting wall, two Green's functions are necessary—one for the interaction between the source and the wall and one for the propagation domain between the wall and the receiver—in addition to the incident field. This case shows that attention has to be paid to situations including wind.

In order to illustrate the proposed methodology, the simple case of a rigid, thin barrier on a rigid, flat ground under a positive, constant sound-speed gradient is presented in this paper. The new method is presented step by step, each step being justified and validated, with comparisons from either measurement or calculation results. First, in Sec. II, the boundary-element method in homogeneous media is briefly recast, and the power of the Green's function is pointed out. The approach used involves layer potentials; emphasis is given here on the most important basic results. Next, in Sec. III, the inhomogeneous model, taking meteorological effects into account, is presented. In the case of a positive linear sound-speed gradient, the normal-mode solution has been found to be the most appropriate "candidate" for the Green's function of the formulation. Then, in Sec. IV, the new method is derived using the results of the previous sections. Comparisons between results from the new method and from experiments are shown. Finally, conclusions and further developments are discussed in Sec. V.

II. THE BOUNDARY-ELEMENT METHOD IN A HOMOGENEOUS ATMOSPHERE

A. A general overview of the BEM

The boundary-element method is a numerical technique developed in the early 1960s, based on the older theory of boundary integral equations. These methods have been extensively discussed in the literature and are still an interesting field of research (see, for example, Refs. 15–18). A few key points about BEM will be given here, but more detailed investigations are not within the scope of this paper. For more information, the reader should refer to the references, and other references cited therein.

In unbounded situations, the BEM has been found to be more appropriate than the other well-known numerical tool, the finite-element method, since it requires only boundary,

instead of domain, discretization. In fact, since the propagation domain does not have to be meshed, the BEM allows the dimension of the problem to be reduced by one and the acoustic field everywhere in the medium is then due to the radiation of the boundaries.

Two families of boundary-element methods can be distinguished: direct and indirect formulations. The direct formulation¹⁵ relies on the use of the Helmholtz integral equation where the unknown functions are pressure and velocity, while the indirect one^{19,20} is based on an integral formulation assuming that the sound field scattered by a boundary can be represented by a linear combination of a distribution of monopoles (a simple-layer potential) and a distribution of dipoles (a double-layer potential). In this latter formulation, the densities of the layer potentials are at first unknown, and found with the help of the boundary integral equation.²⁰ An advantage of the indirect formulation over the direct one is that, in the case of simple boundary conditions, the acoustic field can be represented with only one simple- or double-layer potential. In any case, it is worth mentioning that both formulations depend on a powerful function: the Green's function of the problem; that is, an elementary solution of the Helmholtz equation satisfying the Sommerfeld condition and certain boundary conditions (see Ref. 15). The more information the Green's function accounts for, the smaller the integration domain of the corresponding integral formulation. That is why authors have first looked for Green's functions for the propagation above a rigid plane,⁷ then for Green's functions including ground effects,^{9,10} work is still done in many areas of acoustics to find expressions for these Green's functions suitable for subsequent numerical use in boundary-element methods. Once either a direct or an indirect formulation has been used, the so-called collocation method¹⁶ is one of the best-known and frequently used methods for solving the integral equation obtained by imposing the boundary conditions to the pressure; that is to say, satisfying the integral equation at a set of discrete boundary locations.

In theory, the BEM allows three-dimensional problems to be studied, but the calculation time and the memory size limit the use of these methods to two-dimensional problems or to three-dimensional problems within a reasonable low-frequency range (the meshing size of the boundary depends on the frequency), although a few attempts have been made to extend these formulations to 3D²¹ and to increase the high frequency limits of the BEM.²²

It must be noted that, up to now, boundary-element methods have been used only for propagation in quiescent media. Thus, the aim of this paper is to prove that such powerful formulations can be applied to complex outdoor sound propagation problems, regardless of whether the underlying formulation is direct, indirect, or variational. Considering the discussion above, the formulation adopted in this work, without introducing any restrictions, is an indirect one based on layer potential theory. The next section addresses this issue more precisely in the case of a thin noise barrier on a flat ground.

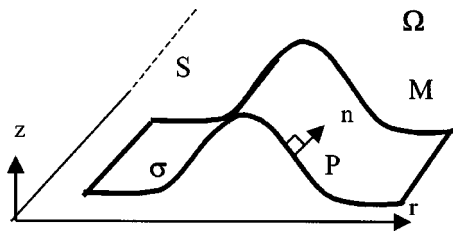


FIG. 1. General problem of outdoor sound propagation.

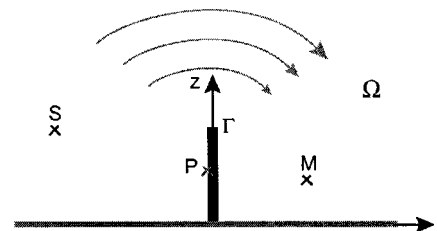


FIG. 2. Thin noise barrier on a flat ground.

B. The indirect BEM based on layer potential theory

Let us consider a harmonic point source S in a semi-infinite domain Ω whose boundary σ is the ground and a barrier (see Fig. 1). M is a point in the space Ω .

Considering linear-acoustical assumptions, and time dependence $\exp(-i\omega t)$, the problem of a homogeneous atmosphere can be described by the following system:

$$(\Delta + k^2)p = \delta_S, \quad \text{for } M \text{ in } \Omega, \quad (1)$$

$$\lim_{M \text{ in } \Omega \rightarrow P \text{ on } \sigma} \left[\partial_{n(M)} p(M) - ik \frac{\rho c}{Z_n} p(M) \right] = 0, \quad (2)$$

$$\text{Sommerfeld condition for } p. \quad (3)$$

Here, p is the total sound pressure, k the wave number, δ_S represents the point-source radiation, ρ is the air density, c the sound speed, and Z_n is the normal acoustic impedance of σ , supposed to be locally reacting.

Using the layer potential formulation, the total sound pressure can be expressed as the sum of the incident pressure (the pressure radiated by the source without the boundary σ) and a linear combination of simple- and double-layer potentials (the pressure scattered by the boundary)²⁰

$$p(M) = p_0(M) + \alpha p_s(M) + \beta p_d(M), \quad (4)$$

in which α and β are complex coefficients.

The incident sound field in free space is

$$p_0(M) = -\frac{\exp(ikr(S,M))}{4\pi r(M,S)} \quad \text{in 3D}, \quad (5)$$

$$p_0(M) = -\frac{i}{4} H_0(kr(S,M)) \quad \text{in 2D},$$

and the simple- and double-layer potentials p_s and p_d are

$$p_s(M) = \int_{\sigma} \nu(P) G(M,P) d\Gamma(P), \quad (6)$$

$$p_d(M) = - \int_{\sigma} \mu(P) \partial_{n(P)} G(M,P) d\Gamma(P).$$

The simple-layer potential can be interpreted as the radiation of a layer of monopole sources located on σ , while the double-layer potential can be seen to be the contribution of dipoles oriented along the normal to σ . These layer potentials have to be carefully handled when crossing the boundary σ . Due to the underlying distribution theory, the simple-layer potential is then a continuous function, but its normal derivative has a discontinuity, while the double-layer potential is a discontinuous function but has a continuous normal

derivative (see Ref. 20 for more details). The functions ν and μ denote, respectively, the simple-layer and double-layer potential densities.

This integral formulation involves the crucial Green's function G that is indeed an elementary solution of the problem satisfying certain boundary conditions. The more boundary conditions included in the Green's function, the smaller the integration domain being considered as a secondary source, so that the total acoustic field is the superposition of the incident field and the contributions of these secondary sources.

As μ and ν are unknown, they have to be determined using the boundary conditions. The introduction of the sound pressure (4) in the boundary conditions (2) leads to a boundary integral equation that has to be solved in order to get the unknown layer potential densities.

Using, for example, a collocation method, the integral equation is satisfied at a few points located on the boundary. The boundary σ is discretized into surface elements on which μ and ν can be approximated by piecewise constant functions or any more appropriate sophisticated shape functions. A linear system then gives these unknown functions; the sound field is finally known over the whole space via the integral formulation.

This BEM is called indirect because μ and ν have to be determined first in order to find the acoustic pressure anywhere in the space Ω via Eq. (4). The mathematical method presented here is exact, and the pressure solution of the boundary value problem is unique, provided that both the propagation medium Ω and the complementary to $\bar{\Omega}$ are infinite.²⁰ In case of a finite associated internal problem, a judicious combination of simple- and double-layer potentials could be used to avoid this nonuniqueness problem at certain characteristic frequencies.

As outlined above, the key point in this formulation is the use of an adequate Green's function. That is why, for example, in the case of outdoor sound propagation in the presence of a sound barrier, different authors have concentrated first on the ground effects in order to reduce the domain σ to the barrier Γ (see Refs. 7 and 10); however, all these works were restricted to a homogeneous atmosphere. In this work, meteorological effects are going to be introduced via the Green's function.

For the sake of clarity, consider the case of a rigid, thin noise barrier Γ , on a rigid, flat ground (see Fig. 2). Boundary condition (2) is then a Neumann condition

$$\lim_{M \text{ in } \Omega \rightarrow P \text{ on } \Gamma} \partial_{n(M)} p(M) = 0 \quad (7)$$

Damas⁷ showed that the solution could be represented by a double-layer potential

$$p(M) = p_0(M) + \int_{\Gamma} \mu(P) \partial_{n(P)} G(M, P) d\Gamma(P) \quad (8)$$

for M in the space Ω .

Including ground effects in the Green's function G allows the integration domain to be reduced to the sound barrier Γ . This Green's function is therefore given by

$$G(P, M) = -\frac{i}{4} H_0(kd(P, M)) - \frac{i}{4} H_0(kd(P', M)), \quad (9)$$

where P' is the image source corresponding to P with respect to the ground plane; H_0 is the Hankel function of the first kind and of order zero; and $d(P, M)$ is the distance between P and M . Here, the 2D problem is addressed for computation time and memory-size reasons.

The incident pressure due to the source S of unit amplitude is given by

$$p_0(M) = G(S, M). \quad (10)$$

Expressing the Neumann condition on the screen, the following Fredholm integral equation of the first kind is obtained:

$$-\partial_{n(M)} p_0(M) = PF \int_{\Gamma} \mu(P) \partial_{n(M)} \partial_{n(P)} G(M, P) d\Gamma(P) \quad (11)$$

for M on Γ .

Because of the singularity of the Green's kernel, the integral is taken in the sense of the Hadamard finite part, represented in (11) by the notation PF . According to Filippi,²³ the definition used is the limit of the normal component of the gradient of the double-layer potential when point M approaches the screen.

This integral equation is solved using N collocation points M_j located on the screen. Looking for a simple piecewise constant approximation for the unknown double-layer potential density, the sound barrier Γ is discretized into sub-elements Γ_i and yields the linear system

$$-\partial_{n(M)} p_0(M_j) = \sum_{i \neq j} \mu_i \int_{\Gamma_i} \partial_{n(M)} \partial_{n(P)} G(M_j, P) d\Gamma(P) + \mu_j PF \int_{\Gamma_j} \partial_{n(M)} \partial_{n(P)} G(M_j, P) d\Gamma(P) \quad (12)$$

$j = 1, \dots, N$.

This equation represents the contribution of the interaction between the source in the presence of the ground and the screen. Following a commonly accepted criterion, the size of the subdivision Γ_i is chosen to be of the same order as one-sixth of the sound wavelength.

Equation (12) can be rewritten as

$$[A][\mu] = [B], \quad (13)$$

with

$$[B] = [B_j] = [-\partial_{n(M)} p_0(M_j)]$$

$$[\mu] = [\mu_i] \quad (14)$$

$$[A] = [A_{ji}] = \left[PF \int_{\Gamma_i} \partial_{n(M)} \partial_{n(P)} G(M_j, P) d\Gamma(P) \right].$$

The integrals are computed using an adaptative Gauss–Legendre scheme and the linear system is solved using a full pivoting Gauss strategy.²⁴

Once the layer density μ is known, the sound pressure can be calculated at any receiver point using the formulation (8). The double-layer potential then represents the contribution of radiation from the sound barrier to the total sound field.

To validate the use of this BEM model in a homogeneous medium with a barrier, one can first compare the numerical results for the BEM with the geometrical theory of diffraction (GTD).³ In order to allow for comparison between the cases (a) with a screen in a homogeneous atmosphere; (b) without any screen in a downward-refracting atmosphere; and (c) with a screen in a downward-refracting atmosphere, the same geometry corresponding to scale-model measurements made above a concave surface¹² and presented in Sec. IV will be used throughout Secs. II B, III, and IV. Figure 3 shows the sound-pressure levels relative to free field calculated by the two methods—BEM and GTD—for three positions of the receiver. The source and screen heights were, respectively, 0.10 and 0.15 m. The source is located 4 m in front of the screen. The three positions of the receiver are: (a) 2 m behind the screen at a height of 0.10 m; (b) 2 m behind the screen at a height of 0.15 m; (c) 3 m behind the screen at a height of 0.10 m. The agreement between the two calculation methods is excellent. The next section presents the method used for the Green's function in an inhomogeneous atmosphere.

III. THE GREEN'S FUNCTION ACCOUNTING FOR METEOROLOGICAL EFFECTS

Meteorological effects (wind and sound-speed gradients, turbulence) are important in outdoor sound propagation, particularly at long ranges.

In the classical boundary-element methods, the Green's functions can include ground effects.^{25,26} The idea of the present work is to take advantage of recent models describing propagation in inhomogeneous media, taking meteorological effects as well as ground effects into account. Here, we concentrate on refraction phenomena. These recent models describing sound-speed gradients are mainly the normal-mode solution for downward refraction, the residue series for upward refraction, and the fast-field program and the parabolic equation for both situations.¹¹

In order to illustrate the methodology used for including this inhomogeneous Green's function in the BEM, consider the case of a positive sound-speed gradient condition.

In the case of a linear sound-speed profile, the normal-mode solution²⁷ is particularly well adapted, since the variables involved in the analytical formulation are uncoupled and straightforward to derive.

The solution p of the pressure wave equation satisfying, on the one hand, the Sommerfeld condition at infinite alti-

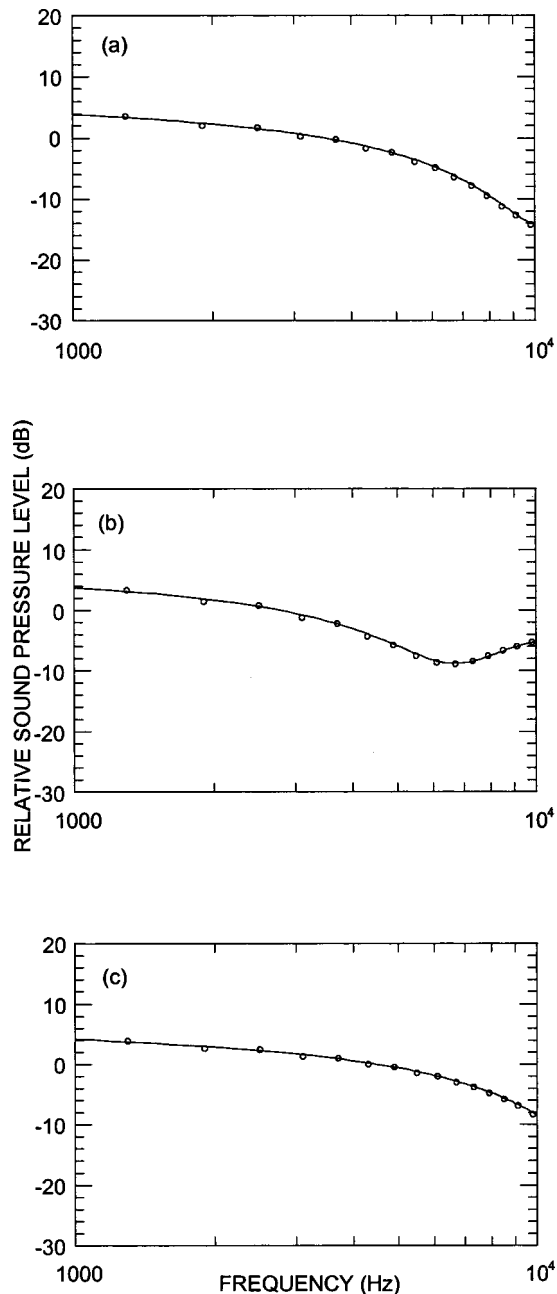


FIG. 3. Sound-pressure level relative to free field versus frequency, obtained in a homogeneous medium behind a rigid barrier of height=0.15 m, distance to the source=4 m. The solid curves are the GTD solution and the circles are the BEM solution. The ground is rigid. Source height=0.1 m in all cases and (a) receiver height=0.1 m, source/receiver distance=6 m; (b) receiver height=0.15 m, source/receiver distance=6 m; (c) receiver height=0.1 m, source/receiver distance=7 m.

tude and the impedance boundary condition at the flat ground, and, on the other hand, the height-dependent sound-speed condition for inhomogeneous media, can be written as follows, using a Hankel transform:²⁷

$$p(r, z) = -S_m \int_{-\infty}^{+\infty} H_0^1(kr) P(z, k) k dk, \quad (15)$$

where r represents the range and z the height. S_m is the monopole source strength. In the case of a linear sound-speed profile,

$$c(z) = c(0)(1 + z/R), \quad (16)$$

the so-called height-dependent Green's function $P(z, k)$ can be expressed in terms of Airy functions and their derivatives

$$P(z, k) = -2\pi e^{i\pi/6} \text{Ai}(\tau + y_>) \left[\text{Ai}((\tau + y_<)e^{2i\pi/3}) - \left(\frac{\text{Ai}'(\tau e^{2i\pi/3}) + q \text{Ai}(\tau e^{2i\pi/3})}{\text{Ai}'(\tau) + q \text{Ai}(\tau)} \right) \text{Ai}(\tau + y_<) \right], \quad (17)$$

where

$$\begin{aligned} k_0 &= 2\pi f/c(0), & q &= (ik_0 \rho c)/Z, \\ l &= (R/2k_0^2)^{1/3}, & R &= c/(dc/dz) \\ \tau &= (k^2 - k_0^2)l^2, & y_> &= z_>/l, & y_< &= z_</l, \\ z_> &= \max(z_s, z_r), & z_< &= \min(z_s, z_r), \end{aligned} \quad (18)$$

R is the radius of curvature of the launched rays, z_s is the source height, and z_r the receiver height.

Next, using the residue theorem to calculate Eq. (15), the poles of the integrand are determined and the contributions of the integrand residue at each pole are summed to obtain the following expression for the sound pressure p_S , in downward refraction, for a point source S radiating spherical waves above a flat locally reacting impedance plane:

$$p_S(r, z) = \frac{i\pi S_m}{1} \sum_n \frac{H_0^1(k_n r) \text{Ai}(\tau_n + z_s/l) \text{Ai}(\tau_n + z/l)}{\tau_n [\text{Ai}(\tau_n)]^2 - [\text{Ai}'(\tau_n)]^2}, \quad (19)$$

in which

$$\tau_n = (k_n^2 - k_0^2)l^2 \quad (20)$$

are the zeros of

$$\text{Ai}'(\tau_n) + q \text{Ai}(\tau_n) = 0, \quad (21)$$

and k_n represents the horizontal wave number of the n th mode. The zeros of (21) are trapped in the complex plane with an adapted Powell hybrid method for nonlinear system solutions.²⁸ Equation (19) gives the expression for the Green's function for sound propagation from a point source above a flat absorbing ground in a medium with a linear sound-speed profile.

One must point out that this derivation is an exact analytical formulation; however, in the last result (19), the continuous spectrum contribution has been disregarded, which leads to negligible error at long range. Furthermore, concerning the numerical implementation, a significant numerical instability gives rise to oscillations in the predicted sound field, due to the oscillatory behavior of the Airy functions for large arguments. This drawback is overcome assuming that, near the vertical, sound-speed gradients do not affect the propagation. Consequently, for small k_n , i.e., important vertical wave numbers, sound propagates almost vertically and we can consider that the propagation happens as if the medium were homogeneous (see Ref. 29). Furthermore, the above sound-pressure formula is valid in 3D (radiation from a point source), so it needs to be adapted to 2D configura-

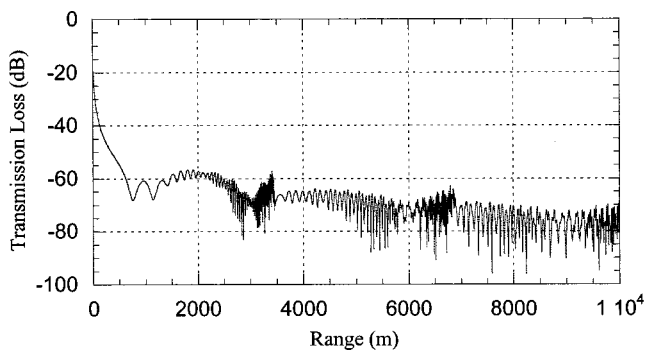


FIG. 4. Normal-mode transmission loss versus range corresponding to the case 2, 100 Hz, Fig. 12, Ref. 11, p. 187.

tions (radiation from a line source) because the BEM approach used in this work is written in 2D. This is done using the idea outlined in Ref. 30, p. 276. Considering the form of the normal modes in 2D and 3D, a trivial modification has to be made to get the 2D solution. Equation (19) becomes, for a line source in plane geometry

$$p_S(r, z) = \frac{iS_1}{21} \sum_n \frac{\exp(ik_n r) \text{Ai}(\tau_n + z_s/1) \text{Ai}(\tau_n + z/1)}{k_n \tau_n [\text{Ai}(\tau_n)]^2 - [\text{Ai}(\tau_n)]^2}, \quad (22)$$

where S_1 is the line source strength.

This last equation (22) gives the expression for the Green's function for sound propagation from a line source above a flat absorbing ground in a medium with a linear sound-speed profile.

The results obtained with the normal-mode solution compared satisfactorily to those from the benchmark¹¹ for downward refraction. Figure 4 shows the results for case 2 of the benchmark (Fig. 12, p. 187 at 100 Hz); the source and receiver heights are 5 and 1 m, respectively; the range varies from 0.1 to 10 000 m, the specific surface impedance of the ground is $Z_c = (12.81, 11.62)$ and the vertical sound-speed gradient is 0.1 s^{-1} . For more clarity, the results of the benchmark are not recalled here in Fig. 4. The instabilities present at short distances, with the normal-mode method, in the result of Fig. 12 of the benchmark are not visible in the result of our Fig. 4. This better result is achieved with the treatment of the vertical modes in the series (22) as presented above.

Next, the normal-mode solution is compared to earlier experimental results for a linear sound-speed profile.¹² There is an analogy between propagation following straight lines above a curved surface and propagation following curved ray paths in the case of a linear sound-speed profile above a plane boundary.^{31,32} Therefore, instead of making measurements downwind outdoors, measurements under controlled conditions indoors have been made above a concave curved surface in Ref. 12. The source and receiver positions are the same as those used in Fig. 3. Figure 5 shows the normal-mode calculation and the measured spectra for the three positions of the receiver. The agreement between calculations and measurements is very good. Figure 5 shows that there are substantial increases in sound-pressure levels in downward refraction above a reflective surface.

These results show that, in the case of a linear sound-speed profile, the normal-mode solution given by Eq. (22) is

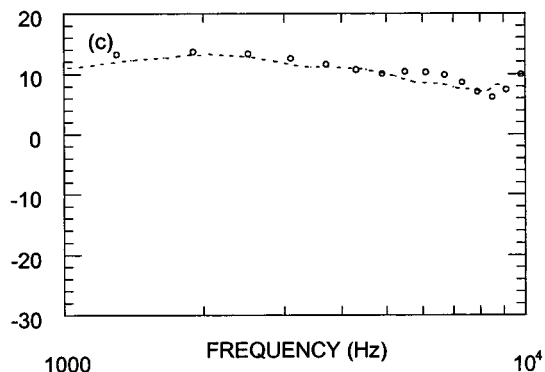
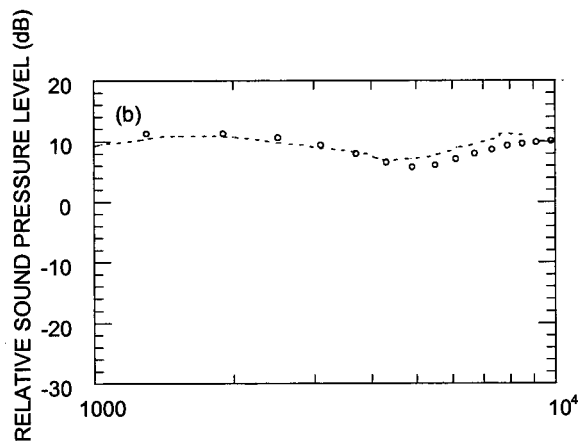
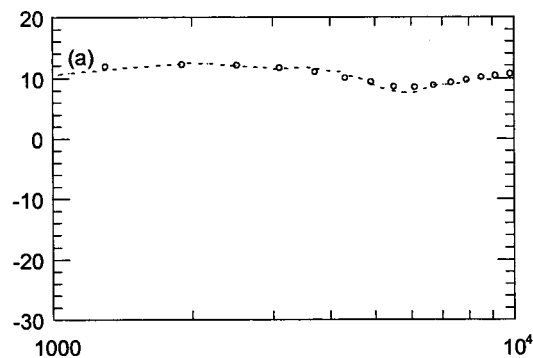


FIG. 5. Sound-pressure level relative to free field versus frequency, obtained in an inhomogeneous medium under downward-refracting conditions in the case of a linear sound-speed profile where $a = 1/R = 0.05 \text{ m}^{-1}$. The circles are the normal-mode solution and the dashed curves are measured levels. The ground is rigid. Source height = 0.1 m in all cases and (a) receiver height = 0.1 m, source/receiver distance = 6 m; (b) receiver height = 0.15 m, source/receiver distance = 6 m; (c) receiver height = 0.1 m, source/receiver distance = 7 m.

a good candidate for the Green's function in an inhomogeneous medium, since the variables involved in the analytical formulation are uncoupled and straightforward to derive. The use of this Green's function in the BEM is presented in the following section.

IV. THE NEW MODEL: METEO-BEM

Using the results of the two theories described above (BEM for noise barrier efficiency in a homogeneous atmosphere, and the normal-mode solution for sound propagation

in inhomogeneous media), the new formulation Meteo-BEM, combining the advantages of both approaches, is now presented. In the following, the subscripts “inhom” and “hom” will denote, respectively, propagation in an inhomogeneous medium and in a homogeneous medium.

For the sake of clarity, consider the case of a rigid, thin noise barrier, on a flat ground, in the presence of downward refraction. In the inhomogeneous case, Eq. (8) Sec. II is rewritten as

$$p(M) = p_{0,\text{inhom}}(M) + \int_{\Gamma} \mu_{\text{inhom}}(P) \partial_{n(P)} G(M, P) d\Gamma(P) \quad \text{for } M \text{ in the space } \Omega. \quad (23)$$

Now, however, the Green’s function describes the sound propagation in an inhomogeneous medium, so the results of Sec. III, Eq. (22) are used

$$G(S, M) = p_S(r(M), z(M)) = \frac{iS_1}{21} \sum_n \frac{\exp(ik_n|r_M - r_S|) \text{Ai}(\tau_n + z_s/1) \text{Ai}(\tau_n + z_M/1)}{k_n \tau_n [\text{Ai}(\tau_n)]^2 - [\text{Ai}'(\tau_n)]^2}. \quad (24)$$

When the ground is rigid, the parameter q in (18) is equal to zero. Thus, Eq. (21) shows that in this case the τ_n are the zeros a'_n of the derivative of the Airy function and we have, for the Green’s function

$$G(S, M) = \frac{iS_1}{21} \times \sum_n \frac{\exp(ik_n|r_M - r_S|) \text{Ai}(a'_n + z_s/1) \text{Ai}(a'_n + z_M/1)}{k_n a'_n [\text{Ai}(a'_n)]^2}. \quad (25)$$

The new inhomogeneous integral equation corresponding to (11) must be solved with the normal-mode solution (25) for the Green’s function as well as for the incident field

$$-\partial_{n(M)} p_{0,\text{inhom}}(M) = PF \int_{\Gamma} \mu_{\text{inhom}}(P) \partial_{n(M)} \partial_{n(P)} \times G(M, P) d\Gamma(P) \quad \text{for } M \text{ on } \Gamma. \quad (26)$$

Using the same collocation method as for the homogeneous BEM, the sound barrier Γ is discretized into subelements on which the unknown double-layer potential density is approximated by a piecewise constant function. Thus, (12) becomes

$$-\partial_{n(M)} p_{0,\text{inhom}}(M_j) = \sum_{i \neq j} \mu_{i,\text{inhom}} \int_{\Gamma_i} \partial_{n(M)} \partial_{n(P)} G(M_j, P) d\Gamma(P) + \mu_{i,\text{inhom}} PF \int_{\Gamma_i} \partial_{n(M)} \partial_{n(P)} G(M_j, P) d\Gamma(P), \quad j = 1, \dots, N. \quad (27)$$

The normal derivative of the pressure for the left-hand side of this equation is

$$\begin{aligned} \partial_{n(M)} p_0(M) \Big|_{\Gamma} &= \frac{\partial G(S, M)}{\partial r_M} \\ &= -\frac{S_1}{21} \sum_n \frac{\exp(ik_n|r_S|) \text{Ai}(a'_n + z_s/1) \text{Ai}(a'_n + z_M/1)}{a'_n [\text{Ai}(a'_n)]^2}. \end{aligned} \quad (28)$$

For the right-hand side of Eq. (27), an approximation based on the idea of Rasmussen²⁹ presented above in Sec. III can be made, considering that vertical propagation is weakly affected by the refraction; thus, this term is at first approximated by the homogeneous term presented in Sec. II.

In this way, a new linear system, involving (a) the normal-mode Green’s function derivative for the right member, and (b) the same matrix as for the homogeneous system Eqs. (13) and (14), is obtained

$$[A_{\text{inhom}}][\mu_{\text{inhom}}] = [B_{\text{inhom}}], \quad (29)$$

with

$$[B_{\text{inhom}}] = [B_{j,\text{inhom}}] = [-\partial_n p_{0,\text{inhom}}(M_j)] \quad [\mu_{\text{inhom}}] = [\mu_{i,\text{inhom}}] \quad (30)$$

$$[A_{\text{inhom}}] = [A_{ji,\text{inhom}}] = \left[PF \int_{\Gamma_i} \partial_{n(M)} \partial_{n(P)} G(M_j, P) d\Gamma(P) \right] \approx [A_{\text{hom}}].$$

Once solved, this new inhomogeneous linear system provides the layer potential density μ for inhomogeneous media calculated using the same numerical schemes as described in Sec. II.

The last step is then to use Eq. (23) with the normal-mode solution for the incident field, as well as for the Green’s function derivative involved in the integral, in the same way as for the left-hand side of the inhomogeneous integral equation (28).

The sound pressure is then computed at any receiver point using the following equation:

$$p(M) = p_{0,\text{inhom}}(M) + \int_{\Gamma} \mu_{\text{inhom}}(P) \partial_{n(P)} G(M, P) d\Gamma(P) \approx p_{0,\text{inhom}}(M) + \sum_i \mu_{i,\text{inhom}} \partial_{n(P)} G(M, P_i) \Delta\Gamma_i. \quad (31)$$

Calculations obtained using this new boundary-element method (Meteo-BEM) are compared (see Fig. 6) to measurements made above a curved concave surface, after setting a rigid thin barrier at a distance of 4 m from the source. In Fig. 6(a) the receiver is within the shadow zone of the barrier for downward refraction, while it was on the limiting ray of the shadow boundary in the homogeneous case [Fig. 3(a)]. Figure 6(b) shows results obtained closer to the limiting curved ray of the shadow boundary in the downward-refraction case.

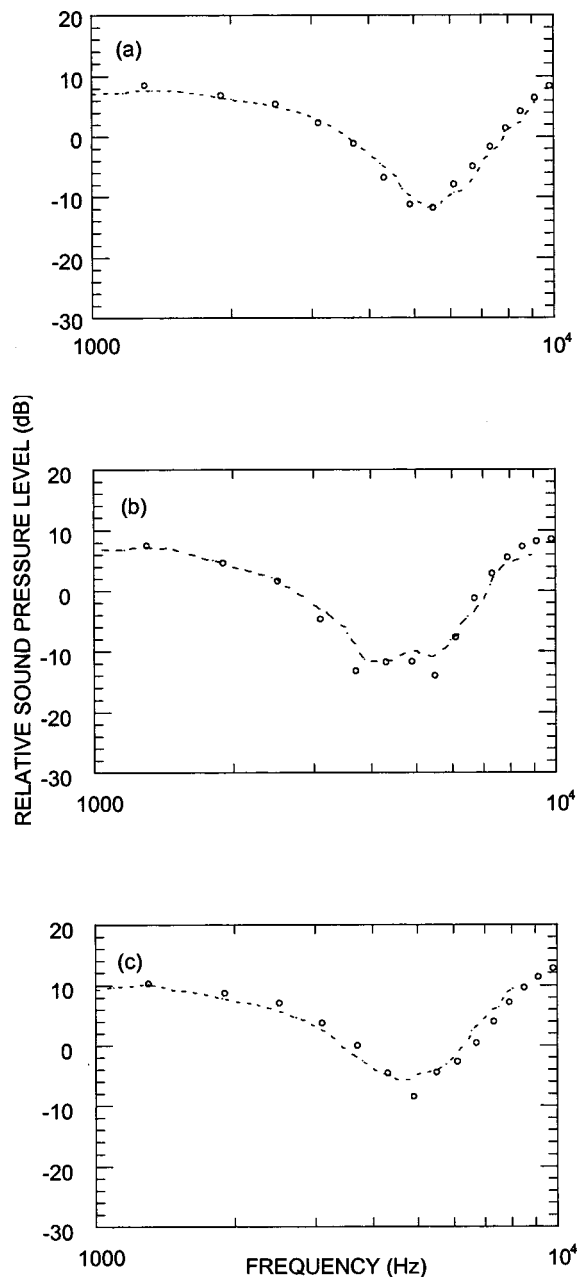


FIG. 6. Sound-pressure level relative to free field versus frequency, obtained in an inhomogeneous medium under downward-refracting conditions behind a rigid barrier of height=0.15 m; distance to the source=4 m. The circles are the BEM solution and the dashed curves are measured levels. The linear sound-speed profile is given by $a=1/R=0.05\text{ m}^{-1}$. The ground is rigid. Source height=0.1 m in all cases and (a) receiver height=0.1 m, source/receiver distance=6 m; (b) receiver height=0.15 m, source/receiver distance=6 m; (c) receiver height=0.1 m, source/receiver distance=7 m.

Figure 6(c) shows results obtained farther from the barrier. In all cases, the agreement between the predicted and measured levels is very good. As mentioned in the earlier paper,¹² the comparison of the results of Figs. 3 and 6 shows, in this case of a scaled model of a practical barrier, that downward refraction does not necessarily destroy the effectiveness of a noise barrier.

V. CONCLUSION

In this paper a new method for calculating the sound field in a medium with a sound-speed profile above complex

boundaries has been presented. First, the theory of BEM, together with that of sound propagation in inhomogeneous media, has been briefly reviewed. Each step of the work has been justified and validated. The new model *Meteo-BEM* has been derived, using results from the two theories. Finally, in order to validate this innovative approach, comparisons have been made with experimental results. The case of a rigid, thin noise barrier under downward refraction has been studied. The results prove that a BEM can be adapted to complex atmospheric sound propagation problems using an appropriate Green's function, and gives good agreement with experimental data. This approach might be interesting in other areas, such as underwater acoustics. This attempt to use non-“classical” Green's functions should be kept in mind when dealing with boundary-element methods for any kind of problem.

This new method allows the sound field in a medium with a sound-speed profile above an uneven impedance ground to be calculated provided that the nonflat part of the terrain is included in the integration domain σ of formulas (2)–(6). The influence of different shapes of the diffracting sound barriers, combined with meteorological effects, on the acoustic field is going to be studied. Further validation with more realistic configurations (finite impedance of the ground, for instance) is in progress. Investigations are also required to provide insight into the physical phenomenon of impedance discontinuity in the presence of refraction. In addition, further work is in progress using the power of the parabolic equation to predict range-dependent propagation in conditions of both downward and upward refraction. Other investigations are also being pursued with other inhomogeneous models, such as the residue series for upward refraction, or FFP for both situations.

ACKNOWLEDGMENTS

Eric Premat wishes especially to acknowledge the contributions of his coauthor, Yannick Gabillet (now deceased), to this particular work. It has been a privilege to collaborate with him during the past four years, and his contributions to the papers we have authored during those years have been immeasurable.

- ¹Z. Maekawa, “Noise reduction by screens,” *Appl. Acoust.* **1**, 157–173 (1968).
- ²U. L. Kurze and G. Anderson, “Sound attenuation by barriers,” *Appl. Acoust.* **4**, 35–53 (1971).
- ³J. B. Keller, “Geometrical theory of diffraction,” *J. Opt. Soc. Am.* **52**, 116–130 (1962).
- ⁴Y. Kawai, “Sound diffraction by a many-sided barrier or pillar,” *J. Sound Vib.* **79**, 229–242 (1981).
- ⁵K. B. Rasmussen, “On the effect of terrain profile on sound propagation outdoors,” *J. Acoust. Soc. Am.* **98**, 35–44 (1985).
- ⁶A. L'Espérance, J. Nicholas, and G. A. Daigle, “Insertion loss of absorbent barriers on ground,” *J. Acoust. Soc. Am.* **86**, 1060–1064 (1989).
- ⁷A. Daumas, “Etude de la diffraction par un écran mince disposé sur le sol,” *Acustica* **40**(4), 213–222 (1978).
- ⁸D. C. Hothersall, S. N. Chandler-Wilde, and M. N. Hajmirzae, “Efficiency of single noise barriers,” *J. Sound Vib.* **146**(2), 303–322 (1991).
- ⁹P. J. Filippi, “Extended sources radiation and Laplace type representation: Application to wave propagation above and within layered media,” *J. Sound Vib.* **91**, 65–84 (1983).
- ¹⁰S. N. Chandler-Wilde and D. C. Hothersall, “Efficient calculation of the

- Green function for acoustic propagation above a homogeneous impedance plane," *J. Sound Vib.* **180**, 705–724 (1995).
- ¹¹ K. Attenborough, S. Taherzadeh, H. E. Bass, X. Di, R. Raspet, G. R. Becker, A. Güdesen, A. Chrestman, G. A. Daigle, A. L'Espérance, Y. Gabillet, K. E. Gilbert, Y. L. Li, M. J. White, P. Naz, J. M. Noble, and H. A. J. M. van Hoof, "Benchmark cases for outdoor sound propagation models," *J. Acoust. Soc. Am.* **97**, 173–191 (1995).
- ¹² Y. Gabillet, H. Schroeder, G. A. Daigle, and A. L'Espérance, "Application of the Gaussian beam approach to sound propagation in the atmosphere: Theory and experiments," *J. Acoust. Soc. Am.* **93**, 3105–3116 (1993).
- ¹³ E. M. Salomons, "Diffraction by a screen in downwind sound propagation: A parabolic equation approach," *J. Acoust. Soc. Am.* **95**, 3109–3117 (1994).
- ¹⁴ Y. Gabillet, G. A. Daigle, and A. L'Espérance, "Sound propagation in a wind tunnel: Comparison of experiments with FFP and residue solution," *Appl. Acoust.* **43**, 321–331 (1994).
- ¹⁵ R. D. Ciskowski and C. A. Brebbia, *Boundary Element Methods in Acoustics*, Computational Mechanics Publications (Elsevier Applied Science, New York, 1991).
- ¹⁶ M. Bonnet, *Equations Intégrales et Éléments de Frontière* (CNRS Editions/Eyrolles, 1995).
- ¹⁷ J. J. do Rêgo Silva, *Acoustic and Elastic Wave Scattering using Boundary Elements*, Computational Mechanics Publications (Elsevier Applied Science, New York, 1994).
- ¹⁸ N. Atalla and R. J. Bernhard, "Review of numerical solutions for low-frequency structural-acoustic problems," *Appl. Acoust.* **43**, 271–294 (1994).
- ¹⁹ V. D. Kupradze, "Potential Methods in the Theory of Elasticity," Israel Program for Scientific Translation, Jerusalem, 1965.
- ²⁰ P. Filippi, "Layer potential and acoustic diffraction," *J. Sound Vib.* **54**(4), 473–500 (1977).
- ²¹ D. Duhamel, "Efficient calculation of the three-dimensional sound pressure field around a noise barrier," *J. Sound Vib.* **197**(5), 547–571 (1996).
- ²² A. Tekatlian and E. Premat, "Computer cost of a 3-D numerical model for noise barriers insertion loss," *Inter-Noise 96*, pp. 3075–3079 (1996).
- ²³ P. Filippi and G. Dumery, "Etude théorique et numérique de la diffraction par un écran mince," *Acustica* **21**, 343–350 (1969).
- ²⁴ W. H. Press, W. T. Vetterling, S. A. Teukolsky, and B. P. Flannery, *Numerical Recipes in FORTRAN*, 2nd ed. (Cambridge University Press, Cambridge, England, 1994).
- ²⁵ D. Habault, "Sound propagation above an inhomogeneous plane: Boundary integral equation methods," *J. Sound Vib.* **100**(1), 55–67 (1985).
- ²⁶ S. Chandler-Wilde, "Sound propagation above an inhomogeneous impedance plane," *J. Sound Vib.* **98**(4), 475–491 (1985).
- ²⁷ R. Raspet and G. Baird, "Normal mode solution for low-frequency sound propagation in a downward refracting atmosphere above a complex impedance plane," *J. Acoust. Soc. Am.* **91**, 1341–1352 (1992).
- ²⁸ M. J. D. Powell, "A Hybrid Method for Nonlinear Algebraic Equations," in *Numerical Methods for Nonlinear Algebraic Equations*, edited by P. Rabinowitz (Gordon and Breach, New York, 1970).
- ²⁹ K. B. Rasmussen, "Sound propagation over ground under the influence of a sound speed profile in the atmosphere," *J. Sound Vib.* **139**(1), 71–81 (1990).
- ³⁰ F. B. Jensen, W. A. Kuperman, M. B. Porter, and H. Schmidt, *Computational Ocean Acoustics*, AIP Series in Modern Acoustics and Signal Processing (AIP, New York, 1994).
- ³¹ T. F. Embleton, "Analogies between nonflat ground and nonuniform meteorological profiles in outdoor sound propagation," *J. Acoust. Soc. Am. Suppl. 1* **178**, S86 (1985).
- ³² A. Berry and G. Daigle, "Controlled experiments on the diffraction of sound by a curved surface," *J. Acoust. Soc. Am.* **83**, 2059–2068 (1988).

Complex Padé approximants for wide-angle acoustic propagators

David Yevick

Department of Physics, University of Waterloo, 200 University Avenue West, Waterloo,
Ontario N2L 3G1, Canada

David J. Thomson

Defence Research Establishment Atlantic, P.O. Box 1012, Dartmouth, Nova Scotia B2Y 3Z7, Canada

(Received 3 April 2000; revised 28 August 2000; accepted 12 September 2000)

Procedures for constructing wide-angle propagators that attenuate evanescent modes in parabolic equation (PE) models of underwater sound propagation are examined. In this context, two new split-step Padé approximations to exponentiated square-root operators are proposed. The first method involves a propagator derived from a Padé approximant of a square-root operator that has been rotated in the complex plane while the propagator of the second method is obtained from a complex coefficient rational approximation of the square-root operator. Numerical evidence confirms that these proposed methods yield improved behavior compared to previously suggested techniques in selected areas of the spectral domain. © 2000 Acoustical Society of America.

[S0001-4966(00)02712-0]

PACS numbers: 43.30.Bp [SAC-B]

I. INTRODUCTION

One-way propagation procedures are routinely used for solving parabolic equations (PEs) relevant to underwater acoustics (see, e.g., Ref. 1 and references therein). An important issue that arises for higher-order PE calculations based on Padé approximations^{2,3} is the proper treatment of evanescent energy for the forward-propagating field. Such contributions are typically quite small and propagate at steep angles to the computational boundary where they can be removed by absorbing boundary conditions. In certain cases, however, evanescent fields can contribute to numerically unstable solutions, for example, if conversion occurs between evanescent and forward-propagating waves in rapidly varying refractive index profiles. Further, the evanescent modes of vector fields may possess complex propagation constants that lead to divergences after a sufficiently long propagation distance.⁴ Evanescent effects are even more pronounced in reflection calculations where evanescent modes can be converted directly into propagating modes by the backward propagation operator.

The source of the numerical instabilities associated with evanescent modes with complex propagation constants can be traced to the analytic behavior of the real Padé approximation for $\sqrt{1+X}$ employed in finite-difference propagation algorithms. In fact, the analytic structure of the standard Padé approximant of the square-root operator, whose coefficients are constructed from simple analytic formulas, reflects that of the exact square-root operator with a branch cut taken to lie along the negative real axis, assuming an $e^{-i\omega t}$ time-dependence. Physical forward-propagating modes that satisfy the proper boundary conditions at infinity possess propagation constants that lie along the positive imaginary axis. At infinite Padé order, the Padé approximant maps the real part of X to the real axis while modes with imaginary propagation constant components infinitesimally different from zero are mapped to points along either the positive or negative imaginary axis. At finite Padé order the branch cut is replaced by

poles along the line $X < -1$ which impart uncontrollably large real and rapidly varying imaginary components to values of $X \pm i\varepsilon$ with small $\varepsilon > 0$ close to the pole positions. Since the complex modes of vector fields appear in pairs with eigenvalues that differ only in the sign of their imaginary propagation constant component, this behavior will lead to rapidly diverging propagating fields if a complex propagation constant with a negative imaginary part is located close to a pole.

The first attempt to address the problems associated with evanescent fields in underwater sound propagation was made by Wetton and Brooke,⁵ who employed a first-order rational-linear approximation to $\sqrt{1+X}$ with complex coefficients to restore stability to a vector PE formulation derived for propagation in elastic media.⁶ This procedure was subsequently generalized by Collins *et al.*,⁷⁻¹⁰ who provided several numerical techniques for generating higher-order complex Padé approximations. These methods are based on nonlinear search procedures and can be difficult to implement at high Padé order (in our experience for $n > 7$). However, a least-squares procedure¹¹ was later proposed that requires only the solution of a linear problem for a set of coefficients. The multiplicative factors appearing in the partial fraction expansion of the propagator are then given in terms of the roots of a polynomial formed from these coefficients. With this improved method, Dacol *et al.*¹² obtained an accurate [12/14] rational Padé approximation in a finite-difference implementation of the self starter¹³ that suppresses both the source function singularity and unwanted evanescent spectral components. Unfortunately although all such treatments yield propagation constants for evanescent modes with a positive imaginary component, ensuring that these modes are damped during propagation, the calculated damping rate is unphysical.

To address these issues, Milinazzo *et al.*¹⁴ introduced an alternative procedure for handling evanescent modes—although it is limited somewhat by a fundamental trade-off

between the accuracy with which the evanescent modes are modeled and the accuracy of the propagating part of the spectrum. In this approach, the analytic behavior of the Padé approximant is altered so that its branch cut will be positioned along the line $-1 - Xe^{i\theta}$ with $\theta < \frac{1}{2}\pi$ instead of being located along $X < -1$ with X real. Mapping the principal branch, (the negative real line) of the square-root operator in this fashion only requires that a simple algebraic transformation be applied to the Padé coefficients for the real problem. For any nonzero value of θ , the square-root operator then maps the line $X < -1$ onto the positive imaginary axis. Unfortunately, the error of such a transformation along the real axis can be significant since the Padé expansion of the square-root operator is performed at $X=0$, but the real line is rotated in the complex plane to $-1 + (1+X)e^{-i\theta}$ before this expansion is performed. As a result, for appreciable values of θ , a much higher-order Padé approximant is required compared to the $\theta=0$ case in order to maintain the same level of accuracy near $X=0$. An additional problem with this rotation method, as we will demonstrate below, is that the resulting expression necessarily introduces divergences into the exponentiated propagator at any Padé order. The origin of these divergences is associated with the rapid variation that occurs close to each pole in the finite-order Padé representation of $\sqrt{1+X}$ for $X < -1$. Since certain poles are located close to the real axis near the point $X = -1$, regions of the real line with X slightly larger than -1 may be mapped into the negative imaginary half-plane. In practical calculations, however, the effects of these divergences are usually removed by absorbing boundary conditions since they are generally confined to grazing angles near $\frac{1}{2}\pi$.

An alternative to Milinazzo *et al.*'s procedure, based on the Padé-type approximants of Brezinski,¹⁵ was put forward by Lu.¹⁶ This method is equivalent to first constructing the continued fraction expansion of the square-root operator, which is straightforward, and then terminating this expansion after its $2n$ th term with a purely imaginary value. Writing the resulting expression as a partial fraction yields an excellent approximation to the square-root operator that additionally possesses a uniformly positive imaginary part.

Recently, Lingeitch and Collins¹⁷ investigated the possibility of rotating the Padé approximation to the full propagation propagator in the complex plane as opposed to simply rotating the exponent of this operator. Their results indicate that satisfactory accuracy can again be achieved in this manner at sufficiently high Padé order. However, our subsequent analysis indicates that this method exhibits intrinsic divergences that are suppressed but not eliminated at high approximation order.

In this paper, we introduce two further procedures for rotating high-order PE propagators that properly treat the decay of evanescent fields. These are derived from the observation¹⁸ that a real $[n/n]$ Padé approximant to $\exp(-\delta + \delta\sqrt{1+X})$ is equivalent to first performing an $[n/n]$ approximant to $Y = \sqrt{1+X}$ and then applying an $[n/n]$ approximant to $\exp(-\delta + \delta Y)$. By extension, an $[n/n]$ Padé approximant to the full propagator can be obtained by first rotating the $[n/n]$ Padé approximant to the square-root operator and then performing an $[n/n]$ Padé expansion of its

exponential—although in this case the result now differs from the corresponding rotated $[n/n]$ approximant of the full exponential operator. We show that such a procedure is not only simple to implement, but leads to either improved accuracy for evanescent fields (in the case of the Milinazzo *et al.* rotation) or a propagator that is entirely free of spurious divergences (starting instead with the Lu recursion). Extensions of this result could be used to design additional families of rotated propagators with more specialized properties.

II. FIELD EQUATIONS

We consider one-way propagation equations in two dimensions (range r , depth z) that are derived from the evolution equation¹⁹

$$\psi(r + \Delta r, z) = \exp(-\delta + \delta\sqrt{1+X})\psi(r, z), \quad (1)$$

for a depth-dependent medium characterized by sound speed, density, and absorption profiles $c(z)$, $\rho(z)$, and $\alpha(z)$, respectively. Here $\delta = ik_0\Delta r$, $k_0 = \omega/c_0$, and X is given by

$$X = N^2 - 1 + k_0^{-2}\rho \frac{\partial}{\partial z} \left(\rho^{-1} \frac{\partial}{\partial z} \right), \quad (2)$$

where $N(z) = c_0[1 + i\alpha(z)]/c(z)$. For an $e^{-i\omega t}$ time-dependence, the pressure p is related to ψ via

$$p(r, z) = \psi(r, z) \frac{\exp ik_0 r}{\sqrt{k_0 r}}. \quad (3)$$

In the absence of reflection effects, the discrete version of Eq. (1) together with appropriate boundary conditions yields an exact numerical solution of the discretized one-way propagation problem.

A. Wide-angle propagators

The evaluation of $\sqrt{1+X}$ appearing in Eq. (1) requires knowledge of the relevant eigenvalues and eigenfunctions of the operator X . Provided that some residual error associated with field components that propagate nearly transversely to the r -axis can be tolerated, however, sound propagation can be determined more readily using wide-angle equations derived from approximations to $\sqrt{1+X}$. Wide-angle equations based on Padé approximations are energy-conserving and do not account for the decay of the physical evanescent fields associated with the exact propagator.

Standard wide-angle formalisms are generally derived from one of two procedures. The first of these is based on the $[n/n]$ Padé approximation to $\sqrt{1+X}$ given by^{2,20}

$$Y = \sqrt{1+X} \approx 1 + \sum_{j=1}^n (1 + b_{j,n}X)^{-1} a_{j,n}X, \quad (4)$$

where the coefficients $a_{j,n}$ and $b_{j,n}$ have the analytic form

$$a_{j,n} = \frac{2}{2n+1} \sin^2 \frac{j\pi}{2n+1}, \quad (5)$$

$$b_{j,n} = \cos^2 \frac{j\pi}{2n+1}. \quad (6)$$

For small δ , a $[1/1]$ Padé approximant with respect to δ can be applied to the exponential propagation operator, yielding

$$\begin{aligned}\psi(r + \Delta r, z) &= \exp(-\delta + \delta Y) \psi(r, z) \\ &\approx (1 - \frac{1}{2}\delta + \frac{1}{2}\delta Y)^{-1} (1 + \frac{1}{2}\delta - \frac{1}{2}\delta Y) \psi(r, z).\end{aligned}\quad (7)$$

The propagator in Eq. (7) can be recast using partial fractions to yield

$$\begin{aligned}\psi(r + \Delta r, z) &= \psi(r, z) + \sum_{j=1}^n \psi_j(r, z) \\ &= \psi(r, z) + \sum_{j=1}^n (1 + b'_{j,n} X)^{-1} a'_{j,n} X \psi(r, z).\end{aligned}\quad (8)$$

Because each partial field $\psi_j(r, z)$ involves a [1/1] Padé approximant operating on the same total field $\psi(r, z)$, Eq. (8) can be solved in parallel by assigning a separate processor to each term in the sum. In two dimensions, the numerical evaluation of Eq. (8) simply involves the multiplication and inversion of the tridiagonal matrix representation of the operator X .

An alternate formalism that admits larger values of δ for a given level of accuracy is obtained by applying an [n/n] Padé approximation with respect to X directly to the exact exponential propagation operator.³ This generates a propagator of the form¹⁸

$$\exp(-\delta + \delta Y) \approx [1 + G_n^*(\delta, X)]^{-1} [1 + G_n(\delta, X)], \quad (9)$$

in which * denotes complex conjugate. For $n=2$, Eq. (9) is given explicitly by

$$G_2(\delta, X) = \frac{g_{2,1}(\delta)X + g_{2,2}(\delta)X^2}{c_2(\delta)}, \quad (10)$$

with

$$\begin{aligned}c_2(\delta) &= \delta^2 - 3, \quad g_{2,1}(\delta) = \frac{1}{4}\delta^3 + \frac{1}{2}\delta^2 - \frac{3}{4}\delta - \frac{9}{4}, \\ g_{2,2}(\delta) &= \frac{1}{48}\delta^4 + \frac{1}{16}\delta^3 - \frac{1}{16}\delta^2 - \frac{27}{16}\delta - \frac{27}{16}.\end{aligned}\quad (11)$$

This equation can also be obtained by applying a [2/2] approximation to the square-root operator followed by a [2/2] Padé approximation to the resulting exponential function.

The above expression for G_2 is observed to contain powers of δ up to fourth order. In fact, the corresponding expression for G_n contains powers of δ up to order n^2 . As a result, the analytic form of the propagator is algebraically cumbersome for $n > 3$. However, we have found previously that the n th order counterpart of Eq. (10) can be obtained numerically by applying first an [n/n] Padé approximation with respect to X to the square-root operator as in Eq. (4) and then an [n/n] Padé approximation with respect to δ of the resulting exponential propagator.¹⁸

B. Rotated Padé approximants

The Padé approximants given in the preceding section incorrectly describe the exponential decay of the physical evanescent modes during forward propagation as given by the exact one-way propagator of Eq. (1). Indeed, the coefficients in both the Padé approximations Eq. (4) and Eq. (9) are explicitly real. Accordingly, the real line is mapped onto itself yielding zero evanescent mode attenuation. As noted above, however, a potentially even more serious source of

error is that these Padé approximations possess poles at certain negative values of $X < -1$. Near these values, the Padé approximant to the square-root operator varies between $\pm \infty$. Thus certain evanescent modes propagate with propagation constants of the same order as those of actual physical modes, providing an obvious source of error in calculations of modal field distributions or modal weights. Additionally, as is often the case for two-component vector fields, the operator X may itself possess positive imaginary eigenvalues. If one of these eigenvalues is located in the complex plane close to a pole of the Padé propagator, the propagator may transform the imaginary part of the eigenvalue into a large positive quantity which can lead to a very rapid divergence as the field is propagated.

To avoid this difficulty, Milinazzo *et al.*¹⁴ rotated the argument of the square-root operator, namely $1 + X$, by $e^{-i\theta}$ in the complex plane before a standard Padé approximation about $X=0$ is applied. To correct for the effects of this rotation, the resulting expression for the square-root approximation is rotated back by $e^{i\theta/2}$. By this procedure, Milinazzo *et al.* obtained the rotated Padé approximation

$$\sqrt{1 + X} = e^{i\theta/2} \sqrt{1 + X'} \approx e^{i\theta/2} + e^{i\theta/2} \sum_{j=1}^n \frac{a_{j,n} X'^j}{1 + b_{j,n} X'}, \quad (12)$$

where $X' = -1 + (1 + X)e^{-i\theta}$ and the coefficients $a_{j,n}$ and $b_{j,n}$ are given in Eq. (5) and Eq. (6), respectively.

The standard Padé approximation in Eq. (4) has a branch cut along the real axis for $X < -1$. In contrast, the rotated Padé approximation in Eq. (12) has a branch cut along the ray $X = -1 + se^{i(\pi + \theta)}$ (with $s > 0$) in the complex X plane. This ensures that eigenvalues with propagation constants near the negative real axis will be mapped onto the upper half plane upon application of the square-root operator. In the limit of infinite Padé order, the rotation $\theta = \frac{1}{2}\pi$ yields the correct physical positions of the evanescent mode propagation constants.

The Milinazzo *et al.* procedure, while simple to implement, does introduce two sources of error. First, because the Padé approximant is effectively applied in the direction of a ray that is rotated from the real axis, its accuracy for a given Padé order along the real line segment $X > -1$ (corresponding to the physical propagating modes) is less than that obtained for the unrotated approximant. Second, while the unrotated Padé approximant maps the real line onto the real line by virtue of all its coefficients being real, the introduction of complex coefficients for the rotated Padé approximant does not preserve the location of the real line in the propagating region of the spectrum ($X > -1$). As a result, a certain fraction of the proper modal acoustic field components ψ_i with $X\psi_i > -1$ have positive imaginary parts and undergo damping with range.

Although the magnitudes of these imaginary parts can be made arbitrarily small by increasing n , modes that are amplified with range as a result of the analytic structure of the rotated Padé approximant will generally be induced in the propagating field as a result of numerical errors. As a result, the field will eventually diverge at large ranges unless this spurious amplification is counteracted by a physical or

artificial absorber. In underwater sound applications, the required damping is often effected with absorbing or radiating boundary conditions since the divergences occur primarily at steep grazing angles for the associated field components and interact with the boundary many times over a short propagation distance. To remove the singularities completely while preserving accuracy at $X=0$ (corresponding to a field with propagation constant k_0), $e^{i\theta}X$ can be substituted for X at the same time that c_0 is assigned the smallest sound speed in the waveguide. The effective propagation constants are then bounded by unity so that the propagation constants of all modes except the one with wave number k_0 will develop a small positive imaginary part proportional to the magnitude of X . Evanescent modes accordingly decay to varying degrees even in the case that X has positive imaginary eigenvalues, as long as θ is chosen sufficiently large. While simple to implement, the drawback of this technique is that all propagating modes become slightly damped so that transmission losses cannot be evaluated precisely. A similar concept, as detailed below, is to employ a modified continued fraction expansion together with a complex rotation. However, as the modified continued fraction expansion yields a very small imaginary contribution away from the vicinity of $X=0$, the success of such a procedure for a particular choice of algorithmic parameters is difficult to predict in advance.

To circumvent the above difficulties, an alternate procedure for addressing the evanescent behavior of $\sqrt{1+X}$ has been proposed by Lu.¹⁶ Using the Padé-type approximants of Brezinski,¹⁵ Lu's method derives from the observation that the standard continued fraction expansion for the Padé approximant of $f(X) = -1 + \sqrt{1+X}$ can be obtained from the rational recursion

$$f_{i+1}(X) = \frac{X}{2 + f_i(X)} \quad (13)$$

supplemented by the initial condition $f_0=0$. The $[n/n]$ diagonal Padé approximant for $\sqrt{1+X}$ is then given by $g_n(X) = f_{2n}(X) + 1$ which, when expressed as a partial fraction, is identical to Y of Eq. (4) with coefficients given by Eq. (5) and Eq. (6). On the other hand, replacing $f_0=0$ in Eq. (13) with the initial condition $f_0=i\beta$ ($\beta>0$) results in a "modified Padé approximant."¹⁶ In this case, the first $n-1$ derivatives of the resulting approximation for $g_n(X)$ can be shown to agree with the equivalent derivatives of $g_n(X)$ obtained using a zero initial condition. As well, both sequences approach the same function as $n \rightarrow \infty$. The reason for this behavior becomes clear if we write down a few steps of the continued fraction expansion for the case $X=1$ and $f_0=i$,

$$f_1(1) = \frac{1}{2+i}, \quad (14)$$

$$f_2(1) = \frac{1}{2+1/(2+i)} = \frac{2+i}{5+2i}, \quad (15)$$

$$f_3(1) = \frac{1}{2+(5+2i)/(2+i)} = \frac{5+2i}{12+5i}. \quad (16)$$

The coefficients of i in the numerator and denominator of each successive expression are the same as the numerator

and denominator that are obtained by setting $i=0$ in the preceding expression. As a consequence, the sequence $f_i(1)$, $i=1,2,\dots$, is guaranteed to approach $f(1) = \sqrt{2}-1$ as $i \rightarrow \infty$. Similar considerations apply as well for general values of X . In fact, it can be shown that the imaginary parts of all even-order continued fraction approximations to $f(x)$ are always greater than zero while the imaginary parts of the odd approximations are instead less than zero. Consequently, a propagation operator based on the even-order approximants will be free of divergences. However, as the modified Padé type approximant differs little from the real Padé approximant, except, of course, for arguments close to the poles of the real approximant along the negative real axis, it does not give correct values for the complex propagation constants of the evanescent modes.

A variant of the Milinazzo *et al.* approach was considered by Lingeitch and Collins¹⁷ who applied a rational approximation directly to the rotated propagator along the lines of Eq. (9). That is, writing the exponentiated square-root operator as

$$\exp(\delta\sqrt{1+X}) = \exp(\delta e^{i\theta/2}\sqrt{1+X'}), \quad (17)$$

with $X' = (1+X)e^{-i\theta} - 1$, yields

$$\exp(-\delta' + \delta'\sqrt{1+X'}) = 1 + \sum_{j=1}^n (1+A'_{j,n}X')^{-1}B'_{j,n}X', \quad (18)$$

where $\delta' = \delta e^{i\theta/2}$. Subsequently, X' is reexpressed in terms of X to construct the final expression for the propagator. We note that Eq. (18) continues to hold if θ is complex. The additional degree of freedom afforded by assigning a small imaginary component to θ can improve the accuracy of the results near $X \approx -1$ by a factor of 2.

We now propose two new procedures for constructing rotated Padé approximants to the exponentiated operator that offer improved accuracy over the entire spectrum of X . In the first procedure, a Padé or partial fraction expansion is applied to the propagator after first rotating and then expanding the square root operator $Y = \sqrt{1+X}$ in partial fractions. That is, representing a branch cut rotation by $\mathcal{R}\{\cdot\}$ and a Padé expansion by $\mathcal{P}\{\cdot\}$, our first method can be written in symbolic form as

$$\exp \delta Y \approx \mathcal{P}\{\exp \mathcal{Q}_1(Y)\}, \quad (19)$$

in which $\mathcal{Q}_1(Y) = \mathcal{P}\{\delta \mathcal{R}\{Y\}\}$. For zero rotation, this procedure yields a result identical to that obtained if a Padé expansion is applied directly to the exponential of the square-root operator, cf. Eq. (9) which is $\mathcal{P}\{\exp \delta Y\}$. The two methods differ, however, once a rotation is applied. In particular, rotating the square-root operator in isolation ensures that its poles lie (for a $\frac{1}{2}\pi$ rotation) as near as possible to the positive imaginary axis, which improves the accuracy of the resulting approximation in the exponentially decaying region of the spectrum. This accuracy, however, is obtained at the expense of the propagating part of the spectrum, which additionally contains propagation constants for which the magnitude of the propagator is slightly greater than unity. Even at small Padé order (e.g., $n \leq 3$), we have found that for moderate propagation step sizes ($k_0 \Delta r \approx 1$) the magnitude of

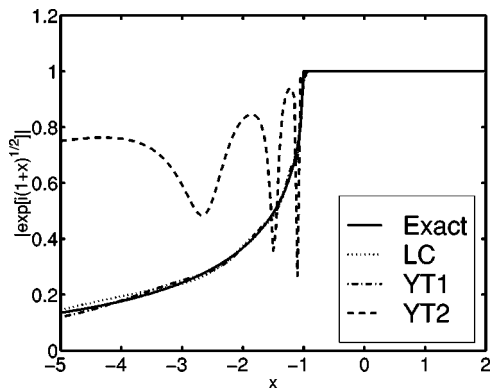


FIG. 1. Comparison of Padé approximants to the exact propagator $|\exp \delta\sqrt{1+X}|$ for $\delta=i$, $n=5$, $\theta=\frac{1}{4}\pi$ and $-5 < X < 5$. LC is the method of Lingeitch and Collins; YT1 is the Padé approximant of rotated $\sqrt{1+X}$ followed by a Padé approximant to the resulting propagator; YT2 is the modified Padé approximant of $\sqrt{1+X}$ followed by a Padé approximant to the resulting propagator.

the error introduced by the Padé expansion of the propagator in Eq. (19) is far smaller than the error introduced by the rotated and expanded square-root approximation to the exact square-root operator, i.e., $Q_1(Y)$.

The above limitation can be overcome to a large extent by our second procedure, which consists of applying a Padé or partial fraction expansion to the propagator formed from a modified Padé approximant to the square-root operator. That is, representing the modified Padé expansion by $\mathcal{P}_M\{\cdot\}$, we implement the operations denoted by

$$\exp \delta Y \approx \mathcal{P}\{\exp Q_2(Y)\}, \quad (20)$$

where $Q_2(Y) = \delta \mathcal{P}_M\{Y\}$. Since the imaginary part of the modified Padé approximant is everywhere positive, the exponential of $\delta = ik_0\Delta r$ times this expression is less than unity for all propagation constants. For long range propagation, the essential requirement in most applications is stability and accuracy in the propagating part of the spectrum. As a result, our second procedure should be nearly optimal in many practical contexts. It should also be noted that, as in our first procedure, the main source of error in the approximation of Eq. (20) for moderate step sizes results from applying the modified Padé approximant to $\sqrt{1+X}$.

The methods we have introduced possess one additional degree of freedom compared to previous techniques, namely, the Padé order used for the square-root operator may differ from that employed to expand the propagator. For example, to enable large range-step sizes ($k_0\Delta r \gg 1$), it may be convenient to combine a high-order Padé expansion of the propagator with a low-order Padé expansion of the square-root operator. This option is appropriate for the small grazing angles of interest in long range propagation with absorbing or radiating boundary conditions. In this case, the long range behavior of the propagator is determined principally by the accuracy of the high-order propagator expansion for large δ and not by the intrinsic accuracy of the Padé approximant employed for the square-root operator. By adapting the Padé expansion orders of the square-root and exponential in this

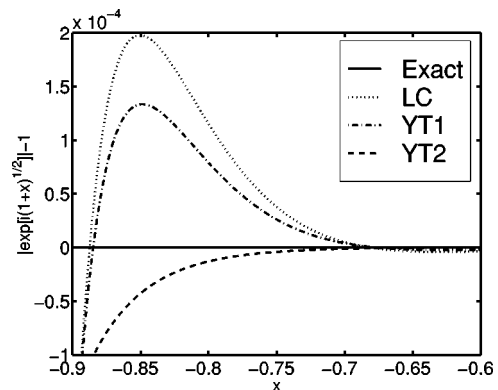


FIG. 2. Comparison of Padé approximants for the quantity $-1 + |\exp \delta\sqrt{1+X}|$ for $\delta=i$, $n=5$, $\theta=\frac{1}{4}\pi$, and $-0.9 < X < -0.6$. The legends have the same meaning as in Fig. 1.

manner to the underlying features of the propagation problem, the computational effort can be optimized for any required level of numerical accuracy.

III. NUMERICAL RESULTS

In this section, we compare three Padé-type approximants to the exact one-way propagator $\exp i\sqrt{1+X}$ that are obtained using $n=5$ and $k_0\Delta r=1$. Although $|\delta|$ is generally chosen far larger in realistic PE applications, the value $\delta=i$ provides a convenient illustration of our technique. The expressions that are used in these comparisons are: LC, the Padé approximant of Lingeitch and Collins¹⁷ for a rotation angle of $\theta=\frac{1}{4}\pi$, YT1, the Padé approximant to the propagator obtained using the first method of this paper for a square-root operator rotated by $\frac{1}{4}\pi$ —which leads to results that clearly differentiate between the various approaches—and YT2, the Padé approximant to the propagator obtained using the second method of this paper based on the modified Padé approximant obtained using Eq. (13) initiated with $f_0=i$. The comparisons are presented in Figs. 1–3. Note that the range of X is different in each of the three figures.

In Fig. 1, we observe that both the LC and YT1 propagator approximations to $|\exp i\sqrt{1+X}|$ have nearly the same accuracy in the evanescent region of the spectrum ($X < -1$). On the other hand, the YT2 approximant yields

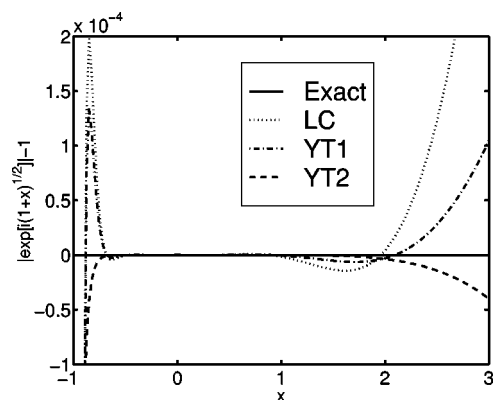


FIG. 3. Comparison of Padé approximants for the quantity $-1 + \exp \delta\sqrt{1+X}$ for $\delta=i$, $n=5$, $\theta=\frac{1}{4}\pi$, and $-1 < X < 4$. The legends have the same meaning as in Fig. 1.

completely incorrect results for the damping constants of the evanescent modes (although the evanescent energy is still suppressed). As discussed above, the two former methods would be preferable in calculations in which a correct description of the short range behavior of the field is required.

The trade-off between the relative accuracy between the evanescent and propagating parts of the spectrum is evident in Figs. 2 and 3, which show the deviation of the magnitude of the various propagator approximations from unity in the propagating part of the spectrum ($X > -1$). The YT2 curve for $-1 + |\exp i\sqrt{1+X}|$ is observed to be damped over the entire spectral region and, in particular, is very accurate in the propagating mode regime. In contrast, both the LC and YT1 propagators exhibit positive values for $-1 < X < -0.7$ and for $X > 1$ that may lead to numerical instabilities. The region $X > 0$, however, is not accessible if the reference phase speed is chosen to correspond to the lowest-order mode of the waveguide. Further, modes with $X \approx -1$ generally travel at very steep propagation angles and repeatedly reflect from the computational window boundary over a short propagation distance. As a result, the application of absorbing boundary conditions will often remove divergences associated with such spectral components.

Overall, it is evident that, especially in the evanescent region, a split-step Padé procedure based on a Padé approximant of the rotated square-root operator (YT1) is somewhat more accurate than a split-step Padé procedure derived from direct rotation of the entire exponential operator (LC). In the propagating region of the spectrum, however, the accuracy of both of these methods is far less than that associated with a split-step procedure based on the modified Padé approximation to the square-root operator (YT2). On the other hand, the latter technique is completely inaccurate in the evanescent region of the spectrum. Consequently, the choice of an optimal procedure is highly problem-dependent.

IV. CONCLUSIONS

This paper has analyzed and extended procedures for generating rotated Padé approximants of one-way propagators. The results of our investigation indicate that a fundamental trade-off exists between accurately representing the spectrum and suppressing divergences in the propagating region on the one hand and minimizing the error in the evanescent spectral region on the other. Thus methods that very accurately describe the evanescent part of the field can exhibit large errors and have regions of positive imaginary components in the propagating part of the spectrum (although the resulting divergences are generally removed through appropriate boundary conditions). Conversely, techniques that accurately resolve the propagating modes and that are free of artificial divergences generate substantial errors in the evanescent spectral region, although they do generally ensure that evanescent modes always decay during propagation. In our estimation, the vast majority of propagation problems require only modest accuracy in the evanescent part of the modal spectrum, since these modes are usually removed by absorbing boundary conditions. Further, except for certain nonlocal formulations (e.g., Refs. 21,22),

the numerical boundary conditions are themselves inexact and thus provide an additional unphysical damping to the evanescent modes. Instead, propagation methods should possess a high degree of accuracy in the propagating part of the spectrum to handle long propagation ranges, especially for modes with effective refractive indices near the reference refractive index (i.e., $X \approx -1$). Thus expressions obtained by expanding the exponential of the uniformly damped Padé-type approximant to the square-root operator appear optimal for field propagation.

In contrast, scattering problems, such as those involving reflection from rough surfaces, require far greater accuracy in the evanescent part of the spectrum, as evanescent modes can be coupled into backward-propagating modes upon reflection. At the same time the intrinsic stability of the method is far less critical, since the longitudinal distances over which the reflected field is evaluated are generally either zero or relatively small compared to the ranges over which the field diverges. Here the preferred procedure is to first rotate the square-root operator by a sufficiently large angle such that the effects of the discrete pole structure which replace the rotated branch cut on the evanescent spectrum is small, and then to perform a Padé approximant to the exponential of the result. While a rotated Padé approximant for the full propagator be employed as well, the resulting accuracy appears to be somewhat less than that associated with the exponentiated rotated square-root operator at an identical Padé order.

ACKNOWLEDGMENTS

Financial support for one of us (D.Y.) was provided through the scientific research Contract No. W7708-8-6293 with the Defence Research Establishment Atlantic. The same author would like to acknowledge the continued funding provided by the National Science and Engineering Research Council of Canada, Nortel Networks, and the Canadian Institute for Photonic Innovation.

- ¹F. B. Jensen, W. A. Kuperman, M. B. Porter, and H. Schmidt, *Computational Ocean Acoustics* (AIP Press, New York, 1994), Chap. 6.
- ²M. D. Collins, "Benchmark calculations for higher-order parabolic equations," *J. Acoust. Soc. Am.* **87**, 1535–1538 (1990).
- ³M. D. Collins, "A split-step Padé solution for the parabolic equation method," *J. Acoust. Soc. Am.* **93**, 1736–1742 (1993).
- ⁴D. Yevick, J. Yu, W. Bardyszewski, and M. Glasner, "Stability issues in vector electric field propagation," *IEEE Photonics Technol. Lett.* **7**, 656–658 (1995).
- ⁵B. T. R. Wetton and G. H. Brooke, "One-way wave equations for seismic propagation in elastic waveguides," *J. Acoust. Soc. Am.* **87**, 624–632 (1990).
- ⁶R. R. Greene, "A high-angle one-way wave-equation for seismic wave propagation along rough and sloping interfaces," *J. Acoust. Soc. Am.* **77**, 1991–1998 (1985).
- ⁷M. D. Collins and E. K. Westwood, "A higher-order energy-conserving parabolic equation for range-dependent ocean depth, sound-speed and density," *J. Acoust. Soc. Am.* **89**, 1068–1075 (1991).
- ⁸M. D. Collins, "Higher-order Padé approximations for accurate and stable elastic parabolic equations with application to interface wave propagation," *J. Acoust. Soc. Am.* **89**, 1050–1057 (1991).
- ⁹M. D. Collins and R. B. Evans, "A two-way parabolic equation for acoustic backscattering in the ocean," *J. Acoust. Soc. Am.* **91**, 1357–1368 (1992).
- ¹⁰M. D. Collins, "Generalization of the split-step Padé solution," *J. Acoust. Soc. Am.* **96**, 382–385 (1994).

- ¹¹R. J. Cedarbeg and M. D. Collins, "Application of an improved self-starter to geoacoustic inversion," *IEEE J. Ocean Eng.* **22**, 102–109 (1997).
- ¹²D. K. Dacol, M. D. Collins, and J. F. Lingeitch, "An efficient parabolic equation solution based on the method of undetermined coefficients," *J. Acoust. Soc. Am.* **106**, 1727–1731 (1999).
- ¹³M. D. Collins, "A self-starter for the parabolic equation method," *J. Acoust. Soc. Am.* **92**, 2069–2074 (1992).
- ¹⁴F. A. Milinazzo, C. A. Zala, and G. H. Brooke, "Rational square-root approximations for parabolic equation algorithms," *J. Acoust. Soc. Am.* **101**, 760–767 (1997).
- ¹⁵C. Brezinski and J. Van Iseghem, "Padé Approximations," in *Handbook of Numerical Analysis, Vol. III*, edited by P. G. Ciarlet and J. L. Lions (Elsevier, North Holland, 1994), pp. 47–222.
- ¹⁶Y. Y. Lu, "A complex coefficient rational approximation of $\sqrt{1+x}$," *Appl. Numer. Math.* **27**, 141–154 (1998).
- ¹⁷J. F. Lingeitch and M. D. Collins, "Wave propagation in range-dependent poro-acoustic waveguides," *J. Acoust. Soc. Am.* **104**, 783–790 (1998).
- ¹⁸D. Yevick and D. J. Thomson, "Impedance-matched absorbers for finite-difference parabolic equation algorithms," *J. Acoust. Soc. Am.* **107**, 1226–1234 (2000).
- ¹⁹F. D. Tappert, "The parabolic approximation method," in *Wave Propagation and Underwater Acoustics*, edited by J. B. Keller and J. S. Papadakis (Springer, New York, 1977), Chap. 5, pp. 224–287.
- ²⁰A. Bamberger, B. Engquist, L. Halpern, and P. Joly, "Higher order paraxial wave equation approximations in heterogeneous media," *SIAM (Soc. Ind. Appl. Math.) J. Appl. Math.* **48**, 129–154 (1988).
- ²¹J. S. Papadakis, "Exact, nonreflecting boundary conditions for parabolic-type approximations in underwater acoustics," *J. Comput. Acoust.* **2**, 83–98 (1994).
- ²²D. Yevick and D. J. Thomson, "Nonlocal boundary conditions for finite-difference parabolic equation solvers," *J. Acoust. Soc. Am.* **106**, 143–150 (1999).

Complex-image approximations to the half-space acousto-elastic Green's function

John A. Fawcett

Defence Research Establishment Atlantic, P.O. Box 1012, Dartmouth, Nova Scotia B2Y 3Z7, Canada

(Received 18 January 2000; revised 31 July 2000; accepted 6 September 2000)

In this paper the complex-image method is used to efficiently approximate the half-space Green's function for acousto-elastic propagation. This approximation is valid for both the near and far fields and hence should be very useful in scattering codes. [S0001-4966(00)01712-4]

PACS numbers: 43.30.Dr, 43.20.Ef [SAC-B]

I. INTRODUCTION

Many of the standard approaches to computing the scattered field from objects near or on the seabed (or methods which can be modified to account for the seabed), e.g., boundary integral equation methods (BIEM),¹ finite element methods (FEM),² and wavefield superposition methods,³ involve the computation of the appropriate half-space Green's function. This Green's function must be computed for many different source/receiver pairs, possibly involving very near field (singular), far field, and moderate (in terms of wavelengths) distances. Thus it is important to have a computationally efficient method for computing this Green's function, which is accurate for all distance regimes.

In this paper we investigate the efficient computation of the wave number integral representation of the Green's function. In particular, we will investigate the complex-image representation as outlined for electromagnetic problems in Refs. 4–6. This approach is straightforward in the case of the seabed being a fluid; if the shear velocity is included in the seabed the approach is a little more complicated, but still very accurate and efficient.

II. THEORY

We start with the wave number integral representation for the acousto-elastic Green's function, with the source and receiver in the upper fluid half space,

$$G(r, z; r=0, z_s) = \frac{e^{ikD}}{4\pi D} + \frac{1}{2\pi} \int_0^\infty J_0(hr) R(h) \frac{e^{i\gamma(z+z_s)}}{2i\gamma} h dh, \quad (1)$$

where $D \equiv \sqrt{r^2 + (z - z_s)^2}$ and $\gamma \equiv \sqrt{\omega^2/c^2 - h^2}$. For the rest of the paper we will only consider the wave number integral, yielding the reflection term. It is important to note that the integral depends only on the two parameters r and $z + z_s$. Thus one way to efficiently compute the Green's function, when a large number of evaluations will be required, is to compute this integral (or its derivatives) for a specified range of r and $z + z_s$ on a sufficiently fine grid, with a subsequent look-up and interpolation algorithm. We will investigate a more analytical approach in this paper. However, the look-up table approach, either alone or combined with other representations for some domains, could be considered.

The branch cut of γ in Eq. (1) is chosen so that it has a positive imaginary part. The reflection coefficient $R(h)$ is defined as

$$R(h) = \frac{\rho_2 \Gamma(h) \gamma_1 - \rho_1 \gamma_2}{\rho_2 \Gamma(h) \gamma_1 + \rho_1 \gamma_2}, \quad (2)$$

where ρ_1 is the density and γ_1 is the compressional vertical wave number of the upper half space and similarly for ρ_2 and γ_2 . For a fluid lower half space $\Gamma(h) \equiv 1$; otherwise,

$$\Gamma(h) \equiv (1 - 2h^2/\beta)^2 + 4\gamma_2 h^2 \gamma_s / \beta^2, \quad (3)$$

where $\beta \equiv (\omega/c_s)^2$ for c_s the shear speed in the bottom; γ_s is the shear vertical wave number in the bottom. We also use the identity that

$$\frac{e^{ikD}}{4\pi D} = \frac{1}{2\pi} \int_0^\infty J_0(hr) \frac{e^{i\gamma(z-z')}}{2i\gamma} h dh. \quad (4)$$

Taking $z' = -z_s + i\alpha$ (i.e., a complex image point for the true source location z_s), then Eq. (4) becomes

$$\frac{e^{ikD}}{4\pi D} = \frac{1}{2\pi} \int_0^\infty J_0(hr) \frac{e^{i\gamma(z+z_s)}}{2i\gamma} e^{\gamma\alpha} h dh, \quad (5)$$

or, more generally, we can write for a sum of sources

$$\sum_{j=1}^N a_j \frac{e^{ikD_j}}{4\pi D_j} = \frac{1}{2\pi} \int_0^\infty J_0(hr) \frac{e^{i\gamma(z+z_s)}}{2i\gamma} \sum_{j=1}^N a_j e^{\gamma\alpha_j} h dh, \quad (6)$$

where

$$D_j \equiv \sqrt{(x - x_s)^2 + (y - y_s)^2 + (z + z_s - i\alpha_j)^2}. \quad (7)$$

From Eqs. (6) and (1), it can be seen that if a_j and α_j are determined so that

$$\sum_{j=1}^N a_j \exp(\gamma(h)\alpha_j) \approx R(h), \quad (8)$$

then the corresponding sum of complex-source points will accurately approximate the wave number integral. Thus the problem of approximating the wave number integral has been reduced to that of fitting a sum of complex exponentials to $R(h)$.

To improve the numerical behavior of the wave number integral for $h \rightarrow \infty$ we note that in the fluid case $R(h) \rightarrow (\rho_2 - \rho_1)/(\rho_2 + \rho_1)$. For the elastic case, $R(h) \rightarrow 1$. Denoting these limiting values as R_∞ we can write for Eq. (1),

$$G(r, z; r=0, z_s) = \frac{e^{ikD}}{4\pi D} + R_\infty \frac{e^{ikD_1}}{4\pi D_1} + \frac{1}{2\pi} \int_0^\infty J_0(hr) \times (R(h) - R_\infty) \frac{e^{i\gamma(z+z_s)}}{2i\gamma} h dh. \quad (9)$$

The integrand in Eq. (9) should approach zero as $h \rightarrow \infty$.

It is interesting that for the elastic case, as the shear speed in the bottom approaches zero, then we would expect to achieve the fluid limit. However, from above, the elastic limit R_∞ is not the same as the fluid limit. This implies that in the case of low shear speed that although the singular behavior is described by $R_\infty = 1$, the integral must produce a nearly singular term which accounts for the difference between the fluid and elastic singular terms. In the elastic case there is one more additional singularity to remove from the wave number integral; this is the pole corresponding to the Scholte⁷ wave. In particular, we wish to determine the value of h such that

$$\Omega(h) = \rho_2 \Gamma(h) \gamma_1 + \rho_1 \gamma_2 = 0, \quad (10)$$

where $R(h) = N(h)/\Omega(h)$. For the example of this paper this pole, h^* , occurs for h slightly larger than ω/c_s . The residue at this pole yields the term

$$S(r, z) = H_0(h^*r) \frac{N(h^*)}{2\gamma(h^*)} \Omega'(h^*) h^* e^{i\gamma(h^*)(z+z_s)}. \quad (11)$$

In order to derive this expression, the half-infinite integral of Eq. (9) is written in terms of an integral from $-\infty$ to ∞ , involving the Hankel function $H_0(hr)$. Then the Scholte pole in the upper-half of the complex plane yields the expression of Eq. (11). It should be noted that the term $\exp[i\gamma(h^*)(z+z_s)]$ is highly evanescent and will only be significant for $z+z_s \approx 0$.

The question arises as to how to best handle the Scholte singularity. The best approach we have found is to fit exponentials to the spectrum with the asymptotic constant, R_∞ , subtracted out but with the Scholte pole contribution left in; however, we do a weighted fit with the weighting approaching zero as the Scholte pole is approached. In particular we use the weighting

$$w(h) = 1 - \exp\left[-\left(\frac{|(h-h^*)|}{10}\right)^2\right]. \quad (12)$$

An efficient method of fitting exponentials to data is by using Prony's⁸ method. This method can be used in the fluid case. At the start of the wave number integral, $h=0$ and $\gamma_{in} = \omega/c_p$; at the end of the wave number integral $\gamma_f = i\sqrt{h_{max}^2 - (\omega/c_p)^2}$. We compute $\tilde{R}(\gamma_k)$ for $\gamma_k = \gamma_{in} + (k-1)\Delta$ where

$$\Delta = \frac{\gamma_f - \gamma_{in}}{2N-1}. \quad (13)$$

It is possible using Prony's method to uniquely determine N values of a_j and α_j from the $2N$ values of $\tilde{R}(\gamma)$. The linearly varying values of γ correspond to a curved contour in the complex- h domain. The values (a_j, α_j) may provide an adequate fit to the wave number integrand or they may be used as starting values of a nonlinear fit to the data.

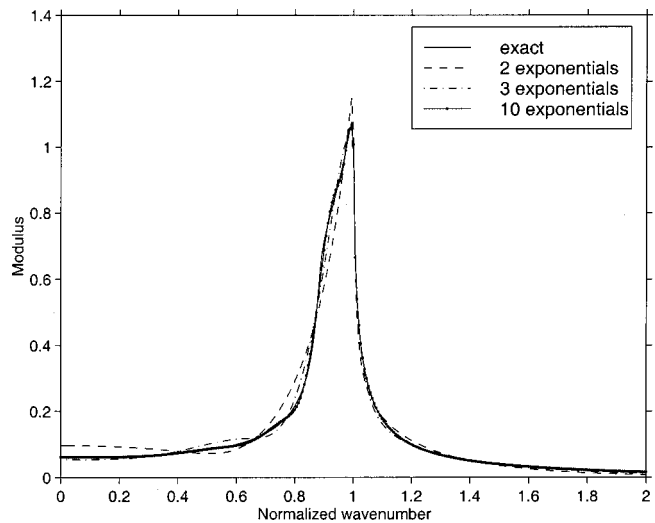


FIG. 1. A comparison of the exact reflection coefficient (with the asymptotic constant subtracted) with fitted exponentials. The wave number coordinate is normalized by $\omega/1500$. The seabed parameters are $c_p=1700$ m/s and $\rho=1.5$ g/cm³.

For the elastic case, where the spectrum is over a large part of the h domain and where we use a weighted fit to nullify the effects of the Scholte pole, the Prony approach is not very appropriate. In order to improve the Prony estimates in the fluid case, or in the elastic case to estimate the exponentials, we use a nonlinear optimization method. In particular, we compute the Jacobian matrix for the derivatives of the functional

$$F(\alpha) = \sum_{n=1}^N |r_n - f_n(\alpha)|^2 w_n, \quad (14)$$

with respect to the real and imaginary parts of the parameter vector α which includes the unknown complex amplitudes and exponents. Here r_n are the given reflection coefficient values along the real- h axis (perhaps shifted by a small imaginary amount), f_n are the computed values using the

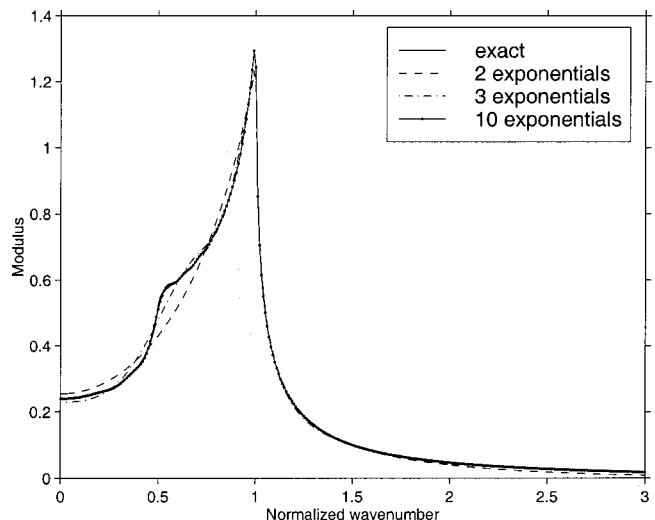


FIG. 2. A comparison of the exact reflection coefficient (with the asymptotic constant subtracted) with fitted exponentials. The wave number coordinate is normalized by $\omega/1500$. The seabed parameters are $c_p=3000$ m/s and $\rho=2.5$ g/cm³.

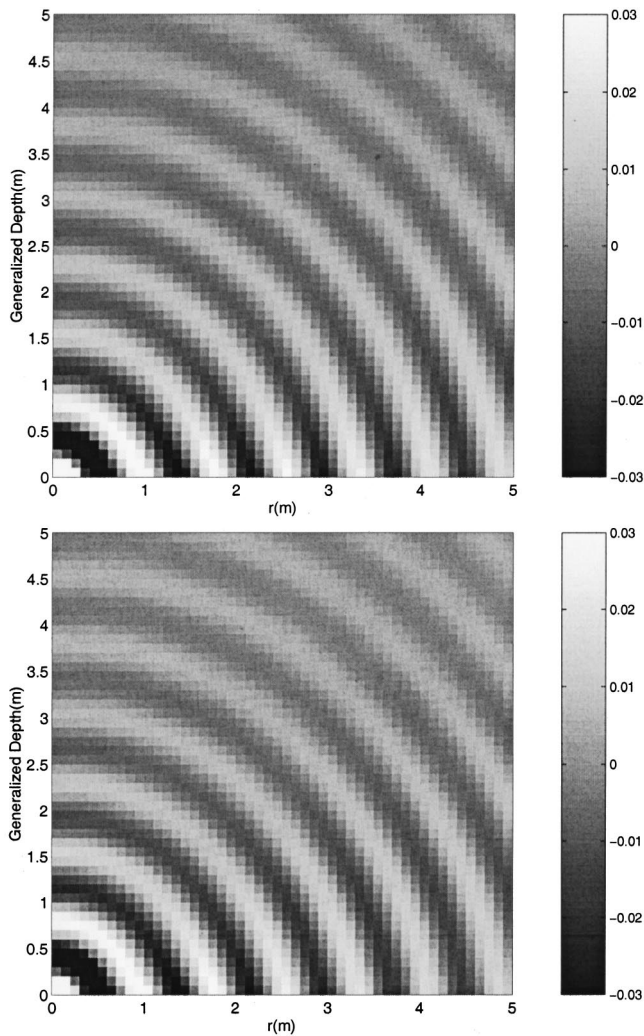


FIG. 3. The two-dimensional range-generalized depth ($z+z_s$) reflected pressure field for (top) the exact reflection coefficient and (bottom) two-term exponential expression with asymptotic term.

values of the parameters α , and w_n are the weightings. With the Jacobian matrix, we use the Levenberg–Maquard⁹ method of optimization. We found that with one or two initial estimates of the parameter vector we would obtain convergence. For the elastic case, there seemed to be a false minimum to which the solution could converge. However, by trying various initial estimates a good fit was always obtained.

III. NUMERICAL EXAMPLES

A. Fluid half space

In this example we first consider a fluid half space, $c_p=1500$ m/s and $\rho=1$ g/cm³ overlying a half space with $c_p=1700$ m/s and $\rho=1.5$ g/cm³. There is an attenuation of 0.5 dB/ λ in the bottom and the frequency considered is 2 kHz. For the optimization technique, the reflection coefficient $R(h)$ was computed for 301 values along the real- h axis (displaced by $-0.01i$) between $h=0$ and $h=2k_0$ ($k_0 \equiv \omega/1500$). The complex exponential parameters were obtained by first applying Prony's method and then refining these estimates with several iterations of the nonlin-

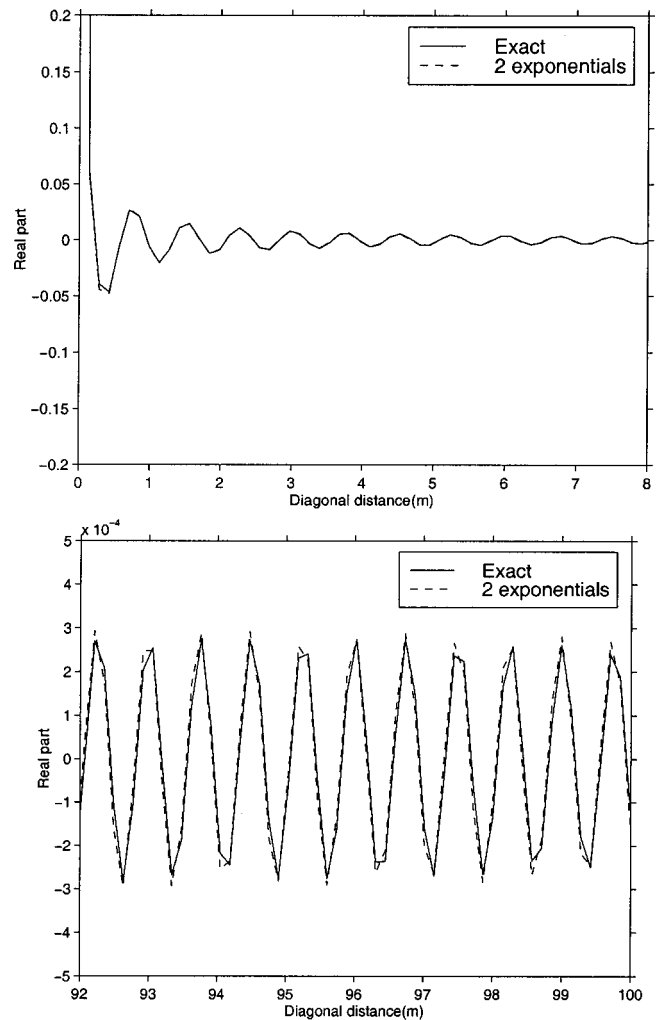


FIG. 4. A comparison of the exact pressure field along the line $z+z_s=x$ with that computed by the three-term exponential expression for (a) the near field and (b) the far field.

ear optimization algorithm. In Fig. 1, we show the wave number integrand along the real h -axis with R_∞ subtracted off and the resulting fits using two, three, and ten exponential terms. The values of α and the amplitudes for the two- and three-term fits are

$$\begin{aligned} \alpha_1 &= -0.431 - 0.476i, & \alpha_1 &= -0.189 + 0.308i, \\ \alpha_2 &= -0.894 + 0.703i, & \alpha_2 &= -0.346 + 0.951i, \end{aligned}$$

and for the the three-term case,

$$\begin{aligned} \alpha_1 &= -0.283 - 0.308i, & \alpha_1 &= -0.127 + 0.249i, \\ \alpha_2 &= -1.20 + 0.173i, & \alpha_2 &= -0.324 + 0.788i, \\ \alpha_3 &= 0.315 - 0.052i & \text{and } \alpha_3 &= -0.281 + 1.75i. \end{aligned}$$

As can be seen the fit is very good for the two- and three-term cases and almost exact for the ten-term case. We computed the ten-term fit to illustrate that the method does not become unstable as more terms are considered. However, the convergence rate of the optimization technique seems to be poorer for large numbers of parameters. In Fig. 2 we show the results for a faster seabed ($c_p=3000$ n/s and $\rho=2.5$

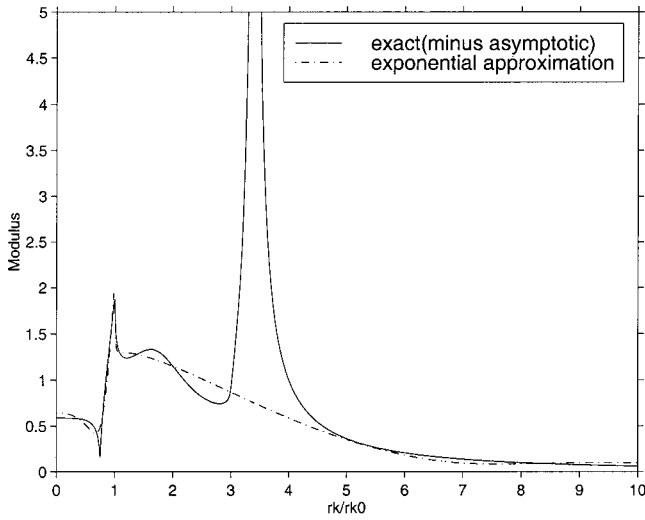


FIG. 5. A comparison of exact reflection coefficient (with the asymptotic constant subtracted) with fitted exponentials.

g/cm^3). Here the fit has been carried out to $k/k_0=3$. Once again, the fits are excellent.

The values of a_i and α_i determined by the fit are then used in the expression,

$$p_{\text{exp}}(r, z) = R_{\infty} \frac{e^{ikD_0}}{4\pi D_0} + \sum_{j=1}^N a_j \frac{e^{ikD_j}}{4\pi D_j}, \quad (15)$$

where

$$D_0 \equiv \sqrt{(x-x_s)^2 + (z+z_s)^2}$$

and

$$D_j \equiv \sqrt{(x-x_s)^2 + (z+z_s - i\alpha_j)^2}.$$

The exact wave number expression with the R_{∞} term analytically added in is used to compute the pressure field for a 5×5 -m square. The real part of this field is shown in Fig. 3(a) for the seabed with $c_p = 1700$ m/s and $\rho = 1.5$ g/cm^3 . The depth coordinate is the generalized depth $z+z_s$. In other words, there is no specific source or receiver depth in these computations; it is their sum which is the important parameter. In Fig. 3(b) the corresponding values, as computed using the expression of Eq. (15) with $N=2$ is shown. As can be seen the two sets of results are very similar in appearance. The fields become singular for $r \rightarrow 0$ and $z+z_s \rightarrow 0$; also, it is interesting to note that the wavefronts are not spherical in appearance for small values of r and $z+z_s$. To further emphasize the agreement between the exact and approximate results, we show in Fig. 4(a) a line plot of the real part along the line $z+z_s=r$ for distance values along this line of between 0 and 8 m and in Fig. 4(b) for distance values between 92 and 100 m. It can be seen here that the agreement between the exact and approximate values is excellent for both small and large values of distance.

B. Elastic half space

We now consider the problem of approximating the reflection response of an elastic half space. For this example we take the lower half space to have a compressional speed of 2000 m/s (attenuation of 0.2 dB/ λ) and a shear speed of

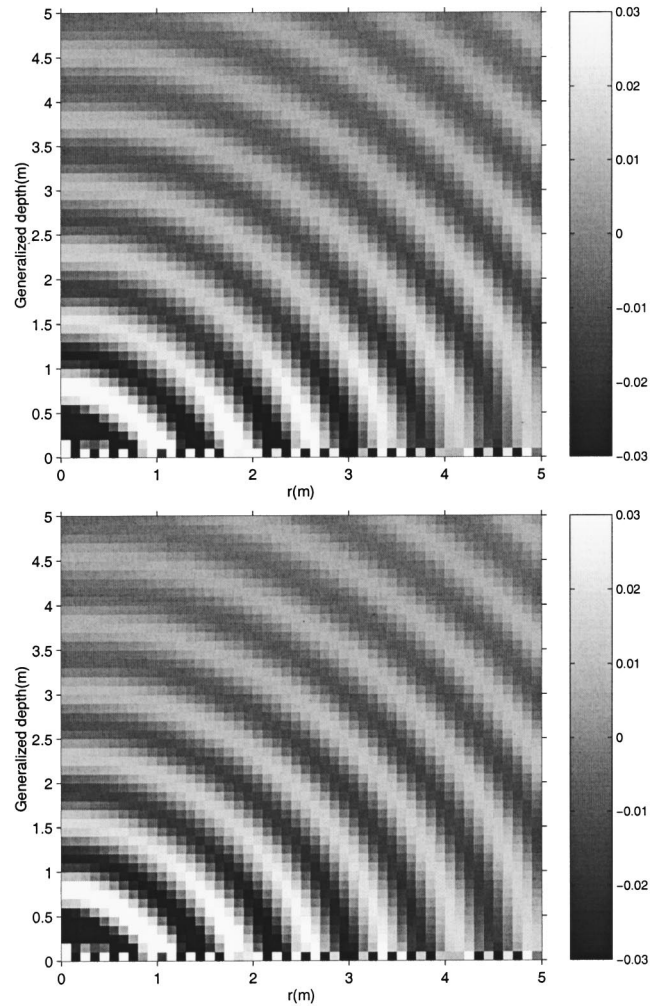


FIG. 6. The two-dimensional range-generalized depth reflected pressure field for (top) the exact reflection coefficient and (bottom) three-term exponential expression with asymptotic term and Scholte residue.

500 m/s (attenuation of 0.4 dB/ λ). The density is 1.8 g/cm^3 . In Fig. 5 we show the reflection coefficient modulus as a function of wave number; in order to include the shear wave number and beyond it is necessary to consider wave numbers $3k_0$ ($k_0 \equiv \omega/1500$) and larger (we consider up to $10k_0$). The contribution from the Scholte pole is evident. The location of this pole, the zero of the function $\Omega(h)$ [i.e., the denominator in the expression for $R(h)$] is determined using Newton's method. In this example the pole is located at $h^* = 28.4796 + 0.205i$ or in terms of k_0 , $h^* = (3.40 + 0.0245i)k_0$.

We now fit a three-term exponential model to the spectrum with the asymptotic term ($R_{\infty} = 1$) subtracted off and the weighting going to zero near the Scholte pole. The resulting values for a_k and α_k are given by

$$a_1 = -0.794 + 0.941i, \quad \alpha_1 = -0.220 + 0.694i,$$

$$a_2 = -0.401 - 1.06i, \quad \alpha_2 = -0.124 + 0.0441i,$$

$$a_3 = -0.762 + 0.526i \quad \text{and} \quad \alpha_3 = -0.0427 + 0.0286i.$$

The approximate reflection curve computed by the three-term exponential expression is shown in Fig. 5; the fit passes smoothly through the Scholte pole.

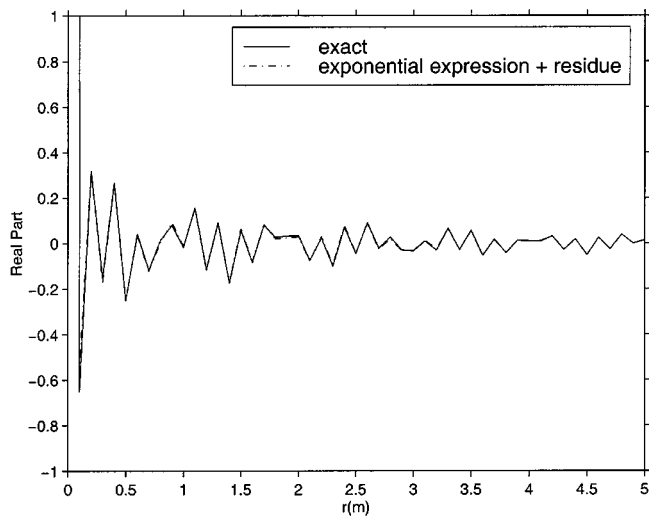


FIG. 7. A comparison of the exact pressure field along the line $z+z_s=0$ with that computed by the three-term exponential expression with asymptotic term and Scholte residue.

As in the fluid case we now compute the pressure field in a 5×5 -m square and display its real part in Fig. 6. For this computation we add in the residue term $S(r, z)$ of Eq. (11) to model the Scholte wave behavior. This term is incorrect for $r \rightarrow 0$ (it is incorrectly singular); to include this term we weight it with the factor $(1 - \exp[-(r/\sigma)^2])$ where $\sigma = 0.8 \times \lambda_s$, with λ_s the shear wavelength. This term goes to zero as $r \rightarrow 0$ and approaches unity for r greater than a few shear wavelengths. As can be seen in the two panels of Fig. 6, the agreement between the exact and approximate computations is excellent. The highly oscillatory behavior of the pressure fields along the line $z+z_s=0$ is due to the Scholte wave which is only evident for values of $z+z_s$ very near zero. To further emphasize the agreement, a line plot for the real parts of the fields along $z+z_s=0$ is shown in Fig. 7. The agree-

ment between the exact and approximate computations is excellent.

IV. SUMMARY

We have demonstrated that for fluid–fluid and fluid–elastic half-space problems the Green’s function can be accurately approximated by a few complex images (and possibly a term representing the Scholte wave) for small, moderate, and large values of source/receiver separation. The determination of the complex-image positions and amplitudes involves a nonlinear optimization procedure which is straightforward to implement. In the future we hope to utilize these Green’s function representations in modeling scattering from objects on or near the seabed.

- ¹J. A. Fawcett, “Acoustic scattering from cylindrical objects embedded between two half-spaces,” *J. Acoust. Soc. Am.* **100**, 3053–3060 (1996).
- ²I. C. Mathews, “Numerical techniques for three-dimensional steady-state fluid structure interaction,” *J. Acoust. Soc. Am.* **79**, 1317–1325 (1986).
- ³A. Sarkissian, “Method of superposition applied to scattering from a target in shallow water,” *J. Acoust. Soc. Am.* **95**, 2340–2345 (1994).
- ⁴S. Vitebskiy, K. Sturgess, and L. Carin, “Short-pulse plane-wave scattering from buried perfectly conducting bodies of revolution,” *IEEE Trans. Antennas Propag.* **44**, 143–151 (1996).
- ⁵R. M. Shubair and Y. L. Chow, “A simple and accurate complex image interpretation of vertical antennas present in contiguous dielectric half spaces,” *IEEE Trans. Antennas Propag.* **41**, 806–812 (1993).
- ⁶J. J. Yang, Y. L. Chow, and D. G. Fang, “Discrete complex images of a three-dimensional dipole above and within a lossy ground,” *IEE Proc., Part H: Microwaves, Opt., and Antennas* **138**, 319–326 (1991).
- ⁷D. Rauch, “On the role of bottom interface waves in ocean seismo-acoustics,” in *Ocean Seismo-Acoustics*, Proceedings of a SACLANT ASW Research Center Symposium, June 10–14, 1985, Lerici, Italy, edited by T. Akal and J. M. Berkson (Plenum, New York, 1986), pp. 623–641.
- ⁸S. Marple, Jr., *Digital Spectral Analysis with Applications* (Prentice-Hall, Englewood Cliffs, NJ, 1987).
- ⁹W. H. Press, B. P. Flannery, S. A. Teukolsky, and W. T. Vetterling, *Numerical Recipes in C* (Cambridge University Press, Cambridge, 1988).

Wave propagation, stress relaxation, and grain-to-grain shearing in saturated, unconsolidated marine sediments

Michael J. Buckingham

Marine Physical Laboratory, Scripps Institution of Oceanography, University of California, San Diego, 9500 Gilman Drive, La Jolla, California 92093-0238 and Institute of Sound and Vibration Research, The University, Southampton SO17 1BJ, United Kingdom

(Received 1 February 1999; revised 23 February 2000; accepted 9 September 2000)

A linear theory of wave propagation in saturated, unconsolidated granular materials, including marine sediments, is developed in this article. Since the grains are unbonded, it is assumed that the shear rigidity modulus of the medium is zero, implying the absence of a skeletal elastic frame. The analysis is based on two types of shearing, translational and radial, which occur at grain contacts during the passage of a wave. These shearing processes act as stress-relaxation mechanisms, which tend to return the material to equilibrium after the application of a dynamic strain. The stress arising from shearing is represented as a random stick-slip process, consisting of a random succession of deterministic stress pulses. Each pulse is produced when micro-asperities on opposite surfaces of a contact slide against each other. The quantity relevant to wave propagation is the *average* stress from all the micro-sliding events, which is shown to be a temporal convolution between the deterministic stress, $h(t)$, from a single event and the probability, $q(t)$, of an event occurring between times t and $t+dt$. This probability is proportional to the velocity gradient normal to the tangent plane of contact between grains. The pulse shape function, $h(t)$, is derived by treating the micro-sliding as a strain-hardening process, which yields an inverse-fractional-power-law dependence on time. Based on two convolutions, one for the stress relaxation from translational and the other from radial shearing, the Navier–Stokes equation for the granular medium is derived. In a standard way, it is split into two equations representing compressional and shear wave propagation. From these wave equations, algebraic expressions are derived for the wave speeds and attenuations as functions of the porosity and frequency. Both wave speeds exhibit weak, near-logarithmic dispersion, and the attenuations scale essentially as the first power of frequency. A test of the theory shows that it is consistent with wave speed and attenuation data acquired recently from a sandy sediment in the Gulf of Mexico during the SAX99 experiment. If dispersion is neglected, the predicted expressions for the wave speeds reduce to forms which are exactly the same as those in the empirical elastic model of a sediment proposed by Hamilton. On this basis, the concept of a “skeletal elastic frame” is interpreted as an approximate, but not equivalent, representation of the rigidity introduced by grain-to-grain interactions. © 2000 Acoustical Society of America. [S0001-4966(00)01112-7]

PACS numbers: 43.30.Ma, 43.30.Xm [DLB]

LIST OF SYMBOLS

a	radius of circle of contact between grains	$h_s(j\omega)$	Fourier transform of $h_s(t)$
\mathbf{A}	vector potential	j	$\sqrt{-1}$
c_0	compressional wave speed in equivalent suspension	m	translational (shear) stress-relaxation exponent
c_p	compressional wave speed in saturated granular medium	n	radial (compressional) stress-relaxation exponent
c_s	shear wave speed in saturated granular medium	N	porosity of granular medium
d	depth beneath seawater-sediment interface	$p(t)$	acoustic pressure
d_0	reference depth in sediment	$q(t)$	probability density function
D	root-mean-square (r.m.s.) roughness of mineral grain	t	time
E	spring constant in Maxwell element	t_p	radial stress-relaxation time constant
E_g	Young's modulus of mineral grains	t_s	translational stress-relaxation time constant
$h_p(t)$	radial (compressional) material impulse response function (MIRF)	u_g	mean grain diameter
$H_p(j\omega)$	Fourier transform of $h_p(t)$	u_0	reference grain diameter
$h_s(t)$	translational (shear) material impulse response function (MIRF)	\mathbf{v}	particle velocity
		x, y, z	Cartesian coordinates
		α_p	attenuation coefficient of compressional wave in saturated granular medium
		α_s	attenuation coefficient of shear wave in saturated granular medium

β_p	loss tangent of compressional wave in saturated granular medium	λ_p	radial (compressional) stress-relaxation coefficient
β_s	loss tangent of shear wave in saturated granular medium	μ_p	radial (compressional) stress-relaxation modulus
γ_p	compressional rigidity coefficient	μ_s	translational (shear) stress-relaxation modulus
γ_s	shear rigidity coefficient	ξ_0	residual viscosity of thin pore-fluid film between asperities
Γ_p	normalized compressional rigidity coefficient	$\xi(t)$	coefficient of strain-hardening dashpot in Maxwell element
Γ_s	normalized shear rigidity coefficient	ρ_g	density of mineral grains
Δ	density fluctuation	ρ_0	bulk density of saturated granular medium
η_s	translational (shear) stress-relaxation coefficient	ρ_w	density of pore fluid
θ	strain-hardening coefficient	σ	internal stress
θ_g	Poisson's ratio for mineral grains	χ	stress in Maxwell element
κ_0	bulk modulus of equivalent suspension	ψ	scalar potential
κ_g	bulk modulus of mineral grains	ω	angular frequency
κ_w	bulk modulus of pore fluid		

I. INTRODUCTION

In 1956 Biot published two distinguished papers^{1,2} on the propagation of stress waves in a porous elastic solid containing a compressible viscous fluid in the pore spaces. An example of such a material is a water-saturated sedimentary rock. The mineral grains in a rock are strongly bonded together to form an elastic matrix, or skeletal frame. Like any other elastic solid, the consolidated skeletal frame obeys Hooke's law. In fact, Biot begins his analysis with the stress tensor for the Hookean elastic forces acting on the frame. Later in his development, two coefficients emerge, the familiar Lamé constants of elasticity theory. One of these, the shear modulus, is a measure of the rigidity of the medium, which supports the propagation of a rotational, or shear, wave. Biot also showed that the relative motion between the pore fluid and the skeletal frame leads to two compressional waves, designated dilatational waves of the first and second kind, or colloquially as the "fast" and "slow" wave. Usually the slow wave is very heavily attenuated, making it difficult to detect experimentally.

In a series of papers, culminating in a monograph,³ Biot's theory has been adapted by Stoll in an attempt to describe wave propagation in a saturated, unconsolidated marine sediment. Unlike a rock, the mineral particles in such a sediment are unbonded. To some extent, the grains are mobile, and recent evidence indicates that, in dry sands at least, the packing arrangement evolves slowly in time due to the presence of a propagating wave.⁴ Moreover, the stresses in an unconsolidated granular material under compression appear to run through the medium along random pathways, known as force chains.⁵ These pathways of high stress follow routes through the medium where the grains are in tight contact. Elsewhere, the grains are looser and the stress is lower.

Such behavior indicates that, unlike a rock, the unbonded mineral grains in an unconsolidated granular material do not form a macroscopic elastic skeletal frame. The primary forces within the unconsolidated medium arise from grain-to-grain interactions. Such interactions give rise to the force chains. In the presence of a wave, grain-to-grain shearing occurs, driven by the velocity gradient across the grain

contacts. In this sense, the unconsolidated granular medium is more like a viscous fluid, where the shear flow is driven by the velocity gradient normal to the flow, rather than an elastic solid in which the stress-strain relationships are governed by Hooke's law.

If the material possesses no elastic skeletal frame, the Biot theory, including Stoll's adaptations of it, does not provide an appropriate theoretical basis for describing wave propagation in an unconsolidated granular medium. An alternative approach is needed which addresses explicitly the forces associated with grain-to-grain shearing. Recently, such a treatment was developed by Buckingham and published in two articles, hereafter referred to as I⁶ and II.⁷

Although the mathematical formalism describing wave propagation in an unconsolidated sediment is established in I and II, the treatment is inductive rather than deductive. For instance, the relationship presented in I and II between internal stress and rate of strain is not deduced from a specific physical mechanism, and the general form of the Navier-Stokes equation used in the analysis is not derived in the original papers but is merely stated, largely by analogy with wave propagation in a viscous fluid.

The purpose of the present article is to rectify these deficiencies. Central to the argument is a stochastic treatment of intergranular shearing, based on a random "stick-slip" process. Each "slip" is a microscopic, stress-relaxation event between micro-asperities, which are separated by a very thin film of interstitial fluid (seawater). Recent developments in tribology⁸ have established that thin aqueous films, less than about ten molecular diameters thick, exhibit an effective viscosity which is considerably higher than the viscosity of the bulk fluid and which increases rapidly as the force compressing the contact grows. It is proposed that, in a saturated granular medium, the viscosity of the lubricating fluid film between micro-asperities increases as the slip progresses, a phenomenon known as strain hardening.⁹ In a granular medium, strain hardening makes a microscopic shearing event more difficult to sustain as the sliding continues.

The wave properties that derive from the random stick-slip, strain-hardening model are similar to those observed experimentally in saturated marine sediments. Since relative

motion between the pore fluid and the mineral grains is not included in the model, only one dilatational wave emerges from the theory (no slow wave is predicted), and interestingly, the new grain-shearing mechanism introduces rigidity into the medium, which weakly supports a rotational wave. Both the dilatational and the shear wave exhibit weak, near-logarithmic dispersion and an attenuation that scales, over many decades, essentially as the first power of frequency.

Before developing the model and deriving the properties of the dilatational and the shear wave, some recent experimental observations on unconsolidated granular media are reviewed. As noted by Jaeger *et al.*,¹⁰ a (dry) granular material behaves differently from a solid, a liquid, and a gas, even though it may possess some of the properties of each. They even suggest that it represents an additional state of matter in its own right. Similar comments could be made about a saturated unconsolidated granular material, not only in connection with its mechanical behavior but also its wave properties.

II. FORCE CHAINS

In a recent series of laboratory experiments on dry sand, Nagel and colleagues^{4,5,11-14} found that granular media exhibit unique properties, most if not all of which are a result of grain-to-grain interactions. In particular, they observed that the stress in a sand pile tends to concentrate along random pathways passing through the points of contact between grains. By using a system of crossed polarizers, Liu *et al.*⁵ were able to visualize the elongated regions of relatively high stress (see their Fig. 1), which they refer to as force chains.

Acoustic waves within the granular medium tend to propagate along the force chains. Since more than one force chain may connect an acoustic source and receiver buried in the medium, interference may occur between waves propagating along each of the force-chain pathways, giving rise to a received signal that fluctuates strongly with changing frequency (as illustrated in Fig. 3 of Liu and Nagel⁴). The experimental findings suggest that the contacts between mineral grains are very fragile. A minuscule mechanical disturbance to the arrangement of the grains causes a substantial change in the level of the received signal, behavior that Nagel and co-authors attribute to the shifting of the packing structure, and hence the force chain pathways, in response to a very small applied strain.

Even the presence of a propagating, small-amplitude wave introduces sufficient strain to alter the medium on a microscopic level. As a result, the level of the received signal from a single-frequency source slowly evolves in time, continually making excursions about its average value as the wave itself modifies the random arrangement of the grains in the host material. This evolutionary behavior is illustrated in Fig. 1(a) of Liu and Nagel,⁴ which shows a time series, lasting approximately 8 h, of the received signal level from a 4-kHz, constant-amplitude source. Fluctuations in the level of the signal arrival can be seen to occur over a wide range of time scales.

The continuous evolution of the amplitude fluctuations suggests that, during the passage of the wave, intergranular

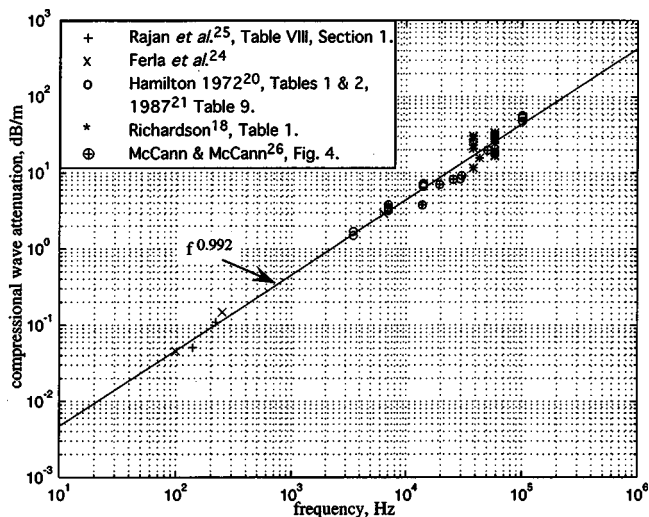


FIG. 1. Compilation of *in situ* data showing compressional wave attenuation as a function of frequency in sands. The solid line is a least-squares fit of a frequency power law to the data.

shearing occurs continuously. Each microscopic grain-to-grain shearing event leads to a new realization of the medium, which differs almost imperceptibly from the previous realization. Since the changes are cumulative, the packing structure of the grains after a long transmission may be significantly different from the original arrangement. A summary of the experiments and conclusions from Nagel's group can be found in a recent article on waves in granular media by Nagel and Jaeger.¹⁵

Variability in the wave properties of granular materials is observed, not only in the laboratory, but also in wave data collected from the seabed. Using their ISSAMS frame,¹⁶⁻¹⁸ Richardson and colleagues have performed numerous *in situ* measurements of compressional and shear waves in unconsolidated marine sediments. In one of their recent experiments in medium sand in the Gulf of Mexico, they observed strong fluctuations¹⁹ in the received signal from a frequency-modulated (chirp) source. These fluctuations are much like those seen in Liu and Nagel's⁴ Fig. 3. As in the laboratory experiments, interference between arrivals that propagated along two or more force-chain pathways would appear to be a plausible explanation for the origin of the fluctuations in the *in situ* measurements.

III. WAVE PROPERTIES OF UNCONSOLIDATED SEDIMENTS

Spot-frequency measurements of wave attenuation in sediments exhibit considerable scatter, possibly due partly to the slow evolution of arrival amplitudes. Consequently, most authors adopt a statistical approach when reporting attenuation data. Thus Hamilton,^{20,21} Wood and Weston,²² and Bjørnø,²³ have reported measurements of the average attenuation of the compressional wave as a function of frequency in unconsolidated marine sediments. Over limited frequency ranges, they all found that the attenuation scales as f^s , where the index s is close to unity.

This linear scaling with frequency is exemplified in Fig. 1, which shows a compilation of compressional wave attenu-

ation data for saturated sands. The data points in the figure are from tables in Hamilton,^{20,21} Richardson,¹⁸ Ferla *et al.*,²⁴ and Rajan *et al.*,²⁵ and from Fig. 4 in McCann and McCann.²⁶ All the data points in Fig. 1 were collected *in situ* and are representative of the sediment just beneath the sea floor. No data from laboratory measurements, or from deep in the sediment, or from materials other than sand, appear in Fig. 1. The solid curve in Fig. 1 is a power-law, least-squares fit to the data, which varies as $f^{0.992}$. The near-linear scaling of the attenuation with frequency, f , is clearer in Fig. 1 than in some of Hamilton's plots, which superimpose data from all types of sediment (sands, silt/sands, silts, and clays), data taken *in situ* and under laboratory conditions, and data taken at great and shallow depths.

In a recent survey article, Bowles,²⁷ in his Fig. 1, plotted a compilation of data showing compressional wave attenuation as a function of frequency in fine-grained sediments, mostly muds, clays, and turbidites. Over a frequency range extending from 10 Hz to 500 kHz he found that the attenuation exhibits a near-linear scaling with frequency: his best power-law fit to the data varies as $f^{1.12}$.

No published, *in situ* measurements are known on the frequency dependence of the shear wave attenuation in sands. Laboratory measurements of shear wave attenuation in a water-saturated medium sand, from Table II in Brunson and Johnson,²⁸ are shown in Fig. 2(a). The solid line, varying as $f^{1.11}$ and passing through the data points, is a least-squares fit of a frequency power law to the data. Although Brunson and Johnson²⁸ themselves suggest otherwise, the shear attenuation data appear to exhibit a near-linear scaling with frequency over the bandwidth (0.45 to 7 kHz) of the experiment.

Brunson²⁹ found similar behavior for the attenuation of the shear wave in water-saturated, sorted glass beads. Figure 2(b) shows the data from his Table 2, along with a least-squares fit of a frequency power law varying as $f^{1.06}$. Curiously, Brunson²⁹ interpreted the measurements in Fig. 2(b) as showing "evidence of viscous attenuation due to fluid-to-grain relative motion." This unfortunate statement, which has been accepted at face value in at least one review article,³⁰ does not appear to be consistent with the data in Fig. 2(b). These shear attenuation data can be seen to exhibit a near-linear dependence on frequency over a band from 1 to 20 kHz.

A medium with an attenuation that essentially scales with frequency should, according to the Kramers–Kronig relationships, exhibit near-logarithmic dispersion.^{31–36} The level of the dispersion is proportional to the loss tangent (or inversely proportional to the Q) of the material and, for the compressional wave in a typical sand, is in the region of 1.5% per decade of frequency. This is too low to be detected in many experiments, even under laboratory conditions.

Nevertheless, several investigators have attempted to detect the frequency dependence of the compressional wave speed in sand.^{20,37,38} All concluded that dispersion, if present at all, is very weak. In a more recent laboratory experiment, Wingham³⁹ observed logarithmic dispersion at a level of approximately 1% per decade in a medium sand over a frequency range between 100 and 350 kHz. Although this band-

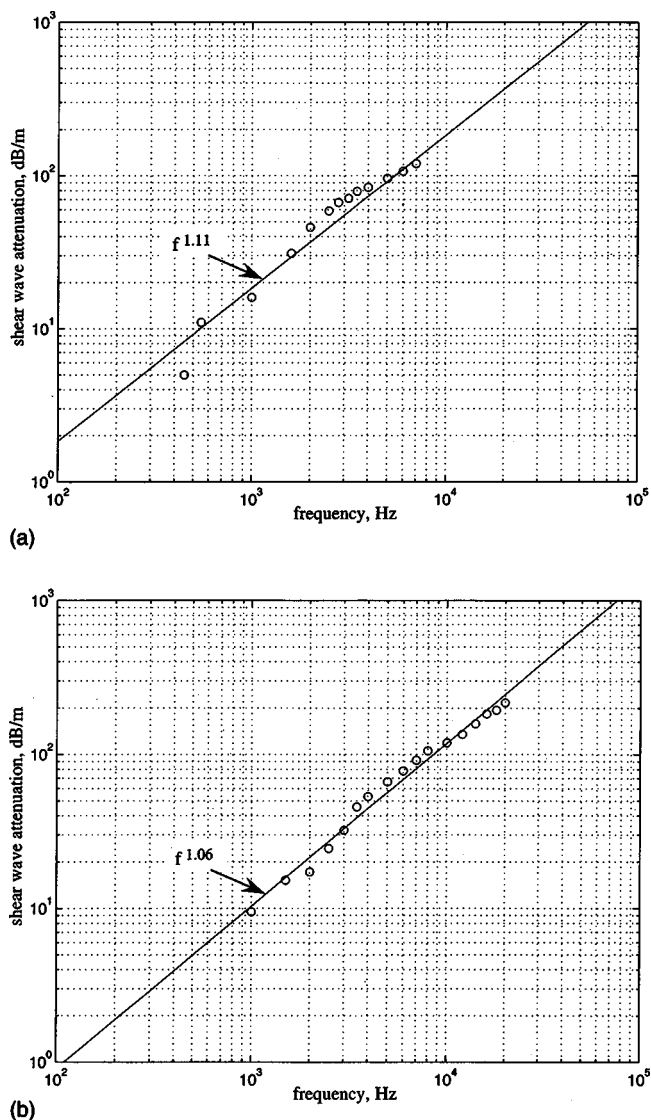


FIG. 2. Laboratory data showing the attenuation of the shear wave as a function of frequency and a least-squares fit of a frequency power law. (a) Saturated medium sand, data from Brunson and Johnson (Ref. 28). (b) Saturated glass beads, data from Brunson (Ref. 29).

width is limited, Wingham's observation is not inconsistent with the Kramers–Kronig requirement for a material with an attenuation that scales linearly with the frequency.

In a critical discussion of the published experimental evidence on frequency dispersion in sands and sediments, Hamilton²⁰ concluded that "velocity dispersion is negligible or absent in water-saturated sediments." He was also of the opinion that wave attenuation in marine sediments is dominated by grain-to-grain interactions, which is consistent with the observations of force-chains in dry sands by Nagel and colleagues. Viscous losses associated with the relative movement of the pore fluid through the mineral structure, the primary dissipation mechanism in the Biot theory, were considered by Hamilton²⁰ to be negligible. He based this conclusion on the fact that the velocity dispersion is negligible, which would not be the case if viscous dissipation were significant.

A secondary piece of evidence indicating that viscous flow has little effect on wave propagation was reported by

Wyllie *et al.*⁴⁰ They found that the speed of compressional waves through water-saturated glass beads remained unchanged as the permeability was varied by a factor of 4.6×10^4 . This insensitivity to the permeability implies that relative motion between the viscous pore fluid and the unbonded mineral grains is insignificant.

If the flow of pore-fluid between grains is negligible, the slow wave predicted by the theory of Biot^{1,2} and its modifications by Stoll³ should be extremely weak, if not absent altogether. A steadily accumulating body of experimental evidence indicates that this is indeed the case. Despite several attempts to detect it under controlled laboratory conditions,^{41–46} the slow wave in unconsolidated, saturated granular media has never been observed. (The slow wave has been detected in a *consolidated* porous medium consisting of lightly fused glass spheres).^{45,46}

Hamilton's²⁰ contention that grain-to-grain interactions largely determine the properties of waves in unconsolidated granular media is supported by the fact that the compressional and shear wave speeds show a pronounced dependence on grain size. Experimental data, compiled from a number of published sources and showing the functional dependence of compressional and shear wave speeds on grain size, are plotted, respectively, in Fig. 8 in I and Fig. 5 in II. Similar grain-size data, acquired using the ISSAMS frame, have been presented by Richardson,¹⁸ who fitted empirical curves to the experimental points using a regression analysis.

Not all the published evidence is unequivocal in supporting grain-to-grain interactions as being responsible for the wave properties of saturated granular materials. For instance, Simpson and Houston⁴⁴ recently reported laboratory measurements of the dispersion and attenuation of the compressional wave in a fine-to-medium sand over the frequency range 4 to 100 kHz. Their acoustic source was in the water column above the sediment and a single hydrophone buried in the sand was moved systematically from run to run to form a synthetic-aperture receiver array. The attenuation was found to vary approximately as $f^{0.61}$, a slope that is somewhat slower than would be expected from grain-to-grain interactions. Dispersion, on the other hand, was not evident in the sound-speed data, which is consistent with a grain-to-grain argument.

It is quite possible that more than one mechanism is responsible for the wave properties of saturated, unconsolidated granular media. Nevertheless, from the weight of experimental evidence that has accrued over the years, it is difficult to avoid the conclusion that grain-to-grain interactions play an important role in characterizing wave behavior in these materials. The remainder of the paper is devoted to developing a model of grain-to-grain shearing, which, as will be shown, gives rise to many of the observed properties of waves in unconsolidated sediments.

IV. THE MODEL

It is assumed that the unconsolidated, saturated granular material consists of mineral grains of essentially uniform size, that there are no large inclusions such as shell fragments that would act as scattering centers, that there is no gas in the pores, and that the wavelength is considerably longer

than the size scale of the grains and pore spaces. Taking the grain boundaries as orientated randomly throughout, the medium is treated as statistically homogeneous and isotropic. Boundary reflections are assumed to be negligible. No skeletal mineral frame is included in the analysis, that is to say, the elastic rigidity modulus of the medium is taken to be zero. (The elasticity of the mineral grains themselves is not neglected.) In effect, the granular medium is treated as a fluid in which the stress-strain relationships are governed by shearing at the embedded grain contacts. It is implicit in these assumptions that only intrinsic attenuation is addressed in the model. Phenomena such as high-frequency scattering from individual grains are excluded from the analysis.

By treating the medium as a homogeneous continuum, it is implicit that relative motion between the viscous pore fluid and the mineral grains is neglected in the model. This is the "closed system" of Gassmann⁴⁷ in which the pore fluid does not circulate between grains under the influence of the very low stress from a propagating wave. The absence of viscous flow through the pore spaces has several consequences, the most obvious being that the model does not lead to a slow wave of the type that emerges from the Biot theory. Another is that the predicted wave properties are independent of the permeability, the tortuosity, and the structure factor, which in the Biot–Stoll treatment characterize the fluid flow between the grains. In the grain-shearing theory, the material parameter which governs the wave properties is the porosity, which is commonly reported along with the wave properties of unconsolidated granular materials.

Central to the theoretical development is the shearing that occurs at grain contacts during the passage of a wave. On a microscopic level, the contacts themselves are taken to be at discrete high points, that is, at micro-asperities on the nominally smooth surface of the grains. Each such micro-contact is assumed to be lubricated by a very thin layer of pore fluid. When sliding occurs at one of these points of contact, the drag opposing the motion is not due to dry friction, but to the effective viscosity of the thin lubricating fluid film, which may be considerably higher than the viscosity of the bulk fluid.

The model is statistical in the sense that many micro-asperities contribute randomly in time to the shearing. An ensemble average over all the shearing events provides the basis for determining the relationship between stress and strain in the medium. This relationship turns out to be a convolution integral, one term of which is a material impulse response function, or MIRF. In fact, two MIRFs appear in the analysis, corresponding to the two types of shearing that can occur between grains. In effect, a MIRF is the stress relaxation that occurs in the material in response to a step-function strain or, equivalently, an impulse of strain rate.

The stress-strain convolutions appear in the Navier–Stokes equation of motion, which splits into two equations, one for compressional and the other for transverse disturbances. Both are genuine wave equations, implying that grain shearing introduces rigidity into the medium, and the rigidity supports a shear wave. Dissipation is also associated with grain shearing, which gives rise to an attenuation in

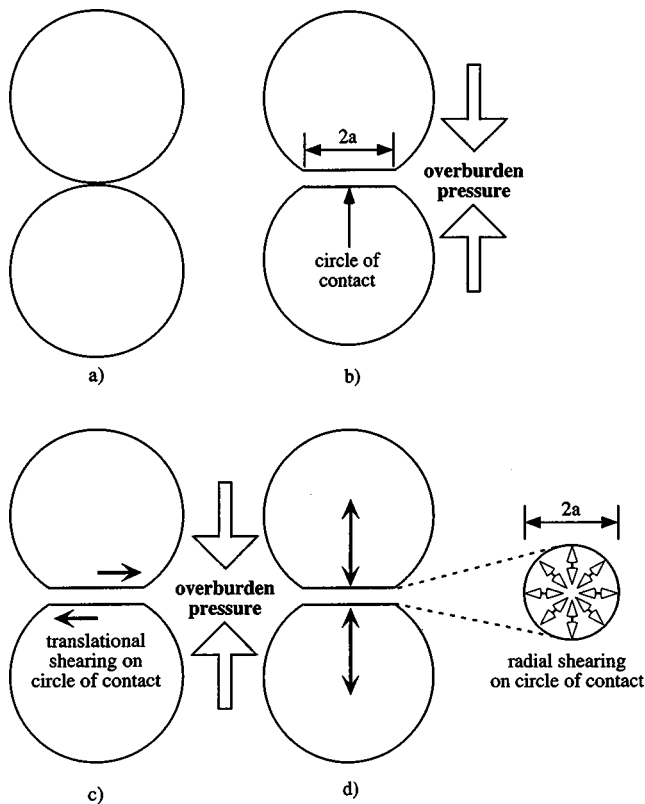


FIG. 3. Cross section through the centers of two contiguous, spherical, mineral grains. (a) Touching lightly, with no elastic deformation at the point of contact. (b) Pressed together by static overburden pressure, elastic deformation occurs, creating a small circle of contact. (c) Translational shearing due to dynamic tangential strain (horizontal black arrows) and (d) compressive shearing along radials of the circle of contact (small open arrows) due to dynamic normal strain (vertical black arrows).

both waves that scales essentially as the first power of frequency.

V. GRAIN-BOUNDARY SHEARING

Since shearing between grains is central to the model, it is important to consider how such shearing may occur. Figure 3(a) is a schematic of two identical elastic spheres in light contact. The spheres are an idealization of contiguous mineral (often quartz) grains in a sediment. When a static force, F , is applied normal to the tangent plane of contact, the grains are pressed together, local elastic deformation occurs, and a small circle of contact is formed [Fig. 3(b)]. In a sediment, the force F may be identified with the overburden pressure.

During the passage of a wave, a small, dynamic, elastic deformation takes place in the vicinity of the contact in addition to the static deformation illustrated in Fig. 3(b). The result of the dynamic deformation is relative motion (shearing) between the two grains. The shearing relieves the stress produced by the wave and tends to restore equilibrium between the grains. Two types of shearing may occur: translational shearing and radial shearing, illustrated in Figs. 3(c) and (d), respectively.

Under translation, the grain centers are displaced relative to each other in a direction parallel to the tangent plane of contact. In response to this shear strain, tangential shear

stress relaxation occurs as micro-asperities slide against one another on the surfaces of the circles of contact. Radial shearing occurs under compressive or tensile strain, that is, when the grain centers are displaced in a direction normal to the tangent plane of contact. Such normal strains produce compressional (tensile) stress relaxation as micro-asperities on the radials of the circle of contact slide against one another. It is to be emphasized that, for typical stress waves in a sediment, the translational and radial displacements are extremely small, corresponding to strains of 10^{-6} or less.

In passing, it should be mentioned that if the two spheres in Fig. 3 were smooth and of the same size, then the shearing along the radials of the circle of contact due to compression (tension) would be zero: the two spheres would deform identically, and no radial sliding would occur. In practice, sliding will be present even when the spheres are of the same size because sand grains are not perfectly smooth but are covered with randomly distributed, microscopic asperities. Note also that radial shearing will occur under not only positive (compressional) but also negative (tensile) dynamic strains. These positive and negative strains produce very small excursions about the equilibrium state maintained by the overburden pressure. Radial shearing occurs under dynamic tension because of the slight relaxation of the deformations on either side of the contact, and under dynamic compression because of the slight enhancement of those same deformations.

The presence of micro-asperities means that the contact between the two spheres is not perfect. Based on recent advances in tribology,⁴⁸ it is expected that many discrete points of contact will exist, distributed randomly over the rough surfaces of the circle of contact. A similar situation has been described by Bengisu and Akay⁴⁹ in their analysis of friction at microscopically rough surfaces. When grain-to-grain shearing occurs in response to a dynamic strain, stress relaxation occurs at the microscopic points of contact. The shearing events are triggered randomly in time with a probability that depends on the normal gradient of the strain across the micro-contact. The resultant random sequence of discrete, stress-relaxation pulses constitutes the mechanism by which equilibrium between two grains is restored.

According to this picture, in the presence of a wave, as the stress relaxation proceeds, the micro-geometry of the surfaces of contact changes irreversibly. After a microscopic sliding event, the disposition of the two asperities involved is slightly different from beforehand. These minute changes on the circle of contact are cumulative, and are thus expected to produce a slowly evolving grain-packing structure as wave propagation through the medium continues. Such behavior appears to be consistent with the stochastic properties of waves in dry granular media observed by Nagel and colleagues. It seems evident that the slow evolution of the packing structure from micro-slip events could be responsible for a changing pattern of force chains within the granular material. The expected result would be fluctuations in the amplitude of signal arrivals, much like those observed over a period of several hours by Liu and Nagel⁴ and illustrated in their Fig. 1(a).

VI. RANDOM STICK-SLIP STRESS RELAXATION

To model the stress relaxation that occurs as two grains slide against each other, the process is represented as a random succession of pulses. Each pulse is the deterministic stress arising from the slippage of one microscopic asperity past another on the circle of contact. The sliding is triggered by the normal velocity gradient across the contact due to the wave disturbance itself. Once triggered, the pulse amplitudes are taken to be independent of the velocity gradient. Since the micro-pulses of stress are the fundamental constituents of both translational [Fig. 3(c)] and radial [Fig. 3(d)] shearing, an identical argument applies to the two cases.

The stress relaxation associated with a particular micro-shearing event occurring at time $t=0$ is represented by the pulse shape function, $h(t)$, where, to satisfy causality, $h(t)=0$ for $t<0$. Letting t_k be the time at which the k th event of amplitude a_k occurs, the total stress from the random succession of events may be written as

$$\sigma(t) = \sum_{k=1}^{\infty} a_k h(t-t_k), \quad (1)$$

where the onset times, t_k , and the time-independent amplitudes, a_k , are random variables, all of which are taken to be independent of one another. The summation on the right of Eq. (1) is known as a random pulse train.⁵⁰

Within an elementary volume of the granular medium, which is large compared with the grain size but small relative to a wavelength, many grain contacts are expected to exist, and thus the quantity of interest in connection with the macroscopic wave properties is the average stress over a large number of contacts. The mean stress is derived below as an ensemble average of the random pulse train in Eq. (1), following a generalized version of the argument that holds for the more familiar Poisson process.⁵¹

Consider shearing at a single grain boundary. During an observation interval $[0, T]$, the probability of a particular micro-sliding event occurring between times t and $t+dt$ is

$$\nu dt = \bar{K} q(t) dt, \quad (2)$$

where \bar{K} is the average number of events in time interval T , and $q(t)$ is a function of time that satisfies the condition

$$\int_0^T q(t) dt = 1, \quad (3)$$

because the event must occur sometime during the interval $[0, T]$. Note that the probability in Eq. (2) is independent of what occurred before time t and what will happen after time $t+dt$. A Poisson process would have $q(t)=1/T$, a constant, and ν would be the mean rate of events, that is, \bar{K}/T . The random stick-slip that occurs at a grain boundary is not, however, Poisson distributed, but is triggered by the velocity gradient across the boundary at any instant, t . Thus the probability density function, $q(t)$, is governed by the instantaneous magnitude of the wave field in the medium: the greater the velocity gradient, the more likely that a slip will be triggered.

To perform the required averaging of Eq. (1), consider the random pulse trains associated with a very large number, M , of observation intervals, each of duration T . If $p(K)$ is the probability of an interval in the ensemble containing *exactly* K events, then the number of such intervals is $Mp(K)$. Thus at a fixed time t into each interval, as $M \rightarrow \infty$, the average value of the stress, $\sigma_K(t)$, in the intervals containing *exactly* K events is

$$\begin{aligned} \overline{\sigma_K(t)} &= \overline{a_K} \int_0^T q(t_1) dt_1 \cdots \int_0^T q(t_K) dt_K \sum_{k=1}^K h(t-t_k) \\ &= \overline{a_K} \sum_{k=1}^K \int_0^T q(t_k) h(t-t_k) dt_k \\ &= \overline{a_K} K \int_0^T q(t_k) h(t-t_k) dt_k, \end{aligned} \quad (4)$$

where the overbar denotes an ensemble average, and $\overline{a_K}$ is the mean value of the pulse amplitudes a_k in the intervals containing exactly K events. Note that the stress-relaxation amplitudes, a_k , will all have the same sign and hence $\overline{a_K} \neq 0$. The final expression in Eq. (4) holds because the integral is independent of the index k and hence may be taken outside the summation.

Now, the average value of the stress relaxation in *all* the intervals $[0, T]$ is

$$\overline{\sigma(t)} = \sum_{K=1}^{\infty} p(K) \overline{\sigma_K(t)} = \bar{a} \int_0^T q(t_k) h(t-t_k) dt_k \sum_{K=1}^{\infty} K p(K). \quad (5)$$

The summation in the last expression is simply the mean number of events in the interval $[0, T]$,

$$\bar{K} = \sum_{K=1}^{\infty} K p(K), \quad (6)$$

an expression which holds for any probability distribution $p(K)$, and hence

$$\overline{\sigma(t)} = \bar{a} \bar{K} \int_0^T q(t_k) h(t-t_k) dt_k, \quad (7)$$

where $\bar{a} \neq 0$ is the mean value of the pulse amplitudes in all the intervals $[0, T]$. Equation (7) is an ensemble average for the mean stress relaxation that occurs when one grain slides against another. Notice that the onset time, t_k , of the k th event in the random pulse train is the integration variable in Eq. (7), that is to say, the distribution of the onset times has no effect on the value of the average.

In view of the fact that the probability $q(t_k)=0$ for $t_k < 0$ and $h(t)=0$ for $t < 0$, the limits on the integral in Eq. (7) may be extended from $-\infty$ to $+\infty$ without changing its value,

$$\overline{\sigma(t)} = \bar{a} \bar{K} \int_{-\infty}^{\infty} q(t_k) h(t-t_k) dt_k. \quad (8)$$

The integral on the right of Eq. (8) will be recognized as a convolution integral, allowing the average stress to be expressed in the form

$$\overline{\sigma(t)} = \bar{a} \bar{K} q(t) \otimes h(t), \quad (9)$$

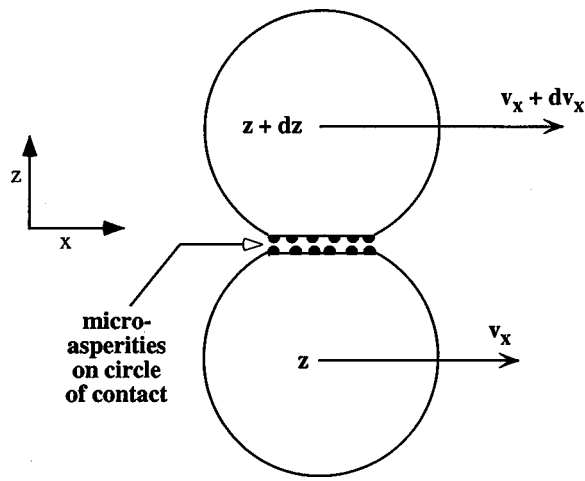


FIG. 4. Shearing of contiguous grains due to the velocity gradient normal to the plane of contact. The micro-asperities (small solid hemispheres) on the circle of contact are not to scale.

where the symbol \otimes denotes a temporal convolution. Equation (9) is a generally valid result for any random pulse train for which the probability density function is $q(t)$ and the pulse shape function is $h(t)$. To proceed, it is necessary to determine the functional forms for $q(t)$ and $h(t)$ that are appropriate to grain-to-grain shearing in an unconsolidated granular medium.

VII. THE PROBABILITY DENSITY FUNCTION, $q(t)$

It is clear that the difference in velocity of the two grains on either side of the circle of contact must trigger the stick-slip process. When boundary shearing occurs, the grain centers move relative to each other in a direction which may be resolved into components parallel to (translational shearing) and normal to (radial shearing) the tangent plane of contact. Similar arguments apply to the two cases, but to be specific we shall discuss the probability function $q(t)$ in the context of translational shearing.

To establish the form of $q(t)$, consider for the moment just two-dimensional motion in the $x-z$ plane, with the plane of the contact parallel to the x -direction, as sketched in Fig. 4. The density function, $q(t)$, is the probability that a single micro-shearing event will contribute to the stress relaxation between times t and $t+dt$. Since each event is triggered by the magnitude of the velocity difference across the plane of contact, the probability that a given event occurs between times t and $t+dt$ is

$$q(t) = \frac{b}{T} \left| \frac{dv_x(t)}{dz} \right|, \quad (10)$$

where b is a (positive) constant of proportionality, and the derivative on the right is the velocity gradient normal to the grain boundary at time t . To account for planes of contact that are not parallel to the x -direction, b may be replaced by its average value, \bar{b} , taken over the random orientation of the slip planes,

$$q(t) = \frac{\bar{b}}{T} \left| \frac{dv_x(t)}{dz} \right|. \quad (11)$$

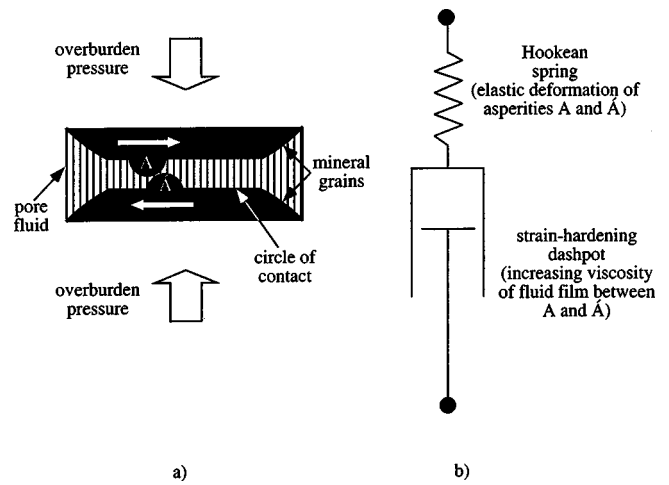


FIG. 5. (a) Asperities A and A' shearing against each other (not to scale) on the circle of contact. A thin film of pore fluid is shown between A and A' . (b) Equivalent Maxwell element consisting of a Hookean spring and nonlinear, strain-hardening dashpot in series.

By writing the velocity as $v_x = dx/dt$, it becomes evident that the derivative in Eqs. (10) and (11) is identical with the rate of strain across the contact. Thus the probability of an event occurring between t and $t+dt$ is proportional to the rate of strain rather than the strain itself, which is physically reasonable since a static strain represents a steady-state condition in which no shearing could occur.

When the expression in Eq. (11) is substituted into Eq. (9), the average stress becomes

$$\overline{\sigma_{xz}(t)} = \nu \bar{a} \bar{b} \left| \frac{dv_x(t)}{dz} \right| \otimes h(t), \quad (12)$$

where $\nu = \bar{K}/T$ is the mean rate of sliding events and the subscripts xz on the left denote in the usual way the shear stress in the $x-z$ plane. An analogous expression holds for radial shearing, in which case the subscript x is replaced by z .

VIII. STRAIN HARDENING AND THE PULSE SHAPE FUNCTION, $h(t)$

The pulse shape function, $h(t)$, is a deterministic, material impulse response function (MIRF). It represents the time dependence of the stress relaxation that occurs as one micro-asperity slides against another in response to an impulse of strain rate.

Two forces are at work when individual asperities on opposite faces of the circle of contact slide against each other: a conservative elastic force of deformation, and a drag force resisting the motion [Fig. 5(a)]. The elastic force may be represented by a simple Hookean spring. Opposing the motion, the drag force is due to friction from the viscosity of the thin film of pore fluid trapped between the asperities. Viscous drag scales with the speed of sliding, and hence may be represented by a dashpot. Since they support the same stress, the spring and the dashpot should be connected in series [Fig. 5(c)] to represent the micro-shearing, a combination which is sometimes known as a Maxwell element.⁹ Usually, a Maxwell element is employed to represent the elastic or plastic behavior of a macroscopic sample of the material

of interest but, in the present instance, it serves as an equivalent mechanical model of the micro-sliding between individual asperities on the circle of contact.

In its simplest form, the coefficients of the spring and dashpot in the Maxwell element are constants, in which case the MIRF, $h(t)$, would decay exponentially in time. Such behavior, however, is not characteristic of the stress relaxation that occurs in granular media. The physical processes underlying the grain-to-grain interactions in granular materials are still not well understood, although the subject has received considerable attention,^{52–56} as summarized in a review article by Deresiewicz.⁵⁷ Much of this prior work addresses the contact mechanics of elastic spheres arranged in regular arrays. A different approach is taken here, where it is postulated that “strain hardening,” originating in the thin fluid film separating two sliding asperities, may be the mechanism that governs the properties of waves in unconsolidated granular media.

Strain hardening is an increase in the resistance to motion as intergranular shearing proceeds. Thus after it is triggered, the shearing becomes progressively more difficult to sustain, behavior which is represented by a time-dependent coefficient for the dashpot in the Maxwell element in Fig. 5(b). It is well-known that a Maxwell element in which the dashpot hardens with time can exhibit behavior that is representative of stress relaxation in plastic materials, as discussed in a number of contexts by Gittus.⁹ However, since a granular material is not plastic, at least, not in the usual sense, the details of the strain hardening mechanism will differ in the two cases.

The thinness of the pore fluid sandwiched between the asperities depicted in Fig. 5(a) could be responsible for strain hardening in the granular medium. It is known that the properties of aqueous solutions confined in a very thin layer (several molecular diameters thick) between solid surfaces are significantly different from those of the bulk material.⁸ In particular, the effective viscosity of a thin fluid film can be much higher than the viscosity of the bulk fluid, and the effective viscosity increases as the film is squeezed harder.^{48,58} This may be what happens as the asperities A, \bar{A} in Fig. 5(a) slide against each other.

Before sliding begins, the two asperities are effectively pinned (the “stick” part of “stick-slip”). On being triggered into slipping, the contact between the two asperities will always become tighter, because of the overburden pressure, and the effective viscosity of the lubricating fluid film will increase, giving rise to the condition of strain hardening. In terms of the Maxwell element in Fig. 5(b), the strain hardening is represented by allowing the coefficient of the dashpot, $\xi(t)$, to be an increasing function of time. Since the stress in such a dashpot is neither in phase nor in quadrature with the strain, the element is not purely dissipative, as it would be if the coefficient were constant. In fact, the strain-hardening dashpot is nonlinear, with cross-coupling between different Fourier components in the stress-strain relationship, and hence the Maxwell element in Fig. 5(b) does not obey the principle of superposition.

The coefficient of the spring in the Maxwell element is taken to be a constant, E , representing the compressibility of

the asperities A, \bar{A} and the fluid film between them. It should be noted that, although the compressibility of the bulk pore fluid is considerably greater than that of the mineral grains, the situation may be reversed for the molecularly thin film of pore fluid between asperities. As discussed by Granick,⁸ such thin fluid films are highly incompressible. Thus as indicated in Fig. 5(b), the predominant factor governing the spring constant E may actually be the elasticity of the mineral asperities rather than the compressibility of the pore fluid separating them.

Be that as it may, the solution for the stress in the Maxwell element in response to a step-function strain, ε , applied at $t=0$ will provide an expression for the MIRF $h(t)$. The applied strain, ε , is governed by material properties alone, that is to say, it is taken to be independent of the wave amplitude.

Since they are in series, the stresses in the spring and the dashpot are the same. Taking the stress at time t to be $\chi = \chi(t)$, then in the spring

$$\chi = E\varepsilon_s, \quad (13)$$

which is simply Hooke’s law, and in the strain-hardening dashpot

$$\chi = \xi(t) \frac{d\varepsilon_d}{dt}. \quad (14)$$

In these expressions, ε_s and ε_d , respectively, are the time-dependent strains in the spring and the dashpot. After $t=0$ the total strain, ε , in the Maxwell element is just the sum of the strains in the two components,

$$u(t)\varepsilon = \varepsilon_s + \varepsilon_d, \quad (15)$$

where $u(t)$ is the unit step function. On combining Eqs. (13) to (15), the following nonlinear differential equation for the stress, χ , is obtained:

$$\frac{1}{E} \frac{d\chi}{dt} + \frac{1}{\xi(t)} \chi = \varepsilon \delta(t), \quad (16)$$

where $\delta(t)$ is the Dirac delta function.

To solve Eq. (16) for the stress, the time-dependence of $\xi(t)$, the coefficient of the dashpot, must be specified. The Taylor expansion of this coefficient about time $t=0$ when sliding begins is

$$\xi(t) = \xi_0 + \left. \frac{d\xi}{dt} \right|_{t=0} t + \left. \frac{d^2\xi}{dt^2} \right|_{t=0} \frac{t^2}{2!} + \dots \approx \xi_0 + \theta t, \quad (17)$$

where the zero-order term, ξ_0 , represents the viscosity of the fluid film before the onset of sliding, and $\theta \geq 0$ is the strain-hardening coefficient or, equivalently, the rate coefficient of the drag. The linear approximation for $\xi(t)$ in Eq. (17) would seem to be justified, given the very short time scales and extremely small strains associated with linear wave propagation in granular media. Later, it will be shown that the theoretical results derived on the basis of the approximation in Eq. (17) agree with the available experimental data.

By employing the linear form in Eq. (17), the solution of Eq. (16) is obtained, after rearranging terms, by straightforward integration,

$$\chi = \chi_0 \left(1 + \frac{\theta}{\xi_0} t \right)^{-E/\theta} \text{sgn}[\varepsilon \delta(t)], \quad (18)$$

where

$$\chi_0 = |\varepsilon| E \quad (19)$$

is the initial value of the stress, $\delta(t)$ is the Dirac delta function, and the signum function represents the arithmetic sign of the driving rate of strain. Equation (18) states that at $t = 0+$ all the strain appears across the spring, as expected because the dashpot cannot respond instantaneously to the input. Note that the limiting behavior of the solution in Eq. (18) is correct: as $\theta \rightarrow 0$ (i.e., as the effect of strain-hardening is eliminated), χ reduces identically to an exponential decay in time. When, in addition, the elasticity is removed by allowing $E \rightarrow \infty$, χ becomes the delta function, $\delta(t)$, which is simply the impulse response of a dashpot with a constant coefficient. The latter is, of course, representative of a purely viscous medium.

The pulse shape function, $h(t)$, is identified as the time-dependent part of the solution in Eq. (18),

$$h(t) = \frac{\theta}{\xi_0} \left(1 + \frac{\theta}{\xi_0} t \right)^{-E/\theta}, \quad (20)$$

where the leading factor on the right has been included only to give $h(t)$ the dimensions of reciprocal time [the same as the delta function, $\delta(t)$]. The mean pulse amplitude is

$$\bar{a} = \chi_0 \frac{\xi_0}{\theta}, \quad (21)$$

and hence the time-dependence of the ensemble-averaged stress relaxation in Eq. (12) is

$$\begin{aligned} \overline{\sigma_{xz}(t)} &= \chi_0 \nu \bar{b} \left| \frac{dv_x(t)}{dz} \right| \otimes \left(1 + \frac{\theta}{\xi_0} t \right)^{-E/\theta} \text{sgn} \left(\frac{dv_x(t)}{dz} \right) \\ &= \chi_0 \nu \bar{b} \frac{\xi_0}{\theta} \frac{dv_x(t)}{dz} \otimes \frac{\theta}{\xi_0} \left(1 + \frac{\theta}{\xi_0} t \right)^{-E/\theta}, \end{aligned} \quad (22)$$

where the leading coefficients on the right (i.e., $\chi_0 \nu \bar{b} \xi_0 / \theta$) are independent of the velocity gradient across the contact. Note that the signum function in Eq. (22) has the same arithmetic sign as that in Eq. (18).

Since the functional form on the right of Eq. (22) represents the average stress relaxation from individual micro-asperities sliding against one another, it holds for both translational and radial shearing. As can be seen from Eq. (22), an important property of the average stress is that it satisfies the principle of superposition, and hence is strictly linear, even though the strain-hardening Maxwell element representing an individual component of the random succession of stress pulses is nonlinear.

IX. TRANSLATIONAL (SHEAR) AND RADIAL (COMPRESSIONAL) GRAIN SHEARING

The internal stress relaxation arising from both translational and radial shearing is given by Eq. (22), with appropriate values for the various coefficients in the two cases. In particular, the grain-size dependence, which appears through

the presence of the mean rate of events, ν , is different for the two types of shearing, as discussed in the Appendix. Incidentally, the translational and radial shearing processes may be thought of as being analogous to shear and bulk viscosity,⁵⁹ respectively, in a viscous fluid.

For convenience in discussing the coefficients in Eq. (22), the expressions for the stress associated with radial (compressional) and translational (shear) sliding are now written separately, as follows:

$$\sigma_{zz}(t) = \lambda_p h_p(t) \otimes \frac{dv_z(t)}{dz} \quad (23)$$

and

$$\sigma_{xz}(t) = \eta_s h_s(t) \otimes \frac{dv_x(t)}{dz}, \quad (24)$$

where the subscripts p and s identify the associated quantity with radial and translational shearing, respectively. The overbars denoting ensemble averaging have now been omitted for brevity. The $h_{p,s}(t)$ functions in Eqs. (23) and (24) are the material impulse response functions (MIRFs) for radial and translational shearing,

$$h_p(t) = t_p^{-1} \left(1 + \frac{t}{t_p} \right)^{-n}, \quad (25)$$

and

$$h_s(t) = t_s^{-1} \left(1 + \frac{t}{t_s} \right)^{-m}, \quad (26)$$

where, from inspection of Eq. (20), the stress-relaxation time constants are

$$t_p = \frac{\xi_{op}}{\theta_p}, \quad t_s = \frac{\xi_{os}}{\theta_s}, \quad (27)$$

and the material exponents are

$$n = \frac{E_p}{\theta_p}, \quad m = \frac{E_s}{\theta_s}. \quad (28)$$

Several of the scaling constants in the analysis conveniently collapse into just two coefficients, the radial and translational stress-relaxation coefficients, λ_p and η_s , in Eqs. (23) and (24). From comparison with Eq. (22),

$$\lambda_p = \chi_{op} \nu_p \bar{b}_p t_p \quad (29)$$

and

$$\eta_s = \chi_{os} \nu_s \bar{b}_s t_s. \quad (30)$$

The temporal convolutions for the radial and translational stresses in Eqs. (23) and (24), respectively, are identical to those introduced inductively in I and II. It is also apparent that the MIRFs in Eqs. (25) and (26) reduce to the inverse-time power laws used in I and II for times that are greater than the stress-relaxation time constants t_p, t_s . Since these time constants scale with the residual viscosity of the fluid in the film, ξ_0 [see Eq. (27)], which in granular materials appears to be negligible, it follows that for all time scales of interest the inverse-time power-law form for the MIRFs is an excellent approximation.

The time constants t_p, t_s and the exponents n, m defined in Eqs. (27) and (28) characterize a single, deterministic event, the sliding of one micro-asperity over another. Such events are the building blocks of both translational and radial stress relaxation. These constitutive events are physically indistinguishable in the two types of grain shearing, and therefore the following equalities are expected to hold:

$$t_p = t_s, \quad (31a)$$

$$m = n, \quad (31b)$$

and hence

$$h_p(t) \equiv h_s(t). \quad (32)$$

These equalities imply that the compressional and shear wave properties, that is, the two wave speeds and the two attenuations, are all causally connected. This linking imposes a strong constraint on the predicted wave properties, which will provide a demanding test of the grain-shearing theory.

Limited experimental evidence in support of the predicted equality between n and m has been presented in II. Further evidence indicating that $n = m$ is presented below in Figs. 6 and 7. However, in the interest of being explicit, the distinctions between t_p, t_s , between n, m , and between $h_p(t), h_s(t)$ are maintained throughout the remainder of the analysis. The identities in Eqs. (31) and (32) should be borne in mind, however, because they will be used later in evaluating the theoretical expressions for the wave speeds and attenuations.

It will turn out that the compressional and shear attenuations, respectively, scale in direct proportion to the material exponents n and m . According to Eqs. (28), these (dimensionless) exponents provide a relative measure of the conservative and dissipative forces in the microscopic sliding process represented by the nonlinear Maxwell element: n (or m) is the elastic modulus of the spring divided by the strain-hardening coefficient of the dashpot. As strain-hardening decreases ($n, m \rightarrow \infty$), grain sliding is facilitated and attenuation rises, and as strain-hardening increases ($n, m \rightarrow 0$) grains tend to lock together, little or no sliding can occur, and attenuation approaches zero. By comparison, the compressional and shear wave speeds are only weakly dependent on n and m , and hence are relatively insensitive to strain-hardening in the granular medium.

X. GENERALIZED NAVIER-STOKES EQUATION

To establish the equation of motion, the granular medium is treated, macroscopically, as a homogeneous, fluid continuum, which, like a viscous fluid, is capable of supporting a shear “flow.” The continuum representation is valid for the wavelengths of interest, which are considerably longer than the size scale of the grain structure and the pore spaces in the material. The microscopic, randomly orientated grain boundaries may be thought of as being embedded in the continuum in such a way as to support the compressive and shear stresses described by Eqs. (23) and (24), respectively.

The assumption of homogeneity is obviously not consistent with Liu *et al.*'s⁵ observations of force chains and the

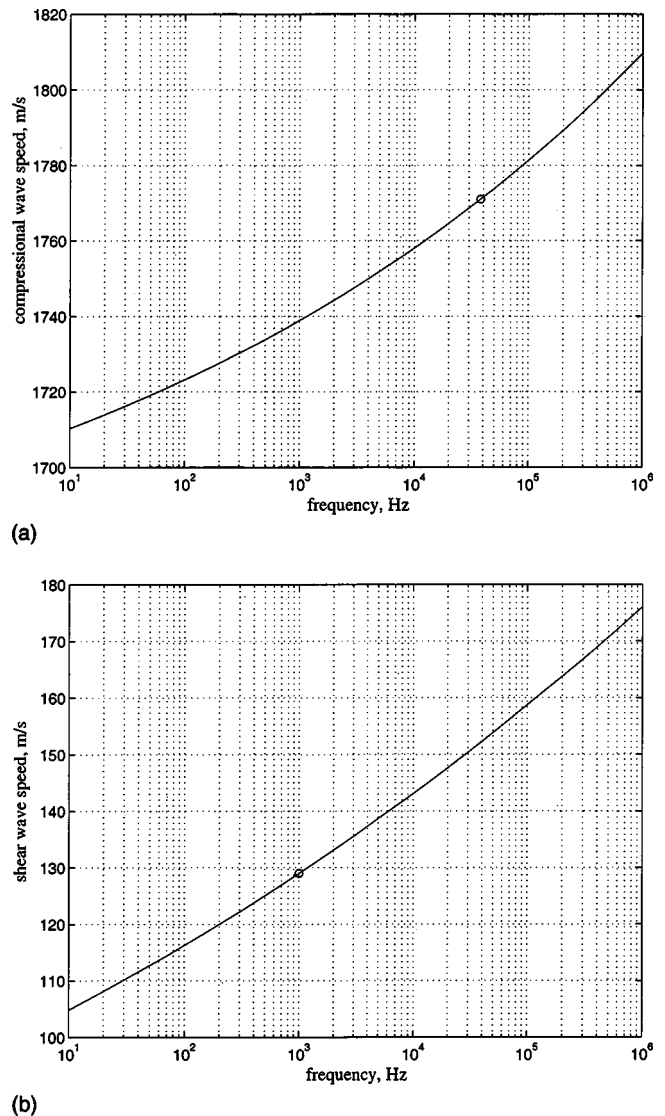


FIG. 6. Theoretical dispersion in the wave speeds for the SAX99 sediment. (a) The compressional wave and (b) the shear wave. The data points (○) used in determining the unknown coefficients fall on the theoretical curves.

associated fluctuations in wave propagation, which are effects of inhomogeneity in the medium. By treating the material as (macroscopically) homogeneous, smoothed wave properties will be obtained, for instance, the average attenuation as a function of frequency. Once the average behavior has been established, the assumption of homogeneity could be relaxed in order to investigate interference between waves propagating along different force-chain pathways. This, however, is beyond the scope of the present article.

To set up the equation of motion, the full stress tensor, σ , for the granular medium must be derived. The terms in this tensor relate stress to rate of strain at a point (x, y, z) in the three-dimensional medium. The argument is analogous to that for a homogeneous, isotropic, viscous fluid, as discussed by Morse and Ingard,⁵⁹ except that the stress, instead of being proportional to the velocity gradient, is in the form of the convolutions in Eqs. (23) and (24).

The tensor for the shear flow may be written as

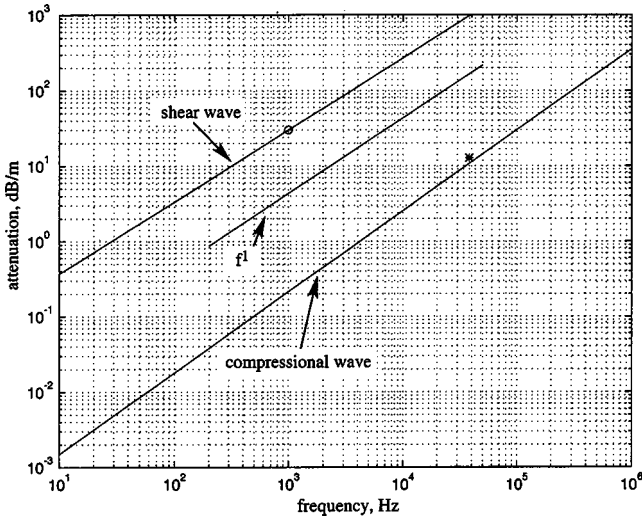


FIG. 7. Theoretical attenuation as a function of frequency for the SAX99 sediment. The shear wave data point (\circ), used in determining the unknown coefficients, falls on the theoretical curve. The compressional wave data point ($*$) lies about 2 dB/m above the theoretically predicted curve. The line labeled f^1 illustrates the slope of any attenuation that scales as the first power of frequency.

$$\mathbf{V} = \begin{pmatrix} V_{xx} & V_{xy} & V_{xz} \\ V_{yx} & V_{yy} & V_{yz} \\ V_{zx} & V_{zy} & V_{zz} \end{pmatrix}, \quad (33)$$

where the diagonal components are

$$V_{ii} = \frac{\partial v_i}{\partial x_i} - \frac{1}{3} \operatorname{div} \mathbf{v}, \quad (34)$$

and the off-diagonal components ($i \neq j$) are

$$V_{ij} = \frac{1}{2} \frac{\partial v_i}{\partial x_j} + \frac{1}{2} \frac{\partial v_j}{\partial x_i} = V_{ji}. \quad (35)$$

Equations (34) and (35) represent pure shear strains with no change in fluid content. Thus the tensor \mathbf{V} in Eq. (33) is a measure of the rate at which one part of the medium slides past another at the point (x, y, z) , excluding the effects of rotation and outflow of material from the unit volume around (x, y, z) . The outflow has been removed by subtracting equal parts of the divergence of the velocity,

$$\operatorname{div} \mathbf{v} = \frac{\partial v_x}{\partial x} + \frac{\partial v_y}{\partial y} + \frac{\partial v_z}{\partial z}, \quad (36)$$

from the diagonal components of the tensor [Eq. (34)].

The stress tensor must include several components in addition to the term $-2\eta_s h_s(t) \otimes \mathbf{V}$ representing the translational shear between grains. [The factor of 2 is included here to maintain consistency with the simple case in Eq. (24).] Clearly, the hydrostatic pressure, including the acoustic pressure, p , must be added into the diagonal elements of $\boldsymbol{\sigma}$. A further term must also be included in the diagonal elements to account for the compressive stress associated with shearing along radials of the circle of contact. From Eq. (23), the appropriate term to be included is $-\lambda_p \operatorname{div} h_p(t) \otimes \mathbf{v}$, representing the stress relaxation arising from the rate of change of compression.

When the acoustic pressure, p , the radial compressive stress, and the translational shear stress are included, the stress tensor can be written as

$$\boldsymbol{\sigma} = \left\{ p - \lambda_p \operatorname{div} [h_p(t) \otimes \mathbf{v}] + \frac{2}{3} \eta_s \operatorname{div} [h_s(t) \otimes \mathbf{v}] \right\} \delta_{ij} - \eta_s \left[h_s(t) \otimes \left\{ \frac{\partial v_i}{\partial x_j} + \frac{\partial v_j}{\partial x_i} \right\} \right], \quad (37)$$

where δ_{ij} is the Kronecker delta. The hydrostatic pressure has been neglected in Eq. (37) since it plays no part in the wave equations. If $h_p(t)$ and $h_s(t)$ were set equal to $\delta(t)$, then Eq. (37) would reduce identically to the stress tensor for a viscous fluid. This should be obvious, since the convolution of a delta function with any continuous function is the function itself. However, with the MIRFs taking the forms in Eqs. (25) and (26), the properties of the stress tensor in Eq. (37) are significantly different from those of the stress tensor for a viscous fluid.

If external forces such as gravity are neglected, the equations of motion may be written as

$$(\rho_0 + \Delta) \frac{d\mathbf{v}}{dt} = (\rho_0 + \Delta) \left[\frac{\partial \mathbf{v}}{\partial t} + (\mathbf{v} \cdot \operatorname{grad}) \mathbf{v} \right] = -\nabla \cdot \boldsymbol{\sigma}, \quad (38)$$

where ρ_0 is the bulk density of the material and Δ is the density fluctuation associated with the presence of a propagating wave. On linearizing this expression, the first-order, Navier–Stokes equation is obtained,

$$\begin{aligned} \rho_0 \frac{\partial \mathbf{v}}{\partial t} = & -\nabla \cdot \boldsymbol{\sigma} = -\operatorname{grad} p + \lambda_p \operatorname{grad} \operatorname{div} [h_p(t) \otimes \mathbf{v}] \\ & + \frac{4}{3} \eta_s \operatorname{grad} \operatorname{div} [h_s(t) \otimes \mathbf{v}] \\ & - \eta_s \operatorname{curl} \operatorname{curl} [h_s(t) \otimes \mathbf{v}], \end{aligned} \quad (39)$$

where the following relationships have been used:

$$(\nabla \mathbf{v})_{ij} = \frac{\partial v_j}{\partial x_i}, \quad (40)$$

$$(\mathbf{v} \nabla)_{ij} = \frac{\partial v_i}{\partial x_j}, \quad (41)$$

$$[\nabla \cdot (\mathbf{v} \nabla)]_j = [\operatorname{grad}(\operatorname{div} \mathbf{v})]_j, \quad (42)$$

and

$$[\nabla \cdot (\nabla \mathbf{v})]_j = [\operatorname{grad}(\operatorname{div} \mathbf{v})]_j - [\operatorname{curl} \operatorname{curl} \mathbf{v}]_j. \quad (43)$$

Equation (39) is the equation of motion appropriate to an unconsolidated granular medium in which radial (compressional) and translational (shear) stress relaxation is as given by Eqs. (23) and (24).

XI. WAVE EQUATIONS

The wave speeds and the associated attenuations are determined from the compressional and shear wave equations, which are developed below from the Navier–Stokes equation [Eq. (39)]. In addition, the equation of state is required, which for the granular medium is, to first order,

$$p = c_0^2 \Delta, \quad (44)$$

where

$$c_0 = \sqrt{\frac{\kappa_0}{\rho_0}}. \quad (45)$$

Physically, c_0 is the compressional wave speed that would be observed in the absence of grain-to-grain stress relaxation, that is, if the granular medium were a suspension with no contact forces. Such a medium will be referred to as the ‘‘equivalent suspension.’’ The bulk modulus, κ_0 , of the equivalent suspension is essentially defined through Eq. (45). Notice that in the limit of low frequency, because the rate of strain is zero, the three convolutions in Eq. (39) vanish and hence the wave properties of the granular medium are expected to be the same as those in the equivalent suspension.

The value of the wave speed, c_0 , is not accessible through direct measurement. It can, however, be evaluated from Wood’s equation,⁶⁰ that is, Eq. (45) with the bulk modulus, κ_0 , and the bulk density, ρ_0 , given by the weighed means

$$\frac{1}{\kappa_0} = N \frac{1}{\kappa_w} + (1-N) \frac{1}{\kappa_g} \quad (46)$$

and

$$\rho_0 = N\rho_w + (1+N)\rho_g. \quad (47)$$

In these expressions, N is the porosity of the granular medium, κ_w , κ_g are, respectively, the bulk moduli of seawater and of the mineral grains, and ρ_w , ρ_g are the corresponding densities. Since values for all these parameters are usually available, c_0 may be considered as known.

As an aside, N is governed by the packing arrangement of the grains. In a typical marine sediment, the sand grains form a random close-packing structure, which, by definition, is the tightest random packing arrangement possible. In a homogeneous material, the random packing is expected to hold at all depths in the sediment, from which it follows that N should be invariant with depth (at least, until the overburden pressure becomes so great as to crush the asperities on the grains). Data exhibiting the depth-invariance of N immediately beneath the sediment interface have been presented by Richardson and Briggs⁶¹ and Richardson.⁶² If N is invariant with depth, it follows from Eqs. (46) and (47) that the bulk modulus and density must behave similarly.

Returning to the derivation of the wave equations, conservation of mass requires that

$$\frac{\partial \Delta}{\partial t} + \rho_0 \nabla \cdot \mathbf{v} = 0, \quad (48)$$

which, when combined with Eq. (44), yields

$$\frac{1}{c_0^2} \frac{\partial p}{\partial t} + \rho_0 \nabla \cdot \mathbf{v} = 0. \quad (49)$$

On eliminating the acoustic pressure, p , from Eqs. (39) and (49), by differentiating the former with respect to time, the following equation for the velocity \mathbf{v} is obtained:

$$\begin{aligned} \rho_0 \frac{\partial^2 \mathbf{v}}{\partial t^2} &= \kappa \text{grad div } \mathbf{v} + \lambda_p \text{grad div } \frac{\partial}{\partial t} [h_p(t) \otimes \mathbf{v}] \\ &+ \frac{4}{3} \eta_s \text{grad div } \frac{\partial}{\partial t} [h_s(t) \otimes \mathbf{v}] \\ &- \eta_s \text{curl curl } \frac{\partial}{\partial t} [h_s(t) \otimes \mathbf{v}]. \end{aligned} \quad (50)$$

According to Helmholtz’s theorem,⁶³ any vector field, \mathbf{v} , can be expressed as the sum of the gradient of a scalar potential, ψ , and the curl of a zero-divergence vector potential, \mathbf{A} ,

$$\mathbf{v} = \text{grad } \psi + \text{curl } \mathbf{A}; \quad \text{div } \mathbf{A} = 0. \quad (51)$$

On substituting the first of these expressions into Eq. (49) and performing a straightforward separation of terms, the following two equations are obtained:

$$\begin{aligned} \nabla^2 \psi - \frac{1}{c_0^2} \frac{\partial^2 \psi}{\partial t^2} + \frac{\lambda_p}{\rho_0 c_0^2} \frac{\partial}{\partial t} \nabla^2 [h_p(t) \otimes \psi] \\ + \frac{(4/3)\eta_s}{\rho_0 c_0^2} \frac{\partial}{\partial t} \nabla^2 [h_s(t) \otimes \psi] = 0 \end{aligned} \quad (52)$$

and

$$\frac{\eta_s}{\rho_0} \nabla^2 [h_s(t) \otimes \mathbf{A}] - \frac{\partial \mathbf{A}}{\partial t} = 0, \quad (53)$$

where ∇^2 is the Laplacian, and the identities $\text{curl grad } \psi = 0$, $\text{div curl } \mathbf{A} = 0$, and $\text{curl curl } \mathbf{A} = -\nabla^2 \mathbf{A}$ have been used. Equations (52) and (53), representing, respectively, the propagation of compressional and shear disturbances in an unconsolidated granular medium, were stated in II but without the formal derivation given above. A minor error in II in the compressional-wave equation has been corrected in Eq. (52).

At first glance, the presence of the first derivative with respect to time might suggest that Eq. (53) for shear disturbances is diffusionlike rather than wavelike in character. This would, in fact, be the case if $h_s(t)$ were a delta function, representative of viscous dissipation. According to Eq. (53), shear disturbances in a viscous fluid are evanescent, decaying away exponentially in time and space, which is why it is said that shear is not supported by a fluid. When $h_s(t)$ is not a delta function, however, but takes the form in Eq. (26), solutions of Eq. (53) exist which represent propagating shear waves, as discussed in II. Physically, the rigidity introduced by strain-hardening during translational shearing is the factor responsible for the predicted shear wave.

XII. WAVE SPEEDS AND ATTENUATIONS

Expressions for the speed and attenuation of the compressional and shear wave are obtained by Fourier transforming the wave equations in Eqs. (52) and (53) with respect to time. This yields the reduced wave equations

$$\nabla^2 \Psi + \left[\frac{\omega^2/c_0^2}{1 + \frac{j\omega}{\rho_0 c_0^2} \{ \lambda_p H_p(j\omega) + (4/3)\eta_s H_s(j\omega) \}} \right] \Psi = 0 \quad (54)$$

and

$$\nabla^2 \hat{\mathbf{A}} + \frac{\omega^2 \rho_0}{j\omega \eta_s H_s(j\omega)} \hat{\mathbf{A}} = 0, \quad (55)$$

where $(\Psi, \hat{\mathbf{A}}, H_p, H_s)$ are the Fourier transforms with respect to time of $(\psi, \mathbf{A}, h_p, h_s)$, ω is angular frequency, and $j = \sqrt{-1}$. Note that the temporal convolutions in Eqs. (52) and (53), representing compressive and shear stress relaxation, appear as products in the frequency domain [Eqs. (54) and (55)]. From the plane-wave solution of Eq. (54), the phase speed, c_p , loss tangent, β_p , and attenuation coefficient, α_p , of the compressional wave can immediately be written as

$$\frac{1}{c_p} = \frac{1}{c_0} \operatorname{Re} \left[1 + \frac{j\omega}{\rho_0 c_0^2} \{ \lambda_p H_p(j\omega) + (4/3) \eta_s H_s(j\omega) \} \right]^{-1/2}, \quad (56a)$$

$$\beta_p = -\frac{c_p}{c_0} \operatorname{Im} \left[1 + \frac{j\omega}{\rho_0 c_0^2} \{ \lambda_p H_p(j\omega) + (4/3) \eta_s H_s(j\omega) \} \right]^{-1/2}, \quad (56b)$$

and

$$\alpha_p = \frac{\omega \beta_p}{c_p}. \quad (56c)$$

Similarly for the shear wave, the phase speed, c_s , the loss tangent, β_s , and the attenuation coefficient, α_s , are, from the plane-wave solution of Eq. (55),

$$\frac{1}{c_s} = \sqrt{\frac{\rho_0}{\eta_s}} \operatorname{Re} [j\omega H_s(j\omega)]^{-1/2}, \quad (57a)$$

$$\beta_s = -c_s \sqrt{\frac{\rho_0}{\eta_s}} \operatorname{Im} [j\omega H_s(j\omega)]^{-1/2}, \quad (57b)$$

and

$$\alpha_s = \frac{\omega \beta_s}{c_s}. \quad (57c)$$

Incidentally, the loss tangents can be expressed as $\beta = 1/2Q$, where Q is the quality factor of the medium. [N.B., The coefficients in Eqs. (56c) and (57c) give the attenuation of a planar pressure wave in nepers/m; they should be doubled to give the attenuation of intensity.]

The temporal Fourier transforms of the MIRFs in Eqs. (25) and (26) are, respectively,

$$\begin{aligned} H_p(j\omega) &= (j\omega t_p)^{n-1} e^{j\omega t_p} \Gamma(1-n, j\omega t_p) \\ &\approx \frac{\Gamma(1-n)}{(j\omega t_p)^{1-n}} \end{aligned} \quad (58)$$

and

$$\begin{aligned} H_s(j\omega) &= (j\omega t_s)^{m-1} e^{j\omega t_s} \Gamma(1-m, j\omega t_s) \\ &\approx \frac{\Gamma(1-m)}{(j\omega t_s)^{1-m}}, \end{aligned} \quad (59)$$

where ω is angular frequency and $\Gamma(\dots, \dots)$ is the complement of the incomplete gamma function. The approximations in Eqs. (58) and (59) hold at all frequencies for which $\omega t_{p,s}$

$\ll 1$, conditions which are satisfied in unconsolidated, saturated marine sediments, where viscous effects, represented by the time constants t_p and t_s , appear to be negligible.

When Eqs. (58) and (59) are substituted into the expressions for the wave speeds and loss tangents, Eqs. (56) and (57) become

$$\frac{1}{c_p} = \frac{1}{c_0} \operatorname{Re} \left[1 + \frac{\mu_p}{\rho_0 c_0^2} (j\omega t_p)^n + \frac{4}{3} \frac{\mu_s}{\rho_0 c_0^2} (j\omega t_s)^m \right]^{-1/2}, \quad (60a)$$

$$\beta_p = -\frac{c_p}{c_0} \operatorname{Im} \left[1 + \frac{\mu_p}{\rho_0 c_0^2} (j\omega t_p)^n + \frac{4}{3} \frac{\mu_s}{\rho_0 c_0^2} (j\omega t_s)^m \right]^{-1/2}, \quad (60b)$$

$$\alpha_p = -\frac{\omega}{c_0} \operatorname{Im} \left[1 + \frac{\mu_p}{\rho_0 c_0^2} (j\omega t_p)^n + \frac{4}{3} \frac{\mu_s}{\rho_0 c_0^2} (j\omega t_s)^m \right]^{-1/2}, \quad (60c)$$

and

$$\begin{aligned} \frac{1}{c_s} &= \frac{1}{c_0} \operatorname{Re} \left[\frac{\mu_s}{\rho_0 c_0^2} (j\omega t_s)^m \right]^{-1/2} \\ &= \frac{1}{c_0} \sqrt{\frac{\rho_0 c_0^2}{\mu_s}} |\omega t_s|^{-m/2} \cos\left(\frac{m\pi}{4}\right), \end{aligned} \quad (61a)$$

$$\beta_s = -\frac{c_s}{c_0} \operatorname{Im} \left[\frac{\mu_s}{\rho_0 c_0^2} (j\omega t_s)^m \right]^{-1/2} = \operatorname{sgn}(\omega) \tan\left(\frac{m\pi}{4}\right), \quad (61b)$$

$$\alpha_s = \frac{|\omega|}{c_0} \sqrt{\frac{\rho_0 c_0^2}{\mu_s}} |\omega t_s|^{-m/2} \sin\left(\frac{m\pi}{4}\right). \quad (61c)$$

The parameters μ_p, μ_s in these expressions are, respectively, radial and translational stress-relaxation moduli, which are related to the stress-relaxation coefficients λ_p and η_s as follows:

$$\mu_p = \frac{\lambda_p}{t_p} \Gamma(1-n) \quad (62a)$$

and

$$\mu_s = \frac{\eta}{t_s} \Gamma(1-m). \quad (62b)$$

It is evident from Eq. (60a) that one effect of these moduli is to raise the compressional wave speed of the sediment above the value c_0 of the equivalent suspension.

The expressions for the wave speeds and attenuations in Eqs. (60) and (61) can be simplified, first by adopting the predicted equalities in Eq. (31), and second by amalgamating the stress-relaxation moduli with the time constant $t_0 \equiv t_p = t_s$. Then, the speed, loss tangent, and attenuation of the compressional wave can be written as

$$\frac{1}{c_p} = \frac{1}{c_0} \operatorname{Re} \left[1 + \frac{3\gamma_p + 4\gamma_s}{3\rho_0 c_0^2} (j\omega T)^n \right]^{-1/2}, \quad (63a)$$

$$\beta_p = -\frac{c_p}{c_0} \operatorname{Im} \left[1 + \frac{3\gamma_p + 4\gamma_s}{3\rho_0 c_0^2} (j\omega T)^n \right]^{-1/2}, \quad (63b)$$

$$\alpha_p = -\frac{\omega}{c_0} \operatorname{Im} \left[1 + \frac{3\gamma_p + 4\gamma_s}{3\rho_0 c_0^2} (j\omega T)^n \right]^{-1/2}, \quad (63c)$$

and for the shear wave,

$$\frac{1}{c_s} = \frac{1}{c_0} \sqrt{\frac{\rho_0 c_0^2}{\gamma_s}} |\omega T|^{-n/2} \cos\left(\frac{n\pi}{4}\right), \quad (64a)$$

$$\beta_s = \operatorname{sgn}(\omega) \tan\left(\frac{n\pi}{4}\right), \quad (64b)$$

$$\alpha_s = \frac{|\omega|}{c_0} \sqrt{\frac{\rho_0 c_0^2}{\gamma_s}} |\omega T|^{-n/2} \sin\left(\frac{n\pi}{4}\right). \quad (64c)$$

In these expressions, γ_p and γ_s are, respectively, compressional and shear rigidity coefficients,

$$\gamma_p = \mu_p \left(\frac{t_0}{T}\right)^n \quad (65a)$$

and

$$\gamma_s = \mu_s \left(\frac{t_0}{T}\right)^n, \quad (65b)$$

where T is an arbitrary time that has been introduced solely to keep terms raised to the fractional power of n dimensionless. It should be clear that the expressions in Eqs. (63) and (64) are independent of the value of T , which is conveniently taken to be $T = 1$ s.

XIII. EVALUATION OF THE GRAIN-SHEARING COEFFICIENTS

Equations (63) and (64) are our final, exact expressions for the wave speeds and attenuations in the granular medium. It can be seen that, besides the mechanical properties of the two constituent materials and the porosity of the granular system, all of which may be taken as known, these expressions involve just three unknown coefficients γ_p , γ_s , and n , which must be determined from data. Two of the coefficients, γ_p and γ_s , respectively, represent the ensemble-averaged stresses associated with radial and translational sliding. The third coefficient, the material exponent n , characterizes the deterministic interaction between individual micro-asperities at the contacts between grains.

To evaluate these coefficients, only three of the expressions for the wave properties are required, the two wave speeds [Eqs. (63a) and (64a)] and the shear attenuation [Eq. (64c)]. The fourth expression, for the compressional attenuation, can then be evaluated to yield a prediction, which may be tested against data.

It is assumed that measurements of the compressional wave speed and attenuation are available at a spot frequency, f_p , and similarly for the shear wave at spot frequency f_s . By forming the product of the shear wave speed and attenuation from Eqs. (64a) and (64c), an expression is obtained which involves only n ,

$$c_s(\omega_s) \alpha_s(\omega_s) = |\omega_s| \tan \frac{n\pi}{4}, \quad (66)$$

where $\omega_s = 2\pi f_s$. It follows that n is uniquely specified as

$$n = \frac{4}{\pi} \tan^{-1} \left\{ \frac{c_s(\omega_s) \alpha_s(\omega_s)}{|\omega_s|} \right\}. \quad (67)$$

Note that α_s in these expressions is in nepers/m, which is obtained by dividing dB/m by $20 \log_{10}(e) = 8.686$.

The coefficient γ_s may be obtained either from the speed or attenuation of the shear wave. Taking the wave speed in Eq. (64a), it follows that

$$\gamma_s = \frac{\rho_0 c_s^2(\omega_s)}{|\omega_s|^n} \cos^2 \frac{n\pi}{4}, \quad (68)$$

where we have set $T = 1$ s. Equation (68) specifies γ_s uniquely. The remaining parameter, γ_p , may now be evaluated in a straightforward manner from Eq. (63a) for the compressional wave speed. It is easier to do this numerically using a simple algorithm, rather than develop a clumsy analytical solution.

Once γ_p , γ_s , and n have been evaluated, the expressions in Eqs. (63) and (64) provide the full frequency dependence for the wave speeds and attenuations. At present, a difficulty in testing the theory is that few data sets are available in the literature which fully characterize a sediment. The required data are: the porosity, N , the shear wave speed and attenuation at frequency f_s , and the compressional wave speed and attenuation at frequency f_p . Often, four out of these five parameters are reported, but usually the attenuation of the shear wave is not available.

Recently, however, as part of an O.N.R. research initiative designated SAX99, a quartz sand sediment in the northeastern Gulf of Mexico off the Florida Panhandle was intensively investigated. Preliminary data from SAX99, including all five parameters required for the test, have been reported by Richardson *et al.*⁶⁴ The values are: $N = 0.39$ (from electrical conductivity measurements); $c_p = 1771$ m/s and $\alpha_p = 12.7$ dB/m, both at $f_p = 38$ kHz; $c_s = 129$ m/s and $\alpha_s = 30$ dB/m, both at $f_s = 1$ kHz. The temperature of the pore water was 22°C , giving $\rho_w = 1024.2$ g/m³, $\kappa_w = 2.388 \times 10^9$ Pa, and $c_w = 1527$ m/s. For quartz, $\rho_g = 2650$ kg/m³ and $\kappa_g = 3.36 \times 10^{10}$ Pa. Thus the sound speed in the equivalent suspension is $c_0 = 1653.4$ m/s and the bulk density of the sediment is $\rho_0 = 2015.9$ kg/m³. These data (excluding α_p) yield: $n = 0.09014$; $\gamma_p = 2.48 \times 10^8$ Pa; and $\gamma_s = 1.517 \times 10^7$ Pa.

Figures 6(a) and (b) show the compressional and shear wave speeds as functions of frequency, from Eqs. (63a) and (64a), respectively, for the SAX99 site. The small circles, lying precisely on the theoretical lines, are two of the data points that were used in determining the coefficients. For the same site, Fig. 7 shows the compressional and shear wave attenuations as functions of frequency, from Eqs. (63c) and (64c), respectively. The small circle in this figure, lying precisely on the theoretical curve for the shear attenuation, is the third data point that was used in evaluating the coefficients.

The asterisk in Fig. 7, the measured compressional attenuation, was not used in evaluating the coefficients. At a frequency of 38 kHz, the theoretically predicted curve lies at 10.7 dB/m, about 16% (2 dB/m) below the data point represented by the asterisk. In view of the fact that the compressional and shear attenuations differ by over two orders of

magnitude, the correspondence between the predicted compressional attenuation and the data in Fig. 7 is considered to be very satisfactory. It is only fair to point out, however, that the values of the SAX99 wave properties used to obtain the prediction are preliminary and may be revised as the data are examined in greater detail. This serves to emphasize the need for more complete data sets on the wave properties of sediments.

In performing a test like that illustrated in Fig. 7 it is important, first, to take proper account of the temperature of the pore fluid⁶⁵ and, second, to use the best available measure of porosity. Both affect the computed value of c_0 , which in turn influences the predicted value of α_p . To illustrate the effect of the porosity, suppose that N is raised by 1% from 0.39, as in the above calculation, to 0.40. Then, with the same input wave properties, the predicted compressional attenuation is $\alpha_p = 11.65$ dB/m, an increase of about 1 dB/m or approximately 10%. In sandy sediments, the wave properties are highly sensitive to the porosity.

XIV. APPROXIMATIONS

Although the exact expressions for the wave speeds and attenuations are easy to compute, the functional trends are not immediately apparent from Eqs. (63) and (64). Approximations for these expressions are derived in I and II, from which the various dependencies are more evident. Just a summary of the results is given below.

By expanding Eqs. (63) and (64) in Taylor series to first order in the small parameter n , the following results are obtained:

$$c_p \approx c_0 \sqrt{1 + \Gamma_p + \frac{4}{3} \Gamma_s} \left[1 + \frac{2\beta_p}{\pi} \ln|\omega T| \right], \quad (69a)$$

$$\beta_p \approx \frac{n\pi\Gamma_p}{4(1 + \Gamma_p)} \operatorname{sgn}(\omega), \quad (69b)$$

$$\alpha_p \approx \frac{n\pi|\omega|\Gamma_p}{4c_0(1 + \Gamma_p)^{3/2}}, \quad (69c)$$

and

$$c_s \approx c_0 \sqrt{\Gamma_s} \left[1 + \frac{2\beta_s}{\pi} \ln|\omega T| \right], \quad (70a)$$

$$\beta_s \approx \frac{n\pi}{4} \operatorname{sgn}(\omega), \quad (70b)$$

$$\alpha_s \approx \frac{n\pi|\omega|}{4c_0\sqrt{\Gamma_s}}. \quad (70c)$$

For brevity, normalized stress-relaxation moduli have been introduced in these expressions,

$$\Gamma_p = \frac{\gamma_p}{\rho_0 c_0^2} \quad (71a)$$

and

$$\Gamma_s = \frac{\gamma_s}{\rho_0 c_0^2}. \quad (71b)$$

It is clear from the approximations in Eqs. (69c) and (70c) that the predicted attenuation of the compressional and shear wave both scale as the first power of frequency. This is confirmed in Fig. 7, where the exact expressions for the attenuations can be seen to follow an essentially linear scaling with frequency over several decades.

The approximate wave speeds in Eqs. (69a) and (70a) show logarithmic dispersion, the form of which is identical with that found by several other authors³¹⁻³⁶ for a wave whose attenuation scales as the first power of frequency. The dispersion scales with the loss tangent, β , or inversely as the Q . Thus the level of dispersion in the shear wave is significantly higher than that in the compressional wave. For the SAX99 site, $\beta_p \approx 0.01$ and $\beta_s \approx 0.07$, yielding dispersion of approximately 1.5% and 10.3% per decade of frequency in the compressional and shear wave, respectively.

At 1.5% per decade, the predicted dispersion in the compressional wave is comparable with the experimental value obtained by Wingham³⁹ for a medium sand. It is also similar to the dispersion in saturated glass beads measured by Hovem and Ingram⁶⁶ in the frequency range between 15 and 300 kHz. The overall trend of their data is logarithmic with a slope of approximately 1.6% per decade. The Biot curve that they attempted to fit to the data (their Fig. 3) seems to have a slope that is too shallow and a magnitude that overestimates the sound speed at the lower frequencies.

An interesting feature of the logarithmic approximations for the wave speeds is that, in the limit of low frequency, the expressions in Eqs. (69a) and (70a) diverge to negative infinity. In contrast, the exact expressions in Eqs. (63a) and (64a) are well-behaved throughout the entire range of frequency. At zero frequency, the exact wave speeds reduce to $c_p = c_0$ and $c_s = 0$, and both attenuations are zero. These are just the properties of the equivalent suspension in which there are no grain-to-grain stresses. As mentioned earlier, this limiting behavior is to be expected because the intergranular shearing depends on the rate of strain, which is zero in the limit of low frequency.

Although the logarithmic approximations and the exact expressions for the wave speeds diverge at low frequency, there is nevertheless a wide frequency range in which Eqs. (69) and (70) accurately approximate the exact forms in Eqs. (63) and (64). The logarithmic trend in the exact wave speeds is evident in Figs. 6(a) and (b). A comparative discussion of the exact versus approximate forms has been given by Buckingham.⁶⁷

XV. "FRAME" ELASTICITY

Hamilton⁶⁸ developed an empirical model of wave propagation in unconsolidated granular materials in which the medium is treated as a Hookean elastic solid. In his model, the compressional and shear wave speeds are given by the familiar expressions for an isotropic elastic medium,

$$\hat{c}_p = \sqrt{\frac{\hat{K} + \frac{4}{3}\hat{\mu}}{\hat{\rho}_0}} \quad (72)$$

and

$$\hat{c}_s = \sqrt{\frac{\hat{\mu}}{\hat{\rho}_0}}, \quad (73)$$

where the tilde denotes one of Hamilton's elastic parameters. The bulk modulus of the saturated granular system is $\hat{\kappa}$, the bulk density is $\hat{\rho}_0$, and the shear modulus is $\hat{\mu}$. Hamilton⁶⁸ extended the elastic model to include dissipation by making $\hat{\mu}$ and the second Lamé constant, $\hat{\lambda} = \hat{\kappa} - 2/3\hat{\mu}$, complex. This he referred to as a viscoelastic model. He let the imaginary parts of the Lamé coefficients be independent of frequency simply because this yielded attenuations that scaled as the first power of frequency.

A recurring difficulty with the viscoelastic model, as discussed by Hamilton,⁶⁸ is the evaluation of the system bulk modulus, $\hat{\kappa}$. As others had done before him, Hamilton assumed implicitly that the unconsolidated granular medium possesses a skeletal elastic "frame," and that one component of $\hat{\kappa}$ is the frame bulk modulus, $\hat{\kappa}_f$. He was then faced with the problem of determining $\hat{\kappa}_f$. His solution was to fit Gassman's equation⁴⁷ to available wave data, from which he inferred a value for the frame bulk modulus. With a judicious choice of the remaining elastic parameters, he then found that the equations of the elastic model could be made to fit measured data rather well.

The equations of Hamilton's elastic model may be interpreted in terms of the lowest-order approximations for the wave speeds predicted by the grain-shearing theory. Thus if the first-order, logarithmic terms representing dispersion are neglected, the wave speeds in Eqs. (69a) and (70a) reduce to the zero-order forms

$$c_p \approx \sqrt{\frac{\kappa_0 + \gamma_p + \frac{4}{3}\gamma_s}{\rho_0}} \quad (74)$$

and

$$c_s \approx \sqrt{\frac{\gamma_s}{\rho_0}}. \quad (75)$$

These expressions have exactly the same structure as those in Eqs. (72) and (73) for the wave speeds in an elastic medium.

Obviously, the bulk densities in the two models are identical: $\rho_0 = \hat{\rho}_0$. By comparing the expressions for the shear speed, Hamilton's shear rigidity modulus, $\hat{\mu}$, may be identified directly with γ_s , the shear rigidity conferred by grain-to-grain translation, and, from the compressional speeds, Hamilton's bulk modulus for the system equates as follows:

$$\hat{\kappa} = \kappa_0 + \gamma_p, \quad (76)$$

where γ_p is the compressional rigidity coefficient of the grain-shearing theory. According to Eqs. (74) and (76), two factors are responsible for raising the compressional speed in the granular medium above that in the equivalent suspension. The larger of the two is the rigidity due to radial (compressive) shearing, represented by γ_p . An order of magnitude smaller is the rigidity introduced by translational shearing and represented by γ_s . The frame bulk modulus may be interpreted in terms of the former, that is, the rigidity due to intergranular shearing under compression.

The Gassmann model⁴⁷ yields the bulk modulus of the system in terms of the "frame" bulk modulus, $\hat{\kappa}_f$, and the bulk modulus of the equivalent suspension, κ_0 ,

$$\hat{\kappa} = \kappa_0 + \frac{\hat{\kappa}_f(\kappa_g - \kappa_0)^2}{(\kappa_g^2 - \hat{\kappa}_f\kappa_0)}. \quad (77)$$

This expression is not as formulated by Gassmann, but is readily derived from his original with a little algebra. Apart from Hamilton,⁶⁸ several authors have examined Gassmann's equation, including White and Sengbush⁶⁹ and Wylie *et al.*⁴⁰ As pointed out by Hamilton,⁶⁸ when the bulk modulus of the frame, $\hat{\kappa}_f$, is zero, the Gassmann equation reduces to Wood's equation, that is, $\hat{\kappa} = \kappa_0$, and when the porosity, N , is zero, corresponding to an elastic solid, $\hat{\kappa} = \kappa_0 = \kappa_g$. Hamilton⁶⁸ also states, erroneously, that, when N is zero, the solution of Eq. (77) for the frame bulk modulus is $\hat{\kappa}_f = \kappa_g$. Actually, $\hat{\kappa}_f$ is indeterminate from Gassmann's equation when $N=0$. It follows that the four points on the ordinate in Hamilton's⁶⁸ Fig. 2 are invalid.

From inspection of Eqs. (76) and (77), γ_p of the grain-shearing theory may be linked to the elastic frame bulk modulus $\hat{\kappa}_f$ as follows:

$$\gamma_p = \frac{\hat{\kappa}_f(\kappa_g - \kappa_0)^2}{(\kappa_g^2 - \hat{\kappa}_f\kappa_0)}. \quad (78)$$

This equation may be inverted to yield

$$\hat{\kappa}_f = \frac{\gamma_p \kappa_g^2}{(\kappa_0 - \kappa_g)^2 + \gamma_p \kappa_0}. \quad (79)$$

Thus an "effective" elastic frame with a bulk modulus, $\hat{\kappa}_f$, as given by Eq. (79), is equivalent, at this lowest order of approximation, to the compressional rigidity that arises from radial (compressional) shearing at the grain contacts.

Of course, by assuming an elastic frame at the outset, many of the wave properties will be lost. For instance, as Hamilton⁶⁸ makes clear, his viscoelastic model is purely empirical and does not account for subtleties such as frequency dispersion in the wave speeds. Nor does it identify any correlations between the wave speeds and attenuations, but leaves them unconstrained. There are four free parameters in the viscoelastic model, the bulk modulus, the shear modulus, and the imaginary parts of the two Lamé coefficients. These can be individually adjusted to fit any wave-data set in which the two wave speeds are essentially independent of frequency and the two attenuations scale as the first power of frequency. In contrast, in the grain-shearing analysis, the wave properties are causally connected and hence heavily constrained.

On a historical note, in addition to recognizing that a saturated sediment exhibits shear rigidity, which supports the transmission of a transverse wave, Hamilton⁶⁸ was also aware that the speed of the compressional wave is greater than that predicted by Wood's equation. He attributed the enhanced compressional wave speed to two factors, "the presence of both (shear) rigidity and a frame bulk modulus." His viscoelastic model [Eqs. (72) and (73)] embodies these ideas, and, although he did not specify physical mechanisms, he recognized that the shear rigidity and the frame bulk

modulus both originate in grain-to-grain interactions. This is exactly as has been argued above, where the frame bulk modulus is identified with the rigidity arising from radial (compressional) sliding, and the shear rigidity with translational sliding. Hamilton's⁶⁸ remarkable insights, expressed some three decades ago, provide an excellent foundation for understanding wave propagation in granular media.

XVI. CONCLUDING REMARKS

The linear theory of wave propagation in unconsolidated granular media developed in this paper is based on two distinct types of grain-to-grain interaction, translational and radial shearing, which occur during the passage of a wave through the medium. Both types of shearing are treated as a random stick-slip process consisting of a sequence of discrete "micro-events." Each such event involves one micro-asperity slipping against another to produce a deterministic pulse of stress, a process which occurs as the medium relaxes after the application of a dynamic strain.

The mean stress, which governs the wave properties, is derived as an ensemble average of the random succession of stress-relaxation pulses. This average takes the form of a temporal convolution between the probability that a slip is triggered and the pulse shape function for a single stress-relaxation event. The probability density function is proportional to the velocity gradient normal to a grain contact, or equivalently, to the rate of strain across the boundary. The pulse shape function is established from a simple model of strain-hardening, which is based on the physics of the very thin film of pore fluid separating mineral grains. The resultant pulse shape function, or material impulse response function (MIRF), is essentially an inverse-time fractional power law.

With the stresses due to intergranular interactions specified as temporal convolutions, the Navier–Stokes equation is derived from the full stress tensor for the granular medium. A standard separation of the Navier–Stokes equation yields two wave equations, one for compressional and the other for shear disturbances. Both are true wave equations, even though the medium is treated as a fluid in the sense of possessing no skeletal elastic frame. By Fourier transforming these equations into the frequency domain, simple algebraic expressions for the wave speeds and attenuations are developed. These expressions depend explicitly on frequency and the porosity of the sediment.

The theoretical expressions for the compressional and shear attenuation both scale essentially in proportion to the first power of frequency. They compare very favorably with the published frequency dependence of compressional and shear wave attenuation data over many decades of frequency. The wave speeds are predicted to exhibit weak, near-logarithmic dispersion, the level of which scales with the loss tangent. Thus dispersion in the shear wave is estimated to be significantly higher than that in the compressional wave. These logarithmic expressions for the wave speeds are consistent with the Kramers–Kronig relationships, which lead to an identical form of logarithmic dispersion for any wave exhibiting an attenuation that scales with the first

power of frequency, regardless of the physical mechanism responsible for the attenuation.

ACKNOWLEDGMENTS

I wish to thank Dr. Michael Richardson, N.R.L., Stennis Space Center, for very generously making many of his unpublished data sets available to me. This work was supported by the Ocean Acoustics Code (Dr. J. Simmen), Office of Naval Research under Grant No. N00014-93-1-0054.

APPENDIX: WAVE PROPERTIES VERSUS GRAIN SIZE AND DEPTH IN THE SEDIMENT

The coefficients γ_p and γ_s scale with the mean rate, $\nu_{p,s}$, of stress-relaxation events in the interval $[0, T]$. These mean rates are proportional to the total number of asperities available for sliding. Thus for translational shearing, ν_s is proportional to the area of the surface of contact, and for radial shearing ν_p is proportional to the radius of the circle of contact.

The Hertz theory⁷⁰ of identical elastic spheres pressed together by a force F gives the radius of the circle of contact as

$$a = \sqrt[3]{\frac{3}{8} F \frac{(1 - \theta_g^2)}{E_g} u_g}, \quad (\text{A1})$$

where u_g is the diameter of the spheres and (E_g, θ_g) are Young's modulus and Poisson's ratio for the material comprising the spheres. Equation (A1) applies to spheres that are frictionless. If the spheres are identified with mineral grains, then F scales with depth, d , in the sediment, and it follows that

$$\nu_p \propto (u_g d)^{1/3} \quad (\text{A2})$$

and

$$\nu_s \propto (u_g d)^{2/3}. \quad (\text{A3})$$

Thus according to the Hertz theory, $\gamma_{p,s}$ depend on grain size and depth as follows:

$$\gamma_p = \gamma_{op} \left(\frac{u_g d}{u_0 d_0} \right)^{1/3} \quad (\text{A4})$$

and

$$\gamma_s = \gamma_{os} \left(\frac{u_g d}{u_0 d_0} \right)^{2/3}, \quad (\text{A5})$$

where γ_{op} , γ_{os} are scaling constants, and $u_0 = 1000 \mu\text{m}$, $d_0 = 0.3 \text{ m}$, are normalizing factors, introduced solely to keep the bracketed terms dimensionless.

When the expression for γ_s in Eq. (A5) is substituted into Eq. (75), the speed of the shear wave is found to be

$$c_s \approx \left(\frac{u_g d}{u_0 d_0} \right)^{1/3} \sqrt{\frac{\gamma_{os}}{\rho_0}}. \quad (\text{A6})$$

Figure 5 in II compares this expression, plotted as a function of grain size, with data on the shear wave speed as a function of grain size. The data show some scatter but straddle Eq. (A6) over three decades of grain size. The variation of c_s as the one-third power of depth, d , has been observed in sands

by Richardson *et al.*,⁷¹ and Hamilton⁷² proposed a similar power-law scaling, of the form $c_s \propto d^{0.28}$, based on a curve fit to data for sands.

The speed of the compressional wave varies relatively slowly with grain size and depth in the sediment. As predicted by Eqs. (74) and (A4), the grain-size dependence of c_p compares favorably with data over three decades of grain size (see Fig. 8 in I). The predicted depth dependence of c_p appears to be consistent with data from the West Florida Sand Sheet reported by Richardson and Briggs.⁶¹

It should be borne in mind when evaluating the grain-size dependence of the wave speeds and attenuations that the expressions involve ρ_0 and c_0 , both of which are functions of the porosity, and the porosity varies with the grain size. In I, a relationship between porosity and grain size was proposed, based on a randomly packed, rough-grain model of the sediment,

$$N = 1 - P \left\{ \frac{u_g + 2D}{u_g + 4D} \right\}^3, \quad (\text{A7})$$

where $P=0.63$ is the packing factor of a random, close-packing of smooth spheres, and D is the r.m.s. grain roughness. When $D=0$, Eq. (A7) yields $N=0.37$, which is the correct porosity for a random packing of smooth spheres.⁷³

In sediments, it is well known that N is not single-valued in the grain size, one reason being that the grains of a given size may show different degrees of roughness. For most sands, D lies somewhere between 0 and 10 μm . If D is treated as a parameter, any of the wave properties, say the approximate expression for the shear speed in Eq. (A6), can be evaluated as a function of grain size with the aid of Eq. (A7). A family of curves will be obtained, each associated with a particular value of D . For a specific sediment, D may be estimated from Eq. (A7) if N and u_g are both available from experimental measurements.

Although the Hertz theory yields grain-size and sediment-depth dependencies that appear to align reasonably well with the few existing data sets, it may be found, as new data become available, that a better description of grain contact mechanics is required. For instance, the assumption that the grains are frictionless, which is central to the Hertz theory, may have to be relaxed. This, and other possible refinements to the treatment of the contact mechanics, could lead to grain-size and sediment-depth dependencies that differ from those in Eqs. (A2) and (A3). Corresponding differences would then be expected in the predicted wave speeds and attenuations as functions of grain size and sediment depth.

¹M. A. Biot, "Theory of propagation of elastic waves in a fluid-saturated porous solid: I. Low-frequency range," *J. Acoust. Soc. Am.* **28**, 168–178 (1956).

²M. A. Biot, "Theory of propagation of elastic waves in a fluid-saturated porous solid: II. Higher frequency range," *J. Acoust. Soc. Am.* **28**, 179–191 (1956).

³R. D. Stoll, *Sediment Acoustics* (Springer-Verlag, Berlin, 1989), Vol. 26.

⁴C.-H. Liu and S. R. Nagel, "Sound in sand," *Phys. Rev. Lett.* **68**, 2301–2304 (1992).

⁵C.-H. Liu, S. R. Nagel, D. A. Schechter, S. N. Coppersmith, S. Majumdar, O. Narayan, and T. A. Witten, "Force fluctuations in bead packs," *Science* **29**, 513–515 (1995).

⁶M. J. Buckingham, "Theory of acoustic attenuation, dispersion, and pulse propagation in unconsolidated granular materials including marine sediments," *J. Acoust. Soc. Am.* **102**, 2579–2596 (1997).

⁷M. J. Buckingham, "Theory of compressional and shear waves in fluid-like marine sediments," *J. Acoust. Soc. Am.* **103**, 288–299 (1998).

⁸S. Granick, "Soft matter in a tight spot," *Phys. Today* **52**, 26–31 (1999).

⁹J. Gittus, *Creep, Viscoelasticity and Creep Fracture in Solids* (Wiley, New York, 1975).

¹⁰H. M. Jaeger, S. R. Nagel, and R. P. Behringer, "The physics of granular materials," *Phys. Today* **49**, 32–38 (1996).

¹¹C.-h. Liu and S. R. Nagel, "Sound in a granular material: disorder and nonlinearity," *Phys. Rev. B* **48**, 15646–15650 (1993).

¹²C.-h. Liu and S. R. Nagel, "Sound and vibrations in granular materials," *J. Phys.: Condens. Matter* **6**, A433–A436 (1994).

¹³C.-h. Liu, "Spatial patterns of sound propagation in sand," *Phys. Rev. B* **50**, 782–794 (1994).

¹⁴D. M. Muth, H. M. Jaeger, and S. R. Nagel, "Force distribution in a granular medium," *Phys. Rev. E* **57**, 3164–3169 (1998).

¹⁵S. R. Nagel and H. M. Jaeger, "Sound propagation in sand," in *Echoes*, edited by T. Rossing (Acoustical Society of America, New York, 1998), Vol. 8, pp. 1, 4.

¹⁶A. Barbagelata, M. Richardson, B. Miaschi, E. Muzi, P. Guerrini, L. Troiano, and T. Akal, "ISSAMS: An in situ sediment acoustic measurement system," in *Shear Waves in Marine Sediments*, edited by J. M. Hovem, M. D. Richardson, and R. D. Stoll (Kluwer, Dordrecht, 1991), pp. 305–312.

¹⁷S. R. Griffin, F. B. Grosz, and M. D. Richardson, "In situ sediment geoacoustic measurement system," *Sea Technol.*, 19–22 (1996).

¹⁸M. D. Richardson, "In-situ, shallow-water sediment geoacoustic properties," in *Shallow-Water Acoustics*, edited by R. Zhang and J. Zhou (China Ocean, Beijing, 1997), pp. 163–170.

¹⁹M. D. Richardson, personal communication, 1998.

²⁰E. L. Hamilton, "Compressional-wave attenuation in marine sediments," *Geophysics* **37**, 620–646 (1972).

²¹E. L. Hamilton, "Acoustic properties of sediments," in *Acoustics and the Ocean Bottom*, edited by A. Lara-Saenz, C. R. Cuierra, and C. Carbo-Fité (Consejo Superior de Investigaciones Científicas, Madrid, 1987), pp. 3–58.

²²A. B. Wood and D. E. Weston, "The propagation of sound in mud," *Acustica* **14**, 156–162 (1964).

²³L. Bjørnø, "Features of the linear and non-linear acoustics of water-saturated marine sediments," Technical University of Denmark, Report No. AFM76-06, June 1976.

²⁴M. C. Ferla, G. Dreini, F. B. Jensen, and W. A. Kuperman, "Broadband model/data comparisons for acoustic propagation in coastal waters," in *Bottom-Interacting Ocean Acoustics*, edited by W. A. Kuperman and F. B. Jensen (Plenum, New York, 1980), pp. 577–592.

²⁵S. D. Rajan, G. V. Frisk, and J. F. Lynch, "On the determination of modal attenuation coefficients and compressional wave attenuation profiles in a range-dependent environment in Nantucket Sound," *IEEE J. Ocean Eng.* **17**, 118–128 (1992).

²⁶C. McCann and D. M. McCann, "A theory of compressional wave attenuation in noncohesive sediments," *Geophysics* **50**, 1311–1317 (1985).

²⁷F. A. Bowles, "Observations on attenuation and shear-wave velocity in fine-grained, marine sediments," *J. Acoust. Soc. Am.* **101**, 3385–3397 (1997).

²⁸B. A. Brunson and R. K. Johnson, "Laboratory measurements of shear wave attenuation in saturated sand," *J. Acoust. Soc. Am.* **68**, 1371–1375 (1980).

²⁹B. A. Brunson, "Shear wave attenuation in unconsolidated laboratory sediments," in *Shear Waves in Marine Sediments*, edited by J. M. Hovem, M. D. Richardson, and R. D. Stoll (Kluwer, Dordrecht, 1991), pp. 141–147.

³⁰A. C. Kibblewhite, "Attenuation of sound in marine sediments: A review with emphasis on new low frequency data," *J. Acoust. Soc. Am.* **86**, 716–738 (1989).

³¹W. I. Futterman, "Dispersive body waves," *J. Geophys. Res.* **67**, 5279–5291 (1962).

³²C. W. Horton, Sr., "Dispersion relationships in sediments and sea water," *J. Acoust. Soc. Am.* **55**, 547–549 (1974).

³³C. W. Horton, Sr., "Comment on 'Kramers-Kronig relationship between ultrasonic attenuation and phase velocity' [*J. Acoust. Soc. Am.* **69**, 696–701 (1981)]," *J. Acoust. Soc. Am.* **70**, 1182 (1981).

³⁴M. O'Donnell, E. T. Jaynes, and J. G. Miller, "General relationships

- between ultrasonic attenuation and dispersion," J. Acoust. Soc. Am. **63**, 1935–1937 (1978).
- ³⁵M. O'Donnell, E. T. Jaynes, and J. G. Miller, "Kramers-Kronig relationship between ultrasonic attenuation and phase velocity," J. Acoust. Soc. Am. **69**, 696–701 (1981).
- ³⁶E. Kjartansson, "Constant Q -wave propagation and attenuation," J. Geophys. Res. **84**, 4737–4748 (1979).
- ³⁷E. G. McLeroy and A. DeLoach, "Sound speed and attenuation, from 15 to 1500 kHz, measured in natural sea-floor sediments," J. Acoust. Soc. Am. **44**, 1148–1150 (1968).
- ³⁸C. McCann and D. M. McCann, "The attenuation of compressional waves in marine sediments," Geophysics **34**, 882–892 (1969).
- ³⁹D. J. Wingham, "The dispersion of sound in sediment," J. Acoust. Soc. Am. **78**, 1757–1760 (1985).
- ⁴⁰M. R. Wyllie, A. R. Gregory, and L. W. Gardner, "Elastic wave velocities in heterogeneous and porous media," Geophysics **21**, 41–70 (1956).
- ⁴¹H. J. Simpson and B. H. Houston, "A synthetic array measurement of a fast compressional and a slower wave in an unconsolidated water-saturated porous medium," J. Acoust. Soc. Am. **102**, 3210 (1997).
- ⁴²H. J. Simpson and B. H. Houston, "Analysis of laboratory measurements of sound propagating into an unconsolidated water-saturated porous media," J. Acoust. Soc. Am. **103**, 3095–3096 (1998).
- ⁴³H. J. Simpson, B. H. Houston, and L. S. Couchman, "Measurements and modeling of sound propagating into unconsolidated water-saturated porous media in a laboratory environment," J. Acoust. Soc. Am. **104**, 1787 (1998).
- ⁴⁴H. J. Simpson and B. H. Houston, "Synthetic array measurements of acoustical waves propagating into a water-saturated sandy bottom for a smoothed and a roughened interface," J. Acoust. Soc. Am. **107**, 2329–2337 (2000).
- ⁴⁵T. J. Plona, "Observation of a second bulk compressional wave in a porous medium at ultrasonic frequencies," Appl. Phys. Lett. **36**, 259–261 (1980).
- ⁴⁶D. L. Johnson and T. J. Plona, "Acoustic slow waves and the consolidation transition," J. Acoust. Soc. Am. **72**, 556–565 (1982).
- ⁴⁷F. Gassmann, "Über die elastizität poröser medien," Vierteljahrsscher. Naturforsch. Ges. Zürich **96**, 1–23 (1951).
- ⁴⁸B. Bhushan, J. N. Israelachvili, and U. Landman, "Nanotribology: friction, wear and lubrication at the atomic scale," Nature (London) **374**, 607–616 (1995).
- ⁴⁹M. T. Bengisu and A. Akay, "Stick-slip oscillations: Dynamics of friction and surface roughness," J. Acoust. Soc. Am. **105**, 194–205 (1999).
- ⁵⁰M. J. Buckingham, *Noise in Electronic Devices and Systems* (Ellis Horwood, Chichester, 1983).
- ⁵¹S. O. Rice, "Mathematical analysis of random noise," Bell Syst. Tech. J. **23**, 282–332 (1945).
- ⁵²R. D. Mindlin, "Compliance of elastic bodies in contact," J. Appl. Mech. **16**, 259–268 (1949).
- ⁵³R. D. Mindlin, W. P. Mason, W. P. Osmer, and H. Deresiewicz, "Effects of an oscillating tangential force on the contact surfaces of elastic spheres," presented at First National Congress on Applied Mechanics, Chicago, 1951.
- ⁵⁴R. D. Mindlin and H. Deresiewicz, "Elastic spheres in contact under varying oblique forces," J. Appl. Mech. **20**, 327–344 (1953).
- ⁵⁵R. D. Mindlin, "Mechanics of granular media," presented at Second U.S. National Congress on Applied Mechanics, Ann Arbor, 1954.
- ⁵⁶P. G. Nutting, "The deformation of granular solids," J. Wash. Acad. Sci. **18**, 123–126 (1928).
- ⁵⁷H. Deresiewicz, "Mechanics of granular matter," in *Advances in Applied Mechanics*, edited by H. L. Dryden and T. v. Kármán (Academic, New York, 1958), Vol. 5, pp. 233–306.
- ⁵⁸A. L. Demirel and S. Granick, "Glasslike transition of a confined simple fluid," Phys. Rev. Lett. **77**, 2261–2264 (1996).
- ⁵⁹P. M. Morse and K. U. Ingard, *Theoretical Acoustics* (McGraw-Hill, New York, 1968).
- ⁶⁰A. B. Wood, *A Textbook of Sound*, 3rd ed. (G. Bell, London, 1964).
- ⁶¹M. D. Richardson and K. B. Briggs, "In situ and laboratory geoaoustic measurements in soft mud and hard-packed sand sediments: Implications for high-frequency acoustic propagation and scattering," Geo-Mar. Lett. **16**, 196–203 (1996).
- ⁶²M. D. Richardson, "Spatial variability of surficial shallow water sediment geoaoustic properties," in *Ocean-Seismo Acoustics: Low-Frequency Underwater Acoustics*, edited by T. Akal and J. M. Berkson (Plenum, New York, 1986), pp. 527–536.
- ⁶³P. M. Morse and H. Feshbach, *Methods of Theoretical Physics: Part 1* (McGraw-Hill, New York, 1953), Vol. 1.
- ⁶⁴M. D. Richardson, K. B. Briggs, D. L. Bibee *et al.*, "Overview of SAX99: environmental considerations," IEEE J. Ocean. Eng. (in press).
- ⁶⁵D. W. Bell and D. J. Shirley, "Temperature variation of the acoustical properties of laboratory sediments," J. Acoust. Soc. Am. **68**, 227–231 (1980).
- ⁶⁶J. M. Hovem and G. D. Ingram, "Viscous attenuation of sound in saturated sand," J. Acoust. Soc. Am. **66**, 1807–1812 (1979).
- ⁶⁷M. J. Buckingham, "Precision correlations between the geoaoustic parameters of an unconsolidated, sandy marine sediment," J. Comput. Acoust. (in press).
- ⁶⁸E. L. Hamilton, "Elastic properties of marine sediments," J. Geophys. Res. **76**, 579–604 (1971).
- ⁶⁹J. E. White and R. L. Sengbush, "Velocity measurements in near-surface formations," Geophysics **18**, 54–69 (1953).
- ⁷⁰S. P. Timoshenko and J. N. Goodier, *Theory of Elasticity*, 3rd ed. (McGraw-Hill, New York, 1970).
- ⁷¹M. D. Richardson, E. Muzi, B. Miashi, and F. Turgutcan, "Shear wave velocity gradients in near-surface marine sediment," in *Shear Waves in Marine Sediments*, edited by J. M. Hovem, M. D. Richardson, and R. D. Stoll (Kluwer, Dordrecht, 1991), pp. 295–304.
- ⁷²E. L. Hamilton, "Shear-wave velocity versus depth in marine sediments: A review," Geophysics **41**, 985–996 (1976).
- ⁷³O. K. Rice, "On the statistical mechanics of liquids, and the gas of hard elastic spheres," J. Chem. Phys. **12**, 1–18 (1944).

Physical limitations of travel-time-based shallow water tomography

Orlando C. Rodríguez^{a)} and Sérgio M. Jesus

Unidade de Ciências Exactas e Humanas, Universidade do Algarve, Campus de Gambelas, 8000—Faro, Portugal

(Received 22 November 1999; revised 23 May 2000; accepted 6 September 2000)

Travel-time-based tomography is a classical method for inverting sound-speed perturbations in an arbitrary environment. A linearization procedure enables relating travel-time perturbations to sound-speed perturbations through a kernel matrix. Thus travel-time-based tomography essentially relies on the inversion of the kernel matrix and is commonly called “linear inversion.” In practice, its spatial resolution is limited by the number of resolved and independent arrivals, which is a basic linear algebra requirement for linear inversion performance. Physically, arrival independency is much more difficult to determine since it is closely related to the sound propagating channel characteristics. This paper presents a brief review of linear inversion and shows that, in deep water, the number of resolved arrivals is equal to the number of independent arrivals, while in shallow water the number of independent arrivals can be much smaller than the number of resolved arrivals. This implies that in shallow water there are physical limitations to the number of independent travel times. Furthermore, those limitations are explained through the analysis of an equivalent environment with a constant sound speed. The results of this paper are of central importance for the understanding of travel-time-based shallow water tomography. © 2000 Acoustical Society of America. [S0001-4966(00)01212-1]

PACS numbers: 43.30.Pc, 43.60.Rw [DLB]

I. INTRODUCTION

Ocean acoustic tomography has been suggested in the last two decades as a powerful tool for large-scale ocean temperature monitoring. In contrast with standard “local” and “direct” methods, ocean acoustic tomography can be used to remotely determine mean current and temperature evolution through time in an ocean volume bounded by a system of acoustic sources and receivers.^{1,2} Travel-time-based tomography has been widely used in the context of ocean acoustic tomography to invert for sound-speed perturbations of a background (reference) profile.^{1–5} For instance, tomographic inversion can be performed by linearizing the integral relationship between perturbations in travel time and continuous perturbations in sound speed. After linearization, the perturbations in travel time are related to a set of discrete perturbations in sound speed through a kernel matrix, which depends on stable eigenrays of propagation. Sound-speed perturbations can be estimated by calculating a generalized inverse of the kernel matrix and relating back the set of sound-speed perturbations to travel-time perturbations. This technique is sometimes called “linear inversion” and its spatial resolution (i.e., the number of depths at which sound-speed perturbations can be reliably estimated) is fundamentally limited by the number of resolved—and as we will see independent—arrivals.

Despite the significant number of references related to linear inversion most studies are limited to its application in deep water, where the effects of sound reflection on the ocean boundaries can be, to a certain extent, neglected, and

acoustic arrivals can be easily resolved for long-range propagation. In shallow water the interaction of sound with the ocean boundaries plays an important role and time resolution of closely spaced arrivals is generally an important practical issue. As an example, Fig. 1 shows a typical shallow water channel impulse response estimate. It is clear from that figure that initial arrivals are unresolved, while late arrivals are well resolved and “clustered” in quadruplets. From ray-tracing predictions it can be shown that most of the initial unresolved arrivals correspond to refracted and bottom reflected eigenrays, while the quadruplets correspond to surface and bottom reflected eigenrays. An important feature in this example is the significant number of resolved arrivals. In the context of travel-time-based shallow water tomography, and through linear inversion, it seems reasonable that those arrivals should be used to achieve a high spatial resolution of sound-speed estimates. This would be the case providing that all the resolved arrivals are independent, i.e., that all the acoustic arrivals that can be identified from one transmission to another correspond to “pieces” of information independently related to the perturbation of sound speed. This assumption seems to be implicitly accepted in some of the studies concerning linear inversion.^{1,3,4} Nevertheless, it is shown in this paper that for shallow water the number of independent arrivals is in fact smaller, and in some cases much smaller, than the number of actually measured—resolved—arrivals. This result implies that in shallow water part of the acoustic arrivals carry redundant information and therefore there are fundamental physical limitations to the number of independent arrivals. Furthermore, and most importantly, this paper shows that the redundancy of shallow water stable arrivals can be explained through the compari-

^{a)}Electronic mail: orodrig@ualg.pt

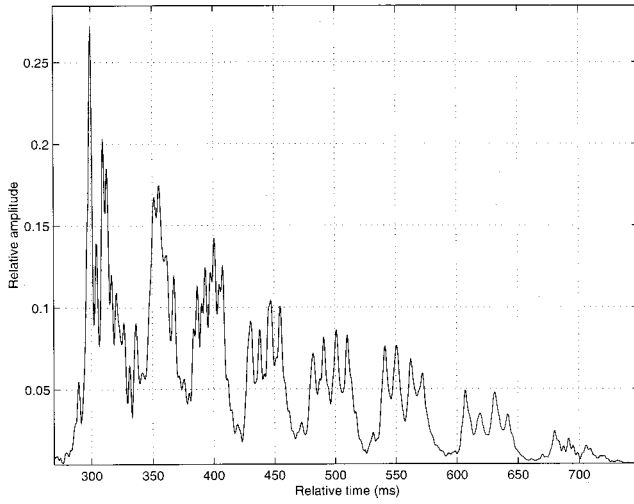


FIG. 1. Typical shallow water short-range arrival pattern showing unresolved (initial) and resolved (late) arrivals; resolved arrivals are “clustered” in groups of quadruplets [real data, taken from Jesus *et al.* (Ref. 6)].

son of the original waveguide with an isovelocity equivalent. Therefore, as a contribution to the general problem of acoustic tomography this paper presents the set of fundamental requirements for successful tomographic inversion of acoustic data in the context of travel-time-based shallow water tomography. This paper is organized as follows: Sec. II presents a brief theoretical review of linear inversion. This review is used in Sec. III to show, through simulations, that for deep water the number of independent arrivals is equal to the number of measured resolved travel times, while in shallow water the number of independent arrivals is much smaller than the number of actually measured resolved arrivals. The results of shallow water simulations are explained in Sec. IV through the comparison of the original acoustic waveguide with an isovelocity equivalent, and conclusions are drawn in Sec. V.

II. LINEAR INVERSION: THEORETICAL BACKGROUND

It can be shown on the basis of ray theory that the perturbation in travel time of an acoustic pulse can be written as^{1,2}

$$\Delta\tau = \int_{\Gamma} \frac{ds}{c(z)} - \int_{\Gamma_0} \frac{ds}{c_0(z)}, \quad (1)$$

where Γ and Γ_0 represent the eigenrays corresponding, respectively, to the perturbed and background sound-speed profiles $c(z)$ and $c_0(z)$. The background sound-speed profile $c_0(z)$ is considered to be known, for instance, from historical data. For small perturbations of sound speed $\delta c(z) = c(z) - c_0(z) \ll c_0(z)$ one can take $\Gamma \approx \Gamma_0$, so the previous equation becomes

$$\Delta\tau_i = \tau_i - \tau_i^0 = \int_{\Gamma_i} \frac{ds}{c(z)} - \int_{\Gamma_i} \frac{ds}{c_0(z)} \approx - \int_{\Gamma_i} \frac{\delta c(z)}{c_0^2(z)} ds, \quad (2)$$

where the integral is taken along the unperturbed eigenray Γ_i . The fundamental statement of this relationship is that a first-order perturbation in sound speed leads only to a first-

order perturbation in travel time, while the path of the eigenray is not affected by this perturbation. In this sense Γ_i corresponds to a stable eigenray and τ_i and τ_i^0 can be considered as resolved travel times (or resolved arrivals). It is clear that the number of perturbations in travel time should be equal to the number of resolved eigenrays or, correspondingly, to the number of resolved arrivals. By “collecting” a set of T perturbations in travel time and representing the acoustic waveguide as a system composed of L layers, one obtains the following linear system:²

$$\mathbf{y} = \mathbf{E}\mathbf{x} + \mathbf{n}, \quad (3)$$

where $\mathbf{y} = [\Delta\tau_1 \Delta\tau_2 \dots \Delta\tau_T]^t$, $\mathbf{x} = [\delta c_1 \delta c_2 \dots \delta c_L]^t$, each δc_j is an average of $\delta c(z)$ in the j th layer, and \mathbf{n} represents the contribution of noise to the set of observations \mathbf{y} . Since the linear inversion will be tested with simulated data it will be considered in the following that there is a perfect match between both sides of the equation and the observations are fully deterministic (i.e., $\mathbf{n} = \mathbf{0}$).

Matrix \mathbf{E} , dimension $T \times L$, is called the “kernel matrix,” the \mathbf{e}_i of which have the following structure:

$$\mathbf{e}_i = \begin{bmatrix} \Delta s_{i1} & \Delta s_{i2} & \dots & \Delta s_{iL} \\ c_{01}^2 & c_{02}^2 & \dots & c_{0L}^2 \end{bmatrix}, \quad (4)$$

where Δs_{ij} stands for the length of ray i inside layer j with $i = 1, 2, \dots, T$ and $j = 1, 2, \dots, L$. The choice of the number of layers L can be done in many different ways. In general L is made as large as possible and in practice it is often larger than T . Under this assumption of $L > T$, Eq. (3) consists of an underdetermined system of equations that has more unknowns than equations, and therefore has an infinite number of solutions. Formally, the columns of matrix \mathbf{E} form a dependent set and, in practice, there is also no guarantee that T rows of \mathbf{E} are linearly independent, which is equivalent to saying that \mathbf{E} may be rank deficient. In terms of the underlying problem of time delays and sound-speed perturbations, rank deficiency means that not all resolved arrivals carry independent sound-speed information. Straight linear algebra tells us that such a system of equations has a solution \mathbf{x} , but that solution is not unique; that is to say that further information is needed to pick one among the possible solutions. The set of possible solutions are those that satisfy the system of equations

$$\mathbf{E}\hat{\mathbf{x}} = \mathbf{p}, \quad (5)$$

where $\hat{\mathbf{x}} = [\mathbf{E}'\mathbf{E}]^{-1}\mathbf{E}'\mathbf{y}$ and therefore \mathbf{p} is the projection of \mathbf{y} onto the column space of \mathbf{E} . If such additional information is not available, the solution of Eq. (5) is the one that has minimum length. That solution is generally called the minimum norm solution and is given by the pseudoinverse

$$\mathbf{x}^\# = \mathbf{E}^\# \mathbf{y}. \quad (6)$$

The pseudoinverse $\mathbf{E}^\#$ is efficiently computed through the singular value decomposition⁷ (SVD) of matrix \mathbf{E} , $\mathbf{E} = \mathbf{U}\mathbf{S}\mathbf{V}'$, which provides a way of dealing with the rank of \mathbf{E} by analysis of the singular spectra, $\sigma_1, \sigma_2, \dots, \sigma_T$, diagonal entries of \mathbf{S} , and further selection of the significant σ_i in the SVD. However, such selection can not be done in a unique manner since it generally depends on the particular charac-

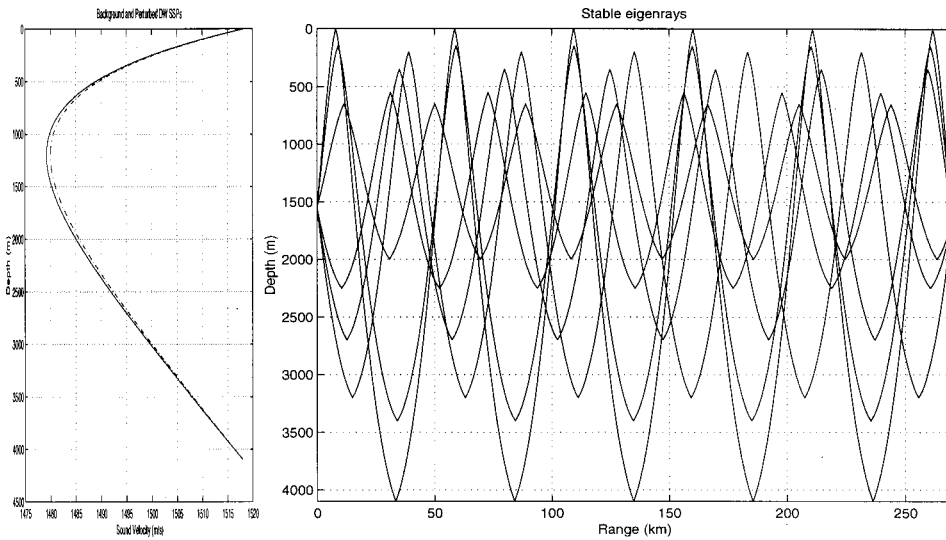


FIG. 2. Deep water test: Background $c_0(z)$ (dotted-dashed line) and perturbed $c(z)$ (continuous line) SSPs (left); stable eigenrays (right).

teristics of the problem. And even with the SVD solution being a minimum norm solution, nothing guarantees that such solution will be close to the searched solution, which is to say that minimizing $\|\mathbf{x}^\#\|$ does not imply the minimization of $\|\mathbf{x}^\# - \mathbf{x}\|$.

Finally, once the rank of the kernel matrix has been calculated, the minimum norm solution can be written as

$$\mathbf{x}^\# = \mathbf{V}_r \mathbf{S}_r^{-1} \mathbf{U}_r^t \mathbf{y}, \quad (7)$$

where subscript $r = \text{rank}(\mathbf{E})$, and denotes that matrices \mathbf{V} and \mathbf{U} are formed by their r first singular vectors, and matrix \mathbf{S}_r is square with its first (highest) singular values along the diagonal.

III. SIMULATION TESTS

Using the theoretical background presented in the previous section, travel-time-based tomographic inversion through ray-tracing simulations is tested to determine the number of independent arrivals in both deep and shallow water scenarios. For each scenario a background and a perturbed sound-speed profile (SSP) are chosen in order to obtain a negative perturbation of sound speed, which corresponds to positive perturbations in travel time. For each SSP a set of eigenrays is calculated and the set of stable eigenrays, resolved arrivals, and corresponding perturbations in travel time are determined. The kernel matrix, \mathbf{E} , is constructed with the stable eigenrays and then the inverse solution is calculated from its SVD. When dealing with real data the number of independent eigenrays N (which is the same as the number of independent arrivals) can be estimated by using statistical criteria.^{6,8} Since the test case presented here is fully deterministic, an alternative method for estimating the rank of matrix \mathbf{E} is proposed. That method takes advantage of the structure of the inverse solution based on the SVD of the kernel matrix, which was discussed in the previous section, and introduces the following functional:

$$E(i) = \frac{\|\mathbf{x}_i^\# - \mathbf{x}\|^2}{\|\mathbf{x}_i^\#\|^2}, \quad (8)$$

where $\mathbf{x}_i^\#$ is the inverse solution obtained from Eq. (7) and calculated with the first i singular values. The ‘‘real’’ perturbation \mathbf{x} is calculated from $\delta c(z)$ (which is known in our simulated case) according to the adopted depth discretization. Using the functional $E(i)$ one can obtain the following estimator of the number of independent arrivals N :

$$\hat{N} = \arg\{\min_i E(i)\}. \quad (9)$$

The minimum of $E(i)$ does not have to be a minimum in the conventional sense since solutions with $N=1$ or $N=T$ will also be admitted. If $N=T$ (which should not be surprising) the natural conclusion is that all resolved arrivals are independent and therefore they all contribute with independent information to the tomographic inversion. However, if $N < T$ (and from ray tracing there is no apparent reason for this to be so), then the unexpected conclusion is that only N of T resolved arrivals are independent, and the remaining $N-T$ convey redundant information. Those redundant arrivals will not contribute with additional information to the tomographic inversion. It will be shown in the following subsections that in deep water one obtains the ‘‘expected’’ conclusion ($N=T$), while in shallow water part of the resolved arrivals are redundant, i.e., $N < T$.

A. Deep water test

The well-known analytical expression for the Munk velocity profile was used to generate the SSPs (see left panel of Fig. 2). Following the geometry of a real experiment⁴ the acoustic source and the receiver depths are $z_s = 1500$ and $z_r = 1650$ m, respectively, the depth of the acoustic waveguide is $D = 4100$ m, and the distance separating the source and the receiver is $R = 270$ km. The asymmetry $z_s \neq z_r$ is intentional. In fact, as discussed by Munk *et al.*,² by locating both source and receiver at the same depth one gets symmetric eigenrays, with turning points at the same depths. Therefore, those eigenrays sample the ocean in the same way and constitute a preliminary source of redundancy in the kernel matrix, which should be avoided. After eigenray ray tracing for the background and the perturbed SSPs, a set of five RR stable eigen-

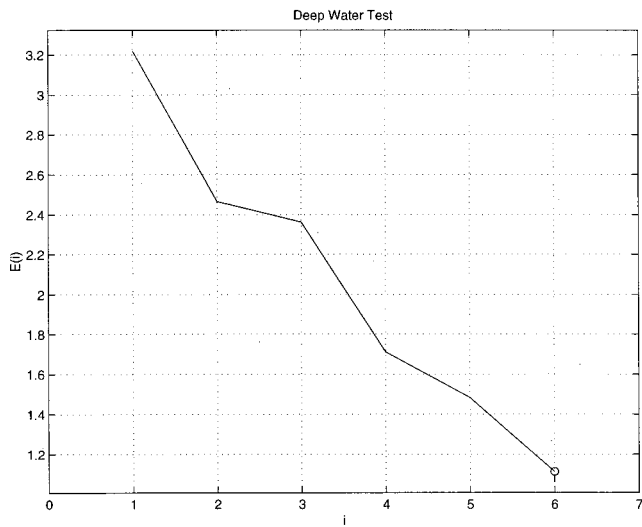


FIG. 3. Deep water test: Estimation of independent arrivals; the projection of the minimum [Eq. (8)] onto the horizontal axis indicates the number of independent arrivals N .

rays and one surface-reflected–bottom-reflected (SRBR) stable eigenray were found (see right panel of Fig. 2). The reflected eigenray should be considered in a somehow formal way (in fact this is the only eigenray that spans the entire water column) since in real conditions the amplitude of SRBR eigenrays is difficult to detect over the level of environmental noise.⁹ Using Eq. (8) it can be found that $N=6$ (see Fig. 3). From this result it can be concluded that all the resolved arrivals are independent and this is the “expected” conclusion.

B. Shallow water test

The shallow water background SSP for this test corresponds to the mean profile from conductivity, temperature, depth (CTD) data used in Jesus *et al.*,⁶ a particular profile from the same data was considered to be representative of the perturbed SSP (see left panel of Fig. 4). The geometry of propagation was taken also from that reference, with the

acoustic source at depth $z_s=90$ m, the hydrophone at depth $z_r=115$ m and range $R=5.6$ km, and the total depth of the waveguide being $D=135$ m. As in the deep water test, the asymmetry $z_s \neq z_r$ avoids the redundancy of symmetric eigenrays with equal turning depths. From ray tracing it can be found that all eigenrays are of RBR or SRBR types (see Fig. 5). The RBR eigenrays [Fig. 5(a)] are not stable (see left box of right panel of Fig. 4) and therefore they can not be used in the tomographic inversion. The SRBR eigenrays [Fig. 5(b)] are stable and “clustered” in quadruplets and are, therefore, suitable for inversion purposes (see right box on right panel of Fig. 4). In general, the clustering of arrivals depends on the particular characteristics of the waveguide geometry and associated SSP. For the shallow water environment and SSP of this test one can remark that each quadruplet contains the arrival times τ , ordered according to the general sequence,

$$(\tau_{2m-1}^+, \tau_{2m}^+, \tau_{2m}^-, \tau_{2m+1}^-), \quad (10)$$

where the index of each τ represents the number of reflections on the surface or bottom of the corresponding eigenray, a “+” or a “-” sign indicates whether that eigenray was launched toward the surface or toward the bottom, respectively. To calculate the kernel matrix an homogeneous layer grid was introduced. Each layer has a thickness $\Delta z=4$ m, which is four times more than the spatial resolution of the discretized sound-speed profile. The depth of every layer interface was coincident with every fourth depth of the discretized sound speed. To simplify the calculations, additional interfaces were added at depths z_s , z_r , and D , which were not included in the homogeneous grid. Thus a total of 36 layers was used to calculate the kernel matrix. The sound speed for each layer was the average of the discretized sound speeds contained within the layer. The functional $E(i)$ was calculated considering a total of 20 resolved arrivals. However, its minimum is reached at $N=4$ (see Fig. 6), which indicates that only 4 of the 20 resolved arrivals are independent, while the other 16 are redundant. It should be remarked that this result is in agreement with a statistical estimation of uncorrelated paths presented in Jesus *et al.*⁶ It is clear that

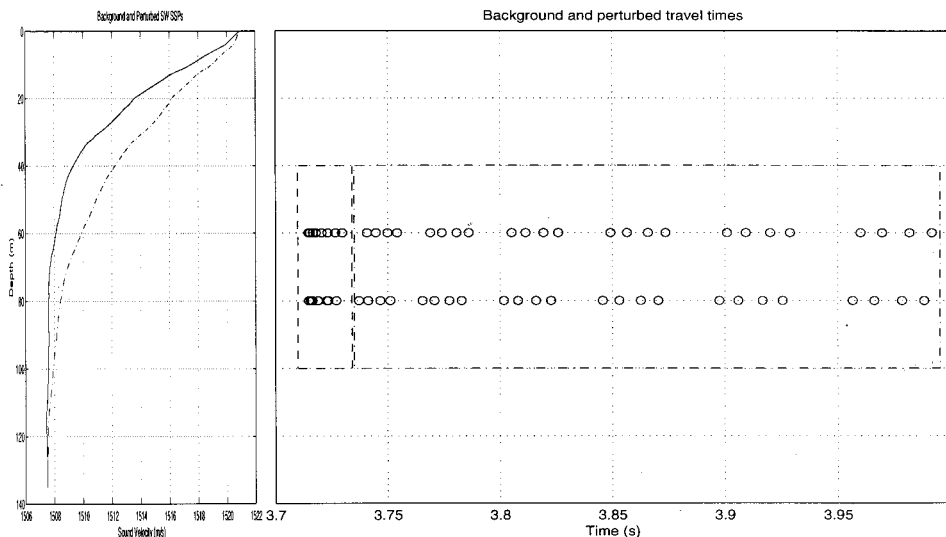


FIG. 4. Shallow water test: Background $c_0(z)$ (dotted-dashed line) and perturbed $c(z)$ (continuous line) SSPs (left); background τ_0 (lower sequence) and τ (upper sequence) travel times (right), left box indicates unstable arrivals, right box indicates resolved arrivals.

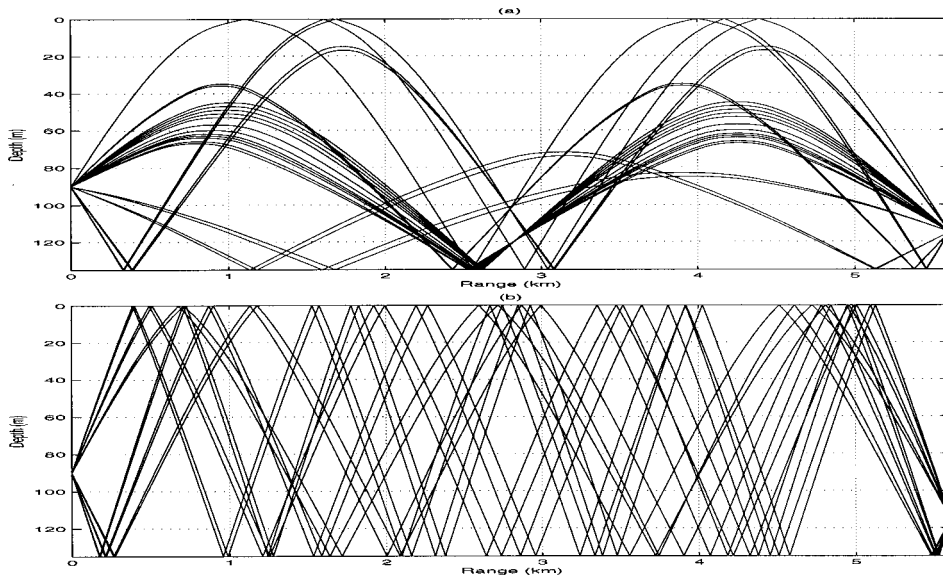


FIG. 5. Rays of propagation for unstable arrivals (a) and stable arrivals (b). (For simplicity only the first three quadruplets are shown.)

the result depends deeply on the particular structure of the kernel matrix, which will be discussed in the following section.

IV. DISCUSSION

The simulation results obtained in the previous section show that the number of independent arrivals (and therefore, of independent eigenrays) can be much lower than the number of resolved arrivals. It follows from those results that there are fundamental physical limitations to the number of independent parameters available for travel-time tomography. However, the general understanding of the simulation results still remains incomplete because those results only say *how many* of the eigenrays are independent, but they do not say *which* are the independent eigenrays and the reason for being so. Intuitively it seems reasonable to admit that each set of eigenrays, corresponding to a particular quadruplet, are independent, and therefore, that each of those eigen-

rays contains a “piece” of independent information. In mathematical terms this assumption states not only that $\text{rank}(\mathbf{E})=4$, but also that for a given quadruplet q the corresponding four rows in \mathbf{E} are linearly independent, and can be used to calculate the four rows of any other quadruplet. However, within the context of ray theory there is not a clear explanation to support this assumption. In part this is due to the fact that, for a generic sound-speed profile $c_0(z)$, one can not derive explicit analytic expressions for each row \mathbf{e}_i of the kernel matrix, thus “hiding” any possible dependence between different sets of rows. In general, for a shallow water waveguide, one can expect that most of the SRBR eigenrays are characterized by steep launching angles and by a significant number of reflections on both surface and bottom. As the number of reflections increases, the shape of the SRBR eigenrays tends to be closer to straight lines. Therefore, for a waveguide geometry like the one discussed in the shallow water test, but with an equivalent—constant—sound-speed profile, the isovelocity kernel matrix can provide a reasonable approximation to the original matrix \mathbf{E} . Moreover, for a constant c_0 , each row of E can be explicitly calculated, making it possible to understand which eigenrays are the independent ones. Those results can provide fundamental knowledge related to the structure of the original kernel matrix, and thus provide an answer to the questions discussed in the beginning of this section.

In general, an SRBR eigenray launched to the surface can arrive at the hydrophone after being reflected an odd number of times $2m-1$, or after being reflected an even number of times $2m$, where m can take the values $1, 2, \dots$. The same kind of reasoning can be applied to an SRBR eigenray being launched to the bottom. Thus for a fixed m , there are four types of eigenrays connecting source and receiver. In the isovelocity case the launching angles of these four eigenrays can be derived by inspection and are given by

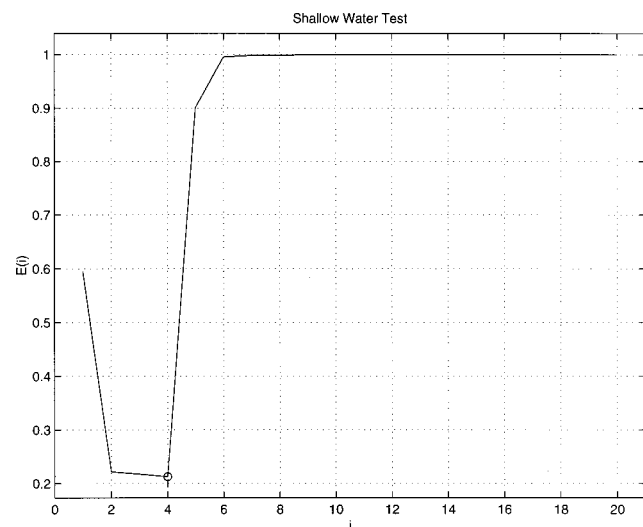


FIG. 6. Shallow water test: Estimation of independent arrivals; the projection of the minimum [Eq. (8)] onto the horizontal axis indicates the number of independent arrivals N .

$$\tan \theta_{2m-1}^+ = \frac{(2m-2)D + z_s + z_r}{R},$$

$$\begin{aligned}\tan \theta_{2m}^+ &= \frac{2mD + z_s - z_r}{R}, \\ \tan \theta_{2m-1}^- &= \frac{2mD - z_s - z_r}{R}, \\ \tan \theta_{2m}^- &= \frac{2mD - z_s + z_r}{R},\end{aligned}\quad (11)$$

where the convention of the “+” or a “-” sign was already introduced in the discussion of the shallow water test. The number of total reflections is given by the index of each θ . There is no practical sense in calculating the θ_m for large values of m because the contribution of a particular eigenray to the pressure field decreases as the number of reflections increases. Furthermore, the arrival times correspond to

$$\tau_m^{+/-} = \frac{R}{c_0 \cos \theta_m^{+/-}}. \quad (12)$$

For an isovelocity SSP the clustering of arrivals depends mainly on the particular values of z_s , z_r , D , and R . However, by taking the values used in the shallow water test, and taking $c_0 = 1510$ m/s, it can be found that the set of four arrivals will be ordered again according to the general sequence Eq. (10). For the sake of simplicity let us consider further that the linear inversion is performed with a set of q quadruplets, so $T = 4q$. A simple choice of the layer system consists in selecting a homogeneous grid composed of L layers, each with a thickness $\Delta z = D/L$. The layer thickness will be taken sufficiently small to separate the source and the receiver with at least a single layer, i.e., the layer indexes will obey the following order:

$$j = 1, 2, \dots, L = 1, 2, \dots, S, S + 1, \dots, R, R + 1, \dots, L. \quad (13)$$

The indexes S and R correspond to the integer parts of $z_s/\Delta z$ and $z_r/\Delta z$, respectively. Furthermore, for the travel-time sequence given by Eq. (10) the isovelocity kernel matrix can be written as

$$\begin{aligned}\mathbf{E} &= \begin{bmatrix} \mathbf{e}_1 \\ \mathbf{e}_2 \\ \mathbf{e}_3 \\ \mathbf{e}_4 \\ \mathbf{e}_5 \\ \vdots \\ \mathbf{e}_T \end{bmatrix} = \begin{bmatrix} [\Delta s_{11} \Delta s_{12} \cdots \Delta s_{1L}] / c_0^2 \\ [\Delta s_{21} \Delta s_{22} \cdots \Delta s_{2L}] / c_0^2 \\ [\Delta s_{31} \Delta s_{32} \cdots \Delta s_{3L}] / c_0^2 \\ [\Delta s_{41} \Delta s_{42} \cdots \Delta s_{4L}] / c_0^2 \\ [\Delta s_{51} \Delta s_{52} \cdots \Delta s_{5L}] / c_0^2 \\ \vdots \\ [\Delta s_{T1} \Delta s_{T2} \cdots \Delta s_{TL}] / c_0^2 \end{bmatrix} \\ &= \begin{bmatrix} \alpha_{2M-1}^+ \times \mathbf{e}_{2M-1}^+ \\ \alpha_{2M}^+ \times \mathbf{e}_{2M}^+ \\ \alpha_{2M}^- \times \mathbf{e}_{2M}^- \\ \alpha_{2M+1}^- \times \mathbf{e}_{2M+1}^- \\ \alpha_{2M+1}^+ \times \mathbf{e}_{2M+1}^+ \\ \vdots \\ \alpha_{2M+2q-1}^- \times \mathbf{e}_{2M+2q-1}^- \end{bmatrix},\end{aligned}\quad (14)$$

where $\alpha_m^{+/-} = (c_0^2 \sin \theta_m^{+/-})^{-1}$, and the index $2M-1$ represents the number of even reflections of the first eigenray within the first quadruplet. The rows $\mathbf{e}_m^{+/-}$ are given by

$$\begin{aligned}\mathbf{e}_{2m-1}^+ &= [2m\Delta z \ 2m\Delta z \cdots (2m-S)\Delta z \\ &\quad + z_s(2m-1)\Delta z \cdots (2m-1-R)\Delta z \\ &\quad + z_r(2m-2)\Delta z \cdots (2m-2)\Delta z], \\ \mathbf{e}_{2m}^+ &= [2m\Delta z \ 2m\Delta z \cdots (2m-S)\Delta z + z_s(2m-1)\Delta z \cdots \\ &\quad (2m-1+R)\Delta z - z_r 2m\Delta z \cdots 2m\Delta z], \\ \mathbf{e}_{2m}^- &= [2m\Delta z \ 2m\Delta z \cdots (2m+S)\Delta z \\ &\quad - z_s(2m+1)\Delta z \cdots (2m+1-R)\Delta z \\ &\quad + z_r 2m\Delta z \cdots 2m\Delta z], \\ \mathbf{e}_{2m+1}^- &= [2m\Delta z \ 2m\Delta z \cdots (2m+S)\Delta z \\ &\quad - z_s(2m+1)\Delta z \cdots (2m+1+R)\Delta z \\ &\quad - z_r(2m+2)\Delta z \cdots (2m+2)\Delta z].\end{aligned}\quad (15)$$

It follows from the previous set of equations that the rows $\mathbf{e}_m^{+/-}$ can be calculated recursively, through the relationship

$$\mathbf{e}_{2m+1}^{+/-} - \mathbf{e}_{2m-1}^{+/-} = \mathbf{e}_{2m+2}^{+/-} - \mathbf{e}_{2m}^{+/-} = [2\Delta z \ 2\Delta z \cdots 2\Delta z]. \quad (16)$$

As shown by Eqs. (15), every four rows \mathbf{e}_i corresponding to a given quadruplet are independent. Furthermore, since α_i is a common factor to all the components of each row \mathbf{e}_i , the set Eqs. (16) indicates the linear dependence between each pair of rows \mathbf{e}_i and \mathbf{e}_{i+4} . In this way, the previous analysis of the isovelocity kernel matrix indicates not only *how many* of the eigenrays are independent [since the analysis shows that $\text{rank}(\mathbf{E}) = 4$], but indicates also in detail *which* are the independent eigenrays. For the case of a more generic sound-speed profile $c_0(z)$, as the number of reflections increases, one notes that the slope of each SRBR eigenray approaches a constant, given by the slope of the launching angle $\tan \theta$. Also significant is that the length of a single eigenray crossing a particular layer approaches the ratio $\Delta z / \sin \theta$. In this way, the general structure of Eqs. (15) suggests that, for the shallow water test, each row of \mathbf{E} can be approximated as

$$\mathbf{e}_i \approx \alpha_i \times \left[M_{i1} \frac{\Delta z}{c_{01}^2} M_{i2} \frac{\Delta z}{c_{02}^2} \cdots M_{iL} \frac{\Delta z}{c_{0L}^2} \right], \quad (17)$$

where $\alpha_i = (\sin \theta_i)^{-1}$ and M_{ij} represents the number of times that the eigenray i crosses the layer j . Through further analogy the set Eqs. (15) guarantees that there are at least four different types of row components (since the layer thickness is not a common factor), and that guarantees the linear independence of those four rows \mathbf{e}_i , corresponding to a particular quadruplet. The analogy to Eqs. (15) allows one to note also that

$$\mathbf{e}_{i+4} \approx \alpha_{i+4} \times \left[(M_{i1} + 2) \frac{\Delta z}{c_{01}^2} (M_{i2} + 2) \frac{\Delta z}{c_{02}^2} \cdots (M_{iL} + 2) \frac{\Delta z}{c_{0L}^2} \right], \quad (18)$$

which brings back the linear dependence between each pair of rows \mathbf{e}_i and \mathbf{e}_{i+4} . Thus the analysis of the isovelocity kernel matrix, and its analogy to the kernel matrix of the original shallow water waveguide, provide a full understanding of the results of the shallow water test.

V. CONCLUSIONS

On the basis of this analysis the following conclusions can be drawn: (1) in the context of travel-time-based shallow water tomography it is of fundamental importance to determine the number of independent resolved arrivals; (2) with real data the estimation of independent arrivals can be done through statistical tests, while in simulations the estimation can be performed by comparison of the inverse and expected solution; (3) it can be shown through ray-tracing simulation and under the condition of placing the source and the receiver at different depths, that in deep water the number of independent arrivals is equal to the number of resolved arrivals; corresponding simulations in shallow water reveal that the number of independent arrivals is much smaller than the number of actually measured—resolved—arrivals; (4) finally, the problem of travel-time redundancy in the shallow water waveguide is fully explained through the detailed analysis of the kernel matrix of an equivalent isovelocity waveguide, where the rows of the isovelocity matrix show a fundamental rank deficiency of the kernel matrix associated with the original shallow water waveguide.

ACKNOWLEDGMENTS

The authors deeply want to thank the reviewers for the interest they have shown in the discussion of the material

presented in this publication. Their detailed remarks concerning some incomplete aspects of the material presented in the first version of the manuscript undoubtedly guided the authors to develop a fundamental improvement of that material.

- ¹W. Munk and C. Wunsch, "Ocean acoustic tomography: A scheme for large scale monitoring," *Deep-Sea Res., Part A* **26**, 123–161 (1979).
- ²W. Munk, P. Worcester, and C. Wunsch, "Ocean acoustic tomography," Cambridge Monographs on Mechanics, New York, 1995.
- ³Y. Stéphan and S. Thiria, "Neural inversions for ocean acoustic tomography," in *Inverse Problems in Engineering Mechanics*, edited by Bui Tanaka *et al.* (Balkema, 1994).
- ⁴S. Prasanna, Y. K. Somayajulu, T. V. Ramana, G. S. Navelkar, A. K. Saran, A. M. Almeida, and C. S. Murty, "Preliminary results of an acoustic tomography experiment (ATE-93) in the eastern Arabian Sea," Proceedings of the 2nd European Conference on Underwater Acoustics, edited by L. Bjorno, 1994.
- ⁵C-S. Chiu, J. H. Miller, and J. F. Lynch, "Inverse techniques for coastal acoustic tomography," in *Environmental Acoustics*, edited by D. Lee and M. Schultz (World Scientific, Singapore, 1994).
- ⁶S. M. Jesus, M. B. Porter, Y. Stephan, X. Démoulin, O. Rodríguez, and E. Coelho, "Single hydrophone source localization," *IEEE J. Ocean Eng.* **25**(3), 337–346 (2000).
- ⁷W. Menke, *Geophysical Data Analysis: Discrete Inverse Theory* (Academic, San Diego, 1989).
- ⁸M. Wax and T. Kailath, "Detection of signals by information theoretic criteria," *IEEE Trans. Acoust., Speech, Signal Process.* **33**, No. 2, 387–392 (1985).
- ⁹I. Tolstoy and C. S. Clay, *Ocean Acoustics, Theory and Experiment in Underwater Sound* (AIP, New York, 1987).

On a novel application of the Helmholtz integral in the development of a virtual sonar

Anthony J. Romano

Naval Research Laboratory, Washington, DC 20375-5350 and SFA, Inc., Largo, Maryland 20785

Joseph A. Bucaro, Brian H. Houston, and Earl G. Williams

Naval Research Laboratory, Washington, DC 20375-5350

(Received 21 April 2000; revised 17 August 2000; accepted 31 August 2000)

A novel application of the Helmholtz integral is presented in the development of a virtual sonar. Given total pressure and normal velocity information over the surface of a structure which has been excited both by incident fields as well as interior noise sources, when the Helmholtz integral is evaluated at field points located within the surface of the structure (using the free-space Green's function characteristic of the exterior medium), only the incident field remains. Therefore, it is possible to remove the effects of both scattering (due to incident excitation) and radiation (due to interior noise sources) throughout a "virtual" volumetric sonar array projected within the structure. This approach will be discussed and demonstrated using numerical results based on finite element simulations. © 2000 Acoustical Society of America. [S0001-4966(00)00112-0]

PACS numbers: 43.30.Vh, 43.30.Wi [DLB]

I. INTRODUCTION

The effects of noise on the response of sonar arrays is an important and relevant problem.¹ Such contamination directly conditions minimum detectable signal levels, and in actual systems can pose limitations on the array response. For hull mounted acoustic arrays, the situation is particularly complicated by the presence of the structure which can contribute to this problem through both structure-borne noise and sensor backing impedance variations.

It is well known that the scattered and radiated response of a structure (for field points exterior to its surface) can be obtained from the evaluation of the Helmholtz integral over the surface of the structure given a knowledge of total pressure and normal velocity. It is also well known that the *incident* field can be recovered by an evaluation of this same integral for field points *inside* the surface of the structure. Previously, these features have been simultaneously implemented to overcome nonuniqueness issues in forward scattering formalisms.²⁻⁴ In this paper however, we investigate the implications of the second feature in the development of a method for dealing with structure-borne noise and impedance effects. With this method, it is possible to construct a "virtual" volumetric sonar array projected within the surface of the structure which is free from the effects of structure-borne noise and variations in the impedance of the structure.

We begin with some fundamental representations of the Helmholtz integral and proceed to demonstrate the ideas outlined above using results from finite element simulations. Finally, we address issues dealing with spatial sampling criteria, measurement error, and sensor noise.

II. THEORETICAL BACKGROUND

Consider an arbitrary structure as shown in Fig. 1, defined by a surface, $\Gamma(r_0)$, with the interior volume represented as $\Omega^-(r)$ and exterior volume as $\Omega^+(r)$. Addition-

ally, consider that the exterior volume is comprised of a fluid with density ρ and wave speed c , and that the interior volume is comprised of an arbitrary medium. Let us assume that the structure is subject to both incident acoustic, $P_i(\mathbf{k}, r)$, and internal structural, $f(\omega)$, monochromatic excitation (at the angular frequency ω), and that we are given a knowledge of the resulting total pressure and normal velocity over the exterior surface, $\Gamma(r_0)$, of this structure. Our goal is then to obtain a knowledge of the incident field free from any scattered or radiated components.

For canonically shaped structures (e.g., geometries expressible in separable coordinates), solutions for the incident and scattered/radiated fields (given a knowledge of total surface pressure and normal velocity) can be obtained in terms of appropriate representations of the incident and scattered/radiated basis functions and a 2×2 solution of the equations relating total pressure and normal velocity to these expansions. For example, in cylindrical coordinates, the incident and scattered/radiated pressure fields may be expressed as

$$P_i(r) = \frac{1}{2\pi} \int_{-\infty}^{\infty} \sum_n P_n^i(k_z) J_n(\sqrt{k^2 - k_z^2} r) e^{in\theta} e^{ik_z z} dk_z$$

and

$$P_s(r) = \frac{1}{2\pi} \int_{-\infty}^{\infty} \sum_n P_n^s(k_z) H_n^{(1)}(\sqrt{k^2 - k_z^2} r) e^{in\theta} e^{ik_z z} dk_z,$$

respectively, where $k = \omega/c$, and k_z is the axial wave number. Since the velocity is related to these expressions through the linear inviscid force equation [$\rho(\partial \mathbf{V}/\partial t) = -\nabla P$, where ρ is the fluid density], a solution for the unknown coefficients ($P_n^i(k_z)$, $P_n^s(k_z)$) can be obtained from the two equations relating total pressure and normal velocity to these expansions. In general, however, many practical structures do not have surfaces which are so accommodating as to permit such

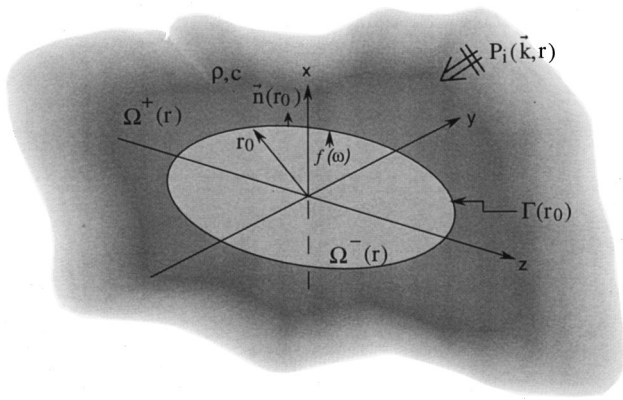


FIG. 1. Arbitrary reference structure.

separability. In such instances, the integral approach presented here remains completely valid.

By way of review, we present the following forms of the Helmholtz integral as shown below in Eqs. (1)–(3):⁵

$$\int_{\Gamma} \left(P_i(r_0) \frac{\partial G}{\partial n_{r_0}}(r, r_0) - j\omega\rho V_i^n(r_0)G(r, r_0) \right) d\Gamma(r_0) = \begin{cases} -P_i(r), & r \in \Omega^-(r); \\ -\frac{1}{2}P_i(r), & r \in \Gamma(r_0); \\ 0, & r \in \Omega^+(r); \end{cases} \quad (1)$$

$$\int_{\Gamma} \left(P_s(r_0) \frac{\partial G}{\partial n_{r_0}}(r, r_0) - j\omega\rho V_s^n(r_0)G(r, r_0) \right) d\Gamma(r_0) = \begin{cases} 0, & r \in \Omega^-(r); \\ \frac{1}{2}P_s(r), & r \in \Gamma(r_0); \\ P_s(r), & r \in \Omega^+(r); \end{cases} \quad (2)$$

$$\int_{\Gamma} \left(P_i(r_0) \frac{\partial G}{\partial n_{r_0}}(r, r_0) - j\omega\rho V_i^n(r_0)G(r, r_0) \right) d\Gamma(r_0) = \begin{cases} -P_i(r), & r \in \Omega^-(r); \\ \frac{1}{2}(P_s(r) - P_i(r)), & r \in \Gamma(r_0); \\ P_s(r), & r \in \Omega^+(r). \end{cases} \quad (3)$$

In these expressions, G is the free space Green's function represented as

$$G(r, r_0) = \frac{e^{ik|r-r_0|}}{4\pi|r-r_0|},$$

$P_i(r_0) = P_i(r_0) + P_s(r_0)$, where $P_i(r_0)$ and $P_s(r_0)$ are the incident and scattered/radiated pressure fields, respectively, and $V_i^n(r_0) = V_i^n(r_0) + V_s^n(r_0)$, where $V_i^n(r_0)$ and $V_s^n(r_0)$ are the incident and scattered/radiated, normal velocity components.

As can be observed from Eq. (3), given a knowledge of the total surface pressure and normal velocity, the incident field can be recovered when the field point, r , is evaluated inside $\Gamma(r_0)$ [i.e., $r \in \Omega^-(r)$], the scattered and/or radiated fields can be recovered when the field point is evaluated outside $\Gamma(r_0)$ [i.e., $r \in \Omega^+(r)$], while on $\Gamma(r_0)$, the integral

yields the corresponding limiting value of $\frac{1}{2}(P_s(r_0) - P_i(r_0))$. These are fundamental properties of the Helmholtz integral, and they have rather important implications for our development. In particular, *when the field is evaluated inside $\Gamma(r_0)$ [in $\Omega^-(r)$], only the incident field remains, i.e., the total response due to both an incident waveform and/or any interior noise sources integrate to zero when the field is evaluated within $\Gamma(r_0)$* . The proofs of these results are well known and exist in the literature.⁶ This is significant in that both the scattered structural response due to an incident waveform, as well as any radiation due to interior sources, can be identically removed from an array response when the Helmholtz integral is evaluated for field points *within* the surface of the sensor array. It should be pointed out here that the integral in all cases utilizes the density and wave number of the exterior medium. Therefore, when the integral is evaluated at field points interior to the surface, it does not yield the actual sound field *inside* the structure. But rather, it represents a “virtual” array which provides the incident field at the interior points *as though the structure were absent*. If it were of interest to compute the real interior field, ρ and $G(r, r_0)$ would assume values characteristic of the interior medium. However, our goal is to determine the incident field which is impinging on the structure from the exterior medium.

In what follows, we will demonstrate this feature for particular cases with numerical examples using the finite element method.

III. NUMERICAL DEMONSTRATION

A. Numerical model

The numerical results presented in this paper utilized an axisymmetric finite element model consisting of a cylindrical steel shell ($E = 19.995 \times 10^{10}$ Pa, $\nu = 0.3$, $\rho = 7799$ kg/m³, $\eta = 0.005$) with spherical endcaps and a length to diameter ratio of ≈ 8 , with 85 regular frames and 8 king frames attached to the interior surface. The response of the structure to both plane wave and point force excitation was simulated using the NRL developed finite element code SONAX.⁷

B. Helmholtz integral evaluation

As a typical example, consider the response to both a plane wave (of magnitude 1 Pa) incident at 45 degrees and a point force (of magnitude 1 N) driving the shell at its center for $ka = 5$. The finite element program yielded total pressure and velocity information on the surface for 1191 equally spaced axial locations and 411 equally spaced circumferential locations. This discretization led to equally spaced data points both axially and circumferentially over the cylindrical section such that $\Delta z = a\Delta\theta$, where a is the cylinder radius, and appropriate discretizations over the spherical endcaps. This spacing permitted approximately eight samples over the smallest structural wavelength of interest, with a resulting spatial (axial) Nyquist frequency of 175.6 radians/meter. With a knowledge of the total surface pressure and velocity, Eqs. (1)–(3) were then implemented for determining the pressure field both outside ($r \in \Omega^+(r)$) and inside ($r \in \Omega^-(r)$) the surface of the structure.

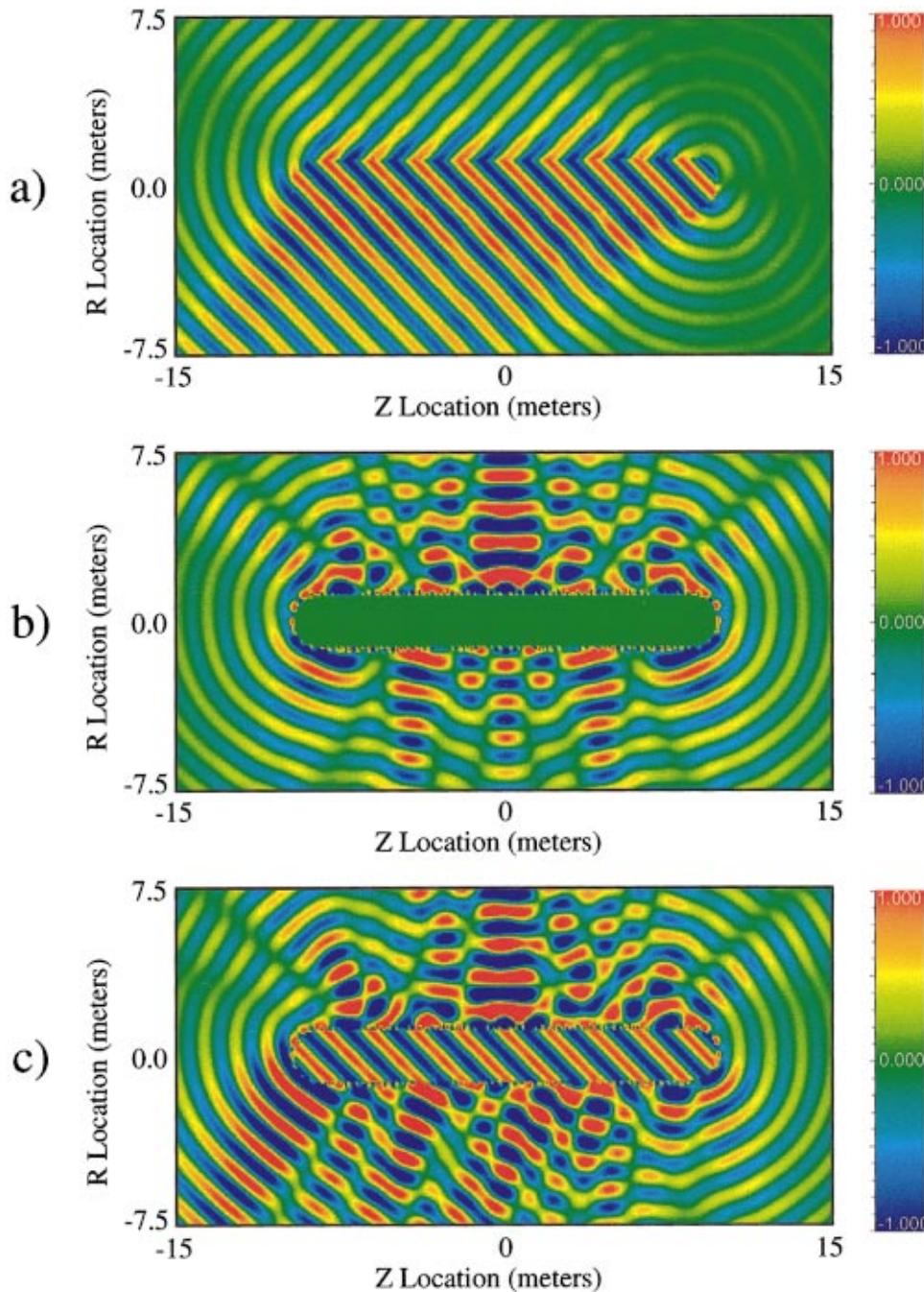


FIG. 2. Helmholtz integral results due to (a) incident field at 45° , (b) point force, (c) total field.

In Fig. 2(a), we show the exterior and virtual interior pressure fields due to the plane wave response alone, in Fig. 2(b), we show the exterior and virtual interior pressure fields due to the point force response, and in Fig. 2(c), we show their linear superposition. Although the figures have amplitude limits of ± 1 Pa, the actual resulting pressure amplitude due to the point force has maxima reaching ≈ 50 Pa, clearly dominating the superposition in the exterior domain. For our virtual interior array inside the structure, however, Eqs. (1)–(3) require that the point force and scattered field responses integrate to zero, while the incident field contribution yields $-P_i$. It should be pointed out that the surface “jitter” in Figs. 2(b) and (c) is due to the surface and near field response caused by the frames attached to the interior.

In Fig. 3, we show the Helmholtz integral evaluation

[Eq. (3)] with r both inside and outside the structure compared with the negative of the incident field over the same area. We then compare these fields along the line $(0,0,z)$ through the axis of the cylinder. As can be seen, for evaluation within the structure, recovery of the incident field is excellent. Outside the structure, the integral yields the scattered field. The “spikes” in the pressure amplitude for the predicted field (red curve in Fig. 3) at either end of the structure are due to the actual values on the exterior surface.

In Fig. 4, we compare the spatial Fourier transform along the z axis over the length of the cylindrical section of (a) the incident field evaluated along the central axis, (b) the interior field evaluated by means of the Helmholtz integral along the central axis of the structure, and (c) the total surface field on a line on $\Gamma(r_0)$ along the lateral surface on the

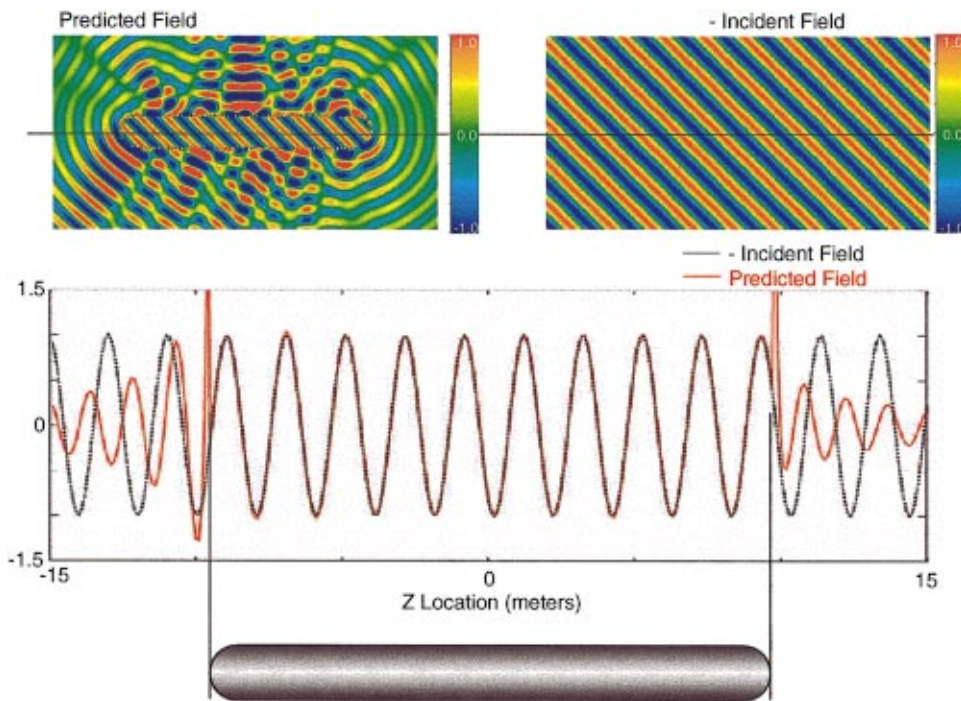


FIG. 3. Comparison of the virtual field along a line through the center of the structure, and the negative of the incident field.

cylindrical structure. This comparison was intended to demonstrate the effect of noise contamination on the response of a surface mounted line array and the corresponding lack of noise contamination on the response of a virtual line array projected within the interior of the structure. As can be seen, the transform of the interior array response is nearly identical to the transform of the incident field, while the transform of the surface array response contains a broad spectrum of wave number components, thus masking the incident field response.

IV. EFFECTS OF SENSOR SAMPLING, PLACEMENT ERROR, NONUNIFORMITY OF SENSOR RESPONSE, AND SENSOR NOISE

In this section, we investigate the effects of some practical issues such as required spatial sensor sampling, random

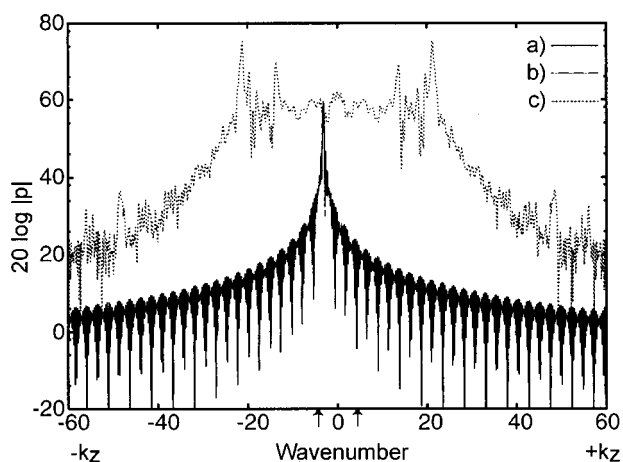


FIG. 4. Comparison of the spatial (axial) Fourier transform over the length of the cylindrical section of the pressure for (a) the incident field evaluated along the central axis of the cylinder, (b) the interior field projection along the central axis of the cylinder, and (c) the total surface response along a line on the lateral surface of the cylinder. Arrows indicate fluid wave numbers.

error in sensor location estimation, nonuniformity of sensor response, and sensor noise. As will be seen, other than being subject to standard spatial sampling requirements, the integral is rather impervious to placement and noise issues.

A. Sensor sampling criteria

As mentioned above, the finite element code yielded surface pressure and normal velocity over the surface of the structure at 1191 equally spaced data locations along the z axis and 411 equally spaced data locations around the circumference. It was also pointed out that this discretization permitted approximately eight spatial samples over the smallest structural wavelength of interest. With this sampling, the error in the interior projection was within 0.001% of the known incident field. To investigate the dependence of the integral on subsampling, we then decreased our spatial discretization by a factor of 5 and 10 (i.e., we *skipped* every four and every nine data points, respectively, both axially and circumferentially). Once the new subsampled array of data points was obtained, cubic splines were utilized to interpolate these sparse data points (both axially and circumferentially) to obtain the predicted surface values at the original 1191 axial and 411 circumferential data points. This was performed because experience has demonstrated that the use of cubic spline interpolation on sparse data sets can dramatically improve the results in the implementation of the Helmholtz integral.

In Fig. 5, we compare the spatial Fourier transform of the interior response evaluated along the central axis of the cylinder for (a) the fully sampled structure, (b) every fifth sample over the structure, and (c) every tenth sample over the structure. As can be seen, the virtual interior projection is still fairly good for the fifth subsample case with side band levels only slightly higher than the fully sampled integration, while the projection noticeably breaks down for every tenth subsample. This error can be understood in terms of the in-

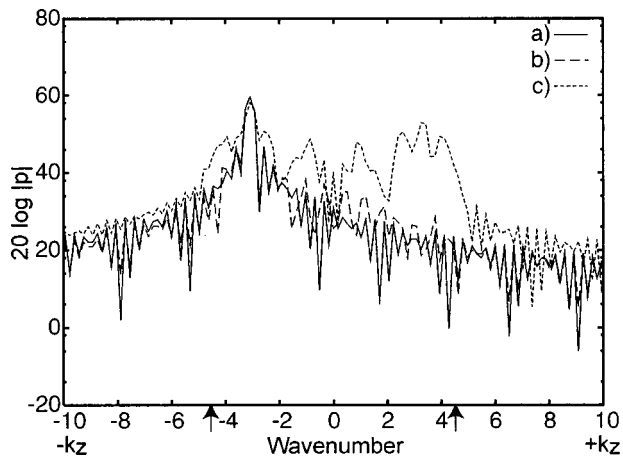


FIG. 5. Comparison of the spatial (axial) Fourier transform over the length of the cylindrical section of the pressure for interior field projection along the central axis of the cylinder for (a) full sampling, (b) every fifth sample, and (c) every tenth sample in the subsampling study. Arrows indicate fluid wave numbers.

sufficient spatial sampling of the noise spectrum induced by the point force excitation. Specifically, for the tenth subsample case, the maximum wave number associated with the spatial sampling (before cubic spline fitting) is 17.56 radians/meter. With regard to Fig. 4, we see that the surface response contains significant wave number components well above this limit. Therefore, one would expect aliasing to occur in the interior projection, which is the cause of the observed error.

B. Error induced by sensor location estimation

In this section, we investigate the effects of errors in the estimation of sensor location for the fully sampled and subsampled cases discussed above. To simulate this effect, cubic splines were first fit to the original data set at the original locations. The following manipulations were then performed for the cases specified.

For the fully sampled case, a random number generator determined both circumferential and axial perturbations from the original sampling coordinates within the spatial deviations of $\pm a\Delta\theta/4$ and $\pm\Delta z/4$. Values for the pressure and velocity at these new data points were then obtained from the original cubic spline interpolated data. These perturbed data values were then assumed to be situated at the original 411×1191 locations. That is to say, we calculated interpolated values of pressure and velocity, and assumed these values to be located at the original coordinates. In this way, we attempted to simulate errors in sensor location estimation.

For the subsampled case of every fifth sample, a random number generator determined both circumferential and axial perturbations from every fifth data location (axially and circumferentially) within spatial deviations of $\pm 5a\Delta\theta/4$ and $\pm 5\Delta z/4$. Values for the pressure and velocity at these new data points were then obtained from the original cubic spline interpolated data. These perturbed data values were then assumed to be situated at their original subsampled locations. Cubic splines were then fit to this subsampled data set and

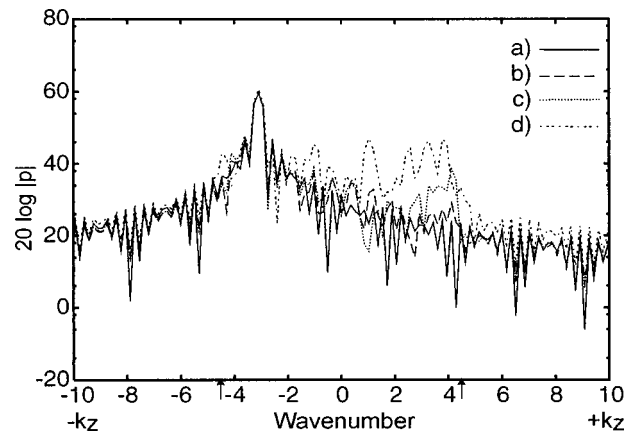


FIG. 6. Comparison of error due to sensor location estimation as a function of subsampling: Spatial Fourier transform of the virtual interior field evaluated along the central axis of the cylinder for (a) full integration, no spatial error (b) full integration with spatial error of $\pm a\Delta\theta/4$ and $\Delta z/4$, (c) every fifth sample with spatial error of $\pm 5a\Delta\theta/4$ and $\pm 5\Delta z/4$, and (d) every tenth sample with spatial error of $\pm 10a\Delta\theta/4$ and $\pm 10\Delta z/4$. Arrows indicate fluid wave numbers.

data was interpolated to the original array of 411×1191 data locations, as performed in the preceding section for improvement of integration.

For the subsampled case of every tenth sample, a random number generator determined both circumferential and axial perturbations from every tenth data location (axially and circumferentially) within spatial deviations of $\pm 10a\Delta\theta/4$ and $\pm 10\Delta z/4$. Values for the pressure and velocity at these new data points were then obtained from the original spline interpolated data. These perturbed data values were once again assumed to be situated at their original subsampled locations. Cubic splines were then fit to this subsampled data set and data was interpolated to the original array of data locations, as discussed above.

In Fig. 6, we show the spatial Fourier transform of the virtual interior field evaluated along the central axis of the cylinder for a comparison of the error due to sensor location estimation as a function of subsampling: (a) Full integration, no spatial error; (b) full integration with spatial error of $\pm a\Delta\theta/4$; and $\pm\Delta z/4$; (c) every fifth sample with spatial error of $\pm 5a\Delta\theta/4$ and $\pm 5\Delta z/4$; and (d) every tenth sample with spatial error of $\pm 10a\Delta\theta/4$ and $\pm 10\Delta z/4$. As can be observed, no significant error is incurred until subsampling approaches $\approx \pm 10a\Delta\theta/4$, $\approx \pm 10\Delta z/4$. Once again, this error can be understood in terms of spatial aliasing as discussed above.

C. Error induced by nonuniformity of sensor response and sensor noise

In this section, we investigate the effects of random nonuniformity of response among sensors and random noise present in the sensor itself. Concerning nonuniformity of response among sensors, let us assume that each sensor can measure the true pressure or velocity only to within a certain random bias for each monochromatic component of a time signal. Concerning random noise present in the sensor itself, let us assume that each sensor measures the true pressure or velocity plus an added random noise term for each mono-

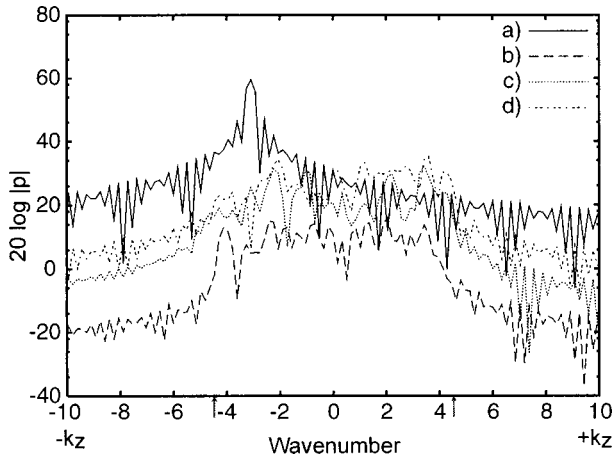


FIG. 7. Comparison of induced error in sensor noise: Spatial Fourier transform over the length of the cylindrical section of the pressure for interior field projection along the central axis of the cylinder for (a) full integration of P_t and V_t only (no error terms), (b) integration of error terms only using full sampling, (c) integration of error terms only using every fifth sample, (d) integration of error terms only using every tenth sample. Arrows indicate fluid wave numbers.

chromatic component of a time signal. Both of these effects can be generally represented as a linear superposition of the true field quantities and respective random noise terms. Let us then define our measured fields as $\hat{P}_t(r_0) = P_t(r_0) + \epsilon_p(r_0)$ and $\hat{V}_t^n(r_0) = V_t^n(r_0) + \epsilon_v^n(r_0)$, where $P_t(r_0)$ and $V_t^n(r_0)$ are defined in Sec. II, $\epsilon_p(r_0)$ is the random bias and/or noise present in the pressure sensors, and $\epsilon_v^n(r_0)$ is the random bias and/or noise present in the velocity sensors. Using Eq. (3) for $r \in \Omega^-(r)$, we have

$$\int_{\Gamma} \left(\hat{P}_t(r_0) \frac{\partial G}{\partial n_{r_0}}(r, r_0) - j\omega\rho \hat{V}_t^n(r_0) G(r, r_0) \right) d\Gamma(r_0) = \hat{P}_{\text{int}}(r), \quad (4)$$

where $\hat{P}_{\text{int}}(r)$ is the resulting virtual interior projection. Substitution of the expressions for $\hat{P}_t(r_0)$ and $\hat{V}_t^n(r_0)$ into Eq. (4) yields

$$\int_{\Gamma} \left((P_t(r_0) + \epsilon_p(r_0)) \frac{\partial G}{\partial n_{r_0}}(r, r_0) - j\omega\rho (V_t^n(r_0) + \epsilon_v^n(r_0)) G(r, r_0) \right) d\Gamma(r_0) = \hat{P}_{\text{int}}(r). \quad (5)$$

Upon inspection, we can see that $\hat{P}_{\text{int}}(r) = -P_t(r) + \epsilon_s(r)$, where $\epsilon_s(r)$ is the resulting contribution due to the sensor bias and/or noise consisting of the second and fourth terms in the integrand of Eq. (5). Therefore, the error due to either nonuniform response or inherent sensor noise ($\epsilon_s(r)$) is independent of the incident and scattered fields. A subsequent integration of the integral demonstrating the effects of random sensor bias and/or noise is shown in Fig. 7. Here, we

show the spatial Fourier transform over the cylindrical length of the structure for the virtual interior projection along the central axis of the cylinder for a comparison of induced error in sensor noise: (a) full integration of P_t and V_t only (no error terms), (b) integration of error terms only using full sampling, (c) integration of error terms only using every fifth sample, (d) integration of error terms only using every tenth sample. In this study, $\epsilon_p(r_0)$ and $\epsilon_v^n(r_0)$ were determined by a random number generator within magnitudes of ± 1 Pa and $\pm 1/\rho c$, respectively, and random phase.

As can be observed, even though the amplitude of the induced noise is on the same order as the incident field, since it has random magnitude and phase, its contributions are diminished upon integration, which is a logical result. It is also logical that as the surface fields are subsampled, the contribution of the noise would increase, as Fig. 7 demonstrates.

V. CONCLUSIONS

A novel application of the Helmholtz integral has been presented for the processing of distributed pressure and velocity sensor data for hull mounted sonar applications. It was shown that, given a measurement of total surface pressure and normal velocity over the structure, the incident field could be recovered when the integral was evaluated for field points located within the surface of the structure, even though the sensor outputs have been affected by structure-borne noise and structural impedance variations. This approach was then demonstrated using results from finite element simulations. In addition, practical issues such as required spatial sensor sampling, placement error, nonuniformity of response, and noise were also addressed. It was found that when the surface data is sufficiently sampled, the integral performance is fairly impervious to such issues. Therefore, this approach appears to yield a potentially powerful method for the development of noiseless sonar systems.

Future research in this area will focus on special cases of partial sensor coverage, the implications of using pressure or velocity contributions only, the potential of the full volumetric response of the virtual array, and the capability of determining the range of nearfield sources or scatterers.

ACKNOWLEDGMENT

This work was supported by ONR.

- ¹R. O. Nielsen, *Sonar Signal Processing* (Artech House, London, 1991).
- ²H. A. Schenck, "Improved integral formulation for acoustic radiation problems," *J. Acoust. Soc. Am.* **44**, 41–58 (1967).
- ³R. E. Kleinman and G. F. Roach, "Boundary integral equations for the three-dimensional Helmholtz equation," *SIAM Rev.* **16**, 214–236 (1974).
- ⁴D. T. Wilton, "Acoustic radiation and scattering from elastic structures," *Int. J. Numer. Methods Eng.* **13**, 123–138 (1978).
- ⁵B. B. Baker and E. T. Copson, *The Mathematical Theory of Huygen's Principle*, 2nd ed. (Oxford University Press, London, 1950).
- ⁶E. G. Williams, *Fourier Acoustics* (Academic, London, 1999).
- ⁷J. J. Shirron, "Solution of exterior Helmholtz problems using finite and infinite elements," Ph.D. thesis, Department of Applied Mathematics, University of Maryland, 1995.

Mode-selective resonance ultrasound spectroscopy of a layered parallelepiped

Hirotsugu Ogi

Graduate School of Engineering Science, Osaka University, Machikaneyama 1-3, Toyonaka, Osaka 560-8531, Japan

Paul Heyliger

Department of Civil Engineering, Colorado State University, Fort Collins, Colorado 80523

Hassel Ledbetter and Sudook Kim

Materials Science and Engineering Laboratory, National Institute of Standards and Technology, Boulder, Colorado 80303

(Received 1 March 2000; revised 11 September 2000; accepted 15 September 2000)

The resonance frequencies of mechanical free vibration of a three-layer material calculated by a discrete-layer model and measured by acoustic-resonance methods were compared. The material was composed of an aluminum parallelepiped sandwiched by two stainless-steel parallelepipeds. The discrete-layer model developed here used linear Lagrange basis functions through the layered dimension and continuous global power-series basis functions in the plane perpendicular to the layer thickness. Using such a basis function for the layer-thickness direction allows discontinuity in the elastic properties across the interface between dissimilar layers. The resonance frequencies were measured using two methods: mode-selective electromagnetic acoustic resonance (EMAR) and resonance ultrasound spectroscopy (RUS). The measurements agreed with the calculations typically within 1%. The EMAR method allows the selective detection of vibrational modes possessing particular displacement patterns. This selectivity was supported by the model calculation. Thus, using the EMAR method makes mode identification clear and this is essential for developing and improving the model calculation of such a complicated structure. Internal friction was also measured by the two acoustic methods, which reveals the mechanical-contact effect on the internal-friction measurement in the RUS method. © 2000 Acoustical Society of America.

[S0001-4966(00)04812-8]

PACS numbers: 43.35.Cg, 43.35.Zc [SGK]

I. INTRODUCTION

Layered systems are prominent in modern engineering components and applications. A layered geometry can be formed as part of shape or stiffness control, to adjust material properties for different applications, or to provide different properties in particular directions. In all cases, the characteristics of both local and global component response become significantly more complicated than for a single homogeneous layer. This is especially so in the calculation of laminate-material elastic properties. In this study, we present comparisons between a laminate-continuum model that takes into account the distinct material properties of each individual layer and experimental observations for the problem of unrestrained free mechanical vibration. Such a comparison is first made here, and it is critical to establish the model calculation to represent layered systems and to eventually adopt such a model to compute the properties for a material of unknown constitution, including a thin film on a substrate.

Concerning measurement of the resonance frequency of free vibration, we principally use electromagnetic acoustic resonance (EMAR),¹⁻⁴ which is an acoustically contactless method and can select particular vibrational modes of interest by controlling the deformation symmetry of vibration using the Lorentz-force mechanism. This mode-selective prin-

ciple provides a significant advantage for making exact correspondence between the measured and calculated resonance frequencies. Along with the resonance frequency, we measure internal friction by the free-decay method of EMAR. Also, we use the usual resonance ultrasound spectroscopy (RUS)^{5,6} for the resonance frequencies and internal friction, and discuss the effect of contacting transduction in the RUS method by comparing with the contactless EMAR results.

For the calculation of resonance frequencies, we adopt the discrete-layer model developed by Heyliger.⁷ The calculated resonance frequencies essentially showed good agreement with the measured frequencies, but agreed less well for higher modes.

II. MATERIAL

We used a diffusion-bonded three-layer parallelepiped, consisting of stainless steel (SS304), aluminum (Al3004), and stainless-steel (SS304) polycrystals. (Two stainless-steel parallelepipeds sandwiched the aluminum parallelepiped.) The dimensions of each layer are given in Table I. We measured elastic constants using the Pulse-echo method and density using Archimedes method before bonding. They are given in Table II.

TABLE I. Dimensions of the layered specimen in mm.

x	y	z_1 (SS304)	z_2 (Al3004)	z_3 (SS304)
2.982	3.988	0.394	1.477	0.465

III. DISCRETE-LAYER MODEL

The resonance frequencies of natural vibration of solids are obtainable by solving the equations of motion with boundary conditions at free surfaces. However, since the direct solutions are unobtainable for rectangular parallelepipeds, we seek approximate solutions by solving the weak form of the equations of motion. Assuming periodic particle motion and using Cartesian coordinates, where u , v , and w denote displacements along x , y , and z axes, respectively, the weak form of the equations of motion for a linear solid is reduced as^{7,8}

$$\int_V \left\{ \rho \omega^2 (u \delta u + v \delta v + w \delta w) - \left[C_{11} \frac{\partial u}{\partial x} \frac{\partial \delta u}{\partial x} + C_{12} \frac{\partial u}{\partial x} \frac{\partial \delta v}{\partial y} + C_{13} \frac{\partial u}{\partial x} \frac{\partial \delta w}{\partial z} + C_{12} \frac{\partial v}{\partial y} \frac{\partial \delta u}{\partial x} + C_{22} \frac{\partial v}{\partial y} \frac{\partial \delta v}{\partial y} + C_{23} \frac{\partial v}{\partial y} \frac{\partial \delta w}{\partial z} + C_{13} \frac{\partial w}{\partial z} \frac{\partial \delta u}{\partial x} + C_{23} \frac{\partial w}{\partial z} \frac{\partial \delta v}{\partial y} + C_{33} \frac{\partial w}{\partial z} \frac{\partial \delta w}{\partial z} + C_{44} \left(\frac{\partial v}{\partial z} + \frac{\partial w}{\partial y} \right) \left(\frac{\partial \delta v}{\partial z} + \frac{\partial \delta w}{\partial y} \right) + C_{55} \left(\frac{\partial u}{\partial z} + \frac{\partial w}{\partial x} \right) \left(\frac{\partial \delta u}{\partial z} + \frac{\partial \delta w}{\partial x} \right) + C_{66} \left(\frac{\partial u}{\partial y} + \frac{\partial v}{\partial x} \right) \right. \right. \\ \left. \left. \times \left(\frac{\partial \delta u}{\partial y} + \frac{\partial \delta v}{\partial x} \right) \right\} dV + \int_S \bar{T}_k \delta u_k dS = 0. \quad (1)$$

Hence, δ denotes the variational operator, C_{ij} the elastic stiffnesses, ω the periodic angular frequency of vibration, and \bar{T}_k the components of the specified surface tractions. V and S denote the volume and surface occupied by and bounding the solid, respectively.

Our model for computing estimates of the natural frequencies of vibration follows, with minor variation, the approach of Heyliger.⁷ The nature of the approximations used to solve Eq. (1) for layered parallelepipeds must take into account the behavior of the elastic stress and strain fields through the interfaces as it undergoes deformation during resonance. Specifically, traction continuity across a dissimilar material interface that is perpendicular to the z axis requires that the stress components σ_{zz} , σ_{xz} , σ_{yz} must all be continuous across the interface. Also, displacements u , v , and w must be continuous. Therefore, the fact that there is a

TABLE II. Elastic constants and mass density of the individual material measured before bonding.

	C_{11} (GPa)	C_{44} (GPa)	ρ (kg/m ³)
Al3004	110.7	26.16	2699
SS304	261.4	77.40	7489

discontinuity in the shear moduli μ implies that the shear strain components are discontinuous. For example, we consider the strain component γ_{xz} defined as

$$\gamma_{xz} = \frac{\partial u}{\partial z} + \frac{\partial w}{\partial x}. \quad (2)$$

It is clear that if this function is discontinuous at the interface, then the displacement component u must have a jump in slope with respect to z as one travels through the thickness of the specimen. Hence, conventional Legendre polynomials or power series, which have been used with outstanding results in many past studies^{9,10} to compute the resonance frequency of free vibration, are unacceptable candidates for vibration studies of layered media.

In the discrete-layer approximation, the dependence of the displacements on the z coordinate is separated from the functions in x and y , and it is allowed to have a break in slope with respect to the layer (or z) coordinate. This allows for global functions in x and y that are continuous and have continuous derivatives in the x - y plane, but still maintains the necessary physical features in z required by the mismatch in material properties. Hence, approximations for the displacement u can be expressed as¹¹

$$u(x, y, z, t) = \sum_{j=1}^n U_j(x, y, t) \bar{\Psi}_j^u(z) \\ = \sum_{i=1}^m \sum_{j=1}^n U_{ji}(t) \Psi_i^u(x, y) \bar{\Psi}_j^u(z). \quad (3)$$

As seen in Ref. 11, approximations for v and w can take similar forms. n denotes the number of layers and m the number of in-plane basis functions $\Psi_i(x, y)$. The approximations for each of the three field quantities are constructed in such a way as to separate the dependence in the plane from that in the direction perpendicular to the interface. In the thickness direction, we used one-dimensional Lagrangian interpolation polynomials for $\bar{\Psi}_j(z)$. For the in-plane approximations, we used power series $x^p y^q$ ($p, q = 0, 1, 2, \dots$). For a parallelepiped with n layers, $(n-1)$ is the number of subdivisions through the parallelepiped thickness, and U_{ji} , for example, denotes the coefficient of u at height j corresponding to the i th in-plane approximation function.¹¹

Substituting these approximations into Eq. (1), collecting the coefficients of the variations of the displacements, and placing the results in matrix form yields the result

$$\omega^2 [\mathbf{M}] \{\xi\} = [\mathbf{K}] \{\xi\}. \quad (4)$$

Here, $[\mathbf{M}]$ denotes the mass matrix, associated with the kinetic energy of the system, and $[\mathbf{K}]$ denotes the stiffness matrix, associated with the potential energy of the system. $\{\xi\}$ denotes the vector of constants that multiplies the displacement functions. Hence, the final problem results in the form of an eigenvalue problem.

In general, it is possible to split the groupings of the approximation functions to coincide with specific modal displacement patterns to reduce the size of the computational problem that must be solved. This behavior has been previously discussed by Ohno⁹ and Visscher *et al.*¹² One of the

TABLE III. Group structure for layered specimen.

Group	Displacement		
		x	y
1	u	E	E
	v	O	O
	w	O	E
2	u	E	O
	v	O	E
	w	O	O
3	u	O	O
	v	E	E
	w	E	O
4	u	O	E
	v	E	O
	w	E	E

disadvantages of our discrete-layer model is that we lose some of the splitting properties in the z direction when we use the discontinuous Lagrangian shape functions. However, it is still possible to make this split for the functions in the x - y plane. Instead of the eight groupings allowed for homogeneous orthotropic or isotropic materials,⁹ four groups are allowable.⁷ We give the displacement patterns corresponding to the four vibration groups in Table III. For example, group 1 includes vibration modes whose displacement component u is an even function about x and y . Hence, if power series are being used, the functions used would appear as $1, x^2, y^2, x^2y^2, x^4$, etc. As our freedom in choosing the odd or even character of our functions in z has vanished when we select piecewise linear functions, no grouping is allowed in z . However, and more important, we may thus model the break in displacement gradient. Our model can also be directly applied to specimens with no symmetry about the x - y plane. Concerning the material used in the present study, we can discuss the z -direction symmetry because of nearly symmetrical structure in the layered thickness.

In practical terms for our calculations, we used a total of 15 layers to model the 3 primary material layers. In plane, we use terms up to and including 8th order for each of the 3 displacement components. This leads to a total number of unknowns equal to $(15+1)(8)(8)(3)=3072$ in Eq. (4).

Splitting the functions as we do allows for solving 4 problems of size 768, a much more appealing proposition.

IV. ACOUSTIC-RESONANCE MEASUREMENTS

Resonance ultrasound spectroscopy, or RUS, is widely adopted to study elastic properties of solids.^{5,6} The specimen can be a sphere, cylinder, rectangular parallelepiped, or other regular shape, which is put between two ultrasonic transducers; one transducer generates a sinusoidal continuous-wave oscillation and the other detects the amplitude of mechanical vibrations at the contact point. By measuring the amplitude as a function of the driving frequency, we obtain a spectrum consisting of many resonance peaks, which are input to an inverse calculation to find the complete set of elastic con-

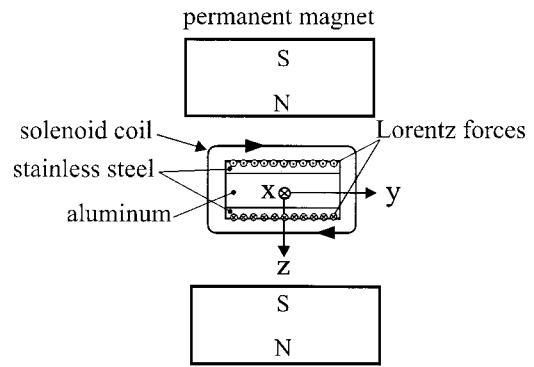


FIG. 1. EMAR-measurement setup for group 1.

stants of the material. The RUS method can determine all independent elastic constants with a single frequency scan for a single small specimen.

For a rectangular parallelepiped of orthorhombic or higher elastic symmetry, we can divide free mechanical vibrations into eight groups depending on the deformation symmetry.⁹ The computation of the resonance frequencies is based on such groupings. Therefore, successful use of the RUS method requires exact correspondence between the measured and calculated resonance frequencies, otherwise the resultant elastic properties have no physical significance. In the usual RUS method, however, such mode identification is not straightforward because all of the eight vibration

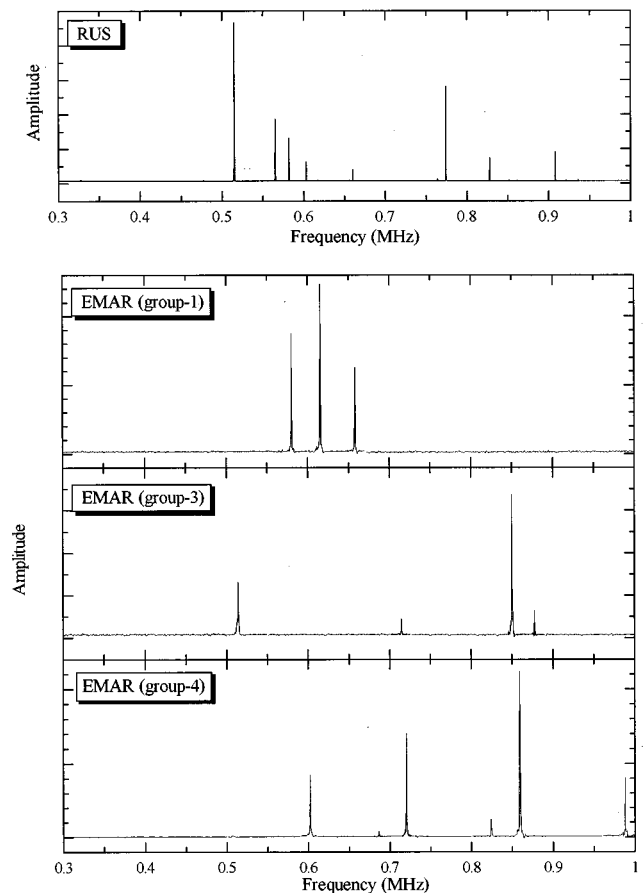


FIG. 2. RUS resonance spectrum and EMAR resonance spectra measured by the three different measurement setups.

TABLE IV. Calculated resonance frequencies f_{calc} by the discrete-layer model; measured resonance frequencies by the EMAR (f_{EMAR}) and RUS (f_{RUS}) methods; and internal friction measured by the EMAR (Q^{-1}_{EMAR}) and RUS (Q^{-1}_{RUS}) methods.

Group	f_{calc} (MHz)	f_{RUS} (MHz)	f_{EMAR} (MHz)	Diff			Q^{-1}_{RUS} (10^{-4})	Q^{-1}_{EMAR} (10^{-4})
				$f_{\text{calc}}-f_{\text{RUS}}$	$f_{\text{calc}}-f_{\text{EMAR}}$	$f_{\text{RUS}}-f_{\text{EMAR}}$		
2	0.330 618	0.327 540	...	0.93	6.41	...
4	0.444 477
2	0.475 870	0.477 209	...	-0.28	1.49	...
1	0.483 995	0.480 354	...	0.75	5.4	...
3 ^b	0.511 266	0.515 126	0.513 816	-0.75	-0.50	0.25	2.11	0.83
1 ^a	0.577 386	0.565 280	0.580 562	2.10	-0.55	-2.63	2.91	0.86
2	0.578 794	0.582 057	...	-0.56	1.74	...
4 ^c	0.603 155	0.603 177	0.602 211	0.00	0.16	0.16	1.53	1.98
1 ^a	0.619 723	0.617 616	0.615 400	0.34	0.70	0.36	2.77	1.46
4	0.655 140	0.656 059	...	-0.14	1.96	...
1 ^a	0.667 090	0.660 323	0.658 002	1.01	1.36	0.35	1.36	1.48
3	0.688 171	0.684 499	...	0.53	1.16	...
4 ^c	0.690 143	0.688 024	0.687 352	0.31	0.40	0.1	1.3	1.48
3 ^b	0.716 305	...	0.714 567	...	0.24	1.74
4 ^c	0.721 124	...	0.720 579	...	0.08	0.99
1	0.761 508	0.752 794	...	1.14	0.8	...
2	0.768 587	0.764 560	...	0.52	0.78	...
2	0.781 888	0.774 563	...	0.94	1.71	...
3	0.806 825
4	0.831 013	0.825 310	...	0.69	2.21	...
1	0.831 996	0.828 144	...	0.46	1.15	...
4 ^c	0.832 514	0.839 802	0.824117	-0.88	1.01	1.9	1.17	0.97
3	0.845 328
3 ^b	0.855 176	0.851 729	0.849 814	0.40	0.63	0.23	1.23	1.17
4 ^c	0.866 047	0.861 784	0.859 193	0.49	0.79	0.3	1.71	1.66
4	0.869 413	0.868 335	...	0.12	2.05	...
3	0.885 307	0.878 115	...	0.81	2.04	...
3 ^b	0.890 438	...	0.877 694	...	1.43	1.41
2	0.915 726	0.908 094	...	0.83	1.18	...
1	0.918 189	0.921 349	...	-0.34	1.54	...
2	0.933 194
3	0.935 763	0.936 009	...	-0.03	1.69	...
4	0.943 766
4 ^c	0.999 864	...	0.986 506	...	1.34	1.6
1	1.006 263
2	1.017 014
1 ^a	1.036 230	...	1.023 532	...	1.23	2.5
4	1.037 997
4 ^c	1.056 968	...	1.040 538	...	1.55	1.4
2	1.060 712
3 ^b	1.072 812	...	1.067 099	...	0.53	1.72
2	1.093 049
1	1.122 839
4 ^c	1.129 148	...	1.112 440	...	1.48	1.28
1 ^a	1.132 007	...	1.115 818	...	1.43	0.49
3 ^b	1.154 532	...	1.111 587	...	3.72	1.84

^a u -odd-in- z modes.

^b v -odd-in- z modes.

^c w -odd-in- z modes.

groups are simultaneously excited and many resonance peaks overlap, which causes inability to track overtones. The best way for mode identification would be to independently produce only one group of vibrations, filtering out the others. This is possible with EMAR, as described below.

In the typical EMAR-measurement setup, the specimen is inserted in a solenoid coil located between two permanent-magnet blocks (see Fig. 1). We drive the solenoid coil with high-power rf bursts to induce eddy currents near the surface

region of the specimen and then the Lorentz forces through interaction between eddy currents and the static magnetic field from the permanent magnets. The Lorentz forces oscillate with the same frequency as the driving bursts, causing the mechanical vibration. After the excitation, the same coil detects the vibrations through the reversed-Lorentz-force mechanism, the received signals are fed to the superheterodyne phase-sensitive detectors, and the amplitude spectrum at the operating frequency is determined. A single frequency

scan provides many resonance peaks (but fewer than in the RUS case), and the resonance frequencies are determined by Lorentzian-function fitting.

Such an EMAR configuration enables us to easily change the Lorentz-force direction and then select particular vibration modes. For example, in Fig. 1, the magnetic field is applied along the z axis and the Lorentz forces occur on the x - y faces along the x axis. The Lorentz forces produce the x component of displacement u . The displacement is most effectively detected by the same coil through the reversed-Lorentz-force mechanism when u is an even function about x and y , and an odd function about z . Among the vibration modes classified into four groups in Table III, only the vibration modes having an odd deformation pattern of u along the z axis in group 1 satisfy this condition. Thus, only those vibration modes should be generated and detected with this configuration. Similarly, we can independently generate and detect the v -odd-in- z modes in group 3 and w -odd-in- z modes in group 4, with different EMAR configurations (see Ref. 3).

For internal friction, we measured the amplitude decay after EMAR excitation with a tone burst. The amplitude free-decay curve provides the internal friction at the resonance frequency.¹³

We also made the usual RUS measurement using two pinducers sandwiching the specimen. In this case, we determined internal friction from the resonance-peak width. The typical measurement reproducibility of EMAR and RUS was 10^{-6} to 10^{-5} for resonance frequencies and 10^{-5} to 10^{-4} for internal friction.

V. RESULTS AND DISCUSSION

We show the resonance spectra measured by the RUS and EMAR methods in Fig. 2. The different EMAR measurement configurations produced different spectra, as expected. Table IV gives the measured and calculated resonance frequencies. In the model calculation, we investigated the eigenvector to predict the deformation pattern for each mode and found the particular vibration modes that u is odd about z in group 1, v is odd about z in group 3, and w is odd about z in group 4. Those modes were faultlessly detected by the three different EMAR configurations described above, indicating that the mode-selective principle of EMAR worked well. The differences between calculated frequencies and frequencies measured with EMAR were less than 1% for lower modes, but larger for higher modes. What is the most important observation here is that the closest pair between the measurement and calculation did not always provide exact mode correspondence. For example, the seventh mode of group 4 detected by EMAR occurred at 0.824 117 MHz and the closest frequency predicted from the model was the sixth mode of group 4. However, this is an undetectable mode with EMAR because it fails to satisfy the condition of detection of EMAR. If we had no information about the symmetry of the excited modes, we may have incorrectly identified this mode. The same thing could occur more easily for higher modes because of larger differences between the calculations and measurements. Thus, the mode-selective or mode-identified method is very significant and essential in

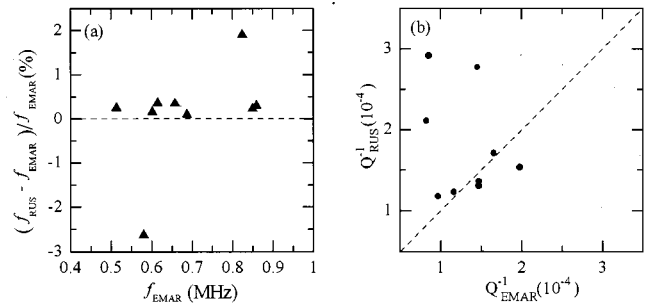


FIG. 3. Comparisons of RUS and EMAR measurements for (a) resonance frequencies and (b) internal friction of corresponding modes.

resonance-ultrasound-spectroscopy study. The fact that there were larger differences between calculated and measured frequencies of higher modes suggests that we need to use a larger number of discrete layers. Also, the discrete-layer model is based on the Ritz method, which typically gives less accurate frequencies as the mode number increases.

The RUS spectrum showed a better signal-to-noise ratio than the EMAR spectra. The RUS measurements agreed with calculations typically with 1% difference. But, we failed to identify the higher-frequency modes because of small amplitude and peak overlapping. An important observation is that the RUS method gave higher resonance frequencies than those of the EMAR method for almost all modes, as seen in Table IV and Fig. 3(a). We attribute this to the applied force of sandwiching transducers which is needed for mechanical coupling in the RUS method. Such an applied force constrains the specimen and prevents it from ideal free vibration, leading to upward shifts in resonance frequencies.¹⁴

Comparisons of internal friction measured by EMAR and RUS are shown in Table IV. Figure 3(b) also demonstrates the coupling effect. For most matching modes, RUS internal friction was noticeably larger than EMAR internal friction. This indicates the energy loss into the contacting transducers in the RUS method, which was pointed out in a previous study.³

VI. CONCLUSIONS

- (1) We have presented the first comparisons between the measurement and calculation of a free-vibration problem of a layered-parallelepiped material. The agreements between measured and calculated resonance frequencies were typically within 1%. This difference is expected to decrease by increasing the number of the discrete layers in the calculation.
- (2) The discrete-layer model explained the nature of vibration well. The deformation pattern of a vibration estimated by the model calculation was supported by the mode-selective EMAR measurements. Such an exact mode identification is absolutely necessary for developing and improving the model.
- (3) The comparisons between the RUS and EMAR results show the effect of contact coupling, even for the relatively weak point contacting of RUS made in this study.

ACKNOWLEDGMENTS

The contribution of the second author was completed during an Alexander von Humboldt Fellowship at the Staatliche Materialprüfungsanstalt (MPA) at the University of Stuttgart. This support is gratefully acknowledged. Professor V. Kinra (Texas A & M) contributed the studied material.

- ¹M. Hirao and H. Ogi, "Electromagnetic Acoustic Resonance and Materials Characterization," *Ultrasonics* **35**, 413–421 (1997).
- ²W. Johnson, "Ultrasonic Damping in Pure Aluminum at Elevated Temperatures," *J. Appl. Phys.* **83**, 2462–2468 (1998).
- ³H. Ogi, H. Ledbetter, S. Kim, and M. Hirao, "Contactless Mode-Selective Resonance Ultrasound Spectroscopy: Electromagnetic Acoustic Resonance," *J. Acoust. Soc. Am.* **106**, 660–665 (1999).
- ⁴H. Ogi, K. Takashima, H. Ledbetter, M. Dunn, G. Shimoike, M. Hirao, and P. Bowen, "Elastic Constants and Internal Friction of an SiC-Fiber-Reinforced Ti-Alloy-Matrix Crossply Composite: Measurement and Theory," *Acta Mater.* **47**, 2787–2796 (1999).
- ⁵J. Maynard, "Resonant Ultrasound Spectroscopy," *Phys. Today* **49**, 26–31 (1996).
- ⁶A. Migliori and J. L. Sarrao, *Resonant Ultrasound Spectroscopy* (Wiley, New York, 1997).
- ⁷P. R. Heyliger, "Traction-Free Vibration of Layered Elastic and Piezoelectric Rectangular Parallelepipeds," *J. Acoust. Soc. Am.* **107**, 1235–1245 (2000).
- ⁸H. F. Tiersten, *Linear Piezoelectric Plate Vibrations* (Plenum, New York, 1969).
- ⁹I. Ohno, "Free Vibration of A Rectangular Parallelepiped Crystal and Its Application to Determination of Elastic Constants of Orthorhombic Crystals," *J. Phys. Earth* **24**, 355–379 (1976).
- ¹⁰A. Migliori, J. L. Sarrao, W. M. Visscher, T. M. Bell, M. Lei, Z. Fisk, and R. G. Leisure, "Resonant Ultrasound Spectroscopy technique for measurement of the elastic moduli of solids," *Physica B* **183**, 1–24 (1993).
- ¹¹J. N. Reddy, "A Generalization of Two-Dimensional Theories of Laminated Composite Plates," *Commun. Appl. Numer. Methods* **3**, 173–180 (1987).
- ¹²W. M. Visscher, A. Migliori, T. M. Bell, and R. A. Reinert, "On the Normal Modes of Free Vibration of Inhomogeneous and Anisotropic Elastic Objects," *J. Acoust. Soc. Am.* **90**, 2154–2162 (1991).
- ¹³H. Ogi, M. Hirao, and T. Honda, "Ultrasonic Attenuation and Grain Size Evaluation Using Electromagnetic Acoustic Resonance," *J. Acoust. Soc. Am.* **98**, 458–464 (1995).
- ¹⁴Y. Sumino, I. Ohno, T. Goto, and M. Kumazawa, "Measurement of Elastic Constants and Internal Friction on Single-Crystal MgO by Rectangular Parallelepiped Resonance," *J. Phys. Earth* **24**, 263–273 (1976).

Experiments with a flow-through thermoacoustic refrigerator

R. S. Reid

Energy and Process Engineering Group, Los Alamos National Laboratory, Los Alamos, New Mexico 87545

G. W. Swift

*Condensed Matter and Thermal Physics Group, Los Alamos National Laboratory,
Los Alamos, New Mexico 87545*

(Received 1 March 2000; revised 1 September 2000; accepted 15 September 2000)

Deliberate superposition of steady flow parallel to the thermoacoustic oscillations in a stack is used to cool the steady flow as it passes through the stack. The loudspeaker-driven refrigerator described here cools a flowing helium–argon mixture from 35 to 27 °C and provides additional cooling power at a traditional cold heat exchanger. The dependence of the stack's temperature profile and of the additional cooling power on the steady flow rate are in agreement with a simple theory based on augmentation of the well-known thermoacoustic momentum, continuity, and energy equations with a single new term in the energy equation that describes the steady flow. © 2000 Acoustical Society of America. [S0001-4966(00)04712-3]

PACS numbers: 43.35.Ud, 05.70.-a, 44.27.+g [SGK]

I. INTRODUCTION

The selection of technology for real-world applications depends on many factors, such as capital cost, operating cost, efficiency, size, weight, and reliability. Practical, economic considerations often favor technologies with nonoptimal efficiency. For example, the reverse Brayton-cycle refrigeration technology used aboard turbine aircraft provides weight savings that indirectly lead to lower aircraft operating cost, despite a cooling efficiency¹ that is less than 10% of the upper bound set by the laws of thermodynamics. The nascent technology of thermoacoustics seems attractive because the small number (often zero) of moving parts and sliding seals suggests low cost and reliability. Especially when both engine and refrigerator are present in one system, thermoacoustic devices are very simple: little more than heat exchangers of conventional design in large vessels that confine the thermoacoustic working gas and define the geometry in which the gas resonates.

In an attempt to enhance this inherent simplicity, we have begun to explore whether some of the heat exchangers can be eliminated from thermoacoustic devices. Figure 1 illustrates the idea for a thermoacoustic refrigerator used to cool air. Figure 1(a) shows the main parts of an air-conditioning system using a conventional standing-wave thermoacoustic refrigerator. In addition to the stack, four heat exchangers are required: two in the thermoacoustic working gas and one in each of the two air streams. Heat transfer between the working-gas heat exchangers and the air heat exchangers, indicated by heavy black arrows, is accomplished via heat-transfer loops such as pumped water, heat pipes, thermosyphons, etc. In mass production, the four heat exchangers and two heat-transfer loops would probably account for most of the capital cost of this system.

The air-conditioning system in Fig. 1(b) illustrates the simplification that is possible by using the indoor air itself as the thermoacoustic gas. A midwall in the indoor-air duct separates two acoustic resonators, driven 180° out of phase from each other by an oscillating driver piston in the center

of the midwall. The drive frequency is chosen to make the acoustic wavelength equal to twice the midwall length, so pressure nodes will be at the ends of the midwall and, hence, negligible acoustic power will be radiated to distant parts of the duct. The position of the stack relative to the nodal pattern of the standing wave is chosen so that conventional standing-wave thermoacoustic phenomena pump heat from right to left. Superimposed on these thermoacoustic phenomena, the air is forced slowly rightward through the stack from ambient to cold, so that cold air leaves the right end of the apparatus. Compared to Fig. 1(a), two heat exchangers are eliminated, suggesting a reduction in capital cost.

This intimate superposition of steady flow of the air with its own oscillating thermoacoustic flow might also give the system of Fig. 1(b) a higher efficiency than that of the system of Fig. 1(a), for two reasons. First, the internal temperature differences of two heat exchangers are eliminated and the acoustic power dissipation in the missing thermoacoustic heat exchanger is eliminated. Second, a much more subtle yet significant improvement in efficiency can occur because the system of Fig. 1(b) puts the air stream sequentially in thermal contact with a large number of refrigerators in series—a continuum limit of staged refrigerators. To understand this point, imagine that thermoacoustic refrigerators were ideal, having Carnot's coefficient of performance $T_C/(T_0 - T_C)$, where T is temperature and the subscripts C and 0 represent cold and ambient. Then, in the case of Fig. 1(a), the removal of heat $\dot{m}c_p(T_0 - T_C)$ from the air stream with mass flow rate \dot{m} and isobaric specific heat c_p by the refrigerator's cold heat exchanger at temperature T_C would require that work

$$\dot{W} = \dot{m}c_p(T_0 - T_C)^2/T_C \quad (1)$$

must be supplied to the refrigerator by the driver piston. This is more than twice the minimum work required by the first and second laws of thermodynamics for this process, which is given by the difference between the outgoing and incoming flow availabilities,²

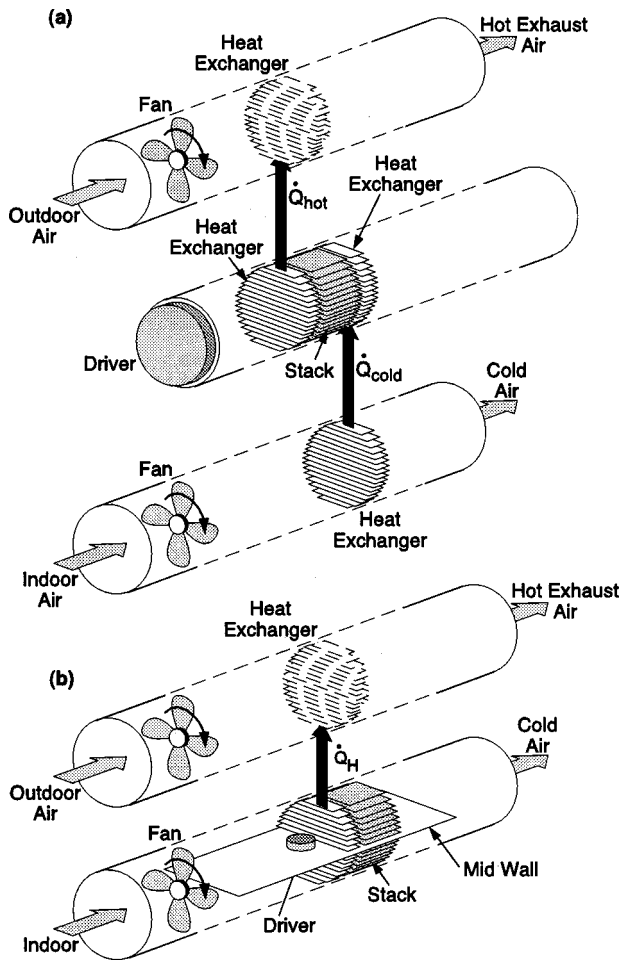


FIG. 1. An air conditioner is used to illustrate the potential simplification of hardware that is possible if the process gas is used as the thermoacoustic working gas and parallel steady flow is superimposed on the thermoacoustic oscillations. The air-conditioning system must remove heat from a stream of indoor air (the “process gas”) and reject waste heat to a stream of outdoor air. (a) A conventional thermoacoustic air-conditioning system would require four heat exchangers and two heat-transfer loops in addition to the stack. (b) By using the indoor air itself as the thermoacoustic working gas and superimposing steady flow on the oscillating flow, two heat exchangers and one heat-transfer loop are eliminated.

$$\dot{W} = \dot{m}[(h_C - h_0) - T_0(s_C - s_0)] \quad (2)$$

$$= \dot{m}c_p[T_C - T_0 + T_0 \ln(T_0/T_C)], \quad (3)$$

where h is enthalpy per unit mass and s is entropy per unit mass. [Equation (3) results from using ideal-gas expressions for h and s .] The lower efficiency of the simple refrigerator of Fig. 1(a) occurs because it removes *all* the heat from the air stream at T_C , where every unit of cooling power requires $(T_0 - T_C)/T_C$ units of input power. It is more efficient to remove as much of the heat load as possible at higher temperatures T'_C , where $T_0 > T'_C > T_C$, so that each unit of cooling power requires only $(T_0 - T'_C)/T'_C$ units of input power. The flow-through thermoacoustic refrigerator of Fig. 1(b) is an imperfect embodiment of this idea, with each differential length dx of the stack essentially a tiny refrigerator unto itself, lifting heat from T'_C to $T'_C + dT'_C$, removing each unit of heat from the flowing air stream at the highest possible temperature.

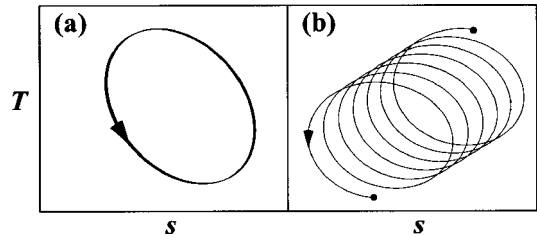


FIG. 2. When $\dot{m} = 0$, a typical parcel of gas in a thermoacoustic stack follows one elliptical temperature–entropy ($T-s$) cycle repeatedly, as shown schematically in (a). When $\dot{m} \neq 0$, a given parcel of gas follows a much more complicated path through $T-s$ space, as shown schematically in (b).

With the addition of a small nonzero steady flow along x , the air moves through the stack in a repetitive, “51 steps forward, 49 steps back” manner in position, and also in temperature, density, and entropy as illustrated in Fig. 2(b). This violates one assumption on which most prior thermoacoustic equations^{3–5} are based—that the x component of gas velocity is given by $u = \text{Re}[u_1 e^{i\omega t}]$, with zero average value. (The subscript 1 indicates a complex amplitude.) However, the derivation of corresponding thermoacoustic equations in the presence of nonzero steady flow is straightforward.^{6,7} The thermoacoustic momentum, continuity, and wave equations are unchanged to lowest order, but the steady flow appears in the thermoacoustic energy equation, which becomes

$$\begin{aligned} \dot{H}_2 = \dot{m}c_p(T_m - T_0) + \frac{1}{2}\rho_m c_p \\ \times \int \text{Re}[T_1 \tilde{u}_1] dA - (Ak + A_{\text{solid}}k_{\text{solid}}) \frac{dT_m}{dx} \end{aligned} \quad (4)$$

for an ideal gas. The subscript m indicates the local mean value, \dot{H}_2 is the total energy flow in the x direction, A is the cross-sectional area in the stack that is available to the gas, k is the thermal conductivity of the gas, and k_{solid} is the thermal conductivity of the stack walls. The complex temperature oscillation amplitude T_1 can be expressed in terms of pressure and velocity amplitudes p_1 and u_1 . In Eq. (4), the new, first term represents enthalpy carried by the steady flow, the familiar⁴ second term represents enthalpy carried by the oscillating flow, and the third term represents ordinary conduction of heat down the temperature gradient in the gas and solid. Note that the second term is second order in the acoustic oscillation amplitude, so this equation will be most interesting and valid when the steady flow \dot{m} is smaller than or roughly comparable to a second-order mass flow such as $A|\rho_1||u_1|$, where ρ is gas density; hence, we retain the traditional subscript “2” on \dot{H}_2 . This bound on \dot{m} also ensures that the steady flow is always in excellent local thermal contact with the stack channel walls, as long as these walls are separated by no more than several thermal penetration depths.

For the usual situation in which the stack is laterally thermally insulated, energy conservation requires that \dot{H}_2 is independent of x . Hence, if p_1 and u_1 are known, Eq. (4) can be used as a differential equation for $T_m(x)$ to predict the temperature profile in the stack. Numerical integration of this differential equation, self-consistently with the momentum and continuity equations, is straightforward.⁸ However,

qualitative insight about the temperature profile can be obtained more easily by making some approximations. Several sets of approximations are plausible, but all lead to qualitatively similar results;^{6,9} here, we choose a mathematically simple set of approximations. Following the inviscid boundary-layer “short-stack” approximation,⁵ suppose that the stack is short enough and spans a small enough temperature difference that thermophysical properties and sound-wave properties can be regarded as independent of x to lowest order, and suppose that the ordinary conduction of heat down the temperature gradient is small. Then Eq. (4) reduces to

$$\dot{H}_2 = \dot{m}c_p(T_m - T_0) + \frac{1}{4}A \frac{\delta_\kappa}{r_h} |p_1| |u_1| \left(\frac{dT_m/dx}{\nabla T_{\text{crit}}} - 1 \right), \quad (5)$$

where δ_κ is the thermal penetration depth, r_h is the hydraulic radius of the pores in the stack, and $\nabla T_{\text{crit}} = -\omega |p_1| / \rho_m c_p |u_1|$. Treating everything except the two explicit occurrences of T_m in Eq. (5) as independent of x and setting $d\dot{H}_2/dx = 0$ yields

$$\frac{T_0(x) - T_m(x)}{T_0 - T_C} = \frac{1 - e^{-\Xi x}}{1 - e^{-\Xi L}}, \quad (6)$$

where L is the length of the stack and

$$\Xi = \frac{4\dot{m}c_p \nabla T_{\text{crit}}}{A |p_1| |u_1| \delta_\kappa / r_h}. \quad (7)$$

In this approximation, Eq. (5) shows that $T_m(x)$ is linear when $\dot{m} = 0$. For nonzero \dot{m} , Eq. (6) shows that $T_m(x)$ is exponential, with characteristic length $1/\Xi$, so that the curvature increases with increasing $|\dot{m}|$ and the sign of the curvature depends on the sign of \dot{m} .

The elimination of heat exchangers by superimposing parallel steady flow and thermoacoustic oscillation should be possible in engines as well, but we chose to investigate this idea in the context of a refrigerator. The next section describes the apparatus, topologically similar to that illustrated in Fig. 1(b). In this first exploration of the idea of superimposed parallel steady flow and of Eq. (4), we had no reason to demonstrate a practical device, so we used ordinary inefficient loudspeakers to drive the acoustic resonance, in what roughly resembles a full-wavelength torus with side branches for injection and removal of steady flow. Our primary intent was the verification of the qualitative features of Eq. (6), so the stacks were equipped with many thermocouples to measure $T_m(x)$. Power-measuring instrumentation was also included, to investigate Eq. (4) more directly. In the course of the measurements, it was easy to change the direction of \dot{m} , so we did this, to expand the range of these investigations, creating a type of steady-flow heat pump as \dot{m} flowed up the temperature gradient. The results of these investigations, described in the final section, provide qualitative and quantitative confirmation of the ideas presented in this introduction. A more complete description of the ideas, the experiment, and the analysis is available elsewhere.⁶

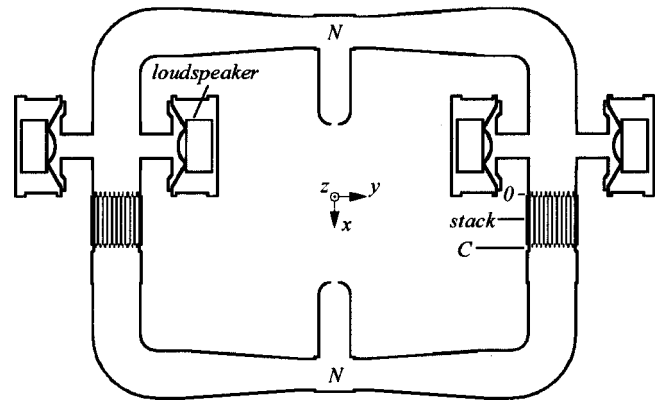


FIG. 3. Schematic of the experimental apparatus, with internal resonator dimensions drawn to scale. Spacings between plates in the stacks and heat exchangers are not to scale. The apparatus is left-right symmetric. The heat exchangers at T_0 and T_C are indicated by “0” and “C.”

II. APPARATUS AND INSTRUMENTS

A schematic of the apparatus built for these investigations is shown in Fig. 3, with internal dimensions drawn to scale. The toroidal resonator had a total internal volume of 0.0915 m^3 filled with a mixture of 92% helium and 8% argon at 3.23-bar mean pressure. (The system was also successfully operated with atmospheric air, but the helium-argon mixture provided larger, more accurately measurable powers.) Four speakers drove the fundamental gas resonance, with the speaker pair on one side of the resonator moving out of phase from the speaker pair on the other side. The two pressure nodes of the standing wave (marked “N”) divided the resonator into symmetric left and right halves and provided convenient locations for injection and removal of steady flow. The stacks and their heat exchangers were positioned in the standing wave so that $|p_1|/\rho_m a |u_1| \approx 1.5$ in mid stack, where a is the sound speed. Although this location generated significant viscous losses, it lowered the temperature gradient so that thermal conduction losses were negligible. For convective stability under normal operating conditions, the apparatus was oriented as shown in the figure, with the ambient ends of the stacks up.

The resonator was made of polyvinyl-chloride pipe and fittings, aluminum housings containing the speakers, and a few other custom-fabricated parts, sealed together with glue or bolted rubber gaskets. The four long conical diffusers reduced harmonic content¹⁰ in the standing wave to negligible levels. Dynamic pressure sensors¹¹ at six locations in the resonator were used to verify that the pressure nodes were indeed nodes and that the wave shape was as expected. The amplitudes and phases of the oscillating pressures, here and elsewhere, were measured with a dynamic signal analyzer,¹² and sometimes checked with a lock-in amplifier. The 94-Hz fundamental resonance frequency measured at low amplitude in the resonator when filled with commercially procured mixed gas agreed within 0.5 Hz with similar measurements using our own mixtures made from pure helium and argon, indicating that the commercial and home-made helium fractions agreed within 0.2%. The measured frequency also agreed within 1 Hz with the value calculated using a DeltaE⁸ model of the complete apparatus with as-built dimensions,

and the low-amplitude quality factor (measured by sweeping frequency) agreed within a few percent with the calculated value, helping to build our confidence in this numerical model.

Each stack consisted of 142 parallel, 0.25-mm-thick fiberglass plates with length 15.24 cm along the acoustic-oscillation direction, contained in a 15.32-cm-i.d. polyvinyl-chloride resonator pipe. The separation between plates was 0.81 mm, maintained by straight lengths of epoxy-coated nylon monofilament, aligned along the acoustic-oscillation direction, and located on 13.5-mm centers. Thus, 70% of the pipe's cross-sectional area was open to gas flow, through many channels 15.24 cm long, each with a rectangular cross section 0.81 mm high by 12.7 mm wide, except near the circumference of the stack where the circular package perimeter truncated the width of many channels. The separation between plates was about two thermal penetration depths of the helium-argon mixture at the operating conditions. Fiberglass and nylon were used to minimize heat conduction along the stack plate in the direction of sound propagation. The stack length was much less than the radian length of the sound wave but many times larger than the oscillatory gas displacements. The fabrication of these stacks is described fully in Ref. 6.

Five 3.2-mm-diameter fiberglass support tubes, extending along the stack diameter, perpendicular to the plates, with 2.54-cm center-to-center spacings, guided 0.5-mm-diameter sheathed copper-constantan thermocouples¹³ with "special limits of error" into the stack. The junctions of ten thermocouples were epoxied to one plate's surface at ten axially equally spaced positions along the full 15.24-cm length of the rectangular channel at the center of the stack. The thermocouples were attached to the plate 3 mm to one side of the fiberglass support tubes. The channel containing the thermocouples was blocked at each end to eliminate thermoacoustic effects on the thermocouple sheaths and wires in that channel. Thus, the temperature measured was produced primarily by thermoacoustic effects in the adjacent, unblocked channels.

Adjacent to and above each stack was a water-cooled, ambient-temperature heat exchanger used to transfer waste heat from the refrigerator to the ambient environment. This exchanger extended 1.27 cm along the acoustic-oscillation direction. Rubber O-rings sealed its case to the stack's pipe below and to another polyvinyl-chloride pipe above. The exchanger's single bank of eight 0.48-cm-o.d. copper tubes were soft-soldered into its 14.8-cm-i.d. brass case and to its 80 copper fins, which had 0.53-mm thicknesses and 1.27-mm separations. A copper-constantan thermocouple measured the temperature of one of the copper fins. A total of 90 cm² (52% of the case inside area) was open to oscillating gas. The thermal resistance measured between the copper tubes and the water flowing through them was 77 °C/kW; the thermal resistance from the middle of each fin to its nearby tubes was calculated to be 3.4 °C/kW.

Manifolds connected the tubes at the inlet and outlet of the ambient exchanger. A copper-constantan thermocouple immersed in the water inside each manifold measured the water temperature entering or leaving the exchanger. The

water flow rate to the exchanger was measured with a variable-area rotameter. The heat rejection rate from the exchanger was calculated from the flow rate and manifold temperature measurements. Uncertainty in the calculated heat-rejection rate was typically less than $\pm 10\%$ of reading, but was a strong function of thermoacoustic conditions and water flow rate.

Other heat exchangers were placed at the cold ends of the two stacks. These electrically heated "cold" heat exchangers were unnecessary for cooling the steady flow of gas, but they allowed versatile measurements and control in the experiments. For example, by using these heat exchangers to hold the stack ends at constant temperature while steady flow was varied, the only temperature equilibration required was inside the stacks, so equilibration time was minimized and system resonance frequency stayed constant. Each cold heat exchanger consisted of a continuous nichrome ribbon, 50.8- μm thick and 6.35-mm wide, supported by a fiberglass frame to form a back-and-forth grid. The room-temperature electrical resistance of the ribbon was about 30 Ω . Power from voltage-controlled alternating electric current was dissipated in the nichrome ribbon. A digital multimeter detected root-mean-square (rms) voltage across the ribbon; a thermocouple near the center of the exchanger's fiberglass frame monitored the local temperature.

The four speakers¹⁴ used to drive the resonator were well suited to this low-cost proof-of-principle experiment. Speaker pairs were contained in machined and welded aluminum housings with penetrations for electrical power and cooling water. These speakers were factory-equipped with a cooling system, in which motion of the diaphragm caused high-velocity gas motion around the voice coil and through three ports in the magnet. Nevertheless, additional cooling was needed to keep the voice coils at acceptable temperatures during typical operation, so a small plate was added to the rear of each speaker's magnet to form a small sealed chamber, and water was circulated through this chamber. The temperatures of the entering and exiting flows were measured with chromel-alumel thermocouples, and a variable-area rotameter indicated the water flow rate through each speaker chamber, so that heat removal from the speakers could be determined.

The properties of each speaker were characterized by measuring Bl product, mechanical resistance, electrical resistance, voice-coil inductance, and diaphragm stiffness. The Bl product of each speaker was measured by applying increasing amounts of weight to the speaker diaphragm and increasing the direct current applied to the voice coil while keeping the diaphragm stationary. Mechanical properties were found by measuring the electromechanical resonance frequency with the speaker in vacuum, and simply using the manufacturer's supplied data for the mass of the moving diaphragm. Strong temperature dependence was noted in diaphragm stiffness, so these measurements were taken at several temperatures to characterize this dependence. The inductance was found by epoxying the voice coil of one speaker to its magnet to prevent motion and measuring the electrical resonance frequency with the voice coil in series with a known capacitance.

The mechanical spring constant and moving mass were small enough, and the associated mechanical resonance frequency was close enough to 94 Hz, that the impedance of the speakers was small compared to that of the acoustic standing wave in the gas, and the pressure amplitude in the cavity behind each speaker was nearly equal to the pressure amplitude just in front of the speaker. This design¹⁵ places such a power transducer at an optimal location in the standing wave, neither at a pressure node nor at a velocity node, and allows the pressure difference across the speaker to be due only to the power delivered to the wave by the speaker. The four speakers were driven by a single sinusoidal function generator with variable frequency and amplitude, through four adjustable “microphone mixers,” each feeding a power amplifier. The mixers were set so that the four speakers produced nearly equal acoustic powers, thereby accommodating minor differences in Bl product among the speakers. The electrical power supplied to each speaker was obtained with a dynamic signal analyzer,¹² which measured the voltage across the speaker terminals, the voltage across a precision, temperature-controlled current-sensing resistor in series with the speaker, and the phase between these voltages.

Accelerometers attached to speaker diaphragms have been used previously¹⁶ to measure the volume velocity so that the acoustic power delivered by the speaker can be determined. A simpler method to measure volume velocity was attempted in this experiment, requiring only measurement of $p_{1,\text{back}}$ in the cavity behind the speaker’s diaphragm using a piezoresistive pressure transducer. Assuming adiabatic oscillations in the cavity volume V_{back} , the complex volume velocity U_1 of the diaphragm is

$$U_1 = - \frac{i \omega V_{\text{back}}}{\gamma p_m} p_{1,\text{back}}, \quad (8)$$

with the signs chosen so that positive volume velocity flows into the resonator from the front of the diaphragm. The time-averaged acoustic power transferred to the resonator by the front of the speaker is then

$$\dot{W}_{ac} = \frac{\omega V_{\text{back}}}{2 \gamma p_m} \text{Im}[p_{1,\text{back}} \tilde{p}_{1,\text{front}}]. \quad (9)$$

Correcting this expression to account for laminar thermal-relaxation effects on the surface area A_{back} of the cavity behind the speaker leads^{17,18} to a factor $1 - i(\gamma - 1)A_{\text{back}}\delta_\kappa/2V_{\text{back}}$ inside the square bracket of Eq. (9), but this is negligible here.

Calculating acoustic power delivered to the resonator using Eq. (9) requires knowledge of the volume V_{back} behind the speaker diaphragm. This volume was estimated using fabrication drawings of the speaker housing, measuring the speaker frame’s volumetric displacement in water, and accounting for the volume occupied by cooling lines and other minor irregularities. The volume behind each speaker diaphragm was estimated to be $7.9 \times 10^{-3} \text{ m}^3 \pm 4\%$. Including uncertainties in pressure measurements, the result obtained from Eq. (9) was typically uncertain by $\pm 8\%$.

The deliberate steady flow was delivered to and removed from the resonator at the two pressure nodes, so that the connections to the steady-flow pumping system did not

perturb the resonance or absorb significant acoustic power. Two compressors¹⁹ in series, with water-cooled heat exchangers downstream of each, circulated the steady flow of the helium–argon mixture through the resonator. The gas flow rate was controlled by throttling the flow to the suction side of the first compressor and by allowing some of the gas discharged by the second compressor to return to the suction side of the first compressor through a bypass. An expansion chamber between this compressor assembly and the resonator, together with the inertance of the connecting tubing, acted as a low-pass acoustic filter to keep velocity and pressure oscillations generated by the compressor assembly out of the resonator. The sign of the gas flow through the resonator could be reversed by interchanging the connections between the compressor assembly and the resonator.

Before entering the resonator, the steady flow passed through a filter to remove dust and then through a laminar flow resistance.²⁰ The differential pressure that formed across the laminar flow resistance as gas flowed through it caused a pressure difference proportional to flow rate. The flow resistance was calibrated by the manufacturer using a NIST-traceable ANSI Z540-1 standard. After months of preliminary experiments, just before the measurements discussed in detail below were made, the flow resistance was returned to the manufacturer for recalibration and was found to be within tolerance. Two redundant piezoresistive pressure transducers¹¹ detected the differential pressure across this resistance. The transducers were calibrated at 323-kPa mean pressure using a water manometer. The mass flow rate \dot{m} through each stack was found by correcting for absolute temperature and pressure and assuming that the flow was evenly divided between resonator sides. The uncertainty in \dot{m} was estimated to range from $\pm 3\%$ at the lowest flow rate, where uncertainty in the temperature correction dominated, to $\pm 0.9\%$ at the highest flow rate, where the uncertainty in the calibrated flow resistance was most important.

Stationary thermocouples near the pressure nodes and movable thermocouples above and below the stack–heat-exchanger assemblies detected temperatures in the moving gas; the tips of these sheathed thermocouples were oriented perpendicular to the oscillating flow to minimize measurement error from thermoacoustic heat pumping along the sheaths.

To thermally insulate the refrigerator from the room, the entire resonator/speaker system was suspended by nylon rope inside a large box filled with 10-mm-diameter polystyrene packing beads. Instrument cables, power leads, and water lines entered through the open top of the box. The efficacy of this insulating method was revealed in comparisons of the total electrical power dissipation with the total thermal power carried by the water cooling lines and steady-flow circuit. When the refrigerator was allowed to operate long enough (typically 6 h) to reach equilibrium, the fractional difference between the heat rejected to the water and the algebraic sum of the other powers was typically less than 3%.

III. RESULTS

As \dot{m} was varied during measurements, the values of $|p_1|$, T_0 , and T_C were held constant by adjusting the electric power to the speakers, the water flow rate through the ambient heat exchanger, and the electric power \dot{Q}_C supplied to the cold heat exchanger. This resulted in a condition that also kept resonator temperature constant, so the resonance frequency was fixed. The effects of \dot{m} on the dependent variables $T_m(x)$, \dot{W}_{ac} , and \dot{Q}_C were then measured. We selected $|p_1|/p_m = 0.020$ as a reasonable compromise between power (more accurately measurable at higher amplitudes) and consistency with the low-amplitude approximation inherent in thermoacoustic analysis based on Rott's work.^{3,4} We selected $T_0 = 308.0$ and $T_C = 300.5$ K; this temperature difference was large enough for accurate temperature measurements yet small enough that the refrigerator could provide a large, accurately measurable cooling power.

Although a complete numerical model (described in Ref. 6) of the entire apparatus was used for some comparisons, the most important numerical results were obtained with a much simpler partial model that integrated⁸ from the pressure node at the bottom of the resonator up through one stack-heat-exchanger assembly just to the location of the pressure sensor above the stack-heat-exchanger assembly. Thus, uncertainty about speaker power (see below) did not affect the results of this integration. The usual thermoacoustic momentum and continuity equations were integrated throughout the model, and were augmented in the stack by Eq. (4). The geometry, the gas pressure and mixture composition, the operating frequency, the temperatures at the two ends of the stack, the steady mass flow rate, the pressure amplitude at the pressure transducer above the stack-heat-exchanger assembly, and $p_1 = 0$ at the pressure node were set equal to their experimental values and treated by the integration as given. Results of the integration then included the complex pressure and volume velocity everywhere, the temperature profile within the stack, the cooling load applied at the cold heat exchanger, and the acoustic power supplied at the top of the stack-heat-exchanger assembly.

The dramatic effect of \dot{m} on $T_m(x)$ is illustrated in Fig. 4, which shows the temperature as a function of distance from the ambient end of the stacks for a few representative values of \dot{m} . The filled and open symbols represent the measured values, with the error bars showing the uncertainties in the thermocouple readings. At $\dot{m} = 0$ the temperature profile is nearly linear, as discussed in the Introduction. Nonzero \dot{m} distorts the temperature profile with sign and shape consistent with the qualitative description in the Introduction and the approximate Eq. (6). The similarity between Figs. 4(a) and (b) also shows that the steady flow is substantially equal in the two stacks, although the steady-flow delivery system guarantees only that the sum of the flow rates through the two stacks is fixed. The fact that the steady flow always automatically split evenly between the two stacks is encouraging for possible practical applications; we had no *a priori* reason to be certain of such stability.

The solid curves in the figure represent numerical

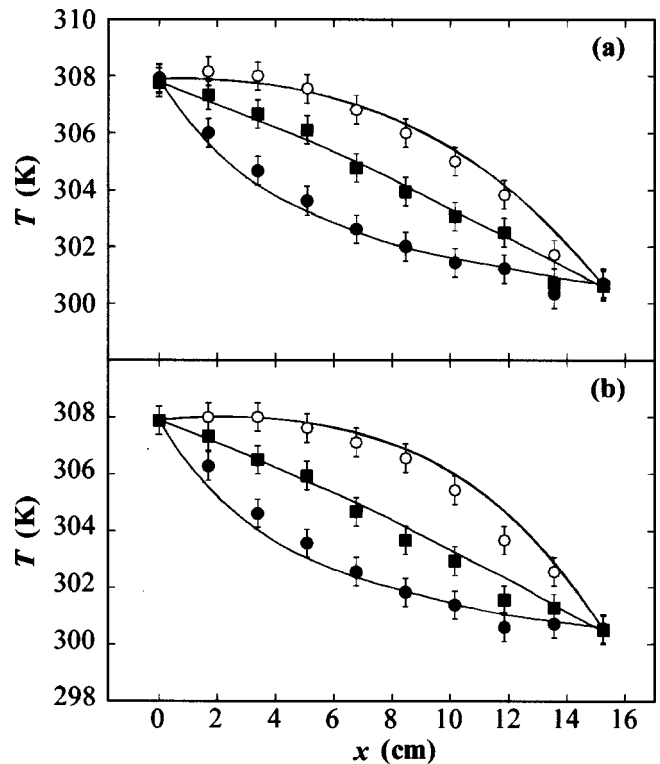


FIG. 4. Mean temperature as a function of distance from the ambient end of the stack, at representative steady flow rates. (a) Left stack. Squares, $\dot{m} = 0$; open circles, $\dot{m} = 3.35$ g/s; filled circles, $\dot{m} = -4.34$ g/s. (b) Right stack. Squares, $\dot{m} = 0$; open circles, $\dot{m} = 4.51$ g/s; filled circles, $\dot{m} = -4.34$ g/s. The curves are the results of numerical integrations of Eq. (4) and the thermoacoustic momentum and continuity equations.

integration⁸ of the partial model described above, incorporating Eq. (4). Overall, the measurements and numerical integrations of $T_m(x)$ are in good agreement, confirming the understanding of superimposed thermoacoustic and steady flow embodied in Eq. (4). It is difficult to provide quantitative estimates for the uncertainty in the calculated curves, which could be due to uncertainties in fabricated geometry (such as the presence of the fiberglass stack supports, slightly nonparallel nylon-monofilament stack spacers, etc.) and to the low-amplitude acoustic model's assumption that the gas displacement amplitude is much smaller than the stack length (see below).

Obtaining the experimental power \dot{Q}_C absorbed by the stack from the cold heat exchanger required some care, because some of the electric power \dot{Q}_{elec} dissipated in the cold heat exchanger was transferred to the steady flow, causing a small difference between the temperature T_C of the cold end of the stack and the time-averaged temperature of the gas just below the heat exchanger, T_{below} . The heat load absorbed by the cold end of the stack was obtained from \dot{Q}_{elec} by measuring these two temperatures and using

$$\dot{Q}_C = \dot{Q}_{elec} - \dot{m}c_p(T_{below} - T_C). \quad (10)$$

This steady-flow correction for obtaining \dot{Q}_C was, of course, zero at $\dot{m} = 0$. It was largest for the largest \dot{m} and smallest \dot{Q}_C , where for example $\dot{Q}_C = 3$ W and $\dot{Q}_{elec} = 19$ W for $\dot{m} = 3.5$ g/s for the left stack. At the opposite extreme for the

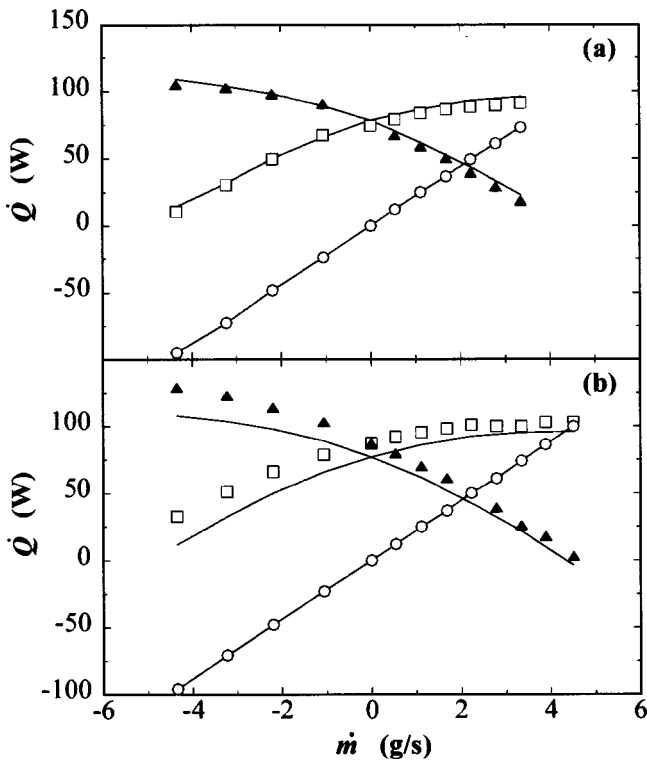


FIG. 5. Several thermal powers \dot{Q} as a function of steady flow rate \dot{m} , (a) for left stack and (b) for right stack. Symbols are experimental results and lines are numerical results. The circles are steady-flow enthalpy change, the triangles are the heat \dot{Q}_C extracted from the cold heat exchanger by the stack, and the squares are the sum of these two. (At $\dot{m} > 0$, the curves end where \dot{Q}_C drops to zero.)

left stack, $\dot{Q}_C = 129$ W and $\dot{Q}_{\text{elec}} = 100$ W for $\dot{m} = -4.2$ g/s.

Figure 5 shows some powers as a function of steady mass flow rate, all at $|p_1|/p_m = 0.020$, $T_0 = 308.0$ K, and $T_C = 300.5$ K. Signs for all \dot{Q} 's and for \dot{m} are chosen so that positive values correspond to operation as a refrigerator: Positive heat transfer rates flow into the stack, removing heat from the steady flow or from the cold heat exchanger. Symbols are measured values, with the uncertainties in the data typically lying within the areas covered by the symbols. The curves are the results of numerical integrations of the partial model.

The open circles and associated straight lines are simply $\dot{m}c_p(T_0 - T_C)$, representing the enthalpy removed from the steady flow as it passed through the stack. The dark triangles are cold-end cooling powers \dot{Q}_C , obtained from measured values of electric power dissipation in the cold heat exchanger and corrected for steady flow using Eq. (10). The open squares represent the total refrigeration power: the sum of \dot{Q}_C and the steady flow's enthalpy change across the stack. The curves associated with the triangles and squares are numerical integrations of the relevant equations, obtained in the same fashion as the curves in Fig. 4.

The qualitative trends in the observed dependences of \dot{Q}_C and $\dot{Q}_C + \dot{m}c_p(T_0 - T_C)$ on \dot{m} are predicted very well by the numerical integrations of Eq. (4) and the other thermoacoustic equations, reinforcing our confidence in Eq. (4).

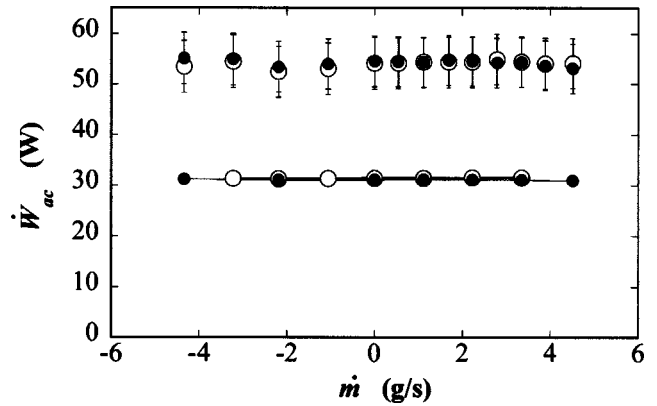


FIG. 6. Acoustic power delivered by the speakers as a function of steady flow rate. Open symbols are for the left speaker pair, and filled symbols for the right speaker pair. The values near 55 W are the result of Eq. (9), using experimental values for pressure amplitudes obtained during the measurements described in Sec. II. The values near 33 W are the result of a DeltaE model, using the speaker parameters obtained during preliminary measurements described in Sec. I.

Quantitative disagreements between the measurements and numerical integrations are less than 20 W, typically 10% of total power, and are probably due to a combination of uncertainty in geometrical parameters of the hardware that are used in the numerical integration and inappropriateness of the low-amplitude acoustic model's assumption that the gas displacement amplitude is much smaller than the stack length. The systematic differences between the right and left stacks' disagreements suggest hardware imperfections. However, the shared disagreements suggest a common cause. The peak-to-peak gas displacement amplitude in the stack was 2 cm, of the order of 10% of the length of the stack, so we would not be surprised by 10% errors in results predicted by the low-amplitude thermoacoustic equations, which are based in part on the assumption of negligibly small displacement amplitudes.

Figure 6 shows acoustic power delivered to the resonator from the fronts of the speakers, as a function of steady flow rate. The open circles with error bars represent the measured acoustic power delivered on the left side, found using measured complex pressure amplitudes and the speaker-diaphragm displacement relation given by Eq. (9); the corresponding dark circles are similar values for the right side. The near equality of the left and right results indicates the control achieved by the microphone mixers in balancing the acoustic power delivered to each side of the resonator, but the independence from \dot{m} is a more interesting, less direct consequence of the experimental conditions. The acoustic power delivered to the resonator was independently estimated using an enclosed-speaker algorithm with the measured speaker parameters in the complete numerical model of the apparatus. The circles connected by lines in Fig. 6 represent the values of acoustic power calculated with this numerical model. The numerically estimated acoustic power delivered to the resonator exhibits the same independence of \dot{m} as the measured data, but disagrees in magnitude by almost a factor of 2.

This large disagreement indicates a failure of either or

both of these methods of obtaining \dot{W}_{ac} . In hindsight, we suspect that the factory-equipped cooling system built into each speaker causes both methods to be inaccurate for this apparatus. At typical operating conditions, gas velocities induced by the cooling system past the voice coil and through the ports in the magnet were of the order of 50 m/s, and pressure differences of the order of $\rho|u_1|^2/2 \approx 1$ kPa and power dissipations of the order of 10 W per speaker are to be expected in the unstreamlined passages through which this high velocity passed. Neither the numerical model nor Eq. (9) (which assumes that the cavity volume V_{back} experiences spatially uniform oscillating pressure) can account for this complicated situation. Future modeling of such speakers in similar circumstances will require either a more sophisticated analysis than that which led to Eq. (9) here or an effort to choose (or modify) the speakers in order to simplify the cavity geometry.

IV. CONCLUSIONS

Deliberate superposition of steady flow parallel to the thermoacoustic oscillations in a stack can indeed be used to cool the steady flow as it passes through the stack. The agreement between measurements and numerical integrations for stack temperature profile and cooling power summarized in Figs. 4 and 5 suggests that Eq. (4) describes the total power flow in a stack when such steady flow exists.

As \dot{m} was increased, adding steady-flow heat load to the refrigerator, it was necessary to reduce \dot{Q}_C in order to maintain $T_0 - T_C$ constant. Figure 5 shows the details of this tradeoff: The total refrigeration power $\dot{Q}_C + \dot{m}c_p(T_0 - T_C)$ rose with \dot{m} . This increase in total cooling power while the acoustic power needed to drive the device remained constant illustrates the increase in efficiency, discussed in the Introduction, that occurs as some of the total heat load is shifted from T_C to temperatures greater than T_C as steady flow increases. If we define the coefficient of performance (COP) as total cooling power divided by acoustic power, the COP increases about 20% as the cooling power is shifted completely from \dot{Q}_C to $\dot{m}c_p(T_0 - T_C)$. This is much less than the ideal factor-of-two efficiency increase discussed in the Introduction, but our refrigerator was also far from ideal in many other respects. At $\dot{m} = 0$, its COP was only roughly 4% of Carnot's COP, and apparently most of the irreversibilities responsible for this low COP are not improved by steady flow. Future exploration of these details will be interesting and important.

Determination of the acoustic power delivered by a speaker based on measurements of complex pressure amplitude on both sides of the speaker diaphragm and knowledge

of the enclosed volume on one side requires attention to the details of the enclosed volume, lest pressure differences within the enclosed volume invalidate the theory of the measurement.

This work focused on a standing-wave thermoacoustic refrigerator with parallel superimposed steady flow, but we hope that engines, traveling-wave devices, and devices with perpendicular superimposed steady flow will also demonstrate interesting phenomena and lead to practical applications.

ACKNOWLEDGMENTS

This work was supported by the Office of Basic Energy Sciences in the U.S. Department of Energy. We thank Bill Ward for designing the speaker system.

- ¹ASHRAE Handbook: 1995 Applications (American Society of Heating, Refrigerating, and Air-Conditioning Engineers, Inc., New York, 1995), pp. 9.4–9.6.
- ²A. Bejan, *Advanced Engineering Thermodynamics*, 2nd ed. (Wiley, New York, 1997).
- ³N. Rott, "Damped and thermally driven acoustic oscillations in wide and narrow tubes," *Z. Angew. Math. Phys.* **20**, 230–243 (1969).
- ⁴N. Rott, "Thermally driven acoustic oscillations, Part III: Second-order heat flux," *Z. Angew. Math. Phys.* **26**, 43–49 (1975).
- ⁵G. W. Swift, "Thermoacoustic engines," *J. Acoust. Soc. Am.* **84**, 1145–1180 (1988).
- ⁶R. S. Reid, "Open cycle thermoacoustics," Ph.D. thesis, Georgia Institute of Technology, School of Mechanical Engineering, 1999.
- ⁷G. W. Swift, "Thermoacoustics: A unifying perspective for some engines and refrigerators," Rough draft available at www.lanl.gov/thermoacoustics/, 1999.
- ⁸W. C. Ward and G. W. Swift, "Design environment for low amplitude thermoacoustic engines (DeltaE)," *J. Acoust. Soc. Am.* **95**, 3671–3672 (1994). Fully tested software and user's guide available from Energy Science and Technology Software Center, U.S. Department of Energy, Oak Ridge, Tennessee. To review DeltaE's capabilities, visit the Los Alamos thermoacoustics web site at www.lanl.gov/thermoacoustics/. For a beta-test version, contact ww@lanl.gov (Bill Ward) or swift@lanl.gov (Greg Swift) by email.
- ⁹R. S. Reid, W. C. Ward, and G. W. Swift, "Cyclic thermodynamics with open flow," *Phys. Rev. Lett.* **80**, 4617–4620 (1998).
- ¹⁰G. W. Swift, "Analysis and performance of a large thermoacoustic engine," *J. Acoust. Soc. Am.* **92**, 1551–1563 (1992).
- ¹¹Endevco, San Juan Capistrano, California 92675, Model 8510B.
- ¹²Hewlett Packard, Santa Clara, California 95054, Model 35665A.
- ¹³Omega Engineering, Stamford, Connecticut 06906.
- ¹⁴JBL Professional, Northridge, California 91329, Model 2206H/J.
- ¹⁵R. S. Wakeland, "Use of electrodynamic drivers in thermoacoustic refrigerators," *J. Acoust. Soc. Am.* **107**, 827–832 (2000).
- ¹⁶T. J. Hofler, "Accurate acoustic power measurements with a high-intensity driver," *J. Acoust. Soc. Am.* **83**, 777–786 (1988).
- ¹⁷S. Ballantine, "Technique of microphone calibration," *J. Acoust. Soc. Am.* **3**, 319–360 (1932).
- ¹⁸A. M. Fusco, W. C. Ward, and G. W. Swift, "Two-sensor power measurements in lossy ducts," *J. Acoust. Soc. Am.* **91**, 2229–2235 (1992).
- ¹⁹Fuji Electric, Tokyo, Japan, blower model 4Z753.
- ²⁰Meriam Instruments, Cleveland, Ohio 44102, Model 50MW20-1 1/2.

Modeling piezoceramic transducer hysteresis in the structural vibration control problem

S.-H. Lee and T. J. Royston^{a)}

University of Illinois at Chicago, Chicago, Illinois 60607

To appropriately assess, compensate for and/or potentially utilize piezoceramic transducer nonlinearities, reversible and irreversible, in the structural vibration control problem, a suitable theoretical framework is needed. In this study such a framework is developed and experimentally evaluated for a basic pedagogical structural vibration control system, the simply supported beam with a monolithic piezoceramic wafer bonded to it that can be both electrically shunted and/or driven by an external electric source. A constitutive model for the piezoceramic (PZT) wafer by itself is formulated that incorporates reversible (higher order polynomial) and irreversible (hysteretic) dielectric nonlinearity. An identification scheme for the model is validated experimentally. The nonlinear PZT model is then integrated into the coupled dynamic equations of the overall system consisting of the simply supported beam and the electrically shunted PZT wafer bonded to the beam. The theoretical system model is then evaluated by comparing its predictions to experimental results. Energy loss and transduction mechanisms in the integrated structural system are investigated. © 2000 Acoustical Society of America. [S0001-4966(00)04012-1]

PACS numbers: 43.40.At, 43.40.Ga, 43.38.Fx [CBB]

I. INTRODUCTION

A number of studies have shown that, in addition to minor reversible nonlinearity, significant irreversible nonlinearity in the form of dielectric hysteresis is present in piezoceramic transducers, such as those based on lead zirconate (PZT).¹⁻¹⁷ Hysteresis can have a detrimental effect on the performance of the piezoceramic in structural vibration control applications. Hysteresis can cause multiple output states for a given input state, frustrating open-loop control, and it can generate unwanted amplitude-dependent phase shifts and harmonic distortion which reduce the effectiveness of feedback control. On the other hand, it can be argued that hysteresis could potentially be harnessed as a means of unwanted vibratory energy dissipation in passive, adaptive and active control scenarios.

In order to appropriately assess the impact of, compensate for, and potentially utilize piezoceramic transducer nonlinearities, reversible and irreversible, in the structural vibration control problem, a suitable theoretical system model is needed. For design robustness, parameters used in this model should be obtainable from studies on the individual components that make up the complex structural system, such as the individual transducers and elements of the mechanical structure. Additionally, overall performance assessment should be based on both the resulting reduction in vibratory energy and the level of control energy required. In other words, an analysis of vibratory power generation, transduction and dissipation throughout the structure and integrated transducers is desirable.

In the study reported in this article, the issues mentioned above are addressed in the context of a basic pedagogical structural vibration control problem, the simply supported

beam with a monolithic piezoceramic wafer bonded to it that can be both electrically shunted and/or driven by an external electric source. Specific objectives are as follows:

- (1) Formulate a constitutive model for the piezoceramic (PZT) wafer that incorporates reversible (higher order polynomial) and irreversible (hysteretic) nonlinearity.
- (2) Devise an experimental identification scheme for the constitutive model and validate it experimentally.
- (3) Integrate the nonlinear PZT model into the coupled dynamic equations of the overall system consisting of a simply supported beam and electrically shunted PZT wafer bonded to the beam.
- (4) Numerically simulate the coupled system equations and evaluate the theoretical developments by comparison to experimental results.
- (5) Investigate energy loss and transduction mechanisms in the integrated structural system.

II. NONLINEAR MODEL FOR PIEZOCERAMIC MONOLITHIC WAFER

A. Quasistatic piezoelectric nonlinear constitutive equation

Consider a monolithic piezoceramic wafer with geometry depicted in Fig. 1. Take the case where $T_3 = T_2 = D_1 = D_2 = E_1 = E_2 = 0$. Then the linear constitutive equations may be expressed in the following form:

$$S_1 = s_{11}^D T_1 + g_{31} D_3, \quad (1a)$$

$$E_3 = -g_{31} T_1 + \beta_{33}^T D_3. \quad (1b)$$

Here, nomenclature follows that of ANSI/IEEE standard 176-1987 on piezoelectricity. In this formulation independent variables are mechanical stress T and electric displacement D . Dependent variables are mechanical strain S and electric field E . Superscripts D and T refer to “at constant”

^{a)} Author to whom correspondence should be addressed: Department of Mechanical Engineering, University of Illinois at Chicago, 842 West Taylor St., MC 251, Chicago, Illinois, 60607. Electronic mail: troyston@uic.edu

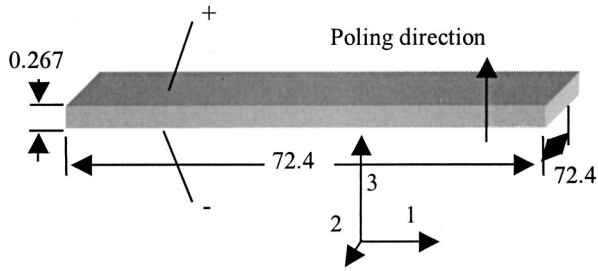


FIG. 1. Schematic of the piezoceramic (PZT-5H) monolithic wafer. Nickel electrode sputtered on “3” sides. Dimensions in millimeters.

electrical displacement or mechanical stress, respectively, and numerical subscripts refer to geometric direction (see Fig. 1). Coefficients s , g , and β refer to the elastic compliance coefficient, piezoelectric constant, and the dielectric impermeability, respectively.

A number of studies have shown that, even at relatively low electrical and/or mechanical stress levels, piezoelectric ceramics exhibit substantial rate-independent nonlinear behavior, primarily hysteretic, in their electroelastic interaction which is not accounted for in the linear formulation of the electroelastic equations for the piezoceramic material. For example, Goldfarb and Celanovic⁴ and Main and Garcia⁵⁻⁷ have measured a strong hysteretic relation between electrical displacement D and field E . Take nonlinear behavior in the PZT to be in the dielectric β^T relation. It will be denoted as a bracket $\{ \}$ in the following equations:

$$S_1 = s_{11}^D T_1 + g_{31} D_3, \quad (2a)$$

$$E_3 = -g_{31} T_1 + \{\beta_{33}^T D_3\}. \quad (2b)$$

These equations do agree with experimental observations of PZT reported in the literature. For example, Goldfarb and Celanovic⁴ observed that the applied electrical displacement (D) versus strain (S) relation under zero stress (T) was reversible, but that applied electric field (E) versus S under zero T was not. They also observed that the mechanical stress-strain relation under constant electric displacement was reversible whereas the relation under constant electric field was hysteretic. Damjanovic *et al.*⁸⁻¹⁰ observed that the applied stress versus electrical displacement relation was hysteretic.

B. A generalized Maxwell resistive capacitor hysteresis model with reversible nonlinearity

In previous articles of the authors,¹⁻³ it has been shown that hysteretic behavior in another type of PZT-based transducer, the 1-3 composite, was accurately modeled using a Maxwell resistive capacitor (MRC) hysteresis model for electric field/displacement levels sufficiently less than saturation (less than 80% of the coercive field to avoid depoling). A new generalized version of the MRC model is applied to the monolithic PZT wafer in the present study. The modification is to account for minor reversible nonlinearity present in the dielectric relationship in addition to the irreversible hysteretic relationship. Also, in previous articles,^{2,3} it has been proven that the MRC hysteresis model represents a subset of classical Preisach (CPM) hysteresis models. In fact,

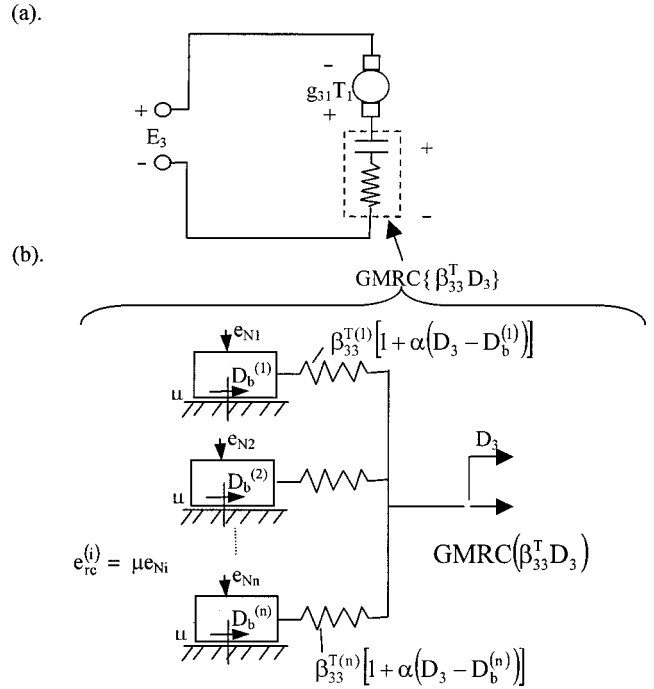


FIG. 2. Generalized Maxwell resistive capacitor (GMRC) hysteresis model. (a) Equivalent electric circuit of Eq. (3b). (b) Equivalent mechanical analogy of GMRC operator of Eq. (3c).

this relationship can be used to develop an efficient online identification routine for the MRC model and its inverse. These developments will be extended to the generalized MRC (GMRC) model of the present study.

The GMRC model is schematically represented in Fig. 2 where the formulation is in terms of electrical field and displacement, E and D . Referring to Fig. 2, the model may be implemented into the otherwise linear constitutive equations (1a) and (1b) as follows:

$$S_1 = s_{11}^D T_1 + g_{31} D_3, \quad (3a)$$

$$E_3 = -g_{31} T_1 + \text{GMRC}\{\beta_{33}^T D_3\}, \quad (3b)$$

with $\text{GMRC}(\beta_{33}^T D_3) = \sum_{i=1}^n E_{rc}^{(i)}$ where

$$\begin{aligned} & \text{if } |\beta_{33}^{T(i)} [1 + \alpha(D_3 - D_b^{(i)})] (D_3 - D_b^{(i)})| < e_{rc}^{(i)}, \\ & \text{then } E_{rc}^{(i)} = \beta_{33}^{T(i)} [1 + \alpha(D_3 - D_b^{(i)})] (D_3 - D_b^{(i)}), \\ & \text{otherwise } E_{rc}^{(i)} = e_{rc}^{(i)} \text{ sign}[\dot{D}_3] \end{aligned} \quad (3c)$$

and $D_b^{(i)}$ is set such that

$$|\beta_{33}^{T(i)} [1 + \alpha(D_3 - D_b^{(i)})] (D_3 - D_b^{(i)})| = e_{rc}^{(i)}.$$

Here, the terms β_{33}^T , e_N , μ , e_{rc} , and D_b may be viewed as electrical analogies to a mechanical spring stiffness, normal force, Coulomb friction coefficient, the force due to Coulomb friction and the displacement from an equilibrium position of the massless box, respectively. The parameter α accounts for a reversible nonlinear “spring stiffness” effect. If $\alpha=0$, the MRC model is recovered. Certainly, additional higher order polynomial terms could be included in the dielectric impermeability expression and a different value of

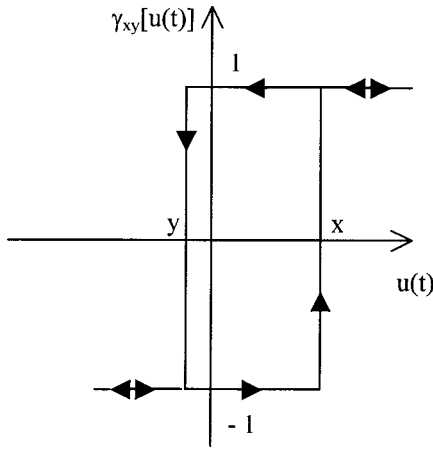


FIG. 3. Preisach hysteresis relay operator, $\gamma_{xy}[u(t)]$.

$\alpha^{(i)}$ could be used for each $\beta_{33}^{T(i)}$. However, the above generalization is sufficient to illustrate the new concepts presented in this work without unnecessary complexity.

The authors have established that the MRC hysteresis model and its inverse are particular cases of the classical Preisach hysteresis model.^{2,3} [Indeed, the basic MRC unit or operator is an elementary stop hysteron, as defined in the magnetics literature;^{18,19} hysterons are also the basic building blocks of the Prandtl-Ishlinskii hysteresis models. Additionally, the MRC operator is related to the Krasnosel'skii and Pokrovskii (KP) operator mentioned in recent studies that use it for actuator hysteresis compensation.²⁰ The KP operator is, in the terminology of Krasnosel'skii and Pokrovskii,²¹ a play hysteron, for which the stop hysteron is, in some cases, its inverse.] Put simply, the classical Preisach model (CPM) combines the outputs of a collection of independent bi-stable relays to form its output according to the following formula:²²

$$f(t) = \int \int_{x \geq y} \mu(x, y) \gamma_{xy}[u(t)] dx dy. \quad (4)$$

Here, $f(t)$ is the output (in our case $\{\beta_{33}^T D_3\}$), $u(t)$ is the input (in our case D_3), $\mu(x, y)$ is a weighting function and γ_{xy} is the simple hysteresis relay operator whose value is determined by the input operation depicted in Fig. 3.

Consider a GMRC model with $n=1$ elasto-slide elements as shown in Fig. 4(a). The following Preisach function approximately represents this behavior for $|\alpha D_3| < 1$:²³

$$\mu(x, y) \approx \frac{1}{2} \beta_{33}^{T(1)} [1 + \alpha(x+y)] \{ \delta[x-y] - \delta[x-y-w_1] \}, \quad (5)$$

where δ denotes the Dirac delta function and $w_1 = 2e_{rc}^{(1)}/\beta_{33}^{T(1)}$. For the single elasto-slide element of Fig. 4(a) an inverse is not well defined due to the horizontal portions of the relationship. To address this issue, now consider the model depicted in Fig. 4(b) with one completely reversible nonlinear “spring” element $\beta_{33}^{T(2)}$ and one nonlinear spring element $\beta_{33}^{T(1)}$ that is a part of a slip element with a “slip force” of $e_{rc}^{(1)}$. More generally, one may consider that there are slip elements associated with both springs, but $e_{rc}^{(2)}$ is sufficiently large that it is never reached and $D_b^{(2)} = 0$ for

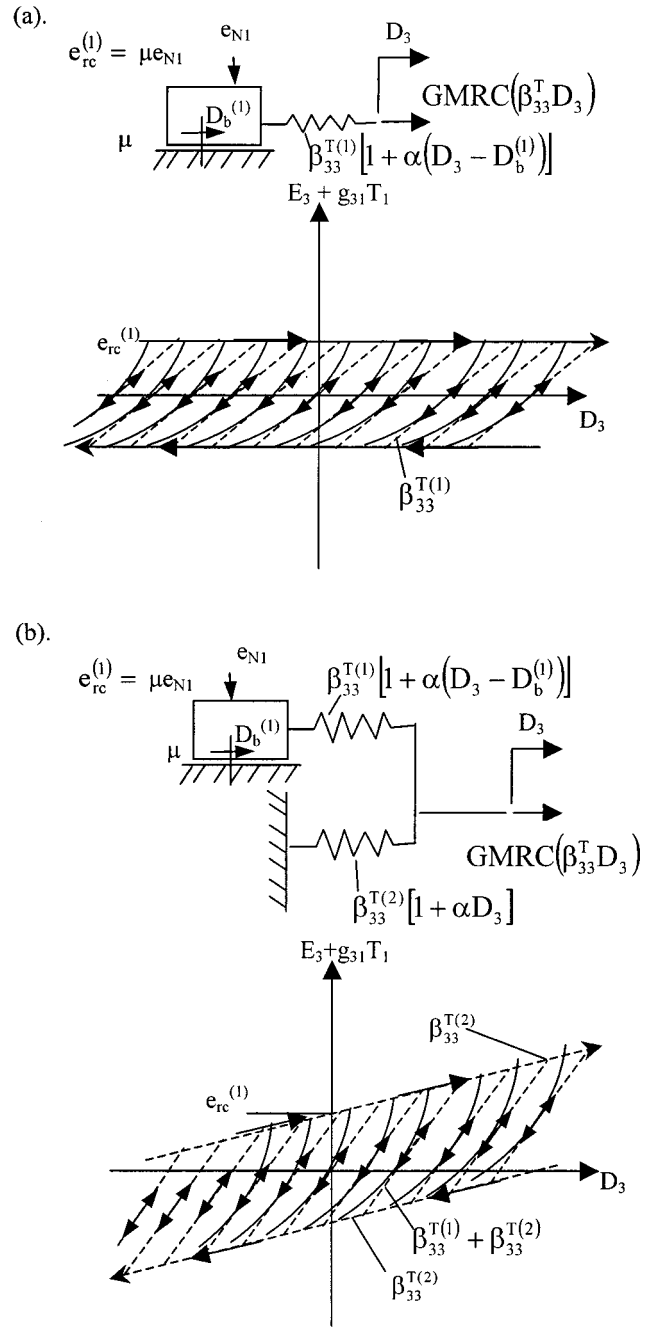


FIG. 4. Simple GMRC models. (a) Single MRC (dashed) and GMRC (solid) elasto-slide element. (b) Single MRC (dashed) and GMRC (solid) elasto-slide element in parallel with elastic element.

all time. Unlike the MRC model, the GMRC model does not satisfy the two necessary and sufficient conditions for it to be considered a classical Preisach model.²² While it satisfies the wiping out property, it does not satisfy the property of congruent minor loops. However, minor loops resulting from back-and-forth input variations between the same two consecutive extrema will have equal vertical chords. Consequently, the GMRC is a subset of the nonlinear Preisach hysteresis model (NPM).²² In general, the NPM requires dependence on three variables in the weighting function μ . But, in the approximate analysis here, dependence on only x and y is reasonable.²³

For the relationship depicted in Fig. 4(b), the Preisach

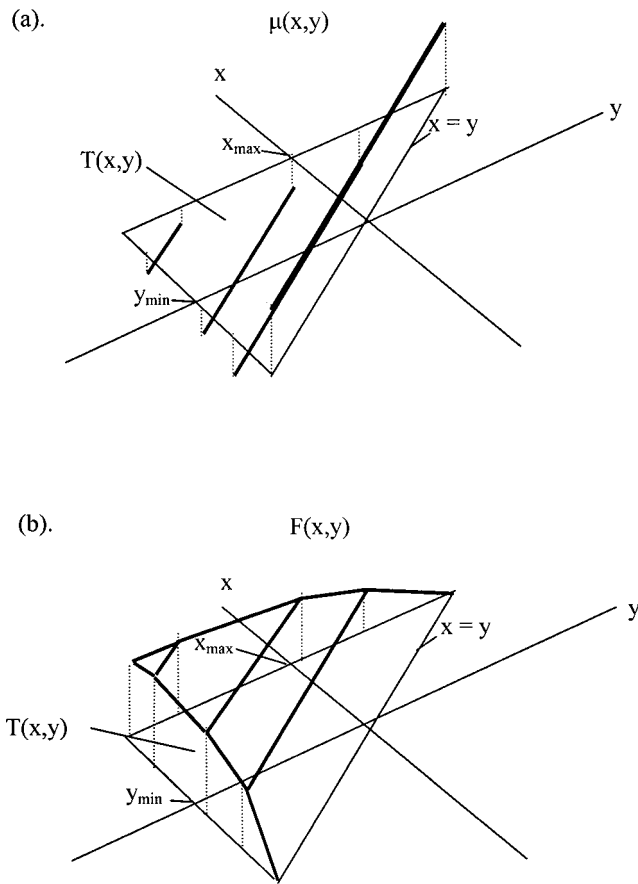


FIG. 5. Functional relationships of classic Preisach representation of the MRC hysteresis model. (a) Weighting function $\mu(x,y)$. (b) Everett function $F(x,y)$ based on first order transition curves.

weighting function can be expressed as follows:

$$\mu(x,y) \approx \frac{1}{2} \{ (\beta_{33}^{T(1)} + \beta_{33}^{T(2)}) [1 + \alpha(x+y)] \delta[x-y] - \beta_{33}^{T(1)} [1 + \alpha(x+y)] \delta[x-y-w_1] \}. \quad (6)$$

The above formulation can be generalized to the case of Fig. 2. Suppose that $e_{rc}^{(n)}$ is sufficiently large that it is never reached and $D_b^{(n)} = 0$ for all time. Then we have the following:

$$\mu(x,y) \approx \frac{1}{2} \left\{ \sum_{i=1}^n (\beta_{33}^{T(i)}) [1 + \alpha(x+y)] \delta[x-y] - \sum_{i=1}^{n-1} (\beta_{33}^{T(i)}) [1 + \alpha(x+y)] \delta[x-y-w_i] \right\}. \quad (7)$$

For the case that $\alpha=0$ (the MRC model) the Preisach weighting function has some unique features as can be observed in Fig. 5(a) where $\mu(x,y)$ is graphed. Essentially, the MRC model represents a subset of classical Preisach weighting functions with the following properties:

- (1) The $\mu(x,y)$ function consists of a countable number of lines parallel to the $x=y$ line.
- (2) The number of lines corresponds to the number of MRC hysteretic elasto-slide elements.
- (3) Each line has a constant value along its length.

- (4) This constant value and the line's distance from the $x=y$ line are directly related to MRC elasto-slide element properties.

In terms of MRC model identification, one could first establish whether or not a particular hysteretic relationship meets the criterion of congruency and wiping out to be described by the CPM.²² Having established this, one then could check for the validity of a MRC representation by checking for a constant value along lines parallel to the $x=y$ line. For the case that $\alpha \neq 0$ (GMRC model) the Preisach weighting function is modified in the following sense. For a given line parallel to the $x=y$ line, there is not a constant value along its length, but rather a value that is linearly increasing or decreasing for increasing x and y values. In fact, the slope of this line is proportionally related to the value of α .

Preisach model identification is accomplished by determining the first order transition (reversal) curves. These can be graphically represented in terms of the following Everett function,

$$F(x',y') = \frac{1}{2} (f_{x'} - f_{x'y'}) \quad (8)$$

in the $T(x,y)$ triangle, similar to $\mu(x,y)$ as shown in Fig. 5(b). These are obtained by first monotonically increasing the input value from negative saturation to x' , obtaining the output value $f_{x'}$. Then, the input is monotonically decreased to y' , obtaining the output value $f_{x'y'}$. This results in the following:

$$F(x',y') = \int \int_{T(x',y')} \mu(x,y) dx dy, \quad (9)$$

where $T(x',y')$ denotes the triangular region bordered by the maximum value of x' , the minimum value of y' and the line $x=y$. Note that the prime is used on x and y where necessary to denote a specific value.

Based on Eqs. (7)–(9) we have the following for the GMRC model in Fig. 2:

$$F(x,y) \approx \left\{ \frac{1}{2} \sum_{i=1}^n \beta_{33}^{T(i)} \right\} [1 + \alpha(x+y)] (x-y) - \frac{1}{2} \sum_{i=1}^{n-1} \{ \beta_{33}^{T(i)} [1 + \alpha(x+y)] (x-y-w_i) \} \times H[x-y-w_i], \quad (10)$$

where $H[\lambda]$ denotes the Heaviside function with

$$H[\lambda] = \begin{cases} 1, & \lambda > 0, \\ 0, & \lambda < 0. \end{cases} \quad (11)$$

Like $\mu(x,y)$, the function $F(x,y)$ of the GMRC hysteresis model has a constant slope along lines parallel to the $x=y$ line. Unlike the representation of $\mu(x,y)$, for finite GMRC elements (finite n) the resulting graph of $F(x,y)$ is continuous over the region $T(x,y)$ but its derivatives are discontinuous. Consequently, having experimentally determined $F(x,y)$ based on the first order transition curves, one could then check if it has the property of a constant slope along lines parallel to the $x=y$ line. If so, then it may be approxi-

mated by the GMRC model. Note that the level of accuracy or resolution that is needed in approximating the experimentally measured relationship will determine the number of GMRC elasto-slide elements and whether or not additional higher order polynomial terms are required to describe reversible nonlinearity. As a final comment here, it is noted that, in general, nonlinear Preisach models require second order reversal curves for their determination. But, for the specific case of the GMRC model, first order reversal curves (which are used to construct the Preisach and Everett functions) are sufficient for the approximate analysis here when $|\alpha D_3| < 1$.²³

C. GMRC model identification

A method for identification of the GMRC model is now presented. It is virtually identical to the identification routine for the MRC model² except for the last step that is required to identify α . The developed methodology assumes that $|x_{\max}| = |y_{\min}|$ but can be easily generalized. The $T(x, y)$ triangle is divided by n lines parallel to the $x = y$ line that are equally separated in distance with the n th line intersecting the point $(x, y) = (x_{\max}, -x_{\max})$. Hence, we have w_i values of equal increments in length denoted by the following:

$$w_i = \frac{i2}{n} x_{\max}, \quad i = 1, \dots, n. \quad (12)$$

Then, given the experimentally determined function $F(x, y)$, it is possible to average its values along lines parallel to the $x = y$ line at distances w_i from the $x = y$ line. These averaged values will be denoted

$$F_{x'i} = \frac{1}{\sqrt{2}(2x_{\max} - w_i)} \int_{y_{\min}}^{x_{\max}} F(x', x' - w_i) dx, \quad (13)$$

and we define

$$\mathbf{F}_{x'} = \begin{bmatrix} F_{x'1} \\ \vdots \\ F_{x'n} \end{bmatrix}. \quad (14)$$

Equations (10)–(14) may be written in the following form, solving for the vector β_{33}^T of the unknown MRC elastic coefficients:

$$\beta_{33}^T = \begin{bmatrix} \beta_{33}^{T(1)} \\ \vdots \\ \beta_{33}^{T(n)} \end{bmatrix} = \frac{n}{x_{\max}} \begin{bmatrix} 1 & 1 & \cdots & 1 & 1 \\ 1 & 2 & \cdots & 2 & 2 \\ \vdots & \vdots & 3 & \cdots & 3 \\ 1 & 2 & \vdots & \ddots & \vdots \\ 1 & 2 & 3 & \cdots & n \end{bmatrix}^{-1} \mathbf{F}_{x'}. \quad (15)$$

Upon determining the elastic coefficients, the sliding constants can be determined using the following:

$$e_{rc}^{(i)} = \frac{ix_{\max}}{n} \beta_{33}^{T(i)}, \quad i = 1, \dots, n-1. \quad (16)$$

Note that a value for $e_{rc}^{(n)}$ is not needed as this is not used in Eq. (10) since it is assumed that the input values do not exceed the region of $T(x, y)$.

To estimate α , the average value of the Everett function along the line $x = y + w_1$ is subtracted and, based on a least squares linear curve fit, the average slope $\partial F_{w1} / \partial r$ of the Everett function along this line is determined. Then we have the following:

$$\alpha = \left(\frac{\partial F_{w1}}{\partial r} \right) / \left[\frac{\sqrt{2}x_{\max}}{n} \sum_{i=1}^n \beta_{33}^{T(i)} \right]. \quad (17)$$

The inverse MRC model and its identification can be found in previous works of the authors³ and extension to the inverse of the GMRC model will be discussed in an upcoming publication.²³ Extension of the identification scheme to the case of higher order polynomials in the dielectric relationship is left for future work. It is sufficient to state here that one would expect additional higher order terms to correspond to curvature on the Everett surface along lines parallel to $x = y$. The coefficients of a least squares polynomial curve fit could be related to the coefficients of higher order terms for the ‘‘spring stiffness’’ in the dielectric GMRC model.

D. Hysteretic energy loss for the general loading condition

Following the derivation in Section 3.5 of Mayergoyz,²² the hysteretic energy loss Q for a monotonic increase in input u from u_- to u_+ in a CPM system can be expressed as follows:

$$Q(u_-, u_+) = (u_+ - u_-)F(u_+, u_-) - \int_{u_-}^{u_+} F(u_+, y) dy - \int_{u_-}^{u_+} F(x, u_-) dx. \quad (18)$$

It is also proved in Ref. 22 that $Q(u_-, u_+) = Q(u_+, u_-)$. From this it follows that an expression for dielectric energy loss in a MRC hysteresis model for a monotonic increase (or decrease) in D_3 is

$$Q(D_{3-}, D_{3+}) = Q(D_{3+}, D_{3-}) = \frac{1}{2} \sum_{i=1}^{n-1} \beta_{33}^{T(i)} w_i (D_{3+} - D_{3-} - w_i) \times H[D_{3+} - D_{3-} - w_i]. \quad (19)$$

The units are in energy per unit volume (e.g., J/cm³). A logical extension of it to the GMRC model is as follows:

$$Q(D_{3-}, D_{3+}) = Q(D_{3+}, D_{3-}) \approx \frac{1}{2} \sum_{i=1}^{n-1} \beta_{33}^{T(i)} [1 + \alpha(D_{3+} + D_{3-})] \times w_i (D_{3+} - D_{3-} - w_i) H[D_{3+} - D_{3-} - w_i]. \quad (20)$$

An alternative means of calculating hysteretic energy loss in this case is to utilize its physical analogy as a collection of Coulomb friction components denoted in Fig. 2. Work done against the friction force for each of the slide elements represents energy dissipation from the system. The total hys-

TABLE I. Manufacturer^a and experimentally determined (*) parameter values of monolithic PZT wafer.

PZT density	ρ_p	7800	kg/m ³
PZT width	b_p	0.072 39	m
PZT thickness	h_p	0.000 266 7	m
Coupling coefficient	k_{31}	0.44	
Young's modulus	E_{11}	6.2×10^{10}	N/m ²
	E_{33}	5.0×10^{10}	N/m ²
Piezoelectric constants	d_{31}	-320×10^{-12}	m/V
	d_{33}	650×10^{-12}	m/V
	g_{31}	-9.5×10^{-3}	V-m/N
Capacitance		610×10^{-9}	Farads
Mechanical stiffness* (based on experiment)	\bar{c}_{11}^D	13.64×10^{10}	N/m ²
	\bar{c}_{12}^D	-5.68×10^{10}	N/m ²
Piezoelectric constants* (based on experiment)	g_{31}	-10.1×10^{-3}	V-m/N
	h_{31}	-1.35×10^9	V/m

^aPiezo Systems, Inc. (Piezoelectric Single Sheet, PSI-5H4E, Part no.: T110-H4E-602).

etic energy dissipation could be expressed in the following form:

$$Q = \sum_{i=1}^{n-1} Q_i \quad (21a)$$

where

$$Q_i = \int_{D_b^{(i), \text{start}}}^{D_b^{(i), \text{finish}}} e_{rc}^{(i)} \partial |D_b^{(i)}|. \quad (21b)$$

For a monotonically increasing input this would be approximated as follows:

$$\begin{aligned} & \sum_{i=1}^{n-1} \int_{D_b^{(i), -}}^{D_b^{(i), +}} e_{rc}^{(i)} \partial D_b^{(i)} \\ & \approx \frac{1}{2} \sum_{i=1}^{n-1} \beta_{33}^{T(i)} [1 + \alpha(D_{3+} + D_{3-})] w_i (D_{3+} - D_{3-} - w_i) \\ & \quad \times H[D_{3+} - D_{3-} - w_i]. \end{aligned} \quad (22)$$

Hence, the calculation of hysteretic energy dissipation using the Preisach argument agrees with the calculation using a physical argument.

III. EXPERIMENTAL STUDY OF PZT MONOLITHIC WAFER

Manufacturer and experimentally measured specifications for the piezoceramic (PZT) wafer considered in this study are provided in Table I. Relations between E_3 , D_3 and S_1 were measured up to several hundred Hz and 80 V amplitude. A Trek Model P0623A-G high-voltage amplifier was used. Here, electric current and voltage across the “3” direction are measured by the Trek amplifier and mechanical strain in the “1” direction is measured using a Polytec PI CLV 800 laser Doppler vibrometer. Sample measurements shown in Figs. 6 and 7 qualitatively confirm the proposed hysteresis model of Eqs. (3a) and (3b) for the case of $T_1 = 0$. However, the measurements do show some rate-dependence, particularly with respect to mechanical strain, S_1 . It is expected that, as frequency increases, mechanical

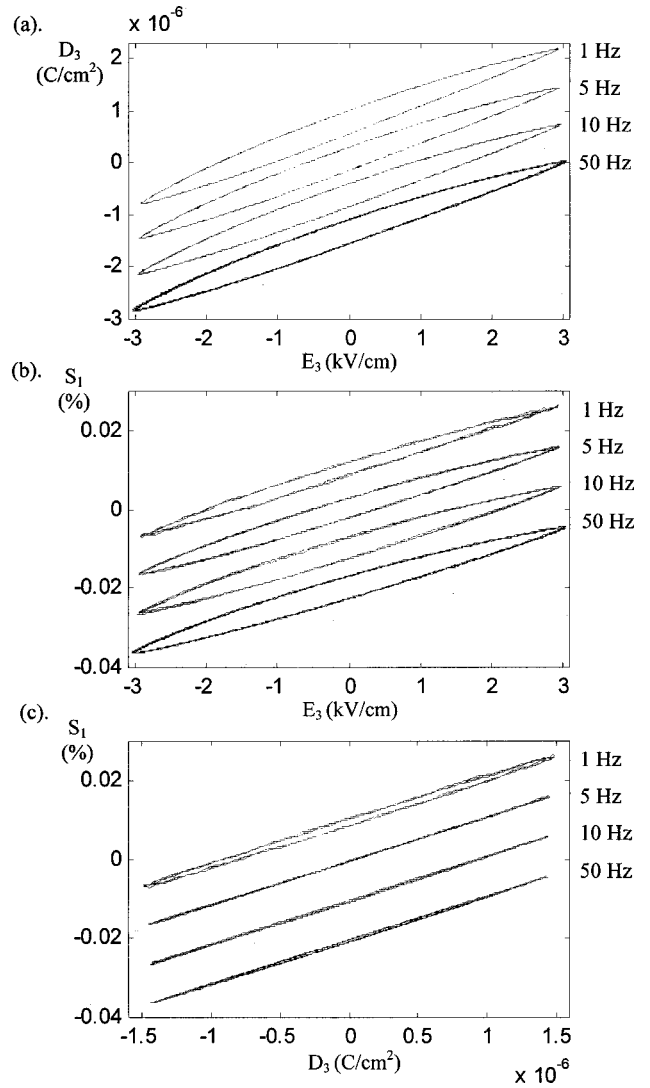


FIG. 6. Experimental measurements of the PZT wafer for sinusoidal voltage (electric field) excitation from 1 to 50 Hz with amplitude 80 V. Vertical offset added for ease of visual comparison.

dissipative effects will introduce rate-dependence. Additionally, it was found at very low frequencies, 1 Hz or less, that there was drift in the electrical and mechanical variables, possibly due both to meta-stability issues as well as instrumentation limitations. Consequently, for most of this study, the excitation was set to 5 Hz to avoid rate-dependence; the focus here is on modeling the underlying rate-independent behavior.

Under these constraints, the dielectric PZT hysteresis can be accurately modeled using the classical Preisach model. This was verified by testing wiping-out and congruent properties for $T_1 = 0$.²² Based on experimental first order reversal curves the Everett function surface can be generated as shown in Fig. 8. First, three MRC models with different numbers of elements, $n = 2, 5$ and 20 , were determined and are given in Table II. Simulation results using the identified Preisach model and different MRC models ($\alpha = 0$) were compared with experimental results for sinusoidal and arbitrary voltage input waveforms as shown in Figs. 9–11. There is a definite asymmetry in the experimental relationship par-

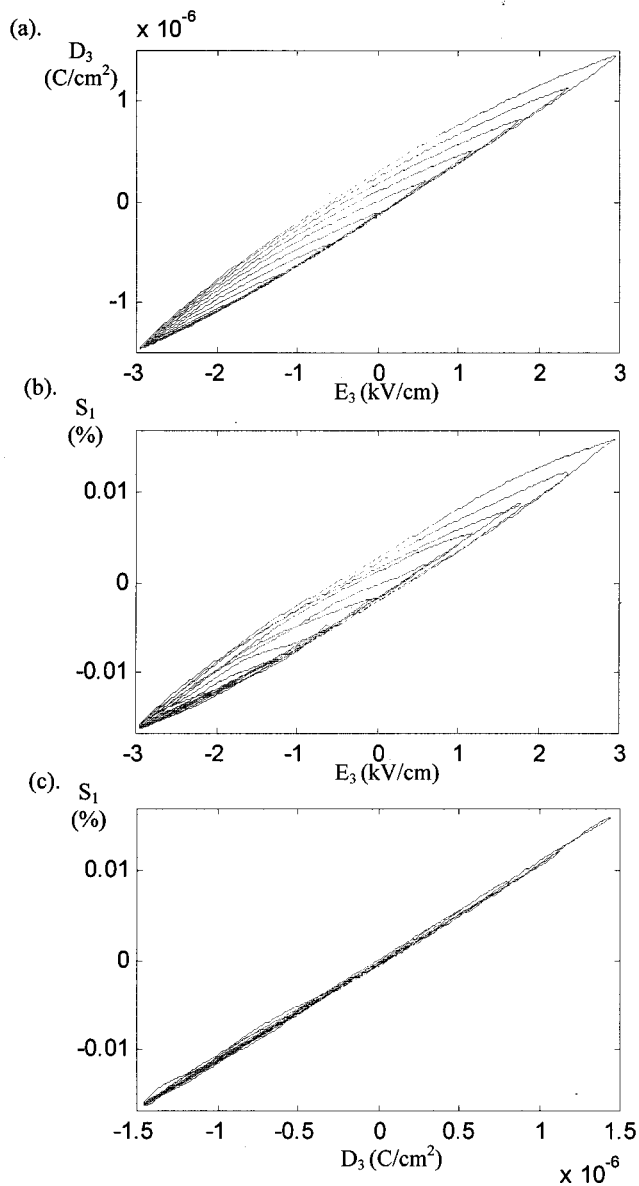


FIG. 7. Experimental measurements of the PZT wafer for sinusoidal voltage (electric field) excitation at 5 Hz with amplitude from 8 to 80 V (and decreasing negative dc bias).

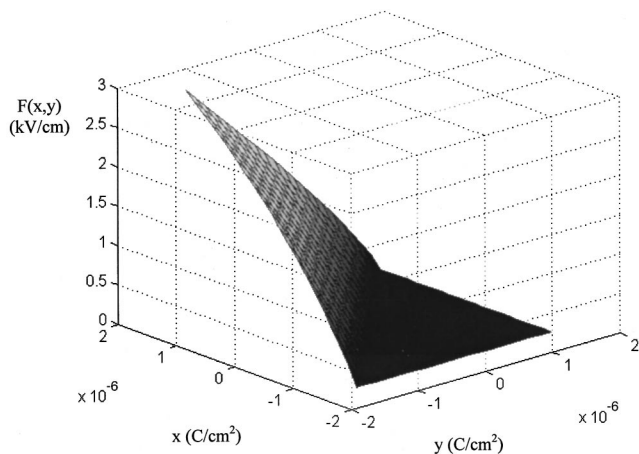


FIG. 8. Experimental Everett surface for the PZT wafer.

TABLE II. Identified MRC parameter values for the monolithic PZT wafer.

$n=2$	$\beta_{33}^{T(i)} \times 10^{-6}$	0.53325, 1.78940
	$e_{rc}^{(i)}$	0.38850, ∞
$n=5$	$\beta_{33}^{T(i)} \times 10^{-6}$	0.30868, 0.23188, 0.18356, 0.41700, 1.67796
	$e_{rc}^{(i)}$	0.08996, 0.13515, 0.16048, 0.16529, ∞
$n=20$	$\beta_{33}^{T(i)} \times 10^{-6}$	0.15688, 0.08362, 0.07663, 0.07183, 0.06788, 0.06433, 0.06102, 0.05784, 0.05476, 0.05174, 0.04877, 0.04584, 0.04294, 0.04009, 0.03730, 3.46269, 0.03223, 0.03083, 0.03527, 1.62803
	$e_{rc}^{(i)}$	0.01142, 0.01218, 0.01675, 0.02093, 0.02472, 0.028123, 0.03112, 0.03371, 0.03590, 0.03769, 0.03908, 0.04007, 0.040675, 0.04089, 0.04076, 0.04036, 0.03992, 0.04043, 0.04882, ∞

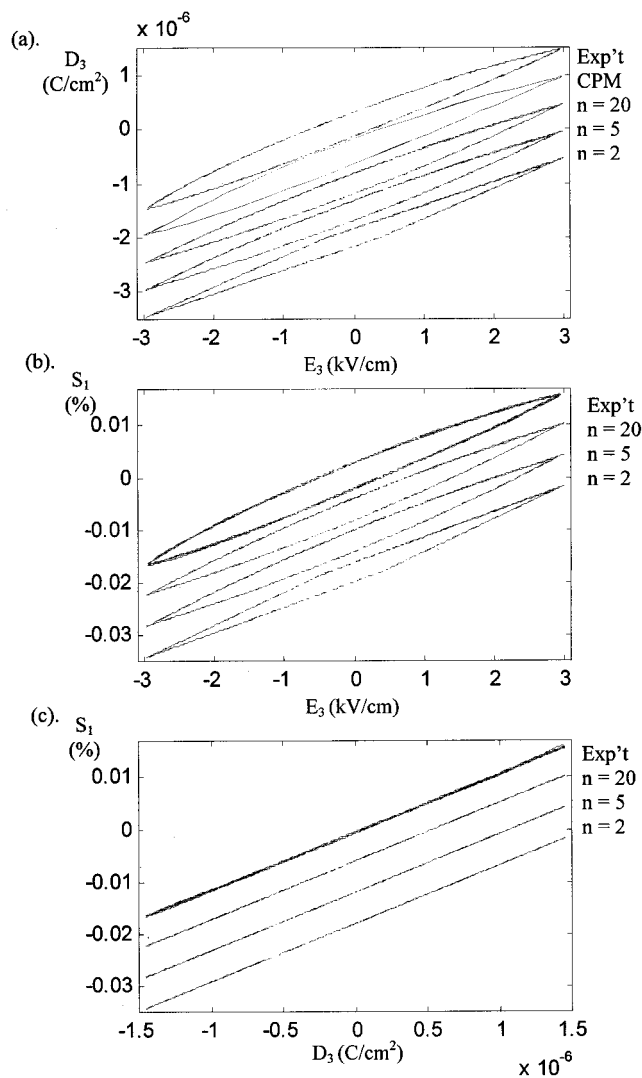


FIG. 9. Comparison of experiment, CPM and MRC ($n=2,5,20$) hysteresis model simulations for the PZT wafer with sinusoidal input at 5 Hz. Vertical offset added for ease of visual comparison.

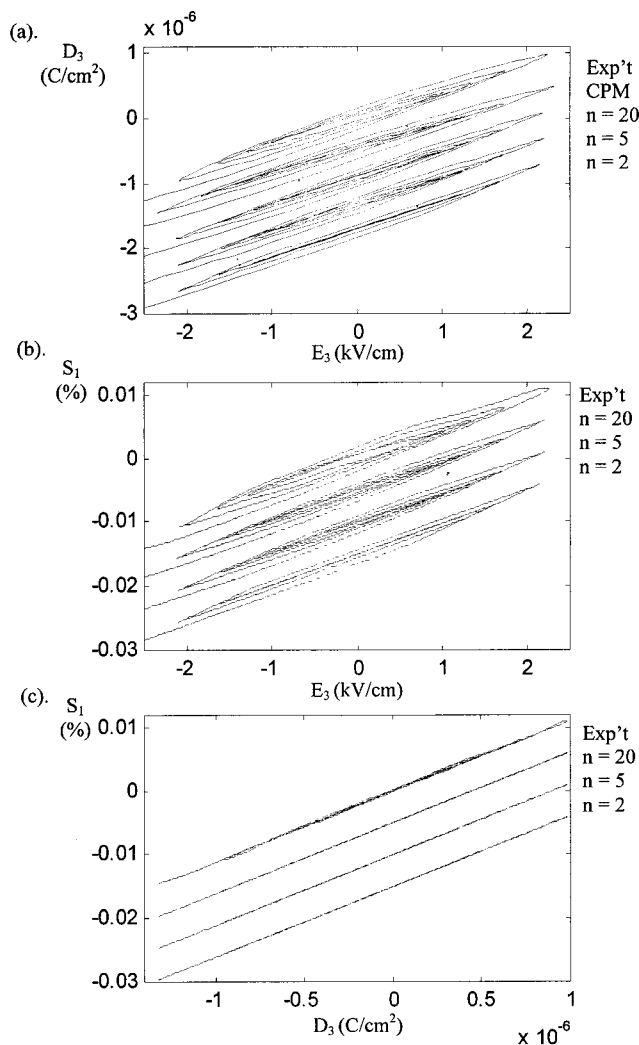


FIG. 10. Comparison of experiment and CPM and MRC ($n=2,5,20$) hysteresis model simulations for the PZT wafer with decaying sinusoidal input at 5 Hz. Vertical offset added for ease of visual comparison.

ticularly evident in Fig. 11 that is not captured by the MRC model.

Following the developments of Sec. I, an $n=20$ GMRC model was identified with $\alpha=5.2513 \times 10^4 \text{ cm}^2/\text{C}$ based on the Everett function of the experimental data and Eq. (17). In Fig. 11, this GMRC model is also compared to the optimal MRC and CPM models as well as experimental results for a sinusoidal input. While the GMRC model is an improvement over the MRC model, the classical Preisach (CPM) model is still the most accurate. In Fig. 12, lines parallel to $x=y$ on the Everett surface do not have constant value or constant slope. Consequently, for greater accuracy additional higher order terms in the MRC dielectric relationship would be needed, or use of the more numerically complex CPM might be required. Nonetheless, the GMRC model is an improvement over the MRC model, but with a cost in complexity. Yet, it is substantially less complex in its implementation relative to the CPM or other Preisach models and may be a reasonable compromise in speed versus accuracy in simulation or real-time model-reference control applications.

The MRC and GMRC models were used to study hysteretic energy loss in the PZT wafer for the case of sinusoidal

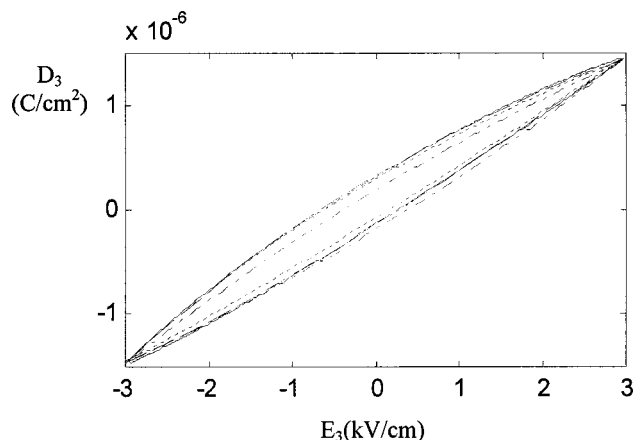


FIG. 11. Comparison of experiment with CPM, GMRC and MRC hysteresis model simulations for sinusoidal voltage input at 5 Hz. Key: — experiment, ---CPM, --GMRC ($n=20$), and -.-MRC ($n=20$).

and arbitrary excitation histories. For sinusoidal excitation, a simple solution can be obtained by conservation principles. For the case $T_1 \approx 0$ there is no mechanical energy output and the hysteretic energy dissipation should equal the electrical energy input. With harmonic voltage excitation at 5 Hz E_3 and D_3 were recorded, as shown in Fig. 9(a). The energy loss per cycle per unit volume is equal to the area within the closed curve. Its value is $0.95 \times 10^{-3} \text{ J/cm}^3$. Equations (18)–(22) were also used with the time record of E_3 and identified MRC model parameters with $n=2, 5$ and 20 that are listed in Table II, as well as the $n=20$ GMRC model with $\alpha=5.2513 \times 10^4 \text{ cm}^2/\text{C}$. Values for energy loss per cycle per unit volume were calculated to be $0.56, 0.73$ and $0.76 \times 10^{-3} \text{ J/cm}^3$, respectively, for the MRC models ($n=2,5,20$). The GMRC model with $n=20$ yielded nearly identical results as that of the MRC model with $n=20$. Time histories of energy quantities are shown in Fig. 13.

Hysteretic energy loss as a function of time was calculated for the arbitrary input E_3 denoted in Fig. 10(a). Given E_3 and D_3 , Eq. (22) and the MRC model parameters of Table II, it is possible to calculate the energy input and hysteretic energy loss as a function of time. These curves can be integrated over time to determine the cumulative energy input and hysteretic loss as a function of time. Since mechanical energy output should be negligible with $T \approx 0$, the cumulative electrical energy input and hysteretic energy losses should asymptotically agree. This trend is evident in Fig. 14. Here again, MRC and GMRC models with more slide elements yield more accurate results.

IV. NONLINEAR SYSTEM MODEL

The system under consideration is schematically shown in Fig. 15. For the derivation of the equations of motion of the electro-elastic continuum, it is assumed that the transverse displacement $w(x,t)$ is the same for the PZT wafer and beam and that there is perfect bonding between them. Under this assumption, Hamilton's principle can be employed to derive the equations of motion for the coupled electromechanical system.^{24–26}

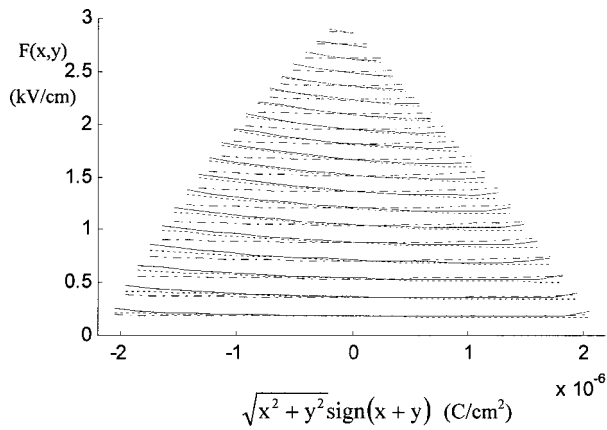


FIG. 12. Comparison of lines on the Everett surface $F(x,y)$ that are parallel to the $x=y$ line and are equally separated in the $x=-y$ direction, spanning the triangular region $T(x,y)$. Key: ———experiment and CPM, --- GMRC ($n=20$), and - - - MRC ($n=20$).

$$\int_{t_1}^{t_2} \delta L dt = \int_{t_1}^{t_2} [\delta K - \delta U_b - \delta U_p + \delta W] dt = 0. \quad (23)$$

Here, K is the kinetic energy of the beam and PZT wafer, U_b is the mechanical strain energy of the beam, U_p is the mechanical and electrical energy of the PZT wafer, and W is the work done by the applied electric voltage and external mechanical forces. Employing the Euler–Bernoulli beam theory with simply supported boundary conditions, each term of the generalized Lagrangian function, L , can be expressed as follows:

$$K = \frac{1}{2} \int_0^{L_b} \rho_e A_e \left(\frac{\partial w}{\partial t} \right)^2 dx, \quad (24a)$$

$$U_b = \frac{1}{2} \int_0^{L_b} E_b I_b \left(\frac{\partial^2 w}{\partial x^2} \right)^2 dx, \quad (24b)$$

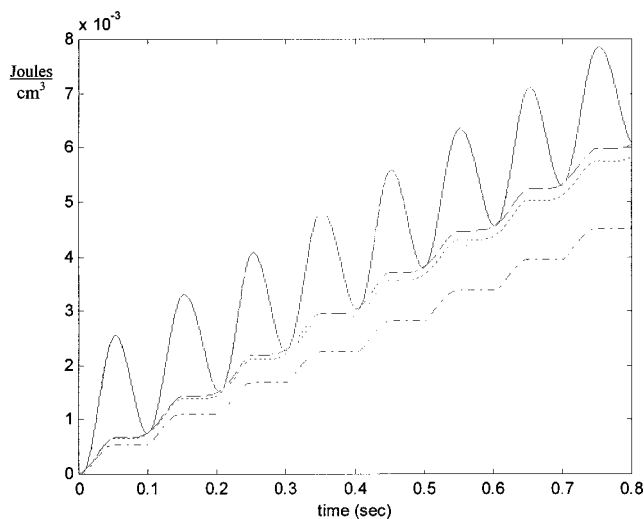


FIG. 13. Electrical energy input and hysteretic energy dissipation as a function of time for sinusoidal voltage input as shown in Fig. 9 (5 Hz, $T_1=0$). Key: ———energy input from MRC simulation with $n=20$, ---, - - - hysteretic energy dissipation from MRC simulation with $n=20$, $n=5$, and $n=2$, respectively.

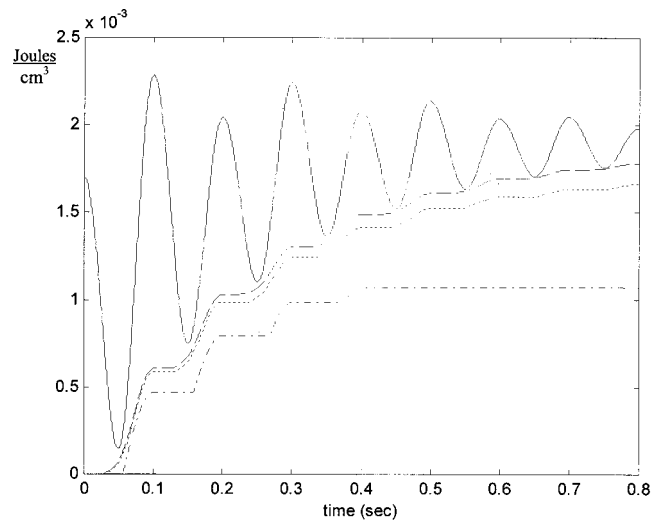


FIG. 14. Electrical energy input and hysteretic energy dissipation as a function of time for decaying sinusoidal voltage input as shown in Fig. 10 (5 Hz, $T_1=0$). Key: ———energy input from MRC simulation with $n=20$, ---, - - - hysteretic energy dissipation from MRC simulation with $n=20$, $n=5$, and $n=2$, respectively.

$$U_p = \frac{1}{2} \int_v (T_1 S_1 + E_3 D_3) dv, \quad (24c)$$

$$W = \int_0^{L_b} \left(f(x,t) - c_b \left(\frac{\partial w}{\partial t} \right) \right) w(x,t) dx + \int_A \tilde{q} \cdot \phi dA. \quad (24d)$$

Here, w is the transverse displacement, f is the externally applied transverse forces, c_b is the beam's damping coefficient and v is the volume of PZT. Also, \tilde{q} is the surface electric charge density per unit area of the electrode (electric displacement, D_3), and ϕ is the electric potential with the relation of $E_3 = -\partial\phi/\partial z$. The properties of the beam and the piezoelectric ceramic wafer with edges at x_1 and x_2 along the x direction may be expressed as follows:

$$\rho_e A_e = \rho_b A_b + \rho_p A_p \chi(x) = \rho_b h_b b_b + \rho_p h_p b_p \chi(x), \quad (25a)$$

$$E_e A_e = E_b A_b + E_p A_p \chi(x) = E_b h_b b_b + E_p h_p b_p \chi(x), \quad (25b)$$

$$E_e I_e = E_b I_b + E_p I_p \chi(x) = \frac{E_b h_b^3 b_b}{12} + \frac{E_p b_p}{3} \left(\left(\frac{h_b}{2} + h_p \right)^3 - \left(\frac{h_b}{2} \right)^3 \right) \chi(x), \quad (25c)$$

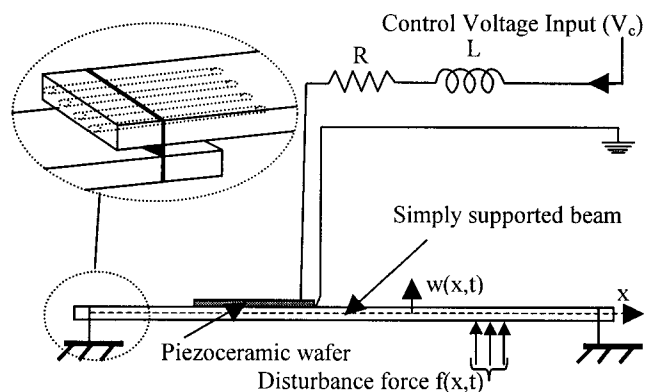


FIG. 15. Schematic diagram of the experimental test system.

where $A_b = h_b b_b$, $A_p = h_p b_p$, $I_b = h_b^3 b_b / 12$, $I_p = (b_p / 3) \times ((h_b / 2 + h_p)^3 - (h_b / 2)^3)$, and $\chi(x) = H(x - x_1) - H(x - x_2)$.

Here, the subscript denotes each structural member: beam (b) and PZT wafer (p). Subscript (e) denotes the effective material constants, and ρ is the material mass density, A is the cross sectional area, I is the moment of inertia of cross sectional area, L_b is the length of the beam, h is the thickness, b is the width, $\chi(x)$ is the characteristic function, and H is the Heaviside function (unit step function). In the Helmholtz free energy term, mechanical stress (T) and electric field (E) on the PZT may have the following nonlinear constitutive relationships:

$$T_1 \approx (c_{11}^D - \nu_p c_{13}^D) S_1 - h_{31} D_3 = \bar{c}_{11}^D S_1 - h_{31} D_3, \quad (26a)$$

$$T_2 \approx (c_{12}^D - \nu_p c_{23}^D) S_1 - h_{31} D_3 = \bar{c}_{12}^D S_1 - h_{31} D_3, \quad (26b)$$

$$\begin{aligned} E_3 &\approx -g_{31} T_1 - g_{32} T_2 + \{\beta_{33}^T D_3\} \\ &= -g_{31} (T_1 + T_2) + \{\beta_{33}^T D_3\} \\ &= -g_{31} (\bar{c}_{11}^D + \bar{c}_{12}^D) S_1 + 2h_{31} g_{31} D_3 + \{\beta_{33}^T D_3\}, \end{aligned} \quad (26c)$$

where $\nu_p = -S_3 / S_1$, $\bar{c}_{11}^D = c_{11}^D - \nu_p c_{13}^D$, $\bar{c}_{12}^D = c_{12}^D - \nu_p c_{23}^D$, $h_{31} = h_{32}$, $g_{31} = g_{32}$, $S_2 \approx 0$, and $T_3 = 0$.

Note that T_1 and T_2 denote the stress terms in the x and y directions of the PZT wafer, respectively. Here, $T_2 \neq 0$ due to the differences in Poisson's ratio of PZT (≈ 0.4) and the beam material (≈ 0.33). Also, S_1 is the strain in the x direction of the PZT wafer ($S_1 \approx -z \partial^2 w / \partial x^2$), E_3 is the electric field [$E_3 = V / h_p$ (volts/length)], D_3 is the electric displacement [$D_3 = Q / A_s$ (charge/area)], Q is the electric charge in the transverse direction, and A_s is the surface area of electrode, $A_s = b_p (x_2 - x_1)$. Here, S_2 is assumed to be negligible due to the differences in Poisson's ratio.

Substituting Eq. (26) into the variational Eq. (24c), the strain energy of a piezoelectric ceramic actuator adhered to the beam may be expressed as follows,

$$\begin{aligned} U_p &= \frac{1}{2} \int_v (T_1 S_1 + E_3 D_3) dv \\ &= \frac{1}{2} \int_0^{L_b} \left(\bar{c}_{11}^D I_p \left(\frac{\partial^2 w}{\partial x^2} \right)^2 + 2g_{31} (\bar{c}_{11}^D + \bar{c}_{12}^D) J_p D_3 \frac{\partial^2 w}{\partial x^2} \right. \\ &\quad \left. + 2A_p h_{31} g_{31} D_3^2 + A_p \{\beta_{33}^T D_3^2\} \right) \chi(x) dx \end{aligned} \quad (27)$$

where

$$Q_a = A_s D_3, \quad J_p = \frac{b_p}{2} \left(\left(\frac{h_b}{2} + h_p \right)^2 - \left(\frac{h_b}{2} \right)^2 \right),$$

$$V_a = E_3 h_p = -L \frac{\partial^2 Q_a}{\partial t^2} - R \frac{\partial Q_a}{\partial t} + V_c.$$

In here, V_a is the actuation voltage and V_c is the applied control voltage. Provisions are made for consideration of an electrical inductor L and resistor R in series with the control voltage V_c for hybrid (passive and active) vibration control.

The derivation then proceeds closely following the linear derivation of Tsai and Wang²⁶ with the addition of the

nonlinear expression denoted by the bracket $\{ \}$. The boundary conditions are those of a simply supported beam,

$$w(0, t) = \frac{\partial^2 w(0, t)}{\partial x^2} = w(L_b, t) = \frac{\partial^2 w(L_b, t)}{\partial x^2} = 0. \quad (28)$$

A Rayleigh–Ritz approximation is employed with the selected eigenfunctions satisfying the boundary conditions

$$\hat{w} = \sum_{n=1}^N a_n \sin\left(\frac{n\pi x}{L_b}\right) e^{j\omega t} = \sum_{n=1}^N a_n \phi(x) e^{j\omega t} \quad (29)$$

We obtain

$$[k_{ij} - \hat{\omega}^2 m_{ij}] [a_j] = [0], \quad (30a)$$

where

$$m_{ij} = \frac{1}{2} \rho_b A_b L_b \delta_{ij} + \rho_p A_p \int_{x_1}^{x_2} \sin\left(\frac{n_i \pi x}{L_b}\right) \sin\left(\frac{n_j \pi x}{L_b}\right) dx, \quad (30b)$$

$$\begin{aligned} k_{ij} &= \frac{1}{2} \left(\frac{n_i \pi}{L_b} \right)^4 E_b I_b L_b \delta_{ij} + \bar{c}_{11}^D I_p \left(\frac{n_i \pi}{L_b} \right)^2 \left(\frac{n_j \pi}{L_b} \right)^2 \\ &\quad \times \int_{x_1}^{x_2} \sin\left(\frac{n_i \pi x}{L_b}\right) \sin\left(\frac{n_j \pi x}{L_b}\right) dx. \end{aligned} \quad (30c)$$

Solving this eigenvalue problem, one can obtain the natural frequencies $\hat{\omega}_r$ and eigenvectors

$$\hat{\phi}_r(x) = \sum_{n=1}^N a_{nr} \sin\left(\frac{n\pi x}{L_b}\right). \quad (31)$$

The external mechanical force vector \mathbf{f} is approximated by the following:

$$\hat{\mathbf{f}}(t) = [\hat{f}_1(t) \quad \cdots \quad \hat{f}_N(t)],$$

where

$$\hat{f}_r(t) = \int_0^{L_b} f(x, t) \hat{\phi}_r(x) dx. \quad (32)$$

The resulting system equations are

$$\begin{aligned} [M_b] \ddot{\mathbf{q}} + [C_b] \dot{\mathbf{q}} + [K_b] \mathbf{q} + \left(\left(\frac{h_b}{2} + h_p \right)^2 - \left(\frac{h_b}{2} \right)^2 \right) \\ \times g_{31} (\bar{c}_{11}^D + \bar{c}_{12}^D) \frac{[\boldsymbol{\sigma}'(x_2) - \boldsymbol{\sigma}'(x_1)]}{2(x_2 - x_1)} Q_a = \hat{\mathbf{f}}, \end{aligned} \quad (33)$$

$$\begin{aligned} L \ddot{Q}_a + R \dot{Q}_a + h_p \left[\left\{ \beta_{33}^T \frac{Q_a}{b_p (x_2 - x_1)} \right\} + \frac{2h_{31} g_{31} Q_a}{b_p (x_2 - x_1)} \right] \\ + \left(\left(\frac{h_b}{2} + h_p \right)^2 - \left(\frac{h_b}{2} \right)^2 \right) g_{31} (\bar{c}_{11}^D + \bar{c}_{12}^D) \\ \times \frac{[\boldsymbol{\sigma}'(x_2) - \boldsymbol{\sigma}'(x_1)]^T}{2(x_2 - x_1)} \mathbf{q} = V_c, \end{aligned} \quad (34)$$

where \mathbf{q} is the vector of generalized displacements and $[M_b]$, $[K_b]$, and $[C_b]$ are the mass, stiffness, and damping matrices, respectively. Only Eq. (34) is nonlinear, but Eqs. (33) and (34) are coupled. Note that this formulation is independent of which hysteresis function is used to describe dielectric nonlinearity. For example, depending on the level

TABLE III. Natural frequencies of the simply supported beam.

Mode	Beam w/o patch (Hz)		Beam with patch (Hz)	
	Theory	Experiment	Theory	Experiment
1	55.79	56.0	55.92	56.09
2	223.18	220.44	224.80	220.61
3	502.16	494.67	508.26	494.19

of needed accuracy versus computational cost one could employ the MRC, GMRC or Preisach functions.

V. EXPERIMENTAL STUDY OF NONLINEAR STRUCTURAL SYSTEM

A. Experimental test setup

To obtain modal parameter values for the simply supported beam, measurements with an instrumented hammer and an accelerometer were conducted and analyzed using a HP 35670a spectrum analyzer and STAR MODAL[®] software. Table III compares experiment and linearized theory for the beam structure with PZT and without PZT. In simulations, parameter values in Table IV are used. Bonding of the PZT onto the beam and soldering of wire leads to its nickel gray electrodes were done according to the PZT manufacturer's manual (Piezo Systems, Inc.) using Epo-Tek 301 epoxy (Epoxy Technology, Inc.), #30 gage wires, S60 Sn/40Pb solder and Supersafe #67 DSA liquid flux. In theoretical calculations, the bond layer is assumed to be even and thin such that its effects can be ignored.

For data acquisition and voltage signal generation, an Agilent Technologies (formerly HP) VXI system (E1433A for Data Acquisition and E1434A for Arbitrary Source Generation) was used. HP VEE GUI software with an embedded MATLAB[®] connection for the interface of input and output and data post processing was used. The electric field-displacement relationship for the PZT patch was determined by controlling the voltage applied to the PZT through a Trek High-Voltage Amplifier Model P0623A-G. Electric displacement D_3 was determined by integration of the current applied to the PZT that was monitored by the Trek amplifier. Electric voltage applied to the PZT was also monitored by the Trek amplifier and used to determine the electric field E_3 . Mechanical velocity of the beam surface was measured using a Polytec CLV 800 laser Doppler vibrometer. All tests were controlled from the MATLAB workspace interactively using programs supplied by Agilent and modified for the purpose of generating the arbitrary input source and for the proper test conditions such as frequency span and data block size, etc.

TABLE IV. Physical parameters of the simply supported beam.

Length	L_b	0.508	m
Thickness	h_b	0.00635	m
Width	b_b	0.1016	m
Density	ρ_b	2698.5	kg/m ³
Young's modulus	E_b	6.748e10	N/m ²
Damping ratio ^a	$\zeta_{1,2,3}$	0.0061, 0.0021, 0.0017	

^aBased on experimental modal analysis.

B. Simulation and experimental evaluation

In this section, based on the MRC identification results of the PZT by itself in Sec. III, the case of $T \neq 0$ is considered with the PZT bonded to the beam. (The MRC model with $\alpha=0$ was judged sufficiently accurate for the purpose of this study.) In this case, energy input may be dissipated via loss mechanisms in the dielectric and mechanical domains. The applied electric signal for simulations and experiments was a sinusoidal voltage with the magnitude of 80 V. With Eqs. (3a) and (3b) and the identified dielectric coefficients of the MRC model with $n=2, 5$ and 20 of Table II, dielectric field in the PZT/beam system may be calculated based on Eqs. (33) and (34). Using the experimental electric field E_3 , simulations were carried out to predict the electric displacement D_3 . Figure 16(a) shows the comparison of experimental data and simulation results for $n=2, 5$ and 20. Simulated electric displacements have a maximum error of 6.4% when compared to experimental data. Also, based on these simulated dielectric displacements, one can extract the dielectric field. Figure 16(b) shows the relations between the dielectric field $E_3 + g_{31}(T_1 + T_2) = \{\beta_{33}^T D_3\}$ and D_3 . Simulation results and experimental data compare favorably. Also in this figure, the effect of nonzero stress is indicated by superimposing the dielectric displacement of the PZT by itself when subjected to the same input E_3 .

Energy studies were carried out using a sinusoidal voltage input to the PZT. Figure 17 shows a simulation of the energy distributions in the beam/PZT wafer system in terms of cumulative electric energy input, dielectric energy levels, dielectric energy loss, and mechanical strain energy levels. This distribution was obtained based on Sec. ID and the identified MRC model parameters with $n=20$ that are listed in Table II. Note that, in this simulation, zero mechanical energy dissipation was assumed. This model could be easily modified to account for mechanical structural damping or linear viscous damping in the form of a modal damping ratio.

VI. CONCLUSION

In this article, the nonlinear smart structural system was investigated via analytical and experimental studies of a PZT patch bonded to a simply supported beam. First, the PZT wafer by itself was investigated and constitutive models incorporating reversible (higher order polynomial) and irreversible (hysteretic) dielectric hysteresis were formulated. An identification scheme was devised and experimental studies validated the theoretical model. The nonlinear PZT model was then integrated into the coupled dynamic equations of the overall system consisting of the simply supported beam and electrically shunted PZT wafer bonded to the beam. The theoretical system model was then evaluated by comparison of its predictions with experimental results showing good agreement. Energy loss and transduction mechanisms in the integrated structural system were investigated.

The developed nonlinear modeling approach is robust in that the integrated system response could be predicted based on models that were experimentally identified for the individual components, the beam and patch by themselves. Additionally, while a few particular hysteresis models for the

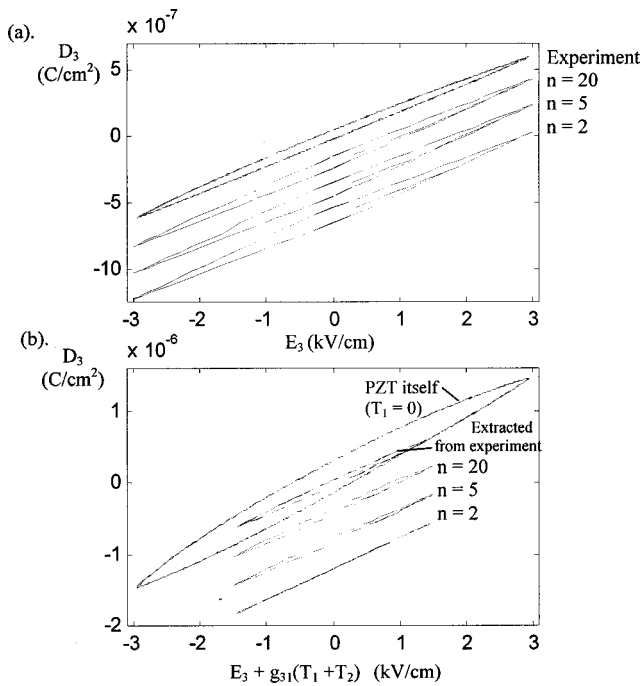


FIG. 16. Experiment versus simulation studies of beam + PZT system subject to 5-Hz sinusoidal voltage excitation. Vertical offset added for ease of visual comparison.

PZT were developed and shown to match experiment, alternate hysteresis models could be easily integrated in the overall system model to simulate its nonlinear response and study real-time active control strategies that may include hysteresis compensation.

ACKNOWLEDGMENTS

This research was supported by a grant from the National Science Foundation (Project monitor: Alison Flatau) and a grant from the Office of Naval Research (Project monitor:

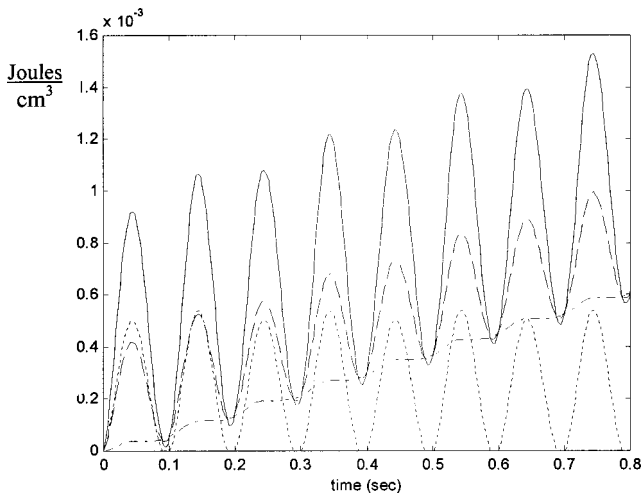


FIG. 17. Comparison of energy quantities of the beam + PZT system subject to 5-Hz sinusoidal voltage excitation. Rate of electric energy input and hysteretic energy dissipation as a function of time. Key: — electrical energy input, --- dielectric energy input, - - - dielectric energy loss, and ... mechanical strain energy.

Dr. Gary Friedman is also acknowledged for numerous fruitful discussions regarding Preisach hysteresis models.

- ¹ T. J. Royston and B. H. Houston, "Modeling and measurement of nonlinear dynamic behavior in piezoelectric ceramics with application to 1–3 composites," *J. Acoust. Soc. Am.* **104**, 2814–2827 (1998).
- ² T. J. Royston, S.-H. Lee, and G. Friedman, "Comparison of Two Rate-Independent hysteresis models with Application to Piezoceramic Transducers," in *Proceedings of ASME Design Engineering Technical Conference Symposium on Nonlinear Response of Hysteretic Oscillators*, Las Vegas, NV, 12–15 September 1999.
- ³ S.-H. Lee, T. J. Royston, and G. Friedman, "Modeling and compensation of hysteresis in piezoceramic transducers for vibration control," *Proc. ASME Int. Mech. Eng. Congress and Exposition (IMECE) Symposium on Adaptive Structures and Material Systems*, **AD-59**, Nashville, TN, pp. 11–18 (1999). Also accepted for publication in *J. Intell. Mater. Syst. Struct.*
- ⁴ M. Goldfarb and N. Celanovic, "A lumped parameter electromechanical model for describing the nonlinear behavior of piezoelectric actuators," *ASME J. of Dyn. Systems, Measurement and Control* **119**, 478–485 (1997).
- ⁵ J. A. Main and E. Garcia, "Design impact of piezoelectric actuator nonlinearities," *J. Guid. Control Dyn.* **20**, 327–332 (1997).
- ⁶ J. A. Main and E. Garcia, "Piezoelectric stack actuators and control system design: strategies and pitfalls," *J. Guid. Control Dyn.* **20**, 479–485 (1997).
- ⁷ J. A. Main, E. Garcia, and D. V. Newton, "Precision position control of piezoelectric actuators using charge feedback," *J. Guid. Control Dyn.* **18**, 1068–1073 (1995).
- ⁸ D. Damjanovic, "Stress and frequency dependence of the direct piezoelectric effect in ferroelectric ceramics," *J. Appl. Phys.* **82**, 1788–1797 (1997).
- ⁹ D. V. Taylor and D. Damjanovic, "Evidence of domain wall contribution to the dielectric permittivity in PZT thin films at sub-switching fields," *J. Appl. Phys.* **82**, 1973–1975 (1997).
- ¹⁰ D. Damjanovic and R. E. Newnham, "Electrostrictive and piezoelectric materials for actuator applications," *J. Intell. Mater. Syst. Struct.* **3**, 190–208 (1992).
- ¹¹ D. Hughes and J. T. Wen, "Preisach modeling of piezoceramic and shape memory alloy hysteresis," *Smart Mater. Struct.* **6**, 287–300 (1997).
- ¹² P. Ge and M. Jouaneh, "Modeling hysteresis in piezoceramic actuators," *Precis. Eng.* **17**, 211–221 (1995).
- ¹³ P. Ge and M. Jouaneh, "Tracking control of a piezoceramic actuator," *IEEE Trans. Control Syst. Technol.* **4**, 209–216 (1996).
- ¹⁴ P. Ge and M. Jouaneh, "Generalized Preisach model for hysteresis nonlinearity of piezoceramic actuators," *Precis. Eng.* **20**, 99–111 (1997).
- ¹⁵ R. C. Smith and Z. Ounaies, "A hysteresis model for piezoceramic materials," *Proc. ASME Int. Mech. Eng. Congress and Exposition (IMECE) Symposium on Adaptive Structures and Material Systems*, **AD-59**, Nashville, TN, pp. 27–32 (1999).
- ¹⁶ S. Chonan, Z. Jiang, and T. Yamamoto, "Nonlinear hysteresis compensation of piezoelectric ceramic actuators," *J. Intell. Mater. Syst. Struct.* **7**, 150–156 (1996).
- ¹⁷ J. Tang and K. W. Wang, "Vibration control using piezoelectric material with high order nonlinearity," *Proc. ASME Int. Mech. Eng. Congress and Exposition (IMECE) Symposium on Adaptive Structures and Material Systems*, **AD-59**, Nashville, TN, pp. 159–160 (1999).
- ¹⁸ G. Miano, C. Serpico, and C. Visone, "A new model of magnetic hysteresis, based on stop hysteron: an application to the magnetic field diffusion," *IEEE Trans. Magn.* **32**, 1132–1135 (1996).
- ¹⁹ S. Bobbio, G. Miano, C. Serpico, and C. Visone, "Models of magnetic hysteresis based on play and stop hysteron," *IEEE Trans. Magn.* **33**, 4417–4426 (1997).
- ²⁰ G. Webb, A. Kurdila, and D. Lagoudas, "Adaptive hysteresis model for model reference control with actuator hysteresis," *J. Guid. Control Dyn.* **23**, 459–465 (2000).
- ²¹ M. A. Krasnosel'skii and A. V. Pokrovskii, *Systems with Hysteresis* (Springer-Verlag, Heidelberg, 1989).
- ²² I. D. Mayergoyz, *Mathematical Models of Hysteresis* (Springer-Verlag, New York, 1991).
- ²³ T. J. Royston, S.-H. Lee, and M. B. Ozer, "Hysteresis models for piezoceramic transducers," in *Proceedings of Hysteresis, Metastability and Af-*

- tereffect 2000 (Chicago, IL, 2000). Also to be published in *J. of Materials Processing and Manufacturing Science*.
- ²⁴M. S. Tsai and K. W. Wang, "On the structural damping characteristics of active piezoelectric actuators with passive shunt," *J. Sound Vib.* **221**, 1–22 (1999).
- ²⁵W. H. Liao and K. W. Wang, "Characteristics of enhanced active constrained layer damping treatments with edge elements, Part 1: Finite element model development and validation," *Trans. ASME, J. Vib. Acoust.* **120**, 886–893 (1998).
- ²⁶W. H. Liao and K. W. Wang, "Characteristics of enhanced active constrained layer damping treatments with edge elements, Part 2: System analysis," *Trans. ASME, J. Vib. Acoust.* **120**, 894–900 (1998).

An illustration of analytical/numerical matching with finite-element analysis for structural vibration problems

Linda P. Franzoni and Christopher D. Park

Department of Mechanical Engineering and Materials Science, Duke University, Box 90300, Durham, North Carolina 27708-0300

(Received 25 February 1999; revised 15 June 2000; accepted 16 September 2000)

Analytical/numerical matching (ANM) is an accurate and efficient method for solving many types of problems with discontinuities. The method separates local and global effects, and solves separate subproblems using high resolution around the discontinuity and low resolution away from the discontinuity. The work presented in this manuscript demonstrates a methodology for applying ANM to a dynamic structure using finite-element analysis (FEA) for the solution of the high-resolution (local) and the low-resolution (global) subproblems. The ANM method is illustrated on a thick, two-dimensional beam having several displacement constraints attached to its lower surface. Ordinarily (and here, for verification purposes) this problem would be solved using two-dimensional plane elements due to the local discontinuities around the constraints and the thickness of the beam. Using ANM, these discontinuities and through-thickness effects are modeled in the geometrically compact local problem using a high-resolution mesh of two-dimensional eight-node plane elements. The much larger global problem contains no discontinuities and is reduced to the solution of a low-resolution finite-element mesh of two-node Bernoulli–Euler beam elements. A third subproblem (matching) is solved analytically (no computational overhead). The agreement between the ANM solution and the purely FEA solution is excellent, and the computational savings are significant. © 2000 Acoustical Society of America.
[S0001-4966(00)04412-X]

PACS numbers: 43.40.Cw [CBB]

I. INTRODUCTION

In structural dynamics, problems arise where there are structural discontinuities along an otherwise smooth structure such as a beam, plate, or shell. For problems of particular interest, such as a submarine or airplane fuselage, structural discontinuities exist in great numbers in the form of bulkhead stiffeners, rivets, ribs, and various types of structural mating surfaces. Due to the overall complexity of these problems, analytical solutions are generally not available. Historically, numerical methods such as finite-element analysis (FEA) have been used to solve these types of structural dynamics problems. By using FEA, structural coupling, fluid loading, and complicated geometry can often be adequately addressed with some approximations. However, the modeling and solution times can be lengthy in order to achieve an acceptable convergence of the numerical solutions. To reduce the extensive computational effort, methodologies within FEA such as submodeling (or substructuring) and the use of more sophisticated transitional meshing have been developed. Some of the alternatives include hybrid approaches,^{1–5} which have been successful in reducing the computation required for an accurate solution. Many of these hybrid approaches share similar themes as the work presented here. For instance, many of these methods make use of local/global or matching/patching techniques. However, these methods differ from this work in that their approaches to the decomposition (or partitioning), followed by reassembly (or patching) of the problem are not mathematically exact. Therefore, the results are usually not accurate in all regions of the structure (local and global regions). A new

hybrid method that formally combines analytical and numerical (FEA, for example) solutions for structural/acoustic analysis is analytical/numerical matching (ANM).

ANM is a method that divides a given problem with discontinuities into subproblems that are solved independently using either analytical or numerical methods. The solutions to these subproblems are superimposed to yield a solution that is valid on the whole domain. Using this methodology, ANM is capable of determining local effects of discontinuities at high resolution while obtaining a computationally efficient solution of the overall problem.

The ANM method was originally developed by Bliss^{6–8} for the analysis of free-vortex wakes in rotorcraft aerodynamics. ANM increased the efficiency of this computationally intensive problem by orders of magnitude. More recently, fluid applications of ANM include the analysis and solution of wing aerodynamics for compressible unsteady flow and the development of an acoustic boundary element method.^{9–11}

The first application of ANM to fluid radiation problems was implemented by Bliss and Franzoni.¹² In this work, ANM was applied to simple wave propagation problems to demonstrate that the solution method was applicable to hyperbolic problems. Subsequently, Loftman and Bliss extended this work to the calculation of acoustic radiation from fluid-loaded membranes and curved shells with structural discontinuities.^{13–16} For these applications, the numerical subproblems were solved using modal methods.

In this paper, analytical/numerical matching is applied to a structural vibration problem containing localized areas of

rapid variation on an otherwise slowly varying domain. The original problem is separated into constituent subproblems. Two of the separate subproblems are solved using standard finite-element analysis (one at high resolution, the other at low resolution) and the third subproblem is solved analytically. The local problem, requiring high resolution, is solved on a small domain using eight-node, two-dimensional plane elements and a finely gridded mesh; the remaining global problem only requires low resolution and can be solved using a low-density grid and lower-order elements (two-node beam elements) on a much larger domain.

The method will be demonstrated for the solution of the structural vibrations of a thick beam with multiple identical discontinuities along the lower edge of the beam. The mathematical procedures that are applied using the ANM method will be explained in the context of a single constraint. The problem involving multiple identical constraints, which couple to each other, will be solved using the single constraint solution as a building block. The results, which compare the ANM/FEA solution method to a full high-resolution finite-element solution, show excellent agreement and a large reduction in computational cost. This work represents the first use of FEA with ANM, and demonstrates that ANM can be used in conjunction with a traditional finite-element analysis.

II. BACKGROUND

The types of problems considered in the areas of structural vibrations and/or acoustics are generally not amenable to a purely analytical solution due to the presence of discontinuities, irregular geometry, etc. In many instances, FEA is the preferred numerical method.

To ensure that all of the discontinuities are fully resolved in a very large or complex structure, an extraordinarily high number of finite elements are required for the full solution of the structure. The resulting model contains many degrees of freedom and is computationally cumbersome to solve. In order to minimize the number of degrees of freedom, a typical analysis uses a transitional mesh of elements between high and low mesh density regions. For a 2D plane stress model, for example, a transition zone is usually developed where the mesh density gradually lessens by using a combination of six-node triangular and eight-node quadrilateral elements. At the opposing edge of the transition zone, the mesh could again return to uniform quadrilateral elements, if desired. A disadvantage of this method for a 2D case is that the triangular elements are less accurate than quadrilateral elements with similarly ordered shape functions.¹⁷ Also, it may take considerable effort to model and mesh certain structures without producing poorly shaped elements that would create inaccuracies in the solution.¹⁸ Improvements such as quality-based quad splitting for all-quad meshing have been made to most commercial FEA packages to address some of these issues.¹⁹

Transition regions are used minimally with ANM because the area requiring high resolution is solved as a separate finite-element analysis on a small local domain. The

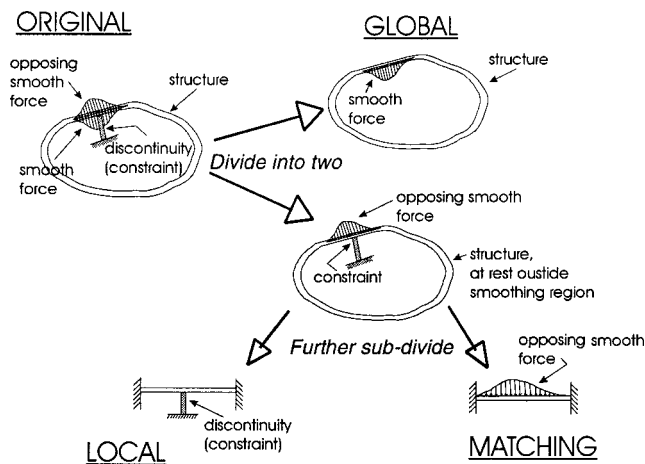


FIG. 1. Decomposition of the original problem into ANM components.

global problem, consisting of the original structure with an applied smooth distributed force, is modeled using a low-resolution finite-element mesh of lower-order element types. Separating the problem into separate finite-element subproblems eliminates the large disparity in resolution requirements within a single model.

Within finite-element analysis, a technique that is often used on problems of this type is called substructuring, where a separate FEA model is constructed for a part of the main structure. The mass and stiffness matrices of the submodel are reduced down to the important degrees of freedom, which are then imbedded in the overall matrices of the entire system. In the sense that portions of the structure are solved separately, ANM is similar to submodeling. However, the ANM local model contains a portion of the master structure and uses specially constructed smooth forces as a means to pass information between the subproblems. In other words, the effects of the discontinuity are transferred to the ANM global model through the smooth distributed forces that are applied in place of the discontinuity. On the other hand, in FEA substructuring, the dynamic information is passed through reduced mass and stiffness matrices.

III. GENERAL ANM DESCRIPTION

The basic principle of superposition must apply in order to utilize analytical/numerical matching. The ANM method applies two identical, but opposing, smooth distributed forcing functions (to be determined) to a structure around a discontinuity. The smooth forces are distributed over a local region that encompasses the discontinuity. The application of these two smooth-force distributions does not change the original problem because they cancel each other exactly. Applying the principle of superposition, the problem is then divided into two separate problems: (1) the structure with only a smooth force, and (2) the structure with the discontinuity and the opposing smooth force. Figure 1 shows schematically the ANM decomposition for a generic structural vibration problem.

The structure with only the smooth force becomes known as the global problem, for it contains the entire struc-

ture and will exhibit a smoothly varying response. In fact, there is no need for this problem to be solved with high resolution, and it can often be represented accurately using a simplified theoretical model.

The remaining problem consisting of the structure with the discontinuity and the opposing smooth force can be subdivided further. Conditions are placed on the smooth force, such that the combination of this force and the original discontinuous force brings the structure to rest outside the smoothing region (the area over which the smooth force is applied). Thus, the motion of the structure in this subproblem is “local” and it extends over the smoothing region only (i.e., the rest of the structure can be eliminated from this part of the analysis). The structure can then be modeled as fixed at the boundaries of the smoothing region. Again referring to Fig. 1, this constituent problem is further divided into two subproblems: (1) a structure with fixed boundaries containing the discontinuity within its domain, and (2) an identical structural counterpart but with an opposing smooth force, instead of the discontinuity.

The two subproblems on the reduced domain are known as the local and matching problems in ANM. The subproblem with the discontinuity contains rapid gradients and must be analyzed with high resolution; it is termed the local problem. The subproblem with only the applied smooth distributed forcing extending over its length and with fixed boundaries contains *no rapid gradients* and is called the matching problem. The smooth distributed force and its derivative, as well as the displacement of the structure and its derivative, are made to go to zero at the boundaries. The matching problem is solved analytically using the lower-order theory that was applied to the global problem.

To ensure that it is valid to use the lower-order theory on the matching problem, the reactions (stress resultants) at the fixed-fixed boundary should be checked against the same reactions using a higher-order theory (or numerics) on the same smooth problem. If the reactions are not identical in the two cases, the smoothing region is not large enough. Usually, a smoothing length that is equal to several structural thicknesses on either side of the discontinuity is sufficient (application of St. Venant’s principle).

The size of the high-resolution local problem, as well as the size of the matching problem, is determined by the size of the smoothing region chosen. Therefore, if the local problem is to be solved numerically, it is advantageous (most efficient computationally) to choose the smallest smoothing region possible, while retaining a large enough smoothing scale to still render the global problem computationally efficient.

It should be noted that there are no approximations being made in the addition and subtraction of smooth forces and the decomposition of the original problem into the three subproblems by the principle of superposition. However, when the lower-order theories are invoked for solution of the smoothly varying problems (global and matching), a certain level of approximation is being made. By comparing the end reactions of the matching problem using elasticity theory with no approximation to the end reactions given by the lower-order theory, one can check that the model reduction

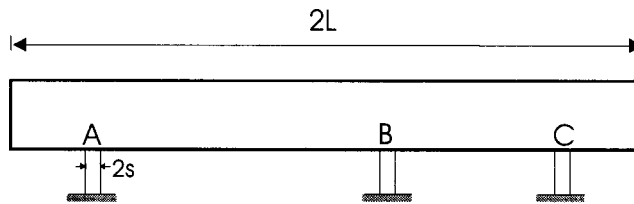


FIG. 2. Thick beam with multiple, nonperiodically spaced supports.

to lower order is valid. This model reduction is important because it makes significant computational savings possible.

IV. MODEL PROBLEM: THICK BEAM WITH MULTIPLE SUPPORTS

The details of applying ANM to a structural vibration problem will now be exhibited for the problem of a two-dimensional thick beam with multiple supports, as shown in Fig. 2. The supports are not periodically spaced; however, they are geometrically identical to each other. The supports are attached to the thick beam at its bottom surface, and therefore it is expected that local stress concentrations will arise in their vicinity. This problem cannot be analyzed with Bernoulli–Euler beam theory due to the through-the-thickness effects. An accurate traditional FEA model of this problem would require the use of 2D plane elements that must be finely meshed around the supports. A model of this type is subsequently analyzed for verification of the ANM/FEA model. For the sample problem, the supports are driven with prescribed displacements and rotations and the response at the lower edge of the beam is predicted, using a traditional FEA approach and using an ANM/FEA approach.

A. Solution of the model problem by ANM

Due to the geometric similarity of the supports, it is only necessary to solve a local problem consisting of one of the supports. A transfer function between the input at a single support and the smooth force associated with it can be used repeatedly in the same problem as long as the supports are geometrically identical. Therefore, first consider a thick beam with a single support over a narrow portion of its bottom edge.

1. ANM for a single constraint

The first step in the ANM process is to add and subtract smooth forces through the thickness over a region of the beam that extends L_s to the right and L_s to the left of the center of the support. Applying the principle of superposition, the problem of the thick beam with a positive smooth distributed force, applied through the thickness and extending over a region $2L_s$, can be made into a separate *global* problem, see Fig. 3.

The remaining problem is that of the thick beam with a displacement constraint over a small region ($2s$) of the bottom edge of the beam and an applied smooth force in the negative direction, distributed through the thickness. The applied smooth force is assumed to have the functional form of a polynomial with as many undetermined coefficients as necessary to satisfy all the conditions that will be imposed. In order for the force to smoothly and exactly cancel the effects

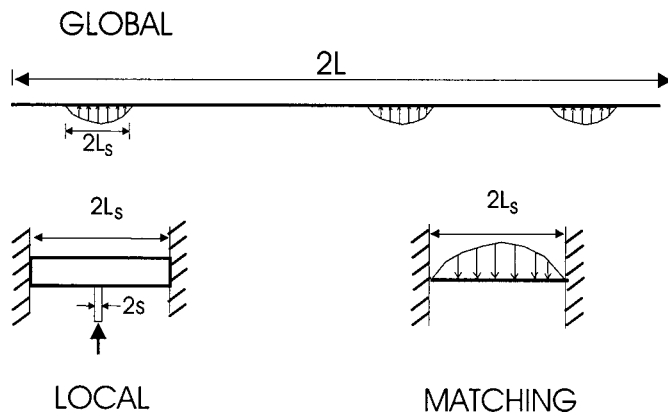


FIG. 3. Schematic of constituent ANM problems for the example problem.

of the discontinuity at the smoothing boundary ($\pm L_s$), six conditions must be specified (as discussed in the following section). Assuming that the smooth force cancels the motion caused by the discontinuity beyond $\pm L_s$ allows the structure within that region to be analyzed as a separate problem with fixed boundary conditions.

Applying the principle of superposition again, the isolated portion of the structure which only extends $\pm L_s$, can be divided into two subproblems, one for each of the two loading conditions; see Fig. 3. The first subproblem (*local*) is the thick beam of length $2L_s$ with the displacement constraint over a region $2s$ of the bottom edge; the boundaries of the region are fixed (no displacement and no slope). The second subproblem (*matching*) is the thick beam of length $2L_s$, with the smooth distributed force applied in the direction opposite that of the subproblem that was initially separated from the others.

At this point, no approximations have been made. The original problem has simply been separated into three subproblems. However, recognizing that two of the subproblems (global and matching) are smoothly varying, i.e., contain no rapid gradients, simplifying approximations can be made which will increase the computational efficiency. A schematic of the ANM constituent parts for this problem is shown in Fig. 3.

In the *global* problem (the full-length thick beam with a smooth distributed force and no discontinuities), the length of the beam is long compared to the thickness, the forcing is smooth, and it is expected that the response through the thickness of the beam will essentially be constant. Therefore, instead of using a two-dimensional solid model to represent this thick beam, a neutral-axis model (i.e., beam theory) can be used. In fact, if rotary inertia and shear effects can be neglected, then Bernoulli–Euler beam theory can be assumed. In some cases, an analytical solution may be available for the global problem; however, in general, *the global problem will be solved using low-resolution numerical methods, such as finite-element analysis with low-order elements on a coarse grid.*

The *matching* problem consists of the thick beam segment of length $2L_s$ with the smooth distributed force directed opposite that of the previous (global) subproblem. The matching problem can also be reduced to a simple beam

model since there are no rapid gradients, the beam segment is long compared to the cross-sectional dimension of the beam, and there are no variations through the thickness. Note, invoking Bernoulli–Euler beam theory on this beam segment imposes the well-known length restriction on the size of the smoothing region; namely, $2L_s$ must be greater than or equal to several beam thickness. *The matching subproblem just described is usually solved analytically.*

The *local* subproblem contains the discontinuity, represented in this example as a displacement constraint of short width $2s$ on the lower edge of the thick beam segment. If the displacement constraint is moved vertically, horizontally, or rotated in any way, large stresses and strains will appear in the vicinity of the constraint. In order to capture this behavior, including the rapid gradients near the constraint, a high-resolution model must be used. In previous applications of ANM, the local problems have been solved analytically (using a Green’s function approach, for example); here, *the local problem will be solved using a high-resolution finite-element analysis.*

2. Determination of the smooth force

After the original problem has been decomposed into the subproblems, the next step in the ANM process is to solve the high-resolution local problem. For a given motion of the constraint, the solution of the local problem includes: displacements at any station through the thickness of the beam segment (of length $2L_s$) including the drive point displacement, the stresses at the boundaries ($\pm L_s$) from which a net moment reaction and shear force reaction can be determined, and the force applied to the drive point. The amplitudes of moment reaction and shear force are divided by the input force that was applied to the constraint, resulting in transfer functions \bar{V} and \bar{M} for the shear force and moment reaction, respectively. The displacements, including the drive point displacement, are also normalized by the input force. The normalized displacements of the local problem are \bar{w}_L and vary through the beam thickness.

The smooth force is prescribed such that its application, along with the motion of the displacement constraint, produces no motion outside the smoothing region and no net reactions on the beam segment at $\pm L_s$. Therefore, the shear-force reaction of the matching problem must equal the normalized net shear-force reaction of the local problem, and the moment reaction of the matching problem must equal the normalized net moment reaction of the local problem. Using Bernoulli–Euler theory to solve the smooth matching problem, these conditions put restrictions on the second and third derivatives of the normalized matching displacements, \bar{w}_m .

In addition, the fixed-end boundary conditions for the matching problem require that the displacement \bar{w}_m and its first derivative be zero. Finally, smoothness conditions are placed on the forcing function, such that the force and its derivative equal zero at the boundaries. In Bernoulli–Euler theory, this means that the fourth and fifth derivatives of displacement must equal zero. In all, there are a total of six conditions on the matching displacement and its derivatives, up through the fifth derivative. Therefore, the smooth forcing

can be assumed to be a polynomial with six unknown coefficients. The matching problem is solved analytically using Bernoulli–Euler beam theory.

3. Solution of the matching problem

The matching problem is the subproblem that contains a smooth distributed force on a beam segment of length $2L_s$. The equation of motion for the matching problem is

$$L_m[\bar{w}_m(\bar{x}, t)] = \bar{f}_s(\bar{x}, t), \quad (1)$$

where \bar{f}_s is the smoothly varying distributed force applied to the beam, \bar{w}_m is the displacement, and L_m is the operator. The coordinate \bar{x} is the spatial coordinate centered at the midspan and nondimensionalized by half the smoothing length, L_s . For Bernoulli–Euler theory, the operator is given by²⁰

$$L_m[\] = EI \frac{\partial^4}{\partial \bar{x}^4} + \rho A \frac{\partial^2}{\partial t^2}, \quad (2)$$

where E is the Young's modulus, ρ is the density of the beam material, I and A are the moment of inertia and area of the cross section, respectively. The functional form of f_s , and therefore w_m , is assumed to be a polynomial. Arbitrary motion of the constraint can be constructed from a superposition of symmetric and asymmetric motions. Therefore, symmetric and asymmetric motion of the constraint will be considered separately. If the motion of the constraint caused symmetric beam motion, then the forcing polynomial would have only even powers of \bar{x} , whereas if the motion of the constraint caused asymmetric beam motion, the forcing would have only odd powers of \bar{x} .

Assume that the constraint is given a rotational displacement producing asymmetric beam motion. The displacement along the beam would then be written as

$$\bar{w}_m(\bar{x}) = a_1\bar{x} + a_3\bar{x}^3 + a_5\bar{x}^5 + a_7\bar{x}^7 + a_9\bar{x}^9 + a_{11}\bar{x}^{11}. \quad (3)$$

The six unknown coefficients, a_1, a_3, \dots, a_{11} will be determined by the aforementioned conditions on displacement and its derivatives (through the fifth derivative). Mathematically, these conditions are

$$\begin{aligned} \bar{w}_m(\pm 1) &= 0, \\ \bar{w}'_m(\pm 1) &= 0, \\ EI\bar{w}''_m(\pm 1) &= \bar{M}, \\ EI\bar{w}'''_m(\pm 1) &= \bar{V}, \\ \bar{w}^{i\nu}_m(\pm 1) &= 0, \\ \bar{w}^{\nu}_m(\pm 1) &= 0. \end{aligned} \quad (4)$$

Satisfying these conditions on $\bar{w}_m(\bar{x})$ guarantees that the displacement, its slope, the applied distributed forcing (\bar{f}_s), and its slope will be zero at the boundaries. Recall that \bar{V} and \bar{M} , which are the transfer functions for the shear-force reaction and moment reaction at the boundaries, come from the solution of the local problem. They will be of equal magnitude and opposite direction for the matching and local sub-

problems. Therefore, when these subproblems are superimposed there will be no residual moments or forces that get transmitted beyond the smoothing region ($\pm L_s$). The above equations [Eq. (4)] represent six equations for the six unknown coefficients in Eq. (3). Solving this system of equations determines $\bar{w}_m(\bar{x})$, and therefore \bar{f}_s from Eq. (1). Note that the local and matching displacements (\bar{w}_L, \bar{w}_m) and the smooth force \bar{f}_s are actually transfer functions between displacement or smooth force and input force applied at the constraint. These transfer functions will be used in the global problem. They will also be used to assemble the ANM composite solution, which is the solution of the original problem.

The previously outlined solutions for the local and matching problems should be repeated for the symmetric case as well, in order to accommodate arbitrary motion of the constraint. The results that are needed from the solutions to the local and matching problems are the displacement transfer functions for each case (\bar{w}_L -symmetric, \bar{w}_L -asymmetric, \bar{w}_m -symmetric, \bar{w}_m -asymmetric) and the transfer function for the distributed forces (\bar{f}_s -symmetric and \bar{f}_s -asymmetric). The smooth-force distributions are applied to the global problem, as explained in the next section, and the appropriately weighted displacement transfer functions from the local and matching subproblems will be superimposed with the displacements of the global problem (w_g) to form the ANM solution to the original problem.

4. The solution of the global problem

In this example problem, the global subproblem is solved numerically, with a low-resolution finite-element analysis. To apply the smooth distributed force to the FEA model, it must first be discretized using either a statically equivalent or work equivalent loading method.¹⁷ In this study, the statically equivalent method is sufficient.

The three small constraints that are attached to the bottom edge of the thick beam are displaced vertically and/or rotated in the local problem. Since the constraints are geometrically identical, a high-resolution local symmetric problem, a high-resolution local asymmetric problem, and the two corresponding matching problems are solved. Two smooth-force transfer functions are obtained, \bar{f}_{sym} and \bar{f}_{asym} , for the symmetric and asymmetric cases, respectively. These force distributions are applied over the smoothing region associated with each constraint and they must be appropriately weighted in order to achieve the amount of displacement and/or rotation desired at each constraint of the full (original or ANM composite) structure.

For a problem where the forces at each constraint of the original problem are specified, the smooth forcing that is applied to the global subproblem around a given constraint equals the smooth-forcing transfer function \bar{f}_s times the amplitude of the specified force. Applying the appropriately weighted smooth forces to the global problem and solving for displacements yields the global displacement, w_g . The solution of the original problem is the sum of the weighted \bar{w}_L and \bar{w}_m plus w_g . The situation is slightly more complicated when the *displacements* of the constraints are prescribed, rather than the *forces* at the constraints.

In a displacement driven problem, the magnitudes of displacement that are *known* are those of the constraints in the *original* problem before it is decomposed. For the global problem, there are unknown displacements and rotations (d_i, θ_i) at every node in the finite-element model. However, at the three constraint locations (where the actual displacements and rotations are known), d_i and θ_i can be rewritten in terms of known quantities and unknown weighting factors. For example, the unknown global displacement of node A can be written as

$$d_A = -\alpha(\bar{w}_L + \bar{w}_m)_A + D_A, \quad (5)$$

where D_A corresponds to the known displacement of constraint A in the actual problem, and α is a factor that appropriately weights the displacement transfer functions from the local and the matching solutions. This factor must also be applied to the smooth forcing. In a multiple constraint problem, these scaling factors are present at each support. Since the local and matching problems are only solved once for translation and once for rotation, these solutions (and the related smooth forcing) must be superimposed at each constraint location with the appropriate weighting, α, β, γ , etc. The physical interpretation of α is that it is the amount of force required at the constraint to produce the desired displacement. These factors are solved for explicitly in the global formulation. The finite-element representation of this, for the stiffness operation, is given in abbreviated form by

$$[K_{\text{global}}] \begin{pmatrix} d_1 \\ \theta_1 \\ \vdots \\ -\alpha(\bar{w}_L + \bar{w}_m)_A + D_A = d_A \\ -\beta(\bar{\theta}_L + \bar{\theta}_m)_A + \Theta_A = \theta_A \\ \vdots \\ -\gamma(\bar{w}_L + \bar{w}_m)_B + D_B = d_B \\ -\eta(\bar{\theta}_L + \bar{\theta}_m)_B + \Theta_B = \theta_B \\ \vdots \\ -\xi(\bar{w}_L + \bar{w}_m)_C + D_C = d_C \\ -\chi(\bar{\theta}_L + \bar{\theta}_m)_C + \Theta_C = \theta_C \\ \vdots \\ d_n \\ \theta_n \end{pmatrix} = \begin{pmatrix} 0 \\ 0 \\ \vdots \\ \{\alpha\{\bar{f}_{\text{sym}}\} + \beta\{\bar{f}_{\text{asym}}\}\} \\ \vdots \\ 0 \\ \vdots \\ \{\gamma\{\bar{f}_{\text{sym}}\} + \eta\{\bar{f}_{\text{asym}}\}\} \\ \vdots \\ 0 \\ \vdots \\ \{\xi\{\bar{f}_{\text{sym}}\} + \chi\{\bar{f}_{\text{asym}}\}\} \\ \vdots \\ 0 \\ \vdots \\ 0 \end{pmatrix}, \quad (6)$$

where $D_A, \Theta_A, D_B, \Theta_B$, etc. are the prescribed displacements and rotations at the nodal locations of the constraints A, B , and C . Lower case d_i and θ_i are the unknown global displacements and rotations at each node, respectively. Each of the smooth forces spans many nodes (vector representation on the right-hand side of the equation). The six unknown factors, α, β, γ , etc., can be traded for the six known displacements D_A, Θ_A, D_B , etc., and the linear set of equations can be rewritten accordingly. Essentially, the stiffness matrix times the known displacements becomes the right-

TABLE I. Material properties, geometry, and forcing conditions for example problem.

Material properties	Geometric dimensions	Forcing conditions
$E = 2.0684 \times 10^{11}$ Pa	$2L = 1016$ cm	$D_A = 2.54$ cm, $\Theta_A = -0.01$ rad
$\nu = 0.0$	$h = 2.54$ cm	$D_B = 0, \Theta_B = 0.01$ rad
$\rho = 8.9057 \times 10^2$ kg/m ³	$d = 2.54$ cm	$D_C = 2.54$ cm, $\Theta_C = 0$.
	$2s = 0.508$ m	$\omega = 31.416$ rad/s

hand side, and the smooth forces get imbedded in a modified K matrix on the left-hand side. The unknown vector contains the remaining global displacements and rotations plus the six scaling constants.

Solving the set of equations results in a solution for the global displacements, as well as the scaling factors. The complete ANM solution is then the superposition of the appropriately weighted local and matching displacements plus the global displacements, where the weighting factors are given by the associated factors α, β, γ , etc. The composite ANM solution, which equals the solution to the original problem, is

$$w_{\text{ANM}} = \alpha(\bar{w}_L + \bar{w}_m) + w_g, \quad (7)$$

where α is used symbolically to represent whichever scaling factor applies for the particular section of beam. Note, except inside the smoothing regions, the solution to the composite (original) problem is simply the solution to the global problem, since outside the smoothing regions \bar{w}_L and \bar{w}_m are zero.

B. Results for the model problem

The model problem consists of a thick beam with three constraints along the bottom edge. The material properties, geometric dimensions, and forcing conditions are given in Table I. The three constraints are located $-\frac{3}{4}L, -\frac{1}{4}L$, and $+\frac{1}{2}L$ from the center of the thick beam, where $2L$ is the length of the beam. The smoothing length ($2L_s$) is chosen to be $0.05L$ (or 25.4 cm). This is ten times the beam thickness and approximately 50 times the size of the discontinuity (constraint). The choice of smoothing length is not unique and the results are presented for other smoothing lengths as well. The high-resolution local solution is solved using two-dimensional, eight node, 16-degree-of-freedom quadrilateral structural solid elements in a plane stress state. The boundary conditions at the end nodes are zero displacement and zero slope.

Two local problems are solved, one in which the constraint is displaced harmonically by an amount D , and one in which the constraint is rotated an amount Θ . The displacement used in this local problem is 2.54 cm and the rotation is 0.01 radians. Although these are actually the prescribed displacements of the original problem, they need not be the same for the local problem, since ANM is performed using transfer functions. The amplitude of the force and/or moment applied to the constraint in the local problem is used to obtain the transfer functions \bar{f}_s, \bar{w}_m , and \bar{w}_L .

The stress resultants, shear and moment, are extracted from the finite-element results of the local problem. In addi-

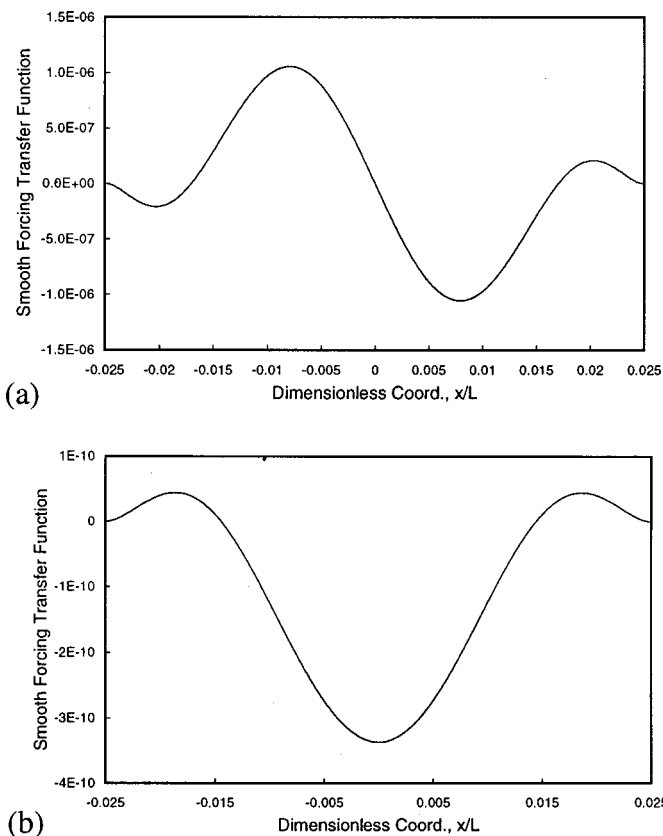


FIG. 4. Smooth forcing transfer functions: (a) asymmetric, and (b) symmetric.

tion, it is verified that the stresses are distributed uniformly about the theoretical neutral axis of the thick beam, proving that the smoothing region is large enough to apply beam theory simplifications on the smooth matching subproblem.

From the stress resultants, the coefficients of the matching displacement polynomial and smooth force polynomial are determined [see Eqs. (1) and (3)] for both the symmetric and asymmetric cases. The transfer functions for the smooth-force distributions in the asymmetric and symmetric cases are shown in Fig. 4. The smooth-force transfer function \bar{f}_s is discretized and applied to the global finite-element analysis problem.

The global problem consists of two-node simple beam elements extending over the full length of the beam (1016 cm). The length of the global problem is 40 times larger than the length of the local problem (for a smoothing length $2L_s = 25.4$ cm). The global problem consists of elements only in the span-wise direction, whereas the local problem has elements in both the span-wise and thickness directions.

1. Traditional FEA full solid model for comparison

As an alternative and for verification purposes, this problem is solved using a full solid model of 2D plane elements. Around each constraint the model is finely meshed to the same resolution as the high-resolution local problems in ANM. Transition regions are used to convert to lower density meshes away from the discontinuities. However, even at the lowest resolution, the model still contains 2D plane ele-

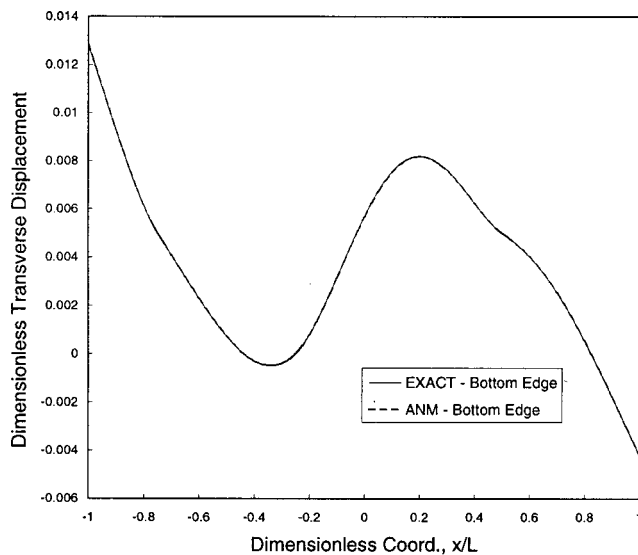


FIG. 5. ANM vs traditional FEA (exact) solutions along the bottom edge of the beam with multiple supports.

ments because beam elements cannot be combined with 2D plane elements in the same model using a traditional FEA approach.

2. Comparisons

In the model problem, shown in Fig. 2, the first support (at $-\frac{3}{4}L$ from the center of the beam) is rotated and displaced by the amounts D_A and Θ_A given in Table I. The second support (at $-\frac{1}{4}L$) is rotated by Θ_B , and the third support (at $\frac{1}{2}L$) is displaced by D_C . The displacements of the bottom edge of the thick beam are plotted in Fig. 5, for both the ANM solution and the traditional FEA solution. The results are indistinguishable.

In Fig. 6, a closer view of the first support is shown. Again, the difference between the ANM solution and the traditional FEA solution cannot be seen. In fact, the largest difference between the two solutions (at any point) is less than a fraction of a percent ($<0.1\%$). Although they are not

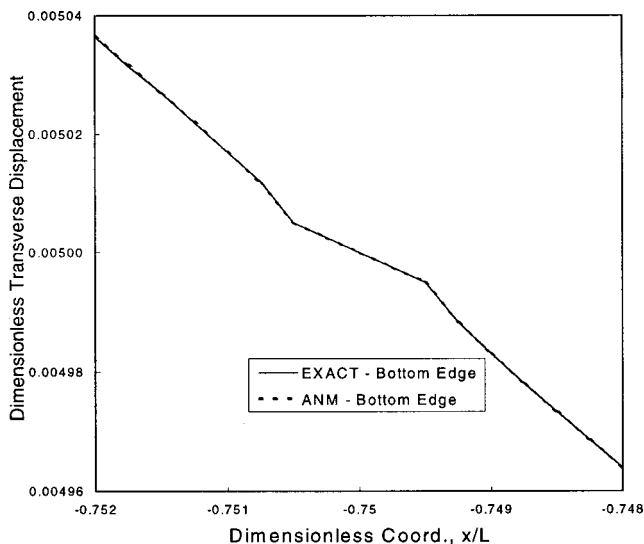


FIG. 6. Close-up of ANM vs traditional FEA (exact) solutions along the bottom edge of the first support.

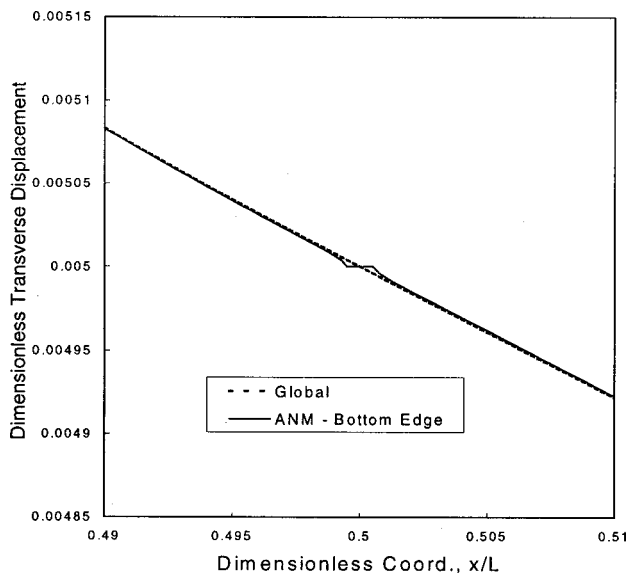


FIG. 7. Global solution vs ANM solution plotted in the near vicinity of the third support, a harmonic displacement constraint.

shown, the displacements throughout the thickness were also compared and included in the previous statistic.

In Fig. 7, a close-up of the third support, which is displaced by D_C , but constrained in rotation, is shown. Here, a comparison is made between the actual solution (ANM) and the contribution of the global solution, for the range inside the chosen smoothing region. The global and ANM solutions are identical outside the smoothing region (since the local and matching solutions are zero there). The global problem contains only smoothly varying forces and does not pick up the sharp gradients. The high-resolution local solution, which is added to the global, gives the ANM solution the detailed information around the support. The matching solution essentially negates the global solution on the domain of the smoothing region, leaving the local solution.

The choice of smoothing region is not unique, and in fact many smoothing lengths will produce equally precise ANM solutions. In Fig. 8, the traditional FEA solution and

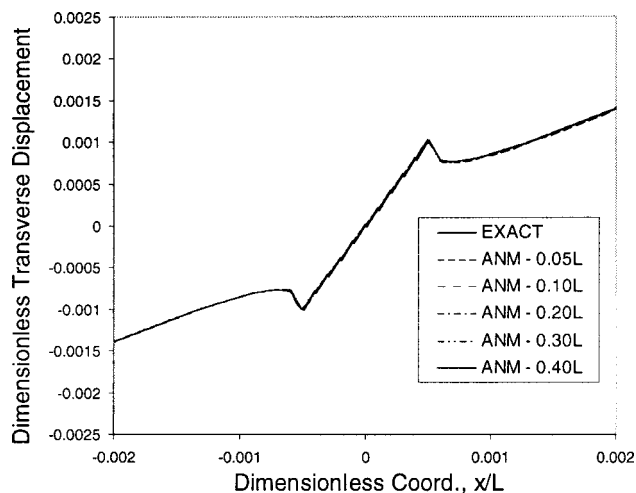


FIG. 8. Comparison of ANM for different smoothing lengths. Results are indistinguishable; scale has been expanded around a constraint.

five different smoothing-length ANM solutions are shown around a single support that has been rotated.

3. Computational savings

The traditional FEA model used for verification of the ANM results is made up entirely of two-dimensional solid elements using approximately 51 000 degrees of freedom. In the ANM submodels, the high-resolution local model made up of two-dimensional solid elements contains 7550 degrees of freedom. Two local models are used, one for symmetric forcing and one for asymmetric forcing. The low-resolution global model is made up of 104 Bernoulli–Euler beam elements, resulting in 210 degrees of freedom. The net total degrees of freedom used for the ANM solution is 15 200. This is approximately a threefold savings in computation time for the same degree of accuracy. It is possible that the savings could have been increased, without significant reduction in accuracy, had the models been optimized for efficiency. However, the most significant reduction in computational time occurs when the structure contains a large number of repeated constraints.

Each subsequent identical support that is added to the thick beam does not add to the computational burden of ANM, since the local solutions are already done. The traditional FEA solution, however, would suffer increased computational cost since another region of finely meshed modeling (i.e., around the new support) would be required. Therefore, in problems with many geometrically identical discontinuities, the savings from ANM could be substantial.

In addition, if other constraint motions are to be considered, the additional ANM cost involves running the low-resolution global model only. The local and matching solutions are done once and for all using transfer functions and do not have to be recalculated, whereas, the entire traditional FEA model would have to be rerun for each additional constraint motion considered. This illustrates another opportunity for computational savings using ANM.

V. CONCLUSION

Three small identical constraints along the edge of a thick beam were harmonically displaced and/or rotated, and the structural vibrations along the bottom edge of the beam (or elsewhere through the thickness) were calculated using analytical/numerical matching and a traditional finite-element model of two-dimensional structural solid elements. The comparisons show excellent agreement over a range of ANM smoothing lengths. It is expected that the results would continue to be excellent for smaller smoothing lengths, as long as the beam theory assumptions still apply.

Analytical/numerical matching allows the region requiring high resolution to be solved as a separate problem and retain all of its structural dynamic content. In contrast to FEA submodeling, the ANM high-resolution local subproblem is not reduced before incorporation with the other subproblems to form the complete solution.

For problems where there are geometrically identical discontinuities, ANM provides a means for significant computational savings over a traditional FEA method. In the ex-

ample problem, only two high-resolution local FEA problems were needed with ANM, one for symmetric loading and one for asymmetric loading. The results of the local problems were applied, using ANM, to each of the three constraints. In the traditional FEA approach, each of the three constraints was modeled with a high-resolution mesh. In problems with substantially more identical geometrical constraints, the computational savings would be more pronounced. In addition to the reduced number of high-resolution degrees of freedom around the constraint, ANM saves computation time by modeling the larger (global) problem with reduced order elements. In the ANM global model, only two-node beam elements are needed, whereas in the traditional FEA model, the full beam is meshed with two-dimensional eight-node solid structural quadrilateral elements. The mesh density can vary, but the element types must be the same throughout the model. Again, these savings would be more dramatic on a larger problem with many more constraints.

In addition to computational savings, ANM provides a means to separate local effects from global effects. This may be important in furthering the understanding of the role of discontinuities in fluid-loaded problems. Furthermore, ongoing research suggests that ANM may be able to provide a mechanism to remove fluid loading from the local problem and account for it entirely in the global problem, by rendering the local problems nonradiating (an additional constraint on the smooth force). If this is possible, ANM has the potential to more efficiently solve fluid-loaded structures with discontinuities.

Work in progress includes extension of ANM to fluid-loaded cylindrical shells with discontinuities. For that application, the structure is decomposed in azimuth using modal analysis, and a three-dimensional (including shell thickness) FEA problem must be solved for each mode. This work has provided a sound basis for applying ANM to that specific problem, and should provide the reader with a guide for applying ANM to more complicated problems in general.

ACKNOWLEDGMENTS

The authors would like to thank the inventor of analytical/numerical matching, Professor Donald B. Bliss at Duke University, for his guidance and suggestions on this research. This work was sponsored by the Office of Naval Research and the North Carolina Supercomputing Center.

- ¹R. Langley and P. Bremner, "A Hybrid Method for the Vibration Analysis of Complex Structural-Acoustic Systems," *J. Acoust. Soc. Am.* **105**, 1657–1671 (1999).
- ²J. Montgomery and P. Barbone, "Diffraction from Simple Shapes by a Hybrid Asymptotic-Finite Element Method," *J. Acoust. Soc. Am.* **104**, 1964–1972 (1998).
- ³N. Kawashima, M. Kashihara, and M. Sugimoto, "A combination of the finite element method and the rigid-body spring model for plane problems," *Finite Elem. Anal. Design* **11**, 67–76 (1992).
- ⁴S. Vijayakar "A Combined Surface Integral and Finite Element Solution for a Three-Dimensional Contact Problem," *Int. J. Numer. Methods Eng.* **31**, 525–545 (1991).
- ⁵J. Lee and H. Gao, "Hybrid Finite Element Analysis of Interface Cracks," *Int. J. Numer. Methods Eng.* **38**, 2465–2482 (1995).
- ⁶D. B. Bliss, M. E. Teske, and T. R. Quackenbush, "A New Methodology for Free Wake Analysis Using Curved Vortex Elements," NASA CR 3958 (1987).
- ⁷D. B. Bliss and W. O. Miller, "Efficient Free Wake Calculations Using Analytical/Numerical Matching and Far-Field Linearization," in *Proceedings of the 45th Annual Forum of the American Helicopter Society*, Boston, MA (1989).
- ⁸D. B. Bliss and R. J. Epstein, "Free Vortex Problems Using Analytical/Numerical Matching with Solution Pyramiding," *AIAA J.* **33**, 894–903 (1995).
- ⁹D. B. Bliss and R. J. Epstein, "Novel Approach to Aerodynamic Analysis Using Analytical/Numerical Matching," *AIAA J.* **34**, 2225–2232 (1996).
- ¹⁰R. J. Epstein and D. B. Bliss, "An Acoustic Boundary Element Method Using Analytical/Numerical Matching," *J. Acoust. Soc. Am.* **101**, 92–106 (1997).
- ¹¹R. J. Epstein and D. B. Bliss, "Aeroacoustic Boundary Element Method Using Analytical/Numerical Matching," *AIAA J.* **35**, 244–254 (1997).
- ¹²D. B. Bliss and L. P. Franzoni, "Analytical/Numerical Matching (ANM) for the Predictions of Acoustic Radiation," *J. Acoust. Soc. Am.* (to be published).
- ¹³R. C. Loftman and D. B. Bliss, "The Application of Analytical/Numerical Matching to Structural Discontinuities in Structural/Acoustic Problems," *J. Acoust. Soc. Am.* **101**, 925–935 (1997).
- ¹⁴D. B. Bliss and R. C. Loftman, "Local and Global Effects in Structural-Acoustic Scattering Using Analytical/Numerical Matching," in *Proceedings of the 15th Annual International Congress on Acoustics*, Trondheim, Norway, June 1995 (Acoustical Society of Norway, Trondheim, Norway, 1995).
- ¹⁵R. C. Loftman and D. B. Bliss, "Analytical/Numerical Matching for Efficient Calculation of Scattering from Cylindrical Shells with Lengthwise Constraints," *J. Acoust. Soc. Am.* **103**, 1885–1896 (1998).
- ¹⁶R. C. Loftman and D. B. Bliss, "Scattering from Fluid-Loaded Cylindrical Shell with Periodic Circumferential Constraints using Analytical/Numerical Matching," *J. Acoust. Soc. Am.* **106**, 1271–1283 (1999).
- ¹⁷T. Y. Yang, *Finite Element Structural Analysis* (Prentice-Hall, Englewood Cliffs, NJ, 1986).
- ¹⁸J. Steele, *Applied Finite Element Modeling Finite Element Modeling* (Marcel Dekker, New York, 1989).
- ¹⁹S. A. Canann, "All-Quad Free Meshing" in *Analysis Solutions* (Connect, Santa Fe, Winter 1997/1998).
- ²⁰K. F. Graff, *Wave Motion In Elastic Solids* (Dover, New York, 1991).

A numerical model for the low frequency diffuse field sound transmission loss of double-wall sound barriers with elastic porous linings

F. C. Sgard

Laboratoire des Sciences de l'Habitat, DGCB URA CNRS 1652, Ecole Nationale des Travaux Publics de l'Etat, 69518 Vaulx-en-Velin Cedex, France

N. Atalla and J. Nicolas

Groupe d'Acoustique de l'Université de Sherbrooke, Department of Mechanical Engineering, Université de Sherbrooke, Sherbrooke, Quebec J1K 2R1, Canada

(Received 26 October 1999; accepted for publication 3 September 2000)

This paper discusses the prediction of the low frequency diffuse field transmission loss through double-wall sound barriers with elastic porous linings. The studied sound barriers are made up from a porous-elastic decoupling material sandwiched between an elastic skin and a septum. The prediction approach is based on a finite element model for the different layers of the sound barrier coupled to a variational boundary element method to account for fluid loading. The diffuse field is modeled as a combination of uncorrelated freely propagating plane waves with equal amplitude, no two of which are traveling in the same direction. The corresponding vibroacoustic indicators are calculated efficiently using a Gauss integration scheme. Also, a power balance is presented to explain the dissipation mechanisms in the different layers. Typical results showing the effects on the transmission loss of several parameters such as the septum mass, the decoupling porous layer properties and the multi-layer mounting conditions are presented. © 2000 Acoustical Society of America. [S0001-4966(00)01512-5]

PACS numbers: 43.50.Gf [MRS]

I. INTRODUCTION

The design of sound barriers is of utmost importance in several industries including automotive, aerospace and buildings. These barriers are typically made up of a decoupling layer sandwiched between a thin skin and a limp massive impervious layer classically known as a septum. As such, they may be considered a double-wall system. The decoupling layer is usually made up from a porous-elastic material such as cellular (e.g., polyurethane foam) and fibrous (e.g., glass fibers) materials. In designing sound barriers for multiple engineering applications, the engineer must select the type and geometric configuration of the barrier and decoupler materials to be used. This task necessitates a thorough understanding of the mechanisms governing the transmission loss of such systems together with an accurate data bank of the mechanical and acoustical properties of these materials. Up to now, design engineers have relied on classical analytical formulae¹⁻³ and Transmission Loss (TL) measurements to design sound barriers. Recent advances concerning the modeling and experimental characterization of porous-elastic material authorized the development of accurate numerical prediction tools.⁴⁻⁸ However, current prediction methods (i.e., the transfer matrix method: TMM) are limited to laterally infinite sound barriers.^{4,6,9} At low frequencies, where the modal behavior of the system is important, prediction methods are still limited.^{7,10,11} In particular, these models usually assume plane wave excitation which represents a limitation since diffuse field excitation is the basis of standardized

transmission loss measurements. Also, it is classically assumed in the above cited references that fluid loading is negligible. However, there are situations where such an assumption is questionable (e.g., steel and water in marine application). More importantly, to simulate correctly a diffuse field excitation at low frequencies, fluid-structure loading must be accounted for. The approach proposed in this article eliminates these two limitations.

The paper discusses the prediction of the low frequency diffuse field transmission loss through double-wall sound barriers with elastic porous linings. The studied sound barriers are made from a porous-elastic decoupling material sandwiched between an elastic skin and a septum. It uses a numerical model based on a finite element method for the different layers of the sound barrier coupled to a variational boundary element method to account for fluid loading. In particular a mixed displacement-pressure formulation of Biot's poroelasticity equations is used to model the porous-elastic layer.⁵ The diffuse field is modeled as a superposition of uncorrelated freely propagating plane waves with equal amplitude, no two of which are traveling in the same direction. The corresponding vibroacoustic indicators are calculated efficiently using a Gauss integration scheme. Finally, expressions for the powers dissipated through the different mechanisms governing dissipation in porous-elastic media are derived, which has not been done in earlier works.

The developed prediction tool is used to investigate a classical configuration in the automotive industry wherein a

decoupling porous layer is sandwiched between the body sheet metal and a septum. Several examples are shown to investigate the effects of several parameters such as the septum mass, the decoupling porous layer properties and the multi-layer mounting conditions on the diffuse field transmission loss of such systems. In particular, a power balance based on the computation of the powers dissipated in the elastic and the porous medium is used to explain the dissipation mechanisms within such systems.

II. THEORY

A. Description of the problem

The problem consists of a double-panellike structure with arbitrary boundary conditions. The system is excited either mechanically or acoustically by a plane wave or diffuse sound field. The air space between the excited plate (skin) and the barrier (septum) is filled with a porous-elastic material which may be either bonded or unbonded to the plates. The system is inserted into an infinite rigid baffle which separates two semi-infinite fluid media V_1 (emission) and V_2 (receiver). The density and sound speed of fluid medium V_i , $i=1,2$ are noted ρ_i and c_i , respectively. The inner and outer layers are subjected to fluid loading induced by their acoustic radiation in their respective exterior medium. In the following, a temporal dependency $e^{j\omega t}$ for all the fields is assumed. The theory regarding the modeling of the plate, the septum, the acoustic domain is classical and can be found in Morand.¹² The finite element model associated with the porous-elastic media is based on the mixed finite element (u,p) formulation of Biot's poroelasticity equations and is detailed in Ref. 5. The limitations of this model are intimately linked to the size of the systems to be solved together with the used poroelastic finite elements. Indeed, the porous medium finite element discretization requires 4 degrees of freedom per node. In addition, classical modal expansions cannot be used for the porous medium due to the frequency nonlinearity of the associated eigenvalue problem so that the system size cannot be reduced as in classical fluid-structure interaction problems. As pointed out by Panneton^{8,13} and Rigobert,¹⁴ the number of linear poroelastic elements needed to achieve convergence of the solution varies and may prove to be very large according to the porous material involved and the vibroacoustic indicators of interest. Also, the convergence of the solution is affected by the dynamic compartments of the elastic and fluid phases which behave differently. An approach has been recently proposed to improve the convergence of the finite element poroelastic models by using hierarchical porous finite elements.¹⁴ The modeling of the complex radiation impedance matrix due to fluid loading assumes the plate to be baffled (i.e., based on Rayleigh's integral¹⁵). The details of its numerical evaluation may be found in Ref. 16.

B. Powers dissipated in porous media

In this section, expressions for the powers dissipated through the different mechanisms governing dissipation in

porous-elastic media are derived. This derivation follows from the weak integral form of Biot-Allard's poroelasticity equations.⁵ A variant form of this equation is presented here. It has the advantage of depicting the boundary terms in a more suitable form for application of the coupling conditions with other media. The modified weak integral form of the porous media according to Atalla⁵ can be written as

$$\begin{aligned} & \int_{\Omega^p} [\tilde{\boldsymbol{\sigma}}^s(\mathbf{u}) : \boldsymbol{\epsilon}^s(\delta\mathbf{u}) - \omega^2 \tilde{\rho} \mathbf{u} \cdot \delta\mathbf{u}] d\Omega \\ & + \int_{\Omega^p} \left[\frac{h^2}{\omega^2 \tilde{\rho}_{22}} \nabla p \cdot \nabla \delta p - \frac{h^2}{\tilde{R}} p \delta p \right] d\Omega \\ & - \int_{\Omega^p} \left(\frac{h^2 \rho_0}{\tilde{\rho}_{22}} - 1 \right) \delta(\nabla p \cdot \mathbf{u}) d\Omega - \int_{\partial\Omega^p} \delta(p u_n) dS \\ & - \int_{\partial\Omega^p} (\boldsymbol{\sigma}^t \cdot \mathbf{n}) \cdot \delta\mathbf{u} dS - \int_{\partial\Omega^p} h(U_n - u_n) \delta p dS \\ & = 0 \quad \forall (\delta\mathbf{u}, \delta p). \end{aligned} \quad (1)$$

Here Ω^p and $\partial\Omega^p$ refer to the porous-elastic domain and its bounding surface. \mathbf{u} and p are the solid phase displacement vector and the interstitial pressure of the porous-elastic medium, respectively; $\delta\mathbf{u}$ and δp refer to their admissible variation, respectively. \mathbf{n} denotes the unit normal vector external to the bounding surface $\partial\Omega^p$. $\tilde{\boldsymbol{\sigma}}^s$ and $\boldsymbol{\epsilon}^s$ are the *in vacuo* stress and strain tensors of the porous material. Tensor $\tilde{\boldsymbol{\sigma}}^s$ is related to the total stress tensor $\boldsymbol{\sigma}^t$ of the material through the following relation: $\tilde{\boldsymbol{\sigma}}^s = \boldsymbol{\sigma}^t + h(1 + \tilde{Q}/\tilde{R})p \mathbf{1}$ where \mathbf{U} and \mathbf{u} refer to the solid and fluid macroscopic displacement vectors, respectively, h stands for the porosity of the material, \tilde{Q} is an elastic coupling coefficient between the two phases, and \tilde{R} may be interpreted as the bulk modulus of the air occupying a fraction h of a unit volume aggregate⁴. Note that $\tilde{\boldsymbol{\sigma}}^s$ accounts for structural damping in the skeleton through a complex Young's modulus $E(1 + j\eta)$. $\tilde{\rho}_{22}$ is the modified Biot's density of the fluid phase accounting for viscous dissipation, $\tilde{\rho}$ is a modified density given by $\tilde{\rho} = \tilde{\rho}_{11} - \tilde{\rho}_{12}^2/\tilde{\rho}_{22}$ where $\tilde{\rho}_{11}$ is the modified Biot's density of the solid phase accounting for viscous dissipation. $\tilde{\rho}_{12}$ is the modified Biot's density which accounts for the interaction between the inertia forces of the solid and fluid phase together with viscous dissipation. Equation (1) assumes that $h(1 + \tilde{Q}/\tilde{R}) \approx 1$, which is valid for most of the porous materials. Following the classical steps leading to the weak integral form Eq. (1) with the following particular choice for the admissible functions: “ $-j\omega\mathbf{u}^*$ ” for the solid-phase displacement u equation and $-j\omega p^*$ for the fluid-phase interstitial pressure p equation, where f^* denotes the complex conjugate of f , one gets

$$\begin{aligned}
& \underbrace{-j\omega \int_{\Omega^p} \tilde{\boldsymbol{\sigma}}^s(\mathbf{u}) : \boldsymbol{\varepsilon}^s(\mathbf{u}^*) d\Omega}_{\Pi_{\text{elas}}^s} + \underbrace{j\omega^3 \int_{\Omega^p} \tilde{\rho} \mathbf{u} \cdot \mathbf{u}^* d\Omega}_{\Pi_{\text{iner}}^s} + \underbrace{j\omega \int_{\Omega^p} \frac{h^2}{\tilde{R}} p p^* d\Omega}_{\Pi_{\text{elas}}^f} - \underbrace{j\omega \int_{\Omega^p} \frac{h^2}{\omega^2 \tilde{\rho}_{22}} \nabla p \cdot \nabla p^* d\Omega}_{\Pi_{\text{iner}}^f} \\
& + \underbrace{j\omega \int_{\Omega^p} \left(\frac{h\rho_0}{\tilde{\rho}_{22}} - 1 \right) (\nabla p \cdot \mathbf{u}^* + \nabla p^* \cdot \mathbf{u}) d\Omega + j\omega \int_{\partial\Omega^p} (p \mathbf{u}^* \cdot \mathbf{n} + p^* \mathbf{u} \cdot \mathbf{n}) d\Omega}_{\Pi_{\text{coup}}^{fs}} \\
& + \underbrace{j\omega \int_{\partial\Omega^p} [\tilde{\boldsymbol{\sigma}}^f \cdot \mathbf{n} \mathbf{u}^*] dS + j\omega \int_{\partial\Omega^p} h(U_n - u_n) p^* d\Omega}_{\Pi_{\text{exc}}} = 0. \tag{2}
\end{aligned}$$

This provides the following power balance equation:

$$\Pi_{\text{elas}}^s + \Pi_{\text{iner}}^s + \Pi_{\text{elas}}^f + \Pi_{\text{iner}}^f + \Pi_{\text{coup}}^{fs} + \Pi_{\text{exc}} = 0, \tag{3}$$

where Π_{elas}^s , Π_{iner}^s represent the power developed by the internal and inertia forces in the solid-phase *in vacuo*, respectively; Π_{elas}^f , Π_{iner}^f represent the power developed by the internal and inertia forces in the interstitial fluid, respectively; Π_{coup}^{fs} represents the power exchanged between the two phases; and Π_{exc} represents the power developed by external loading.

The time-averaged power dissipated within the porous medium can be subdivided into contributions from powers dissipated through structural damping of the skeleton, viscous and thermal effects: $\Pi_{\text{diss}} = \Pi_{\text{diss}}^s + \Pi_{\text{diss}}^v + \Pi_{\text{diss}}^t$. The time-averaged power dissipated through structural damping is obtained from Π_{elas}^s , namely:

$$\Pi_{\text{diss}}^s = \frac{1}{2} \Im \left[\omega \int_{\Omega^p} \tilde{\boldsymbol{\sigma}}^s(\mathbf{u}) : \boldsymbol{\varepsilon}^s(\mathbf{u}^*) d\Omega \right]. \tag{4}$$

The power dissipated through viscous effects is obtained from $\Pi_{\text{iner}}^s + \Pi_{\text{iner}}^f + \Pi_{\text{coup}}^{fs}$, namely:

$$\begin{aligned}
\Pi_{\text{diss}}^v = & -\frac{1}{2} \Im \left[\omega^3 \int_{\Omega^p} \tilde{\rho} \mathbf{u} \cdot \mathbf{u}^* d\Omega - \int_{\Omega^p} \frac{h^2}{\omega \tilde{\rho}_{22}} \nabla p \right. \\
& \left. \cdot \nabla p^* d\Omega + 2 \int_{\Omega^p} \omega \left(\frac{h^2 \rho_0}{\tilde{\rho}_{22}} - 1 \right) \Re(\nabla p \cdot \mathbf{u}^*) d\Omega \right]. \tag{5}
\end{aligned}$$

Finally, the power dissipated through thermal effects is obtained from Π_{elas}^f , namely:

$$\Pi_{\text{diss}}^t = -\frac{1}{2} \Im \left[\omega \int_{\Omega^p} \frac{h^2}{\tilde{R}} p p^* d\Omega \right]. \tag{6}$$

C. Diffuse field indicators

The diffuse field excitation can be considered as a combination of freely propagating plane waves with equal amplitude, no two of which are traveling in the same direction and with the propagation vector pointing toward the plate.¹⁵ Accounting for fluid loading, the system equations are solved for each incident plane wave with incidence angle (θ, φ) and complex amplitude p_{inc} , to yield the corresponding acoustic

power radiated by the plate or the septum in medium i , $\Pi_{i,(\theta,\varphi)}$ ($i=1,2$). The diffuse field radiated in medium i is then obtained through an integration over the half space:

$$\Pi_i^d = \int_0^{2\pi} \int_0^{\pi/2} \Pi_{i,(\theta,\varphi)} \sin \theta d\theta d\varphi, \tag{7}$$

where

$$\Pi_{i,(\theta,\varphi)} = \frac{1}{2} \Re \left[\int_{\Sigma_i} p_{i,(\theta,\varphi)}(\mathbf{x}) \mathbf{v}_{i,(\theta,\varphi)}^*(\mathbf{x}) \cdot \mathbf{n}_i(\mathbf{x}) dS(\mathbf{x}) \right], \tag{8}$$

where v_i is the structural velocity of the plate or the septum. Equation (8) can be rewritten in terms of the radiation impedance operator of the plate or the septum in medium i , $Z_i(\omega, \mathbf{x}, \mathbf{y})$ as

$$\begin{aligned}
\Pi_{i,(\theta,\varphi)} = & \frac{1}{2} \Re \left[\omega^2 \int_{\Sigma_i} \int_{\Sigma_i} \mathbf{u}_{i,(\theta,\varphi)}^*(\mathbf{y}) \cdot Z_i(\omega, \mathbf{x}, \mathbf{y}) \right. \\
& \left. \cdot \mathbf{u}_{i,(\theta,\varphi)}(\mathbf{x}) dS(\mathbf{y}) dS(\mathbf{x}) \right]. \tag{9}
\end{aligned}$$

Because of symmetry, only the regular part of the impedance operator (i.e., the one which corresponds to the imaginary part of the Green's function) is needed to compute the radiated acoustic power. However, from the computational viewpoint, it is more efficient to evaluate the radiated power directly from Eq. (8).

The diffuse field incident power is given by:

$$\begin{aligned}
\Pi_{\text{inc}}^d = & \int_0^{2\pi} \int_0^{\pi/2} \Pi_{\text{inc}}(\theta, \varphi) \sin \theta d\theta d\varphi \\
= & \frac{\Sigma_1}{2\rho_1 c_1} \int_0^{2\pi} \int_0^{\pi/2} |p_{\text{inc}}|^2 \cos \theta \sin \theta d\theta d\varphi, \\
= & \frac{\Sigma_1 |p_{\text{inc}}|^2 \pi}{2\rho_1 c_1}. \tag{10}
\end{aligned}$$

The diffuse field transmission loss is given by:

$$TL^d = \frac{\Pi_2^d}{\Pi_{\text{inc}}^d}. \tag{11}$$

The diffuse field powers dissipated within the porous media are computed in a similar way to Π_i^d . Finally, it is

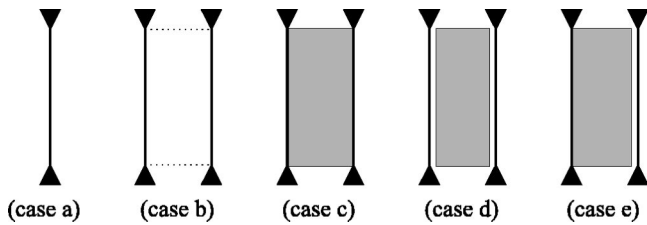


FIG. 1. Design configurations of interest: (case a) single plate; (case b) unlined; (case c) bonded layer; (case d) unbonded layer; (case e) bonded-unbonded layer.

worth mentioning that in the present work, all the diffused field indicators are calculated using a Gauss integration scheme.

III. NUMERICAL RESULTS

The different finite element formulations used in this paper have been previously validated experimentally^{13,17} and numerically for classical mechanical and acoustical excitations.^{5,16,18,19} However, the diffuse field excitation has not been investigated. In the following, the diffuse field transmission loss obtained from the presented approach is first compared to a Rayleigh–Ritz approach in the particular case of a single simply supported panel, the fluid loading effects being neglected. Next, results will be presented regarding the diffuse field transmission loss of the geometrical configurations summarized in Fig. 1. In particular, several points are studied such as the effect of the septum mass per unit area, the influence of the interface conditions between the different layers and the relevance of a septum model compared to a plate model. Also, the importance of the dissipation mechanisms in the system is studied according to the interface conditions. Two different poroelastic materials are considered: a polyester urethane foam and an unreinforced fiberglass which may be bonded or unbonded to the plates. The unbonded condition is obtained by inserting a very thin air gap between the plate and the porous layer. The investigated porous materials have slipping conditions on their lateral faces (i.e., the normal solid-phase displacements are prevented on their edges) and the plate is supposed simply supported. The physical data for the porous materials are given in Table I. In the following, the plate has dimensions $0.35\text{ m} \times 0.22\text{ m}$ and is 0.001 m thick. The emission and reception domains are supposed to contain air. In all cases, fluid loading is accounted for, unless otherwise specified. Finally, note that the finite element meshes have been checked to ensure the convergence of the presented calculations.

A. Single plate excited by a diffuse field

In this section, the diffuse field transmission loss of a single aluminum plate with Young’s modulus $E_s = 7.1 \times 10^{10}\text{ Pa}$, Poisson’s ratio $\nu_s = 0.33$, mass density $\rho_s = 2814\text{ kg/m}^3$ and loss factor $\eta_s = 0.001$, is considered [Fig. 1(a)]. The present approach is compared with a semi-analytical method based on the Rayleigh–Ritz method for plate vibrations together with a simple trapezoidal numerical integration scheme for the diffuse field indicators. Fluid loading is

TABLE I. Physical properties and dimensions.

Sound absorbing layer (fiberglass)	
Flow resistivity	$\sigma = 25\,000\text{ Nm}^{-4}\text{ s}$
Porosity	$h = 0.95$
Tortuosity	$\alpha_\infty = 1.4$
Viscous characteristic length	$\Lambda = 93.2 \times 10^{-6}\text{ m}$
Thermal characteristic length	$\Lambda' = 93.2 \times 10^{-6}\text{ m}$
Poisson’s ratio	$\nu = 0$
<i>In vacuo</i> Young’s modulus	$E = 14 \times 10^3\text{ Pa}$
Loss factor	$\eta = 0.05$
Solid phase mass density	$\rho_1 = 30\text{ kg/m}^3$
Sound absorbing layer (foam)	
Flow resistivity	$\sigma = 25\,000\text{ Nm}^{-4}\text{ s}$
Porosity	$h = 0.90$
Tortuosity	$\alpha_\infty = 7.8$
Viscous characteristic length	$\Lambda = 2.26 \times 10^{-6}\text{ m}$
Thermal characteristic length	$\Lambda' = 2.26 \times 10^{-6}\text{ m}$
Poisson’s ratio	$\nu = 0.4$
<i>In vacuo</i> Young’s modulus	$E = 800 \times 10^3\text{ Pa}$
Loss factor	$\eta = 0.265$
Solid phase mass density	$\rho = 30\text{ kg/m}^3$

neglected. In the semi-analytical method, 360 plane waves (spacing of 10 degrees along φ and θ) were used to model the diffuse field whereas only 16 (16 Gauss points) were utilized in the present approach. Both the diffuse field and normal incidence transmission loss are compared. Figure 2 shows excellent agreement between the presented approach and the semi-analytical approach.

In the next three sections, the plate is made up of steel with Young’s modulus $E_s = 2 \times 10^{11}\text{ Pa}$, Poisson’s ratio $\nu_s = 0.32$, mass density $\rho_s = 7841\text{ kg/m}^3$ and loss factor $\eta_s = 0.007$. The air cavity [case (b) in Fig. 1] is 0.0375 m thick and the air gap [cases (d) and (e) in Fig. 1] is 0.0001 m thick. The density and the sound speed of the air are $\rho_0 = 1.213\text{ kg/m}^3$ and $c = 342.2\text{ m/s}$, respectively.

B. Influence of the septum mass per unit area

In this section, the effects of the septum mass per unit area on the transmission loss are studied. Figures 3 and 4

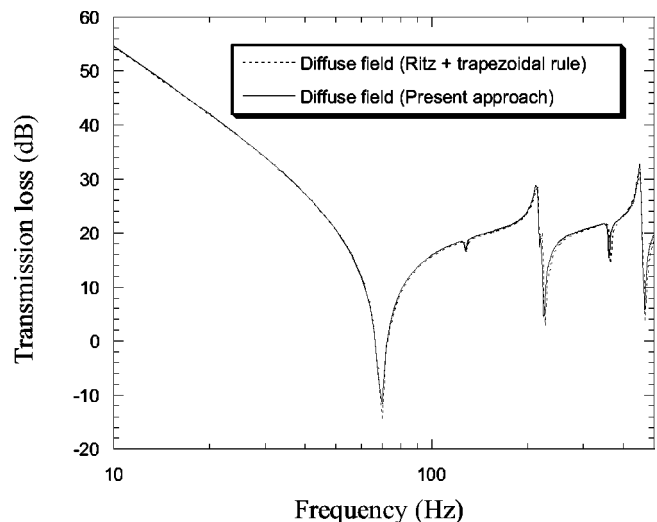


FIG. 2. Diffuse field transmission loss through a single plate. Comparison between the present approach and a Rayleigh–Ritz method combined with a trapezoidal integration scheme for the diffuse field transmission loss.

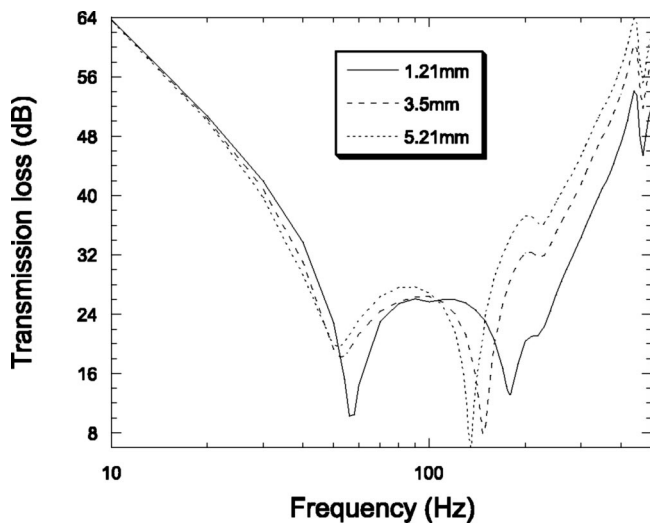


FIG. 3. Diffuse field transmission loss through a finite plate lined with fiberglass and a vinyl septum (bonded case): influence of the septum thickness.

present the diffuse field transmission loss through the system depicted in Fig. 1(c) for three thicknesses (1.71 mm, 3.5 mm, 5.21 mm) of a vinyl septum with a mass density equal to 1400 kg/m^3 for two different porous materials (a fiberglass and a foam). The chosen thickness for the inner layer corresponds to masses per unit area of 2.4, 4.9 and 7.3 kg/m^2 , respectively. These values coincide with classical values encountered in the automotive industry. It is seen that increasing the septum mass per unit area induces an added mass effect which decreases the first dip and second dip frequencies for all of the tested materials. It has been verified by analyzing the mode shapes of the system that the first dip corresponds to a plate-controlled mode and the second dip to the double-wall resonance. Below the first plate-controlled mode resonance frequency, the increase of the septum thickness is effectless since in this frequency band the stiffness of the system governs the transmission loss. Above the double-wall resonance, a thicker septum induces an increase of the transmission loss, as expected from laterally infinite behav-

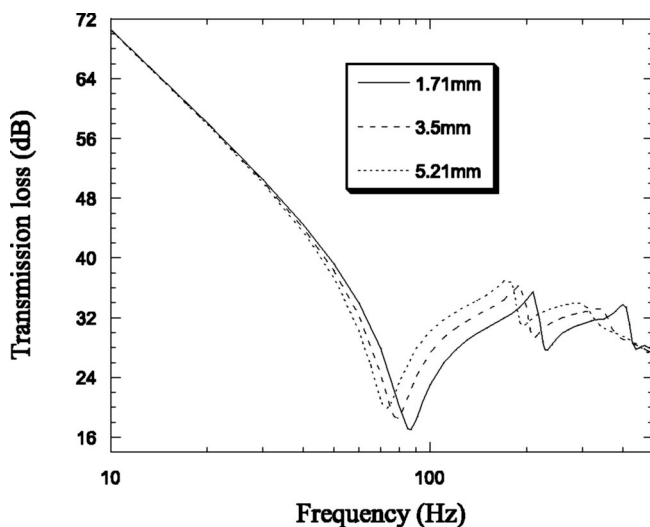


FIG. 4. Diffuse field transmission loss through a finite plate lined with foam and a vinyl septum (bonded case): influence of the septum thickness.

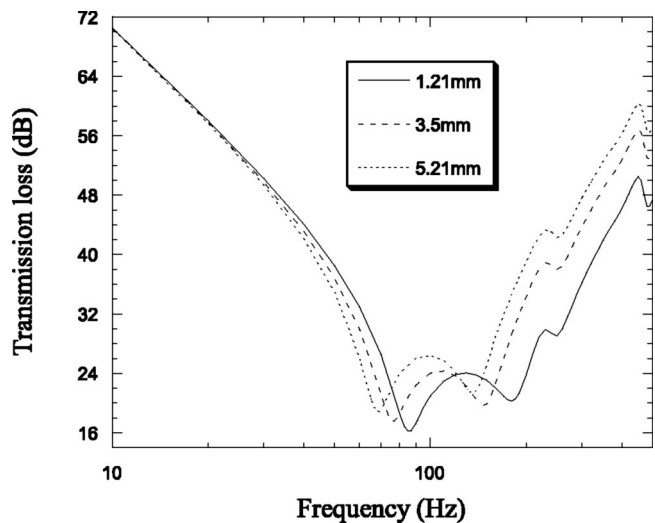


FIG. 5. Diffuse field transmission loss through a finite plate lined with foam and a vinyl septum (bonded-unbonded case): influence of the septum thickness.

ior. This effect is particularly strong when the cavity is filled with a soft material such as fiberglass or a limp wool whatever the interface conditions.

For stiffer materials, the interface conditions are very important. Thus for the case of a foam with bonded interface conditions (Fig. 4), the transmission loss of the system falls down at frequencies higher than the double-wall resonance, instead of increasing. This is a consequence of the strong coupling between the inner and outer layers induced by the foam: there is a solidien transmission through the foam. However, at higher frequencies (not shown in the figure), the transmission loss increases again. As soon as the foam is decoupled through a thin air space from the inner layer [pictured in Fig. 1(d)], Fig. 5 indicates that the transmission loss increases above the double-wall resonance, like soft materials.

C. Influence of the interface conditions

In the following, the influence of the interface conditions between the plate, the poroelastic material, and a 1.71 mm thick vinyl septum are studied. Figures 6 and 7 present the diffuse field transmission loss through the systems depicted in Fig. 1 in the case of a fiberglass and a foam porous layer, respectively. In the two cases, the porous material of thickness 3.75 cm is either bonded, unbonded to both plate and septum or bonded to the first plate and unbonded to the septum. In the three cases, the results are compared to the plate/air/septum case [Fig. 1(b)].

It is seen in Fig. 6 that the fiberglass induces an added mass effect compared to the air case which shifts the dip frequencies leftward. The presence of fiberglass improves the transmission loss at system resonances. The bonded, unbonded and bonded-unbonded cases are very similar. At this point, it is interesting to see how the power is dissipated into the system. Calculation of the powers dissipated in the porous medium has been presented in Sec. I B. The expressions of the powers dissipated in an elastic medium or a fluid are classical and can be found in Ref. 20. Figure 8 shows the part of the powers dissipated within each layers relative to

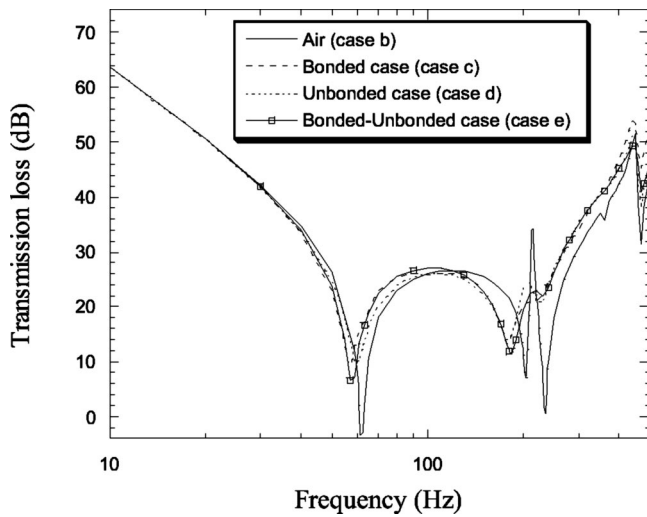


FIG. 6. Diffuse field transmission loss through a finite plate lined with fiberglass and a 1.71 mm thick vinyl septum. Comparison between the unlined, bonded, unbonded and bonded–unbonded configurations, case b, case c, case d, case e, respectively.

the total power Π_{diss} dissipated into the system, for the bonded case. In this figure (and also in Fig. 9 and Fig. 10), Π_1^d and Π_2^d refer to the powers dissipated through acoustic radiation in the emitting and receiving medium, $\Pi_{\text{diss}}^{\text{pl}}$ refers to the power dissipated through structural damping within the plate, $\Pi_{\text{diss}}^{\text{s}}$ refers to the power dissipated through structural damping within the porous skeleton, $\Pi_{\text{diss}}^{\text{t}}$ refers to the power dissipated through thermal effects in the porous material, and $\Pi_{\text{diss}}^{\text{v}}$ refers to the power dissipated through viscous effects in the porous material. At very low frequencies, the power is mainly dissipated through structural damping within the plate which is logical since the transmission loss is controlled by the plate stiffness. As the frequency increases the dominant dissipation mechanism becomes viscous effects dissipation in the fiberglass layer. The same observations can be made for the other interface conditions. However, the part of the total power dissipated by structural

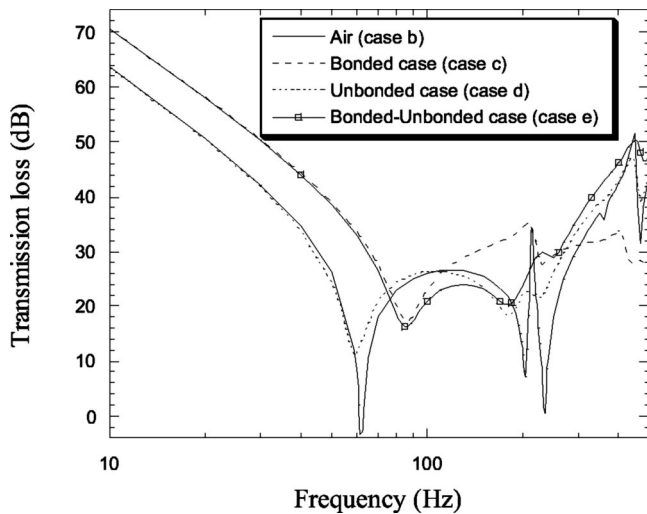


FIG. 7. Diffuse field transmission loss through a finite plate lined with foam and a 1.71 mm thick vinyl septum. Comparison between the unlined, bonded, unbonded and bonded–unbonded configurations, case b, case c, case d, case e, respectively.

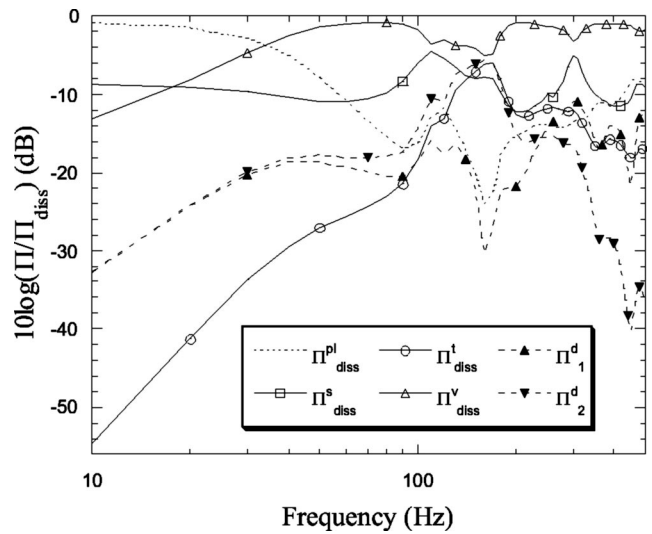


FIG. 8. Ratio of the powers dissipated in the different layers of a finite plate lined with fiberglass (bonded case) and terminated with a vinyl 1.71 mm thick septum to the total power dissipated in the system Π_{diss} .

damping within the plate is slightly more important in the bonded case. These observations explain the similar performance of the three configurations: since the used fiberglass is gently soft, it does not add any significant stiffness to the inner and outer panels.

The situation is quite different in the case of a foam decoupling layer (Fig. 7). When the foam is bonded onto the first panel, the first resonance of the system is shifted rightward compared to the air case because of the bending stiffness added by the foam; the transmission loss is greatly improved in the stiffness-controlled region. However, when the foam is also bonded to the inner layer, the transmission loss deteriorates rapidly since in this case the foam couples, rather than decouples, the inner and outer layers. In the unbonded configuration [Fig. 1(d)], the foam stiffness effect is negligible and only its decoupling and dissipation effects get into play. To confirm these interpretations, Fig. 9 and Fig. 10

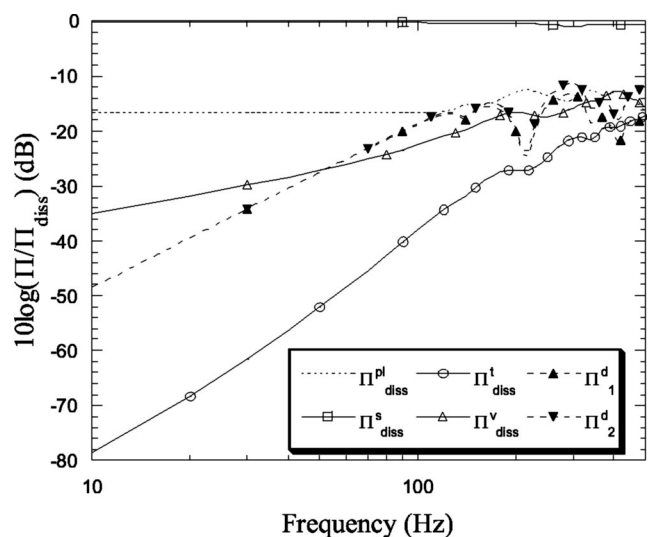


FIG. 9. Ratio of the powers dissipated in the different layers of a finite plate lined with foam (bonded case) and terminated with a vinyl 1.71 mm thick septum to the total power dissipated in the system Π_{diss} .

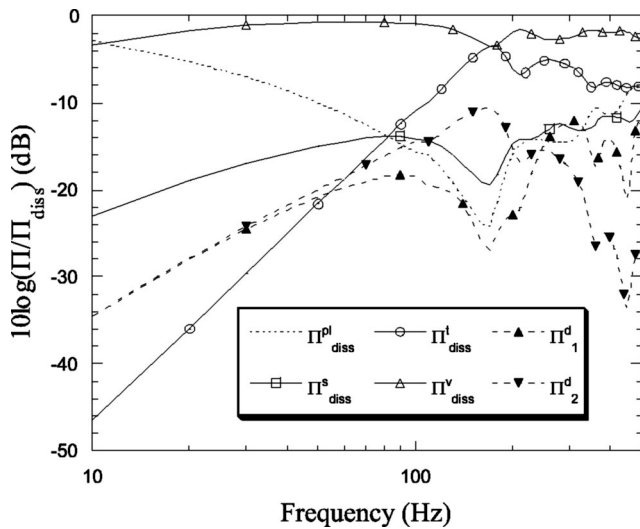


FIG. 10. Ratio of the powers dissipated in the different layers of a finite plate lined with foam (unbonded case) and terminated with a vinyl 1.71 mm thick septum to the total power dissipated in the system Π_{diss} .

present the powers dissipated within each layer compared to the total power dissipated into the system, in the bonded and unbonded cases, respectively. It is seen that in the bonded case, the power is mainly dissipated through structural damping within the foam skeleton which has a large damping factor (0.265) while in the unbonded case, viscous dissipation is predominant since the flow is not restrained to zero on each side of the porous material. The bonded–unbonded case seems the right compromise (Fig. 7), since in this case both the stiffness and damping effects (in the stiffness-controlled region) and decoupling effects (viscous dissipation above the double-wall resonance) get into play.

D. Septum modeling versus plate modeling

The presented results concentrated on a double panel system with a stiffnessless inner layer (= septum). The purpose of this section is to verify the stiffness effect in the case of a metallike inner layer. It compares the diffuse field transmission loss of a double panel system with an inner 0.89 mm thick aluminum panel modeled (i) as a septum: $\rho_s = 2700 \text{ kg/m}^3$ and (ii) as a thin plate: $E = 6.83 \times 10^{10} \text{ Pa}$, $\nu = 0.33$, $\rho_s = 2700 \text{ kg/m}^3$, $\eta_s = 0.007$. Figures 11 and 12 show the results for the previous porous materials with bonded and bonded–unbonded interface conditions. It is seen that additional peaks appear in the frequency response when the last layer is modeled as a plate due to coupled modes of the plate–porous–plate system. The first resonance frequency of the system (plate-controlled mode) is lower when the septum model is used since it only has a mass effect whereas when the plate model is used, the stiffness of the whole system is larger and the first resonance frequency of the coupled plate–porous–plate mode is higher. This explains in turn the increase of the transmission loss, obtained with the plate model, in the stiffness-controlled region. Above the double-wall resonance, the two models are sensibly (i.e., on average) equivalent. It is, however, worth mentioning that the position of the double-wall resonance depends on the decoupling material. In the case where a soft material is used, the double-

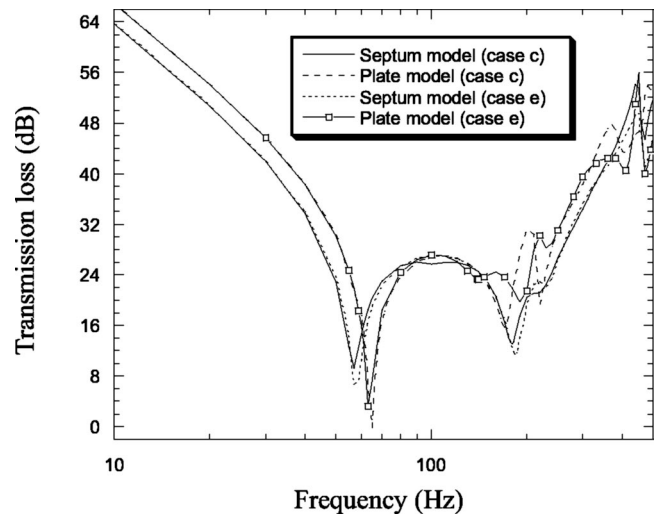


FIG. 11. Diffuse field transmission loss through a finite plate lined with fiberglass and an aluminum septum or an aluminum plate (bonded and bonded–unbonded cases): influence of the choice of the modeling for the last layer.

wall resonance frequency is slightly lower when the plate model is used compared with the septum model. In the case of the foam, especially in the bonded case, the opposite is observed because of the importance of the foam added stiffness and coupling. Overall, the transmission loss calculated with the septum model is underestimated in the stiffness-controlled region.

IV. CONCLUSION

In this paper, a simulation tool has been proposed to predict the low frequency diffuse field transmission loss of 3D multilayered planar complex structures made up of elastic, acoustic, poroelastic and septum media and separating two semi-infinite media. This tool is based on a finite element model for the complex structure coupled to a variational boundary element method to account for fluid loading. The diffuse field is modeled as a superposition of uncorre-

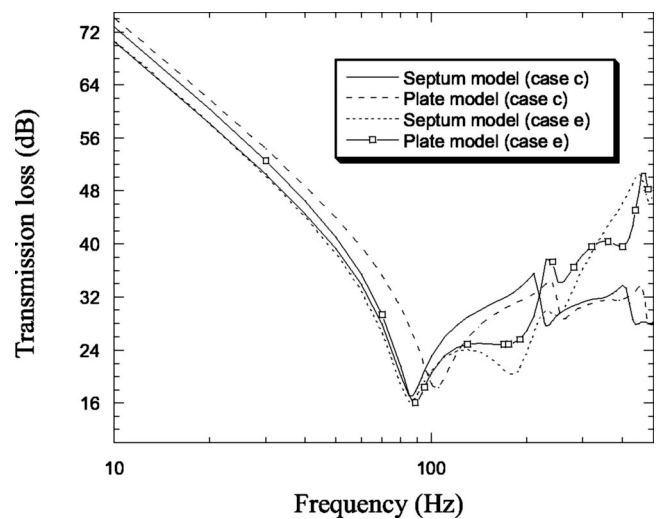


FIG. 12. Diffuse field transmission loss through a finite plate lined with foam and an aluminum septum or an aluminum plate (bonded and bonded–unbonded cases): influence of the choice of the modeling for the last layer.

lated freely propagating plane waves with equal amplitude, no two of which are traveling in the same direction. The corresponding vibroacoustic indicators are calculated efficiently using a Gauss integration scheme. Moreover, expressions for the powers dissipated through visco-elastic, thermal and viscous effects within the porous layer have been derived.

Numerical results have been presented in the case of a double panel system made of a plate lined with a porous material and terminated with a septum. The effects of several parameters on the diffuse field transmission loss have been studied. Also a power balance has been used to explain the main dissipation mechanisms in the studied systems. The main conclusions are as follows: (i) The increase of the septum mass improves the transmission loss above the double-wall resonance of the system for soft materials. (ii) The mounting conditions play an important role and the performance depends strongly on the nature of the decoupling porous layer. (iii) When a foam-type material is used, a compromise must be made between stiffness effects and dissipation effects: the best compromise is a bonded-unbonded type of configuration. Finally, it has been shown that when dealing with metal septa, the septum model underestimate the transmission loss in the stiffness-controlled region.

ACKNOWLEDGMENTS

This work has been made possible with the combined financial support of NSERC (National Sciences and Engineering Research Council of Canada) and IRSST (Institut de Recherche en Santé et Sécurité au Travail, Quebec).

¹L. L. Beranek and I. L. Ver, *Noise and Vibration Control Engineering, Principles and Applications* (Wiley, New York, 1992).

²F. Fahy, *Sound and Structural Vibration* (Academic, London, 1989).

³C. Lesueur, *Rayonnement Acoustique des Structures, Vibro-acoustique, Interactions Fluide-structure* (Eyrolles, Paris, France, 1988).

⁴J. F. Allard, *Propagation of Sound in Porous Media, Modelling Sound Absorbing Materials* (Elsevier Application Science, New York, 1993), pp. 284.

⁵N. Atalla, R. Panneton, and P. Debergue, "A mixed displacement-pressure formulation for poroelastic materials," *J. Acoust. Soc. Am.* **104**, 1444–1452 (1998).

⁶U. Ingard, *Notes on Sound Absorption Technology* (Bk and Disk edition, 1994).

⁷Y. J. Kang and J. S. Bolton, "A finite element model for sound transmission through foam-lined double panel structures," *J. Acoust. Soc. Am.* **99**, 2755–2765 (1996).

⁸R. Panneton and N. Atalla, "Numerical prediction of sound transmission through finite multilayer systems with poroelastic materials," *J. Acoust. Soc. Am.* **100**, 346–353 (1996).

⁹J. S. Bolton and E. R. Green, "Normal incidence sound transmission through double panel systems lined with relatively stiff, partially reticulated polyurethane foam," *Appl. Acoust.* **39**, 23–51 (1993).

¹⁰N. Atalla and R. Panneton, "The effects of multilayer sound-absorbing treatments on the noise field inside a plate backed cavity," *Noise Control Eng. J.* **44**, 235–243 (1996).

¹¹R. Panneton, N. Atalla, and F. Charon, "A finite element formulation for the vibroacoustic behavior of double-plate structures with cavity absorption," *Can Aero. Space J.* **41**, 5–12 (1995).

¹²H. P. Morand and R. Ohayon, *Fluid Structure Interaction* (Wiley, New York, 1995).

¹³R. Panneton, "Modélisation numérique tridimensionnelle par éléments finis des milieux poroélastiques," Ph.D. Thesis, University of Sherbrooke, Canada, 1996.

¹⁴S. Rigobert, N. Atalla, and F. C. Sgard, "Numerical implementation of the mixed displacement-pressure formulation for poroelastic materials using hierarchical elements," submitted to *Int. J. Numer. Methods Eng.* (2000).

¹⁵A. D. Pierce, *Acoustics, an Introduction to its Physical Principles and Applications* (McGraw-Hill, New York, 1981), 678 pp.

¹⁶F. C. Sgard and N. Atalla, "Mean flow effects on a plate-backed cavity, Part 1: Theory," *Acta Acust. (China)* **83**, 243–251 (1997).

¹⁷N. Dauchez, "Etude vibroacoustique des matériaux poreux par éléments finis," Ph.D. thesis, Université du Maine, France, 1999.

¹⁸R. Panneton and N. Atalla, "An efficient finite element scheme for solving the three-dimensional poroelasticity problem in acoustics," *J. Acoust. Soc. Am.* **101**, 3287–3298 (1997).

¹⁹P. Debergue, "Développement d'une formulation mixte en déplacement pression pour les matériaux poro-élastiques," Master's Thesis, University of Sherbrooke, Canada, 1998.

²⁰P. Millot, "Rayonnement acoustique de plaques couplées dans une cavité," Ph.D. thesis, INS de LYON, France, 1987.

Three-dimensional optical measurement of instantaneous pressure

Todd A. Pitts^{a)} and James F. Greenleaf

Ultrasound Research Laboratory, Department of Physiology and Biophysics, Mayo Clinic and Foundation, Rochester, Minnesota 55905

(Received 5 April 1999; revised 22 November 1999; revised 3 August 2000; accepted 24 August 2000)

Local perturbations in material density induced in a material by a compressional wave give rise to local perturbations in refractive index. Accurate, high-resolution, three-dimensional, optical measurements of an instantaneous refractive index perturbation in a homogeneous, optically transparent medium may be obtained from measurements of scattered optical intensity alone. The method of generalized projections allows incorporation of optical intensity measurements into an iterative algorithm for computing the phase of the interrogating optical pulse as the solution of a fixed point equation. The complex optical field amplitude, computed in this manner, is unique up to a constant unit magnitude complex coefficient. The three-dimensional refractive index distribution may be computed via the Fourier slice reconstruction algorithm from the optical phase data under the assumption of weak optical scattering. The refractive index perturbation is related to local instantaneous pressure under a linear, small-displacement model for the mechanical wave. A numerical simulation of the measurement experiment, phase recovery, and reconstruction process for a plane piston ultrasound transducer with a semicircular aperture and center frequency of 1.5 MHz is described and corresponds very well with experiment. Experimental data obtained using an 810-nm laser source are used to reconstruct the three-dimensional pressure field from two elements of a 2.5-MHz linear array. Comparison with a measurement obtained via a 500- μm needle hydrophone shows excellent agreement. © 2000 Acoustical Society of America. [S0001-4966(00)05511-9]

PACS numbers: 43.58.Fm, 43.35.Yb, 43.35.Sx, 78.20.Hp [SLE]

I. INTRODUCTION

Modeling and measurement of acoustic wave propagation in various media have long histories in both pure and applied research. Optical measurement of acoustic fields in transparent media has been the subject of numerous investigations since Raman and Nath¹⁻⁵ offered the first accurate model of the physics involved in optical scattering by narrow bandwidth acoustic fields. Nearly all research has focused on deduction of narrow-band beam cross-sectional power or amplitude from far-field measurements of scattered optical intensity. Typically, analog signal processing elements are used in the optical beam path to obtain the necessary measurements. Some have investigated the utility of optical near-field measurements.⁶⁻⁸ This paper establishes the viability of a new optical method for high-resolution three-dimensional measurement of instantaneous pressure in a wide bandwidth ultrasound pulse.

The experiment records the forward-scattered optical intensity from the interaction of a collimated laser pulse with the ultrasound field via a two-lens imaging system. The phase of the optical field immediately after passage through the ultrasound pulse is computed from this intensity. Reconstruction of the instantaneous acoustic field via tomographic methods requires recording the forward-scattered optical intensity at several angles as the ultrasound transducer is ro-

tated through 180 deg about an axis normal to the propagation direction of the incident optical pulse (see Fig. 1). Instantaneous three-dimensional pressure in the ultrasound pulse is then obtained from the set of recovered optical phase distributions.

This paper is organized as follows. The physical theory underlying the method is explained in Sec. II. Section II A gives a model relating local refractive index to the ratio of local to ambient density (this ratio is related to the acoustic field variables of displacement and pressure). Section II B describes the relationship between optical refractive index and the acoustic field parameters of density and pressure. Specific parameter values for water (the medium used in the physical experiments presented in this report) are given. Section II C gives a simple delay model for optical scattering. This model determines the algorithm used to reconstruct the pressure field from optical phase measurements. Optical phase is computed from optical intensity as the solution of a fixed point equation via the MGP (method of generalized projections) as described in Sec. III A. Reconstruction of the instantaneous acoustic pressure field is discussed in Sec. III B. Section IV presents a numerical simulation of the measurement experiment including optical phase retrieval and three-dimensional pressure field reconstruction. Section V B compares hydrophone measurements of a complicated wide bandwidth ultrasound field to those obtained via the optical method presented in this paper. The paper ends with conclusions. The Appendix briefly reviews the scalar Fresnel

^{a)}Electronic mail: pitts.todd@ieec.org

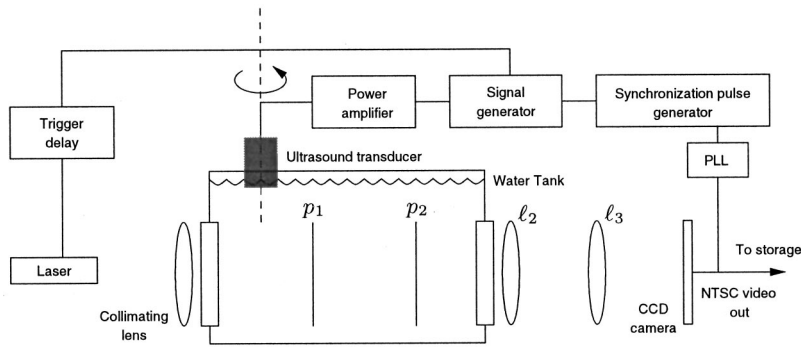


FIG. 1. A description of the basic experiment. The ultrasound transducer and laser are fired with timing that allows the collision of optical and acoustic pulses to take place near the optical axis of the imaging system. The lenses ℓ_2 and ℓ_3 provide a means of imaging arbitrary planes within the imaging volume onto the CCD array. Plane p_1 is the plane immediately subsequent to passage of the optical pulse through the acoustic field and is sometimes referred to as the "transducer" plane. Plane p_2 is an arbitrary diffraction plane. The dimensions of the water tank used in this experiment are approximately $18 \times 18 \times 32$ cm.

model used for optical field propagation and the implications of this approximation for this measurement.

II. THEORY

Here we describe the relationship between the continuum mechanics of ultrasound and the electromagnetics of the optical scattering problem. The purpose of this section is to show under what assumptions we may consider the optical phase delay induced by a wide bandwidth ultrasound pulse in water to be approximately a line integral of local *pressure* variations in the acoustic field. This approximation allows the use of computed tomography algorithms to quantitatively measure the three-dimensional distribution of pressure in the ultrasound pulse at a selected point in time. An understanding of how an acoustic wave alters the optical refractive index of the supporting medium is central to this study. Section II A describes a simple model relating refractive index to the ratio of local to ambient material density. The ratio of local to ambient material density appears as a Jacobian determinant in the nonlinear continuum model for the acoustic equations of motion (see Ref. 9).

For small amplitude acoustic fields we may linearize this model and use a constitutive relation between particle dis-

placement and pressure to develop a linear wave equation in these field variables. We then model the refractive index perturbation induced by the acoustic field as being approximately linearly proportional to *pressure* via a piezo-optic coefficient as described in Sec. II B. This model is used in Sec. II C to describe a simple accumulative phase delay model for optical scattering by small amplitude wideband ultrasound fields. The Appendix briefly reviews the basic optical propagation physics used in this study. We begin with the description of how a mechanical wave alters local refractive index.

A. Acoustic perturbation of refractive index

In a dielectric material the dominant charges in atoms and molecules are bound. That is, they are not free to move about in the material as they are in conductors. Simple descriptions of how such materials interact with electromagnetic fields model the constituent molecules of a medium as charge distributions that distort in the presence of an electric field.¹⁰ This distortion constitutes the formation of an electric dipole. As the electric field oscillates this dipole will follow, emitting a field of its own. The total field in the medium is then the sum of the applied and induced dipole fields. At a macroscopic level this effect may be accounted for by the introduction of a polarization vector \mathbf{P} .¹⁰ We expect its magnitude to be proportional to the molecular dipole strength and the *number* of molecules per unit volume. The complex component of \mathbf{P} accounts for absorption. Wave speed in the medium is determined by both the real and imaginary components. Its units are those of electric flux density (or electric induction), and in fact we may write

$$\mathbf{D} - \mathbf{P} = \epsilon_0 \mathbf{E} \quad (1)$$

or

$$\mathbf{D} = \epsilon_0 \mathbf{E} + \mathbf{P} = \epsilon_0 \mathbf{E} + \epsilon_0 \chi \mathbf{E} = \epsilon_0 (1 + \chi) \mathbf{E},$$

where $\epsilon_0 \approx 8.85 \times 10^{-12}$ F/m is the permittivity of free space and χ is the electric susceptibility. Hence, this model predicts changes in the permittivity of the medium corresponding to changes in the number of molecules per unit volume. The number of molecules per unit volume changes if the density of the material is perturbed by an acoustic wave in the medium. Refractive index,

$$n = \sqrt{\epsilon_r} = \sqrt{1 + \chi}, \quad (2)$$

is a function of permittivity and thus dipole moment per unit volume under this model. Refractive index is therefore a

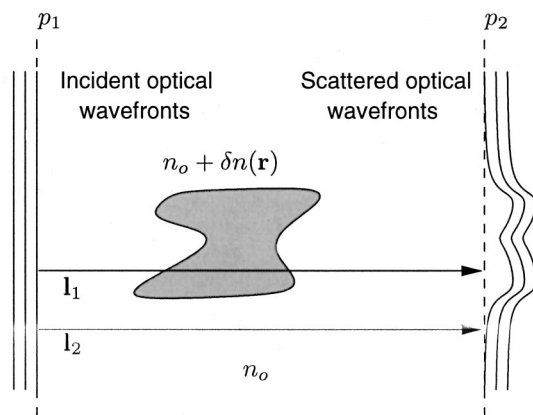


FIG. 2. Planar optical wavefronts impinging on a refractive index object $n_o + \delta n(\mathbf{r})$. The background refractive index is n_o . Planes p_1 and p_2 are parallel to the incident optical wavefronts. For sufficiently small $\delta n(\mathbf{r})$ the optical wave experiences essentially only phase delay (the complex magnitude remains approximately uniform after passage through the sound field represented by $\delta n(\mathbf{r})$). Paths I_1 and I_2 represent two possible path choices for the line integral in Eq. (11). The relative phase delay at plane p_2 between any two such paths is used in the method of this paper to estimate ultrasonic pressure from the three-dimensional variation of refractive index obtained via computed tomography.

function of density in a dielectric material. An increase in the number of dipoles per unit volume (higher density) implies an increase in permittivity and thus refractive index. We expect to observe slower light wave speed in areas of greater dipole density. Although greater pressure in a region implies greater density, the two are not generally linearly related. The ratio of local to ambient density describes the percent increase in the number of molecules per unit volume. Hence, for a homogeneous material of density ρ_o , we may write

$$n(\mathbf{r},t) = \sqrt{\epsilon_r} = \sqrt{1 + \chi \rho(\mathbf{r},t) / \rho_o}, \quad (3)$$

where $\rho(\mathbf{r},t)$ is the density at location \mathbf{r} at time t . Next we use the model for the propagation of a mechanical disturbance in an elastic medium described in Ref. 9 to relate pressure to the optical refractive index perturbation in Eq. (3).

B. Piezooptic coefficient

Currently, no physical data for the elasto- and piezo-optic coefficients at the temperature and wavelength used in our experiment (see Sec. V) is available in the literature. In the following we derive a theoretical estimate of the change in refractive index with density and pressure. Under the refractive index model discussed in Sec. II A the electric susceptibility χ is proportional to the local number of molecules per unit volume. We thus expect the net susceptibility to change in direct proportion to the Jacobian determinant, yielding

$$n(\mathbf{r},t) = \sqrt{1 + \chi J^{-1}(\mathbf{r},t)}, \quad (4)$$

where the Jacobian $J(\mathbf{r},t)$ is given by

$$J(\mathbf{r},t) = \left| \mathbf{I} + \begin{bmatrix} \xi_{x,x}(\mathbf{r},t) & \xi_{y,x}(\mathbf{r},t) & \xi_{z,x}(\mathbf{r},t) \\ \xi_{x,y}(\mathbf{r},t) & \xi_{y,y}(\mathbf{r},t) & \xi_{z,y}(\mathbf{r},t) \\ \xi_{x,z}(\mathbf{r},t) & \xi_{y,z}(\mathbf{r},t) & \xi_{z,z}(\mathbf{r},t) \end{bmatrix} \right|. \quad (5)$$

The quantity $\xi_{i,j}(\mathbf{r},t)$ for $i,j=x,y,z$ is the partial derivative of the i -coordinate component of the displacement function $\xi(\mathbf{r},t)$ with respect to the j -coordinate variable, and \mathbf{I} is the 3×3 identity matrix.

The refractive index perturbation induced by the mechanical wave depends simply on the Jacobian determinant describing the local distortion in the supporting medium. For small amplitude acoustic waves the Jacobian differs little from unity. In the linear acoustic model the Jacobian determinant J is approximated as one. For an isotropic, dielectric material such as water the relationship between refractive index, $n(\mathbf{r},t)$, and the ultrasound field may be described as given in Eq. (4) and written as

$$n(\mathbf{r},t) = \sqrt{\epsilon_r} = \sqrt{1 + \chi \rho(\mathbf{r},t) / \rho_o}, \quad (6)$$

where $\rho(\mathbf{r},t)$ is the density at location \mathbf{r} at time t . Equation (6) may be rewritten as

$$n(\mathbf{r},t) = \sqrt{\epsilon_r} = \sqrt{1 + \chi} \sqrt{1 + \frac{\chi}{\rho_o(1 + \chi)} (\rho(\mathbf{r},t) - \rho_o)}. \quad (7)$$

A Taylor series expansion of Eq. (7) gives

$$n(\mathbf{r},t) = n_o + \frac{n_o^2 - 1}{2\rho_o n_o} (\rho(\mathbf{r},t) - \rho_o). \quad (8)$$

Assuming water behaves as an isentropic fluid during our measurement and that the amplitude of our ultrasonic waves is sufficiently small, the over-density ($\rho(\mathbf{r},t) - \rho_o$) may be related to the over-pressure $p(\mathbf{r},t)$ by a simple coefficient¹¹ giving

$$n(\mathbf{r},t) = n_o + \frac{n_o^2 - 1}{2n_o \rho_o n_o^2} p(\mathbf{r},t). \quad (9)$$

For a temperature of 30 °C we have $\rho_o = 995.65 \text{ kg/m}^3$, $c_o = 1509.5 \text{ m/s}$ (see Ref. 12). An optical wavelength of $\lambda = 810 \text{ nm}$ at 30 °C gives $n_o = 1.3273$ (see Ref. 13). We therefore calculate the piezo-optic coefficient in Eq. (9) to be

$$\left(\frac{\partial n}{\partial p} \right) = 1.2648 \times 10^{-10} \text{ pascal}^{-1}. \quad (10)$$

In our measurement the refractive index perturbation is small. This results in minimal coupling between the components of the electric field vector. We therefore use a scalar model for the electromagnetic field propagation and scattering.¹⁴⁻¹⁶

It should be clear from the above discussion that the actual optical scatterer is the Jacobian displacement determinant and not the pressure field. The actual relationship between pressure and density in water is very complicated and several sophisticated models have been developed. We emphasize, however, that the relationship described in Eq. (4) does not depend on a constitutive relationship and may *always* be used. For the purpose of comparing hydrophone (pressure) measurements to those obtained optically we use the simple model relationship given in Eqs. (9) and (10).

C. Optical scattering model

In this section the weak scattering model for the interaction of the optical and acoustic pulses is explained. The FSR (Fourier slice reconstruction) algorithm (see Sec. III B) is used to reconstruct the instantaneous pressure in the ultrasound pulse from optical phase delay data. Thus it is assumed that the ultrasound pulse may be considered a *phase* object. A phase object induces essentially only phase variations in the optical wavefront. To consider the sound field a phase object the amount of optical scattering must be small. Consider a plane wave impinging on a region of space with varying refractive index $n(\mathbf{r})$ as shown in Fig. 2. The refractive index variations will induce breadth into the angular plane wave spectrum, scattering the optical wave. If we write the refractive index function as

$$n(\mathbf{r}) = n_o + \delta n(\mathbf{r}),$$

where $\delta n(\mathbf{r})$ is a small change in the local refractive index representing the scatterer, the relative phase delay is given as

$$\theta = k \int_1 \delta n(\mathbf{r}) ds, \quad (11)$$

where the wave number k is given by $k = \omega/c$ and s is a parameter describing distance along the path $\mathbf{1}$.

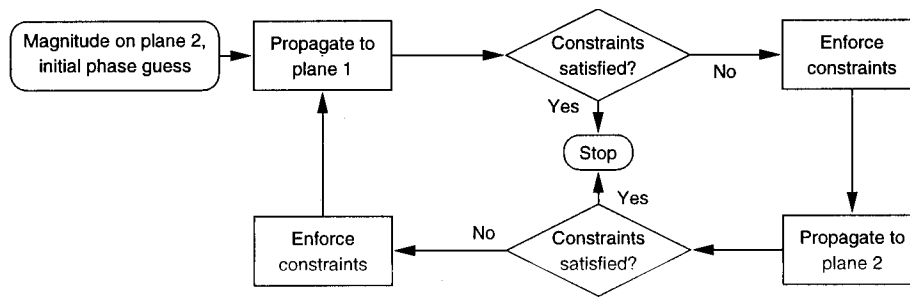


FIG. 3. The above algorithm may be viewed as reconstruction via projection onto constrained sets. We begin with the magnitude data measured in plane 2 of Fig. 1 and an initial phase guess. We then propagate this field to plane 1 and apply any known constraints such as region of support for the phase function or a magnitude constraint. After enforcing the constraints we propagate the resulting field back to plane 2 in Fig. 1 and apply any known constraints on values in that plane. In our case the principal constraint on plane 2 is the measured magnitude. We continue this process until the constraints are satisfied (within some tolerance) without explicit enforcement.

III. SIGNAL PROCESSING

A. Optical phase recovery from magnitude

If we are to infer the desired pressure information we need to know the *phase* of the optical field in the plane immediately after the ultrasound pulse. Much work has been done on the problem of *phase recovery*.^{17,18} In this paper we use a version of the Gerchberg–Saxton algorithm applied to Fresnel diffraction (see Fig. 3). We begin with the magnitude of the field in plane 1 and an estimate for the phase. We then propagate this estimated field to plane 2 and apply any known constraints to the field. In this case we have measured the intensity and thus know the magnitude. The propagated phase is retained. Propagating the field back to plane 1 and applying the magnitude constraint again completes a single iteration and yields an estimate for the complex valued field over this plane. In our model the acoustic pulse is a phase object and therefore the magnitude in plane 1 is always unity. Iteration stops when the corrected (measured) magnitude and the predicted magnitude in one of the planes are not

significantly different. It has been shown that the algorithm possesses a property of error reduction guaranteeing a monotonic decrease in a metric known as the SDE (summed distance error).^{19,20}

Definition (Summed distance error). Let C_1, C_2 be any two closed sets with projection operators P_1, P_2 , respectively. Let f_n be the estimate of f at the n th iteration of the equation

$$f_{n+1} = P_1 P_2 f_n, \quad f_0 \text{ arbitrary.}$$

Then the performance measure at f_n , denoted by $J_e(f_n)$, is the sum of the distances between the points f_n and the sets C_1 and C_2 . Thus the performance is measured by

$$J_e(f_n) \triangleq \|P_1 f_n - f_n\| + \|P_2 f_n - f_n\|.$$

The quantity $J_e(f_n)$ is referred to as the SDE (summed distance error).

Note that

$$J_e(P_2 f_n) = \|P_1 P_2 f_n - P_2 f_n\| + \|P_2 f_n - P_2 f_n\|, \quad (12)$$

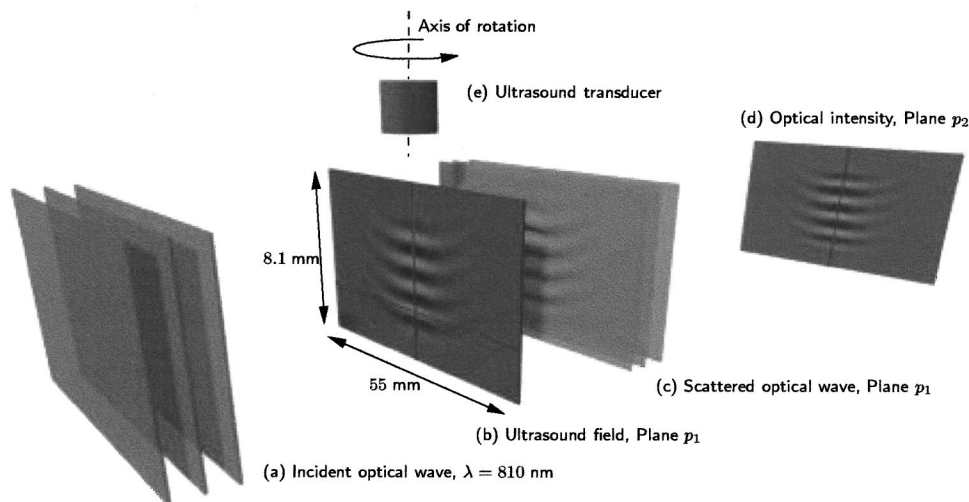


FIG. 4. A schematic of the simulated experiment. (a) Planar optical wavefronts propagating toward the two-dimensional phase delay function representing the ultrasound in (b). In the actual experiment these are produced with the laser and collimating lens in Fig. 1. (b) The ray sum (taken in the direction of the optical wave propagation) of the ultrasound field. The field is produced by the transducer in (e). (c) Optical wavefronts immediately after passing through the ultrasound field. The amplitude remains essentially unchanged. The phase delay is proportional to the “projection” (in the direction of optical wave propagation) of the ultrasound field. Their location corresponds to plane p_1 in Fig. 1. (d) Optical intensity after propagating a known distance beyond interaction with the ultrasound field. In Fig. 1 this location is specified by plane p_2 . (e) The ultrasound transducer producing the field in (b). In the simulation a Fresnel model for acoustic propagation is used.

where we have used $P_2 P_2 h = P_2 h$. Correcting the magnitude of the complex field distribution over planes 1 and 2 corresponds to the projections $P_{1,2}$ respectively.¹⁴ It has also been shown that the phase which satisfies the fixed point equation defined by the iterative process described above is unique up to a constant unit magnitude complex factor.^{14,21}

B. Inversion of Radon transform

During the basic measurement experiment described in Figs. 1 and 4 a recording of the forward-scattered optical intensity is obtained for several angles θ as the transducer is rotated about an axis perpendicular to the impinging optical pulse. The method described in Sec. III A allows computation of the optical phase immediately after passage through the ultrasound pulse. As shown in Sec. II C [see Eq. (11)] this phase represents a ray sum of the instantaneous local optical delay in the direction of the incident optical pulse. Thus for each angle θ , a ray sum $p_\theta(r_2)$ through the object distribution $o(\mathbf{r})$ is obtained. Rotation of the object about the origin in the spatial domain rotates the Fourier transform through the same angle.²² Thus we obtain the two-dimensional Fourier transform of an object by recording a complete set of projections for $0 \leq \theta < \pi$. This set of projections is referred to as a Radon transform.²⁰ It is clearly invertible as the original object distribution can be obtained from it via the Fourier transform. A function may therefore be described in the Radon transform domain as well as in the spatial or Fourier domains.

In practice, however, only a finite set of points $\{r_{2,k}, \theta_k\}$ is measured. Sampled Radon transforms are not, in general, invertible. Sampling is not one-to-one. Shannon's sampling theorem explains how two different vectors (sinusoidal signals) are mapped to the same coefficient through aliasing or "spectral folding." In practice, adequate sampling takes place at twice the frequency of the lowest frequency signal we are willing to alias.

It is clear from the development of the Fourier slice theorem²² that sampling in angle occurs in the Fourier domain. That is, the density of angular samples must be based on the angular frequencies present in the Fourier domain representation of the signal. Required angular sampling rates will increase with increasing angular asymmetry of the spatial domain signal.

In applying sampling criteria to the measurement experiment it must be remembered that intensity is the actual physical quantity sampled. It is necessary to relate the frequencies present in the phase function to those present in the optical intensity pattern. For the purpose of obtaining an estimate of the required spatial sampling density the optical field immediately after passage through the ultrasound pulse may be approximated via Taylor's series expansion of $\exp(\phi'(\mathbf{r}_\perp))$ as

$$u(\mathbf{r}_\perp, z) = 1 + j\phi'(\mathbf{r}_\perp), \quad (13)$$

where $\phi'(\mathbf{r}_\perp)$ represents the spatial variations induced in the optical wave front and \mathbf{r}_\perp coordinate vector representing directions transverse to the direction of propagation of the impinging optical wave. We obtain an approximate spectrum for $u(\mathbf{r}_\perp, z)$ by transforming Eq. (13). For sufficiently small

amplitude pressure variations, the portion of the optical angular plane wave spectrum that represents spatial variations and the corresponding portion of the sound field spectrum are related by the factor j .

Thus under weak scattering assumptions it is approximately correct to consider the bandwidth of the phase function and the bandwidth of the optical signal to be the same. The bandwidth of the optical intensity will be twice that of the complex optical amplitude. Thus the projection sampling rate computed from the optical phase function is multiplied by a factor of two to obtain the correct sampling rate for the optical intensity in the experiment. The angular sampling rate is computed directly from the Fourier domain data.

C. Background suppression

Ring artifacts resulting from errors that occur consistently in each view are a source of problems in tomography. Examples of this are an improperly calibrated sensor, optical amplitude variations caused by multiple reflections, stationary Airy patterns in the image resulting from small particles in the beam path, etc. Such corruption will result in a ridge (or ridges) in the Radon transform domain parallel to the angular coordinate axis. During the reconstruction process the one-dimensional Fourier transform of each view is computed. The addition of the same local feature in each view may be considered an identical perturbation of one-dimensional Fourier coefficients. This results in circular rings or ridges in the two-dimensional Fourier transform domain of the object distribution. Enforcing the conjugate symmetry of real objects in the Fourier domain does not eliminate the artifact. The conjugate symmetric part of the artifact remains and reconstructs to ringlike features centered about the tomographic axis of rotation in the spatial position domain.

In our experiment the Radon transform is not measured directly. Rather, intensity images are recorded as a function of angle and a set of phase functions representing the Radon transform is computed. The similarity of features between the intensity in plane p_2 of Figs. 1 and 4 and the retrieved phase in plane p_1 allows discussion of ring artifacts in the above fashion. Any number of methods are available for filtering out such corruption. The results presented in this paper are obtained using a simple FIR (finite impulse response) filter designed to reject spectral components representing high frequencies parallel to the sensor axis (a row of the CCD (charged coupled device) array and low frequencies parallel to the angular axis simultaneously. For a discussion of the use of wavelets to accomplish this filtering task please see Pitts.¹⁴

IV. NUMERICAL SIMULATION

To more completely understand the nature of the physics and signal processing involved in the measurement technique described in this paper, a simulation of the complete experiment and reconstruction process was computed. Figure 4 depicts the measurement of a single view of the field. Incident from the left are planar optical wavefronts [see Fig. 4(a)]. In the diagram of the physical experiment in Fig. 1 these are

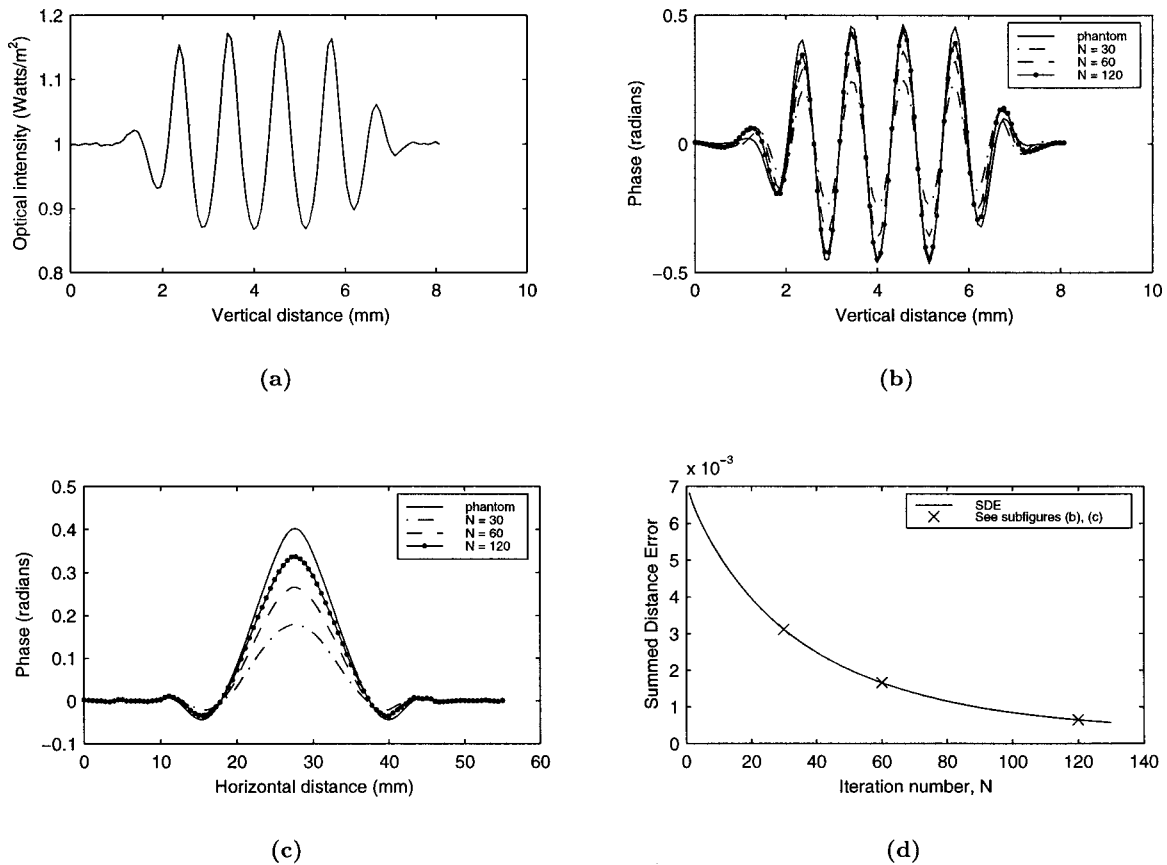


FIG. 5. A comparison of phantom and retrieved phase for increasing iteration number in the phase retrieval algorithm. The solid line plots the phantom phase. (a) A line plot showing the intensity data under the vertical line in Fig. 4(d) for the first view in the simulated experiment. (b) A line plot comparing the retrieved phase indicated by vertical line Fig. 4(b) after 30, 60, and 120 iterations of the phase retrieval algorithm with the original phantom. (c) A line plot comparing the retrieved phase indicated by horizontal line Fig. 4(b) after 30, 60, and 120 iterations of the phase retrieval algorithm with the original. (d) The SDE (summed distance error) through 130 iterations in the phase retrieval.

produced by the laser source and collimating lens. The output of the transducer in Fig. 4(e) is simulated via a Fresnel model for a simple acoustic aperture function. The accumulated (in the direction normal to the optical wavefronts) optical refractive index is pictured beneath the transducer aperture in Fig. 4(b). The data indicated by the vertical line in this image are plotted in Fig. 5(b). In Fig. 4(c) is a representation of the optical *phase* or optical wavefront shape indicating the accumulated delays and advances experienced by the wavefront as it passes through the ultrasound pulse. Under our weak scattering model, points on this surface plot deviate from zero in direct proportion to the ray sum of the refractive index variation induced by the acoustic disturbance. The magnitude of the optical wave over this plane is approximately uniform. The location of Fig. 4(c) corresponds to plane p_1 in Fig. 1. Figure 4(d) depicts the optical intensity that is imaged onto the CCD (charge coupled device) array. The data indicated by the vertical line in this image are plotted in Fig. 5(a). Plane p_2 is the corresponding location in Fig. 1. Lenses ℓ_2 and ℓ_3 in Fig. 1 image this plane onto the CCD array.

The simulation used an ultrasound pulse of four cycles at a center frequency of 1.25 MHz. The time series was filtered to approximately represent a transducer with 80% bandwidth. A plane piston D-shaped aperture was driven and a Fresnel model used to propagate the pulse 40 acoustic wavelengths from the aperture. The two-dimensional projec-

tion of the pressure field onto a plane transverse to the propagation direction of the impinging optical pulse was used to create a phase perturbation on a planar optical wave with a maximum deviation from zero equal to $\pi/5$. A Fresnel model was then used to propagate this optical distribution 8 cm (plane p_2 in Fig. 4). The squared modulus in this plane represents the experimentally measured optical intensity. Figure 5(a) plots the optical intensity in plane p_2 . The location of the data in this plot is indicated in Fig 4(d) by the vertical line. Similarly indicated in Fig. 4(b) are the locations of the simulated optical phase delay data plotted in Figs. 5(b) and (c). A practical signal-peak-to-noise variance ratio of 8.6×10^{-6} in the diffraction plane intensity measurements was estimated from a single experimentally obtained image (see Sec. V) under the assumption that the measurement noise may be represented by a Gaussian white noise random field. Zero mean Gaussian noise was then added to each simulated intensity image to produce the same apparent signal-peak-to-noise variance ratio. A total of 60 views, evenly spaced over 180 deg, were taken for reconstruction.

One hundred thirty iterations per view were used to retrieve the phase (plane p_1 in Figs. 1 and 4) from the noisy intensity plane images (plane p_2 in Figs. 1 and 4) under the assumption of uniform optical intensity over plane p_1 . Figure 5 shows the phase retrieved image corresponding to the first view. A typical difficulty evident in both line plots is the reduction in amplitude of the higher peaks in the phase im-

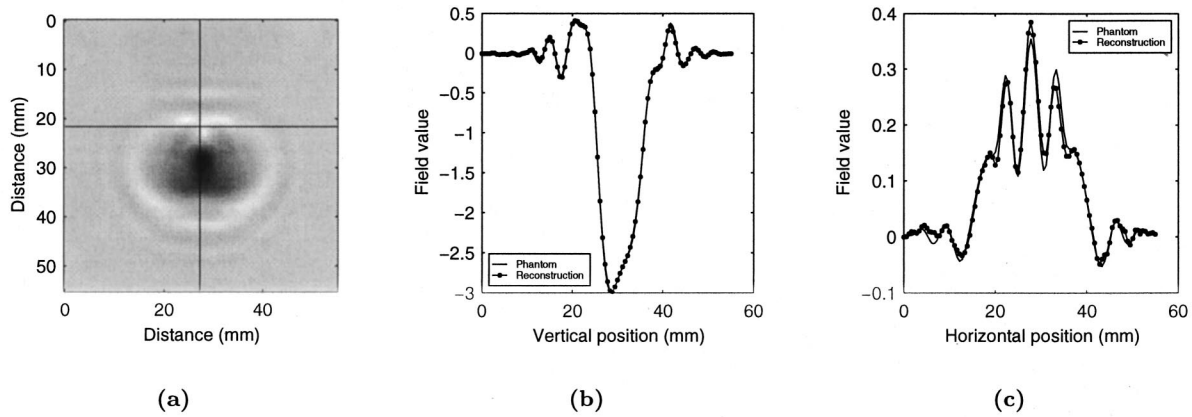


FIG. 6. (a) Reconstruction of a level parallel to the transducer aperture. (b) Data under the vertical line are plotted against corresponding data from the original phantom in (c). (c) Data under the horizontal line are plotted against corresponding data from the original phantom.

age. Figure 5(d) shows the monotonically decreasing SDE (summed distance error). The collection of phase retrieved views constitutes the Radon transform of the instantaneous refractive index distribution. Rows in a single view are always oriented orthogonal to the axis about which the transducer (and hence the acoustic field) is rotated during data collection. Some care must be taken during the experiment to ensure orthogonality or the images must be adjusted appropriately during a post-processing step. The two-dimensional function obtained by considering how the optical phase in a single row varies with view angle is the Radon transform of a single level slice through the refractive index perturbation. This slice is oriented normal to the rotational axis and is therefore approximately parallel to the emitting surface of the transducer.

The complete set of phase retrieved views provides a set of Radon transforms (one for each row in a given image) which are reconstructed independently to yield a complete description of the refractive index distribution in the pulse. Figure 6(a) shows the results of applying the FSR (Fourier slice reconstruction) algorithm to a single level slice (taken parallel to the emitting aperture). Figures 6(b) and (c) show line plots comparing the reconstructed and simulated pressure distributions. Very good fidelity is apparent in both plots. The greatest discrepancy is observed in the high narrow peaks of Fig. 6(c).

V. EXPERIMENTS

The first step in determining the viability of the method described in this paper is to test its linearity as described by Eq. (14) in Sec. V A. This was done explicitly in the two experiments described in Secs. V A 1 and V A 2. Finally, the method is validated in Sec. V B via a point-by-point comparison of hydrophone and optical measurements of the acoustic field produced by two elements of a 64-element, 2.5-MHz linear array.

A. Measurement linearity

If the optical measurement method is linear it will satisfy the scaling and superposition properties in Eq. (14).

$$\mathcal{M}\{as_1(\mathbf{r}) + bs_2(\mathbf{r})\} = a\mathcal{M}\{s_1(\mathbf{r})\} + b\mathcal{M}\{s_2(\mathbf{r})\}. \quad (14)$$

In Eq. (14) $\mathcal{M}\{\}$ is the measurement operator, a and b are different scalar coefficients, and $s_{1,2}(\mathbf{r})$ represent the pressure in two different ultrasound pulses. The ability of the optical method to provide quantitative measurements of sound fields was tested explicitly in the following two experiments.

1. Superposition of refractive index perturbations

Three different driving voltage waveforms w_1 , w_2 , and $w_3 = w_1 + w_2$ were used to drive a Panametrics, 12.5-mm diameter, 2.25-MHz ultrasound transducer. The voltage waveform w_1 was 2.22 μs of a 2.5-MHz tone burst. Voltage waveform w_2 was 2.22 μs of a 2-MHz tone burst. In each case, foreground (sound on) and background (sound off) images in planes p_1 and p_2 of Fig. 1 (also see Fig. 4) were taken. These data were used to recover the phase of the optical pulse immediately after passage through the sound field. The sum of the phase delay produced using voltage waveforms w_1 and w_2 is plotted with that produced by driving voltage w_3 in Fig. 7. Excellent agreement is apparent, thus demonstrating the presence of the superposition property in the measurement process.

2. Scaling of refractive index perturbation

To test the amplitude scaling property of the measurement operator several linearly scaled versions of the same driving waveform (five cycles at 2.25 MHz) were applied to the transducer. The resulting pressures ranged from 6.59 to 111 kPa (spatial peak amplitude at a propagation delay of approximately 10 μs). In each case foreground (sound on) and background (sound off) images from the transducer and diffraction planes were used in conjunction with the phase retrieval algorithm to compute the phase delay introduced into the optical wavefront by the ultrasound pulse.

Figure 7(d) shows a line plot of the peak (both positive and negative) optical phase delays introduced into the optical wavefront by the ultrasound pulse as a function of applied voltage amplitude on the transducer. Also shown is a plot of peak pressure in the wave as measured via a calibrated membrane hydrophone. The peak positive and negative pressures measured by the hydrophone were the same. The linearity of the optical measurement is excellent for lower pressures. As

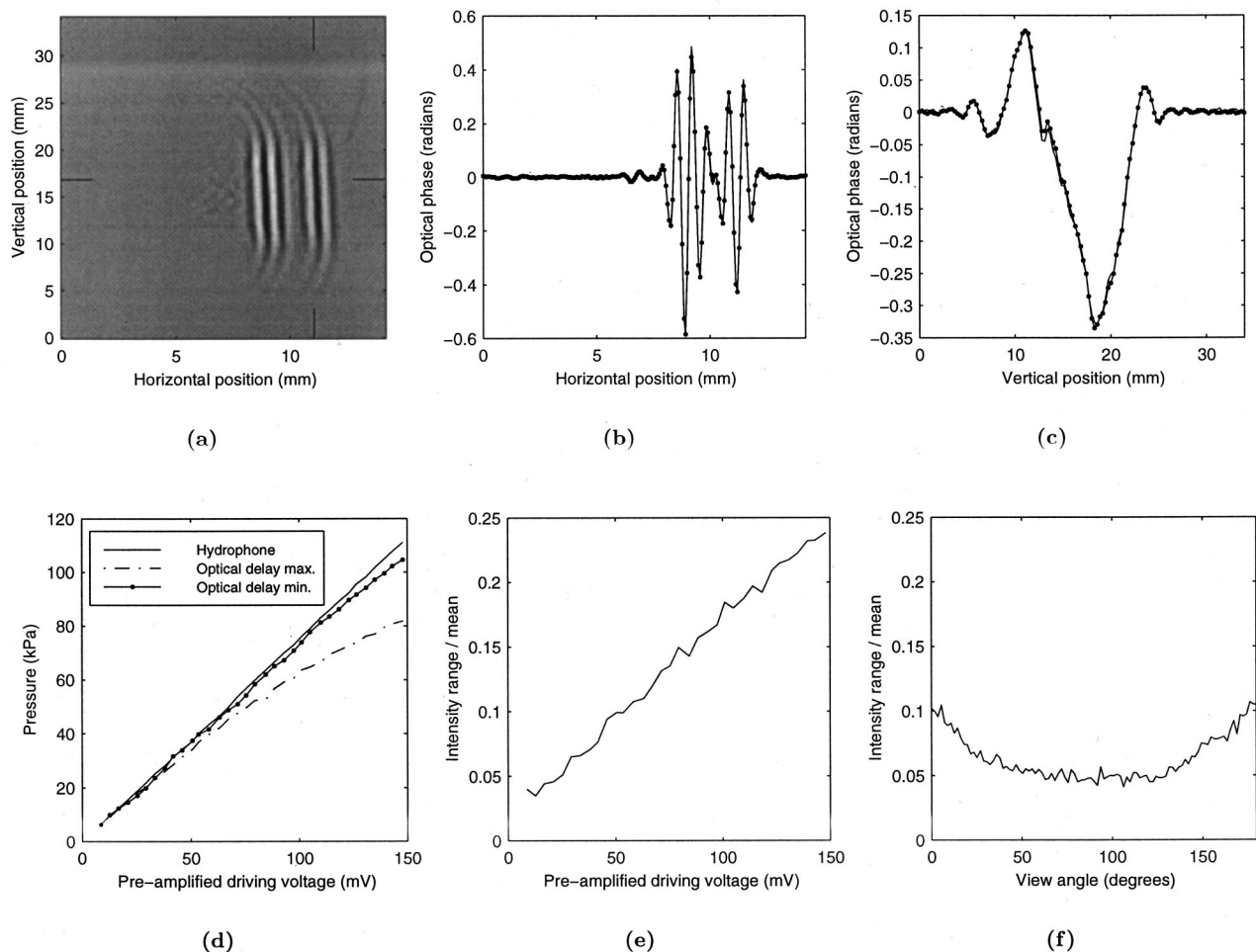


FIG. 7. The above plots demonstrate the linearity of the measurement operator. (a) The image is 34 mm in the vertical and 14.2 mm in the horizontal dimension, respectively, and depicts the phase retrieved image of the waveform produced when the transducer is driven with the algebraic sum of waveforms w_1 and w_2 . Figures (c) and (d) show line plots comparing the result in (a) (solid line) with the sum of optical phase distributions obtained by driving the transducer with w_1 and w_2 separately. (d) Comparison of integrated optical phase delay (maxima and minima) with peak pressure values as a function of applied voltage on a Panametrics 12.5-mm, 2.25-MHz, plane piston transducer. Excellent linearity is observed for peak pressures below about 75 kPa. (e) Normalized peak optical intensity variation (image range divided by the mean background value) immediately after passage of the optical pulse through the sound field as a function of applied voltage amplitude on the ultrasound transducer. A true phase object (see Sec. II C) produces a value of zero. (f) Normalized peak optical intensity variation immediately after passage of the optical pulse through the sound field as a function of tomographic view angle for the field measurement described in Sec. V B. The ultrasound field may be approximated as a phase object in this case due to the small deviation from the mean background value.

the peak pressure in the ultrasound transducer is increased we begin to deviate from our model (which requires no diffraction during propagation through the ultrasound field). The authors believe this to be a result of optical scattering during passage through the acoustic field (see Sec. II C). Pressures used in the experiment were sufficiently low so as to eliminate the nonlinear relationship between pressure and density or density and refractive index as the source of the discrepancy at higher amplitudes.

Figure 7(e) shows a plot of normalized optical intensity variation immediately after passage through the acoustic field. Normalized optical intensity variation is computed as image range (difference between maximum and minimum intensities in background normalized image) divided by the mean of the background. Clearly, under the scattering model described in Sec. II C this value should be zero because the amplitude of the impinging optical wave remains unaltered during propagation through the sound field. The plots in Figs. 7(e) and (f) thus provide a means of assessing how

closely the measurement experiment conforms to this requirement. Figure 7(f) shows the normalized optical intensity variation immediately after passage through the ultrasound field measured in Sec. V B as a function of view angle. Any optical measurement should be checked in this fashion prior to reconstruction. The excellent comparison between optical and hydrophone measurements given in Sec. V B shows that the perturbation of optical amplitude during propagation through the ultrasound field indicated in Fig. 7(f) may be considered minimal.

B. Optical versus hydrophone measurement

To validate the fidelity of the optical method, this section presents a comparison between data obtained with a calibrated NTR Systems, Inc. 500- μm diameter hydrophone and that acquired via the optical imaging technique discussed in this paper. In this experiment elements 32 and 34 of a 2.5-MHz, 64-element linear array were used to create a

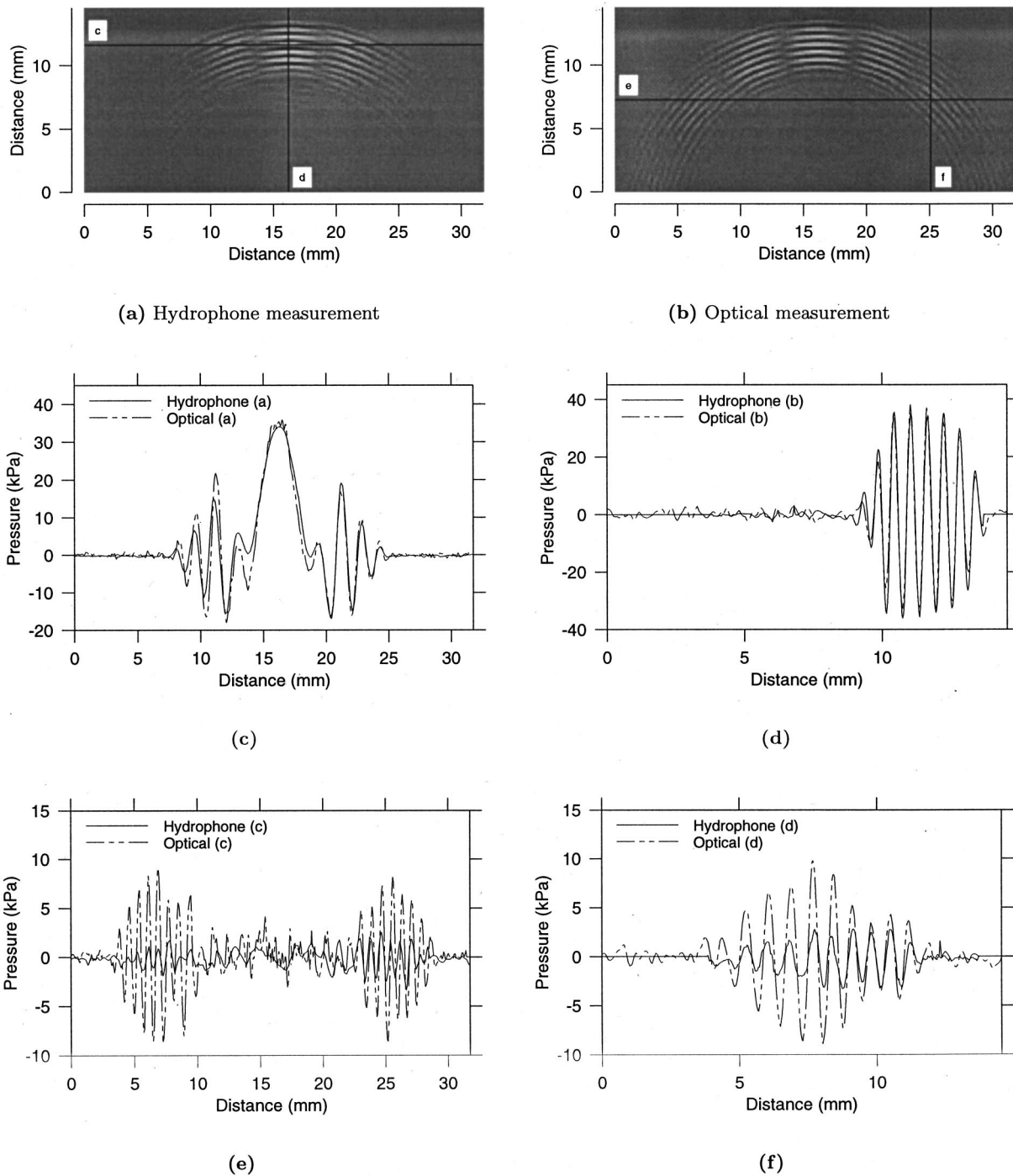


FIG. 8. (a) Hydrophone measurement of pulse from elements 32 and 34 of a 2.5-MHz, 64-element linear array at a delay of $12 \mu\text{s}$. (b) Optical measurement of the same field. (c)–(f) Line profile comparisons between optical and hydrophone measurements at the indicated locations in image plots. The reason for the poor agreement in panels (e) and (f) is the directivity pattern (spatial averaging property) of the $500\text{-}\mu\text{m}$ diameter hydrophone.

double slit pattern. A short tone burst at the transducer center frequency was applied to the two elements. All other elements were grounded. The field was imaged approximately $12 \mu\text{s}$ into its temporal evolution. The optical intensity was imaged approximately 7.33 cm after passage through the ultrasound pulse (this distance is the separation between planes p_1 and p_2 in Figs. 1 and 4). The same drive signals were used to generate the pulse for the hydrophone measurement.

The optical data for the double slit experiment using array elements 32 and 34 were taken at a temporal delay of

$12 \mu\text{s}$. Two slices from approximately the same location in the hydrophone and optical data volumes were selected and registered by hand. Figures 8(a) and (b) show the hydrophone and laser data slices, respectively. Line plot comparisons between the two slices are shown in Fig. 8. Figures 8(c) and (d) show excellent agreement between hydrophone and optical measurements. The plots in Figs. 8(e) and (f) demonstrate an advantage of the optical method. The averaging property or directivity pattern of the hydrophone leads to inaccurate field measurement in these regions.

VI. CONCLUSIONS

This paper describes an optical method for detailed three-dimensional measurement of instantaneous pressure in a wide bandwidth ultrasound pulse propagating in water. The method records the forward-scattered optical intensity from the interaction of a collimated laser pulse with an ultrasound field via a two-lens imaging system (see Sec. V). The optical intensity is recorded as a function of angle as the ultrasound transducer is rotated through 180 deg about an axis normal to the propagation direction of the incident optical pulse. The phase of the optical field immediately after passage through the ultrasound pulse is computed from this intensity via the MGP (method of generalized projections) (see Sec. III A) under a scalar Fresnel model for optical wave propagation (see the Appendix). A rigorous model for acoustic wave propagation is used, precisely defining the nature of the optical scatterer and its relationship to the acoustic pulse independent of a particular constitutive relationship between pressure and density. A linear model for the relationship between local pressure and local refractive index perturbation is described in Sec. II A assuming a simple pressure-density relationship. A simple delay model is described in Sec. II C for the interaction of the optical wave with the ultrasound pulse. This allows the reconstruction of the instantaneous three-dimensional refractive index distribution from the optical phase via the Fourier slice reconstruction algorithm (see Secs. V and III B). A numerical simulation of the measurement experiment and reconstruction process for a plane piston ultrasound transducer with a semicircular aperture and center frequency of 1.5 MHz in Sec. IV demonstrates the theoretical viability of the measurement. Laboratory measurements obtained using the method described in this paper are compared with 500- μm needle hydrophone measurements of a pressure field from two elements of a 2.5-MHz linear array. Excellent agreement is observed everywhere except those regions where the hydrophone directivity pattern prevents accurate measurement.

The method presented in this paper provides an accurate, quantitative means for obtaining the three-dimensional, instantaneous refractive index perturbation induced in water via an ultrasonic wave. There are no restrictions on the bandwidth of the ultrasound field. In general this refractive index perturbation is a simple function of the ratio of local instantaneous to ambient material density. For small amplitude pressure waves the change in refractive index is related linearly to pressure. The resolution of the method is limited principally by the quality of the optics employed. As the amplitude of the ultrasound pulse increases, the linear relationship between pressure and refractive index deteriorates and the more complete description in terms of local density ratios is needed. Also, the delay model for optical scattering must give way to one including scattering within the sound field. This is also the case if the dimension of the sound field traversed by the optical pulse is sufficiently large, or the ultrasound frequency is high enough so that features of the optical scatterer approach the order of a light wavelength. The method depends only on optical intensity measurements and uses an iterative phase retrieval algorithm to compute the optical phase delay necessary for the reconstruction of three-

dimensional pressure. The method may find application in calibration, practical transducer design and manufacture, investigation of processes important in ultrasonic imaging systems such as phase aberration, and studies in acoustic wave propagation and scattering.

ACKNOWLEDGMENTS

The authors gratefully acknowledge the assistance of Randy Kinnick and Tom Kinter in the experimental and computational aspects of this research. We also thank Elaine C. Quarve for her secretarial and organizational assistance. This research was supported in part by Grant No. CA 43920 from the National Institutes of Health.

APPENDIX: OPTICAL FIELD MODEL

Fundamental to this study is the model used for optical wave propagation. The measurement method inverts this model to provide the three-dimensional distribution of refractive index. We briefly review the approximations made in developing the Fresnel model for optical wave propagation from Maxwell's equations and verify that our experimental conditions satisfy these constraints. The discussion is extended from Balanis,¹⁰ Goodman,¹⁵ and Kong.²³

Under the assumption of no magnetic monopoles, constant permeability μ , no impressed current sources, zero conductivity, no electric charge in the solution region, and the constitutive material models,

$$\mathcal{D} = \epsilon \mathcal{E}, \quad (\text{A1})$$

$$\mathcal{B} = \mu \mathcal{H}, \quad (\text{A2})$$

the following vector electromagnetic wave equation for the electric field may be developed from Maxwell's equations,

$$\nabla^2 \mathcal{E} = \frac{1}{c^2} \left(\frac{\partial^2}{\partial t^2} \right) (1 + \chi) \mathcal{E} - \frac{\nabla(\mathcal{E} \cdot \nabla \chi)}{1 + \chi}. \quad (\text{A3})$$

In Eq. (A3), $c = 1/\sqrt{\mu_o \epsilon_o}$, χ is susceptibility, and \mathcal{E} is the electric field vector. Equation (A3) is a linear, second-order partial differential equation for electromagnetic fields in an isotropic medium. The second term on the right-hand side of Eq. (A3) provides coupling between the three vector components of the electric field. If the spatial variations in the susceptibility occur sufficiently slowly this term may be neglected. In this case, we have the three separate scalar wave equations

$$\nabla^2 \mathcal{E}_n = \frac{1}{c^2} \left(\frac{\partial^2}{\partial t^2} \right) (1 + \chi) \mathcal{E}_n, \quad \text{where } n = x, y, z. \quad (\text{A4})$$

The form of the second term in Eq. (A3) also indicates that high gradients in the electric susceptibility do not create coupling if they are perpendicular to the electric field vector.

From the discussion in Sec. II A it is clear that a medium at rest (in the absence of a mechanical wave) has an intrinsic polarizability or electric susceptibility χ_i . This value is perturbed by an acoustic wave in proportion to the induced density change. If we neglect Doppler shift induced in the optical wave by the acoustic wave motion we may consider the refractive index perturbation stationary and write

$$\nabla^2 u(\mathbf{r}, t) = \frac{1}{c^2} (1 + \chi_i J^{-1}(\mathbf{r}, t)) \left(\frac{\partial^2}{\partial t^2} \right) u(\mathbf{r}, t). \quad (\text{A5})$$

Here we use a generic scalar variable $u(\mathbf{r}, t)$ for the electric field under the assumption that coupling between field components may be neglected. Note that c is the speed of light in a vacuum and that the dependence of $J^{-1}(\mathbf{r}, t)$ on the variable t is merely that of an index (to define a point in the temporal evolution of the ultrasound pulse).

From the above it is clear that under certain restrictions it is appropriate to use a scalar model for electromagnetic wave propagation and scattering. Here we review conditions under which an additional simplification, known as the Fresnel approximation, may be used.^{15,16} Consider the following free space wave equation:

$$\left(\nabla^2 - \frac{1}{c^2} \frac{\partial^2}{\partial t^2} \right) u(\mathbf{r}, t) = 0. \quad (\text{A6})$$

If $u(\mathbf{r}, t)$ is time harmonic we assume $u(\mathbf{r}, t) = \text{Re}\{u(\mathbf{r})e^{j\omega t}\}$ and solve

$$(\nabla^2 + k^2)u(\mathbf{r}) = 0. \quad (\text{A7})$$

Expansion of $u(\mathbf{r}, t)$ in a complex exponential basis together with an assumption on the possible directions of propagation for the various plane wave components of the solution yields (see Goodman¹⁵)

$$U(\mathbf{r}_\perp, z) = \int_{-\infty}^{\infty} d^2\mathbf{k}_\perp U(\mathbf{k}_\perp, 0) e^{jk_z z}, \quad (\text{A8})$$

where $k_z = \sqrt{k^2 - k_\perp^2}$, k is the wave number, and $\mathbf{k}_\perp = (k_x, k_y)$ is the transverse wave number. Assumption of a *band limited* spectrum (see Solimeno *et al.*¹⁶) implies $k_\perp^2 \ll k^2$ and we may write, using the first two nonzero terms in Taylor's expansion,²⁴

$$k^2 \sqrt{1 - (k_\perp/k)^2} \approx k - \frac{1}{2} \frac{k_\perp^2}{k},$$

giving

$$U(\mathbf{r}_\perp, z) = \int_{-\infty}^{\infty} d^2\mathbf{k}_\perp U(\mathbf{k}_\perp, 0) e^{j[k - (1/2)(k_\perp^2/k)]z}. \quad (\text{A9})$$

This approximation will be acceptable if the resulting phase error is much less than 2π . We may approximate the error α_e with the third nonzero term in Taylor's expansion to give

$$\alpha_e = \frac{1}{8} k_\perp^4 z_b / k^3. \quad (\text{A10})$$

Given a phase error α_e , Eq. (A10) defines a *maximum* distance z for which the model is valid.

Using a Green's function approach in the spatial domain it has been shown that under assumptions of a *space-limited* field (see for example Goodman¹⁵) that the model in Eq. (23) may be used from infinity up to some *minimum* distance z . We write the error β_e as

$$\beta_e = \frac{1}{8} \frac{a^4 k}{z_s^3}, \quad (\text{A11})$$

where $a^2 = x^2 + y^2$ is the radius of a circle in the xy -plane that contains the entire aperture. While no signal may be

both strictly band and space-limited, the required approximations are satisfied in both cases if $z_s < z_b$. Setting $\alpha_e = \beta_e$ we obtain the required condition,¹⁶

$$a < 8 \alpha_e k^2 / k_\perp^3, \quad (\text{A12})$$

which allows use of the Fresnel approximation from distances very close to the aperture out to infinity. It should be noted that a is the aperture of our system, k is the optical wave number, and k_\perp is the spectral breadth induced into the optical angular plane wave spectrum by the ultrasound field (see Sec. II C). Assuming an acoustic wave speed of 1480 m/s, that the highest frequency the ultrasound transducer can pass is 5 MHz, an optical wavelength of $\lambda = 810$ nm, and $\alpha_e = 0.1$, we obtain a maximum aperture of

$$a_{\max} = 8 \alpha_e k^2 / k_\perp^3 \approx 5 \text{ m}.$$

¹C. Raman and N. N. Nath, "The diffraction of light by high frequency sound waves: Part I," Proc. Indian Acad. Sci. **2**, 406–412 (1935a).

²C. Raman and N. N. Nath, "The diffraction of light by high frequency sound waves: Part II," Proc. Indian Acad. Sci. **2**, 413–465 (1935b).

³C. Raman and N. N. Nath, "The diffraction of light by high frequency sound waves: Part III," Proc. Indian Acad. Sci. **3**, 75–84 (1936a).

⁴C. Raman and N. N. Nath, "The diffraction of light by high frequency sound waves: Part IV," Proc. Indian Acad. Sci. **3**, 119–125 (1936b).

⁵C. Raman and N. N. Nath, "The diffraction of light by high frequency sound waves: Part V," Proc. Indian Acad. Sci. **3**, 459–465 (1936c).

⁶E. Blomme, P. Kwiek, O. Leroy, and R. Reibold, "On the near field of light diffraction by an ultrasonic phase-amplitude grating: Theory and experiment," Acustica **73**, 134–143 (1991).

⁷H. Colbert and K. Zankel, "Light diffraction by ultrasonic waves—Fresnel region," J. Acoust. Soc. Am. **35**, 359–363 (1963).

⁸B. D. Cook, "Interference patterns of ultrasonic optical gratings," J. Opt. Soc. Am. **53**, 429–430 (1963).

⁹J. E. Marsden and T. J. Hughes, *Mathematical Foundations of Elasticity* (Dover, New York, 1993).

¹⁰C. A. Balanis, *Advanced Engineering Electromagnetics* (Wiley, New York, 1989).

¹¹*Encyclopedia of Acoustics*, edited by M. J. Crocker (Wiley, New York, 1997), Vol. 1.

¹²*CRC Handbook of Chemistry and Physics*, 79th ed., edited by W. H. Beyer (CRC, Boca Raton, 1998).

¹³I. Thormahlen, J. Straub, and U. Grigull, "Refractive index of water and its dependence on wavelength, temperature, and density," J. Phys. Chem. Ref. Data **14**, 933–945 (1985).

¹⁴T. Pitts, Ph.D. thesis, Mayo Graduate School, Rochester, Minnesota, 1998.

¹⁵J. Goodman, *Introduction to Fourier Optics*, 2nd ed. (McGraw-Hill, New York, NY, 1994).

¹⁶S. Solimeno, B. Crosignani, and P. DiPorto, *Guiding, Diffraction, and Confinement of Optical Radiation* (Harcourt Brace Jovanovich, New York, 1986).

¹⁷M. H. Maleki and A. J. Devaney, "Phase-retrieval and intensity-only reconstruction algorithms for optical diffraction tomography," J. Opt. Soc. Am. A **10**, 1086–1092 (1993).

¹⁸J. Cederquist, J. Fienup, C. Wackerman, S. Robinson, and D. Kryskowski, "Wave-front phase estimation from Fourier intensity measurements," J. Opt. Soc. Am. A **6**, 1020–1026 (1989).

¹⁹A. Levi and H. Stark, "Image restoration by the method of generalized projections with application to restoration from magnitude," J. Opt. Soc. Am. A **1**, 932–943 (1984).

²⁰H. Stark, *Image Recovery: Theory and Application* (Academic, Orlando, FL, 1987).

²¹M. Hayes, "The reconstruction of a multidimensional sequence from the phase or magnitude of its Fourier transform," IEEE Trans. Acoust., Speech, Signal Process. **ASSP-30**, 140–154 (1982).

²²A. K. Jain, *Fundamentals of Digital Image Processing* (Prentice Hall, New York, 1989).

²³J. A. Kong, *Electromagnetic Wave Theory* (Wiley, New York, 1990).

²⁴J. E. Marsden and A. J. Tromba, *Vector Calculus* (Freeman, San Francisco, 1988).

Two-dimensional noise source imaging with a T-shaped microphone cross array

Marinus M. Boone

University of Technology, Faculty of Applied Physics, P.O. Box 5046, 2600 GA, Delft, The Netherlands

Niels Kinneging^{a)}

Institute of Applied Physics, Stieltjesweg 1, 2628 CK Delft, The Netherlands

Teun van den Dool

Institute of Applied Physics, Stieltjesweg 1, 2628 CK Delft, The Netherlands

(Received 16 December 1996; revised 21 July 1999; accepted 24 August 2000)

Spatial cross-correlation beamsteering with a T-shaped sparse array can provide an efficient procedure to identify the directions and to obtain the emission levels of multiple uncorrelated noise sources. The procedure can be applied to stationary or moving sources. It provides two-dimensional image resolution equivalent to that of a full array, but requires significantly fewer microphones. This results in substantially reduced requirements for data acquisition and signal processing, with a material cost reduction. Simulation, laboratory measurement, and field measurement of a train moving at high speed illustrate application of the procedure. © 2000 Acoustical Society of America. [S0001-4966(00)00812-2]

PACS numbers: 43.60.Gk, 43.20.Ye [JCB]

I. INTRODUCTION

In many practical situations it is desirable to measure the sound field of a source distribution in such a way that it is possible to analyze the position and source strengths of different radiating parts. Examples are the quantification of the acoustic sources of machinery, but also from moving sources, like vehicles, trains, and aircraft. Especially in those cases where it is not possible to examine these sources from nearby, the use of highly directive microphone systems is advantageous. Conventional single microphone methods to obtain directivity are based on gradient and interference tube microphones.¹ Directivity can also be obtained in combination with parabolic mirrors.² These solutions have physical limitations in resolution and frequency range, mainly due to the limited dimensions in relation to the relevant wavelengths. Higher resolution can be obtained with microphone arrays in combination with adequate signal processing.³⁻⁷ Such microphone arrays can basically be divided into one-, two-, and three-dimensional systems. Another classification can be made based on the applied signal processing. There are several approaches, ranging from simple time domain beamsteering to advanced processing schemes, based on the cross-spectral matrix of the array signals. Many of these techniques stem from seismics,⁸ radar,⁹ sonar,¹⁰ and radio astronomy.¹¹ Time domain beamsteering processing is often applied, because of the simple signal processing that is required. It also gives the most stable results and in some sense the best signal to noise ratios. However, cross-spectral density matrix processing may lead to higher spatial resolution. Well-known examples of the latter are the Capon method¹² and the MUSIC algorithm.¹³ A special class of cross-spectral

matrix processing is optimized for the use of so-called sparse arrays with the benefit that many fewer sensors are needed. Here, use is made of the properties of the spatial correlation function of the wave field. Examples are found in radio astronomy,¹¹ sonar,¹⁴ and noise control.^{5,6} For instance the one-dimensional cross-correlation antenna SYNTACAN^{5,6} uses only 15 microphones in one octave band to obtain almost the same angular resolution as a full linear array with 128 microphones and direct beamsteering. Notice that the spatial cross-correlation (or cross-spectrum) function of the wave field is related to, but not identical with the cross-spectral density matrix of the sensor signals.

An essential difference between direct beamsteering and spatial cross-correlation beamsteering is that with direct beamsteering the source signals can be found as a function of time, whereas with spatial cross-correlation beamsteering only the root-mean-square (rms) values of the source signals can be obtained. However, in many cases the latter is sufficient. For many applications, spatial processing in one dimension is not sufficient to separate the noise sources, for instance, if the noise sources are distributed in both horizontal and vertical directions. In those cases one needs at least a two-dimensional microphone array. In the two-dimensional situation, the choice of an efficient signal processing procedure is even more important than in the one-dimensional situation, because of the high reduction that can be obtained in the number of required microphones. Two-dimensional planar array techniques in the near field of the sources have become known as acoustic holography.¹⁵ Under certain conditions, when the source signals are repeatable in place and time, aperture synthesis techniques can be used, where the response function over a measurement surface is scanned with a single sensor.¹⁶ A related method is spatial transformation of sound fields (STSF),¹⁷ where the necessity to carry out all measurements over the measurement plane simulta-

^{a)}Present address: Survey Department of the Ministry of Transport, Public Works and Water Management, Kanaalweg 3b, 2628 EB Delft, The Netherlands.

neously, is avoided by measuring the cross spectra between the scanning microphones and a limited number of reference microphones. A prerequisite for this procedure is that the noise sources are stationary.

There are many instances where one needs or wants to carry out all measurements simultaneously (nonstationarity, limited measuring time) with angular resolution in two perpendicular directions. To limit the number of microphones, several types of sparse planar arrays have been proposed. Some results have been reported in the literature of beamsteering with sparse two-dimensional arrays. Time delay beamsteering with cross-arrays results in high side lobes.^{18,19} Other sparse planar arrays have also been tested,²⁰⁻²³ also with less than ideal side lobe patterns when direct beamsteering is applied. With direct beamsteering, good results are only obtained with full planar arrays.¹⁸

With cross-spectral matrix processing these limitations can be overcome. For instance, Elias²⁴ gives a method to obtain spatial source images with low side lobes from a cross-shaped array by taking advantage of the structure of the cross-spectral density matrix of the array sensor signals.

The signal processing method that we propose in this paper is directly based on the two-dimensional cross-correlation function of the wave field and is hence a two-dimensional extension of our one-dimensional SYNTACAN design.⁵ It was found that the proposed T-shaped cross array is very efficient for this processing method.

In the following sections we will first summarize the theory of two-dimensional microphone arrays, based on both direct signal beamsteering and spatial correlation beamsteering. Special attention will be given to the use of cross-shaped arrays to reduce the number of microphones. It will be shown that beamsteering of the spatial cross-correlation function will result in beampatterns without severe side lobes. Next, simulations will be presented to show the potential of this method for side lobe reduction as compared with direct signal beamsteering. We also present the results of an illustrative laboratory measurement that confirms this theoretical approach and results of a practical measurement with a T-shaped array on a passing train. We end with conclusions about the applicability of the new method.

II. THEORY

Let us assume that all sound sources to be measured are at a large distance from the aperture of a multichannel receiver system (the Fraunhofer condition). In that case the sound pressure of the sound field can be written as

$$p(\mathbf{r}, t) = \sum_{a=1}^N s_a(t - \mathbf{n}_a \cdot \mathbf{r}/c), \quad (1)$$

where \mathbf{r} denotes the spatial coordinates, $s_a(t)$ is the sound pressure of source a at the origin of the coordinate system, which is in the antenna region, \mathbf{n}_a is the normal to the wave front from source a and c is the sound velocity. There are a total of N sources. The sound pressure can also be written in the frequency domain:

$$P(\mathbf{r}, f) = \sum_{a=1}^N S_a(f) \exp(-j\mathbf{k}_a \cdot \mathbf{r}), \quad (2)$$

where $\mathbf{k}_a = (2\pi f/c)\mathbf{n}_a$ is the wave vector of the wave field of source a , and $S_a(f)$ is the Fourier transform of $s_a(t)$.

A. Direct signal beamsteering

Direct signal beamsteering is obtained by integration over a receiver aperture surface A with appropriate travel-time corrections and including some weighting function $w(\mathbf{r})$. (In practice a summation is carried out. However, in this theoretical section we prefer to use integrals instead of summations. If the sample interval between the transducers is small enough to avoid spatial aliasing, the applied DFT theory will give the same results as the Fourier transforms that are used here.) The output of such a beamformer, steering at direction $-\mathbf{n}_0$, can be written in the time domain as

$$q(\mathbf{n}_0, t) = \int \int_A \sum_{a=1}^N s_a(t - \mathbf{n}_a \cdot \mathbf{r}/c + \mathbf{n}_0 \cdot \mathbf{r}/c) w(\mathbf{r}) dA \quad (3)$$

or in the frequency domain as

$$Q(\mathbf{n}_0, f) = \int \int_A \sum_{a=1}^N S_a(f) \exp(-j\mathbf{k}_a \cdot \mathbf{r}) \times \exp(j\mathbf{k}_0 \cdot \mathbf{r}) w(\mathbf{r}) dA, \quad (4)$$

where $\mathbf{k}_0 = (2\pi f/c)\mathbf{n}_0$. Notice from Eqs. (3) and (4) that delay and sum beamsteering in the time domain is equivalent with phase filtering and sum beamsteering in the frequency domain.

In the case that A is a plane surface in the $x-z$ plane, the beamsteering corresponds to a two-dimensional Fourier transform from the spatial coordinates x and z to the wave numbers k_x and k_z :

$$\begin{aligned} \tilde{P}(k_x, k_z, f) &= \int \int_A \sum_{a=1}^N S_a(f) \exp(-jk_{ax}x - jk_{az}z) \\ &\quad \times w(x, z) \exp(jk_x x + jk_z z) dA \\ &= \sum_{a=1}^N S_a(f) W(k_x - k_{ax}, k_z - k_{az}). \end{aligned} \quad (5)$$

This result shows that a good beamforming is obtained if $W(k_x, k_z)$, being the Fourier transform of $w(x, z)$, has a large value around $k_x=0$ and $k_z=0$ while being small for all other values of k_x and k_z .

A separation between the signals from the different sources is now possible by selective integration. From the inverse Fourier transform

$$P(x, z, f) = \int_{-\infty}^{\infty} \int_{-\infty}^{\infty} \tilde{P}(k_x, k_z, f) e^{-jk_x x - jk_z z} dk_x dk_z \quad (6)$$

we find by inserting $x=0$ and $z=0$ and restricting the integration over the wave vector components due to one source a , assuming that the sources are well separated:

$$P_a(0, 0, f) \approx S_a(f). \quad (7)$$

Notice that source signal $s_a(t)$ can be obtained by inverse Fourier transformation of Eq. (7):

$$p_a(0,0,t) \approx s_a(t). \quad (8)$$

B. Spatial correlation beamsteering

Instead of direct beamsteering, which can be seen as a decomposition of the received sound field with a spatial Fourier transform, it is also possible to carry out a decomposition of the spatial correlation function of the sound field.

The spatial correlation function of a sound field is defined as the temporal cross-correlation function between different points \mathbf{r}_1 and \mathbf{r}_2 in the sound field:

$$R(\mathbf{r}_1, \mathbf{r}_2, \tau) = E\{p(\mathbf{r}_1, t)p(\mathbf{r}_2, t + \tau)\}, \quad (9)$$

where $E\{ \}$ denotes the expectation operator, obtained by time averaging.

If the wave field fulfills Eq. (1) we find

$$\begin{aligned} R(\mathbf{r}_1, \mathbf{r}_2, \tau) &= E\left\{ \sum_{a=1}^N s_a(t - \mathbf{n}_a \cdot \mathbf{r}_1 / c) \right. \\ &\quad \left. \times \sum_{b=1}^N s_b(t + \tau - \mathbf{n}_b \cdot \mathbf{r}_2 / c) \right\} \\ &= \sum_{a=1}^N \sum_{b=1}^N R_{ab}(\tau + \mathbf{n}_a \cdot \mathbf{r}_1 / c - \mathbf{n}_b \cdot \mathbf{r}_2 / c), \end{aligned} \quad (10)$$

where $R_{ab}(\tau)$ is the temporal correlation function between source signal a and source signal b at $\mathbf{r} = \mathbf{0}$. It is interesting to look at the special case where $\mathbf{r}_1 = \mathbf{0}$ (the origin of our coordinate system). The spatial cross-correlation function of the sound pressure is then given by

$$R(\mathbf{0}, \mathbf{r}, \tau) = \sum_{a=1}^N \sum_{b=1}^N R_{ab}(\tau - \mathbf{n}_b \cdot \mathbf{r} / c). \quad (11)$$

Transformation of this expression to the frequency domain yields

$$\tilde{R}(\mathbf{0}, \mathbf{r}, f) = \sum_{a=1}^N \sum_{b=1}^N \tilde{R}_{ab}(f) \exp(-j\mathbf{k}_b \cdot \mathbf{r}). \quad (12)$$

Note the strong relationship between Eq. (12) and Eq. (2).

Let us also assume that the receivers are placed on a plane surface in the x - z plane. Applying a spatial windowing function $w(x, z)$ and carrying out a two-dimensional Fourier transform to k_x and k_z gives the result

$$\tilde{R}'(k_x, k_z, f) = \sum_{a=1}^N \sum_{b=1}^N \tilde{R}_{ab}(f) W(k_x - k_{bx}, k_z - k_{bz}). \quad (13)$$

This result shows that if $W(k_x, k_z)$ has a large value around $k_x = 0$ and $k_z = 0$ and a small value for other values of k_x and k_z that a good separation will be obtained between the different cross-spectra $\tilde{R}_{ab}(f)$.

C. Comparison between direct beamsteering and cross-correlation beamsteering

Much insight in the spatial resolution of direct beamsteering as well as cross-correlation beamsteering is obtained by inspection of Eqs. (5) and (13). An important difference between both methods is that with direct beamsteering it is possible to find the complete time signal from one direction; with the cross-correlation approach only the auto- and cross-spectra can be obtained. In many instances one is only interested in average spectral values and the result of Eq. (5) will be further processed to obtain spectral information only, just like Eq. (13).

It was already stated that a good separation of the contributions from different source directions will be obtained, if $W(k_x, k_z)$ is a narrow peak function. For W to behave like a narrow peak function with low side lobes, it is necessary that $w(\mathbf{r})$ is a smooth function over a large area in the x - z plane. As a consequence, the direct beamsteering method requires the use of a sampled plane array and not just a cross array. Application of a cross array with direct beamsteering results in a beam pattern with very high side lobes. In the same way, application of the cross-correlation method according to Eq. (11) makes it necessary to measure over a large planar region. However, in the special case where the noise sources are mutually uncorrelated, a situation occurs, where a cross array can give the necessary input for a full two-dimensional spatial Fourier transform.

To understand this, we rewrite Eq. (11) for $\mathbf{r} = (\xi, \zeta)$ and $\mathbf{n}_b = (n_{bx}, n_{bz})$:

$$R(\xi, \zeta, \tau) = \sum_{a=1}^N \sum_{b=1}^N R_{ab}(\tau - n_{bx}\xi/c - n_{bz}\zeta/c). \quad (14)$$

If the noise sources are uncorrelated, this expression reduces to

$$R(\xi, \zeta, \tau) = \sum_{a=1}^N R_{aa}(\tau - n_{ax}\xi/c - n_{az}\zeta/c). \quad (15)$$

Let us now compute the cross-correlation function between two positions on a cross-shaped array with receivers at the x and z axes. The position along the x axis is at $-\xi$ and along the z axis at $+\zeta$. Substitution of these coordinates in Eq. (10) under the assumption of uncorrelated sources gives

$$\begin{aligned} R_+(\xi, \zeta, \tau) &= E\left\{ \sum_{a=1}^N s_a(t + n_{ax}\xi/c) s_a(t + \tau - n_{az}\zeta/c) \right\} \\ &= \sum_{a=1}^N R_{aa}(\tau - n_{ax}\xi/c - n_{az}\zeta/c). \end{aligned} \quad (16)$$

As we see, the results of Eqs. (15) and (16) are the same. When the noise sources are uncorrelated, the cross-correlation function only depends on the difference in x and z positions and not on the absolute position. This is further illustrated in Fig. 1.

By making use of this property, we are able to compute $R(\xi, \zeta, \tau)$ for a complete set of ξ and ζ values, as would be possible with a full planar array. This result is directly com-

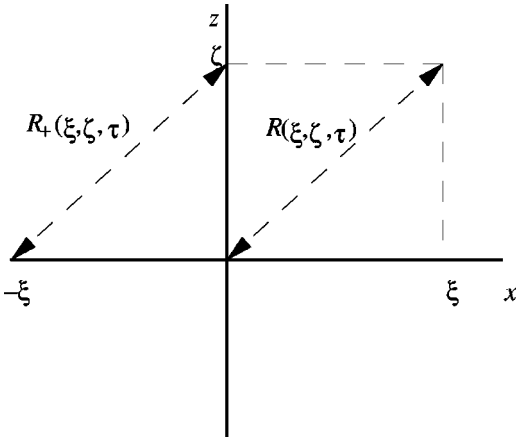


FIG. 1. Comparison of spatial cross-correlation functions at different positions in the x - y plane.

parable with the one-dimensional situation, where the cross-correlation technique can be used with a sparse array in case of uncorrelated noise sources.⁵

In the case of uncorrelated sources, it follows from Eq. (16) that

$$\tilde{R}'_+(k_x, k_z, f) = \sum_{a=1}^N \tilde{R}_{aa}(f) W(k_x - k_{ax}, k_z - k_{az}) \quad (17)$$

and the auto-spectrum of an individual source is found by selective integration. Notice that the auto-spectrum of a source is directly related to its rms pressure by the Parseval relation.

Another important observation that can be made is that only half of the total number of cross-correlation functions needs to be measured. The second half can be computed from the first. This is easily understood by realizing that the result in the k_x, k_z, f domain must be real, because all $\tilde{R}_{aa}(f)$ are real. Consequently, the following complex-conjugate relation holds for the spatial cross-spectrum function:

$$R(-\xi, -\zeta, f) = R^*(\xi, \zeta, f). \quad (18)$$

This means that one of the two arms of the microphone cross can be one-sided; the cross reduces to a T.

III. SIMULATIONS

The theory of the previous section is illustrated and confirmed with a number of simulations. First, simulations are shown for two simultaneous plane waves that are assumed to be uncorrelated. The simulations are carried out for one small frequency band around 1000 Hz. The sound velocity is 340 m/s. The receivers are placed at a constant distance between each other of 0.1 m. The two plane waves have directions such that for the first source $k_x = 0.5k$ and $k_z = 0.3k$ and the relative amplitude $A = 1$. For the second source these values are $k_x = -0.2k$, $k_z = -0.4k$, and $A = 0.5$.

The first simulation illustrates the result of direct beamsteering with a full planar array of 64×64 elements. To suppress the side lobes due to the finite beamsteering surface, a Hanning window is applied to the receiver signals in the x and z directions. The result is obtained by Fourier transform

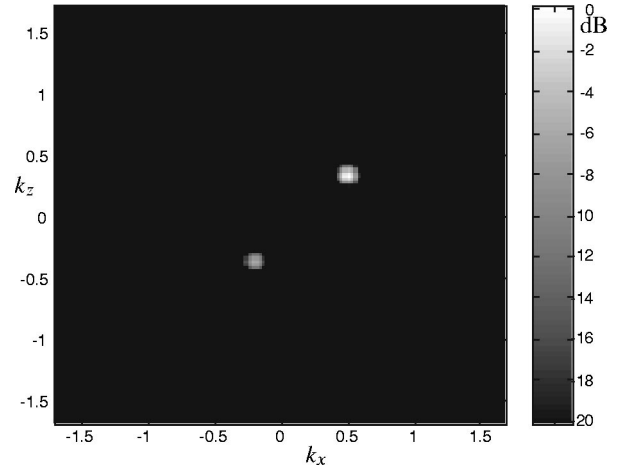


FIG. 2. Simulated images of two uncorrelated sources with direct beamsteering of a full planar array.

ation as given by Eq. (5), after which the squared amplitude is computed as a measure for the intensity in each direction. An interpolation by a factor 2 is carried out to obtain a smoother presentation of the result. The resulting $\tilde{R}'(k_x, k_z, f)$ is shown in Fig. 2 on a dB scale over a range of 40 dB. Notice that the sources are well separated.

The second simulation shows the result of direct beamsteering with a cross array with 64 receivers in both x and z direction. Here also a Hanning window is applied and the squared magnitude is computed. The result in Fig. 3 clearly shows the high side lobes due to the poor spatial window function of the cross array. Notice especially the high outputs at the crossing of the side lobes of the two sources.

The third simulation shows the result of a T-shaped cross array, obtained by beamsteering of the spatial cross-correlation function of the wave field. In this case 64 elements were used in the x direction and 32 elements in the z direction. Use was made of the redundancy given by Eq. (18). The result was obtained from a two-dimensional Fourier transform of the spatial cross-spectra, also including a Hanning window in both directions. This results directly in an amplitude that is a measure for the intensity. The result is

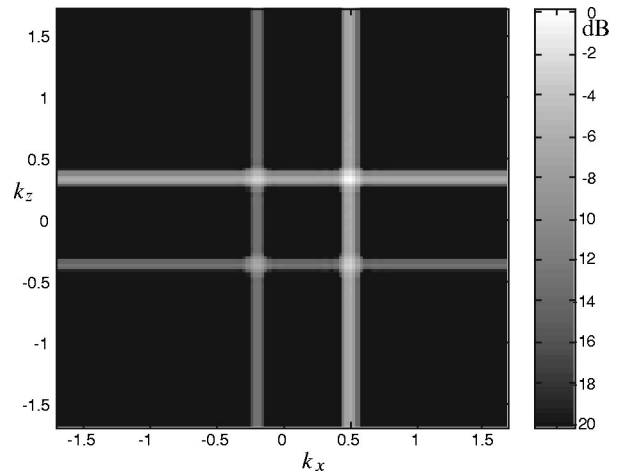


FIG. 3. Simulated images of two uncorrelated sources with direct beamsteering of a cross array.

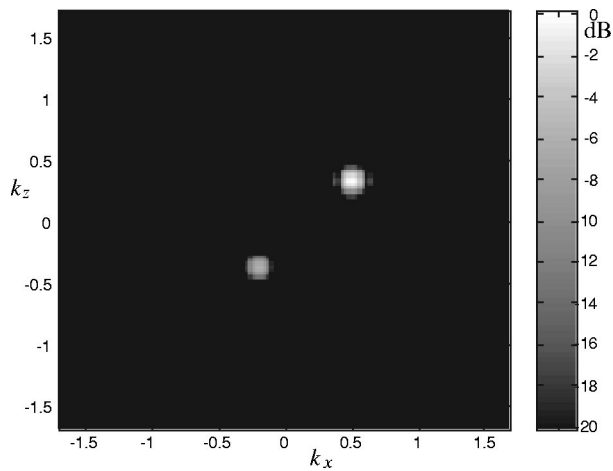


FIG. 4. Simulated images of two uncorrelated sources with cross correlation beamsteering of a T-shaped cross array.

shown in Fig. 4. We see that the source responses are well separated.

Comparison with Fig. 2 also shows that the main lobe is wider and the side lobes are higher. This is due to the fact that the direct beamsteering method leads to a result that has to be squared, while the cross-correlation method gives a linear result in the intensity. Hence, the beam pattern of the Hanning window shows more clearly in the latter case. The concept of the T-shaped cross array was further tested in a simulation that closely matched a laboratory measurement that is discussed in the next section. Here use is made of a horizontal array of 30 microphones in the x direction and 16 microphones in the z direction, forming a T-shaped cross array, as illustrated in Fig. 5. The origin of the Cartesian coordinate system is at the crossing of the horizontal and vertical subarrays. The distance between the microphones is $\Delta x = 0.1$ m. A source model was used of 3 monopole sources that radiated uncorrelated Gaussian white noise. These sources were placed at the plane $y = 5.94$ m, at positions $x_1 = 0.00$ m, $z_1 = 0.33$ m, $x_2 = 0.00$ m, $z_2 = 2.90$ m, $x_3 = 1.90$ m, $z_3 = 0.28$ m. For each noise source a Gaussian pseudo-random-noise sequence of 4096 data samples was computed. A sample frequency of 11 025 Hz was assumed. The microphone signals were computed by adding the white noise contributions from the different sources with the appropriate delays. The amplitude differences were neglected.

From these simulated noise data the cross-spectra were

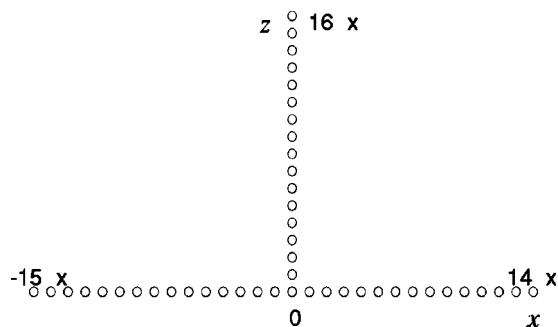


FIG. 5. Configuration of the T-shaped cross array that was used in the simulation of Fig. 6 and the measurement of Fig. 7.

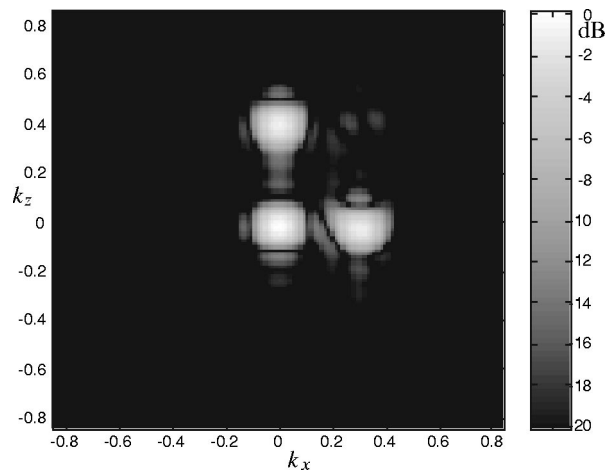


FIG. 6. Simulated images of three uncorrelated sources with cross-correlation beamsteering of the T-shaped cross array of Fig. 5.

computed, for all combinations of x and z indices. These cross-spectra were averaged by numerically integrating over a frequency range of 1/3 octave band around 2 kHz. This results in a BT product of 172, giving an estimated error in the average intensity level of 0.6 dB with a 95% confidence limit. These integrated complex spectrum values are used as samples of the two-dimensional spatial cross-spectrum function, according to the theory of Sec. II B. With this procedure it is assumed that all frequency components from one source result in the same phase component, which is not exactly true, but the errors are negligible for the given array length and frequency interval.

The spatial cross-spectrum is further preprocessed with a focussing operator that compensates for the fact that the sources are at a finite distance from the microphone array. The focussing is carried out by compensation of the phase differences that occur for a source at the position $(0, 0, 5.94)$. Next, the complex-conjugate property of Eq. (18) is applied to obtain the spatial cross-spectrum data that correspond with the missing microphones along the z axis. The spatial cross-spectrum is weighted with a two-dimensional Hanning window, zero padding is applied to obtain a 128×128 matrix (this acts as an interpolator after transformation), and the matrix is Fourier transformed to the k_x - k_z - f domain. Finally the result is scaled and converted to decibels and plotted in Fig. 6.

IV. MEASUREMENTS

A. Laboratory measurements

Measurements were carried out in an anechoic room with the same setup as the last simulation of the preceding section. The three sources were small loudspeakers, fed with uncorrelated broadband noise. The microphone signals of the T-shaped array were fed to a 48 channel digital signal acquisition system. A 11 025 Hz sample frequency was used and the simultaneously sampled signals were recorded on disk. All microphone channels were calibrated to compensate for amplitude and phase errors. Further processing was carried out in the same way as outlined in the previous section. The results are shown in Fig. 7. Comparison of Figs. 6 and 7

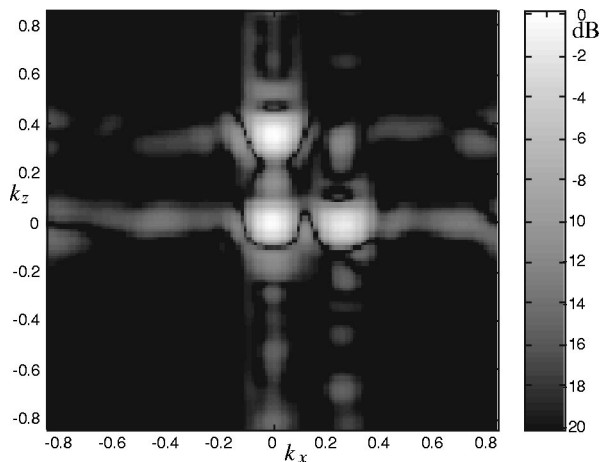


FIG. 7. Measured images of three uncorrelated sources with cross-correlation beamsteering of the T-shaped cross array of Fig. 5.

shows that the measurements correspond very well with the simulations. The measurements locate the sources at the correct positions and with the same resolution as the simulations. Differences occur at low levels, showing that the side lobes and background levels are different. This is mainly caused by small errors in the microphone positions and remaining amplitude and phase errors between the microphone signals.

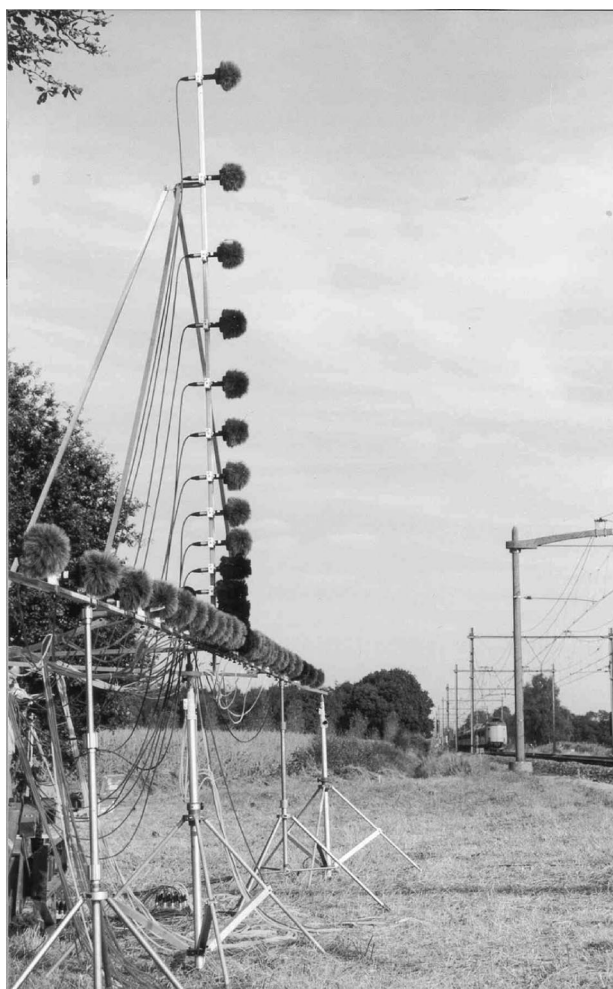


FIG. 8. The T-shaped cross array in use for measurements of a passing train.

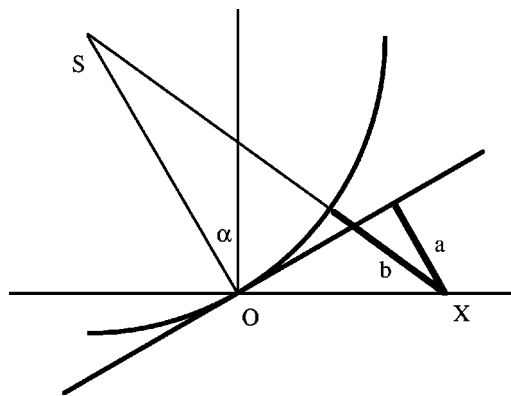


FIG. 9. Travel path differences a and b between a plane and a spherical wave from the same direction α as seen from the origin O of the array.

B. Practical measurements

A T-shaped array has been constructed to be used with a dedicated multichannel acquisition and data processing system for practical measurements. Results are presented of measurements on a high-speed passing train. For these measurements the system was optimized for analysis in the 500, 1000, and 2000 Hz octave bands. A total of 44 microphones were used with a microphone separation of 0.1 m. The x axis consisted of 31 microphones and the z axis consisted of 14 microphones (with one microphone common with the x axis). See Fig. 8.

The array was positioned at a distance of 7.35 m from the track and the train passed with a speed of 138 km/h, or 38.3 m/s. The software was adapted for this special situation by implementation of a swept focus technique. It is a combination of Doppler shift corrections to the array signals according to the propagation theory of moving sources²⁵ to make the passing noise sources appear to be standing still, and travel time corrections that make the spherical waves appear as plane waves.⁶ The latter method is easily explained for a one-dimensional array as shown in Fig. 9, which shows a spherical wave and a plane wave from the same direction as observed from the reference position O of the array. The travel time difference of both waves to the array microphone

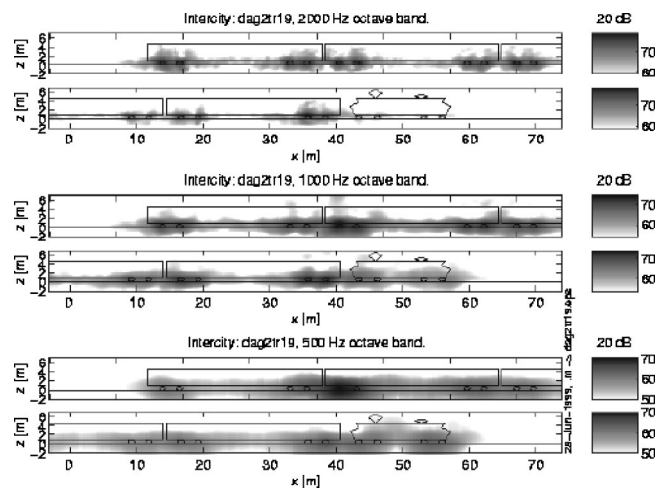


FIG. 10. T-array processed noise from a train passage (138 km/h). The array was at 7.35 m from the track as shown in Fig. 8.

at position X equals $(b-a)/c$, where a and b are shown in Fig. 9 and c is the sound velocity. By compensating for this travel time difference, the spherical wave appears to be a plane wave. After this precorrection a plane wave decomposition of the spatial correlation function of the wave field is carried out. In this way the area around the true focus point also appears to be in focus. The method was repeated for parts of the train with a length of 40 m each and an overlap of 20 m. The resulting two-dimensional images were added with a smooth weighting function, giving an acoustical image of the complete passing train. The results are presented for the three octave bands in Fig. 10. Notice that the emitted noise is dominated by wheel and rail noise.

V. CONCLUSIONS

In this paper we have introduced a new method to calculate two-dimensional images of uncorrelated acoustic sources by means of a T-shaped cross array. The method is based on calculation of the spatial cross-correlation function of the wave field, and use is made of the complex conjugate properties of the spatial cross-spectrum function for uncorrelated noise sources in the far field. It is shown by simulations and a laboratory measurement under anechoic conditions that the method is applicable to distinguish between spatially separated sources. The method is further illustrated with a practical measurement of a train, passing with high speed. In this case sharp images were obtained with a swept focus technique.

The benefit of the proposed method is that a relatively small number of microphones is needed, compared with direct beamsteering techniques which would require a full planar array of microphones. Application of direct beamsteering on the T-shaped array would result in much higher sidelobes and reduced resolution.

The proposed method is very well applicable to situations where a distinction has to be made between sources that are spatially distributed. It has been shown by example that the method is not restricted to sources in the far field. Because all measurements are taken simultaneously, the sources also do not need to be stationary in time. The method can be calibrated to find the true emission spectra or rms values of the sound pressures of the separate sources at the microphone array by integration over the main lobes in the wave number domain of the spatial correlation function.

¹H. F. Olson, "Directional Microphones," *J. Audio Eng. Soc.* **15**(4), 420–424 (1967).

²S. Wahlström, "The parabolic reflector as an acoustical amplifier," *J. Audio Eng. Soc.* **33**, 418–429 (1985).

³J. Billingsley and R. Kinns, "The acoustic telescope," *J. Sound Vib.* **48**, 485–510 (1976).

⁴M. J. Fisher, M. Harper-Bourne, and S. A. L. Glegg, "Jet engine noise source localization: The polar correlation technique," *J. Sound Vib.* **51**, 23–54 (1977).

⁵M. M. Boone and A. J. Berkhout, "Theory and applications of a high-resolution synthetic acoustic antenna for industrial noise measurement," *Noise Control Eng. J.* **23**, 60–68 (1984).

⁶M. M. Boone, Ph.D. thesis, TU-Delft, 1987.

⁷B. Barsikow, W. F. King III, and E. Pfizenmaier, "Wheel/rail noise generated by a high-speed train investigated with a line array of microphones," *J. Sound Vib.* **118**, 99–122 (1987).

⁸A. J. Berkhout, *Seismic Migration*, 3rd ed. (Elsevier Scientific, Amsterdam, 1985).

⁹M. I. Skolnik, *Radar Handbook* (McGraw-Hill, New York, 1970).

¹⁰A. B. Baggeroer, *Applications of Digital Signal Processing: Sonar Signal Processing* (Prentice-Hall, Englewood Cliffs, NJ, 1978).

¹¹*Synthesis Imaging in Radio Astronomy* (Astronomical Society of the Pacific, San Francisco, 1989).

¹²J. Capon, "High-resolution frequency-wavenumber spectrum analysis," *Proc. IEEE* **57**, 1408–1418 (1969).

¹³R. O. Schmidt, Ph.D. thesis, Stanford University, 1982.

¹⁴A. H. Nuttall, G. C. Carter, and E. M. Montavon, "Estimation of the two-dimensional spectrum of the space-time noise field of a sparse line array," *J. Acoust. Soc. Am.* **55**, 1034–1041 (1974).

¹⁵J. D. Maynard, E. G. Williams, and Y. Lee, "Nearfield acoustic holography: I. Theory of generalized holography and the development of NAH," *J. Acoust. Soc. Am.* **78**, 1395–1413 (1985).

¹⁶E. G. Williams and H. D. Dardy, "Generalized nearfield acoustical holography for cylindrical geometry: Theory and experiment," *J. Acoust. Soc. Am.* **81**, 389–407 (1987).

¹⁷J. Hald, "STSF - a unique technique for scan-based Near-field Acoustic Holography without restrictions on coherence," *Brüel&Kjær Technical Review No. 1*, pp. 1–50 (1989).

¹⁸J. Hamet, M. Pallas, and K. P. Schmitz, Deufrako-1: Microphone array techniques used to locate acoustic sources on ICE, TGV-A and TRANSRAPID 07, presented at *Internoise 94*, Yokohama, Japan, 1994.

¹⁹B. Barsikow, "Experiences with various configurations of microphone arrays used to locate sound sources on railway trains operated by the DB AG," *J. Sound Vib.* **193**, 283–293 (1996).

²⁰R. P. Dougherty, Source location with sparse acoustic arrays: Interference cancellation, presented at *First ASC Workshop*, DNW, Noordoostpolder, The Netherlands, 1997.

²¹W. M. Humphreys, Jr., T. F. Brooks, W. W. Hunter, Jr., and K. R. Meadows, Design and use of microphone directional arrays for aeroacoustic measurements, presented at *36th Aerospace Sciences Meeting & Exhibit*, Reno, NV, AIAA 98-0471, 1998.

²²U. Michel, B. Barsikow, J. Helbig, and M. Hellmig, Flyover noise measurements on landing aircraft with a microphone array, presented at *4th AIAA/CEAS Aeroacoustics Conference*, Toulouse, France, 1998.

²³P. F. Wang, P. Davies, and H. Takata, 2-D Sensor array configurations and its use in noise source visualisation, presented at *Internoise 95*, Newport Beach, 1995.

²⁴G. Elias, "Source localization with a two-dimensional focused array: optimal signal processing for a cross-shaped array," presented at *Internoise 95*, Newport Beach, 1995.

²⁵A. D. Pierce, *Acoustics: An Introduction to Its Physical Principles and Applications* (McGraw-Hill, New York, 1981), p. 453.

Target parameter estimation using resonance scattering analysis applied to air-filled, cylindrical shells in water

A. Tesei, W. L. J. Fox,^{a)} A. Maguer,^{b)} and A. Løvrik^{c)}

SACLANT Undersea Research Centre, Viale San Bartolomeo 400, 19138, La Spezia, Italy

(Received 7 July 1998; revised 26 June 2000; accepted 26 July 2000)

Current research on classification of submerged objects is concerned with using broadband sonar signals to insonify the targets, and applying signal-processing techniques to the backscattered signals. One characteristic of target echoes which may provide classification clues is the so-called resonance scattering response, the characteristics of which depend on target elastic properties. This paper presents algorithms for extracting resonance information based on autoregressive (AR) spectral estimation techniques. The AR-based representation is useful for detecting and accurately localizing resonances in the frequency domain. The extracted resonance frequencies are grouped into identified wave families, and processed in order to characterize the scatterer in terms of elastic and geometrical parameters on the basis of equations derived from resonance scattering theory. The targets considered are water-loaded elastic, cylindrical, thin-walled shells immersed in salt water under free-field conditions. Analysis was performed on data collected at sea at low-intermediate frequencies [$ka \in (0,50)$] and provided good results. The proposed approach is a first step towards the characterization of more complex targets either lying proud on the seabed or buried in bottom sediments. © 2000 Acoustical Society of America. [S0001-4966(00)01111-5]

PACS numbers: 43.60.Pt, 43.40.Ey, 43.20.Tb [JCB]

LIST OF SYMBOLS

f	frequency	ρ_o	outer fluid density
r	range	c_o	outer fluid sound speed
a	shell outer radius	$k = 2\pi f/c_o$	wave number
b	shell inner radius	$\epsilon_i; \epsilon_0 = 1, \epsilon_i = 2$	Neumann factor
$d = a - b$	shell thickness	(for $i > 0$)	
ρ	shell material density	c_g^l	group speed of the surface wave l
c_p	shell material compressional speed	c_{ph}^l	phase speed of the surface wave l
c_s	shell material shear speed		

I. INTRODUCTION

This work applies direct and inverse acoustic scattering theory to the characterization and classification of submerged elastic objects via geometrical and physical parameter estimation. The analysis presented concerns broadband acoustic scattering at low-intermediate frequencies [$ka \in (0,50)$] by elastic manmade objects in the free field. The investigation is limited to fluid-loaded, air-filled (or empty), circular cylindrical shells insonified at broadside aspect (aspect angle refers to the angle between the direction of incidence and the cylinder axis). The analysis is based on theoretical considerations derived from resonance scattering theory (RST),^{1,2} specifically regarding *far-field backscattering by infinite circular cylindrical targets excited by plane waves at normal incidence*. The scattered acoustic pressure consists of two

main contributions: a nonresonant background that varies smoothly with frequency, and a resonance component characterized by a series of echoes corresponding to resonance frequencies. RST is the study of the relation between the resonance frequencies of the target response and the peripheral waves traveling around the target. The nature and frequency behavior of the generated waves depend on the geometrical and elastic properties of the target.

In the case study proposed here, the target is of finite length, but the receiver is close enough to the target so that the cylinder end effects on the backscattered response can be considered negligible for $f > 4$ kHz.³ The constraints that must be satisfied (at least approximately) for maintaining the validity of the selected theory are the hypotheses concerning the target shape (a circular shell), the incidence angle (roughly $\pm 5^\circ$ around normal incidence⁴) and the shell inner medium (vacuum or air).

II. RESONANCE SCATTERING THEORY

The mathematical approach of RST^{1,2} is based on the normal-mode series formulation of the scatterer transfer function (TF), namely $H(\cdot)$, at normal incidence as²

^{a)}Currently at Applied Physics Laboratory, 1013 NE 40th St., Seattle, WA 98105-6698.

^{b)}Currently at Thomson Marconi Sonar PTY, 274 Victoria Road, Rydalmere NSW 2116, Australia.

^{c)}Currently at Kongsberg Defense Aerospace AS, P.O. Box 1003, N-3601 Kongsberg, Norway.

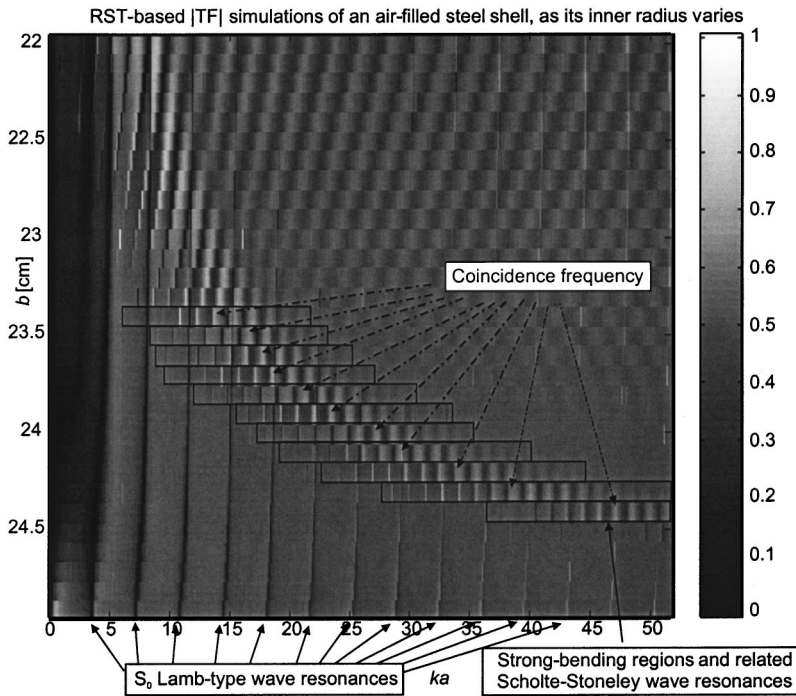


FIG. 1. Scattering TF spectrum $|H(ka)|$ of an air-filled steel in sea water (linear scale); $a=25$ cm, $b \in [22,24.9]$ cm, $\Delta b=0.1$ cm. Nominal steel parameters used: $c_s=3240$ m/s, $c_p=5950$ m/s, $\rho=7.7$ g/cm³. Some examples of features are outlined.

$$H(\cdot) = \left(\frac{a}{2r} \right) \sum_{i=0}^{\infty} \epsilon_i (j\pi ka)^{-1/2} \frac{D_i^1(\omega)}{D_i(\omega)}, \quad (2.1)$$

where $D_i^1(\omega)$ and $D_i(\omega)$ are determinants computed from the boundary conditions of the problem, and depend on all the mechanical and geometrical parameters of the target shell and of the physical properties of the outer (sea water) and inner (air) media. It is known² that the zeros of $D_i(\omega)$ correspond to shell resonance frequencies, generated by the surface acoustic waves of different types circulating around the target cross section. The frequency behavior of a generic peripheral wave l in terms of target geometrical and elastic parameters is well described by the dispersion curves of its group and phase speeds, c_g^l and c_{ph}^l , respectively.⁵ It may be deduced that the study of elastic wave properties in terms of target parameters can be applied to target characterization. Investigations have focused on the TF of a scatterer, because resonance frequency location is the information of concern.

A. Feature selection and physical interpretation

Figure 1 presents a case which is taken as a reference for the interpretation of scattering phenomena. It consists of the simulated TF modulus $|H(ka)|$ of a water-loaded, steel, air-filled shell with fixed outer radius a and variable inner radius b . Scattering by thick- and thin-walled shells is characterized by different physical phenomena.⁶ Shell-wall thickness is relative to the incident pulse wavelength. Here, we focus the analysis on shells with quasithin to very thin walls ($d \in [1,30]$ mm) in the frequency range $f \in (0,50]$ kHz, which corresponds to $ka \in (0,51.6370]$ given the outer radius fixed to 25 cm and the outer medium sound speed c_0 equal to 1521 m/s. The following subsections describe specific features outlined in Fig. 1 which are selected as significant for inversion.

1. Lamb-type waves

The Lamb-type waves are a class of shell-borne surface waves revolving around a thin-walled shell in the target material. In the selected frequency range, only the zero-order symmetric and asymmetric Lamb-type waves can be detected. The *symmetric Lamb-type waves of zero order* (S_0) are analyzed as evident in the TF modulus and usually identifiable as distinct, equally spaced dips. The near-constant distance between adjacent resonance frequencies derives from the fact that this wave family is almost nondispersive, only slightly attenuated by reradiation into the loading fluid. Resonance therefore corresponds to dips among the sharpest and deepest of the TF spectrum and, for very thin-walled shells (for which no other resonance phenomenon is evident in the same range), among the easiest to detect and identify (see Fig. 1). Dip location in frequency is nearly constant as the wall thickness and the properties of the outer medium vary, but does depend on the shell material parameters, c_s and c_p , and on the outer radius.

The *asymmetric zero-order* family A_0 is subsonic from very low frequency up to the so-called coincidence frequency, and supersonic at higher frequencies.⁷ As its energy is damped very quickly outside the shell, however, its contribution to backscattering is minimal.

2. Scholte–Stoneley waves and coincidence frequency

The *Scholte–Stoneley waves*, also called A waves because of the asymmetric nature of the corresponding waves generated in the plane-plate case,² are fluid borne and travel around the target cross section at the shell–fluid interface with a phase speed always subsonic but asymptotically approaching c_0 . Around the coincidence frequency, where the phase speed of the Scholte–Stoneley wave family ap-

proaches the phase speed of the A_0 Lamb-type waves, the TF amplitude increases and reaches its maximum. This means that at the coincidence frequency, the two types of waves travel in phase. At higher frequencies, the A_0 wave phase speed further increases, hence deviating from the Scholte–Stoneley wave phase speed, which remains subsonic. This causes a gradual TF amplitude decrease.⁸

The frequency window, characterized by the above-mentioned energy enhancement and by a sequence of dip/peak pairs having a roughly Gaussian envelope spread, is called the *strong-bending region* (Fig. 1). In this window, at frequencies lower than the coincidence frequency, the A_0 wave resonances are highly attenuated by radiation into the outer fluid and provide very weak energy contribution to the scatterer TF. The Scholte–Stoneley waves, however, are almost unattenuated and are identifiable with the very sharp discontinuities at the beginning of the strong-bending region and with the smooth peak–dip pairs around the coincidence frequency. The distance between adjacent resonances is essentially constant with f around the coincidence frequency. It depends strongly on the outer medium and on the outer radius, while it is roughly constant as the inner radius and shell material vary.

The frequency width of the strong-bending domain is nearly constant as a function of the inner radius. Its location and the coincidence frequency vary not only with the outer medium, but also with the shell-wall thickness. In particular, they shift to higher frequencies for thinner walls, and appear at very low frequencies for intermediate thickness (see Fig. 1). Further, the coincidence frequency varies with the outer medium and the shell material shear speed, but is nearly constant with the shell material density and compressional speed. The strong-bending region, the related resonances, and the coincidence frequency are particularly evident in the case of thin-walled shells, but may be difficult to detect either when they fall at low frequencies for possible interference with S_0 wave modes or when walls are so thin that they are beyond the range of interest (i.e., here for $ka > 50$).

B. Matching models between TF features and target parameters

A list of selected theoretical equations and empirical matching models, linking resonance analysis with target geometrical and physical parameters, is now presented and discussed. The models are characterized by analytical simplicity and easy applicability to real data.

1. Outer radius estimation

For estimating the outer radius from resonance scattering analysis, a set of at least three resonance frequencies belonging to the Scholte–Stoneley wave family must be detected in the examined frequency range. This is a critical point, as the location of the strong-bending region varies significantly with wall thickness, material, and outer medium. The higher the number of the wave frequencies detected, the higher the robustness and accuracy of the estimate.

The numerical property to extract from these features is the frequency distance Δf_n^A between adjacent modes of or-

ders n and $(n-1)$. As adjacent Scholte–Stoneley resonance frequencies are roughly equidistant where they can be detected, i.e., when they tend to approach the outer fluid sound speed, an average distance Δf^A computed on a set of distances between adjacent resonances can be used in order to make feature extraction more robust. Starting from the known property that Scholte–Stoneley waves travel around the target outer interface in the outer fluid, the following equation between Δf^A and a has been built by equating the Scholte–Stoneley wave group speeds of a reference and an unknown shell:

$$a \approx \frac{c_o K_{\text{ref}}}{\Delta f^A 2\pi}, \quad (2.2)$$

where K_{ref} is computed on the basis of a reference case (generally simulated) in which each quantity is known, i.e.,

$$K_{\text{ref}} = \frac{\Delta f_{\text{ref}}^A 2\pi a_{\text{ref}}}{c_{o,\text{ref}}}. \quad (2.3)$$

The radius estimate can be computed more precisely if $c_{o,\text{ref}}$ is chosen close to c_o .

2. Shell material estimation

From the detection and identification of S_0 frequency modes $f_n^{S_0}$ ($n = 1, 2, \dots$), and the estimate of the distance $\Delta f_n^{S_0}$ between adjacent frequencies of modal orders n and $(n-1)$, one property of the shell material can be estimated from the following equation:

$$c_* \approx c_{g,n}^{S_0} \approx 2\pi a \Delta f_n^{S_0}, \quad (2.4)$$

where the outer radius a must be known, and c_* is the shell material membrane speed, defined as a combination of the longitudinal and shear speeds

$$c_* = 2 \frac{c_s}{c_p} \sqrt{c_p^2 - c_s^2}. \quad (2.5)$$

When c_* is estimated by Eq. (2.4), the material for which the characteristic speed is closest to the estimated value is selected as the shell material. For steel the c_* value is 5435 m/s. If the phase speed is introduced, Eq. (2.4) can be replaced by

$$f_n^{S_0} = \frac{nc_{ph,n}^{S_0}}{2\pi a} \approx \frac{nc_*}{2\pi a}. \quad (2.6)$$

The equations above reflect the well-known property of near nondispersiveness of the S_0 waves. Hence, an average distance $\Delta f_n^{S_0}$ between adjacent resonances can replace $\Delta f_n^{S_0}$ in Eq. (2.4), which makes the estimate more robust to resonance measurement inaccuracy

$$c_* \approx 2\pi a \Delta f^{S_0}, \quad (2.7)$$

where the modal order identification is not required.

3. Shell thickness estimation

The method used here for thickness estimation starts from the localization of the maximum energy peak f^{me} inside the strong-bending region, which approximately corresponds

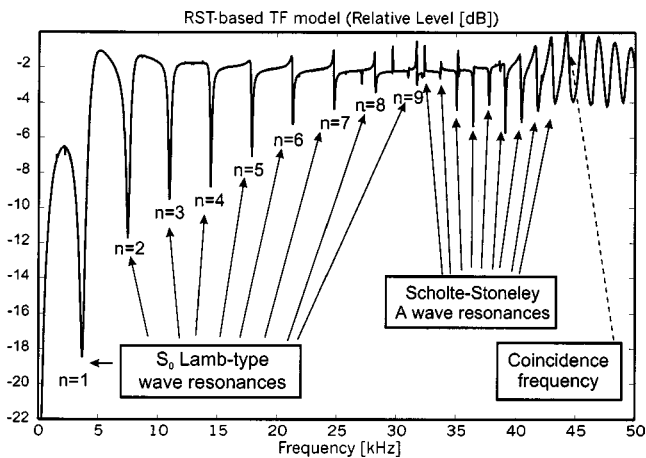


FIG. 2. Simulated scattering by an air-filled, steel shell at broadside in sea water.

to the coincidence frequency f^c . From the empirical matching model proposed in Ref. 8 for thin, air-filled, aluminum, steel, and similar shells, the following formula, independent from a , directly follows:

$$d \approx \frac{c_o}{2\pi f^{me}}. \quad (2.8)$$

C. Model of a reference scattering response

According to the selected approach a known case is needed as a reference. Figure 2 plots the ideal TF spectrum of a steel, air-filled, thin-walled shell with $a=25$ cm and $b=24.4$ cm. The plot represents a section of Fig. 1, and the selected features are outlined. In particular, from the localization of the Scholte–Stoneley resonance frequencies, the constant quantity K_{ref} [useful for outer radius estimates according to Eq. (2.2)] can be computed through Eq. (2.3) as $K_{ref}=1.3904$. The dispersion curves of the Scholte–Stoneley waves can be estimated, given a set of wave resonances in terms of their location and modal order (see Fig. 3). The plane-plate theory (PPT) dispersion curves are plotted for comparison. They are derived from the analytical solution of the vibration of a thin plane steel plate having the same

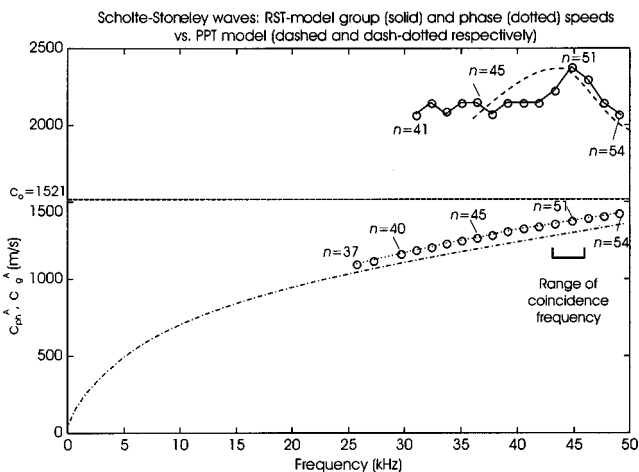


FIG. 3. Estimated group and phase dispersion curves of the A waves. Some estimated modal orders n are included (circles).

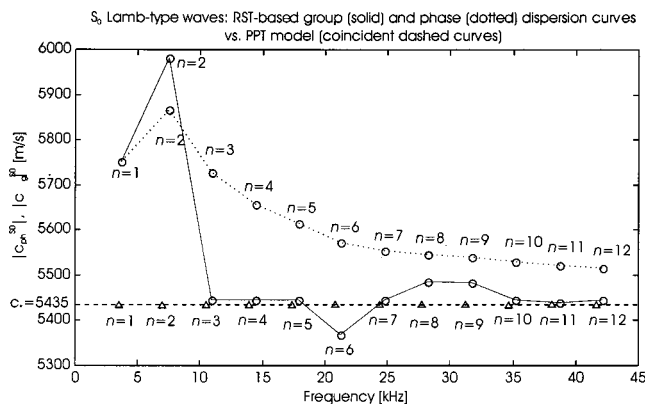


FIG. 4. Group and phase dispersion curves of the S_0 Lamb-type waves. Modal orders n are included.

thickness and being water loaded at one side and dry at the other. The group dispersion curve presents a mode around the coincidence frequency, which is confirmed by other authors (e.g., Ref. 9). Analogously, the S_0 Lamb-type wave phase and group dispersion curves are computed. Figure 4 presents the plots compared with the corresponding dispersion curves derived from PPT.¹⁰ The solution obtained from the RST-based model approximates the plate theory as the frequency increases, while in the low-frequency range, the dispersion appears more significant. A possible justification is that applying the plane-plate theory to the study of a circular shell implies neglecting the curvature effect, which causes the wave attenuation to increase due to a stronger reradiation into the outer fluid. The plots presented and their comparison would suggest the application of Eq. (2.7) to S_0 wave resonances with $n > 2$. Moreover, because of the better agreement of the two theories on the group speed dispersion curves, it is confirmed that Eq. (2.7) should be more robust than Eq. (2.6), being independent from n and, hence, in this case, from the contribution of wave attenuation to the wave frequency characteristics.

III. AUTOREGRESSIVE-BASED METHODS OF DATA REPRESENTATION

A. ARMA-based parametric approaches to data representation

In Sec. II the scattering response of an elastic object has been represented according to RST as the linear superposition of an infinite number of modes, each characterized by a frequency-dependent coefficient [see Eq. (2.1)]. Each coefficient has been represented as the ratio of two determinants expressed in terms of all the elastic properties of the scatterer. In Ref. 2 the modal resonances have been proven to correspond to the poles of each coefficient. As most of the features selected in Sec. II that are significant for target characterization are based on the detection and localization of resonance frequencies, a useful method for representing scattered data should allow one to easily compute the TF poles. A possible solution is to describe the scatterer as a linear time-invariant (LTI) discrete-time system, and represent its TF with a parametric model. On the basis of the above considerations derived from RST, the models discussed here are

the *rational* TF models, which are explicitly formulated in terms of the set of TF poles in the z plane. Unattenuated resonances are defined as those poles of the TF of an LTI discrete-time system that lie on the unit circle in the z domain. An input driving sequence $u[m]$ (where $m=1,\dots,M$ denotes the discrete time index) and the corresponding output series $y[m]$ that must model the data are related by the linear constant-coefficient difference equation

$$\sum_{i=0}^p a[i]y[m-i] = \sum_{i=0}^q b[i]u[m-i], \quad (3.1)$$

with $a[0]=1$. This most general linear model (with both the orders p and q different from 0) is called autoregressive moving average (ARMA), particular cases of which are the autoregressive (AR) model if $q=0$, and the moving-average (MA) model if $p=0$.¹¹ The properties of LTI systems represented by an equation like Eq. (3.1) are best described by the z -transform relationship

$$\left(\sum_{i=0}^p a[i]z^{-i} \right) Y(z) = \left(\sum_{i=0}^q b[i]z^{-i} \right) U(z), \quad (3.2)$$

where $z=e^{j\omega}$, if a unit sampling interval is assumed. Hence, the system transfer function $H(z)$ for the process of Eq. (3.1) is the rational function

$$H(z) = \frac{B(z)}{A(z)}, \quad (3.3)$$

where $A(z)$ and $B(z)$ are the z transform of the AR and MA branches, respectively,

$$A(z) = \sum_{i=0}^p a[i]z^{-i}, \quad B(z) = \sum_{i=0}^q b[i]z^{-i}. \quad (3.4)$$

It is assumed that $A(z)$ has all its zeros within (or, at least, on) the unit circle of the z plane. This guarantees that $H(z)$ is stable (asymptotically, if one or more zeros lie on the unit circle) and causal. As a real impulse response is to be modeled, all complex poles (or zeros) included in the TF rational pattern imply the presence of their respective complex conjugates among the poles (or zeros). Parametric modeling is particularly useful for representing signals characterized by a set of peaks/dips in very close vicinity in the frequency domain, as it can provide higher frequency resolution of the spectral estimate than FFT-based nonparametric methods, given the number of input time samples.¹¹

B. ARMA models applied to acoustic scattering

From the theoretical RST analysis of acoustic scattering,^{2,12} it is clear that a scattering frequency response presents both poles and zeros. While poles are fundamental for extracting resonances, zeros generally influence the spectrum global shape and some of them correspond to the frequencies of the generated creeping waves revolving around the target in the outer fluid. This means that the best scattering model is of the ARMA type. Nevertheless, from the results of feature selection proposed in Sec. II, attention is limited to detecting and accurately localizing the resonances. In this case, AR models are addressed as they are more

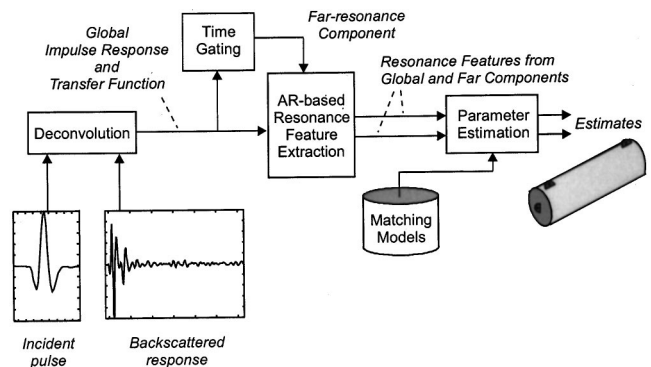


FIG. 5. Block diagram of the selected processing steps.

straightforward. A crucial aspect of AR modeling optimization is the determination of the polynomial order p . In the literature, various methods exist;¹¹ a cross-validation method is used to compare different AR-model structures as p varies. The method for selecting the optimal structure is the well-known Akaike's information theoretic criterion (AIC).¹¹ It consists of the minimization of a cost functional with respect to the parameters of the structure. It requires the user to suggest possible ranges of variability of the structure. Once the parametric model (AR, MA, or ARMA) and its polynomial order(s) are fixed, many parameter estimation algorithms exist for building the optimal representation of the signal sequence examined. In the present work, focused on modeling a system on the basis of known output and input data sequences, the least-squares method is used.¹¹ It is suitable for high signal-to-noise ratio (SNR) values; otherwise, its accuracy can decay and more refined AR-based estimation techniques are preferred, such as the so-called principal component autoregressive (PCAR) method¹³ and its extension to modal analysis,¹⁴ which although more robust to noise, are more computationally intensive.

C. Proposed processing method of cylindrical target characterization

By using the AR-based technique of feature extraction and the analytical matching models presented in Sec. II, a method of data analysis has been developed, the block diagram of which is presented in Fig. 5. A preliminary nonparametric deconvolution phase is applied to the time response in order to recover an approximate impulse response (and corresponding TF) of the scattering system. Deconvolution requires a replica of the incident pulse as input and is computed in a broadband frequency range in which SNR is high in order to limit noise-increasing effects typical of deconvolution (the range [0.5, 46] kHz is used in this application). The selection of the best bandwidth to apply deconvolution is critical. Notice that the coincidence frequency is extracted from the TF spectral shape (see Secs. II A and II B), the accurate estimation of which is of great importance.

AR modeling is then applied to the deconvolved data in order to estimate the TF poles. In theory only the poles lying on the unit circle in the z plane are resonances of nondispersive waves. However, as they are generally damped and, in addition, their estimation is generally affected by error, a

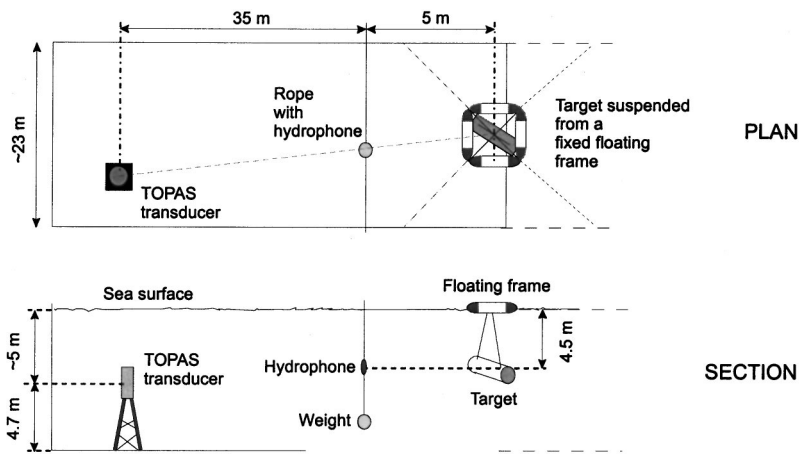


FIG. 6. Scheme of the experiment configuration in a basin (not to scale).

finite annulus is defined in the z plane: each couple of complex conjugated poles and each real-valued pole estimated to lie within the annulus correspond to a different resonance frequency. For this work the annulus is such that $0.95 \leq |z| \leq 1$. Once the scattered resonance frequencies are extracted among the poles, two subsets of resonances are identified as belonging to the S_0 Lamb-type waves and to the Scholte–Stoneley A waves, respectively. These two families are those most contributing to the scattering response as the S_0 waves are almost nondispersive in the whole frequency range where they are generated, and the A waves are extracted and processed only around the coincidence frequency, where they are less dispersive. The A_0 waves, being so highly dispersive as to be damped almost completely before the first target circumnavigation (and reradiation to the observer), do not contribute significantly to the target response and, in any case, give rise to resonances that are expected to lie out of the selected annulus.

The identification method applied to the extracted set of resonance poles is based on the criterion of constant distance between adjacent resonances belonging to the same wave family, as detailed in Ref. 15. The A -wave mode identification allows the outer radius estimation [from Eq. (2.2)], which, in turn, is used together with the localized S_0 resonance modes in Eq. (2.7) for the shell material estimation. If the material is estimated to be aluminum or similar and the coincidence frequency is localized, Eq. (2.8) is applied to determine the shell-wall thickness.

The same processing steps can be also applied to the *far-resonance* component of the scatterer impulse response, which is defined as the tail of the target response in time, and is obtained by applying a time gate so distant from the specular echo that the target background response is negligible. This response tail is characterized by low energy, and in many cases can be insufficiently long for allowing a high-resolution frequency analysis, but remains useful for isolating and hence, localizing resonances at intermediate frequencies, partially or completely concealed in the global spectra.¹⁵ The point at which to apply the time gate is computed by evaluating scattered energy variation over time.¹⁶ If the time series obtained is long enough, the exact time location of the gate is not a critical parameter for resonance-extraction accuracy. A separate AR model is applied for es-

timating the scattered resonances from this data segment, independently of the global response analysis. In this case, only the resonance features (and not those features derived from the TF shape) can be extracted; hence, the number of estimated target parameters will be less, but the absence of reflection and diffraction phenomena cut off by time gating may lead to more accurate localization of resonance frequencies, hence more accurate inversion results.

IV. APPLICATION OF ANALYSIS TO DATA SCATTERED BY A CYLINDRICAL SHELL IN SEA WATER

The proposed method was applied to acoustic scattering responses of air-filled, thin-walled steel shells measured at sea. The experimental geometry is sketched in Fig. 6 and detailed in Ref. 3. Targets consisted of steel, circular, cylindrical shells with flat ends 2 m long, outer radius $a = 25$ cm, inner radius $b = 24.4$ cm. The present analysis addresses an air-filled shell insonified at nominal broadside.

The inner and outer media properties and the target shape are *a priori* known. As incident acoustic signals, Ricker pulses with different central frequencies transmitted by a parametric array sonar (TOPAS PS 040)¹⁷ were selected. The frequency-domain plot of the pulse used (Fig. 7) was obtained by zero padding before FFT computation in order to show a smoother curve. This technique was applied,

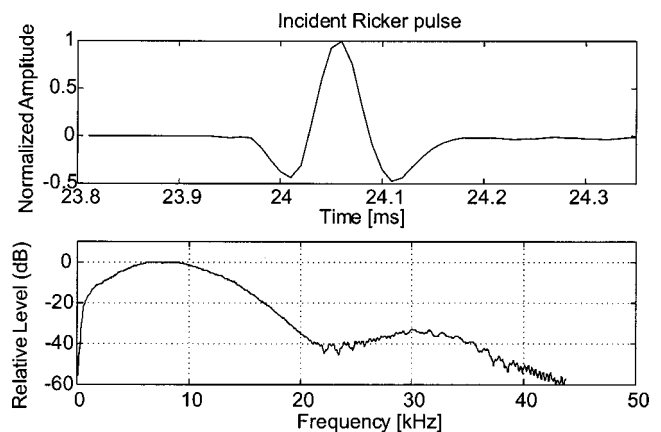


FIG. 7. Real incident Ricker pulse (time- and frequency domains).

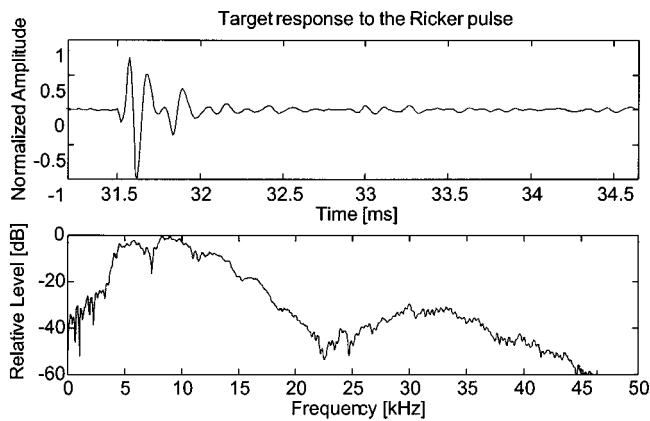


FIG. 8. Target response (time- and frequency domains).

when needed, to each time sequence analyzed. The incident pulses and scattered responses were averaged across 100 pings. The TOPAS generates secondary frequencies in the range [2,16] kHz by transmitting a broadband pulse near 40 kHz (primary frequency) and using the nonlinear properties of water. For this reason, two main spectral components, corresponding to the secondary and primary frequencies, can be seen in the spectrum plotted in Fig. 7. System filters have affected the overall frequency response. However, as the outgoing pulse is recorded on the same system as the scattered data, and the signal path is the same for both, we have all the information needed to estimate the scatterer TF. In the processing phases, even the primary frequency signal component was considered, in order to be able to test whether or not it could excite target resonance scattering. The frequency range [4,45] kHz was analyzed.

The target response to the selected incident pulse was simulated and used as a reference during the data analysis.³ Tests on real scattering data guided by a reference model allow validation of the used model which simplifies the real scattering system, validation of expectations as to the generation of certain resonance wave families and phenomena, and evaluation of capabilities and accuracy of resonance extraction AR-based method.

A. Analysis of deconvolved global response

The scattering response measured from the target is considered (see Fig. 8). From its spectrum it is clear that it consists of the response to the secondary pulse (centered

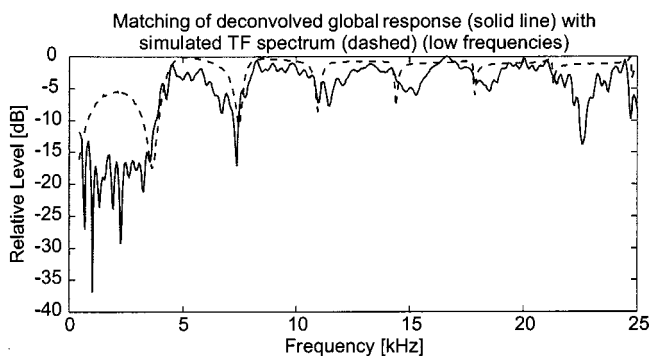


FIG. 9. Matching between predicted and estimated TF spectra in the low-frequency domain.

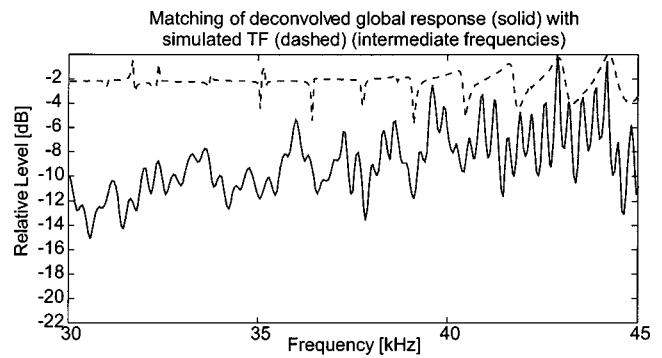


FIG. 10. Matching between predicted and estimated TF spectra at higher frequencies.

around 8 kHz), and to the primary pulse component. The SNR of the secondary frequency response is estimated to be roughly 25–30 dB, while the SNR of the primary frequency response component is around 20 dB less.

Fitting between the expected and estimated TF spectra (computed by FFT) is shown in Figs. 9 and 10. Resonance matching is in Figs. 11 and 12. The numerical results in terms of extracted feature characteristics and estimated parameters are reported in Table I, in which the estimates are denoted by the symbol $\hat{\cdot}$ and the nominally true values (known by construction) with a superscript “ \circ .”

If compared with the simulation, the measured spectrum is characterized by additional fluctuations. They may derive from scattering diffraction phenomena disregarded by the RST-based model (and influencing the TF *background* component). They might also be caused, for example, by the cylinder end caps, several external steel structures used for hanging and weighting the air-filled target, or two large steel plugs. Another cause of partial model-data mismatching might contribute to the *resonance* component and derive from shell cross-section and wall-thickness nonuniformities due to construction inaccuracies and the mentioned external structures. These phenomena increase the TF complexity and consequently the AR order p required to appropriately estimate the TF; hence, they make the interpretation and the resonance detection and identification less reliable. In particular, according to the considerations presented in Ref. 3, discrepancies between model and data for $f < 4$ kHz can derive mainly from the cylinder end effects. Model-data fitting in terms of the TF spectrum is better in the frequency range

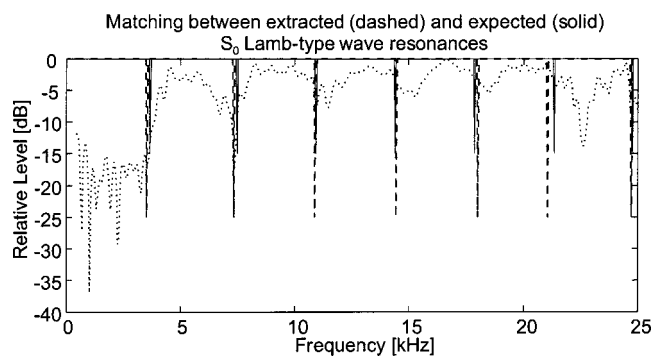


FIG. 11. Estimated TF (dotted) at low frequencies; estimated and expected S_0 Lamb-type wave resonances (AR model order $p = 110$).

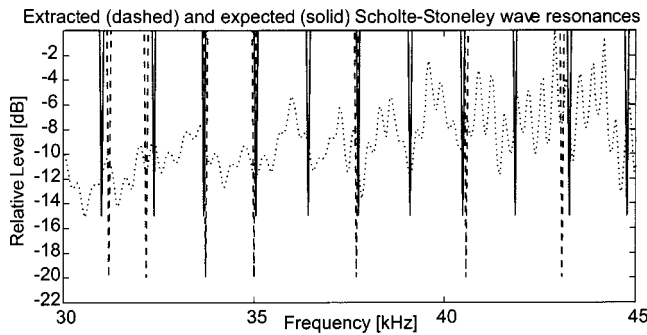


FIG. 12. Estimated TF (dotted) at higher frequencies, extracted and expected Scholte–Stoney wave resonances.

[4,25] kHz. At higher frequencies ($f \in [30,45]$ kHz) curve fitting is poor, but around 45 kHz the shape (although not the relative level) of the strong-bending region is approximately recovered, which is an important result for feature extraction purposes.

In the range $f \in [4,25]$ kHz, where S_0 Lamb-type waves are examined (see Fig. 11), resonance fitting is accurate; hence, the shell material estimate may be considered reliable. However, even a small error in estimating the outer radius causes low confidence in the shell material classification. Hence, the relation used is shown to be very sensitive to minor changes of outer radius, which constitutes a significant limitation.

At intermediate frequencies, only some Scholte–Stoney wave resonances fit the modeled resonances well (Fig. 12). The detection of a certain energy enhancement corresponding to the strong-bending region leads to a rough localization of the coincidence frequency, and hence, to the wall-thickness estimate. This result is achieved because matching with the ideal TF spectral shape confirms a good fit with the strong-bending region. Under uncontrolled experimental conditions, one might interpret this energy enhancement as the deconvolution side effect of noise-level enhancement, and thus, disregard it. For this reason, the thickness estimate is included with low confidence.

Scholte–Stoney resonance localization and identification lead to the estimation of the related phase-speed dispersion curve, plotted and fitted with the simulated curve (from Fig. 3) in Fig. 13. Curve fitting is good in a wide range. Scholte–Stoney wave resonances detected and matched correctly are too sparse to provide their group dispersion curve. The S_0 Lamb-type group and phase dispersion curves are presented in Fig. 14. The estimated curves compared with corresponding patterns derived from the analysis of the RST-based TF model (see Fig. 4) are computed on the basis of the true outer radius value a^o .

TABLE I. Estimation results from the global response.

Extracted feature	Estimated value	True value
$\Delta f^A = 1.327$ kHz	$\hat{a} = 25.36$ cm	$a^o = 25$ cm
$\Delta f^{S_0} = 3.471$ kHz	with $a^o: \hat{c}_* = 5452.7$ m/s, with $\hat{a}: \hat{c}_* = 5531.2$ m/s \Rightarrow material=steel (low confidence)	$c_*^o = 5435$ m/s \Rightarrow material=steel
$f^{me} = 44.459$ kHz	$\hat{d} = 5.4$ mm (low confidence)	$d^o = 6$ mm

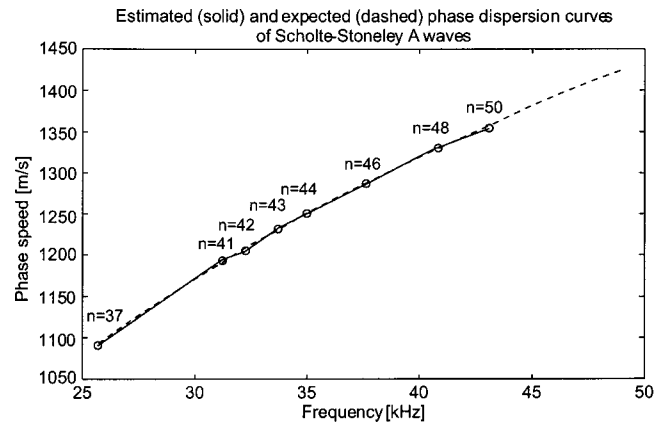


FIG. 13. Phase dispersion curve of the Scholte–Stoney wave resonances.

B. Analysis of deconvolved far-resonance response

The feasibility and advantages of far-resonance processing is analyzed here when the SNR level is appreciable but the data length is limited. Time gating allows isolation of the far resonance from the rigid (diffraction) response contributions, hence simplifying the TF shape. However, several spectral fluctuations remain (consequently the estimated p order is still high), in part because of the lower SNR value, and in part due to the resonance effects unexpected by RST and assumed to derive from the shell nonuniformity (as explained in Sec. IV A). Here, the time gate is applied at 32.38 ms (see Fig. 8 above). With reference to TF-pattern matching in Fig. 15, this component allows individualization of many of the peaks related to the S_0 Lamb-type wave resonances. S_0 Lamb-type resonance matching is shown in Fig. 16. Even at higher frequencies ($f > 25$ kHz), the estimated TF spec-

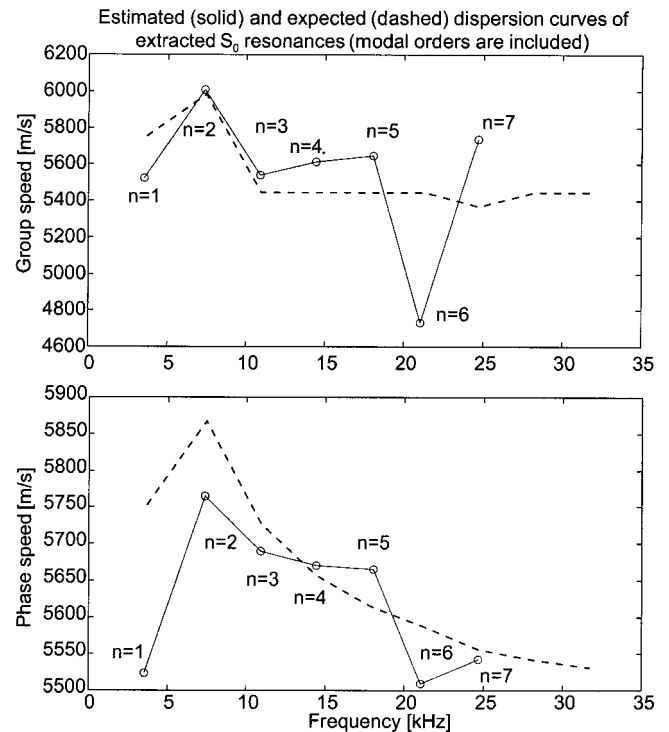


FIG. 14. Estimated S_0 Lamb-type group (up) and phase (down) dispersion curves.

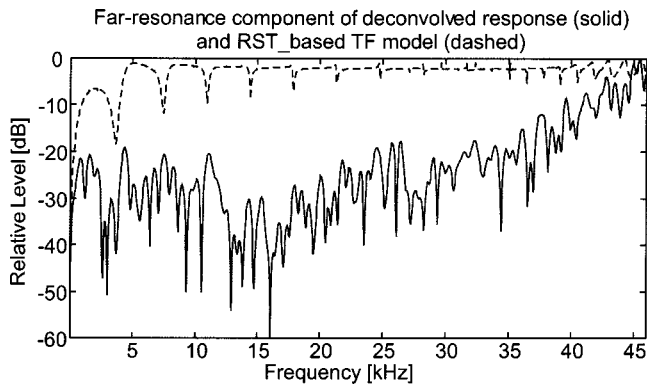


FIG. 15. Deconvolved far-resonance spectrum fitted with the TF model. Some resonances can be seen as peaks, as predicted.

trum is characterized by peaks roughly corresponding to the Scholte–Stoneley wave resonance (see Fig. 17). Few resonances are detected and well fitted (hence, the low-confidence level of the radius computation), but allow good estimates, summarized in Table II. In this case, resonance response isolation can be considered redundant, as good model-data fitting and parameter estimation results have been obtained by processing the global response. Decomposition is fundamental when global response analysis results are inadequate for resonance feature extraction, matching, and processing.

V. CONCLUSIONS AND FUTURE RESEARCH

A. Proposed method of feature selection and analysis

The main purpose of this study was to determine the applicability of resonance analysis to target characterization and classification. On the basis of analysis of experimental data fitted with RST modeling, this paper has shown that this kind of approach is not only feasible, but can provide accurate target parameter estimation. The results obtained are:

- (i) The generation of resonance phenomena and in particular, of some wave families, forecast by RST under ideal conditions, have been verified on at-sea data.
- (ii) The energy contribution of the generated resonance component from scattered data collected at sea was shown to be significant and has made high-resolution resonance analysis feasible and reliable in most cases.

Extracted (dashed) and predicted (solid) S_0 Lamb-type wave resonances (far-resonance component)

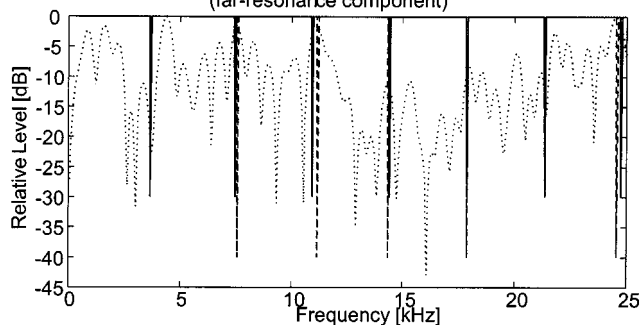


FIG. 16. Estimated and expected S_0 Lamb-type wave resonances (AR order $p = 100$), referred to the estimated TF (dotted).

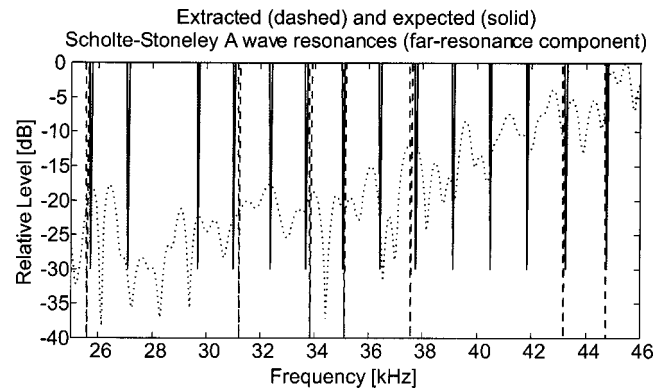


FIG. 17. Estimated Scholte–Stoneley wave resonances, matched with expected ones. Reference: estimated TF (dotted).

- (iii) Although the adopted RST-based model assumes a canonical cylindrical shell which is an approximation of the measured target, model-data matching in the frequency domain is acceptable in the broadband range [4,45] kHz, and has resulted in good parameter estimation.
- (iv) The number and accuracy of inversion results is also due to the *broadband* nature of the selected approach, which allows the extraction and processing of sets of resonances related to several target parameters; however, the frequency domain of interest varies with the elastic parameters of the inner and outer media, and with the shell material and wall thickness.

These observations justify the employment of the proposed model-based method for extracting resonance frequencies from scattered responses (see the next subsection) and for inversion. However, the assumption of *a priori* knowledge on the target shape, filler, and aspect (see also Sec. V C), the low confidence associated with estimation results when few resonances of a certain family are identified, and the sensitivity of shell material estimation to the outer radius estimation accuracy are among the main limitations.

B. The parametric approach to data representation

The proposed approach to data representation consists of preliminary deconvolution followed by AR-based modeling applied to the scatterer estimated impulse response. It has the significant advantage of also providing the scattering TF recovery, from which significant features can be used. Further, the recovered TF can be used as a guideline for selecting the most reliable resonance frequencies, which correspond to TF spectral troughs or peaks.

Although the TF of a scattering system should be represented by an ARMA model, the AR-based approach can be

TABLE II. Analysis of the response far resonance component.

Feature	Estimate	True value
$\Delta f^A = 1.3393$ kHz	$\hat{a} = 25.13$ cm	$a^o = 25$ cm
$\Delta f^{S_0} = 3.4531$ kHz	with $a^o: \hat{c}_* = 5424.0$ m/s,	$c_*^o = 5435$ m/s
	with $\hat{a}: \hat{c}_* = 5452.0$ m/s	\Rightarrow material=steel
	\Rightarrow material=steel	

sufficient for the extraction of the main resonances of the scattering field. Further, when signals are complicated and/or noisy, it is difficult to optimize the orders p and q of an ARMA model. In fact, this is the most suitable and immediate method for providing the poles of a system and, hence, the scatterer resonance frequencies. In any case, ARMA modeling may be taken as an extension of the present work, as including zeros in the parametric model can lead to more complete and more realistic data representation, as explained in Sec. III.

C. Future research

Research in the field of acoustic resonance scattering can be further investigated for the purposes of target characterization and classification, and extended to more complicated real cases. Further work will address the relaxation of imposed constraints:

- (1) extension of RST-based investigations to *shells filled with fluids* other than air (in particular, liquids);
- (2) extension to *multiple-aspect scattering analysis* which is expected to make the approach more robust and reliable and to extend its applicability; and
- (3) study of scattering by *natural objects and irregular complicated manmade objects*.

ACKNOWLEDGMENTS

Many thanks go to John Fawcett for his fundamental contribution to scattering modeling, the Engineering Tech-

nology Division, and the SACLANTCEN technicians for their help and availability in the experiment design and performance, and the Italian Navy for their support during the trial.

- ¹L. Flax, L. R. Dragonette, and H. Überall, *J. Acoust. Soc. Am.* **63**, 723–731 (1978).
- ²N. D. Veksler, *Resonance Acoustic Spectroscopy* (Springer, Berlin, 1993).
- ³W. L. J. Fox, J. A. Fawcett, D. Jourdain-Albonico, and A. Tesei, SM-331, SACLANT Undersea Research Centre, La Spezia, Italy (unpublished).
- ⁴J. D. Kaplunov and N. D. Veksler, *Acustica* **72**, 131–139 (1990).
- ⁵M. Talmant and G. Quentin, *J. Appl. Phys.* **63**, 1857–1863 (1988).
- ⁶E. D. Breitenbach, H. Überall, and K.-B. Yoo, *J. Acoust. Soc. Am.* **74**, 1267 (1983).
- ⁷L. R. Dragonette, C. F. Gaumont, D. H. Hughes, B. T. O'Connor, N.-C. Yen, and T. J. Yoder, *Proc. IEEE* **84**, 1249–1263 (1996).
- ⁸F. Magand and P. Chevret, *Acust. Acta Acust.* **82**, 707–716 (1996).
- ⁹J.-P. Sessarego, J. Sageloli, C. Gazanhes, and H. Überall, *J. Acoust. Soc. Am.* **101**, 135–142 (1997).
- ¹⁰G. Quentin and M. Talmant, in *Elastic Wave Propagation*, edited by M. F. McCarthy and M. A. Hayes (Elsevier Science, North-Holland, Amsterdam, 1989), pp. 477–482.
- ¹¹S. M. Kay, *Modern Spectral Estimation: Theory and Application* (Prentice-Hall, New York, 1988).
- ¹²G. C. Gaunard and D. Brill, *J. Acoust. Soc. Am.* **75**, 1680–1693 (1984).
- ¹³S. Kay, *Personal Eng.* **12**, 37–43 (1997).
- ¹⁴R. Kumaresan and D. W. Tufts, *IEEE Trans. Acoust., Speech, Signal Process.* **ASSP-30**, 833–840 (1982).
- ¹⁵A. Tesei, W. L. J. Fox, A. Maguer, and A. Løvik, SR-265, SACLANT Undersea Research Centre, La Spezia, Italy (unpublished).
- ¹⁶M. de Billy, *J. Acoust. Soc. Am.* **79**, 219–221 (1986).
- ¹⁷*Simrad TOPAS PS 040 Operator Manual*, Bentech Subsea AS, Stjørdal, Norway (1994).

Resolution of front-back confusion in virtual acoustic imaging systems

P. A. Hill, P. A. Nelson, and O. Kirkeby

Institute of Sound and Vibration Research, University of Southampton, SO17 1BJ, United Kingdom

H. Hamada

Department of Information and Communication Engineering, Tokyo Denki University, Tokyo 101, Japan

(Received 9 September 1998; revised 6 April 2000; accepted 8 September 2000)

A geometric model of the scattering of sound by the human head is used to generate a model of localization cues based on interaural time delay (ITD). The ITD is calculated in terms of the interaural cross-correlation function (IACC) for sources placed at a series of azimuthal angles in the horizontal plane. This model is used to simulate the pressures generated at the ears of a listener due to real sources and due to a two-channel and a four-channel virtual source imaging system. Results are presented in each case for the variation of ITD with head rotation. The simulations predict that the rate of change of the ITD with head rotation produced by a real source and replicated by the four-channel virtual source imaging system, cannot be replicated by the two-channel system. These changes to the ITD provide cues which allow resolution of front-back confusion. The results of subjective experiments are also presented for the three cases modeled. These results strongly support the findings from the modeling work indicating that, for the systems described here, front-back confusion is resolved through changes to the ITD arising from head motion. © 2000 Acoustical Society of America. [S0001-4966(00)03112-X]

PACS numbers: 43.60.Pt, 43.66.Qp, 43.38.Md [JCB]

I. INTRODUCTION

The duplex theory of sound localization, originating with Rayleigh,¹ has long been accepted as the dominant model of the way the human hearing system processes the cues presented by the surrounding environment. At its simplest level, this model separates the audible spectrum, for the purposes of localization, into two parts. In the lower frequency band, stretching from the lowest audible frequency to about 1.6 kHz, localization is dominated by the use of interaural time delays (ITD). In the upper frequency band, stretching from 1.6 kHz to the upper limit of hearing, localization is dominated by the use of interaural level differences (ILD). In addition to these simple cues, which originate from diffraction of sound around the head, there are also interaural envelope shifts and spectral cues originating from interaction of the incident sound with the pinna.² However, it is now generally accepted that the pinna spectral cues are associated with the discrimination of the angle of elevation of sources above or below the horizontal plane.³⁻⁶

The use of the cross-correlation function was first proposed by Jeffress⁷ as the mechanism by which the hearing system interprets ITD cues. Other authors, such as Lindemann,^{8,9} have expanded greatly on the original Jeffress cross-correlation model and have proposed more complex models, explaining other related phenomena such as the law of the first wavefront. Work has also been undertaken on the physiology of animals such as the barn owl¹⁰ and the cat¹¹ which has indicated that there is a neurological basis for this IACC-based model. The medial superior oliveary complex (MSO) has been identified as the region of the hindbrain associated with this function in mammals. It has also been demonstrated that there is an increased ability to localize

using ITD cues in mammals where this region is well developed.¹²

One of the well-known characteristics of the hearing system, when localizing sources on the horizontal plane, is the problem of "front-back confusion." This refers to instances where a subject localizes a source to the front that should be in the rear, or less commonly, to the rear when it should be in the front. Subjects maintain the ability to localize with the expected degree of accuracy for the prevailing conditions, yet the perceived location of a source is reflected in a vertical plane running through the ears. An example of this phenomenon would be where a source placed at 120° (where 0° is directly in front of the subject) was perceived as being at 60°. i.e., $90 \pm 30^\circ$. The early work of Wallach,¹³ Thurlow *et al.*,¹⁴ and Burger¹⁵ demonstrated experimentally that head movements play a very important role in the resolution of front-back confusions. Clearly it is the effect that head movements have on the ILD, ITD, and spectral cues that allow the hearing mechanism to use this movement to help resolve such errors. Leaky¹⁶ indicated analytically that, in this context, the changes in the ITD's are of much greater significance than changes in the ILD's. The work of Wallach¹³ on the importance of head movement in the resolution of front-back confusions has been recently supported by the experimental work of Wightman and Kistler.¹⁷ Interestingly, their work has indicated that head movement *per se* is not necessary and that similar results can be obtained through movement of the source under the control of the subject. The recent work of Perrett and Noble^{18,19} has also further supported this view. These authors show the importance of head rotation to the resolution of ambiguities in relation to elevation discrimination. Their work also shows

that this is a low-frequency effect and does not appear to occur for high-pass test signals.

This paper describes an investigation into the origins of differences between the performance of two multichannel virtual acoustic imaging systems with regard to the incidence of front-back confusions. These differences came to light during the course of subjective experimental work intended to characterize the performance of the two systems. This work is reported in full by Hill.²⁰

The work described here used a simple geometrical model of the scattering of sound by the human head to calculate the ITD for sources placed around the head. Calculation of the ITD was achieved using the interaural cross-correlation function (IACC). Results are presented from the simulation of a series of sources placed around a listener as well as from virtual source imaging systems using either two loudspeakers (placed to the front of the listener) or four loudspeakers (with two placed to the front and two placed to the rear of the listener). Subjective results based on these simulations are also presented together with simulated results of the effect of head rotation on the ITD as measured using the IACC function. The results from the subjective experiments correlate very well with the simulated ITD data, indicating that it is possible to predict accurately the prevalence of front-back confusion in a given set of experimental data from these simulations. This work indicates that in relation to the systems described here, the resolution of front-back confusion can be predicted through the changes in the ITD function resulting from head movement.

II. HEAD MODEL

The head model used here is based on a fixed rigid sphere in a free field.²⁰ Calculation of the pressure on the surface of a sphere due to a plane wave is from the analysis of this scattering problem presented by Rayleigh²¹ and reworked by Morse and Ingard,²² Malechi,²³ and Rschevkin.²⁴ This model has also been used in the context of sound localization by other authors such as Cooper²⁵ and Kuhn.²⁶

The pressure on the surface of the sphere is calculated according to the equation

$$p_t = -p_0 e^{j\omega t} \sum_{n=0}^{\infty} \frac{j^{n+1} (2n+1) (ka)^{-2} P_n(\cos \theta)}{j'_n(ka) - j n'_n(ka)}, \quad (1)$$

where $p_0 e^{j\omega t}$ represents the incident wave, $j'_n(ka)$ and $n'_n(ka)$ are, respectively, the first derivatives of the spherical Bessel and spherical Neuman functions of the first kind and of order n , the wave number is given by k , and a is the radius of the sphere, $P_n(\cos \theta)$ is the Legendre polynomial of order n , and θ is the angle of plane-wave incidence. The coordinate system used in this work is defined in Fig. 1. The radius of the sphere used in the simulation studies described below was chosen to be 8.75 m. The derivation of Eq. (1) from the analyses presented in Refs. 22–24 is presented in full in Ref. 20.

From the above expression it is possible to calculate the pressure at any point on the surface of a sphere due to an incident plane wave. In using this as a head model, the ears were simulated by calculating the pressures at a pair of

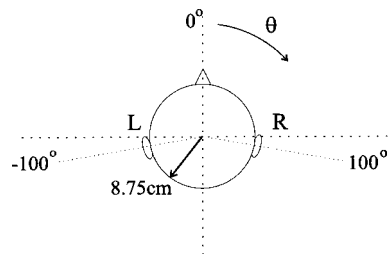


FIG. 1. Spherical head model showing coordinate system with sphere of radius 0.0875 m and location of ear positions at $\pm 100^\circ$.

points $\pm 100^\circ$ from straight in front, with no account being taken of the pinnae. The complex pressure was then computed at 256 discrete evenly distributed frequencies between 0 and 20 kHz and for a range of angles of plane-wave incidence from 0 to 360° in 5° increments. It was found that convergence of the summation could be achieved for all values in the desired frequency range if the first 50 terms were evaluated. The complex conjugate of each of the resulting 256 point frequency domain sequences was then reflected in the highest frequency point (the Nyquist frequency) to give a two-sided frequency domain representation. These 512 point sequences were then windowed using a Hanning window before inverse Fourier transformation into the time domain. Finally, an identical time delay was introduced into each sequence in order to shift the peak in the response into the center of the data window.

The resulting 72 left ear and 72 right ear pressure responses in the time domain formed a database of sphere model head related transfer functions (HRTF's) for sources on the horizontal plane. These left and right ear HRTF's form the basis of all of the modeling work described below and are referred to here as the "sphere model database." Figure 2 shows the impulse responses from the right ear of this database.

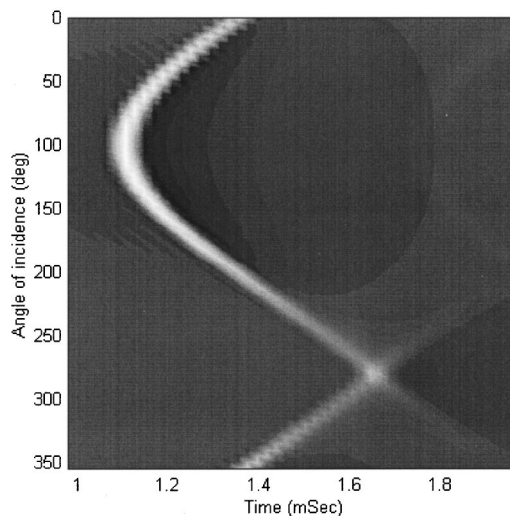


FIG. 2. Gray-scale plot of simulated data showing changes in the delay as the source is moved round the head. (Note: The gray scale is linear from 0 to +1 with these extremes being represented by black and white, respectively.)

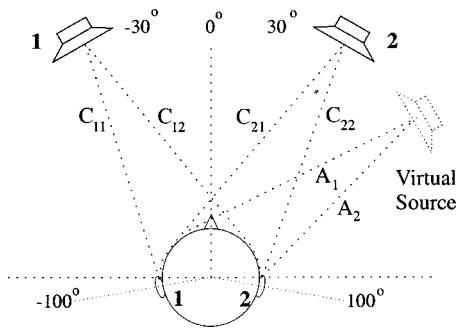


FIG. 3. Two-channel reproduction system showing source-to-ear transfer functions for both real and virtual sources.

III. REPRODUCTION SYSTEM

Two virtual source imaging systems were studied in both the simulation work and later in the subjective work. These systems are characterized by the number of inputs and outputs used in the system design. They are referred to as the “2by2 system” and the “4by4 system” and utilized two measurement points with two reproduction sources in the former case and four measurement points with four reproduction sources in the latter case. Figure 3 shows the layout of the 2by2 system. The objective of the system is to design the filters $H_1(z)$ and $H_2(z)$ that are used on the inputs to sources 1 and 2, respectively. These operate on the virtual source signal $U(z)$ in order to produce the time histories of the pressures at the listener’s ears that would be produced by the virtual source. Similarly for the four-channel system shown in Fig. 4, the objective is to design the filters $H_1(z)$, $H_2(z)$, $H_3(z)$, and $H_4(z)$.

The design of the filters for both of these systems was based on the fast Fourier transform (FFT)-based deconvolution method of Kirkeby *et al.*²⁷ This method provides a very efficient means of designing the digital filters for a multichannel sound reproduction system and a brief outline of the technique is given as follows. Here we restrict the analysis to the case of a single virtual source and refer to the general block diagram given in Fig. 5. It is assumed that this

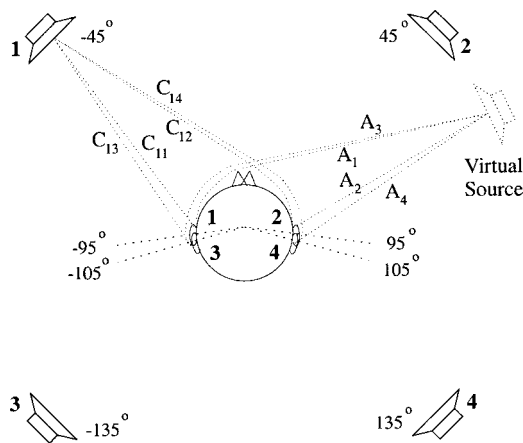


FIG. 4. Four-channel reproduction system showing source-to-ear transfer functions for both real and virtual sources. Both head positions used for the system definition are shown. (Note: For clarity only the source-to-ear transfer functions for reconstruction source 1 and the virtual source have been shown.)

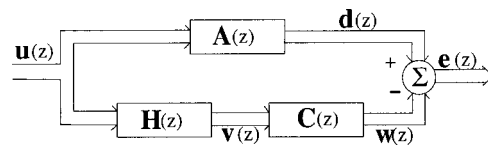


FIG. 5. Generalized block diagram of the inverse filtering problem, where $A(z)$ is the matrix of target functions, $C(z)$ is the electroacoustic transfer function matrix, $H(z)$ is the inverse filter matrix, $u(z)$ is the system input, and $e(z)$ is the error vector.

source, whose output signal we denote as $U(z)$, produces signals at R points in the region of the listener’s head and that these signals are represented by the elements of the vector $\mathbf{d}(z)$. We also denote the transfer functions that relate the signals comprising $\mathbf{d}(z)$, to the virtual source signal $U(z)$ by the vector $\mathbf{a}(z)$ such that $\mathbf{d}(z) = \mathbf{a}(z)U(z)$. We now assume that S sources are used to reproduce the field and that these sources produce the signals $\mathbf{w}(z)$ at the R points in the sound field. We denote the vector of source input signals by $\mathbf{v}(z)$ and the matrix of electroacoustic transfer functions between the source inputs and the reproduced signals as $\mathbf{C}(z)$ such that $\mathbf{w}(z) = \mathbf{C}(z)\mathbf{v}(z)$. The source inputs are in turn generated by operating on the virtual source signal $U(z)$ by the vector of filters $\mathbf{h}(z)$ whose elements we wish to find. In order to determine $\mathbf{h}(z)$, we use a least-squared error criterion having first defined a vector of error signals that quantifies the differences between the desired virtual source signals $\mathbf{d}(z)$ and the reproduced signals $\mathbf{w}(z)$ such that

$$\mathbf{e}(z) = \mathbf{d}(z) - \mathbf{w}(z). \quad (2)$$

Since $\mathbf{d}(z) = \mathbf{a}(z)U(z)$ and $\mathbf{w}(z) = \mathbf{C}(z)\mathbf{h}(z)U(z)$, then this vector of error signals can also be written as

$$\mathbf{e}(z) = [\mathbf{a}(z) - \mathbf{C}(z)\mathbf{h}(z)]U(z). \quad (3)$$

We now seek to minimize the cost function given by

$$J = \mathbf{e}^H(z)\mathbf{e}(z) + \beta \mathbf{v}^H(z)\mathbf{v}(z), \quad (4)$$

where H denotes the complex conjugate of the transposed vector. This cost function consists of the sum of the squared errors $\mathbf{e}^H(z)\mathbf{e}(z)$ plus a term quantifying the effort used in the minimization which is given by the product of the regularization parameter β and the sum of the squared source input signals $\mathbf{v}^H(z)\mathbf{v}(z)$. Since $\mathbf{v}(z) = \mathbf{h}(z)U(z)$, and using Eq. (3) for the error vector, the cost function J can be written as a quadratic function of the error vector whose minimum is defined by²⁷

$$\mathbf{h}_{\text{opt}}(z) = [\mathbf{C}^H(z)\mathbf{C}(z) + \beta\mathbf{I}]^{-1}\mathbf{C}^H(z)\mathbf{a}(z). \quad (5)$$

This therefore defines the optimal vector of filters which, as shown clearly by Kirkeby *et al.*²⁷ can be effectively computed in the frequency domain provided that β is correctly chosen and that the target vector $\mathbf{a}(z)$ associated with a given virtual source position includes a suitable modeling delay in order to enable the effective inversion of nonminimum phase components in the electroacoustic transfer function matrix $\mathbf{C}(z)$. It is also useful to define the cross-talk cancellation matrix

$$\mathbf{H}_x(z) = [\mathbf{C}^H(z)\mathbf{C}(z) + \beta\mathbf{I}]^{-1}\mathbf{C}^H(z), \quad (6)$$

such that for a given virtual source position specified by the vector $\mathbf{a}(z)$, the vector of filters that minimizes the cost function J is given by

$$\mathbf{h}_{\text{opt}}(z) = \mathbf{H}_x(z) \mathbf{a}(z). \quad (7)$$

Thus $\mathbf{H}_x(z)$ can be computed for a given arrangement of listener and reproduction sources [and corresponding matrix $\mathbf{C}(z)$] and then the optimal vector of filters $\mathbf{h}_{\text{opt}}(z)$ can be computed for a given virtual source position. Note that the inclusion of the regularization parameter β is crucial to the proper functioning of the inversion technique. By controlling the ratio between the amount of energy in the error function and in the inverse filters, β allows the problems associated with an ill-conditioned electroacoustic transfer function matrix to be overcome.²⁷

For the 2by2 system mentioned above, two measurement points and two reconstruction sources were used. The measurement point locations chosen were the same as the location of the ears in the above model. The source positions were chosen in accordance with the conventional stereo placement positions of $\pm 30^\circ$. Thus the four transfer functions, one from each source to each measurement point, were obtained directly from the sphere model database. The matrix containing these four transfer functions, which is often referred to as the electroacoustic transfer function matrix, $\mathbf{C}(z)$, was then inverted using Eq. (6) with β set to 0.01 and a suitable modeling delay of half the inverse filter length. The elements of the target function vectors, $\mathbf{a}(z)$, were also chosen from the sphere model database as the transfer functions resulting from a source placed at the desired virtual source location. Thus the filters for a given virtual image location were obtained by multiplying the cross-talk cancellation matrix from the above inversion with the appropriate target function vectors.

The design of the 4by4 system was very similar to the above 2by2 system. The added complexity of having to deal with four measurement points and four reconstruction sources was exacerbated by the placement of the measurement points away from the sphere model ear locations, although it was still possible to obtain the required transfer functions from the sphere model database. The reconstruction sources were placed at $\pm 45^\circ$ and $\pm 135^\circ$ for the frontal and rear sources, respectively. The measurement points were placed at $\pm 100 \pm 5^\circ$. The inversion for the 4by4 system was again carried out using Eq. (14) with β set to 0.02 and a modeling delay of again half the inverse filter length. The cross-talk cancellation matrix was then multiplied with the target transfer function vector, $\mathbf{a}(z)$, for each virtual image placement, the elements of which were obtained in a similar manner to the above system transfer functions, giving the four filters associated with each virtual source location. A more detailed explanation of this inversion technique can be found in Kirkeby.²⁷ This paper also contains plots of typical elements from the \mathbf{C} and \mathbf{H} matrices, as does the paper by Kahana et al.²⁸ The paper by Kahana et al. also illustrates the complexity of the sound field in the region of the head when multiple sources are used.

IV. SIMULATIONS

Three separate simulation models were studied, using the sphere model with the two ears placed at $\pm 100^\circ$ in all three cases. First, the ear pressures due to real sources placed at locations around the head were modeled, providing a reference of ideal ear pressure impulse responses. The ear pressures were then modeled that resulted from the reconstruction of virtual sources at various locations around the listener using the 2by2 system and the 4by4 system. In each case the source positions used were all equidistant from the center of the sphere (although this only affected the time delay used in the model since plane waves were assumed throughout) and were placed at angles from 0 to 355 in 5° increments.

The virtual image reconstruction filters were calculated for each source and each model using the cross-talk cancellation matrix based method discussed in the previous section. Thus the ear pressures resulting from the 2by2 and the 4by4 systems were obtained by filtering a broadband (20–20 k-Hz) random noise input signal with the convolution of the appropriate virtual imaging filter and source-to-ear transfer function for that particular ear and reconstruction system.

For any given system, the pressure at the ears for a given input signal can be obtained in the time domain by the convolution of that input signal with the system transfer function. Grouping the various filters and electroacoustic transfer functions together we can define a single system impulse response relating the virtual source signal to the pressure at each ear. We can refer to these as $s_L(n)$ and $s_R(n)$ for the left and right ears, respectively.

The interaural cross-correlation function (IACC) can be defined as²⁹

$$R_{LR}(k) = E[p(n)p(n+k)], \quad (8)$$

where $E[\]$ denotes the expectation operator. For a white noise virtual source signal it is straightforward to show²⁰ that

$$R_{LR}(k) = \sum_{n=0}^{\infty} s_L(n)s_R(n+k). \quad (9)$$

One of the main objectives of the simulations was to evaluate the effect of head rotation on the IACC. This was obtained by recalculating the ear pressures as described above but with the head rotated by $\pm 5^\circ$. From this new ear pressure data the rotated head IACC's were calculated and the difference between the nonrotated IACC and the rotated head IACC was calculated. Thus

$$R_{LR}^{0 \rightarrow 5}(k) = R_{LR}^0(k) - R_{LR}^5(k) \quad (10)$$

is the IACC difference for a right rotation of the head by 5° . A similar expression can be defined for a left rotation of the head.

V. RESULTS OF SIMULATIONS

The results of the simulations of the IACC and the changes in the IACC with head rotation for the real source case, the 2by2 system, and the 4by4 system are presented in Figs. 5–8. These data are presented in the form of a series of gray-scale plots of angle of source incidence (x -axis) from 0 to 355° in increments of 5° against time (y -axis). The time

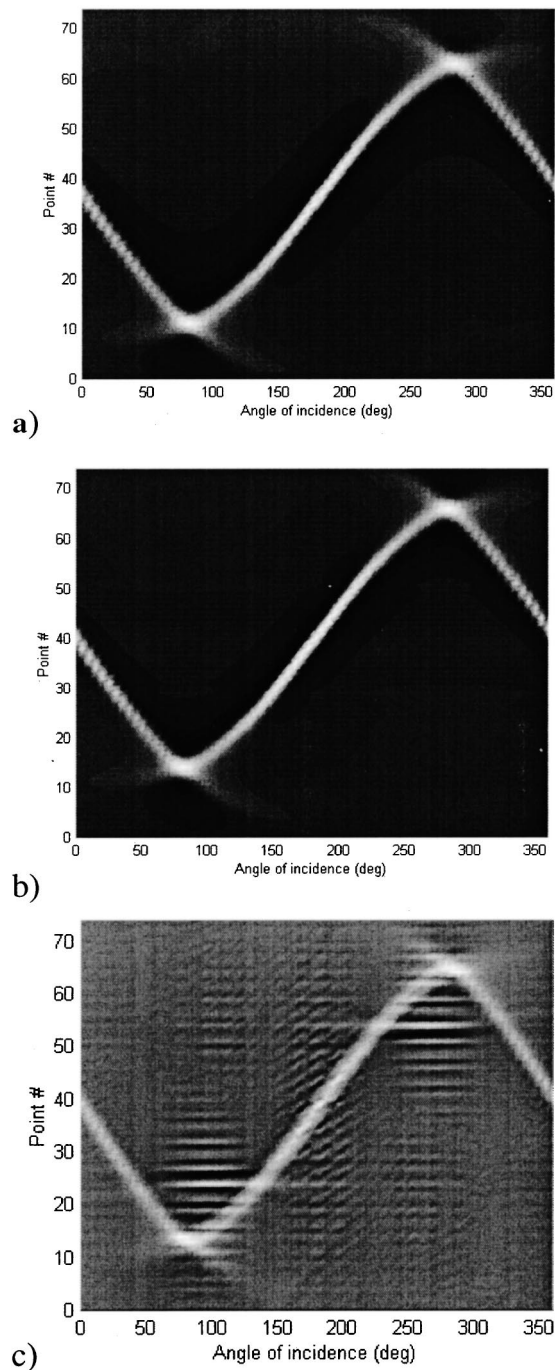


FIG. 6. Gray-scale plot of IACC plotted against angle of source incidence for (a) real sources, (b) the two-channel system, and (c) the four-channel system. (Note: The gray scale is linear from 0 to +1 with these extremes being represented by black and white, respectively.)

information is represented nondimensionally in terms of the correlation point number since its absolute value is dependent on the dimension of the sphere. A positive correlation of unity is represented by white for all three figures and a negative correlation of unity is represented by black in Figs. 7 and 8. In Fig. 6 the minimum value shown on the plot is zero, which is represented by black. In all three plots there is a linear graduation along the gray scale from black to white. Three plots are presented for each model, the IACC data for a single fixed head with no rotation (Fig. 6) and the IACC difference data for head rotations of $\pm 5^\circ$ (Figs. 7 and 8).

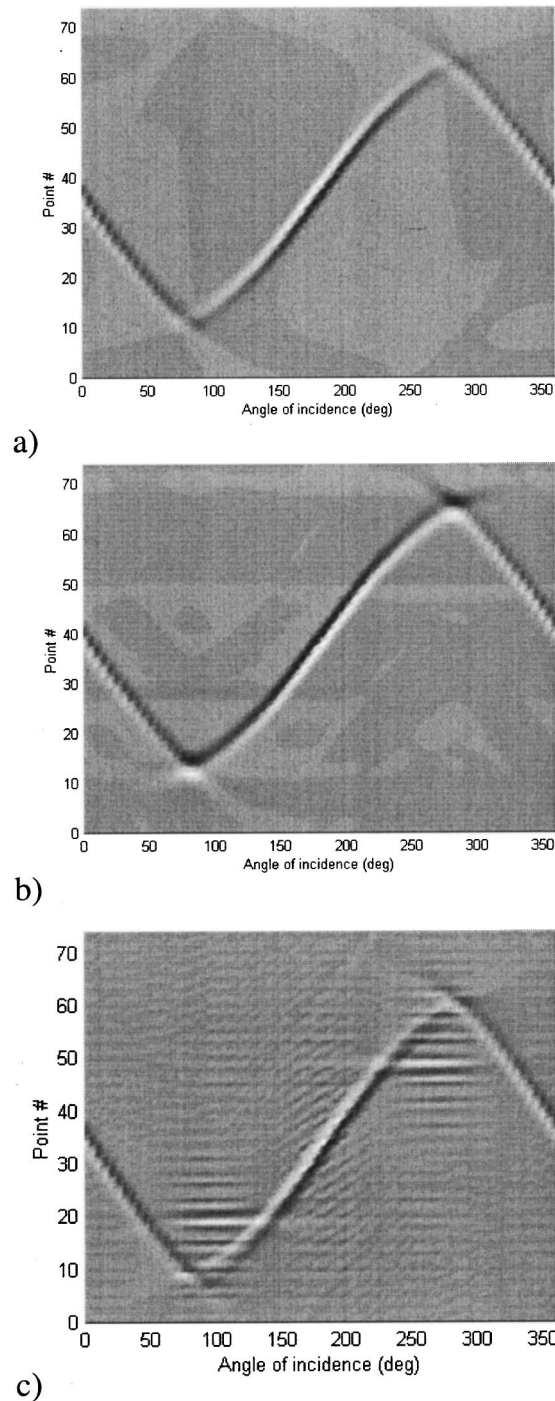


FIG. 7. Gray-scale plot of IACC difference plotted against angle of source incidence due to left head rotation of 5° for (a) real sources, (b) the two-channel system, and (c) the four-channel system. (Note: The gray scale is linear from -1 to $+1$ with these extremes being represented by black and white, respectively.)

It is clear from the IACC data presented here that there is a high degree of consistency between the different systems in terms of the relative interaural time delays for a given source position. However, from the plots for the three systems without rotation (Fig. 6), it is also clear that there is a front-back ambiguity present in this time delay information. For example, with reference to Fig. 6(a), the value of the interaural time delay is the same for a source placed at $90 \pm x^\circ$ (where $x < 90^\circ$). This is also true for a source placed at

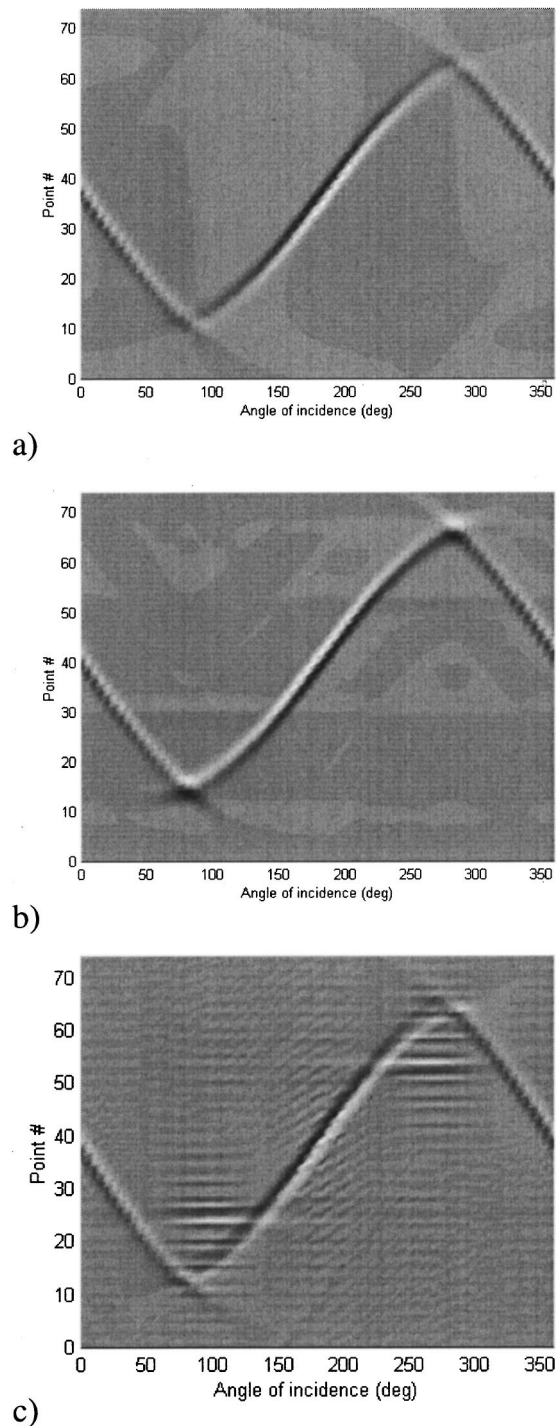


FIG. 8. Gray-scale plot of IACC difference plotted against angle of source incidence due to right head rotation of 5° for (a) real sources, (b) the two-channel system, and (c) the four-channel system. (Note: The gray scale is linear from -1 to $+1$ with these extremes being represented by black and white, respectively.)

$270 \pm x^\circ$. It is therefore not possible, from the information contained in these data alone, to determine whether a given source is in the frontal or the rear quadrant, even though it is possible to accurately determine the value of x . These are exactly the conditions which lead to the phenomenon of front-back confusion.

The plots of the IACC difference for -5° and $+5^\circ$ rotation for the sphere model, Figs. 7(a) and 8(a), respectively,

show that the ambiguity with regard to front-back confusion can be resolved with head rotation. There is a clear and unambiguous pattern of positive and negative correlations that is different depending on the quadrant in which the source is located. For example, if a source is located at either $90^\circ \pm x$, where x is 30° , then from the data given in Fig. 6(a) alone it is not possible to determine whether x is positive or negative even though it is possible to say that the magnitude of x is 30° , this being exactly the condition necessary for front-back confusion to occur. If the head is moved by -5° , then, from the IACC difference data [Fig. 7(a)], this ambiguity is resolved. If the source is at $90+30^\circ$, the changes in the IACC will result in a positive followed by a negative correlation (increasing point number represents a forward movement in time) whereas if the source is at $90-30^\circ$ there will be a negative followed by a positive correlation. Thus front-back confusions can be resolved using this new information. It is also clear from Fig. 8(a) that this pattern of positive and negative correlation is reversed for all source locations if the head is rotated in the opposite direction. It is therefore essential to know the direction in which the head is rotated. This observation, that knowledge of the direction of rotation of the head is important for accurate localization, is supported by the early work of Klensch.³⁰ Klensch demonstrated the importance of an accurate knowledge of the direction of rotation of the head by performing experiments which involved placing equal length flexible tubes attached to funnels into the ears of subjects. The funnels were then moved synchronously with rotations of the head or in contrary motion to the head and the movement of the perceived source image was recorded. When the funnels were moved in contrary motion to the head, or when the tubes were swapped between the left and right ear, and the funnels moved synchronously with the head, the source was perceived to be in the rear when it should have been in front and vice versa. This experiment indicated that knowledge of the direction of rotation of the head is used by the localization mechanism in the resolution of front-back confusion.

The other sets of simulated data for the 2by2 system [Figs. 6(b), 7(b), and 8(b)] and the 4by4 system [Figs. 6(c), 7(c), and 8(c)] show similar patterns of change in the time delay with angle of incidence for the fixed head ITD data. The ITD difference data for the 4by4 system simulations [Figs. 7(c) and 8(c)] indicate that this system is behaving in a very similar manner to the real source model. Thus it would be expected that with this system, listeners would be able to localize sources in the rear using head rotation in a very similar manner to real sources. The results of the subjective experiments presented later will show that this is indeed the case.

The IACC difference data for the 2by2 system [Figs. 7(b) and 8(b)] do not show this discrimination between frontal and rear virtual source placement. These data show that the characteristic pattern of positive and negative correlation for a given head rotation is what would be expected of a frontal source regardless of the actual source location. The appropriate delay associated with determining the angular location of a source is preserved in these data and it is only the second IACC difference based cue that is misleading. We

again take the previous example of a source being placed at $90^\circ \pm x$. If x is $+30^\circ$, then the cues resulting from a $+5^\circ$ rotation of the head would be a positive followed by a negative correlation [Fig. 8(b)] which is exactly what would be expected from the example of the sphere model. If the source is instead placed at -30° , Fig. 8(b) shows that for the same $+5^\circ$ rotation of the head as before, there is again a positive followed by a negative correlation, indicating that the source is placed in front at $+30^\circ$. Given that the interaural time delays used to resolve the magnitude of x in the above example are not affected, it would be expected that subjects using this system would accurately determine x but reflect all rear sources into the frontal half plane. These data indicate that there should be a significant difference between the ability of subjects to localize using all three systems depending on whether the subject's head is free to move or not. In the case of the real source and the 4by4 virtual source system, there should be a decrease in the incidence of front-back confusion when the head is free to move. With the 2by2 virtual source system, freedom of head movement should result in all images being localized in the frontal half of the horizontal plane.

VI. SUBJECTIVE EXPERIMENTS

The subjective experiments described here were designed to test the hypothesis drawn from the simulated results.²⁰ Fourteen volunteer subjects were used in the experiment, which was carried out in a large (78 m^3) anechoic chamber. A preliminary test was repeated using a single subject to check for repeatability and gave almost identical responses the second time. Subjects were seated in a fixed chair in the center of the anechoic chamber. Surrounding them was a thin metal frame supporting an acoustically transparent, visually opaque screen and a series of numbers denoting azimuth angle in 10° increments with 0° being placed directly in front. The subjects were asked to identify the location of each of the test presentations, in 5° increments, with reference to these numbers. During the first part of the experiment a headrest, adjusted for each subject, was used to restrain the subject's head movement. Subjects were explicitly and repeatedly told of the importance of "keeping their head absolutely motionless while the signals were audible." This headrest was then removed for the second half of the experiment, when each set of presentations was repeated, and the subject encouraged to rotate their head a small amount to facilitate localization. Each presentation was of about 5 sec duration with a short break being given between each set of presentations. The whole test lasted about 45 min.

Three prerecorded sets of presentations were used in the experiment, one for each of the 2by2, 4by4, and real source conditions. The subjects listened to each of these sets twice, once with a headrest restraining head movement and again with this headrest removed. In the case of the 2by2 and the 4by4 systems the same filters used in the simulation work were also used here. The choice of measurement point and reconstruction source locations was also the same as for the simulation work. Each of the eight presentations in each set was for a different virtual or real source location and was

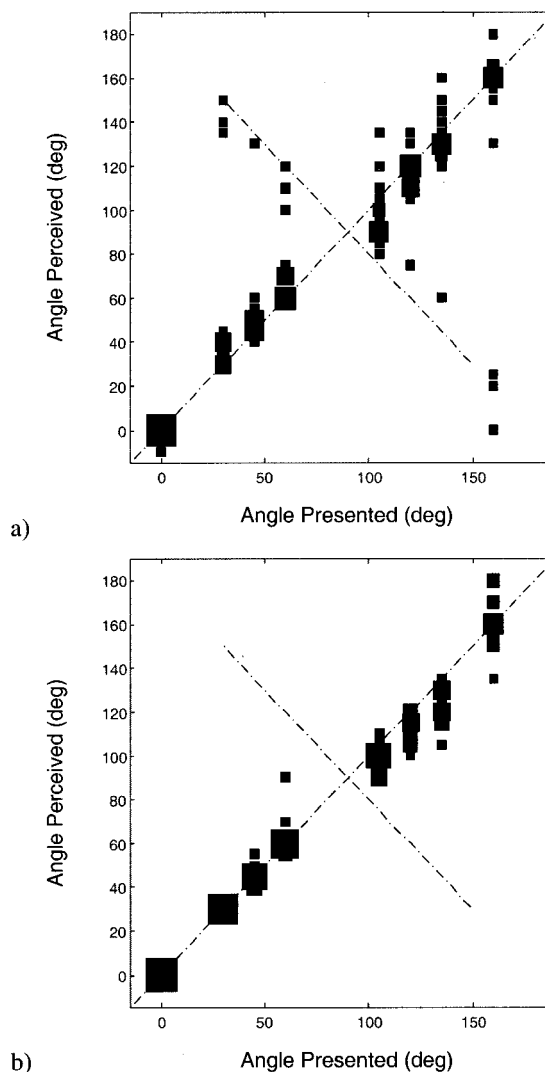


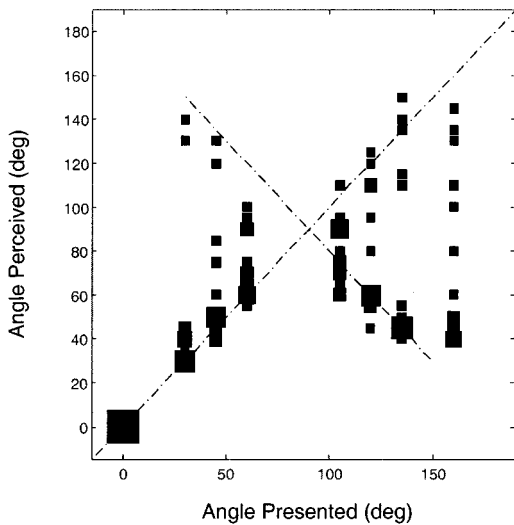
FIG. 9. Subjective results for real sources showing fixed head (a) and free head (b) data, using a 3-kHz band-limited pink noise signal. (Note: The squares have an area proportional to the number of answers given.)

preceded by a presentation of the same noise signal from a real source placed at 0° . The test signal used was pink noise restricted to a frequency content below 3 kHz, with the intention of avoiding undue pinna spectral effects.

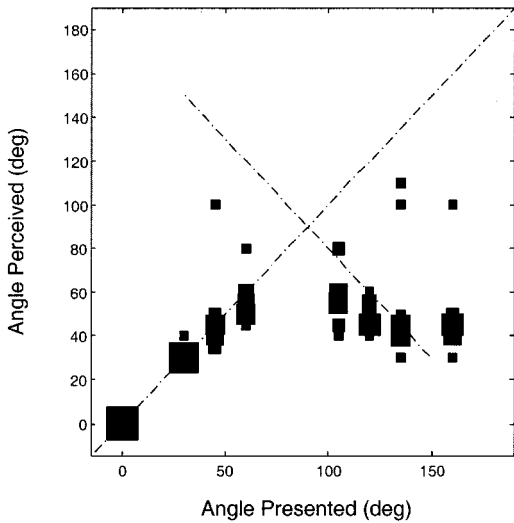
The subjects were informed of the location of the reference (0°) source and that a presentation of the noise from there would precede each test presentation. The presentation angles used for both real and virtual sources were $0, 30, 45, 60, 105, 120, 135,$ and 160° . In all cases the noise was ramped up and down in level to avoid switching transients. The order of presentation of the chosen source locations was randomly arranged within each set and the same arrangement used for each set.

Figures 9–11 show the results from the subjective experiments. The form of presentation for the raw data is to show the angle answered plotted against the angle presented. The area of each of the boxes in the plots is proportional to the number of answers at that particular value. The two lines on the plots indicate the correct answers (45° line) and the front-back confusion answers (-45° line).

The importance of head rotation to the ability of subjects



a)

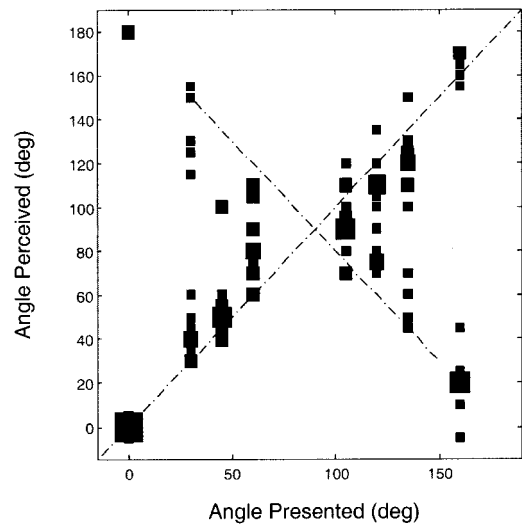


b)

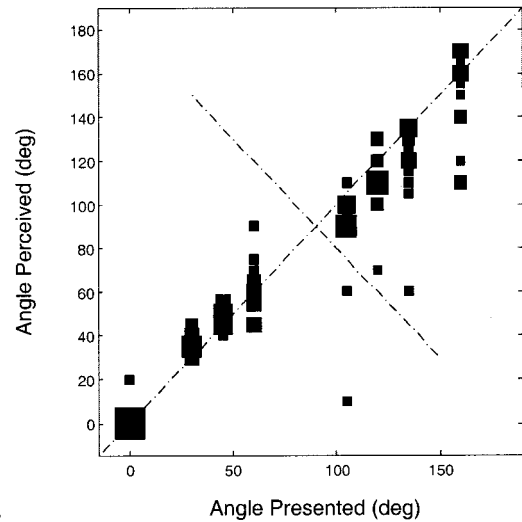
FIG. 10. Subjective results for virtual sources generated using the 2by2 system showing fixed head (a) and free head (b) data, using a 3-kHz band-limited pink noise signal. (Note: The squares have an area proportional to the number of answers given.)

to resolve front-back confusions is clear from these data. For real sources [Figs. 9(a) and (b)], some front-back confusions occurred when the head was fixed, but when the head was free not a single incidence of front-back confusion occurs. This provides further evidence for the importance of head movement in the resolution of front-back confusion, supporting the work of Wallach,¹³ Thurlow *et al.*,¹⁴ and Burger.¹⁵ The data also show clearly that the 4by4 virtual source imaging system performs much better than the 2by2 system in producing rear images when listeners are allowed head rotations.

There appears to be a systematic bias in the data for all three free head data sets. The most likely source of this bias was in the physical difficulty the subjects experienced in accurately pointing to a source behind them, especially since they were not permitted to look toward the source while it was audible. This would have been further compounded by the action of turning the head to read the appropriate number, thus shifting the whole frame of reference. A number of subjects complained of this in discussions following their



a)



b)

FIG. 11. Subjective results for virtual sources generated using the 4by4 system showing fixed head (a) and free head (b) data, using a 3-kHz band-limited pink noise signal. (Note: The squares have an area proportional to the number of answers given.)

participation in the experiment. All six raw data plots indicate that this trend is present to a lesser or greater extent; however, in the plots for the fixed head data it is less apparent since the scatter of the errors is greater.

Another problem was observed while running the experiment which may have had an effect on the data for the virtual source presentations. The nature of the experiments was such that each signal presentation was ramped up and down in level at the beginning and end rather than being abruptly switched on and off. This led to the problem that, if the output from one of the reconstruction sources was significantly greater than the output from the other sources, as would be the case when a virtual source was placed at or very near the location of one of the reconstruction sources, then as the overall signal level was increased, the output from this source would exceed the subject's hearing threshold before the other sources. A similar effect occurred when the signals were ramped down. Thus the first and last thing that the subject would hear would be this reconstruction source rather than the combined effect of all the reconstruction

sources. The bias introduced by this mechanism is unlikely to have been of any great significance except where the virtual source location was very near to one of the reconstruction sources, since it is only for these virtual images that the output amplitude of any one source is considerably larger than the other sources. However, this effect would certainly have caused far fewer problems than switching transients.

As well as the systematic error discussed above, both for the fixed and free head, the 4by4 data appear to show another trend drawing the frontal data toward 90°. This is not understood. For the 2by2 system, the dominant error, for both fixed and free head data, is clearly the almost complete inability of subjects to localize rear images. The fixed head data do appear to show some tendency toward localization of rear images, although correct localizations of rear images are not sufficiently plentiful to be able to draw any firm conclusions from these data. All that can be said is that although it is extremely difficult to localize rear images using this system with a fixed head, this does appear to be possible for some subjects. It is interesting to note at this point that Takeuchi *et al.*³¹ have shown that it is possible to achieve rear localizations from a modified version of the 2by2 system described here when individualized HRTF's are used in the filter design procedure.

VII. DISCUSSION

The results of the simulation of the effects of head rotation on the ITD appear to provide a reliable predictor of the ability of subjects to resolve front-back confusions. Assuming that this ITD-based cue is the primary mechanism for resolution of front-back confusion for these systems, then, for the real sources and the virtual sources generated using the 4by4 system, the simulated data predict that there should be a much greater incidence of front-back confusion when the subject's head movement is restrained. The subjective experimental results support this prediction and show this to be the case. The ability of subjects to localize sources in the rear when head movement is restricted is a testament to the robustness of the hearing mechanism.

Furthermore, it indicates that the hearing system is able to recover from the loss of an important contributor to the localization mechanism and to make good use of whatever cues are still available. The bandwidth restriction imposed on the test signal should have prevented much use being made of pinna spectral differences for horizontal plane localization. What should have remained, therefore, was just the low-frequency (< 3 kHz) ILD and ITD cues. It is also possible that small involuntary head movements did occur during the fixed head part of the experiment since no attempt was made to restrict subject's head movement apart from the head rest and verbal instruction. Head rotations as small as 1 or 2° may provide the necessary cues.

There appears to be evidence from this and other work (discussed earlier) to indicate that the resolution of front-back confusion for low-frequency sources is based on the changes in the ITD with head rotation which are processed by the auditory system through a mechanism such as the evaluation of the IACC. Furthermore, the work of Wightman and Kistler³ indicates that, for broadband signals, the low-

frequency ITD's, where they are present, provide the dominant localization cues. The work of Perrett and Noble¹⁸ also indicates that the dynamic cues for the resolution of spatial ambiguities in relation to source elevation do not function above 2 kHz. It may therefore be possible to say that the mechanism discussed here holds true for broadband signals.

VIII. CONCLUSIONS

The analytical model of the human head presented here represents a credible low-frequency model of the acoustic conditions leading to interaural time delays for sources in the horizontal plane. The results of the simulations of the ITD and the changes to the ITD with head movement resulting from sources placed on the horizontal plane appear to provide an accurate predictor of the ability of subjects to resolve front-back confusions. This appears to hold true for both real and virtual images generated using the two systems discussed here. The subjective experimental data presented here strongly support the hypothesis that front-back confusion, in these systems and for the bandwidths studied, can be resolved using the changes in the ITD resulting from head movement.

¹Lord Rayleigh, "Acoustical observations," *Philos. Mag.* **3**, 456–464 (1877).

²J. Blauert, *Spatial Hearing* (MIT Press, Cambridge, MA, 1983).

³F. L. Wightman and D. J. Kistler, "The dominant role of low-frequency interaural time differences in sound localization," *J. Acoust. Soc. Am.* **91**, 1648–1661 (1992).

⁴S. Oldfield and S. Parker, "Acuity of sound localization: A topography of auditory space. I. Normal hearing conditions," *Perception* **13**, 581–600 (1984).

⁵S. Oldfield and S. Parker, "Acuity of sound localization: A topography of auditory space. II. Pinna cues absent," *Perception* **13**, 601–617 (1984).

⁶S. Oldfield and S. Parker, "Acuity of sound localization: A topography of auditory space. III. Monaural hearing conditions," *Perception* **15**, 67–81 (1986).

⁷L. A. Jeffress, "A place theory of sound localization," *J. Comp. Physiol. Psychol.* **61**, 468–486 (1948).

⁸W. Lindemann, "Extension of a binaural cross-correlation model by contralateral inhibition. I. Simulation of lateralization for stationary signals' sounds," *J. Acoust. Soc. Am.* **80**, 1608–1622 (1986).

⁹W. Lindemann, "Extension of a binaural cross-correlation model by contralateral inhibition. II. The law of the first wavefront," *J. Acoust. Soc. Am.* **80**, 1623–1630 (1986).

¹⁰C. E. Carr and M. Konishi, "A circuit for detection of interaural time differences in the brain stem of the barn owl," *J. Neurosci.* **10**, 3227–3264 (1990).

¹¹T. C. T. Yin and J. C. K. Chan, "Interaural time sensitivity in medial superior olive of the cat," *J. Neurophysiol.* **64**, 465–489 (1994).

¹²R. B. Masterton, G. C. Thompson, J. K. Bechtold, and M. J. Robards, "Neuroanatomical basis of binaural phase-difference analysis for sound localization: A comparative study," *J. Comp. Physiol. Psychol.* **89**, 379–386 (1975).

¹³H. Wallach, "The role of head movement and vestibular and visual cues in sound localization," *J. Exp. Psychol.* **27**, 339–368 (1940).

¹⁴W. R. Thurlow, J. W. Mangels, and P. S. Runge, "Head movement during sound localization," *J. Acoust. Soc. Am.* **42**, 489–493 (1967).

¹⁵J. F. Burger, "Front back discrimination of the hearing system," *Acustica* **8**, 301–302 (1958).

¹⁶D. M. Leaky, "Some measurements on the effects of interchannel intensity and time differences in two channel sound systems," *J. Acoust. Soc. Am.* **31**, 977–986 (1959).

¹⁷F. L. Wightman and D. J. Kistler, "Resolution of front-back ambiguity in spatial hearing by listener and source movement," *J. Acoust. Soc. Am.* **105**(5), 2841–2853 (1999).

¹⁸S. Perrett and W. Noble, "The contribution of head motion cues to localization of low-pass noise," *Percept. Psychophys.* **59**, 1018–1026 (1997).

- ¹⁹S. Perrett and W. Noble, "The effects of head rotation on vertical sound localization," *Percept. Psychophys.* **102**, 2325–2332 (1997).
- ²⁰P. A. Hill, "Front back confusion in systems for the production of virtual acoustic images," Ph.D thesis, Institute of Sound and Vibration Research, University of Southampton, 1998.
- ²¹Lord Rayleigh, *The Theory of Sound* (Dover, New York, 1897), Vol. II.
- ²²P. M. Morse and K. U. Ingard, *Theoretical Acoustics* (McGraw-Hill, New York, 1968).
- ²³I. Malechi, *Physical Foundations of Technical Acoustics* (Pergamon, New York, 1969).
- ²⁴S. N. Rschevkin, *A Short Course of Lectures on The Theory of Sound* (Pergamon, New York, 1963).
- ²⁵D. H. Cooper, "Calculator program for HRTF," *J. Audio Eng. Soc.* **30**, 34–38 (1982); **31**, 760(E) (1986).
- ²⁶G. Kuhn, "Physical acoustics and measurements pertaining to directional hearing," in *Directional Hearing*, edited by W. Yost and G. Gourevitch (Springer-Verlag, New York, 1987).
- ²⁷O. Kirkeby, P. A. Nelson, H. Hamada, and F. Orduna-Bustamante, "Fast deconvolution of multi-channel systems using regularization," *IEEE Trans. Speech Signal Process.* **6**(2), 189–194 (1998).
- ²⁸Y. Kahana, P. A. Nelson, O. Kirkeby, and H. Hamada, "A multiple microphone recording technique for the generation of virtual acoustic images," *J. Acoust. Soc. Am.* **105**(3), 1503–1516 (1999).
- ²⁹R. Shiavi, *Introduction to Applied Statistical Signal Analysis* (Askin, 1991).
- ³⁰H. Klensch, "Beitrag zur Frage der Lokalisation des Schalles im Raum (A contribution to the localization of sound in space)," *Pflugers Arch.* **250**, 492–500 (1948).
- ³¹T. Takeuchi, P. A. Nelson, and H. Hamada, "Influence of individual head related transfer function on the performance of virtual acoustic imaging systems," *Audio Eng. Soc. 104th Convention*, Amsterdam, May 16–19, 1998, Reprint 4700 (P4-3).

Modeling the combined effects of basilar membrane nonlinearity and roughness on stimulus frequency otoacoustic emission fine structure

Carrick L. Talmadge^{a)}

National Center for Physical Acoustics, University of Mississippi, University, Mississippi 38677

Arnold Tubis

Department of Physics, Purdue University, West Lafayette, Indiana 47907

Glenis R. Long

Department of Audiology and Speech Sciences, Purdue University, West Lafayette, Indiana 47907

Christopher Tong

Department of Physics, Purdue University, West Lafayette, Indiana 47907

(Received 21 March 2000; revised 31 August 2000; accepted 1 September 2000)

A theoretical framework for describing the effects of nonlinear reflection on otoacoustic emission fine structure is presented. The following models of cochlear reflection are analyzed: weak nonlinearity, distributed roughness, and a combination of weak nonlinearity and distributed roughness. In particular, these models are examined in the context of stimulus frequency otoacoustic emissions (SFOAEs). In agreement with previous studies, it is concluded that only linear cochlear reflection can explain the underlying properties of cochlear fine structures. However, it is shown that nonlinearity can unexpectedly, in some cases, significantly modify the level and phase behaviors of the otoacoustic emission fine structure, and actually enhance the pattern of fine structures observed. The implications of these results on the stimulus level dependence of SFOAE fine structure are also explored. © 2000 Acoustical Society of America. [S0001-4966(00)01012-2]

PACS numbers: 43.64.Bt, 43.64.Ha, 43.64.Jb [BLM]

I. INTRODUCTION

Otoacoustic emissions (OAEs) are signals that are generated in the cochlea, either in the absence of external stimulation, in which case they are known as spontaneous otoacoustic emissions or SOAEs (see review by Bright, 1997), or in response to external stimulation, in which case they are known as evoked otoacoustic emissions or EOAEs (see, e.g., Norton and Stover, 1994; Robinette and Glatke, 1997). When present, SOAEs in humans have been shown to occur with a periodic frequency spacing corresponding to approximately 0.4 Bark (cf. Zwicker and Peisl, 1990; Talmadge *et al.*, 1993b). EOAEs also exhibit periodic variations in amplitude and phase with frequency, which have been referred to as “fine structure,” with spacings very similar to those of SOAEs (e.g., Zwicker and Peisl, 1990; Zweig and Shera, 1995). Collectively, these periodic variations with frequency are known as “cochlear fine structure” (see, e.g., Talmadge *et al.*, 1998). The EOAEs whose fine structures have been investigated in great detail are stimulus frequency otoacoustic emissions or SFOAEs (e.g., Zweig and Shera, 1995; these emissions are sometimes referred to as synchronous evoked OAEs or SEOAEs) and distortion product otoacoustic emissions or DPOAEs (e.g., He and Schmiedt, 1993; Talmadge *et al.*, 1996; Heitmann *et al.*, 1998; Talmadge *et al.*, 1999; Shera and Guinan, 1999; Mauermann *et al.*, 1999). Both of these types of fine structures also exhibit frequency spacings

in humans between fine structure maxima corresponding to approximately 0.4 Bark (e.g., Zwicker and Peisl, 1990) or the approximate equivalent of 1/16 octave (e.g., He and Schmiedt, 1993).

Early attempts to describe cochlear OAE fine structure were mostly rooted in the assumption that they originated from nonlinear reflection (e.g., Kemp, 1997; see also review and discussion in Shera and Guinan, 1999). Nonlinear reflection results from the nonlinear distortion of an initial apically traveling wave of frequency f , which produces a mixture of apical and basal traveling waves, with the latter being associated with nonlinear reflection. Ascribing fine structure to nonlinear reflection was based in part on overwhelming experimental evidence that nonlinear distortion plays a critical role in the generation of many types of OAEs, especially DPOAEs, whose very existence depends on the nonlinear interaction of the cochlear waves from the two primary tones.

Recent studies have cast doubt on this point of view (Kemp and Brown, 1983; Strube, 1989; Zweig, 1991; Shera and Zweig, 1993; Zweig and Shera, 1995; Talmadge *et al.*, 1998; Shera and Guinan, 1999; Mauermann *et al.*, 1999) and give support to linear reflection as the main source of cochlear fine structure. In particular, it has been proposed that this type of reflection is due to low level inhomogeneities which are strewn along the cochlea (Shera and Zweig, 1993; Zweig and Shera, 1995). It has also been argued that linear cochlear reflection plays an important role in the generation of many types of OAEs, including SFOAEs and click-evoked otoacoustic emissions (Zweig and Shera, 1995; Tal-

^{a)}Current address: Institute for Nonlinear Science, University of California, San Diego, La Jolla, CA 92093-0357.

madge *et al.*, 1997, 1998; Shera and Guinan, 1999), and is also the principal mechanism responsible for the generation of SOAEs (Talmadge and Tubis, 1993a; Zweig and Shera, 1995; Talmadge *et al.*, 1997, 1998; Shera and Guinan, 1999).

To date, most attempts to model OAE fine structures in terms of linear cochlear reflection have completely ignored the influence of nonlinearity. However, both nonlinearity and distributed roughness are thought to be present and to play significant roles in the function of the cochlea. It is thus important to characterize more precisely their combined effects. Taking into account of the influence of nonlinearity on cochlear fine structure provides the basis for extending the range of levels over which these phenomena can be analytically described.

Some attempts to qualitatively discuss the combined effects of nonlinearity and distributed roughness have been made in the context of transient otoacoustic emissions (TEOAEs), mostly recently by Yates and Withnell (1999). The nonlinear differential response of the cochlea to external clicks, such as that developed by Bray and Kemp (1987), involves the subtracting out of the purely linear response of the cochlea, including that due to linear coherent reflection in the absence of nonlinearity. The observed residual presence of TEOAE fine structure implies that linear coherent reflection must still be playing an important role in the generation and emission of the measured TEOAEs (e.g., Zweig and Shera, 1995; Talmadge *et al.*, 1998; Shera and Guinan, 1999).

It is initially puzzling that a linear process could play a role in the measured nonlinear differential response, which is designed to subtract off any linear component. This puzzle is resolved by noting that one of the generation mechanisms of TEOAEs is intermodulation distortion (Yates and Withnell, 1999), and that linear coherent reflection will still play a role in the emission of the generated TEOAE components, especially through reflection of TEOAE components which have a lower frequency than the place frequency of the region where the TEOAE component is initially generated. In this picture, such TEOAE components are very similar to ordinary DPOAEs generated by steady-state external tones.

Experimentally, the question of the influence of nonlinearity on OAE fine structure is best tested by sweeping a single-frequency primary (or primaries) through a range of frequencies with fixed stimulus level(s), in order to study the effect of level on fine structure. Such a procedure was performed by He and Schmiedt (1993, 1997) for the case of DPOAEs with fixed primary frequency ratio. He and Schmiedt also tried to model the effects of the nonlinearity, and assumed an underlying model in which the fine structure is the result of linear reflection (Sun *et al.*, 1994a, b). He and Schmiedt (1993) also noted the difficulties of interpreting input–output curves of DPOAE level versus primary level in the presence of large fine structure.

In the present paper, the theoretical framework developed in Talmadge *et al.* (1998) is extended to include the effects of weak nonlinearity on cochlear reflection and cochlear fine structure. The underlying theoretical formalism is identical to that of Talmadge *et al.* (1998), and, as such, this manuscript may be regarded as a companion paper to that

study. A critical examination of some of the main assumptions of the model and their possible effect on the results obtained here are given in Sec. II. Models of cochlear reflection involving nonlinearity, distributed roughness, and a combination of nonlinearity and distributed roughness are considered in Sec. III. These models are applied in Sec. IV to the case of SFOAE fine structure. A summary and further discussion of the results of this paper may be found in Sec. V. A list of symbols is given in Appendix A, and in order to improve continuity between the two papers, a brief review of the basis function formalism, together with definitions and some basic properties of cochlear reflection, is given in Appendix B.

II. THEORY AND METHODS

As discussed in the Introduction, the analysis in this paper is based on the theoretical framework developed in Talmadge *et al.* (1998), to which the reader is referred for a detailed discussion of the methodology, explanation of notation, and discussions of assumptions and approximations involved. In this section, a summary is given of the underpinnings of the formulation used in this paper together with its main implications about cochlear wave reflection.

A. Modeling the cochlear partition

As described in Appendix B, the cochlear partition is modeled in terms of a single dynamical equation, written in terms of the displacement ξ of the basilar membrane (BM). In this model, the dynamical behavior of the organ of Corti is incorporated into the fast and slow stiffness feedback terms in Δ given by Eq. (B5). (For correspondence to the usual BM place-impedance function Z_{bm} , note that $\Delta = i\omega Z_{\text{bm}}/\sigma_{\text{bm}}$.)

The fast and slow stiffness feedback contributions are those suggested by Zweig (1991) based on Rhode's BM measurements of the squirrel monkey (e.g., Rhode, 1971; Rhode and Robles, 1974) in order to produce "realistic" basilar membrane excitation patterns. Although the assumption of a "macromechanical" model may appear as a limitation of the current framework, it should be noted that any currently proposed micromechanical model of the cochlear partition can be recast in terms of a single equation involving the displacement of the basilar membrane (e.g., de Boer, 1995).

The advantage of this phenomenological approach is that it is "guaranteed" to produce the realistic active patterns on the basilar membrane, which are in turn needed to generate realistic otoacoustic emissions. The main limitation of this approach is the lack of a clear connection between the phenomenological parameters of this model and the underlying detailed anatomy and physiology of the cochlear partition.

B. Modeling the effects of nonlinearity

As discussed in Sec. III A, the only assumed nonlinearity is introduced as a cubic nonlinearity in damping,

$$\gamma_{\text{bm}}(x) = \gamma_0(x) + \gamma_2(x)\xi^2(x,t) \equiv \gamma_0(x)[1 + \xi^2(x,t)/b_m^2], \quad (1)$$

where b_{nl} is the so-called “nonlinear saturation level.” The basis of this choice deserves further comment. First, it should be noted that the existence of spontaneous otoacoustic emissions (SOAEs) and their statistical properties (e.g., Wit, 1986) requires a nonlinear active cochlea (e.g., Talmadge *et al.*, 1991), i.e., one with negative damping for small displacements and some kind of positive nonlinear damping for stabilization. Nonlinear active cochlear models have proven successful in accounting for not only the characteristic properties of SOAEs, including their frequency distribution (e.g., Zwicker and Peisl, 1990; Talmadge *et al.*, 1993b), but also the observed properties of evoked otoacoustic emissions and the microstructure of the hearing threshold (e.g., Talmadge and Tubis, 1993a; Talmadge *et al.*, 1997, 1998). Cochlear nonlinearity could also occur in the BM stiffness. The role of nonlinear stiffness can be assessed by considering the correlations between amplitude and frequency fluctuations of SOAEs. From the results of van Dijk *et al.* (1994), it may be concluded that for a BM amplitude at the nonlinear saturation level b_{nl} , the increase in stiffness is between -1.0% and 1.5% .

The choice of a *cubic* nonlinearity was made by noting that the most general damping function, $\gamma_{nl}(x, \xi)$ must be of the form,

$$\gamma_{bm}(x, t) \dot{\xi}(x, t) = \mathcal{E}(x, \xi, \dot{\xi}) \dot{\xi}(x, t), \quad (2)$$

where \mathcal{E} is an even function in ξ and $\dot{\xi}$. If it is further assumed that \mathcal{E} is analytic at $\xi=0$ and $\dot{\xi}=0$, then this function may be expanded in small quantities to find,

$$\gamma_{bm}(x) \dot{\xi}(x, t) = [\mathcal{E}_0(x) + \mathcal{E}_{20}(x) \xi^2(x, t) + \mathcal{E}_{02}(x) \dot{\xi}^2(x, t) + \dots] \dot{\xi}(x, t). \quad (3)$$

[The initial odd order terms $\xi(x, t)$ and $\dot{\xi}(x, t)$ have been set to zero, by noting that \mathcal{E} must be even in both ξ and $\dot{\xi}$.] Since $\dot{\xi}^2(x, t) \rightarrow -\omega^2 \xi^2(x, t)$ by Eq. (B1), for current purposes, $\mathcal{E}_{20}(x) \xi^2(x, t)$ and $\mathcal{E}_{02}(x) \dot{\xi}^2(x, t)$ may be treated as equivalent.

The resulting simple form of the nonlinearity [Eq. (1)] is justified by noting that even-order DPOAES are much reduced compared to odd-order (“cubic”) DPOAES (e.g., Kim, 1980). Furthermore, except at very high stimulation levels, our simulation results suggest that a simple cubic nonlinearity is able to reproduce most or all of the essential features of the growth of otoacoustic emissions.

C. Modeling the fluid dynamics

As discussed in Talmadge *et al.* (1998) and Appendix B of this paper, the underlying physical model of the cochlea is based on one-dimensional fluid flow. This class of models (“1D” models) have long been known (e.g., de Boer, 1991) to give an accurate description of cochlear mechanics *only* in the basal portion of the traveling wave. This region is referred to as the long-wave region, because the characteristic wavelength λ of the transpartition pressure traveling wave is comparable to or longer than the height H_{sc} of the cochlear scalae.

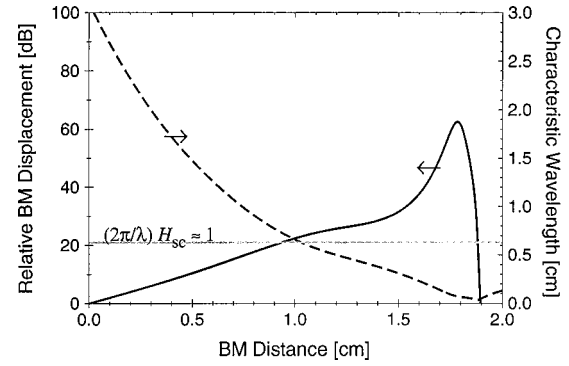


FIG. 1. Plot of basilar membrane (BM) displacement amplitude (solid line) and the characteristic wavelength $\lambda = 2\pi/k$ of the transpartition pressure traveling wave (dashed line) versus distance along the basilar membrane from the base for $f = 1500$ Hz. The BM amplitude has been normalized to unity at the base. The intersection of the $(2\pi/\lambda)H_{sc} \approx 1$ line (shown in gray) and the wavelength curve indicates the location along the basilar membrane where the wavelength is approximately equal to the height H_{sc} of the cochlear scalae. As is discussed in Sec. II C, this shows that the assumption of 1D flow is expected to be roughly valid for the basal 50% of the traveling wave’s propagating distance from the base to its peak region.

A precise criterion for the validity of the one-dimensional model comes from the study of models incorporating three-dimensional fluid flow (i.e., “3D” models). This criterion states that $kH_{sc} \lesssim 1$, where $k = 2\pi/\lambda$ is the wave number of the propagating wave (e.g., Steele and Taber, 1979b). The wavelength of the traveling wave, together with the resulting displacement of the BM, is shown in Fig. 1. The “break-point” for one-dimensional flow is also shown as the horizontal gray line. Expressed in terms of wavelength, this criterion gives $\lambda \approx 2\pi/H_{sc} \approx 0.63$ cm, where $H_{sc} \approx 0.1$ cm for the human cochlea. From the figure, the distance from the base at which the assumption of one-dimensional flow is violated is roughly 1.0 cm. For this case, the location of the BM activity pattern maximum is approximately 1.8 cm, which indicates that the assumption of one-dimensional flow is expected to be roughly valid for the basal 50% of the traveling wave’s propagating distance from the base to the peak region.

For the 1D cochlear model, the basis function formulation can be understood by considering the principal results of this model. In essence, this formulation connects the pressure in the ear canal to the motion on the basilar membrane via a set of so-called pressure basis functions. The ψ_r and ψ_l basis functions describe the right or apically traveling and the left or basally traveling transpartition pressure waves *under the assumption of a smooth, linear cochlear model*. Any deviations from this smooth, linear system are treated as *sources of wave reflection*.

The connection between the cochlear model and the basis functions is provided by the Helmholtz (or 1D wave) equation, for these functions

$$\psi''_{r,l}(x, \omega) + k^2(x, \omega) \psi_{r,l}(x, \omega) = 0, \quad (4)$$

where $k(x, \omega)$ is the wave number of the traveling wave in a smooth cochlea, and depends on both frequency and position along the BM. By convention, $\psi_{r,l}(x, \omega)$ are dimensionless and normalized so that $\psi_{r,l}(0, \omega) \equiv 1$ [Eq. (B26)]. The 1D model gives

$$k^2(x, \omega) = \frac{k_0^2 \omega^2}{\Delta(x, \omega)}, \quad (5)$$

where $\Delta(x, \omega)$ [defined in Eq. (B5)] specifies the mechanics of the BM. In the Wentzel–Kramers–Brillouin (WKB) approximation (e.g., Zweig *et al.*, 1976), the $\psi_{r,l}(x, \omega)$ have semi-analytic solutions in terms of $k(x, \omega)$ and its integral over x ,

$$\psi_{r,l}(x, \omega) = \sqrt{\frac{k(0, \omega)}{k(x, \omega)}} \exp\left[\mp i \int_0^x k(x', \omega) dx'\right]. \quad (6)$$

If $k(x, \omega)$ is smooth (in the sense defined in Appendix B), then in the absence of source terms, the transpartition pressure P_d is given exactly by

$$P_d(x, \omega) = a_r(\omega) \psi_r(x, \omega) + a_l(\omega) \psi_l(x, \omega), \quad (7)$$

where $a_r(\omega)$ and $a_l(\omega)$ are the (constant) pressure amplitudes of the right (apical) moving and left (basal) moving traveling waves. As discussed above, $\psi_{r,l}$ are dimensionless, implying that a_r and a_l carry dimensions of pressure.

In the context of this model, it is not an assumption that both left and right moving traveling waves exist, but rather a consequence of the fact that the Helmholtz equation [Eq. (4)] is a second-order differential equation. Note, of course, that $P_d(x, \omega)$ also satisfies Helmholtz's equation [Eq. (4)].

D. Sources of reflection

In the presence of roughness, nonlinearity, or other sources of reflections, the definition of wave number makes it necessary to distinguish the smooth part of the wave number from that due to roughness or other sources of internal reflection. In this case the total $k^2(x, \omega)$, still given by Eq. (5), is written as

$$k^2(x, \omega) = k_{\text{sm}}^2(x, \omega) + \delta k^2(x, \omega), \quad (8)$$

where

$$k_{\text{sm}}^2(x, \omega) = \frac{k_0^2 \omega^2}{\Delta_{\text{sm}}(x, \omega)}, \quad (9)$$

$$\Delta(x, \omega) = \Delta_{\text{sm}}(x, \omega) + \delta \Delta(x, \omega).$$

Here $\Delta_{\text{sm}}(x, \omega)$ describes the mechanics of the underlying smooth, linear BM, and $\delta \Delta(x, \omega)$ parameterizes any deviations from smoothness and nonlinearity on the BM that will produce internal reflection.

E. Parametrizing cochlear reflection

Since the dynamics of the organ of Corti enter through the basilar membrane equation, all sources of reflection will be characterized via the $\delta \Delta(x, \omega)$ deviation (that is through deviations on the basilar membrane). As illustrated in Fig. 1, the basilar membrane activity pattern is sharply peaked near the traveling-wave tonotopic location. The reflection due to any point is necessarily proportional to the amplitude of the BM displacement (or the amplitude to some power for the case of nonlinear reflection); this also means that $\delta \Delta$ (and hence δk^2) are small except near the BM activity pattern maximum.

Thus even for a highly nonlinear or very rough BM, the solution to the 1D Helmholtz equation [Eq. (4)] given by Eq. (7) will remain valid near the base. For an initially apical traveling wave, this allows *all* the effects of roughness and nonlinearity to be parameterized through a single *apical reflectance*, R_a .

Given an initial apical traveling-wave packet with transpartition pressure P_{r0} at the base, and a reflected basal traveling wave with pressure P_{l1} , the apical reflectance is just given by

$$R_a(\omega) = \frac{P_{l1}(0, \omega)}{P_{r0}(0, \omega)}. \quad (10)$$

Note that in this formulation, all of the physics at the peak region of the traveling wave (including the 3D nature of the fluid motion) are encapsulated in R_a . An important example of a source of internal reflection is that due to distributed BM inhomogeneities. As discussed by Shera and Zweig (Shera and Zweig, 1993; Zweig and Shera, 1995), the resulting apical reflectance is expected to be of the form

$$R_{\text{rough}}(\omega) = |R_{\text{rough}}(\omega)| e^{-i \varphi_{\text{rough}}(\omega)}, \quad (11)$$

$$|R_{\text{rough}}| \approx \text{constant}, \quad \varphi_{\text{rough}}(\omega) \approx \varphi_0 \log(\omega/\omega_0), \quad (12)$$

where $\varphi_0 \approx 17\pi$ in humans. (See the following sections for further details on the functional form of R_a .) As discussed by Shera and Zweig (Shera and Zweig, 1993; Zweig and Shera, 1995), the underlying quasi-periodicity of otoacoustic emission fine structure has its origins in the phase dependence of the apical reflectance due to roughness.

Internal reflection also occurs for basally traveling waves at the middle-/inner-ear interface. For an initial basal traveling-wave packet with pressure P_{l0} at the base impinging on the stapes, and a reflected apical traveling-wave packet with pressure P_{r1} , the *basal reflectance* R_b is defined as

$$R_b(\omega) = \frac{P_{r1}(0, \omega)}{P_{l0}(0, \omega)}. \quad (13)$$

It can be shown that R_b depends entirely on the cochlear properties at the base, and on the impedance of the middle and outer ear looking out through the stapes. In summary, R_a describes the physics at the peak region of the BM activity pattern, R_b the physics of the ear canal, middle-ear, and cochlear base, and ψ_r and ψ_l describe the propagation of disturbances between these two extremities.

F. Effect of internal resonance

Because partial reflections of both apical and basal traveling wave will in general be present, the response of the cochlea to continuous tones will exhibit a resonance effect. In particular, if it is assumed that the apical reflectance R_a is independent of the level of stimulation, the apical component of pressure P_r at the base can be shown to be related to the calibrated driving pressure P_{dr} in the ear canal by

$$P_r(0, \omega) \propto \frac{1}{1 - R_a(\omega) R_b(\omega)} P_{\text{dr}}(\omega), \quad (14)$$

where the proportionality constant depends only the physics of the outer ear, middle ear, and cochlear base. If the product $|R_a||R_b|$ is assumed small, Eq. (14) can be approximated by its first-order Taylor series expansion. If the apical reflectance is due to roughness, then

$$|P_r(0, \omega)| \propto |P_{dr}(\omega)| [1 + 2|R_a| \cos(\varphi_0 \log(\omega/\omega_0) + \varphi_1)], \quad (15)$$

where φ_1 is a phase constant. Equation (15) predicts that $P_r(0, \omega)$ will exhibit a quasi-periodic fluctuation in amplitude with a frequency spacing between adjacent maxima of

$$\frac{\Delta f}{f} \approx \frac{2\pi}{\varphi_0}. \quad (16)$$

The interested reader is referred to Talmadge *et al.* (1998) for more details on the modeling of specific types of cochlear fine structure that are predicted by the above considerations.

G. Relationship between the apical reflectance R_a and the physics at the activity pattern maximum

If it is assumed that a 1D Helmholtz equation can be used to describe wave propagation near the activity pattern maximum, then the underlying sources of reflection parameterized by $\delta\Delta$ can be related to the apical reflectance via (see Appendix B for details)

$$\begin{aligned} R_a(\omega) &\approx -\frac{1}{W_0(\omega)} \int_0^\infty \delta k^2(x', \omega) \psi_r^2(x', \omega) dx' \\ &\approx \frac{k_0^2 \omega^2}{W_0(\omega)} \int_0^\infty \delta\Delta(x', \omega) \chi_r^2(x', \omega). \end{aligned} \quad (17)$$

Since $\chi_r(x', \omega)$ is sharply peaked near $x \approx \hat{x}(\omega)$, it is possible to evaluate Eq. (17) using either saddle-point integration (e.g., Zweig and Shera, 1995), or by approximating χ_r by a Gaussian (e.g., Zweig and Shera, 1995; Talmadge *et al.*, 1998). The latter approach, in particular, allows one to relate the behavior of the apical reflectance to very general details of the basilar membrane mechanics, such as the place-frequency map, the mechanical damping, the wavelength of the traveling wave at its activity pattern maximum, and so on. This also allows modeling of the effects of manipulations such as administration of ototoxic drugs, heartbeat rate, noise exposure, etc. on otoacoustic fine structure.

H. Extension of the basis-function formalism to multiple dimensions

The consequences of including the effects of 2D or 3D fluid flow on the basis function formalism is an ongoing topic of research. Since the fluid flow is known to be essentially 1D near the base, the primary effect will be to modify the dependence of the apical reflectance R_a on the specific underlying physiological parameters. It is well known (e.g., Steele and Taber, 1979a, b) that the functional dependence of the BM impedance function needed to produce the same BM activity pattern is quite different for a 2D or 3D model than for a 1D model. The reason is that in the ‘‘short-wave’’ region (where $\lambda \ll H_{sc}$), the wave number k is related to the basilar membrane mechanics Δ via

$$k(x, \omega) \approx \frac{2\rho\omega^2 W_{bm}}{\sigma_{bm} W_{sc} \Delta(x, \omega)}, \quad (18)$$

where W_{sc} is the width of the cochlear scalae. The important point of Eq. (18) is the linear dependence of k on $1/\Delta$ in the short-wave region. This result should be compared to the $1/\sqrt{\Delta}$ dependence in the long-wave region.

One consequence of this result is that 2D and 3D fluid action tends to ‘‘sharpen’’ the cochlear response to a given mechanical tuning of the basilar membrane. The place-frequency map of the basilar membrane is well understood. This suggests that a smaller mechanical Q is needed to produce the same magnitude of response of the basilar membrane. A second potential consequence is the possible modification of the form of Eq. (17). Preliminary model results suggest that the form of the results for 2D or 3D models may be very similar to that found for 1D models. This result will be explored in greater detail in a future publication. Because of the great simplification of presentation allowed by its use, the 1D model will be assumed in the formal development of this paper.

III. MODELS OF REFLECTION

A. Nonlinear damping

Although nonlinear damping is not a form of basilar membrane discontinuity, it has the same effect of transforming an apical traveling wave into a ‘‘mixed state’’ of both apical and basal traveling waves. There have been several studies of approximate solutions of the nonlinear cochlear model equations in the frequency domain (e.g., Kanis and de Boer, 1994). In these studies, the cochlear equations are typically solved in an iterative fashion to arrive at a self-consistent solution for the pressure wave in the presence of nonlinearity. In the present paper, as in Talmadge *et al.* (1998), the effects of nonlinearity will be assumed to be small enough to be treated in a perturbative manner.

In this section, only the case of a weak nonlinearity will be considered. For this situation, the resulting pressure solutions can still be decomposed using the basis functions appropriate to the underlying linear model. For the sake of simplicity, a Van der Pol type nonlinearity of the form (see Talmadge *et al.*, 1998),

$$\gamma_{bm}(x, \xi) = \gamma_0(x) + \gamma_2(x) \xi(x, t)^2, \quad (19)$$

is assumed. However, the general character of our results would be expected to hold for low-level excitation for other more complex forms of nonlinear damping (for further discussion of this point, see Secs. II B and V E of this paper as well as, e.g., van Hengel *et al.*, 1996).

If the complex representation of Eq. (B1) is used for real quantities, and only the ω frequency component is retained for terms such as $\xi^2(x, t) \dot{\xi}(x, t)$, it is easily verified that,

$$\xi^2(x, t) \dot{\xi}(x, t) \equiv i\omega |\xi(x, \omega)|^2 \xi(x, \omega) + \text{complex conjugate}, \quad (20)$$

where terms involving 3ω that arise from the presence of the nonlinearity have been neglected. Then, the approximate frequency domain expression for Eq. (19) is

$$\gamma_{bm}(x, \xi) = \gamma_0(x) + \gamma_2(x) |\xi^2(x, \omega)|^2. \quad (21)$$

In analogy to Eqs. (B3) and (B5), the resulting dynamical equation is given by

$$\begin{aligned} & [\omega_0(x)^2 - \omega^2 + i\omega(\gamma_0(x) + \gamma_2(x))|\xi(x, \omega)|^2] \\ & + \rho_f \omega_0(x) e^{-i\psi_f \omega / \omega_0(x)} \\ & + \rho_s \omega_0(x) e^{-i\psi_s \omega / \omega_0(x)} \xi(x, \omega) = \frac{1}{\sigma_{\text{bm}}} P_d(x, \omega). \end{aligned} \quad (22)$$

Finally, if $\gamma_2(x)|\xi(x, \omega)|^2$ is sufficiently small, the effects of nonlinearity can be assessed using the methodology of Appendix B 4. The change in the effective $k^2(x, \omega)$ due to the nonlinearity, $\delta k_{\text{nl}}^2(x, \omega)$, is given by

$$\delta k_{\text{nl}}^2(x, \omega) \equiv \frac{-i\gamma_2(x)|\xi(x, \omega)|^2 k_0^2 \omega^3}{\Delta^2(x, \omega)}. \quad (23)$$

In order to assess the effect of the nonlinearity, this contribution can be inserted into either Eq. (B45) for an initial apical moving wave, or into Eq. (B48) for an initial basal moving one.

Only the apical moving wave, which corresponds, for example, to a cochlea driven at the base or in the ear canal, will be considered here. From Eq. (B45), the apical reflectance is given by

$$\begin{aligned} R_{\text{nl}}(\omega) & \equiv - \frac{i\epsilon_\gamma k_0^2 \omega^3 |b_r|^2}{W_0(\omega) \Delta^2(0, \omega) b_{\text{nl}}^2(\omega)} \\ & \times \int_0^\infty dx' \omega_0(x') |\chi_r(x', \omega)|^2 \chi_r^2(x', \omega), \end{aligned} \quad (24)$$

where we use the notation $R_{\text{nl}}(\omega)$ to refer to the apical reflectance due to nonlinearity. Also, the nonlinear stiffness has been rewritten as $\gamma_2(x) = \gamma_0(x)/b_{\text{nl}}^2(\omega) = \epsilon_\gamma \omega_0(x)/b_{\text{nl}}^2(\omega)$, where $b_{\text{nl}}(\omega)$ parameterizes the basilar membrane displacement at which the nonlinearity becomes important, and $\epsilon_\gamma = \gamma_0(x)/\omega_0(x)$. For an active cochlea, $\chi_r(x, \omega)$ is sharply peaked about the maximum of the activity pattern, a fact that can be used to approximately evaluate the above integral. In particular, it is assumed that $\chi_r(x, \omega)$ can be approximately written as a product of a phase term and a Gaussian,¹

$$\chi_r(x, \omega) \approx e^{-2\pi i N_\lambda - i\pi/2} e^{-i\hat{k}[x - \hat{x}(\omega)]} |\hat{\chi}_r| e^{-[x - \hat{x}(\omega)]^2 / (2\sigma_x^2)}, \quad (25)$$

where $\hat{k} = \text{Re}[k(\hat{x}(\omega), \omega)]$, $\hat{\chi}_r = \chi_r(\hat{x}(\omega), \omega)$, and σ_x is the full-width half-maximum of the activity pattern. In obtaining Eq. (25), the WKB phase for $\psi_r(x, \omega)$ [i.e., Eq. (B39)] was assumed, and it was further assumed that $\text{Re}[k(x, \omega)]$ slowly varies about $x = \hat{x}(\omega)$. By construction, $|\hat{\chi}_r|$ is the ratio of the peak amplitude of the activity pattern divided by the value at its base. (Hence, $|\hat{\chi}_r|$ parametrizes how ‘‘tall’’ the activity pattern is, and σ_x parametrizes how ‘‘broad’’ the activity pattern is for a given cochlear model.) In practice, \hat{k} , χ_r , and σ_x are only weakly dependent on frequency for the frequencies considered in this paper, and for most considerations can be assumed constant. Substituting Eq. (25) into (24) gives

$$\begin{aligned} R_{\text{nl}}(\omega) & \equiv - \frac{i\epsilon_\gamma k_0^2 \omega^4 |b_r|^2 |\hat{\chi}_r|^4}{W_0(\omega) \omega_0^4 b_{\text{nl}}^2(\omega)} e^{-4\pi i N_\lambda - i\pi} \\ & \times \int_0^\infty dx' e^{-k_\omega[x' - \hat{x}(\omega)]} e^{-2i\hat{k}[x' - \hat{x}(\omega)]} \\ & \times e^{-2[x' - \hat{x}(\omega)]^2 / (\sigma_x^2)}. \end{aligned} \quad (26)$$

In obtaining Eq. (26), it was further assumed that

$$\begin{aligned} \omega_0(x) & \approx \omega_0 e^{-k_\omega x} = \omega_0 e^{-k_\omega \hat{x}(\omega)} e^{-k_\omega[x - \hat{x}(\omega)]} \\ & = \hat{\omega} e^{-k_\omega[x - \hat{x}(\omega)]} = \omega e^{-k_\omega[x - \hat{x}(\omega)]}, \end{aligned} \quad (27)$$

where $\hat{\omega} = \omega$ by definition. Since $\sigma_x \ll L_{\text{bm}}$, for $x \ll \hat{x}(\omega) - 2\sigma_x$, the lower limit of Eq. (26) can be replaced by negative infinity, which gives the new integral expression

$$\begin{aligned} R_{\text{nl}}(\omega) & = - \frac{i\epsilon_\gamma k_0^2 \omega^4 |b_r|^2 |\hat{\chi}_r|^4}{W_0(\omega) \omega_0^4 b_{\text{nl}}^2(\omega)} e^{-4\pi i N_\lambda - i\pi} \\ & \times \int_{-\infty}^{+\infty} dy e^{-k_\omega y} e^{-2i\hat{k}y} e^{-(2y^2)/(\sigma_x^2)} \quad (x \ll \hat{x} - 2\sigma_x), \end{aligned} \quad (28)$$

where the change of variables $y = x' - \hat{x}(\omega)$ has been made. This integral can be explicitly evaluated to give

$$\begin{aligned} R_{\text{nl}}(\omega) & \equiv - \frac{i\epsilon_\gamma k_0^2 \omega^4 |b_r \hat{\chi}_r|^2 \sigma_x |\hat{\chi}_r|^2 \sqrt{\pi}}{W_0(\omega) \omega_0^4 b_{\text{nl}}^2(\omega)} \sqrt{\frac{\pi}{2}} \\ & \times e^{-4\pi i N_\lambda - i\pi} e^{-(1/2)(\hat{k}^2 - k_\omega^4)\sigma_x^2} e^{i(1/2)\hat{k}k_\omega \sigma_x^2} \\ & (x \ll \hat{x} - 2\sigma_x). \end{aligned} \quad (29)$$

Equation (29), with appropriate definitions, can be written in either of the forms,

$$\begin{aligned} R_{\text{nl}}(\omega) & \equiv \frac{|a_r(\omega)|^2}{a_{\text{nl}}^2(\omega)} e^{-i\varphi_{\text{nl}}(\omega)} \\ & = \frac{|P_{\text{dr}}(\omega)|^2}{P_{\text{nl}}^2(\omega)} e^{-i\varphi_{\text{nl}}(\omega)} \quad (x \ll \hat{x} - 2\sigma_x), \end{aligned} \quad (30)$$

$$\varphi_{\text{nl}}(\omega) \equiv 4\pi N_\lambda + \frac{3\pi}{2} - \frac{1}{2} \hat{k} k_\omega \sigma_x^2, \quad (31)$$

where $a_{\text{nl}}(\omega)$ and $P_{\text{nl}}(\omega)$ are themselves functions of the various parameters of the model. The final form of the result given in Eq. (30) could easily have been guessed, given the cubic nature of the nonlinearity that was assumed. However, the ‘‘full version’’ of the solution given in Eq. (29) allows effects such as systematic variations in \hat{k} , $|\hat{\chi}_r|$ or σ_x along the basilar membrane to be explored. This full solution also provides an explicit dependence of $\varphi_{\text{nl}}(\omega)$ on the various cochlear parameters.

Several points should be noted in Eq. (29). First, the quantity $|\hat{\xi}| = |b_r \hat{\chi}_r|$ measures the maximum displacement of the basilar membrane for an apical moving traveling wave of amplitude $a_r(\omega)$. Hence, the amount of reflectance from nonlinearity depends on the square of the maximum basilar membrane displacement. Second, the term $\sigma_x |\hat{\chi}_r|^2$ measures the ‘‘equivalent rectangular window power’’ of the basilar

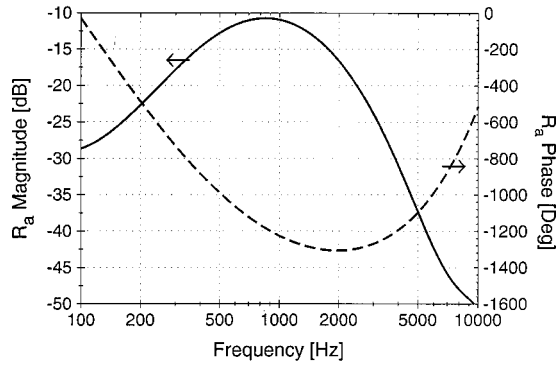


FIG. 2. Nonlinear apical cochlear reflectance $R_a(\omega) = R_{nl}(\omega)$ magnitude (solid line) and phase (dashed line) from Eq. (29) for a 20-dB swept tone. The results are for the cochlear model of Talmadge *et al.* (1998), which contains BM nonlinear damping of the form given by Eq. (19) of the text. The apical reflectance quantifies the fraction of an initial apical traveling pressure wave which is basally reflected. Note that the frequency range used, 100–10 000 Hz, is greatly expanded compared to that used for most of the following plots. $R_{nl}(\omega)$ is characterized by a very slow variation of its phase in comparison to that of the apical reflectance $R_{rough}(\omega)$ due to roughness (compare to Fig. 3).

membrane activity pattern near its peak, and is a sensitive function of the particular cochlear model. Since the quantity $\sigma_x |\hat{\chi}_r|^2$ is expected to be smaller near the apex as well as in cochlear models with less tall and broad activity patterns, the predicted nonlinearity-induced reflectance is also expected to be smaller for these cases. Finally, it should be noted that the phase of the nonlinear apical reflectance $R_{nl}(\omega)$ is nearly independent of frequency over the range of the basilar membrane for which the cochlear parameters are nearly scale invariant. This latter feature is a general characteristic of any reflectance originating from “wave-fixed” phenomena, such as nonlinearity (e.g., Strube, 1989; Zweig and Shera, 1995; Shera and Guinan, 1999).

The behavior of the magnitude and phase of $R_{nl}(\omega)$ is shown in Fig. 2 for a wide range of frequencies. The reflectance was computed by maintaining a constant stimulus level of 20 dB SPL, with $a_{nl}(\omega) = 10^{-6}$ dyne cm^{-2} . Unlike the reflectance for a pointlike discontinuity, both the magnitude and phase of the reflectance are slowly varying. As is expected from Eq. (29), the dominant variation in both the magnitude and phase of the nonlinear reflectance arises from the scale-invariance violating elements of the cochlear model (for example, finite L_{bm} , effects of the middle-outer ear, and variation of the Q of the traveling wave with frequency).

B. Distributed discontinuities

Since this model of reflectance has been extensively studied elsewhere (e.g., Shera and Zweig, 1993; Zweig and Shera, 1995; Talmadge *et al.*, 1997, 1998), only the main results for this case will be summarized here. As in Talmadge *et al.* (1998), the distributed inhomogeneities are assumed to be of the form,

$$\tilde{\omega}_0(x) = \omega_0(x)[1 + r_0(x)\tilde{r}(x)], \quad (32)$$

where, as in that publication, the tilde in a quantity $\tilde{A}(x)$ signifies that this quantity contains inhomogeneities. Here $\tilde{r}(x)$ is a function that gives a pseudorandom Gaussian num-

ber with a variance of unity. The magnitude of the roughness is parametrized by $r_0(x)$, with $0 \leq r_0(x) \leq 1$ for all x . The source contribution to $k^2(x, \omega)$ is then

$$\delta k_{rough}^2(x, \omega) = - \frac{2k_0^2 \omega^2 \omega_0^2(x) r_0(x) \tilde{r}(x)}{\Delta_{sm}^2(x, \omega)}. \quad (33)$$

Following the same assumption outlined in Appendix B 6, and the use of Eq. (25), the apical reflectance is given by

$$R_{rough}(\omega) \cong - \frac{2\sqrt{\pi} r_0 k_0^2 \omega^4 \sigma_x |\hat{\chi}_r|^2}{W_0(\omega) \omega_0^4} \times e^{-4\pi i N \lambda - i\pi e^{k_0^2 \sigma_x^2} e^{2i\hat{k}\hat{x}(\omega)}} \times \tilde{r}_f(\hat{x}(\omega) + k_0 \sigma_x^2, \omega) \quad (x \ll \hat{x} - 2\sigma_x), \quad (34)$$

where $R_{rough}(\omega)$ is the apical reflectance due to roughness, and where $\tilde{r}_f(x)$ is the basilar membrane roughness which has been filtered around the spatial frequency region centered at twice the spatial wave number ($2\hat{k}$). The presence of the $\tilde{r}_f(x)$ term results in a slow fluctuation in the magnitude and phase of $R_a(\omega)$ with ω in the manner of narrow-band filtered noise. As with nonlinear reflectance, Eq. (34) can be written in a simpler looking form,

$$R_{rough}(\omega) \cong |R_{rough}(\omega)| e^{-i\varphi_{rough}(\omega)} \quad (x \ll \hat{x} - 2\sigma_x), \quad (35)$$

$$\varphi_{rough}(\omega) \cong -2\hat{k}\hat{x}(\omega) + \arg[R_{rough}(\omega)] + \varphi_{0a} \quad (36)$$

$$\cong (2\hat{k}/k_\omega) \log(\omega/\omega_0) + \arg[R_{rough}(\omega)] + \varphi_{0a}, \quad (37)$$

where φ_{0a} is a constant. An alternative form of this derivation is given by Zweig and Shera (1995), which also includes a more precise analysis in which an asymptotic expansion of the integral is obtained using saddle-point integration.

The reflectance due to roughness in a linear model is shown in Figs. 3(a) and (b) for a limited range of frequencies. The two models shown are that of the model of Talmadge *et al.* (1998) in Fig. 3(a), and a version of that model with modified parameter values in Fig. 3(b). (These models will hereafter be referred to as Models A and B.) The modified parameters are $\rho_f = 0.14$, $\mu_f = 0.21$, $\rho_s = 0.13$, $\mu_s = 1.76$, $\gamma_0 = 7000 \text{ s}^{-1}$, and $\gamma_1 = 100 \text{ s}^{-1}$. The roughnesses in the two cases are 0.02% for Model A and 1% for Model B.

As discussed above, the variation in the magnitude of $R_{rough}(\omega)$ and the departure of the phase of $R_{rough}(\omega)$ from $\log(\omega/\omega_0)$ are the results of the spatial filtering of the cochlear wave (e.g., Zweig and Shera, 1995; Talmadge *et al.*, 1998), which results in a behavior of $R_{rough}(\omega)$ similar to that of band-pass filtered noise. The differences in results for these two models can be understood in terms of the differences in the height and shape of $|\chi_r(x, \omega)|$ near its maximum value, as well as in the different values for \hat{k} . For Model A:

$$|\hat{\chi}_r(1250 \text{ Hz})| = 84 \text{ dB}, \quad \sigma_x = 0.44 \text{ cm}, \quad \hat{k} = 143 \text{ cm}^{-1}, \quad (38)$$

and for Model B:

$$|\hat{\chi}_r(1250 \text{ Hz})| = 65 \text{ dB}, \quad \sigma_x = 0.85 \text{ cm}, \quad \hat{k} = 86 \text{ cm}^{-1}. \quad (39)$$

The increased sensitivity of Model A to small scale discontinuities can be understood from the fact that the product

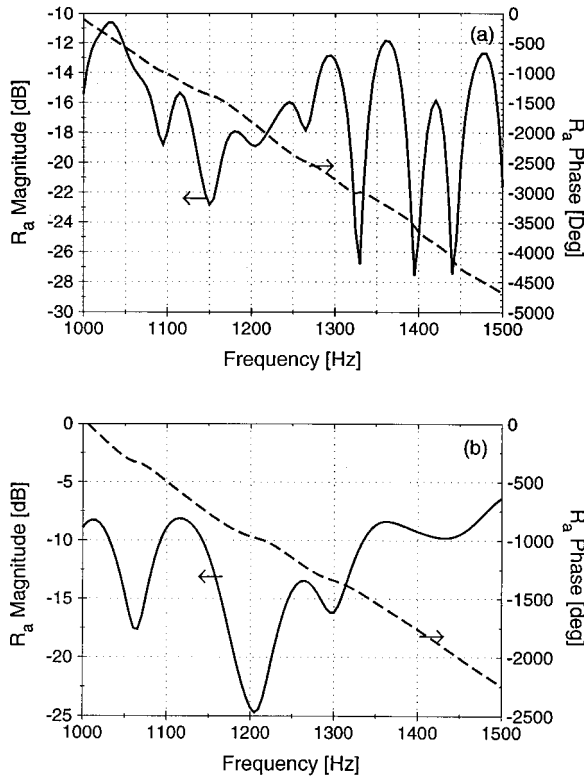


FIG. 3. Apical cochlear reflectance $R_a(\omega) = R_{\text{rough}}(\omega)$ for distributed discontinuities (roughness) in stiffness evaluated using the cochlear model of Talmadge *et al.* (1998). Results are shown for two different choices of model parameters, as discussed in Sec. III B. Model A and B results are given in the upper (a) and lower (b) panels, respectively. Note that the frequency range (1000–1500 Hz) is very narrow compared to that used for nonlinear reflectance (see Fig. 2). The rapid phase variation of $R_{\text{rough}}(\omega)$ is mainly responsible for the typical SFOAE fine structure that is observed experimentally.

$\sigma_x |\hat{\chi}_r^2|$ which appears in Eq. (34) is approximately 40 times larger than that in Model B. The increased variability of $|R_a|$ in Fig. 3(a) can be related to the smaller value of σ_x for Model A, and the larger slope for $\varphi_{\text{rough}}(\omega)$ is due to the larger value of \hat{k} , since the slope of $\varphi_{\text{rough}}(\omega)$ is just $2\hat{k}/k_\omega$.

C. Combined nonlinearity and distributed discontinuities

The real basilar membrane very likely contains both nonlinearities as well as distributed discontinuities. For this reason, it is useful to study the combined effect of both of these sources of reflection. Under the assumption that both effects are calculated to first order in perturbation theory, the resulting source contribution to $k^2(x, \omega)$ is then simply given by

$$\delta k_{\text{nl+rough}}^2(x, \omega) = \delta k_{\text{nl}}^2(x, \omega) + \delta k_{\text{rough}}^2(x, \omega), \quad (40)$$

and the resulting apical reflectance of an initial apical moving wave of amplitude $a_r(\omega)$ is given by

$$\begin{aligned} R_{\text{nl+rough}}(\omega) &= R_{\text{nl}}(\omega) + R_{\text{rough}}(\omega) \\ &= |R_{\text{nl}}(\omega)| e^{-i\varphi_{\text{nl}}(\omega)} \\ &\quad + |R_{\text{rough}}(\omega)| e^{-i\varphi_{\text{rough}}(\omega)}. \end{aligned} \quad (41)$$

Additional insight is provided by studying the level and phase of $R_{\text{nl+rough}}(\omega)$:

$$\begin{aligned} |R_{\text{nl+rough}}(\omega)|^2 &= |R_{\text{nl}}(\omega)|^2 + |R_{\text{rough}}(\omega)|^2 + 2|R_{\text{nl}}(\omega)||R_{\text{rough}}(\omega)| \\ &\quad \times \cos[\varphi_{\text{nl}}(\omega) - \varphi_{\text{rough}}(\omega)], \end{aligned} \quad (42)$$

$$\begin{aligned} |R_{\text{nl+rough}}(\omega)| \sin \varphi_{\text{nl+rough}}(\omega) &= |R_{\text{nl}}(\omega)| \sin \varphi_{\text{nl}}(\omega) + |R_{\text{rough}}(\omega)| \sin \varphi_{\text{rough}}(\omega), \end{aligned} \quad (43)$$

$$\begin{aligned} |R_{\text{nl+rough}}(\omega)| \cos \varphi_{\text{nl+rough}}(\omega) &= |R_{\text{nl}}(\omega)| \cos \varphi_{\text{nl}}(\omega) + |R_{\text{rough}}(\omega)| \cos \varphi_{\text{rough}}(\omega), \end{aligned} \quad (44)$$

where $\varphi_{\text{nl+rough}}(\omega) \equiv -\arg[R_{\text{nl+rough}}(\omega)]$. When $|R_{\text{nl}}(\omega)| \ll |R_{\text{rough}}(\omega)|$ or when $|R_{\text{nl}}(\omega)| \gg |R_{\text{rough}}(\omega)|$, these equations reduce to their expected limits: namely, at low excitation levels, the reflectance will resemble reflectance due purely to roughness and, at high levels, reflectance due purely to nonlinearity. When the magnitudes of the two components of reflectance are comparable, however, these results indicate that the reflectance will exhibit interference between these two components. The frequency spacing of this reflectance fine structure will be principally associated with the variation of $\varphi_{\text{rough}}(\omega)$, because of its more rapid phase behavior.

These observations are borne out in the simulation results shown in Fig. 4 for the magnitude and phase of the apical reflectance $R_a = R_{\text{nl}} + R_{\text{rough}}$. Note that the phase variation of R_a is much more rapid for low-level stimuli, which is consistent with the dominance of R_{rough} , as the phase variation of R_{rough} is much more rapid than R_{nl} . At higher levels of stimulation, the phase variation of R_a decreases dramatically, which is consistent with a dominance of R_{nl} .

IV. SINGLE TONE STIMULATION AND SFOAES

In this section, the cochlear response to a single tone stimulation and the resulting SFOAEs is considered for the models studied in Sec. III. By considering the response of the cochlea to a single tone, the phenomenology of the sources of reflection considered in the previous section can be illustrated. By comparing the results of these simulations to experimental observations, important conclusions can be drawn as to the nature of the underlying physical source of reflection, as was originally done for SFOAEs by Shera and Zweig (1993) (see also Zweig and Shera, 1995).

A. SFOAE fine structure equation

As derived in Talmadge *et al.* (1998), the car canal pressure due to a stimulation of level P_{dr} and frequency ω is

$$\begin{aligned} P_e(\omega) &= \left[T_{\text{dr}}(\omega) - G_{me}(\omega) T_{pd}(\omega) \right. \\ &\quad \left. \times \frac{k_r(0, \omega) k_{ow}(\omega)}{k_r(0, \omega) + k_{ow}(\omega)} \frac{1 + R_a(\omega) \mathcal{R}_s(\omega)}{1 - R_a(\omega) R_b(\omega)} \right] P_{\text{dr}}(\omega), \end{aligned} \quad (45)$$

where

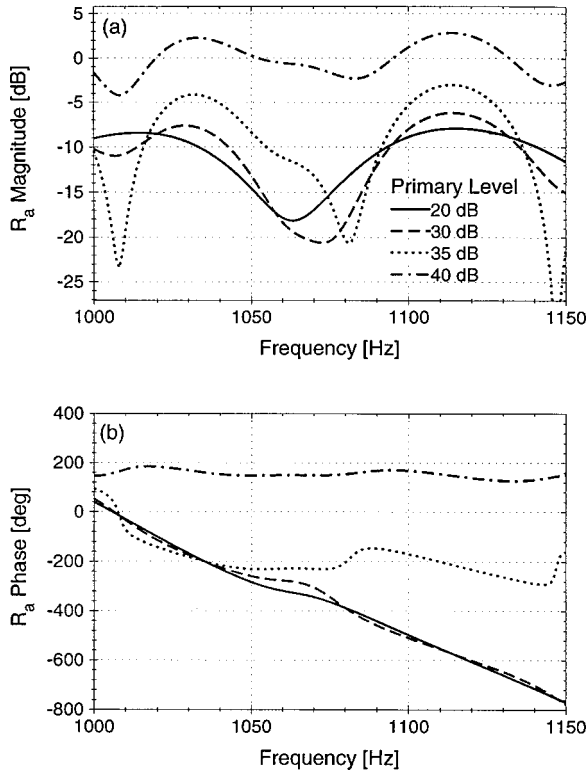


FIG. 4. Apical cochlear reflectance $R_a(\omega) = R_{nl+rough}(\omega)$ for the cochlear model of Talmadge *et al.* (1998) that contain nonlinear damping and roughness, as discussed in Sec. III C. The magnitude and phase of the reflectance are shown as functions of the stimulus level. At high stimulation levels, the reflectance is dominated by nonlinearity and its amplitude and phase vary slowly with frequency. At low stimulation levels, it is dominated by roughness and has a characteristically rapid phase variation. At levels for which roughness and nonlinear effects are comparable, there may be strong interference, as is indicated by the behaviors for a primary level of 35 dB SPL.

$$\mathcal{R}_s(\omega) = \frac{\psi'_l(0, \omega)}{\psi'_r(0, \omega)}. \quad (46)$$

Equation (45) was derived under the assumption that the reflectance represented a linear phenomenon (such as coherent reflection from distributed roughness), and will in general not be correct when dealing with nonlinear phenomena. However, the expansion of Eq. (45) in powers of $R_a(\omega)$ is valid through first order in $R_a(\omega)$.

Some insight into the structure of Eq. (45) can be obtained by studying the frequency dependence of $\mathcal{R}_s(\omega)$. From Fig. 5, it is apparent that $|\mathcal{R}_s(\omega)| \cong 1$ and $\arg[\mathcal{R}_s(\omega)]$ is slowly varying. For the active cochlear model used in this paper, the total phase change between $f = 500$ Hz and $f = 1500$ Hz is about -40° , and between 1500 Hz and 10 000 Hz, a phase change of less than -20° is observed.

Although the expressions for the reflectance from the various models could, in principle, be inserted directly into Eq. (45), further insight is obtained by focusing on the contribution to this equation that gives rise to cochlear fine structure, namely

$$\mathcal{F}_{sfoae}(\omega) = \frac{1 + R_a(\omega)\mathcal{R}_s(\omega)}{1 - R_a(\omega)R_b(\omega)}. \quad (47)$$

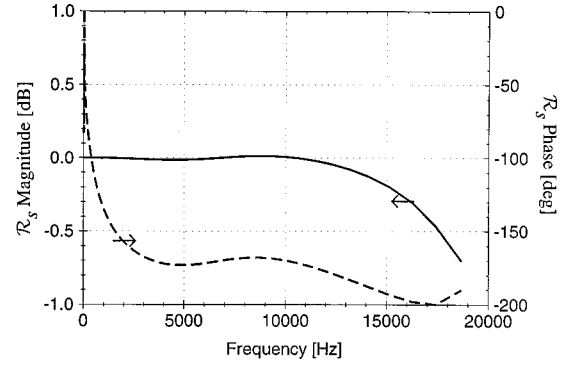


FIG. 5. Magnitude (solid line) and phase (dash line) of the ratio of the derivatives of cochlear basis functions, $\mathcal{R}_s(\omega) = \psi'_l(0, \omega) / \psi'_r(0, \omega)$, evaluated at the base. As expected, the magnitude of $\mathcal{R}_s(\omega)$ varies only slightly with frequency, and for frequencies above 1500 Hz, $\arg[\mathcal{R}_s(\omega)] \cong -160^\circ$.

The coefficient of this term in Eq. (45) describes the effects of the forward and reverse signal transmission through the middle ear and ear canal, while the other term $[T_{dr}(\omega)]$ represents the effect of the ear canal. In general, neither of these effects will give rise to rapid phase or amplitude changes in $P_e(\omega)$, and this is the basis for focusing attention only on $\mathcal{F}_{sfoae}(\omega)$. Equation (47) can be further simplified by assuming that $\mathcal{R}_s(\omega) \cong e^{i\varphi_s(\omega)}$ [where $\varphi_s(\omega) \equiv \arg[\mathcal{R}_s(\omega)]$ is the phase of $\mathcal{R}_s(\omega)$], $|R_a(\omega)| \ll 1$, and $|R_b(\omega)| \ll 1$, which gives

$$\mathcal{L}_{sfoae} \equiv \log|\mathcal{F}_{sfoae}(\omega)| \cong |R_a(\omega)| \cos[\varphi_a(\omega) + \varphi_s(\omega)], \quad (48)$$

$$\varphi_{sfoae} \equiv \arg[\mathcal{F}_{sfoae}(\omega)] \cong |R_a(\omega)| \sin[\varphi_a(\omega) + \varphi_s(\omega)], \quad (49)$$

where $\varphi_a(\omega) \equiv \arg[R_a(\omega)]$ and $\log(x)$ is the natural logarithm of x .

B. Model SFOAEs

1. SFOAEs for nonlinear reflectance

The SFOAE fine structure function for the smooth, nonlinear basilar membrane model described in Sec. III A is obtained by combining the $R_a(\omega)$ given by Eq. (29) (and shown in Fig. 2) with Eq. (48). The result, as displayed in Fig. 6, indicates that some fine structure may be expected at

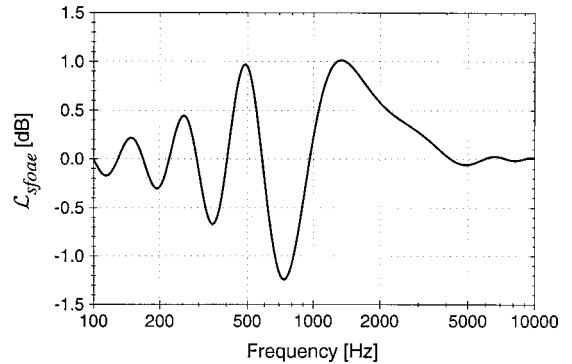


FIG. 6. Fine structure function \mathcal{L}_{sfoae} [defined by Eqs. (48) and (49)] for the nonlinear basilar membrane described in Sec. III A for a 20-dB swept tone. As for the plot of nonlinear reflectance shown in Fig. 2, note the greatly expanded frequency scale (100–10 000 Hz). The fine structure for frequencies below 1000 Hz arise from scale-invariance violations as discussed in Sec. IV B 1.

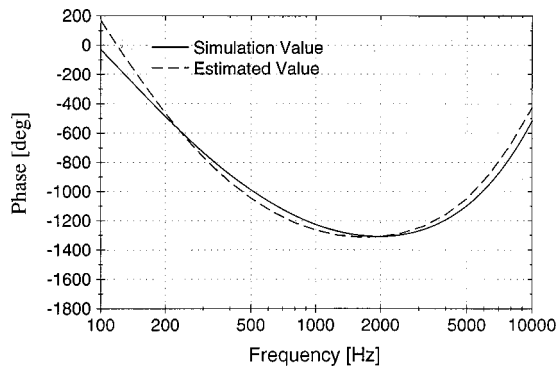


FIG. 7. Comparison of the simulation result for the phase $\varphi_{nl}(\omega)$ of the apical reflectance $R_a(\omega)$ from nonlinearity with that obtained by computing $N_\lambda(\omega)$, $\hat{k}(\omega)$, and $\sigma_x(\omega)$ and substituting these values into the approximate expression given by Eq. (31).

lower frequencies $f < 1000$ Hz in this model. It should be emphasized that this fine structure arises from scale-invariance violations. For SFOAE fine structure resulting from nonlinearity, the most important of these is the variation in the Q of the basilar membrane traveling wave envelope.

The variation of Q built into the cochlear model was based on estimates of Q ranging from 5 at the apex to 15 at the base (see Talmadge *et al.*, 1998). This variation is generated in the model by the differing scale-invariance violations of $\omega_0(x)$ and $\gamma_0(x)$. As a consequence of these violations, N_λ , \hat{k} , and σ_x all vary with frequency. Since these are the parameters that directly appear in Eq. (31), a variation in any of these parameters will result in a corresponding variation in $\varphi_{nl}(\omega)$.

This assertion can be tested by estimating the functions $N_\lambda(\omega)$, $\hat{k}(\omega)$, and $\sigma_x(\omega)$ using numerical solutions to the cochlear model of Appendix B, and then substituting these functions into Eq. (31). The result of this calculation is shown in Fig. 7, in which comparable variations in the $\varphi_{nl}(\omega)$ obtained directly from the simulation (solid line) and from Eq. (31) are observed. Note that some discrepancy is expected due to the approximations made in obtaining the closed-formed results, such as those given in Eqs. (25) and (27). Even with the application of these approximations, Eq. (31) is expected to be qualitatively similar to the direct simulation result, and this is what is found. The maximum deviation between the two curves is less than 80° degrees, compared to a total variation of 1300° in $\varphi_{nl}(\omega)$. It should be cautioned that the precise variation of Q with frequency is not well-measured experimentally, and consequently the fine structure pattern observed in this model is not expected to closely correspond to that observed in real human cochleas for the case of a smooth nonlinear basilar membrane.

Finally, it should be noted that the large scale-invariance violations found in this model at low frequencies $\omega \lesssim 1000$ Hz give a significant variation in $\mathcal{L}_{\text{sfoae}}(\omega)$ at these lower frequencies. Thus for cochleas with smooth nonlinear basilar membranes, physically measurable cochlear fine structure can still be present at low frequencies.

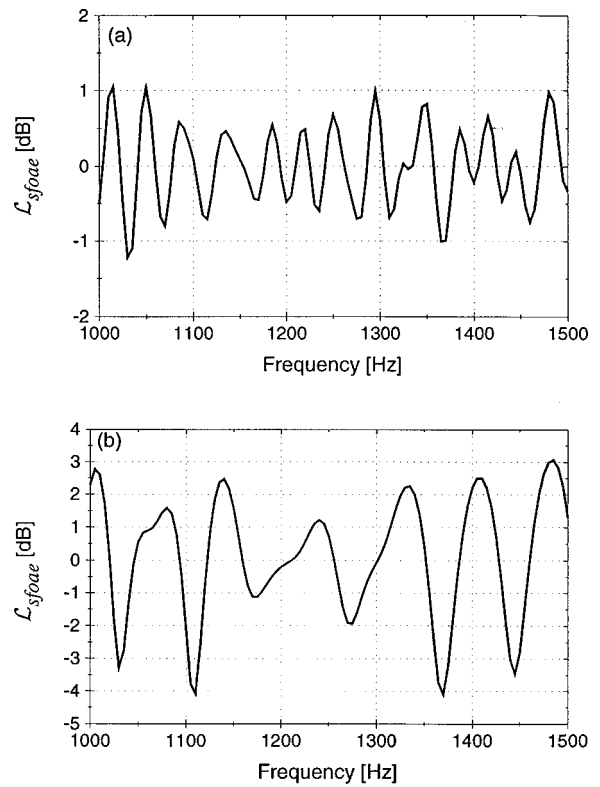


FIG. 8. Fine structure function $\mathcal{L}_{\text{sfoae}}$ for distributed discontinuities as described in Sec. II B. Plotted in (a) and (b) are the predictions for Models A and B (which are described in Sec. III B), respectively. As is discussed in Sec. IV B 2, the fine structure spacing for Model A is much smaller than in typical humans because of an unrealistically large wave number in the activity peak region.

2. SFOAEs for reflectance due to roughness

The SFOAE fine structures for the models with distributed discontinuities described in Sec. III B are shown in Figs. 8(a) and (b). These results were obtained by combining Eqs. (34) and (48). Note that the frequency spacing in Fig. 8(a) (corresponding to Model A of Sec. III B) between adjacent fine structure maxima is narrow compared to that found for human SFOAEs (Zwicker and Peisl, 1990). The difference in these results can be understood by noting that the relative frequency spacing between adjacent maxima located at angular frequencies ω and $\omega + \Delta\omega$ is given by the condition

$$\varphi_{\text{sfoae}}(\omega + \Delta\omega) - \varphi_{\text{sfoae}}(\omega) \cong \varphi_{\text{rough}}(\omega + \Delta\omega) - \varphi_{\text{rough}}(\omega) = 2\pi, \quad (50)$$

where the much smaller variation in $\varphi_s(\omega)$ has been neglected. Using Eq. (37) gives

$$\frac{2\hat{k}}{k_\omega} \log\left(\frac{\omega + \Delta\omega}{\omega}\right) \cong 2\pi. \quad (51)$$

Under the assumption that $\Delta\omega/\omega \ll 1$, this reduces to

$$\frac{\omega}{\Delta\omega} = \frac{f}{\Delta f} \cong \frac{\hat{k}}{\pi k_\omega}, \quad (52)$$

where $f = \omega/2\pi$ as usual, and $\Delta f = \Delta\omega/2\pi$ is the spacing between adjacent fine structure maxima. (For previous derivations of this result in a slightly different form, see Zweig and Shera, 1995 and Talmadge *et al.*, 1998.) Comparing the

simulation result to the prediction from Eq. (52) gives for Model A

$$\left. \frac{f}{\Delta f} \right|_{\text{simulation}} \approx \left(\frac{1030 \text{ Hz} + 1475 \text{ Hz}}{2} \right) \times \left(\frac{1475 \text{ Hz} - 1030 \text{ Hz}}{12 \text{ maxima}} \right)^{-1} \cong 33.8, \quad (53)$$

$$\left. \frac{f}{\Delta f} \right|_{\text{prediction}} \approx \frac{\pi \cdot 1.382 \text{ cm}^{-1}}{143 \text{ cm}^{-1}} \cong 32.9. \quad (54)$$

The value of $\hat{k}[1250 \text{ Hz}] = 143 \text{ cm}^{-1}$ quoted in Eq. (38) was obtained from the full simulation results. This value should be compared to the value of $k \cong 75 \text{ cm}^{-1}$ (e.g., Talmadge *et al.*, 1998) suggested by experiment; a similar value can be inferred from Zweig and Shera (1995). Thus the deviation between the model and observation can be understood as a consequence of a value of \hat{k} in Model A which is too large.²

3. SFOAEs for reflectance due to combined nonlinearity and roughness

The final case that will be considered is combined nonlinearity and distributed discontinuities, for which the fine structure equation is given by

$$\begin{aligned} \mathcal{F}_{\text{sfoae}}(\omega)|_{\text{nl+rough}} \cong & 1 + |R_{\text{nl}}(\omega)| e^{-i[\varphi_{\text{nl}}(\omega) + \varphi_s(\omega)]} \\ & + |R_{\text{rough}}(\omega)| e^{-i[\varphi_{\text{rough}}(\omega) + \varphi_s(\omega)]}, \end{aligned} \quad (55)$$

where the assumed forms of $R_{\text{nl}}(\omega)$ and $R_{\text{rough}}(\omega)$ are those given by Eq. (41) and the text that follows it.

To illustrate the phenomenology that arises when roughness is combined with nonlinearity, the magnitude of the reflectance due to roughness, $|R_{\text{rough}}(\omega)|$, will be assumed small, so that higher order terms in $|R_{\text{rough}}(\omega)|$ can be neglected. However, the relative magnitude of $R_{\text{nl}}(\omega)$ will be allowed to be large compared to $R_{\text{rough}}(\omega)$ in order to illustrate the influence of level on the fine structure due to the combined effects of nonlinearity and roughness. The analysis proceeds by first evaluating $|\mathcal{F}_{\text{sfoae}}(\omega)|$ and then expanding in terms of small quantities (for clarity, the dependence on ω is temporarily suppressed):

$$\begin{aligned} |\mathcal{F}_{\text{sfoae}}|^2 = & 1 + |R_{\text{nl}}|^2 + |R_{\text{rough}}|^2 + 2|R_{\text{nl}}|\cos(\varphi_{\text{nl}} + \varphi_s) \\ & + 2|R_{\text{rough}}|\cos(\varphi_{\text{rough}} + \varphi_s) \\ & + 2|R_{\text{nl}}||R_{\text{rough}}|\cos(\varphi_{\text{rough}} - \varphi_{\text{nl}}). \end{aligned} \quad (56)$$

Defining the quantity,

$$\begin{aligned} A_{\text{nl}}(\omega) \equiv & |1 + R_{\text{nl}}(\omega)e^{-i\varphi_s(\omega)}| \\ = & \sqrt{1 + |R_{\text{nl}}(\omega)|^2 + 2|R_{\text{nl}}(\omega)|\cos[\varphi_{\text{nl}}(\omega) + \varphi_s(\omega)]}, \end{aligned} \quad (57)$$

and using this definition in Eq. (56) gives

$$\begin{aligned} |\mathcal{F}_{\text{sfoae}}(\omega)|^2 \approx & A_{\text{nl}}^2(\omega) \\ & + 2|R_{\text{rough}}(\omega)|A_{\text{nl}}(\omega)\cos[\varphi_{\text{rough}}(\omega) \\ & + \varphi_s(\omega) - \bar{\varphi}_{\text{nl}}(\omega)], \end{aligned} \quad (58)$$

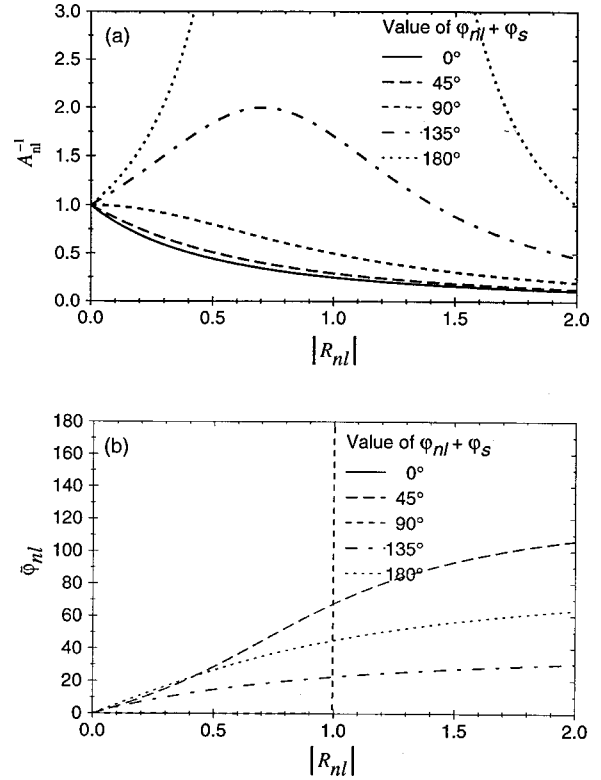


FIG. 9. Variation of the functions (a) $A_{\text{nl}}^{-1}(\omega)$ [Eq. (57)] and (b) $\bar{\varphi}_{\text{nl}}(\omega)$ [Eqs. (59) and (60)] for various choices of $\varphi_{\text{nl}}(\omega)$. These functions govern the effect of nonlinearity upon the SFOAE fine structure. See the text for details.

$$A_{\text{nl}}(\omega)\sin\bar{\varphi}_{\text{nl}}(\omega) = |R_{\text{nl}}(\omega)|\sin[\varphi_{\text{nl}}(\omega) + \varphi_s(\omega)], \quad (59)$$

$$A_{\text{nl}}(\omega)\cos\bar{\varphi}_{\text{nl}}(\omega) = 1 + |R_{\text{nl}}(\omega)|\cos[\varphi_{\text{nl}}(\omega) + \varphi_s(\omega)], \quad (60)$$

where quantities of order $|R_{\text{rough}}(\omega)|^2$ have been neglected. Finally, assuming that $|R_{\text{rough}}(\omega)| \ll A_{\text{nl}}(\omega)$, applying the definition of $\mathcal{L}_{\text{sfoae}}(\omega)$ given by Eq. (48), and expanding gives

$$\begin{aligned} \mathcal{L}_{\text{sfoae}}(\omega) \cong & \log A_{\text{nl}}(\omega) + \frac{|R_{\text{rough}}(\omega)|}{A_{\text{nl}}(\omega)} \\ & \times \cos[\varphi_{\text{rough}}(\omega) + \varphi_s(\omega) - \bar{\varphi}_{\text{nl}}(\omega)]. \end{aligned} \quad (61)$$

Since $A_{\text{nl}}(\omega)$, $\varphi_{\text{nl}}(\omega)$, and $\varphi_s(\omega)$ are expected to vary slowly compared to $\varphi_{\text{rough}}(\omega)$, the first term in Eq. (61) simply produces a vertical shift in $\mathcal{L}_{\text{sfoae}}(\omega)$. The origin of the second term can be understood by noticing that the first two terms in Eq. (55) are slowly varying in phase compared to the $R_{\text{rough}}(\omega)$ term. Thus the effect of the nonlinearity to lowest order is to modify the ratio of the rapidly varying phase term to the slowly varying phase term. Increasing this ratio, for example, increases the amplitude of the fine structure.

The variation of $A_{\text{nl}}^{-1}(\omega)$ with $|R_{\text{nl}}(\omega)|$ is illustrated in Fig. 9(a) for several choices of $\varphi_{\text{nl}} + \varphi_s$. For $0^\circ \leq \varphi_{\text{nl}}(\omega) + \varphi_s(\omega) \leq 90^\circ$ [corresponding to $\cos[\varphi_{\text{nl}}(\omega) + \varphi_s(\omega)] \geq 0$], $A_{\text{nl}}^{-1}(\omega)$ is monotonically decreasing with $|R_{\text{nl}}(\omega)|$. Consequently, the fine structure amplitude is expected to increase with increasing $|R_{\text{nl}}(\omega)|$, and thus with increasing stimulus level $|P_{\text{dr}}|$. If, on the other hand, for $90^\circ < \varphi_{\text{nl}}(\omega) + \varphi_s(\omega)$

$\leq 180^\circ$ [corresponding to $\cos[\varphi_{nl}(\omega) + \varphi_s(\omega)] < 0$], $A_{nl}^{-1}(\omega)$ initially increases with $|R_{nl}(\omega)|$ until it reaches a maximum, and then decreases for larger values of $|R_{nl}(\omega)|$. For $\varphi_{nl} + \varphi_s = 180^\circ$ and $|R_{nl}(\omega)| \rightarrow 1$, $A_{nl}^{-1}(\omega) \rightarrow \infty$, and the assumptions used to obtain Eq. (61) are formally violated, as are the assumptions used to obtain an approximate expression for $R_{nl}(\omega)$ in Eq. (29).

Although the first-order perturbation calculation for $R_{nl}(\omega)$ is unlikely to be correct for $|R_{nl}(\omega)| > 1$, it is instructive to compare the SFOAE fine structure predictions of this first-order theory to the reflectance computed using a time-domain model, for which the full order of nonlinearity is implicitly retained. The difference between the first-order theory and the ‘‘full solution’’ will thus indicate the relative importance of the higher-order corrections to $R_{nl}(\omega)$. It is found that the chief distinction between the first-order theory and the full solution is that $|R_{nl}(\omega)| \rightarrow 0$ for $|P_{dr}(\omega)|/P_{nl}(\omega) \rightarrow \infty$, where $P_{nl}(\omega)$ is given by Eq. (30); however, the phase is only weakly affected by values of $|P_{dr}(\omega)| \gg P_{nl}(\omega)$.

The frequency shift of the fine structure pattern with primary level $|P_{dr}(\omega)|$ is governed by $\bar{\varphi}_{nl}(\omega)$. This can be demonstrated by implicitly defining the frequency shift due to nonlinearity, $\Delta\omega_{nl}(\omega)$, in terms of the equation,

$$\bar{\varphi}_{nl}(\omega) = \frac{2\hat{k}}{k_\omega} \log \left[1 - \frac{\Delta\omega_{nl}(\omega)}{\omega} \right], \quad (62)$$

and then combining Eq. (62) with Eq. (37),

$$\varphi_{rough}(\omega) - \bar{\varphi}_{nl}(\omega) = \frac{2\hat{k}}{k_\omega} \log \left[\frac{\omega - \Delta\omega_{nl}(\omega)}{\omega_0} \right] + \varphi_{0a}. \quad (63)$$

From Eqs. (62) and (63), it can be seen that a positive (negative) value of $\bar{\varphi}_{nl}(\omega)$ gives rise to a shift in the fine structure maximum and minima to higher (lower) frequencies. For $|R_{nl}(\omega)| < 1$, the sign of $\bar{\varphi}_{nl}(\omega)$ will be the same as $\sin[\varphi_{nl}(\omega) + \varphi_s(\omega)]$. The variation of $\bar{\varphi}_{nl}(\omega)$ with $|R_{nl}(\omega)|$ is illustrated in Fig. 9(b) for several (positive valued) choices of $\varphi_{nl}(\omega) + \varphi_s(\omega)$.

Representative behaviors of the SFOAE level fine structure are shown in Figs. 10(a) and (b) for various levels of the driving pressure $|P_{dr}(\omega)|$. These simulated results were obtained by computing separately $R_{nl}(\omega)$, $R_{rough}(\omega)$, and $\mathcal{R}_s(\omega)$, and then using these values in Eq. (55).

Notice in Fig. 10(a) that the fine structure amplitude becomes progressively smaller and the fine structure mean level shifts to a higher value with increased $|P_{dr}(\omega)|$. This behavior is consistent with a monotonic increase in $A_{nl}(\omega)$. In this frequency range, $\cos[\varphi_{nl}(\omega) + \varphi_s(\omega)]$ varies from 0.911 to 0.985, a behavior consistent with the theory outlined above. Note also that the fine structure pattern shifts to higher frequency with increased $|P_{dr}(\omega)|$. This shift is consistent with the values of $\sin[\varphi_{nl}(\omega) + \varphi_s(\omega)]$, which range from 0.173 to 0.412.

In Fig. 10(b), the fine structure amplitude initially becomes enhanced and is accompanied by a decreasing mean value of the fine structure level with increasing $|P_{dr}(\omega)|$. At higher levels [e.g., $|P_{dr}(\omega)| = 45$ dB], the fine structure amplitude again decreases as implied by the approximate

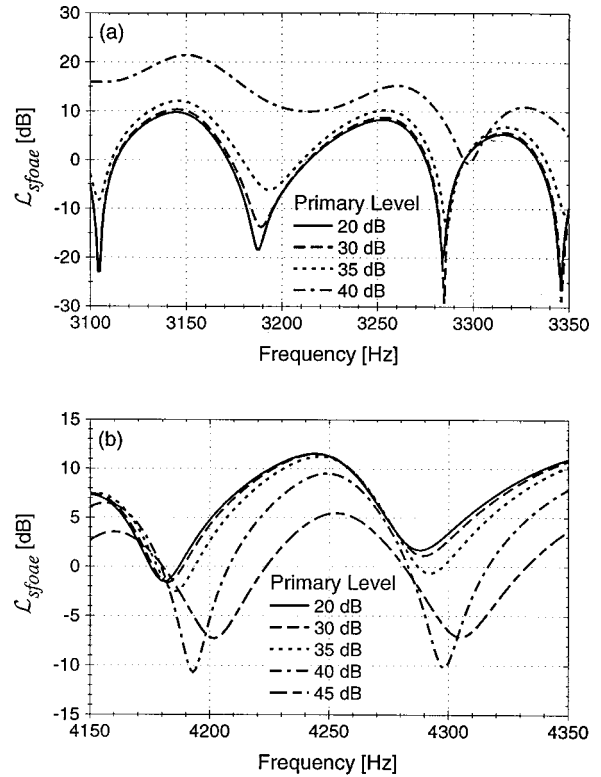


FIG. 10. Fine structure function \mathcal{L}_{sfoae} obtained from combined nonlinearity and roughness using Model A of Sec. III C, shown as a function of level for two separate frequency regions, which have been chosen to illustrate some of the effects of nonlinearity on SFOAE fine structure.

theory. For comparison, $\cos[\varphi_{nl} + \varphi_s]$ varies from 0.011 at 4150 Hz to -0.218 at 4350 Hz, which is again consistent with the theory given above. Finally, the fine structure pattern again shifts to higher frequency with increased $|P_{dr}(\omega)|$. This behavior is consistent with the values of $\sin[\varphi_{nl}(\omega) + \varphi_s(\omega)]$, which range from 0.976 to 1.00.

It should be noted that these figures exhibit a trend of decreased (increased) mean level of the fine structure accompanied by an enhanced (diminished) fine structure amplitude. This trend is a general property of SFOAEs which results from combined nonlinearity and roughness, as predicted by Eq. (61). On the other hand, the shift of the fine structure pattern to higher frequencies with increased primary levels should not be regarded as a general property of SFOAEs, but rather a consequence of the frequency ranges chosen for these simulations.

Finally, the general trends expected in the fine structure amplitude and the corresponding frequency shifts are summarized in Fig. 11. This figure shows the effects of the level of the tone and the relative phase, $\varphi_{nl}(\omega) + \varphi_s(\omega)$, on the fine structure. The arrow in this figure shows the direction of increasing phase. Note from Fig. 2 that the nonlinear phase decreases with frequency until it reaches approximately 2000 Hz, where it starts to increase with frequency. This means that the shift in behavior with increasing stimulus frequency below this break-point frequency corresponds to a clockwise rotation on the circle. Above the break-point frequency, the shift will correspond to a counterclockwise behavior.

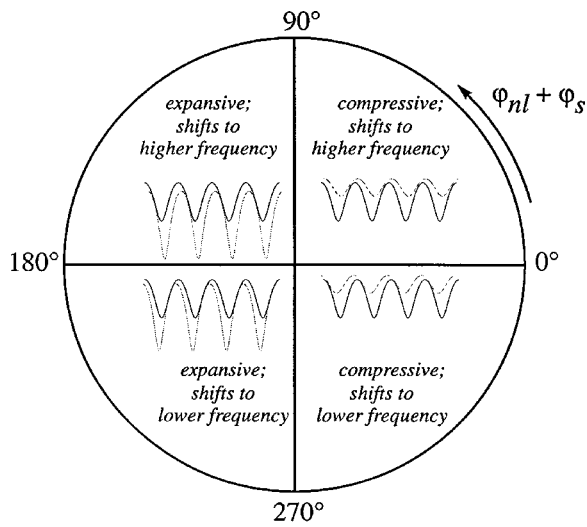


FIG. 11. Illustration of the effects of combined nonlinearity and roughness on the fine structure function $\mathcal{L}_{\text{SFOAE}}$. This figure relates the phase $\varphi_{nl} + \varphi_s$ to the effect of stimulus on SFOAE fine structure. Shown are the effects of a low-level (black line) and a high-level (gray line) tone on the SFOAE fine structure for the four quadrants of the phase $\varphi_{nl} + \varphi_s$. The variation in the effects of stimulus level on SFOAE fine structure with stimulus frequency can be understood by consideration of the effects of frequency on $\varphi_{nl} + \varphi_s$ (see Figs. 2 and 5, respectively). In this model, below approximately 2000 Hz, $\varphi_{nl} + \varphi_s$ decreases with increasing stimulus frequency, corresponding to a clockwise rotation of phase in the figure. Above 2000 Hz, this phase increases with stimulus frequency, corresponding to a counterclockwise rotation of phase in the figure.

V. DISCUSSION

Additional details are given in this section regarding extensions to the formalism outlined in this paper. Unless specifically stated otherwise, the discussion in this section is based on the assumption of a combination of nonlinear reflection and coherent linear reflection.

A. Effect of nonlinearity on R_{rough}

The effects of combined nonlinearity and roughness were considered in Secs. III C and IV B 3. In these sections, however, the direct effects of nonlinearity on the value of R_{rough} were ignored. These direct effects occur as a result of the reduced height, $|\hat{\chi}_r(\omega)|$, and increased width, σ_x , of the basilar membrane traveling wave, as is illustrated in Fig. 12. In this figure, the basilar membrane amplitude (normalized to its response at the base) and phase are plotted as functions of stimulus level. Only the basilar membrane level is significantly affected by the nonlinearity. This result is due to the assumption that the nonlinearity occurs only in the basilar membrane damping function [see Eq. (19)]. The lack of influence of the nonlinearity on the phase also means that the local wave number will be relatively insensitive to the level of the stimulus, since $k(x, \omega) = -\partial\varphi(x, \omega)/\partial\omega$. Another significant effect of the nonlinearity is a basal shift of the peak of the activity pattern with increased level of stimulation.

It was demonstrated in Sec. III B that using two different sets of parameters for the cochlear model (the so-called Models A and B) gives a dramatic effect on the apical reflectance due to roughness. In a similar manner, increasing the stimulus level will systematically reduce the magnitude of the reflectance. This is due to the broadening of the activ-

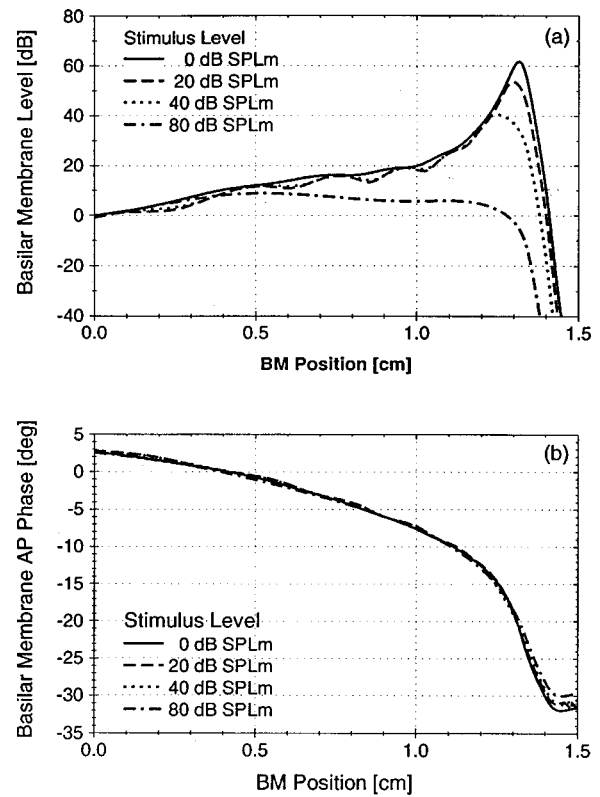


FIG. 12. Effect of the stimulus level on the basilar membrane activity pattern (a) amplitude and (b) phase for a nonlinear cochlear model. The basilar membrane response is plotted relative to its value at the base. Note that the primary effect of the nonlinearity is on the activity pattern level (a result of the assumption that the nonlinearity is rooted in the basilar membrane damping function).

ity pattern and decreased relative BM response for high level stimuli. The peak of the activity pattern also shifts to a slightly more basal region of the cochlea, and therefore “samples” a slightly different region of the roughness. A lower frequency tone will then be needed to sample a region of the basilar membrane that, at lower stimulus levels, gives fine structure effects at higher frequencies. Thus the fine structure pattern will shift to lower frequencies. However, this description was made by neglecting the reflection due to nonlinearity, and therefore is an incomplete description at best.

When the direct effects of nonlinear saturation of the activity pattern on the reflectance due to roughness are combined with the apical reflectance induced by nonlinearity, the results are slightly modified from those given in Sec. IV B 3. If $|R_{\text{rough}}(\omega)|$ is sufficiently large, then at moderate levels of stimulation the initial effects of the nonlinearity on the fine structure will be a slight reduction in the mean level and a shift of the fine structure pattern to lower frequency. In cochleae with little roughness, it is also expected that nonlinear reflectance will be observable at lower stimulus levels. This is due to the fact that the apical reflectance due to roughness R_{rough} will be smaller in magnitude, so that a lower stimulation level is needed to produce a comparable magnitude for the nonlinear reflectance P_{nl} . In addition, the effects of the nonlinearity will be compressed into a narrow range of levels in a cochlea with little fine structure compared to that for

cochleae with larger fine structure. This is a consequence of the saturation of the nonlinear effects for higher level stimuli (the growth of nonlinear effects occurs more slowly for high stimuli levels compared to lower ones).

B. Relationship of $\mathcal{F}_{\text{sfoae}}(\omega)$ to experimentally measured quantities

Several procedures have been proposed for estimating values of $\mathcal{F}_{\text{sfoae}}(\omega)$ [Eq. (47)], or a simple expression involving $\mathcal{F}_{\text{sfoae}}(\omega)$, from experimental measurements. One protocol, originally proposed by Kemp and Chum (1980), is based on the assumptions that at sufficiently high stimulation levels, $R_a(\omega) \rightarrow 0$ as a consequence of the compressive nature of the cochlear nonlinearity, and that

$$\Gamma(\omega) = G_{me}(\omega) T_{pd}(\omega) \frac{k_r(0, \omega) k_{ow}(\omega)}{k_r(0, \omega) + k_{ow}(\omega)} \quad (64)$$

is independent of stimulus level. Then the difference between $P_e(\omega)$ and $P_e(\omega)|_{\text{scaled}}$ (which is the ear canal pressure at a high level of stimulation scaled to the low stimulation level) is

$$\begin{aligned} P_e(\omega) - P_e(\omega)|_{\text{scaled}} &= -\Gamma(\omega) [\mathcal{F}_{\text{sfoae}}(\omega) - 1] P_{dr}(\omega) \\ &\cong -\Gamma(\omega) R_a(\omega) R_s(\omega) P_{dr}(\omega), \end{aligned} \quad (65)$$

where it is assumed that $|R_b(\omega)| \ll 1$. If this quantity is further divided by the scaled $P_e(\omega)$ for high level stimulation, this results in

$$\begin{aligned} \frac{P_e(\omega) - P_e(\omega)|_{\text{scaled}}}{P_e(\omega)|_{\text{scaled}}} &= \frac{\Gamma(\omega)}{\Gamma(\omega) - 1} [\mathcal{F}_{\text{sfoae}}(\omega) - 1] \\ &\cong -\frac{\Gamma(\omega)}{\Gamma(\omega) - 1} R_a(\omega) R_s(\omega). \end{aligned} \quad (66)$$

A major problem with this and other variants of this approach, in addition to the necessity of having to independently obtain an estimate of $\Gamma(\omega)$, is that it is difficult to determine how high the stimulation level must be in order for $R_a(\omega) \rightarrow 0$. The nonappearance of fine structure is not a sufficient criterion since, except at very low frequencies, $R_a(\omega)$ from nonlinearity does not give fine structure that varies rapidly with frequency.

An alternative approach is to fit the SFOAE measurements of $P_e(\omega)$ with a low order polynomial for each level of stimulation and subtract this best-fit background contribution. Because of the slow variation in $\mathcal{F}_{\text{sfoae}}(\omega)$ arising from the nonlinear reflection contribution, this procedure will remove most of this contribution and leave a ‘‘linearized’’ residual.

A third approach is to normalize $P_e(\omega)$ to the calibrated pressure $P_{dr}(\omega)$. This has many of the advantages of the first method described above, but does not subtract off the additive component due to nonlinear reflection [i.e., the first term in Eq. (61)]. The trade-off is a slightly more complex relationship between the fine structure and the underlying mechanics, which is offset by the preservation of the important qualitative features of the SFOAE due both to nonlinearity and roughness.

A promising new technique for estimating $\mathcal{F}_{\text{sfoae}}(\omega)$ has been proposed by Dreisbach *et al.* (1998, 1999), in which $P_e(\omega)$ is measured at the same level of stimulation with and without a suppressor close in frequency to ω . The measurement in the presence of the suppressor tone is assumed to correspond to $R_a(\omega) = 0$ as a consequence of the assumption that the suppressor reduces $|\hat{\chi}_r(\omega)|$ enough so that $R_a(\omega)$ becomes negligible.

C. Modulation of $|R_a(\omega)|$

A surprising phenomenological result of the analysis of Sec. III C is that the introduction of nonlinearity to the linear coherent reflection process is an apparent modulation of $R_a(\omega)$. For the case of purely linear coherent reflection, $|R_a(\omega)|$ is expected to vary slowly with frequency, as described in Sec. III B. In this picture, fine structure in OAEs is the result of the interference of a component with a phase that varies slowly with the frequency and a component due to coherent linear reflection which has a phase that varies rapidly with frequency. However, as shown by Fig. 4, introducing nonlinearity results in an amplitude $|R_a(\omega)|$ which itself has a fine structure due to the interference of the $R_{nl}(\omega)$ and $R_{\text{rough}}(\omega)$ components of reflection. This result is of particular interest for pulses of very short duration, for which there may be no components with slowly varying phases.

D. Physical scale of roughness

The 1D cochlear model with embedded roughness is unable to *a priori* predict the exact pattern (if any) of spontaneous otoacoustic emissions (SOAEs) which will be produced. However, a qualitative estimate of the magnitude r_0 of the roughness needed to produce SOAEs can be obtained using the criterion that the magnitude of the apical reflectance $|R_a| > 1$. [See Talmadge and Tubis (1993a) and Sec. IV of Talmadge *et al.* (1998) for detailed discussions of the criteria necessary for the generation of SOAEs.]

Using the 1D model results, it is possible to estimate the magnitude of roughness r_0 needed to generate SOAEs using, e.g., Eq. (34). Using the WKB solution to estimate the Wronskian, $W_0(\omega) \cong -2ik(0, \omega)$, assuming an activity pattern maximum width $\sigma_x \approx 0.1$ cm, a basilar membrane ‘‘gain’’ of $|\hat{\chi}| \approx 10^3$, and a SOAE frequency ≈ 2000 Hz gives

$$r_0 \approx 0.02\% \times \left(\frac{f}{2000 \text{ Hz}} \right)^3 \times \left(\frac{\sigma_x}{0.1 \text{ cm}} \right) \times \left(\frac{|\hat{\chi}_r|}{10^3} \right)^2. \quad (67)$$

Since the values for f , σ_x and $|\hat{\chi}_r|$ represent nominal values for those quantities, the value $r_0 \approx 0.02\%$ for the appearance of SOAEs in a given model is a reasonable estimate. Since $r_f(\omega)$ is a pseudorandom quantity and can vary in magnitude from 0.01 to a value of order 1, this low level of roughness is not expected to produce a large family of SOAEs, but rather a few weaker SOAEs (plus their associated distortion product SOAEs).

This qualitative prediction is consistent with modeling results using the time-domain implementation of the 1D cochlear model described in Appendix B. Of course, the results

vary somewhat depending on the exact values of σ_x and $|\hat{\chi}_r|$ produced by a given model. A detailed comparison of the model simulation results versus predicted performance, however, is outside of the scope of this paper, nor given the limitations of the 1D model outlined in Sec. II, is such a detailed comparison particularly meaningful.

E. Dependence of the results on the form of the nonlinearity

As was discussed in Sec. II B, justification for the particularly simple form of the nonlinearity is based both on experimental and theoretical observations, and it is further assumed that the level of BM excitation is small enough so that the Taylor series expansion of Eq. (3) can be justified. It is expected that this simple damping function should hold approximately at low-to-moderate stimulation levels ($L_{dr} \equiv |P_{dr}| \leq 50$ dB SPL) where an interference between the reflectance due to nonlinearity R_{nl} and R_{rough} is expected. At higher stimulation levels, the validity of Eq. (3) is highly suspect, and for these levels the variation of R_{nl} with L_{dr} may vary radically from that described using the simple cubic damping function of this paper.

F. Relative magnitudes of reflectance due to roughness and nonlinearity

It was shown in Sec. IV that, under certain circumstances, the effects of nonlinear reflectance can significantly modify and even dominate the generated fine structure of SFOAEs. In order to assess how general this result is, it is necessary to first discuss the link between phenomenology and model parameters. In practice, the scale of basilar membrane roughness is set by the amplitude of SFOAE or DPOAE fine structure of otoacoustic emissions generated by low-level stimulation.

The BM nonlinear saturation scale b_{nl} is defined as the level at which the nonlinear component of damping is approximately equal to that due to passive linear damping. It can be set using a number of different methodologies, all of which ultimately prove to be equivalent. One means of setting the nonlinear saturation level b_{nl} is by fixing the maximum SOAE level to the maximum observed experimentally. Once this is done, any further saturation effects become a prediction of the model. A similar approach is to fix the ‘‘roll-over’’ or ‘‘bend-over’’ of DPOAE I/O curves (that is, where the DPOAE I/O curve ceases to have a straight-line behavior on a log–log plot). In the simulations reported on in this paper, the latter method was used. More specifically, the I/O curve for equal-level primaries was chosen so as to have a maximum at primary levels of 65 dB SPL. This value was chosen as typical of our own data as well as that of published data (e.g., Nelson and Zhou, 1996).

Except in regions where $|R_{rough}| \geq 1$ (for which the above analysis is invalid in any case), some stimulation level L_{dr} will exist for which the magnitude of nonlinear reflectance $|R_{nl}|$ will become comparable to that due to roughness $|R_{rough}|$. For a very ‘‘smooth’’ basilar membrane, such as that discussed in this paper, the approximate equivalence $|R_{nl}| \approx |R_{rough}|$ corresponds to a moderately low level of

stimulation, that is, driving pressure levels in the range 30–40 dB SPL. For more realistic amounts of roughness, which generate more typical SFOAE amplitudes, the corresponding driving pressure levels are in the range 40–50 dB SPL. Models which have $|R_a| > 1$ will require time-domain simulation to establish the levels (if any) at which equivalence between the two reflectances will occur.

G. Applicability of results to other cochlear fine structures

A complete framework for modeling the various classes of OAEs was given in Talmadge *et al.* (1998) for the case of linear coherent reflection. The extension of the current work to include other classes of cochlear fine structures is, for the most part, quite straightforward, and many of the qualitative results, e.g., of level on the cochlear fine structures, are expected to carry over to these other types of emissions.

A case which is more subtle is that of DPOAEs. The reason for this is that the fine structure in this case is thought to be a combination of that originating from the generator site and that from the DP best place (the ‘‘reflection’’ site). If, for example, the level of the lower frequency primary is held fixed, while the higher level primary is varied in frequency, an effect on the position of maximum overlap of the two sources is expected (e.g., He and Schmiedt, 1993). This shift in the maximum overlap, in turn, will translate into a shift in the position of the DP fine structure, as was discussed by He and Schmiedt (1993). Nonetheless, a level effect of nonlinear reflection on the DPOAE fine structure is expected, including the previously discussed results of a shift of the fine structure pattern to either higher or lower frequency (for an assumed stationary primary overlap position), as well as either enhancement or reduction of the fine structure amplitude. Detailed discussion of these points will be deferred to a future publication.

VI. SUMMARY

In agreement with previous investigations (Zweig and Shera, 1995; Talmadge *et al.*, 1998; Shera and Guinan, 1999), it was found that the phenomenology of cochlear fine structures resulting from low-level stimuli is best described by a linear cochlear model with embedded roughness. It was found that although nonlinearity does give a significant reflection at higher levels, the relatively slow phase variation of the reflectance (see Fig. 2) results in a fine structure which varies too slowly in level (see Fig. 6) to account for the much more rapid variation in level observed in real cochlear fine structure (e.g., Shera and Guinan, 1999).

For higher level stimulation, it was also found necessary to incorporate both roughness and nonlinearity in order to give a realistic description of the level behavior of SFOAEs. The effects of nonlinearity, which were insignificant at low levels, give rise to a surprisingly rich phenomenology when incorporated into models of SFOAEs. The properties of SFOAEs described in this paper will be more fully tested against experiment in a future publication. The inclusion of this class of nonlinear effects into models of DPOAEs may

help to identify behaviors that have not been previously recognized as systematic. This topic will also be dealt with in detail in a separate paper.

ACKNOWLEDGMENTS

The authors would like to thank Jont Allen, Diek Duifhuis, Egbert de Boer, Paul Fahey, Peter van Hengel, Douglas Keefe, Chris Shera, Hero Wit, and George Zweig for many stimulating discussions concerning cochlear mechanics and sometimes provocative comments that have stimulated our research on this topic. This research was supported in part by NIH/NIDCD Grant No. R29 DC03094.

APPENDIX A: FREQUENTLY USED SYMBOLS AND THEIR MEANING

Frequently used mathematical symbols employed in this study and their meanings are summarized below. In the cases for which the symbol has a defining equation, its corresponding equation number is also included. When values are available in Table I of Talmadge *et al.* (1998) this is so indicated.

Operators

$\text{Re}(z)$	real part of z
$\text{Im}(z)$	imaginary part of z
$\arg(z)$	phase of z
$ z $	magnitude of z
\hat{A}	denotes that the quantity A contains a random component.
$\hat{A}(x, \dots)$	the value of the cochlear quantity evaluated at the tonotopic position $\hat{x}(\omega)$
δA	denotes the difference $A - A_{\text{sm}}$, where A_{sm} is the value of the underlying quantity for a smooth linear cochlea.

Independent variables

f	frequency
k	wave number ($2\pi/\lambda$), also used to signify quantities with dimensions of inverse length
P	pressure
t	time
x	position along basilar membrane ($x=0$ corresponds to base)
λ	characteristic wavelength of the transpartition traveling wave
ω	angular frequency ($2\pi \times f$)
ξ	linear displacement

Physical quantities (cochlea)

b_{nl}	scale for nonlinear saturation, assumed independent of x (see Table I of Talmadge <i>et al.</i> , 1998)
H_{sc}	height of the cochlear scalae (≈ 0.1 cm in humans)
\hat{k}	real value of wave number at activity pattern maximum (\hat{k} is assumed independent of frequency)
k_0	geometric wave number of cochlea [Eq. (B8)]
k_ω	exponential constant of frequency map
$k(x, \omega)$	complex wave number [Eq. (B4)]

$k_{\text{sm}}(x, \omega)$	smooth component of wave number [Eq. (B19)]
L_{bm}	length of basilar membrane (see Table I of Talmadge <i>et al.</i> , 1998)
$P_d(x, \omega)$	complex amplitude of basilar membrane motion [Eq. (B2)]
S_{avg}	reciprocal average of cross-sectional areas of cochlear scalae (see Table I of Talmadge <i>et al.</i> , 1998)
W_{bm}	average width of basilar membrane (see Table I of Talmadge <i>et al.</i> , 1998)
$\hat{x}(\omega)$	tonotopic location of traveling wave of frequency ω
$\hat{\chi}_{r,l}(\omega)$	level of right, left basilar membrane basis functions at tonotopic frequency of traveling wave ($\hat{\chi}_{r,l}$ is assumed independent of frequency)
$\gamma_0(x)$	linear (with displacement) basilar membrane damping function [Eq. (B7); see also Table I of Talmadge <i>et al.</i> , 1998]
$\gamma_2(x)$	nonlinear (with displacement) basilar membrane damping function [$\gamma_2(x) = \gamma_0(x)/b_{\text{nl}}^2$]
$\omega_0(x)$	passive linear (with displacement) component of basilar membrane frequency map [Eq. (B6)]
ρ	density of the perilymph
$\rho_{f,s}$	“fast, slow” feedback coupling strength coefficients [Eq. (B5)]
$\psi_{f,s}$	“fast, slow” feedback constant [Eq. (B5)]
σ_{bm}	effective mass per unit area of basilar membrane
$\xi(x, \omega)$	complex amplitude of basilar membrane motion [Eq. (B3)]

Derived quantities (cochlea)

$a_{\text{nl}}(\omega)$	nonlinear saturation amplitude of pressure traveling waves [Eq. (30)]
$a_{r,l}$	right, left pressure wave basis function amplitudes [Eq. (B25)]
$b_{\text{nl}}(\omega)$	basilar membrane nonlinear saturation amplitude [Eq. (24)]
$b_{r,l}$	right, left basilar membrane basis function amplitudes [Eq. (B35)]
$\mathcal{F}_{\text{sfoae}}(\omega)$	fine structure function for SFOAEs [Eq. (47)]
$\mathcal{L}_{\text{sfoae}}(\omega)$	level of fine structure function for SFOAEs [Eq. (48)]
N_λ	number of wavelengths of pressure traveling wave from base to activity maximum [Eq. (B41)]
$P_{\text{nl}}(\omega)$	ear canal driving pressure nonlinear saturation level [Eq. (30)]
$R_a(x, \omega)$	ratio of basal to apical traveling waves [Eq. (B49)]
$R_b(x, \omega)$	ratio of apical to basal traveling waves [Eq. (B53)]
$R_a(\omega)$	reflectance function at the base for an initially apical moving wave [Eq. (B51)]
$R_b(\omega)$	reflectance function at the base for an initially basally moving wave [Eq. (B55)]
$\mathcal{R}_a(x, \omega)$	ratio of basal to apical traveling basis functions [Eq. (B54)]

$\mathcal{R}_b(x, \omega)$	ratio of apical to basal traveling basis functions [Eq. (B54)]
$R_{nl}(\omega)$	apical reflectance due to nonlinearity [e.g., Eq. (30)]
$R_{nl+rough}(\omega)$	apical reflectance due to combined nonlinearity and roughness [e.g., Eq. (41)]
$R_{rough}(\omega)$	apical reflectance due to roughness [e.g., Eq. (35)]
$\mathcal{R}_s(\omega)$	ratio of derivatives of basis function evaluated at $x=0$ [Eq. (46)]
$W_0(\omega)$	Wronskian [Eq. (B27)]
$\chi_{r,l}(x, \omega)$	right, left basilar membrane basis functions [Eq. (B33)]
$\Delta(x, \omega)$	denominator of wave number [Eq. (B5)]
$\delta k^2(x, \omega)$	deviation of a particular cochlear model from underlying ‘‘smooth’’ model [Eq. (B19)]
$\varphi_{sfoae}(\omega)$	phase of fine structure function for SFOAEs [Eq. (49)]
$\varphi_s(\omega)$	phase of $R_s(\omega)$
$\varphi_{nl}(\omega)$	phase of $R_{nl}(\omega)$
$\rho_{source}(x, \omega)$	cochlear pressure source density [Eq. (B21)]
$\psi_{r,l}(x, \omega)$	right, left pressure wave basis functions [Eq. (B25)]
σ_x	Width of the activity-pattern maximum.

Physical and derived quantities (middle/outer ear)

$G_{me}(\omega)$	generalized mechanical gain of ossicles for general middle ear models [Eq. (B13); see also Table I of Talmadge <i>et al.</i> , 1998]
$k_{ow}(\omega)$	wave number function of middle ear [Eq. (B11); see also Table I of Talmadge <i>et al.</i> , 1998]
$k_{ow,0}$	geometrical constant relating pressure in ear canal to pressure difference at base [Eq. (B14); see also Table I of Talmadge <i>et al.</i> , 1998]
$L_{dr}(\omega)$	level of complex ‘‘calibrated driving pressure’’ amplitude ($L_{dr} \equiv P_{dr} $)
m_{ow}	effective mass of the oval window
$P_e(x, \omega)$	complex pressure amplitude in ear canal [Eq. (B16)]
$P_{dr}(\omega)$	complex ‘‘calibrated driving pressure’’ amplitude
P_e^a	adiabatic bulk modulus of air in ear canal
$T_{dr}(\omega)$	transfer function relating $P_{dr}(\omega)$ to $P_e(\omega)$ [Eq. (B18)]
$T_{pd}(\omega)$	transfer function relating $P'_d(0, \omega)$ to $P_e(\omega)$ [Eq. (B18)]
Δ_{ow}	denominator of middle ear wave number function [Eq. (B12)]
Γ_{mi}	lever ratio of long-to-short incus process (see Table I of Talmadge <i>et al.</i> , 1998)
S_{ty}	effective area of the tympanic membrane (see Table I of Talmadge <i>et al.</i> , 1998)
S_{ow}	effective area of the oval window (see Table I of Talmadge <i>et al.</i> , 1998)
γ_{ow}	damping constant for the middle ear (see Table I of Talmadge <i>et al.</i> , 1998)
σ_{ow}	effective areal density of the oval window (see also Table I of Talmadge <i>et al.</i> , 1998)

ω_{ow}	frequency of middle ear, corrected for loading of tympanic and ear canal cavities
$\xi_{ow}(x, \omega)$	complex amplitude of oval window [Eq. (B15)]

APPENDIX B: SUMMARY OF THE THEORETICAL FORMULATION

The theoretical formulation is exclusively based on the frequency-domain formulation of a one-dimensional cochlear model. All space–time dependent quantities, $A(x, t)$ are assumed periodic in time, and are represented in terms of a complex amplitude $A(x, \omega)$, where

$$A(x, t) = A(x, \omega)e^{i\omega t} + \text{complex conjugate.} \quad (\text{B1})$$

{For the nonmathematical reader, note that $A(x, \omega) = |A(x, \omega)|\exp[\arg(A)]$, so that Eq. (B1) has the alternative representation $A(x, t) = 2|A(x, \omega)|\cos[\omega t + \arg(A)]$.} As in Talmadge *et al.* (1998) the linear part of the cochlear mechanics is based on time-delayed stiffness of the type described by Zweig (1991) and distributed roughness of the form discussed by Shera and Zweig (Shera and Zweig, 1993; Zweig and Shera, 1995). A simple single-piston middle ear model is also incorporated as described in Talmadge *et al.* (1998).

1. Cochlear model

The underlying linear frequency domain model is given by

$$P'_d(x, \omega) + k^2(x, \omega)P_d(x, \omega) = 0, \quad (\text{B2})$$

$$\xi(x, \omega) = \frac{1}{\sigma_{bm}\Delta(x, \omega)}P_d(x, \omega), \quad (\text{B3})$$

$$k(x, \omega) = \frac{k_0\omega}{\sqrt{\Delta(x, \omega)}}, \quad (\text{B4})$$

$$\Delta(x, \omega) = \omega_0^2(x) - \omega^2 + i\omega\gamma_0(x) + \rho_f\omega_0^2(x)e^{-\psi_f\omega/\omega_0(x)} + \rho_s\omega_0^2(x)e^{-\psi_s\omega/\omega_0(x)}, \quad (\text{B5})$$

$$\omega_0(x) = \omega_0e^{-k\omega x} + \omega_1, \quad (\text{B6})$$

$$\gamma_0(x) = \gamma_0e^{-k\omega x} + \gamma_1, \quad (\text{B7})$$

$$k_0 = \sqrt{\frac{2\rho W_{bm}}{\sigma_{bm}S_{avg}}}, \quad (\text{B8})$$

where $P_d(x, \omega)$ is the differential pressure between the scala tympani and scala vestibuli, $\xi(x, \omega)$ is the upward displacement of the basilar membrane (considered positive if it is toward the scala vestibuli), x is the distance along the basilar membrane from the basal end, and $k(x, \omega)$ is the complex wave number of the traveling wave. The other parameters are defined in Appendix A, and have values given by Table I of Talmadge *et al.* (1998).

The boundary conditions for these equations are,

$$P'_d(0, \omega) + k_{ow}(\omega)P_d(0, \omega) = -G_{me}(\omega)k_{ow}(\omega)P_{dr}(\omega), \quad (\text{B9})$$

$$P_d(L_{bm}, \omega) = 0, \quad (\text{B10})$$

$$k_{ow}(\omega) = \frac{\sigma_{bm} k_{ow,0} \omega^2}{\sigma_{ow} \Delta_{ow}(\omega)}, \quad (\text{B11})$$

$$\Delta_{ow}(\omega) = \omega_{ow}^2 - \omega^2 + i\omega \gamma_{om}, \quad (\text{B12})$$

$$G_{me}(\omega) = G_{me} = \frac{\Gamma_{mi} S_{ry}}{S_{ow}}, \quad (\text{B13})$$

$$k_{ow,0} = \frac{2\rho S_{ow}}{\sigma_{bm} S_{avg}}, \quad (\text{B14})$$

where L_{bm} is the length of the basilar membrane. The equations governing the middle and outer ears are

$$\xi_{ow} = \frac{1}{\sigma_{ow} \Delta_{ow}(\omega)} [P_d(0, \omega) + G_{me}(\omega) P_{dr}(\omega)], \quad (\text{B15})$$

$$P_e(\omega) = T_{dr}(\omega) P_{dr}(\omega) - \frac{P_e^a G_{me}(\omega) S_{ow} \xi_{ow}(\omega)}{V_e}, \quad (\text{B16})$$

$$P_e(\omega) = T_{dr}(\omega) P_{dr}(\omega) + T_{pd}(\omega) P_d'(0, \omega), \quad (\text{B17})$$

$$T_{dr}(\omega) = 1, \quad T_{pd}(\omega) = \frac{S_{avg} P_e^a G_{me}(\omega)}{2\rho V_e \omega^2}. \quad (\text{B18})$$

Note that Eqs. (B16) and (B17) are alternative formulations for the pressure in the external ear. In more complex middle ear models, the basic form of Eqs. (B11) and (B15)–(B17) are retained, although the forms of $\Delta_{ow}(\omega)$, $G_{me}(\omega)$, $T_{dr}(\omega)$, and $T_{pd}(\omega)$ become correspondingly more complex.

2. Basis functions

Equation (B2) governs the evolution of a pressure difference traveling wave for general $k(x, \omega)$, where $k(x, \omega)$, in a generalized sense, could include effects due, e.g., to nonlinearity or basilar membrane roughness. Additional insight is obtained by writing

$$k^2(x, \omega) = k_{sm}^2(x, \omega) + \delta k^2(x, \omega), \quad (\text{B19})$$

where $k_{sm}^2(x, \omega)$ characterizes the ‘‘smooth,’’ linear portion of $k^2(x, \omega)$ and $\delta k^2(x, \omega)$ the deviation from this underlying model. Inserting Eq. (B19) into Eq. (B2) gives the modified wave equation,

$$P_d''(x, \omega) + k_{sm}^2(x, \omega) P_d(x, \omega) = \rho_{source}(x, \omega), \quad (\text{B20})$$

$$\rho_{source}(x, \omega) = -\delta k^2(x, \omega) P_d(x, \omega). \quad (\text{B21})$$

Here $\rho_{source}(x, \omega)$ and any other nonzero term on the right-hand side of Eq. (B20) will be referred to as ‘‘source terms.’’ It is also assumed that $k_{sm}^2(x, \omega)$ satisfies the validity condition for the Wentzel–Kramers–Brillouin (WKB) approximation (e.g., Zweig *et al.*, 1976; de Boer and Viergever, 1984; Mathews and Walker, 1964),

$$\left| \frac{1}{k_{sm}^2(x, \omega)} \frac{\partial k_{sm}^2(x, \omega)}{\partial \omega} \right| \ll \frac{1}{2\pi}, \quad (\text{B22})$$

as well as the condition,

$$\frac{\partial \text{Re}[k_{sm}^2(x, \omega)]}{\partial \omega} > 0 \quad (\text{for all } x). \quad (\text{B23})$$

With the inclusion of these assumptions, it can be shown that the solution of the homogeneous version of Eq. (B20) given by

$$P_d''(x, \omega) + k_{sm}^2(x, \omega) P_d(x, \omega) = 0, \quad (\text{B24})$$

may be written as

$$P_d(x, \omega) = a_r(\omega) \psi_r(x, \omega) + a_l(\omega) \psi_l(x, \omega), \quad (\text{B25})$$

where $\psi_r(x, \omega)$ and $\psi_l(x, \omega)$ have the interpretations of being the solutions to the ‘‘smooth’’ homogeneous wave equation, Eq. (B24), which are purely ‘‘right’’ (apical) and ‘‘left’’ (basal) moving.

By convention,

$$\psi_r(0, \omega) = \psi_l(0, \omega) = 1, \quad (\text{B26})$$

so that $\psi_{r,l}(x, \omega)$ are dimensionless and $a_{r,l}(\omega)$ have the dimension of pressure. It is easy to show that the Wronskian, $W_0(\omega)$, of the basis functions, given by

$$W_0(\omega) = \psi_r(x, \omega) \psi_l'(x, \omega) - \psi_r'(x, \omega) \psi_l(x, \omega), \quad (\text{B27})$$

is independent of x . In terms of the defined quantities,

$$k_{r,l}(x, \omega) = \frac{\psi_{r,l}'(x, \omega)}{\psi_{r,l}(x, \omega)}, \quad (\text{B28})$$

it follows that

$$W_0(\omega) = \psi_l'(0, \omega) - \psi_r'(0, \omega) = k_l(0, \omega) - k_r(0, \omega). \quad (\text{B29})$$

The solution of the inhomogeneous wave equation can be cast in terms of the homogeneous solution by writing

$$P_d(x, \omega) = a_r(x, \omega) \psi_r(x, \omega) + a_l(x, \omega) \psi_l(x, \omega), \quad (\text{B30})$$

which is the direct analogue of Eq. (B25), with the coefficients, $a_{r,l}(x, \omega)$, now being allowed to vary with x . These coefficients are sometimes referred to as osculating functions (see, e.g., Mathews and Walker, 1964; Shera and Zweig, 1991).

Because $a_{r,l}(x, \omega)$ are underspecified in Eq. (B30), the additional derivative condition,

$$P_d'(x, \omega) = a_r(x, \omega) \psi_r'(x, \omega) + a_l(x, \omega) \psi_l'(x, \omega), \quad (\text{B31})$$

can be imposed. This in turn implies the auxiliary condition (Shera and Zweig, 1991),

$$a_r'(x, \omega) \psi_r(x, \omega) + a_l'(x, \omega) \psi_l(x, \omega) = 0. \quad (\text{B32})$$

Using Eq. (B3), basilar membrane basis functions, $\chi_{r,l}(x, \omega)$, can be defined in terms of the pressure difference basis functions,

$$\chi_{r,l}(x, \omega) = \frac{\Delta_{sm}(0, \omega)}{\Delta_{sm}(x, \omega)} \psi_{r,l}(x, \omega), \quad (\text{B33})$$

where $\Delta_{sm}(x, \omega)$ represents the ‘‘smooth’’ component of $\Delta(x, \omega)$, and $\chi_{r,l}(x, \omega)$ represent the apical and basal traveling waves on the basilar membrane for the underlying smooth cochlea. Note that $\chi_{r,l}(x, \omega)$ have been defined so that

$$\chi_r(0, \omega) = \chi_l(0, \omega) = 1. \quad (\text{B34})$$

The motion of the basilar membrane is then given by

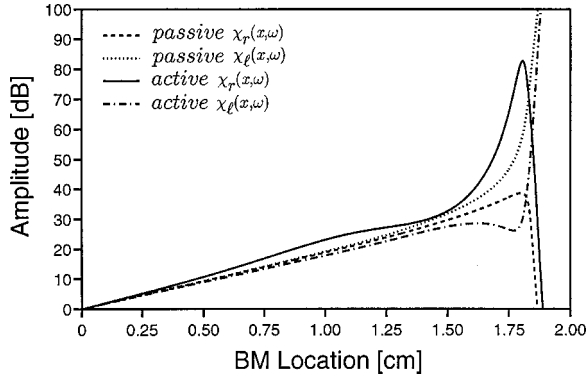


FIG. B1. Basilar membrane basis functions for an active model which incorporates stiffness feedback, and for a passive model in which the stiffness feedback is removed. The stimulus frequency is 2000 Hz, and the parameter values of these models are listed in Table I of Talmadge *et al.* (1998).

$$\xi(x, \omega) = b_r(x, \omega)\chi_r(x, \omega) + b_l(x, \omega)\chi_l(x, \omega), \quad (\text{B35})$$

$$b_{r,l}(x, \omega) = \frac{1}{\sigma_{\text{bm}}\Delta_{\text{sm}}(0, \omega)} \frac{\Delta_{\text{sm}}(x, \omega)}{\Delta(x, \omega)} a_{r,l}(x, \omega). \quad (\text{B36})$$

3. WKB approximation

The WKB method can be used to obtain approximate expressions for the basis functions (see, for example, Mathews and Walker, 1964; Zweig *et al.*, 1976; Shera and Zweig, 1991) which are valid in the “long-wave” region. This method yields the solutions,

$$\psi_r(x, \omega) = \sqrt{\frac{k(0, \omega)}{k(x, \omega)}} e^{-i\varphi_{\text{WKB}}(x)}, \quad (\text{B37})$$

$$\psi_l(x, \omega) = \sqrt{\frac{k(0, \omega)}{k(x, \omega)}} e^{+i\varphi_{\text{WKB}}(x)}, \quad (\text{B38})$$

$$\varphi_{\text{WKB}}(x) = \int_0^x dx' k(x', \omega). \quad (\text{B39})$$

Approximate closed form solutions for $\psi_{r,l}(x, \omega)$ using the WKB method are given in Talmadge *et al.* (1998). Shera and Zweig (1991) provide alternative closed form solutions as well.

Numerical solutions for $\chi_{r,l}(x, \omega)$ using the WKB method are shown in Fig. B1. Solutions for $\psi_{r,l}(x, \omega)$ are given for the active cochlear model used in this analysis, by Talmadge *et al.* (1998). As illustrated in Fig. B1, in active models, $\chi_r(x, \omega)$ is sharply peaked near $x \cong \hat{x}$ whereas $\chi_l(x, \omega)$ has a shallow minimum near $x \cong \hat{x}$.

If the basilar membrane damping and timed-delayed stiffness terms are ignored, then the wave number is given approximately by

$$k(x, \omega) \cong \frac{k_0 \omega}{\sqrt{\omega_0(x)^2 - \omega^2}}. \quad (\text{B40})$$

Making the further approximation that $\omega_0(x) \cong \omega_0 e^{-k_0 x}$, neglecting the phase variation of $\sqrt{k(0, \omega)/k(x, \omega)}$, and inserting Eq. (B40) into Eq. (B39) allow this integral to be explicitly evaluated to obtain an approximate expression for the total phase change, $\hat{\varphi}$, of a pressure wave of frequency ω

from the base to the activity pattern maximum:

$$\hat{\varphi} = \arg[\psi_r(\hat{x}(\omega), \omega)] \cong \varphi_{\text{WKB}}(\hat{x}(\omega)) \cong \frac{\pi k_0}{2k_\omega},$$

$$\Leftrightarrow N_\lambda \cong \frac{k_0}{4k_\omega}. \quad (\text{B41})$$

Here $\hat{x}(\omega)$ is the basilar membrane place-frequency map, and N_λ is generally defined as the number of wavelengths of the transpartition pressure wave from the base to the point of maximum basilar membrane activity.

4. Solutions of the inhomogeneous pressure wave equation

The solution of the inhomogeneous pressure wave equation of Eq. (B20) can formally be written in terms of the basis functions (Talmadge *et al.*, 1998),

$$P_d(x, \omega) = \left[a_r(0, \omega) - \frac{1}{W_0(\omega)} \int_0^x dx' \right. \\ \left. \times \rho_{\text{source}}(x', \omega) \psi_l(x', \omega) \right] \psi_r(x, \omega) \\ + \left[a_l(\infty, \omega) - \frac{1}{W_0(\omega)} \int_x^\infty dx' \rho_{\text{source}}(x', \omega) \right. \\ \left. \times \psi_r(x', \omega) \right] \psi_l(x, \omega). \quad (\text{B42})$$

This formal solution can be applied to the case when $\rho_{\text{source}}(x, \omega)$ contains $P_d(x, \omega)$, as in Eq. (B21). When $\delta k^2(x, \omega) \ll k_{\text{sm}}^2(x, \omega)$, Eq. (B42) can be used to calculate the corrections to $P_d(x, \omega)$ to first order in $\delta k^2(x, \omega)$. For example, if in the limit of $\delta k^2(x, \omega) = 0$,

$$P_d^{(0)}(x, \omega) = a_{0r}(\omega) \psi_r(x, \omega), \quad (\text{B43})$$

corresponding to a right or apical moving traveling wave, then to first order in $\delta k^2(x, \omega)$,

$$\rho_{\text{source}}(x, \omega) = \rho_{\text{source}}^{(1)}(x, \omega) \\ = -\delta k^2(x, \omega) a_{0r}(x, \omega) \psi_r(x, \omega). \quad (\text{B44})$$

It is convenient to normalize $P_d(x, \omega)$ so that $a_r(0, \omega) = a_{0r}(\omega)$, and if the region for which $\delta k^2(x, \omega)$ is nonzero is bounded in x , then on physical grounds, $a_l(\infty, \omega) = 0$. Equation (B42) then gives an expression for $P_d(x, \omega)$ correct to first order in $\delta k^2(x, \omega)$:

$$P_d(x, \omega) \cong a_{0r}(\omega) \left[1 + \frac{1}{W_0(\omega)} \int_0^x dx' \delta k^2(x', \omega) \right. \\ \left. \times \psi_r(x', \omega) \psi_l(x', \omega) \right] \psi_r(x, \omega) + a_{0r}(\omega) \\ \times \left[\frac{1}{W_0(\omega)} \int_x^\infty dx' \delta k^2(x', \omega) \psi_r^2(x', \omega) \right] \\ \times \psi_l(x, \omega). \quad (\text{B45})$$

Note that the presence of a nonzero value of $\delta k^2(x, \omega)$ results in a backscattered wave depending on all scattering elements apical to the position x together with a forward traveling wave which is modified by all scattering elements basal to x . There is no loss of generality of results if $a_r(x, \omega)$ is set equal to $a_{0r}(\omega)$ for values of x other than zero. For example, if $P_d(x, \omega)$ is normalized so that $a_r(\infty, \omega)$, instead of $a_r(0, \omega)$, is set equal to $a_{0r}(\omega)$, then it can easily be shown that to first order in $\delta k^2(x, \omega)$, $P_d(x, \omega)$ is again given by Eq. (B45), except for an extra multiplicative factor,

$$1 - \frac{1}{W_0(\omega)} \int_0^\infty dx' \delta k^2(x', \omega) \psi_r(x', \omega) \psi_l(x', \omega). \quad (\text{B46})$$

As will be seen from the analysis to be given at the end of Sec. III B, this extra factor has no effect on the determination of the cochlear response to stimulation [$P_{\text{dr}}(\omega)$] in the ear canal.

This same methodology can be applied for the case of an initial basal moving traveling wave in the absence of reflections from the cochlear base (Talmadge *et al.*, 1998),

$$P_d^{(0)}(x, \omega) = a_{0l}(\omega) \psi_l(x, \omega), \quad (\text{B47})$$

where $a_r(0, \omega) = 0$, $a_l(\infty, \omega) = a_{0l}(\omega)$ in Eq. (B42). $P_d(x, \omega)$, correct to first order in $\delta k^2(x, \omega)$, is found from Eq. (B42) to be

$$\begin{aligned} P_d(x, \omega) \cong & a_{0l}(\omega) \left[1 + \frac{1}{W_0(\omega)} \int_x^\infty dx' \delta k^2(x', \omega) \right. \\ & \left. \times \psi_r(x', \omega) \psi_l(x', \omega) \right] \psi_l(x, \omega) + a_{0l}(\omega) \\ & \times \left[\frac{1}{W_0(\omega)} \int_0^x dx' \delta k^2(x', \omega) \psi_l^2(x', \omega) \right] \\ & \times \psi_r(x, \omega). \end{aligned} \quad (\text{B48})$$

5. Cochlear reflection

The apical reflectance of a traveling wave is defined as

$$R_a(x, \omega) = \frac{a_l(x, \omega) \psi_l(x, \omega)}{a_r(x, \omega) \psi_r(x, \omega)} = r_a(x, \omega) \mathcal{R}_a(x, \omega), \quad (\text{B49})$$

$$r_a(x, \omega) = \frac{a_l(x, \omega)}{a_r(x, \omega)}, \quad \mathcal{R}_a(x, \omega) = \frac{\psi_l(x, \omega)}{\psi_r(x, \omega)}. \quad (\text{B50})$$

It is understood that $a_r(\omega) \psi_r(x, \omega)$ represents an initial apical moving wave, and $a_l(\omega) \psi_l(x, \omega)$ the resulting basal moving wave due to reflectance within the cochlea from more apical positions. Note that $r_a(x, \omega)$ is constant except in regions which contain sources, since by definition, both $a_r(\omega)$ and $a_l(\omega)$ are constant outside of regions with sources, but $\mathcal{R}_a(x, \omega)$ varies throughout the cochlea. The quantity $\mathcal{R}_a(x, \omega)$ is plotted in Fig. 6 of Talmadge *et al.* (1998) for both passive and active cochlear models. Of special importance is the apical reflectance, given by

$$R_a(\omega) \equiv R_a(0, \omega) = r_a(0, \omega). \quad (\text{B51})$$

For the case of an initial apical moving wave, the application of Eq. (B45) gives $R_a(x, \omega)$ to lowest order in $\delta k^2(x, \omega)$:

$$R_a(x, \omega) \cong \frac{\mathcal{R}_a(x, \omega)}{W_0(\omega)} \int_x^\infty dx' \delta k^2(x', \omega) \psi_r^2(x', \omega). \quad (\text{B52})$$

The basal reflectance of a traveling wave is defined in a similar manner:

$$R_b(x, \omega) = \frac{a_r(x, \omega) \psi_r(x, \omega)}{a_l(x, \omega) \psi_l(x, \omega)} = r_b(x, \omega) \mathcal{R}_b(x, \omega), \quad (\text{B53})$$

$$r_b(x, \omega) = \frac{a_r(x, \omega)}{a_l(x, \omega)}, \quad \mathcal{R}_b(x, \omega) = \frac{\psi_r(x, \omega)}{\psi_l(x, \omega)}. \quad (\text{B54})$$

It is understood that $a_l(\omega) \psi_l(x, \omega)$ represents an initial basal moving wave, and $a_r(\omega) \psi_r(x, \omega)$ the resulting apical moving wave due to reflectance within the cochlea from more basal positions. The reflectance at the base ($x=0$) is

$$R_b(\omega) \equiv R_b(0, \omega) = r_b(0, \omega). \quad (\text{B55})$$

To first order in $\delta k^2(x, \omega)$, Eq. (B48) may be used to give

$$R_b(x, \omega) \cong - \frac{\mathcal{R}_b(x, \omega)}{W_0(\omega)} \int_0^x dx' \delta k^2(x', \omega) \psi_l^2(x', \omega). \quad (\text{B56})$$

It should be noted that Eq. (B56) only gives the contribution due to cochlear inhomogeneities and other cochlear sources. Since this contribution vanishes at $x=0$, a nonzero value for $R_b(x, \omega)$ at $x=0$ is due entirely to the cochlea-middle ear interface. As was discussed in Talmadge *et al.* (1998) (see also the next section), $R_b(\omega) = R_b(0, \omega)$ depends only on the physics of the middle and outer ear and on the properties of the cochlea at the base.

6. Pressure wave equation solutions in the presence of cochlear wave reflection

As discussed in Talmadge *et al.* (1998), the basal reflectance can be obtained by formally writing,

$$P_d(0, \omega) = a_l(0, \omega) [1 + R_b(\omega)], \quad (\text{B57})$$

$$P_d'(0, \omega) = a_l(0, \omega) [k_l(0, \omega) + R_b(\omega) k_r(0, \omega)], \quad (\text{B58})$$

and combining these equations with Eq. (B9) with $P_{\text{dr}}(\omega) = 0$, which gives

$$R_b(\omega) = - \frac{k_{ow}(\omega) + k_l(0, \omega)}{k_{ow}(\omega) + k_r(0, \omega)} = -1 - \frac{W_0(\omega)}{k_{ow}(\omega) + k_r(0, \omega)}, \quad (\text{B59})$$

where the latter expression follows from Eq. (B29). The quantity $R_b(\omega)$ is plotted in Fig. 7 of Talmadge *et al.* (1998) for the simple one-piston middle ear model of that paper.

The response of the cochlea to an external tone when $R_a(\omega)$ is nonzero can also be obtained under the assumption that $R_a(x, \omega)$ is approximately constant near the base. In this case, $P_d(0, \omega)$ and $P_d'(0, \omega)$ are written as

$$P_d(0, \omega) = a_r(0, \omega) [1 + R_a(\omega)], \quad (\text{B60})$$

$$P_d'(0, \omega) = a_r(0, \omega) [k_r(0, \omega) + R_a(\omega) k_l(0, \omega)]. \quad (\text{B61})$$

Combining these equations with Eq. (B9) and using Eq. (B59) gives

$$a_r(0, \omega) = -\frac{G_{me}(\omega)k_{ow}(\omega)}{k_{ow}(\omega) + k_r(0, \omega)} \frac{1}{1 - R_a(\omega)R_b(\omega)} P_{dr}(\omega), \quad (\text{B62})$$

and

$$P_d(0, \omega) = -\frac{G_{me}(\omega)k_{ow}(\omega)}{k_{ow}(\omega) + k_r(0, \omega)} \frac{1 + R_a(\omega)}{1 - R_a(\omega)R_b(\omega)} P_{dr}(\omega). \quad (\text{B63})$$

Letting

$$b(\omega) \equiv -\frac{G_{me}(\omega)k_{ow}(\omega)}{k_{ow}(\omega) + k_r(0, \omega)} P_{dr}(\omega), \quad (\text{B64})$$

and expanding in $R_a(\omega)R_b(\omega)$ gives

$$P_d(0, \omega)/b(\omega) = 1 + R_a(\omega) + R_a(\omega)R_b(\omega) + R_a^2(\omega)R_b(\omega) + R_a^2(\omega)R_b^2(\omega) + \dots. \quad (\text{B65})$$

This series has the simple physical interpretation of multiple internal scattering of an incident wave of amplitude $b(\omega)$, as illustrated by Fig. 8 of Talmadge *et al.* (1998).

The discussion in Appendix B 4 following Eq. (B42) of the perturbative effect of $\delta k^2(x, \omega)$ on an initial basal moving cochlear wave can be generalized to include the case of basal reflection at the cochlea/middle ear interface. The unperturbed wave is now

$$P_d^{(0)}(x, \omega) = a_{l0}(\omega)[\psi_l(x, \omega) + R_b(\omega)\psi_r(x, \omega)], \quad (\text{B66})$$

and $\rho_{\text{source}}(x, \omega)$ in Eq. (B42) is

$$\begin{aligned} \rho_{\text{source}}(x, \omega) &= \rho_{\text{source}}^{(1)}(x, \omega) \\ &= -\delta k^2(x, \omega)P_d^{(0)}(0, \omega) \\ &= -\delta k^2(x, \omega)a_{l0}(\omega)[\psi_l(x, \omega) \\ &\quad + R_b(\omega)\psi_r(x, \omega)]. \end{aligned} \quad (\text{B67})$$

The boundary conditions in Eq. (B42) may be taken as

$$a_l(\infty, \omega) = a_{l0}(\omega), \quad (\text{B68})$$

$$a_r(0, \omega) = R_b(\omega)a_l(0, \omega), \quad (\text{B69})$$

where Eq. (B69) is valid if $\delta k^2(x, \omega) = 0$ in the neighborhood of $x = 0$. Then to first order in $\delta k^2(x, \omega)$, $P_d(x, \omega)$ is given by

$$\begin{aligned} P_d(x, \omega) &= a_{l0}(\omega) \left[R_b(\omega) \left(1 + \frac{1}{W_0(\omega)} \int_0^\infty dx' \delta k^2(x', \omega) [\psi_l(x', \omega) + R_b(\omega)\psi_r(x', \omega)] \psi_r(x', \omega) \right) \right. \\ &\quad \left. + \frac{1}{W_0(\omega)} \int_0^x \delta k^2(x', \omega) [\psi_l(x', \omega) + R_b(\omega)\psi_r(x', \omega)] \psi_l(x', \omega) \right] \psi_r(x, \omega) \\ &\quad + a_{l0}(\omega) \left[1 + \frac{1}{W_0(\omega)} \int_x^\infty dx' \delta k^2(x', \omega) [\psi_l(x', \omega) + R_b(\omega)\psi_r(x', \omega)] \psi_r(x', \omega) \right] \psi_l(x, \omega). \end{aligned} \quad (\text{B70})$$

¹It should be pointed out that Eq. (24) contains an extra constant phase factor of $e^{-i\pi/2}$ compared with Eq. (133) of Talmadge *et al.* (1998). This additional phase arises from phase variation in the $\Delta(0, \omega)/\Delta(x, \omega)$ term from the base to the activity pattern maximum, and is included because N_λ , by definition, is the number of wavelengths of the *pressure* (rather than basilar membrane displacement) traveling wave. [For simplicity, the time-delayed stiffness terms in $\Delta(0, \omega)/\Delta(x, \omega)$ are neglected. However, it can be demonstrated numerically that inclusion of this stiffness feedback does not significantly affect the computed value of N_λ .] Although technically this term could have been included in the analysis of Talmadge *et al.* (1998), this phase factor has no effect on the analysis of the reflectance, as a result of the random (and therefore arbitrary) phase term appearing in the apical reflectance due to roughness [see Eq. (37)]. While it is also true that the $2\pi N_\lambda$ phase contribution is assumed constant across frequencies in this analysis, this phase contribution has been included both in the current paper and in Talmadge *et al.* (1998) to allow the modeling of the effects of a variation in N_λ with frequency. Since the nonlinear phase depends on the absolute phase change in the traveling wave, it is necessary to include the additional factor of $e^{-i\pi/2}$ to properly characterize the phase of the nonlinear reflectance.

²Values for \hat{k} ranging from 45 cm⁻¹ to over 200 cm⁻¹ can be obtained by ‘‘fine-tuning’’ the cochlear model parameters [e.g., by increasing $\gamma_0(\omega)$ or decreasing the positive feedback term ρ_f , without changing the structure of the underlying model]. This was done for Model B of Sec. III B [see Eq. (39) for the changes to the parameter values]. The defect in the predicted

fine structure spacing using this particular choice of model parameters thus illustrates how the fine structure generated by a particular cochlear model can be used to control the parameter choices for that model. On the other hand, the (hypothetical) inability of a particular cochlear model to generate cochlear fine structure that qualitatively agrees with the observed fine structure (see Shera and Guinan, 1999, for a review) for *any* choice of model parameters, must be viewed as a fundamental defect of the underlying cochlear model.

Bray, P., and Kemp, D. T. (1987). ‘‘An advanced cochlear echo technique suitable for infant screening,’’ *Br. J. Audiol.* **21**, 191–204.

Bright, K. E. (1997). ‘‘Spontaneous otoacoustic emissions,’’ in *Otoacoustic Emissions: Clinical Applications*, edited by M. Robinette and T. J. Glatte (Theime, New York), pp. 46–62.

de Boer, E. (1991). ‘‘Auditory physics, physical principles in hearing theory. iii,’’ *Phys. Rep.* **203**, 125–231.

de Boer, E. (1995). ‘‘On equivalence of locally active models of the cochlea,’’ *J. Acoust. Soc. Am.* **98**, 1400–1409.

de Boer, E., and Vieregger, M. A. (1984). ‘‘Validity of the Liouville–Green (or WKB) method for cochlear mechanics,’’ *Hear. Res.* **8**, 131–155.

Dreisbach, L. E. (1999). ‘‘Characterizing the $2f(1)-f(2)$ distortion-product otoacoustic emission and its generators measured from 2 to 20 kHz in humans (intermodulation distortion),’’ Ph.D. thesis, Northwestern University.

Dreisbach, L. E., Siegel, J. H., and Chen, W. (1998). ‘‘Stimulus-frequency otoacoustic emissions measured at low- and high-frequencies in untrained

- human subjects," in *Abstracts of the Twenty First Midwinter Research Meeting of the Association for Research in Otolaryngology*, edited by G. R. Popelka (Association for Research in Otolaryngology, Mt. Royal, NJ), p. 88.
- He, N.-J., and Schmiedt, R. A. (1993). "Fine structure of the $2f_1 - f_2$ acoustic distortion product: Changes with primary level," *J. Acoust. Soc. Am.* **94**, 2659–2669.
- He, N.-J., and Schmiedt, R. A. (1997). "Fine structure of the $2f_1 - f_2$ acoustic distortion product: Effects on primary level and frequency ratio," *J. Acoust. Soc. Am.* **101**, 3554–3565.
- Heitmann, J., Waldmann, B., Schnitzler, H. U., Plinkert, P. K., and Zenner, H.-P. (1998). "Suppression of distortion product otoacoustic emissions (dpoae) near $2f_1 - f_2$ dp-gram fine structure—Evidence for a secondary generator," *J. Acoust. Soc. Am.* **103**, 1527–1531.
- Kanis, L. J., and de Boer, E. (1994). "Two-tone suppression in a locally active nonlinear model of the cochlea," *J. Acoust. Soc. Am.* **96**, 2156–2165.
- Kemp, D. T. (1997). "Otoacoustic emissions in perspective," in *Otoacoustic Emissions: Clinical Applications*, edited by M. S. Robinette and T. J. Glatke (Thieme, New York), pp. 1–21.
- Kemp, D. T., and Brown, A. M. (1983). "A comparison of mechanical nonlinearities in the cochlea of man and gerbil from ear canal measurements," in *Hearing—Physiological Bases and Psychophysics. Proceedings of the 6th International Symposium on Hearing*, edited by R. Klinke and R. Hartman (Springer Verlag, Berlin), pp. 82–88.
- Kemp, D. T., and Chum, R. (1980). "Properties of the generator of stimulated acoustic emissions," *Hear. Res.* **2**, 213–232.
- Kim, D. O. (1980). "Cochlear mechanics: Implications of electrophysiological and acoustical observations," *Hear. Res.* **2**, 297–317.
- Mathews, J., and Walker, R. (1964). *Mathematical Methods of Physics* (Benjamin, New York).
- Mauermann, M., Uppenkampf, S., van Hengel, P. W. J., and Kollmeier, B. (1999). "Evidence for the distortion product frequency place as a source of distortion product otoacoustic emission (dpoae) fine structure in humans. I. Fine structure and higher-order dpoae as a function of the frequency ratio f_2/f_1 ," *J. Acoust. Soc. Am.* **106**, 3473–3483.
- Nelson, D. A., and Zhou, J. Z. (1996). "Slopes of distortion-product otoacoustic emission growth curves corrected for noise-floor levels," *J. Acoust. Soc. Am.* **99**, 468–474.
- Norton, S. J., and Stover, L. J. (1994). "Otoacoustic emissions: An emerging clinical tool," in *Handbook of Clinical Audiology*, edited by J. Katz (Williams and Wilkins, Maryland), pp. 448–462.
- Rhode, W. S. (1971). "Observations of the vibration of the basilar membrane in squirrel monkeys using the Mössbauer technique," *J. Acoust. Soc. Am.* **49**, 1218–1231.
- Rhode, W. S., and Robles, L. (1974). "Evidence from Mössbauer experiments for nonlinear vibrations in the cochlea," *J. Acoust. Soc. Am.* **55**, 558–596.
- Robinette, M. S., and Glatke, T. J. (Eds.). (1997). *Otoacoustic Emissions: Clinical Applications* (Thieme, New York).
- Shera, C. A., and Guinan, J. J. (1999). "Evoked otoacoustic emissions arise from two fundamentally different mechanisms: A taxonomy for mammalian DAEs," *J. Acoust. Soc. Am.* **105**, 782–798.
- Shera, C. A., and Zweig, G. (1991). "Reflection of retrograde waves within the cochlea and at the stapes," *J. Acoust. Soc. Am.* **89**, 1290–1305.
- Shera, C. A., and Zweig, G. (1993). "Order from chaos: Resolving the paradox of periodicity in evoked otoacoustic emission," in *Biophysics of Hair Cell Sensory Systems*, edited by H. Duifhuis, J. W. Horst, P. van Dijk, and S. M. van Netten (World Scientific, Singapore), pp. 54–63.
- Steele, C. R., and Taber, L. A. (1979a). "Comparison of WKB calculations and experimental results for two-dimensional cochlear models," *J. Acoust. Soc. Am.* **65**, 1001–1006.
- Steele, C. R., and Taber, L. A. (1979b). "Comparison of WKB calculations and experimental results for three-dimensional cochlear models," *J. Acoust. Soc. Am.* **65**, 1007–1018.
- Strube, H. W. (1989). "Evoked otoacoustic emission as cochlear Bragg reflections," *Hear. Res.* **38**, 35–46.
- Sun, X. M., Schmiedt, R. A., He, N.-J., and Lam, C. F. (1994a). "Modeling the fine structure of the $2f_1 - f_2$ acoustic distortion product. 1. Model development," *J. Acoust. Soc. Am.* **96**, 2166–2174.
- Sun, X. M., Schmiedt, R. A., He, N.-J., and Lam, C. F. (1994b). "Modeling the fine structure of the $2f_1 - f_2$ acoustic distortion product. 2. Model evaluation," *J. Acoust. Soc. Am.* **96**, 2175–2183.
- Talmadge, C., and Tubis, A. (1993a). "On modeling the connection between spontaneous and evoked otoacoustic emissions," in *Biophysics of Hair Cell Sensory Systems*, edited by H. Duifhuis, J. W. Horst, P. van Dijk, and S. M. van Netten (World Scientific, Singapore), pp. 25–32.
- Talmadge, C., Long, G. R., and Tubis, A. (1993b). "New off-line method for detecting spontaneous otoacoustic emissions in human subjects," *Hear. Res.* **71**, 170–182.
- Talmadge, C., Long, G. R., Tubis, A., and Dhar, S. (1999). "Experimental confirmation of the two-source interference model for the fine structure of distortion product otoacoustic emissions," *J. Acoust. Soc. Am.* **105**, 275–292.
- Talmadge, C., Tubis, A., Long, G. R., and Piskorski, P. (1998). "Modeling otoacoustic emission and hearing threshold fine structures in humans," *J. Acoust. Soc. Am.* **104**, 1517–1543.
- Talmadge, C., Tubis, A., Piskorski, P., and Long, G. R. (1997). "Modeling otoacoustic emission fine structure," in *Diversity in Auditory Mechanics*, edited by E. Lewis, G. Long, R. Lyon, P. Narins, C. Steele, and E. Hecht-Poinar (World Scientific, Singapore), pp. 462–471.
- Talmadge, C. L., Tubis, A., Long, G. R., and Piskorski, P. (1996). "Evidence for multiple spatial origins of the fine structure of distortion product otoacoustic emissions in humans, and its implications: Experimental and modeling results," in *Abstracts of the Nineteenth Midwinter Research Meeting of the Association for Research in Otolaryngology*, edited by D. J. Lim (unpublished), p. 94, Abstract.
- Talmadge, C. L., Tubis, A., Wit, H. P., and Long, G. R. (1991). "Are spontaneous otoacoustic emissions generated by self-sustained cochlear oscillators?," *J. Acoust. Soc. Am.* **89**, 2391–2399.
- van Dijk, P., Wit, H. P., Tubis, A., Talmadge, C. L., and Long, G. R. (1994). "Correlation between amplitude and frequency fluctuations of spontaneous emissions," *J. Acoust. Soc. Am.* **96**, 163–169.
- van Hengel, P. W., Duifhuis, H., and van den Raadt, M. P. (1996). "Spatial periodicity in the cochlea: The result of interaction of spontaneous emissions?," *J. Acoust. Soc. Am.* **99**, 3566–3571.
- Wit, H. P. (1986). "Statistical properties of a strong spontaneous otoacoustic emission," in *Peripheral Auditory Mechanisms*, edited by J. B. Allen, A. Hubbard, S. T. Neely, and A. Tubis (Springer-Verlag, Berlin), pp. 221–228.
- Yates, G. K., and Withnell, R. H. (1999). "The role of intermodulation distortion in transient-evoked otoacoustic emissions," *Hear. Res.* **136**, 49–64.
- Zweig, G. (1991). "Finding the impedance of the organ of Corti," *J. Acoust. Soc. Am.* **89**, 1229–1254.
- Zweig, G., and Shera, C. A. (1995). "The origins of periodicity in the spectrum of evoked otoacoustic emissions," *J. Acoust. Soc. Am.* **98**, 2018–2047.
- Zweig, G., Lipes, R., and Pierce, J. R. (1976). "The cochlear compromise," *J. Acoust. Soc. Am.* **59**, 975–982.
- Zwicker, E., and Peisl, W. (1990). "Cochlear processing in analog models, in digital models, and in human inner ear," *Hear. Res.* **44**, 206–216.

Interrelations among distortion-product phase-gradient delays: Their connection to scaling symmetry and its breaking

Christopher A. Shera^{a)}

Eaton-Peabody Laboratory of Auditory Physiology, Massachusetts Eye and Ear Infirmary, 243 Charles Street, Boston, Massachusetts 02114 and Department of Otology and Laryngology, Harvard Medical School, Boston, Massachusetts 02115

Carrick L. Talmadge

National Center for Physical Acoustics, University of Mississippi, University, Mississippi 38677

Arnold Tubis

Department of Physics, Purdue University, West Lafayette, Indiana 47907 and Institute for Nonlinear Science, University of California, San Diego, La Jolla, California 92093

(Received 1 June 2000; revised 6 September 2000; accepted 12 September 2000)

Distortion-product-otoacoustic-emission (DPOAE) phase-versus-frequency functions and corresponding phase-gradient delays have received considerable attention because of their potential for providing information about mechanisms of emission generation, cochlear wave latencies, and characteristics of cochlear tuning. The three measurement paradigms in common use (fixed- f_1 , fixed- f_2 , and fixed- f_2/f_1) yield significantly different delays, suggesting that they depend on qualitatively different aspects of cochlear mechanics. In this paper, theory and experiment are combined to demonstrate that simple phenomenological arguments, which make no detailed mechanistic assumptions concerning the underlying cochlear mechanics, predict relationships among the delays that are in good quantitative agreement with experimental data obtained in guinea pigs. To understand deviations between the simple theory and experiment, a general equation is found that relates the three delays for any deterministic model of DPOAE generation. Both model-independent and exact, the general relation provides a powerful consistency check on the measurements and a useful tool for organizing and understanding the structure in DPOAE phase data (e.g., for interpreting the relative magnitudes and intensity-dependencies of the three delays). Analysis of the general relation demonstrates that the success of the simple, phenomenological approach can be understood as a consequence of the mechanisms of emission generation and the approximate local scaling symmetry of cochlear mechanics. The general relation is used to quantify deviations from scaling manifest in the measured phase-gradient delays; the results indicate that deviations from scaling are typically small and that both linear and nonlinear mechanisms contribute significantly to these deviations. Intensity-dependent mechanisms contributing to deviations from scaling include cochlear-reflection and wave-interference effects associated with the mixing of distortion- and reflection-source emissions (as in DPOAE fine structure). Finally, the ratio of the fixed- f_1 and fixed- f_2 phase-gradient delays is shown to follow from the choice of experimental paradigm and, in the scaling limit, contains no information about cochlear physiology whatsoever. These results cast considerable doubt on the theoretical basis of recent attempts to use relative DPOAE phase-gradient delays to estimate the bandwidths of peripheral auditory filters. © 2000 Acoustical Society of America. [S0001-4966(00)03012-5]

PACS numbers: 43.64.Bt, 43.64.Ha, 43.64.Jb, 43.64.Kc [BLM]

I. INTRODUCTION

Since their discovery by Kemp (1979), distortion-product otoacoustic emissions (or DPOAEs) have proved a powerful noninvasive probe of cochlear function. Distortion products at combination-tone frequencies [i.e., $f_{dp} = f_1 - n(f_2 - f_1)$, with $f_2 > f_1$ and n an integer] are typically evoked by stimulating the ear with two primary tones at frequencies f_1 and f_2 . Although most research has focused on DPOAE amplitudes, distortion-product phases have recently received considerable attention, both because of their

relevance to understanding mechanisms of emission generation and for the insight they may provide on mechanical delay within the cochlea (e.g., Kemp and Brown, 1983; Kimberley *et al.*, 1993; Brown *et al.*, 1994; O'Mahoney and Kemp, 1995; Moulin and Kemp, 1996a, 1996b; Stover *et al.*, 1996; Wable *et al.*, 1996; Whitehead *et al.*, 1996; Fahey and Allen, 1997; Bowman *et al.*, 1997, 1998; Mills and Rubel, 1997; Shera and Guinan, 1999; Schneider *et al.*, 1999, 2000; Talmadge *et al.*, 2000; Faulstich and Kössl, 2000; Tubis *et al.*, 2000a; Bowman *et al.*, 2000; Prijs *et al.*, 2000). DPOAE phase-versus-frequency functions and corresponding phase-gradient delays have been measured using two principal sweep paradigms, obtained by fixing one of the two

^{a)} Author to whom correspondence should be addressed; electronic mail: shera@epl.meei.harvard.edu

primary frequencies and varying the other. For example, in the fixed- f_2 measurement paradigm, the frequency f_2 is held constant and DPOAE phase measured as the frequency f_1 is swept.² Analogous relations hold for the fixed- f_1 paradigm. A third sweep paradigm sometimes employed is the fixed-ratio paradigm during which both primaries are varied in such a way that their ratio, f_2/f_1 , remains constant.

For the cubic distortion product at frequency $2f_1 - f_2$ and other lower-side-band DPOAEs (i.e., for $n \geq 1$), the three measurement paradigms yield significantly different phase-gradient delays (e.g., Kemp and Brown, 1983; Whitehead *et al.*, 1994, 1996), and the problem of understanding the relationship among them has been extensively explored (e.g., O'Mahoney and Kemp, 1995; Moulin and Kemp, 1996a, 1996b; Bowman *et al.*, 1997, 1998; Schneider *et al.*, 1999, 2000; Prijs *et al.*, 2000; Tubis *et al.*, 2000b). The traditional approach has been to explain observed DPOAE phase-gradient delays using conceptual or mathematical arguments based on detailed theoretical assumptions about cochlear mechanics. For example, assumptions are made about the nature of the emission sources (e.g., whether they can be approximated as points or must be distributed over a region), about their spatial location within the cochlea (e.g., whether the sources reside near the peak of the f_2 traveling wave and/or the distortion-product place), about the character of the cochlear traveling wave (e.g., the effective dimensionality of its hydrodynamics, the nature of its spatial and frequency dispersion, the degree of its amplification, the form of its nonlinear dependence on stimulus intensity, and the relative time delays attributable to "wave travel" versus "filter build-up"), and so on. Expanding on earlier work relating DPOAE phase-gradient delays to auditory-filter bandwidth (Moulin and Kemp, 1996b), Bowman *et al.* (1997) provide perhaps the most ambitious theoretical analysis to date by attempting to derive the response properties of gammatone-filter models of human peripheral auditory filters from relative DPOAE phase-gradient delays.

Here we take a simpler, more phenomenological approach to the problem. In particular, we ask how much of the emission data can one account for by making *no detailed assumptions about cochlear mechanics*? The answer, it turns out, is a surprisingly large amount. Indeed, the success of our naive phenomenological approach is considerable: Not only do we provide a quantitative account of the major known relationships between DPOAE phase-gradient delays—including those used to "derive" properties of cochlear tuning (Bowman *et al.*, 1997; Moulin and Kemp, 1996b)—but we deduce other heretofore unrecognized relationships as well. We test these relationships among the phase-gradient delays using emission data from guinea pigs and conclude by discussing the implications of our findings, both for cochlear mechanics and for attempts to characterize cochlear tuning using DPOAE phase measurements.

II. THEORETICAL PHASE-GRADIENT DELAYS

To explore the frequency dependence of the DPOAE phase we represent the complex DPOAE pressure at frequency f_{dp} in the ear canal in the form $|P_{dp}|e^{i\varphi_{dp}}$. We wish to

determine theoretical values of the fixed- f_1 , fixed- f_2 , and fixed-ratio phase-gradient delays defined by the equations

$$\tau_1 \equiv - \left. \frac{1}{2\pi} \frac{\partial \varphi_{dp}}{\partial f_{dp}} \right|_{\text{fixed-}f_1}; \quad (1)$$

$$\tau_2 \equiv - \left. \frac{1}{2\pi} \frac{\partial \varphi_{dp}}{\partial f_{dp}} \right|_{\text{fixed-}f_2}; \quad (2)$$

and

$$\tau_r \equiv - \left. \frac{1}{2\pi} \frac{\partial \varphi_{dp}}{\partial f_{dp}} \right|_{\text{fixed-}r}. \quad (3)$$

The symbol r denotes the primary-frequency ratio, f_2/f_1 , and the subscripts indicate the variable held constant. The quantities τ_1 , τ_2 , and τ_r defined by Eqs. (1)–(3) are often referred to as DPOAE "latencies" or "group delays." Since relations between frequency derivatives of DPOAE phase (measured in the sinusoidal steady state) and physical delays (measured in the time domain) are not always straightforward (e.g., Tubis *et al.*, 2000a), we adopt the descriptive but more hermeneutically neutral term "phase-gradient delay."

How do we determine the phase-gradient delays theoretically? In general, φ_{dp} depends parametrically on the primary frequencies and on other fixed parameters in the problem, so that we can write

$$\varphi_{dp} = \varphi_{dp}(f_1, f_2; \dots), \quad (4)$$

where f_1 and f_2 are the primary frequencies. The frequency f_{dp} of the measured distortion component does not appear among the list of independent variables because its value is not independent of f_1 and f_2 . In particular, for odd-order distortion products,

$$f_{dp} = f_1 - n(f_2 - f_1) \quad (n = \dots, -3, -2, 1, 2, \dots), \quad (5)$$

where the cubic distortion product at frequency $f_{dp} = 2f_1 - f_2$ corresponds to $n = 1$.

The ellipsis after the semicolon in Eq. (4) represents the fixed parameters that characterize the model under study or specify features of the stimuli that are held constant during the phase measurement. Examples of such parameters include the frequency scales defining the cochlear map; resonant frequencies associated with middle-ear transfer functions; the relative strength of efferent feedback at different cochlear locations; the index, n , of the measured distortion product; the amplitudes and phases of the primary tones; and so on. Note that Eq. (4) is completely generic: both the fixed parameters and the functional form of φ_{dp} remain unspecified.

A. The simplest model

Although we will later return to the general model, it proves instructive first to consider the simplest nontrivial case. In the simplest model, the primary frequencies f_1 and f_2 themselves constitute the only frequency scales in the problem. In this case, Eq. (4) for φ_{dp} can be simplified further using the Buckingham Π theorem from dimensional analysis (e.g., Bridgman, 1931). Application of this theorem amounts to the recognition that the value of the dimension-

less angle φ_{dp} must be independent of the units chosen to measure frequency (e.g., whether those units be Hz or cycles/light-smoot).³ Consequently, the units of frequency must cancel. The only dimensionless combination of the independent variables f_1 and f_2 is some function of their ratio. Therefore,

$$\varphi_{dp} = \varphi_{dp}(r; \dots), \quad (6)$$

where $r \equiv f_2/f_1$; thus in the simplest nontrivial model, the phase φ_{dp} depends on a single dimensionless variable, r . We could, of course, just as well have defined r as its reciprocal, f_1/f_2 . Since any function of r is also a function of $1/r$, our conclusions do not depend upon this arbitrary choice. Note that since we leave the fixed parameters represented by the ellipsis unspecified, the simplest model defined by Eq. (6) actually represents an entire *class* of models.

The fixed- f_1 , fixed- f_2 , and fixed-ratio phase derivatives appearing in Eqs. (1)–(3) for τ_1 , τ_2 , and τ_r now follow from a straightforward application of the chain rule:⁴

$$\left. \frac{\partial \varphi_{dp}}{\partial f_{dp}} \right|_{f_1} = \left. \frac{\partial r}{\partial f_{dp}} \right|_{f_1} \frac{d\varphi_{dp}}{dr} = -\frac{1}{nf_1} \varphi'_{dp}; \quad (7)$$

$$\left. \frac{\partial \varphi_{dp}}{\partial f_{dp}} \right|_{f_2} = \left. \frac{\partial r}{\partial f_{dp}} \right|_{f_2} \frac{d\varphi_{dp}}{dr} = -\frac{r}{(n+1)f_1} \varphi'_{dp}; \quad (8)$$

and

$$\left. \frac{\partial \varphi_{dp}}{\partial f_{dp}} \right|_r = \left. \frac{\partial r}{\partial f_{dp}} \right|_r \frac{\partial \varphi_{dp}}{\partial r} = 0, \quad (9)$$

where $\varphi'_{dp} \equiv d\varphi_{dp}/dr$. As before, the subscripts on the derivatives indicate the quantity held fixed. For example, the derivative $\partial r/\partial f_{dp}|_r$ in Eq. (9) is zero because the value of r is held constant during the sweep.

Substituting the derivatives (7)–(9) into Eqs. (1)–(3) yields expressions for the phase-gradient delays τ_1 , τ_2 , and τ_r . For example, our analysis immediately predicts that

$$\boxed{\tau_r = 0}. \quad (10)$$

Although we cannot predict the absolute values of τ_1 or τ_2 without knowledge of φ'_{dp} , our analysis does predict the value of their ratio,⁵

$$\boxed{\tau_1/\tau_2 = \rho_n}, \quad (11)$$

where

$$\rho_n \equiv \left(\frac{n+1}{n} \right) r^{-1}. \quad (12)$$

Note that all the messy details of cochlear mechanics—generally unknown and model-dependent, but neatly encapsulated in the function $\varphi'_{dp}(r)$ —have canceled in the ratio. For the cubic DPOAE ($n=1$), the proportionality in Eq. (11) reduces to

$$\tau_1 = \rho_1 \tau_2 \quad (\text{for } 2f_1 - f_2), \quad (13)$$

where $\rho_1 = 2/r$. We emphasize again that predictions (10) and (11) apply to *any* model of the class defined by Eq. (6), irrespective both of its parameter values and of whatever additional assumptions it may make about cochlear mechanics and the mechanisms of DPOAE generation. In the following section we test these predictions using measurements in the guinea pig.

III. EMPIRICAL PHASE-GRADIENT DELAYS

A. Methods

The methods and equipment used to measure DPOAEs were generally similar to those detailed elsewhere (Shera and Guinan, 1999); we discuss relevant differences below.

1. Animal care and preparation

Five male albino guinea pigs weighing between 250 and 350 g were used in these experiments. All procedures were conducted in accordance with National Institutes of Health guidelines and were approved by the Animal Care and Use Committee of the Massachusetts Eye and Ear Infirmary. Preparatory to anything else, the animals were anesthetized with Nembutal (15 mg/kg i.p.) and fentanyl/droperidol (0.2 and 10 mg/kg i.m., respectively). Surgical levels of anesthesia were maintained with booster injections as necessary (1/3 of original dose every 2 h). All measurements and procedures were performed in a soundproofed, vibration-isolated chamber (Ver *et al.*, 1975) in which the temperature was held between 32–35 °C. Animal rectal temperature was maintained between 37 and 39 °C using a heating pad, and heart rate was monitored continuously. After tracheotomy, the skin and muscle layers were removed from the back of the skull to expose the bullae, which were opened by carefully shaving the bone with a scalpel blade. The pinnae were removed and the cartilaginous ear canals severed near the skull to allow placement of the acoustic transducers within 2–3 mm of the eardrum for subsequent calibration, stimulus delivery, and recording. The acoustic assembly consisted of two 1/4-in. Bruel and Kjaer condenser microphones (used as sound sources) and an Etymotic Research ER10c probe system (used as a microphone).

2. Measurement methods

We measured DPOAEs at the frequency $2f_1 - f_2$ (i.e., $n=1$) using three different sweep paradigms: fixed- f_1 , fixed- f_2 , and fixed-ratio. In each paradigm, we chose initial primary frequencies based on specified nominal values of f_2 and r . Together, these nominal values, denoted $\langle f_2 \rangle$ and $\langle r \rangle$, determine the nominal value of f_1 , namely $\langle f_1 \rangle = \langle f_2 \rangle / \langle r \rangle$. The nominal values $\langle f_1 \rangle$ and $\langle f_2 \rangle$ represent center frequencies about which the primaries were varied to obtain the phase measurements necessary to compute the three phase-gradient delays. In the fixed- f_2 paradigm, for example, the primary frequency f_2 was fixed at the value $\langle f_2 \rangle$ and the frequency f_1 then varied, in steps of size Δf , over the range defined by

$$f_1 = \langle f_1 \rangle + m\Delta f, \quad m = \{-k, -k+1, \dots, k-1, k\}, \quad (14)$$

where k is an integer and Δf is the minimum frequency interval between measurement points allowed by our choice of sampling rate (approximately 59.94 kHz) and the length of the discrete Fourier transform used in the frequency analysis (4096 points). Thus DPOAEs were measured at a total of $2k + 1$ values of f_1 about $\langle f_1 \rangle$. In the measurements reported here, $k = 5$ and $\Delta f \approx 15$ Hz, so that f_1 was swept over a range of approximately ± 75 Hz centered at $\langle f_1 \rangle$. Similarly, in the fixed- f_1 paradigm, the frequency f_1 was fixed at $\langle f_1 \rangle$ and f_2 varied over the range

$$f_2 = \langle f_2 \rangle + 2m\Delta f, \quad m = \{-k, -k + 1, \dots, k - 1, k\}. \quad (15)$$

The extra factor of two guarantees that the resulting value of $2f_1 - f_2$ varies over approximately the same range as in the fixed- f_2 paradigm.

Note that because one of the two primary frequencies changes during the fixed- f_1 and fixed- f_2 sweeps, the ratio r must depart from its nominal value during the measurements. In order to provide a simple test of prediction (13) for τ_1/τ_2 , we sought to keep r as close to $\langle r \rangle$ as possible, thereby holding the predicted proportionality factor, ρ_1 , nearly constant during the measurements. The largest change in r occurs during the fixed- f_1 sweeps, for which r varies over the range

$$r/\langle r \rangle \approx 1 \pm 2k\Delta f \langle r \rangle / \langle f_2 \rangle. \quad (16)$$

Using our values $k = 5$ and $\Delta f \approx 15$ Hz at the typical frequency $\langle f_2 \rangle \sim 9$ kHz and ratio $\langle r \rangle = 1.21$ yields a variation of roughly 2% about $\langle r \rangle$.

Finally, in the fixed-ratio paradigm, the frequency f_2 was varied over the range defined by Eq. (15); at each frequency f_2 , a corresponding f_1 was chosen so that $f_2/f_1 \approx \langle r \rangle$. To ensure that our ability to maintain a constant ratio during the sweep was not systematically compromised by the frequency quantization imposed by digital stimulus generation, we modified our data acquisition system to allow the sampling frequency to vary between measurement points by up to $\pm 10\%$ about its nominal value (59.94 kHz). This flexibility enabled us to choose f_1 and f_2 values so that the ratio f_2/f_1 varied by less than a hundredth of a percent about $\langle r \rangle$.

Our stimulus parameters were generally selected with an eye toward maximizing overall DPOAE levels. For example, we worked with primary stimulus levels satisfying $L_1 \geq L_2$ (specifically, $L_1 = L_2 + 10$ dB SPL). Likewise, we sought a nominal primary frequency ratio satisfying $\langle r \rangle \approx (f_2/f_1)_{\text{optimal}}$. Since we required measurements at one value of $\langle r \rangle$ over a wide range of $\langle f_2 \rangle$ —and since the value $(f_2/f_1)_{\text{optimal}}$ varies with f_2 (e.g., Allen and Fahey, 1993; Schneider *et al.*, 2000)—we chose the value $\langle r \rangle = 1.21$ as a compromise that yields good results over a wide range of frequencies.

To allow time for multiple internal reflections that might occur within the cochlea to settle into a steady-state response, we measured P_{dp} over time intervals much longer than the estimated round-trip travel time for cochlear waves (cf. Shera and Zweig, 1993a). Real-time artifact rejection was implemented as described elsewhere (Shera and Guinan, 1999) by comparing the time waveforms in successive data buffers before adding them to the averaged responses. The difference between successive data buffers was used to pro-

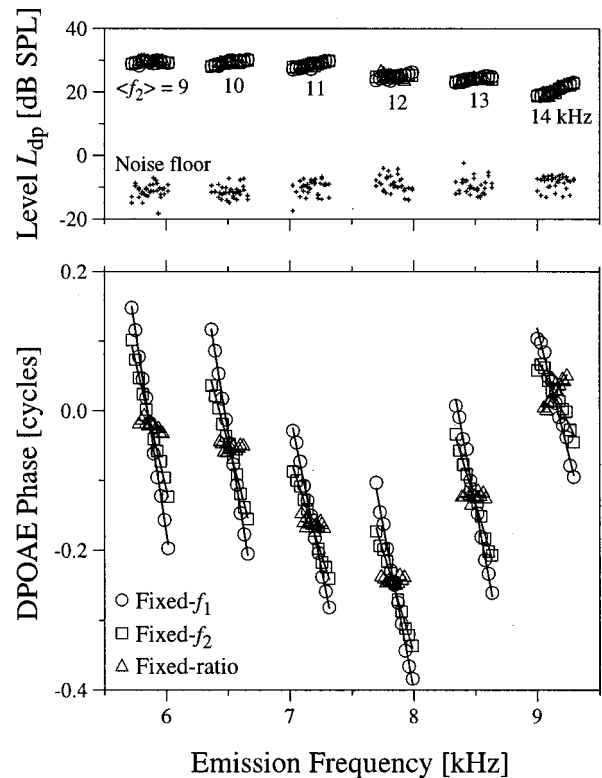


FIG. 1. A typical set of DPOAEs measured using the three different sweep paradigms: fixed- f_1 (\circ), fixed- f_2 (\square), and fixed-ratio (\triangle). The figure shows the amplitude (top) and phase (bottom) of the $2f_1 - f_2$ distortion product measured in one guinea pig (animal CAS-52) at the six nominal values of $\langle f_2 \rangle$ indicated in the top panel. Each sweep was measured at the nominal value $\langle r \rangle = 1.21$ using primary levels of $\{L_1, L_2\} = \{60, 50\}$ dB SPL. The solid lines represent best-fit straight lines to the unwrapped phase measurements obtained using weighted least-squares linear regression. To reduce clutter, the error bars on the measurements, which are used in the fitting procedure and are typically on the order of 1–2 deg in the phase, are not shown.

vide a measure of the noise floor at the frequencies of measurement. Uncertainties in the real and imaginary parts of the measured pressure were estimated from the noise floor and used to compute estimates of the uncertainty in pressure amplitude and phase using standard formulas for error propagation (e.g., Meyer, 1975).⁶

3. Analysis methods

We measured DPOAEs in five guinea pigs and found qualitatively similar results in all animal subjects. Typical DPOAE measurements are shown in Fig. 1.

To determine phase-gradient-delay triplets $\{\tau_1, \tau_2, \tau_r\}$ at various values of $\langle f_2 \rangle$ and $\langle r \rangle$, we extracted DPOAE phase responses obtained using the three sweep paradigms from the measured ear-canal pressure using Fourier analysis. In each case, the DPOAE phase, φ_{dp} , was unwrapped by removing 2π discontinuities and corrected for phase variations in the primaries by subtracting $2\varphi_1 - \varphi_2$, where φ_1 and φ_2 are the measured phases of the primaries.⁷ Measurement frequency resolution was always sufficient to prevent ambiguities due to phase unwrapping. Only phase data for which the corresponding emission amplitudes, $|P_{\text{dp}}|$, were at least 20 dB above the measured noise floor were analyzed further. When at least three data points (of the possible $2k + 1 = 11$ per

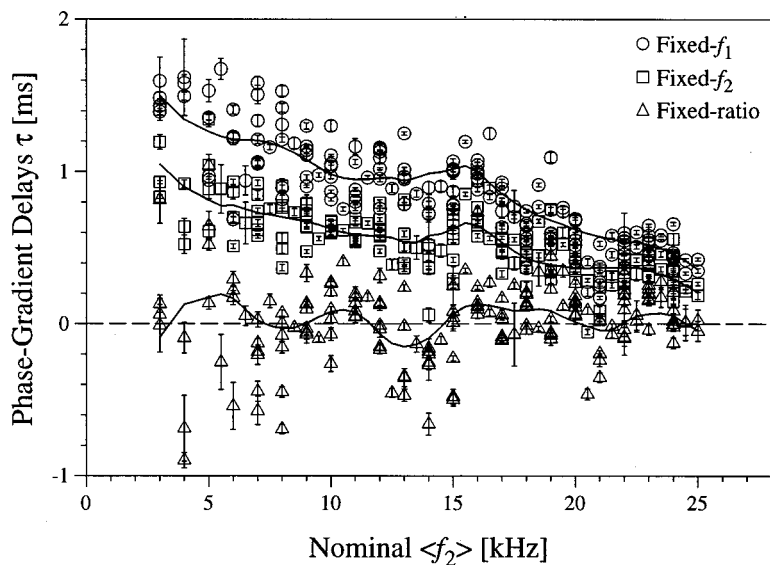


FIG. 2. Phase-gradient-delay triples $\{\tau_1, \tau_2, \tau_r\}$ and their estimated uncertainties. Delay triplets ($n=164$ from 5 ears) were computed from DPOAE phase measurements obtained using three different sweep paradigms: fixed- f_1 (\circ), fixed- f_2 (\square), and fixed-ratio (\triangle). The nominal value of $\langle f_2 \rangle$ is given along the abscissa. Triplets were measured at the value $\langle r \rangle = 1.21$ using primary levels of $\{L_1, L_2\} = \{60, 50\}$ dB SPL. Robust loess trend lines (Cleveland, 1993) computed from the data for each sweep paradigm are shown for comparison. As predicted, the values of τ_r straddle the zero line. Furthermore, the τ_1 - and τ_2 -trend lines suggest considerable correlation in their values.

sweep) satisfied this criterion,⁸ the selected data and their uncertainties were plotted against the emission frequency, f_{dp} , and the parameters of the best-fit straight line (i.e., the phase-gradient delay and intercept) determined using weighted least-squares linear regression (e.g., Press *et al.*, 1992). Uncertainties in the determined parameters were estimated using bootstrap resampling (e.g., Efron and Tibshirani, 1993).

A small fraction of the computed phase-gradient delays were obvious outliers. Including these values had negligible effect on our conclusions but their display required greatly expanded scales on many of the graphs. We therefore chose to eliminate them from our initial analysis using an automated procedure, described here for the fixed- f_1 data. First, to equalize the variance in the phase-gradient delay τ_1 across $\langle f_2 \rangle$, the values τ_1 measured at a given value of $\langle r \rangle$ were multiplied by $\sqrt{\langle f_2 \rangle}$ (cf. Neely *et al.*, 1988; Shera and Guinan, 2000a). The results, pooled across animals, were plotted against $\langle f_2 \rangle$ and a robust loess trend line (Cleveland, 1993) computed from the scatterplot. Data points were discarded when their distance from the trend line (i.e., the trend residual) put them in the 98th percentile or higher, a criterion based on examination of the residual distribution.⁹ Identical procedures and selection criteria were applied, separately for each sweep type, to the fixed- f_2 and fixed-ratio data. Taken together, these procedures eliminated roughly 5% of the triplets $\{\tau_1, \tau_2, \tau_r\}$.

B. Empirical correlation between τ_1 and τ_2

Figure 2 shows phase-gradient delays versus $\langle f_2 \rangle$ measured using each of the three sweep paradigms at $\langle r \rangle = 1.21$ and at primary levels of $\{L_1, L_2\} = \{60, 50\}$ dB SPL. The data indicate that both τ_1 and τ_2 are positive and generally decrease with increasing $\langle f_2 \rangle$, in agreement with earlier reports (e.g., O'Mahoney and Kemp, 1995; Moulin and Kemp, 1996a; Whitehead *et al.*, 1996; Bowman *et al.*, 1997; Schneider *et al.*, 1999). The fixed-ratio phase-gradient delays, in contrast, straddle the line $\tau_r = 0$, as predicted by Eq. (10). The data indicate that $\tau_1 > \tau_2$ throughout the measured range, in qualitative agreement both with the reports cited

above and with Eq. (13), which predicts $\tau_1 / \tau_2 = \rho_1 > 1$ when evaluated for $n = 1$ with the nominal value $\langle r \rangle = 1.21$. In addition, inspection of the τ_1 - and τ_2 -trend lines suggests considerable correlation in their values.

We explore further the empirical correlation between the delays τ_1 and τ_2 in Fig. 3(a). The scatterplot indicates that the two phase-gradient delays are indeed highly correlated. Equation (13) predicts that the data will fall about a straight line through the origin with slope $\rho_1 = 2 / \langle r \rangle \approx 1.653$. As shown in the figure, this simple proportionality quantitatively captures the major trend in the data.¹⁰ Fitting a line to the data—using a weighted least-squares technique that accounts for the estimated uncertainties in both τ_1 and τ_2 (e.g., Press *et al.*, 1992)—yields $\tau_1 = (1.53 \pm 0.1) \tau_2 + (0.005 \pm 0.06)$, where the uncertainties in the slope and intercept represent the 95%-confidence intervals estimated by bootstrap resampling (e.g., Efron and Tibshirani, 1993). The importance of taking measurement uncertainty into account is underscored by the observation that our estimate of the best-fit straight line differs substantially from that obtained using standard linear regression in which uncertainties in the coordinates are ignored.¹¹ As illustrated in the residual-dependence plots [Figs. 3(b), (c)], deviations about the predicted line certainly have a nonrandom component, suggesting additional structure in the data not accounted for by Eq. (13). Given the simplicity of the analysis, however, the overall agreement between theory and experiment is striking.

Other phase-gradient-delay data in the literature appear at least qualitatively consistent with the empirical relations reported here [e.g., Bowman *et al.* (1997), Table I]. Unfortunately, definitive quantitative comparisons are precluded by the absence of error bars and the wide range of f_2 / f_1 ratios typically employed during the phase measurements used to determine phase-gradient delays. The work of Schneider *et al.* (1999, 2000; Prijs *et al.*, 2000) proves a happy exception to this rule: In their recent conference report they show that their measurements of τ_1 and τ_2 (including DPOAEs with indices $n = \{1, 2, 3\}$) are generally consistent with Eq. (11), a relation they obtained independently by exploring the consequences of theoretical assumptions about

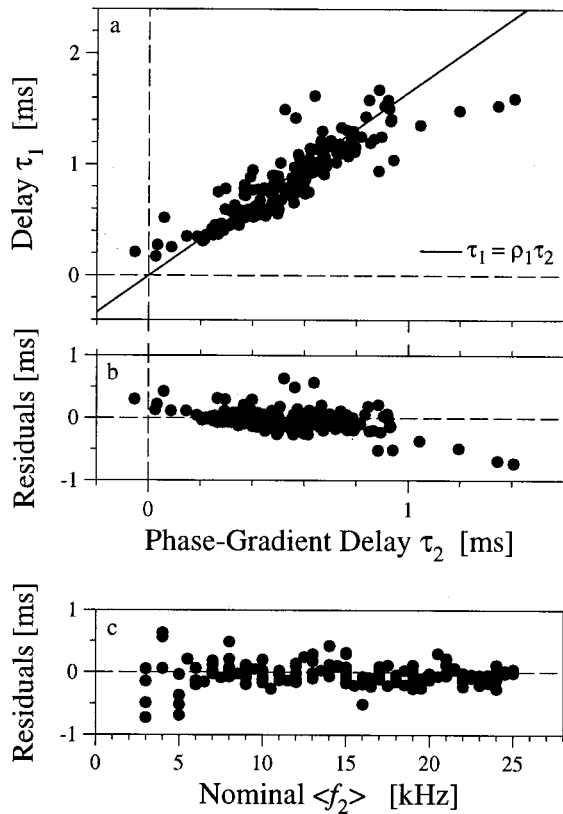


FIG. 3. Empirical correlation between τ_1 and τ_2 . The figure (panel a, top) shows a scatterplot of τ_1 vs τ_2 constructed using the data from Fig. 2. The simple proportionality with slope $\rho_1 = 2/\langle r \rangle \approx 1.653$ predicted by Eq. (13) is shown for comparison. The lower panels illustrate the residual dependence by plotting the deviations from the predicted line in two different ways: vs τ_2 (panel b, center) and vs $\langle f_2 \rangle$ (panel c, bottom). Although the residuals have a nonrandom component suggesting additional structure in the data not accounted for by the simple model of Eq. (13), the theoretical line captures the dominant trend in the data.

DPOAE generation in a scaling-symmetric, nonlinear transmission-line model of cochlear mechanics.

C. Why does the simple model work so well?

As illustrated in Fig. 3, the dominant trends in the phase-gradient-delay data are well captured by the simplest model consistent with dimensional constraints. In this model—or, rather, in the entire class of models defined by Eq. (6)—the primary frequencies themselves are assumed to constitute the only frequency scales in the problem; distortion-product phase φ_{dp} then depends solely on the ratio f_2/f_1 . The model correctly predicts both the approximate proportionality between τ_1 and τ_2 (see Fig. 3) and the relation $\tau_r \approx 0$ (see Fig. 2). This latter prediction is equivalent to the statement that distortion-product phase measured using a fixed-ratio frequency sweep is approximately constant (e.g., Kemp and Brown, 1983; Shera and Guinan, 1999).

The success of this simple model can be understood as a consequence of the mechanisms of DPOAE generation within the cochlea. Considerable evidence now suggests that DPOAEs are mixtures of emissions generated by two fundamentally different mechanisms: nonlinear distortion and linear coherent reflection (Shera and Guinan, 1999; Talmadge *et al.*, 1999; Mauermann *et al.*, 1999a; Kalluri and Shera,

2000; Knight and Kemp, 2000b). For the measurement parameters in common use [i.e., $n > 0$, $L_1 \geq L_2$, and $f_2/f_1 \approx (f_2/f_1)_{\text{optimal}}$], the distortion-source component of the mixture is generally larger than the reflection-source component (Talmadge *et al.*, 1999; Kalluri and Shera, 2000; Knight and Kemp, 2000b), and consequently the secular variation of the DPOAE phase is determined by the mechanisms of nonlinear intermodulation distortion.

Cochlear intermodulation distortion depends upon the interaction between the two primary traveling waves. When produced using frequency-scaled stimuli (e.g., with the fixed-ratio paradigm), the spatial envelopes of the stimulus traveling waves simply shift along the cochlear partition as the stimulus frequencies are varied. This approximate shift similarity follows from the approximate local scaling symmetry (Zweig, 1976; Siebert, 1968; Sondhi, 1978) manifest by basilar- and tectorial-membrane transfer functions (Rhode, 1971; Gummer *et al.*, 1987; Rhode and Cooper, 1996) and neural tuning curves (e.g., Kiang and Moxon, 1974; Liberman, 1978). Local scaling symmetry implies that rather than depending on position and frequency independently, as might be expected, cochlear mechanical responses in fact depend on the two variables x and f primarily in the combination $f/f_{cf}(x)$, where $f_{cf}(x)$ is the cochlear position-frequency map. When the cochlear map is exponential, local scaling symmetry implies that traveling-wave envelopes are locally “shift-similar.”

The approximate shift-similarity ensures that the amplitude and phase of the primary traveling waves—and hence any nonlinear interactions between them—remain nearly invariant in a coordinate system that moves with the envelope of the f_2 traveling wave as the primary frequencies are swept. Otoacoustic emissions recorded using the fixed-ratio paradigm therefore manifest a nearly constant phase (Shera and Guinan, 1999). Consequently, the fixed-ratio phase-gradient delays, τ_r , generally straddle the zero line. In the following section, we demonstrate that the predictions $\tau_r = 0$ and $\tau_1 = \rho_n \tau_2$ [Eqs. (10) and (11)] are not independent: Any model that predicts one also predicts the other. The simple model works so well, then, because cochlear mechanical responses—and thus the mechanisms of distortion generation—are themselves “simple.” To a good first approximation, local scaling symmetry applies and cochlear mechanical responses are functions of the single dimensionless variable $f/f_{cf}(x)$.

IV. UNDERSTANDING DEVIATIONS FROM THE SIMPLE MODEL

Although the simple model discussed above—in which distortion-product phase depends solely on the ratio of primary frequencies—accounts for the major trends in the data, the residual-dependence plots in Fig. 3 clearly hint at additional structure in the measurements. A clue to the form of this structure can be found in Fig. 4, which shows τ_1 and τ_2 in a scatterplot vs τ_r , the fixed-ratio phase-gradient delay. To render the two data sets more directly comparable, the τ_2 data have been rescaled by the factor ρ_1 suggested by Eq. (11). Careful examination of the scatterplot reveals that the relationship between the two delays τ_1 (circles) and τ_2

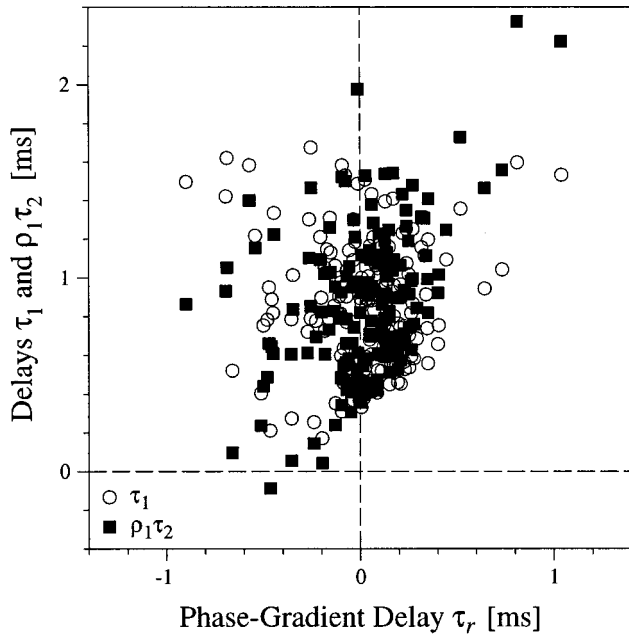


FIG. 4. Additional structure in the τ_1 and τ_2 data. The figure shows a scatterplot of τ_1 (○) and $\rho_1\tau_2$ (■) vs τ_r constructed using the data from Fig. 2. The τ_2 data have been rescaled by the factor ρ_1 [cf. Eq. (11)] in order to make two data sets more comparable. The figure suggests that the relationship between τ_1 and τ_2 varies systematically with τ_r : At any given value of $\tau_r < 0$, the delay τ_1 is usually greater than $\rho_1\tau_2$ (circles above squares); for $\tau_r > 0$, however, $\rho_1\tau_2$ is usually greater than τ_1 (squares above circles).

(squares) varies systematically with τ_r . In particular, note that for negative τ_r (shown left of center), the delay τ_1 is generally greater than $\rho_1\tau_2$ (so that the circles generally appear *above* the squares); for positive τ_r , however, the relative magnitudes of these two quantities are reversed (and the circles appear *below* the squares).

A. A general relation among the phase-gradient delays

To elucidate this structure, we return to the general case described by Eq. (4). Rewritten using dimensionless variables, Eq. (4) becomes

$$\varphi_{\text{dp}} = \varphi_{\text{dp}}(r, s; \dots), \quad (17)$$

where $r \equiv f_2/f_1$ as before. Without loss of generality, we take the second independent variable to be $s \equiv f_2/f_0$, where f_0 represents an additional fixed frequency scale chosen for convenience.¹² Including s among the list of independent variables thus allows φ_{dp} to depend on the absolute primary frequencies, f_1 and f_2 , rather than simply on their ratio.

The second independent variable modifies the theoretical phase-gradient delays. As before, derivatives are evaluated using the chain rule. The derivative that defines τ_r in Eq. (3) becomes

$$-2\pi\tau_r \equiv \left. \frac{\partial \varphi_{\text{dp}}}{\partial f_{\text{dp}}} \right|_r = \left. \frac{\partial r}{\partial f_{\text{dp}}} \right|_r \frac{\partial \varphi_{\text{dp}}}{\partial r} + \left. \frac{\partial s}{\partial f_{\text{dp}}} \right|_r \frac{\partial \varphi_{\text{dp}}}{\partial s}. \quad (18)$$

Analogous relations hold for the derivatives that define τ_1 and τ_2 . Again, the first term in Eq. (18) is zero (since r is constant). Evaluating the derivative $\partial s / \partial f_{\text{dp}}|_r$ in the second term yields¹³

$$2\pi f_2 \tau_r = - \frac{s}{(n+1)r-n} \frac{\partial \varphi_{\text{dp}}}{\partial s}. \quad (19)$$

Thus the fixed-ratio phase-gradient delay, τ_r , is no longer necessarily zero, in contrast to the results of our earlier analysis, in which φ_{dp} was assumed to depend only on r . In a similar manner one obtains expressions for τ_1 and τ_2 :

$$2\pi f_2 \tau_1 = \frac{1}{n} \left(r \frac{\partial \varphi_{\text{dp}}}{\partial r} + s \frac{\partial \varphi_{\text{dp}}}{\partial s} \right), \quad (20)$$

and

$$2\pi f_2 \tau_2 = \frac{r^2}{n+1} \frac{\partial \varphi_{\text{dp}}}{\partial r}. \quad (21)$$

Equations (19)–(21) can be combined to yield an expression relating the three phase-gradient delays,

$$\tau_1 = \rho_n \tau_2 - (\rho_n - 1) \tau_r, \quad (22)$$

where ρ_n is defined by Eq. (12). Equation (22) implies that not all vectors $\{x, y, z\}$ represent realizable triplets $\{\tau_1, \tau_2, \tau_r\}$: Legitimate phase-gradient delay triplets are constrained to a two-dimensional surface—i.e., the plane defined by Eq. (22)—in the full three-dimensional space of possibilities.

Equation (22) is a consequence of Eq. (17) and the mathematical relationships among the three sweep paradigms, as defined by the derivatives in Eqs. (1)–(3) and Eq. (5) for f_{dp} . Equation (22) therefore constitutes a *general relation that holds for any model*. As such, the relation has no additional physical content. Nevertheless, by providing an exact relation among measurable quantities, Eq. (22) proves useful for organizing and understanding the structure in phase-gradient-delay data. Note, for example, that the direct proportionality between τ_1 and τ_2 predicted by models in the class defined by Eq. (6) is recovered in the limit $\tau_r \rightarrow 0$. The predictions $\tau_r = 0$ and $\tau_1 = \rho_n \tau_2$ are therefore not independent: Any model that predicts one also predicts the other. Thus the general relation effectively reduces the problem of understanding the relative values of τ_1 and τ_2 to the problem of understanding τ_r ; this latter problem is simplified by the existence of a ready conceptual framework involving local scaling symmetry and its breaking.

For the interested reader, we derive Eq. (22) as a special case of an even more general relation in the Appendix. In the following sections, we demonstrate that our measurements satisfy Eq. (22) and then apply it to understand deviations from the simple model.

B. Comparison with experiment

Equation (22) provides at least a qualitative account of the trends apparent in Fig. 4: Specialized to the case $n = 1$, Eq. (22) predicts that when $(\rho_1 - 1) > 0$, the delay τ_1 will appear corresponding greater than (less than) $\rho_1\tau_2$ according to whether τ_r is less than (greater than) zero. We perform a more quantitative evaluation by rearranging the terms in Eq. (22) to obtain a relation convenient for plotting in the manner of Fig. 3,

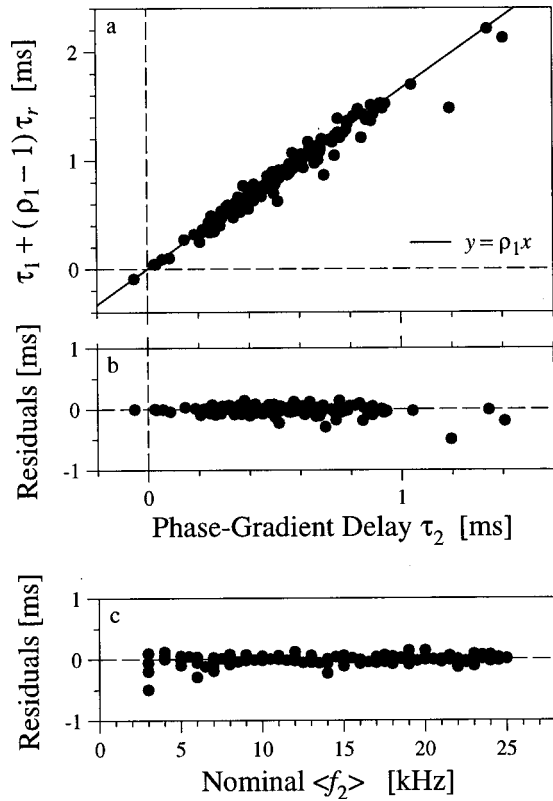


FIG. 5. Relationship among the phase-gradient delays. The figure (panel a, top) shows a scatterplot of $y \equiv [\tau_1 + (\rho_1 - 1)\tau_r]$ vs $x \equiv \tau_2$ constructed using the data from Fig. 2. The theoretical line of slope ρ_1 predicted by Eq. (23) is shown for comparison. As in Fig. 3, the bottom panels illustrate the residual dependence by plotting the deviations from the predicted line in two different ways: vs τ_2 (panel b, center) and vs $\langle f_2 \rangle$ (panel c, bottom). All the points with large residuals have unusually large estimated uncertainties. The excellent agreement provides a strong check on the internal consistency of our data.

$$\underbrace{\tau_1 + (\rho_1 - 1)\tau_r}_y = \rho_1 \underbrace{\tau_2}_x \quad (23)$$

This equation predicts a proportionality, with slope $\rho_1 = 2/\langle r \rangle \approx 1.653$, between the quantity $y \equiv \tau_1 + (\rho_1 - 1)\tau_r$ appearing on the left-hand side and the phase-gradient delay $x \equiv \tau_2$ on the right. Figure 5(a) shows that our data satisfy this relation. Indeed, fitting a straight line to the data—again accounting for errors in both coordinates—yields empirical values for the slope and intercept that agree, within estimated uncertainties, with theoretical predictions. Specifically, the best-fit slope and intercept have values of 1.66 ± 0.04 and -0.014 ± 0.024 , respectively.¹⁴ Furthermore, the residual-dependence plots [Figs. 5(b), (c)] indicate little systematic variation in the residuals. In addition to illustrating the power of our phenomenological analysis, the strong quantitative agreement we find constitutes an important check on the internal consistency of our data.

1. Eliminating spurious measurements

Consistency with general relation (22) provides an objective criterion for identifying spurious measurements. To avoid apparent circularity in the argument, however, we have not as yet applied this criterion to our data. With Eq. (22)

now established, we proceed to eliminate erroneous phase-gradient-delay triplets from further analysis.¹⁵ For each delay triplet (including those previously eliminated based on their trend residual), we computed the quantity $\Delta \equiv \tau_1 - \rho_1 \tau_2 + (\rho_1 - 1)\tau_r$. In the absence of measurement noise or other experimental error, internal consistency of the data requires $\Delta = 0$. We therefore discarded those delay triplets with values $|\Delta|$ larger than 95% of their companions (a criterion based on examination of the distribution of Δ values). Only 20% of the triplets eliminated in this way (3 of 14) had failed the selection test based on trend residuals. Henceforth, all figures and analysis are based on this revised data set.

C. Intensity-dependence of the phase-gradient delays

Figure 5 illustrates the general relation using phase-gradient-delay data obtained at one stimulus-level pair $\{L_1, L_2\}$. The general relation, however, holds at all levels and can be applied to help elucidate the intensity-dependence of the phase-gradient delays. Figure 6 shows triplets $\{\tau_1, \tau_2, \tau_r\}$ vs L_2 , the level of the higher frequency primary (with $L_1 = L_2 + 10$ dB SPL). Points connected by solid lines constitute a level series made in the same ear and at the same nominal values of $\langle f_2 \rangle$ and $\langle r \rangle$. Note that most series appear roughly linear when plotted versus log intensity. We therefore quantified the overall dependence on intensity by fitting a straight line to each level series and averaging the results to compute the mean slope, $d\tau/dL$, for each of the three phase-gradient delays. [Note that because we varied both primary levels together (with $L_1 = L_2 + 10$ dB SPL), we write $d\tau/dL$, rather than $d\tau/dL_2$, to indicate an overall change in primary level, rather than a change in L_2 specifically.] In agreement with earlier reports (e.g., Bowman *et al.*, 1997), we find a significant ($p < 0.01$) level dependence in both τ_1 and τ_2 . The mean slopes have values $d\tau_1/dL = -14.2 \pm 1.6 \mu\text{s}/\text{dB}$ and $d\tau_2/dL = -10 \pm 1.5 \mu\text{s}/\text{dB}$, indicating that τ_1 varies more strongly with level than τ_2 (again in agreement with Bowman *et al.*). The uncertainties here represent standard errors of the mean and statistical significance was assessed by testing the null hypothesis (level-independence) using permutation tests (e.g., Efron and Tibshirani, 1993; Sprent, 1998). The mean slope for the τ_r level series (namely, $d\tau_r/dL = -3.8 \pm 2.4 \mu\text{s}/\text{dB}$), although significantly different from zero ($p < 0.05$), is considerably shallower than the slopes for τ_1 and τ_2 .

In Fig. 6(d) (right-most panel) we demonstrate that the $\{\tau_1, \tau_2, \tau_r\}$ level series are described by the general relation (22). The data points represent values of τ_1 predicted by Eq. (22) using corresponding values of τ_2 and τ_r taken from panels (b) and (c). As expected, overall agreement is excellent; the measured and predicted τ_1 level series are statistically indistinguishable. Note, in addition, that the mean slopes obtained above can be related by differentiating Eq. (22) with respect to L . For $n = 1$,

$$\frac{d\tau_1}{dL} = \rho_1 \frac{d\tau_2}{dL} - (\rho_1 - 1) \frac{d\tau_r}{dL} \quad (24)$$

Substituting the value $\rho_1 = 2/\langle r \rangle$ and using our mean-slope estimates for $d\tau_2/dL$ and $d\tau_r/dL$ yields the value $d\tau_1/dL$

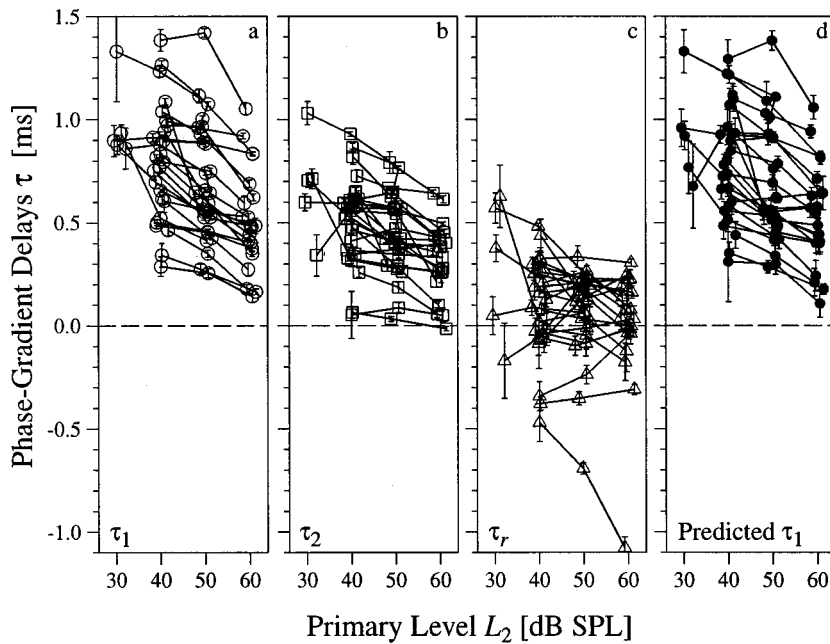


FIG. 6. Intensity dependence of phase-gradient-delay triplets $\{\tau_1, \tau_2, \tau_r\}$. Empirical values of τ_1 (\circ in panel a, left), τ_2 (\square in panel b), and τ_r (\triangle in panel c) and their estimated uncertainties are plotted vs L_2 , the level of the higher-frequency primary (with $L_1=L_2+10$ dB SPL and $\langle r \rangle=1.21$). Solid lines connect measurements in a level series made in the same ear at the same values of $\langle f_2 \rangle$ and $\langle r \rangle$. Only series consisting of measurements at three or more different levels are shown ($n=26$ series). For comparison, the right-most panel (\bullet in panel d) shows values of τ_1 and their uncertainties as predicted from Eq. (22) using corresponding values of τ_2 and τ_r from panels (b) and (c). Although all measurements were made at L_2 levels corresponding to integer multiples of 10 dB SPL, the L_2 values on the graph were dithered randomly (but identically in all four panels) to make individual data points somewhat easier to distinguish.

$\approx -14 \pm 3 \mu\text{s}/\text{dB}$, in close agreement with the empirical value reported above ($d\tau_1/dL = -14.2 \pm 1.6 \mu\text{s}/\text{dB}$). Note that since the $d\tau_r/dL$ term in Eq. (24) is relatively small, most of the difference in level dependence between τ_1 and τ_2 can be understood as a trivial consequence of the proportionality factor $\rho_1 > 1$. [Indeed, simply neglecting the $d\tau_r/dL$ term in Eq. (24) yields the estimate $d\tau_1/dL \approx -16.5 \pm 2.5 \mu\text{s}/\text{dB}$.]

D. Deviations from the simple model

The simple approximate analysis presented and interpreted in Sec. III predicts that the phase-gradient-delay ratio τ_1/τ_2 has the value ρ_n [Eq. (11)]. More generally, Eq. (22) implies that the delay ratio has the form

$$\tau_1/\tau_2 = \rho_n(1 - \varepsilon_{sd}), \quad (25)$$

where

$$\varepsilon_{sd} \equiv (1 - 1/\rho_n) \frac{\tau_r}{\tau_2}. \quad (26)$$

Our sign convention guarantees that ε_{sd} and τ_r usually have the same sign (since, typically, $\tau_2 > 0$ and $\rho_n > 1$). Equation (25) thus modifies the simple-model prediction for the ratio τ_1/τ_2 with a ‘‘correction term’’ proportional to τ_r/τ_2 . The quantity ε_{sd} provides a dimensionless measure of the effect of deviations from scaling on DPOAE phase-gradient delays (the subscript stands for ‘‘scaling deviations’’).¹⁶ Equation (25) indicates that the approximate proportionality between τ_1 and τ_2 holds whenever $|\varepsilon_{sd}| \ll 1$; that is, whenever deviations from scaling are small. In the ‘‘scaling limit’’ ($\varepsilon_{sd} \rightarrow 0$), the phase-gradient delays τ_1 and τ_2 become exactly proportional. Figure 7 illustrates this analysis by showing how the delay ratio, τ_1/τ_2 , depends on the value of ε_{sd} . Note that the scales along both axes have been warped to accommodate the wide range of positive and negative values

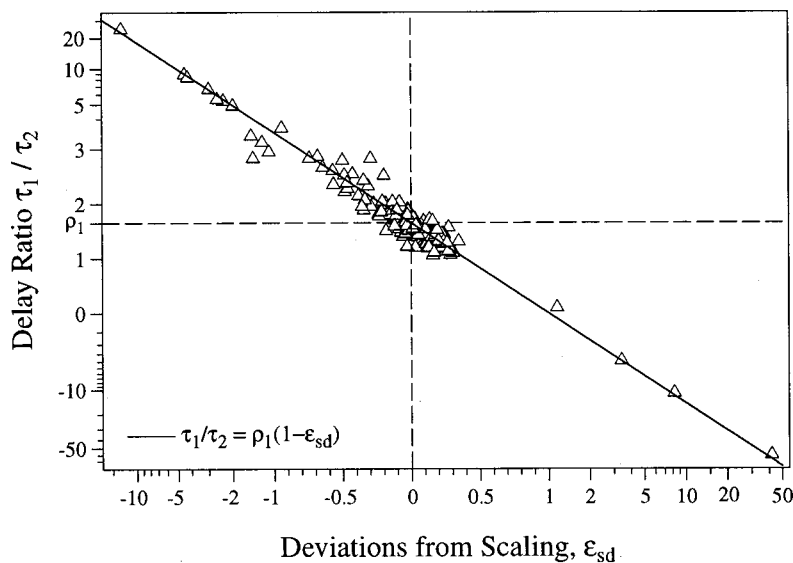


FIG. 7. Phase-gradient-delay ratio τ_1/τ_2 and its dependence on ε_{sd} . The figure shows τ_1/τ_2 vs $\varepsilon_{sd} \equiv (1 - 1/\rho_1)\tau_r/\tau_2$. Since the predicted relation between these quantities applies independent of stimulus level, data at $L_2=50$ dB SPL (as in Fig. 2) have been pooled with measurements made at $L_2=\{30,40,60\}$ dB SPL with $L_1=L_2+10$ dB (for a total of $n=259$ triplets in 5 ears). The scales have been warped to accommodate the wide range of positive and negative values in the data (see Note 17). Both the ordinate and the abscissa are linear over intervals centered on the dashed lines: The ordinate is linear for $0 < \tau_1/\tau_2 < 2\rho_1$; the abscissa is linear for $|\varepsilon_{sd}| < 1$. Both scales are logarithmic outside their linear range. The solid line shows the theoretical prediction obtained in Eq. (25), namely a line of slope $-\rho_1$ intersecting the line $\varepsilon_{sd}=0$ at the value $\rho_1=2/\langle r \rangle \approx 1.653$. In the scaling limit ($\varepsilon_{sd} \rightarrow 0$), the phase-gradient delays τ_1 and τ_2 become exactly proportional.

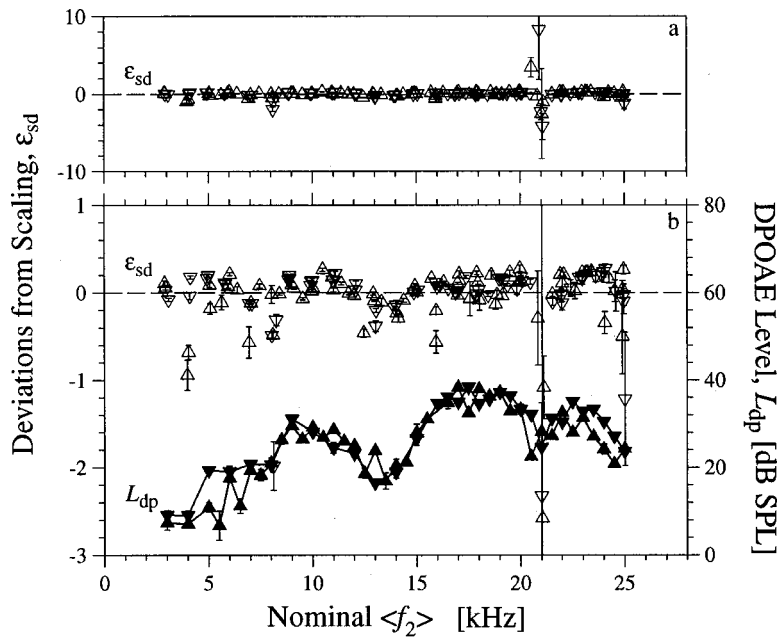


FIG. 8. Deviations from scaling quantified by ϵ_{sd} . Both panels show the parameter $\epsilon_{sd} \equiv (1 - 1/\rho_1)\tau_r/\tau_2$ (Δ and ∇) and its estimated uncertainty vs $\langle f_2 \rangle$. The downwards- and upwards-pointing triangles distinguish data from different animals [CAS-51 ($n=68$) and CAS-52 ($n=75$), respectively]. The bottom panel (b) shows the same data as the top (a) on an expanded vertical scale (axis on the left). For comparison, the bottom panel also shows corresponding DPOAE levels, L_{dp} , measured at primary stimulus levels of $\{L_1, L_2\} = \{60, 50\}$ dB SPL and $f_2/f_1 = 1.21$ (\blacktriangle and \blacktriangledown connected by solid lines; axis on the right). As quantified by ϵ_{sd} , deviations from scaling are usually small ($|\epsilon_{sd}| \leq 0.2$) and slightly positive. Larger deviations, typically negative (cf. Fig. 7), often occur at $\langle f_2 \rangle$ values associated with prominent notches in DPOAE amplitude.

represented in the figure.¹⁷ Our data verify that departures from the strict proportionality $\tau_1/\tau_2 = \rho_1$ predicted by the simple model are linearly related to deviations from scaling quantified by ϵ_{sd} .

In addition to an estimate of the magnitude of scaling deviations, our data provide information about their variation with location in the cochlea. As demonstrated in Fig. 8, which shows ϵ_{sd} as a function of $\langle f_2 \rangle$, the data indicate that scaling deviations are generally small (typically, $|\epsilon_{sd}| \leq 0.2$) and, on average, slightly positive ($\epsilon_{sd} > 0$). Larger deviations from scaling, often corresponding to values of $\epsilon_{sd} < 0$, typically occur at values of $\langle f_2 \rangle$ associated with prominent notches in DPOAE amplitude. Amplitude notches—or, indeed, any variation in emission amplitude with frequency measured using the fixed-ratio paradigm—also constitute deviations from scaling. Since DPOAE amplitude and phase appear strongly correlated, the association noted here is not surprising. The generally small size of the scaling deviations evident in Figs. 7 and 8 explains the considerable success of the simple model [Eq. (6)] in capturing the major trends in the data. With regard to variations in ϵ_{sd} along the length of the cochlea, obvious systematic variations with $\langle f_2 \rangle$ are not apparent.

1. Sources of the deviations from scaling

As suggested above, values $\tau_r \neq 0$ correspond to deviations from scaling symmetry.¹⁸ Such deviations can occur on a variety of frequency scales. For example, although fixed-ratio DPOAE phase is nearly constant at high frequencies [for $f_2/f_1 \approx (f_2/f_1)_{\text{optimal}}$], a secular variation in human DPOAE phase (corresponding to $\tau_r > 0$) occurs at frequencies less than approximately 3 kHz (Shera and Guinan, 1999). This slow phase variation reflects a gradual breaking of scaling symmetry in the apical turns of the cochlea, perhaps corresponding to deviations from scaling at similar frequencies apparent in the shapes of cat auditory-nerve tuning curves (e.g., Kiang and Moxon, 1974; Liberman, 1978). Measurements of stimulus-frequency-emission phase pro-

vide further evidence for gradual deviations from scaling in the mammalian cochlea (Shera and Guinan, 2000a, 2000b). These deviations—apparent in cats, guinea pigs, and humans—are in qualitative agreement with trends expected from the gradual sharpening of neural and mechanical tuning at high characteristic frequencies. Deviations from scaling are also apparent over smaller intervals. Although DPOAE phase appears to vary smoothly when considered over intervals of an octave or more, on smaller scales the phase manifests reproducible “irregularities” or fine structure (e.g., O’Mahoney and Kemp, 1995; Moulin and Kemp, 1996a; Talmadge *et al.*, 1999, and references therein). This phase fine structure, often highly correlated with fine structure in DPOAE amplitude, is magnified by the computation of phase derivatives and can yield both positive and negative values of τ_r .

Thus nonzero values of τ_r due to phase microstructure and other more clearly location-dependent variations indicate deviations from perfect scale invariance. Possible sources for nonzero values of τ_r include (1) the frequency dependence of middle-ear transfer functions; (2) end effects due to the finite length of the cochlea (presumably most important at the highest and lowest frequencies); (3) variations in the shapes of mechanical transfer functions across characteristic frequency; and (4) wave-reflection and interference effects in the cochlea due to the distributed nature of nonlinear distortion, mixing from multiple emission sources, interactions with spontaneous emissions, and multiple internal reflection.

Since all of these sources may contribute to some extent—with magnitudes and signs that presumably vary from species to species, between subjects, and with characteristic frequency within a given subject—the phase-gradient delay τ_r may depend on cochlear mechanics and physiology in a complicated way. Extracting useful information from τ_r by teasing apart the relative contributions thus becomes a difficult problem. Some insight, however, can be obtained by examining the dependence of τ_r on a primary level. Of the possible sources enumerated above, items (1) and (2) would

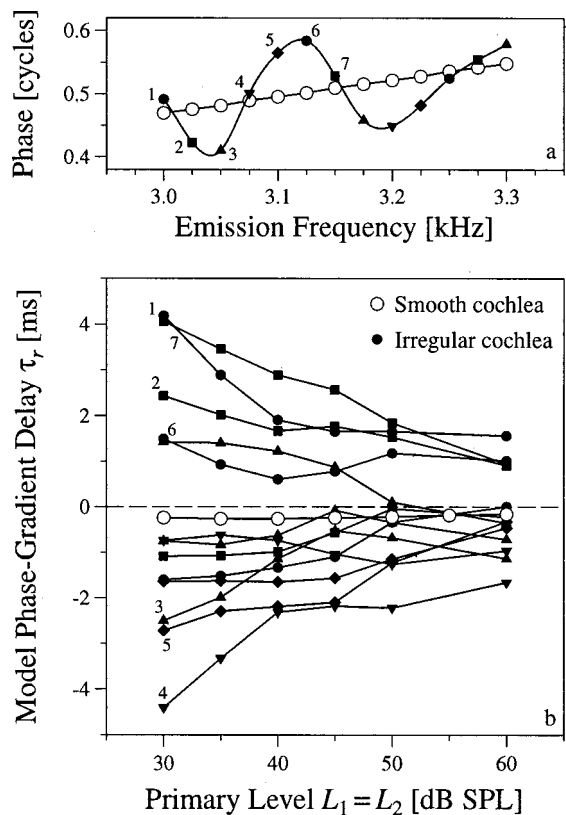


FIG. 9. Simulated DPOAE fine structure and its effects on τ_r . The figure shows fixed-ratio DPOAE phase (panel a, top) and values of τ_r (panel b, bottom), computed for the human ear using two variants of the model of Talmadge *et al.* (1998). The only difference between the two models is the presence (solid symbols) or absence (○) of random micromechanical impedance perturbations (and, thus, the presence or absence of reflection-source emissions and DPOAE fine structure). The top panel shows DPOAE phase vs frequency computed at 25-Hz intervals with $L_1=L_2=30$ dB SPL and $f_2/f_1=1.225$; the smooth interpolant was obtained using cubic spline interpolation. The five solid symbols (●, ■, ▲, ▼, ◆) are used in rotation and appear again in the bottom panel to help distinguish series at different frequencies. The bottom panel shows corresponding values of τ_r , together with values calculated at higher primary levels (connected in level series by solid lines). The numerals 1–7 identify series computed at frequencies spanning one full cycle of DPOAE fine structure (see top panel). In the smooth cochlea, the level series obtained at different frequencies are indistinguishable on the scale of the graph.

be expected to yield values of τ_r that are nearly independent of stimulus intensity. Sources (3) and, especially, (4), however, could generate significant variation across level since their effects presumably depend on the relative amplitudes and phases of interfering waves, both of which can change substantially with level.

Support for this reasoning comes from cochlear-model simulations of the effect of DPOAE fine structure on τ_r . As illustrated in Fig. 9, we simulated human DPOAEs using two variants of the model of Talmadge *et al.* (1998).¹⁹ The two models, denoted “smooth” and “irregular,” are identical in every way but one: In the smooth cochlea, the mechanical parameters characterizing the organ of Corti vary smoothly with position; in the irregular cochlea, random micromechanical impedance perturbations are densely arrayed along its length. The traveling wave scatters off these perturbations as it propagates, generating reflection-source emissions through the mechanism of coherent reflection filtering

(Shera, 1992; Shera and Zweig, 1993b; Zweig and Shera, 1995). As illustrated in Fig. 9(a), DPOAE fine structure then results from the mixing of reflection- and distortion-source emissions in the model ear canal. In the smooth cochlea, reflection-source emissions and DPOAE fine structure are entirely absent.

The considerable effect of wave-interference phenomena—in this case, the mixing of reflection- and distortion-source emissions—is evident in the very different values of τ_r obtained in the two models [see Fig. 9(b)]. In the absence of DPOAE fine structure (smooth cochlea), τ_r is small and essentially independent of both frequency and level. The small negative value of τ_r (positive phase slope) apparent in the figure results from mechanism (2) discussed above, namely weak deviations from scaling caused by the finite length of the cochlea (Tubis *et al.*, 2000b; see also Zweig and Shera, 1995, footnote 19). The presence of DPOAE fine structure (irregular cochlea) changes this picture dramatically: predicted values of τ_r , now much larger and of either sign, can vary considerably with both frequency and level. Ultimately, these deviations from scaling due to wave interference effects arise from a more fundamental breaking of scaling symmetry caused by the existence of small, place-fixed perturbations in the mechanics that partially reflect the traveling wave (Shera and Zweig, 1993b; Zweig and Shera, 1995).

In Fig. 10 we look for similar effects in our data. The two panels in the figure show values of τ_r and their estimated uncertainties measured as a function of L_2 (with $L_1=L_2+10$ dB SPL). As in Fig. 6, points connected by solid lines constitute a level series made in the same ear and at the same nominal values of $\langle f_2 \rangle$ and $\langle r \rangle$. If τ_r were always independent of level, each level series would appear approximately horizontal on the graph, with the only variation due to uncertainty in the measurement. Many level series are indeed roughly horizontal (top panel); a sizable fraction (roughly half), however, vary considerably more than can be accounted for by measurement uncertainty alone (bottom panel). These results suggest that nonlinear mechanisms, such as the wave-reflection and interference effects simulated in Fig. 9, constitute a significant source of scale-invariance deviations.

V. DISCUSSION

Experimental and theoretical investigations are often considerably simplified by exploiting symmetries and constraints, exact or approximate, arising both from universal physical principles (e.g., causality, covariance, dimensional homogeneity) and from the particular dynamics of the system (e.g., linearity, reciprocity, analyticity properties such as minimum-phase behavior, scaling). Applying this general lesson, we have used simple phenomenological arguments, which make no detailed assumptions concerning the underlying cochlear mechanics, to establish relationships among the fixed- f_1 , fixed- f_2 , and fixed-ratio DPOAE phase-gradient delays (τ_1 , τ_2 , and τ_r) that find good agreement with experimental data. Indeed, the dominant trends in the

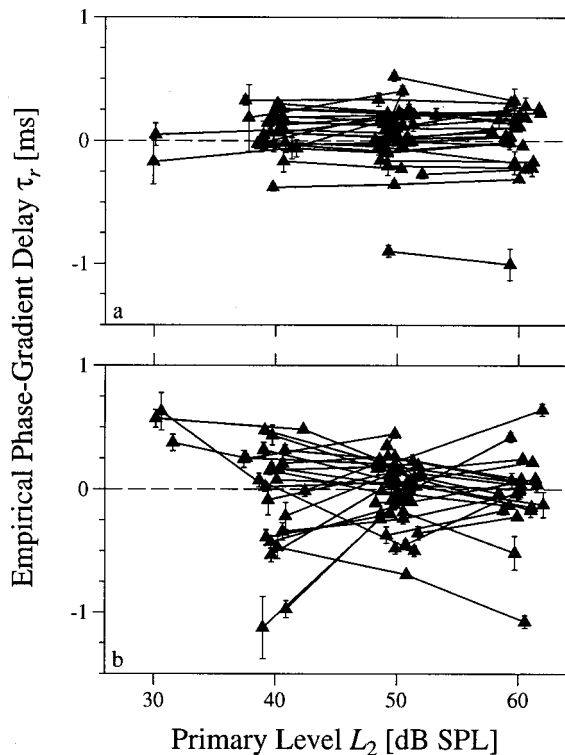


FIG. 10. Intensity dependence of τ_r . Empirical values of τ_r and their estimated uncertainties are plotted vs L_2 , the level of the higher-frequency primary (with $L_1 = L_2 + 10$ dB SPL and $\langle r \rangle = 1.21$). Solid lines connect measurements in a level series made in the same ear at the same values of $\langle f_2 \rangle$ and $\langle r \rangle$. The level series are separated into two groups (which happen to be of roughly equal size) based on their variation with level. The bottom panel (b) shows those series ($n=36$) whose mean variance is significantly greater than that expected by chance ($p \leq 0.05$, as determined by Monte Carlo simulation), given the estimated measurement uncertainties. The top panel (a) shows the remaining series ($n=38$), whose variation with level falls within the range expected by chance alone. As in Fig. 6, the L_2 values on the graph were dithered randomly to make individual data points somewhat easier to distinguish.

phase-gradient-delay data are shown to be well captured by the simplest class of models consistent with dimensional constraints.

To understand deviations between the simple model and experiment, we derived a general equation relating the three phase-gradient delays. Since the general relation is model-independent and exact, it provides a powerful consistency check on DPOAE phase-gradient-delay measurements and a tool for organizing and understanding the structure in DPOAE phase data. For example, the general relation reduces the much-debated problem of understanding the relative values of τ_1 and τ_2 , and their dependence on cochlear physiology, to that of understanding τ_r —a more theoretically tractable case because of its relation to local scaling symmetry.

In the limit of perfect scaling ($\tau_r \rightarrow 0$), the general relation reproduces the predictions of the simple model, namely an exact proportionality between τ_1 and τ_2 characterized by a proportionality constant, ρ_n , dependent on the index, n , of the distortion product and the f_2/f_1 ratio. An approximate proportionality holds whenever deviations from scaling are small. We quantified the magnitude of deviations from scaling in DPOAE phase-gradient delays by introducing the di-

dimensionless parameter ε_{sd} , defined by Eq. (26). As measured by ε_{sd} , deviations from scaling manifest in our data are typically small ($|\varepsilon_{sd}| \leq 0.2$), except in frequency regions associated with prominent notches in DPOAE amplitude. Since the corresponding DPOAE phase is nearly independent of frequency (Shera and Guinan, 1999), we expect $|\varepsilon_{sd}| \ll 1$ whenever fixed-ratio DPOAEs are dominated by backward-traveling waves created by nonlinear distortion [e.g., for $n > 0$, $L_1 \geq L_2$, and $f_2/f_1 \approx (f_2/f_1)_{\text{optimal}}$]. Exploration of the intensity dependence of τ_r suggests that both linear and nonlinear mechanisms contribute significantly to deviations from scaling. Intensity-dependent mechanisms contributing to such deviations include cochlear-reflection and wave-interference effects, such as those associated with the mixing of distortion- and reflection-source emissions (as in DPOAE fine structure).

Thus by exposing directly much of the underlying structure in DPOAE phase-gradient delays, and by doing so in a manner unobscured by extraneous theoretical assumptions, our simple phenomenological approach highlights the origin of that structure in fundamental properties of cochlear mechanics (e.g., in scaling symmetry and its deviations).

A. Implications for noninvasive estimates of cochlear tuning

On the basis of intuitive conceptual arguments about wave propagation in the cochlea, several recent studies have suggested that relative DPOAE phase-gradient delays can be used to provide a noninvasive measure of cochlear tuning. Moulin and Kemp (1996b), for example, argue that the latency ratio τ_1/τ_2 reflects the “sharpness” of the spatial pattern of the traveling wave within the cochlea, supporting their arguments with a comparison between the frequency dependence of τ_1/τ_2 and psychophysical estimates of the relative bandwidths of tuning. Bowman *et al.* (1998) go further by attempting to determine the parameters of gammatone models of human auditory filters from DPOAE measurements. They begin by supposing the total cochlear delay partitioned into components corresponding to “wave-travel time” and “filter-build-up time.”²⁰ They then argue that these two delay components can be extracted from DPOAE phase gradients. Their formulation implies, for example, that the relative delay attributable to “filter-build-up time” versus “wave-travel time” can be estimated, for the f_2 traveling wave, from the relation

$$\frac{\text{filter-build-up time}}{\text{wave-travel time}} \approx \frac{\tau_1 - \tau_2}{\tau_2} = \tau_1/\tau_2 - 1. \quad (27)$$

Auditory filter shapes are then approximated by requiring that gammatone-filter group delays match the estimated “filter-build-up times” for various values of f_2 .

Our results, however, demonstrate that neither of these proposals has any compelling theoretical basis, even in the idealized cases their proponents analyze (e.g., when wave-reflection and interference phenomena due to multiple DPOAE sources can be neglected). Consider, for example, the Bowman *et al.* (1997) argument sketched above. Although “wave-travel” and “filter-build-up” times are never precisely defined, Bowman *et al.* certainly intend them to

depend on parameters of cochlear mechanics (e.g., on the stiffness of the cochlear partition or on characteristics of the filters whose responses are building up). But in the idealized case they consider—for which local scaling applies—our analysis demonstrates that the phase-gradient-delay ratio appearing in Eq. (27) has the value $\tau_1/\tau_2 \approx 2/r = 2f_1/f_2$. In other words, the empirical, emission-based estimates of relative “wave-travel” and “filter-build-up” times that undergird the proposed procedure *depend only on the particular stimulus configuration employed during the DPOAE measurement* (i.e., the primary frequency ratio) and *do not depend on any aspect of cochlear mechanics other than local scaling symmetry* (e.g., the sharpness of the cochlear filters).²¹ Similar remarks apply to the latency ratio discussed by Moulin and Kemp (1996b). In short, our simple phenomenological analysis undercuts these proposals by providing a quantitative account of the relevant data—namely, the longer delays (i.e., $\tau_1 > \tau_2$) and greater intensity dependence (i.e., $|d\tau_1/dL| > |d\tau_2/dL|$) observed using the fixed- f_1 sweep paradigm—without reference to “filter-build-up times” or other elusive concepts.

In the real world, if not always in the idealized models amenable to intuitive argument, the DPOAE phase-gradient-delay ratio τ_1/τ_2 does, of course, contain information about cochlear mechanics [i.e., through its dependence on ε_{sd} as indicated in Eq. (25)]. This information, however, is present in a form not readily recovered by hand-waving conceptual analyses. Our general relation, coupled with the obvious complexity of the data (e.g., Fig. 10), indicates that extracting valid and reliable information about cochlear physiology from DPOAE phase-gradient delays requires coming to grips with a jumble of nonlinear wave-interference effects and other deviations from scaling.

As illustrated here, much of the difficulty in interpreting evoked otoacoustic emissions arises because of interference effects due to the mixing of emissions originating both from different spatial locations (e.g., Kim, 1980; Gaskill and Brown, 1990; Brown *et al.*, 1996; Engdahl and Kemp, 1996; Brown and Beveridge, 1997; Heitmann *et al.*, 1998; Fahey and Allen, 1997; Siegel *et al.*, 1998) and, more fundamentally, by different physical mechanisms within the cochlea (Shera and Guinan, 1999; Talmadge *et al.*, 1999; Mauer-mann *et al.*, 1999a, 1999b; Kalluri and Shera, 2000; Knight and Kemp, 2000b). Mitigating these interpretive difficulties as much as possible by focusing first on the simplest cases—namely, the different emission types measured separately rather than in confounding combination—thus represents an attractive strategy for understanding DPOAEs.

Fortunately, several promising methods now exist for unmixing emissions. For example, the reflection- and distortion-source components of DPOAEs can often be effectively dissected from the total emission using techniques based on selective suppression (Kemp and Brown, 1983; Heitmann *et al.*, 1998; Siegel *et al.*, 1998; Kalluri and Shera, 2000) and/or on emission latency, such as phase-rotation averaging (Whitehead *et al.*, 1996; Talmadge *et al.*, 1999) or time windowing (Kalluri and Shera, 2000; Knight and Kemp, 2000a). Perhaps simplest of all, reflection-source emissions can be studied directly using stimulus-frequency

or transient emissions evoked by sufficiently low-level stimuli.

When pursued within an appropriate interpretive framework, simplification through unmixing or other means shows considerable potential as a strategy for understanding OAEs and the information they carry back to the ear canal about cochlear function. Consider two examples that focus on OAE phase. For distortion-source emissions detailed models of their phase-gradient delays are now appearing (e.g., Schneider *et al.*, 2000; Tubis *et al.*, 2000b); careful comparisons between such models and experiment will establish how these delays depend on parameters of cochlear mechanics. And for reflection-source emissions, the model of coherent reflection filtering (Shera and Zweig, 1993b; Zweig and Shera, 1995; Talmadge *et al.*, 1998) provides a quantitative theoretical foundation for using these emissions to probe cochlear function. Preliminary applications of the theory to stimulus-frequency-emission phase-gradient delays (Shera and Guinan, 2000a, 2000b) confirm the rich potential inherent in OAE phase measurements for obtaining valuable new information about cochlear tuning.

ACKNOWLEDGMENTS

We gratefully acknowledge the help of Leslie Liberman, who assisted with animal care and preparation, and the efforts of Jont Allen, Paul Fahey, John Guinan, Radha Kalluri, William Peake, Susan Voss, and two anonymous reviewers, all of whom provided valuable comments on the manuscript. Finally, we thank Laurel Carney, who asked whether relative DPOAE phase-gradient delays provide a noninvasive measure of cochlear tuning. This work was supported by Grant Nos. R01 DC03687 and R29 DC03094 from the NIDCD, National Institutes of Health.

APPENDIX: THE GENERAL RELATION REVISITED

In this Appendix we obtain our general relation (22) as a special case of an even more general equation. Consider two arbitrary functions, $p(x, y)$ and $q(x, y)$, that depend continuously on two variables, x and y . [In the specific case of interest, revisited at the end, these two functions correspond to $-\varphi_{dp}(f_1, f_2)/2\pi$ and $f_{dp}(f_1, f_2)$, respectively.] We wish to compute derivatives $\tau \equiv dp/dq$ under certain special conditions (i.e., fixed- x , fixed- y , and fixed- r , where $r \equiv y/x$). Toward this end, we compute the differentials dp and dq :

$$dp = p_x \partial x + p_y \partial y, \quad (A1)$$

$$dq = q_x \partial x + q_y \partial y, \quad (A2)$$

where we adopt the notational shorthand $p_x \equiv \partial p / \partial x$, and similarly for the other partial derivatives. When dq is non-zero, the desired derivative, dp/dq , becomes

$$\tau \equiv \frac{dp}{dq} = \frac{p_x \partial x + p_y \partial y}{q_x \partial x + q_y \partial y}. \quad (A3)$$

Consider now our three special cases:

Fixed-x: In this case, $\partial x = 0$; consequently,

$$\tau_x \equiv \left. \frac{dp}{dq} \right|_x = \frac{p_y}{q_y}. \quad (\text{A4})$$

Fixed- y : In this case, $\partial y = 0$; consequently,

$$\tau_y \equiv \left. \frac{dp}{dq} \right|_y = \frac{p_x}{q_x}. \quad (\text{A5})$$

Fixed- r : In this case, $\partial r = 0$, where $r \equiv y/x$; consequently, $\partial y = r \partial x$, and

$$\tau_r \equiv \left. \frac{dp}{dq} \right|_r = \frac{p_x + r p_y}{q_x + r q_y}. \quad (\text{A6})$$

Note that we can use Eq. (A6) to obtain a relation among the three derivatives τ_x , τ_y , and τ_r by using definition (A4) to replace p_y by the product $q_y \tau_x$ (and p_x by $q_x \tau_y$). By doing so we obtain the general equation

$$\tau_r = \frac{q_x \tau_y + r q_y \tau_x}{q_x + r q_y}. \quad (\text{A7})$$

We could, of course, have chosen to replace q_y by p_y / τ_x and so on; Eq. (A7) would then have involved partial derivatives of $p(x, y)$ rather than of $q(x, y)$. The choice is a matter of convenience; in our application, we know the functional form of q but not of p .

We now apply this general relation to DPOAE phase-gradient delays. We wish to obtain the fixed- f_1 , fixed- f_2 , and fixed- r derivatives of DPOAE phase as defined by Eqs. (1)–(3). The functions $p(x, y)$ and $q(x, y)$ therefore correspond to the functions $p(x, y) \mapsto -\varphi_{\text{dp}}(f_1, f_2)/2\pi$ and $q(x, y) \mapsto f_{\text{dp}}(f_1, f_2)$, where, for odd-order distortion products,

$$f_{\text{dp}}(f_1, f_2) = (n+1)f_1 - n f_2 \quad (n = \dots, -3, -2, 1, 2, \dots). \quad (\text{A8})$$

The required derivatives follow immediately:

$$\{q_x, q_y\} \mapsto \left\{ \frac{\partial f_{\text{dp}}}{\partial f_1}, \frac{\partial f_{\text{dp}}}{\partial f_2} \right\} = \{n+1, -n\}. \quad (\text{A9})$$

Substituting these values into Eq. (A7) yields the general relation (22) obtained in the text.

As another application, we derive a corresponding relation valid for even-order distortion products, for which

$$f_{\text{dp}}(f_1, f_2) = m(f_2 - f_1) \quad (m = 1, 2, \dots). \quad (\text{A10})$$

The derivatives are simply $\{q_x, q_y\} \mapsto \{-m, m\}$. Therefore,

$$\tau_1 = \tau_2 / r + (1 - 1/r) \tau_r \quad (\text{even order}), \quad (\text{A11})$$

independent of m .

¹Distortion products with indices $n \geq 1$, for which f_{dp} is less than the primary frequencies, are known as lower-side-band DPOAEs (or apical DPOAEs because their characteristic places are closer to the cochlear apex than those of the primaries). Distortion products with $n \leq -2$, for which f_{dp} is greater than the primary frequencies, are known as upper-side-band (or basal) DPOAEs. Indices $n = 0$ and $n = -1$ correspond to the primary frequencies themselves.

²In the literature, the fixed- f_2 paradigm is usually described as ‘‘swept- f_1 .’’ For clarity, and consistency with the fixed-ratio paradigm, our nomencla-

ture emphasizes the frequency (or parameter) held fixed during the measurement rather than one of the several (e.g., f_1 , f_2 , and f_{dp}) that may be varied.

³A light-smoot is the time it takes light to travel a distance of one smoot in vacuum. One light-smoot is approximately 5.677×10^{-9} s (Leibowitz, 1990).

⁴The value of $\partial r / \partial f_{\text{dp}}|_{f_2}$ can be obtained by writing the defining equation for f_{dp} in the form

$$f_{\text{dp}} = [(n+1)/r - n] f_2.$$

Since f_2 is constant, $\partial f_{\text{dp}} / \partial r|_{f_2} = -(n+1)f_2/r^2 = -(n+1)f_1/r$. Similarly, the value of $\partial r / \partial f_{\text{dp}}|_{f_1}$ follows from the equation

$$f_{\text{dp}} = [(n+1) - nr] f_1;$$

since f_1 is constant, $\partial f_{\text{dp}} / \partial r|_{f_1} = -n f_1$.

⁵By analyzing scaling-symmetric models for distortion emissions, Schneider *et al.* (2000), Talmadge *et al.* (2000), and Tubis *et al.* (2000a) have obtained this relation independently.

⁶To compute uncertainties in pressure amplitude and phase we used error-propagation formulas valid to second order; second-order approximations were necessary in this case because first-order terms could vanish.

⁷In practice, this correction had negligible effect because our in-the-ear ear-phone calibrations guaranteed that the stimulus tones had constant starting phase in the ear canal.

⁸For more than 85% of the sweeps, all 11 points satisfied the selection criterion; less than 2% of the sweeps had 4 or fewer points.

⁹Our initial data-selection criteria, based on trend residuals, may preferentially eliminate data from intervals over which the data vary rapidly with $\langle f_2 \rangle$. Later, when reducing the potential for such bias becomes important, we adopt an alternate selection criterion (described in Sec. IV B 1) based on the results of Sec. IV A.

¹⁰Additional measurements (not shown here) taken at other primary levels and at other values of $\langle r \rangle$ —as well as more limited data from human subjects—support this conclusion.

¹¹Fitting a line using standard linear regression yields the line $\tau_1 = (1.28 \pm 0.15) \tau_2 + (0.17 \pm 0.06)$ and a corresponding correlation coefficient of $r_{\text{corr}}^2 = 0.78$.

¹²Although our analysis does not depend on the value or physical interpretation of this additional frequency scale, a natural choice for f_0 would be the characteristic frequency at the basal end of the cochlea. With this identification, $-\log(s)$ becomes proportional to the location of the peak of the f_2 traveling wave (in the basal turn of the cochlea, where the cochlear mapping between frequency and position is logarithmic).

¹³The derivative $\partial s / \partial f_{\text{dp}}|_r$ can be written in the form

$$\left. \frac{\partial s}{\partial f_{\text{dp}}|_r} \right| = \frac{\partial s}{\partial f_2} \frac{\partial f_2}{\partial f_{\text{dp}}|_r},$$

with $s = f_2 / f_0$, the derivative $\partial s / \partial f_2 = 1/f_0 = s/f_2$. Similarly, the derivative $\partial f_2 / \partial f_{\text{dp}}|_r$ follows immediately from the expression

$$f_{\text{dp}} = [(n+1)/r - n] f_2.$$

¹⁴Fitting a line using standard linear regression in which uncertainties in the coordinates are ignored yields estimates for the slope and intercept of 1.59 ± 0.08 and 0.02 ± 0.04 , respectively. The corresponding correlation coefficient has the value $r_{\text{corr}}^2 = 0.97$.

¹⁵Interactions between the measured DPOAE and a strong nearby spontaneous emission (SOAE) provide one possible cause of erroneous phase-gradient measurements. Unfortunately, we performed no systematic screening for SOAEs in our animals and so cannot explore this possibility further. We note, however, that SOAEs at frequencies greater than 2 kHz appear relatively uncommon in guinea pigs (Ohyama *et al.*, 1991).

¹⁶General relation (22) implies that the scaling-violation parameter $S \equiv \tau_1 / \rho_1 \tau_2$ used by Tubis *et al.* (2000b) has the value $S = 1 - \epsilon_{\text{sd}}$.

¹⁷We define here the transformation used to warp the axes in Fig. 7. Let z denote the quantity represented along the axis (e.g., ϵ_{sd} , for the abscissa). The axis warping is defined so that values $\hat{z}(z)$ are arrayed uniformly along the axis. The transformation \hat{z} is defined by the composition $\hat{z}(z) = a^{-1}(W(a(z)))$, where the affine transformation, a , is defined by $a(z) = (z - z_0)/z_1$, and the warping, W , by

$$W(\gamma) = \begin{cases} \gamma & \text{for } |\gamma| \leq 1 \\ \text{sgn}(\gamma)[\log(|\gamma|) + 1] & \text{for } |\gamma| > 1 \end{cases}$$

In this expression, the signum function, sgn , yields the sign of its argument. For the abscissa in Fig. 7, $z = \varepsilon_{\text{sd}}$, with $z_0 = 0$ and $z_1 = 1$; for the ordinate, $z = \tau_1 / \tau_2$, with $z_0 = z_1 = \rho_1$.

¹⁸The converse, however, does not hold. Although sufficient to yield $\tau_r = 0$, scaling is not necessary because the multiple deviations discussed below can, in principle, combine in τ_r with opposite signs and cancel one another.

¹⁹Model parameter values were modified slightly from those of Talmadge *et al.* (1998) in order to achieve a better match to human fine-structure spacings.

²⁰Although not the issue here, this dichotomy strikes us as specious and any such division as essentially arbitrary. [An anonymous reviewer summarized the point nicely: "In cochlear mechanics, the 'filter-build-up time' is inseparable from the 'wave-travel time' because the wave amplitude builds up while it is traveling."] We therefore agree with de Boer (1997), whose analysis underscores the artificiality of regarding the total delay as somehow precisely and meaningfully divisible into components representing "wave-travel" and "filter-build-up" time. So lest we unintentionally contribute to the reification of these dubious concepts, we place the terms in quotation marks, mindful of the fallacy identified by John Stuart Mill (1874),

The tendency has always been strong to believe that whatever received a name must be an entity or being, having an independent existence of its own. And if no real entity answering to the name could be found, men did not for that reason suppose that none existed, but imagined that it was something particularly abstruse and mysterious.

²¹Tubis *et al.* (2000b) provide a concrete illustration of the decoupling of the issue of filter sharpness from the value of the ratio τ_1 / τ_2 . Working in the context of a specific cochlear model, they find that the assumption of scale-invariance of the wavelength gives approximate scale-invariance of the DPOAE phase, and hence Eq. (11), to a good approximation. By itself, however, the assumption of scale-invariance of the wavelength tells one nothing about the actual sharpness of the cochlear filters.

Allen, J. B., and Fahey, P. F. (1993). "A second cochlear-frequency map that correlates distortion product and neutral tuning measurements," *J. Acoust. Soc. Am.* **94**, 809–816.

Bowman, D. M., Brown, D. K., Eggermont, J. J., and Kimberley, B. P. (1997). "The effect of sound intensity on f_1 -sweep and f_2 -sweep distortion product otoacoustic emissions phase delay estimates in human adults," *J. Acoust. Soc. Am.* **101**, 1550–1559.

Bowman, D. M., Eggermont, J. J., Brown, D. K., and Kimberley, B. P. (1998). "Estimating cochlear filter response properties from distortion product otoacoustic emission (DPOAE) phase delay measurements in normal hearing adults," *Hear. Res.* **119**, 14–26.

Bowman, D. M., Brown, D. K., and Kimberley, B. P. (2000). "An examination of gender differences in DPOAE phase delay measurements in normal-hearing human adults," *Hear. Res.* **142**, 1–11.

Bridgman, P. W. (1931). *Dimensional Analysis* (Yale University Press, New Haven).

Brown, A. M., and Beveridge, H. A. (1997). "Two components of acoustic distortion: Differential effects of contralateral sound and aspirin," in *Diversity in Auditory Mechanics*, edited by E. R. Lewis, G. R. Long, R. F. Lyon, P. M. Narins, C. R. Steele, and E. L. Hecht-Poinar (World Scientific, Singapore), pp. 219–225.

Brown, A. M., Harris, F. P., and Beveridge, H. A. (1996). "Two sources of acoustic distortion products from the human cochlea," *J. Acoust. Soc. Am.* **100**, 3260–3267.

Brown, D., Kimberley, B., and Eggermont, J. (1994). "Cochlear traveling-wave delays estimated by distortion-product emissions in normal hearing adults and term-born neonates," *J. Otolaryngol.* **23**, 234–238.

Cleveland, W. S. (1993). *Visualizing Data* (Hobart, Summit, NJ).

de Boer, E. (1997). "Cochlear models and minimum phase," *J. Acoust. Soc. Am.* **102**, 3810–3813.

Efron, B., and Tibshirani, R. J. (1993). *An Introduction to the Bootstrap* (Chapman and Hall, New York).

Engdahl, B., and Kemp, D. T. (1996). "The effect of noise exposure on the details of distortion product otoacoustic emissions in humans," *J. Acoust. Soc. Am.* **99**, 1573–1587.

Fahey, P. F., and Allen, J. B. (1997). "Measurement of distortion product phase in the ear canal of the cat," *J. Acoust. Soc. Am.* **102**, 2880–2891.

Faulstich, M., and Kössl, M. (2000). "Evidence for multiple DPOAE com-

ponents based upon group delay of the $2f_1 - f_2$ distortion in gerbil," *Hear. Res.* **140**, 99–110.

Gaskill, S. A., and Brown, A. M. (1990). "The behavior of the acoustic distortion product, $2f_1 - f_2$, from the human ear and its relation to auditory sensitivity," *J. Acoust. Soc. Am.* **88**, 821–839.

Gummer, A. W., Smolders, J. W. T., and Klinke, R. (1987). "Basilar membrane motion in the pigeon measured with the Mössbauer technique," *Hear. Res.* **29**, 63–92.

Heitmann, J., Waldman, B., Schnitzler, H. U., Plinkert, P. K., and Zenner, H.-P. (1998). "Suppression of distortion product otoacoustic emissions (DPOAE) near $2f_1 - f_2$ removes DP-gram fine structure—Evidence for a secondary generator," *J. Acoust. Soc. Am.* **103**, 1527–1531.

Kalluri, R., and Shera, C. A. (2000). "Are DPOAEs a mixture of emissions generated by different mechanisms?," *Assoc. Res. Otolaryngol. Abs.* **23**, 480.

Kemp, D. T. (1979). "Evidence of mechanical nonlinearity and frequency selective wave amplification in the cochlea," *Arch. Oto-Rhino-Laryngol.* **224**, 37–45.

Kemp, D. T., and Brown, A. M. (1983). "An integrated view of cochlear mechanical nonlinearities observable from the ear canal," in *Mechanics of Hearing*, edited by E. de Boer and M. A. Viergever (Martinus Nijhoff, The Hague), pp. 75–82.

Kiang, N. Y. S., and Moxon, E. C. (1974). "Tails of tuning curves of auditory-nerve fibers," *J. Acoust. Soc. Am.* **55**, 620–630.

Kim, D. O. (1980). "Cochlear mechanics: Implications of electrophysiological and acoustical observations," *Hear. Res.* **2**, 297–317.

Kimberley, B. P., Brown, D. K., and Eggermont, J. J. (1993). "Measuring human cochlear traveling wave delay using distortion product emission phase responses," *J. Acoust. Soc. Am.* **94**, 1343–1350.

Knight, R., and Kemp, D. T. (2000a). "Separation of 'wave' and 'place' fixed $2f_1 - f_2$ DPOAE," *Assoc. Res. Otolaryngol. Abs.* **23**, 987.

Knight, R. D., and Kemp, D. T. (2000b). "Indications of different distortion product otoacoustic emission mechanisms from a detailed f_1, f_2 area study," *J. Acoust. Soc. Am.* **107**, 457–473.

Leibowitz, B. (1990). *The Journal of the Institute for Hacks, Tomfoolery, and Pranks at MIT* (MIT Museum, Cambridge).

Lieberman, M. C. (1978). "Auditory-nerve response from cats raised in a low-noise chamber," *J. Acoust. Soc. Am.* **63**, 442–455.

Mauermann, M., Uppenkamp, S., van Hengel, P. W. J., and Kollmeier, B. (1999a). "Evidence for the distortion product frequency place as a source of distortion product otoacoustic emission (DPOAE) fine structure in humans. II. Fine structure for different shapes of cochlear hearing loss," *J. Acoust. Soc. Am.* **106**, 3484–3491.

Mauermann, M., Uppenkamp, S., van Hengel, P. W. J., and Kollmeier, B. (1999b). "Evidence for the distortion product frequency place as a source of distortion product otoacoustic emission (DPOAE) fine structure in humans. I. Fine structure and higher-order DPOAE as a function of the frequency ratio f_2 / f_1 ," *J. Acoust. Soc. Am.* **106**, 3473–3483.

Meyer, S. L. (1975). *Data Analysis for Scientists and Engineers* (Wiley, New York).

Mill, J. S. (1874). *A System of Logic, Ratiocinative and Inductive: Being a Connected View of the Principles of Evidence and the Methods of Scientific Investigation* (Harper, New York).

Mills, D. M., and Rubel, E. W. (1997). "Development of distortion product emissions in the gerbil: 'Filter' response and signal delay," *J. Acoust. Soc. Am.* **101**, 395–411.

Moulin, A., and Kemp, D. T. (1996a). "Multicomponent acoustic distortion product otoacoustic emission phase in humans. I. General characteristics," *J. Acoust. Soc. Am.* **100**, 1617–1639.

Moulin, A., and Kemp, D. T. (1996b). "Multicomponent acoustic distortion product otoacoustic emission phase in humans. II. Implications for distortion product otoacoustic emissions generation," *J. Acoust. Soc. Am.* **100**, 1640–1662.

Neely, S. T., Norton, S. J., Gorga, M. P., and Jesteadt, W. (1988). "Latency of auditory brain-stem responses and otoacoustic emissions using tone-burst stimuli," *J. Acoust. Soc. Am.* **83**, 652–656.

Ohyama, K., Wada, H., Kobayashi, T., and Takasaka, T. (1991). "Spontaneous otoacoustic emissions in the guinea pig," *Hear. Res.* **56**, 111–121.

O'Mahoney, C. F., and Kemp, D. T. (1995). "Distortion product otoacoustic emission delay measurement in human ears," *J. Acoust. Soc. Am.* **97**, 3721–3735.

Press, W. H., Teukolsky, S. A., Vetterling, W. T., and Flannery, B. P. (1992). *Numerical Recipes in C: The Art of Scientific Computing* (Cambridge University Press, Cambridge).

- Prijs, V. F., Schneider, S., and Schoonhoven, R. (2000). "Group delays of distortion product otoacoustic emissions: Relating delays measured with f_1 - and f_2 -sweep paradigms," *J. Acoust. Soc. Am.* **107**, 3298–3307.
- Rhode, W. S. (1971). "Observations of the vibration of the basilar membrane in squirrel monkeys using the Mössbauer technique," *J. Acoust. Soc. Am.* **49**, 1218–1231.
- Rhode, W. S., and Cooper, N. P. (1996). "Nonlinear mechanics in the apical turn of the chinchilla cochlea *in vivo*," *Aud. Neurosci.* **3**, 101–121.
- Schneider, S., Prijs, V. F., and Schoonhoven, R. (1999). "Group delays of distortion product otoacoustic emissions in the guinea pig," *J. Acoust. Soc. Am.* **105**, 2722–2730.
- Schneider, S., Prijs, V. F., Schoonhoven, R., and van Hengel, P. (2000). " f_1 versus f_2 -sweep group delays of distortion product otoacoustic emissions in the guinea pig: Experimental results and theoretical predictions," in *Recent Developments in Auditory Mechanics*, edited by H. Wada, T. Takasaka, K. Ikeda, K. Ohyama, and T. Koike (World Scientific, Singapore), pp. 360–366.
- Shera, C. A. (1992). "Listening to the ear," Ph.D. thesis, California Institute of Technology.
- Shera, C. A., and Guinan, J. J. (1999). "Evoked otoacoustic emissions arise by two fundamentally different mechanisms: A taxonomy for mammalian OAEs," *J. Acoust. Soc. Am.* **105**, 782–798.
- Shera, C. A., and Guinan, J. J. (2000a). "Frequency dependence of stimulus-frequency-emission phase: Implications for cochlear mechanics," in *Recent Developments in Auditory Mechanics*, edited by H. Wada, T. Takasaka, K. Ikeda, K. Ohyama, and T. Koike (World Scientific, Singapore), pp. 381–387.
- Shera, C. A., and Guinan, J. J. (2000b). "Reflection-emission phase: A test of coherent reflection filtering and a window on cochlear tuning," *Assoc. Res. Otolaryngol. Abs.* **23**, 545.
- Shera, C. A., and Zweig, G. (1993a). "Noninvasive measurement of the cochlear traveling-wave ratio," *J. Acoust. Soc. Am.* **93**, 3333–3352.
- Shera, C. A., and Zweig, G. (1993b). "Order from chaos: Resolving the paradox of periodicity in evoked otoacoustic emission," in *Biophysics of Hair Cell Sensory Systems*, edited by H. Duifhuis, J. W. Horst, P. van Dijk, and S. M. van Netten (World Scientific, Singapore), pp. 54–63.
- Siebert, W. M. (1968). "Stimulus transformations in the peripheral auditory system," in *Recognizing Patterns*, edited by P. A. Kolars and M. Eden (MIT Press, Cambridge), pp. 104–133.
- Siegel, J. H., Dreisbach, L. E., Neely, S. T., and Spear, W. H. (1998). "Vector decomposition of distortion-product otoacoustic emission sources in humans," *Assoc. Res. Otolaryngol. Abs.* **21**, 347.
- Sondhi, M. M. (1978). "Method for computing motion in a two-dimensional cochlear model," *J. Acoust. Soc. Am.* **63**, 1468–1477.
- Sprent, P. (1998). *Data Driven Statistical Methods* (Chapman and Hall, New York).
- Stover, L. J., Neely, S. T., and Gorga, M. P. (1996). "Latency and multiple sources of distortion product otoacoustic emissions," *J. Acoust. Soc. Am.* **99**, 1016–1024.
- Talmadge, C. L., Tubis, A., Long, G. R., and Piskorski, P. (1998). "Modeling otoacoustic emission and hearing threshold fine structures," *J. Acoust. Soc. Am.* **104**, 1517–1543.
- Talmadge, C. L., Long, G. R., Tubis, A., and Dhar, S. (1999). "Experimental confirmation of the two-source interference model for the fine structure of distortion product otoacoustic emissions," *J. Acoust. Soc. Am.* **105**, 275–292.
- Talmadge, C. L., Tubis, A., Long, G. L., and Dhar, S. (2000). "Temporal aspects of otoacoustic emissions," in *Recent Developments in Auditory Mechanics*, edited by H. Wada, T. Takasaka, K. Ikeda, K. Ohyama, and T. Koike (World Scientific, Singapore), pp. 353–359.
- Tubis, A., Talmadge, C. L., and Tong, C. (2000a). "Modeling the temporal behavior of distortion product otoacoustic emissions," *J. Acoust. Soc. Am.* **107**, 2112–2127.
- Tubis, A., Talmadge, C. L., Tong, C., and Dhar, S. (2000b). "On the relationships between the fixed- f_1 , fixed- f_2 , and fixed-ratio phase derivatives of the $2f_1-f_2$ distortion product otoacoustic emission," *J. Acoust. Soc. Am.* **108**, 1772–1785.
- Ver, I. L., Brown, R. M., and Kiang, N. Y. S. (1975). "Low-noise chambers for auditory research," *J. Acoust. Soc. Am.* **58**, 392–398.
- Wable, J., Collet, L., and Chéry-Croze, S. (1996). "Phase delay measurements of distortion product otoacoustic emissions at $2f_1-f_2$ and $2f_2-f_1$ in human ears," *J. Acoust. Soc. Am.* **100**, 2228–2235.
- Whitehead, M. L., Stagner, B. B., Lonsbury-Martin, B. L., and Martin, G. K. (1994). "Comparison of the onset latency and group latency of distortion-product otoacoustic emissions in human ears," *Assoc. Res. Otolaryngol. Abs.* **17**, 182.
- Whitehead, M. L., Stagner, B. B., Martin, G. K., and Lonsbury-Martin, B. L. (1996). "Visualization of the onset of distortion-product otoacoustic emissions and measurement of their latency," *J. Acoust. Soc. Am.* **100**, 1663–1679.
- Zweig, G. (1976). "Basilar membrane motion," in *Cold Spring Harbor Symposia on Quantitative Biology* (Cold Spring Harbor Laboratory, Cold Spring Harbor, NY), Vol. XL, pp. 619–633.
- Zweig, G., and Shera, C. A. (1995). "The origin of periodicity in the spectrum of evoked otoacoustic emissions," *J. Acoust. Soc. Am.* **98**, 2018–2047.

A concept for a research tool for experiments with cochlear implant users

Luc Geurts^{a)} and Jan Wouters^{b)}

Laboratoire Experimental ORL, KULeuven, Kapucijnenvoer 33, B 3000 Leuven, Belgium

(Received 8 December 1999; revised 26 July 2000; accepted 1 September 2000)

APEX, an acronym for computer Application for Psycho-Electrical eXperiments, is a user friendly tool used to conduct psychophysical experiments and to investigate new speech coding algorithms with cochlear implant users. Most common psychophysical experiments can be easily programmed and all stimuli can be easily created without any knowledge of computer programming. The pulsatile stimuli are composed off-line using custom-made MATLAB (Registered trademark of The Mathworks, Inc., <http://www.mathworks.com>) functions and are stored on hard disk or CD ROM. These functions convert either a speech signal into a pulse sequence or generate any sequence of pulses based on the parameters specified by the experimenter. The APEX personal computer (PC) software reads a text file which specifies the experiment and the stimuli, controls the experiment, delivers the stimuli to the subject through a digital signal processor (DSP) board, collects the responses via a computer mouse or a graphics tablet, and writes the results to the same file. At present, the APEX system is implemented for the LAURA (Registered trademark of Philips Hearing Implants) cochlear implant. However, the concept—and many parts of the system—is portable to any other device. Also, psycho-acoustical experiments can be conducted by presenting the stimuli acoustically through a sound card. © 2000 Acoustical Society of America.

[S0001-4966(00)00912-7]

PACS numbers: 43.66.Ts, 43.58.Ta [SLE]

I. INTRODUCTION

Until now, numerous psychophysical experiments have been conducted with cochlear implant users. These provide a better understanding of the perceptual effect of varying the parameters of electrical stimulation such as current amplitude, stimulation mode, pulse rate or frequency, place of stimulation, pulse width, or more complex parameters such as the modulation depth of amplitude modulated pulse trains and the duration of a silent gap between successive pulse trains. Various methods are used to obtain quantitative measures of the effect of these parameter variations, such as the method of adjustment, method of limits, method of constant stimuli, rating scales, and triad experiments (Stevens, 1951). Also, several researchers have developed new speech processing algorithms to enhance the implantee's speech perception or to investigate the effect of parameter variations of known algorithms on speech intelligibility.

For psychophysical experiments and the evaluation of speech processors, an interface is needed that connects a personal computer (PC) to the cochlear implant, enabling the delivery of the electric stimuli to the subject under test. Preferably, the PC program also controls the experiment. The cochlear implant manufacturers provide some tools to build such a setup, but some specific technical knowledge is still indispensable to carry out any experiment. This article describes a computer tool that allows any researcher to program an experiment and create the stimuli with no knowledge of either computer programming or electrical

engineering. Currently, this tool is implemented for experiments with the LAURA cochlear implant,¹ and the stimuli can vary within all technical degrees of freedom of this device. However, the concept—and many parts of the system—is portable to any implant system.

II. GENERAL DESCRIPTION

A schematic representation of APEX is shown in Fig. 1. The experiment is controlled by the PC program *Apex.exe*, which runs on the Windows 95 operating system. The input of the program is a simple text file, which contains all parameters specifying the experiment (top left). No specific programming skills are required to define a new experiment. Stimuli are created off-line in MATLAB,² enabling easy and flexible manipulation of all stimulus parameters. Several custom-made MATLAB functions are available for stimulus generation, i.e., functions that convert sampled speech to pulse sequences and functions that generate stimuli specified by the input parameters. At this level, the amplitudes of the current pulses are not yet patient dependent, so the same stimuli can be used for all subjects. The stimuli can be stored in files on hard disk or CD ROM (top right). The PC program loads the required files during the experiment and sends the data to a DSP board (bottom left), together with some subject and implant dependent parameters. The DSP program converts the subject independent amplitudes to current values within the subject's dynamic range. A fast link connects the DSP to a BTE hearing aid of the same type as the one all subjects use. The DSP program also generates the signal containing the code for each current pulse and sends it through the link. The subject can give his response on a graphics tablet, which usually is the number of the stimulus

^{a)}Electronic mail: Luc.Geurts@uz.kuleuven.ac.be

^{b)}Electronic mail: Jan.Wouters@uz.kuleuven.ac.be

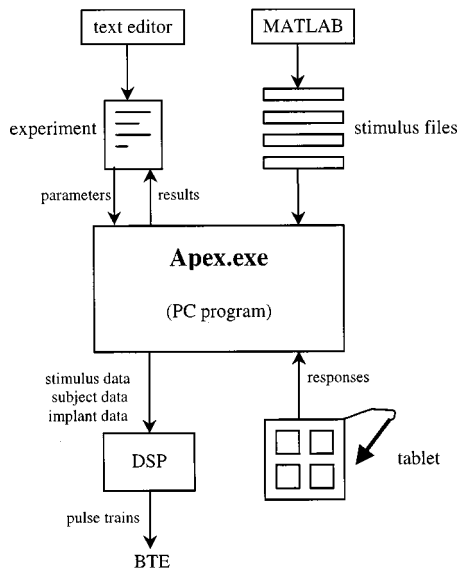


FIG. 1. Schematic representation of APEX. The arrows indicate the direction of the information flow. (DSP: Digital Signal Processor; BTE: Behind The Ear.)

in a series of possible responses or a speech token from a closed set. Alternatively, a mouse can be used. The PC program collects the responses, calculates some statistical values, and appends the results to the input text file.

III. HARDWARE

Three important requisites are imposed on the hardware. First, it may not induce additional limitations on the performance of the internal part of the cochlear implant. Second, the whole setup should be portable, enabling participating subjects to be tested at their homes. Third, to limit the risks to the patient, no galvanic coupling is allowed between computer and implant. Therefore, information about the current pulses to be generated and the power for the internal electronic circuits is preferably transmitted transcutaneously through two inductively coupled coils, as is the case with the LAURA device. The subject should be able to easily remove the external coil, if a stimulus sounds very loud or irritating. Two additional securities of the LAURA device limit the risks even further. First, if there is an error in the code received by the internal processor, no current pulse will be generated. Second, there is a built-in technical limit on the highest current that can be generated of about 1.5 mA.

The current implementation for the LAURA device consists of a laptop computer with 486DX processor, which is inserted in a docking station holding the TMS320C30³ DSP board. The board is connected to the PC via an ISA bus. The DSP processor on this board contains integer and floating-point arithmetic units and parallel and serial interfaces. The processor is capable to perform 16.7 million instructions per second. The board contains 256 kB of RAM memory, of which 64 kB is directly accessible from the PC. Further, the board contains two 16-bit A/D and D/A convertors, two serial ports and a 16-bit wide parallel interface, DSPLINK, of which three pins used for the connection to the cochlear im-

plant. The subject can give his or her response with a pen and a graphics tablet (ACECAT II⁴), which is connected to the PC through the serial port.

IV. SOFTWARE

A. Requisites

The experimenter who creates the stimuli and designs the experiment should not have to be familiar with computer programming. The stimulus editing software should be simple and easy to work with. Another requirement is that all degrees of freedom of the internal part can be exploited.⁵ It is also desirable that all parameters specifying the experiment can easily be set, preferably in a simple text file. The software should be applicable to all patients, so it must take account of possible technical differences between their devices. Also, not all subject dependent stimulus parameters are known in advance, such as the optimal current levels. Mostly, these are determined during a so-called fitting procedure. The software should allow easy and fast manipulation of these subject data. In short, the generated stimuli should be independent of subject parameters, and the software should be able to fit these stimuli to the subject under test.

B. MATLAB functions

The stimuli are either the output of a speech processing algorithm or consist of a pulse sequence of which the stimulation parameters are set by the experimenter. Instead of generating the stimuli in real time on the DSP processor, these are created off-line using custom-made MATLAB functions, which have several benefits compared to DSP programs—programming, debugging, changing, and extending MATLAB code is easier, the user interface is more flexible, the output can be verified easily and several toolboxes are available containing useful functions, such as the Signal Processing Toolbox. The MATLAB functions are either speech processing algorithms, converting an array of speech samples at the input into a pulse sequence, or synthesizers of more elementary stimuli as specified by the input parameters. Although each pulse within a stimulus can be applied on any stimulation channel with any amplitude, there is generally a logic structure in such a stimulus. So, a limited set of simple functions is sufficient for most desired stimuli. The currently created functions always operate on one channel and enable the following: generation of a regular pulse train (i.e., amplitude and inter-pulse interval are constant throughout the stimulus), modulation of this pulse train with some function (e.g., a sine wave), application of some gating function at the onset and the off-set, deletion of the pulse train on a particular channel, and creation of a plot that displays the stimulus on a time scale for each channel. For multiple-channel stimuli, the functions are applied on each channel, and, if applicable, delays between the pulse trains or the modulating functions can be set. Stimuli can also easily be concatenated in MATLAB. At this level, the electrode channels and the amplitudes are not patient dependent. During the experiment, each channel is mapped to one of the implant channels and the value of the amplitude will be mapped within the subject's

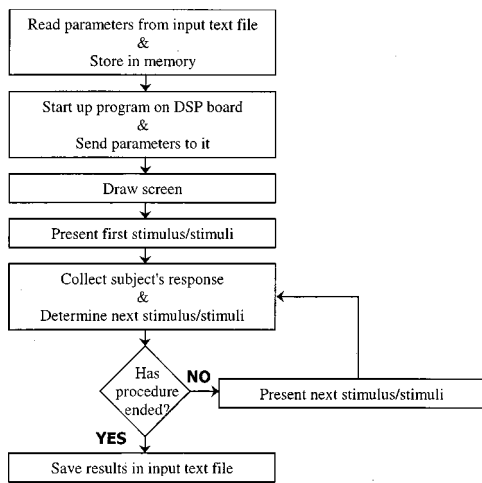


FIG. 2. General flow-chart of the classes implemented in APEX. Each class corresponds to a specific psychophysical method.

dynamic range on that channel in real time. After editing, the stimulus is verified and compressed before it is saved in a file. In the verification step, it is checked that there are no impossible stimulation patterns (e.g., simultaneous pulses for a device that does not permit this). In the compression step, the stimulus is transformed to another format in order to utilize as few bits as possible.

In the case of the LAURA implementation, stimuli are defined in a matrix with twice as many columns as there are channels, and as many rows as ten times the length of the stimulus in milliseconds. Every row corresponds to a 100 μ s interval and contains the pulses that will be applied during that interval. The amplitudes are specified in the first half of the columns, the modes in the second half. Every column in each half corresponds to one channel. The value of the mode specifies the length of the biphasic pulse (40 or 100 μ s/phase) and its polarity (apical or basal electrode cathodic first). An example illustrating how a stimulus is generated in MATLAB is given in Appendix A.

In addition, there are a few more MATLAB functions that are part of the APEX system, but that are not intended to generate stimuli. In some experiments, stimuli are presented in a random order, e.g., in word or phoneme identification experiments or when the method of constant stimuli is used. Several functions are available for the generation of a random list of numbers appropriate for the experiment. There is also one function that calculates the information transfer from a confusion matrix, as suggested by Miller and Nicely (1955).

C. PC program

The PC program is the core of the APEX system and controls every action during the running of the experiment. It is written in Visual C++ (Microsoft Developer Studio 4.0), and the object oriented design contains several classes corresponding to different psychophysical methods. The program recognizes the class by the extension of the input text file, and reads all the parameters specifying the experiment. In general, a series of stimuli is presented to the subject under test, who has to make a judgement about these stimuli.

TABLE I. Overview of the methods of the experiments, implemented in Apex.exe.

Class name	Task	Example of application
CIidentify	Identify a phoneme, word or sentence	Closed set identification
CDiscriminate	Indicate whether two stimuli are the "same" or "different"	Pitch discrimination
CBalance	Balance two stimuli in loudness	Typically used prior to a discrimination task
CAdjust	Find the best match to a given stimulus from a list of stimuli	Pitch matching
CAadaptive	Identify the "signal" from a list of stimuli	Exploration of the limit of performance in a discrimination task
CConstantStimuli	Identify the "signal" from a list of stimuli	Measurement of a psychometric curve
CTriade	Give the most similar or the most dissimilar pair out of three stimuli	Exploration of the perceptual most important features of different stimuli
CThreshold	Indicate the interval where the stimulus was presented	Determination of the threshold of hearing
CCount	Count the number of presented stimuli	Determination of the threshold of hearing

S/he gives a response using the graphics tablet or the mouse. The program collects and summarizes all the responses, and in some cases calculates one or more statistical measures (e.g., average scores, confusion matrices, ...). The results are appended to the input text file, so that both the conditions and the results of the experiment are always stored in one file. A general flow-chart for the classes implemented in the PC program is given in Fig. 2. The classes mainly differ in the kind of variables needed from the experimenter, the kind of questions asked to the subject under test, and the way in which the next stimulus is determined. Table I gives an overview of all the experiments that are currently implemented and an example of a typical application. More details about these experiments are given in Appendix B. Two example input text files are given in Appendix C.

D. DSP program

The DSP program receives three types of data from the PC program: subject data, stimulus data, and implant data. The latter are read from a short text file containing some information about the code that drives the subject's implant and are sent each time the PC program starts executing. Subject and stimulus data are sent to the DSP for each stimulus to be presented to the subject. The task of the DSP program is to combine and convert all of these data to a code which specifies each electrical pulse of the stimulus.⁶ This code signal is sent to the BTE where a high frequency carrier is amplitude modulated with this signal. The modulated signal is applied to the external coil, received through inductive coupling by the internal coil, and demodulated and decoded by the internal circuitry, where a current source generates the pulse to be applied on the electrodes.

In the implementation for the LAURA device, the stimulus data are stored in files, in which each 16 bit word contains the information for a single pulse (channel, mode, and amplitude). The PC program sends the data in this format to the DSP. At this level, the channel and the current amplitude of each pulse do not yet depend on the subject, so the DSP program must still adjust the stimulus to the subject. For each channel of each stimulus, the actual channel to be stimulated and the two subject dependent current levels for the mapping must be defined in the input files of the PC program. Two points specify the linear mapping function, i.e., the currents that correspond to MATLAB value “0.0” and to MATLAB value “100.0.” These currents are determined in a subjective manner, mostly at the start of a test session. In general, they correspond to the subject’s threshold and most comfortable level. However, the experimenter is free to interpret both values in any way. The last step is to convert the three parameters, mode, channel, and current, to three timings which characterize the pulse code signal that is transmitted to the implant. This pulse train is generated with the C30 processor’s FLAGOUT bit, which is connected to the DSPLINK. This bit can be set high or low at processor speed, i.e., every 60 ns its value can be changed. Refreshment is not needed: the bit holds its value after it is set or cleared. Also the ground (GND) and the +5 V supply voltage (VCC) are connected to the BTE, to provide the necessary power.

V. CONCLUSIONS

The APEX system is developed to easily design and conduct experiments with cochlear implantees: various existing methods for classical psychophysical tests and various speech tests to investigate new speech processing algorithms are implemented. Stimuli are created off-line using MATLAB functions, the procedures of the experiments are programmed off-line in simple text files. The PC program controls the experiments, while the DSP board serves as the interface to the implant. Expansion of the system is also relatively easy: new MATLAB functions can be created to generate stimuli, and new classes can be implemented in the PC program to conduct an experiment according to some new method. Also, the system allows acoustical stimuli to be presented through a sound card. Many experiments have already been conducted with APEX. The concept and the implementation has been very suitable for all the experiments that were designed for several studies. The description of the experimental methods can be found in the corresponding articles (Geurts and Wouters, 1999, 2000; Carlyon, Geurts, and Wouters, 2000; van Wieringen and Wouters, 1999a,b). Readers interested in obtaining APEX are advised to contact the authors.

ACKNOWLEDGMENTS

We would like to thank Philips Hearing Implants, currently Cochlear Technology Center Europe, and Stefaan Peeters of the University of Antwerp for providing the necessary details to drive the LAURA implant. This study was partly supported by the Fund for Scientific Research—Flanders (Belgium).

APPENDIX A: EXAMPLE OF STIMULUS EDITING WITH THE CUSTOM-MADE MATLAB FUNCTIONS

The first step in the synthesis of a new stimulus is to create an empty matrix with twice as many columns as there are channels, and as many rows as ten times the length of the stimulus in ms. The following command generates the matrix for a 100 ms long stimulus, containing pulses on two channels:

```
x = zeros (100*10,2*2).
```

The second step is to generate a pulse train on one or more channels. Amplitude, channel, mode, inter-pulse interval (in ms), and time instance of the first pulse (in ms) can be specified with the function *train.m*. The first command below creates a pulse train on channel 1, inter-pulse interval is 0.8 ms, amplitude is 100, mode is 1 (40 μ s/phase, apical electrode cathodic first), and the first pulse starts at 0 ms. The second command creates an identical pulse train on channel 2, starting with a delay of 0.4 ms:

```
x = train (x,1,0.8,100,1,0);
```

```
x = train (x,2,0.8,100,1,0.4).
```

The pulse trains are amplitude modulated with the following commands. First, a sinusoidal amplitude modulation is applied with a modulation frequency of 100 Hz (period=10 ms) and a modulation depth of 50%. The sine wave starts at 0 deg at time instant 0 ms on channel 1, and at time instant 5 ms on channel 2. The third command applies a window with linear ramps having a rise/fall time of 20 ms:

```
x = samtrain (x,1,10,0.5,0);
```

```
x = samtrain (x,2,10,0.5,5);
```

```
x = gate (x,20).
```

Finally, after compressing and saving stimulus *x*, the following output is given, meaning that there are 125 pulses in each channel (length is 100 ms and inter-pulse interval is 0.8 ms), and that no pulses overlap in time:

```
col =
125  0
  0 125
```

APPENDIX B: DETAILS OF PSYCHOPHYSICAL METHODS

CIIdentify (*.idn): This class is generally used for closed-set word identification tasks, e.g., consonants in vowel context or numbers. A randomized series of stimuli from a limited list will be presented to the subject under test. Next, the subject points with the pen to the word on the tablet that he has heard. The program constructs a confusion matrix and appends it to the input file. Each entry of such a matrix indicates the number of times a particular stimulus (row) evoked a particular response (column).

CDiscriminate (*.dsc): In a discrimination task, the subject undergoing the test is presented with either two dif-

ferent stimuli or two identical stimuli. These stimuli can either be speech tokens or more elementary stimuli for psychophysical research. The subject must indicate if the two stimuli were the same or different. The program output is a list of all presented stimuli pairs with the number of times each of the two possible responses was given.

CBalance (*.bln): In psychophysical research, it is often necessary to balance a set of stimuli in loudness. This is to prevent the loudness of a specific stimulus from being used as a cue to distinguish it from others. In a balancing task two stimuli are presented from which one has to be adjusted by the subject so that it sounds equally loud as the other stimulus. The parameter which is varied is the amplitude of the current pulses presented at the electrode array. The final amplitudes for each balanced pair are appended to the input file.

CAdjust (*.adj): An adjustment task is comparable with a balancing task, the difference being that not the amplitude, but some other parameter is varied. The criterion which must be equalized is not restricted to loudness only, but can be any other cue, such as pitch or timbre. The input file contains a list of stimuli in which one or more parameters are varied, e.g., the pulse rate. A stimulus from this list and a fixed reference stimulus, which can have a totally different configuration, is presented. The subject can “move” through the list and has to indicate which stimulus resembles the reference stimulus the most, following a given criterion. The output consists of the file-name of the chosen stimulus.

CAdaptive (*.adp): An adaptive procedure is often used for a discrimination task: the subject is presented with a series of stimuli consisting of one so-called “signal” and one or more “standards.” The signal differs from the standard stimuli in one or more parameters. This results in a cue that the subject can use to differentiate between two or more stimuli. At the start of an adaptive procedure, the value of the parameter is made large resulting in a salient difference between the stimuli. The following presentation is determined by an X-down Y-up procedure (Levitt, 1971): the difference is made larger after X incorrect responses, while Y correct responses will make it smaller again. A *reversal* occurs when X or more incorrect responses are followed by Y correct responses, or vice versa. The values of X and Y may be chosen by the experimenter. The procedure stops after a predefined number of reversals. The program output is the followed sequence of the parameter values, the number of presentations and correct responses for each value and the mean of the values at the last *n* reversals, with *n* a number chosen by the experimenter.

CConstantStimuli (*.cst): The method of constant stimuli is also typically used for a discrimination task. The difference with an adaptive procedure is that the parameter value of the next presentation does not depend on the subject’s response: a fixed number of presentations of a limited set of stimuli with different parameters will be presented in a random order. The output of the program leads to a psychometric curve, which represents the number or the percentage of correct responses for each parameter value.

CTriade (*.trd): In a triade experiment, the subject can listen to three distinct stimuli at once by simply clicking the

corresponding box on the screen or the graphics tablet. The task is to indicate which two of those three stimuli sounds the most similar and which two consists of the most unlike stimuli. The program output is a list of all possible stimuli pairs and the number of times they were chosen to be the most similar and/or dissimilar pair.

CThreshold (*.thr): This class provides one way to determine the threshold of hearing. Two to four boxes appear on the screen, which will light up consecutively for several hundreds of ms, according to the length of the used stimulus. Only during one interval will the stimulus be presented, and the task for the subject is to indicate this interval. The amplitude of the stimulus is adaptively varied using an X-down Y-up procedure. The initial amplitude and the stepsize are set by the experimenter. The program output is a list of the amplitudes at the reversals and the mean amplitude at the last predefined number of reversals.

CCount (*.cnt): Another way to determine the threshold is the counted threshold estimate (Skinner *et al.*, 1995). The stimulus is presented a random number of times, and the subject has to count the stimuli. The minimum and maximum number can be set by the experimenter, but are limited to two and five, respectively. The amplitude is also adaptively varied using an X-down Y-up procedure. The program output is a list of the amplitudes at the reversals and the mean amplitude at the last *n* reversals.

APPENDIX C: TWO EXAMPLES OF INPUT TEXT FILES

Each of the next two sections contains an example of an input file and the corresponding output. The first is for an identification experiment; the second for a discrimination experiment with adaptive procedure. The purpose is to illustrate the use of the software, and not to describe its full capabilities.

1. Example.idn: An identification experiment

The following experiment is a closed set stop consonant identification task, as used for the evaluation of a speech processing algorithm. The stimulus set consists of six stop consonants, /p/, /t/, /k/, /b/, /d/, /g/, in intervocalic /a/ context (apa, ata,...) of two male speakers. Each token will be presented twice to the subject under test in random order. The input file contains four sections. The first section specifies the size, position, and text content of the six rectangles which will appear on the screen and/or on the graphics tablet. The text corresponds to the words presented during the experiment. The second section consists of the list of 12 stimulus files. First, the directory containing the stimulus files is specified. The second line includes the mapping data, which are valid for all stimuli. Then, for each stimulus the file name, the number of the corresponding rectangle, and a condition number corresponding to the speaker are given. A confusion matrix will be constructed for all stimuli having the same condition number. The last line includes the file name of the DSP program, which will be downloaded to the DSP and executed when the experiment starts. The first pa-

parameter of the third section is a list of numbers, which specifies the order of presentation of the stimuli. The subsequent parameter indicates the number of initial stimulus/response pairs that will not be included in the confusion matrices. The last section contains some additional parameters for the experiment: the pause in ms between the subject's response and the presentation of the next stimulus, the feedback parameter, and the training parameter. In the case feedback is wanted, the correct answer will be shortly highlighted after the subject's response. Training means that the experiment is inverted: the subject first points to a word and subsequently is presented with the corresponding stimulus:

```
[screen]
box=5,5,45,30,apa
box=55,70,95,95,ata
box=55,5,95,30,aka
box=5,35,45,60,aba
box=55,35,95,60,ada
box=5,70,45,95,aga
font=28,Times
```

```
[input]
path=c:\tippex\stimuluspattens\nonsens\cis\8ch\
mapping=1,1,10,1470,2,2,30,1470,3,3,140,630,4,4,90,68
0,5,5,80,910,6,6,220,640,7,7,430,1470,8,8,430,840
file=jwapa.stm
box=1
condition=1
file=jwata.stm
box=2
condition=1
file=jwaka.stm
box=3
condition=1
file=jwaba.stm
box=4
condition=1
file=jwada.stm
box=5
condition=1
file=jwakda.stm
box=6
condition=1
file=mdapa.stm
box=1
condition=2
file=mdata.stm
box=2
condition=2
file=mdaka.stm
box=3
condition=2
file=mdaba.stm
box=4
condition=2
file=mdada.stm
box=5
condition=2
file=mdakda.stm
```

```
box=6
condition=2
c30=c:\tippex\30electr.out
```

```
[randomlist]
list=12,5,7,12,5,1,5,11,9,8,3,7,7,4,4,2,6,9,10,12,11,6,8,2,1,3,10
skip=3
```

```
[procedure]
feedback=no
pause=1000
practice=no
```

Each time an experiment is completed, the results are appended to the input file. The first line specifies day and time of the completion of the experiment. The following section contains the two confusion matrices, one for each speaker. For example, the first row of the first matrix shows that the word /apa/ was once identified correctly, and once as /ata/. The last section contains all stimulus response pairs, in the order of presentation.

The following results were collected on Wed 22Apr98 at 15:10

[confusion matrices]

```
condition 1
apa  ata  aka  aba  ada  aga
1    1    0    0    0    0
0    0    2    0    0    0
0    0    2    0    0    0
0    0    0    1    1    0
0    0    0    1    1    0
0    0    0    2    0    2
```

```
condition 2
apa  ata  aka  aba  ada  aga
0    2    0    0    0    0
0    2    0    0    0    0
1    0    1    0    0    0
0    0    0    1    1    0
0    0    0    0    2    0
0    0    0    0    0    2
```

[stimulus/response pairs]

```
aga2/aga, ada1/aba, apa2/ata, aga2/aga, ada1/aba,...
apa1/apa, ada1/ada, ada2/ada, aka2/apa, ata2/ata,...
aka1/aka, apa2/ata, apa2/ata, aba1/aba, aba1/ada,...
ata1/aka, aga1/aba, aka2/aka, aba2/ada, aga2/aga,...
ada2/ada, aga1/aba, ata2/ata, ata1/aka, apa1/ata,...
aka1/aka, aba2/aba
```

2. A discrimination experiment with adaptive procedure

The following experiment is a so-called two interval—two alternative forced choice task (2I2AFC). The subject is presented with two stimuli, a *standard* and a *signal*, in random order, and has to point to the *signal*. As long as the subject correctly identifies the *signal*, the difference between both stimuli is made smaller. The difference arises from

some parameter characterizing the stimuli, in this case the delay in ms between two concurrent pulse trains on two different channels. The first section contains a list of *signal* or *variable* files, in which the parameter changes in discrete steps from file to file. The order of the files is such that discrimination varies from difficult to easy. For each stimulus, the file name, the mapping vector, and a value are given. This is typically the value of the varying parameter. The second section contains the file name and the mapping data of the *standard* or *reference* stimulus. Details of the *method* or *procedure* of the experiment are given in the last section. The first line indicates that a 2I2AFC task will be used, with a silent interval of 500 ms between the stimuli. The first *signal* is the ninth file in the list (line 2). A 2-down 1-up procedure is used (line 3 and 4). At the start, the stepsize is 2 *signal* files; after four reversals it is 1 *signal* file (line 5). The experiment ends after 12 reversals (line 6), correct response feedback will be given (line 7), and the mean value of the parameter values at the last 8 reversal points will be calculated (line 8). The next presentation of stimuli starts 1500 ms after the subject's response (line 9), and there is no training (line 10). Training means in this case that the correct answer will be displayed on the screen before and during the presentation of the stimuli.

```
[varlist]
file=C:\Tippex\StimulusPatterns\Bob1Per100\del32.stm
mapping=1,2,400,600,2,7,450,723
value=3.2
file=C:\Tippex\StimulusPatterns\Bob1Per100\del34.stm
mapping=1,2,400,600,2,7,450,723
value=3.4
file=C:\Tippex\StimulusPatterns\Bob1Per100\del36.stm
mapping=1,2,400,600,2,7,450,723
value=3.6
file=C:\Tippex\StimulusPatterns\Bob1Per100\del38.stm
mapping=1,2,400,600,2,7,450,723
value=3.8
file=C:\Tippex\StimulusPatterns\Bob1Per100\del40.stm
mapping=1,2,400,600,2,7,450,723
value=4.0
file=C:\Tippex\StimulusPatterns\Bob1Per100\del42.stm
mapping=1,2,400,600,2,7,450,723
value=4.2
file=C:\Tippex\StimulusPatterns\Bob1Per100\del44.stm
mapping=1,2,400,600,2,7,450,723
value=4.4
file=C:\Tippex\StimulusPatterns\Bob1Per100\del46.stm
mapping=1,2,400,600,2,7,450,723
value=4.6
file=C:\Tippex\StimulusPatterns\Bob1Per100\del48.stm
mapping=1,2,400,600,2,7,450,723
value=4.8
file=C:\Tippex\StimulusPatterns\Bob1Per100\del50.stm
mapping=1,2,400,600,2,7,450,723
value=5.0
```

```
[reflist]
file=C:\Tippex\StimulusPatterns\Bob1Per100\del11.stm
mapping=1,2,400,600,2,7,450,723
```

```
[procedure]
sequence=afc,500,afc,-1
start=9
up=2
down=1
stepsize=2/0,1/4
stop=12
feedback=yes
numrevsformean=8
pause=1500
practice=no
```

The output of the program contains for each *visited* signal file the parameter value, the number of correct responses, and the number of presentations, in that order. Also, the sequence of the parameter values of the visited signal files is given, and finally the mean value of the parameters at the last eight reversal points.

The following results were collected on Wed 04Jun97 at 14:47

```
Score for value 3.4: 1/3
Score for value 3.6: 6/8
Score for value 3.8: 7/11
Score for value 4: 4/5
Score for value 4.2: 7/8
Score for value 4.4: 3/4
Score for value 4.6: 2/2
Sequence= 3.8,4.2,3.8,4.2,3.8,4.4,2,4.4,4.6,4.4,4.2,...
4,3.8,4,3.8,3.6,3.4,3.6,3.4,3.6,3.8,3.6
mean= 3.775
```

¹LAURA is a registered trademark of Philips Hearing Implants.

²MATLAB is a registered trademark of The Mathworks, Inc. (<http://www.mathworks.com>).

³The TMS320C30 DSP board is a product of Blue Wave Systems, Inc. (<http://www.bluews.com>).

⁴The ACECAT II graphics tablet is a product of Acecad, Inc. (<http://www.acecad.com>).

⁵In the case of the LAURA device, this means that every 100 μ s a biphasic current pulse with any amplitude and any polarity can be delivered on any stimulation channel. The LAURA electrode array holds eight channels, each consisting of two bipolarly coupled electrodes (see Fig. 1 in van Wieringen and Wouters, 1999b).

⁶With current, more powerful PC's, it should be easy to include these calculations in the PC program. The only function of DSP is then to provide a link between the PC and the implant through which the code may be sent.

Carlyon, R. P., Geurts, L., and Wouters, J. (2000). "Detection of small across-channel timing differences by cochlear implantees," *Hear. Res.* **141**, 140–154.

Geurts, L., and Wouters, J. (1999). "Enhancing the speech envelope of CIS processors for cochlear implants," *J. Acoust. Soc. Am.* **105**, 2476–2484.

Geurts, L., and Wouters, J. (2000). "Coding of the fundamental frequency in continuous interleaved sampling processors for cochlear implants," *J. Acoust. Soc. Am.* (Submitted).

Levitt, H. (1971). "Transformed up-down methods in psychoacoustics," *J. Acoust. Soc. Am.* **49**, 467–477.

Miller, G. A., and Nicely, P. E. (1955). "An analysis of perceptual confusions among some English consonants," *J. Acoust. Soc. Am.* **27**, 338–352.

Skinner, M. W., Holden, L. K., Holden, T. A., and Demorest, M. E. (1995). "Comparison of procedures for obtaining thresholds and maximum acceptable loudness levels with the Nucleus cochlear implant system," *J. Speech Hear. Res.* **38**, 677–689.

Stevens, S. S. (1951). "Mathematics, measurement and psychophysics," in *Handbook of Experimental Psychology*, edited by S. S. Stevens (Wiley, New York), pp. 1–49.

van Wieringen, A., and Wouters, J. (1999a). "Natural vowel and consonant

recognition by Laura cochlear implantees," *Ear Hear.* **20**, 89–103.

van Wieringen, A., and Wouters, J. (1999b). "Gap detection in single- and multiple-channel stimuli by Laura cochlear implantees," *J. Acoust. Soc. Am.* **106**, 1925–1939.

Independence of frequency channels in auditory temporal gap detection

Dennis P. Phillips^a) and Susan E. Hall

Hearing Research Laboratory, Department of Psychology, Dalhousie University, Halifax, Nova Scotia B3H 4J1, Canada

(Received 21 March 2000; revised 27 July 2000; accepted 31 August 2000)

The ability of listeners to detect a temporal gap in a 1600-Hz-wide noiseband (target) was studied as a function of the absence and presence of concurrent stimulation by a second 1600-Hz-wide noiseband (distractor) with a nonoverlapping spectrum. Gap detection thresholds for single noisebands centered on 1.0, 2.0, 4.0, and 5.0 kHz were in the range from 4 to 6 ms, and were comparable to those described in previous studies. Gap thresholds for the same target noisebands were only modestly improved by the presence of a synchronously gated gap in a second frequency band. Gap thresholds were unaffected by the presence of a continuous distractor that was either proximate or remote from the target frequency band. Gap thresholds for the target noiseband were elevated if the distractor noiseband also contained a gap which “roved” in time in temporal proximity to the target gap. This effect was most marked in inexperienced listeners. Between-channel gap thresholds, obtained using leading and trailing markers that differed in frequency, were high in all listeners, again consistent with previous findings. The data are discussed in terms of the levels of the auditory perceptual processing stream at which the listener can voluntarily access auditory events in distinct frequency channels. © 2000 Acoustical Society of America. [S0001-4966(00)00412-4]

PACS numbers: 43.66.Ba, 43.66.Mk [DWG]

I. INTRODUCTION

Gap detection is one measure of auditory temporal acuity. The listener is usually presented with two streams of sound, one of which has a brief silent period (“gap”) at its temporal midpoint. The task of the listener is to identify this signal, and some form of adaptive tracking procedure (after Levitt, 1971) is used to determine the shortest detectable gap (“gap threshold”). At least three different stimulus paradigms have been used to study the mechanisms mediating gap detection performance. Historically, the acoustic markers delimiting the gap have been spectrally identical, and so the temporal task is, in practice, the detection of a discontinuity in the activity aroused in the neural representation activated by the stimulus (and/or in the perceptual channel supported by that representation: after Moray, 1969; Johnson, 1980; Phillips *et al.*, 1997; Taylor *et al.*, 1999). The “within-channel” nature of this paradigm has permitted exploration of the temporal acuity supported in different frequency regions, and for signals of different bandwidth (e.g., Eddins *et al.*, 1992; Moore *et al.*, 1993). Depending on signal bandwidth, gap thresholds in this paradigm can be as short as a few milliseconds (e.g., Plomp, 1964; Penner, 1977; Eddins *et al.*, 1992), and the threshold is usually insensitive to the temporal location of the gap in the signal stimulus, at least in highly experienced listeners (Forrest and Green, 1987; Phillips *et al.*, 1997, 1998; Snell and Hu, 1999).

A second paradigm, which has been termed “between-channel” gap detection, requires the listener to detect a gap bounded by markers that are different in frequency content,

ear stimulated (Phillips *et al.*, 1997; Formby *et al.*, 1998a, b; Taylor *et al.*, 1999), or location in free-field space (Phillips *et al.*, 1998; Boehnke and Phillips, 1999). Gap thresholds are longer in this paradigm (Phillips *et al.*, 1997, 1998; Formby *et al.*, 1998a, b; see also Grose *et al.*, 1999), and they increase as the leading marker is shortened (Phillips *et al.*, 1997, 1998). The higher gap thresholds in the between-channel paradigm presumably reflect the poorer central representational overlap of the markers delimiting the gap (see Formby *et al.*, 1998b; Taylor *et al.*, 1999; Boehnke and Phillips, 1999). That is, each marker has its own “representation” in a spatiotemporal pattern of activity in the central auditory system; between-channel gap thresholds approach within-channel values when the markers become sufficiently similar and coactivate neural representations whose responses can be input to a discontinuity detection process. In the absence of such representational overlap, gap detection relies entirely on the relative timing of activity in the two channels, and gap thresholds remain asymptotically high (Phillips *et al.*, 1997; Formby *et al.*, 1998a; Boehnke and Phillips, 1999).

Finally, there is considerable interest in “across-channel” gap detection. In this paradigm, identical markers bound the silent period, but the markers themselves are composed of more than one spectral element (e.g., Grose, 1991; Grose and Hall, 1988; Hall *et al.*, 1996). Using any single narrow-band stimulus, gap detection thresholds are high (Eddins *et al.*, 1992). If listeners are presented with gaps bounded by multiple narrow-band markers, and if the cumulative marker bandwidth is kept narrow, then gap thresholds improve when the spectral energy is presented in multiple frequency channels (Grose, 1991). Using relatively widely

^aElectronic mail: ears@is.dal.ca

spaced pairs of 20-Hz-wide noise markers, Hall *et al.* (1996) showed that gap thresholds were better for pairs of noisebands than for single noisebands, and that the benefit was independent of the spectral separation of the bands. One important point to emerge from this line of research is that the auditory system appears in some way to integrate spectral information across very wide frequency ranges in order to detect the temporal event. Viemeister (1979) has discussed the recovery of temporal information from wideband analyses of more periodic temporal events. His account suggests that whatever the nature of the integration mechanism, the inputs to it must preserve information about the temporal event in a frequency-specific fashion.

The existence of a, presumably central, mechanism executing a spectral integration for gap detection raises a question regarding the extent to which the listener is able to access information in the frequency-specific representational or processing channels. Grose and Hall (1993) addressed this question using narrow (25-Hz-wide) noiseband stimuli centered on 1.0 and 1.5 kHz. They showed that the ability to detect a gap in the 1.0-kHz band was impoverished by energy in the flanking band, particularly if the flanking band was comodulated or synchronously gated with the target. This suggests that the listener's ability to detect a temporal event in one frequency channel can be degraded by concurrent activity in another channel.

The general purpose of the present study was to re-examine this general question, but using stimuli with broader bandwidths. There are at least two reasons for suspecting that the stimuli used by Grose and Hall (1993) represent a limiting case. First, to reduce spectral splatter, the exceptionally narrow bandwidths of their stimuli required very slow gating (10 ms) and presentation of the stimuli against a background notched-noise masker. In turn, even under the most optimal stimulus conditions, gap thresholds were in the range from 30 to 50 ms, which is an order of magnitude greater than that seen with wider-band stimuli. Thus, without disputing Grose and Hall's (1993) findings, we sought to study the effect on gap detection performance within one frequency sector of the presence of energy in a second band, but using stimuli with bandwidths great enough to elicit within-channel gap thresholds in the ms range. Second, Grose and Hall (1993) attributed the interference effect of the flanking noiseband to modulation detection interference (MDI, after Yost and Sheft, 1989; but see also Moore and Jorasz, 1992), because the interference was present when the flanking stimulus was a gated tone, but not a continuous tone. MDI is presumably most likely to occur with sounds which have low-frequency envelope amplitude fluctuations. Again, without disputing the earlier findings, these data suggest that the interference effects seen with very narrow-band stimuli might not generalize to more wideband sounds.

This general issue takes on further significance when one considers that many of the foregoing experiments have recently been performed in listeners with cochlear implants (e.g., Chatterjee *et al.*, 1998; Hanekom and Shannon, 1998; Van Wieringen and Wouters, 1999). Thus, within-(stimulating)-channel gap thresholds are in the ms range when the markers are electrically identical, but are elevated

if the markers are applied to different stimulating channels, or if the markers delivered to one channel are different (e.g., if the electrical marker signals differ in pulse rate). Insofar as the present question is concerned, Van Wieringen and Wouters (1999) reported that the presence of a continuous masker in one channel was inconsequential to gap thresholds for markers delivered to a second channel.

We are thus left with a complex picture. First, studies using very narrow bandwidth noises in normal listeners suggest that gap detection performance for one noiseband can be *degraded* by a flanking band, though this might be a result of the noises containing temporal components that interfere with detection of the gap (Grose and Hall, 1993). Second, gap thresholds for narrow-band noises can be *improved* if bands containing a synchronous gap are dispersed across frequency channels (Grose, 1991; Hall *et al.*, 1996). Third, studies in cochlear implant patients, in whom the meaning of "bandwidth" is less clear, suggest that gap detection through one (stimulating) channel is *unaffected* by the presence of activity in a second channel. This state of affairs prompted us to examine the conditions under which the normal listener has unfettered access to within-channel processing in the presence of concurrent activity in another channel. Preliminary data have been presented in abstract form (Phillips and Hall, 2000).

II. METHOD

A. Subjects

The present report is based on data from seven (five female) listeners, ages 21–44 years. Six of the listeners had no history of otologic disease, and had absolute sensitivities within laboratory norms. Four of these listeners (two male) had extensive prior experience in other gap detection studies using wider-band stimuli ("experienced listeners"). Two of these six listeners (both female) had never previously participated in auditory perception experiments ("inexperienced listeners"). A seventh listener, also inexperienced, completed the study. We detected a >20-dB hearing loss for frequencies above 2 kHz in this listener. Her data have been included because they were indistinguishable from those of the other two inexperienced listeners.

B. Gap stimuli and apparatus

All noise stimuli were generated digitally on a custom-programmed Macintosh G3 computer. The bandpass stimuli had nominal bandwidths of 1600 Hz, and they were centered on frequencies of 1.0, 2.0, 4.0, and 5.0 kHz. The roll-off slopes were nominally specified as 70 dB/90 Hz. The standard and signal stimuli each had total durations of 400 ms. Gaps were inserted destructively into the signal (and, where appropriate, the standard) stimuli at their temporal midpoints, unless otherwise specified. The rise–fall times were 2.0 ms in duration, and were raised cosine in shape. Gap duration was specified as the duration of the silent period plus the fall time (i.e., the "equivalent rectangular" period of silence, in ms). To address problems attendant to the use of "frozen" noise (i.e., the same sample of noise in all trials), each standard and signal stimulus (or component

thereof, see below) was drawn pseudorandomly from four different bandpass noise samples. The generated stimuli were saved as “resource files” by SOUNDEDIT™ software on a Power Macintosh 8600 computer. The experiment was then programed in HYPERCARD™, which called up the resource files as needed.

Stimuli were transduced by Koss TD/64 headphones. Stimulation was monaural, to the listener’s preferred ear (right, in five of the seven listeners). Absolute stimulus levels were in the range from 70 to 75 dB SPL (sound-pressure level: dB *re* 20 μ Pa, A-weighted; Bruel & Kjaer Instruments) for single noiseband stimuli; by design, these levels roughly equated the noisebands for subjective loudness. Levels were close to 3 dB greater (up to 78 dB SPL) for stimuli containing two noisebands. Across the seven listeners, these stimulus levels were in the range from about 45 to 55 dB above detection threshold, i.e., about 45 to 55-dB sensation level.

C. Design and procedure

All listeners were tested individually. There were 14 stimulus conditions (see below) and a minimum of three gap thresholds was measured for each. Each gap threshold was determined in a single block of trials. Each trial presented the listener with a standard and a signal, separated in time by 1.25 s, in a random order. The task of the listener was to indicate by mouseclick which stimulus was the signal (i.e., a two-interval, two-alternative, forced choice). A two-down/one-up adaptive tracking procedure (after Levitt, 1971), with a step factor of 1.2, was used to determine the gap threshold. Starting gap durations were in the range from 15–53 ms (depending on task difficulty). The block of trials was terminated after ten reversals in the direction of change of the adaptive step, and the gap threshold was defined as the mean gap duration associated with the last six reversals. Listeners were tested on each stimulus condition until their thresholds stabilized (3–8 thresholds). A listener’s final gap threshold for any specified stimulus condition was defined as the mean of those obtained in the last three blocks for that condition. Trials were self-paced, and no feedback was provided.

The 14 stimulus conditions fell into five groups. The first four stimulus conditions tested listeners for temporal gap detection thresholds for each of the noisebands separately [Fig. 1(A)]. There was no gap in the standard stimulus. Thresholds for these simple, within-channel conditions served (a) to confirm that the stimulus bandwidths were sufficient to produce gap thresholds in the ms range, and (b) to serve as benchmarks against which to measure the effects of concurrent stimuli at different frequencies.

The next set of two stimulus conditions each contained two stimulus noisebands: either the conjunction of the 2.0- and 4.0-kHz noises, or the conjunction of the 1.0- and 5.0-kHz noises [Fig. 1(B)]. Both components of the signal contained the target gap, and the adaptive step in the threshold tracking procedure was applied to both components. The standard stimulus did not contain a gap in either frequency component. The task of the listener was to specify which of the noiseband pairs was the signal. These two conditions explored whether (a) a perceptual benefit would result from

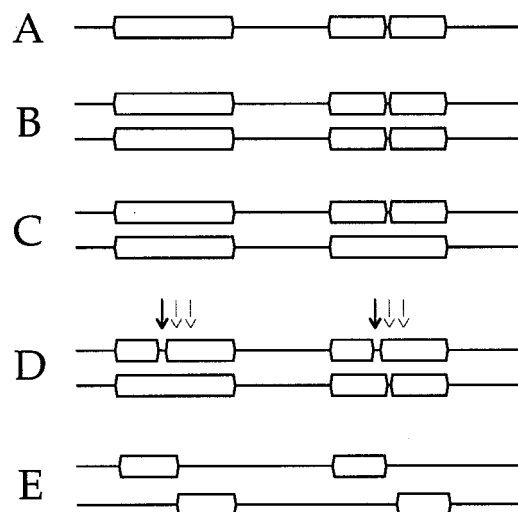


FIG. 1. Schematic depictions of the stimulus configurations used in the present experiments. In (A), the stimulus was a single noiseband shaped into standard and signal elements. In (B), all stimuli contained two noisebands, and the signal stimulus contained a gap in both noisebands. In (C), one noiseband contained the signal, while the distractor noiseband did not. In (D), the target noiseband contained a gap at the temporal midpoint of the signal stimulus. The distractor noiseband contained a 20-ms gap that was initiated roughly 30 ms before, synchronously with, or 30 ms after the gap in the target noiseband [arrows in (D)]. In (E), the leading and trailing markers were different noisebands.

the presence of the temporal event in more than one cochlear sector, and (b) whether that benefit depended on the frequency separation of the noisebands.

A third stimulus set of four conditions was used to determine the effect on within-channel gap thresholds in one cochlear sector of continuous activity in another frequency region [Fig. 1(C)]. In two conditions, the standard and signal each contained the 2.0- and 4.0-kHz noises, but the signal contained the target gap in only one noiseband. In separate blocks of trials, the listener was informed whether it was the 2.0- or 4.0-kHz noiseband that contained the gap. The “distractor” noiseband was, with the exception of the presence of the gap in the signal, simultaneously gated with the noiseband containing the gap. The remaining two conditions were identical to those just described, with the exception that the two noisebands used were centered on 1.0 and 5.0 kHz.

The fourth set of stimulus conditions [Fig. 1(D)] also probed the effects of activity in one cochlear sector on gap detection mediated by another. There were two relevant conditions. In the first, the standard and signal stimuli each contained the 2.0- and 4.0-kHz noises, and the listener was informed that the target gap was in the 4.0-kHz noise. The distractor (2.0 kHz) noiseband also contained a temporal gap, and it did so in both the standard and the signal. Its duration was always 20 ms, and its midpoint occurred at either 170, 200, or 230 ms after the onset of the noise burst. Since the target gap was centered at 200 ms, this meant that the distractor gap’s onset occurred before, in close temporal proximity to, or after the onset of the gap in the signal. The second stimulus condition was identical, except that the noisebands were centered on 1.0- and 5.0 kHz, and the target gap was in the 5.0-kHz component. These stimulus condi-

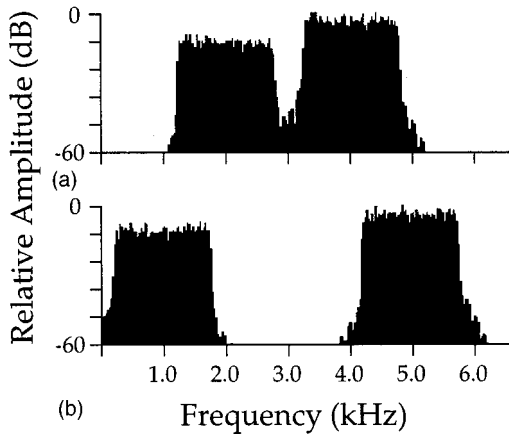


FIG. 2. Sample stimulus spectra of two of the stimulus pairs used. Spectra are of the electrical signals, obtained after all stimulus shaping (including stimulus onset and offset, the insertion of the temporal gap, and equating the amplitudes of the noisebands for equal subjective loudness through the Koss earphones).

tions explored the effect of a temporal event in one frequency channel having an unpredictable temporal relation to the gap in the target channel on the detectability of the gap in the target frequency band. The conditions were repeated for two frequency separations of the target and distractor frequency channels. Note that the distractor frequency band contained a gap in both the signal and the standard stimulus; this ensured that the only difference between the standard and signal stimuli was the presence of a gap in the target channel of the signal, i.e., the gap in the distractor noiseband was noninformative about which noiseband pair was the signal.

The fifth, and final, set of two conditions contained routine, between-channel markers in which gap thresholds were obtained using the same noise bands as above [Fig. 1(E)]. In one condition, the gap was bounded by a 2.0-kHz leading marker and a 4.0-kHz trailing marker. In the other condition, the gap was bounded by 5.0-kHz leading and 1.0-kHz trailing markers. Thresholds obtained in these two conditions served (a) to confirm the acuity difference of within- and between-channel gap thresholds, and (b) to do so for two marker frequency separations.

Listeners were given the option of completing all testing within a single session (about 3 h: one experienced and one naive listener), or of distributing the testing across 2–5 sessions. Listeners were also given the choice of the serial order of conditions tested. The two listeners who completed testing in one session each stabilized their thresholds on one condition before proceeding to the next. All other listeners obtained one or more thresholds on a given condition and then proceeded to the next, and repeated that sequence as necessary on subsequent days until testing was complete. In practice, gap thresholds for the experienced listeners were already stable within the first 3–4 measures. The inexperienced listeners more often required 4 to 6 threshold determinations before the thresholds were judged as stable.

Figure 2 shows two sample stimulus spectra, measured using Blackman windowing. The spectra are of electrical signals generated to study gap thresholds obtained when the two

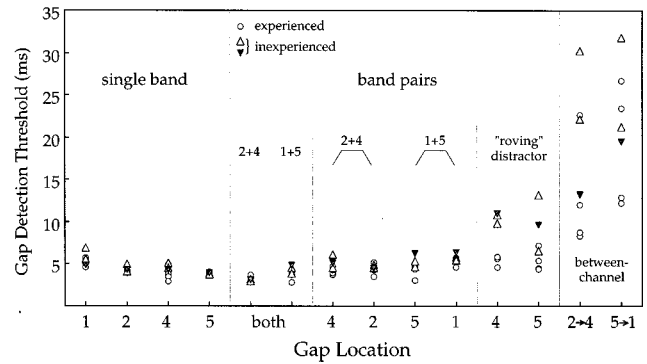


FIG. 3. Mean data for each of the 14 stimulus conditions tested, plotted separately for experienced listeners (open circles) and inexperienced listeners (open triangles). Data for the inexperienced listener with a high-frequency hearing loss are shown as the filled, inverted triangles. All data are the averages from each listener of the last three thresholds obtained for each stimulus condition.

frequency components of the signal were simultaneously gated. The two spectra differ in the identity of the component noise bands. In Fig. 2(a), the noises were centered on 2.0 and 4.0 kHz; in Fig. 2(b), they were centered on 1.0 and 5.0 kHz. Note that the rolloffs of the spectra were very steep, and that the amplitude of any “splatter” associated with the stimulus gating was lower than about 45 dB below that of the pass-band frequencies.

III. RESULTS

Data collected were the means of the last three gap thresholds obtained for each of the 14 stimulus conditions, in each of the seven listeners. Figure 3 shows the mean thresholds of each listener for each stimulus condition. Data are shown separately for the experienced listeners (open circles), the normal-hearing inexperienced listeners (open triangles), and for the inexperienced listener with a high-frequency sensitivity loss (filled, inverted triangles).

The mean gap thresholds for the single noiseband stimuli (stimulus configuration A in Fig. 1) were all in the single-digit range. For both the experienced and inexperienced listeners, there was a small effect of noiseband frequency, with the gap thresholds tending to be highest for the lowest frequency stimuli. Thus, for the experienced listeners, grand mean gap thresholds for the 1.0-, 2.0-, 4.0-, and 5.0-kHz noisebands were 5.2, 4.2, 3.8, and 3.8 ms, respectively, while those for the inexperienced listeners were 5.8, 4.8, 4.7, and 3.8 ms, respectively.

The individual mean gap thresholds for the simultaneously gated noiseband pairs [Fig. 1(B)] were also in the single-digit range, and again for both experienced and inexperienced listeners, were among the lowest thresholds obtained in the study. For the experienced listeners the grand mean thresholds for the 2.0/4.0-kHz and the 1.0/5.0-kHz noiseband pairs were 3.3 and 3.7 ms, respectively, and those for the inexperienced listeners were 3.1 and 4.4 ms, respectively.

Gap thresholds for target-frequency noisebands occurring in the presence of continuous distractors [Fig. 1(C)] were again usually in the low, single-digit range. The gap

thresholds for the two listener groups were almost completely overlapping for each stimulus condition. Moreover, the grand mean gap thresholds (i.e., averaged across all listeners) for each of the four target-frequency bands were very close (within 0.1 to 0.9 ms of) to those obtained for the same frequency bands in the absence of a concurrent stimulus.

Data for conditions in which the distractor frequency band contained a temporally roving, 20-ms gap were more variable. For three of the experienced listeners, gap thresholds for both the 4.0-kHz and the 5.0-kHz target noisebands were unaffected by the presence of the roving distractor. For each of the inexperienced listeners, gap thresholds for both target-frequency bands were elevated to values nonoverlapping with all of the foregoing thresholds. The same was true for one experienced listener for the 5.0-kHz target. This listener's thresholds for this condition were obtained in a single test session, suggesting that the high thresholds were not attributable to a lack of within-session practice effects. Interestingly, all of the listeners described this stimulus condition as the most difficult, despite the fact that some of the listeners ultimately obtained gap thresholds that were comparable to those obtained without a distractor frequency band.

The final stimulus conditions were those with between-channel markers [Fig. 1(E)]. In these conditions, the leading and trailing markers of the temporal gap had nonoverlapping spectra. The two between-channel conditions differed in the frequency separation of the markers and in the direction of frequency change between them. The gap thresholds for every listener were higher for these conditions than for any of the preceding conditions. Six of the seven listeners had higher gap thresholds for the between-channel condition with the larger frequency separation of markers, although the difference was less than 2 ms for one inexperienced listener. The seventh listener had nearly identical thresholds for the two conditions (22.1 and 21.3 ms for the close and distant between-channel markers, respectively).

IV. DISCUSSION

The general purpose of this study was to examine the extent to which listeners have unfettered access to temporal events arising from one cochlear sector in the presence of concurrent activity at another cochlear site. The study was prompted by two lines of previous evidence. One was the demonstration that the auditory system is able to execute some form of spectral integration prior to the recovery of a temporal event (after Viemeister, 1979; Hall *et al.*, 1996). That line of evidence left unaddressed the question posed by the present study; that is, the availability of such a spectral integration process does not directly speak to whether listeners have access to activity within frequency-specific processing channels prior to the integration process, or in some other perceptual module.

The second line of pre-existing evidence came from two studies of across-channel gap detection. In one (Grose and Hall, 1993), it was found that the detection of a temporal gap in one 25-Hz-wide noiseband was compromised by the presence of a flanking 25-Hz-wide band. [Note that this finding is not at all incompatible with those of Hall *et al.* (1996), who showed the perceptual *benefit* of having synchronous gaps in

widely spectrally separated noisebands. This is because the stimuli in Hall *et al.*'s study were designed to be exploited by a spectral-averaging process to recover the gap. In Grose and Hall's (1993) study, the stimuli were specifically designed to test for the presence of *interference* as well as any enhancing effects. In this instance, the interference effect was attributed to MDI, to which very narrow-band noises may be prone because of their low-frequency envelope fluctuations.] Now, in an independent study of cochlear implant patients (Van Wieringen and Wouters, 1999), it was shown that continuous activity in one stimulus channel was inconsequential to gap detection performance through another. The present study sought to readdress this general question, in normal-hearing listeners, but using bandpass noises with bandwidths great enough that gap detection thresholds for either noise were in the ms range, and were not likely affected by the modulation detection interference suspected to affect gap detection in very narrow-band noises (after Grose and Hall, 1993).

The 1600-Hz-wide bandpass noises in the present study (see Fig. 2) each supported gap detection thresholds in the ms range in all listeners. The absolute values of those thresholds were within the range of those described by Eddins *et al.* (1992). This suggests that the stimuli and methodology employed in the present study were uncontroversial, while satisfying the goal of achieving relatively focal stimulation of the cochlea. The absolute gap thresholds obtained are comparable to those seen in cochlear implant patients in cases of single-channel stimulation (Hanekom and Shannon, 1998; Van Wieringen and Wouters, 1999).

When two noisebands contained simultaneously gated gaps, gap detection thresholds for the pair were as low as, or slightly lower than, those seen with single noisebands. This appeared to be independent of the frequency separation of the noisebands. The improvement in gap thresholds in these conditions (albeit exceptionally modest) was consistent with the findings of Hall *et al.* (1996). This small effect likely reflected the fact that the bandwidths and levels of the individual noisebands were already supporting gap thresholds close to minima in duration.

Gap thresholds for a target noiseband, obtained in the presence of concurrent activity in a second noiseband containing no gap, were very similar to those obtained with the target noise band alone (Fig. 3). This finding is concordant with the observations of Van Wieringen and Wouters (1999) in cochlear implant patients. It is also consistent with the finding by Grose and Hall (1993) that gap thresholds in one 25-Hz-wide band were unaffected by the presence of a flanking continuous tone. Viewed from an attentional standpoint (after Scharf *et al.*, 1987; Botte, 1995; Phillips *et al.*, 1997), these findings suggest that the listener can access a temporal event in one cochlear sector in the presence of irrelevant, unmodulated activity in another when the stimulus levels are comparable.

A temporally roving gap in a distractor frequency band elevated gap thresholds for a target noiseband in some listeners, especially the inexperienced ones (Fig. 3). This was found despite the fact that listeners were informed that activity in the distractor frequency band was irrelevant. In the

parlance of the attentional literature (after Posner, 1980), the occurrence of an event in the distractor noiseband (i.e., the temporal gap in the standard or the signal stimulus) might have exerted an exogenous attraction of attentional resources from the target-frequency band. Following Scharf *et al.* (1987) and Phillips *et al.* (1997), this resulted in impoverished judgments about activity in the target-frequency band. The fact that our most experienced listeners were less prone to such interference suggests that the allocation of attentional resources to particular frequency bands can be trained. The intriguing feature of the training effect here was that the “experience” which differentiated the two listener groups was not in the across-frequency tasks that formed the bulk of the present experiments. It was in other gap detection tasks, often using wideband noise. This suggests that one element of a “training effect” is a generalized improvement in performance across similar tasks. In the present study, the inexperienced listeners took more threshold determinations to reach stable performance than did the experienced listeners (see Sec. II). This “within-task” practice did not offset the broader training effect seen in the experienced listeners, at least over the short term of the present study.

Finally, the now-familiar, between-channel gap thresholds of the present listeners were always longer than those seen in any other stimulus condition. The magnitudes of these gap thresholds was consistent with previous demonstrations of the poorer temporal acuity of the between-channel gap detection process (Phillips *et al.*, 1997, 1998; Formby *et al.*, 1998a, b; Chatterjee *et al.*, 1998; Taylor *et al.*, 1999; Grose *et al.*, 1999) and gap discrimination (Fitzgibbons *et al.*, 1974; Divenyi and Danner, 1977).

The next question concerns the reasons for the poor acuity of the between-channel gap detection process. We have previously argued that where the markers bounding a temporal gap have little or no central representational overlap, the detection of the gap must rely on a relative timing of the offset of activity in the perceptual channel activated by the leading marker, and the onset of activity evoked in the channel driven by the trailing marker (Phillips *et al.*, 1997, 1998; Taylor *et al.*, 1999). Following the general arguments of Fitzgibbons *et al.* (1974), it is possible that once attentional resources have been allocated to the channel representing the leading marker, there is a mandatory “dwell time” before an attentional shift can be executed, and that the attentional shift to the perceptual channel representing the trailing marker itself takes time. Such an account would require that the minimal detectable gap have a duration at least equaling the shift time, *plus* any obligatory dwell time not occupied by the leading marker duration; of necessity, this gap duration would be longer than the thresholds seen in within-channel tasks. A less sophisticated account is that the allocation of attentional resources to one channel reduces those available for the time-stamping of events in a second channel (Phillips *et al.*, 1997). This is simply an extension of the account generated by the data of Scharf *et al.* (1987, 1994), i.e., that at sound detection threshold, allocation of attentional resources to one frequency channel raises detection thresholds for tones outside that channel.

Taken together, these observations suggest that it is not

the presence of activity *per se* in a distractor channel that can impoverish gap detection thresholds in a target channel, but rather, it is the occurrence of perceptible auditory *events* in the distractor channel, particularly when they have temporal proximity to the target gap. This is a high-level, “active” description of the listener, i.e., an account built around the voluntary or involuntary allocation of attentional processes to particular channels or events. The kinds of interactions between frequency channels seen in this account are separable from those between frequency channels at lower levels of the perceptual processing stream. Thus, the low gap thresholds seen for broadband sounds (e.g., Eddins *et al.*, 1992), and the improvement in gap detection performance for very narrow-band sounds when the gap is carried by more than one band (Hall *et al.*, 1996) likely does reflect a low-level “integrative” process, at least in the sense that the recovery of a threshold-duration temporal event is statistically more likely if the event is being carried in more than one channel at a time to a central “integrator.” This kind of processing does not reflect attentional allocation across the audible spectrum any more than does the superiority of sound localization for broadband sources over tones. The events carried through the more low-level frequency channels in these cases may be neither individuated nor perceptible. Similarly, some interference effects between channels (e.g., Grose and Hall, 1993, 1996), may well be phenomena occurring prior to the conscious perceptual elaboration of the relevant events.

The foregoing discussion has been heavily predicated on the assumption that central mechanisms significantly contribute to gap detection acuity, perhaps especially in these more complex paradigms (see also Phillips *et al.*, 1997, 1998; Taylor *et al.*, 1999; Boehnke and Phillips, 1999). Such an assumption is supported by the finding of deficits in gap detection performance following cortical lesions (Buchtel and Stewart, 1989; Kelly *et al.*, 1996). Nevertheless, Oxenham (2000) has provided a cautionary counterpoint to this assumption. In his experiments using gap markers distinguished either by subjective pitch or by acoustic spectrum, Oxenham (2000) showed that gap thresholds were elevated more when markers differed in acoustic spectrum (i.e., peripheral factors) than when the markers differed in pitch but not spectrum (central factors). However, when the markers differed in pitch alone, gap thresholds were elevated by a factor of 2–3. This finding does not, therefore, dispute the contribution of central processes to gap detection. Moreover, it remains the case that in the absence of spectral overlap between a gap’s markers (e.g., Formby *et al.*, 1998a; Phillips *et al.*, 1997), or in the case of markers presented to different ears (e.g., Phillips *et al.*, 1997), the temporal gap detection process must be central in locus. This is because there is no peripheral mechanism available for the temporal correlation required to detect the gap in those cases. In the eight across-channel conditions used in the present study, facilitative (synchronous gap in the distractor) and interference effects (roving gap in the distractor) were largely independent of the frequency separation of the noisebands (Fig. 3, middle). Accordingly, while “peripheral” accounts alone might have explained the present findings for spectrally adjacent noise-

bands (whose abutting spectral edges might have been within channel for frequency channels tuned close to the border frequency), they have difficulty with the findings for stimulus conditions with spectrally remote noisebands. None of this disputes the contribution of peripheral factors to the temporal and spectral fidelity of the signals transmitted as cochlear output; it simply emphasizes that gap detection processes as “low” in level as the recovery of the temporal event through wideband spectral integration, or as “high” in level as the voluntary allocation of perceptual resources to a particular frequency channel, are necessarily more central in locus than cochlear output.

ACKNOWLEDGMENTS

This work was supported by grants from the Natural Sciences and Engineering Research Council of Canada to DPP. Sean Maclean wrote the software (“AUDIODEN”) which generated the noise stimuli. We thank Susan Boehnke for her input at all stages of this work, and Leanna Rutherford and Mary Ellen Large for their participation in the research.

- Boehnke, S. E., and Phillips, D. P. (1999). “Azimuthal tuning of human perceptual channels for sound location,” *J. Acoust. Soc. Am.* **106**, 1948–1955.
- Botte, M.-C. (1995). “Auditory attentional bandwidth: Effect of level and frequency range,” *J. Acoust. Soc. Am.* **98**, 2475–2485.
- Buchtel, H. A., and Stewart, J. D. (1989). “Auditory agnosia: Apperceptive or associative disorder?” *Brain Lang.* **37**, 12–25.
- Chatterjee, M., Fu, Q.-L., and Shannon, R. V. (1998). “Within-channel gap detection using dissimilar markers in cochlear implant listeners,” *J. Acoust. Soc. Am.* **103**, 2515–2519.
- Divenyi, P. L., and Danner, W. F. (1977). “Discrimination of time intervals marked by brief acoustic pulses of various intensities and spectra,” *Percept. Psychophys.* **21**, 125–142.
- Eddins, D. A., Hall, J. W., and Grose, J. H. (1992). “The detection of temporal gaps as a function of frequency region and absolute noise bandwidth,” *J. Acoust. Soc. Am.* **91**, 1069–1077.
- Fitzgibbons, P. J., Pollatsek, A., and Thomas, I. B. (1974). “Detection of temporal gaps within and between perceptual tonal groups,” *Percept. Psychophys.* **16**, 522–528.
- Formby, C., Gerber, M. J., Sherlock, L. P., and Magder, L. S. (1998a). “Evidence for an across-frequency, between-channel process in asymptotic monaural temporal gap detection,” *J. Acoust. Soc. Am.* **103**, 3554–3560.
- Formby, C., Sherlock, L. P., and Li, S. (1998b). “Temporal gap detection measured with multiple sinusoidal markers: Effects of marker number, frequency, and temporal position,” *J. Acoust. Soc. Am.* **104**, 984–998.
- Forrest, T. G., and Green, D. M. (1987). “Detection of partially filled gaps in noise and the temporal modulation transfer function,” *J. Acoust. Soc. Am.* **82**, 1933–1943.
- Grose, J. H. (1991). “Gap detection in multiple narrow bands of noise as a function of spectral configuration,” *J. Acoust. Soc. Am.* **90**, 3061–3068.
- Grose, J. H., and Hall, J. W. (1988). “Across-frequency processing in temporal gap detection,” in *Basic Issues in Hearing*, edited by H. Duifhuis, H. P. Wit, and J. B. Horst (Academic, New York), pp. 308–316.
- Grose, J. H., and Hall, J. W. (1993). “Gap detection in a narrow band of noise in the presence of a flanking band of noise,” *J. Acoust. Soc. Am.* **93**, 1645–1648.
- Grose, J. H., and Hall, J. W. (1996). “Across-frequency processing of multiple modulation patterns,” *J. Acoust. Soc. Am.* **99**, 534–541.
- Grose, J. H., Hall, J. W., and Buss, E. (1999). “Modulation gap detection: Effects of modulation rate, carrier separation, and mode of presentation,” *J. Acoust. Soc. Am.* **106**, 946–953.
- Hall, J. W., Grose, J. H., and Saju, J. (1996). “Gap detection for pairs of noise bands: Effects of stimulus level and frequency separation,” *J. Acoust. Soc. Am.* **99**, 1091–1095.
- Hanekom, J., and Shannon, R. V. (1998). “Gap detection as a measure of electrode interaction in cochlear implants,” *J. Acoust. Soc. Am.* **104**, 2372–2384.
- Johnson, K. O. (1980). “Sensory discrimination: Neural processes preceding discrimination decision,” *J. Neurophysiol.* **43**, 1793–1815.
- Kelly, J. B., Rooney, B. J., and Phillips, D. P. (1996). “Effects of bilateral auditory cortical lesions on gap-detection thresholds in the ferret (*Mustela putorius*),” *Behav. Neurosci.* **110**, 542–550.
- Levitt, H. (1971). “Transformed up-down methods in psychoacoustics,” *J. Acoust. Soc. Am.* **49**, 467–477.
- Moore, B. C. J., and Jorasz, U. (1992). “Detection of changes in modulation depth of a target sound in the presence of other modulated sounds,” *J. Acoust. Soc. Am.* **91**, 1051–1061.
- Moore, B. C. J., Peters, R. W., and Glasberg, B. R. (1993). “Detection of temporal gaps in sinusoids: Effects of frequency and level,” *J. Acoust. Soc. Am.* **93**, 1563–1570.
- Moray, N. (1969). *Attention: Selective Processes in Vision and Hearing* (Hutchinson Educational, London), p. 28.
- Oxenham, A. J. (2000). “Influence of spatial and temporal coding on auditory gap detection,” *J. Acoust. Soc. Am.* **107**, 2215–2223.
- Penner, M. J. (1977). “Detection of temporal gaps in noise as a measure of the decay of auditory sensation,” *J. Acoust. Soc. Am.* **61**, 552–557.
- Phillips, D. P., and Hall, S. E. (2000). “Independence of frequency channels for within-channel gap detection,” *Assn. Res. Otolaryngol. Abstr.* **23**, 104, Abstract #364.
- Phillips, D. P., Hall, S. E., Harrington, I. A., and Taylor, T. L. (1998). “‘Central’ auditory gap detection: A spatial case,” *J. Acoust. Soc. Am.* **103**, 2064–2068.
- Phillips, D. P., Taylor, T. L., Hall, S. E., Carr, M. M., and Mossop, J. E. (1997). “Detection of silent intervals between noises activating different perceptual channels: Some properties of ‘central’ auditory gap detection,” *J. Acoust. Soc. Am.* **101**, 3694–3705.
- Plomp, R. (1964). “Rate of decay of auditory sensation,” *J. Acoust. Soc. Am.* **36**, 277–282.
- Posner, M. I. (1980). “Orienting of attention,” *Quarterly J. Exp. Psychol.* **32**, 3–25.
- Scharf, B., Magnan, J., Collet, L., Ulmer, E., and Chays, A. (1994). “On the role of the olivocochlear bundle in hearing: A case study,” *Hear. Res.* **75**, 11–26.
- Scharf, B., Quigley, S., Aoki, C., Peachey, N., and Reeves, A. (1987). “Focused auditory attention and frequency selectivity,” *Percept. Psychophys.* **42**, 215–223.
- Snell, K. B., and Hu, H.-L. (1999). “The effect of temporal placement on gap detectability,” *J. Acoust. Soc. Am.* **106**, 3571–3577.
- Taylor, T. L., Hall, S. E., Boehnke, S. E., and Phillips, D. P. (1999). “Additivity of perceptual channel-crossing effects in auditory gap detection,” *J. Acoust. Soc. Am.* **105**, 563–566.
- Van Wieringen, A., and Wouters, J. (1999). “Gap detection in single- and multiple-channel stimuli by LAURA cochlear implantees,” *J. Acoust. Soc. Am.* **106**, 1925–1939.
- Viemeister, N. F. (1979). “Temporal modulation transfer functions based upon modulation thresholds,” *J. Acoust. Soc. Am.* **66**, 1364–1380.
- Yost, W. A., and Sheft, S. (1989). “Across-critical-band processing of amplitude-modulated tones,” *J. Acoust. Soc. Am.* **85**, 848–857.

Specificity of perceptual learning in a frequency discrimination task

Dexter R. F. Irvine^{a)}

Department of Psychology, Monash University, Victoria 3800, Australia

Russell L. Martin

*Aeronautical and Maritime Research Laboratory, Defence Science and Technology Organisation,
P.O. Box 4331, Melbourne, Victoria 3001, Australia*

Ester Klimkeit and Rachel Smith

Department of Psychology, Monash University, Victoria 3800, Australia

(Received 5 August 1999; revised 28 October 1999; accepted 12 September 2000)

On a variety of visual tasks, improvement in perceptual discrimination with practice (perceptual learning) has been found to be specific to features of the training stimulus, including retinal location. This specificity has been interpreted as evidence that the learning reflects changes in neuronal tuning at relatively early processing stages. The aim of the present study was to examine the frequency specificity of human auditory perceptual learning in a frequency discrimination task. Difference limens for frequency (DLFs) were determined at 5 and 8 kHz, using a three-alternative forced choice method, for two groups of eight subjects before and after extensive training at one or the other frequency. Both groups showed substantial improvement at the training frequency, and much of this improvement generalized to the nontrained frequency. However, a small but statistically significant component of the improvement was specific to the training frequency. Whether this specificity reflects changes in neural frequency tuning or attentional changes remains unclear.

© 2000 Acoustical Society of America. [S0001-4966(00)04112-6]

PACS numbers: 43.66.Fe, 43.66.Ba [RVS]

I. INTRODUCTION

Improvements in perceptual judgments with practice have been known for well over a century [see Gibson (1953) and Goldstone (1998) for reviews]. In recent years there has been considerable interest in the *specificity* of some forms of visual perceptual learning. Improvements with practice on tasks such as Vernier acuity and texture discrimination have been reported to be highly specific for such features as locus of retinal stimulation, stimulus orientation and size, and (in some cases) the trained eye (e.g., Ramachandran and Brad-dick, 1973; Fiorentini and Berardi, 1980; Karni and Sagi, 1991; Gilbert, 1994; Schoups *et al.*, 1995; Ahissar and Hochstein, 1993, 1996). A common interpretation of this specificity is that the learning reflects plastic changes in the tuning of neurons at a relatively early stage of visual processing. For example, Karni and Sagi (1991) interpreted the fact that learning of a texture discrimination task was specific to retinal locus, orientation, and the trained eye as indicating that the learning reflected neural plasticity in primary visual cortex. However, alternative explanations of the specificity of perceptual learning in attentional terms have also been proposed (Mollon and Danilova, 1996).

Although there have been a number of studies of auditory perceptual learning and generalization [see Watson (1980, 1991) for reviews], only a few recent studies have explicitly examined the question of whether any component of the learning is specific to the training stimulus (e.g., Trem-

blay *et al.*, 1997; Wright *et al.*, 1997). Specificity of visual perceptual learning on a number of tasks with respect to the retinal location at which the stimuli are presented suggests that there might be an analogous specificity of auditory perceptual learning with respect to cochlear locus of activation, i.e., with respect to frequency. Although improvements in frequency discrimination with practice have been reported by a number of authors (e.g., Campbell and Small, 1963; Moore, 1973, 1976), the only investigation of the frequency specificity of this learning in humans is that by Demany (1985). He trained four different groups of subjects on a frequency discrimination task at 0.2, 0.36, 2.5, and 6 kHz, and determined the effect of this training on frequency difference limens (DLFs) at 0.2 kHz. His results indicated that training at the first three frequencies resulted in similar (statistically indistinguishable) improvement in discrimination at the test frequency (0.2 kHz), whereas training at 6 kHz resulted in less improvement. He suggested that this difference might be attributable to the fact that the three lower frequencies were in the frequency range likely to be coded peripherally by temporal mechanisms, whereas the highest frequency (6 kHz) was in the place coding range. Although Demany's results indicate a lack of specificity of frequency discrimination learning in the frequency range likely to be coded by temporal mechanisms, they leave open the possibility that there might be some degree of specificity of such learning in the frequency range coded by place mechanisms.

A recent study of frequency discrimination learning in owl monkeys has provided important data on the nature and locus of neural changes associated with perceptual learning

^{a)}Electronic mail: d.irvine@sci.monash.edu.au

in frequency discrimination. Recanzone *et al.* (1993) reported that improvements in frequency discrimination (at 2.5, 3.0, 5.0, and 8.0 kHz) were characterized by an early fast phase in which large improvements in performance were seen, and by a later, slower phase in which smaller improvements occurred [see also Prosen *et al.* (1990)]. Generalization was tested in two animals, from 2.5 to 8 kHz in one case and from 5 to 3 kHz in the other. Improvements in the fast phase generalized to frequencies other than that at which the monkeys were trained, and were attributed to “conceptual” learning of the task and the development of appropriate strategies. Improvements in the second, slower phase did not generalize to other frequencies, and in one case were associated with a decrement in performance at a previously trained frequency. These results are therefore in accordance with those of Demany (1985) in indicating some degree of specificity of perceptual learning when generalization is tested across frequency ranges likely to be coded peripherally by different mechanisms. Recanzone *et al.* attributed the second phase of improvement to an enhancement of the central representation of the training frequencies. In accordance with this suggestion, and with the proposal that stimulus-specific perceptual learning reflects changes in neural response characteristics at relatively early processing stages, they reported that learning was associated with an enlarged representation of the training frequencies in the primary auditory cortex (AI).

The aim of the study reported here was to determine whether perceptual learning by human subjects on a frequency discrimination task using frequencies in the range coded peripherally by place rather than temporal mechanisms is specific to the training frequency.

II. METHOD

A. Subjects

Sixteen normal hearing, right-handed volunteers (12 female) in the age range 18–31 years (mean 22.9 years) served as subjects. One subject was one of the authors (EK); all other subjects were paid for their participation. Normality of hearing was established by determining thresholds at 1, 5, and 8 kHz using a three-alternative forced choice (3AFC) procedure. All Ss had thresholds within 1.5 standard deviations of age- and gender-related norms (Corso, 1963). No subject had any previous experience in psychoacoustics; the use of untrained subjects was necessary in order to ensure that any perceptual learning in frequency discrimination took place predominantly in the course of the experiment. Subjects were assigned randomly to one of two experimental groups (see Sec. II C).

B. Stimuli

Tone-burst stimuli were generated digitally using a digital signal processing board [Tucker Davis Technologies (TDT) AP2] and a sampling rate of 200 kHz. The tone bursts were 220 ms in duration, incorporating 10-ms rise–fall times shaped with a \cos^2 function, and the interval between successive tones in a trial was 520 ms. Digitized waveforms were delivered to a 16-bit digital-to-analog converter (TDT

DD1), followed by a programmable attenuator (TDT PA4) and an audio amplifier (Yamaha AX350). Stimuli were presented monotonically to the right ear via Sennheiser HD265 headphones, at a level 60 dB above the subject’s absolute threshold in that ear for the particular frequency (60 dB SL). To control for the possibility of loudness fluctuations providing a cue to frequency differences (Henning, 1966), tone level was randomly varied over a ± 1 -dB range around the specified level.

C. Procedure

The experiment consisted of a preliminary task-practice phase, followed by a pretest, a training phase, and a posttest. In the pre- and posttest phases, DLFs were measured for all 16 subjects at 5 and 8 kHz. In the training phase, eight subjects received extensive frequency discrimination training at one of these frequencies, and the remaining eight at the other. The preliminary task-practice phase was designed to reduce the magnitude of the task-related learning component in the training phase, so that this component would be less likely to mask small perceptual learning effects. During the task-practice phase, DLFs were determined at a frequency (1 kHz) in the temporal coding range, and well removed from those to be used in training.

In each phase of the experiment, DLFs were estimated using an adaptive, three-interval, 3AFC method. Each trial consisted of three intervals indicated by lights. In two of the intervals the frequency of the stimulus was the same; in the third, selected at random, it was higher. The subject’s task was to detect the interval containing the higher frequency. Subjects responded using a hand-held three-button key pad, and initiated each new trial by pushing the first button. Subjects were not given trial-by-trial feedback but, in an attempt to maintain motivation, they were informed of their threshold after each DLF estimation.

A two-down one-up rule was used to estimate the frequency difference corresponding to the 70.7% correct point on the psychometric function (Levitt, 1971). The initial difference in frequency was 20% of the base frequency; after two consecutive correct responses the frequency difference was reduced by a factor of 1.4, and after one incorrect response it was increased by the same factor. For each DLF estimate, the adaptive procedure was terminated after 11 reversals (i.e., six downward runs) and the threshold was taken as the geometric mean of the frequency differences at the last eight reversals.

In the task-practice phase, four DLF estimates were obtained at 1 kHz. In the pre- and posttest phases, three estimates were obtained at each of 5 and 8 kHz, with the order of testing frequencies alternated and counterbalanced across subjects. In the training phase, each session comprised eight DLF estimates, with a rest period of five minutes between the first and last four. The median of the threshold estimations made at a given frequency within the task-practice, pretest, and posttest phases, or within a training session, was taken as the DLF for that phase/session. The median was used because in our experience it has proved to be a more reliable measure than the mean with respect to thresholds measured using this procedure.

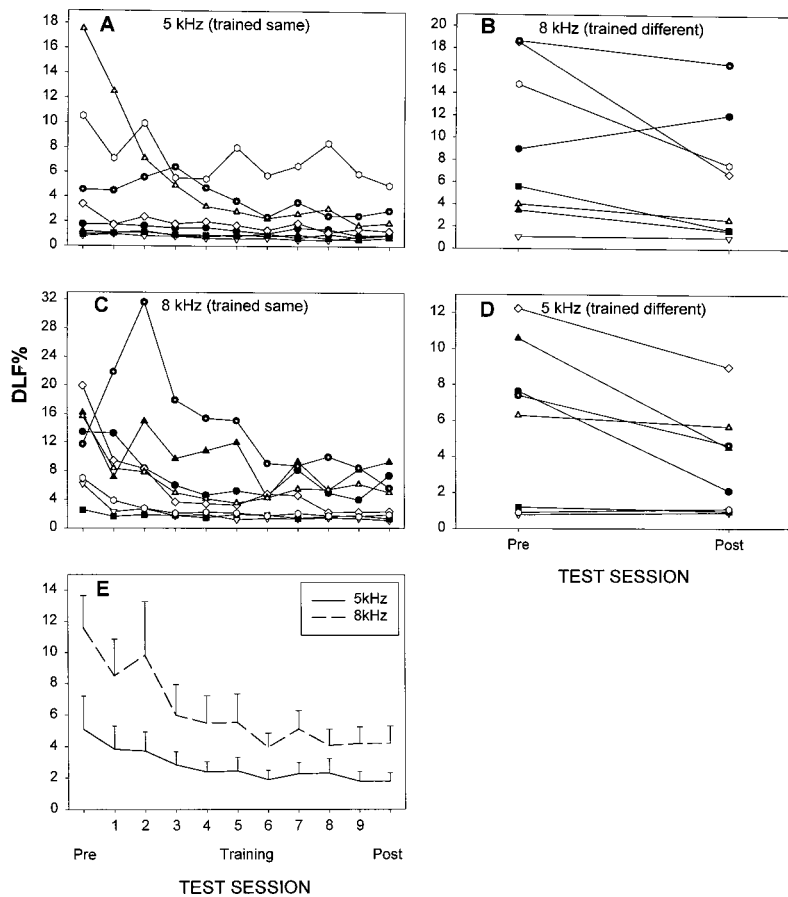


FIG. 1. Improvement in frequency discrimination with training. (a) and (b) Changes in DLF% across sessions at training frequency (5 kHz) (a), and pre- and post-training DLF% estimates at 8 kHz (b), for individual subjects in the 5-kHz training group. Each subject is represented by the same symbol in the two panels. (c) and (d) Corresponding data for subjects in the 8-kHz training group. (e) Mean functions showing learning curves for the two groups at their training frequencies. Error bars indicate the standard error of the mean (SEM).

Nine training sessions were run, with a maximum of two sessions per day and a minimum interval of 2 h between sessions. Task practice and the pretest, separated by a 5-min rest interval, were completed on day 1 of testing. Two training sessions were completed on each of days 2–5, and the ninth training session and posttest, separated by a 5-min rest interval, were completed on day 6. In the course of the experiment each subject spent 6–7 h and completed 4000–5000 trials in making frequency discriminations at the training frequency.

III. RESULTS

The major aim of this study was to determine whether improvement in frequency discrimination with training (perceptual learning) is specific to the training frequency. A prerequisite, therefore, is to establish the occurrence of perceptual learning at the training frequency. In Figs. 1(a) and 1(c) median DLFs [expressed as percentage of base frequency (DLF%)] for individual subjects trained at 5 and 8 kHz, respectively, are shown as a function of test session. In both groups, there was considerable intersubject variability in both DLF magnitude and the amount by which DLF changed as a result of training, but the posttest threshold was lower than the pretest threshold for seven of the eight subjects trained at 5 kHz [Fig. 1(a)] and for all of the eight subjects trained at 8 kHz [Fig. 1(c)]. The overall improvement in discrimination is illustrated by the mean functions in Fig. 1(e), which show that asymptotic or near-asymptotic group performance was achieved over the last five sessions. Mean

DLFs were larger, and the improvement with practice also appeared to be somewhat greater, at the higher frequency. These differences were examined statistically by means of a repeated-measures two-way analysis of variance (ANOVA) incorporating a Greenhouse–Geiser correction, after subjecting the data to a square-root transformation to correct for non-normality in some cells. The analysis yielded a highly significant effect of session [$F(10,140)=12.25$; $p=0.00001$], confirming the reduction in DLF with training. The difference between groups just failed to achieve significance at the 0.05 level [$F(1,14)=4.42$; $p=0.054$], and the interaction was not significant [$F(10,140)=1.35$; $p=0.211$]. Thus, while the difference in DLFs in the 5- and 8-kHz groups approached significance, there was no significant difference between the groups with respect to the effect of training.

Given a significant perceptual learning effect, the question of the specificity of this effect to the training frequency can be examined. The pre- and posttest DLFs of individual subjects at the untrained frequencies are shown in Figs. 1(b) and 1(d). Again, there are large individual differences, but seven of the eight subjects trained at 5 kHz showed a decrease in threshold at 8 kHz [Fig. 1(b)], and six of the eight trained at 8 kHz showed a decrease at 5 kHz. Mean pre- and posttest DLFs at 5 and 8 kHz are shown in Figs. 2(a) and 2(b), respectively, for subjects trained at the same frequency (“trained same;” solid lines) and at the other frequency (“trained different;” broken lines). The “trained-same” lines show the substantial improvement already illustrated in Fig. 1(e). At each of the test frequencies, there also appears to be improvement in DLF for those subjects trained at the

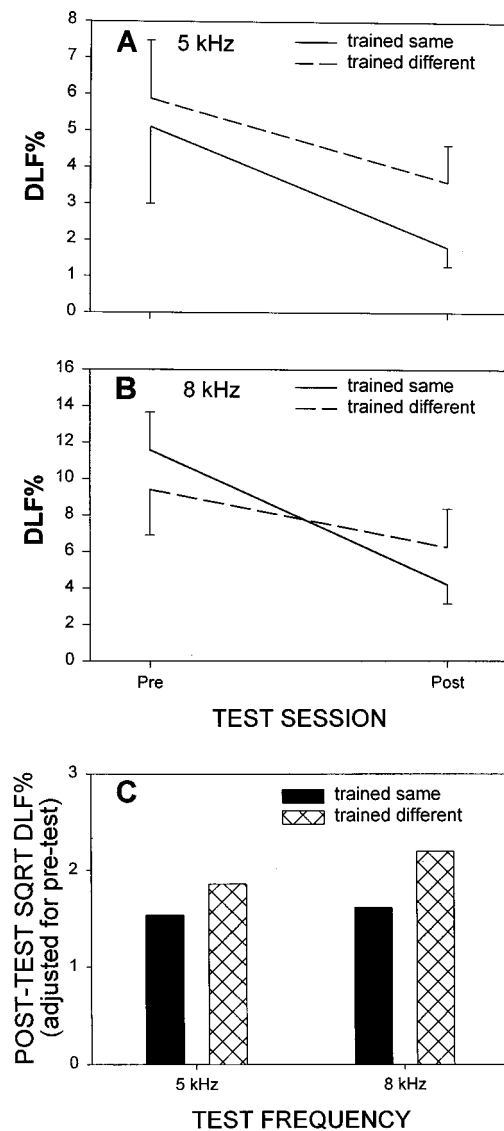


FIG. 2. Comparison of improvements at training and non-training frequencies. (a) and (b) Mean pre- and posttest DLF% values at 5 and 8 kHz [(a) and (b), respectively] for subjects trained at that frequency (“trained same”) and subjects trained at the other frequency (“trained different”). Note different ordinate scales. Error bars indicate the SEM. (c) Mean posttest square root DLF% values, adjusted for differences in pretest values, at 5 and 8 kHz for subjects trained at the same and at the other frequency.

other frequency (broken lines), suggesting a degree of generalization of perceptual learning across frequencies. However, the slope of the “trained-same” line is steeper than that of the “trained-different” line in each case, indicating a greater degree of improvement at the trained frequency, and suggesting that some proportion of the improvement with practice was specific to the training frequency. As in Demany’s (1985) study, this difference in slope is confounded with differences in the pretest DLFs, so its interpretation is unclear. In order to control for the effects of pretest scores, a two-way analysis of covariance (ANCOVA) of the posttest scores, using pretest scores as a covariate (Keppel and Zedek, 1989), was carried out. The two factors were training frequency and whether the training and test frequencies were the same or different (the “trained-same/trained-different” factor). Again, a square-root transformation was applied to

the data to correct for non-normality. In Fig. 2(c) the mean posttest square-root DLF% values, adjusted for the correlation with the pretest covariate, are shown, and illustrate that for each of the test frequencies the adjusted posttest DLF was smaller for subjects trained at the same frequency. The ANCOVA revealed that the main effect of the trained-same/trained-different factor was significant [$F(1,13)=4.70$; $p=0.049$], but that neither the main effect of training frequency [$F(1,13)=0.51$; $p=0.489$] nor the interaction between the two factors [$F(1,13)=0.53$; $p=0.479$] approached significance. Thus, it appears that there is a component of the improvement in frequency discrimination with training that is specific to the training frequency.

IV. DISCUSSION AND CONCLUSIONS

The results confirm the occurrence of perceptual learning in a frequency discrimination task, and indicate that although a large component of the improvement in frequency discrimination generalizes across frequencies, a small but statistically significant component of the improvement is specific to the training frequency. The mean posttraining DLFs at 5 and 8 kHz were considerably larger than those reported in previous studies in which subjects were screened for low DLFs (e.g., Wier *et al.*, 1977) or had musical or psychoacoustical skills (e.g., Henning, 1966; Moore, 1973; Sek and Moore, 1995). However, the range of DLFs was comparable to that reported for unskilled listeners at 1 kHz by Moore (1976) (when his difference limens are converted to DLF% values), and the posttraining DLFs of the best-performing subjects were similar to those reported for selected/highly skilled listeners in previous studies. The greater magnitude of DLFs at 8 kHz than at 5 kHz, a difference that approached significance, is also in agreement with previous data (Moore, 1993).

The major aim of this study was to examine the specificity of perceptual learning on a frequency discrimination task. As in Demany’s (1985) study, there was evidence of improvement in frequency discrimination at a frequency other than that on which subjects were trained, suggesting generalization of perceptual learning across frequencies. The extent to which this improvement reflects a true generalization of the effects of training cannot be established in the absence of a control group that received no training between pre- and posttest. It is possible that such a group would show some improvement as a consequence of some form of long-term consolidation of learning that took place during the pretest itself.

The most important feature of the present data, however, is the finding that a component of the improvement with training was specific to the training frequency. The finding of partial specificity of perceptual learning in the frequency range coded by place mechanisms is in contrast to the complete generalization shown by Demany (1985) within the frequency range coded peripherally by temporal mechanisms. However, comparison between our and Demany’s studies is qualified by the fact that he used only 700 training trials, in contrast to the 4000–5000 trials at the training frequency in the present study. Furthermore, his experiment did not in-

clude a task-practice session to minimize the contribution of task-related learning. It is therefore possible that a substantial proportion of the improvement shown by his subjects reflected task-related learning which generalized completely and masked a small frequency-specific perceptual learning effect. As noted in the Introduction, both Demany (1985; in humans) and Recanzone *et al.* (1993; in monkeys) found some degree of specificity when generalization was tested across frequency ranges coded by different mechanisms. Considered together, the data from all three studies suggest the possibility of differences in the specificity of perceptual learning in different frequency ranges. This possibility requires further examination in experiments using the same testing and data analysis procedures to examine specificity of perceptual learning within and across different frequency ranges.

As discussed in the Introduction, specificity of visual perceptual learning to the locus of retinal stimulation (and to a number of other features) has commonly been interpreted as indicating that the learning involves changes in the tuning of neurons at relatively early processing stages (perhaps in primary visual cortex). Recanzone *et al.*'s (1993) finding that improvement in frequency discrimination performance was associated with increases in the area of representation of the training frequencies (defined as the area in which neurons had characteristic frequencies in the frequency range used in training) in AI is in accordance with this interpretation. In this context, the possible difference between frequency ranges discussed above is of interest, given that temporal coding mechanisms are not preserved at levels above the midbrain.

Finally, as alluded to in the Introduction, the interpretation of specificity of perceptual learning requires some consideration. Except in animal studies in which cortical neural tuning can be examined directly [as in Recanzone *et al.* (1993)], evidence for the relationship between perceptual learning and changes in neuronal tuning in cortex is indirect. As Mollon and Danilova (1996) have argued, other explanations of the specificity of perceptual learning are possible. For example, it could be that the subject learns which subset of central channels provides the most useful information on which to base the discrimination and "how variations in the signals on these channels map onto the external discriminanda" (Mollon and Danilova, 1996, p. 52). This proposed mechanism would not involve any change in the tuning or other properties of the neurons comprising the channels.

ACKNOWLEDGMENTS

This research was supported by a grant from the Australian Research Council. We are grateful to Frank Devlin, Caroline Molloy, and Lorraine Park for technical assistance, and to Ken McAnally and two reviewers for extremely helpful comments on earlier versions of the manuscript.

- Ahissar, M., and Hochstein, S. (1993). "Attentional control of early perceptual learning," *Proc. Natl. Acad. Sci. U.S.A.* **90**, 5718–5722.
- Ahissar, M., and Hochstein, S. (1996). "Learning pop-out detection: Specificities to stimulus characteristics," *Vision Res.* **36**, 3487–3500.
- Campbell, R. A., and Small, A. M. (1963). "Effect of practice and feedback on frequency discrimination," *J. Acoust. Soc. Am.* **35**, 1511–1514.
- Corso, J. F. (1963). "Age and sex differences in pure-tone thresholds," *Arch. Otolaryngol.* **77**, 385–405.
- Demany, L. (1985). "Perceptual learning in frequency discrimination," *J. Acoust. Soc. Am.* **78**, 1118–1120.
- Florentini, A., and Berardi, N. (1980). "Perceptual learning specific for orientation and spatial frequency," *Nature (London)* **287**, 43–44.
- Gibson, E. J. (1953). "Improvement in perceptual judgements as a function of controlled practice or training," *Psychol. Bull.* **50**, 401–431.
- Gilbert, C. D. (1994). "Early perceptual learning," *Proc. Natl. Acad. Sci. U.S.A.* **91**, 1195–1197.
- Goldstone, R. L. (1998). "Perceptual learning," *Annu. Rev. Psychol.* **49**, 585–612.
- Henning, G. B. (1966). "Frequency discrimination of random-amplitude tones," *J. Acoust. Soc. Am.* **39**, 336–339.
- Karni, A., and Sagi, D. (1991). "Where practice makes perfect in texture discrimination: Evidence for primary visual cortex plasticity," *Proc. Natl. Acad. Sci. U.S.A.* **88**, 4966–4970.
- Keppel, G., and Zedeck, S. (1989). *Data Analysis for Research Designs* (Freeman, New York).
- Levitt, H. (1971). "Transformed up-down methods in psychoacoustics," *J. Acoust. Soc. Am.* **49**, 467.
- Mollon, J. D., and Danilova, M. V. (1996). "Three remarks on perceptual learning," *Spatial Vis.* **10**, 51–58.
- Moore, B. C. J. (1973). "Frequency difference limens for short-duration tones," *J. Acoust. Soc. Am.* **54**, 610–619.
- Moore, B. C. J. (1976). "Comparison of frequency DL's for pulsed tones and modulated tones," *Br. J. Audiol.* **10**, 17–20.
- Moore, B. C. J. (1993). "Frequency analysis and pitch perception," in *Human Psychophysics*, edited by W. A. Yost, A. N. Popper, and R. R. Fay (Springer-Verlag, New York), pp. 56–115.
- Prosen, C. A., Moody, D. B., Sommers, M. S., and Stebbins, W. C. (1990). "Frequency discrimination in the monkey," *J. Acoust. Soc. Am.* **88**, 2152–2158.
- Ramachandran, V. S., and Braddick, O. (1973). "Orientation-specific learning in stereopsis," *Perception* **2**, 371–376.
- Recanzone, G. H., Schreiner, C. E., and Merzenich, M. M. (1993). "Plasticity in the frequency representation of primary auditory cortex following discrimination training in adult owl monkeys," *J. Neurosci.* **13**, 87–103.
- Schoups, A. A., Vogels, R., and Orban, G. A. (1995). "Human perceptual learning in identifying the oblique orientation: retinotopy, orientation specificity and monocularly," *J. Physiol. (London)* **483**, 797–810.
- Sek, A., and Moore, B. C. J. (1995). "Frequency discrimination as a function of frequency, measured in several ways," *J. Acoust. Soc. Am.* **97**, 2479–2486.
- Tremblay, K., Kraus, N., Carrell, T. D., and McGee, T. (1997). "Central auditory system plasticity: Generalization to novel stimuli following listening training," *J. Acoust. Soc. Am.* **102**, 3762–3773.
- Watson, C. S. (1980). "Time course of auditory perceptual learning," *Ann. Otol. Rhinol. Laryngol. (Suppl.)* **74**, 96–102.
- Watson, C. S. (1991). "Auditory perceptual learning and the cochlear implant," *Am. J. Otolaryngol. (Suppl.)* **12**, 73–79.
- Wier, C. C., Jesteadt, W., Green, D. (1977). "Frequency discrimination as a function of frequency and sensation level," *J. Acoust. Soc. Am.* **61**, 178–184.
- Wright, B. A., Buonomano, D. V., Mahncke, H. W., Merzenich, M. M. (1997). "Learning and generalization of auditory temporal-interval discrimination in humans," *J. Neurosci.* **17**, 3956–3963.

Generalization of tactile perceptual skills to new context following tactile-alone word recognition training with the Tickle Talker™

Karyn L. Galvin

CRC for Cochlear Implant and Hearing Aid Innovation, 384-388 Albert Street, East Melbourne 3002, Australia and The Bionic Ear Institute, 384-388 Albert Street, East Melbourne 3002, Australia

Peter J. Blamey

Department of Otolaryngology, The University of Melbourne, 2nd Floor, RVEEH, 32 Gisborne Street, East Melbourne 3002, Australia

Robert S. C. Cowan

CRC for Cochlear Implant and Hearing Aid Innovation, 384-388 Albert Street, East Melbourne 3002, Australia; The Bionic Ear Institute, 384-388 Albert Street, East Melbourne 3002, Australia; and Department of Otolaryngology, The University of Melbourne, 2nd Floor, RVEEH, 32 Gisborne Street, East Melbourne 3002, Australia

Michael Oerlemans

Department of Otolaryngology, The University of Melbourne, 2nd Floor, RVEEH, 32 Gisborne Street, East Melbourne 3002, Australia

Graeme M. Clark

CRC for Cochlear Implant and Hearing Aid Innovation, 384-388 Albert Street, East Melbourne 3002, Australia; The Bionic Ear Institute, 384-388 Albert Street, East Melbourne 3002, Australia; and Department of Otolaryngology, The University of Melbourne, 2nd Floor, RVEEH, 32 Gisborne Street, East Melbourne 3002, Australia

(Received 11 May 1999; revised 26 May 2000; accepted 28 August 2000)

The Tickle Talker™ is an electrotactile speech perception device. Subjects were evaluated using the device in various tactile-alone and tactile–visual contexts to assess the generalization to other contexts of tactile-alone perceptual skills. The subjects were from a group of six normally hearing subjects who had previously received 12 to 33 h of tactile-alone word recognition training and had learned an average vocabulary of 50 words [Galvin *et al.*, *J. Acoust. Soc. Am.* **106**, 1084–1089 (1999)]. The tactile-alone evaluation contexts were sentences, unfamiliar talkers, and untrained words. The tactile–visual evaluation contexts were closed-set words, open-set words, and open-set sentences. Tactile-alone perceptual skills were generalized to unfamiliar speakers, sentences, and untrained words, though scores indicated that generalization was not complete. In contrast, the generalization of skills to tactile–visual contexts was minimal or absent. The potential value of tactile-alone training for hearing-impaired users of the Tickle Talker™ is discussed. © 2000 Acoustical Society of America. [S0001-4966(00)00612-3]

PACS numbers: 43.66.Wv, 43.71.Es, 43.71.Ky, 43.71.Ma [DOS]

I. INTRODUCTION

Tactile devices supply speech information to supplement that available via audition and vision, and are one option for improving the sound awareness and speech perception of people with a severe-profound or profound hearing impairment. Multichannel tactile devices generally provide time, intensity, and spectral information that can be used to discriminate speech features, and to recognize vowels and consonants in closed sets. Studies in the literature have reported variation in the level of enhancement demonstrated on speechtracking evaluations, with relatively small improvements of 5 to 13 words per minute (wpm) being common when the tactile was combined with auditory, visual, or auditory-plus-visual information (see, for example, Cowan *et al.*, 1988, 1989, 1990; Kishon-Rabin *et al.*, 1996; Plant, 1992, 1998; Reed and Delhorne, 1995; and summary articles by Bernstein, 1992; Weisenberger, 1995). Superior

speechtracking enhancement rates of over 40 words per minute have also been reported (Weisenberger *et al.*, 1989). Despite the potential demonstrated by these results, the level of clinical usage of tactile devices remains relatively low. In contrast, an alternative speech perception device, the cochlear implant, has achieved widespread clinical success (see, for example, Geers and Moog, 1995; Kessler, 1993; Osberger *et al.*, 1996; Parkinson *et al.*, 1998; Staller *et al.*, 1995). An implant has clear advantages over a tactile device, including utilizing the natural auditory neural pathway, typically providing an individual with a benefit to speech perception greater than that to be expected from a tactile device, and providing a realistic possibility for device-alone perception of connected speech.

Given the advantages and success of cochlear implants, some clinicians and researchers have questioned the need for tactile devices. However, it is important to recognize that a cochlear implant is not the answer for every person who

TABLE I. Details of devices used in previous studies examining the post-training performance of subjects trained in tactile-alone word recognition.

Reference	Lynch <i>et al.</i> , 1989	Lynch <i>et al.</i> , 1988, 1989	Engelmann and Rosov, 1975	Brooks <i>et al.</i> , 1986a, 1986b
Device	Tactaid II	Tacticon 1600	Oregon vocoder	Queen's University vocoder
Stimulation	vibrotactile	electrotactile	vibrotactile	vibrotactile
Site	wrist	abdomen	arm	arm
Channels	2	16	23	16

meets the audiological criteria for candidature. For some there are medical contraindications to surgery, such as an obliterated cochlea, a recurring middle-ear infection, or unsuitability for general anesthetic. For others with multiple handicaps, their potential to cooperate with device fitting and to utilize the information provided may be difficult to predict. Even if candidacy is established, some adults and parents of candidates do not wish to proceed with the operation. Reasons for this decision include unwillingness to undergo surgery, the likely destruction of any remaining hearing in the implanted ear, the fact that performance predictions are based on general group experience and cannot be guaranteed for an individual, and the cost of the surgery and the device. Parents may also agree with the view of some in the deaf community that hearing impairment is not a disability to be ‘‘corrected’’ (Lane and Bahan, 1998; Tucker, 1998).

For individuals who cannot or do not wish to obtain a cochlear implant, a tactile device is an alternative for supplying supplementary acoustic information. Tactile device use may also have other important outcomes. Positive experience with a tactile device motivates some individuals to improve their communication, perhaps through participating in aural rehabilitation classes, increased social participation, or investigation of cochlear implant candidacy. Tactile device use by established pediatric cochlear implant candidates may provide useful information relating to such factors as the child’s ability to cooperate with programming and to learn to use new speech information, and the commitment of the child and family to session attendance and consistent device use.

Given that, for the foreseeable future, tactile devices will be used by some hearing-impaired people, it is important to establish what type of training is most likely to help such users to learn to obtain and utilize tactile information quickly and effectively. The importance of training has been emphasized previously (see, for example, Alcantara, 1991; Galvin *et al.*, 1993; Plant, 1995; Oller, 1995); however, the optimum configuration of training remains unclear. Unfortunately, clarifying the effective components of training is a complex task as many interacting factors influence speech perception. The limited number of hearing-impaired tactile device users who are potential subjects for such research also makes the task more difficult. One compromise approach is to employ hearing subjects in studies examining limited aspects of training. With continued research each such study should contribute to an overall picture of the most appropriate training for hearing-impaired tactile device users. One such specific area of investigation has been the value of unimodal and combined-modality training, and this topic is further examined in the present study.

The subjects in the present study used the Tickle Talker™ electrotactile device, which was originally developed by The University of Melbourne’s Department of Otolaryngology for use in the preoperative evaluation of cochlear implant candidates (Blamey and Clark, 1985). Earlier training studies with the device considered some effects of providing unimodal and bimodal training to device users (Alcantara *et al.*, 1993; Oerlemans and Blamey, 1998). In a recent investigation of the potential for naive subjects to learn a vocabulary using the Tickle Talker™ alone, six normally hearing subjects learned to recognize an average of 50 words when provided with 12 to 33 h of tactile-alone word recognition training (Galvin *et al.*, 1999). As discussed previously (Galvin *et al.*, 1993), some basic tactile-alone work is included in the Tickle Talker™ training program, with the aim of introducing the tactile signal, allowing the user to focus on the tactile information only, and developing an understanding that the tactile signal provides useful speech information. However, the results of Galvin *et al.*’s (1999) tactile-alone word recognition training study raise the question of whether providing further tactile-alone training at the word level would be a productive use of training time for hearing-impaired device users. Such training would only be worthwhile if the skills learned during training were generalized to other contexts which were representative of the variation encountered in daily communication.

Previous studies have evaluated the performance in a variety of contexts of subjects trained in tactile-alone word recognition using other tactile devices (the details of these devices are presented in Table I and further discussion of tactile devices in general is provided in the Method section) (Engelmann and Rosov, 1975; Reed *et al.*, 1982; Brooks *et al.*, 1986a, 1986b; Lynch *et al.*, 1988, 1989). As the main aim of these studies varied, the subjects in some studies (Engelmann and Rosov, 1975; Reed *et al.*, 1982; Lynch *et al.*, 1989) gained experience or received training other than the tactile-alone word recognition training. As a consequence, it was not always possible to determine the extent to which performance in other contexts was due to the tactile-alone training. The present study involved subjects whose only experience of tactile speech information was the tactile-alone word recognition training reported in Galvin *et al.* (1999). Given this, the performance of these subjects in other contexts can be attributed to the generalization of skills learned during the tactile-alone word recognition training.

The general aim of the present study was to consider the value of tactile-alone word recognition training for hearing-impaired users of the Tickle Talker™ by evaluating the flexibility of the tactile perceptual skills developed through such

training. The specific aim was to assess whether perceptual skills acquired during tactile-alone word recognition training using the Tickle Talker™ were generalized to other selected tactile-alone and tactile–visual contexts. The other tactile-alone contexts were the perception of sentences, untrained words, and words presented by unfamiliar talkers. The other tactile–visual contexts were the perception of closed-set words and open-set words and sentences.

II. METHOD

A. Design

Four adults with normal hearing completed evaluations of tactile-alone and tactile–visual perception with the Tickle Talker™ using a variety of test materials. The subjects' only experience with tactile speech perception was an earlier program of tactile-alone word recognition training, so that their performance in other contexts could be attributed to this type of training.

B. Tactile devices and the Tickle Talker™

As background information to the subsequent description of the Tickle Talker™, and to allow comparison of the Tickle Talker™ with other tactile devices referred to in the Discussion section, some basic points relating to tactile devices in general will be reviewed here. Characteristics of the tactile sense are important in determining the type of information to be presented via a tactile device. Verrillo and Gescheider (1992) reviewed research into perception via the sense of touch. These authors concluded that the skin is ‘poor’ at discriminating frequency differences, that the vibrotactile system has a comfortable intensity range of just 55 dB, and that masking of simultaneous or consecutive stimuli was a significant issue for tactile device developers. A tactile device usually consists of a microphone to collect the acoustic input, a speech processor to process (if necessary) and relay the signal, and transducer(s) to present the information to the skin. Devices are commonly classified by the level of processing applied to the acoustic input (bandpass filter or speech feature selection), the site of stimulation, the number of transducers used to present information, and the type of stimulation (electrotactile or vibrotactile). In devices employing a speech-feature selection approach to processing the acoustic input, the system extracts particular features of the acoustic signal for presentation to the user. In the bandpass filter or vocoder approach, the input passes through a set of filters, with each filter corresponding to a particular tactile transducer. This latter approach essentially presents the raw signal to the user. Vibrotactile devices present information to the user via mechanical depression of the skin, with the skin being more sensitive to vibrations in the frequency range 200 to 250 Hz (Sherrick and Craig, 1982). Electrotactile devices present information via electrical stimulation of the sensory receptors or nerve fibers in the skin. This stimulation is most efficiently conducted using current pulses, with rates in the range of 20 to 400 pulses per second ensuring that individual pulses are not felt but that the nerve has sufficient time to recover between pulses (Brown and Stevens, 1992). The disadvantages of vibrotactile stimulation are that relatively large

transducers and a relatively high rate of power consumption are required (Sherrick, 1984). The disadvantages of electro-tactile stimulation are the greater potential for unpleasant stimulation (Brown and Stevens, 1992), and the limited dynamic range of the tactile system for responding to variation in the intensity of electrotactile stimulation; this latter disadvantage requires that sound input be compressed or intensity coded in an alternative manner (Weisenberger, 1992).

The Tickle Talker™ consists of a lapel microphone, a handset, and a speech processor. The eight electrodes in the four rings of the handset are positioned over the digital nerve bundles, which lie along the sides of the fingers. Information is presented to the user via electrocutaneous stimulation of these nerve bundles. The original Tickle Talker™ speech processor was based on the WSP II processor used with the original version of the Nucleus 22-channel cochlear implant (Blamey and Clark, 1985). The speech processor used in the present study was the Mk III version, which incorporated a number of design improvements including the use of the nonactive finger electrodes as the ground/return electrode during stimulation. The speech-processing strategy implemented in this processor extracted estimates of the fundamental frequency and the second formant frequency of speech, and the overall amplitude of speech in the band up to 4 kHz and in a second band above 4 kHz (Cowan *et al.*, 1991). These features were encoded as electrical stimulus parameters, with F_0 being encoded as pulse rate, F_2 being encoded as electrode position on electrodes 2 to 7, overall amplitude being encoded as stimulus intensity, and high-frequency information resulting in stimulation on electrode 8. In addition to the frequency-specific stimulation on electrodes 2 to 7, the voiced/unvoiced contrast was presented as stimulation on electrode 1 for unvoiced sounds. No stimulation was presented on electrode 1 for voiced sounds. The crossover boundaries for the electrodes were 1100, 1300, 1500, 1800, 2000, 2200, and 4000 Hz.

C. Subjects

The subjects were two females (S1 and S5) and two males (S2 and S3) from the group of six normally hearing adults who participated in a previous training study (Galvin *et al.*, 1999). Subject numbering is consistent with that study. Personal commitments prevented S4 and S6 from being involved in the present study. By coincidence, S4 and S6 demonstrated the fastest and the slowest rates, respectively, of word learning in the training study, so that the four remaining subjects form a relatively homogeneous group with respect to learning rate. The number of hours of tactile-alone word recognition training received, the number of words learned, and the learning rate for each subject in the training study are presented in Table II. The subjects had received no visual-alone or combined-modality training, and no tactile-alone training other than the word-level training provided in the previous training study.

D. Experimental setup

The experimental setup was identical to that used for the training study (Galvin *et al.*, 1999). To ensure that the

TABLE II. Number of hours of training received, number of words learned, and learning rate for subjects in a previous tactile-alone word recognition training study.^a

Subject	Hours of training ^b	Words learned	Rate (words/h)
S1	33.1	77	2.3
S2	17.8	46	2.6
S3	12.3	34	2.8
S4	17.7	27	1.5
S5	18.5	62	3.4
S6	12.5	52	4.2

^aGalvin *et al.* (1999).

^bExcludes evaluation time.

stimuli were not audible, the subject wore foam earplugs, received white noise via headphones, and was isolated from the talker inside a soundproof booth. During visual-alone and tactile–visual evaluations, the subject viewed the talker through the booth window. A Mirage DM520 microphone, positioned approximately 15 cm from the talker’s mouth, replaced the standard Tickle Talker™ lapel microphone, allowing the input signal to be delivered through a mixer.

E. Evaluation

Details of the training and evaluation procedures implemented in the training study were reported in Galvin *et al.* (1999). Briefly, the subjects received tactile-alone training on a closed set of words that increased in size as evaluations indicated that the vocabulary was being recognized with 70%–80% accuracy. Within 10 days of the cessation of training, the subjects were evaluated in the present study with a variety of tactile-alone and tactile–visual materials.

The generalization of tactile-alone word recognition skills to unfamiliar talkers was assessed with an unfamiliar male talker and an unfamiliar female talker. A 34-word list, on which all subjects had been trained and evaluated in the training study, was used. The evaluation protocol was the same as that used during the training study; that is, the test list consisted of two random presentations of each word, and subjects responded from a closed-set list. Initial evaluation was with the familiar male talker, followed directly by the two other unfamiliar talkers. The order of these two talkers was randomized across subjects.

The generalization of tactile-alone perceptual skills to the perception of words in sentences was assessed using sentences constructed only from the words each subject learned during training. Details of the individual test list constructed for each subject are presented in Table III, and examples of the sentences used are presented as Appendix A. Two to four words in each sentence were designated as key words, and the sentences were scored by the number of key words perceived correctly. The first subject evaluated, S2, had learned 46 words. Construction of a sentence list based on the presentation of each learned word twice as a key word resulted in 92 key words in 33 sentences. This test list was too long, making it difficult for the subject to maintain concentration. For subsequent subjects, the evaluation protocol used in the training study was followed, so that the number of key words was limited to a maximum of 70, with each learned word

TABLE III. Details of the test list for each subject for the tactile-alone perception of key words in sentences constructed from trained words.

Subj.	Trained words used to construct sentences	Sentences/ list	Key words/ list	Chance ^a (%)	Score (%)
S1	70	24	70	3.0	14.2
S2	46	33	92	7.4	6.5
S3	34	24	68	8.6	17.6
S5	62	24	70	3.5	22.8

^aCalculated by dividing the average number of words per response sentence by the number of trained words used to construct the sentences.

being presented as a key word at least once but no more than twice. Note that subjects were not provided with a word list to refer to during the sentence testing.

The generalization of tactile-alone word recognition skills to the perception of untrained words, and the generalization of tactile perceptual skills to the tactile–visual perception of trained and untrained words, were assessed with a single word list containing both word types. The list (attached as Appendix B) was constructed from 20 untrained words and 20 trained words (these being the first 20 words used in the training study). The untrained words were constructed from the phonemes of the trained words, with each phoneme used only once and no consideration given to phoneme position within a word. This procedure was used to achieve the maximum similarity between the lists. It is not claimed that the procedure produced word lists that were phonemically balanced, as changes in the word position of the phonemes clearly change their acoustic properties. Such balancing would be impossible to achieve, given that the content and order of the trained word list was fixed. Each administration of the list consisted of two random presentations of each word, with subjects responding from a closed-set list. Subjects were evaluated in the tactile-alone, visual-alone, and tactile–visual conditions, with the order of conditions balanced across subjects.

The generalization of tactile perceptual skills to the tactile–visual perception of open-set material was assessed using the Consonant–Nucleus–Consonant (CNC) words test (Peterson and Lehiste, 1962) and the Speech Intelligibility Test (SIT) sentences (Magner, 1972). For the CNC words, each list contained 50 words, and responses were scored for the number of phonemes correct and the number of words correct. For the SIT sentences, each list contained 16 sentences with a total of 80 key words, and responses were scored for the number of key words correct. For each test, two lists were presented in each of the visual-alone and tactile–visual conditions. The lists used were randomized across subjects and conditions, and the order of conditions was balanced across subjects.

The evaluation materials were administered in the following order: sentences constructed from trained words; closed-set trained and untrained words; words presented by unfamiliar talkers; and the CNC words test and the SIT sentences. Nearly all evaluations were completed in the 10-day period following the cessation of training. The only exception was that S3 completed the unfamiliar talker assessment 1 month after the cessation of training, due to other commitments of this subject and the unfamiliar male talker. This

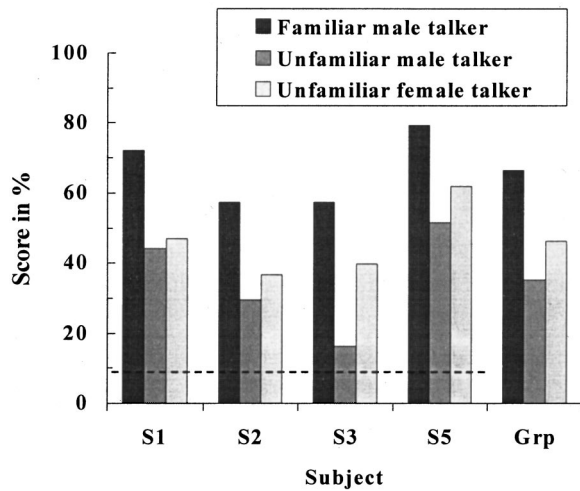


FIG. 1. Individual and group scores for tactile-alone word recognition with the familiar male talker, the unfamiliar male talker, and the unfamiliar female talker. The dashed line represents the 95% confidence limit for scores greater than chance [based on the binomial approximation of Thornton and Raffin (1978)].

deviation from the protocol did not affect the conclusions drawn, as the most important comparison of scores was made across talkers, and S3 completed the evaluations with all three talkers on the same day. For the CNC words test and the SIT sentences, the post-training evaluation was designated evaluation 2. For these tests only, evaluation 1 was conducted during the training study, after the subjects had learned 25 to 30 words. Evaluation 1 was defined as a “midtraining” evaluation.

The evaluation materials were presented live-voice without feedback. With the exception of the evaluations specified as involving unfamiliar talkers, all materials were presented by the same male talker who previously provided the training. The familiar and the two unfamiliar talkers were researchers or clinicians experienced in producing clear speech for artificially deafened research subjects or hearing-impaired clients. The talkers were instructed to present the evaluations using the clear speech they would normally use for communicating with hearing-impaired or artificially deafened individuals. For the sentence evaluations, a medium-paced rate of presentation was used so that the speech was clear but the rate was not slowed to the extent that natural intonation patterns were affected.

III. RESULTS

Figure 1 presents the individual and group scores for tactile-alone word recognition with the familiar talker and the two unfamiliar talkers. The dashed line represents the 95% confidence limit for scores greater than chance, which was calculated using the binomial approximation of Thornton and Raffin (1978). As shown, all subjects scored significantly above chance with the familiar talker and both of the unfamiliar talkers. When evaluated with the familiar talker, S1 and S5 scored above the 70% evaluation criterion used in the training study, whilst S2 and S3 scored just 57.4%. The word recognition skills of S2 and S3 may have been more affected by the fact that training was no longer being re-

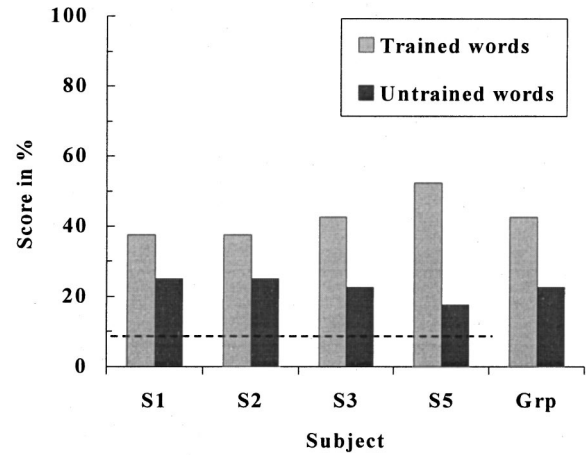
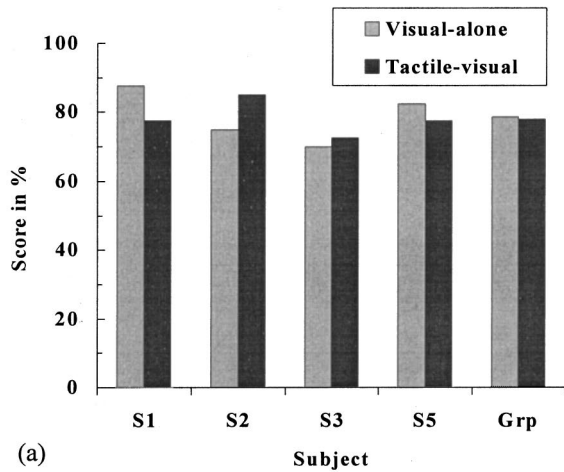


FIG. 2. Individual and group ($n=4$) scores for the tactile-alone recognition of closed-set trained and untrained words. The dashed line represents the 95% confidence limit for scores greater than chance [based on the binomial approximation of Thornton and Raffin (1978)].

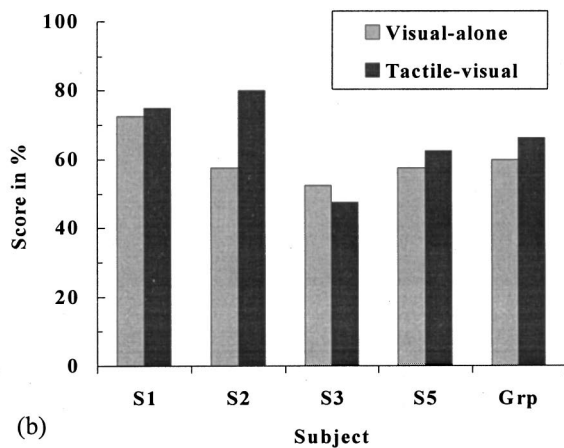
ceived when these evaluations were completed. The skills of S3 may have been particularly affected due to this subject completing this evaluation 4 weeks after training ceased, while the other subjects completed this evaluation within the 10-day post-training period. In addition, in the previous training study, S1 had received more training, and S5 had demonstrated a faster rate of word learning, and these factors may have contributed to the superior scores of these two subjects. The chi-square test for goodness of fit indicated that, for each subject and the group, the scores with the familiar talker were significantly higher than the scores with the unfamiliar male talker [$\chi^2(1, n=68) > 10.8, p < 0.001$] and the unfamiliar female talker [$\chi^2(1, n=68) > 4.2, p < 0.04$]. The chi-square test also indicated that there was no significant difference between the scores with the two unfamiliar talkers for S1, S2, S5, or the group [$\chi^2(1, n=68) < 1.9, p > 0.19$]. For S3, the score with the unfamiliar male talker was significantly lower than the score with the unfamiliar female talker ($\chi^2=9.3, p=0.002$). It should be noted that S3 reported after the event that the voice of the unfamiliar male talker was presented at a lower level than those of the other talkers and had been difficult to detect at times. A possible equipment malfunction may explain the poor score of this subject with this unfamiliar talker.

Table III presents the key-word scores for the tactile-alone perception of sentences constructed from trained words. Chance scores for each subject were calculated by dividing the average number of words per response sentence by the number of trained words used to construct the sentences. The chi-square test for goodness of fit indicated that scores were significantly above chance for S1 [$\chi^2(1, n=70) = 31.3, p < 0.001$], S3 [$\chi^2(1, n=68) = 7.3, p = 0.007$], and S5 [$\chi^2(1, n=70) = 77.7, p < 0.001$], but not for S2 [$\chi^2(1, n=92) = 0.1, p = 0.75$].

Figure 2 presents the individual and group scores for the tactile-alone recognition of a closed set of trained and untrained words. The dashed line represents the 95% confidence limit for scores greater than chance, which was calculated using the binomial approximation of Thornton and



(a)



(b)

FIG. 3. Individual and group scores for the visual-alone and tactile-visual recognition of closed-set trained words (a) and untrained words (b).

Raffin (1978). As shown, all subjects scored significantly above chance on trained and untrained words. The group score of 42.5% on trained words was lower than that reported for the 34-word list in Fig. 1 and the criterion used in the training study. This difference is most likely due to the fact that the 20 trained words were presented in a single list that also included 20 untrained words. An analysis of variance (ANOVA) was conducted on the scores of all subjects for trained and untrained words. The factors in the analysis were subject and word type (trained or untrained). The main effect of word type was significant [$F(1,3)=14.2$, $p=0.033$], indicating that the mean score of 42.5% on trained words was significantly higher than the mean score of 22.5% on untrained words. The main effect of subject was not significant, indicating that performance was similar across subjects.

Figures 3(a) and (b) present the individual and group scores for the visual-alone and tactile-visual recognition of a closed set of trained words and untrained words, respectively. An ANOVA was conducted on the visual-alone and tactile-visual scores of all subjects for trained and untrained words. The factors in the analysis were subject, word type (trained or untrained), and condition. The resulting F statistics and p values are presented in Table IV. The main effect of subject was significant, indicating that, when scores were

TABLE IV. F statistics and p values for the main effects and interaction effects of the ANOVA conducted on the scores for the perception of closed-set words. Scores were obtained from the four subjects for trained and untrained words in the visual-alone and tactile-visual conditions. Boldface type indicates effects which reached significance at $\alpha=0.05$.

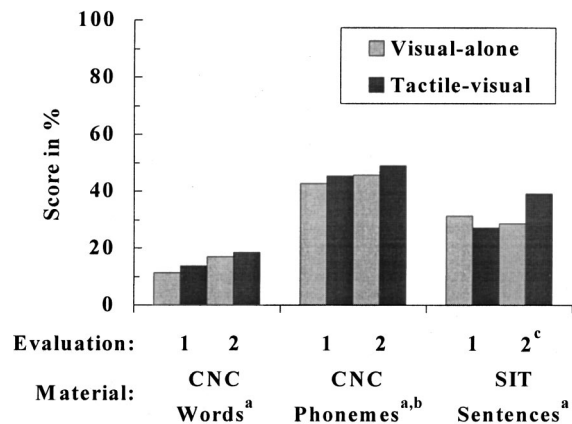
Effect	F	p
Subject ^a	9.8	0.047
Word type ^b	40.2	0.008
Condition ^b	1.4	0.33
Cond \times word type ^b	2.0	0.25
Cond \times subj ^a	3.6	0.16
Word type \times subj ^a	1.7	0.34

^aDegrees of freedom=(3,3).

^bDegrees of freedom=(1,3).

collapsed across conditions and word type, the scores varied significantly across subjects. Tukey's test indicated that the mean score of S3 was significantly lower ($p=0.04$) than that of S1. The main effect of word type was significant, indicating that, when scores were collapsed across subjects and conditions, the mean score of 78.4% for trained words was significantly higher than the mean score of 63.1% for untrained words. The main effect of condition was not significant, indicating that, when scores were collapsed across subjects and word type, there was no significant difference between the mean scores in the visual-alone and tactile-visual conditions. The absence of any significant interaction effects indicated that the findings for the main effects were not significantly different across subjects, conditions, or word types.

Figure 4 presents the mean group scores (collapsed across two lists and four subjects) for CNC words, CNC phonemes, and SIT sentences. Scores were obtained in the visual-alone and tactile-visual conditions at evaluation 1 (midtraining) and evaluation 2 (post-training). For each material, an ANOVA was conducted on the visual-alone and tactile-visual scores of all subjects. The factors in the analysis were subject, evaluation, and condition. The resulting F statistics and p values are presented in Table V. The main effect of subject was significant for all materials, indicating



^a evaluation effect ($p<0.05$); ^b condition effect ($p<0.05$); ^c condition \times evaluation interaction effect ($p<0.05$)

FIG. 4. Group ($n=4$) scores for CNC words, CNC phonemes, and SIT sentences. Scores were obtained in the visual-alone and tactile-visual conditions at evaluation 1 and evaluation 2.

TABLE V. *F* statistics and *p* values for the main effects and interaction effects of the ANOVAs conducted on scores for CNC words, CNC phonemes, and SIT sentences. Scores were obtained from the four subjects at evaluation 1 and evaluation 2 in the visual-alone and tactile–visual conditions. Boldface type indicates effects which reached significance at $\alpha = 0.05$.

Effect		CNC words	CNC phonemes	SIT sentences
Subject ^a	<i>F</i>	18.0	44.8	164.9
	<i>p</i>	<0.001	<0.001	<0.001
Evaluation ^b	<i>F</i>	7.4	7.4	7.2
	<i>p</i>	0.015	0.015	0.017
Condition ^b	<i>F</i>	1.1	5.8	3.3
	<i>p</i>	0.32	0.028	0.089
Cond×eval ^b	<i>F</i>	0.1	0.04	17.0
	<i>p</i>	0.8	0.84	0.001
Cond×subj ^a	<i>F</i>	2.7	1.6	2.4
	<i>p</i>	0.08	0.23	0.11
Eval×subj ^a	<i>F</i>	1.4	2.7	2.3
	<i>p</i>	0.3	0.082	0.12
Eval×subj×cond ^a	<i>F</i>	1.0	0.6	2.3
	<i>p</i>	0.42	0.66	0.12

^aDegrees of freedom=(3,16).

^bDegrees of freedom=(1,16).

that, when scores were collapsed across conditions and evaluations, the scores of some subjects were significantly different from some others. Tukey's test indicated that the mean scores of S1 were significantly higher ($p < 0.002$) than the scores of the other subjects for each material. Furthermore, the mean score of S3 was significantly lower ($p < 0.008$) than those of all other subjects for SIT sentences, and lower than that of S2 for CNC phonemes. The main effect of evaluation was significant for all materials, indicating that, when scores were collapsed across subjects and conditions, the mean scores at evaluation 2 were higher than the mean scores at evaluation 1. However, the actual difference in scores at the two evaluations was quite small, being just 3.4% for CNC phonemes, 5.3% for CNC words, and 4.6% for SIT sentences. The main effect of condition was significant for CNC phonemes, indicating that, when scores were collapsed across subjects and evaluations, the mean score of 47.2% in the tactile–visual condition was significantly higher than the mean score of 44.2% in the visual-alone condition. The only significant interaction effect was a condition by evaluation interaction effect for SIT sentences. This effect indicated that, when scores were collapsed across subjects, the mean score at evaluation 2 of 39% in the tactile–visual condition was significantly higher than the mean score of 27.3% in the visual-alone condition. The absence of any other significant interaction effects indicated that, with the exception of the condition effect for SIT sentences, the findings for the main effects were not significantly different across subjects, evaluations, or conditions.

IV. DISCUSSION

The results demonstrate that the tactile-alone perceptual skills learned during word recognition training were generalized to new tactile-alone contexts, with subjects able to recognize trained words presented by unfamiliar talkers of either gender, trained words presented in sentences, and

tactually new untrained words. The scores achieved were lower than the evaluation criterion used in training, indicating that complete generalization of skills did not occur. This was not surprising, given that the training was limited in amount, type, and number of trainers. In contrast to the tactile-alone results, the generalization of skills to tactile–visual contexts was very limited, with no improvement in tactile–visual over visual-alone scores for the perception of closed-set trained and untrained words or open-set words, and minimal improvement for phonemes in open-set words and words in open-set sentences. It should be acknowledged at this point that it is possible that the subjects' above-chance performance on the tactile-alone evaluations may have been due to their baseline capacity for tactile-alone perception with the Tickle Talker™; i.e., their performance was not influenced by the tactile-alone word recognition training received. However, the extensive clinical experience gained with the device by the authors strongly suggests that such a level of tactile-alone perception could not be achieved without experience and/or training, and that the performance of the present subjects was a function of the training received in the previous study.

Clinical experience with the Tickle Talker™ and previous evaluations of vowel and consonant recognition (Cowan, 1991) suggested that tactile perceptual skills do generalize to unfamiliar talkers, and this was confirmed by the present scores for unfamiliar talkers. However, talkers vary in aspects of production such as pronunciation, vowel duration, vowel *F2*, and frication (Peterson and Barney, 1952; Nabelek, Czyzewski, and Krishnan, 1992). The lower scores for unfamiliar as compared with familiar talkers indicates that some tactile cues varied sufficiently between talkers that they were not recognized when an unfamiliar talker presented the words. The additional variation between male and female talkers did not appear to affect word recognition performance. In particular, female talkers have a higher *F2* frequency than males, with the median difference for American talkers reported as 250 Hz (Peterson and Barney, 1952). Depending upon the frequency of a particular *F2* in relation to the frequency boundaries of the electrodes, a change in the *F2* frequency with a change in talker gender could result in the movement of stimulation to an adjacent electrode. However, it appears that this either did not occur consistently, or did affect word recognition. Female talkers also have a higher *F0* than males. Prosodic information is conveyed by the Tickle Talker™ as relative changes in the rate of stimulation. The perception of relative changes may have been unaffected by the increase in *F0* with the change to a female talker. It is also possible that, irrespective of the talker's gender, the subjects were just not using the *F0* information provided by the Tickle Talker™, as previous research has indicated that stimulus rate is the most difficult parameter to perceive in the tactile signal (Blamey and Clark, 1987).

In the study of Brooks and colleagues (Scilley, 1980), the two subjects trained with female talkers also demonstrated generalization of tactile-alone word recognition skills to unfamiliar talkers that was independent of gender. Further information regarding the generalization of skills to unfamiliar talkers would be gained through using a new talker to

repeat the training study with the present subject group. Given the results so far, an accelerated rate of word learning could be expected during training with a second talker. Such a result was reported for one subject of Brooks and Frost (1983), who demonstrated a continuing decrease in the number of training sessions required to learn 100 words as each of four unfamiliar talkers was introduced.

Three of the present subjects demonstrated generalization of tactile-alone word recognition skills to the perception of key words in sentences, with a mean score of 15.3%. This score was higher than the 1% tactile-alone score of a previous group evaluated on BKB (Bamford–Kowal–Bench) sentences following visual and tactile–visual training using the Tickle Talker™ (Blamey *et al.*, 1989), but lower than the scores generally demonstrated in the present study for words in isolation. Compared to the presentation of isolated words, the sentence format provides additional syntactic and semantic information (Boothroyd and Nittrouer, 1988; Olsen, Van Tasell, and Speaks, 1997), so that subjects performing reasonably well in auditory or visual speech perception typically obtain higher scores for the recognition of words in sentences. In the present study, the predictability of most of the sentences was low, and subjects usually recognized only one or two words per sentence. Therefore, the potential to utilize semantic and syntactic information was limited, and subjects were most likely to be attempting to recognize individual words within the sentences. The lower scores were likely due to the difficulty of perceiving word boundaries and recognizing words whose tactile pattern was altered by coarticulatory effects. Memory may also have played a role. If subjects made perceptual decisions at the completion of a stimulus, then the tactile pattern of the whole sentence would need to have been retained. If, on the other hand, subjects made decisions during the stimulus presentation, then only the recognized words would need to be retained. As the subjects were not queried on this point, it is not known which of these scenarios occurred.

This study does not suggest that the tactile-alone perception of conversational-level speech could be achieved in practice with the Tickle Talker™ at normal rates of speech, and provides only minimal evidence that this could be achieved at a slow, word-by-word rate. Tactile-alone running speech perception has only been reported for users of Tadoma, a communication method developed for deaf–blind people to obtain tactile speech information by resting a hand across the face and throat of a talker. Tadoma was taught in the mid-twentieth century as the primary communication method in a small number of American schools for hearing-impaired children (Schultz *et al.*, 1984). A major social disadvantage of the method was the requirement of touching the talker. Speechtracking scores of 30 to 40 words per minute have been reported for experienced Tadoma users (Reed *et al.*, 1985). Such success has been attributed, in particular, to the rich multidimensional articulatory display provided by the face and the extensive training and experience of the subjects (Reed *et al.*, 1989, 1992). It is impractical for subjects in tactile device studies to obtain levels of training and experience comparable with those of experienced Tadoma users. As a consequence, valid comparisons can only be

made between the performance of tactile device users and the results reported for naive Tadoma users. The present results can be compared with those of two inexperienced Tadoma users who received 26 h of training and learned 43 words (Reed *et al.*, 1982). Average post-training scores for the tactile-alone perception of sentences constructed from trained words were 40% and 20%. Superior scores to those of the present subjects were to be expected, given that Reed's subjects received more training than most of the present subjects, their training included sentence-level tasks, and they were using Tadoma, which is known to supply sufficient information for running speech perception. Nevertheless, with a score of 20%, Reed's poorer performing subject scored similarly to S3 (17.6%) and S5 (22.8%) of the present group. Although interesting, this result does not suggest that experienced Tickle Talker™ users could emulate the performance of experienced Tadoma users.

In our previous training study, it was assumed that subjects were learning to perceive tactile speech cues and then using these skills to recognize new words, given that the subject group required less training time to learn new words as the study progressed (Galvin *et al.*, 1999). The scores in the present study for untrained word perception support the assumption that skills were generalized to untrained words. Lynch *et al.* (1988) also concluded from post-training word recognition scores that their subjects were applying phonologically based tactile knowledge. Brooks *et al.* (1987) concluded that subjects were able to apply general rules about the tactile representation of speech features, as their subjects' post-training score for consonant feature recognition was around 87%.

The incomplete generalization demonstrated by the higher scores on trained as compared with untrained words was possibly due to one or more of four factors. First, tactile speech cues may have been easier to detect in the context of a trained word as this particular context would be familiar to the subject. Second, the subtle differences between some words may have become clearer with repeated exposure during training. Third, the subjects reported that the tactile representation of some words (for example, words containing /s/ or /ʃ/ or long vowels) was highly distinctive so that, with repeated exposure, these words were easily recognized as whole words. Finally, the subjects reported that if a word was recognized as a trained word they often responded without consulting the response list, whereas for untrained words the memory of the tactile pattern had to be retained while the list was scanned. Previous studies have also evaluated untrained word recognition, with reported scores of 4% to 5% for two adults using the Tacticon 1600 (Lynch *et al.*, 1988), 4% for four children using the Tacticon 1600, around 30% for four children using the Tactaid II or the Tacticon 1600 and selecting from a limited response set (Lynch *et al.*, 1989), and 5.1% for one subject evaluated with open-set words (Brooks *et al.*, 1986a).

The generalization of tactile-alone skills to tactile–visual perception was very limited. This was an unexpected result, given that the tactile signal provided information not easily available visually, such as final consonant voicing and vowel second formant. On the other hand, some previous

studies with the Tickle Talker™ (Blamey *et al.*, 1989) and with other tactile devices [see a review by Bernstein (1992)] have demonstrated that subjects may be able to obtain significant amounts of tactile speech-feature information without necessarily gaining an equivalent level of benefit in the combined-modality condition.

These results for combined-modality perception are in contrast to those reported in other studies of tactile-alone word recognition training. Brooks *et al.* (1986a, 1986b) reported percentage-point improvements of 29.3% on open-set words and 17% on open-set sentences when the Queen's University vocoder was added to vision. The very experienced subject had received 65 h of tactile-alone training. Lynch and colleagues compared tactile-alone and tactile-auditory performance. Lynch *et al.* (1989) reported that children using the Tacticon 1600 or the Tactaid II demonstrated respective percentage-point improvements of 39% and 22% for trained words, and 27% and 8% for untrained words. Lynch *et al.* (1988) reported that two adults using the Tacticon 1600 demonstrated percentage-point improvements of 24% for trained words and 15% for untrained words. Lynch's studies differed from the present study in the use of the tactile-auditory evaluation condition, hearing-impaired subjects, and pediatric subjects who had months of multimodality experience using the device in the classroom. In addition, the adults received an average of 44 h of tactile-alone training.

The results of previous studies examining tactile-alone and combined-modality perception using the Tickle Talker™ may contribute to understanding the present results. Blamey *et al.* (1989) compared observed and predicted information transmission scores for combined modalities, and concluded that combining tactile information with visual or auditory information was less effective than combining auditory and visual information. The authors suggested that the effectiveness of the auditory and visual combination might be due to experience and/or the presence of neural mechanisms specialized to this task. Alcántara *et al.* (1993) provided unimodal or tactile-auditory speech-feature perception training. The unimodally trained subjects demonstrated the greatest pre- to post-training improvements in tactile-auditory vowel and consonant recognition, and combined the tactile and auditory information as effectively as the tactile-auditory trained subjects. The authors concluded that improved unimodal perception would contribute to improved tactile-auditory perception without combined-modality training. However, it is important to note that these conclusions were limited to analytic training, the tactile-auditory condition, and speech-feature perception (as similar results were not achieved for the perception of phonemes in words). In a speech-feature training study by Oerlemans and Blamey (1998), subjects received tactile-visual training or unimodal training or tactile-visual training whilst concentrating on one specified modality (bimodal-cued). A greater pre- to post-training increase in scores was demonstrated by the bimodal group for the perception of the vowel, but not consonant, features in words. The authors proposed that the complementary nature of the tactile and visual modalities resulted in greater benefits being gained from bimodal training, while

the redundancy of the auditory and tactile information used in the earlier study of Alcántara *et al.* (1993) resulted in nothing "extra" to be gained from bimodal training.

In conclusion, these previous studies with the Tickle Talker™ and those with other tactile devices suggest a number of factors relating to the tactile device, the subjects, the training, and the evaluation modality may have influenced the results obtained. First, the Tickle Talker™ may have provided less useful speech information than the other tactile devices, although scores reported previously for hearing-impaired adults (Alcántara, 1991; Cowan *et al.*, 1988) suggest it is unlikely that this is the sole explanation. Second, the normally hearing subjects of the present study may not have been as skilled as other hearing-impaired subjects at integrating incomplete speech signals and/or may have ignored the tactile signal when the more familiar visual signal was available. It has previously been suggested that lower than predicted tactile-visual scores may be due to a poor strategy being employed in combined-modality perception (Summers and Du, 1997). Third, the use of "higher level" training materials (i.e., words) may not have been effective in developing combined-modality perceptual skills if, as has previously been suggested for auditory and visual information (Blamey, 1990; Massaro, 1987), visual and tactile information are combined at or before the speech-feature level. Fourth, the amount of training provided may have been insufficient to achieve improved perception at the word and sentence level. Finally, the use of the relatively complementary tactile and visual conditions in the post-training evaluations may have resulted in no benefit being shown from the unimodal training. It is not possible to determine from the present study how influential each of these factors may have been.

The results of this study can be used to consider the potential benefits of tactile-alone training for hearing-impaired users of the Tickle Talker™. As the device was designed to provide supplementary speech information, the usual training program emphasizes combined-modality training, and only includes some basic tactile-alone tasks, such as sound detection and phoneme discrimination (Galvin *et al.*, 1993). Given the information provided by the device, the results of previous speech perception studies, and the tactile-alone sentence scores in the present study, it is clear that the role of the Tickle Talker™ will remain that of providing supplementary speech information. The failure here to demonstrate generalization of skills to the tactile-visual condition suggests that extensive tactile-alone, word-level training would not achieve maximum benefits for hearing-impaired device users. Nevertheless, the generalization of skills to new tactile-alone contexts indicates that there may be a role for more tactile-alone training than has been included previously. Tactile-alone training at the word level may be useful for establishing tactile perceptual skills and introducing the device to the user, and will definitely provide a good opportunity to focus only on the tactile information and to develop the understanding that the tactile signal provides useful speech information.

V. CONCLUSION

The tactile-perceptual skills learned by these subjects in tactile-alone word recognition training generalized to the tactile-alone perception of sentences, untrained words, and words presented by unfamiliar talkers. There was minimal evidence of generalization to the tactile-visual perception of closed-set words, open-set words, or open-set sentences. The tactile-alone results suggest that tactile-alone training at the word level may be a useful component of a training program; however, the tactile-visual results reinforce the importance of combined-modality training. It appears from this result that the emphasis of tactile training programs for hearing-impaired device users should be on combined-modality training. However, future research needs to consider this point in more detail for, unlike the subjects of the present study, hearing-impaired device users will gain combined-modality experience with a tactile device in daily communication. The question that remains unanswered by this study is whether hearing-impaired device users need *formal* combined-modality training, or whether combined-modality experience gained in daily device use may be equally effective in developing the important combined-modality perceptual skills. Clearly, if daily experience were equally effective it would be possible to spend more of the usually finite training time on learning to detect and discriminate the speech cues in the tactile signal. It is possible that this may be most effectively achieved through tactile-alone training. Further investigation of this issue is required.

ACKNOWLEDGMENTS

The authors are grateful for the technical support provided by Anne Lu, and the contributions of three anonymous reviewers. The study was funded by the Commonwealth of Australia, Department of Industry, Science and Tourism through the Cooperative Research Centres Program. The contribution of the parties to the then CRC for Cochlear Implant, Speech and Hearing Research is acknowledged, in particular those of The Bionic Ear Institute and The University of Melbourne's Department of Otolaryngology. The Tickle Talker™ was developed with financial support from the then Department of Industry, Technology and Commerce and the Department of Employment, Education and Training of the Commonwealth Government of Australia, the Australian Research Council through the funding of the Human Communication Research Centre, the National Health and Medical Research Council of Australia, Cochlear Limited, the George Hicks Foundation, and the Ian Potter Foundation.

APPENDIX A

Examples of sentences used in the assessment of tactile-alone sentence perception. Key words used for scoring the subject's response are underlined.

- (1) Put the paper under the house.
- (2) The best jam is red.
- (3) The baby doesn't drink much.
- (4) Did they see the plane?
- (5) The music show is over.

APPENDIX B

Word list for the tactile-alone, visual-alone, and tactile-visual perception of trained and untrained words. The 20 trained words were the first 20 words used in the training study (Galvin *et al.*, 1999). The 20 untrained words were constructed from the phonemes of the 20 trained words, with each phoneme used only once and no consideration given to phoneme position within a word.

Trained words	Untrained words
(1) boy	(1) stork
(2) put	(2) peel
(3) we	(3) wood
(4) see	(4) grave
(5) door	(5) wing
(6) they	(6) geese
(7) house	(7) shower
(8) show	(8) goat
(9) go	(9) thief
(10) thing	(10) soy
(11) what	(11) though
(12) sing	(12) ping
(13) speak	(13) thongs
(14) talking	(14) swung
(15) something	(15) soap
(16) radio	(16) wart
(17) giving	(17) bake
(18) over	(18) doing
(19) little	(19) later
(20) paper	(20) theme

- Alcántara, J. I. (1991). "The effect of training on tactile speech perception," Unpublished Doctoral thesis (University of Melbourne, Australia).
- Alcántara, J. I., Blamey, P. J., and Clark, G. M. (1993). "Tactile-auditory speech perception by unimodally and bimodally trained normal hearing subjects," *J. Am. Acad. Audiol.* **4**, 98-108.
- Bernstein, L. E. (1992). "The evaluation of tactile aids," in *Tactile Aids for the Hearing Impaired*, edited by I. R. Summers (Whurr, London).
- Blamey, P. J. (1990). "Multimodal stimulation for speech perception," in *Information Processing in Mammalian Auditory and Tactile Systems*, edited by M. Rowe and L. Aitkin (Wiley-Liss, New York).
- Blamey, P. J., and Clark, G. M. (1985). "A wearable multiple-electrode speech processor for the profoundly deaf," *J. Acoust. Soc. Am.* **77**, 1619-1620.
- Blamey, P. J., and Clark, G. M. (1987). "Psychophysical studies relevant to the design of a digital electrotactile speech processor," *J. Acoust. Soc. Am.* **82**, 116-125.
- Blamey, P. J., Cowan, R. S. C., Alcántara, J. I., Whitford, L. A., and Clark, G. M. (1989). "Speech perception using combinations of auditory, visual and tactile information," *J. Rehabil. Res. Dev.* **26**, 15-24.
- Boothroyd, A., and Nittrouer, S. (1988). "Mathematical treatment of context effects in phoneme and word recognition," *J. Acoust. Soc. Am.* **84**, 101-114.
- Brooks, P. L., Frost, B. J., Mason, J. L., and Gibson, D. M. (1986a). "Continuing evaluation of the Queen's University tactile vocoder. I. Identification of open set words," *J. Rehabil. Res. Dev.* **23**, 119-128.
- Brooks, P. L., Frost, B. J., Mason, J. L., and Gibson, D. M. (1986b). "Continuing evaluation of the Queen's University tactile vocoder. II. Identification of open set sentences and tracking narrative," *J. Rehabil. Res. Dev.* **23**, 129-138.
- Brooks, P. L., Frost, B. J., Mason, J. L., and Gibson, D. M. (1987). "Word and feature identification by profoundly deaf teenagers using the Queen's University tactile vocoder," *J. Speech Hear. Res.* **30**, 137-141.
- Brooks, P. L., and Frost, B. J. (1983). "Evaluation of a tactile vocoder for word recognition," *J. Acoust. Soc. Am.* **74**, 34-39.
- Brown, B. H., and Stevens, J. C. (1992). "Electrical stimulation of the

- skin," in *Tactile Aids for the Hearing Impaired*, edited by I. R. Summers (Whurr, London).
- Cowan, R. S. C. (1991). "Speech feature encoding through an electrotactile speech processor," Unpublished Doctoral thesis (University of Melbourne, Australia).
- Cowan, R. S. C., Alcántara, J. I., Blamey, P. J., and Clark, G. M. (1988). "Preliminary evaluation of a multichannel electrotactile speech processor," *J. Acoust. Soc. Am.* **83**, 2328–2338.
- Cowan, R. S. C., Alcántara, J. I., Whitford, L. A., Blamey, P. J., and Clark, G. M. (1989). "Speech perception studies using a multichannel electrotactile speech processor, residual hearing, and lipreading," *J. Acoust. Soc. Am.* **85**, 2593–2607.
- Cowan, R. S. C., Blamey, P. J., Galvin, K. L., Sarant, J. Z., Alcántara, J. I., and Clark, G. M. (1990). "Perception of sentences, words, and speech features by profoundly hearing-impaired children using a multichannel electrotactile speech processor," *J. Acoust. Soc. Am.* **88**, 1374–1384.
- Cowan, R. S. C., Blamey, P. J., Sarant, J. Z., Galvin, K. L., and Clark, G. M. (1991). "Perception of multiple electrode stimulus patterns: Implications for the design of an electrotactile speech processor," *J. Acoust. Soc. Am.* **89**, 360–368.
- Engelmann, S., and Rosov, R. (1975). "Tactual hearing experiment with deaf and hearing subjects," *Except. Child.* **41**, 243–253.
- Galvin, K. L., Cowan, R. S. C., Sarant, J. Z., Blamey, P. J., and Clark, G. M. (1993). "Factors in the development of a training program for use with tactile devices," *Ear Hear.* **14**, 118–127.
- Galvin, K. L., Blamey, P. J., Oerlemans, M., Cowan, R. S. C., and Clark, G. M. (1999). "Acquisition of a tactile-alone vocabulary by normally hearing users of the Tickle Talker™," *J. Acoust. Soc. Am.* **106**, 1084–1089.
- Geers, A. E., and Moog, J. S. (1995). "Effectiveness of cochlear implants and tactile aids for deaf children: The sensory aids study at Central Institute for the Deaf," *Volta Rev.* **95**(5).
- Kessler, D. K. (1993). "The CLARION multi-strategy cochlear implant," *Ann. Otol. Rhinol. Laryngol.* **177**, 8–16.
- Kishon-Rabin, L., Boothroyd, A., and Hanin, L. (1996). "Speechreading enhancement: A comparison of spatial–tactile display of voice fundamental frequency (F_0) with auditory F_0 ," *J. Acoust. Soc. Am.* **100**, 593–602.
- Lane, H., and Bahan, B. (1998). "Ethics of cochlear implantation in young children: a review and reply from a Deaf-World perspective," *Otolaryngol.-Head Neck Surg.* **119**, 297–313.
- Lynch, M. P., Eilers, R. E., Oller, D. K., and LaVoie, L. (1988). "Speech perception by congenitally deaf subjects using an electrocutaneous vocoder," *J. Rehabil. Res. Dev.* **25**, 41–50.
- Lynch, M. P., Eilers, R. E., Oller, D. K., and Cobo-Lewis, A. (1989). "Multisensory speech perception by profoundly hearing-impaired children," *J. Speech Hear. Dis.* **54**, 57–67.
- Magner, M. E. (1972). *A Speech Intelligibility Test for Deaf Children* (Clarke School for the Deaf, Northampton, MA).
- Massaro, D. W. (1987). *Speech Perception by Ear and Eye: A Paradigm for Psychological Inquiry* (Erlbaum, Hillsdale, NJ).
- Nabelek, A. K., Czyzewski, Z., and Krishnan, L. A. (1992). "The influence of talker differences on vowel identification by normal-hearing and hearing-impaired listeners," *J. Acoust. Soc. Am.* **92**, 1228–1246.
- Oerlemans, M., and Blamey, P. J. (1998). "Touch and auditory–visual speech perception," in *Hearing By Eye II*, edited by R. Campbell, B. Dodd, and D. Burnham (Psychology, Hove, UK).
- Oller, D. K. (1995). "Tactile aids for the hearing impaired: An overview," *Semin. Hearing* **16**, 289–295.
- Olsen, W. O., Van Tasell, D. J., and Speaks, C. E. (1997). "Phoneme recognition for words in isolation and in sentences," *Ear Hear.* **18**, 175–186.
- Osberger, M. J., Fisher, L., and Murad, C. (1996). "Clinical results with the CLARION® multi-strategy cochlear implant in children," *Cochlear Implants, Proceedings of the XVI World Congress of Otorhinolaryngology Head and Neck Surgery, Sydney, 2–7 March 1997*, edited by G. M. Clark (Monduzzi Editore, Bologna, Italy).
- Parkinson, A. J., Parkinson, W. S., Tyler, R. S., Lowder, M. W., and Gantz, B. J. (1998). "Speech perception performance in experienced cochlear-implant patients receiving the SPEAK processing strategy in the Nucleus Spectra-22 cochlear implant," *J. Speech Lang. Hear. Res.* **41**, 1073–1087.
- Peterson, G. E., and Barney, H. L. (1952). "Control methods used in a study of the vowels," *J. Acoust. Soc. Am.* **24**, 585–597.
- Peterson, G. E., and Lehiste, I. (1962). "Revised CNC lists for auditory tests," *J. Speech Hear. Res.* **27**, 62–70.
- Plant, G. (1992). "The use of tactile aids with congenitally deaf adults. Is it worthwhile? A case study," *Proceedings of the Second International Conference on Tactile Aids, Hearing Aids, and Cochlear Implants*, edited by A. Risberg, S. Felicetti, G. Plant, and K.-E. Spens [Royal Institute of Technology (KTH), Department of Speech Communication & Music Acoustics, Stockholm, Sweden].
- Plant, G. L. (1995). "Training approaches with tactile aids," *Semin. Hear.* **16**, 394–403.
- Plant, G. (1998). "Training in the use of a tactile supplement to lipreading: A long-term case study," *Ear Hear.* **19**, 394–406.
- Reed, C. M., and Delhorne, L. A. (1995). "Current results of a field study of adult users of tactile aids," *Semin. Hear.* **16**, 305–315.
- Reed, C. M., Doherty, M. J., Braidia, L. D., and Durlach, N. I. (1982). "Analytic study of the Tadoma method: Further experiments with inexperienced observers," *J. Speech Hear. Res.* **25**, 216–223.
- Reed, C. M., Durlach, N. I., Delhorne, L. A., Rabinowitz, W. M., and Grant, K. W. (1989). "Research on tactual communication of speech: Ideas, issues, and findings," *Volta Rev. Mono.* **91**, 65–78.
- Reed, C. M., Rabinowitz, W. M., Durlach, N. I., Braidia, L. D., Conway-Fithian, S., and Schultz, M. C. (1985). "Research on the Tadoma method of speech communication," *J. Acoust. Soc. Am.* **77**, 247–257.
- Reed, C. M., Rabinowitz, W. M., Durlach, N. I., Delhorne, L. A., Braidia, L. D., Pemberton, J. C., Mulcahey, B. D., and Washington, D. L. (1992). "Analytic study of the Tadoma method: Improving performance through the use of supplementary tactual displays," *J. Speech Hear. Res.* **35**, 450–465.
- Schultz, M. C., Norton, S. J., Conway-Fithian, S., and Reed, C. M. (1984). "A survey of the use of the Tadoma method in the United States and Canada," *Volta Rev.* **86**, 282–292.
- Scilley, P. L. (1980). "Evaluation of a vibrotactile auditory prosthetic device for the profoundly deaf," Unpublished Masters thesis (Queen's University, Ontario).
- Sherrick, C. E. (1984). "Basic and applied research on tactile aids for deaf people: Progress and prospects," *J. Acoust. Soc. Am.* **75**, 1325–1342.
- Sherrick, C. E., and Craig, J. C. (1982). "The psychophysics of touch," in *Tactual Perception*, edited by W. Schiff and E. Foulke (Cambridge University Press, Cambridge).
- Staller, S. J., Beiter, A. L., and Brimacombe, J. A. (1995). "Use of the Nucleus 22-channel cochlear implant system with children," *Volta Rev. Mono.* **96**, 15–39.
- Summers, I. R., and Du, J. (1997). "Integration of visual and tactile modalities," *Scand. Audiol. Suppl.* **47**, 29–33.
- Thornton, A. R., and Raffin, M. J. (1978). "Speech discrimination scores modelled as a binomial variable," *J. Speech Hear. Res.* **21**, 507–518.
- Tucker, B. P. (1998). "Deaf culture, cochlear implants, and elective disability," *Hastings Cent. Rep.* **28**(4), 6–14.
- Verrillo, R. T., and Gescheider, G. A. (1992). "Perception via the sense of touch," in *Tactile Aids for the Hearing Impaired*, edited by I. R. Summers (Whurr, London).
- Weisenberger, J. M. (1992). "Communication of the acoustic environment via tactile stimuli," in *Tactile Aids for the Hearing Impaired*, edited by I. R. Summers (Whurr, London).
- Weisenberger, J. M. (1995). "Factors influencing benefit from tactile aids," *Semin. Hear.* **16**, 343–355.
- Weisenberger, J. M., Broadstone, S. M., and Saunders, F. A. (1989). "Evaluation of two multichannel tactile aids for the deaf," *J. Acoust. Soc. Am.* **86**, 1764–1775.

Simultaneous effects on vowel duration in American English: A covariance structure modeling approach

Molly L. Erickson

*Department of Audiology and Speech Pathology, University of Tennessee—Knoxville,
457 South Stadium Hall, Knoxville, Tennessee 37996-0740*

(Received 9 November 1999; accepted for publication 5 September 2000)

The powerful techniques of covariance structure modeling (CSM) long have been used to study complex behavioral phenomenon in the social and behavioral sciences. This study employed these same techniques to examine simultaneous effects on vowel duration in American English. Additionally, this study investigated whether a single population model of vowel duration fits observed data better than a dual population model where separate parameters are generated for syllables that carry large information loads and for syllables that specify linguistic relationships. For the single population model, intrinsic duration, phrase final position, lexical stress, post-vocalic consonant voicing, and position in word all were significant predictors of vowel duration. However, the dual population model, in which separate model parameters were generated for (1) monosyllabic content words and lexically stressed syllables and (2) monosyllabic function words and lexically unstressed syllables, fit the data better than the single population model. Intrinsic duration and phrase final position affected duration similarly for both the populations. On the other hand, the effects of post-vocalic consonant voicing and position in word, while significant predictors of vowel duration in content words and stressed syllables, were not significant predictors of vowel duration in function words or unstressed syllables. These results are not unexpected, based on previous research, and suggest that covariance structure analysis can be used as a complementary technique in linguistic and phonetic research. © 2000 Acoustical Society of America.

[S0001-4966(00)01812-9]

PACS numbers: 43.70.Aj, 43.70.Bk [AL]

I. INTRODUCTION

The prediction of vowel duration in connected speech has suffered from five methodological weaknesses. First, experimental studies that examine the effects of specific factors on vowel duration in controlled environments do not provide insight regarding how these factors interact to affect vowel duration in continuous speech. Second, observational studies that fit *post hoc* models to continuous speech, while contributing a great deal to our understanding of the distributional properties of speech, may not necessarily have any theoretical significance, nor can they be generalized to other data. Third, many of the factors that are believed to affect vowel duration in speech, for example, intrinsic duration, are essentially unmeasurable constructs; that is, their effects are mediated or obscured by other factors during speech production. Fourth, many factors that affect vowel duration may covary. A model of vowel duration must be able to include expected covariances. Fifth, durational models are typically constructed using categorical variables and factorial designs. Such designs work well with balanced data sets, but not with continuous speech.

In this paper, covariance structure modeling (CSM) is used to test an additive linear model of vowel duration. CSM, as implemented in this study, minimizes the methodological weaknesses described above because: (1) it requires the researcher to specify theoretical relationships prior to application of the statistical technique so that outcomes are less likely to be specific to one set of data and may be generalized to other contexts; (2) it incorporates a factor analysis

component that allows the estimation of latent variables through the use of multiple measurable, or manifest, variables; (3) it can simultaneously incorporate covariances between factors; and (4) it requires only that data be normally distributed, not balanced.

A. Organization of the paper

The paper consists of five major sections. This section, the Introduction, includes subsections dealing with the following topics: factors affecting vowel duration, models of vowel duration, covariance structure analysis, and covariance structure models of vowel duration. The next major section, Preliminary Experiment (Sec. II), describes the method and results of an experiment designed to calculate the means and medians necessary for the development of a covariance structure model of vowel duration. The preliminary experiment is followed by major sections presenting the methods (Sec. III), results (Sec. IV), discussion (Sec. V), and summary and conclusions (Sec. VI) of the main experiment, i.e., the analysis of a covariance structure model of vowel duration.

B. Factors affecting vowel duration

Early research examining vowel duration utilized highly controlled experimental paradigms in order to deduce the effects of specific factors. Typically, vowel duration was examined in stressed syllables of minimally contrasting one-, two-, or three-syllable content words. These studies suggest

that vowel duration is predicted by numerous factors, including: intrinsic duration, post-vocalic consonant voicing, position in word, lexical stress, and phrase final position.

Experimental studies have provided converging evidence that English vowels exhibit an intrinsic duration (House, 1961; Peterson and Lehiste, 1960). These studies have shown that tense vowels exhibit longer durations than lax vowels and low vowels exhibit longer durations than high vowels.

Researchers long have recognized that English vowels in prepausal position are longer when followed by a voiced consonant than they are when followed by a voiceless consonant (Heffner, 1937; House, 1961; House and Fairbanks, 1953; Jones, 1940; Kenyon, 1924). This effect has also been demonstrated in monosyllabic content words embedded in carrier phrases (Peterson and Lehiste, 1960).

Numerous researchers have constructed highly controlled studies designed to test the effect of number of syllables in the word on vowel duration. In English, such research has focused almost exclusively on vowel duration in a stressed root syllable followed by multiple suffix syllables (Klatt, 1973; Lehiste, 1972; Port, 1981). This research has demonstrated that vowels in stressed roots are shortened as suffix syllables are added. However, research by Umeda and colleagues showed that vowel duration is affected by the number of syllables in the word in carrier sentences (Harris and Umeda, 1974), but not in continuous speech (Umeda, 1972, 1975). Nootboom (1972) examined the effect of number of syllables in the word on both stressed and unstressed vowel duration in Dutch. He found that both stressed and unstressed vowels were shortened as the number of syllables in the word increased; however, the effect was reduced for unstressed syllables.

Controlled studies have shown that increased vowel duration is one of several correlates of lexical stress (Fry, 1955, 1958; Lieberman, 1960; Morton and Jassem, 1965). Other correlates of lexical stress included increased intensity, change in fundamental frequency, and vowel quality.

Finally, phrase final position has been shown to affect vowel duration. Numerous researchers have found evidence of phrase final lengthening of stressed and unstressed syllable nuclei in English (Berkovits, 1984; Klatt, 1975; Oller, 1973).

C. Models of vowel duration

Each of the five factors presented above has been shown to predict vowel duration in controlled studies. The next logical step for researchers has been to determine the degree to which such factors in combination may predict vowel duration in connected speech. Several approaches have been taken to this problem. The choice of approach is often dictated by the purpose of the model. One purpose of modeling is to test theory. As van Santen (1992) points out, there are great differences between theoretical models and empirical models. Theoretical models are concerned more with underlying processes. Completeness or even a high degree of predictive accuracy are not as important in such models as is evidence of fundamental processes. Predictive models, on

the other hand, are less concerned with theory and more concerned with simple and accurate prediction of duration.

In an attempt to develop a predictive model of duration for speech synthesis, Klatt (1973) considered a model combining two shortening factors, voiceless post-vocalic consonant and the number of following syllables in the word. He found that the simultaneous shortening effect of these two factors was less than would be expected if they were linearly combined, and thus concluded that speech was “incompressible.” In 1976, Klatt published the following model:

$$D_o = k(D_i - D_{\min}) + D_{\min}, \quad (1)$$

where D_o = output duration, D_i = intrinsic duration, D_{\min} = minimum possible duration, and k is a constant that is specific to each effect. While this model has been shown to account for between 70% (Campbell, 1990a) and 90% (Klatt, 1976) of the durational variance in some speech samples, such predictive ability is accomplished by “fitting” the model atheoretically to each data set.

On the other hand, other researchers have developed durational models based on phonetic and linguistic theory. Such research seems to suggest that phonologically specified shortening factors (Port, 1981) and lengthening factors (Cunimins, 1999) combine additively, while nonphonological factors such as number of syllables in the word (Port, 1981) combine subadditively, and are therefore “incompressible.”

Early durational models attempted to predict duration at the segment level. However, English has long been perceived as stress-timed (Classe, 1939). Numerous researchers believe that timing is to some degree controlled at the stress-foot level (Lehiste, 1977; Scott, 1980). Recent research suggests that timing may be controlled at multiple levels, including the phrase level and the syllable level (Campbell and Isard, 1991; Edwards and Beckman, 1988). Models incorporating higher-level timing factors typically examine duration at the syllable level (Bailly, 1989; Campbell, 1990b) and include factors such as the number of phonemes in the syllable, pitch accent, position of syllable in the foot, position of syllable in the phrase, and lexical stress (Campbell and Isard, 1991).

Regardless of level, all durational models must overcome two difficulties—nonlinearity and interactional effects. The inherent “incompressibility” of speech implies that durations may asymptotically approach a minimum. Some researchers also believe that expandability constraints are placed on speech durations (Cooper *et al.*, 1985; Berkovits, 1991). Thus at least for extreme values, vowel duration is likely a nonlinear phenomenon.

Durational effects have also been shown to interact. Both Klatt (1973) and Port (1981) have shown that the effect of post-vocalic consonant voicing reduces as the number of syllables in the word increases. Likewise, the effect of post-vocalic consonant voicing increases in sentence final position (van Santen, 1992). Completeness and accuracy of duration modeling requires the inclusion of interaction terms. However, when modeling any natural phenomenon, completeness must be balanced with parsimony. In an attempt to develop a complete, yet parsimonious model of vowel duration, van

Santen (1992) examined the effects of vowel identity, accent, syllabic stress, pre-vocalic consonant, post-vocalic consonant, number of preceding syllables, number of following syllables, and utterance position on vowel duration. He concluded that the model required only two major interactions; one between pitch accent and syllabic stress and a second between post-vocalic consonant voicing and position in utterance.

D. Covariance structure analysis

The techniques of covariance structure analysis allow researchers to test complicated models of behavioral and natural phenomena. The term ‘‘covariance structure analysis’’ was introduced by Bock and Bargmann (1966) to describe their confirmatory factor analytic procedure. Since then, the model has been expanded and generalized. Today, the term ‘‘covariance structure modeling’’ (CSM) is applied to many of these generalized models. However, the term is most commonly associated with the form of the model developed by several researchers in the early 1970s (Jöreskog, 1973; Jöreskog and van Thillo, 1972; Keesling, 1972; Wiley, 1973). It is this form of the model that will be discussed in this paper. For a more complete description of covariance structure modeling, the reader is referred to the following: Asher (1983), Long (1983), Maruyama (1998), Peyrot (1996), and Youngblut (1994a, b).

Many factors of interest in science are latent or unobserved. These latent factors may often be defined by one or more manifest or observed variables. Covariance structural modeling provides a method of testing the linear relationships between latent dependent factors and latent independent factors through observing the inter-correlations of the manifest independent and dependent variables.

Covariance structure modeling is based on the general linear model, as are many other important statistical techniques (e.g., multiple regression and factor analysis). However, covariance structure modeling differs from techniques such as multiple regression and factor analysis in one important way: covariance structure modeling is a confirmatory (or, more accurately, disconfirmatory) technique. Unlike the more commonly used exploratory multivariate techniques, covariance structure modeling forces the researcher to specify the relationships between the variables of interest prior to applying the technique, rather than simply allowing the statistical algorithm to atheoretically choose the model which best fits the data.

1. The model

Essentially, covariance structure analysis combines the techniques of path analysis, factor analysis, and multiple regression in a manner that allows the testing of hypothesized models, which are represented by specified patterns of covariances, factor loadings, and simultaneous regressions. Covariance structure models merge two component models: (1) the measurement model and (2) the structural equation model.

a. Measurement model. Because covariance structure models typically employ latent independent and dependent factors, the parameters of the structural model may not be

estimated until the relationships between these latent factors and their corresponding manifest independent and dependent variables are specified. The measurement model specifies these relationships with two linear equations. The first equation specifies the relationships between the independent manifest variables and the latent independent factors:

$$x = \Lambda_x \xi + \delta, \quad (2)$$

where x is a vector of the manifest independent variable measures; Λ_x is a matrix of loadings of x on the latent dependent factors; and δ is a vector of measurement errors, or unique variance, associated with x .

The second equation specifies the relationships between the manifest dependent variables and the latent dependent factors:

$$y = \Lambda_y \eta + \epsilon, \quad (3)$$

where y is a vector of the manifest dependent variable measures; Λ_y is a matrix of loadings of y on the latent dependent factors; and ϵ is a vector of measurement errors, or unique variance, associated with y .

b. The structural equation model. The structural equation model specifies the linear relationships between multiple independent and one or more dependent variables. Usually, these variables are unmeasurable constructs, and, therefore, latent factors; however, they also may be manifest variables. These relationships are specified by the linear equation:

$$\eta = \Gamma \xi + \zeta, \quad (4)$$

where η is a vector of latent dependent factors or variables; ξ is a vector of latent independent factors or variables; Γ represents a matrix of the regression coefficients for the regression of the latent independent factors on latent dependent factors; and ζ is a vector of residuals.

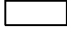


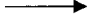

2. Defining a covariance structure model

The relationships among the variables and factors described in the two models are simultaneously examined in covariance structure modeling. It is necessary for the researcher to specify the hypothetical relationships between the variables and factors prior to employing covariance structure techniques. Typically, the researcher constructs a path diagram reflecting the hypothesized relationships among the variables and factors. Conventionally, measured variables are represented by rectangles, latent factors are represented by ovals, and error terms are represented by circles. Hypothesized linear relationships are indicated by straight lines, while covariances are indicated with curved lines. These symbols are illustrated in Table I.

3. Estimation of the model parameters and calculation of the expected covariances

Parameters for covariance structure models may be estimated by least squares, unweighted least squares, generalized least squares, or maximum likelihood estimation techniques. Estimated parameters are used to calculate a matrix of expected covariances among the observed variables. The model fit is determined by comparing the expected covariance matrix to the actual covariance matrix.

TABLE I. Common symbols used in CSM.

Symbol	Meaning
	Measured variable
	Latent variable
	Error
	Linear equation
	Covariance

4. Evaluation of the model

Covariance structure models may be evaluated in several ways. The most important of these methods are described below.

a. Chi-square goodness-of-fit test. The estimated covariance matrix may be compared to the actual covariance matrix by calculating a chi-square goodness-of-fit statistic (Bentler and Weeks, 1980). The null hypothesis H_0 is that there is no difference between the actual and estimated covariance matrices. Large chi-square values in relation to degrees of freedom yield lower alpha probabilities that observed differences occur by chance. Thus models that generate large chi-square values would not be considered to fit the data well. Unfortunately, because chi-square values are partly a function of N , models with large sample sizes, and, consequently, large chi-square values, may be rejected unnecessarily.

b. Fit indexes. Numerous fit indexes have been designed to overcome dependence on sample size. These fit indexes are based on the concept of nested models. The hypothesized model is compared to a highly restricted version of itself, the null model, and to an unrestricted version of itself, the saturated model. The null model constrains all covariances to be equal to zero and would be unlikely to fit any data well. The saturated model contains as many estimated parameters as there are nonredundant variances and covariances and will always fit the data exactly. Since the hypothesized model of interest lies somewhere on the continuum between these two extreme models, its chi-square goodness-of-fit statistic and degrees of freedom also lie between those generated by these extreme models.

A detailed description of the numerous fit indexes is beyond the scope of this paper. For more information, the reader is directed to Hu and Bentler (1995) and Maruyama (1998). One commonly used fit index, the Comparative Fit Index (CFI), has been described by Bentler (1995). The CFI is based on the idea that, in large samples, if the model of interest is a true model, then its goodness-of-fit statistic is asymptotically distributed as a central chi-square variate with a noncentrality parameter, τ_k , which equals zero. Larger values of τ_k reflect greater model misspecifications. The CFI is determined as follows:

$$CFI = (\tau_i - \tau_k) / \tau_i, \quad (5)$$

where τ_i equals the noncentrality parameter of the null

model and τ_k equals the noncentrality parameter of the model of interest. Thus CFI values close to one imply that the model fits the data well. CFI values close to zero imply that the model does not fit the data well.

A fit index such as the CFI can show whether or not a given model is an improvement over the null model. That is, a CFI value of 0.5 indicates that the model of interest lies midway between the null model and the best fit model. However, there are no rigorous methods to determine the “significance” of improvement over the null model. A rule-of-thumb interpretation is that a model with a fit index of less than 0.90 could be improved (Bentler and Bonnet, 1980; Maruyama, 1998). This does not necessarily mean that models with fit index values of less than 0.90 should be discarded. As Bollen (1989) points out, the 0.90 cutoff value is arbitrary. Maruyama reminds us that often the purpose of the model is not to describe the most complete model, but rather to specify relationships between parameters. In such cases, the model fit may not be optimal, but the parameter estimates may be significant and supportive of theory.

Neither can an index such as the CFI be used to demonstrate that the proposed model is significantly better than any number of arbitrary models. Instead, fit index values must be evaluated in the context of the theoretical viability of the model. Consider two situations: models that are essentially equivalent, and models that have been improved through atheoretical manipulation. The three models, A predicts B, B predicts A, and A covaries with B, are equivalent and generate identical fit indices. Yet it is possible that only one may be theoretically valid. Likewise, one could, through analysis of the covariance structure, devise an arbitrary model that generates larger fit index values than the theoretical model. In fact, the best fitting model may be one with no theoretical significance and may not represent the true underlying processes (MacCallum *et al.*, 1993). Thus models must always be assessed by simultaneous evaluation of fit index values and theoretical significance.

5. Comparisons of competing models

Two competing models may be tested using covariance structure analysis if one of the models is restricted in such a way that it is a subset of the other (Bentler and Bonnet, 1980). This situation is identical to that presented above where the model of interest was compared to a highly restricted version of itself, the null model. The same goodness-of-fit tests and improvement-of-fit indexes apply.

One such test, the Lagrange Multiplier (LM), evaluates the effect of adding free parameters to a more restricted model. This test is asymptotically equivalent to the chi-square difference test. LM tests also can be used to test the model parameter invariance across separate populations.

6. Cautions concerning the use of CSM

The powerful statistical analysis technique of covariance structure modeling may be misused by the unwary. It is important to keep in mind that the basic principles of scientific inference still apply, regardless of which statistical or mathematical modeling technique is employed to analyze data.

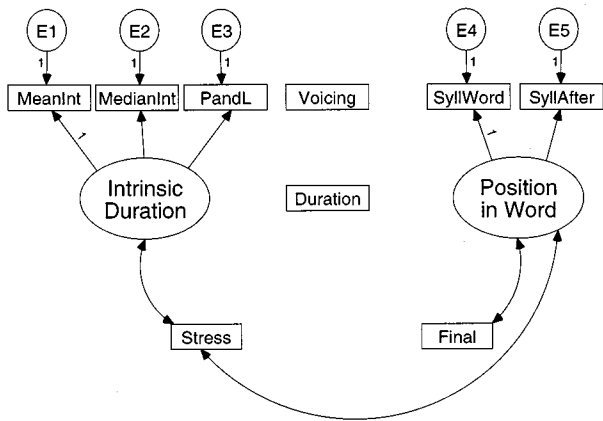


FIG. 1. Measurement component for a covariance structure model of English vowel duration.

Many possible models will fit a given set of data equally well (Cliff, 1983; MacCallum *et al.*, 1993). Thus a model cannot be confirmed by the data, only disconfirmed. The legitimacy of a model rests in its theoretical significance, not in its statistical significance. Cliff points out that correlational data based on observation do not allow for the systematic manipulation of variables necessary to suggest causation. Instead, causation must be suggested by converging evidence in the literature.

E. A covariance structure model of vowel duration

CSM typically has been used to model complex behavioral phenomenon (e.g., Boyle and Pickles, 1997; Prussia *et al.*, 1993). Rarely has this powerful modeling technique been used in the speech, language, and hearing sciences. This paper proposes a covariance structure model of vowel duration based on converging evidence provided by previous highly controlled experimental research. The proposed model examines the effects on vowel duration of the following five factors: (1) intrinsic vowel duration; (2) post-vocalic consonant voicing; (3) position in word; (4) lexical stress; and (5) phrase final position.

1. The measurement model

The measurement component of the proposed covariance structure model of vowel duration specifies the relationship of the manifest variables to the latent factors and also specifies hypothesized covariances between independent factors and variables. The measurement component proposed in this study is presented graphically in Fig. 1.

The proposed measurement component is comprised of two hypothesized independent latent factors, intrinsic duration and position in word, three independent manifest variables, post-vocalic consonant voicing, lexical stress, and phrase final position, and the dependent manifest variable, vowel duration.

In 1960, Peterson and Lehiste defined intrinsic vowel duration as the average duration of syllable nuclei in minimally contrasting monosyllables whose final consonants differ only in terms of presence or absence of voicing. This definition implies that intrinsic duration is a latent factor that

only can be deduced by reducing the effects of other durational factors through processes such as averaging. CSM is an ideal modeling strategy for such an unmeasurable phenomenon. For this study, three measurable estimations of intrinsic duration were used to define this latent factor. These measures, indicated in rectangles and connected by arrows to the factor intrinsic duration, are precisely defined in Sec. II.

The effect of position in word on vowel duration is typically measured by calculating the number of following syllables in the word (Lehiste, 1972; Port, 1981). However, some researchers have also considered the total number of syllables in the word as a predictor of duration (Oller, 1973). Others have examined the effect of the number of preceding syllables on duration (van Santen, 1992). All of these measures are highly correlated. The proposed model considers word positional effects on duration to be a latent factor defined in part by the number of following syllables in the lexical word and in part by the number of total syllables in the lexical word.

The proposed covariance structure model assumes three theoretical covariances. First, lexical stress is hypothesized to covary with position in word because this model treats lexical stress as a relative measure that is only realized in polysyllabic words. Second, lexical stress is hypothesized to covary with intrinsic duration because unstressed syllables are often associated with intrinsically short vowels (Fry, 1964). Third, phrase final position is hypothesized to negatively covary with position in word because it is impossible for any but the last syllable of a polysyllabic word to occur in phrase final position.

The measurement component of the proposed covariance structure model requires the estimation of the following parameters:

- (1) Regression coefficients of the hypothesized factors on the measured variables.
- (2) Residual variances of the measured independent variables. These variances apply only to those measured variables that actually contribute to a factor. Single variables have no residuals and, therefore, no residual variances.
- (3) Covariances among factors and/or single variables.

The general equations specifying the relationships in the measurement component are listed below. Λ_X represents loadings of the latent factor on the manifest variable.

$$\text{MeanInt} = \Lambda_1(\text{intrinsic duration}) + E1, \quad (6)$$

$$\text{MedianInt} = \Lambda_2(\text{intrinsic duration}) + E2, \quad (7)$$

$$\text{PandL} = \Lambda_3(\text{intrinsic duration}) + E3, \quad (8)$$

$$\text{SyllWord} = \Lambda_4(\text{position in word}) + E4, \quad (9)$$

$$\text{SyllAfter} = \Lambda_5(\text{position in word}) + E5. \quad (10)$$

Variances to be estimated include those for $E1$, $E2$, $E3$, $E4$, $E5$, post-vocalic consonant voicing, lexical stress, and phrase final position. Covariances to be estimated include those between lexical stress and position in word, lexical

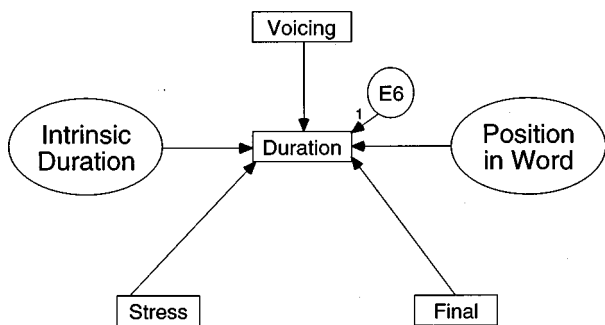


FIG. 2. Structural equation component for a covariance structure model of English vowel duration.

stress and intrinsic duration, and phrase final position and position in word.

2. The structural equation model

The structural equation component of the proposed model specifies direct effects on vowel duration and is depicted graphically in Fig. 2.

The parameters to be estimated in the direct effects structural equation are as follows:

- (1) All regression coefficients of the independent latent factors and solitary manifest variables on the dependent variable of vowel duration.
- (2) The residual variance of the dependent variable vowel duration, $E6$.

The direct effects structural equation appears below:

$$D_o = \gamma_{DI}D_i + \gamma_VV + \gamma_WW + \gamma_SS + \gamma_PP + E6, \quad (11)$$

where D_o =output duration, D_i =intrinsic duration, V =post-vocalic consonant voicing, W =position in word, S =lexical stress, P =phrase final position, and E =error.

3. Populations

It has long been understood that words serve very different linguistic functions. The largest division of function is believed to be between those words that carry meaning, i.e., content words, and those that specify linguistic relationships, i.e., function words (i.e., Bolinger, 1975). It also appears that not all syllables serve equal linguistic functions. Van Bergem (1990) argues that stressed syllables act as an anchor point for word retrieval. Carter (1987) has shown that stressed syllables have an “informational” advantage over unstressed syllables. That is, word uniqueness is defined by the stressed syllable(s) in the word.

It is possible that durational effects operate differently on syllables that carry large information loads (i.e., content words and stressed syllables) than on those whose function is to specify linguistic relationships (i.e., function words and unstressed syllables). Van Bergem (1993) compared vowel durations of stressed syllables, unstressed syllables, and function words in both accented and unaccented conditions. He concluded that the effect of sentence accent on duration is of minor importance compared to the effect of lexical stress and word class. Specifically, he found that unaccented unstressed syllables, accented function words, and unaccented

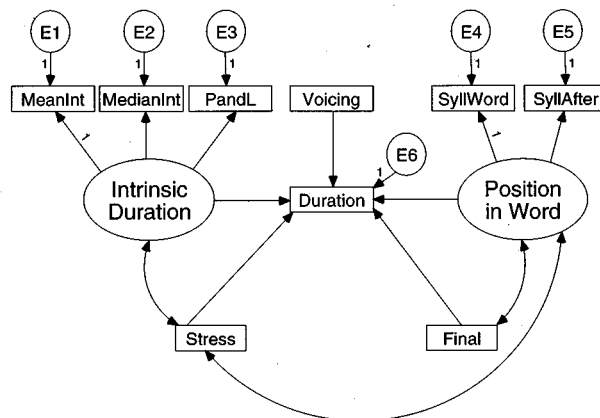


FIG. 3. Single population covariance structure model of vowel duration.

function words did not significantly differ in vowel duration. On the other hand, these three syllable groups were significantly shorter in vowel duration than either accented stressed syllables or unaccented stressed syllables.

To test the hypothesis that durational effects operate differently on content words and lexically stressed syllables (content/stressed) than on function words and lexically unstressed syllables (function/unstressed), two covariance models of vowel duration are considered: the single population model and the dual population model.

a. Single population model. The single population covariance structure model assumes that a single set of parameter estimates can be generated that fits all syllables well. In such a model, vowel duration is considered to be a direct effect of all independent factors or variables (Fig. 3).

b. Dual population model. The dual population model assumes that duration factors operate differently on syllables from the content/stressed population than on syllables from the function/unstressed population. The dual population covariance structure model is hypothesized to consist of identical path structures to the single population model with the omission of the variable stress (Fig. 4). It is hypothesized that parameter estimates of this model will differ across the two populations: content/stressed and function/unstressed.

4. Appropriateness of an additive linear model

Van Santen (1992) has described a sums-of-products model that is essentially linear with the inclusion of two multiplicative terms: one between pitch accent and syllabic

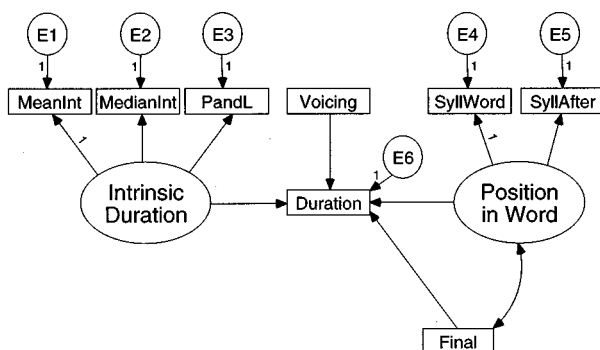


FIG. 4. Dual population covariance structure model of vowel duration.

stress, and a second one between the influence of post-vocalic consonant voicing and position in utterance. While other interactions are possible and even likely, this parsimonious model accounted for 87% of the variance. Factors included in the model were vowel identity, accent, syllabic stress, pre-vocalic consonant, post-vocalic consonant, number of preceding syllables, number of following syllables, and utterance position. The proposed covariance structure model is an additive linear model that includes most of these factors, with the exception of accent and pre-vocalic consonant. Traditional CSM does not easily accommodate the inclusion of interaction terms. Thus this proposed model fails to include the interaction of post-vocalic consonant voicing with position in utterance. Thus it is possible that vowel duration in some phrase final syllables may be underestimated using an additive covariance structure model.

II. PRELIMINARY EXPERIMENT

A preliminary experiment was performed to obtain means for the effects of intrinsic duration and post-vocalic consonant voicing that could be used to transform these categorical variables into ratiolike measures that behave like continuous variables. Using methodology partially borrowed from previous studies (e.g., Peterson and Lehiste, 1960; House, 1961), the preliminary experiment intended to:

- (1) calculate the mean and median vowel duration for each of 14 English vowels across voiced and voiceless environments;
- (2) calculate the mean and median vowel duration for voiced post-vocalic consonant across all 14 vowels;
- (3) calculate the mean and median vowel duration for voiceless post-vocalic consonant across all 14 vowels.

A. Method

1. Stimuli

Stimuli were nonsense words consisting of ‘‘h’’ followed by a vowel and consonant. Nonsense words were imbedded in the carrier phrase ‘‘Say ___ again.’’ Nonsense words were composed of all possible combinations of 14 vowels and 14 post-vocalic consonants (7 voiced/voiceless cognates), for a total of 196 stimuli. These are presented in Table II. Each sentence was written on a separate three by five card with the stimulus word transcribed in the International Phonetic Alphabet (IPA). A sample sentence is as follows: ‘‘Say /hud/ again.’’

2. Subjects

Two adult males and two adult females participated in the preliminary study. All subjects were native speakers of American English and had never been diagnosed with a language or speech disorder. Each subject passed a standard hearing screening at 20 dB HL for the frequencies 500 Hz, 1000 Hz, and 2000 Hz. Subjects were trained in phonetics, were familiar with the International Phonetic Alphabet (IPA), and were able to read IPA transcriptions fluently.

TABLE II. Fourteen vowels and fourteen consonant sounds used in the preliminary study.

Vowel	Post-vocalic consonant
i	p
ɪ	b
eɪ	t
ɛ	d
æ	k
ə	g
ɑ	s
oʊ	z
ʊ	f
u	v
aʊ	θ
ɜː	ð
ɔ	tʃ
aɪ	dʒ

3. Recording procedure

Subjects participated in three recording sessions spaced at least one week apart. During each session, subjects were recorded reading a randomized list of all 196 stimuli for an N of 2352 (196 stimuli \times 3 sessions \times 4 subjects).

Subjects were recorded while reading stimulus materials in a double-walled sound booth (Industrial Acoustics Company model 1203) at the University of Tennessee, Knoxville. Recordings were made on a Sony PCMR500 digital audio tape recorder using a Sennheiser MD 441-U microphone. Subjects were instructed to read at a comfortable rate, but to keep the rate consistent throughout the session.

4. Analysis

Stimuli were low-pass filtered at 5000 Hz and digitized at a sampling rate of 10 000 Hz using the Computerized Speech Laboratory (CSL) from Kay Elemetrics. Wide-band and narrow-band spectrograms were computed for each stimulus word. The author measured the duration of the vowel in each stimulus word from the spectrogram using segmentation criteria developed by Peterson and Lehiste (1960). The beginning of the vowel after the initial /h/ was determined by the onset of periodic energy in the region of the first formant. The end of the vowel before a voiceless plosive was marked at the abrupt cessation of energy in all formants. The end of the vowel before a voiced plosive was determined by the cessation of energy in the higher harmonics. The end of the vowel before final voiceless fricatives was marked at the onset of random noise. The end of the vowel before final voiced fricatives was marked at the onset of random noise in the higher frequencies.

Two months after the vowel duration measurements had been completed, the author recoded a randomly selected session from one subject ($n=196$). Intra-rater reliability as measured by the Pearson product moment correlation coefficient was 0.93 for vowel duration. A graduate student trained in the segmentation procedures described by Peterson and Lehiste (1960) coded a randomly selected subset of the data ($n=204$). Inter-rater reliability for vowel duration as measured by the Pearson product moment correlation coefficient was 0.89.

TABLE III. Mean and median durations of syllable nuclei by vowel ($n = 480$).

Vowel	Mean duration (ms)	Median duration (ms)	Peterson and Lehiste mean duration (ms)
i	168.8	146.9	240
ɪ	141.8	128.7	180
eɪ	196.7	179.8	270
ɛ	156.5	135.8	200
æ	203.6	185.3	330
ə	145.9	132.5	230
ɑ	195.3	175.2	260
ɔ	199.7	188.3	310
oʊ	192.2	167.9	220
U	152.2	137.5	200
u	167.9	150.9	260
aʊ	209.6	160.1	300
aɪ	214.9	187.7	350
ɜ	179.7	136.2	240

Estimations of intrinsic duration were obtained by calculating mean and median vowel durations for each of the 14 vowels across the 14 consonants that constituted the 7 voiced/voiceless cognate pairs ($n = 480$). Estimations of the effect of post-vocalic consonant voicing on vowel duration were obtained by calculating mean and median vowel durations across all vowels for vowels followed by voiceless consonants ($n = 1176$) and for vowels followed by voiced consonants ($n = 1176$).

B. Results

Overall mean and median intrinsic durations for each vowel are presented in Table III along with mean intrinsic durations obtained by Peterson and Lehiste (1960). The preliminary experiment data exhibited mean and median durations that were shorter than the intrinsic durations obtained by Peterson and Lehiste; however, the relative durations are quite similar between the two sets of data. For example, while the mean durations for /i/ and /ɪ/ in the preliminary data (168.8 ms and 141.8 ms, respectively) are noticeably shorter than those in the Peterson and Lehiste data (240 ms and 180 ms, respectively), the ratio of the mean duration of /i/ to the mean duration of /ɪ/ for the preliminary data is similar to the same ratio calculated from the Peterson and Lehiste data (1.2 and 1.3, respectively). Thus it appears that both sets of data provide a relative measure of intrinsic duration.

Mean and median vowel durations for voiced and voiceless post-vocalic consonant environments are presented in Table IV. Examination of these means and medians reveals that these vowels were longer when followed by voiced con-

TABLE IV. Mean and median durations of syllable nuclei by post-vocalic consonant voicing.

Post-vocalic consonant	Mean duration (ms)	Median duration (ms)	N
Voiced	218.7	205.0	1176
Voiceless	142.0	137.1	1176

sonants, a finding consistent with previous research (e.g., Peterson and Lehiste, 1960; House, 1961). The ratio of vowel duration before a voiceless consonant to vowel duration before a voiced consonant was 0.65. This ratio is slightly greater than the same ratio as reported by other researchers: 0.61 (Chen, 1970); 0.54 (House, 1961); and 0.53 (Mack, 1982).

III. METHOD

A. Data collection

1. Reading material

The reading material consisted of six passages written in the style of newspaper articles. Each reading passage was presented in a 12-point font on a separate sheet of paper.

2. Subjects

Whiteside (1996) has reported sex differences in the temporal patterns of speech. In order to remove sex differences from the model, only male native English speakers were eligible to participate. Subjects were recruited from the University of Southern California Psychology 100 subject pool. Thirty-eight male monolingual European-American English speakers were recorded reading the six passages. All subjects were native to southern California and spoke a variation of Standard American English common to the area. Subjects ranged in age from 18 to 22 years.

3. Recording

a. Equipment. Each subject was recorded while reading the materials in a single-walled sound booth (IAC 402A). Recordings were made on a calibrated Tandberg 9021X reel-to-reel tape deck with an Uher M857 microphone. All reel-to-reel recordings were transferred onto digital audio tape using a Sony PCMR500 digital audio tape recorder.

b. Procedures. Each reading passage was presented in full. Subjects were allowed to silently read through the material prior to recording. Subjects were recorded while seated 12 in. from the microphone. Subjects were instructed to read at a constant and comfortable rate.

4. Data reduction

a. Sentences. In order to ensure that sentences of various lengths were included, the reading material first was divided into short (<15 syllables), medium (15–24 syllables), and long sentences (>24 syllables). For each group (short, medium, or long), the three sentences with the highest voiceless to voiced post-vocalic consonant ratio were chosen. For each category (short, medium, and long) the sentence produced with the greatest number of disfluencies or mispronunciations was eliminated, resulting in six sentences. Disfluencies were coded according to criteria developed by Williams *et al.* (1969). Mispronunciations were coded as any pronunciation resulting in a change in word or in a nonsense word. One of these six sentences was later eliminated due to severe segmentation problems resulting from the phonetic composition of the sentence. The resulting data set is presented in the

Appendix. The five resulting sentences consisted of the following number of syllables: 10, 9, 22, 18, and 28.

b. Subjects. Highly disfluent subjects were eliminated from the study. Subjects were eliminated if they committed more than three disfluencies or mispronunciations or more than five incorrect word inclusions or omissions during the entire reading. In order to maintain a reasonable balance between short, medium, and long sentences in the data, subjects were also eliminated from the study if they produced disfluencies or mispronunciations in more than one sentence in any of the categories short, medium, or long. The final number of subjects was 16.

c. Syllables. Syllable nuclei that were not coded as one of the 15 vowels included in the Peterson and Lehiste (1960) study were dropped from analysis. Also, any syllable nuclei that could not be segmented accurately were dropped from the analysis. A syllable nucleus was determined to be segmented inaccurately if intra-rater reliabilities were less than 80%. Procedures for intra-rater reliability are discussed in Sec. II B. The data reduction procedure resulted in an N of 893 syllable nuclei extracted from 5 sentences produced by 16 subjects.

5. Data digitization

The recorded speech signals were low-pass filtered at 4000 Hz and digitized at a sampling rate of 10 000 Hz using the Computerized Speech Laboratory (CSL) from Kay Elemetrics.

B. Measures

1. Dependent variable

The dependent variable in this study, i.e., vowel duration, was defined as the duration of the vocalic portion of the syllable. The author measured the duration of each syllable nucleus from digital spectrograms using segmentation criteria developed by Peterson and Lehiste (1960). Aspiration was not included as part of the vowel. Skewness and kurtosis values for duration were 0.99 and -1.35 , respectively.

To test the reliability of segmentation, the author re-measured recordings from one randomly selected subject two weeks after the initial measurement. A third set of measurements was obtained one month after the initial measurement. All three sets of measurements were tested for reliability using Cronbach's α as calculated by the "reliability" procedure provided by version 8 of the Statistical Product and Service Solutions (SPSS, formerly known as Statistical Package for the Social Sciences). The three sets of measurements were found to be consistent ($\alpha=0.99$, $n=54$).

To further assess the reliability of segmentation, a graduate student familiar with segmentation measured vowel durations from 1 subject randomly selected from the full set of 16 subjects. These measurements were compared with the initial measurements made by the author for the same subject. The two sets of measurements were found to be consistent ($\alpha=0.98$, $n=53$).

TABLE V. Frequency of occurrence of the 12 vowels included in the main experiment.

Vowel	N
i	92
ɪ	142
eɪ	60
ɛ	144
æ	78
ə	211
ɑ	67
oʊ	39
ʊ	30
u	13
ɑʊ	31
ɜ˞	46

2. Independent variables

All independent variables were measured by the author. To assess the reliability of these measurements, the author re-measured all data for one randomly selected subject. To further assess the reliability of these measurements, a graduate student from the Department of Speech Science and Technology at the University of Southern California measured all independent variables for a subset of seven randomly selected subjects. All reliabilities were calculated using Cronbach's α . Results of these analyses are presented on a variable-by-variable basis in the following sections.

a. Intrinsic vowel duration. Each syllable nucleus was categorized for vowel identity using a list that included the 15 syllable nuclei analyzed in the Peterson and Lehiste study (1960) plus "not listed" and "cannot tell" and 5 additional phonemic categories that were not used in this study. Three of the Peterson and Lehiste vowels, /ɔɪ/, /aɪ/, and /ɔ/, were not represented in the stimulus materials. The 12 syllable nuclei used in this study are listed in Table V. Inter-rater and intra-rater reliabilities of vowel identity categorization were high ($\alpha=0.99$, $n=68$; $\alpha=0.97$, $n=304$, respectively).

Typically, the unmeasurable factor, intrinsic duration, is estimated using some type of average vowel duration computed from minimal pairs. Using CSM, however, intrinsic duration can be estimated using multiple measures. Intrinsic duration would then be defined as the shared variance of these measures. In this study, three measured variables were used to define the latent factor of intrinsic duration: (1) mean intrinsic, mean vowel duration as calculated in the preliminary study; (2) median intrinsic, median vowel duration as calculated in the preliminary experiment; and (3) Peterson and Lehiste intrinsic, intrinsic duration as calculated by Peterson and Lehiste (1960) (see Table III). These variables were created by assigning the appropriate mean or median to each syllable nuclei in the study based on its phonemic identity. This procedure converted the categorical measure of phonemic identity into three ratiolike measures of intrinsic duration. Thus a syllable with a nucleus of /i/ would be coded as follows: mean intrinsic duration=168.8 ms, median intrinsic duration=146.9 ms, and Peterson and Lehiste intrinsic duration=240 ms.

Conversion of the categorical variable of phonemic identity into one or more ratiolike variable of intrinsic dura-

tion allows the use of statistical procedures typically applied to normally distributed continuous data. It is not necessary for each phoneme to be equally represented. Instead, it is assumed that these measures are normally distributed. Skewness and kurtosis values for the three variables were as follows: mean intrinsic, 0.52 and -1.35 , respectively; median intrinsic duration, 0.76 and -0.76 , respectively; and Peterson and Lehiste intrinsic duration, 0.77 and 0.03, respectively.

b. Post-vocalic consonant voicing. Each vowel was assigned to one of the following categories: (1) “followed by voiceless consonant in same syllable;” (2) “followed by voiced consonant in same syllable;” (3) “followed by voiceless consonant in next syllable in the same word;” (4) “followed by voiced consonant in next syllable in same word;” (5) “followed by voiceless consonant in next word;” (6) “followed by voiced consonant in next word;” and (7) “no following consonant.” A categorization of “no following consonant” was assigned when one of the following was true: vowel was phrase final; vowel was followed by a pause; or vowel was followed by another vowel. Syllables categorized as “no following consonant” were not included in the study. The reliability of these categorizations was assessed by creating a vector for each of the seven categories. For each syllable nucleus, the vector was coded “0” if the category was not assigned or “1” if the category was assigned. Intra-rater reliabilities for the seven categories ranged from 0.93 to 1.00. Inter-rater reliabilities for the seven categories ranged from 0.92 to 1.00.

The influence of post-vocalic consonant voicing on vowel duration has been studied extensively within the syllable. Little is known concerning the strength of this effect across syllable or word boundaries. In a study examining 200 phonetically balanced sentences, Campbell and Isard (1991) found no effect of post-vocalic consonant voicing across word boundaries. Given that the function words “a” and “the” are two of the most frequently occurring words in English, it is likely that, in sentences, word boundary effects are confounded with other effects such as cliticization and position in the stress foot. To assess the effect of post-vocalic consonant voicing across syllable and word boundaries in these data, two Lagrange Multiplier tests (LM) (see Bentler, 1995) were performed. The first LM analysis tested the hypothesis that the influence of post-vocalic consonant voicing on vowel duration is invariant within and across syllable boundaries. The second LM analysis tested the hypothesis that the influence of post-vocalic consonant voicing on vowel duration is invariant within and across word boundaries. Results of these analyses suggest that the influence of post-vocalic consonant voicing on duration is similar within and across syllable boundaries [$\chi^2(1)=0.125$, $p=0.72$] and within and across word boundaries [$\chi^2(1)<0.001$, $p=1.00$] in connected speech. Therefore, the six categorizations for post-vocalic consonant voicing were collapsed into two categories: “followed by voiced consonant” and “followed by voiceless consonant.”

The categorical variable of post-vocalic consonant voicing was converted to the binary variable of mean voicing by assigning mean durations for each voiced/voiceless envi-

ronment obtained from the preliminary experiment to each syllable, thus creating a binary variable with ratiolike qualities. Specifically, vowels categorized as “followed by voiced consonant” were assigned a mean voicing value of 218.7 ms, while vowels categorized as “followed by voiceless consonant” were assigned a mean voicing value of 142.0 ms. Skewness and kurtosis values for this variable were -0.52 and -1.73 , respectively.

c. Position in word. The latent factor of position in word was defined by two measured variables: syllables per word, the number of syllables per word, and syllables after, the number of following syllables in the word. Skewness and kurtosis values for syllables per word were 1.59 and 2.35, respectively. Skewness and kurtosis values for number of following syllables in the word were 2.25 and 5.56, respectively. Intra-rater and inter-rater reliability for the variable syllables/word produced alpha coefficients of 1.00 ($n=68$) and 0.99 ($n=304$). Due to these extremely high reliability coefficients, no analysis of reliability was performed for the variable syllables after.

d. Stress. Each coder was asked to choose the “most stressed” syllable in each polysyllabic word. The measured variable stress was assigned a value of zero if the syllable was not marked as stressed or a value of one if the syllable was marked as stressed. Skewness and kurtosis values for stress were 1.03 and -0.94 , respectively. Reliability analysis revealed high intra-rater and inter-rater agreement ($\alpha=1.00$, $n=68$; $\alpha=0.99$, $n=304$, respectively).

e. Phrase final position. Phrase boundaries were coded following a procedure developed by Wightman *et al.* (1992). This system labels the boundary between each pair of orthographic words with a break index of 0–6. One listener, the author, examined the boundaries between each pair of orthographic words and assigned a break index value for those boundaries meeting the criteria for ratings of 4 or higher. A break index of 4 marked an intonational phrase boundary and was preceded by a boundary tone (Beckman and Pierrehumbert, 1986). A break index of 5 marked a group of intonational phrases. A break index of 6 marked a sentence boundary. Boundaries with break index ratings of 5 or 6 were marked as phrase boundaries.

To assess the reliability of phrase boundary marking, the author relabeled the data from one randomly selected subject. Intra-labeler reliability of phrase boundary marking was 0.96 ($n=68$). Additionally, a graduate student applied the same procedure to seven randomly selected subjects. Inter-labeler reliability for phrase boundary marking was 0.95 ($n=304$).

Cummins (1999) points out that phrase final lengthening refers to the relatively longer durations seen in the rhyme of the syllable that lies at the right edge of a major prosodic group, while utterance final lengthening tends to affect several syllables. Research by Campbell and Isard (1991), Klatt (1976), Oller (1973), van Santen (1992), and Wightman *et al.* (1992) suggests that in final words, the final lengthening occurs primarily in the final syllable, whether stressed or unstressed. Thus only syllables immediately preceding a phrase boundary were marked as phrase final. Phrase final

syllables were coded as one, all others were coded as zero. Skewness and kurtosis for phrase final position were the highest in these data (3.08 and 7.49, respectively).

3. Influence of speaking rate

Experimental studies typically examine the effect of speaking rate on vowel duration by comparing speech at conversational and fast speaking rates (e.g., Cummins, 1999; Gay, 1978; Weismer and Fennell, 1985). In such cases, speaking rate appears to be an important predictor of vowel duration. In the present study, mean speaking rate was calculated per phrase and ranged from 3.8 syllables per second to 7.1 syllables per second with a mean of 5.5 syllables per second and a standard deviation of 0.7 syllables per second. Speaking rate was not highly correlated with vowel duration ($r = -0.20$, $n = 896$). Given the low correlation between speaking rate and vowel duration in these data, this parameter was not included in the model.

C. Data sets

Three data sets were used in the analyses. The main data set ($N = 896$) was used to test the single population model. In order to test the hypothesis that two separate models predict duration better than a single model, the main data set was divided into two data subsets: (1) content/stressed ($N = 426$), consisting of monosyllabic content words and lexically stressed syllables, and (2) function/unstressed ($N = 470$), consisting of monosyllabic function words and lexically unstressed syllables.

IV. RESULTS

A. Single population model

1. Goodness-of-fit

Maximum likelihood (ML) was used to estimate the covariance matrix of the single population model. Comparison of the estimated covariance matrix with the actual covariance matrix produced a large chi-square, as would be expected for models for large N , suggesting that the estimated covariance matrix differed significantly from the actual covariance matrix [$\chi^2(25) = 836$, $p < 0.001$]. However, the null model produced a much larger chi-square goodness-of-fit statistic [$\chi^2(36) = 6692$, $p < 0.001$]. Comparison of the chi-square of the single population model to that of the null model suggests that the single population model is an improvement over the null model (CFI=0.878).

2. Parameter estimates

Unstandardized parameter estimates are presented in Fig. 5. Latent variable loadings are indicated along arrows connecting latent factors (ovals) to manifest variables (rectangles). Covariances are indicated along curved lines connecting factors or variables. Structural equation parameters are indicated along arrows running from independent factors or variables to duration, the dependent variable. All latent variable loadings were significant. All parameter estimates for hypothesized covariances were of the expected sign. All five direct effects on vowel duration were significant.

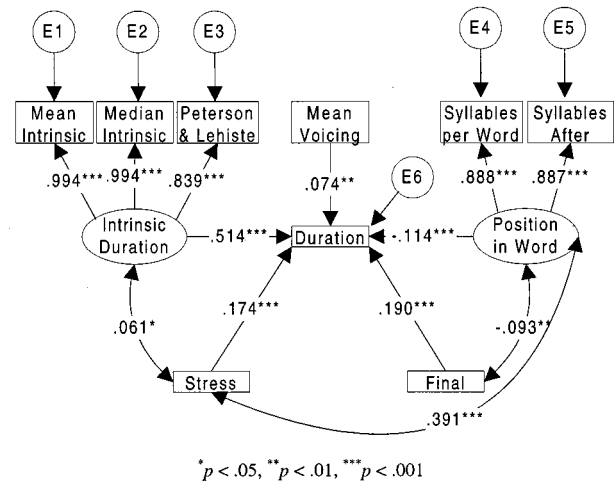


FIG. 5. Single population covariance structure model of vowel duration with unstandardized parameter estimates.

3. Summary

The fit index employed in this study indicated that the single population model fits the data better than the null model. The strongest direct effect on vowel duration was intrinsic duration, followed by the much weaker effects of phrase final position, lexical stress, position in word, and post-vocalic consonant voicing.

B. Dual population model

1. Fully constrained simultaneous solution

The hypothesis that two durational models, one for the population of content/stressed syllables ($N = 426$), and a second for the population of function/unstressed syllables ($N = 470$), predict duration better than a single population model was tested by constraining all structural equation parameters of each model to be equal. In other words, the effects of the independent factors and variables on duration were constrained to be equal across both populations. All other parameters were freely estimated. A Lagrange Multiplier test (LM) was employed to assess whether any improvement in fit results if the structural equation parameters for each sample are freely estimated.

a. Goodness-of-fit. ML estimation was used to calculate parameter estimates. Comparison of the estimated covariance matrix to the actual covariance matrix resulted in a large chi-square goodness-of-fit statistic [$\chi^2(44) = 679$, $p < 0.001$]. The null model yielded a much larger chi-square [$\chi^2(56) = 6533$, $p < 0.001$]. Comparison of the chi-square of the dual population model to that of the null model suggests that the dual population model is an improvement over the null model (CFI=0.902).

b. Parameter estimates. The LM test indicated that the direct structural equation parameters of the two samples should not be simultaneously constrained to be equal across the two samples [$\chi^2(4) = 21.399$, $p < 0.001$]. Results of the univariate LM test are presented in Table VI. If we consider the LM statistic to be zero in the population at probabilities above 0.05, only two parameters should be released from the equality constraint: intrinsic duration and post-vocalic con-

TABLE VI. LM test univariate statistics for removal of structural equation parameter equality constraints between content/stressed ($N=426$) and function/unstressed ($N=470$).

Parameter ^a	χ^2	p
Intrinsic Duration→Duration	7.27	0.007
Voicing→Duration	8.46	0.004
Position in Word→Duration	2.64	0.104
Final→Duration	3.03	0.082

^aIndependent variable→Dependent variable.

sonant voicing. However, great caution must be used in interpretation of the univariate LM statistic. Such statistics cannot be used to determine the effect of releasing multiple restrictions because the statistics may be correlated (Bentler, 1995). Given that there is evidence that position in word affects vowel duration less in unstressed syllables than it does in stressed syllables, it seems theoretically unwise to constrain this parameter to be equal across content/stressed syllables and function/unstressed syllables simply because the probability value of its LM statistic is 0.104. Likewise, phrase final position has been associated with similar vowel durations across stressed and unstressed syllables (van Santen, 1992), but the manner in which this lengthening is achieved may not be identical across these two populations (Edwards *et al.*, 1990). Given that the probability of the LM statistic for phrase final position is only 0.08, it may be unwise to restrict this parameter to be equal across the two populations as well. Thus all four parameter estimates were freely estimated.

c. Summary. The results of the LM test indicate that model fit is improved if the structural equation parameters of the two groups, content/stressed and function/unstressed, are allowed to vary independently, thus supporting the hypothesis that a dual population duration model will fit the data better than a single population duration model.

2. Unconstrained simultaneous solution

Based on the results of the fully constrained LM test, a second LM test was performed in which all four structural equation parameters were freely estimated across the content/stressed and function/unstressed populations.

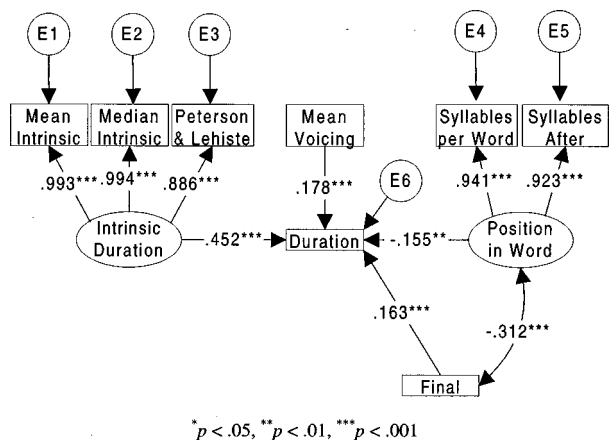


FIG. 6. Content/stressed covariance structure model of vowel duration with unstandardized parameter estimates.

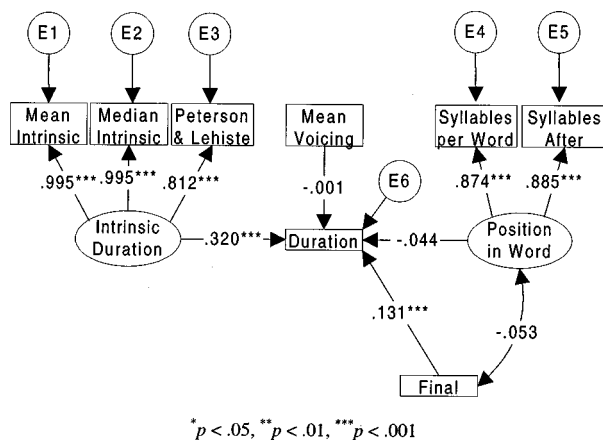


FIG. 7. Function/unstressed covariance structure model of vowel duration with unstandardized parameter estimates.

a. Goodness-of-fit. ML estimation was used to calculate parameter estimates. Comparison of the estimated covariance matrix to the actual covariance matrix resulted in a large chi-square goodness-of-fit statistic [$\chi^2(40) = 661, p < 0.001$]. The null model yielded a much larger chi-square [$\chi^2(56) = 6563, p < 0.001$]. Comparison of the chi-square of the unconstrained model to that of the null model suggests that this model is an improvement over the null model (CFI=0.905).

b. Parameter estimates. The magnitudes and levels of significance for direct structural equation parameters differed for the content/stressed and function/unstressed data subsets. Unstandardized parameter values for the content/stressed data subset are displayed in Fig. 6, while those for the function/unstressed data subset are displayed in Fig. 7. Table VII presents the direct effects on vowel duration for each data subset in decreasing order of magnitude.

Intrinsic duration remained the strongest direct effect on duration in both the content/stressed and function/unstressed data subsets. Likewise, phrase final position remained a moderately strong direct effect on vowel duration in both data subsets. On the other hand, the two models differed with respect to the effect of post-vocalic consonant voicing on vowel duration. For content/stressed syllables, post-vocalic consonant voicing was the second strongest significant effect. Conversely, for function/unstressed syllables, post-vocalic consonant voicing was an insignificant predictor of vowel duration. Likewise, the shortening effect of position in word was a significant predictor of vowel duration in content/stressed syllables, but was not a significant shortening effect on the duration of function/unstressed syllables.

c. Summary. The results of ML analysis of each data

TABLE VII. Direct effects on vowel duration for content/stressed and function/unstressed syllables in descending order of magnitude.

Content/stressed	Function/unstressed
Intrinsic duration ^a	Intrinsic duration ^a
Following voicing ^a	Final ^a
Final ^a	Position in word
Position in word ^b	Following voicing

^a $p < 0.001$.

^b $p < 0.01$.

subset support the hypothesis that the combined effects of several factors on vowel duration differ between the two populations, content/stressed and function/unstressed. Separate modeling of these two groups of syllables fit the data better than a single model of vowel duration.

V. DISCUSSION

This study was able to test simultaneous effects on vowel duration in American English. Additionally, through the use of multiple sample CSM, it has been possible to investigate whether two models of vowel duration, one for content/stressed syllables and a second for function/unstressed syllables, more accurately model vowel duration than does a single model. While this study cannot suggest causation because of its nonexperimental nature, it has provided a more complete picture of the processes that shape vowel duration in continuous speech than have previous experimental studies. The results support many of the findings of experimental studies. However, some effects that frequently have been seen experimentally were not strong effects in these data.

A. Specific effects

1. Intrinsic duration

Intrinsic duration was the strongest predictor of vowel duration in all models studied. It is clear that, at least in these data, the effect is very strong. The unstandardized path coefficient for the effect of intrinsic duration on vowel duration was 0.452 for the content/stressed group and 0.320 for the function/unstressed group, suggesting that this effect was stronger in the content/stressed group than it was in the function/unstressed group. While previous studies have not examined the strength of intrinsic duration in monosyllabic function words, its effect has been examined in unstressed syllables. In his 1992 study, van Santen examined the durational distribution of stressed and unstressed syllables in accented words and found a high degree of similarity in rank ordering of duration, suggesting that this effect is similar in both stressed and unstressed syllables.

2. Post-vocalic consonant voicing

In this study of connected speech, post-vocalic consonant voicing was not a strong predictor of vowel duration in the single population model ($\gamma=0.074$); however, the effect was significant. On the other hand, in the dual population model, a stronger effect on vowel duration was seen ($\gamma=0.178$) for the content/stressed population, while no effect was observed for the function/unstressed population. While no previous studies have examined this effect in function words, the current findings are in agreement with those observed by Crystal and House (1988) in stressed and unstressed syllables.

3. Position in word

In the current research, position in word was indicated by two measured variables, number of syllables in the word and number of syllables after. In the single population model, a small, but significant, inverse relationship between

position in word and vowel duration was observed ($\gamma=-0.114$). In the dual population model, a larger inverse relationship between position in word and vowel duration ($\gamma=-0.155$) was observed in the content/stressed population, while position in word had no significant effect on duration in the function/unstressed population. The finding that position in word inversely affects vowel duration in stressed syllables is supported by numerous studies (Klatt, 1973; Lehiste, 1972; Nooteboom, 1972; Port, 1981). The handful of studies that have examined the effect of position in word on vowel duration in unstressed syllables have seen an effect, but one that is much reduced from that seen in stressed syllables (Nooteboom, 1972; van Santen, 1992). Data provided by van Santen show that vowel duration is longer in word-final unstressed syllables than in unstressed syllables followed by one syllable. However, no obvious difference was seen in vowel duration of unstressed syllables followed by one syllable and those followed by greater than one syllable. These findings suggest that when the effects of word final position are removed, the duration of unstressed vowels are not greatly affected by the number of following syllables.

4. Lexical stress

Lexical stress was the second strongest effect on vowel duration in the single population model ($\gamma=0.174$). This is not surprising since increased duration has long been associated with the perception (Fry, 1955, 1958, 1964) and production (Lieberman, 1960) of lexical stress. Distributional data provided by Crystal and House (1988) show that all categories of vowels, i.e., tense, lax, and diphthong, are longer in stressed syllables.

5. Phrase final position

Evaluation of the effect of phrase final position on vowel duration suggests that this variable is a significant, but moderate, predictor of vowel duration in all three models. The effect of phrase final position on duration was consistent across all three models, single population, content/stressed population, and function/unstressed population ($\gamma=0.190$, $\gamma=0.163$, $\gamma=0.131$, respectively), suggesting that, at least in these data, phrase final position predicts duration similarly in both populations. Such a finding is in agreement with those of Berkovits (1984) and Oller (1973). The finding is also supported by the research of Crystal and House (1988) and van Santen (1992), who concluded that vowels in prepausal position are lengthened independent of stress. However, as Edwards *et al.* (1990) point out, while similar lengthening is observed in stressed and unstressed syllables, the articulatory kinematics of this lengthening differ.

B. Appropriateness of a multisample model

The present study supports the differential modeling of duration for syllables that carry meaning (i.e., monosyllabic content words and stressed syllables) and syllables that specify relationships (i.e., monosyllabic function words and unstressed syllables). While some factors appeared to exert similar effects on duration in these two populations, others appeared to operate differentially on these two groups. Con-

sider the unstandardized parameter estimates for the single population model [Eq. (12)] and those generated by the dual population model for the content/stressed population [Eq. (13)] and the function/unstressed population [Eq. (14)]:

$$D_o = 0.514D_i + 0.074V - 0.114W + 0.174S + 0.190P + E, \quad (12)$$

$$D_o = 0.452D_i + 0.178V - 0.155W + 0.163P + E, \quad (13)$$

$$D_o = 0.320D_i + 0.131P + E, \quad (14)$$

where D_o =output duration, D_i =intrinsic duration, V =post-vocalic consonant voicing, W =position in word, S =lexical stress, P =phrase final position, and E =error. Factors with parameter estimates not significantly different from zero were not included in these equations. The effects of intrinsic duration and phrase final position appear relatively consistent across all three models. Conversely, position in word appears to be a significant predictor of vowel duration in the content/stressed model but is an insignificant predictor of vowel duration in the function/unstressed model. Post-vocalic consonant voicing also had a stronger effect on vowel duration in the content/stressed model than in the function/unstressed model.

Klatt (1976) posited that speech was ultimately “incompressible.” Klatt’s theory predicts that as shortening effects are added to the model, their combined effects are reduced as segment durations asymptotically approach a minimum. Results of the dual population model analysis, while not proving this theory, are consistent with it. The argument could be made that content/stressed syllables are inherently longer than function/unstressed syllables and therefore more “compressible.” It would be expected, then, that shortening factors would be stronger predictors of duration in the content/stressed model than in the function/unstressed model. This was the case in these data.

Other researchers have suggested that factors that are not phonologically specified might exhibit “incompressibility” while those that are phonologically specified would not (Port, 1981). That is, inherently shorter and inherently longer syllables should be similarly affected by phonologically specified factors. Cummins (1999) showed that the phonological factor of final lengthening appeared to operate in a constant ratio manner across contexts. The present study in part supports this finding. In both models, content/stressed and function/unstressed phrase final lengthening operated in a similar manner; however, because the model is additive and not multiplicative, it cannot be said that this factor operated using a constant ratio. On the other hand, the effect of post-vocalic voicing on duration, considered to be a phonologically specified factor in English (House, 1961; Delattre, 1962), did not operate in a similar manner across the two groups. In fact, this factor had no significant effect on syllables from the function/unstressed group.

In summary, it appears that intrinsic duration and phrase final position predict duration in content/stressed and function/unstressed syllables in a similar fashion. On the other hand, the factors of post-vocalic consonant voicing and position in word appear to have little or no affect on the

duration of function/unstressed syllables. It appears that some factors that affect vowel duration operate differentially on these two groups.

C. Interpretation of model fit and parameter estimates

1. Model fit

The chi-square goodness-of-fit statistics generated in this study suggest that for all models tested the actual covariance matrices differed significantly from the estimated covariance matrices. Accordingly, these models should be considered to be poor fitting. However, there are several reasons why these chi-square goodness-of-fit values could be misleading. First, as sample size increases, the chi-square test gains increasing power. Thus for large sample sizes, small differences between the actual covariance matrices and the estimated covariance matrices become significant, increasing the probability of a Type II error. In this study, all sample sizes were quite large. Second, the more complex the model, the more likely a good fit. Recall that the saturated model, where there are as many estimated parameters as there are nonredundant variances and covariances, will always fit the data exactly. As model complexity approaches saturation, fit approaches perfection. The models examined in this study were relatively simple and would, therefore, generate lower chi-square values than a more complex, but theoretically invalid, model.

Several authorities recommend using the relative chi-square to evaluate model fit. The relative chi-square is the chi-square goodness-of-fit statistic divided by the degrees of freedom. In theory, this measure is less dependent on sample size than the simple chi-square statistic. Rule-of-thumb acceptable values for this measure range from 2:1 to 3:1 (Carmines and McIver, 1981; Kline, 1998). However, some researchers accept values as high as 5:1. This measure, in fact, is very useful when sample sizes are just above those minimally required to successfully perform CSM. However, this measure is also dependent on sample size due to the fact that increases in sample size, while resulting in larger chi-square goodness-of-fit statistics, do not also result in an increase in degrees of freedom. Thus as sample size increases beyond that minimally required for stable parameter estimation in CSM, the relative chi-square also increases. Consider the single population model ($N=896$). The relative chi-square generated by this model is 33.44:1 [$\chi^2(25)=836$]. When the same model is generated using a minimally acceptable subset of the data ($N=148$), a much smaller chi-square goodness-of-fit statistic is generated, yet the degrees of freedom are constant [$\chi^2(25)=100$], resulting in a more acceptable relative chi-square of 4:1. Thus for this large data set, the relative chi-square is not a particularly useful measure of fit.

The CFI, while not being immune to the effects of sample size, is much less affected than either the chi-square goodness-of-fit statistic or the relative chi-square. The CFI values generated in this study ranged from slightly below the rule-of-thumb cutoff of 0.90 proposed by Bentler and Bonnet (1980) to slightly above this cutoff, suggesting that these

models should not be discarded, but could be improved. This is not surprising since these models did not incorporate factors at levels higher than the syllable. Also, these models employ a linear estimation technique that suffers from the inability to include nonlinear interaction effects.

2. Parameter estimation

The stability of parameter estimates in CSM is a function of sample size. The parameter estimates generated by these models are quite likely stable, because the sample sizes employed in these models, 896 for the single population model, and 426 and 470 for the dual population model, are many times greater than the sample sizes suggested by typical rule-of-thumb methods. According to Stevens (1996), the sample size should be 15 times the number of measured variables. Using his method, these models require a sample size of only 135. Bentler and Chou (1987) recommend a sample size that contains at least five cases per parameter estimate. Multiplying the 19 estimated parameters by 5 yields a sample size of 95, well below the sample sizes used in this study.

Validity of the parameter estimates is generally determined by model fit; however, there is currently no rigorously defined CFI cutoff below which parameters should be considered invalid. Maruyama (1998) is careful to remind us that the plausibility of a particular relationship in a model can be assessed even when an overall fit index does not exceed rule-of-thumb values. While the CFI values generated in this study suggest that the models could be improved, the parameter estimates obtained in this study generally agree with those obtained using other methodologies.

VI. SUMMARY AND CONCLUSIONS

While the best model of duration likely contains higher level factors, interaction terms, and is nonlinear at its extremes, this study has shown that by using a dual population model, additive linear techniques can be used to obtain a great deal of information concerning the simultaneous effects on vowel duration in connected speech. Intrinsic duration, post-vocalic consonant voicing, position in word, lexical stress, and phrase final position were significant predictors of vowel duration in the single population model. A dual population model of vowel duration where parameter estimates were predicted separately for monosyllabic content words/lexically stressed syllables and monosyllabic function words/lexically unstressed syllables fit the data better than did the single population model. The results obtained in this study generally agree with those obtained using other methodologies, and suggest that covariance structure analysis can be used as a complementary technique in linguistic and phonetic research.

ACKNOWLEDGMENTS

The author would like to express her sincere gratitude to June Shoup, Don Cooper, Edward Purcell, and Stephen Handel for their support and encouragement. Special thanks must be extended to J. M. Pickett for his review of the manuscript.

This research was supported in part by a dissertation fellowship from the University of Southern California.

APPENDIX: SENTENCE ANALYZED

Below are the five sentences analyzed in this study.

- (1) Each lawyer attempts to present his case.
- (2) Husband steps down and wife takes the stand.
- (3) At the Lompoc penitentiary, a convict may get a chance to have his protest heard.
- (4) Warden Jonathon Stout listens to the pleas of the inmates every week.
- (5) This gift, together with the proceeds of last year's celebrity concert, could be used to improve prison programs.

- Asher, H. B. (1983). *Causal Modeling* (Sage, Newbury Park).
- Bailly, G. (1989). "Integration of rhythmic and syntactic constraints in a model of generation of French prosody." *Speech Commun.* **8**, 137–146.
- Beckman, M., and Pierrehumbert, J. (1986). "Intonational structure in Japanese and English," *Phonology Yearbook 3*, edited by J. Ohala (Cambridge University Press, Cambridge), pp. 255–309.
- Bentler, P. M. (1995). *EQS: Structural Equations Program Manual* (Multivariate Software, Inc., Encino, CA).
- Bentler, P. M., and Bonnet, D. G. (1980). "Significance tests and goodness of fit in the analysis of covariance structures," *Psychol. Bull.* **88**, 588–606.
- Bentler, P. M., and Chou, C. P. (1987). "Practical issues in structural modeling," *Sociological Methods Research* **16**, 78–117.
- Bentler, P. M., and Weeks, D. G. (1980). "Linear structural equations with latent variables," *Psychometrika* **45**, 289–308.
- Berkovits, R. (1984). "Duration and fundamental frequency in sentence final intonation," *J. Phonetics* **12**, 255–265.
- Berkovits, R. (1991). "The effect of speaking rate on evidence for utterance-final lengthening," *Phonetica* **48**, 57–66.
- Bock, R. D., and Bargmann, R. E. (1966). "Analysis of covariance structures," *Psychometrika* **31**, 507–534.
- Bolinger, D. (1975). *Aspects of Language* (Harcourt Brace Jovanovich, New York).
- Bollen, K. A. (1989). *Structural Equations with Latent Variables* (Wiley, New York).
- Boyle, M. H., and Pickles, A. R. (1997). "Influence of maternal depressive symptoms on ratings of childhood behavior," *J. Abnorm. Child Psychol.* **25**, 390–412.
- Campbell, W. N. (1990a). "Measuring speech-rate in the Spoken English Corpus," in *Theory and Practice in Corpus Linguistics*, edited by J. Aarts and W. Meijs (Rodopi, Amsterdam), pp. 61–81.
- Campbell, W. N. (1990b). "Analog I/O nets for syllable timing," *Speech Commun.* **9**, 57–62.
- Campbell, W. N., and Isard, S. D. (1991). "Segment durations in a syllable frame," *J. Phonetics* **19**, 37–47.
- Carmines, E. G., and McIver, J. P. (1981). "Analyzing models with unobserved variables: Analysis of covariance structures," in *Social Measurement*, edited by G. W. Bohmstedt and E. F. Borgatta (Sage, Thousand Oaks, CA), pp. 65–115.
- Carter, D. M. (1987). "An information-theoretic analysis of phonetic dictionary access," *Comput. Speech Lang.* **2**, 1–11.
- Chen, M. (1970). "Vowel length variation as a function of the voicing of the consonant environment," *Phonetica* **22**, 129–159.
- Classe, A. (1939). *The Rhythm of English Prose* (Blackwell, Oxford).
- Cliff, N. (1983). "Some cautions concerning the application of causal modeling methods," *Multivariate Behavioral Research* **18**, 115–126.
- Cooper, W. E., Eady, S. J., and Mueller, P. R. (1985). "Acoustical aspects of contrastive stress in question-answer contexts," *J. Acoust. Soc. Am.* **77**, 2142–2156.
- Cummins, F. (1999). "Some lengthening factors in English speech combine additively at most rates," *J. Acoust. Soc. Am.* **105**, 476–480.
- Crystal, T. H., and House, A. S. (1988). "Segmental durations in connected-speech signals: Syllabic stress," *J. Acoust. Soc. Am.* **83**, 1574–1585.
- Delattre, P. (1962). "Some factors of vowel duration and their cross-linguistic validity," *J. Acoust. Soc. Am.* **34**, 1141–1143.

- Edwards, J., and Beckman, M. E. (1988). "Articulatory timing and the prosodic interpretation of syllable duration," *Phonetica* **45**, 156–174.
- Edwards, J., Beckman, M. E., and Fletcher, J. (1990). "The articulatory kinematics of final lengthening," *J. Acoust. Soc. Am.* **89**, 369–382.
- Fry, D. B. (1955). "Duration and intensity as physical correlates of linguistic stress," *J. Acoust. Soc. Am.* **27**, 155–158.
- Fry, D. B. (1958). "Experiments in the perception of stress," *Lang. Speech* **1**, 126–152.
- Fry, D. B. (1964). "The dependence of stress judgments on vowel formant structures," in *Proceedings of the 5th International Congress of Phonetic Science*, edited by E. Zwirner and W. Bethge (S. Karger, Basel), pp. 306–311.
- Gay, T. (1978). "Effect of speaking rate on vowel formant movements," *J. Acoust. Soc. Am.* **63**, 223–230.
- Harris, M. S., and Umeda, N. (1974). "Effect of speaking mode on temporal factors in speech: Vowel duration," *J. Acoust. Soc. Am.* **56**, 1016–1018.
- Heffner, R.-M. S. (1937). "Note on the length of vowels," *Am. Speech* **12**, 128–134.
- House, A. S. (1961). "On vowel duration in English," *J. Acoust. Soc. Am.* **33**, 1174–1178.
- House, A. S., and Fairbanks, G. (1953). "The influence of consonant environment upon the secondary acoustical characteristics of vowels," *J. Acoust. Soc. Am.* **25**, 105–113.
- Hu, L., and Bentler, P. M. (1995). "Evaluating model fit," in *Structural Equation Modeling: Concepts, Issues, and Applications*, edited by R. H. Hoyle (Sage, Thousand Oaks, CA), pp. 158–176.
- Jones, D. (1940). *An Outline of English Phonetics* (E. P. Dutton, New York).
- Jöreskog, K. G. (1973). "A general method for estimating a linear structural equation system," in *Structural Equation Models in the Social Sciences*, edited by A. S. Goldberger and O. D. Duncan (Seminar, New York), pp. 85–112.
- Jöreskog, K. G., and van Thillo, M. (1972). *A General Computer Program for Estimating a Linear Structural Equation System Involving Multiple Indicators of Unmeasured Variables* (Educational Testing Service, Princeton, NJ).
- Keesling, W. (1972). "Maximum likelihood approaches to causal flow analysis," Doctoral dissertation, University of Chicago.
- Kenyon, J. S. (1924). *American Pronunciation* (George Wahr, Ann Arbor, MI).
- Klatt, D. (1973). "Interaction between two factors that influence vowel duration," *J. Acoust. Soc. Am.* **54**, 1102–1104.
- Klatt, D. (1975). "Vowel lengthening is syntactically determined in a connected discourse," *J. Phonetics* **3**, 129–140.
- Klatt, D. (1976). "Linguistic uses of segmental duration in English: Acoustic and perceptual evidence," *J. Acoust. Soc. Am.* **59**, 1208–1221.
- Kline, R. B. (1998). *Principles and Practice of Structural Equation Modeling* (Guilford, New York).
- Lehiste, I. (1972). "Timing of utterances and linguistic boundaries," *J. Acoust. Soc. Am.* **51**, 2018–2024.
- Lehiste, I. (1977). "Isochrony reconsidered," *J. Phonetics* **5**, 253–265.
- Lieberman, P. (1960). "Some acoustic correlates of word stress in American English," *J. Acoust. Soc. Am.* **32**, 451–454.
- Long, J. S. (1983). *Covariance Structure Models: An Introduction to LISREL* (Sage, Newbury Park).
- MacCallum, R. C., Wegener, D. T., Uchino, B. N., and Fabrigar, L. R. (1993). "The problem of equivalent models in applications of covariance structure analysis," *Psychol. Bull.* **114**, 185–199.
- Mack, M. (1982). "Voicing-dependent vowel duration in English and French: Monolingual and bilingual production," *J. Acoust. Soc. Am.* **71**, 173–178.
- Maruyama, G. M. (1998). *Basics of Structural Equation Modeling* (Sage, Thousand Oaks, CA).
- Morton, J., and Jassem, W. (1965). "Acoustic correlates of stress," *Lang. Speech* **8**, 59–181.
- Nooteboom, S. G. (1972). "Production and perception of vowel duration," Doctoral Dissertation, Utrecht, The Netherlands.
- Oller, D. K. (1973). "The effect of position in utterance on speech segment duration in English," *J. Acoust. Soc. Am.* **54**, 1235–1247.
- Peterson, G. E., and Lehiste, I. (1960). "Duration of syllable nuclei in English," *J. Acoust. Soc. Am.* **32**, 693–703.
- Peyrot, M. (1996). "Causal analysis: Theory and application," *J. Pediatr. Psychol.* **21**, 3–24.
- Port, R. F. (1981). "Linguistic timing factors in combination," *J. Acoust. Soc. Am.* **69**, 262–274.
- Prussia, G. E., Kinicki, A. J., and Bracker, J. S. (1993). "Psychological and behavioral consequences of job loss: A covariance structure analysis using Weiner's (1985) attribution model," *J. Appl. Psychol.* **78**, 382–394.
- Scott, D. R. (1980). "Duration as a cue to the perception of a phrase boundary," *J. Acoust. Soc. Am.* **71**, 996–1007.
- Stevens, J. (1996). *Applied Multivariate Statistics for the Social Sciences* (Lawrence Erlbaum Associates, Mahwah, NJ).
- Umeda, N. (1972). "Vowel duration in polysyllabic words in American English," *J. Acoust. Soc. Am.* **52**, 133(A).
- Umeda, N. (1975). "Vowel duration in American English," *J. Acoust. Soc. Am.* **58**, 434–445.
- van Bergem, D. R. (1990). "In defense of a probabilistic view on human word recognition," *Proc. Inst. Phonetic Sci. Amsterdam* **15**, 121–127.
- van Bergem, D. R. (1993). "Acoustic vowel reduction as a function of sentence accent, word stress, and word class," *Speech Commun.* **12**, 1–23.
- van Santen, J. P. H. (1992). "Contextual effects on vowel duration," *Speech Commun.* **11**, 513–546.
- Weismer, G., and Fennell, A. M. (1985). "Constancy of (acoustic) timing measures in phrase-level utterances," *J. Acoust. Soc. Am.* **78**, 49–57.
- Wightman, C. W., Shattuck-Hufnagel, S., Ostendorf, M., and Price, P. J. (1992). "Segmental durations in the vicinity of prosodic phrase boundaries," *J. Acoust. Soc. Am.* **91**, 1707–1717.
- Wiley, D. E. (1973). "The identification problem for structural equation models with unmeasured variables," in *Structural Equation Models in the Social Sciences*, edited by A. S. Goldberger and O. D. Duncan (Seminar, New York), pp. 69–83.
- Williams, D., Silverman, F., and Kools, J. (1969). "Disfluency behavior of elementary school stutterers and nonstutterers: Loci of instance of disfluency," *J. Speech Hear. Res.* **12**, 303–318.
- Whiteside, S. P. (1996). "Temporal-based acoustic-phonetic patterns in read speech: Some evidence for speaker sex differences," *J. Int. Phonetic Association* **26**, 23–40.
- Youngblut, J. M. (1994a). "A consumer's guide to causal modeling: Part I," *J. Pediatr. Nurs.* **9**, 268–271.
- Youngblut, J. M. (1994b). "A consumer's guide to causal modeling: Part II," *J. Pediatr. Nurs.* **9**, 409–413.

Irregular vocal-fold vibration—High-speed observation and modeling

Patrick Mergell^{a)}

Siemens Audiologische Technik GmbH, Gebbertstrasse 125, D-91058 Erlangen, Germany

Hanspeter Herzel^{b)}

Institute for Theoretical Biology, Humboldt University Berlin, Invalidenstrasse 43, D-10115 Berlin, Germany

Ingo R. Titze^{c)}

National Center for Voice and Speech, University of Iowa, 330 Wendell Johnson Building, Iowa City, Iowa 52242

(Received 9 March 2000; accepted for publication 7 August 2000)

Direct observations of nonstationary asymmetric vocal-fold oscillations are reported. Complex time series of the left and the right vocal-fold vibrations are extracted from digital high-speed image sequences separately. The dynamics of the corresponding high-speed glottograms reveals transitions between low-dimensional attractors such as subharmonic and quasiperiodic oscillations. The spectral components of either oscillation are given by positive linear combinations of two fundamental frequencies. Their ratio is determined from the high-speed sequences and is used as a parameter of laryngeal asymmetry in model calculations. The parameters of a simplified asymmetric two-mass model of the larynx are preset by using experimental data. Its bifurcation structure is explored in order to fit simulations to the observed time series. Appropriate parameter settings allow the reproduction of time series and differentiated amplitude contours with quantitative agreement. In particular, several phase-locked episodes ranging from 4:5 to 2:3 rhythms are generated realistically with the model. © 2000 Acoustical Society of America. [S0001-4966(00)02711-9]

PACS numbers: 43.70.Aj [AL]

I. INTRODUCTION

Irregularities in vocalization signals reveal the dynamical complexity of the vocal organs in humans, mammals, and birds (Nowicki and Capranica, 1986; Herzel, 1996; Fee *et al.*, 1998; Mergell *et al.*, 1999; Wilden *et al.*, 1998). Irregular vocal-fold vibrations are mostly perceived as a rough voice sound. They are observed in newborn cries (Sirviö and Michelsson, 1976; Mende *et al.*, 1990), noncry vocalizations of infants (Robb and Saxman, 1988), Russian lament (Mazo *et al.*, 1995), normal conversational speech (Dolansky and Tjernlund, 1968; Kohler, 1996), and especially in patients with vocal-fold lesions, paralysis, and other voice disorders (Herzel *et al.*, 1995). Vocal instabilities can be induced either by dysfunctions of the neural control or by pathological changes of the mechanical properties intrinsic to larynx (Titze, 1994).

There are strong indications that many vocal instabilities are manifestations of bifurcations and low-dimensional attractors of the highly nonlinear voice source. Indeed, subharmonics and the coexistence of two fundamental frequencies (biphonation) have been found in biomechanical simulations of the vocal-fold vibrations (Ishizaka and Isshiki, 1976; Isshiki *et al.*, 1977; Wong *et al.*, 1991; Smith *et al.*, 1992; Steinecke and Herzel, 1995). In all reports, different modifications of the two-mass model developed by Ishizaka and

Flanagan (1972) have been used in order to examine the cause and effect relationships between variations of crucial model parameters and vibratory patterns of the vocal cords. Asymmetric vocal-fold tension, resting glottal gap, and subglottal pressure have been generally pointed out to be the central parameters causing irregular vocal-fold oscillations.

So far, however, no quantitative comparison of observations and model simulations of irregular vocal-fold dynamics has been made. One important focus of this study is the conceptualization of the quantitative description of vocal irregularities. For that purpose, we combine digital high-speed cinematography and biomechanical modeling. We provide evidence that vocal irregularities can be manifestations of sudden dynamical transitions (bifurcations) which are induced by failing neural control of an injured larynx.

II. HIGH-SPEED OBSERVATION AND PARAMETER EXTRACTION

The examined subject is a 23-year-old woman with a complicated injury of the laryngeal branches of the vagus nerve. The complete adduction process and the activities of the ventricular folds were both recorded with the high-speed camera. Visual assessment by an expert provides indications for a complete paralysis of the left superior laryngeal nerve. The left ventricular fold is immobile, whereas the opposite ventricular fold shows a compensatory hyperfunction. The inferior laryngeal nerve appears to be partially injured, since only the rotation and the forward rocking of the vocal processes toward the glottal midline are affected. That means

^{a)}Electronic mail: mergell@med.siemens.de

^{b)}Electronic mail: herzel@itb.biologie.hu-berlin.de

^{c)}Electronic mail: titze@shc.uiowa.edu

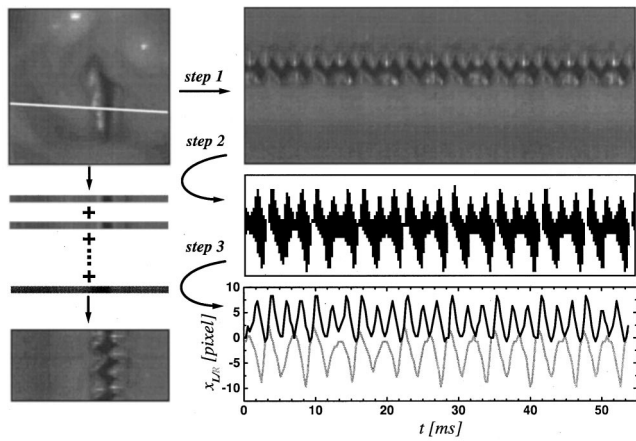


FIG. 1. Image processing and data reduction. The analyzed digital high-speed video has been recorded with the CAMSYS+128 camera system at an image rate of 3704/s. The first step of image processing is the extraction of subsequent image scan lines from the high-speed video sequence. The method is shown on the left side of the figure. The resulting gray-scale array (kymogram, top right) visualizes the trajectories of the midglottal edge points of the left and the right vocal folds. The second step is the binary segmentation of the kymogram. For that purpose, the gray-scale histogram is analyzed in order to detect the glottal components and to determine the corresponding gray-scale threshold. Above this threshold all pixels are coded white; below it all pixels are coded black as can be seen on the middle-right bitmap. The last step is the detection of the black–white boundary which corresponds to the oscillation amplitudes of the vocal folds. As final results one obtains the high-speed glottograms shown in the lower-right diagram. The oscillation pattern of this phonation episode exhibits a 2:3 phase locking. The algorithm for data reduction is a simplified and modified version of the kymographic image processing proposed by Wittenberg (1998).

that no sliding motion on the cricoidarytenoid joint could be observed in the high-speed video. This might be due to a dysfunction of the lateral cricoarytenoid and interarytenoid muscles. In contrast, the narrowing of the vocal folds by drawing the arytenoid cartilages forward due to the thyroarytenoid muscle action was possible. An objective diagnosis of the muscle functions using electromyographic recordings of the laryngeal muscles has not been made.

We use the high-speed camera system CAMSYS+128 described earlier by Bloss *et al.* (1993). The high-speed image sequences are recorded at a sampling rate of 3704 frames/s. A data reduction and pattern recognition algorithm is applied in order to obtain the time series of the vocal-fold oscillations (see Fig. 1). The first step is to extract one single horizontal scan line from each frame intersecting the vocal folds at half vocal-fold length. The resulting gray-scale array (kymogram) visualizes the change of the distance from one to the other vocal fold during phonation. By means of a subsequent binary segmentation, the space between the vocal folds, i.e., the glottis (black coded) is raised from the glottal environment (white coded). The upper and lower separation lines between black and white regions correspond to the left and right vocal-fold vibrations. We call the extracted time series high-speed glottograms (HGG), according to Wittenberg *et al.* (1995) and Eysholdt *et al.* (1996). The oscillation episode which is shown in Fig. 1 is characterized by a 2:3 phase-locking as it can be detected by counting the number of oscillation maxima of each vocal fold. Such an irregular oscillation pattern is typical for laryngeal paralyses (Herzel

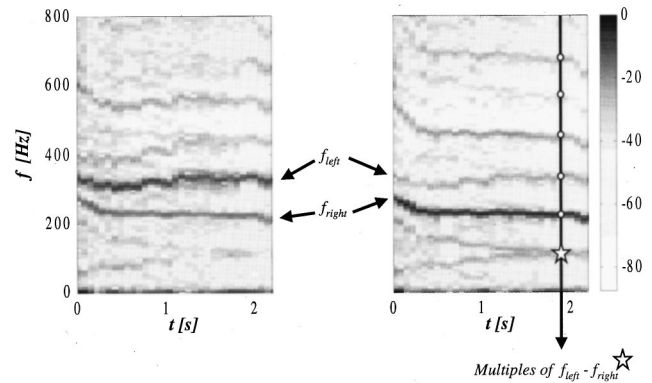


FIG. 2. Spectrograms of nonstationary asymmetric HGG. The spectrograms show subsequent short-time spectra of signal segments. The spectral amplitude is encoded using a gray scale. In this way the temporal evolution of spectral components can be visualized. Left graph: Spectrogram of the observed left vocal-fold oscillation. Right graph: Spectrogram of the observed right vocal-fold oscillation. At a certain point in time, the peak positions of the spectral components can be found at positive linear combinations of the two fundamental frequencies f_{left} and f_{right} .

et al., 1995). More details of the dynamics during the complete sample length emerge from the spectrograms of the left and the right vocal-fold oscillations (Fig. 2). Obviously, the fundamental frequency of the paralyzed vocal fold is detuned with respect to the fundamental frequency of the healthy vocal fold due to a different degree of muscle tonus. As a direct consequence of the asymmetric vocal-fold tensions, the spectra reveal the coexistence of two fundamental frequencies f_{left} and f_{right} . The frequency of the right vocal fold decreases monotonously from about 275 to 220 Hz, indicating a release of vocal-fold tension. In contrast, the frequency of the paralyzed vocal fold f_{left} varies slowly around 325 Hz. This indicates a higher tonus of the paralyzed vocal fold, which is untypical. Since the left vocal fold exhibits no atrophy, one might speculate that reinnervation is the reason for a permanent neural stimulation of the thyroarytenoid muscle which cannot be controlled voluntarily. The fine structure of the short-time spectra shows frequency components at positive linear combinations of the fundamental frequencies, i.e., at $f_{mn} = |mf_{\text{left}} + nf_{\text{right}}|$, where $m, n \in \dots -2, -1, 0, 1, 2, \dots$. These spectra are related to toroidal or quasiperiodic and entrained oscillations as found in many dynamical systems (Glass and Mackey, 1988; Bergé *et al.*, 1984). The laryngeal asymmetry can be parametrized by the coefficient Q , which is the ratio of the lower and the higher fundamental frequency. Consequently, $Q=1$ for symmetric conditions; $Q<1$ for asymmetric conditions. In cases where Q is close to a rational number (e.g., $1/2$, $2/3$, etc.) one obtains a discrete spectrum indicating entrainment or phase locking (f_{mn} are clearly separated). Consider as an example the 2:3 entrainment at about 2 s in Fig. 2 with a stack of frequency components at multiples of $f_{\text{left}} - f_{\text{right}}$. An irrational value of Q produces toroidal oscillations or biphonation with two incommensurate fundamental frequencies f_{left} and f_{right} . The nonstationarity of the measured time series originates mainly from the time-varying asymmetry coefficient. The time dependence can be expressed with a good accuracy by an exponential decay formula yielding an asymmetry coefficient which decreases from about 0.82 to 0.64. This sug-

TABLE I. Standard parameters in the symmetric simplified two-mass model for the simulation of normal phonation (Steinecke and Herzel, 1995).

m_1	m_2	k_1	k_2	k_c	r_1	r_2	c_1
0.125	0.025	0.08	0.008	0.025	0.02	0.02	$3k_1$
c_2	a_{01}	a_{02}	d_1	d_2	l	ρ	P_s
$3k_2$	0.05	0.05	0.25	0.05	1.4	0.001 13	0.008

gests that there are several regions of phase locking, e.g., 4:5, 3:4, and 2:3. We used the following fitting formula in order to determine Q_{exp} from the HGG

$$Q_{\text{exp}}(t) = \frac{f_{\text{right}}(t)}{f_{\text{left}}(t)} = a(1 + be^{-t/\tau}),$$

$$a = 0.64, \quad b = 0.28, \quad \tau = 0.98 \text{ s}, \quad (1)$$

where a , b , and τ are fitting parameters. The choice of the fitting formula depends on the variations of the fundamental frequencies. Since these variations are related to muscle activities and tissue properties, adequate fitting formulas are combinations of linear and exponential functions (Alipour-Haghighi and Titze, 1991; Titze, 1996). The fundamental frequencies f_{left} and f_{right} are determined in three steps. First, the HGG are filtered using a finite impulse response (FIR) filter with a Hamming window and a passband ranging from 30 to 800 Hz in order to remove higher-order harmonics due to vocal-fold contact and low-frequency contamination arising from movements of the endoscope relative to the larynx. The lower cutoff frequency is chosen to be halfway from the lowest difference frequency $f_{\text{left}} - f_{\text{right}} \approx 50$ Hz and the maximum tremor frequency (about 16 Hz) of the tremor frequency band as it was determined by Riviere *et al.* (1998). Second, we use a peak picking algorithm with quadratic interpolation to determine the time intervals between successive oscillation maxima from the resulting smoothed oscillation curves. The algorithm is adopted from Titze *et al.* (1987). Finally, the inverse of these time intervals is taken as the corresponding fundamental frequency. The ratio of these fundamental frequencies serves as the database for the non-linear curve fit.

A. Modeling

The experimentally measured asymmetry is the key for appropriate biomechanical modeling. For that purpose, we use a model which originates from a work by Ishizaka and Flanagan (1972). It has been simplified by Steinecke and Herzel (1995) in order to focus on the essential features causing bifurcations of the vocal-fold dynamics. We choose this model because it represents a good compromise between physiological completeness and computational costs. Moreover, its mathematical structure and its bifurcation behavior is well analyzed. Each vocal fold is represented by two coupled oscillators. The driving Bernoulli force which is influenced by the lung or subglottal pressure and the time-varying glottal geometry induces self-sustained oscillations. The corresponding differential equations and the default parameter settings are given in the Appendix and in Table I. For a detailed discussion of the rationales of the model de-

sign, we refer to the original work by Steinecke and Herzel (1995). Starting from the standard parameter set in Table I, several parameter changes are required to adjust the standard model to the specific patient. For the tuning of the fundamental frequencies to the experimental values the scaling laws $m_i \rightarrow m_i/q$ and $k_i \rightarrow qk_i$ with $q = 2.6$ are used for both vocal folds, where m_i are the model masses and k_i are the stiffness parameters. The glottal rest areas are estimated roughly from the high-speed sequence by determining the ratio of the length and the average vocal-fold distance in pixels, which is approximately 20:1. Consequently, the glottal rest areas are increased $a_{0i} = 0.1 \approx 0.07l$ with the standard vocal-fold length $l = 1.4$ and a vocal-fold distance of about 0.07. Moreover, it is necessary to decrease the damping ratios $r_i = 0.005$ for reproducing the observed oscillation patterns. Laryngeal asymmetry is imposed by using the relations

$$m_{il} = m_i, \quad k_{il} = k_i,$$

$$m_{ir} = m_i/Q, \quad k_{ir} = Qk_i. \quad (2)$$

The subglottal pressure, which could not be measured with our equipment, controls the energy supply of the vocal-fold oscillations and the left-right coupling mediated by the induced airflow. Hence, we have to scan the model dynamics in the Q - P_s plane in order to detect regions which correspond to the observed vocal-fold oscillations. For that purpose, time series are generated by varying the asymmetry coefficient and the subglottal pressure systematically. After a transient time of 800 ms, the oscillation maxima are determined by applying a peak picking algorithm with quadratic interpolation (Titze *et al.*, 1987). The oscillation maxima of one of the model masses m_{i1} at the corresponding (Q, P_s) coordinate is plotted. The result is a *roughness map* providing a good overview of the domains where normal and pathological vocal-fold vibrations can be found (compare Fig. 3).

Within the aphonia domain the subglottal pressure is not sufficient to cause self-sustained oscillations. At the boundary between the regions of aphonia and normal phonation a so-called Hopf bifurcation occurs (a transition from damped to self-sustained oscillations). This bifurcation is closely related to the phonation onset (Mergell *et al.*, 1998; Lucero, 1999). For $Q < 0.8$ and $P_s > 9$ cm H₂O, bifurcations from normal to irregular oscillations occur. Within the instability region Arnold tongues (entrainment) appear at rational Q (e.g., $Q = 2/3$, $Q = 3/4$) values indicated by a smaller number of oscillation maxima.

After analyzing the dynamical behavior within physiologically relevant parameter regions, the next step is to combine the experimental findings with the model equations

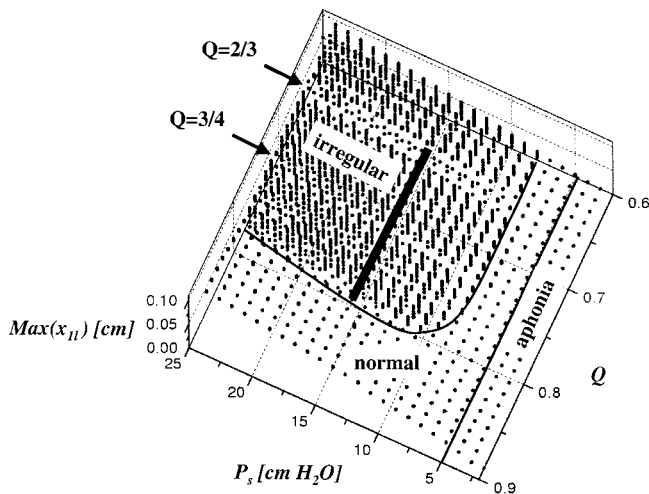


FIG. 3. The dynamic behavior of the simplified two-mass model is explored in the P_s - Q plane, which can be subdivided into three regions. In the region of “aphonia,” phonation cannot set in since the subglottal pressure is below threshold $P_s < 5$ cm H₂O. This region is separated from the region of “normal” phonation by the Hopf bifurcation line. Normal phonation is characterized by one single maximum during one period. Another bifurcation line separates the region of different “irregular” phonation patterns (typically more than one single oscillation maximum per period) from the region of normal phonation. Within the instability region, phase-locked oscillations occur at rational values of $Q = \{2/3, 3/4, \dots\}$ indicated by a smaller number of maxima during one period. The thick line corresponds to the simulation path used for matching the time series of the model to the HGG ($P_s = 16$ cm H₂O, $Q = Q_{\text{exp}}$).

in order to fit the simulated time series to the HGG. In the instability regions of the Q - P_s plane, tori (occurrence of two incommensurate frequencies) are clearly developed, e.g., around $P_s \approx 16$ cm H₂O. Along that pressure level, which is comparable to the upper pressure limit of the voice-range profile of a female around 350 Hz (Titze, 1994), one finds in the Q - P_s plane narrow windows with phase locking and adjacent tori within the asymmetry range of $Q_{\text{exp}}(t)$. For that reason, we use the simulation path at $P_s = 16$ cm H₂O as indicated in Fig. 3 in order to fit the time series of the model to the nonstationary asymmetric HGG.

III. COMPARISON AND RESULTS

An overview of the various nonlinear phenomena occurring in the recorded high-speed video sequence can be obtained from differentiated amplitude contours of the vocal-fold oscillations (Fig. 4). For direct comparison, these diagrams show the differences of subsequent oscillation maxima of the filtered HGG and of the simulated time series plotted over time. The amplitudes are normalized with the maximum value during examination time. Obviously, the characteristic features of the experimental data can be well described by the model simulations. The structural similarity of the differentiated amplitude contours is most evident in the regions where phase locking appears. In these time intervals the right-left comparison of the number of contour branches clearly exhibits a 4:5 relation between 0.2 and 0.3 s ($Q \approx 4/5$), a 3:4 relation between 0.6 and 0.7 s ($Q \approx 3/4$), a 5:7 relation between 1.0 and 1.1 s ($Q \approx 5/7$), and a 2:3 relation between 2.1 and 2.2 s ($Q \approx 2/3$), which are more pro-

nounced in the model contours. However, the model data guide the eyes to episodes of phase locking, as can be verified by zooming into the corresponding time intervals of the HGG. We show in Figs. 4(b)–(e) several phase-locked oscillation cycles for direct comparison of the experimental and simulated time series. The corresponding oscillatory patterns are very similar to each other. Although the observed vocal-fold oscillations are nonstationary and irregular, the simplified two-mass model allows one to reproduce their temporal characteristics apart from small deviations of phase and modulation amplitude adequately.

IV. DISCUSSION AND CONCLUSIONS

One important focus of this study is the conceptualization of the quantitative description of vocal instabilities due to laryngeal paralyses by means of biomechanical modeling. Although it is a single case study, the presented method has general character. The observed vocal-fold oscillations are representative for the class of pathologies characterized by laryngeal asymmetry without morphological changes, increased glottal rest area, and abnormally increased subglottal pressure, i.e., many forms of laryngeal paralyses (Woodson, 1993b, 1993a; Colton and Woo, 1995).

Earlier studies devoted to asymmetric vocal-fold models (Ishizaka and Isshiki, 1976; Smith *et al.*, 1992; Wong *et al.*, 1991) were restricted to simulations at a few parameter values or at one-parameter variations with a rough step size and to stationary vocal-fold vibrations. Later, Steinecke and Herzel (1995) studied the complex bifurcation scenarios by means of systematic two-parameter variations. Their method of detection and classification of instabilities in the resulting two-dimensional bifurcation diagrams in terms of the associated attractors was still lacking direct experimental comparison at that time. In the present study, the groundwork for modeling complex vibratory patterns is made along the same lines. Moreover, the described concept allows for nonstationary vocal-fold oscillations which are typical for many voice disorders.

Additional considerations were required for the fine adjustment of the model, i.e., the determination of the time dependence of the asymmetry coefficient and of the parameter deviations from the standard set. The crucial information, however, can only be obtained by high-speed examination of each vocal fold since the spectral contributions of the left and the right vocal-fold oscillations cannot be separated by stroboscopy, acoustic analysis, or electro-glottography (EGG). Here, our understanding of the term high-speed examination is a measurement of time series of at least one point of each vocal fold with a sampling frequency which is considerably higher than the fundamental frequency of the vocal-fold oscillations, e.g., high-speed glottography (Eysholdt *et al.*, 1996) and videokymography (Svec and Schutte, 1995). At present, the combined application of high-speed glottography, image processing, signal analysis, and biomechanical modeling is the most efficient way to give a quantitative diagnosis of voice disorder by means of the model parameter set. However, several parameters still have to be estimated (e.g., P_s , r_i). Their number and range is limited, and therefore the fitting of the simulated time series to HGG

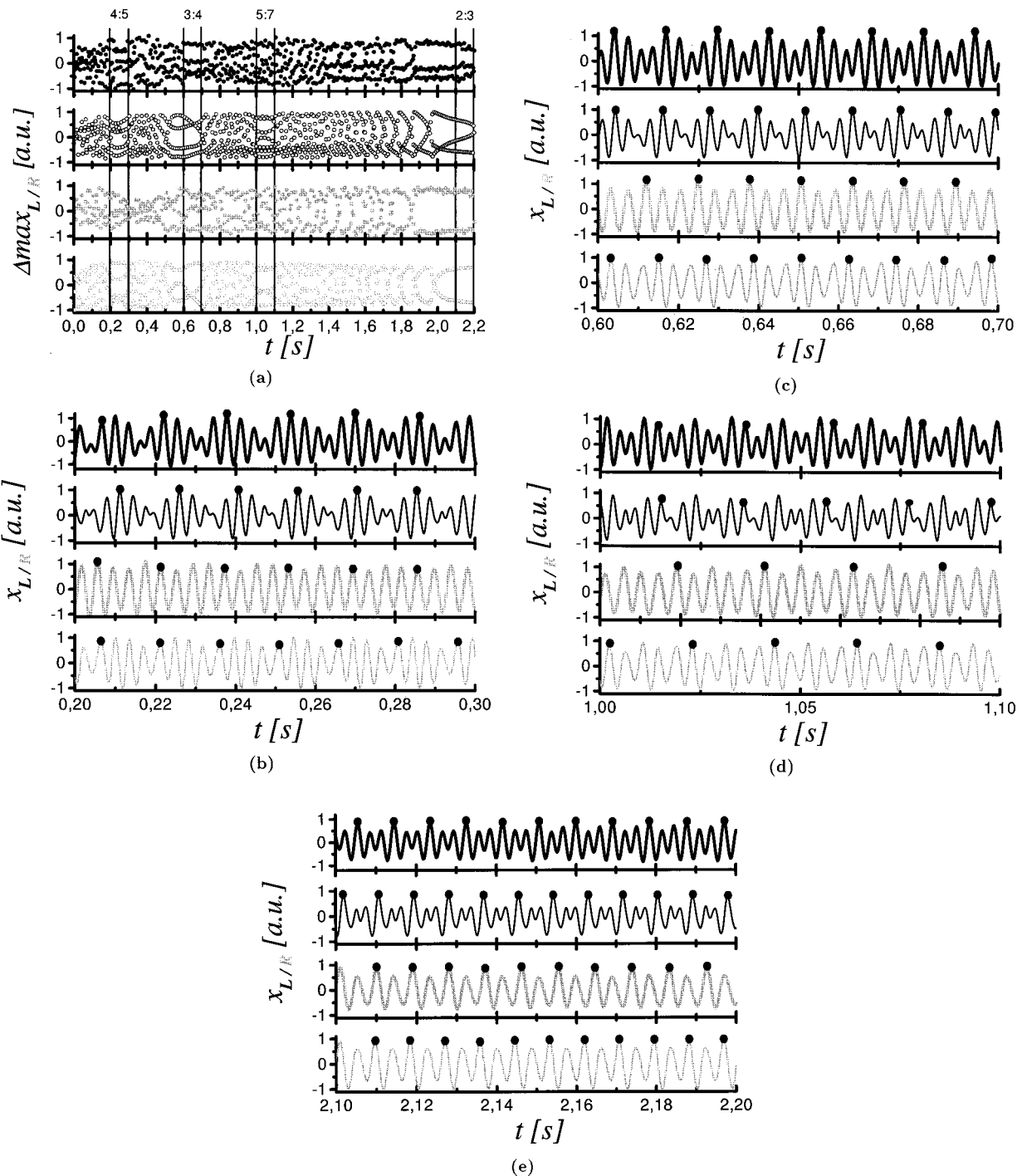


FIG. 4. (a) Differentiated amplitude contours of the nonstationary left (black) and right (gray) asymmetric vocal-fold oscillations. Prior to peak detection the observed vocal-fold oscillations have been filtered using a bandpass FIR filter (passband 30–800 Hz) in order to remove higher-order harmonics due to vocal-fold contact and low-frequency contamination arising from movements of the endoscope relative to the larynx. On the ordinates the differences of subsequent oscillation maxima are plotted (HGG: filled circles; simulations: unfilled circles). The subsequent maxima are extracted by using a peak picking algorithm with quadratic interpolation. Since the amplitudes of the experimental and the simulated data are of the same order of magnitude, the time series have been divided by their maximum values, i.e., about 1 mm. Hence, amplitude values are plotted with arbitrary units (a.u.). (b) Several periods of the simulated time series (thin lines) and the filtered HGG (thick lines) showing 4:5 phase locking. This episode is highlighted by corresponding markers in the differentiated amplitude scatter plots. The subsequent oscillation periods are indicated by filled black circles. (c) Several periods of the simulated time series (thin lines) and the filtered HGG (thick lines) showing 3:4 phase locking. This episode is highlighted by corresponding markers in the differentiated amplitude scatter plots. (d) Several periods of the simulated time series (thin lines) and the filtered HGG (thick lines) showing 5:7 phase locking. This episode is highlighted by corresponding markers in the differentiated amplitude scatter plots. (e) Several periods of the simulated time series (thin lines) and the filtered HGG (thick lines) showing 2:3 phase locking. This episode is highlighted by corresponding markers in the differentiated amplitude scatter plots.

can be done without too much ambiguity. In the future, experimental data of myoelastic properties or other examination methods might be combined to get more fitting constraints.

In the literature, several extensions of the two-mass model have been proposed with the aim to obtain more realistic simulations of laryngeal asymmetries than with competing modifications (Ishizaka and Isshiki, 1976; Isshiki *et al.*,

1977; Wong *et al.*, 1991; Smith *et al.*, 1992). The simplified asymmetric two-mass model used in the present work encompasses the minimum number of degrees of freedom and of parameters in comparison with other versions. According to the findings presented in this section, however, it allows the reconstruction of very complex laryngeal mechanisms with high accuracy.

The presented case study raises many interesting questions which could not be answered by conventional diagnostic handling. The pretherapeutic findings point to the fact that the patient was not able to compensate the laryngeal dysfunctions due to the paralysis. In most cases, the paralyzed vocal fold is flaccid and shows atrophy after degeneration (Titze, 1994). High-speed analysis before therapy revealed in our case that the tension of the nonparalyzed vocal fold was a considerable fraction Q_{exp} lower than the tension of the paralyzed left vocal fold, which is untypical. Certainly, theories relating glottal configurations to diverse impairments of the laryngeal nerve are controversially discussed (Woodson, 1993b, 1993a). However, in some cases, motion analysis of the vocal-fold oscillations, of the adduction and abduction processes might provide sufficient information to make a valuable diagnosis without using an invasive method, i.e., electromyography. After voice training, the compensation mechanisms showed an effect again. The high-speed examination after voice training reveals that the right ventricular fold is moved towards the glottal midline in order to enforce a higher degree of adduction (less glottal area at rest) and the muscle tonus of the right healthy vocal fold approaches the

tonus of the left vocal fold. As a consequence, the vocal-fold oscillations can be synchronized $Q_{\text{exp}}=1$ (symmetry) and therefore, normal vocal-fold vibrations can be produced again.

It has been demonstrated that the analyzed voice disorder can be classified by instability regions in the P_s-Q plane being a subset of the whole parameter space. One might speculate that once a laryngeal configuration is changed pathologically, the central nervous system is temporarily not able to handle the anomalous position in the parameter space. During voice training, compensatory strategies are learned which may help to find the way out of the instability regions. If the laryngeal injury cannot be compensated, adequate phonosurgery might be indicated for readjusting the crucial parameters. Certainly, more research is necessary to verify these hypotheses.

ACKNOWLEDGMENTS

This work has been supported by the Deutsche Forschungsgemeinschaft. We thank U. Eysholdt, M. Tigges, and T. Wittenberg at the Dept. of Phoniatrics and Pediatric Audiology (University Erlangen-Nuremberg) for many fruitful discussions.

APPENDIX

The dynamical system describing the motion of the model masses can be written as follows [according to Stei-
necke and Herzel (1995)]:

$$\frac{d}{dt} \begin{pmatrix} x_{1\alpha} \\ v_{1\alpha} \\ x_{2\alpha} \\ v_{2\alpha} \end{pmatrix} = \begin{pmatrix} 0 & 1 & 0 & 0 \\ -\left(\frac{k_{1\alpha}+k_{c\alpha}}{m_{1\alpha}}\right) & -\frac{r_{1\alpha}}{m_{1\alpha}} & \frac{k_{c\alpha}}{m_{1\alpha}} & 0 \\ 0 & 0 & 0 & 0 \\ \frac{k_{c\alpha}}{m_{2\alpha}} & 0 & -\left(\frac{k_{2\alpha}+k_{c\alpha}}{m_{2\alpha}}\right) & -\frac{r_{2\alpha}}{m_{2\alpha}} \end{pmatrix} \begin{pmatrix} x_{1\alpha} \\ v_{1\alpha} \\ x_{2\alpha} \\ v_{2\alpha} \end{pmatrix} + \begin{pmatrix} 0 \\ I_{1\alpha}(x_{1\alpha}) + \frac{1}{m_{1\alpha}} F_1(x_{1\alpha}, x_{2\alpha}) \\ 0 \\ I_{2\alpha}(x_{2\alpha}) \end{pmatrix}, \quad (\text{A1})$$

where $x_{i\alpha}$ are the oscillation amplitudes and $v_{i\alpha}$ are the corresponding velocities. The indices (i, α) distinguish (upper/lower) and (left/right) mass pairs. The matrix comprises the myoelastic information of the vocal folds and the 4-vector adds the nonlinearities to the model, i.e., the driving Bernoulli force and the contact forces. The parameter set has three subsets:

- (1) Parameters defining the glottal geometry at rest, i.e., vocal-fold length l , the vertical depths of the model masses d_i , and the glottal rest areas $a_{0i\alpha} = l x_{0i\alpha}$ at the level of the corresponding mass pair;
- (2) Parameters specifying the tissue properties, i.e., masses $m_{i\alpha}$, stiffness coefficients $k_{i\alpha}$, the coupling coefficients $k_{c\alpha}$, and damping coefficients $r_{i\alpha}$; and
- (3) Parameters specifying the aerodynamics of the model,

i.e., the air density at body temperature and corresponding humidity ρ and the subglottal pressure P_s .

The collision contribution which acts as an additional restoring force when the vocal folds make contact reads

$$I_{i\alpha}(x_{i\alpha}) = -\Theta(-a_i) \frac{c_{i\alpha}}{m_{i\alpha}} \frac{a_i}{2l}, \quad (\text{A2})$$

where $\Theta(x) = 1$ for $x > 0$ and $\Theta(x) = 0$ for $x < 0$ and $c_{i\alpha}$ are additional stiffness coefficients. $a_i = a_{0i} + l(x_{il} + x_{ir}) = a_{il} + a_{ir}$ with $a_{0i} = a_{0il} + a_{0ir}$ denotes the instantaneous glottal area. Nonlinearities of the elastic forces have been neglected.

For the derivation of the driving forces F_i , constant subglottal pressure and atmospheric pressure above the glottis is assumed, i.e., the effect of the vocal tract is neglected in a first approximation or the vocal-tract input pressure P_T

=0. We assume that an air jet separates at the point of minimum area a_{\min} , inducing an immediate pressure drop to zero. Consequently, in the simplified model without any extensions the driving force of the upper mass, F_2 is identically zero for all glottal configurations. Moreover, quasilinear flow throughout the glottis is assumed, which is a reasonable approximation according to numerical calculations by Liljencrants (1991).

$F_1 = l d_1 P_1$ is the force exerted by the pressure P_1 on the lower portion of the vocal folds. The corresponding pressure P_1 can be obtained from the Bernoulli law

$$P_s = \frac{\rho}{2} \left(\frac{U}{a_{\min}} \right)^2 = P_1 + \frac{\rho}{2} \left(\frac{U}{a_1} \right)^2. \quad (\text{A3})$$

Here, U denotes the glottal volume flow. Using

$$U = \sqrt{\frac{2P_s}{\rho}} a_{\min} \Theta(a_{\min}), \quad (\text{A4})$$

one obtains

$$P_1 = P_s \left[1 - \Theta(a_{\min}) \left(\frac{a_{\min}}{a_1} \right)^2 \right] \Theta(a_1). \quad (\text{A5})$$

In contrast to the model by Ishizaka and Flanagan (1972), the aerodynamic pressure is set to zero for a closed glottis since a pressure equilibrium is assumed at vocal-fold contact. This assumption is a consequence of the chosen glottal geometry.

Alipour-Haghighi, F., and Titze, I. R. (1991). "Elastic models of vocal fold tissues," *J. Acoust. Soc. Am.* **90**, 1326–1331.

Bergé, P., Pomeau, Y., and Vidal, C. (1984). *Order within Chaos* (Hermann and Wiley, Paris).

Bloss, H., Backert, C., and Raguse, A. (1993). CAMSYS high speed camera system. Fraunhofer Gesellschaft IIS, Erlangen, Germany.

Colton, R. H., and Woo, P. (1995). "Measuring vocal fold function," in *Diagnosis and Treatment of Voice Disorders*, edited by J. S. Rubin, R. T. Sataloff, G. S. Korovin, and W. J. Gould (Igaku-Shoin, New York, Tokyo), pp. 290–315.

Dolansky, L., and Tjernlund, P. (1968). "On certain irregularities of voiced-speech waveforms," *IEEE Trans. Audio Electroacoust.* **AU-16**, 51–56.

Eysholdt, U., Tigges, M., Wittenberg, T., and Pröschel, U. (1996). "Direct evaluation of high-speed recordings of vocal fold vibrations," *Folia Phoniatr.* **48**, 163–170.

Fee, M. S., Shraiman, B., Pesaran, B., and Mitra, P. P. (1998). "The role of nonlinear dynamics of the syrinx in vocalizations of a songbird," *Nature (London)* **395**, 67–71.

Glass, L., and Mackey, M. (1998). *From Clocks to Chaos* (Princeton University Press, Princeton).

Herzel, H., Berry, D. A., Titze, I. R., and Steinecke, I. (1995). "Nonlinear dynamics of the voice: Signal analysis and biomechanical modeling," *Chaos* **5**, 30–34.

Herzel, H. (1996). "Possible mechanisms of vocal instabilities," in *Vocal Fold Physiology: Controlling Complexity and Chaos*, edited by P. J. Davies and P. J. Fletcher (Singular, San Diego).

Ishizaka, K., and Flanagan, J. L. (1972). "Synthesis of voiced sounds from a two-mass model of the vocal cords," *Bell Syst. Tech. J.* **51**, 1233–1268.

Ishizaka, K., and Isshiki, N. (1976). "Computer simulation of pathological vocal-cord vibration," *J. Acoust. Soc. Am.* **60**, 1193–1198.

Isshiki, N., Tanabe, M., Ishizaka, K., and Broad, D. (1977). "Clinical significance of asymmetrical vocal cord tension," *Ann. Otol.* **86**, 58–66.

Kohler, K. J. (1996). "Articulatory reduction in German spontaneous speech," in *Proceedings of the 4th Speech Production Seminar (Autrans)*, edited by ESCA (Singular, San Diego), pp. 1–4.

Liljencrants, J. (1991). "Numerical simulation of glottal flow," in *Vocal Fold Physiology: Acoustics, Perception and Physiological Aspects of Voice Mechanisms*, edited by J. Gauffin and B. Hammarberg (Singular, San Diego), pp. 99–104.

Lucero, J. C. (1999). "A theoretical study of the hysteresis phenomenon at vocal fold oscillation onset–offset," *J. Acoust. Soc. Am.* **105**, 423–431.

Mazo, M., Ericson, D., and Harvey, T. (1995). "Emotion and expression: Temporal data on voice quality in Russian lament," in *Vocal Fold Physiology: Voice Quality Control*, edited by O. Fujimura and M. Hirano (Singular, San Diego), pp. 173–178.

Mende, W., Herzel, H., and Wermke, K. (1990). "Bifurcations and chaos in newborn cries," *Phys. Lett. A* **145**, 418–424.

Mergell, P., Herzel, H., Wittenberg, T., Tigges, M., and Eysholdt, U. (1998). "Phonation onset: Vocal fold modeling and high-speed glottography," *J. Acoust. Soc. Am.* **104**, 467–470.

Mergell, P., Fitch, W. T., and Herzel, H. (1999). "Modeling the role of nonhuman vocal membranes in phonation," *J. Acoust. Soc. Am.* **105**, 2020–2028.

Nowicki, S., and Capranica, R. R. (1986). "Bilateral syringeal interaction in vocal production of oscine bird sound," *Science* **231**, 1297–1299.

Riviere, C. N., Rader, R. S., and Thakor, N. V. (1998). "Adaptive canceling of physiological tremor for improved precision in microsurgery," *IEEE Trans. Biomed. Eng.* **45**, 839–846.

Robb, J. B., and Saxman, J. (1988). "Acoustic observations in young children's vocalizations," *J. Acoust. Soc. Am.* **83**, 1876–1882.

Sirviö, P., and Michelsson, K. (1976). "Sound-spectrographic cry analysis of normal and abnormal newborn infants," *Folia Phoniatr.* **28**, 161–173.

Smith, M. E., Berke, G. S., Gerratt, B. R., and Kreiman, J. (1992). "Laryngeal paralyses: Theoretical considerations and effects on laryngeal vibration," *J. Speech Hear. Res.* **35**, 545–554.

Steinecke, I., and Herzel, H. (1995). "Bifurcations in an asymmetric vocal fold model," *J. Acoust. Soc. Am.* **97**, 1878–1884.

Svec, J. G., and Schutte, H. K. (1995). "Videokymography: High-speed line scanning of the vocal fold vibration," *J. Voice* **10**, 201–205.

Titze, I. R., Horii, Y., and Scherer, R. C. (1987). "Some technical considerations in voice perturbation measurements," *J. Speech Hear. Res.* **30**, 252–260.

Titze, I. R. (1994). *Principles of Voice Production* (Prentice-Hall, Englewood Cliffs, NJ).

Titze, I. R. (1996). "Coupling of neural and mechanical oscillators in control of pitch, vibrato, and tremor," in *Vocal Fold Physiology: Controlling Complexity and Chaos*, edited by I. R. Titze (Singular, San Diego), pp. 47–62.

Wilden, I., Herzel, H., Peters, G., and Tembrock, G. (1998). "Subharmonics, biphonation, and deterministic chaos in mammal vocalization," *Bioacoustics* **9**, 171–196.

Wittenberg, T., Moser, M., Tigges, M., and Eysholdt, U. (1995). "Recording, processing and analysis of digital high-speed sequences in glottography," *Mach. Vision Appl.* **8**, 399–404.

Wittenberg, T. (1998). *Wissensbasierte Bewegungsanalyse von Stimmleipenschwingungen anhand digitaler Hochgeschwindigkeitsaufnahmen*. Ph.D. thesis (Shaker Verlag, Aachen).

Wong, D., Ito, M. R., and Cox, N. B. (1991). "Observation of perturbations in a lumped-element model of the vocal folds with application to some pathological cases," *J. Acoust. Soc. Am.* **89**, 383–394.

Woodson, G. E. (1993a). "Configuration of the glottis in laryngeal paralysis. I. Clinical study," *Laryngoscope* **103**, 1227–1234.

Woodson, G. E. (1993b). "Configuration of the glottis in laryngeal paralysis. II. Animal experiments," *Laryngoscope* **103**, 1235–1241.

A finite-element model of vocal-fold vibration

Fariborz Alipour,^{a)} David A. Berry, and Ingo R. Titze

Department of Speech Pathology and Audiology, The University of Iowa, Iowa City, Iowa 52242

(Received 25 April 2000; accepted for publication 20 September 2000)

A finite-element model of the vocal fold is developed from basic laws of continuum mechanics to obtain the oscillatory characteristics of the vocal folds. The model is capable of accommodating inhomogeneous, anisotropic material properties and irregular geometry of the boundaries. It has provisions for asymmetry across the midplane, both from the geometric and tension point of view, which enables one to simulate certain kinds of voice disorders due to vocal-fold paralysis. It employs the measured viscoelastic properties of the vocal-fold tissues. The detailed construction of the matrix differential equations of motion is presented followed by the solution scheme. Finally, typical results are presented and validated using an eigenvalue method and a commercial finite-element package (ABAQUS). © 2000 Acoustical Society of America. [S0001-4966(00)05112-2]

PACS numbers: 43.70.Bk [AL]

I. INTRODUCTION

In the last decade, speech science has benefited from new experimental data on the mechanical properties of human and animal tissues. In parallel, mathematical methods have advanced for highly efficient computer simulations of many dynamical systems. Because of the complexity of many of these systems, computer simulation becomes the only viable tool for solution. With any model of a physical or physiological process, there is always a tradeoff between simplicity and completeness. The model should be simple enough to be useful in conceptualization and prediction, but also complete enough to represent the process accurately.

This certainly applies to vocal-fold models. Early one- and two-mass models (Flanagan and Landgraf, 1968; Ishizaka and Flanagan, 1972) were simple enough to be described in a few pages of print. They were elegant in that they helped conceptualize the interaction between airflow and tissue movement to produce self-oscillation. But, there is considerable doubt that they represented the geometry and the viscoelastic properties of the vocal folds adequately to investigate voice disorders or special vocal qualities. For such purposes, continuum models of the vocal folds have been developed.

Assuming a linear constitutive relation for vocal-fold tissues, early continuum models investigated the vocal-fold resonance structure (Titze and Strong, 1975; Titze, 1976). While such models reported laryngeal eigenmodes and eigenfrequencies, the results were later shown to be inaccurate because improper boundary conditions were applied. In a more recent report (Berry and Titze, 1996), new eigenfrequencies and eigenmodes were computed using an analytical approximation technique known as the Ritz method (Huebner, 1975). Significantly, these latter results converged with *in vivo* studies on human subjects (Švec *et al.*, in press) in their description of the composite resonance of the vocal folds (Berry, submitted).

However, none of the aforementioned studies provided a complete solution to vocal-fold self-oscillation and the analytical techniques were generally limited to simple brick-shaped geometries. Also, eigenvalue studies were conducted in the absence of aerodynamic forces.

In order to consider more realistic geometries (boundary conditions), simulate the layered structure of the vocal folds, and include aerodynamic forces, a continuum model that solves the equations of motion is needed. Since these equations are time dependent and nonlinear partial differential equations, a finite-element model has been developed and presented in this paper. The computer code has been tested and refined in the last 16 years in our lab (Alipour and Titze, 1985a; 1988; 1996) and some typical results and validation cases will be presented later.

II. CONTINUUM MECHANICS OF VOCAL FOLDS

The finite-element method (FEM) to be developed here is based on the continuum mechanics, because the field variable that is solved for (here, the displacement vector) is continuously distributed through each element; as the size of the elements becomes smaller, the solution approaches an analytic solution. An advantage of the FEM is the ability to handle complex boundaries and driving forces. Before the continuum model of vocal-fold vibration is formulated, a few assumptions are stated that help to simplify the job without sacrificing the accuracy. These follow.

- (1) The vibration causes small deformations (linear elasticity).
- (2) The vibration takes place in a single plane only.
- (3) The tissue layers of the vocal fold are either isotropic or transversally isotropic (with the plane of isotropy being perpendicular to the tissue fibers). This assumption is based on measured mechanical properties of the vocal-fold tissues.
- (4) The effect of grids motion during finite-element space integration is neglected, assuming fixed control volume for integration.

^{a)} Author to whom correspondence should be addressed. Electronic mail: alipour@shc.uiowa.edu

The first assumption, which is the most crucial one, will also be supported later by some experimental results. While large deformations are expected in tissue deformations such as tongue movement in speech (Wilhelms-Tricarico, 1995) and the velum (Berry *et al.*, 1999), the time scale and amplitudes of motion are smaller in the vocal folds. For nonlinear static models (e.g., NASTRAN finite-element package developed by NASA), large deformations can be obtained through solution of small deformations iterated at intermediate steps. The dynamic solution of vocal folds naturally has many intermediate steps that are required in the time integration (about 100–200 per cycle), which makes deformation of each time step a small fraction of a millimeter. Dividing these displacements by a characteristic length, such as vocal-fold length, yields a very small strain that satisfies the small deformation requirement in linear elasticity theory.

The second assumption, that of planar oscillatory motion, is based on observations of trajectories of vocal-fold tissue (flesh points) during self-oscillation (Baer, 1981; Saito *et al.*, 1985). In the coronal plane, the trajectories tend to be ellipses, figures of eight, or more complicated figures. From a superior aspect, however, the trajectories are basically straight lines in the medial–lateral direction.

Finally, whenever fibers are present (as in the ligament and the muscle), their direction tends to be anterior–posterior, which is called the longitudinal direction. Experimental data have shown that vocal-fold tissues have stronger stiffness in the longitudinal direction than in the transverse direction (Hirano *et al.*, 1982). The mechanical properties across the fibers are similar in all directions.

Using our first assumption, a constitutive equation for six stress and six strain components can be written as

$$\sigma = [S]\varepsilon, \quad (1)$$

where σ is the stress tensor, ε is the strain tensor, and $[S]$ is a *stiffness matrix*. This is basically Hooke's law and corresponds to the proportionality between displacement and restoring force in a one-dimensional spring. In linear elasticity theory, $[S]$ is a 6×6 symmetric matrix, having 21 independent elastic constants in the most general case (18 plus 3 extra along the diagonal). But, for transverse isotropy, several elastic constants are dependent on each other, and many are zero. The total number of independent elastic constants for transversely isotropic materials becomes five (Lekhnitskii, 1981). These are the (E, ν) , Young's modulus, and Poisson's ratio in the plane transverse to the fibers, (E', μ', ν') , the Young's modulus, shear modulus, and Poisson's ratio along the longitudinal fiber axis. The shear modulus in the transverse plane can be obtained from the relation

$$\mu = \frac{E}{2(1 + \nu)}. \quad (2)$$

The generalized Hooke's law for the transversely isotropic material becomes

$$\varepsilon_x = \frac{1}{E}(\sigma_x - \nu\sigma_z) - \frac{\nu'}{E'}\sigma_y,$$

$$\begin{aligned} \varepsilon_z &= \frac{1}{E}(\sigma_z - \nu\sigma_x) - \frac{\nu'}{E'}\sigma_y, \\ \varepsilon_y &= -\frac{\nu'}{E'}(\sigma_x + \sigma_z) + \frac{1}{E'}\sigma_y, \\ \gamma_{xy} &= \frac{1}{\mu'}\tau_{xy}, \quad \gamma_{yz} = \frac{1}{\mu'}\tau_{yz}, \quad \gamma_{zx} = \frac{1}{\mu}\tau_{zx}. \end{aligned} \quad (3)$$

Using the second assumption of planar strain, a displacement vector is defined as

$$\psi = u(x, y, z, t)\mathbf{i} + w(x, y, z, t)\mathbf{k}, \quad (4)$$

where u and w are the lateral (x) and vertical (z) components of the displacement vector, which will be the focus of the finite-element formulation in this paper.¹ Using linear elasticity theory, the strain tensor is related to the displacement vector as

$$\varepsilon_{ij} = \frac{1}{2} \left(\frac{\partial u_i}{\partial x_j} + \frac{\partial u_j}{\partial x_i} \right) \quad (i, j = x, y, z), \quad (5)$$

where $u_x = u$, $u_y = v$, $u_z = w$, etc. The factor 1/2 facilitates the representation of the strains in indicial notation. However, the shear strains from this equations are 1/2 of the shear strains in Eq. (3). By inverting the equations of (3), solving for stress components, and combining with Eq. (5), one finds the following relation between stress and displacement functions:

$$\begin{aligned} \sigma_x &= c_1\mu \frac{\partial u}{\partial x} + c_2\mu \frac{\partial w}{\partial z}, \\ \sigma_z &= c_2\mu \frac{\partial u}{\partial x} + c_1\mu \frac{\partial w}{\partial z}, \\ \tau_{xy} &= \mu' \frac{\partial u}{\partial y}, \\ \tau_{yz} &= \mu' \frac{\partial w}{\partial y}, \\ \tau_{zx} &= \mu \left(\frac{\partial w}{\partial x} + \frac{\partial u}{\partial z} \right), \end{aligned} \quad (6)$$

where c_1 and c_2 are constants evaluated as

$$\begin{aligned} c_1 &= \frac{2(\alpha - \nu'^2)}{\alpha(1 - \nu) - 2\nu'^2}, \\ c_2 &= \frac{2(\alpha\nu - \nu'^2)}{\alpha(1 - \nu) - 2\nu'^2}, \\ \alpha &= \frac{E'}{E}. \end{aligned} \quad (7)$$

III. FORMULATION OF THE DISPLACEMENT FIELD

The potential energy of the deformed vibrating continuum is

$$\pi = U - W_p, \quad (8)$$

where U is the strain energy calculated from energy density as

$$U = \int \int \int_{cv} \frac{1}{2} (\sigma_x \varepsilon_x + \sigma_z \varepsilon_z + \tau_{xy} \gamma_{xy} + \tau_{yz} \gamma_{yz} + \tau_{zx} \gamma_{zx}) dv. \quad (9)$$

W_p is the virtual work defined as

$$W_p = \int \int \int_{cv} (B_x u + B_z w) dv + \int \int_A (T_x u + T_z w) dA, \quad (10)$$

where B_x and B_z are transverse components of the body force (inertia) and T_x and T_z are transverse components of the surface forces (Ugural and Fenster, 1981). When we discretize the continuum into the finite elements, the domain of the integrations in Eqs. (9) and (10) are the individual elements. To simplify the complexity of three-dimensional geometry, the vocal fold is divided into M thin layers along its length ($M=15$), such that the foregoing planar strain approximations can be applied to each layer. If the layers are thin enough, the displacement field does not change much across the thickness of each layer and may be assumed uniform. With h as the thickness of a layer, the potential energy becomes

$$\begin{aligned} \pi = & \frac{\mu h}{2} \int \int_A \left[c_1 \left(\frac{\partial u}{\partial x} \right)^2 + c_1 \left(\frac{\partial w}{\partial z} \right)^2 + 2c_2 \frac{\partial u}{\partial x} \frac{\partial w}{\partial z} \right] dA \\ & + \frac{\mu h}{2} \int \int_A \left[\frac{\partial u}{\partial z} + \frac{\partial w}{\partial x} \right]^2 dA \\ & + h \int \int_A \rho \left(u \frac{\partial^2 u}{\partial t^2} + w \frac{\partial^2 w}{\partial t^2} \right) dA - h \int_s (T_x u + T_z w) ds. \end{aligned} \quad (11)$$

A term that would normally appear as

$$J = \mu' \left[\left(\frac{\partial u}{\partial y} \right)^2 + \left(\frac{\partial w}{\partial y} \right)^2 \right] \quad (12)$$

is dropped temporarily here due to the assumption of a uniform displacement field across the layer, but the effect of the fiber tension between layers will be included later in the external forces exerted on each layer. Formulation of the vibration problem within each layer as a quasistatic system is now carried out by minimization of the total potential energy of the system via a variational principle (Zienkiewicz, 1977).

IV. FINITE-ELEMENT DISCRETIZATION

The concept of a finite element is based on the ability to interpolate the field variable within the element from the field values at nodes of that element. Using this concept, the integrations in Eq. (11) can be carried out easily. Using a triangular plane element within each layer, the displacement field can be written for each element as

$$\begin{aligned} u &= \sum_{i=1}^3 N_i(x,z) U_i(y,t), \\ w &= \sum_{i=1}^3 N_i(x,z) W_i(y,t), \end{aligned} \quad (13)$$

where U_i is the x component of displacement vector at node i of the element and W_i is the corresponding z component. The interpolation function (also called the shape function) $N_i(x,z)$, which can be selected as linear or higher order polynomial, defines the shape of the displacement field for each layer. The choice of higher order usually gives more accurate results at the price of a heavier computational load. In this version of the model, a linear shape function of the form

$$N_i = \frac{1}{2A} (\alpha_i + \beta_i x + \gamma_i z) \quad (14)$$

is used, where A is the area of the element and α , β , γ are coefficients calculated from the nodal coordinates. The advantage of this linear shape function is that it makes the many partial derivatives in Eq. (11) constants, allowing analytic evaluation of the integrations.

The equations of motion are obtained by setting the variations of potential energy with respect to nodal displacements to zero. Since Eq. (11) has nine terms, we can define the potential energy of each element as

$$\pi^e = \sum_{k=1}^9 I_k. \quad (15)$$

Then, the variational principle gives

$$\begin{aligned} \frac{\partial \pi^e}{\partial U_i} &= \sum_{k=1}^9 \frac{\partial I_k}{\partial U_i} = 0, \\ \frac{\partial \pi^e}{\partial W_i} &= \sum_{k=1}^9 \frac{\partial I_k}{\partial W_i} = 0, \end{aligned} \quad (16)$$

which yields six equations for the nodal displacements U_i and W_i . To carry out these operations with a series of integrations and summations, we can benefit from the linearity of the shape function that yields simple results upon partial derivations, such as

$$\begin{aligned} \frac{\partial u}{\partial x} &= \sum U_i \frac{\partial N_i}{\partial x} = \frac{1}{2A} \sum \beta_i U_i, \\ \frac{\partial w}{\partial z} &= \sum W_i \frac{\partial N_i}{\partial z} = \frac{1}{2A} \sum \gamma_i W_i, \\ \frac{\partial^2 u}{\partial t^2} &= \sum N_i \frac{\partial^2 U_i}{\partial t^2} = \sum N_i \ddot{U}_i, \end{aligned} \quad (17)$$

where the double overdots represent the second time derivative. Similar expressions are obtained for various derivatives in Eq. (11). Substituting these expressions into (16) yields six sets of equations for the displacement vectors at the element's three nodes and the shape functions. However, once the integrations are carried out over the elemental domain, the equations will include only the nodal displacement vector

and other constants. For example, the first integral yields

$$\begin{aligned}
 I_1 &= \frac{1}{2} h c_1 \mu \int \int \left(\frac{\partial u}{\partial x} \right)^2 dA \\
 &= \frac{1}{2} h c_1 \mu \frac{1}{4A^2} \int \int \left[\sum_{A_e} \beta_i U_i \right]^2 dA, \\
 \frac{\partial I_1}{\partial U_i} &= \frac{1}{2} h c_1 \mu \frac{\beta_i}{2A} \sum_{k=1}^3 \beta_k U_k, \quad \frac{\partial I_1}{\partial W_i} = 0.
 \end{aligned} \tag{18}$$

During these operations, one particular integral has specific values that are evaluated analytically (see Huebner, 1975)

$$\begin{aligned}
 S_{ij} &= \int \int_{A_e} N_i N_j dA \\
 &= \frac{1}{6} \text{ for } i=j, \quad = \frac{1}{12} \text{ for } i \neq j.
 \end{aligned} \tag{19}$$

This matrix will be used in the evaluation of some of those integrals. Also, the last two integrals provide the forcing vector as

$$\begin{aligned}
 \frac{\partial I_8}{\partial U_i} &= -h \int T_x N_i ds = -h F_i^x, \\
 \frac{\partial I_9}{\partial W_i} &= -h \int T_z N_i ds = -h F_i^z.
 \end{aligned} \tag{20}$$

Performing all nine integrations similar to (18) yields the following set of equations:

$$\begin{aligned}
 \frac{c_1 \mu \beta_i}{4A} \sum_{k=1}^3 \beta_k U_k + \frac{c_2 \mu \beta_i}{4A} \sum_{k=1}^3 \gamma_k W_k + \frac{\mu \gamma_i}{4A} \sum_{k=1}^3 \gamma_k U_k \\
 + \frac{\mu \gamma_i}{4A} \sum_{k=1}^3 \beta_k W_k + \rho A \sum_{k=1}^3 S_{ik} \ddot{U}_k = F_i^x,
 \end{aligned} \tag{21}$$

and

$$\begin{aligned}
 \frac{c_1 \mu \gamma_i}{4A} \sum_{k=1}^3 \gamma_k W_k + \frac{c_2 \mu \gamma_i}{4A} \sum_{k=1}^3 \beta_k U_k + \frac{\mu \beta_i}{4A} \sum_{k=1}^3 \beta_k W_k \\
 + \frac{\mu \beta_i}{4A} \sum_{k=1}^3 \gamma_k U_k + \rho A \sum_{k=1}^3 S_{ik} \ddot{W}_k = F_i^z.
 \end{aligned} \tag{22}$$

The effects of viscous damping are included by replacing μ with $\mu + \eta \partial/\partial t$ (η stands for viscosity) in the preceding equations. This will add some additional terms containing the first time derivative of displacement vector. The resulting equations are six second-order differential equations for the element nodal displacement vector that resemble the equation for a mass-spring oscillator.

V. STIFFNESS, DAMPING, AND MASS MATRICES

The equations of motion for the elements (21) and (22) can be cast into the elemental matrix differential equations. Then, we can combine all these elemental matrices into global matrices and solve them using appropriate initial and boundary conditions. To facilitate formulation in matrix form, some auxiliary vectors are defined as

$$\begin{aligned}
 \{B\} &= [\beta_1 \beta_2 \beta_3 \beta_1 \beta_2 \beta_3]^T, \\
 \{G\} &= [\gamma_1 \gamma_2 \gamma_3 \gamma_1 \gamma_2 \gamma_3]^T.
 \end{aligned} \tag{23}$$

These vectors are calculated from the element's nodal coordinates. By defining the nodal displacement vector as

$$\{\psi\} = [U_1 U_2 U_3 W_1 W_2 W_3]^T, \tag{24}$$

and the forcing vector as

$$\{F\} = [F_1^x F_2^x F_3^x F_1^z F_2^z F_3^z]^T, \tag{25}$$

where U_i and W_i are x and z components of displacement vector at node i , F^x and F^z are the x and z components of the nodal force vector for the element, respectively. With these definitions, a matrix equation of motion for the element is obtained as

$$[M]\{\ddot{\psi}\} + [D]\{\dot{\psi}\} + [K]\{\psi\} = \{F\}, \tag{26}$$

where $[M]$ is mass matrix, $[D]$ is the damping matrix, and $[K]$ is the stiffness matrix, all of dimension 6×6 . Equating first the terms of $[K]\{\psi\}$ to the corresponding terms in Eqs. (21) and (22), we have the elements of the stiffness matrix as

$$\begin{aligned}
 K_{ij} &= \frac{\mu}{4A} (c_1 B_i B_j + G_i G_j) \quad i=1 \text{ to } 3, j=1 \text{ to } 3, \\
 K_{ij} &= \frac{\mu}{4A} (c_2 B_i G_j + G_i B_j) \quad i=1 \text{ to } 3, j=4 \text{ to } 6, \\
 K_{ij} &= \frac{\mu}{4A} (c_2 G_i B_j + B_i G_j) \quad i=4 \text{ to } 6, j=1 \text{ to } 3, \\
 K_{ij} &= \frac{\mu}{4A} (c_1 G_i G_j + B_i B_j) \quad i=4 \text{ to } 6, j=4 \text{ to } 6,
 \end{aligned} \tag{27}$$

where A is the area of the element. Equating the terms of $[D]\{\dot{\psi}\}$ to the corresponding terms in Eqs. (21) and (22), we have the elements of the damping matrix as

$$\begin{aligned}
 D_{ij} &= \frac{\eta}{4A} (c_1 B_i B_j + G_i G_j) \quad i=1 \text{ to } 3, j=1 \text{ to } 3, \\
 D_{ij} &= \frac{\eta}{4A} (c_2 B_i G_j + G_i B_j) \quad i=1 \text{ to } 3, j=4 \text{ to } 6, \\
 D_{ij} &= \frac{\eta}{4A} (c_2 G_i B_j + B_i G_j) \quad i=4 \text{ to } 6, j=1 \text{ to } 3, \\
 D_{ij} &= \frac{\eta}{4A} (c_1 G_i G_j + B_i B_j) \quad i=4 \text{ to } 6, j=4 \text{ to } 6.
 \end{aligned} \tag{28}$$

Finally, the elements of the mass matrix for a tissue density of ρ are

$$\begin{aligned}
 M_{ij} &= \rho A S_{ij} \quad \text{for } i, j=1 \text{ to } 3, \\
 M_{ij} &= \rho A S_{i-3, j-3} \quad \text{for } i, j=4 \text{ to } 6, \\
 M_{ij} &= 0 \quad \text{otherwise.}
 \end{aligned} \tag{29}$$

VI. NODAL FORCE VECTOR

The nodal force vector is the resultant of the transverse force and the string force (effects of adjacent layers) acting

on each element. When the transverse force is only the aerodynamic pressure force, with components P_x and P_z , we have

$$\begin{aligned} F_i^x &= \int P_x N_i ds \\ F_i^z &= \int P_z N_i ds. \end{aligned} \quad (30)$$

The integration on each side (surface) of the element provides the contribution from that side to the nodal force vector. If we assume the pressure distribution on the surface is linear, then the integration results in the expression in terms of nodal pressure. Consider triangular elements with vertices (nodes) numbered 1, 2, and 3 with their sides sharing the number of opposing nodes. A nodal loading factor f_i defines the existence of the load on its opposite side as

$$\begin{aligned} f_i &= 1 && \text{if its opposite side has pressure load,} \\ f_i &= 0 && \text{if not.} \end{aligned}$$

If a pressure load exists on any side, the load is assumed linearly distributed on that side and can be evaluated at the endpoint nodes of that side by balancing the force and moments. For example, the components of the pressure force at node 1 in the element with nodal pressure P_1 , P_2 , and P_3 at the corresponding nodes are

$$\begin{aligned} F_1^x &= f_2 \beta_2 (2P_1 + P_3)/6 + f_3 \beta_3 (2P_1 + P_2)/6, \\ F_1^z &= f_2 \gamma_2 (2P_1 + P_3)/6 + f_3 \gamma_3 (2P_1 + P_2)/6. \end{aligned} \quad (31)$$

The string (fiber) component acting on each element is proportional to its area, longitudinal shear modulus, and the slope of string or tissue fibers that pass through that element. This force is the resistance of the adjacent layers to the motion of the element due to shear force. The components of this force are calculated from the integration of term J or Eq. (12), assuming derivatives are constant within each element yielding

$$\int_{A_e} J dA = \mu' A \left[\left(\frac{\partial u}{\partial y} \right)^2 + \left(\frac{\partial w}{\partial y} \right)^2 \right]. \quad (32)$$

Taking variations of Eq. (32) with respect to y derivatives yields two additional terms that, when moved to the right-hand side of Eqs. (21) and (22), appear as string shear forces below

$$\begin{aligned} S^x &= -\mu' 2A \frac{\partial u}{\partial y}, \\ S^z &= -\mu' 2A \frac{\partial w}{\partial y}, \end{aligned} \quad (33)$$

where $2A$ is the total area (both sides) of the element in contact with its adjacent layers.

Now that we have obtained a matrix differential equation that is equivalent to six second-order differential equations for each element, we need to combine all the equations within each layer. The resulting global system of equations includes all the nodes in the layer and, in the matrix form, is similar to Eq. (26), with the difference that the vectors have

twice as many elements as the number of nodes. The coefficient matrices are much larger and are obtained by assembling the corresponding elemental matrices. The assembly process can be performed by nodes or by elements. For example, for assembly by elements, one needs to add the contributions of every node of that element to the global matrices. A similar assembly process is required for the global force vector. The global matrices are banded symmetric matrices, where the bandwidth is dependent upon the node numbering which should be arranged to minimize the bandwidth for computational speed and to reduce memory requirement (Zienkiewicz, 1977).

VII. TIME INTEGRATION

The finite-element method yields a solution of the spatial problem, but leaves a second-order matrix differential equation in time. Solution of this equation can be obtained by a finite difference scheme, marching along with a specific time step from a known initial condition. For ease of notation, we drop the vector and matrix brackets from the global equation and write it as

$$M \ddot{\psi} + D \dot{\psi} + K \psi = F. \quad (34)$$

Using a central difference approximation, we can write

$$\begin{aligned} \dot{\psi} &= \frac{\psi_{n+1} - \psi_{n-1}}{2\Delta t} + O(\Delta t)^2, \\ \ddot{\psi} &= \frac{\psi_{n+1} - 2\psi_n + \psi_{n-1}}{(\Delta t)^2} + O(\Delta t)^2, \end{aligned} \quad (35)$$

where the index refers to the vector evaluated at that time step. The stiffness force is replaced by its average at time steps of n and $n+1$ for stability of the system, i.e.,

$$K \psi = K \frac{\psi_n + \psi_{n+1}}{2}. \quad (36)$$

Substitution of this term into Eq. (34) yields

$$\begin{aligned} [M + 0.5(\Delta t)D + 0.5(\Delta t)^2 K] \psi_{n+1} \\ = (\Delta t)^2 F_n - [0.5(\Delta t)^2 K - 2M] \psi_n \\ - [M - 0.5(\Delta t)D] \psi_{n-1}. \end{aligned} \quad (37)$$

The displacement vector ψ_{n+1} is calculated from the two previous time-step vectors ψ_n and ψ_{n-1} . Having two initial conditions, namely ψ_0 and $\dot{\psi}_0$, will enable one to find the displacement vector at any time by using the above recursive relation. The computation across layers is serial rather than simultaneous at this time, which may have some effects on the string force calculations. This can be remedied in the future refinement through three-dimensional modeling of the vocal folds and parallel processing of the computation. Since the purpose of finite-element solution of vocal fold is to simulate speech production, a model of airflow and acoustic model of wave propagation in the vocal tract is used in the following sections, but details are not discussed here and are beyond the purpose and scope of this article. Interested readers may refer to Alipour and Scherer (in press) and Lai and Alipour (submitted) or similar publications for further de-

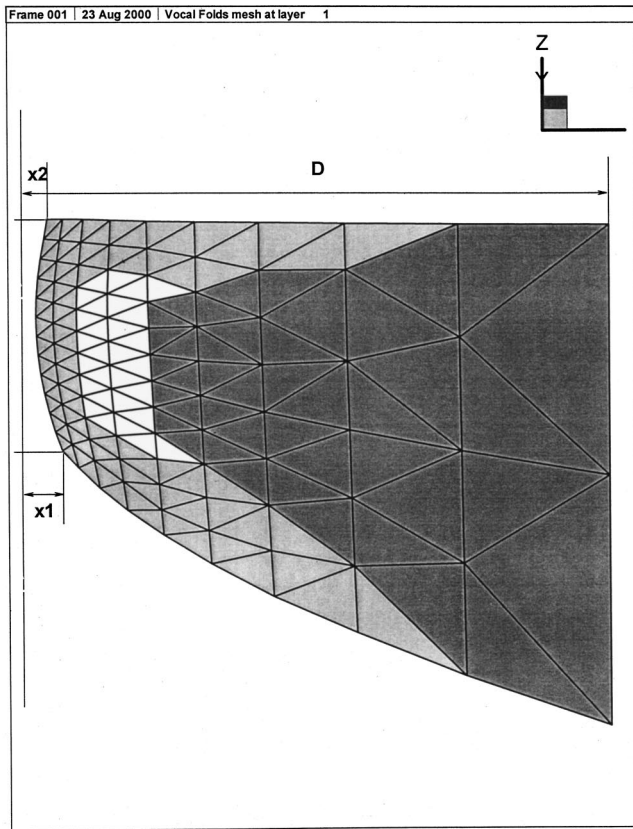


FIG. 1. The vocal-fold mesh in a coronal layer midway between anterior and posterior extremes. The dark gray represents the vocal-fold body, light gray represents the cover, and white region represents ligament. The vocal-fold dimensions are defined by its depth D and thickness T at the posterior end and its length L . The inferior and superior glottal half widths ($X1$ and $X2$) define the glottal adduction.

tails. At every time step (50 microseconds), the global matrices are first calculated; then, the pressure distribution from the airflow is obtained and used to calculate the forcing vector. Once the solution is found for the displacement of left and right vocal folds, the boundary conditions are enforced by looking at the nodal degrees of freedom. The nodes that are stationary or fixed are excluded from the solution scheme after assembly process. When vocal folds touch each other, the contact nodes lose one degree of freedom. Finally, the nodal coordinates are updated for that time step.

VIII. VALIDATION AND TYPICAL RESULTS

Fortunately, many aspects of the proposed finite-element model may be validated by comparing its results with standard FEM packages. As an example, Berry and Titze (1996) calculated the normal modes of a continuum model of vocal-fold tissues. They also duplicated their analytic calculations using ABAQUS, a commercial, nonlinear finite-element package. In a similar manner, the current FEM model is validated by comparing its output with eigenvalue solutions obtained from ABAQUS.

Although the eigenmodes and eigenfrequencies from ABAQUS do not provide solutions identical to those obtained from a self-oscillating model (because self-oscillation is a nonlinear process), the results from the two models should be comparable qualitatively. Because experimental *in vivo*

TABLE I. Input parameters used in model.

Vocal folds static length, L	1.6 cm
Vocal folds depth, D	1.0 cm
Vocal folds thickness, T	0.45 cm
Inferior glottal width	0.06 cm
Superior glottal width	0.02 cm
Lung pressure P_L	0.8 kPa
Longitudinal Poisson's ratio for all tissue layers (ν'_b, ν'_c, ν'_l)	0.0
Transverse Poisson's ratio for all tissue layers (ν_b, ν_c, ν_l)	0.9
Longitudinal shear modulus of the body, μ_b^a	12 kPa
Longitudinal shear modulus of the cover, μ_c^a	10 kPa
Longitudinal shear modulus of the ligament, μ_l^a	40 kPa
Transverse shear modulus of the body, μ_b	1.05 kPa
Transverse shear modulus of the cover, μ_c	0.53 kPa
Transverse shear modulus of the ligament, μ_l	0.87 kPa
Body viscosity, η_b	6 poise
Cover viscosity, η_c	3 poise
Ligament viscosity, η_l	5 poise
Thyroarytenoid muscle activity	70%

^aThis value accounts for the passive aspect of the shear modulus only. An additional "active" shear modulus is added to this amount for the muscle or body, as explained in Alipour and Scherer (in press).

observations have demonstrated that vocal-fold resonance frequencies correlate well with the corresponding phonation frequency (Kaneko *et al.*, 1986), the self-oscillating modes are not driven far from the natural modes. In addition, the empirical eigenfunctions extracted from self-oscillating vocal-fold models have been shown to correspond to the eigenmodes calculated from linearized versions of the models, which ignore the influence of glottal airflow and collision (Berry *et al.*, 1994; Berry and Titze, 1996). In these studies, the correspondence between eigenmodes and empirical eigenfunctions was noted both in terms of modal shape and frequency of oscillation.

To facilitate comparison of the two calculations, the same nodal coordinates and finite-element mesh that were utilized in our self-oscillating FEM model were used to create a finite-element mesh in ABAQUS. Figure 1 shows the finite-element mesh pattern that was used for each layer. More discussion on the vocal-fold geometry and input parameters will be given later, along with some typical waveform results. Although the self-oscillating model was a 2D/3D hybrid to optimize speed of computation (i.e., using the uniform layer assumption), 3D elements were implemented in ABAQUS to compare our results with the output of a complete 3D model, which tested the validity of our 2D/3D hybrid technique. In ABAQUS, standard 6-node, 3-D, linear elements were utilized. Beyond the finite-element mesh, elastic constants have been measured for various vocal-fold tissues (Alipour and Titze, 1985b, 1991, 1999; Hirano *et al.*, 1982; Min *et al.*, 1995; Chan and Titze, 1999) and used in the model, as indicated in Table I.

Using identical input parameters, eigenmodes and eigenfrequencies were calculated in ABAQUS, as shown in Fig. 2, and empirical eigenfunctions were extracted from our self-oscillating finite-element model, as shown in Fig. 3. The eigenfrequencies for the three eigenmodes shown in Fig. 2 were (a) 137 Hz; (b) 165 Hz; and (c) 195 Hz, respectively. The phonation frequency of our self-oscillating finite-

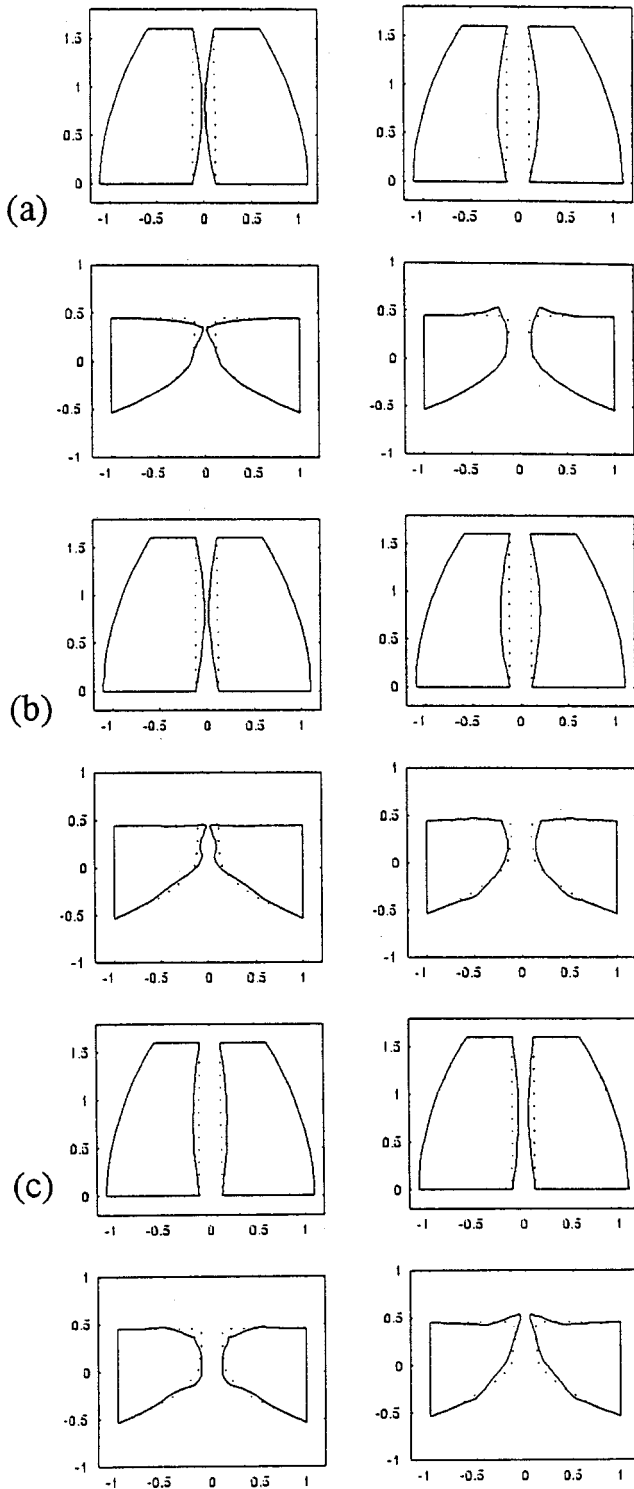


FIG. 2. Eigenmodes (a) one; (b) two; and (c) three obtained from ABAQUS. The top row shows a superior view, and the bottom row a coronal view. Columns one and two show projections of the eigenmodes at their extreme values, separated by a 180° phase difference. The numbers on the axes refer to linear dimensions in centimeters.

element model was 147 Hz, and the two empirical eigenfunctions of Fig. 3 entrained at this frequency. In terms of the previous experimental studies of Kaneko *et al.* (1986), this is a believable result. It is also reasonable that the two lowest eigenmodes would entrain in the vicinity of 150 Hz, roughly the average between the two frequencies.

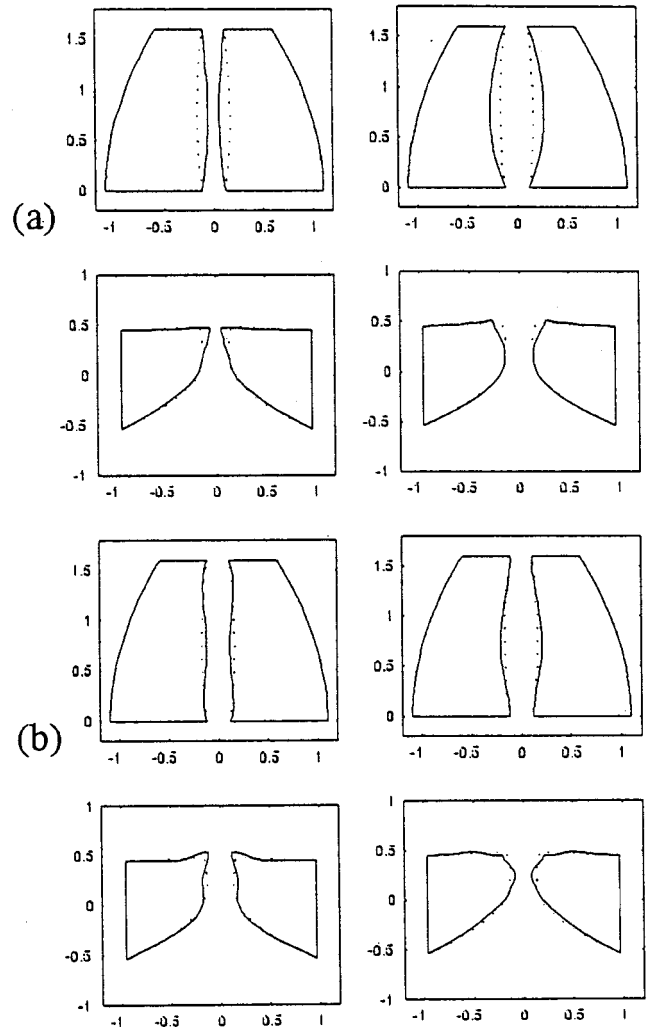


FIG. 3. Empirical eigenfunctions (a) one; and (b) two extracted from the finite-element simulation, explaining 93% and 5% of the vibrational variance, respectively. The row and column descriptions and labels on the axes are similar to Fig. 2.

By itself, the eigenfunction shown in Fig. 3(a) captured most of the oscillation pattern, describing 93% of the variance of the nodal trajectories. This eigenfunction showed a reasonable correspondence with the first eigenmode, as shown in Fig 2(a). The eigenfunction in Fig. 3(b) described an additional 5% of the variance, and showed a reasonable correspondence with the third eigenmode, as shown in Fig. 2(c). In addition, this eigenfunction captured some of the wave-like motion along the medial surface that was manifested in the second eigenmode, as shown in Fig. 2(b). This eigenfunction also captured some subtle higher-order effects in the vibration pattern, as shown in the superior view of Fig. 3(b), i.e., with three half-wavelengths appearing along the medial edge of the anterior–posterior length of the folds. Together, the two eigenfunctions explained 98% of the variance, which is comparable to results obtained from previous finite-element investigations (Berry *et al.*, 1994) and high-speed imaging studies of excised larynges (Berry, submitted). Because the nonlinear effects of glottal airflow and vocal-fold collision are not considered in the computation of eigenfrequencies and eigenmodes, it is expected that the em-

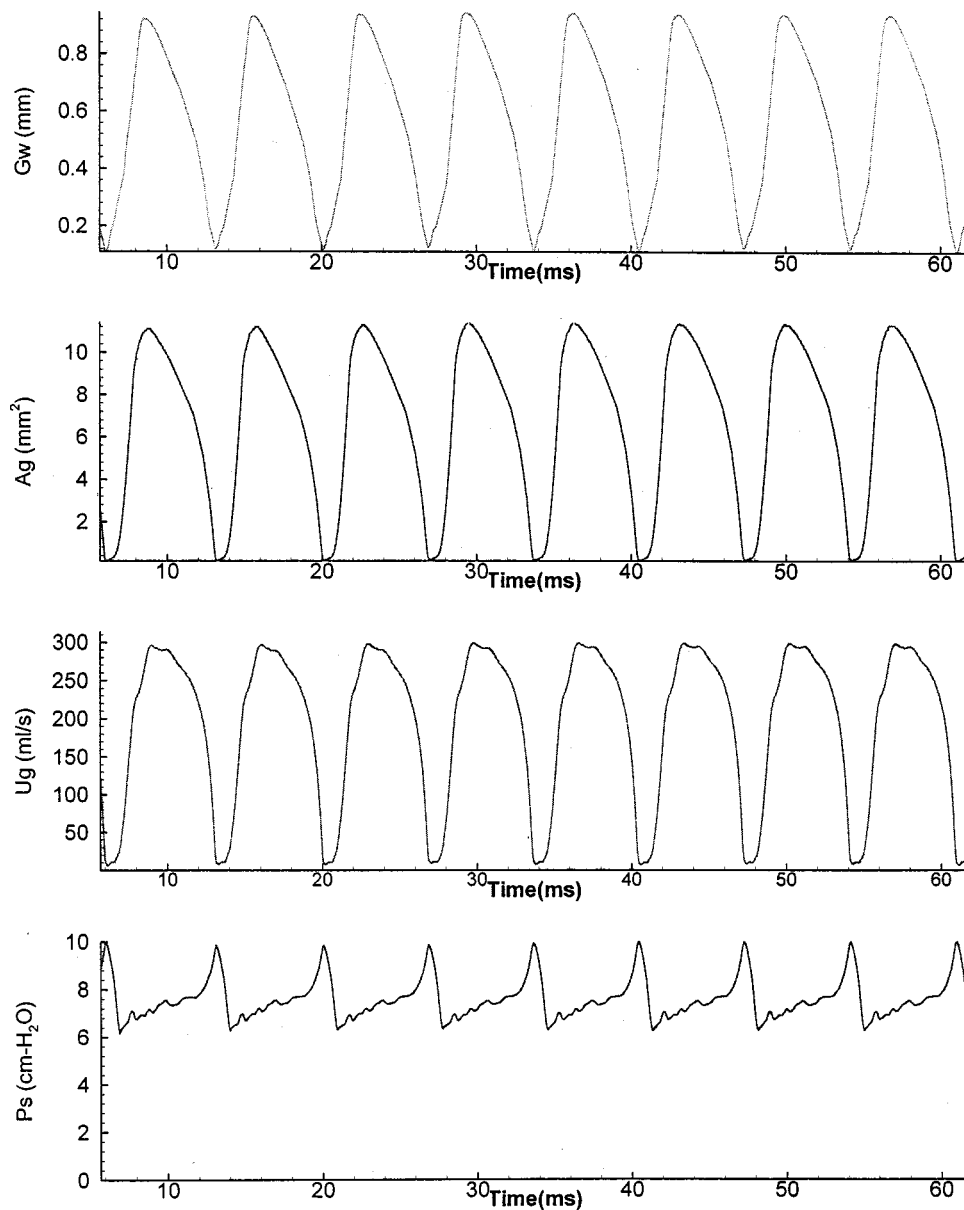


FIG. 4. Glottal waveforms of simulation at a lung pressure of 0.8 kPa. Time is in milliseconds.

pirical eigenfunctions might result in slight changes of the eigenmodes. Nevertheless, an obvious correspondence was evident between the eigenmodes and the empirical eigenfunctions, suggesting the validity of the self-oscillating finite-element model.

Results of the self-oscillating finite-element model were also evaluated by examining other output variables, specifically glottal flow waveforms and typical nodal coordinates. Before we discuss these waveforms, the geometrical and viscoelastic constants need to be clarified for those readers who want to replicate the work. Once the adduction is defined by the inferior (X1) and superior (X2) glottal half width (see Fig. 1) and bulging of the vocal fold is defined by a thyroarytenoid (TA) activation level or bulging factor (Alipour and Scherer, in press), the nodal coordinates are calculated and used to establish static equilibrium. The glottal adduction is defined with inferior and superior openings and vocal-fold bulging as shown in Fig. 1. The bulging is controlled

with the TA activation or bulging factor, a model that was used earlier by Alipour and Scherer (in press) to study the effects of bulging on simulated phonation. The typical values for these parameters are included with the viscoelastic properties in Table I.

Figure 4 shows some typical glottal waveforms simulated by the model. The simulation shown is for a bulging value of 0.7, a lung pressure of 0.8 kPa, and an /a/ vowel configuration. The fundamental frequency was 146 Hz. The lowest trace is the subglottal pressure (Ps) signal. The variations in the pressure correspond mainly to the first subglottal formant frequency of approximately 500 Hz. The trace just above the subglottal pressure is the glottal volume velocity, also called the glottal flow (Ug), with an average value of 197 ml/s and a peak flow of 300 ml/s. The next trace is the projected glottal area (Ag), with a maximum value of about 11 mm². The open quotient is about 0.9, suggesting only a mild collision. The fourth trace is the (maximum) glottal

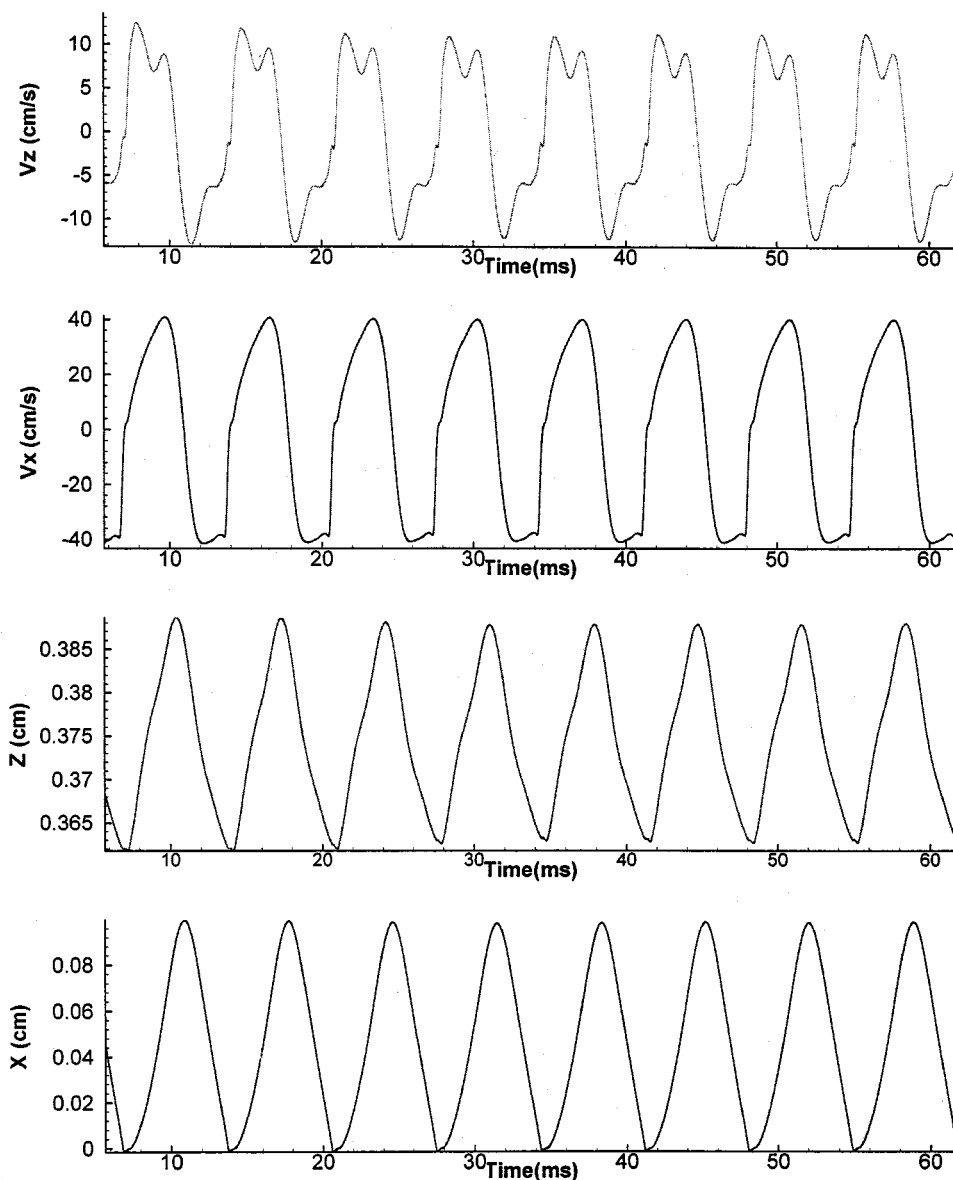


FIG. 5. Waveforms of coordinates and velocities of node number 4 in a coronal layer (layer 8, where layer number 1 corresponds to the most posterior layer).

width (G_w) calculated between the two vocal folds. It also is somewhat triangular in shape, but with some asymmetry. All of these waveforms are in reasonable ranges when compared with experimental observations on human subjects, and output from other computer models.

Figure 5 shows waveforms of x and z coordinates for node #4 (the fourth node from the top left edge in layer 8) and its velocity components. The displacements are nearly triangular shapes with higher excursion in the horizontal direction. The tissue velocity at this node has the largest component in the horizontal (x), direction with values ranging between -40 to 40 cm/s at 0.8 kPa lung pressure.

Figure 6 shows the trajectories of a few selected nodes simulated at a lung pressure of 1.2 kPa overlaid on the equilibrium mesh points. The trajectories indicate the highest excursion of the vocal folds is at the upper left corner, which had a total displacement of about 4 mm in a cycle. Since a sampling interval of 50 microseconds is used, for the frequency 146 Hz, every cycle would have 137 time steps.

Thus, within each time step the displacement is about 0.03 mm, and for the vocal-fold length of 1.6 cm the deformation angles are less than 0.002 , which satisfies small deformation theory.

IX. CONCLUDING REMARKS

The main purpose of this paper was to provide some mathematical detail of finite-element modeling of vocal-fold tissues, along with validation. Typical journal articles cannot accommodate the pages necessary to present both the mathematical detail and a substantial corpus of results. Thus, we opted to do the first. We feel this was appropriate, especially since many results of this model have already been reported (Alipour and Titze, 1985a; Berry *et al.*, 1994; Alipour and Titze, 1996; Alipour and Scherer, in press). In addition, many future reports will follow. Although not every mathematical step is included here, the engineer or mathematician

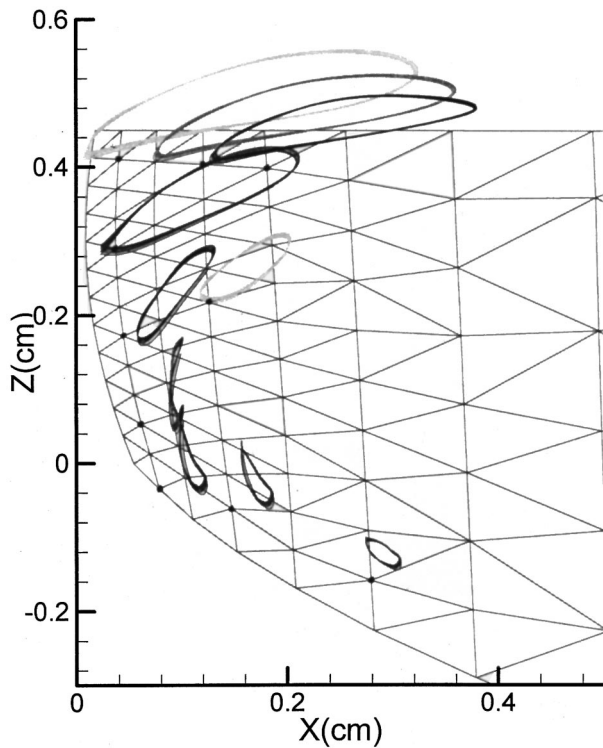


FIG. 6. Trajectories of selected nodes from coronal layer number 8.

familiar with continuum mechanics and some basic concepts of numerical methods should be able to replicate our results, and build upon them.

We feel that the primary significance of this article lies in the statements (and justification) of some assumptions that we have made about isotropy, planar motion, incompressibility, and treatment of the boundary conditions. Other parts of the simulations, such as the exact values of the viscoelastic constants, and the medial shaping of the vocal fold, are likely to evolve even more quickly. Much research is ongoing with high-speed imaging and measurement of viscoelastic properties of tissues.

Finally, the testing of simulation results with independent analytical results (normal modes) via empirical orthogonal eigenfunctions is an approach that will also have a considerable lifetime. It will continue to serve as a measuring rod for investigators in the evaluation and development of their models.

ACKNOWLEDGMENTS

The authors thank two anonymous reviewers for their helpful comments. This work was supported by Grant Nos. R01 DC03566 and R29 DC03072 from the National Institute of Deafness and Other Communication Disorders.

¹In previous writings, we have used ξ and ζ as the components of the displacement vector to avoid confusion with the flow variable u . Flow is not explicitly formulated here, however, which allows us to conform to the more standard elasticity notation.

Alipour, F., and Titze, I. R. (1985a). "Simulation of particle trajectories of vocal fold tissue," in *Vocal Fold Physiology: Biomechanics, Acoustics, and Phonatory Control*, edited by I. R. Titze and R. C. Scherer (Denver

Center for the Performing Arts, Denver), pp. 183–190.

Alipour, F., and Titze, I. R. (1985b). "Viscoelastic modeling of canine vocalis muscle in relaxation," *J. Acoust. Soc. Am.* **78**, 1939–1943.

Alipour, F., and Titze, I. R. (1988). "A finite element simulation of vocal fold vibration," in *Proceedings of the Fourteenth Annual Northeast Bio-engineering Conference*, Durham, NH, edited by J. R. LaCourse, pp. 186–189.

Alipour, F., and Titze, I. R. (1991). "Elastic models of vocal fold tissues," *J. Acoust. Soc. Am.* **90** (No. 3), 1326–1331.

Alipour, F., and Titze, I. R. (1996). "Combined simulation of airflow and vocal fold vibrations," in *Vocal Fold Physiology, Controlling Complexity & Chaos*, edited by P. Davis and N. Fletcher (Singular Publishing Group, San Diego, 1996), pp. 17–29.

Alipour, F., and Titze, I. R. (1999). "Active and passive characteristics of cricothyroid muscles," *J. Voice* **13** (No. 1), 1–10.

Alipour, F., and Scherer, R. C. "Vocal fold bulging effects on phonation using a biophysical computer model," *J. Voice* (in press).

Baer, T. (1981). *Investigation of the phonatory mechanism*. ASHA Reports 11, pp. 38–46.

Berry, D. A., Herzog, H., Titze, I. R., and Krischer, K. (1994). "Interpretation of biomechanical simulations of normal and chaotic vocal fold oscillations with empirical eigenfunctions," *J. Acoust. Soc. Am.* **95**, 3595–3604.

Berry, D. A., and Titze, I. R. (1996). "Normal modes in a continuum model of vocal fold tissues," *J. Acoust. Soc. Am.* **100**, 3345–3354.

Berry, D. A., Moon, J. B., and Kuehn, D. P. (1999). "A finite element model of the soft palate," *Cleft Palate—Craniofac. J.* **36**, 217–223.

Berry, D. A. "Mechanisms of nonmodal phonation," *J. Phonetics* (submitted).

Chan, R. W., and Titze, I. R. (1999). "Viscoelastic shear properties of human vocal fold mucosa: Measurement methodology and empirical results," *J. Acoust. Soc. Am.* **106**, 2008–2021.

Flanagan, J. L., and Landgraf, L. (1968). "Self-oscillating source for vocal tract synthesizers," *IEEE Trans. Audio Electroacoust.* **AU-16**, 57–64.

Hirano, M., Kakita, Y., Ohmaru, K., and Kurita, S. (1982). "Structure and mechanical properties of the vocal fold," *Speech Language* **7**, 271–297.

Huebner, K. H. (1975). *The Finite Element Method for Engineers* (Wiley, New York).

Ishizaka, K., and Flanagan, J. L. (1972). "Synthesis of voiced sounds from a two-mass model of the vocal cords," *Bell Syst. Tech. J.* **51**(6), 1233–1268.

Kaneko, T., Masuda, T., Shimada, A., Suzuki, H., Hayasaki, K., and Komatsu, K. (1986). "Resonance characteristics of the human vocal folds in vivo and in vitro by an impulse excitation," *Laryngeal Function in Phonation and Respiration*, edited by T. Baer, C. Sasaki, and K. Harris (Little Brown, Boston), pp. 349–377.

Lai, Y., and Alipour, F. "A computational study of oscillating flow in a model larynx," *Int. J. Numer. Methods Fluids* (submitted).

Lekhnitskii, S. G. (1981). *Theory of Elasticity of an Anisotropic Body* (Mir, Moscow).

Min, Y. B., Titze, I. R., and Alipour, F. (1995). "Stress-strain response of the human vocal ligament," *Ann. Otol. Rhinol. Laryngol.* **104**(7), 563–569.

Saito, S., Fukuda, H., Kitahara, S., Isogai, Y., Tsuzuki, T., Muta, H., Takayama, E., Fujioka, T., Kokawa, N., and Makino, K. (1985), in *Vocal Fold Physiology: Biomechanics, Acoustics, and Phonatory Control*, edited by I. R. Titze and R. C. Scherer (Denver Center for the Performing Arts, Denver), pp. 169–182.

Švec, J. G., Horáček, J., Sram, F., and Vesely, J. "Resonance properties of the vocal folds: In vivo laryngoscopic investigation of the externally excited laryngeal vibrations," *J. Acoust. Soc. Am.* (in press).

Titze, I. R., and Strong, W. J. (1975). "Normal modes in vocal cord tissues," *J. Acoust. Soc. Am.* **57**, 736–744.

Titze, I. R. (1976). "On the mechanics of vocal fold vibration," *J. Acoust. Soc. Am.* **60**, 1366–1380.

Ugural, A. C., and Fenster, S. K. (1981). *Advanced Strength and Applied Elasticity* (Elsevier North-Holland, New York).

Wilhelms-Tricarico, R. (1995). "Physiological modeling of speech production: Methods for modeling soft-tissue articulators," *J. Acoust. Soc. Am.* **97**, 3085–3098.

Zienkiewicz, O. C. (1977). *The Finite Element Method*, 3rd ed. (McGraw-Hill, London).

Some effects of duration on vowel recognition

James M. Hillenbrand^{a)} and Michael J. Clark

Department of Speech Pathology and Audiology, Western Michigan University, Kalamazoo, Michigan 49008

Robert A. Houde

RIT Research Corporation, 125 Tech Park Drive, Rochester, New York 14623

(Received 14 April 2000; accepted for publication 14 September 2000)

This study was designed to examine the role of duration in vowel perception by testing listeners on the identification of CVC syllables generated at different durations. Test signals consisted of synthesized versions of 300 utterances selected from a large, multitalker database of /hVd/ syllables [Hillenbrand *et al.*, *J. Acoust. Soc. Am.* **97**, 3099–3111 (1995)]. Four versions of each utterance were synthesized: (1) an *original duration* set (vowel duration matched to the original utterance), (2) a *neutral duration* set (duration fixed at 272 ms, the grand mean across all vowels), (3) a *short duration* set (duration fixed at 144 ms, two standard deviations below the mean), and (4) a *long duration* set (duration fixed at 400 ms, two standard deviations above the mean). Experiment 1 used a formant synthesizer, while a second experiment was an exact replication using a sinusoidal synthesis method that represented the original vowel spectrum more precisely than the formant synthesizer. Findings included (1) duration had a small overall effect on vowel identity since the great majority of signals were identified correctly at their original durations and at all three altered durations; (2) despite the relatively small average effect of duration, some vowels, especially /ɑ/-ɔ/-ʌ/ and /æ/-ε/, were significantly affected by duration; (3) some vowel contrasts that differ systematically in duration, such as /i/-ɪ/, /u/-ʊ/, and /ɪ/-e/-ε/, were minimally affected by duration; (4) a simple pattern recognition model appears to be capable of accounting for several features of the listening test results, especially the greater influence of duration on some vowels than others; and (5) because a formant synthesizer does an imperfect job of representing the fine details of the original vowel spectrum, results using the formant-synthesized signals led to a slight overestimate of the role of duration in vowel recognition, especially for the shortened vowels. © 2000 Acoustical Society of America. [S0001-4966(00)03912-6]

PACS numbers: 43.71.An, 43.71.Es [KRK]

I. INTRODUCTION

Duration has long been a key feature in the description and analysis of vowels. The chief phonological question concerns whether duration should be considered a contrastive or redundant feature (Chomsky and Halle, 1968; Roca and Johnson, 1999), and the main phonetic issues have been the measurement of vowel durations under a variety of conditions and the study of duration as a cue in vowel perception. In this study we are neutral regarding the phonological question of whether length should be considered an intrinsic phonological vowel feature in English. Rather we assume the existence of distinct vowel categories that contrast with one another in most phonetic contexts and that are produced with different typical durations in American English. Our focus is on the role played by variations in vowel duration in the recognition of vowel identity. Specifically, we studied the perception of 300 /hVd/ syllables that were synthesized in four different ways: (1) an *original duration* condition in which the duration of each vowel was matched as closely as possible to that of the original utterance, (2) a *neutral duration* condition in which the synthesis control parameters were linearly stretched or contracted to produce a fixed vowel duration of 272 ms (the mean of all 300 utterances),

(3) a *short duration* condition in which vowel duration was fixed at 144 ms (two standard deviations below the mean), and (4) a *long duration* condition in which vowel duration was fixed at 400 ms (two standard deviations above the mean).

A. Measurement studies

The central phonetic fact underlying this study is the well-known observation that American English vowels differ from one another in average duration. Of particular interest are the many pairs of spectrally similar vowels that differ in duration, pairs such as /i/-ɪ/, /u/-ʊ/, /æ/-ε/, /e/-ε/, /ɑ/-ʌ/, and /ɔ/-ɑ/. Average vowel duration measurements for the 12 vowel types used in the present experiment are summarized in Fig. 1. The data from Crystal and House (1988) and van Santen (1992) are from connected speech, while the Hillenbrand *et al.* (1995) and Black (1949) measurements are from CVC syllables. There is, of course, quite a bit of variability in the absolute durations associated with each vowel type across the four studies, reflecting the differences in speech material. As expected, the two connected speech studies show shorter average durations than the two studies using citation-form syllables. The longer durations in Hillenbrand *et al.* than in Black are related primarily to the use of a final voiced stop (/hVd/) in Hillenbrand *et al.* as compared to a final voiceless stop (/tVp/) in Black (House and Fairbanks,

^{a)}Electronic mail: james.hillenbrand@wmich.edu

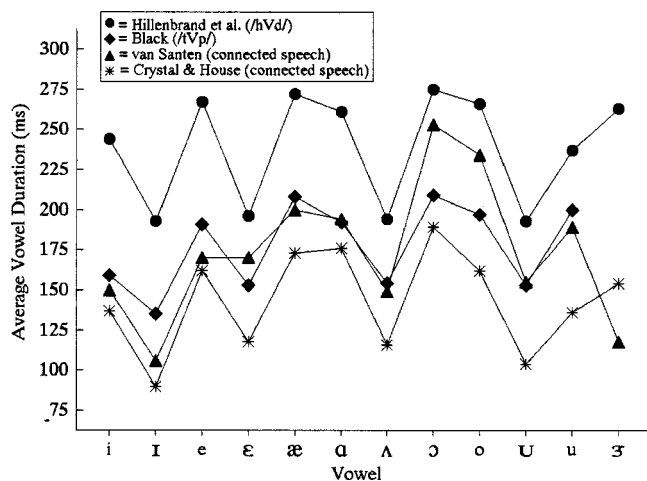


FIG. 1. Average vowel durations from four studies: Hillenbrand *et al.* (1995), Black (1949), van Santen (1992), and Crystal and House (1988). Measurements for /ʊ/ are not available from Black.

1953). Despite these differences in absolute duration, however, the four studies show rather similar patterns of duration differences across the vowel categories. Correlations among the six possible pairings of the four functions shown in Fig. 1 ranged from 0.70 to 0.95, with an average of 0.84. As will be seen later, the results of our synthesis experiments show that listeners are tacitly aware of these differences in typical duration and make some use of this knowledge in making judgments about vowel identity.

B. Pattern recognition studies

The role of duration in vowel identification has been studied indirectly through the use of pattern recognition experiments. In work of this type, a statistically based pattern classifier is used to determine the separability of vowels based on various combinations of acoustic measurements. For example, Zahorian and Jagharghi (1993) used a discriminant classifier to identify signals in a database of 2922 CVC syllables formed from nine initial consonants, 11 vowels, and eight final consonants. Zahorian and Jagharghi's main interest was the comparison of two methods of representing the spectral characteristics of vowels, but they also tested the value of duration for improving vowel categorization. Zahorian and Jagharghi reported a statistically nonsignificant improvement in classification accuracy of less than 1% when duration was added to the spectrally based acoustic measurements that were used to train the pattern classifier, suggesting a very limited role for duration in vowel separability. Very different conclusions were reached by Hillenbrand *et al.* (1995), who used a discriminant classifier to identify signals in a database of /hVd/ syllables produced by men, women, and children (12 vowels \times 139 talkers = 1668 syllables). Results showed that inclusion of duration in the parameter set resulted in consistent improvements in category separability, especially for the simpler parameter sets involving very few spectrum-related variables (e.g., a single sampling of F_1 and F_2 at steady state). Similar findings were reported by Hillenbrand *et al.* (2000) in a discriminant analysis study of CVC syllables formed from seven initial conso-

nants, eight vowels, and six final consonants spoken by 12 talkers. Consistent with Hillenbrand *et al.* (1995), the results showed a modest but consistent improvement in classification accuracy with the addition of duration measures. Particularly large improvements in category separability were seen for /æ/ and /ε/, but there were also substantial improvements for /ɪ/ and /a/. Finally, a study of Australian English vowels by Watson and Harrington (1999) showed a small improvement in classification accuracy when measurements of formant trajectories were augmented by duration measures.

C. Perception studies

More direct evidence on the role of duration in vowel identification comes from a series of perception experiments using synthetic speech or modified natural speech. For example, Tiffany (1953) recorded 12 vowels spoken by four phonetically trained men under a variety of conditions differing by pitch and phonetic context (e.g., /tVp/ syllables versus vowels in isolation). The talkers also produced long sustained vowels, from which segments of different durations were clipped (80 ms, 200 ms, 500 ms, and 8 s). The signals were identified by listeners who had some training in phonetics. Some duration effects emerged from the listening data; for example, some vowels with long typical durations (e.g., /e/ and /a/) were more likely to be correctly identified at longer durations, while others with short typical durations (e.g., /ɪ/ and /u/) were better identified at the shorter durations.

Stevens (1959) synthesized /dVs/ syllables at durations ranging from 25 to 400 ms, one series with front vowels (to be identified by listeners as /i, I, ε, æ/) and another with back vowels (to be identified as /u, U, A, a/). Several effects were observed which are consistent with the idea that listeners use both spectrum and duration in identifying vowels. For example, for durations less than about 100 ms, vowels with formant specifications appropriate for /æ/ were judged to be /ε/. Similarly for vowels with formant specifications appropriate for /a/, the stimuli shorter than 100 ms were judged as /A/. Less robust shifts were seen from /i/ to /ɪ/ and from /u/ to /U/, and these tended to occur only for extremely short vowels. In a related study, Ainsworth (1972) synthesized two-formant vowels with formant values covering the English vowel space with durations ranging from 120 to 600 ms. Listeners were influenced in a manner generally consistent with observed durational differences among vowels. For example, signals with F_1 and F_2 values generally similar to those found for /u/ and /U/ were more likely to be identified as /U/ if short and /u/ if long.

A synthesis experiment by Huang (1986) yielded somewhat equivocal results. Listeners were presented with nine-step synthetic continua contrasting a variety of spectrally similar vowel pairs at durations of 40, 90, 140, and 235 ms. While the expected duration-dependent boundary shifts occurred (e.g., the /i/-/ɪ/ boundary shifted in the direction of /ɪ/ at shorter durations), duration differences much larger than those observed in natural speech were typically needed to move the boundaries. For duration differences approximating those found in natural speech, boundary shifts were small or

nonexistent. Huang also reported unexpected boundary shifts for lax-lax pairs such as /ʊ/-/ʌ/ that do not differ in duration.

The Stevens (1959), Ainsworth (1972), and Huang (1986) studies, which used synthetically generated vowels with static formant patterns, should be interpreted with some caution since it is well known that vowel color tends to be considerably more ambiguous for signals with static formant patterns than for vowels showing natural patterns of spectral change over time (e.g., Hillenbrand and Gayvert, 1993; Hillenbrand and Nearey, 1999; Fairbanks and Grubb, 1961). Consequently, it is possible that studies using static synthetic vowels have overestimated the importance of duration information.

Daniloff *et al.* (1968) measured the intelligibility of naturally produced vowels in /hVd/ syllables under several conditions of time and frequency distortion. Intelligibility was found to be more vulnerable to frequency division than time compression. Except at the most extreme degrees of time compression, syllables were correctly identified as to vowel category at 90% or better. As expected, time compression affected long vowels (/æ, ɑ, ɔ, e/ much more than short vowels (/ɪ, ε, ʌ, ʊ/), with intermediate effects for medium duration vowels (/ɜ, u, i/). As expected, most errors in the Daniloff *et al.* data involved the misidentification of longer vowels as their shorter-duration neighbors.

Mixed results on the effects of duration on vowel identity were reported by Strange *et al.* (1983) in experiments using silent-center stimuli—signals consisting of brief onglides and offglides, with the center vowel nuclei replaced by a variable-duration silent gap. Listeners were presented with three kinds of silent-center stimuli: (1) durational information retained (i.e., onglides and offglides separated by an amount of silence equal to the duration of the deleted vowel nucleus), (2) durational information neutralized by setting the silent intervals for all stimuli equal to the shortest vowel nucleus, and (3) durational information neutralized by setting the silent intervals for all stimuli equal to the longest vowel nucleus. Results were mixed: shortening the silent interval to match the shortest vowels did not increase error rates relative to the natural duration condition, but lengthening the intervals to match the longest vowels produced a significant increase in error rates. The authors speculated that the results for the lengthened signals may have been “... due to the disruption of the integrity of the syllables, rather than misinformation about vowel length; that is, subjects may not have perceived a single syllable with a silent gap in it, but instead, heard the initial and final portions as two discrete utterances” (Strange, 1989, p. 2140). While the experiments using silent-center and related stimuli (see also Nearey and Assmann, 1986) have clearly been quite important, the uncertainty that results from the kind of interpretive problem described by Strange represents an important weakness of this class of experiments. The present experiments adopt an approach that is generally similar to that of Strange *et al.*, but we will attempt to address this limitation by using stimuli modeled on naturally spoken CVC syllables rather than silent-center stimuli.

D. Summary

The picture that emerges from the pattern recognition and perception studies described earlier is not entirely clear. Much of the evidence is consistent with the idea duration plays a modest but measurable role in vowel recognition, but the findings are far from uniform. The present study was designed to explore this question further by testing listeners on the identification of resynthesized /hVd/ utterances under four duration conditions. We were especially interested in conducting a relatively large-scale study in which the spectral properties of the test signals, and especially the patterns of formant frequency change over time, were modeled as closely as possible on naturally spoken speech signals.

II. EXPERIMENT 1

A. Methods

1. Test signals

The test signals consisted of four different synthesized versions of 300 /hVd/ utterances that were sampled from the 1668 utterances recorded by Hillenbrand *et al.* (1995). The full database consisted of recordings of 12 vowels (/i,ɪ,e,ɛ,æ,ɑ,ɔ,o,u,ʌ,ɜ,ɝ/) in /hVd/ syllables spoken by 45 men, 48 women, and 46 10- to 12-year-old children. The 300-stimulus subset was selected at random from the full database, but with the following constraints: (a) signals showing formant mergers involving any of the three lowest formants were omitted, (b) signals with identification error rates (measured in the original 1995 study) of 15% or greater were omitted, and (c) all 12 vowels were equally represented. The 300-stimulus set that was selected by this method included tokens from 123 of the 139 talkers, with 30% of the tokens from men, 36% from women, and 34% from children. This same 300-syllable subset had been used in an earlier study of the effects of formant contour on vowel recognition (Hillenbrand and Nearey, 1999).

2. Acoustic measurements

Acoustic measurements of the /hVd/ syllables consisted of formant contours for F_1 – F_4 measured from LPC spectra (sampled every 8 ms) and edited by hand during the vowel using methods that are described in detail in Hillenbrand *et al.* (1995). Measurements were also made of (a) the F_0 contour (also edited by hand), (b) the onset of the vowel, and (c) the offset of the vowel. Vowel onsets and offsets were judged by visual inspection using standard measurement criteria (Peterson and Lehiste, 1960). The distribution of vowel durations in the 300-stimulus subset was approximately symmetrical with a mean duration of 274.0 ms, a median of 268.5 ms, and a standard deviation of 65.3 ms.

3. Synthesis method

The Klatt and Klatt (1990) formant synthesizer, running at a 16-kHz sample rate, was used to generate four sets of synthetic signals differing in vowel duration (see Fig. 2). An *original duration* (OD) set was generated in a straightforward way from the measured F_0 and formant contours, so the vowel durations of these signals matched those of the

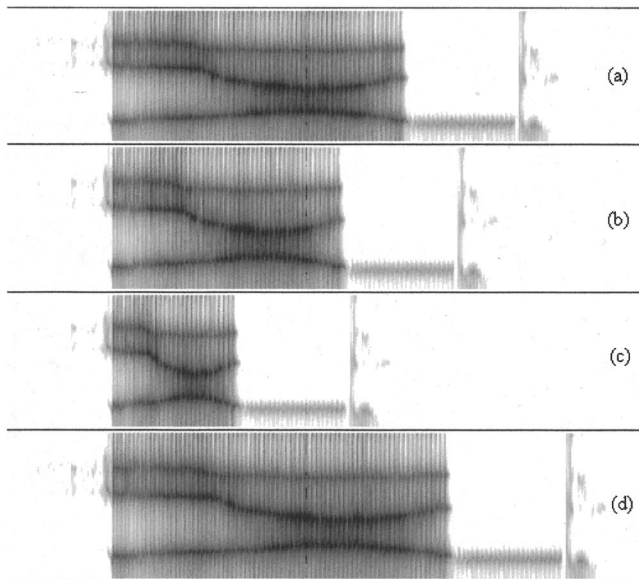


FIG. 2. Spectrograms of the four types of synthetic signals used in experiment 1: (a) original duration (OD), (b) neutral duration (ND), (c) short duration (SD), and (d) long duration (LD). The original signal was /hæd/ spoken by a child.

original signals, within the limits of measurement error and the 8-ms frame rate. Procedures for synthesizing initial /h/ and final /d/ segments for these signals are described in detail in Hillenbrand and Nearey (1999; hereafter HN99). Briefly, the initial /h/ was synthesized by (a) setting the frequencies of all formants to their values measured at vowel onset, (b) setting voicing amplitude to zero and aspiration amplitude to the measured rms intensity of the signal being synthesized, and (c) setting the bandwidth of F_1 to 300 Hz. A final /d/ was simulated by (a) ramping F_1 100 Hz below its measured value at the end of the vowel in four 25-Hz steps, and (b) switching from the cascade to the parallel branch of the synthesizer and setting the resonator gains of F_2 – F_6 30 dB below the F_1 resonator gain, producing a “voice bar” with energy primarily at F_1 . Since we were not satisfied with our efforts to generate natural sounding final release bursts with the synthesizer, the signals were generated unreleased, and release bursts that had been excised from naturally produced signals spoken by one man, one woman, and one child were appended to the end of the stimuli. Formant frequencies for F_1 – F_3 and fundamental frequency during the vowel were set to the original measured values. Formant amplitudes during the /h/ and vowel were set automatically by running the synthesizer in series mode, formant bandwidths were kept at their default values (see HN99), the frequency of F_4 was set separately for each vowel and talker group based on data from Hillenbrand *et al.* (1995), and the frequencies of F_5 and F_6 were based on Rabiner (1968).

The synthesis parameter files for the OD signals [Fig. 2(a)] served as the basis for generating parameter files for (a) a *neutral duration* (ND) set with vowel durations fixed at 272 ms, the grand mean of all vowel durations from Hillenbrand *et al.* (1995), rounded to nearest 8-ms frame; (b) a *short duration* (SD) set with vowel durations fixed at 144 ms, 2 standard deviations below the grand mean (again

TABLE I. Overall recognition rates for the four duration conditions of experiments 1 and 2 (OD=original duration, ND=neutral duration, SD=short duration, LD=long duration). Standard deviations are shown in parentheses.

Duration condition	Experiment 1	Experiment 2
OD	91.7(3.3)	96.0(2.7)
ND	90.4(3.5)	94.1(2.9)
SD	82.4(4.9)	91.4(5.2)
LD	89.5(2.2)	90.9(3.3)

rounded to closest 8-ms frame); and (c) a *long duration* (LD) set with vowel durations fixed at 400 ms, 2 standard deviations above the grand mean. The parameter files for the ND, SD, and LD signals were created from the OD parameter files simply by resampling the contours of F_0 – F_3 during the vowel using linear interpolation. Parameter settings during the /h/ and /d/ segments were unchanged. Examples of ND, SD, and LD signals are shown in panels (b)–(d) of Fig. 2.

4. Listening test

Fifteen phonetically trained subjects served as listeners. Twelve of the listeners were graduate students in the speech-language pathology program at Western Michigan University and the other three were faculty members in the same department. Listeners with training in phonetic transcription were chosen because of the findings of Assmann *et al.* (1982) showing that many apparent identification errors made by untrained subjects are, in fact, simply errors in transcription. The regional dialect characteristics of the listeners were a fairly close match close to those of the talkers. Dialect was assessed by a trained phonetician using an interview procedure similar to that described in Hillenbrand *et al.* (1995). Eight of the listeners were raised in southwest Michigan, three in Chicago, two in the northeast (Massachusetts and New Jersey), and one each in Iowa and California. Listeners were tested one at a time in a quiet room in two sessions lasting about 35–40 min. Listeners identified each of the 1200 test signals (300 OD, 300 ND, 300 SD, and 300 LD) presented unblocked in a single random order. The presentation order was reshuffled prior to each listening session. Stimuli were low-pass filtered at 6.9 kHz, amplified, and delivered at approximately 75 dBA over a single loudspeaker (Boston Acoustics A60) positioned approximately 1 m from the subject’s head. Subjects entered their responses on a computer keyboard labeled with both phonetic symbols and key words for the 12 vowels. Subjects were allowed to repeat stimuli as many times as they wished before entering a response.

B. Results and discussion

Overall recognition rates for the four duration conditions are shown in Table I (experiment 2 results, shown to the right in Table I, will be discussed later). The 91.7% recognition rate for the OD signals is slightly higher than the 89.8% rate for the same set of signals that were used in an earlier study (averaged across the two “OF” conditions from HN99). More importantly, the recognition rate for the OD

signals is lower than the 94.5% rate for the original, naturally produced signals from the full 1668-signal database (Hillenbrand *et al.*, 1995). It is also lower than the 96.0% recognition rate for naturally spoken versions of the 300-utterance subset used in HN99. As will be discussed in greater detail later, the slightly lower recognition rate for the OD synthetic signals as compared to the natural signals is due to a small but important limitation of the formant vocoding method to faithfully model some perceptually relevant details of the original vowel spectrum.

It can be seen that the OD signals were the most intelligible, followed by the ND, LD, and SD signals. The only numerically large effect, however, is the drop in intelligibility that occurred as a result of vowel shortening, with the SD signals being nearly 10 percentage points less intelligible than the OD signals. A two-way repeated measures analysis of variance showed a highly significant effect for duration condition [$F(3,42)=38.3, p<0.0001$] and vowel [$F(11,154)=22.2, p<0.0001$] and a significant duration by vowel interaction [$F(33,462)=19.6, p<0.0001$]. Bonferroni *post hoc* tests showed significant differences among all pairs of duration conditions with the exception of ND versus LD.

A detailed analysis of the specific changes in vowel identity that occurred in the three duration-modification conditions will not be undertaken here. As will be explained below, there are some key aspects of the findings of experiment 1 that do not replicate when a synthesis method is used that more faithfully models the detailed spectrum of the original vowels. Briefly, the vowels that were most affected by shortening were /æ/, which tended to shift to /ɛ/, and /ɑ/, which tended to shift to /ʌ/. Similarly, but to a lesser extent, the opposite shifts in vowel identity tended to occur as the most common effects of vowel lengthening; i.e., lengthened /ɛ/ tended to shift toward /æ/ and lengthened /ʌ/ tended to shift to /ɑ/ or /ɔ/. Considerably less common were duration-induced shifts in vowel identity affecting the /i/-/ɪ/ contrast, the /u/-/ʊ/ contrast, or distinctions among the cluster /ɪ/-/e/-/ɛ/. A more detailed discussion of the effects of duration on the recognition of individual vowels will await the outcome of experiment 2.

In summary, experiment 1 showed that the effect of altering vowel duration was modest overall since the great majority of signals were accurately identified at their original durations and with vowel duration set to a neutral value, shortened, and lengthened. There were some significant effects, however, including (1) vowels with long typical durations, especially /æ/ and /ɑ/, tended to shift to adjacent vowels with shorter typical durations when shortened, (2) vowels with short typical durations, especially /ʌ/ and /ɛ/, tended to shift to adjacent vowels with longer typical durations, and (3) vowel shortening had a considerably greater effect on vowel identity than vowel lengthening.

III. EXPERIMENT 2

The purpose of experiment 2 was to determine the generality of the effects observed in experiment 1 by conducting a similar experiment but using a very different method to synthesize the test signals. The logic that is implicit in ex-

periment 1 is that the spectral properties associated with vowels are held constant across the four duration conditions—and *matched as closely as possible to the original signals*—while vowel duration is varied. A problem that is inherent in this approach is that the spectral properties of vowels are imperfectly represented by the formant synthesis method. The difference in intelligibility between the original signals and the formant synthesized versions of those same signals is not especially large, but it is quite real. For example, in HN99, the recognition rate for the 300 naturally produced /hVd/ signals averaged 6.3 percentage points higher than that of the formant-synthesized versions of the same signals, which are identical to the OD signals used in experiment 1. As a consequence, it might be argued that experiment 1, by failing to faithfully model the perceptually relevant spectral cues to vowel identity, may have overestimated the importance of duration in vowel recognition. Experiment 2 was an attempt to explore this possibility by directly replicating experiment 1 using a synthesis method that more accurately models the spectral characteristics of the original signals. The experiment used the same 300-stimulus database and the same four duration conditions (OD, ND, SD, and LD). However, a synthesizer based on the summation of sinusoidal Fourier components was used to generate the test signals. As will be explained below, this synthesizer does a significantly better job of coding the spectral properties of vowels, resulting in a set of OD signals whose intelligibility is essentially indistinguishable from that of the natural produced signals upon which they are based.

A. Methods

1. Test signals

Four sets of synthetic test signals were generated with a sinusoidal synthesizer that has a number of features in common with the method described by McAuley and Quatieri (1986). As in experiment 1, we generated OD, ND, SD, and LD versions of each of the 300 /hVd/ syllables. Briefly, the sinusoidal synthesizer can be thought of as something akin to resynthesis using an inverse Fourier transform, with the important exceptions that (1) phase relations among spectral components are not preserved,¹ and (2) sinusoidal components are generated only for spectral peaks (i.e., harmonic peaks in voiced regions and harmonically unrelated spectral peaks in unvoiced regions, but not nonpeak Fourier components). The analysis begins with the calculation of a high-resolution Fourier spectrum over a relatively large hamming-windowed segment of the speech signal. A 64-ms window was used in this experiment. Spectral peak frequencies and amplitudes are then measured from the narrow-band spectrum. These peaks will correspond primarily to voice-source harmonics during voiced intervals, but the analysis proceeds in the same way for both voiced and unvoiced intervals. The analysis window is then advanced by some constant (8 ms in the present case), and the measurement of spectral peaks continues to the end of the signal. For each spectral peak that is measured from the Fourier spectrum, a sinusoid is generated at the measured frequency and amplitude and with a duration equal to the frame rate (8 ms in our implementation). Since it is essential that phase discontinuities not occur

at the boundaries between frames, it is necessary to track spectral peaks from one frame to the next in much the same way that envelope peaks are tracked from frame to frame in a formant tracker. If the tracking algorithm determines that a given spectral peak is continuous from one frame to the next, the frequency and amplitude of the peak are linearly interpolated through the frame. Further, the starting phase of the sinusoid in frame $n + 1$ is adjusted to be continuous with the ending phase of the sinusoid in frame n . If the tracking algorithm determines that a spectral peak in frame n does not continue into frame $n + 1$, the amplitude of the sinusoid is ramped down to zero. Similarly, if a spectral peak is found in a given analysis frame that is determined to be new (i.e., not continuous with a peak in the previous frame), the amplitude of the sinusoid is ramped up to its measured amplitude.

One of the many elegant aspects of the sinusoidal approach to synthesis is that the manipulation of speech rate, either globally or frame by frame, is exceedingly simple. Altering duration is simply a matter of changing the durations of the individual sinusoids from the 8-ms frame rate (or whatever the frame rate happens to be) to some other value. For example, for the frame rate used here, decreasing duration by a factor of 2 is simply a matter of changing the durations of the individual sinusoids from 8 to 4 ms. Similarly, increasing duration by a factor of 1.5, for example, is accomplished by changing the durations of the individual sinusoids from 8 to 12 ms. With this rate-manipulation method, the evolution of spectral shape from one frame to the next remains constant from one duration condition to another, and what varies is the rate at which one spectral shape evolves into the next. This is also true of the formant synthesis method that was used in experiment 1. The most important difference between the two methods, in our view, is in the degree to which the detailed spectral shape of the original signal is preserved. With a formant synthesizer the match between the spectral shape of the original signal and that of the resynthesized signal is only approximate since only the frequencies of broad envelope peaks are preserved (and even then, only within the limits of formant estimation, which is imperfect—see HN99 for a discussion). The match is much better with the sinusoidal method since many more spectral details—all narrow-band spectral peaks—are preserved in the resynthesis (see Fig. 3).

In generating a set of OD signals comparable to the set used in experiment 1, the default 8-ms sinusoidal duration was simply left unmodified. For the ND set, this duration was adjusted on a signal-by-signal basis to a value that was sufficient to produce a vowel duration of 272 ms for all signals. Sinusoidal durations were modified only during the vowel and not during the /h/ and /d/ segments of the signal. The SD and LD sets were generated using the same method, but with vowel durations fixed at 144 and 400 ms, respectively.

2. Subjects and procedures

A separate group of 14 listeners participated in experiment 2. As in experiment 1, the listeners were phonetically trained and, based on a dialect interview, were judged to

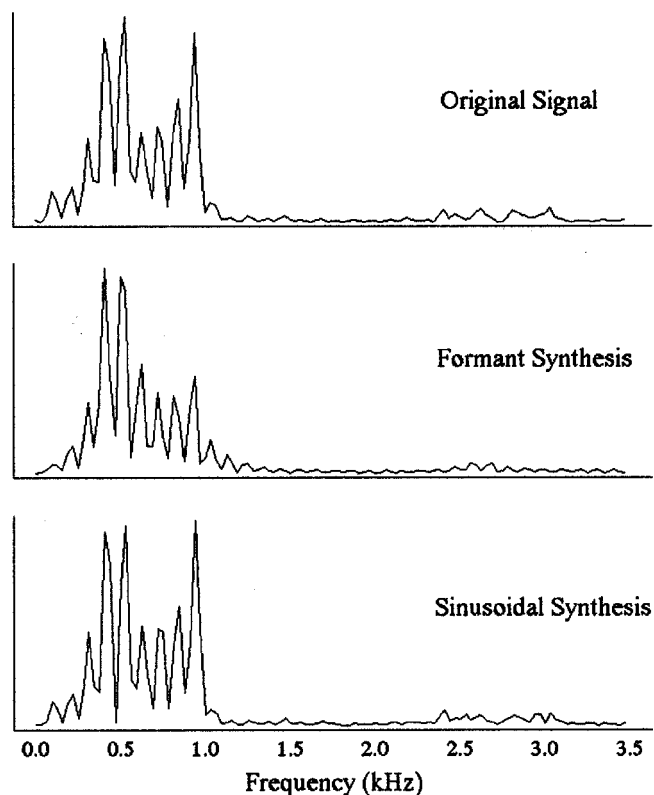


FIG. 3. Fourier spectra computed at roughly the center of the vowel /o/ from (a) the original speech signal, (b) the OD formant synthesized version of the same signal, and (c) the OD sinusoidal synthesized version of the same signal. Note that the match in spectral detail is much closer for the sinusoidal synthesis than for formant synthesis.

speak a dialect that was quite similar to that of the speakers. Instrumentation and experimental procedures were identical to experiment 1.

B. Results and discussion

1. Effects of synthesis method

An assumption underlying the design of experiment 2 was that the sinusoidal synthesizer would preserve the detailed spectral properties of vowels better than the formant synthesizer. We speculated that this may have led to a slight overestimate of the relative importance of duration in vowel recognition in experiment 1. Accordingly, we begin our analysis of experiment 2 by comparing the recognition of the OD signals from experiments 1 and 2. Figure 4 shows average recognition rates by vowel for OD signals produced with the formant synthesizer versus the sinusoidal synthesizer. It can be seen that the sinusoidal OD signals were more intelligible than the formant synthesized versions (96.0% versus 91.7%). The 96.0% recognition rate for the sinusoidal OD signals is virtually identical to the recognition rate reported in HN99 for naturally spoken versions of the same signals.² A two-way analysis of variance for synthesis method and vowel, with repeated measures on the vowel factor, showed significant effects for both factors, as well as a significant interaction [synthesis method: $F(1,27) = 32.1$, $p < 0.0001$; vowel: $F(11,27) = 15.3$, $p < 0.0001$; method by vowel: $F(11,297) = 6.4$, $p < 0.0001$]. The nature of the interaction is readily apparent in Fig. 4, which shows considerable vari-

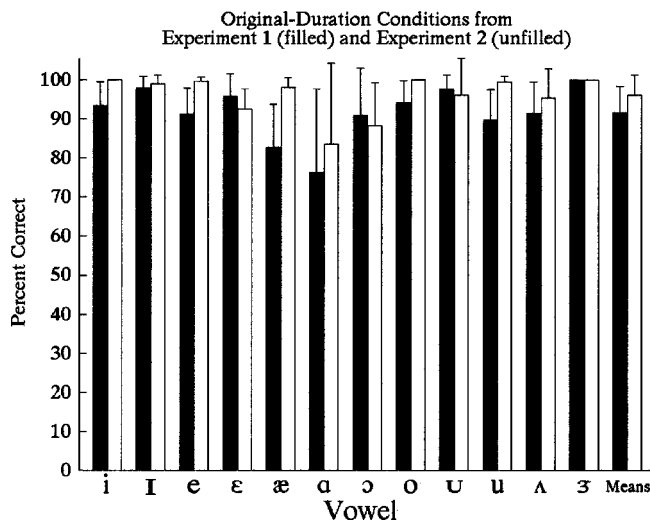


FIG. 4. Percent correct for the original duration conditions from experiment 1 (filled) and experiment 2 (unfilled). Error bars show one standard deviation.

ability across the 12 vowels in the synthesis method effect. As expected, most of the vowels show higher recognition rates when generated with the sinusoidal synthesizer than the formant synthesizer, although the advantage is much larger for some vowels (e.g., /æ/, /u/, and /e/) than others (e.g., /i/ and /ɔ/). Note also that /ε/, /ɔ/, and /u/ were actually slightly *more* intelligible in the formant synthesis condition. The findings for these three vowels are consistent with results from HN99's comparison of formant synthesized and natural speech, which showed *tendencies* for (1) signals with formant values in the /æ/-/ε/ region to be heard as /ε/ when formant synthesized, (2) signals with formant values in the /a/-/ɔ/ region to be heard as /ɔ/ when formant synthesized, and (3) signals with formant values in the /u/-/u/ region to be heard as /u/ when formant synthesized (see especially Fig. 6 of HN99).

2. Effects of duration

Average recognition rates and standard deviations for the four duration conditions of experiment 2 are shown in the right-most columns of Table I. Relative to the original duration signals, there is a modest drop in intelligibility of 1.9% for the neutral duration signals and drops of 4.6% and 5.1% for the shortened and lengthened signals, respectively. A two-way repeated measures analysis of variance showed highly significant effects for duration condition [$F(3,39) = 12.4, p < 0.0001$] and vowel [$F(11,143) = 16.8, p < 0.0001$] and a significant duration by vowel interaction [$F(33,429) = 19.0, p < 0.0001$]. Bonferroni *post hoc* tests showed significant differences among all pairs of duration conditions except ND-SD and SD-LD. The duration effects observed here differ in some important respects from those of experiment 1. A major finding of experiment 1 was a substantial asymmetry in the effects of shortening versus lengthening, with shortening resulting in a much larger drop in vowel intelligibility than lengthening. There was no evidence for this asymmetry in experiment 2: the average effect of vowel shortening in experiment 2 was considerably

TABLE II. The most frequent changes in vowel identity resulting from vowel shortening or vowel lengthening in experiment 2. The percentages in the column to the right reflect the number of shifts in vowel identity (OD→SD or OD→LD) divided by the number of opportunities for such shifts to occur.

Vowel shift	Percentage
Effects of vowel shortening	
/ɔ/ → /a/ or /ɔ/	43.0
/æ/ → /ε/	20.7
/a/ → /ɔ/	9.4
Effects of vowel lengthening	
/ɔ/ → /a/ or /ɔ/	36.0
/ε/ → /æ/	18.9

smaller than in experiment 1, and was not significantly greater than the average effect of vowel lengthening.

Table II provides a summary of the most frequent changes in vowel identity that occurred as a result of shortening and lengthening. The shifts in vowel identity that are shown in this table are based on confusion matrices which focused on instances in which a given listener identified the OD version of a signal correctly (i.e., as the vowel intended by the talker) but the duration-modified version of the same utterance incorrectly. For example, suppose that listener 1 correctly identified an OD signal that was intended as /æ/ by the talker but that same listener identified the SD version of the same stimulus as /ε/. The count in the cell associated with row /æ/ and column /ε/ in the confusion matrix would be incremented by 1. To simplify the presentation, the full confusion matrices are not shown, and only the most frequency shifts in vowel identity are listed in Table II. The percentages that are shown to the right are based on the number of shifts in vowel identity divided by the number of opportunities for such shifts to occur. As the table shows, only /ɔ/ was strongly affected by shortening, with 43.0% of the tokens shifting to /a/ or /ɔ/. The only other vowel shifts of any consequence consisted of the roughly one-fifth of the OD tokens of /æ/ that were heard as /ε/ when shortened, and a modest number of /a/ tokens that shifted to /ɔ/. The effects of vowel lengthening, shown in the bottom half of Table II, are nearly the mirror image, with lengthened /ɔ/ tending to shift to /a/ or /ɔ/, and /ε/ tending to shift to /æ/. Conspicuous by their absence in Table II are several shifts in vowel identity which might have been expected based on observed durational differences among vowels but which occurred rarely or not at all. For example, there were very few cases of shortened /i/ shifting to /i/ (0.6%), no cases of shortened /u/ shifting to /u/, and few cases of shortened /e/ shifting to /i/ or /ε/ (2.2%). Similarly, lengthened /i/ seldom shifted to /i/ (0.6%), lengthened /ε/ or /i/ never shifted to /e/, and lengthened /u/ seldom shifted to /u/ (1.3%).

In summary, experiment 2 showed the following: (1) duration has a measurable but rather modest overall effect on vowel perception since the overwhelming majority of the signals were identified correctly at their original durations and at all three altered durations, (2) vowel shortening and vowel lengthening produced statistically equivalent reductions in vowel intelligibility of 4.5%–5.0%, (3) the vowels

that are most affected by duration are the /a/-/ɔ/-/ʌ/ cluster and the /æ/-/ɛ/ pair, (4) in spite of consistent differences in average durations, vowels that are hardly affected at all by duration are the /i/-/ɪ/ and /u/-/ʊ/ pairs, and the /ɪ/-/e/-/ɛ/ cluster. The similarities and differences between experiments 1 and 2 will be treated in Sec. V.

IV. PATTERN RECOGNITION TESTS

The final question that we wish to consider has to do with the finding that some pairs and clusters of vowels (/a/-/ɔ/-/ʌ/ and /æ/-/ɛ/) were influenced fairly strongly by the modification of duration, while others (/i/-/ɪ/, /u/-/ʊ/, and /ɪ/-/e/-/ɛ/) were minimally affected by duration modification. There is nothing obvious about the magnitude of the durational differences among the vowels that can readily explain these variations in the influence of duration on vowel recognition. For example, based on the Crystal and House (1988) data, /æ/ averages about 18% longer than /ɛ/, while /i/ averages about 41% longer than /ɪ/. However, it is the /æ/-/ɛ/ pair which shows a robust duration effect, while shortening /i/ or lengthening /ɪ/ have very little effect on vowel identity. Similarly, while /u/ is about 51% longer on average than /ʊ/, and /ɔ/ is about 30% longer than /a/, it was the contrast between /a/ and /ɔ/ that was affected by duration and not the contrast between /u/ and /ʊ/. We believe that there is a fairly straightforward explanation for these apparently contradictory findings. A combination of listening to the /hVd/ signals and close examination of the acoustic measurements led us to speculate that non-duration-sensitive pairs such as /i/-/ɪ/ and /u/-/ʊ/ are quite distinct from one another based on their spectral properties (F_0 and formant trajectories) and, as a consequence, less dependent on duration for their separation. On the other hand, vowels such as /a/-/ɔ/-/ʌ/ and /æ/-/ɛ/ show a greater degree of spectral overlap, resulting in a greater reliance on duration for their separation. If this explanation is valid, it ought to be possible to simulate certain features of our listening test results with a simple pattern classifier. In particular, we were interested in determining whether a simple pattern recognition model would show a greater sensitivity to duration for /a/-/ɔ/-/ʌ/ and /æ/-/ɛ/ than for /i/-/ɪ/, /u/-/ʊ/, and /ɪ/-/e/-/ɛ/.

To test this idea, a quadratic discriminant classifier (Johnson and Wincham, 1982) was trained on measurements from the Hillenbrand *et al.* (1995) database. Excluded from the trained data were (1) tokens with identification error rates of 15% or higher, and (2) tokens with missing values for any of the parameters that were used in discriminant analyses. The parameter set consisted to duration, F_0 , and F_1 – F_3 sampled at 20% and 80% of vowel duration. [Justification for this particular choice of parameters can be found in Hillenbrand *et al.* (1995) and Hillenbrand and Nearey (1999)]. The pattern recognizer was then tested on measurements from the four different versions of the 300 /hVd/ utterances that were used in the listening tests. The four versions of each utterance were identical with respect to the spectral measurements, but duration was set to (a) the original measured value (OD), (b) 272 ms (ND), (c) 144 ms (SD), or (d) 400 ms (LD).

TABLE III. The most frequent changes in vowel classification resulting from vowel shortening or vowel lengthening by the quadratic discriminant classifier. The percentages in the column to the right reflect the number of shifts in vowel identity (OD→SD or OD→LD) divided by the number of opportunities for such shifts to occur.

Vowel shift	Percentage
Effects of vowel shortening	
/ɔ/→/a/ or /ʌ/	54.2
/æ/→/ɛ/	25.0
/a/→/ʌ/	8.0
Effects of vowel lengthening	
/ʌ/→/a/ or /ɔ/	60.0
/ɛ/→/æ/	33.0

Overall correct classification rates were 98.0% for the OD signals, 97.3% for the ND signals, 88.3% for the SD signals, and 87.0% for the LD signals. Compared to the listening tests results in experiment 2, the OD and ND recognition rates are some 2%–3% higher, while the SD and LD rates are about 3%–4% lower. In common with the listening test results, setting duration to a neutral value produced a very small drop in overall recognition accuracy, while shortening produced a drop in accuracy that was very similar to that produced by lengthening. Of greater interest are the results in Table III, which show the most common shifts in vowel identity produced by the pattern classifier. These analyses were carried out in the same way as those reported for the listening test; i.e., they are based on confusion matrices which focused on instances in which the pattern recognizer classified the OD version of a signal correctly but classified the duration-modified version of the same utterance incorrectly. The results in Table III show a number of important features in common with the listening test results from experiment 2 (Table II). In particular, as with human listeners, the most frequent shifts in vowel classification for the shortened signals consisted of /ɔ/ shifting to /a/ or /ʌ/, and /æ/ shifting to /ɛ/. Further, the most frequent shifts in vowel classification for the lengthened signals consisted of /ʌ/ shifting to /a/ or /ɔ/, and /ɛ/ shifting to /æ/. With the exception of the substantially larger percentage of lengthened /ʌ/ tokens that shifted to /a/ or /ɔ/, the percentages of shifts in Tables II and III are rather similar. Not shown in Table III, but of equal importance, the pattern classifier produced no shifts between /i/ and /ɪ/ and no shifts between /u/ and /ʊ/. Among the /ɪ/-/e/-/ɛ/ cluster, the only duration-dependent shifts that were observed consisted of a modest number (12.0%) of lengthened /ɛ/ tokens shifting to /e/.

Overall, the pattern recognition results support the idea that the role of duration in vowel recognition depends not only on the magnitude and consistency of observed durational differences among vowels but also on the degree to which pairs and groups of vowels are well separated on the basis of spectral cues. Vowels such as /i/-/ɪ/, /u/-/ʊ/, and /ɪ/-/e/-/ɛ/ show consistent durational differences in production but are sufficiently well separated on the basis of spectral features that duration has a rather small influence on perceived vowel quality. On the other hand, vowels such as /a/-/ɔ/-/ʌ/ and /æ/-/ɛ/ show a greater degree of overlap in

their spectral properties and, as a consequence, duration plays a more important role in the recognition of these vowels.

V. GENERAL DISCUSSION

There were many features in common between the findings of experiments 1 and 2. In both experiments, the effect of altering vowel duration was seen to be relatively modest overall since the great preponderance of signals were accurately identified under all four duration conditions. Further, the duration-related effects that were observed in both experiments were quite sensible; that is, vowels with long typical durations tended to shift to adjacent vowels with shorter typical durations when shortened. Conversely, vowels with short typical durations tended to shift to adjacent vowels with longer typical durations when lengthened. The primary difference between the two experiments was that the effect of vowel shortening was considerably greater for the formant synthesized stimuli than the sinusoidally synthesized stimuli.

The greater overall effect of duration in experiment 1 is consistent with the hypothesis that motivated experiment 2. Since the spectral cues to vowel quality are not preserved quite as well in the formant synthesis conditions—resulting in signals whose vowel quality is a bit more ambiguous—altering vowel duration was expected to exert a slightly larger influence on vowel identity in experiment 1. Although an effect in this direction was observed, the results were not quite so simple since the primary difference between the two synthesis methods had to do with the greater influence of vowel shortening for the formant synthesized stimuli relative to the sinusoidally synthesized signals. We believe that this discrepancy between the two experiments is consistent with the HN99 findings on the recognition of natural versus formant synthesized /hVd/ syllables. As mentioned previously, HN99 found that the natural signals were somewhat more intelligible than the formant synthesized versions (96.1% versus 89.8%). However, there was not a simple across-the-board drop in intelligibility resulting from formant synthesis. Vowels showing relatively large decreases in intelligibility as a result of the formant synthesis method included /u/ (shifting primarily to /ʊ/), /æ/ (shifting primarily to /ɛ/), and /a/ (shifting primarily to /ɔ/ or /ʌ/). The explanation for this differential effect of formant coding across vowels is as yet unclear. However, we assume that in experiment 1 of the present study there were a number of OD tokens of /u/, /æ/, and /a/ that were closer in vowel quality than their sinusoidal counterparts to their shorter-duration neighbors, /ʊ/, /ɛ/, and /ʌ/. The result was that a decrease in duration was sufficient to induce a change in vowel identity for many of these formant-synthesized signals. The sinusoidally synthesized signals, on the other hand, preserved the spectral cues of the original vowels more accurately and were less likely to shift to adjacent vowels with shorter typical durations.

The general principle that is illustrated by the differences between experiments 1 and 2 is that the measured importance of a particular acoustic cue to a phonetic dimension depends not only on the precision with which that cue is modeled in the test signals but also on the degree to which other cues to that same dimension are faithfully preserved in

the those signals. There are other illustrations of this principle in the acoustic phonetics literature. For example, a series of synthetic speech experiments by Raphael and colleagues (Raphael, 1972, 1981, Raphael *et al.*, 1975) suggested that the duration of a preceding vowel was both a necessary and sufficient cue to the voicing of syllable-final consonants. However, subsequent studies using edited natural speech, which preserved the rich cues to final voicing in the vicinity of articulatory closure and/or release, found that alterations in vowel duration alone were unlikely to induce a change in the voicing of the final consonant (e.g., Wardrip-Fruin, 1982; O’Kane, 1978; Hogan and Rozsypal, 1980; Raphael, 1981; Revoile *et al.*, 1982; Hillenbrand *et al.*, 1984). Results such as these, along with the present findings, serve as a reminder that the conclusions that are drawn from acoustic-phonetic studies can depend on the fine details of the stimulus construction methods.

On a related point, it should be noted that the interpretation of these findings is limited by the relatively simple speech material that was employed. It is well known that there is a large, diverse, and often competing set of influences on vowel duration in connected speech (see Klatt, 1976, for a thorough review). In addition to inherent duration, vowel duration is affected by factors such as overall speaking rate, semantic phenomena such as emphatic stress, grammatical effects such as word- and phrase-final lengthening, variations in lexical stress, and phonetic effects such as the voicing property of preceding or following consonants. Given that the test signals used in this study consisted of citation-form CVC syllables, with identical initial and final consonants, it is nearly certain that listeners would attribute a very large share of the variation in vowel duration to the vowel itself. The situation in connected speech is considerably more complicated, so it is possible that the relatively modest duration effects that were observed here would be even smaller in connected speech. On the other hand, it is also possible that the shorter durations and vowel reduction that characterize connected speech might reduce the spectral contrast among vowels, resulting in a greater role for duration than was observed for the citation-form syllables studied here. Extension of methods such as those used in the present study to connected speech would seem to be a fruitful avenue for further work on this question.

ACKNOWLEDGMENTS

This work was supported by the National Institutes of Health under Grant No. DC-01661 to Western Michigan University. Thanks to Terry Nearey for advice on data analysis. The authors are grateful to Keith Kluender and three anonymous reviewers for insightful comments on an earlier draft.

¹This is an important difference between our sinusoidal synthesizer and the synthesizer described by McAuley and Quatieri (1986). McAuley and Quatieri go to considerable lengths to preserve the original phase relations among spectral components, while in our method phase is ignored, with the important exception of the steps that are taken to prevent phase discontinuities at the boundaries between frames.

²HN99 compared natural and formant-synthesized versions of the 300 /hVd/ signals used in the present study in two experiments with separate listener

- groups. In experiment 1 of HN99, the natural signals were 95.4% intelligible versus 88.5% for the formant synthesized signals, used both in HN99 and in experiment 1 of the present study. The corresponding figures for the replication in experiment 2 of HN99 were 96.7% versus 91.0%. Averaged across the two replications, the recognition rate was 96.1% for the natural signals—identical to the recognition rate for the sinusoidal signals used in experiment 2 of the present study—versus 89.8% for the formant synthesized versions.
- Ainsworth, W. A. (1972). "Duration as a cue in the recognition of synthetic vowels," *J. Acoust. Soc. Am.* **51**, 648–651.
- Assmann, P., Nearey, T., and Hogan, J. (1982). "Vowel identification: Orthographic, perceptual, and acoustic aspects," *J. Acoust. Soc. Am.* **71**, 975–989.
- Black, J. W. (1949). "Natural frequency, duration, and intensity of vowels in reading," *J. Speech Hear. Dis.* **14**, 216–221.
- Chomsky, N., and Halle, M. (1968). *The Sound Pattern of English* (Harper and Row, New York).
- Crystal, T. H., and House, A. S. (1988). "The duration of American-English vowels: An overview," *J. Phonetics* **16**, 263–284.
- Daniloff, R. G., Shriner, T. H., and Zemlin, W. R. (1968). "Intelligibility of vowels altered in duration and frequency," *J. Acoust. Soc. Am.* **44**, 700–707.
- Fairbanks, G., and Grubb, P. (1961). "A psychophysical investigation of vowel formants," *J. Speech Hear. Res.* **4**, 203–219.
- Hillenbrand, J. M., and Gayvert, R. T. (1993). "Identification of steady-state vowels synthesized from the Peterson–Barney measurements," *J. Acoust. Soc. Am.* **94**, 668–674.
- Hillenbrand, J. M., and Nearey, T. M. (1999). "Identification of resynthesized /hVd/utterances: Effects of formant contour," *J. Acoust. Soc. Am.* **105**, 3509–3523.
- Hillenbrand, J. M., Clark, M. J., and Nearey, T. M. (2000). "Effects of consonant environment on vowel formant patterns," *J. Acoust. Soc. Am.* (submitted).
- Hillenbrand, J., Getty, L. A., Clark, M. J., and Wheeler, K. (1995). "Acoustic characteristics of American English vowels," *J. Acoust. Soc. Am.* **97**, 3099–3111.
- Hillenbrand, J., Ingrisano, D., Smith, B., and Flege, J. (1984). "Perception of the voiced-voiceless contrast in syllable-final stops," *J. Acoust. Soc. Am.* **76**, 18–26.
- Hogan, J., and Rozsypal, A. (1980). "Evaluation of vowel duration as a cue for the voicing distinction in the following word-final consonant," *J. Acoust. Soc. Am.* **67**, 1764–1771.
- House, A. S., and Fairbanks, G. (1953). "The influence of consonantal environment upon the secondary acoustical characteristics of vowels," *J. Acoust. Soc. Am.* **25**, 105–113.
- Huang, C. B. (1986). "The effect of formant trajectory and spectral shape on the tense/lax distinction in American vowels," *IEEE ICASSP*, 893–896.
- Johnson, R. A., and Winchern, D. W. (1982). *Applied Multivariate Statistical Analysis* (Prentice-Hall, Englewood Cliffs, NJ).
- Klatt, D. H. (1976). "Linguistic uses of segmental duration in English: Acoustic and perceptual evidence," *J. Acoust. Soc. Am.* **59**, 1208–1221.
- Klatt, D. H., and Klatt, L. C. (1990). "Analysis, synthesis, and perception of voice quality variations among female and male talkers," *J. Acoust. Soc. Am.* **87**, 820–857.
- Laver, J. (1994). *Principles of Phonetics* (Cambridge U. P., Cambridge).
- McAuley, R. J., and Quatieri, T. F. (1986). "Speech analysis/synthesis based on sinusoidal representation," *IEEE Trans. Acoust., Speech, Signal Process.* **ASSP-22**, 330–338.
- Nearey, T. M., and Assmann, P. (1986). "Modeling the role of vowel inherent spectral change in vowel identification," *J. Acoust. Soc. Am.* **80**, 1297–1308.
- O'Kane, D. (1978). "Manner of vowel termination as a perceptual cue to the voicing status of post-vocalic stop consonants," *J. Phonetics* **6**, 311–318.
- Peterson, G., and Lehiste, I. (1960). "Duration of syllable nuclei in English," *J. Acoust. Soc. Am.* **32**, 693–703.
- Rabiner, L. (1968). "Digital formant synthesizer for speech synthesis studies," *J. Acoust. Soc. Am.* **24**, 175–184.
- Raphael, L. (1972). "Preceding vowel duration as a cue to the perception of the voicing characteristic of word-final consonants in American English," *J. Acoust. Soc. Am.* **51**, 1296–1303.
- Raphael, L. (1981). "Durations and contexts as cues to word-final cognate opposition in English," *Phonetica* **38**, 126–147.
- Raphael, L., Dorman, M., Freeman, F., and Tobin, C. (1975). "Vowel and nasal duration as cues to voicing in word-final stop consonants: Spectrographic and perceptual studies," *J. Speech Hear. Res.* **18**, 389–400.
- Revoile, S., Pickett, J. M., Holden, L. D., and Talkin, D. (1982). "Acoustic cues to final-stop voicing for impaired- and normal-hearing listeners," *J. Acoust. Soc. Am.* **72**, 1145–1154.
- Roca, I., and Johnson, W. (1999). *A Course in Phonology* (Blackwell, Oxford).
- Stevens, K. N. (1959). "The role of duration in vowel identification," *Quarterly Progress Report* **52**, Research Laboratory of Electronics, MIT.
- Strange, W. (1989). "Dynamic specification of coarticulated vowels," *J. Acoust. Soc. Am.* **74**, 695–705.
- van Santen, J. P. H. (1992). "Contextual effects on vowel duration," *Speech Commun.* **11**, 513–546.
- Tiffany, W. (1953). "Vowel recognition as a function of duration, frequency modulation and phonetic context," *J. Speech Hear. Dis.* **18**, 289–301.
- Wardrip-Fruin, C. (1982). "On the status of temporal cues to phonetic categories: Preceding vowel duration as a cue in final stop consonants," *J. Acoust. Soc. Am.* **71**, 187–195.
- Watson, C. I., and Harrington, J. (1999). "Acoustic evidence for dynamic formant trajectories in Australian English Vowels," *J. Acoust. Soc. Am.* **106**, 458–468.
- Zahorian, S. A., and Jagharghi, A. J. (1993). "Spectral-shape features versus formants as acoustic correlates for vowels," *J. Acoust. Soc. Am.* **94**, 1966–1982.

Children's perception of speech in multitalker babble

Marianne Fallon, Sandra E. Trehub,^{a)} and Bruce A. Schneider

Department of Psychology, University of Toronto at Mississauga, 3359 Mississauga Rd., Mississauga, Ontario L5L 1C6, Canada

(Received 11 August 1999; accepted for publication 14 September 2000)

Children 5, 9, and 11 years of age and young adults attempted to identify the final word of sentences recorded by a female speaker. The sentences were presented in two levels of multitalker babble, and participants responded by selecting one of four pictures. In a low-noise condition, the signal-to-noise ratio (SNR) was adjusted for each age group to yield 85% correct performance. In a high-noise condition, the SNR was set 7 dB lower than the low-noise condition. Although children required more favorable SNRs than adults to achieve comparable performance in low noise, an equivalent decrease in SNR had comparable consequences for all age groups. Thus age-related differences on this task can be attributed primarily to sensory factors. © 2000 Acoustical Society of America. [S0001-4966(00)02812-5]

PACS numbers: 43.71.Ft, 43.71.Bp, 43.71.Pc [CWT]

I. INTRODUCTION

Children are believed to have considerable difficulty perceiving speech in noise (e.g., Mills, 1975; Elliott, 1995). For example, normative estimates [e.g., The Goldman-Fristoe-Woodcock Test of Auditory Discrimination (Goldman *et al.* 1976)] reflect young children's poor speech identification in "cafeteria noise" relative to that of older children and adults. In classroom settings, younger children are more "distracted" by noise than are older children (Héту *et al.*, 1990). Moreover, young children are significantly less accurate at identifying the last word of a sentence presented in multitalker babble than are older children and adults (Elliott, 1979; Elliott *et al.*, 1979). Similarly, children 4 to 6 years of age are significantly poorer than adults at identifying words and sentences in spectrally matched noise (Nittrouer and Boothroyd, 1990).

A number of factors may contribute to children's apparent difficulty with speech in noise. First, young children have higher auditory thresholds than do older children and adults (Roche *et al.*, 1978; Elliott and Katz, 1980; Yoneshige and Elliott, 1981; Berg and Smith, 1983; Sinnott *et al.*, 1983; Schneider *et al.*, 1986; Trehub *et al.*, 1988). Although the relation between auditory sensitivity and speech identification thresholds in quiet and in noise is unclear (Elliott *et al.*, 1979; Summerfield *et al.*, 1994), age-related differences in sensitivity could underlie children's difficulty identifying speech in noise. From 5 years of age, developmental changes in absolute thresholds for octave-band noise mirror the changes in masked thresholds for octave-band noise presented in broadband noise (Schneider *et al.*, 1989). Moreover, thresholds for the identification of words presented in quiet are higher for younger children than for older children and adults (Elliott *et al.*, 1979). Nevertheless, most developmental investigations of speech identification in noise have used identical signal-to-noise ratios (SNRs) across age without adjusting for age-related differences in detection or identification thresholds (e.g., Elliott, 1979; Nittrouer and Boo-

throyd, 1990). Chermak and Dengerink (1981) found, however, that when age-related differences in word identification thresholds were taken into account, adult-child performance differences in noise were minimal.

Second, young children's limited language experience may have adverse effects on their performance. For example, native speakers of English are more proficient at identifying speech in noise than are non-native speakers with several years of exposure to English (Gat and Keith, 1978; Mayo *et al.*, 1997). As words become increasingly familiar, less acoustic information is required for their identification (Rosenwieg and Postman, 1957; Elliott *et al.* 1979; Elliott *et al.*, 1983). In some cases, however, words (e.g., "oath") and sentences (e.g., "Tough guys sound mean") that are unfamiliar to many children have been used as test stimuli (e.g., Elliott, 1979; Nittrouer and Boothroyd, 1990). Moreover, limited phonological awareness on the part of young children (Treiman, 1985; Hnath-Chisholm *et al.*, 1998), especially pre-readers (Wimmer *et al.*, 1991), may also impair performance on speech-identification tasks. For example, a young child hearing "_ike" might not generate "bike" as a candidate word. Even if a child can use phonological strategies to aid identification, noise may disrupt this process.

Third, the typical tasks used in speech-identification studies may pose disproportionate difficulty for young children. As Wightman and Allen (1992) note, some performance differences between children and adults "may reflect nothing more than the influence of nonsensory factors such as memory and attention" (p. 133). These nonsensory factors could contribute to young children's difficulty with verbal material designed for use with adults. For example, some investigators adapted the well-known SPIN (speech perception in noise) test for children (e.g., Elliott, 1979, 1995; Elliott and Katz, 1983, in Elliott, 1995 and references therein). The original (Kalikow *et al.*, 1977) and revised (SPIN-R) versions (Bilger *et al.*, 1984) of the SPIN test, which were normed for native English-speaking adults, require listeners to repeat the last word of low-predictability ("The old man discussed the dive.") and high-predictability ("The watch-

^{a)}Electronic mail: sandra.trehub@utoronto.ca

dog gave a warning growl.’’) sentences presented in multitalker babble. The presumption is that low-predictability sentences depend primarily on sensory function, and that high-predictability sentences engage cognitive as well as sensory functions (Kalikow *et al.*, 1977). Children’s (9- and 11-year-olds’) poor performance on both types of sentences led Elliott (1979) to conclude that the SPIN task was inappropriate for use with children under the age of 15. The required verbal responses are potentially problematic for listeners with limitations in articulation and memory. Indeed, picture-pointing responses yield substantially higher performance levels for young children than do verbal responses (Elliott *et al.*, 1979). Although feedback about performance is also known to enhance accuracy (Green and Swets, 1966; Smith and Hodgson, 1970), such feedback is often excluded from developmental investigations (e.g., Elliott *et al.*, 1979; Nittrouer and Boothroyd, 1990). Its absence may have detrimental consequences on children’s motivation.

Nittrouer and Boothroyd (1990) tested 4- to 6-year-old children on a task that may be even more demanding than the SPIN task. Children were required to repeat various types of verbal material presented in noise, including nonsense syllables, monosyllabic words, and four-word sentences, some of which were semantically and/or syntactically anomalous (e.g., ‘‘Sing his get throw,’’ ‘‘Lend them less joy’’). Semantic and syntactic anomalies are likely to be especially confusing for young children. Unfortunately, Nittrouer and Boothroyd (1990) did not confirm that young children were capable of repeating such anomalous sentences under optimal listening conditions.

The primary goal of the present investigation was to determine whether noise impairs children’s identification of speech to a greater extent than it does for adults. In other words, does noise affect children’s perception of speech beyond what would be expected from adult–child differences in auditory sensitivity? Unlike previous adult–child comparisons that evaluated all listeners at identical SNRs (e.g., Elliott, 1979; Nittrouer and Boothroyd, 1990), the present study identified SNRs that yielded 85% correct performance (i.e., a low-noise condition) for 5-year-olds, 9-year-olds, 11-year-olds, and adults. A high-noise condition was created by adding 7 dB of noise. Based on adult–child differences in the detection of auditory signals in quiet (e.g., Schneider *et al.*, 1986; Trehub *et al.*, 1988) and in noise (Schneider *et al.*, 1989), 5-year-olds were expected to require at least 5-dB less background noise than adults to achieve comparable (85% correct) performance in low noise. Additional noise may differentially affect lexical access, leading to more adverse consequences for young children than for older children and adults. In such circumstances, performance differences between low- and high-noise contexts should be greater for children than for adults. Alternatively, adult–child differences could arise from poor allocation of attention on the part of children. Were this the case, children would have to guess more often than adults. Thus they would require more favorable SNRs to reach 85% correct performance than would be expected from differences in sensory functioning alone (5 dB). Simple models of inattention (e.g., Wightman and Allen, 1992) would predict that performance differences

between low- and high-noise conditions would be less pronounced for children than for adults. If, however, the effects of noise were attributable primarily to sensory factors (i.e., processes involved in converting acoustic-phonetic information into electrical impulses in the brain) rather than some combination of sensory and nonsensory factors (e.g., inattention and/or interference with lexical access), then high noise should produce comparable decrements in performance across age.

The available evidence does not favor a single hypothesis. According to Elliott (1979), perceptual and cognitive factors contribute jointly to children’s poor performance on the SPIN task. Nittrouer and Boothroyd (1990) argue, however, that children’s poor performance on their task resulted from perceptual factors. Although some researchers claim that inattention cannot account for adult–child differences in auditory detection or discrimination tasks (e.g., Schneider and Trehub, 1992), others suggest that inattention is largely responsible for age-related differences, especially when adaptive procedures are used (e.g., Wightman and Allen, 1992). Finally, Hnath-Chisholm *et al.* (1998) attribute young children’s poor speech discrimination to cognitive factors coupled with immature phonological development.

A second goal of the present investigation was to develop a procedure that would minimize cognitive demands and maximize comparability across a broad age range. A four-alternative, picture-pointing task was used because of its documented success with young children (Goldman *et al.*, 1976; Geffner *et al.*, 1996) and its obvious advantages over word-generation tasks (Elliott *et al.*, 1979). Target words were presented in a low-context carrier phrase (‘‘Touch the X’’) because of the present focus on perceptual, or bottom-up, factors and the reported advantage of sentential contexts over words presented in isolation (Craig, 1988). Target words were restricted to those that were familiar to 5-year-olds, the youngest age group in the present study. Moreover, target words and foils were highly contrastive phonologically so that children would not be penalized for their lesser phonological awareness (Treiman, 1985). Sentences were presented in multitalker babble (Bilger *et al.*, 1984) rather than spectrally matched noise (Boothroyd and Nittrouer, 1988; Nittrouer and Boothroyd, 1990) because babble is a more effective masker of speech (Carhart *et al.*, 1969; Elliott *et al.*, 1979; Lewis *et al.*, 1988). A female speaker was used because of the predominance of female caregivers and educators in the lives of young children. Finally, a motivating, gamelike atmosphere was created by presenting the pictorial response options on a touch-sensitive screen and providing automated visual feedback for correct and incorrect responses.

II. METHOD

A. Participants

The participants were 24 children 5.0–5.5 years of age ($M = 5.25$ years), 24 children 9.0–9.5 years of age ($M = 9.25$ years), 24 children 11.0–11.5 years of age ($M = 11.25$ years), and 24 adults 19–28 years of age ($M = 22.7$ years), none of whom had health problems or a his-

tory of hearing loss. Equal numbers of males and females were included in each age group. No participant had experienced frequent ear infections or pressure-equalizing tubes in the past; none had a cold on the day of testing. Children's age and their family's middle- to upper-middle-class status made it unlikely that serious middle-ear problems had gone undetected; thus no tympanometric screening was undertaken. The children were all native English speakers and the adults were either native speakers or had learned English by 6 years of age ($N=3$). Additional children were excluded because of experimenter error (one 9-year-old) or inattentiveness (four 5-year-olds and one 9-year-old), which included the following behaviors: responding before hearing the entire sentence on more than two trials, excessive fidgeting, talking during sentence presentation, talking excessively between test trials, or not completing one or both experimental conditions.

B. Apparatus and stimuli

Testing occurred in a double-wall sound-attenuating booth, $3 \times 2.8 \times 2$ m in size. Participants were seated facing a nonglare touch screen monitor (Goldstar 1465DLs) 33×33 cm. Loudspeakers (KEF Model 101) were 45° to the left and right of the participant (distance of 70 cm) at approximate ear level. All sentences, which were spoken by the same young woman, were digitized at a rate of 20 kHz by means of a 16-bit Tucker Davis (DD1) analog-to-digital converter. The babble portion of SPIN forms used by Pichora-Fuller *et al.* (1995) was similarly digitized and stored. Sentence files and babble files were converted to analog form using Tucker Davis digital-to-analog converters under the control of a computer with a Pentium processor. Sentence and babble amplitudes were controlled separately using programmable attenuators. After mixing, the combined signals were amplified (SAE 2600) and presented over loudspeakers located inside the testing booth. Sound-field levels were determined in the absence of the listener with a Bruel and Kjaer 1/2-in microphone.

The multitalker babble, which did not contain energy above 8 kHz, consisted of eight voices, both male and female, reading from newspapers (see Bilger *et al.*, 1984). The degree to which a speech signal is masked by babble will depend on the spectral characteristics of the speech relative to that of the background babble. Figure 1 (dashed line) shows the distribution of average spectral power in the background babble. This distribution was obtained by averaging the power spectra of 40 independent 1-s samples of the babble background. The average power spectrum was then normalized by dividing it by the total power in the average spectrum. This normalized average power spectrum was converted to decibels and plotted in Fig. 1. The average power in the babble background declines with increasing frequency at a rate of approximately 3-dB/octave for frequencies up to approximately 700 Hz, and 12-dB/octave for frequencies higher than 700 Hz. Also shown in Fig. 1 is the average power spectrum for the male voice used in the modified SPIN test (Bilger *et al.*, 1984). This spectrum was obtained by averaging the power spectra (1-s samples taken from the beginning of each sentence) of the first 40 SPIN sentences

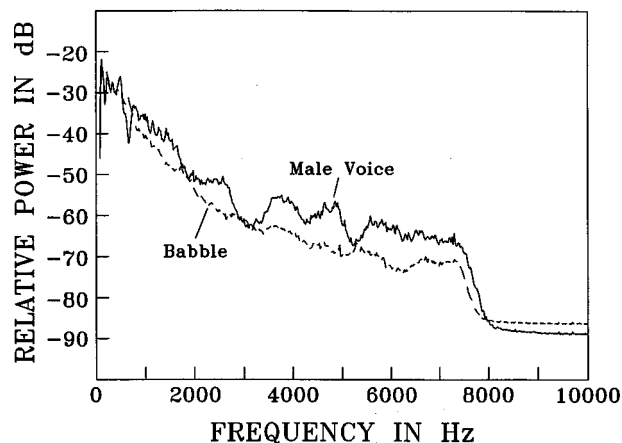


FIG. 1. Averaged power spectra of the babble used in the present study and the male speaker of the SPIN sentences (Bilger *et al.*, 1984).

from Form 1. The average power spectrum was then normalized by dividing it by the total power in the average spectrum. Clearly, the relative power spectrum of the male voice from the SPIN test closely matches that of the babble background. By contrast, Fig. 2 plots the relative power spectrum of the female voice used in the present experiment. This spectrum was obtained by averaging the power spectra of the 40 test sentences (1-s samples taken from the beginning of each sentence). Not only was the fundamental frequency of the female speaker (255 Hz) much higher than that of the male speaker, but the distribution of power in the female voice was heavily weighted toward the higher frequencies.

The female speaker's high degree of power at the high frequencies vastly improves the SNR at these frequencies. If we adjust the total power in the babble to equal the total power in each of the speech signals (an overall SNR of 0 dB), the average SNR for the male speaker is -0.06 dB in the 0–1.5-kHz region and $+4.49$ dB in the 1.5–5-kHz region. By contrast, the average SNR for the female speaker is -2.40 dB in the 0–1.5-kHz region and $+16.92$ dB in the 1.5–5-kHz region. Thus the male speaker enjoys a 2.34-dB advantage at the low frequencies whereas the female speaker enjoys a 12.4-dB advantage at the high frequencies. Because it is usually assumed that the low- and high-frequency por-

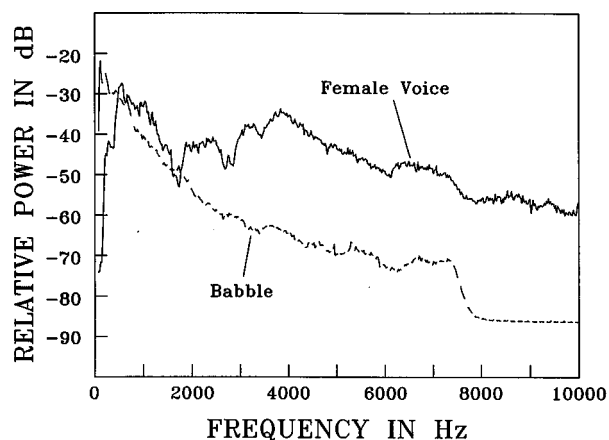


FIG. 2. Averaged power spectra of the babble and the female speaker from the present study.

tions of the spectrum contribute equally to speech recognition, we might expect the female speaker to enjoy a 12-dB advantage relative to the male speaker in the babble background.

Speech stimuli consisted of the prompt, “Touch the —,” and a target word (e.g., “ball”). Target words consisted of 40 monosyllabic nouns for the test phase and an additional 20 words (monosyllabic and polysyllabic) for the training phase. The sentences were presented at approximately 44 dB (A scale). This level was chosen to ensure that young children would not be exposed to sound levels exceeding 80 dB (A). Root-mean-square (rms) values were calculated and adjusted such that each sentence was presented at an equal rms value following the procedure described in Schneider *et al.* (2000). SNR was varied by adjusting the level of babble (F_0 : 185 Hz). Pilot-testing established the SNR at which each age group achieved approximately 85% correct performance: -28 dB for 5-year-olds, -30 dB for 9-year-olds, -31 dB for 11-year-olds, and -33 dB for adults. These levels were designated low-noise conditions. High-noise conditions were created for each age group by decreasing the SNR in the low-noise condition (i.e., the level yielding 85% correct performance) by 7 dB, resulting in SNRs of -35 dB for 5-year-olds, -37 dB for 9-year-olds, -38 dB for 11-year-olds, and -40 dB for adults. SNRs for the training phase were set lower than those in the low-noise conditions: 0, -5 , -6 , and -8 dB for 5-year-olds, 9-year-olds, 11-year-olds, and adults, respectively.

Visual stimuli consisted of 60 black-and-white Snodgrass line drawings of familiar, concrete objects (Snodgrass and Vanderwart, 1980). All pictures were chosen on the basis of 4- and 5-year-olds’ ability to correctly name the image. An independent sample of 32 children 4.0 to 5.5 years of age was asked to verbally identify each of the 60 pictures. Inclusion of a picture in the stimulus set required at least 88% of children correctly identifying it. The average correct identification of pictures was 96.8%.

C. Procedure

All participants were tested individually. A trial, which was initiated by means of a button box located inside the testing booth, consisted of the simultaneous presentation of vocal stimuli (sentence and noise) and visual stimuli (pictures). A sentence in low or high noise was accompanied by an array of four different images, one appearing in each corner of the touch screen. Sentences were selected randomly without replacement. The multitalker babble began with the onset of the sentence and terminated when the sentence ended. The visual array included the target image and three foils selected randomly from the remaining images. A picture could appear as a target only once and as a foil three times during the test phase. The only other restriction on foils was that an item could not serve as a foil immediately after it was presented as a target. The locations of targets and foils were selected randomly on each trial. Feedback for correct performance consisted of the target picture flashing in the middle of the screen. Incorrect selections resulted in the screen going blank.

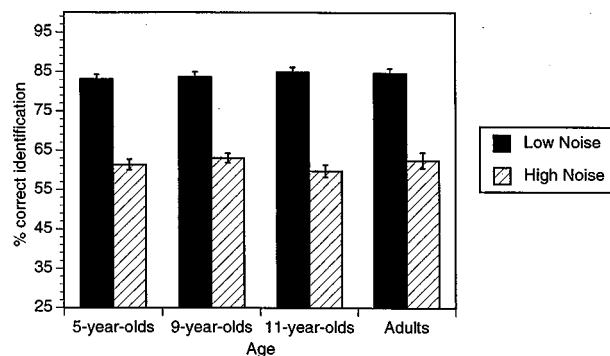


FIG. 3. Percent correct identification as a function of noise level and age. Error bars represent the standard error of the mean.

The instructions were tailored to the age of participants. The experimenter explained to 5-year-old children that if they only hear part of a word, they should choose the picture that sounds similar to what they hear (e.g., “If you hear ‘irt’ and there are pictures of a can, plate, shirt, and boat on the screen, you should pick the shirt since ‘shirt’ sounds the most like ‘irt.’”). Older children and adults were told that the pictures were identifiable by basic-level terms. For example, a picture of a shirt would be identified by the word “shirt,” not “button-down” or “clothing.” No other explicit strategies were provided.

The test session consisted of a training phase and a test phase. All participants had to meet a training criterion of correctly identifying 4 targets in a row within 16 trials; on average, listeners achieved the training criterion in 6.04 trials. After reaching the criterion, participants advanced to the test phase, consisting of 40 trials in the low-noise condition and another 40 trials in the high-noise condition. The two conditions, which were separated by a short break, were counterbalanced such that half of the participants received the low-noise condition first and the other half received the high-noise condition first. Adults and older children initiated trials at their preferred pace. The experimenter initiated trials for 5-year-olds when she judged them to be ready and attentive. The experimenter remained in the testing booth during the entire session for children, offering verbal reinforcement and encouragement when appropriate. An additional motivational technique was used with the 5-year-olds. After every four trials, children received a colored sticker to place in an “incomplete” black-and-white picture. At the end of the 40 trials, the child had completed the picture. A new picture was made in the second condition.

III. RESULTS

Figure 3 plots correct performance at each noise level for each age group. Performance (percent correct) in the low-noise condition did not differ significantly across age groups, as confirmed by a one-way ANOVA, $F(3,92) = .491$, $p = .689$. Recall, however, that SNRs were selected to equalize performance in low noise across age levels. To examine whether the high-noise condition differentially affected younger children, a $2 \times 4 \times 2 \times 2$ repeated-measures ANOVA was calculated with noise level as the within-subject factor and age, sex, and presentation order (low or

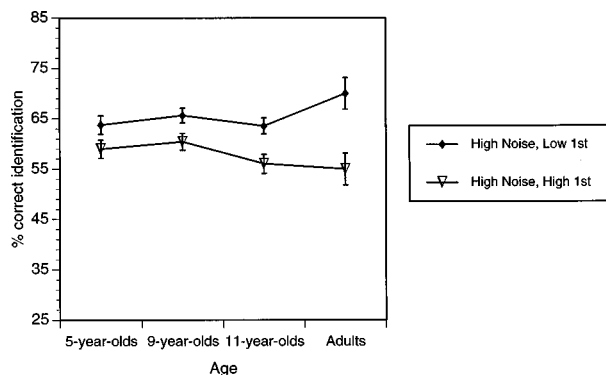


FIG. 4. Percent correct identification in high noise as a function of age and order. Error bars represent the standard error of the mean.

high noise first) as between-subject factors. As expected, listeners performed significantly better in low noise than in high noise, $F(1,80)=677.996$, $p<.00001$ (see Table I). There was no effect of age and no effect of gender, but there was a significant effect of presentation order, $F(1,80)=11.418$, $p=.001$. Participants made more correct selections when the low-noise condition was presented before the high-noise condition than the reverse order ($M_{low\rightarrow high}=74.79\%$, $M_{high\rightarrow low}=70.96\%$). The only two-way interaction that achieved statistical significance was a noise \times order interaction, $F(1,80)=24.899$, $p<.001$, reflecting listeners' improved performance in the high-noise condition when it was preceded by the low-noise condition. No higher-order interactions were significant.

To examine potential age-related differences with regard to the noise \times order interaction, a 2×4 ANOVA was calculated using performance in high noise as the dependent variable, with order and age as independent variables. Not surprisingly, there was a significant effect of order, $F(1,88)=27.15$, $p<.001$, but no effect of age or age \times order interaction (see Fig. 4). However, one-way ANOVAs conducted on each age group separately revealed that the order effect in high noise was somewhat more pronounced for 9-year-olds, 11-year-olds, and adults [$F(1,22)=5.62$, $p<.03$, $F(1,22)=7.16$, $p<.02$, and $F(1,22)=11.48$, $p<.005$, respectively] than for 5-year-olds [$F(1,22)=3.47$, $p=.076$].

Patterns of performance were also examined for potential age-related improvement within the test sessions. Gender was excluded from this analysis because it had no effect in

TABLE I. Percent correct performance across age, noise level, and order of presentation.

	Low→High	High→Low
Low-noise condition	83.85 (6.12) ^a	84.32 (5.62)
5-year-olds	83.96 (4.94)	82.29 (6.17)
9-year-olds	82.71 (7.03)	84.58 (5.52)
11-year-olds	82.92 (7.06)	86.88 (4.41)
Adults	85.83 (5.47)	83.54 (5.88)
High-noise condition	65.73 (7.00)	57.60 (7.85)
5-year-olds	63.75 (6.26)	58.96 (6.35)
9-year-olds	65.62 (5.01)	60.42 (5.72)
11-year-olds	63.54 (6.52)	56.04 (7.19)
Adults	70.00 (10.82)	55.00 (10.87)

^aStandard deviations are in parentheses.

TABLE II. Percent correct performance per half in low noise.

	1st Half	2nd Half
5-year-olds	81.04 (8.97) ^a	85.21 (7.44)
9-year-olds	82.71 (9.09)	84.58 (7.65)
11-year-olds	83.12 (8.05)	86.46 (9.26)
Adults	81.04 (9.09)	88.12 (5.67)

^aStandard deviations are in parentheses.

the main analysis. Given that the order effect was noise-level specific, analyses were conducted separately for each noise condition. A 2×4 repeated measures ANOVA was performed using percent correct per half in low noise (i.e., first 20 trials vs final 20 trials) as the within-subject factor and age as the between-subject factor. Order was excluded from this analysis because it had no effect in low noise. Listeners performed more accurately in the second half of the test session than in the first half, $F(1,92)=12.405$, $p=.001$, ($M=86.09\%$, $M=81.98\%$, respectively). No age effect or age \times half interaction was observed (see Table II). In the high-noise condition, a $2 \times 2 \times 4$ repeated measures ANOVA, with half as the within-subject variable and order and age as between-subject variables, revealed an order effect, $F(1,88)=27.591$, $p<.001$, reflecting the effect found in the main analysis. No additional main effects or higher-order interactions were observed.

Table III indicates the relative difficulty of identifying particular target words, in descending rank order. Note, for example, that MOON (rank=40) was the most difficult target to identify out of this sample of items, with TREE (rank=2.13) being the easiest. To determine whether listeners found the same targets difficult, the average rank across age groups was correlated with the rankings by individual age groups. As shown in Table IV, these strong positive correlations reflect the fact that all listeners, irrespective of age, experienced comparable difficulty with the same target words.

IV. DISCUSSION

When the accuracy of speech identification by 5-year-olds, 9-year-olds, 11-year-olds, and adults was equated in

TABLE III. Average difficulty of targets in descending rank order.

Target	Average rank	Target	Average rank	Target	Average rank
MOON	40.00 ^a	WHEEL	24.75	HOUSE	9.88
BOOK	38.13	CLOCK	23.63	CAT	9.75
BALL	36.63	COW	21.63	GRAPES	9.63
FORK	36.50	BREAD	21.25	KEY	7.25
CORN	36.38	SPOON	21.13	SHOE	6.63
KNIFE	33.00	EAR	19.63	CHAIR	6.50
BELL	32.88	DOG	18.00	SUN	5.38
LEAF	31.63	DUCK	17.88	FISH	4.50
EYE	30.63	HAT	17.75	SNAKE	2.63
FLAG	29.75	CAKE	17.63	TREE	2.13
FROG	29.38	HORSE	17.13		
BED	27.63	BUS	15.38		
HEART	26.75	HAND	14.88		
TRUCK	26.00	KITE	13.50		
PIG	25.50	PANTS	10.88		

^aMaximum rank is 40 (i.e., most difficult), minimum rank is 1 (i.e., easiest).

TABLE IV. Spearman correlation coefficients relating overall average ranking with rankings of individual age groups.

	5-year-olds	9-year-olds	11-year-olds	Adults
Average	.93 ^a	.91	.95	.93

^aAll correlations are significant to the $p = .01$ level at $\alpha = .5$.

low noise, the addition of further noise (7 dB) had comparable consequences for all age groups. Note, however, that 5-year-olds still required SNRs (-28 and -35 dB at low- and high-noise levels, respectively) that were 5 dB more favorable than those of adults (-33 and -40 dB) to obtain comparable performance. These results are consistent with evidence that 5-year-olds' and adults' absolute and masked thresholds for narrow-band noise differ by approximately 5 dB (Trehub *et al.*, 1988; Schneider *et al.*, 1989). Moreover, Elliott *et al.* (1979), using a four-alternative picture-pointing response, found that 5-year-olds' and adults' identification thresholds for monosyllables presented in babble differed by approximately 5 dB. Comparable performance decrements from high noise, regardless of age, imply that children's performance on the present task reflects their perceptual limitations rather than cognitive or attentional limitations. In fact, the minimal impact of nonsensory factors attests to the utility of the present task, which featured low-context sentences, words familiar to the youngest participants, a four-alternative picture-pointing response, and visual reinforcement. Moreover, comparable difficulty with the same target words at all age levels attests further to the role of sensory factors and to the limited contribution of linguistic experience to the present findings. Thus the findings support Nitttrouer and Boothroyd's (1990) contention that age-related differences in word identification in noisy backgrounds are largely due to perceptual factors, provided the task is equally suitable for all age levels.

Children and adults performed better in high noise when it followed the low-noise condition rather than preceding it. In other words, participants showed evidence of learning in the initial low-noise condition that generalized to the subsequent high-noise condition. It is interesting to note that the nonsignificant age trend in high-noise performance as a function of order parallels the nonsignificant age-related improvement in performance over the course of the low-noise condition. Experience in a relatively undemanding situation (low noise) may have allowed listeners to gain information, perhaps about the speaker's voice or other aspects of the task, that facilitated subsequent performance under more difficult circumstances (high noise). By contrast, experience in high noise showed no such transfer effects.

Although the SNR required for word recognition is affected by characteristics of the speaker's voice, the nature of the speech materials, and whether or not the materials are from an open or closed set (Miller *et al.*, 1951; Sumbly and Pollack, 1954), it was still surprising to find young adults recognizing 85% of the words at SNRs as low as -33 dB. The unusually low SNRs result, in part, from the spectral characteristics of the female voice in relation to the background babble. Recall that the speaker's power at the higher frequencies translated to a 12-dB advantage in SNR relative

to the male speaker used in the SPIN task (Bilger *et al.*, 1984). Moreover, the closed-set response (i.e., selecting from four alternatives) undoubtedly contributed to the high levels of performance at such low SNRs. To ascertain the consequences of open-set responding, an independent sample of 20 adults (6 males, 14 females; ages 19–25) was tested on the same target words without the pictorial alternatives. After listening to each of the same sentences in the same babble background at -22 dB SNR or -18 dB SNR, adults identified the last word of the sentence by means of written responses. Listeners achieved 81.125% and 89.17% correct performance at -22 and -18 dB SNR, respectively. Thus the SNR that would yield 85% correct performance with open-set responding is approximately -20 dB. In other words, the change from a closed set of four alternatives to an open set resulted in a 13-dB shift in SNR. Miller *et al.* (1951) found a comparable shift between a 256-word response set and a 4-word response set. The 13-dB advantage attributable to the four-alternative response set coupled with the 12-dB high-frequency advantage for the female voice can account for the performance levels obtained with the unusually low SNRs in the present experiment.

Although equivalent additions of noise had comparable effects on children and adults in the present task, such noise increments could have differential consequences in situations that accord a greater role to cognitive, or top-down, factors. For example, the use of high-predictability as well as low-predictability sentences would reveal whether noise interferes with children's ability to profit from contextual information. The present procedure could be used to investigate this question and others involving the identification of speech in quiet and in noise.

V. CONCLUSIONS

Children 5, 9, and 11 years of age required more favorable SNRs than young adults to achieve comparable accuracy on low-context sentences presented in background babble. Nevertheless, equivalent increases in noise level led to similar performance decrements for all age groups. The findings are consistent with the view that bottom-up (sensory) processing plays the primary role in children's and adults' perception of simple, low-context sentences in noisy backgrounds. The availability of a sensitive means for evaluating children's perception of speech in noise will make it possible to document the impact of noise in situations with varying cognitive demands. In particular, it will allow us to delineate the relative contribution of perceptual and cognitive factors to the identification of spoken messages varying in complexity and listening conditions.

ACKNOWLEDGMENTS

This research was supported by a grant from the Medical Research Council of Canada. We thank Loretta Falco and Michelle Florendo for their assistance in data collection, Kim Yue for technical assistance, and two anonymous reviewers for their valuable comments.

- Berg, K. M., and Smith, M. C. (1983). "Behavioral thresholds for tones during infancy," *J. Exp. Child Psychol.* **35**, 409–425.
- Bilger, R. C., Nuetzel, J. M., Rabinowitz, W. M., and Rzeczkowski, C. (1984). "Standardization of a test of speech perception in noise," *J. Speech Hear. Res.* **27**, 32–48.
- Boothroyd, A., and Nittrouer, S. (1988). "Mathematical treatment of context effects in phoneme and word recognition," *J. Acoust. Soc. Am.* **84**, 101–114.
- Carhart, R., Tillman, T. W., and Greetis, E. S. (1969). "Perceptual masking in multiple sound backgrounds," *J. Acoust. Soc. Am.* **45**, 694–703.
- Chermak, G. D., and Dengerink, J. (1981). "Word identification in quiet and in noise: A re-examination," *Scand. Audiol.* **10**, 55–60.
- Craig, C. H. (1988). "Effect of three conditions of predictability in word-recognition performance," *J. Speech Hear. Res.* **31**, 588–592.
- Elliott, L. L. (1979). "Performance of children aged 9 to 17 years on a test of speech intelligibility in noise using sentence material with controlled word predictability," *J. Acoust. Soc. Am.* **66**, 651–653.
- Elliott, L. L. (1995). "Verbal auditory closure and the Speech Perception in Noise (SPIN) Test," *J. Speech Hear. Res.* **38**, 1363–1376.
- Elliott, L. L., Clifton, A. B., and Servi, D. G. (1983). "Word frequency effects for a closed-set word identification task," *Audiol.* **22**, 229–240.
- Elliott, L. L., Connors, S., Kille, E., Levin, S., Ball, K., and Katz, D. (1979). "Children's understanding of monosyllabic nouns in quiet and in noise," *J. Acoust. Soc. Am.* **66**, 12–21.
- Elliott, L. L., and Katz, D. R. (1980). "Children's pure-tone detection," *J. Acoust. Soc. Am.* **67**, 343–344.
- Gat, I. B., and Keith, R. W. (1978). "An effect of linguistic experience: Auditory word discrimination by native and non-native speakers of English," *Audiol.* **17**, 339–345.
- Geffner, D., Lucker, J. R., and Koch, W. (1996). "Evaluation of auditory discrimination in children with ADD and without ADD," *Child Psychiatry Human Devel.* **26**, 169–180.
- Goldman, R., Fristoe, M., and Woodcock, R. W. (1976). *Test of Auditory Discrimination* (American Guidance Service, Circle Pines, MN).
- Green, D. M., and Swets, J. A. (1966). *Signal Detection Theory and Psychophysics* (Wiley, New York), pp. 317–318.
- Héту, R., Truchon-Gagnon, C., and Bilodeau, S. A. (1990). "Problems of noise in school settings: A review of the literature and the results of an exploratory study," *J. Speech Lang. Pathol. Audiol.* **14**, 31–39.
- Hnath-Chisholm, T. E., Laipply, E., and Boothroyd, A. (1998). "Age-related changes on a children's test of sensory-level speech perception capacity," *J. Speech Lang. Hear. Res.* **41**, 94–106.
- Kalikow, D. N., Stevens, K. N., and Elliott, L. L. (1977). "Development of a test of speech intelligibility in noise using sentence materials with controlled word predictability," *J. Acoust. Soc. Am.* **61**, 1337–1361.
- Lewis, H. D., Benignus, V. A., Muller, K. E., Mallott, C. M., and Barton, C. N. (1988). "Babble and random-noise masking of speech in high and low context cue conditions," *J. Speech Hear. Res.* **31**, 108–114.
- Mayo, L. H., Florentine, M., and Buus, S. (1997). "Age of second-language acquisition and perception of speech in noise," *J. Speech Hear. Res.* **40**, 686–693.
- Miller, G. A., Heise, G. A., and Lichten, W. (1951). "The intelligibility of speech as a function of the context of the test materials," *J. Exp. Psychol.* **41**, 329–335.
- Mills, J. H. (1975). "Noise and children: A review of literature," *J. Acoust. Soc. Am.* **58**, 767–779.
- Nittrouer, S., and Boothroyd, A. (1990). "Context effects in phoneme and word recognition by young children and older adults," *J. Acoust. Soc. Am.* **87**, 2705–2715.
- Pichora-Fuller, M. K., Schneider, B. A., and Daneman, M. (1995). "How young and old adults listen to and remember speech in noise," *J. Acoust. Soc. Am.* **97**, 593–608.
- Roche, A. F., Siervogel, R. M., Himes, J. H., and Johnson, D. L. (1978). "Longitudinal study of hearing in children: Baseline data concerning auditory thresholds, noise exposure, and biological factors," *J. Acoust. Soc. Am.* **64**, 1593–1601.
- Rosenwieg, M., and Postman, L. (1957). "Intelligibility as a function of frequency of usage," *J. Exp. Psychol.* **54**, 412–422.
- Schneider, B. A., Daneman, M., Murphy, D., and Kwong-See, S. (2000). "Listening to discourse in distracting settings: The effects of aging," *Psychol. Aging.* **15**, 110–125.
- Schneider, B. A., and Trehub, S. E. (1992). "Sources of developmental change in auditory sensitivity," in *Developmental Psychoacoustics*, edited by L. A. Werner and E. W. Rubel (APA, Washington, DC), pp. 3–46.
- Schneider, B. A., Trehub, S. E., Morrongiello, B. A., and Thorpe, L. A. (1986). "Auditory sensitivity in preschool children," *J. Acoust. Soc. Am.* **79**, 447–452.
- Schneider, B. A., Trehub, S. E., Morrongiello, B. A., and Thorpe, L. A. (1989). "Developmental changes in masked thresholds," *J. Acoust. Soc. Am.* **86**, 1733–1742.
- Sinnott, J., Pisoni, D., and Aslin, R. (1983). "A comparison of pure tone auditory thresholds in human infants and adults," *Infant Behav. Dev.* **6**, 3–18.
- Smith, K. E., and Hodgson, W. R. (1970). "The effects of systematic reinforcement on the speech discrimination responses of normal and hearing-impaired children," *J. Audiol. Res.* **10**, 110–117.
- Snodgrass, J. G., and Vanderwart, M. (1980). "A standardized set of 260 pictures: Norms for name agreement, image agreement, familiarity, and visual complexity," *J. Exp. Psychol Human Learn. Mem.* **6**, 174–215.
- Sumby, W. H., and Pollack, I. (1954). "Visual contribution to speech intelligibility in noise," *J. Acoust. Soc. Am.* **26**, 212–215.
- Summerfield, Q., Palmer, A. R., Foster, J. R., Marshall, D. H., and Twomey, T. (1994). "Clinical evaluation and test-retest reliability of the IHR-McCormick Automated Toy Discrimination Test," *Br. J. Audiol.* **28**, 165–179.
- Trehub, S. E., Schneider, B. A., Morrongiello, B. A., and Thorpe, L. A. (1988). "Auditory sensitivity in school-age children," *J. Exp. Child Psychol.* **46**, 273–285.
- Treiman, R. (1985). "Phonemic awareness and spelling: Children's judgments do not always agree with adults," *J. Exp. Child Psychol.* **39**, 182–201.
- Wightman, F., and Allen, P. (1992). "Individual differences in auditory capability among preschool children," in *Developmental Psychoacoustics*, edited by L. A. Werner and E. W. Rubel (APA, Washington, DC), pp. 113–133.
- Wimmer, H., Landerl, K., Linortner, R., and Hummer, P. (1991). "The relationship of phonemic awareness to reading acquisition: More consequence than precondition but still important," *Cognition* **40**, 219–249.
- Yoneshige, Y., and Elliott, L. L. (1981). "Pure-tone sensitivity and ear canal pressure at threshold in children and adults," *J. Acoust. Soc. Am.* **70**, 1272–1276.

Relationship between N1 evoked potential morphology and the perception of voicing

Anu Sharma,^{a)} Catherine M. Marsh, and Michael F. Dorman

Department of Speech and Hearing Science, Arizona State University, Tempe, Arizona 85287-0102

(Received 12 July 1999; accepted for publication 22 August 2000)

Auditory evoked potential (AEP) correlates of the neural representation of stimuli along a /ga/–/ka/ and a /ba/–/pa/ continuum were examined to determine whether the voice-onset time (VOT)-related change in the N1 onset response from a single to double-peaked component is a reliable indicator of the perception of voiced and voiceless sounds. Behavioral identification results from ten subjects revealed a mean category boundary at a VOT of 46 ms for the /ga/–/ka/ continuum and at a VOT of 27.5 ms for the /ba/–/pa/ continuum. In the same subjects, electrophysiologic recordings revealed that a single N1 component was seen for stimuli with VOTs of 30 ms and less, and two components (N1' and N1) were seen for stimuli with VOTs of 40 ms and more for both continua. That is, the change in N1 morphology (from single to double-peaked) coincided with the change in perception from voiced to voiceless for stimuli from the /ba/–/pa/ continuum, but not for stimuli from the /ga/–/ka/ continuum. The results of this study show that N1 morphology does not reliably predict phonetic identification of stimuli varying in VOT. These findings also suggest that the previously reported appearance of a “double-peak” onset response in aggregate recordings from the auditory cortex does not indicate a cortical correlate of the perception of voicelessness. © 2000 Acoustical Society of America. [S0001-4966(00)00512-9]

PACS numbers: 43.71.Pc, 43.71.An, 43.64.Qh [CWT]

I. INTRODUCTION

The aim of the research reported here was to examine the relationship between the morphology of the N1 component of the cortical auditory evoked potential (AEP) and the perception of the voicing contrast in syllable initial position. In a previous study (Sharma and Dorman, 1999), we recorded behavioral responses and AEPs in response to stimuli along a synthesized /da/–/ta/ continuum in which the voice-onset time (VOT) of the syllables varied from 0 to 80 ms. The results of the behavioral experiment revealed, as expected, a sharp category boundary between /da/ and /ta/ around the same VOT for all listeners. The results of the electrophysiologic experiment showed two distinct onset responses (N1' and N1) of the AEP that behaved differently in response to VOT. Based on the latencies of the two components, Sharma and Dorman (1999) concluded that the first component (N1') occurred in response to the burst at the beginning of each syllable and that the second component (N1) occurred in response to voicing onset. Of particular interest was their finding that for sounds with a short lag in voicing (perceived as /da/) only a single component (N1) was seen, while for sounds with longer VOTs (perceived as /ta/) two distinct components (N1' and N1) were observed in the AEP waveform. That is, in Sharma and Dorman's study the physiologic discontinuity in N1 morphology coincided with the change in perception from /da/ to /ta/ across the category boundary.

Sharma and Dorman's (1999) findings were consistent with some earlier human and animal work which had also examined VOT encoding in the auditory cortex. For ex-

ample, Steinscheider *et al.* (1995) and McGee *et al.* (1996), who examined evoked responses from the auditory cortex of awake moneys and guinea pigs, respectively, and Steinscheider *et al.* (1999), who examined intracortical evoked responses in humans, reported that voiced syllables and syllables with short VOTs elicited a “single-onset” response in the AEP waveform, and that a robust “double-onset” response was observed only for sounds with longer VOTs (i.e., sounds that are typically perceived as voiceless by human listeners).

In all these studies, the appearance of a clearly apparent double-peaked onset response in the AEP waveform coincided with a stimulus identified as voiceless. Therefore, it is possible that the change in N1 from a single to double-peaked component actually *predicts* a change in perception of phonetic categories. If this were the case, then the N1 might provide a clinically useful technique to measure VOT perception. Towards this end, we examined N1 correlates of neural representation of VOT in a /ba/–/pa/ and /ka/–/ga/ stimulus continuum to determine whether the appearance of VOT-related changes in the N1 waveform is a reliable indicator of perceptual identification of voiced and voiceless sounds. The /ba/–/pa/ and /ga/–/ka/ continua were chosen because the voicing boundaries differ for the two continua.

II. BEHAVIORAL EXPERIMENT

A. Method

1. Subjects

Five females and five males ranging in age from 20–30 years with a mean age of 25 years were paid \$5/h to partici-

^{a)}Electronic mail: anu.sharma@asu.edu

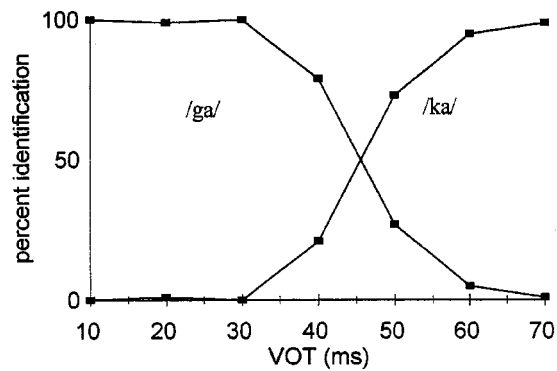


FIG. 1. Mean identification functions for the /ga/-/ka/ continuum. Stimuli with VOTs of 0–30 ms were identified as /ga/, while stimuli with VOTs of 60–70 ms were identified as /ka/. The category boundary between /ga/ and /ka/ was at a VOT of 46 ms.

pate as subjects. All subjects were monolingual native speakers of American English who reported no history of speech or hearing disorders.

2. Stimuli

Two sets of continua of CV speech sounds varying in VOT were generated using the Klatt (1980) speech synthesizer. One continuum consisted of seven tokens varying perceptually from /ga/ to /ka/ and the other continuum consisted of six tokens varying perceptually from /ba/ to /pa/. In each syllable, a brief burst of friction noise was present at syllable onset and from syllable onset to $F1$ onset the higher formants were excited using aspiration noise. For the /ga/-/ka/ continuum, the aspirated interval corresponded to VOT which was varied from 0–70 ms. The center frequency of $F1$ was 310 Hz for the first 10 ms and increased to its steady-state value of 521 Hz at 60 ms. $F2$ decreased from 1920 to 1568 Hz over a 50-ms transition duration and $F3$ remained at 2500 Hz throughout the syllable. For the /ba/-/pa/ continuum, the aspirated interval corresponded to VOT which was varied from 0–60 ms. The center frequency of $F1$ was 435 Hz for the first 10 ms of the syllable and increased to its steady-state value of 650 Hz at 40 ms. $F2$ increased from 1250 to 1490 Hz over a 40-ms transition duration and $F3$ increased from 2300 to 2470 Hz over a 50-ms transition

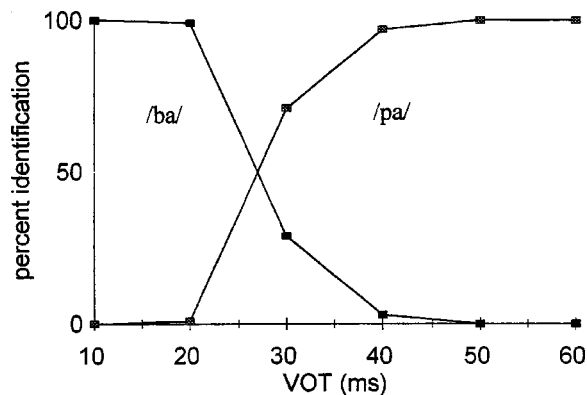


FIG. 2. Mean identification functions for the /ba/-/pa/ continuum. Stimuli with VOTs of 0–20 ms were identified as /ba/, while stimuli with VOTs of 40–60 ms were identified as /pa/. The category boundary between /ba/ and /pa/ lay at a VOT of 27.5.

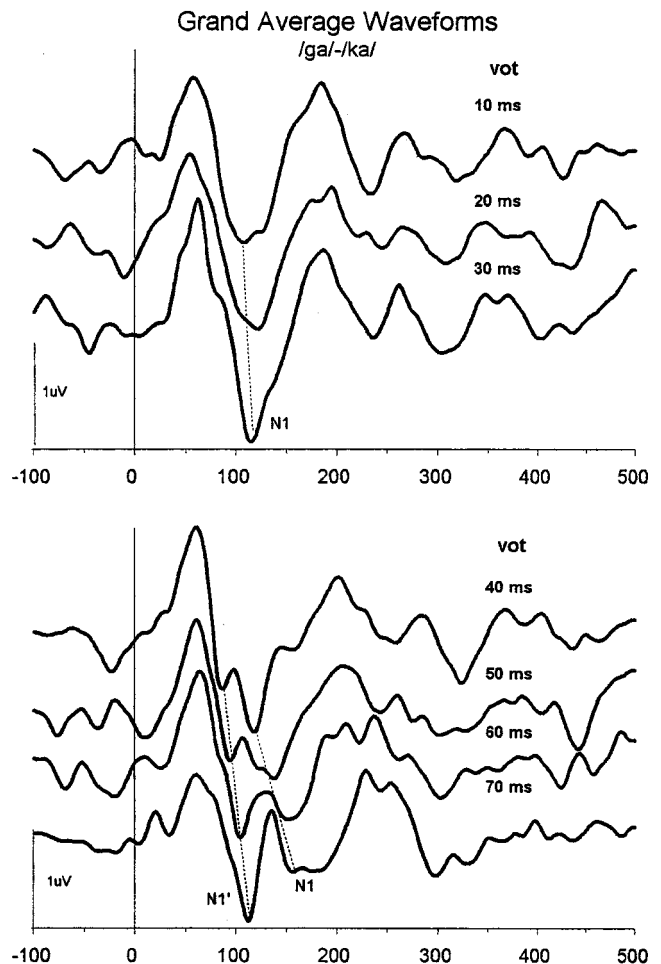


FIG. 3. Grand-averaged $N1$ responses elicited by stimuli in the /ga/-/ka/ continuum. Responses to stimuli with VOTs of 30 ms or less showed a single negativity ($N1$) indicated by the dashed line. Responses to stimuli with VOTs of 40 ms or more showed two distinct negative components ($N1'$ and $N1$) indicated by dashed lines.

duration. In both continua, the overall duration of each syllable was 200 ms. Stimuli were equated in intensity within 1 dB of each other and were presented to subjects at 75 dB SPL binaurally over headphones.

3. Procedure

Subjects performed a two-choice identification experiment with the stimuli from each stimulus continuum. That is, subjects were asked to listen to the syllables and classify them as either /ba/, /pa/ or /ga/, /ka/. Subjects were asked to indicate their responses by clicking with a computer mouse on panels marked BA, PA, GA, and KA appearing on the computer screen. Subjects were given an initial practice session where they heard every stimulus from each continuum once in order. After the practice session, ten repetitions of each stimulus in a continuum were presented to the subject in random order. The order of presentation of the /ga/-/ka/ and /ba/-/pa/ stimulus continua was randomized across subjects.

B. Results

Responses to each of the 13 tokens in the two continua were collapsed across subjects. The group means for each

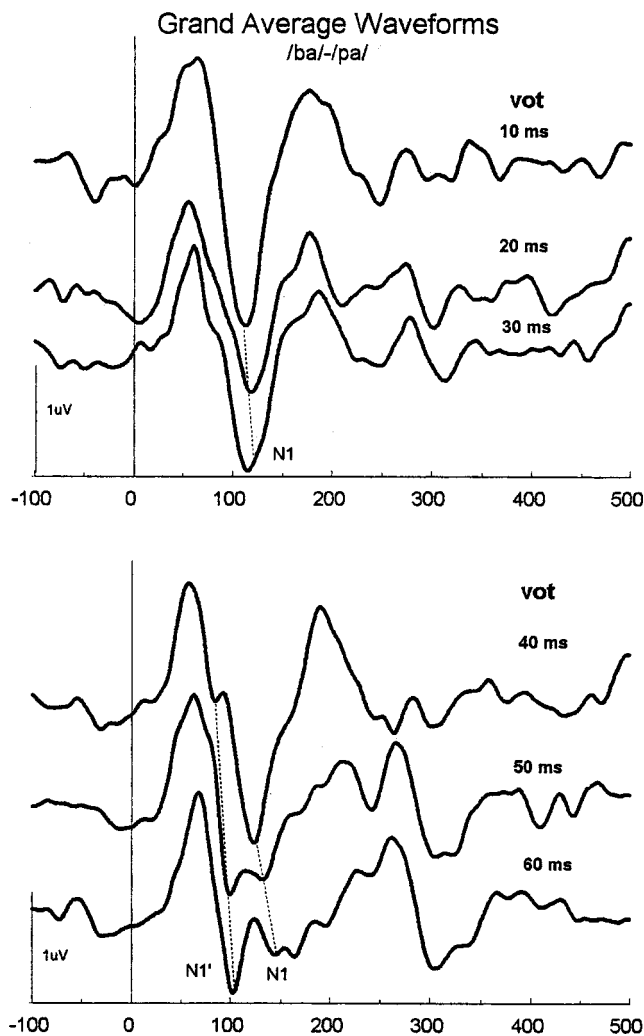


FIG. 4. Grand-averaged *N1* responses elicited by stimuli in the /ba/-/pa/ continuum. Responses to stimuli with VOTs of 30 ms or less showed a single negativity (*N1*) indicated by the dashed line. Responses to stimuli with VOTs of 40 ms or more showed two distinct negative components (*N1'* and *N1*) indicated by dashed lines.

token are shown in Fig. 1 for /ga/-/ka/ and Fig. 2 for /ba/-/pa/. As can be seen in Fig. 1, for the /ga/-/ka/ continuum, stimuli with VOT of 0–30 ms were consistently identified as /ga/ while stimuli with VOT of 60–70 ms were consistently identified as /ka/. The boundary (i.e., the 50% identification point) between the /ga/-/ka/ categories occurred at a VOT of 46 ms. As can be seen in Fig. 2, for the /ba/-/pa/ continuum, stimuli with VOT of 0–20 ms were consistently identified as /ba/ while stimuli with VOT of 40–60 ms were consistently identified as /pa/. The boundary (i.e., the 50% identification point) between the /ba/-/pa/ categories occurred at a VOT of 27.5 ms.

III. ELECTROPHYSIOLOGIC EXPERIMENT

A. Methods

1. Subjects

Electrophysiologic recordings were obtained in the same ten subjects who performed in the behavioral experiment.

N1 /ga/-/ka/

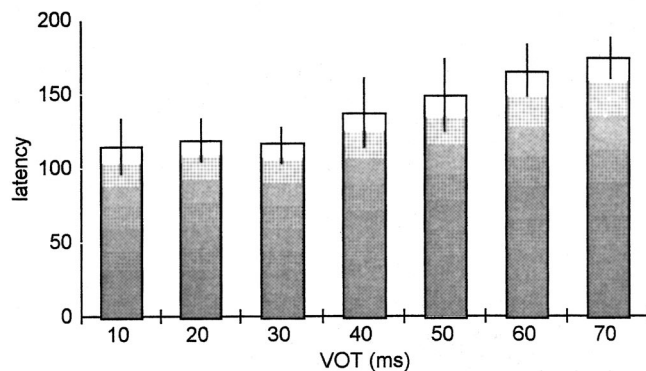


FIG. 5. Mean *N1* response latency values for the /ga/-/ka/ continuum. Error bars indicate ± 1 standard deviation.

2. Stimuli

The /ga/-/ka/ and /ba/-/pa/ stimulus continua were identical to those used in the behavioral identification experiment. Repeated presentations of each stimulus separated by an onset-to-offset interstimulus interval (ISI) of 800 ms were used to elicit the *N1*. The order of presentation of stimuli was counterbalanced across subjects.

3. Recording procedures

During *N1* recordings, subjects were seated comfortably in a sound-treated booth. To control for arousal state and to minimize their attention to the test stimuli, subjects watched a videotaped movie of their choice. Subjects were asked to ignore the stimuli that were presented through an insert earphone at 75 dB SPL in the right ear. Videotape audio levels were kept below 40 dB SPL.

A Neuroscan Inc. data acquisition system was utilized to record the auditory evoked potentials. Silver-chloride electrodes were placed on the scalp at midline (Fz, Cz, and Pz) locations. A reference electrode was placed on the right mastoid and a ground electrode was positioned on the forehead. Eye movements were monitored with a bipolar electrode montage (supraorbital to lateral canthus). Averaging was suspended when the eye channel recorded blinks. The recording window included a 100-ms prestimulus period and 500-ms poststimulus time. Evoked responses were recorded in response to each stimulus; 250–300 sweeps analog filtered on-line from 0.1 to 100 Hz were collected. The digitization rate was 2 kHz. Total testing time for each subject was approximately 2 h and breaks were provided to subjects as necessary.

4. Data analysis

For individual subjects, sweeps were corrected to the average baseline, and sweeps that were greater than ± 100 microvolts were automatically rejected. Sweeps were then averaged to compute an individual averaged waveform. Waveforms were digitally high-pass filtered off-line at 4 Hz (filter slope 12 dB/octave).

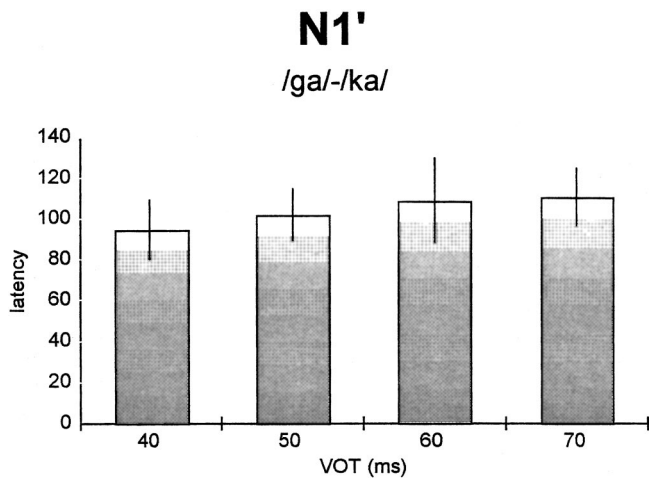


FIG. 6. Mean $N1'$ response latency values for the /ga/-/ka/ continuum. Error bars indicate ± 1 standard deviation.

Response windows were defined around the peak or peaks in the group mean waveforms to aid in peak identification and measurement in data from individual subjects. The time frame was defined as 0–200 ms when one $N1$ component was present. When it was determined that two $N1$ components were present in the grand average waveform, the time window was defined as 0–120 ms for the first ($N1'$) component and 120–200 ms for the second ($N1$) component. Peak latencies were detected based on the recordings from the Cz electrode site because the response amplitudes were the largest at this site in the group mean waveforms. $N1$ and $N1'$ amplitudes were measured relative to preceding positive peak. The author (CM) who marked the $N1$ and $N1'$ latencies and amplitudes was unaware of the eliciting stimulus continuum or stimulus number. Finally, group-averaged waveforms were computed by averaging across the individual average waveforms for the appropriate stimulus condition. Group-averaged waveforms were low-pass filtered at 40 Hz (12 dB/octave) to smooth the waves for the final figures.

B. Results

Grand average waveforms elicited in response to stimuli from the /ga/-/ka/ continuum and in response to stimuli from the /ba/-/pa/ continuum are shown in Fig. 3 and Fig. 4, respectively. Distinct morphological changes related to encoding of VOT are seen in the AEP waveforms. For both the /ga/-/ka/ and the /ba/-/pa/ continua, stimuli with short VOTs (0–30 ms) elicited a single negativity. However, in response to stimuli with long VOTs (40–70 ms) two negative components ($N1'$ and $N1$) were apparent in the AEP waveform.

1. Latency

Mean latency values for the $N1$ and $N1'$ components are shown in Fig. 5 and Fig. 6, respectively, for the /ga/-/ka/ continuum. For the /ga/-/ka/ continuum, a one-way repeated-measures analysis of variance (ANOVA), which revealed a significant main effect of VOT ($F=28$, $p < 0.000001$) on $N1$ latencies. Correlation analysis revealed a significant positive correlation between $N1$ latency and

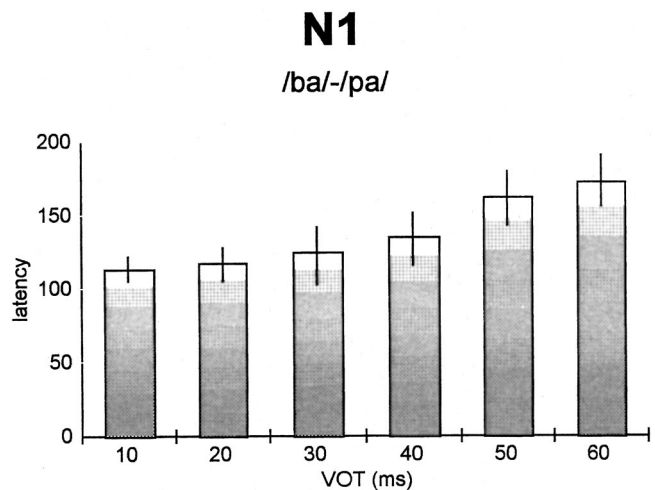


FIG. 7. Mean $N1$ response latency values for the /ba/-/pa/ continuum. Error bars indicate ± 1 standard deviation.

VOT ($r=0.77$, $p < 0.0001$). For the $N1'$ component (Fig. 6), a one-way repeated measures ANOVA did not demonstrate a main effect for VOT ($F=3.73$, $p > 0.01$).

Mean latency values for the $N1$ and $N1'$ components for the /ba/-/pa/ continuum are shown in Fig. 7 and Fig. 8, respectively. For the /ba/-/pa/ continuum, a one-way repeated measures ANOVA was performed which revealed a significant main effect of VOT and $N1$ ($F=43.8$, $p < 0.000001$). Furthermore, a correlation analysis revealed that the $N1$ latency was significantly positively correlated with VOT ($r=0.82$, $p < 0.0001$). For the $N1'$ component (Fig. 8) a one-way repeated measures ANOVA did not demonstrate a main effect for VOT ($F=3.32$, $p > 0.01$).

2. Amplitude

For the /ba/-/pa/ continuum, a repeated measures ANOVA for $N1$ amplitude revealed a significant main effect of VOT ($F=13$, $p < 0.00001$). A correlation analysis revealed that the $N1$ amplitude was significantly negatively

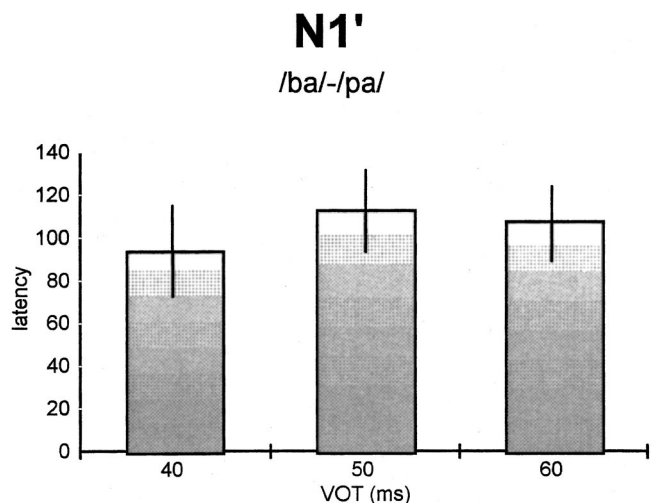


FIG. 8. Mean $N1'$ response latency values for the /ba/-/pa/ continuum. Error bars indicate ± 1 standard deviation.

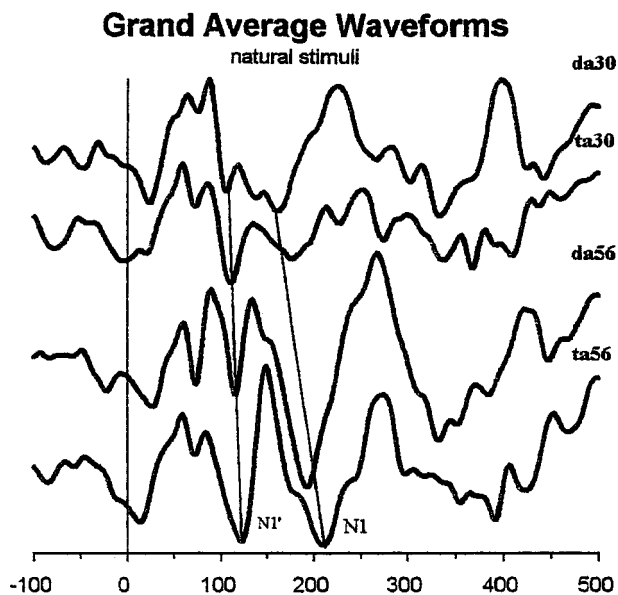


FIG. 9. Mean responses elicited by natural speech stimuli with VOTs of 30 and 56 ms which were perceived as /da/ and /ta/, respectively. Responses to all stimuli show two negative components ($N1'$ and $N1$).

correlated with VOT ($r=0.59$, $p<0.0001$). A one-way repeated measures ANOVA for $N1'$ amplitude did not show a main effect of VOT ($F=1$, $p>0.05$).

For the /ga/-ka/ continuum, a repeated measures ANOVA for $N1$ amplitude revealed a significant main effect of VOT ($F=15.4$, $p<0.0000001$). A correlation analysis revealed that the $N1$ amplitude was significantly negatively correlated with VOT ($r=0.59$, $p<0.0001$). A repeated measures ANOVA for $N1'$ amplitude did not show a main effect of VOT ($F=0.9$, $p>0.05$).

To summarize the results of the electrophysiologic experiment, a double-peaked $N1$ response was observed for stimuli with 40-ms VOT in both the /ga/-ka/ and the /ba/-pa/ continua. As pointed out in the stimulus description section, each stimulus in the two continua began with a brief burst and frication noise. For both continua, given the time frame of the $N1'$ peak latency and given that the latency did not show a significant correlation with VOT, it would appear that the $N1'$ component occurred in response to the burst at syllable onset. Taking into consideration the time frame of the peak latency of the $N1$ component and its significant positive correlation with VOT, it appears that this component occurs in response to the onset of voicing in the syllables.

With respect to the amplitude data, since the burst at syllable onset was identical for stimuli from within a continuum, the amplitude of the component which occurred in response to the burst (i.e., $N1'$) was not significantly different for stimuli from within both continua. However, as the duration between the burst and the onset of voicing increased, the response to the burst became more distinct to visual inspection, and the amplitude of the second component which occurred in response to voicing onset (i.e., $N1$) decreased. These results for the amplitude data are consistent with those of Steinschneider *et al.* (1999) and Simos *et al.* (1998), who have reported that the amplitude of AEP responses elicited by stimuli with long VOTs (i.e., 40, 60, and

80 ms) were significantly smaller than the amplitude of AEP responses elicited by stimuli with short VOTs (i.e., 0 and 20 ms). Overall, results from the present study are consistent with those of Sharma and Dorman (1999), who described similar $N1'$ and $N1$ components in the AEP waveform in response to stimuli varying in VOT across a /da/-/ta/ continuum.

IV. GENERAL DISCUSSION

In the case of the /ba/-/pa/ stimulus continuum, the results of the behavioral experiment revealed that listeners' perception of a change in phonetic categories from voiced to voiceless occurred reliably at a VOT of 40 ms (Fig. 2). The results of the electrophysiologic experiment for the same continuum showed that the change in the AEP waveform morphology from a single to double-peaked $N1$ component also occurred at a VOT of 40 ms (Fig. 4). These results are consistent with those from an earlier study (Sharma and Dorman, 1999), in which we found that the change in $N1$ morphology from single to double-peaked coincided with a change in perception from voiced to voiceless for a /da/-/ta/ continuum. On the other hand, in the present study, for the /ga/-/ka/ stimulus continuum, listeners' behavioral perception of a change in phonetic categories occurred reliably at a VOT of 60 ms (Fig. 1). As seen in Fig. 4, the change in $N1$ morphology from single- to double-peaked occurred at a VOT of 40 ms. That is, in the case of the /ga/-/ka/ continuum, the change in $N1$ morphology to a double-peaked component did not signal behavioral perception of a voiceless sound. Therefore, the results of the present study demonstrate that $N1$ morphology is not a reliable indicator of perception of voicing contrasts in syllable-initial position.

The data were also analyzed with respect to the correspondence between individual boundaries and individual changes in $N1$ morphology. For each subject, for each continuum, the individual VOT boundary was determined (the 50% identification point). We then determined for individual subjects the postboundary stimulus that was perceived as voiceless greater than 75% of the time. Finally, we noted for individual subjects if the $N1$ morphology changed from a single-peaked to a double-peaked response at this stimulus (i.e., the stimulus identified greater than 75% as voiceless). For the /ba/-/pa/ continuum, there was a correspondence between perceptual boundaries and changes in $N1$ morphology for 6 of 11 subjects. For the /ga/-/ka/ continuum, however, there was no correspondence for any subject. Therefore, the individual data conform to the overall findings for the group that the change in $N1$ from single- to double-peaked responses is not a reliable indicator of the perception of voiced and voiceless sounds.

Examination of the grand average waveforms for the two continua in Figs. 3 and 4, indicates that the two components (i.e., $N1'$ and $N1$) are fused in the AEP waveform at short VOTs and that a minimum temporal separation of 40 ms between the burst and voicing onset is required for the two components to be seen discretely in the temporal waveform. As stated above, our results with the synthesized speech continua show that the minimum VOT value (i.e., 40 ms) required for this temporal separation of $N1$ components

is dependent on acoustic properties of the stimulus rather than the perceptual categorization of the stimulus. In a subsequent experiment we confirmed this result using natural speech stimuli (Marsh, 1999). In that study, a /da/ and a /ta/ syllable (with VOTs of 30 and 56 ms, respectively) were recorded by a male speaker. Then, 26 ms of silence was added to the /da/ syllable (between the burst and onset of voicing) to create a new /da/ syllable with a VOT of 56 ms, and 26 ms of aspiration was removed from the /ta/ syllable to create a new /ta/ syllable with a VOT of 30 ms. Behavioral measurements in ten subjects revealed that subjects identified both the /da/ with a 30-ms VOT and the /da/ with a 56-ms VOT as /da/ and identified both the /ta/ with a 56-ms VOT and the /ta/ with a 30-ms VOT as /ta/. *N1* recordings in the same ten subjects (see Fig. 9) revealed that all four stimuli elicited double-peaked *N1* responses (albeit, not with identical morphology). Thus, the presence of a double-peaked *N1* component was independent of the phonetic categorization of the stimulus.

Yet another recent study confirms this outcome. Sharma and Dorman (2000) explored the changes in *N1* latency and morphology which are correlated with changes in VOT ranging from 0 to -90 ms across a prevoiced /ba/-/pa/ continuum. The results of a labeling experiment revealed, as expected, that the sounds along the continuum could be grouped into two categories (/ba/ and /pa/) by Hindi listeners but only into a single category (/ba/) by English listeners. However, *N1* responses were observed to change from single to double peaked at approximately 70 ms of prevoicing for both English listeners and Hindi listeners. Furthermore, the latencies of the *N1* components were not significantly different for the two groups of listeners. Thus, changes in *N1* waveform morphology and latency were independent of phonetic categorization of voicing.

Taken together, the results from the present study, Marsh (1999) and Sharma and Dorman (1999, 2000) suggest that the appearance of the double-peaked *N1* is influenced by multiple stimulus properties, including VOT, burst duration, amplitude of aspiration, and height of *F1*. More studies are

needed to systematically examine the effects of these and other acoustic properties of voicing on the morphology and the topography of the AEP waveform. The present study which examined evoked responses only from the scalp midline shows neither the presence of a double-peaked *N1* response, nor that the latency and amplitude of this response are related to the phonetic categorization of voicing. It is possible that recordings made at other scalp recordings or at intracortical locations may show a different relationship between *N1* morphology and phonetic categorization. In addition, it is possible that a different relationship will be found in children or adults learning phonetic categories.

In conclusion, our results show that a “double-peak” onset response as reported in recordings from the auditory cortex (e.g., Steinschneider *et al.*, 1995, 1999; Eggermont, 1995; McGee *et al.*, 1996, and Sharma and Dorman, 1999) is not a cortical correlate of the perception of voicelessness.

- Eggermont, J. (1995). “Representation of a voice onset time continuum in the primary auditory cortex of the cat,” *J. Acoust. Soc. Am.* **98**, 911–920.
- Klatt, D. (1980). “Software for cascade/parallel formant synthesizer,” *J. Acoust. Soc. Am.* **67**, 971–995.
- Marsh, C. M. (1999). “Cortical Auditory Evoked Potential Correlates of VOT,” Masters thesis, Arizona State University.
- McGee, T., Kraus, N., King, C., and Nicol, T. (1996). “Acoustic elements of speechlike stimuli are reflected in surface recorded responses over the guinea pig temporal lobe,” *J. Acoust. Soc. Am.* **99**, 3606–3614.
- Sharma, A., and Dorman, M. (1999). “Cortical auditory evoked potential correlates of categorical perception of voice-onset time,” *J. Acoust. Soc. Am.* **106**, 1078–1083.
- Sharma, A., and Dorman, M. (2000). “Neurophysiologic correlates of cross-language phonetic perception,” *J. Acoust. Soc. Am.* **107**, 2697–2703.
- Simos, P. G., Diehl, R. L., Breier, J. L., Molis, M. R., Zouridakis, G., and Papanicolaou, G. (1998). “MEG correlates of categorical perception of a voice onset time continuum in humans,” *Brain Res. Cognit. Brain Res.* **7**, 215–219.
- Steinschneider, M., Schroeder, C., Arezzo, J., and Vaughan, H. (1995). “Physiologic correlates of the voice onset time boundary in primary auditory cortex (A1) of the awake monkey: Temporal response patterns,” *Brain Lang* **48**, 326–340.
- Steinschneider, M., Volkov, I., Noh, D., Garell, P., and Howard, M. (1999). “Temporal encoding of voice onset time phonetic parameter by field potentials recorded directly from the human auditory cortex,” *J. Neurophysiol.* **82**(5), 2346–2357.

Spontaneous speech recognition using a statistical coarticulatory model for the vocal-tract-resonance dynamics

Li Deng^{a)} and Jeff Ma

Department of Electrical and Computer Engineering, University of Waterloo, Waterloo, Ontario N2L 3G1, Canada

(Received 9 September 1999; revised 20 June 2000; accepted 7 August 2000)

A statistical coarticulatory model is presented for spontaneous speech recognition, where knowledge of the dynamic, target-directed behavior in the vocal tract resonance is incorporated into the model design, training, and in likelihood computation. The principal advantage of the new model over the conventional HMM is the use of a compact, internal structure that parsimoniously represents long-span context dependence in the observable domain of speech acoustics without using additional, context-dependent model parameters. The new model is formulated mathematically as a constrained, nonstationary, and nonlinear dynamic system, for which a version of the generalized EM algorithm is developed and implemented for automatically learning the compact set of model parameters. A series of experiments for speech recognition and model synthesis using spontaneous speech data from the Switchboard corpus are reported. The promise of the new model is demonstrated by showing its consistently superior performance over a state-of-the-art benchmark HMM system under controlled experimental conditions. Experiments on model synthesis and analysis shed insight into the mechanism underlying such superiority in terms of the target-directed behavior and of the long-span context-dependence property, both inherent in the designed structure of the new dynamic model of speech. © 2000 Acoustical Society of America.

[S0001-4966(00)02911-8]

PACS numbers: 43.72.-p [DOS]

I. INTRODUCTION

Speech recognition technology has achieved significant success using complex models with their parameters automatically trained from large amounts of data.¹ The success based on such an approach, however, has not been extended to spontaneous speech, which exhibits a much greater degree of variability than the less natural speech style for which the current technology has been successful. For the Switchboard spontaneous speech recognition task, even with use of hundreds of hours of speech as training data, the state-of-the-art, hidden Markov model (HMM)-based recognizers still produce more than one-third of errors in the recognized words.² In order to capture the overwhelming variability in spontaneous, conversational speech, it appears necessary to explore some underlying structure in the speech patterns. The fundamental nature of the current acoustic modeling strategy used in the current technology is such that it explores only the surface-level observation data and not their internal structure or generative mechanisms. Because the variability in spontaneous speech is continuously scaled (rather than discretely scaled), an infinite amount of surface-level data would be required, at least in theory, to completely cover such variability without using structural information.

The research reported in this article represents our recent efforts in developing structural models for dynamic patterns of spontaneous speech. The goal of this research is to overcome the inadequacy of the current speech recognition tech-

nology in accounting for the acoustic variability in spontaneous speech, which has been based on ever-expanding the myriad Gaussian mixture components and HMM states in a largely unstructured manner. (This has a small number of exceptions; e.g., Ref. 3.) A particular model we have developed for this purpose describes the long-term (utterance-length) context-dependent or coarticulatory effects in spontaneous speech in the domain of partially hidden vocal-tract-resonance (VTR). The VTR domain is internal to the domain of surface acoustic observation (such as Mel-frequency cepstral coefficients or MFCCs). This coarticulation modeling is accomplished via two separate but related mechanisms. First, the mechanism of duration-dependent *phonetic reduction* allows the VTR variables and the associated surface acoustic variables to be modified automatically according to the varying speech rate and hence the duration of the speech units (e.g., phones). This modification is physically established according to the structured dynamics assigned to the VTR variables in the model. Second, the “*continuity*” mechanism at the utterance level employed in the model constrains the VTR variables so that they flow smoothly from one segmental unit to another. Since this continuity constraint is global (i.e., temporally across an entire utterance), long-span coarticulation is accomplished without the need to use explicit context-dependent units such as triphones. (Use of triphone units is a main factor contributing to the success of current speech recognition technology for read-style speech, but at the expense of requiring unreasonable amounts of training data for the recognizers’ very large number of free parameters. This aspect of the weakness is completely eliminated by the coarticulatory model described in this article.) As a

^{a)}Current address: Microsoft Research, One Microsoft Way, Redmond, WA 98052. Electronic mail: deng@microsoft.com

result, the number of free parameters for the recognizer and the amount of data required for training the recognizer are drastically reduced compared with the conventional HMM-based speech recognizers

The organization of this article is as follows. In Sec. II, a detailed description of our new VTR-based statistical coarticulatory model will be provided. The learning algorithm we have developed for training the model parameters and a scoring algorithm will be presented in Sec. III. A series of experiments conducted for analysis, synthesis, and recognition of Switchboard spontaneous speech using the new coarticulatory model will be reported in Sec. IV. These will include detailed examinations of the model behavior in fitting the Switchboard data and of the quality of the spontaneous speech artificially generated from the model. They also include some small-scale N -best rescoring experiments used to diagnose the cause and nature of the recognition errors, as well as some large-scale N -best rescoring experiments, which provide the performance figures of the new recognizer.

II. A STATISTICAL COARTICULATORY MODEL

In this section, we provide a detailed account of the new speech model we have developed, including the motivation for the model development, the mathematical formulation of the model, and comparisons of the new model with other types of speech models used in the past.

A. Background, motivation, and model overview

The statistical coarticulatory model presented in this article is a drastic departure from the conventional HMM-based approach to speech recognition. In the conventional approach, the variability in observed speech acoustics is accounted for by a large number of Gaussian distributions, each of which may be indexed by a discrete “context” factor. The discrete nature of encoding the contextual (or coarticulatory) effect on speech variability leads to explosive growth of free parameters in the recognizers, and when the true source of the variability originates from causes of a continuous nature (such as in spontaneous speech), this approach necessarily breaks down. In contrast, the new approach we have developed focuses directly on the continuous nature of speech coarticulation and speech variability in spontaneous speech. In particular, the phonetic reduction phenomenon is explicitly modeled by a statistical dynamic system in the domain of the VTR, which is internal to, or hidden from, the observable speech acoustics. In this dynamic model, the system matrix (encompassing the concept of time constants) is structured and constrained to ensure the asymptotic behavior in the VTR dynamics within each speech segment. [In the work reported in this article, we take speech segments as phones defined in the HMM systems on Switchboard tasks as used in the 1997 Workshop on Innovative Techniques for Large Vocabulary Conversational Speech Recognition (http://www.clsp.jhu.edu/ws97/ws97_general.html).] Across speech segments in a speech utterance, a smoothness or continuity constraint is imposed on the VTR variables. The main consequence of this constraint is that the interacting factors of phonetic context, speaking rate, and segment duration at

any local temporal region are in combination exerting their influences on the VTR variable values (and hence the acoustic observations as a noisy nonlinear functions of the VTR values) anywhere in the utterance. This gives rise to the property of long-term context dependence in the model without requiring use of context dependent speech units.

Some background work, which leads to the development of this particular version of the model (i.e., with use of VTRs as the partially hidden dynamic states), has been the extensive studies of spontaneous speech spectrograms and of the associated speech production mechanisms. The spectrographic studies on spontaneous speech have highlighted the critical roles of smooth, goal-directed formant transitions (in vocalic segments, including vowels, glides, and liquids) in carrying underlying phonetic information in the adjacent consonantal and vocalic segments. The smoothness in formant movements (for vocalic sounds) and in VTR movements (for practically all speech sounds) reflects the dynamic behavior of the articulatory structure in speech production. The smoothness is not only confined within phonetic units but also across them. This cross-unit smoothness or continuity in the VTR domain becomes apparent after one learns to identify, by extrapolation, the “hidden” VTRs associated with most consonants, where the VTRs in spectrograms are either masked or distorted by spectral zeros, wide formant bandwidths, or by acoustic turbulences. The properties of the dynamic behavior change in a systematic manner as a function of speaking style and speaking rate, and the contextual variations of phonetic units are linked with the speaking style and rate variations in a highly predictable way.

The VTRs are pole locations of the vocal tract configured to produce speech sounds. They have acoustic correlates of formants which are directly measurable for vocalic sounds, but often are hidden or perturbed for consonantal sounds due to the concurrent spectral zeros and turbulence noises. Hence, formants and VTRs are related but distinct concepts: the former is defined in the acoustic domain and the latter is associated with the vocal-tract properties *per se*. According to the goal-based speech production theory, articulatory structure and the associated VTRs necessarily manifest asymptotic behavior in their temporally smooth dynamics. This dynamic component of the overall speech model for the goal-directed and temporally smooth properties of the VTRs is called the (continuous) “state” model.

Since the temporal dynamics in the VTR variables is distorted, or hidden, in the observable acoustic signal, the overall speech-generative model needs to account for the physical, “quantal” nature of the distortion.⁴ This component of the model is called the “observation” model. In the current implementation of the model, the “observation” model for the distortion is constructed functionally by a static nonlinear function, implemented by artificial neural networks, mapping from the underlying VTRs to acoustic observations (MFCCs in the current system). Since the same VTRs may produce drastically different MFCCs depending on whether the VTR(s) are hidden by spectral zero(s) or other factors, separate networks are used for distinct classes of speech sounds where each class corresponds to similar VTR-to-MFCC mappings. For example, the effects of nasal

coupling are represented by a neural network separate from all other non-nasal speech sounds. Note that this static nonlinear function is clearly separated from the smooth-dynamic model describing the temporal asymptotic behavior for the underlying, hidden VTR dynamic variables. This separation makes it unnecessary, at least in principle, to extract formants from the speech signal in implementing the recognizer. But when formant information is made available with reliability indicator, this information can be and has been effectively used to initialize the model's continuous "states" for the vocalic segments, and has been used in the overall statistical structure (separate static nonlinear and dynamic linear components) of the model to facilitate model parameter learning. For example, to diagnose the accuracy of the state-estimation algorithm, we examine the algorithm's output with reference to the formants extracted from vocalic segments in the training data; see Sec. III.

One key characteristic of this model is the elimination of the need to enumerate contextual factors such as triphones. The contextual variations are automatically built into the goal-directed, globally smooth dynamic "state" equations governing the VTR movements during speech utterances. Moreover, the contextual variations are integrated into speaking rate variations which are controlled by a small number of shared dynamic model parameters. The sharing is based on physical principles of speech production.

To provide an overview, we have proposed a new coarticulatory speech model, which consists of two separate components. They accommodate separate sources of speech variability. The first component has a smooth dynamic property, and is linear but nonstationary. The nonstationarity is described by left-to-right regimes corresponding to sequentially organized phonological units such as context-independent phones. Handling nonstationarity in this way is very close to the conventional HMMs; but for each state (discrete as in the HMM), rather than having an independent and identically distributed (i.i.d.) process, the new model has a phonetic-goal-directed linear dynamic process with the physically meaningful entity of continuous state variables. Equipped with the physical meaning of the state variables (i.e., VTRs in the current version of the model), variability due to phonetic contexts and to speaking styles is naturally represented in the model structure with duration-dependent physical variables and with global temporal continuity of these variables. This contrasts with the conventional HMM approach where the variability is accounted for in a largely unstructured manner by accumulating an ever-increasing model size in terms of the number of Gaussian mixture components. (The increase in the model size is blocked only by use of decision-tree based methods, at the expense of sacrificing modeling accuracy.) The second component, the observation model, is static and nonlinear. This lower-level component in the speech generation chain handles other types of variability including spectral tilts, formant bandwidths, relative formant magnitudes, frication spectra, and voice source differences. The two components combined form a nonstationary, nonlinear dynamic system whose structure and properties are well understood in terms of the general process of human speech production.

B. Mathematical formulation

The coarticulatory speech model with its overview provided in the preceding subsection has been formulated in mathematical terms as a constrained and simplified nonlinear dynamic system. This is a special version of the general statistical hidden dynamic model described in Refs. 5 and 6 using the EM implementation technique. The special structure of the model was also motivated by the speech production model of Ref. 7 based on articulatory gestural representations. While our model structure is much simplified from that of Ref. 7, the new statistical formulation of the model (rather than a deterministic model in Ref. 7) gives its power for use in speech recognition that no previous deterministic model is capable of. Another novelty of our model is its use of vocal tract resonances, rather than vocal tract constrictions, as the dynamic, hidden state variable. This makes it much easier to implement the model and the related recognizer.

The dynamic system model consists of two separate but related components: (1) state equation and (2) observation equation, which are described below.

1. State equation

A noisy, causal, and linear first-order "state" equation is used to describe the three-dimensional (F1, F2, and F3) VTR dynamics according to

$$Z(k+1) = \Phi^j Z(k) + (I - \Phi^j) T^j + W_d(k), \quad j = 1, 2, \dots, J_p, \quad (1)$$

where $Z(k)$ is the three-dimensional "state" vector at discrete time step k , Φ^j and T^j are the system matrix and goal (or target) vector associated with dynamic regime j which is related to the initiation of dynamic patterns in phone j , and J_p is the total number of phones in a speech utterance. (See a derivation of this discrete-time state equation from the continuous-time system in Ref. 5. This is a first-order system since its state has a time lag of one only in the system definition.) Both Φ^j and T^j are a function of time k via their dependence on dynamic regime j , but the time switching points are not synchronous with the phone boundaries. Throughout this article, we define the phone boundary as the time point when the phonetic feature of manner of articulation switches from one phone to its next adjacent phone. The dynamic regime often starts ahead of the phone boundary in order to initiate the dynamic patterns of the new phone. This is sometimes called "look-ahead" or anticipatory coarticulation. The time scale for evolution of dynamic regime j is significantly larger than that for time frame k . In Eq. (1), $W_d(k)$ is the discrete-time state noise, modeled by an i.i.d., zero-mean, Gaussian process with covariance matrix Q . Diagonal covariance matrix Q has been used in the current model, independent of phones (i.e., Q is tied across all phones).

The special structure in the state equation, which is linear in the state vector $Z(k)$ but nonlinear with respect to its parameters Φ^j and T^j , in Eq. (1) gives rise to two significant properties of the VTRs modeled by the state vector $Z(k)$. The first property is local smoothness; i.e., the state vector $Z(k)$ is smooth within the dynamic regime associated with

each phone. The second, attractor or saturation, property is related to the target-directed, temporally asymptotic behavior in $Z(k)$. This target-directed behavior of the dynamics described by Eq. (1) can be seen by setting $k \rightarrow \infty$, which forces the system to enter the local, asymptotic region where $Z(k+1) \approx Z(k)$. With the assumption of mild levels of noise $W_d(k)$, Eq. (1) then directly gives the target-directed behavior in $Z(k)$: $Z(k) \rightarrow T^j$.

An additional significant property of the state equation is the left-to-right structure in Eq. (1) for $j=1,2,\dots,J_P$ and the related global-smoothness characteristics. That is, the local smoothness in state vector $Z(k)$ is extended across each pair of adjacent dynamic regimes, making $Z(k)$ continuous or smooth across an entire utterance. This continuity constraint is implemented in the current model by forcing the state vector $Z(k)$ at the end of dynamic regime j to be identical to the initial state vector for dynamic regime $j+1$. That is, the Kalman filter which implements optimal state estimation (see details in Sec. III) for dynamic regime $j+1$ is initialized by the $Z(k)$ value computed at the end of dynamic regime j .

2. Observation equation

The observation equation in the dynamic system model developed is nonlinear, noisy, and static, and is described by

$$O(k) = h^{(r)}[Z(k)] + V(k), \quad (2)$$

where the acoustic observation $O(k)$ is MFCC measurements computed from a conventional speech preprocessor, and $V(k)$ is the additive observation noise modeled by an i.i.d., zero-mean, Gaussian process with covariance matrix R , intended to capture residual errors in the nonlinear mapping from $Z(k)$ to $O(k)$. (Again, diagonal covariance matrix R has been used in the current model independent of phones.) The multivariate nonlinear mapping, $h^{(r)}[Z(k)]$, is implemented by multiple switching MLPs (multi-layer perceptions), with each MLP associated with a distinct manner (r) of articulation of a phone. A total of ten MLPs (i.e., $r = 1,2,\dots,10$) are used in the experiments reported in this article.

The nonlinearity is used because the physical mapping from VTR frequencies $[Z(k)]$ to MFCCs $[O(k)]$ is highly nonlinear in nature. The noise used in the model Eq. (2) captures the effects of VTR bandwidths (i.e., formant bandwidths for vocalic sounds) and relative VTR amplitudes on the MFCC values. These effects are secondary to the VTR frequencies but they nevertheless contribute to the variability of MFCCs. Such secondary effects are quantified by the determinant of matrix R , which, in combination with the relative size of the state noise covariance matrix Q , plays important roles in determining relative amounts of state prediction and state update in the state estimation procedure.

In implementing the nonlinear function $h[Z(k)]$ (omitting index r for clarity henceforth) in Eq. (2), we used a MLP network of three linear input units $[Z(k)]$ of F1, F2, and F3], of 100 nonlinear hidden units, and of 12 linear output units $[O(k)]$ of MFCC1-12]. Denoting the MLP weights from input to hidden units as w_{jl} , and the MLP weights from hidden to output units as W_{ij} , we have

$$h_i(Z) = \sum_j W_{ij} \cdot g_j \left(\sum_l w_{jl} \cdot Z_l \right), \quad (3)$$

where $i=1,2,\dots,12$ is the index of output units (i.e., component index of observation vector O_k), $j=1,2,\dots,100$ is the index of hidden units, and $l=1,2,3$ is the index of input units. In Eq. (3), the hidden units' activation function is the standard sigmoid function

$$g(x) = \frac{1}{1 + \exp(-x)} \quad (4)$$

with its derivative

$$g'(x) = g(x)(1 - g(x)). \quad (5)$$

The Jacobian matrix for Eq. (3), which will be needed for the extended Kalman filter (EKF; see Sec. III A 3), can be computed in an analytical form:

$$H_z(Z) \equiv \frac{d}{dZ} h(Z) = [H_{il}(Z)] = \begin{pmatrix} \frac{\partial h_1}{\partial Z_1} & \frac{\partial h_1}{\partial Z_2} & \frac{\partial h_1}{\partial Z_3} \\ \frac{\partial h_2}{\partial Z_1} & \frac{\partial h_2}{\partial Z_2} & \frac{\partial h_2}{\partial Z_3} \\ \vdots & \vdots & \vdots \\ \frac{\partial h_{12}}{\partial Z_1} & \frac{\partial h_{12}}{\partial Z_2} & \frac{\partial h_{12}}{\partial Z_3} \end{pmatrix} \quad (6)$$

where

$$H_{il}(Z) = \sum_j W_{ij} g \left[\sum_l w_{jl} g(Z_l) \right] \left[1 - g \left(\sum_l w_{jl} g(Z_l) \right) \right] w_{jl}.$$

The use of the Jacobian above is motivated by the need to linearize the observation equation so that the KF equations can be applied.

C. Comparison with other models

The mathematical model described earlier in this section can be viewed as a significant extension of the linear dynamic system model as a thus-far most general formulation of stochastic segment models for speech described in Ref. 8 and 9. The extension is in the following six major aspects. First, while maintaining linearity in the state equation, the observation equation is extended to a nonlinear one with use of physically motivated nonlinear functions. Second, special structures are built into the state equation to ensure the target-directed property. Third, a physically motivated "global" continuity constraint is imposed on the state variable across phone-correlated dynamic regimes, to provide the long-span context-dependent modeling capability. This makes the current model not just a "segment" model as defined mathematically in Ref. 9, but a "supersegment" model where the correlation structure in the model extends over an entire speech utterance. Fourth, the continuous state variable is endowed with a physically meaningful entity in the realistic speech process (i.e., VTRs), which allows special structures to be built into the state equation and which has been instrumental in the model development (especially in model initialization, learning, and diagnosis). In contrast, in the linear dynamic system model described in Refs. 8 and

9, the continuous state variable was treated merely as a smoothed version of the noisy acoustic observation. Fifth, due to the introduction of nonlinearity in the observation equation and of the structural constraints in the state equation, the model learning and scoring algorithms described in Refs. 8 and 9 have been substantially extended. Finally, due to the compact structure in the current model for speech coarticulation and its elimination of explicit context-dependent units such as triphones, very small amounts of training data are needed for model parameter learning. In contrast, the model described in Refs. 8 and 9 still requires as much training data as the conventional HMM-based recognizers.

Compared with other models of speech developed earlier in our laboratory, the current model offers several significant advantages. The articulatory-dynamic model and task-dynamic model described in Refs. 10–12 all have the dynamic state variables completely hidden (i.e., unobservable). In the case of articulatory-dynamic model, the state variables are articulatory parameters, and in the case of the task-dynamic model, the state variables are vocal tract constriction parameters. The current model uses VTRs as the partially hidden state variables, which are observable for vocalic sounds. In addition to the smaller dimensionality in the dynamic system state (three versus a dozen or so), use of the partially observable VTRs as the system state has been critically important in the model development (model learning and diagnosis) and in the recognizer implementation. Further, use of the learnable MLP architecture for the observation equation provides significant implementation advantages over the earlier use of codebook methods. The acoustic-dynamic models described in Refs. 13–15, on the other hand, lack the physically meaningful internal dynamics capable of piecing together phones in an utterance. Hence, despite the simplicity in the model development and recognizer implementation, it still requires explicit context-dependent units and therefore a large amount of training data. It shares similar weaknesses to those in the model described in Refs. 8 and 9.

The current model shares similar motivations and philosophies of other work aiming at developing better, more compact coarticulatory models than the HMM. The models described in Refs. 16–19 have all used fully hidden internal dynamics, similar to the models described in Refs. 10–12. Some models explicitly use articulatory parameters as the dynamic variable (e.g., Ref. 16), others use more abstract, automatically extracted variables for the purpose of modeling coarticulation (e.g., Refs. 17–19). One main difference between these and the model described in this article lies in mathematical formulation of the models. The models described in Refs. 16, 17, and 18 are largely deterministic, where the outputs of the models need to be explicitly synthesized and compared with the unknown speech in order to reach recognition decision. In contrast, the statistical nature of the current model permits likelihood-score computation against the unknown speech (similar to the conventional HMM formulation in this aspect) directly from the model parameters where the model synthesis is only carried out implicitly. In addition, the deterministic and statistical na-

tures render the models with different learning criteria and hence different learning algorithms.

III. LEARNING AND LIKELIHOOD-SCORING ALGORITHMS

In this section, we will describe the learning and likelihood-scoring algorithms we have developed for the statistical coarticulatory model for fixed dynamic regimes (segmentations). These algorithms enable the training of the recognizer and the use of the recognizer for rescoring N -best hypotheses.

A. Learning algorithm

The learning or parameter estimation method for the new speech model is based on the generalized EM algorithm. The EM algorithm is a two-step iterative scheme for maximum likelihood parameter estimation. Each iteration of the algorithm involves two separate steps, called the expectation step (E-step) and the maximization step (M-step), respectively. A formal introduction of the EM algorithm appeared in Ref. 20. Examples of using the EM algorithm in speech recognition can be found in Refs. 8, 13, and 14. The algorithm guarantees an increase (or strictly speaking, nondecrease) of the likelihood upon each iteration of the algorithm and guarantees convergence of the iteration to a stationary point for an exponential family. Use of local optimization, rather than the global optimization, in the M step of the algorithm gives rise to the generalized EM algorithm.

To derive the EM algorithm for the new model, we first use the i.i.d. noise assumption for $W_d(k)$ and $V(k)$ in Eqs. (1) and (2) so as to express the log-likelihood for acoustic observation sequence $O=[O(1),O(2),\dots,O(N)]$ and hidden VTR-variable sequence $Z=[Z(1),Z(2),\dots,Z(N)]$ as

$$\begin{aligned} \log L(Z, O, \Theta) &= -\frac{1}{2} \sum_{k=0}^{N-1} \{ \log |Q| + [Z(k+1) - \Phi Z(k) - (I - \Phi)T]' \\ &\quad \times Q^{-1} [Z(k+1) - \Phi Z(k) - (I - \Phi)T] \} \\ &\quad - \frac{1}{2} \sum_{k=1}^N \{ \log |R| + [O(k) - h(Z(k))] ' R^{-1} \\ &\quad \times [O(k) - h(Z(k))] \} + \text{const}, \end{aligned}$$

where superscript ' denotes matrix transposition, and the model parameters Θ to be learned include those in the state equation (1) and those in the MLP nonlinear mapping functions Eq. (2): $\Theta = \{T, \Phi, W_{ij}, w_{jl}, i=1,2,\dots,I; j=1,2,\dots,J; l=1,2,\dots,L\}$. To simplify the algorithm description without loss of generality, estimation of additional model parameters of covariance matrices Q, R for state and observation noises will not be addressed in this article. Also, the dynamic-regime index on parameters T, Φ and the phone-class index on parameters W_{ij}, w_{jl} are dropped because supervised learning is used. In the current model implementation, $I = 3, J = 100, L = 12$.

1. E-step

The E-step of the EM algorithm involves computation of the following conditional expectation (together with a set of related sufficient statistics needed to complete evaluation of the conditional expectation):

$$\begin{aligned} Q(Z, O, \Theta) &= E\{\log L(Z, O, \Theta) | O, \Theta\} \\ &= -\frac{N}{2} \log |Q| - \frac{N}{2} \log |R| \\ &\quad - \frac{1}{2} \sum_{k=0}^{N-1} E[e'_{k1} Q^{-1} e_{k1} | O, \Theta] \\ &\quad - \frac{1}{2} \sum_{k=1}^N E[e'_{k2} R^{-1} e_{k2} | O, \Theta], \end{aligned}$$

where $e_{k1} = Z(k+1) - \Phi Z(k) - (I - \Phi)T$ and $e_{k2} = O(k) - h(Z(k))$, and E denotes conditional expectation given observation vectors O .

This can be simplified, by substituting the optimal values of covariance matrix estimates, to

$$\begin{aligned} Q(Z, O, \Theta) &= -\frac{N}{2} \log \left\{ \underbrace{\frac{1}{N} \sum_{k=0}^{N-1} E[e_{k1} e'_{k1} | O, \Theta]}_{Q_1(Z, O, \Phi, T)} \right\} \\ &\quad - \frac{N}{2} \log \left\{ \underbrace{\frac{1}{N} \sum_{k=1}^N E[e_{k2} e'_{k2} | O, \Theta]}_{Q_2(Z, O, W_{ij}, w_{jl})} \right\} + \text{const.} \end{aligned} \quad (7)$$

(For detailed derivation, see Ref. 21.) Note that the state-equation's parameters (Φ, T) are contained in Q_1 only and the MLP weight parameters (W_{ij}, w_{jl}) in the observation equation are contained in Q_2 only. These two sets of parameters can then be optimized independently in the subsequent M-step to be detailed in Sec. III A 2.

2. M-step

The M-step of the EM algorithm aims at optimizing the Q function in Eq. (7) with respect to model parameters $\Theta = \{T, \Phi, W_{ij}, w_{jl}\}$. For the model at hand, it seeks solutions for

$$\begin{aligned} \frac{\partial Q_1}{\partial \Phi} &\propto \sum_{k=0}^{N-1} E \left[\frac{\partial}{\partial \Phi} \{ [Z(k+1) - \Phi Z(k) \right. \\ &\quad \left. - (I - \Phi)T]^2 \} \middle| O, \Theta \right] = 0, \end{aligned} \quad (8)$$

$$\begin{aligned} \frac{\partial Q_1}{\partial T} &\propto \sum_{k=0}^{N-1} E \left[\frac{\partial}{\partial T} \{ [Z(k+1) - \Phi Z(k) \right. \\ &\quad \left. - (I - \Phi)T]^2 \} \middle| O, \Theta \right] = 0, \end{aligned} \quad (9)$$

$$\frac{\partial Q_2}{\partial W_{ij}} \propto \sum_{k=1}^N E \left[\frac{\partial}{\partial W_{ij}} \{ [O(k) - h(Z(k))]^2 \} \middle| O, \Theta \right] = 0, \quad (10)$$

$$\frac{\partial Q_2}{\partial w_{jl}} \propto \sum_{k=1}^N E \left[\frac{\partial}{\partial w_{jl}} \{ [O(k) - h(Z(k))]^2 \} \middle| O, \Theta \right] = 0. \quad (11)$$

Equation (8) is a third-order nonlinear algebraic equation (in Φ and T), of the following form after some algebraic and matrix-calculus manipulation:

$$\begin{aligned} N\Phi TT' - \Phi TA' - \Phi AT' - NTT' - TA' \\ + BT' + \Phi C - D = 0, \end{aligned} \quad (12)$$

where

$$A = \sum_{k=0}^{N-1} E[Z(k) | O, \Theta], \quad B = \sum_{k=0}^{N-1} E[Z(k+1) | O, \Theta],$$

$$C = \sum_{k=0}^{N-1} E[Z(k)Z(k)' | O, \Theta],$$

$$D = \sum_{k=0}^{N-1} E[Z(k+1)Z(k)' | O, \Theta].$$

Equation (9) is another third-order nonlinear algebraic equation (in Φ and T) of the form

$$\begin{aligned} N\Phi' \Phi T - \Phi' \Phi A - N\Phi' T - N\Phi T + \Phi' B \\ + \Phi A + NT - B = 0. \end{aligned} \quad (13)$$

The coefficients in Eqs. (12) and (13), A, B, C , and D , constitute the sufficient statistics, which can be obtained by the standard technique of EKF (see Sec. III A 3).

Solutions to Eqs. (10) and (11) for finding (W_{ij}, w_{jl}) to maximize Q_2 in Eq. (7) have to rely on approximation due to the complexity in the nonlinear function $h(Z)$. The approximation involves first finding estimates of hidden variables $Z(k)$, $Z(k|k)$, via the EKF algorithm. Given such estimates, the conditional expectations in Eqs. (10) and (11) are approximated to give

$$\frac{\partial Q_2}{\partial W_{ij}} \propto \sum_{k=1}^N [O(k) - h(Z(k|k))] \frac{\partial h(Z(k|k))}{\partial W_{ij}}, \quad (14)$$

$$\frac{\partial Q_2}{\partial w_{jl}} \propto \sum_{k=1}^N [O(k) - h(Z(k|k))] \frac{\partial h(Z(k|k))}{\partial w_{jl}}. \quad (15)$$

If the estimated state variable, $Z(k|k)$, is treated as the input to the MLP neural network defined in Eq. (3), and the observation, $O(k)$, as the output of the MLP, then the gradients expressed in Eqs. (14) and (15) are exactly the same as those in the backpropagation algorithm.²² Therefore, the backpropagation algorithm is used to provide the estimates to W_{ij} and w_{jl} parameters. The local-optimum property of the backpropagation algorithm in this M-step makes the learning algorithm described in this section a generalized EM. The approximation used to obtain the gradients in Eqs. (14) and (15) makes the learning algorithm a pseudo-EM.

3. Extended Kalman filter for finding sufficient statistics

We have observed that in the E-step derivation of the EM algorithm shown in this section, the objective functions Q_1 and Q_2 in Eq. (7) contain a set of conditional expectations as sufficient statistics. These conditional expectations, A , B , C , and D in Eqs. (12) and (13), need to be computed during the M-step of the EM algorithm. The extended Kalman filter or EKF algorithm provides a solution to finding these sufficient statistics. (We have also implemented an extended Kalman smoothing algorithm which is expected to provide more accurate solutions. But in this work we have empirically observed no practical differences from the EKF. In this article we only describe the EKF method used.) Also, as shown in Sec. III A 2, the EKF algorithm is needed to approximate the gradients in Eqs. (10) and (11), before the M-step can be formulated as the backpropagation algorithm and can be carried out straightforwardly.

The EKF algorithm gives an approximate minimum-mean-square error estimate to the state of a general nonlinear dynamic system. Our speech model discussed in Sec. II B uses a special structure within the general class of the nonlinear dynamic system models. Given such a structure, the EKF algorithm developed is described here in a standard predictor-corrector format.^{23,24}

Denoting by $\hat{Z}(k|k)$ the EKF state estimate and by $\hat{Z}(k+1|k)$ the one-step EKF state prediction, the prediction equation for the special structure of our model has the form

$$\hat{Z}(k+1|k) = \Phi \hat{Z}(k|k) + (I - \Phi)T. \quad (16)$$

The physical interpretation of Eq. (16) applied to our speech model is that the one-step EKF state predictor based on the current EKF state estimate will always move towards the target vector T for a given system matrix Φ . Such desirable dynamics comes directly from state equation (1), and it is, in fact, in exactly the same form as the noise-free model state equation.

Denote by $H_z(\hat{Z}(k+1|k))$ the Jacobian matrix, as defined in Eq. (6), at the point of $\hat{Z}(k+1|k)$ for the MLP observation equation in our speech model, and denote by $h(\hat{Z}(k+1|k))$ the MLP output for the input $\hat{Z}(k+1|k)$. Then the EKF corrector (or filter) equation applied to our speech model is

$$\begin{aligned} \hat{Z}(k+1|k+1) &= \hat{Z}(k+1|k) + K(k+1) \\ &\quad \times \{O(k+1) - h(\hat{Z}(k+1|k))\}, \end{aligned} \quad (17)$$

where $K(k+1)$ is the filter gain computed recursively according to

$$\begin{aligned} K(k+1) &= P(k+1|k)H_z[\hat{Z}(k+1|k)] \\ &\quad \times \{H_z[\hat{Z}(k+1|k)]P(k+1|k) \\ &\quad \times H_z[\hat{Z}(k+1|k)]' + R(k+1)\}^{-1}, \\ P(k+1|k) &= \Phi P(k|k)\Phi' + Q(k), \\ P(k+1|k+1) &= \{I - K(k+1) \\ &\quad \times H_z[\hat{Z}(k+1|k)]\}P(k+1|k). \end{aligned} \quad (18)$$

In the above, $P(k+1|k)$ is the prediction error covariance and $P(k+1|k+1)$ is the filtering error covariance.

The physical interpretation of Eq. (17) as applied to our speech model is that the amount of correction to the state predictor obtained from Eq. (17) is directly proportional to the accuracy with which the MLP is used to model the relationship between the state $Z(k)$ or VTRs and the observation $O(k)$ or MFCCs. [Correction is necessary because the predictor obtained from Eq. (16) is based solely on the system dynamics discarding the actual observation. Use of the actual observation will improve the accuracy of the state estimation.] Such a matching error in the acoustic domain (called innovation in estimation theory²⁴) is magnified by the time-varying filter gain $K(k+1)$, which is dependent on the balance of the covariances of the two noises Q and R , and on the local Jacobian matrix that measures the sensitivity of the nonlinear function $h(Z)$ represented by the MLP.

In using the EM algorithm to learn the model parameters, we require that all the conditional expectations (sufficient statistics) for the coefficients A , B , C and D in Eq. (13) be reasonably accurately evaluated. This can be accomplished, once the EKF's outputs become available, according to

$$\begin{aligned} E[Z(k)|O] &= \hat{Z}(k|N) \approx \hat{Z}(k|k), \\ E[Z(k+1)|O] &= \hat{Z}(k+1|N) \approx \hat{Z}(k+1|k+1), \\ E[Z(k)Z(k)'|O] &= P(k|N) + \hat{Z}(k|N)\hat{Z}(k|N)' \\ &\approx P(k|k) + \hat{Z}(k|k)\hat{Z}(k|k)', \\ E[Z(k+1)Z(k)'|O] &= P(k+1,k|N) + \hat{Z}(k+1|N)\hat{Z}(k|N)' \\ &\approx P(k+1,k|k+1) \\ &\quad + \hat{Z}(k+1|k+1)\hat{Z}(k|k)'. \end{aligned}$$

All the quantities on the right-hand sides of the above are computed directly from the EKF recursion Eqs. (16)–(18), except for the quantity $P(k+1,k|k+1)$, which is computed separately according to

$$\begin{aligned} P(k+1,k|k+1) \\ = [I - K(k+1)H_z(\hat{Z}(k+1|k+1))] \Phi P(k|k). \end{aligned}$$

It is noted that while the EM algorithm requires Kalman smoothing which takes into account the complete acoustic observation sequences, we found no practical differences with the use of Kalman filtering taking account of only the previous observations. In other words, we used the EKF to approximate the corresponding smoothing algorithm in computing all the sufficient statistics required by the EM algorithm.

B. Likelihood-scoring algorithm for recognizer testing

In addition to the use of the EKF algorithm in the model learning as discussed so far, it is also needed in the likelihood-scoring algorithm (during the recognizer testing phase) which we discuss now.

Using the basic estimation theory for dynamic systems (cf. Theorem 25-1 in Ref. 24; see also in Ref. 8), the log-

likelihood scoring function for our speech model can be computed from the approximate innovation sequence $\tilde{O}(k|k-1)$ according to

$$\log L(O|\Theta) = -\frac{1}{2} \sum_{k=1}^N \{ \log |P_{\tilde{o}\tilde{o}}(k|k-1)| + \tilde{O}(k|k-1)' \times P_{\tilde{o}\tilde{o}}^{-1}(k|k-1) \tilde{O}(k|k-1) \} + \text{const}, \quad (19)$$

where the approximate innovation sequence

$$\tilde{O}(k|k-1) = O(k) - h(\hat{Z}(k|k-1)), \quad k = 1, 2, \dots, N$$

is computed from the EKF recursion, and $P_{\tilde{o}\tilde{o}}$ is the covariance matrix of the approximate innovation sequence:

$$P_{\tilde{o}\tilde{o}}(k|k-1) = H_z(\hat{Z}(k|k-1))P(k|k-1) \times H_z(\hat{Z}(k|k-1))' + R,$$

which is also computed from the EKF recursion.

For a speech utterance that consists of a sequence of phones with the dynamic regimes given, the log-likelihood scoring functions for each phone in the sequence as defined in Eq. (19) are summed to give the total log-likelihood score for the entire speech utterance.

IV. SPEECH RECOGNITION, SYNTHESIS, AND ANALYSIS EXPERIMENTS

In this section, we will report a series of experiments conducted for analysis, synthesis, and recognition of Switchboard spontaneous speech using the statistical, VTR-based coarticulatory model presented so far. After introducing the experimental paradigm and the design parameters of the new recognizer, we will first report a set of small-scale N -best rescoring speech recognition experiments, which permits analysis of the model behavior by manipulating some hand-tuned variables. We will then evaluate the performance of the new recognizer in a set of large-scale N -best rescoring experiment, and compare the performance figures with the conventional triphone HMM-based speech recognizer under similar conditions. Finally, we will present some model-synthesis results and give detailed examinations of the model behavior in fitting the Switchboard data and of the quality of the spontaneous speech artificially generated from the model. Such analysis and synthesis experiments serve to explain why the new coarticulatory model is doing the right job in ‘‘locking into’’ the correct transcription but at the same time it can ‘‘break away’’ from partially correct transcriptions due to contextual influences.

A. Experimental paradigm, HMM benchmark system, and design parameters of the VTR recognizer

In all the experiments reported in this article, we used an N -best list rescoring paradigm, according to the scoring algorithm Eq. (19), to evaluate the new recognizer based on the VTR-based coarticulatory model on the Switchboard spontaneous speech data. The N -best list of word transcription hypotheses and their phone-level segmentation (i.e., alignment) are obtained from a conventional triphone-based HMM that also serves as the benchmark to gauge the recognizer performance improvement via use of the new speech

model. The reasons for using the limited N -best rescoring paradigm in the current experiments are mainly due to computational ones.

The benchmark HMM system used in our experiments is one of the best systems developed earlier [see http://www.clsp.jhu.edu/ws97/ws97_general.html], and it has been described in some detail in Refs. 19 and 25. Briefly, the system has word-internal triphones clustered by a decision tree, with a bigram language model. The total number of the parameters in this benchmark HMM system is approximately 3 276 000, which can be broken down to the product of (1) 39, which is the MFCC feature vector dimension; (2) 12, which is the number of Gaussian mixtures for each HMM state; (3) 2, which includes Gaussian means and diagonal covariance matrices in each mixture component; and (4) 3500, which is the total number of the distinct HMM states clustered by the decision tree.

In contrast, the total number of parameters in the new recognizer is considerably smaller. The total 15 252 parameters in the recognizer consists of those from target parameters $42 \times 3 = 126$, those from diagonal dynamic system matrices $42 \times 3 = 126$, and those from MLP parameters $10 \times 100 \times (12 + 3) = 15\,000$. These numbers are elaborated below while detailing several essential implementation aspects of the recognizer.

First, we choose a total of 42 distinct phonelike symbols, including 8 context-dependent phones, each of which is intended to be associated with a distinct three-dimensional (F1, F2, and F3) vector-valued target (T^j) in the VTR domain. The phonelike symbol inventory and the VTR target values used to initialize the model training discussed in Sec. III A are based on the Klatt synthesizer setup.²⁶ The values are slightly adjusted by examining some spectrograms of the Switchboard training data. Among the 42 phonelike symbols, 34 are context independent. The remaining eight are context dependent because their target VTRs are affected by the anticipatory tongue position associated with the following phone.

The next set of model parameters is the elements in the 42 distinct diagonal dynamic system matrices (Φ^j). Before the training, they are initialized based on the consideration that the articulators responsible for producing different phones have different intrinsic movement rates. This difference roughly translates to the difference in the VTR movement rates across the varying phones. For example, the VTR transitions for labial consonants (/b/, /m/, /p/) marked by ‘‘Lips’’ features are significant faster than those for alveolar consonants (/d/, /t/, /n/) marked by ‘‘Tongue-Blade’’ features. The VTR transitions for both labial and alveolar consonants are faster than those for velar consonants (marked by ‘‘Tongue Dorsum’’ features) and those of vowels marked also by the ‘‘Tongue Dorsum’’ features. (We found that after the model training, the differences in the elements of the system matrices are largely retained from the initialization across the phone classes. However, their values have been changed after the training.)

The final set of model parameters in the recognizer are the MLP weights, W_{ij} and w_{ji} , responsible for the VTR-to-MFCC mapping. Unlike the target and system matrix param-

eters which are phone dependent, we tie the MLPs approximately according to the distinct classes of manner of articulation (and voicing). Such tying reduces the MLP noise resulting from otherwise too many independently trained MLPs. On the other hand, by not tying all phones into one single MLP, we also ensure effective discrimination of phones using differential nonlinear mapping (from the smoothed physical VTR state variables to the MFCCs) even if the VTR targets are identical for different phones (a few phones have nearly identical VTR targets). The ten classes resulting from the tying and used in the current recognizer implementation are (1) aw, ay, ey, ow, oy, aa, ae, ah, ao, ax, ih, iy, uh, uw, er, eh, el; (2) l, w, r, y; (3) f, th, sh; (4) s, ch; (5) v, dh, zh; (6) z, jh; (7) p, t, k; (8) b, d, g; (9) m, n, ng, en; and (10) sil, sp.

In the above tying scheme, all vowels are tied using one MLP, because vowel distinction is based exclusively on different target values in the VTR domain. Here /s/ and /sh/ are associated with separate MLPs, because their target VTR values (not observable in the acoustic domain because of concurrent zeros and large VTR bandwidths) are similar to each other. This can be seen in terms of their similar ways in attracting the VTR (formant) transitions from the adjacent phones. Hence their distinction will be based mainly on the different VTR-to-MFCC mappings. In this case, the acoustic difference between these two phones in terms of the greater amount of energy at lower frequency for /sh/ than for /s/ is captured by different MLP weights (which are trained automatically), rather than by differential VTR target values since the behavior of attracting adjacent phones' VTR transitions is similar between /s/ and /sh/.

Now for each of the 10 distinct MLPs, we use 100 (non-linear) hidden units, 3 (linear) input units, and 12 (linear) output units. This gives a total of $10 \times 100 \times (3 + 12)$ MLP weight parameters.

B. Experiments on small-scale N -best rescoring

In this set of experiments, we train the VTR-based model with the design parameters outlined above using speech data from a single male speaker in the Switchboard data. A total of 30 min of the data are used which consist of several telephone conversations. Due to the use of only a single speaker, we avoid normalization problems for both the VTR targets and for the MFCC observations.

We randomly selected 18 utterances (sentences) in one conversation as the test data from the same speaker that are disjoint from the training set. For these 18 utterances, an N -best list with $N=5$ is generated, together with the phone alignments for each of the five-best hypotheses, by the benchmark HMM system. We then add the reference (correct) hypothesis together with its phone alignments into this list, making a total of six ("ref+5") hypotheses to be rescored by the VTR recognizer.

Under the identical conditions set out above, we rescore these 18 utterances using the following three recognizers with the language model removed: (1) benchmark triphone HMM; (2) VTR model using automatically computed phone alignments (which determine the VTR dynamic regimes for each constituent phone) by the HMM for all the six hypoth-

TABLE I. Performance comparison of three recognizers for 18 utterances with the same speaker in training and testing (ref+5).

	Benchmark HMM	VTR (HMM align)	VTR (true align)
% Reference-at-top	37.0%	38.8%	50.0%
Average word error rate	39.2%	30.4%	22.8%

eses; and (3) VTR model using manually determined "true" dynamic regimes for the reference hypothesis according to spectrogram reading. A performance comparison of these three recognizers is shown in Table I. Two performance measures are used in this comparison. First, among the 18 test utterances we examine the percentage when the correct, reference hypothesis scores higher than all the remaining five hypotheses. Second, we directly compute the word error rate (WER) using the standard NIST scoring software. The new, VTR-based recognizers are consistently better than the benchmark HMM, especially when the "true" dynamic regimes are provided and in this case the performance is considerably better.

We conduct a similar experiment to the above, using the same recognizers trained from a single male but choosing a separate male speaker's ten utterances as the test data. Again, as shown in Table II, the VTR-based recognizer with the "true" dynamic regimes gives significantly better performance than the others.

These experiments demonstrate superior performance of the VTR-based coarticulatory model, when exposed to the reference transcriptions. They also highlight the importance of providing the true or optimal dynamic regimes to the model. Automatic searching for the optimal dynamic regimes is a gigantic computational problem and has not been addressed by the work reported in this article.

C. Experiments on large-scale N -best rescoring

In our large-scale experiments, we keep the same recognizers trained from a single male speaker but significantly increase the size of the test set. All the male speakers from the WS'97 DevTest are selected, resulting in a total of 23 male speakers comprising 24 conversation sides (each side has a distinct speaker), 1241 utterances (sentences), 9970 words, and 50 min of speech as the test data. Because of the large test set and because of lack of an efficient method to automate the optimization of the VTR-model dynamic regimes, we report in this section only the performance comparison between the benchmark HMM recognizer and the VTR recognizer with dynamic regimes suboptimally derived from the HMM phone alignments. In Table III, we provide the performance comparison for the "ref+5" mode, and for

TABLE II. Performance comparison of three recognizers for ten utterances with separate speakers in training and testing (ref+5).

	Benchmark HMM	VTR (HMM align)	VTR (true align)
% Reference-at-top	30.0%	40.0%	50.0%
Average word error rate	27.0%	25.7%	9.2%

TABLE III. Performance comparison of two recognizers for a total of 1241 test utterances when the recognizers are exposed to the reference transcription (ref+5 and ref+100).

	Benchmark HMM	VTR (HMM align)	Chance
Average WER (ref+5)	44.8%	32.3%	45.0%
Average WER (ref+100)	56.1%	50.2%	59.6%

the additional ‘‘ref+100’’ mode where the N -best list contains 100 hypotheses. In Table III, we also add the ‘‘Chance’’ performance which is used to calibrate the recognizers’ performance. The chance WER is computed by ensemble averaging the WERs obtained by having a recognizer randomly choosing one hypothesis from the six possible ones (for the ref+5 mode or $N=5$) or from the 101 possible ones (for the ref+100 mode or $N=100$). For both the $N=5$ and $N=100$ cases, the VTR recognizer performs significantly better than the benchmark HMM recognizer, which is slightly better than the chance performance.

More detailed results of the above experiment for the VTR recognizer are shown in Table IV, where the average WER is shown as a function of N in the N -best list.

We also conduct the same experiment as shown in Table III except no reference transcription is added into the N -best list. The results are shown in Table V, with $N=5$ and $N=100$ in the N -best list, respectively. In the both cases, the VTR recognizer performs nearly the same as the chance, both slightly worse than the benchmark HMM recognizer. This contrasts sharply with the superior performance of the VTR recognizer when it is exposed to the reference transcription shown in Tables I–III. A reasonable explanation is that the long-span context-dependence property of the VTR model naturally endows the model with the capability to ‘‘lock-in’’ to the correct transcription and it at the same time increases the tendency for the model to ‘‘break-away’’ from partially correct transcriptions due to the influence of wrong contexts. Since nearly all the hypotheses in the N -best list contain a large proportion of incorrect words, they affect the matching of the model to the remaining correct words in the hypotheses through the context-dependence mechanism much stronger than the conventional triphone HMM. (Professor Fred Jelinek pointed out to us that similar effects have been found in language modeling using long-span dependency language models.²⁷)

D. Experiments on model synthesis and analysis

The experiments described in this section are devoted to investigating and demonstrating some intrinsic mechanisms responsible for the VTR-based, coarticulatory model’s ability in matching the characteristics of the spontaneous speech patterns. Since this new speech model uses physical parameters of speech as its underlying hidden state, it permits the

TABLE IV. VTR recognizer’s average WER% as a function of N in the N -best list (ref+ N).

N	1	2	3	4	7	10	20	30	40	50	60	70	80	90
WER%	20.5	26.3	29.3	31.2	34.5	36.1	40.6	43.3	44.6	46.4	47.7	48.5	49.5	50.1

TABLE V. Performance comparison of two recognizers for a total of 1241 utterances when the recognizers are not exposed to the reference transcription (5-best and 100-best).

	Benchmark HMM	VTR (HMM align)	Chance
Average WER (5-best)	52.6%	51.8%	54.0%
Average WER (100-best)	58.9%	58.2%	60.2%

analysis of experimental results with physical insight and understanding. (The conventional HMM would have a hard time of doing this because of its lack of physical structure in the model.) To pursue this analysis, we introduce the methodology of ‘‘model synthesis.’’

Model synthesis refers to the process of generating an observation sequence, $\hat{O}(1), \hat{O}(2), \dots, \hat{O}(N)$, artificially from the model *conditioned on* a fixed sequence of observation data, $O(1), O(2), \dots, O(N)$, and on its transcription. When the model used is the current VTR model, we pursue the model-synthesis procedure as follows. First, given the fixed sequence of observation MFCC data, $O(1), O(2), \dots, O(N)$, we apply the EKF algorithm to obtain the predicted VTR state sequence:

$$\hat{Z}(1|0), \hat{Z}(2|1), \dots, \hat{Z}(k|k-1), \dots, \hat{Z}(N|N-1).$$

The parameters in the VTR model used in the EKF algorithm are consistent with the phonelike transcription for the given MFCC data. The dynamic regime for each phonelike unit is fixed in advance, and in moving from one dynamic regime to the next, the continuity constraint is imposed on the VTR state while applying the EKF algorithm. Second, using the predicted VTR state sequence, we generate the MFCC sequence according to the nonlinear mapping:

$$\hat{O}(k) = h(\hat{Z}(k|k-1)), \quad k = 1, 2, \dots, N. \quad (20)$$

While using the MLPs to synthesize the MFCC sequence according to Eq. (20), one of the ten MLPs is selected at each time frame depending on the given alignment of the phonelike units.

The result of the VTR model synthesis applied to a Switchboard test utterance ‘‘*And that’s mostly flat,*’’ which is transcribed as sil, /ae/, /n/, /d/, /dh/, /ae/, /t/, /s/, /m/, /ow/, /s/, /t/, /l/, /f/, /l/, /ae/, /t/, sil, is shown in Fig. 1. It shows the speech waveform with phone segmentation (top), the data MFCC sequence converted and then displayed in a Mel-scaled spectrogram format (middle), and the VTR model-synthesized MFCC sequence displayed also in the Mel-scaled spectrogram format (bottom). The three-dimensional predicted VTR vector by the EKF algorithm, $\hat{Z}(1|0), \hat{Z}(2|1), \dots, \hat{Z}(k|k-1), \dots, \hat{Z}(N|N-1)$, is superimposed on the model-synthesized Mel-scaled spectrogram. The VTRs give a reasonably good match to the spectral peaks derived from the MFCC sequence during all vocalic segments in the

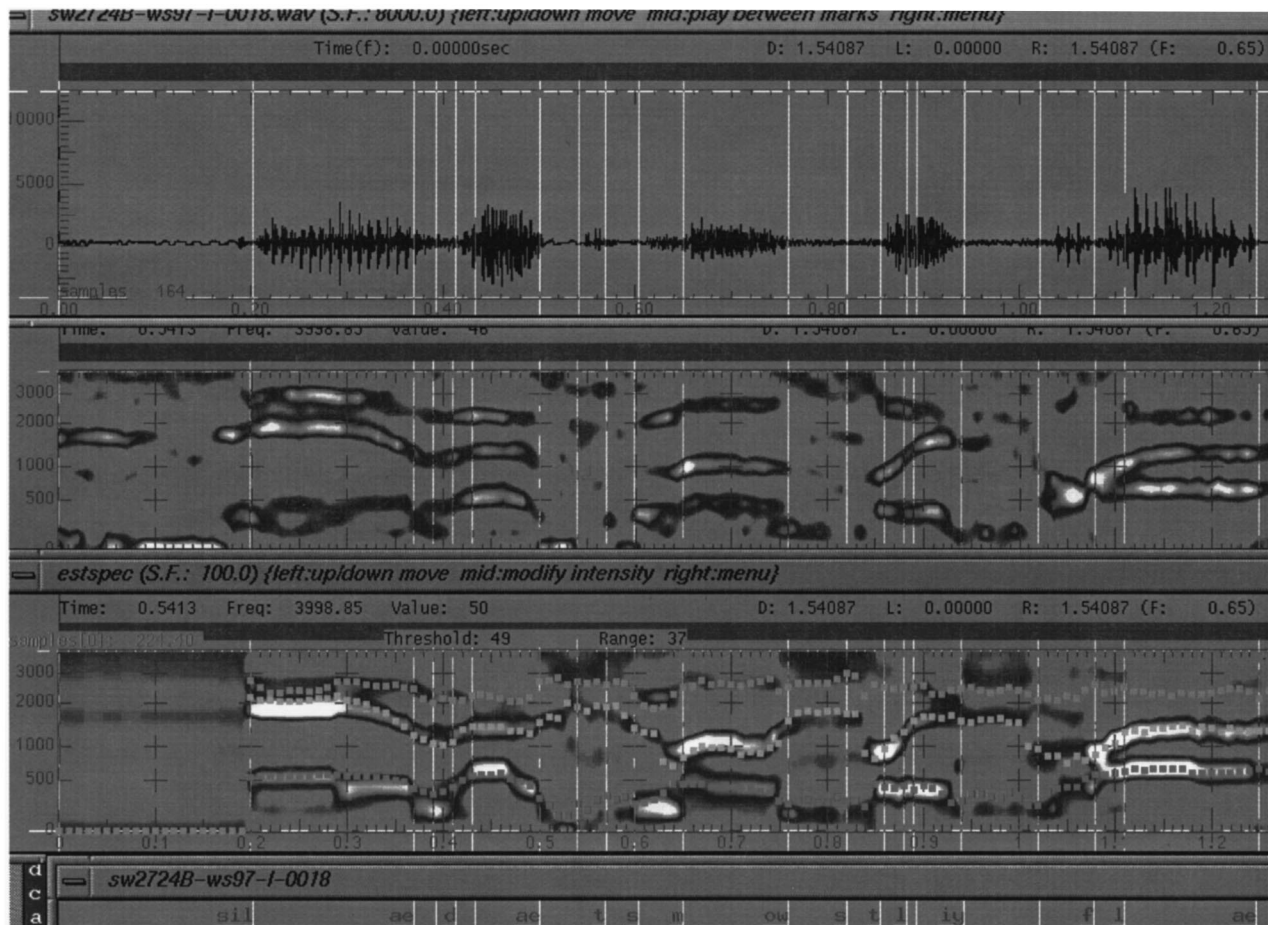


FIG. 1. VTR model synthesis results for spontaneous speech utterance “*And that’s mostly flat*” using the correct transcription.

utterance. Comparing the data MFCCs and the model-synthesized MFCCs, both in the same spectrogram format, we observe a high degree of match across the entire utterance. In particular, most of the observable VTR transitions (those associated with the vocalic segments shown as the spectral prominences) in the data are faithfully synthesized. Use of “correct” target vectors (i.e., consistent with the transcription) is responsible for directing the VTR transitions to and from correct directions across the entire utterance. Then use of such accurate VTRs as inputs to the MLPs naturally generates the MFCCs also accurately matched to the data MFCCs. This makes the likelihood of observation high according to the scoring algorithm of Eq. (19).

In contrast, for most of the incorrect transcriptions in the N -best hypotheses, applying the same model synthesis procedure results in the VTR transitions moving to and from wrong directions. This makes the likelihoods low according to the scoring of Eq. (19). Such disparate likelihoods accounts for the VTR recognizer’s success when exposed to reference transcriptions as demonstrated earlier. In this analysis based on model synthesis, we clearly see that it is the model’s target-directed structure which is responsible for moving the hidden VTRs towards favorable (unfavorable) directions for the correct (incorrect) transcription. This serves as the basis for successfully discriminating the correct from the incorrect transcriptions.

V. SUMMARY AND CONCLUSIONS

The spontaneous speech process is a combination of cognitive (linguistic or phonological) and physical (phonetic) subprocesses. The new statistical coarticulatory model presented in this article focuses on the physical aspect of the spontaneous speech process, where a main novelty is the introduction of the VTR as the internal, structured model state (continuous valued) for representing phonetic reduction and target undershoot in human production of spontaneous speech. The continuity constraint imposed on the VTR state across speech units as implemented in the model is physically motivated, and it enables phonetic information to flow from one unit to another with no use of additional, context-dependent model parameters. Such continuity is not valid in the acoustic domain because of the nonlinear, “quantal” nature of the distortion in the peripheral speech production process,⁴ and in order for the model to ultimately score on the acoustic domain, we explicitly represent the nonlinear distortion as a model component integrated with the VTR dynamic component. With the complex model structure formulated mathematically as a constrained, nonstationary, and nonlinear dynamic system, a version of the generalized EM algorithm has been developed and implemented for automatically learning the compact set of model parameters.

We have shown that in the new VTR model described in

this article the number of model parameters to be estimated is reduced by incorporating the internal structure of the speech production process. This provides the possibility of increased recognizer stability and robustness since it restricts the admissible solutions of the speech recognition problem to those that result only from the possible outcomes of the VTR model. This advantage, however, crucially depends on the capability of the model in explaining the observed acoustic data. In Sec. IV D on model synthesis, we have demonstrated some essential properties of the VTR model in generating the acoustic data. It is our future work to further improve the accuracy (i.e., explanation power) of the VTR model and investigate how the recognizer performance can be enhanced as a result of the improved explanation power on the observed acoustic data.

The new speech model can be viewed as structural decomposition of observed acoustic signals into the dynamic system state (VTR) and the mapping between the VTR (internal) variables and the acoustic (external) variables. It may be possible that when these two structures compensate each other, the convergence of the parameter estimation could be affected. This is so because different combinations of the two components could result in the same observed information used for the parameter estimation. However, the model synthesis results shown in Sec. IV D have convinced us that such undesirable compensation is unlikely to have occurred, because the VTR target parameters estimated from the acoustic data have been shown to largely conform to the physical reality.

We have carried out a series of experiments for speech recognition, model synthesis, and analysis using the recognizer built from the new speech model and using the spontaneous speech data from the Switchboard corpus. The promise of the new recognizer is demonstrated by showing its consistently superior performance over a state-of-the-art benchmark HMM system under similar experimental conditions, especially when exposed to the reference transcription. Experiments on model synthesis and analysis shed powerful insight into the mechanism underlying such superiority in terms of the VTR target-directed behavior and of the long-span context-dependence property, both ensured by the model construct.

While studying the VTR model's (desirable) tendency of automatically "locking in" to the correct transcription, we have also observed and analyzed its opposite (undesirable) tendency of "breaking away" from the locally correct phones by the action of incorrect transcriptions located a distance away. Both of these tendencies are enabled by the inherent long-span context-dependence property of the VTR model. The undesirable, "break-away" tendency, which accounts for the results shown in Table V, can be eliminated if we move on to some more realistic evaluation paradigms than the current N -best rescoring. Most of the transcriptions in the N -best lists used in this work contain more than 30% word errors, artificially accentuating the "break-away" effect. One new evaluation paradigm we are currently pursuing is rescoring on a word lattice rather than on an N -best list. With a sufficiently large lattice, the word errors contained in the lattice is becoming diminishingly small. This provides

the opportunity to completely eliminate the negative effect of "break away" (due to an error a distance away) if cares are taken to avoid early introduction of errors during the lattice search.

A related research effort we are currently also pursuing is motivated by the experiments reported in Sec. IV B (Tables I and II), which underscore the critical role of using true dynamic regimes of the VTR model in speech recognition performance. Algorithms are currently under development which will be capable of joint optimization of dynamic regimes and of the regime-bound acoustic match scores. These algorithms will also be extended to training, enabling the automatic learning of all model parameters without use of heuristically supplied dynamic regimes in the training data.

Our further efforts will include a number of approaches to improving the overall quality of the speech model and subsequently speech recognition performance. These approaches will include interfacing the VTR model to a feature-based phonological model,⁶ use of clusters of target vectors to represent multiple-speaker variability in the VTR target, normalization of speakers in both acoustic and VTR target domains, on-line adaptation and time-varying modeling of state and observation "noise" variances, Bayesian learning of system matrices to allow effective speaking rate and style adaptation, and discriminative training of the model parameters.

ACKNOWLEDGMENTS

The evaluation results reported in this paper were based mainly upon work supported by the National Science Foundation under Grant No. (#IIS-9732388) and carried out at the 1998 Workshop on Language Engineering, Center for Language and Speech Processing, Johns Hopkins University. We thank M. Schuster, J. Picone, J. Bridle, H. Richards, S. Pike, R. Reagan, T. Kamm who contributed neural network programs, HMM benchmark results, discussions, and error-analysis software tools which made this evaluation possible. We also thank F. Jelinek, M. Ostendorf, C. Lee, G. Doddington, T. Crystal, J. Cohen, W. Byrne, S. Khudanpur, and Charles Wayne for support, encouragement, and insightful comments and discussions of this work. We thank three anonymous reviewers and the associate editor who provided constructive comments that significantly improved the quality of the paper.

¹L. Rabiner, B.-H. Juang, and C.-H. Lee, "An overview of automatic speech recognition," in *Automatic Speech and Speaker Recognition—Advanced Topics* (Kluwer Academic, Dordrecht, 1996), pp. 1–30.

²V. Digalakis, E. Bocchieri, C. Boulis, W. Byrne, H. Collier, A. Cordonneau, A. Kannan, and S. Khudanpur, "Rapid speech recognizer adaptation to new speakers," in Final Report of Adaptation Team at the 1998 Workshop on Language Engineering, Center for Language and Speech Processing, Johns Hopkins University, August 1998, pp. 1–29.

³K. Shinoda and C.-H. Lee, "Structural MAP speaker adaptation using hierarchical priors," in *Proceedings of the 1997 IEEE Workshop on Automatic Speech Recognition and Understanding*, Santa Barbara, CA, December 1997, pp. 381–388.

⁴K. Stevens, "On the quantal nature of speech," *J. Phonetics* **17**, 3–45 (1989).

⁵L. Deng, "Computational models for speech production," in *Computa-*

- tional Models of Speech Pattern Processing* (NATO ASI) (Springer, 1999), pp. 199–213.
- ⁶L. Deng, “A dynamic, feature-based approach to the interface between phonology and phonetics for speech modeling and recognition,” *Speech Commun.* **24**(4), 299–323 (1998).
- ⁷E. Saltzman and K. Munhall, “A dynamic approach to gestural patterning in speech production,” *Ecological Psychol.* **1**, 333–382 (1989).
- ⁸V. Digalakis, J. Rohlicek, and M. Ostendorf, “ML estimation of a stochastic linear system with the EM algorithm and its application to speech recognition,” *IEEE Trans. Speech Audio Process.* **1**, 431–442 (1993).
- ⁹M. Ostendorf, V. Digalakis, and K. Owen, “From HMMs to segment models: A unified view of stochastic modeling for speech recognition” *IEEE Trans. Speech Audio Process.* **4**, 360–378 (1996).
- ¹⁰L. Deng, G. Ramsay, and D. Sun, “Production models as a structural basis for automatic speech recognition,” *Speech Commun.* **22**(2), 93–112 (1997).
- ¹¹S. Dusan and L. Deng, “Recovering vocal tract shapes from MFCC parameters,” *Proceedings of the International Conference on Spoken Language Processing*, Sydney, Australia, 30 November–4 December 1998, pp. 3087–3090.
- ¹²L. Deng, “Integrated-multilingual speech recognition using universal phonological features in a functional speech production model,” in *Proceedings of the IEEE International Conference on Acoustics, Speech, and Signal Processing*, Munich, Germany, 1997, Vol. 2, pp. 1007–1010.
- ¹³L. Deng, “A generalized hidden Markov model with state-conditioned trend functions of time for the speech signal,” *Signal Process.* **27**, 65–78 (1992).
- ¹⁴L. Deng, “A stochastic model of speech incorporating hierarchical non-stationarity,” *IEEE Trans. Speech Audio Process.* **1**, 471–474 (1993).
- ¹⁵L. Deng, M. Aksmanovic, D. Sun, and J. Wu, “Speech recognition using hidden Markov models with polynomial regression functions as nonstationary states,” *IEEE Trans. Speech Audio Process.* **2**, 507–520 (1994).
- ¹⁶C. Blackburn and S. Young, “Towards improved speech recognition using a speech production model,” in *Proc. Eurospeech 1995*, Vol. 2, pp. 1623–1626.
- ¹⁷R. Bakis, “Coarticulation modeling with continuous-state HMMs,” in *Proc. IEEE Workshop Automatic Speech Recognition* (Arden House, New York, 1991), pp. 20–21.
- ¹⁸H. Richards and J. Bridle, “The HDM: A segmental hidden dynamic model of coarticulation,” in *Proceedings of the IEEE International Conference on Acoustics, Speech, and Signal Processing*, March 1999, pp. 357–360.
- ¹⁹J. Bridle, L. Deng, J. Picone, H. Richards, J. Ma, T. Kamm, M. Schuster, S. Pike, and R. Reagan, “An Investigation of Segmental Hidden Dynamic Models of Speech Coarticulation for Automatic Speech Recognition,” Final Report for the 1998 Workshop on Language Engineering, Center for Language and Speech Processing at Johns Hopkins University, 1998, pp. 1–61.
- ²⁰A. Dempster, N. Laird, and D. Rubin, “Maximum likelihood from incomplete data via the EM algorithm,” *J. R. Statist. Soc.* **B-39**, 1–38 (1977).
- ²¹L. Deng and X. Shen, “Maximum likelihood in statistical estimation of dynamical systems: Decomposition algorithm and simulation results,” *Signal Process.* **57**(1), 65–79 (1997).
- ²²C. M. Bishop, *Neural Networks for Pattern Recognition* (Clarendon, Oxford, 1995).
- ²³A. H. Jazwinski, *Stochastic Processes and Filtering Theory* (Academic, New York, 1970).
- ²⁴J. M. Mendel, *Lessons in Estimation Theory for Signal Processing, Communications, and Control* (Prentice Hall, Englewood Cliffs, NJ, 1995).
- ²⁵J. Picone, S. Pike, R. Reagan, T. Kamm, J. Bridle, L. Deng, Z. Ma, H. Richards, and M. Schuster, “Initial evaluation of hidden dynamic models on conversational speech,” in *Proceedings of the IEEE International Conference on Acoustics, Speech, and Signal Processing*, March 1999, pp. 109–112.
- ²⁶K. Stevens, Course notes, “Speech Synthesis with a Formant Synthesizer,” MIT, 26–30 July 1993.
- ²⁷F. Jelinek, personal communications.

Time evolution of enhanced ultrasonic reflection using a fibrin-targeted nanoparticulate contrast agent

Christopher S. Hall, Jon N. Marsh, and Michael J. Scott

Washington University School of Medicine, St. Louis, Missouri 63110 and Barnes-Jewish Hospital, St. Louis, Missouri 63110

Patrick J. Gaffney

St. Thomas' Hospital, London SE1 7EH, United Kingdom

Samuel A. Wickline and Gregory M. Lanza

Washington University School of Medicine, St. Louis, Missouri 63110 and Barnes-Jewish Hospital, St. Louis, Missouri 63110

(Received 14 March 2000; accepted for publication 8 September 2000)

Complex molecular signaling heralds the early stages of pathologies such as angiogenesis, inflammation, unstable atherosclerotic plaques, and areas of remote thrombi. In previous studies, acoustic enhancement of blood clot morphology was demonstrated with the use of a nongaseous, fibrin-targeted acoustic nanoparticle emulsion delivered to areas of thrombosis both *in vitro* and *in vivo*. In this study, a system was designed and constructed that allows visualization of the evolution of acoustic contrast enhancement. To evaluate the system, two targets were examined: avidin-complexed nitrocellulose membrane and human plasma clots. The time evolution of enhancement was visualized in 10-min increments for 1 h. A monotonic increase was observed in ultrasonic reflection enhancement from specially treated nitrocellulose membranes for targeted emulsions containing perfluorooctylbromide (1.30 ± 0.3 dB) and for perfluorooctane (2.64 ± 0.5 dB) within the first 60 min of imaging. In comparison, the inherently nonechogenic plasma clots showed a substantial increase of 12.0 ± 0.9 dB when targeted with a perfluoro-octane emulsion. This study demonstrates the concept of molecular imaging and provides the first quantifiable time-evolution report of the binding of a site-targeted ultrasonic contrast agent. Moreover, with the incorporation of specific drug treatments into the nanoparticulate contrast agent, ultrasonic molecular imaging may yield reliable detection and quantification of nascent pathologies and facilitate targeted drug therapy. © 2000 Acoustical Society of America. [S0001-4966(00)02212-8]

PACS numbers: 43.80.Cs, 43.80.Ev, 43.80.Qf, 43.80.Vj [FD]

I. INTRODUCTION

Molecular imaging is a very new but rapidly growing field of medicine that complements and extends traditional imaging modalities.¹ The primary interest of traditional medical ultrasonic imaging has been discerning organ anatomy, blood flow, and for echocardiography, gross function. The area of molecular imaging seeks to extend the traditional imaging approach by adding the ability to differentiate pathology through detection of molecular and cell-surface epitopes. These molecular signatures occur on a microscopic level far below the threshold of resolution of any practical imaging modality.

Historically, molecular imaging has been the domain of positron emission tomography² and nuclear medicine³ where highly specific ligands have been attached to radioactive elements to target specific tissues of the body. Recent developments in the fields of magnetic resonance⁴ and ultrasound imaging⁵ have spawned novel approaches to the goal of molecular imaging using these modalities.

Ultrasonic contrast agents have been the subject of active research for the last decade, especially in recent years with added interest in developing blood-pool agents suitable for determining perfusion of the heart and other organs.^{5,6}

These contrast agents have typically consisted of gaseous microbubbles surrounded by lipid, albumin, polymer, or other proprietary shell materials. The large acoustic impedance mismatch between the blood pool and entrapped gas leads to an extremely echogenic contrast agent. The success of microbubbles depends on their ability to pass through the vasculature of the lungs ($3\text{--}5 \mu\text{m}$) and to resonate at the frequencies of ultrasound typically employed in clinical studies. These blood-pool contrast agents appear to aid in the diagnosis of morphological abnormalities,⁷ aid in border detection for assessment of myocardial function,⁸ and in some instances actually help assess myocardial perfusion.⁹

Site-targeted ultrasonic contrast is a complementary technology to blood-pool contrast agents. The primary function of site-targeted contrast agents is to specifically enhance the acoustic detection of pathologic tissues, e.g., intravascular plaque, thrombosis, inflammation, and new vessel growth around tumors. A highly specific ligand complexed with an ultrasonic contrast agent can selectively highlight a specific pathology previously undifferentiated from surrounding tissue. Because early biochemical changes associated with certain pathologies cannot be resolved with typical ultrasonic imaging systems, the role of site-targeted contrast agents in

molecular imaging is to establish the location and “detection” (although not necessarily the resolution) of a pathogenic molecular marker.

The site-targeted contrast agent employed in this study consists of a liquid-perfluorocarbon, lipid-encapsulated nanoparticulate emulsion. The nanoparticles (~250 nm in diameter) have been successfully demonstrated to enhance thrombus in both *in vitro*¹⁰ and *in vivo* settings.^{11,12} In addition, because of their smaller size, these particles were able to penetrate microfissures in the arterial wall to target the expression of vascular tissue factor, an inducible transmembrane protein, in balloon-injured carotid arteries.¹³ In this study, the targeting of our contrast system occurs in three steps. The first step delivers a biotinylated antibody into the circulating system. For the purposes of targeting human plasma clots, we utilized a well-characterized biotinylated monoclonal antifibrin antibody, NIB 5F3.^{14,15} After the antibody has had adequate time to fix to fibrin B-domains on the substrate surface, avidin is delivered. The avidin particles have a strong natural affinity for the biotin complexed to the antibody. The third stage delivers a biotinylated perfluorocarbon emulsion. The perfluorocarbon emulsion is encapsulated in a monolayer lipid coating¹⁶ which contains the biotin molecules. The perfluorocarbon particles then attach to the antibody-complexed avidin molecules through unoccupied biotin sites.

The primary goal of this study was to design and implement an experimental measure to quantify and image the time dependence of acoustic enhancement achieved by specific binding of the site-targeted contrast agent. This system allows measurements of the acoustic enhancement characteristics of ligand-targeted particles in a setting that can mimic blood flow, and provides a platform for the evaluation of changes to the agent’s formulation with the addition of other ligands or drugs for treatment purposes. Thrombus was selected as the desired target substrate because of its biological importance in the areas of stroke, heart attack, and pulmonary emboli. The present paper describes the temporal evolution of binding of site-targeted contrast agent to a thrombus as distinct from the static approach taken by earlier studies from our group^{10,12} and others^{17,18} which examine the difference between clots at baseline and after long exposure to contrast agent.

By observing the change in ultrasonic reflection as binding of the contrast agent to a substrate progresses over time, the dynamics and physical model that describe the source of ultrasonic enhancement can be tested. Section II briefly summarizes a simple, acoustic transmission line model for the enhancement bestowed by the perfluorocarbon nanoparticles. This section then predicts some features that would be expected in the frequency-dependent reflection enhancement. Sections III and IV describe the methods and results of this study. Finally, in Sec. V we discuss some of the implications of this study in the context of targeted contrast agents and molecular imaging.

II. THEORETICAL MODEL

To explain the observed enhancement of ultrasonic scattering from a surface targeted with the liquid nanoparticle

perfluorocarbon emulsion, a simple acoustic transmission line model has been developed.^{10,19} This model attempts to account for several experimental features of the contrast agent: the lack of enhancement when the emulsion is in suspension, and the observed increase when the contrast agent attaches to a substrate.

The geometry of the experimental situation has been simplified. The incoming wave is modeled as a plane wave approaching the interface provided by a substrate covered with a targeted contrast agent. The incoming wave passes through an attenuating medium that could be phosphate buffer, as in our *in vitro* experiments, or whole blood, as in our *in vivo* situations. The ultrasonic wave then encounters the contrast agent, which is modeled as a continuous thin layer completely covering the substrate. This approximation is an obvious oversimplification as the density of bound contrast particles is not continuous and the surface topography of the substrate often has greater variation than the thickness of single layer of contrast.¹¹ Nevertheless, the predictions of such a simple model are useful for determining the physical mechanism and building intuition for the enhancement observed with this site-targeted contrast agent. The substrate is modeled as having a thickness great enough to preclude reflections from the back wall from interfering with the observed front wall echo. In this study, the experimental substrates consist of plasma clots, as well as a more controlled medium, nitrocellulose membrane.

The amplitude reflection coefficient from the combined system can be expressed as

$$r(k) = r_{12} + \frac{t_{12}t_{21}r_{23}e^{2ikd}}{1 - r_{21}r_{23}e^{2ikd}}, \quad (1)$$

where r and t are the complex reflection and transmission coefficients between water (1), contrast (2), and substrate (3), k is the wave number of the ultrasonic wave in the contrast layer, and d is the thickness of the contrast layer. Typical thickness of a layer consisting of one covering of the substrate by the emulsion particles is about 250 nm. The amplitude reflection and transmission coefficients are merely functions of the complex impedance, and therefore are primarily controlled by the density and speed of sound in each material.

The enhancement provided by the layer of contrast agent can be expressed in decibels as

$$\text{Enhancement} = 20 \log(|r(k)|/|r_0|), \quad (2)$$

where r_0 is the amplitude reflection coefficient of the substrate surface without the contrast agent.

III. METHODS

A. Sample preparation

1. Manufacture of antibody

A frozen (−145 °C) antifibrin hybridoma cell line [NIB 5F3 (Ref. 14)] was resurrected into Dulbecco’s modified Eagle’s medium (DMEM) containing 10% fetal bovine serum (FBS) and 1% glutamine. Cells were maintained in a 37 °C

incubator at 5% CO₂. The hybridomas were split, then passed into larger flasks. As the cells reached confluency, additional fresh DMEM was added to lower the FBS concentration to 3%. The medium was allowed to remain on the cells until the cells began to die. At this time, the supernatant was collected, spun, and passed through a 0.45- μ m filter. The clarified supernatant was then concentrated using a 10 000-molecular weight cutoff (MWCO). The concentrated volume was frozen at -145°C until the NIB 5F3 antifibrin antibody was isolated.

Concentrated medium was thawed at 4°C and loaded onto a protein G Sepharose column (Amersham Pharmacia Biotech) using 20-mM sodium phosphate ($\text{pH}7.0$). The IgG was then eluted with 0.1 M glycine ($\text{pH}2.7$), neutralized with 1.0 M Tris-HCl, while fractions were collected. Protein fractions were detected by ultraviolet spectrophotometry at 280 nm. The IgG fractions were pooled and dialyzed against 20-mM sodium phosphate ($\text{pH}7.0$). Polyacrylamide gel electrophoresis (PAGE) validated the molecular weight of the IgG. The antifibrin monoclonal antibody was then biotinylated using a biotinylation kit (EZ-link Sulfo-NHS-LC-Biotinylation kit 21430, Pierce, Rockford IL). The antibody was used immediately or frozen at -145°C for future experiments.

2. Formulation of the contrast agent

Our first generation agent comprised a three-step process for “pretargeting” a biotinylated antibody and subsequent binding of a biotinylated emulsion to a molecular epitope. The contrast agent itself was produced by incorporating biotinylated phosphatidylethanolamine into the outer lipid monolayer of a perfluorocarbon microemulsion. Briefly, the emulsion was comprised of perfluorocarbon (40% w/v), safflower oil (2.0% w/v), a surfactant comixture (2.0% w/v), and glycerin (1.7% w/v) with a minimum batch size of 25 ml. The surfactant comixture included 64 mole % lecithin (Pharmacia Inc), 35 mole % cholesterol (Sigma Chemical Co.), and 1 mole % N-(6-(biotinoyl)amino)hexanoyl-dipalmitoyl-L-alpha-phosphatidyl-ethanolamine, (Pierce Inc.) which were dissolved in chloroform. The chloroform-lipid mixture was evaporated under reduced pressure, dried in a 50°C vacuum oven overnight, and dispersed into water by sonication. The suspension was transferred into a blender cup (Dynamics Corporation of America) with perfluorocarbon, safflower oil, and distilled, deionized water and emulsified for 30 to 60 s. The emulsified mixture was transferred to an S100 Microfluidics emulsifier (Microfluidics Co.) and continuously processed at 20 000 PSI for 3 min. The completed emulsion was vialled, blanketed with nitrogen, and sealed with a stopper crimp seal until use. A control emulsion was prepared similarly except a nonbiotinylated phosphatidylethanolamine was substituted into the surfactant comixture. Particle sizes were determined in triplicate at 37°C with a laser light scattering submicron particle size analyzer (Malvern Zetasizer 4, Malvern Instruments Ltd., Southborough, MA), which indicated tight and highly reproducible size distribution with average diameters around 250 nm.

3. Nitrocellulose

Nitrocellulose was prepared with a diaminohexane spacer and activated with glutaraldehyde for protein conjugation. Nitrocellulose discs (2.5-cm diameter) were immersed in 1,6 diaminohexane (2.5% w/v, $\text{pH}11.9$) for 60 min under constant rotary agitation. The membranes were next washed under constant agitation for approximately 12 h in 1 M acetic acid followed by 12 h in ultrapure water with several changes of each medium. The diaminoalkane-modified nitrocellulose membranes were then exposed to 1% glutaraldehyde in 0.5 M NaHCO₃/Na₂CO₃, $\text{pH}=10$, for 15 min followed by a 3-h wash in several changes of ultrapure water. The diaminohexane modified, glutaraldehyde-activated nitrocellulose membranes were stored dry at 4°C until use.

Avidin (50 μg) dissolved in 0.1 M phosphate buffered saline (PBS) ($\text{pH}7.2-7.4$) was spotted and dried dropwise onto the center of each membrane with a microliter syringe and allowed to dry. Next, each membrane was washed with three 5-min changes of PBS-0.1% Tween 20. “Blotto” or dried milk in PBS-0.1% Tween 20 was used to block glutaraldehyde activated protein binding sites left unoccupied after the application of avidin for 20 min. Excess blotto was removed with three 5-min isotonic, PBS washes.

Four nitrocellulose discs were utilized for exposure to each perfluorocarbon-based contrast agent using perfluorooctane (PFO) and perfluorooctylbromide (PFOB). Control disks were prepared by utilizing nitrocellulose membranes completely blocked with blotto.

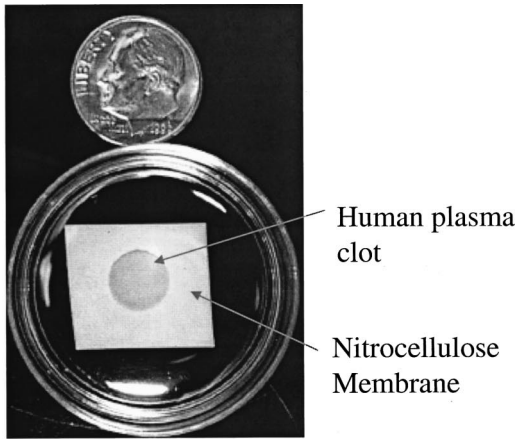
4. Human clot

Plasma clots were produced on nitrocellulose membranes by combining human citrated plasma (375 μl) and 100 mM calcium chloride (25 μl) with 3 units of thrombin in a plastic mold placed on the membranes. The plasma was allowed to coagulate slowly at ambient temperature and then transferred to PBS until exposure to the control or targeted contrast system. A picture of one clot is included in Fig. 1(a).

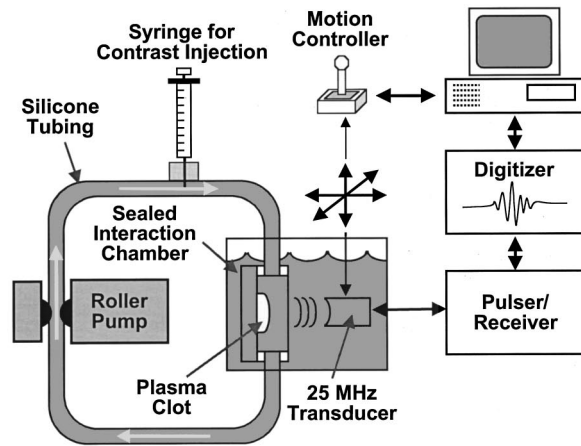
Clots were then incubated with the biotinylated 5F3 antibody overnight in PBS in a 4°C cold room under gentle agitation. The clots were then rinsed and exposed to 100 μg of avidin under gentle agitation for 30 min at room temperature. The clots were then rerinsed and ready for exposure to contrast agent in the manner described in the next subsection. Control clots ($n=4$), not pretargeted with biotinylated antibody or avidin, were exposed in an identical manner to the biotinylated contrast agent. Treated clots ($n=11$) were exposed to the biotinylated contrast agent which contained perfluorooctane.

B. Ultrasonic acquisition

A 25-MHz, spherically focused transducer (0.63-mm diameter, 2.54-mm focal length, Panametrics V324) was mounted on a gantry consisting of three orthogonal sleds. The transducer was translated in a raster scan format by a computer-controlled motion controller (Aerotech Unidex 12) with 100- μm resolution. The pulses sent to the motor from



(a)



(b)

FIG. 1. (a) Human plasma clot shown in petri dish; (b) experimental setup for acquisition of time-dependent site-targeted ultrasonic enhancement.

the motion controller were counted in a digital counter (National Instruments PCI-1200) and then a trigger was generated for a digital delay generator (Stanford Research Systems DG535). The delay generator then sent a trigger for the pulser (Panametrics 5900) and for the digitizing oscilloscope (Hewlett-Packard 54510B), as well as a delayed trigger for the real-time digitizer (Tektronix RTD720A). The delayed trigger was used to capture data with the real-time digitizer within the same time window shown on the oscilloscope. Traces representing the backscattered ultrasonic wave were captured on the fly as the transducer was scanned over the surface of the clot in a 68×68 ($6.8 \text{ mm} \times 6.8 \text{ mm}$) grid at $100\text{-}\mu\text{m}$ resolution. The traces were then transferred from the real-time digitizer to the controlling computer (Apple Power Macintosh 7300) over the general purpose interface bus (GPIB) for image reconstruction and data storage. Acquisition typically took about 4 min per scan. Figure 1(b) shows the block diagram of the experimental setup. The peak pressure at the focus of the transducer was found to be 0.3 MPa with the aid of a calibrated hydrophone (PVDF-Z44-0400, Specialty Engineering).

The sample chamber consisted of a fully enclosed well with an acoustic aperture to allow insonification of the sample. The chamber was attached through two ports to silicone tubing (Masterflex Platinum, i.d. = $1/8$ in.) that allowed

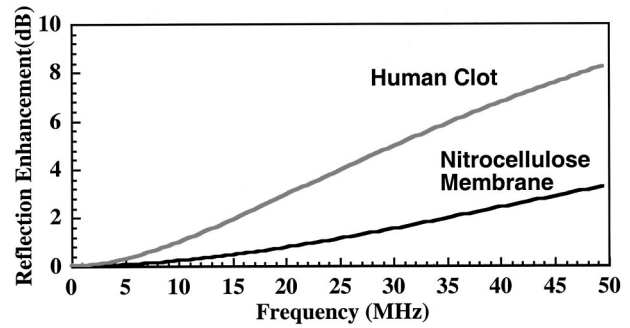


FIG. 2. Theoretical prediction of the frequency-dependent reflection coefficient for a monolayer (250 nm) of targeted perfluoro-octane emulsion on nitrocellulose membrane and human plasma clot.

perfusion of the contrast agent over the sample. A roller pump (Masterflex, Cole-Parmer, Inc.) was used to drive the flow at a rate of 20 mL/min or roughly 4.2 cm/s in the center of the tube. The flow system was filled with 20 mL of 50-nM phosphate buffer. The sample chamber and enclosed sample were positioned vertically so that no passive settling of the contrast agent could occur. After initial location of the sample, a bolus of $100 \mu\text{L}$ of the contrast agent was delivered through an injection port and ultrasonic monitoring was performed at 10-min intervals thereafter for 60 min.

C. Ultrasonic analysis

The reflected ultrasonic signals were full-wave rectified and used to render a peak-detected c-scan image so that a user-defined region of interest could be drawn around the clot or nitrocellulose sample. The signals representing the reflection of the interrogating wave of ultrasound from the surface of the sample were isolated with a rectangular windowing function. The placement of the window was carefully controlled in the case of the thin nitrocellulose samples by an automatic algorithm that placed the end of the window midway between the front and back wall echo of the nitrocellulose paper. The isolated signal was then fast Fourier transformed and the average power over the usable bandwidth (17 to 35 MHz, 10-dB down points) was calculated in the logarithmic domain. This "integrated power" was then sorted for all of the points in the region of interest and the 100 brightest points were retained for analysis. The integrated power was used to render images of the change in ultrasonic enhancement of the clot. The frequency-dependent reflection enhancement was averaged for these 100 points and then normalized by subtracting the reflection enhancement for the 0-min (first postcontrast scan). This process was performed for all of the time points (0 to 60 min in 10-min increments) and for each sample.

IV. RESULTS

A. Theory

The theoretical predictions for the two situations examined experimentally in this paper are shown in Fig. 2. For the case of reflection enhancement of nitrocellulose membrane with the site-targeted contrast agent, the following experimentally determined densities and velocities were used:

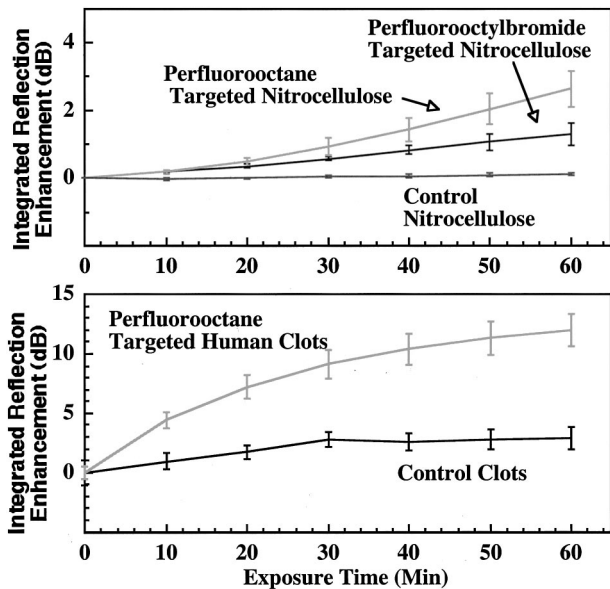


FIG. 3. Time evolution of the enhancement of reflection from nitrocellulose membrane (top panel) for treated ($n=4$) and control ($n=4$). Bottom panel contains results for human plasma clot (treated, $n=11$ and control, $n=4$).

$\rho_{\text{nitrocellulose}}=1.141 \text{ g/cm}^3$, $\nu_{\text{nitrocellulose}}=1.47 \text{ mm}/\mu\text{s}$, $\rho_{\text{water}}=1.0 \text{ g/cm}^3$, $\nu_{\text{water}}=1.49 \text{ mm}/\mu\text{s}$, and $\rho_{\text{PFO}}=1.73 \text{ g/cm}^3$, $\nu_{\text{PFO}}=0.58 \text{ mm}/\mu\text{s}$. The thickness of the layer was assumed to be that of a monolayer of typical contrast particles (250 nm). For predictions of enhancement from the clot, the same parameters were used with the exception of $\rho_{\text{clot}}=1.05 \text{ g/cm}^3$ and $\nu_{\text{clot}}=1.49 \text{ mm}/\mu\text{s}$. The theoretical model predicts an increase in the magnitude of reflection enhancement with increasing frequency within the bandwidth of these measurements and forecasts greater enhancement for the clot than for the nitrocellulose.

B. Nitrocellulose membrane

The more uniform nitrocellulose membranes provided an ideal test of the binding characteristics of our site-targeted emulsion. Although the samples ($n=4$) were initially acoustically reflective, changes in the enhancement were discernible in our serial measurements of ultrasonic reflection. The top panel of Fig. 3 illustrates the change in integrated reflection enhancement during exposure of the membrane to the contrast agent. The enhancement was quite small for contrast agents made with either PFO or PFOB. The total enhancement over the course of 60 min of exposure was $1.30 \pm 0.3 \text{ dB}$ for PFOB and $2.64 \pm 0.5 \text{ dB}$ for PFO versus $0.13 \pm 0.03 \text{ dB}$ for control ($p < 0.05$ at 20 min for PFO and PFOB).

Figure 4 shows the frequency-dependent reflection enhancement at 10-min intervals for PFO and PFOB. There are several interesting features in addition to the obvious monotonic increase in the amount of enhancement from the targeted clots. There is an overall general increase in the enhancement with frequency with the highest frequencies showing greater reflection enhancement than the lower frequencies in our bandwidth. In addition, the slope of the frequency-dependent reflection enhancement increases as the contrast agent binds to the membrane over time.

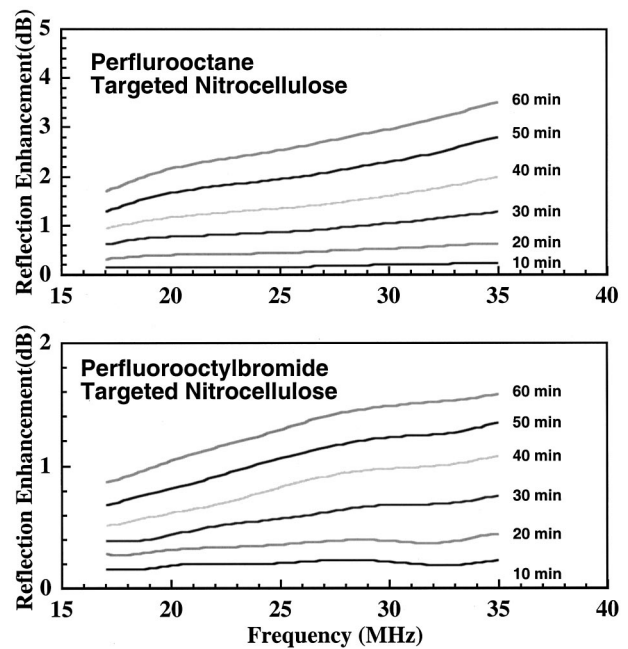


FIG. 4. The frequency-dependent reflection enhancement for nitrocellulose membrane ($n=4$) as a function of exposure time. Typical standard error of the mean is 0.05 dB.

C. Human clots

The human plasma clots were a more biologically relevant substrate for targeting our contrast agent. Figure 5 shows images of a clot rendered with integrated power (17 to 35 MHz) mapped to grayscale. The first picture labeled “baseline” demonstrates the low echogenicity inherently possessed by these clots. The series of pictures made in 10-min intervals shows the morphology of the clot becoming increasingly apparent as the site-targeted contrast agent binds to receptors on fibrin strands. The increase in integrated power was quantified and is shown in the bottom panel of Fig. 3. Like the results for nitrocellulose membranes (top panel of Fig. 3), the curves demonstrated improved reflection enhancement as a function of exposure time to the contrast agent. The increase in reflection enhancement for the clots was substantially greater than for the membranes: $12.0 \pm 0.9 \text{ dB}$ for the treated clots ($n=11$) as opposed to the control clots ($2.9 \pm 2.3 \text{ dB}$, $p < 0.0002$ at 20 min, $n=4$). This result is to be expected because the clots are inherently nonechogenic at baseline.

The frequency-dependent reflection enhancement is shown in Fig. 6 for both the fibrin-targeted and control clots. There is no discernible increase in the reflection enhancement for the control clots, while the targeted clots’ frequency-dependent reflection enhancement has many of the same features as the experiment with nitrocellulose membrane. In particular, there is a monotonic increase in the amount of reflection enhancement with time, as well as a positive slope in the frequency dependence of the observed reflection enhancement. Although there may appear to be some structure in the frequency-dependent reflection enhancement, it is worth noting that the curves have been normalized to the frequency-dependent reflection from an unenhanced clot which itself has very low signal-to-noise ratio.

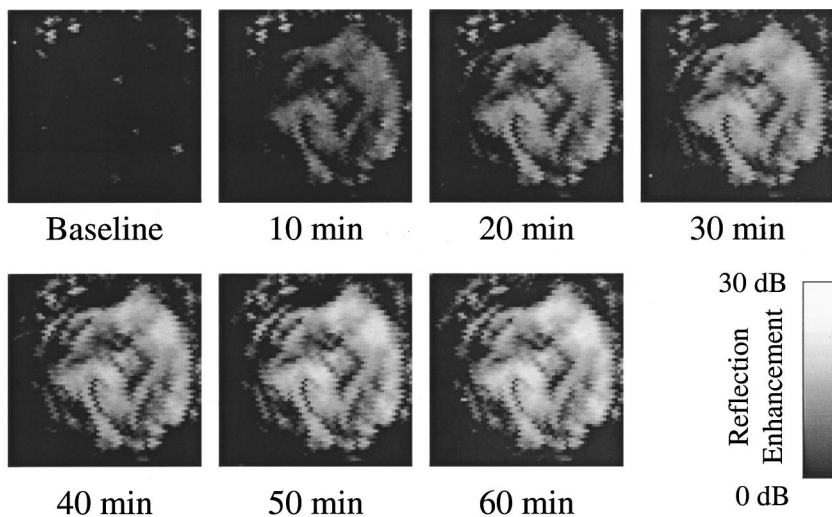


FIG. 5. C-scan images of the integrated reflection enhancement for specific exposure times of human clot to site-targeted ultrasonic contrast agent. Each image is 68×68 sites at $100\text{-}\mu\text{m}$ resolution.

We also include preliminary data that demonstrate the dependence of the contrast effect on the directionality of the insonifying wave with respect to the substrate, shown in Fig. 7. This experiment consisted of a normal measurement of enhancement, but at the 60-min mark rotating the transducer by a 5-deg angle. The resulting structure of the reflection image can be seen to be highly dependent on the angle of insonification. This effect is believed to be due to the variability of the surface geometry of the biological samples.

V. DISCUSSION

“Molecular imaging” entails detecting the presence of molecular markers such as proteins or other cellular receptors associated with pathology. This approach promises to increase the certainty and timeliness of diagnosis and to aid the treatment of a disease before it progresses. Unlike traditional imaging techniques, which concentrate primarily on

the ability to *resolve* a change in morphology or function of tissue, molecular imaging attempts to *detect* and localize biochemical changes within the body. Accordingly, site-targeted contrast agents are designed to adhere to specific receptors within a pathology and provide imaging contrast with respect to the surrounding materials.

The natural extension of perfusion contrast agents to site-targeted applications was the attachment of a ligand to a microbubble contrast agent. This technique has been employed by several researchers to examine an *in vitro* avidin/biotin targeted petri dish,²⁰ activated carotid endothelial cells,²¹ and thrombus.^{12,17} Other investigators have examined the interaction of thrombus with site-targeted agents. In particular, Unger *et al.* have observed successful binding of MRX-408, a bubble-based contrast agent, both *in vitro*^{17,22} and *in vivo*.¹⁸ In subsequent studies, he demonstrated that lysing the clot with bound microbubbles could induce a therapeutic effect.²³ Liposome suspensions also represent another technology that shows some promise as a site-targeted acoustic contrast agent.²⁴ Studies have shown that the multilamellar lipid bilayers form internal vesicles within a liposome and lead to increased acoustic reflectance.²⁵ Demos *et al.* have shown successful binding of these agents to fibrin on slides,²⁶ fibrin-coated filter paper,²⁷ and in plaques of arterial segments.²⁵

In this paper, we have described a different agent, a liquid-perfluorocarbon, lipid-encapsulated nanoparticle, which has been used successfully as an ultrasonic contrast agent.¹⁰⁻¹³ The agent is stable in the bloodstream and has a circulating half-life of roughly 1 h.²⁸ The nanoparticles are

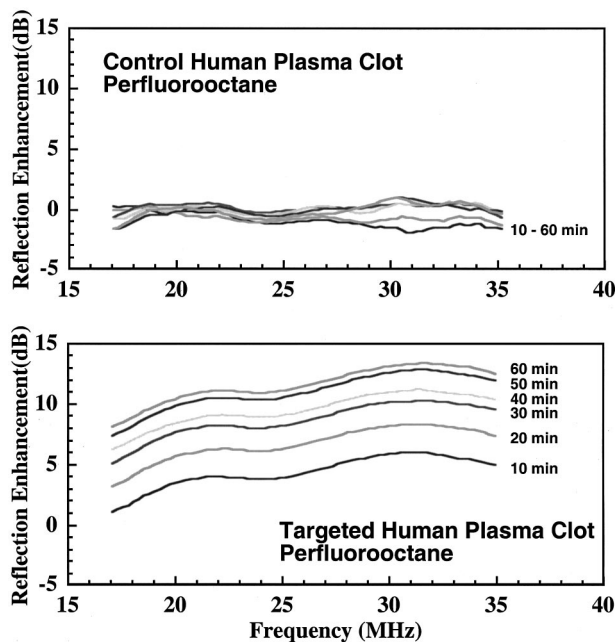


FIG. 6. The frequency-dependent reflection enhancement for human clot ($n=11$) as a function of exposure time. Typical standard error of the mean is 1.5 dB.

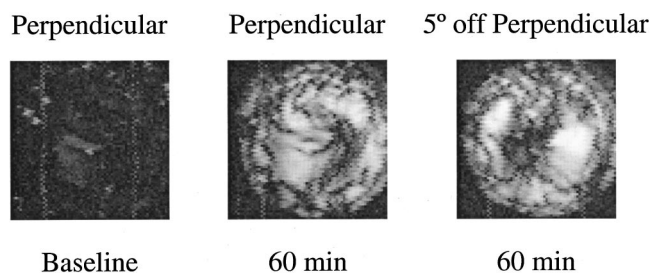


FIG. 7. Comparison of integrated enhancement for two different orientations of the transducer with respect to the surface of a human plasma clot.

not echogenic in suspension (i.e., the volumetric scattering is quite small) but provide enhancement only when bound in adequate density on the targeted surface. We have described a very simple physical model that provides a general explanation for this effect.^{10,19} An important element in the design of a site-targeted contrast agent is a preliminary evaluation of the binding and enhancement characteristics of the agent when attached to the targeted substrate. To accomplish this goal, we designed and experimentally verified a system which quantifies the acoustic enhancement of our site-targeted contrast agent as it bound to a synthetic target, nitrocellulose membrane, and a biological target, thrombus.

To measure the effect of binding of the site-targeted contrast agent on ultrasonic enhancement, we utilized a clot made from human plasma. The increase in ultrasonic reflection coefficient after introduction of the agent was monitored with the clot mounted in an interaction chamber attached to a system designed to mimic blood flow. Figure 3 shows the results for ultrasonic reflection enhancement versus time of exposure for both nitrocellulose membrane and human clot. There are several interesting features to note about these two graphs. The obvious interpretation is that the enhancement of the substrate was successful for the site-targeted agents and demonstrates a monotonic increase in the amount of reflection enhancement with exposure time. The nitrocellulose is expected to show a much smaller enhancement according to the theory presented in Sec. II (see Fig. 2) due to its inherent impedance mismatch with the surrounding fluid. Human clot, which is much more water-like in density and longitudinal acoustic velocity, shows a substantial increase in ultrasonic reflection enhancement as the theory would predict. One of the interesting, although at this time unexplained, features of Fig. 2 in comparison to Figs. 4 and 6 is that the predicted ultrasonic enhancement is somewhat less than that observed experimentally at 60 min. One possible explanation for this difference is the fact that the contrast agent does not bind in a smooth 250-nm layer, but may in fact be approximated by a thicker layer with the acoustic attributes of the surrounding medium combined with the perfluorocarbon. The effect of a thicker layer may account for the increased acoustic contrast.

One of the predictions of the simple acoustic transmission line model presented in Sec. II is that the frequency-dependent reflection enhancement increases with frequency for both nitrocellulose membrane and human clot targeted substrates. Figures 4 and 6 show the experimentally determined frequency-dependent reflection enhancement as contrast agent exposure time increases. These figures illustrate that the reflection enhancement increases as a function of frequency. This observation concurs with the predictions shown in Fig. 2. The frequency-dependent reflection enhancement for the human clots show peaks and troughs with frequency, although the authors believe these are an artifact due to referencing all enhancement to the relatively noisy ultrasonic reflectance from unenhanced clot. An interesting feature is noticeable on the nitrocellulose membrane curves in Fig. 4: the frequency dependence increases from an almost frequency-independent reflection enhancement as one might expect from a flat surface to the predicted positive slope with the presence of contrast agent.

In addition to the magnitude of the time-exposure curves which is due primarily to the initial or baseline echogenicity of the substrate, another distinguishing characteristic in Fig. 3 is the shape of the time-exposure curve. The human clots near an apparent asymptote at 60 min. All of the measurements for targeted thrombi demonstrate that peak enhancement is reached near 60 min, while the asymptote for the nitrocellulose appears to occur later in time. The enhancement observed for substrates is a function of many factors: epitope density, binding efficiency, surface topography, and flow rate, among others. The fact that the nitrocellulose does not appear to have reached an asymptote could be due to several reasons. We surmise that the surface topography may have a large influence. Unlike the membrane, the human clot is a rough surface with limited surfaces that are roughly perpendicular to the insonifying wave. Further proof for this interpretation can be seen in Fig. 5, where only certain portions of the clot become bright as exposure time increases. These regions of enhancement are likely to be areas of sufficiently flat topography.

The importance of the angle between the direction of insonification and the surface topography of the targeted substrate is demonstrated in Fig. 7. A small change in this angle, 5 deg, resulted in a substantially different pattern of ultrasonic enhancement, although the overall magnitude was similar. Interestingly, the patterns of enhancement changed in a complementary manner such that regions that were once less echogenic became brighter and vice versa. One likely explanation for this effect is that the sites that were perpendicular to the insonifying wave changed as the transducer's angle changed. These results imply that the surface topography of the target is an extremely important factor in the enhancement of the substrate. Fortunately, most biological targets have enough variation in surface roughness that the importance of careful alignment of the transducer should not be a great concern. In addition, the clots used in these studies are artificially constructed plasma clots that have a tight weave of fibrin which prevents the deep penetration of the nanoparticles into the clot. In an *in vivo* thrombus, the contrast agent (250 nm) would be able to penetrate and adhere to fibrin throughout the volume of the clot due to the interposition of red blood cells (8 μm) and other cellular elements (>8 μm),¹⁰ thereby increasing the echogenicity as if the target were a multilevel mixture of fibrin and perfluorocarbon contrast.

Several interesting questions can be answered with the construction of this imaging approach, including: what is the effect of flow rate on the binding efficiency of site-targeted contrast agent and once bound, what is the ability of the agent to stay attached to the substrate when encountering various shear rates? The flow rate chosen for these experiments was chosen to be below typical maximum systolic flow velocities in the body of about 1 m/s.²⁹ The shear rate and resulting drag forces on the bound particle are small due to the fact that there is low flow velocity near the edges of the vessel where the particles bind and the small cross-sectional area of the particle. Using a model described by Hyman³⁰ to describe the shear force on a particle attached to a planar surface in flow, we calculate that the drag force on

the particle is on the order of 1×10^{-9} newtons. Further studies will characterize the effect of flow on binding rate and persistence of the contrast agent.

Another utility of the system described in this paper is the ability to check the effect of changing the nanoparticle composition by conjugating different ligands, drugs, and imaging agents to the particles. The top panel of Fig. 3 shows the result of changing the formulation of the contrast agent by substituting different perfluorocarbons. The contrast agent incorporating the perfluorooctylbromide had less overall reflection enhancement at each time point than the agent including the perfluorooctane. This assessment was made possible and more credible by the easily tracked monotonic increase of reflection enhancement for both agents at each time point. In future studies, we wish to assess the effect of other formulation changes including the effect of incorporating other perfluorocarbons³¹ and direct conjugation of the antibody to the particle¹³ as opposed to the three-step, avidin-biotin approach utilized in this and previous studies. By tracking the enhancement of a substrate targeted with different antibodies, we will be able to confirm the bioactivity of the particles and also characterize their relative contrast efficiency.

In addition, we would eventually like to extend this work by attaching a drug to the particle so that we can simultaneously image and treat an area of pathology. The system employed in this study is ideally suited to examine the possible steric hindrance or other effects that the incorporation of other moieties may have on the binding characteristics of the agent.

VI. SUMMARY

We have successfully designed and constructed a system for visualizing and measuring the time course of ultrasonic enhancement due to binding of a site-targeted contrast agent. The enhancement showed monotonic increase with time for the targeted clots and nitrocellulose membranes and the features of the frequency-dependent reflection enhancement qualitatively matched a simple, acoustic transmission line model used to describe the source of the enhancement. To the best of our knowledge, this paper is the first to describe the direct visualization of the time course of binding of site-targeted contrast agent to thrombus. The methodology reported here can be extended to aid the delineation of the effects of different ligands (antibodies, proteins, aptamers, etc.), incorporation of drugs and other imaging agents, and formulation changes to the contrast agent.

ACKNOWLEDGMENTS

The authors would like to thank the NIH for No. R01-59865, Bracco Diagnostics, Inc. SCA&I Fellowship Award, AHA Heartland Affiliate No. 9960282Z, and sponsorship from Abbott Laboratories.

¹R. Weissleder, "Molecular imaging: Exploring the next frontier," *Radiology* **212**, 609–614 (1999).

²T. Jones, "The imaging science of positron emission tomography," *Eur. J. Nucl. Med.* **23**, 807–813 (1996).

³J. Katz, "Pharmaceutical discovery and development: Nuclear and mo-

lecular imaging technologies recognized," *J. Nucl. Med.* **40**, 22N–23N, 26N (1999).

⁴H. Gupta and R. Weissleder, "Targeted contrast agents in MR imaging," *MRI Clinics North Am.* **4**, 171–184 (1996).

⁵F. Forsberg, D. A. Merton, J. B. Liu, L. Needleman, and B. B. Goldberg, "Clinical applications of ultrasound contrast agents," *Ultrasonics* **36**, 695–701 (1998).

⁶B. P. Paelinck and J. D. Kasprzak, "Contrast-enhanced echocardiography: Review and current role," *Acta Cardiologica* **54**, 195–201 (1999).

⁷H. L. Nisenbaum and S. E. Rowling, "Ultrasound of focal hepatic lesions," *Sem. Roentgenol.* **30**, 324–346 (1995).

⁸J. D. Kasprzak and F. J. TenCate, "New ultrasound contrast agents for left ventricular and myocardial opacification," *Herz.* **23**, 474–482 (1998).

⁹T. Jansson, H. W. Persson, and K. Lindstrom, "Estimation of blood perfusion using ultrasound," *Proceedings of the Institution of Mechanical Engineers. Part H—Journal of Engineering in Medicine* **213**, 91–106 (1999).

¹⁰G. Lanza, R. Trousil, K. Wallace, J. Rose, C. Hall, M. Scott, J. Miller, P. Eisenberg, P. Gaffney, and S. Wickline, "In vitro characterization of a novel, tissue-targeted ultrasonic contrast system with acoustic microscopy," *J. Acoust. Soc. Am.* **104**, 3665–3672 (1998).

¹¹G. Lanza, K. Wallace, M. Scott, W. Cacheris, D. Abendschein, D. Christy, A. Sharkey, J. Miller, P. Gaffney, and S. Wickline, "A novel site-targeted ultrasonic contrast agent with broad biomedical application," *Circulation* **94**, 3334–3340 (1996).

¹²G. Lanza, K. Wallace, S. Fischer, D. Christy, M. Scott, R. Trousil, W. Cacheris, J. Miller, P. Gaffney, and S. Wickline, "High frequency ultrasonic detection of thrombi with a targeted contrast system," *Ultrasound Med. Biol.* **23**, 863–870 (1997).

¹³G. M. Lanza, D. R. Abendschein, C. S. Hall, J. N. Marsh, M. J. Scott, D. E. Scherrer, and S. A. Wickline, "Molecular imaging of stretch-induced tissue factor expression in carotid arteries with intravascular ultrasound," *Invest. Radiol.* **35**, 227–234 (2000).

¹⁴S. Raut and P. J. Gaffney, "Evaluation of the fibrin binding profile of two antifibrin monoclonal antibodies," *Thromb. Haemostasis* **76**, 56–64 (1996).

¹⁵T. Edgell, F. McEvoy, P. Webbon, and P. J. Gaffney, "Monoclonal antibodies to human fibrin: Interaction with other animal fibrins," *Thromb. Haemostasis* **75**, 595–599 (1996).

¹⁶*Encyclopedia of Emulsion Technology*, (Dekker, New York, 1988), Vol. 3.

¹⁷E. C. Unger, T. P. McCreery, R. H. Sweitzer, D. Shen, and G. Wu, "In vitro studies of a new thrombus-specific ultrasound contrast agent," *Am. J. Cardiol.* **81**, 58G–61G (1998).

¹⁸M. Takeuchi, K. Ognyankin, N. Pandian, T. P. McCreery, R. H. Sweitzer, V. E. Caldwell, E. C. Unger, E. Avelar, M. Sheahan, and R. Conolly, "Enhanced visualization of intravascular and left atrial appendage thrombus with the use of a thrombus-targeting ultrasonographic contrast agent (MRX-408A1): In vivo experimental echocardiographic studies," *J. Am. Soc. Echocardiogr.* **12**, 1015–1021 (1999).

¹⁹C. S. Hall, G. M. Lanza, J. H. Rose, R. J. Kaufmann, R. W. Fuhrhop, S. H. Handley, K. R. Waters, J. G. Miller, and S. A. Wickline, "Experimental determination of phase velocity of perfluorocarbons: Applications to targeted contrast agents," *IEEE Trans. Ultrason. Ferroelectr. Freq. Control* **47**, 75–84 (2000).

²⁰A. L. Klibanov, M. L. Hughes, J. K. Wojdyla, J. N. Marsh, C. S. Hall, J. G. Miller, J. H. Wible, and G. H. Brandenburger, "Targeting of ultrasound contrast material: Selective imaging of microbubbles in vitro," *Acad. Radiol.* **5**, S243–S246 (1998).

²¹F. S. Villanueva, R. J. Jankowski, S. Klibanov, M. L. Pina, S. M. Alber, S. C. Watkins, G. H. Brandenburger, and W. R. Wagner, "Microbubbles targeted to intercellular adhesion molecule-1 bind to activated coronary artery endothelial cells," *Circulation* **98**, 1–5 (1998).

²²W. H. Wright, T. P. McCreery, E. A. Krupinski, P. J. Lund, S. H. Smyth, M. R. Baker, R. L. Hulett, and E. C. Unger, "Evaluation of new thrombus-specific ultrasound contrast agent," *Acad Radiol* **5**, S240–S242 (1998).

²³Y. Wu, E. C. Unger, and T. P. McCreery, "Binding and lysing of blood clots using MRX-408," *Invest. Radiol.* **33**, 880–885 (1998).

²⁴H. Alkan-Onyuksel, S. M. Demos, G. M. Lanza, M. J. Vonesh, M. E. Klegerman, B. J. Kane, J. Kuszak, and D. D. McPherson, "Development of inherently echogenic liposomes as an ultrasonic contrast agent," *J. Pharm. Sci.* **85**, 486–490 (1996).

²⁵S. M. Demos, H. Alkan-Onyuksel, B. J. Kane, K. Ramani, A. Nagaraj, R.

- Greene, M. Klegerman, and D. D. McPherson, "In vivo targeting of acoustically reflective liposomes for intravascular and transvascular ultrasonic enhancement," *J. Am. Coll. Cardiol.* **33**, 867–875 (1999).
- ²⁶S. M. Demos, H. Onyuskel, J. Gilbert, S. I. Roth, B. Kane, P. Jungblut, J. V. Pinto, D. D. McPherson, and M. E. Klegerman, "In vitro targeting of antibody-conjugated echogenic liposomes for site-specific ultrasonic image enhancement," *J. Pharm. Sci.* **86**, 167–171 (1997).
- ²⁷S. Demos, S. Dagar, M. Klegerman, A. Nagaraj, D. McPherson, and H. Onyuskel, "In vitro targeting of acoustically reflective immunoliposomes to fibrin under various flow conditions," *J. Drug Targeting* **5**, 507–518 (1998).
- ²⁸G. Lanza, C. Lorenz, S. Fischer, M. Scott, W. Cacheris, R. Kaufman, P. Gaffney, and S. Wickline, "Enhanced detection of thrombi with a novel fibrin-targeted magnetic resonance imaging agent," *Acad. Radiol.* **5** (suppl. 1), s173–s176 (1998).
- ²⁹L. Hatle and B. Angelsen, *Doppler Ultrasound in Cardiology*, 2nd ed. (Lea & Febiger, Philadelphia, 1985).
- ³⁰W. A. Hyman, "Shear flow over a protusion from a plane wall," *J. Biomech.* **5**, 45–48 (1972).
- ³¹J. N. Marsh, C. S. Hall, M. J. Scott, R. J. Fuhrhop, P. J. Gaffney, S. A. Wickline, and G. M. Lanza, "Enhancement of reflectivity by specific perfluorocarbon emulsions used in site-targeted ultrasound contrast agent," *SPIE International Symposium on Medical Imaging*, San Diego, CA, 2000, pp. 333–341.

Analysis of the axial transmission technique for the assessment of skeletal status

Estelle Camus^{a)}

Laboratoire d'Imagerie Paramétrique CNRS UMR 7623-Université Paris VI 15, rue de l'Ecole de Médecine 75006 Paris, France and Diagnostic Medical Systems, Parc de la Méditerranée, District de Montpellier, 34470 Perols, France

Maryline Talmant, Geneviève Berger, and Pascal Laugier

Laboratoire d'Imagerie Paramétrique CNRS UMR 7623-Université Paris VI 15, rue de l'Ecole de Médecine 75006 Paris, France

(Received 10 March 2000; accepted for publication 7 July 2000)

Ultrasonic wave propagation in human cortical bone has been investigated *in vitro* using the so-called axial transmission technique. This technique, which relies on velocity measurement of the first arriving signal, has been used in earlier investigations to study bone status during fracture healing or osteoporosis. Two quasi-point-source elements, one transmitter and one receiver (central frequency 0.5 MHz), were used to generate a wide ultrasonic beam, part of which strikes the sample surface at the longitudinal critical angle, and to receive the signals reflected from the sample surface. The analysis of the field reflected from a fluid–solid interface for an incident spherical wave predicts the existence of a lateral wave propagating along the sample surface at a velocity close to the longitudinal velocity, in addition to the ordinary reflected wave and vibration modes. The transducer–sample and the transmitter–receiver distances were chosen such that the lateral wave is the first arriving signal. Validation of the measuring technique was performed on test materials and was followed by experiments on human cortical bones. Experimental results (arrival time and velocity) strongly suggest that the first detected signal corresponds to the lateral wave predicted by theory. © 2000 Acoustical Society of America. [S0001-4966(00)03610-9]

PACS numbers: 43.80.Ev, 43.80.Jz, 43.80.Qf, 43.80.Vj [FD]

I. INTRODUCTION

In recent years quantitative ultrasound measurements of bone have played a growing role in the assessment and management of osteoporosis and are gradually becoming an integrated part of the diagnosis of osteoporosis. This development is attributable to the now-wide availability of ultrasonic equipment which provides equivalent fracture risk assessment compared to conventional x-ray absorptiometric techniques (Glüer, 1997). Ultrasound investigations of bone properties include transverse transmission techniques in which the ultrasound wave passes through bone, e.g., the heel bone and the phalanges (Fredfeldt, 1986; Duboëuf *et al.*, 1996), and the so-called axial transmission techniques in which the ultrasound wave propagates along the long axis of bone, such as the tibia (Foldes *et al.*, 1995) or radius (Hans *et al.*, 1999). The transverse transmission technique uses two transducers, one acting as a transmitter and the second one acting as a receiver. Both transducers are placed on each side of the bone to be tested and the speed of sound- and frequency-dependent attenuation of a broadband ultrasonic pulse transmitted through the sample are calculated. The axial transmission technique currently uses a set of transducers (transmitters and receivers) to measure ultrasound velocity along a fixed distance of the cortical layer of the bone, parallel to its long axis. This set of transducers is placed on

the skin along the bone and measures the arrival time of the wave which propagates along and just below the bone's surface after entering it at the critical angle (Hans *et al.*, 1999). This technique was first developed in 1958 to study cortical bone status during fracture healing (Siegel *et al.*, 1958). Lowet and Van der Perre (1996) have reported that in the axial transmission technique the wave which propagates between a piezoelectric transmitter placed on the bone and a similar receiving transducer placed at a known distance from the transmitter propagates along bone surface at the longitudinal velocity. However, to the best of our knowledge, the nature of the propagating waves has not been documented. The present paper, based on the theoretical analysis of the field reflected from a fluid–solid interface, is a contribution to the understanding of the propagation mode involved in these measurements. Theory predicts the existence of a longitudinal lateral (or head) wave propagating along the interface in the case of a spatially confined source (Brekhovskikh and Godin, 1992; Officer, 1958; Cerveny and Ravindra, 1971). The properties of lateral waves have been described extensively in related fields such as geophysics (Officer, 1958; Galea, 1992), optics (Wabia, 1992), or acoustic microscopy (Chan and Bertoni, 1991). In the present paper, we briefly describe the lateral wave propagation in terms of arrival time and propagation velocity, then compare the experimental arrival times and propagation velocity in two test materials immersed in water with the predicted values for the longitudinal lateral wave, and finally apply this technique to cortical bone specimens (immersed in water) and determine

^{a)} Author to whom correspondence should be addressed. Electronic mail: Estelle.Camus@lip.bhdc.jussieu.fr

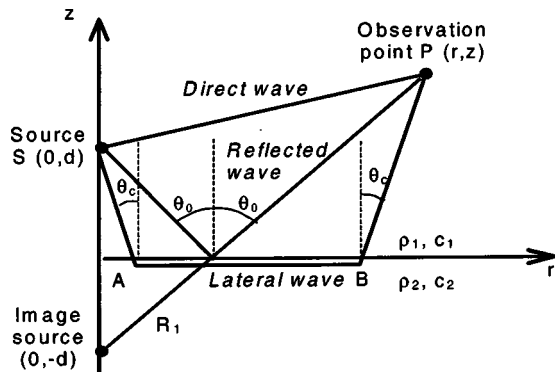


FIG. 1. Fluid–fluid interface with a point source and a point receiver: ray representations of the direct, reflected, and lateral waves.

the longitudinal velocity along the long axis of the bone. The full understanding of the physical mechanisms involved in these measurements may allow further advances in addressing several important issues regarding the potential of the technique to characterize bone acoustical properties (attenuation, velocity) and their precision.

II. THEORETICAL BACKGROUND

As cited by many authors, the first report about the lateral or head wave dates back to 1910 when it was empirically inferred from earthquake records. Later, numerous theoretical papers were devoted to this type of propagation, which is not described by the pure geometrical laws. The wave integral method and/or the geometrical theory of diffraction were used. Details of the investigation are given in several textbooks (Brekhovskikh and Godin, 1992; Ewing *et al.*, 1957; Cerveny and Ravindra, 1971; Officer, 1958; Aki and Richards, 1980) and we summarize here only the basic properties of the lateral wave.

The lateral wave appears as an effect closely related to the total reflection phenomenon. An illustration is given here in the simplest case of two homogeneous fluid half-spaces separated by a flat interface. The bulk wave velocity denoted by c_1 in the upper medium (medium 1, which contains the source) is assumed to be lower than the bulk wave velocity in the lower medium (medium 2) denoted by c_2 . The critical angle θ_c is defined by

$$\sin \theta_c = \frac{c_1}{c_2}. \quad (1)$$

Let us consider a spherical incident wave. Analogous results may be obtained with cylindrical waves or bounded beams. When using the integral representation of the field and the contour integration method, the total reflected pressure can be calculated analytically assuming that the distance R_1 between the image source and the observation point (Fig. 1) is large with respect to the wavelength ($k_1 R_1 \gg 1$ where k_1 is the wave number in medium 1) (Brekhovskikh and Godin, 1992; Ewing *et al.*, 1957; Officer, 1958; Aki and Richards, 1980). Expanding the pressure in powers of the small parameter $1/k_1 R_1$, the dominant term gives the specularly reflected wave while a correction of higher order is found which contains the so-called lateral wave contribution, valid only for

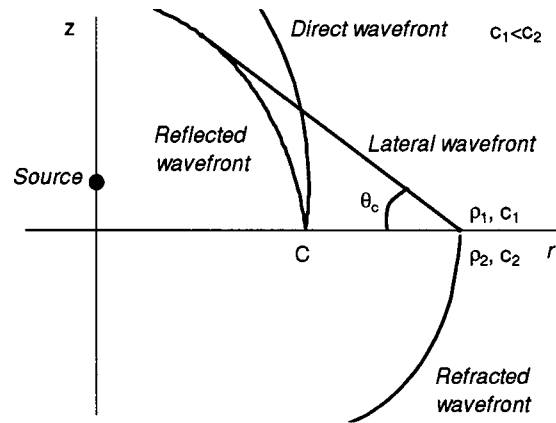


FIG. 2. Direct, reflected, refracted, and lateral wavefronts from a point source at a fluid–fluid interface.

specific regions of space such that the specular reflection angle is higher than the critical one. It means that, using the pure geometrical viewpoint, the lateral wave has a zero amplitude, and with a more precise evaluation its amplitude is smaller than that of the reflected wave by a factor of the order of $1/k_1 R_1$. The energy associated with this propagation originates in the second-order terms of the refracted wave, which arises only when the wavefronts are curved (Heelan, 1953).

Using the ray interpretation, the pressure corresponding to the lateral wave is (Brekhovskikh and Godin, 1992)

$$P = 2i \frac{c_1}{c_2} \left[k_1 \frac{\rho_2}{\rho_1} \left(1 - \frac{c_1^2}{c_2^2} \right) r^{1/2} [r - (z+d) \tan \theta_c]^{3/2} \right]^{-1} \times e^{ik_1(SA+BP+[c_1/c_2]AB)}, \quad (2)$$

where SA is the distance between the source S and point A , BP the distance between point B and observation point P , AB the distance between points A and B along the interface, ρ_1 (respectively, ρ_2) the density of medium 1 (respectively, medium 2), r the transmitter–receiver distance along the interface (also called range), and d (respectively, z) the distance from the source (respectively, the observation point) to the interface. This expression leads easily to the propagation path shown in Fig. 1. The lateral wave is excited at the critical angle (SA), propagates along the interface (AB) with the bulk wave velocity c_2 and radiates back into medium 1 at the critical angle (BP). The lateral wave is observable only from and beyond the critical point which is located at the critical range r_c , corresponding to the limiting case of lack of propagation along the interface (Brekhovskikh and Godin, 1992)

$$r_c = (z+d) \tan \theta_c. \quad (3)$$

The lateral wavefront is not of infinite extent, as shown in Fig. 2 (Ewing *et al.*, 1957; Cerveny and Ravindra, 1971). At a given time t such that $t \leq d/(c_1 \cos \theta_c)$, the incident and reflected wavefronts are connected on the interface at point C together with the refracted wavefront. With increasing time, this point moves along the interface at velocity $v(C) = c_1/\sin \theta(C)$ [$\theta(C)$, angle of incidence corresponding to point C]. When $\theta(C)$ becomes greater than the critical angle

θ_c , the velocity of point C becomes lower than velocity c_2 : $v(C) < c_2$. As a consequence, the refracted wavefront will be more advanced than the incident and reflected wavefronts (Fig. 2). Therefore, the lateral wavefront appears as the wavefront required to link the reflected and the refracted wavefronts on the interface or, in other words, the additional wavefront required to satisfy the boundary conditions (continuity of pressure on each side of the interface and continuity of the displacement normal to the interface). It is connected on the interface to the refracted wavefront and is tangential to the reflected wavefront at the critical range r_c . The lateral wavefront may also be obtained using Huygens construction (Officer, 1958): considering the disturbance propagating along the interface in the lower medium with velocity c_2 , the wavelets generated in the upper medium overlap because the velocity c_2 is greater than the velocity c_1 ; the envelope which results from this overlap forms a plane wavefront, the perpendicular of which gives the ray direction and is oriented at the critical angle with respect to the z axis.

The phases of the lateral and reflected waves are related to different propagation paths and propagation velocities, which results in different arrival times. The wavefronts show that, at a given observation point, the lateral wave arrives before the reflected one and in some regions of space before the direct one. The propagation path of the lateral wave corresponds to the minimum propagation time between the source S and the observation point P ; this is in accordance with the Fermat principle (Officer, 1958).

Because a lateral wave is so closely related to the critical angle, it contributes to the reflected pressure in most of the more complicated systems such as the fluid–solid interface or the layered media with or without absorption. The total pressure reflected by the system contains the specularly reflected wave, the eigenmodes (e.g., Lamb waves), and the lateral waves. In some cases, (e.g., the solid–solid interface) several lateral waves may be identified, depending on the number of critical angles, corresponding to conversion of compressional to shear wave, shear to shear wave, etc. Lateral waves and eigenmodes have analogous propagation paths, but correspond to two specific attenuation behaviors. For distances large compared to the source–interface and observer–interface distances, the lateral wave type amplitude varies as r^{-2} with range r , while the amplitude of the specular wave and of the eigenmodes varies at most as r^{-1} (Ewing *et al.*, 1957). Therefore, the lateral wave type is poorly excited compared to the other phenomena and attenuates strongly with range r . Despite this, the longitudinal lateral wave may be of interest in a nondestructive evaluation procedure because it arrives prior to all other contributions in some regions of space.

III. SIMULATIONS

In order to unambiguously identify the lateral wave, it is desirable that it be separated in the time domain from the other signals. As mentioned in the theoretical part, several waves arrive at the observation point P in medium 1: the direct wave which travels in medium 1 directly from the

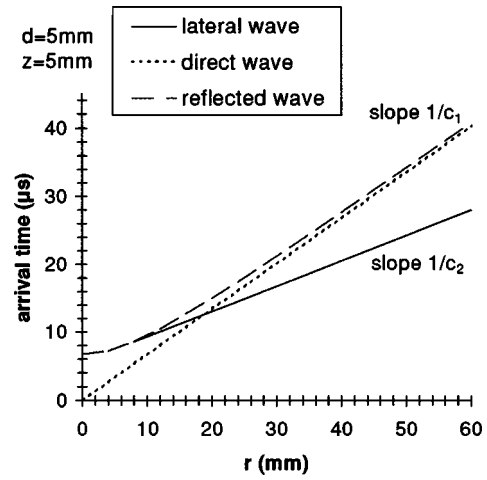


FIG. 3. Theoretical arrival times of the direct, reflected, and lateral waves from a fluid–solid interface; $c_1 = 1490 \text{ m s}^{-1}$, $c_2 = 2680 \text{ m s}^{-1}$.

source to point P (Fig. 1), the wave specularly reflected on the interface between medium 1 and medium 2, the lateral wave which travels on the interface and is radiated back into medium 1 at the critical angle, and other propagation modes such as Lamb modes which arrive at a later time.

The equations of the arrival times of the direct, reflected, and lateral waves, respectively, $t_{\text{direct wave}}$, $t_{\text{reflected wave}}$, and $t_{\text{lateral wave}}$, are

$$t_{\text{direct wave}} = \frac{[r^2 + (z-d)^2]^{1/2}}{c_1}, \quad (4)$$

$$t_{\text{reflected wave}} = \frac{[r^2 + (z+d)^2]^{1/2}}{c_1}, \quad (5)$$

$$t_{\text{lateral wave}} = \frac{r}{c_2} + \frac{(z+d)}{c_1} \left(1 - \frac{c_1^2}{c_2^2}\right)^{1/2}. \quad (6)$$

Theoretical predictions of the arrival times of the direct, reflected, and lateral waves at the receiver (observation point P) are plotted in Fig. 3 as a function of the transmitter–receiver separation r for a water–solid interface with $c_1 = 1490 \text{ m s}^{-1}$ and $c_2 = 2680 \text{ m s}^{-1}$ (bulk wave velocity in Plexiglas).

As previously reported in Sec. II of this paper, the lateral wave can be detected only at some observation points P in medium 1; that is to say Eq. (6) is valid for r values larger than the critical distance r_c [Eq. (3)].

Figure 3 shows that, as the transmitter–receiver separation increases, the arrival times of the direct and reflected waves increase more rapidly than that of the lateral wave and eventually reach the same asymptote of slope $1/c_1$, while the lateral wave reaches an asymptote of slope $1/c_2$. It can be shown that the lateral wave always arrives before the direct wave only for r values larger than r_{min} defined by

$$r_{\text{min}} = (1 - n^2)^{-1/2} [n(z+d) + 2(zd)^{1/2}], \quad (7)$$

where $n = c_1/c_2$.

Figure 4 shows for two different sample materials the predicted relationship between the transducer–sample distance and the transmitter–receiver distance r along the interface corresponding to simultaneous arrival of the direct and

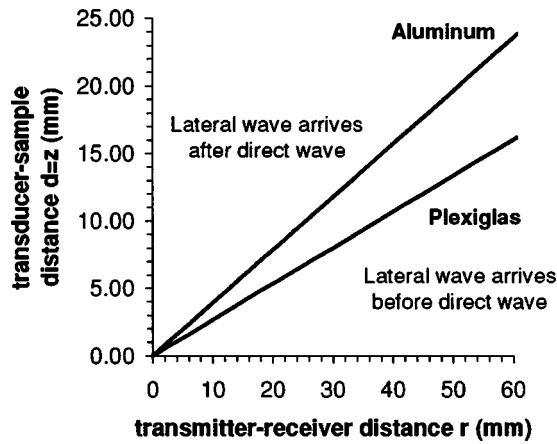


FIG. 4. Predicted limits for separation in the time domain of the direct and longitudinal lateral waves at a water–solid interface ($c_1 = 1490 \text{ m s}^{-1}$; $c_2 = 2680 \text{ m s}^{-1}$ and 6300 m s^{-1} for Plexiglas and aluminum, respectively).

lateral waves, under the assumption that the transmitter– and receiver–sample distances d and z are equal. The two samples, Plexiglas and aluminum with longitudinal velocities of 2680 and 6300 m s^{-1} , respectively, were used as test materials in our experiments. For each sample material, the area defined by (r, d) values under the limit curve defined by

$$z = \frac{r}{2} \left(\frac{1-n}{1+n} \right)^{1/2} \quad (8)$$

corresponds to the case of a lateral wave arriving before the direct wave [Eq. (9)], while in the area above the curve, it is the opposite

$$t_{\text{lateral wave}} \leq t_{\text{direct wave}} \Leftrightarrow z \leq \frac{r}{2} \left(\frac{1-n}{1+n} \right)^{1/2}. \quad (9)$$

Since the longitudinal velocity in cortical bone ranges from 3400 to 4200 m s^{-1} , the limit curve for cortical bone lies in between that of Plexiglas and that of aluminum.

This is the basis of our experimental setup. Equation (3) is useful in determining the area in space where the lateral wave can be observed and Eq. (9) specifies which experimental configuration (transmitter–receiver distance) must be used so that the first arriving signal corresponds to the lateral wave. Note that harmonic theory predicts that the lateral wave is nondispersive; therefore, Eq. (6) may be used with pulses.

IV. EXPERIMENTS

We present here the experimental results of identification of the lateral wave in two test materials with a point source and a point receiver. The technique was then applied *in vitro* to cortical bone specimens immersed in water.

A. Experimental setup

All measurements were performed in a water tank at room temperature (range 18.6 – $23.9 \text{ }^\circ\text{C}$). Two 2×2 -mm 0.5 -MHz quasi-point-source broadband piezoelectric elements (Vermon, Tours, France), one transmitter and one receiver, were placed at normal incidence to the interface (Fig. 5). The transmitter was excited with a broadband 180V pulse

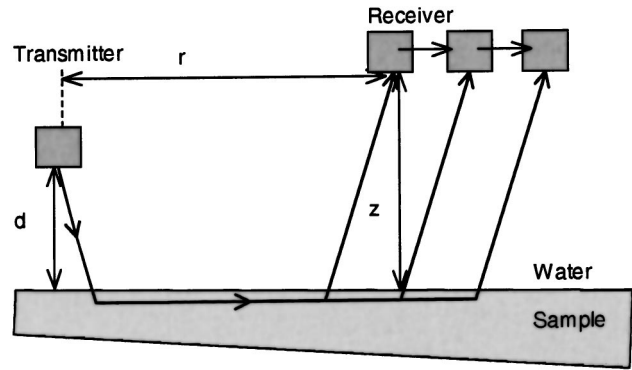


FIG. 5. Experimental setup.

(5052PR, Panametrics, Waltham, MA) and the received signals were recorded at different transmitter–receiver r positions by moving the receiver stepwise (1-, 2-, or 5-mm steps) along the interface. These recordings include the direct wave, the reflected wave, the lateral wave, and all other propagation modes. As mentioned above, the transmitter–receiver, transmitter–sample, and receiver–sample distance (respectively, r , d , and z) were chosen such that the lateral wave was the first arriving signal. In all experiments, the r values were in the range 23 – 60 mm and d or z varied from 2 to 14 mm . In these conditions, the parameter kR introduced in Sec. II is such that $kR \gg 1$.

Two parameters were used to identify the lateral wave:

- (1) the difference in times of flight of the first arriving signal between two measurements at consecutive r positions, from which the propagation velocity c_2 can be calculated using

$$\Delta t = t_{LW_i} - t_{LW_{i+1}} = \frac{r_i - r_{i+1}}{c_2^i}, \quad (10)$$

where t_{LW_i} (respectively, $t_{LW_{i+1}}$) is the time of flight of the first arriving signal when the receiver is at position r_i (respectively, r_{i+1});

- (2) the absolute time-of-flight measurements as a function of distance r which can be compared to the theoretical predictions given by Eq. (6).

In order to determine the experimental quantities d and z , the transmitter– and receiver–sample distances which are used in the theoretical predictions, the transmitter and the receiver were driven individually in the pulse echo mode and the two quantities were measured from the time of flight of the first echo reflected from the interface. The experimental transmitter–receiver separation r , which is also needed to compute the theoretical predictions, was measured from a series of recordings of direct transmission of an ultrasonic pulse from the transmitter to the receiver for each receiver position r with the sample removed from the water tank. The water velocity taken in the time-of-flight predictions was 1490 m s^{-1} (velocity at $22.5 \text{ }^\circ\text{C}$) and the experimental value of the propagation velocity of the first arriving signal was used for the longitudinal velocity in the sample (denoted by c_2).

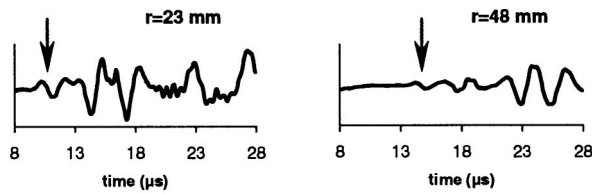


FIG. 6. The rf signals and associated (r,t) diagram for a water–aluminum interface.

B. Specimens/materials

Ultrasonic measurements of the lateral and direct waves were first performed on test materials of known acoustical properties: a 28-mm-thick aluminum plate with a longitudinal ultrasound velocity of 6300 m s^{-1} and a critical angle for excitation of a longitudinal lateral wave at a water–aluminum interface of 13.7° ; and a 25-mm-thick Plexiglas plate with a longitudinal ultrasound velocity of 2680 m s^{-1} and a longitudinal critical angle at a water–Plexiglas interface of 33.8° (Ensminger, 1973). The experimental method was then applied to two human femur specimens with soft tissue and marrow removed. The least irregularly shaped area of the femur specimens was chosen for investigation. The longitudinal velocity in the cortical part of the femur reported in the literature ranges from 3480 to 4200 m s^{-1} along the axial direction (Lee *et al.*, 1997; Lowet and Van der Perre, 1996, 1992; Siegel *et al.*, 1958), which gives a longitudinal critical angle at a water–femur interface in the range 20.8° – 25.4° .

C. Results

Typical recordings [rf signals and associated (r,t) diagrams] are shown in Figs. 6 and 7 for the aluminum and Plexiglas samples. The arrow indicates the first arriving signal which is analyzed. In the (r,t) diagram, the amplitude of the radio-frequency signals has been converted into gray level and plotted versus the transmitter–receiver distance r (vertical axis). The different waves received at distance r from the source are shown with their associated trajectories in the (r,t) plane. In Fig. 7 the signals directly following the first arriving signal correspond to the direct and reflected waves. The direct wave was identified with the additional measurements performed to determine the r values. The following signals of higher amplitude correspond to the eigenmodes of the Plexiglas plate.

The plot of the absolute time of flight versus the transmitter–receiver separation r is shown in Figs. 8 and 9 for the aluminum and Plexiglas samples, respectively, and corresponds to the data shown in Figs. 6 and 7. The mea-

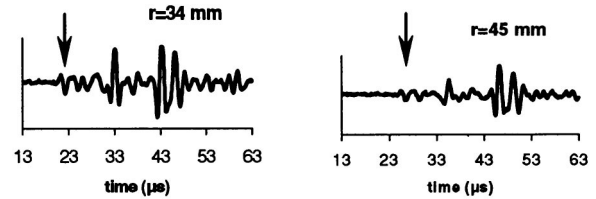


FIG. 7. The rf signal and associated (r,t) diagram for a water–Plexiglas interface.

asured velocities (mean \pm standard deviation) are $6100 \pm 300 \text{ m s}^{-1}$ and $2650 \pm 150 \text{ m s}^{-1}$ for the aluminum and the Plexiglas samples, respectively; they are in good agreement with the reported values for these materials (Ensminger, 1973). The standard deviation of the velocity measurements was calculated from a series of experiments performed at various transducer–sample distances (d,z).

Figure 10 displays the rf recordings [rf signal and associated (r,t) diagram] obtained in one human femur sample. The arrow indicates the first arriving signal which is analyzed. Figure 10 is an interesting case in that several waves seem to arrive at the same time and interfere with each other at small transmitter–receiver distances. In this experiment, we suspected that the requirements given in Eq. (9) were not met, i.e., that the direct wave arrived first, shortly followed by the lateral wave, or both waves arrived at the same time and interfered with each other. Therefore, the first arriving signal was studied after digital subtraction of the data set

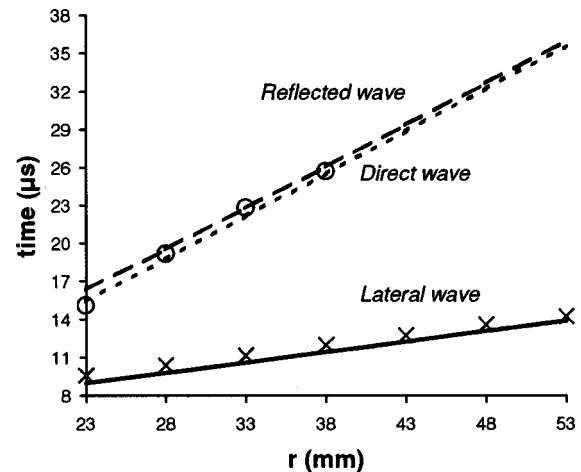


FIG. 8. Time-of-flight versus transmitter–receiver separation r for a water–aluminum interface. The solid, dashed, and dotted lines represent the predicted times of flight of the lateral, reflected, and direct waves, respectively. The dots correspond to the experimental times of flight of the lateral and direct waves.

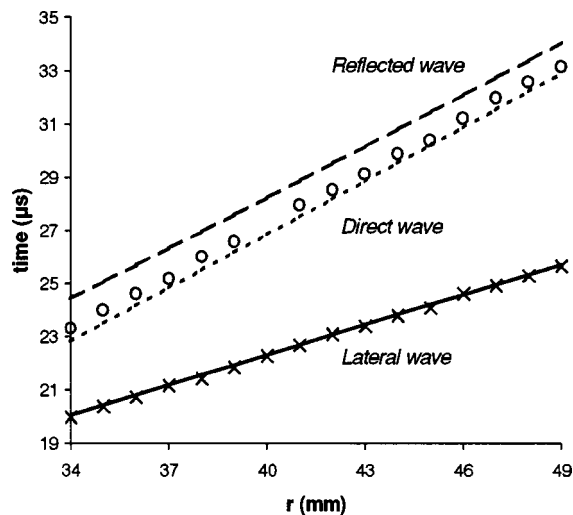


FIG. 9. Time-of-flight versus transmitter–receiver separation r for a water–Plexiglas interface. The solid, dashed, and dotted lines represent the predicted times of flight of the lateral, reflected, and direct waves, respectively. The dots correspond to the experimental times of flight of the lateral and direct waves.

containing only the direct wave from the first data set containing all waves. The result of this digital subtraction on the (r,t) diagram is shown in Fig. 11. The corresponding plot of the absolute time of flight versus the transmitter–receiver separation r for this femur sample is displayed in Fig. 12.

The velocities (mean \pm s.d.) measured in this femur sample are $3750 \pm 150 \text{ m s}^{-1}$ and in another femur sample $3600 \pm 100 \text{ m s}^{-1}$ and $4050 \pm 100 \text{ m s}^{-1}$ at two different sites, all in agreement with reported values.

V. DISCUSSION

The time-of-flight determinations of the direct wave and first arriving signal on the test materials are in good agreement with the theoretical predictions of the direct and lateral waves. As the transmitter–receiver separation r increases, the lateral wave separates more and more in the time domain from the other received signals and therefore it is easier to track it on the rf recordings. However, its amplitude drops

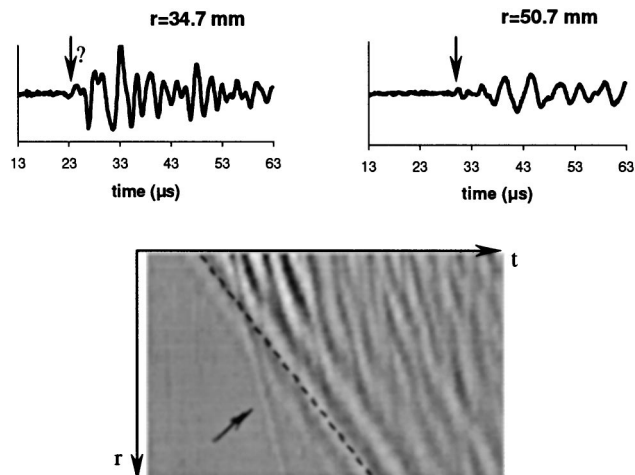


FIG. 10. The rf signal and associated (r,t) diagram for a water–femur interface. The dotted line indicates the direct wave.

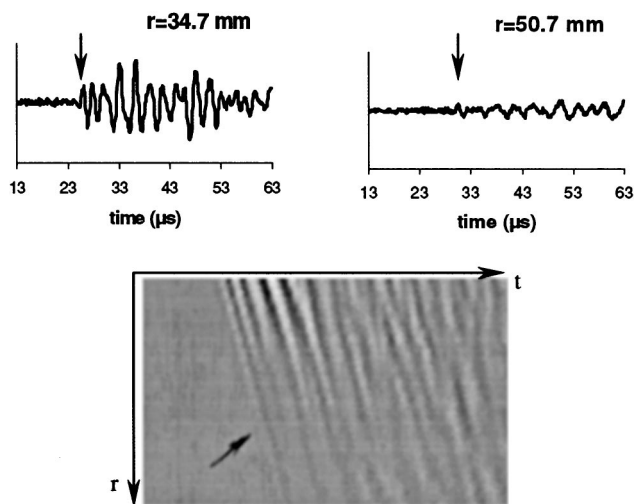


FIG. 11. The rf signal and associated (r,t) diagram for a water–femur interface after digital subtraction of the direct wave.

swiftly with increasing transmitter–receiver separation r and the performance of the data acquisition system may limit the detection of the lateral wave for large r values. This is confirmed in the rf recordings on both aluminum and Plexiglas: the first arriving signal is of very low amplitude compared with the direct, reflected, and other waves. Agreement in the times of flight of the first arriving signal and the lateral wave validates the ultrasonic path followed by the first arriving signal.

For both test materials, the propagation velocities of the first arriving signal measured from the time-of-flight method are close to the longitudinal velocities found in the literature. The standard deviation is larger for aluminum than for Plexiglas. This can be explained by the fact that the velocity is determined by a time-of-flight method (r -step value over difference in times of flight between two consecutive r positions): higher velocities are associated with smaller times of flight and thus lower slopes of time of flight versus r ; there-

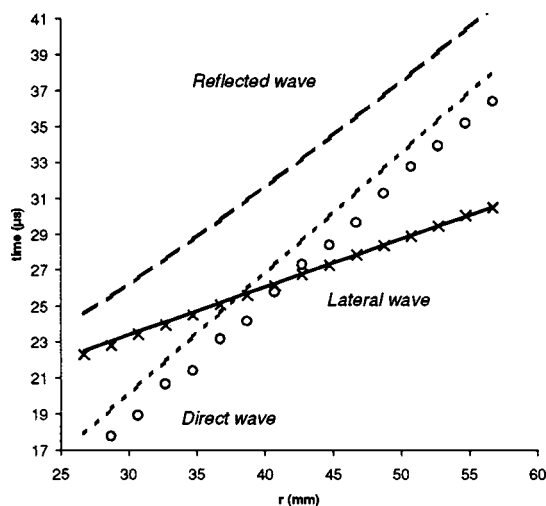


FIG. 12. Time-of-flight versus transmitter–receiver separation r for the water–femur interface corresponding to Fig. 10. The solid, dashed, and dotted lines represent the predicted times of flight of the lateral, reflected, and direct waves, respectively. The dots correspond to the experimental times of flight of the lateral and direct waves.

fore, measurements of higher velocities require a better precision on the time of flight, and thus slope, determination (for example, higher sampling frequency).

The results obtained in one of the human femur specimens and shown in Fig. 10 are very interesting in that for small r values the direct wave arrives slightly before the lateral wave. This is predicted by the theoretical analysis and confirmed by the experimental (r,t) diagram and measurements of the time of flight as a function of transmitter–receiver separation r : on both representations the trajectory of the direct wave clearly crosses that of the studied signal at a r value close to 36–38 mm. As mentioned previously, the direct wave data set was subtracted from the original one in order to analyze the first arriving signal at any r value. The measured propagation velocities range from 3600 to 4050 for two femur specimens and are in agreement with reported values.

These *in vitro* results in test materials and human bone specimens show that the longitudinal lateral wave was successfully excited and detected as the first arriving signal under specific experimental conditions for (r,d,z) . Our results also indicate that the approximation of a planar interface separating two half-spaces seems acceptable in the case of cortical bone specimens immersed in water. Chubachi *et al.* (1992, 1997) have studied the propagation of leaky surface-skimming compressional waves in bone specimens using the defocusing method developed in acoustic microscopy with focused transducers; these waves are in nature similar to the lateral wave described here with quasi-point-source transducers.

Error sources on the velocity measurements include the determination of the accurate time of flight of the first arriving signal and the variation of the receiver–sample distance z with the distance r along the interface. Indeed, improvements on the signal-to-noise ratio could be made by optimizing the sensitivity of the transmitting and the receiving transducers and would result in better time-of-flight determinations. In our experiments, the receiver–sample distance z varied only slightly, so that the assumption $z = \text{constant}$ could easily be made. If necessary, correction for this variation which we have already described (Camus *et al.*, 1998) can be done in the velocity calculations: assuming a plane interface, only the ratio of the receiver–sample distance variation to the distance r (and not the exact value of the receiver–sample distance for each r position) needs to be evaluated to perform this correction.

This axial transmission technique offers a great potential in the study of the mechanical properties of bone in relation to the diagnosis of osteoporosis as it may be applied *in vivo* at various skeletal sites, in particular at peripheral sites. Indeed, the acoustical properties of soft tissue are similar to those of water (sound velocity around 1500–1600 m s^{-1}) so that the transducers may be applied directly onto the skin with a coupling gel. The important parameters are the soft-tissue thickness under the receiver which determines the minimum distance between transmitter and receiver so as to detect the lateral wave as the first arriving signal. In contrast to the transverse transmission technique, which is based on the transmission of ultrasound through bone and requires

placement of a transducer on each side of the bone, the axial transmission technique with its easy transducer setup may be applied to a greater number of skeletal sites.

Finally, it is important to note that we have considered the model of a plane interface between a homogeneous fluid and an isotropic homogeneous nonattenuating solid. These conditions might not be met when experimenting with biological tissues (soft tissue and bone). Therefore, further work should include the influence of heterogeneity, density, anisotropy, and attenuation on the propagation of a longitudinal lateral wave. Effects of the sample thickness in relation to the extension in depth of the lateral wave in the sample should also be investigated.

VI. CONCLUSION

Theoretical predictions of the arrival times of the waves received from a fluid–solid interface with a quasi-point-source ultrasonic transmitter, in particular the lateral wave, have been performed along with experimental investigations on test materials and cortical bone specimens. The first arriving signal was analyzed in terms of arrival time and propagation velocity along the interface. For all samples, good agreement was found between the experimental data and the theoretical predictions of the lateral wave. These results strongly suggest that, in our experimental setup, the lateral wave has been successfully excited and corresponds to the first arriving signal. In conclusion, the nature of the ultrasonic wave which is analyzed in the axial transmission technique has been identified and this work serves as a basis for the development of the technique and the evaluation of the mechanical properties of human cortical bones in relation to the diagnosis of osteoporosis.

ACKNOWLEDGMENT

We acknowledge the support of GIP Ultrasons, Tours, France for providing the transducers.

- Aki, K., and Richards, P. G. (1980). *Quantitative Seismology: Theory and Methods* (Freeman, San Francisco), Vol. 1.
- Brekhovskikh, L., and Godin, O. (1992). *Acoustics of Layered Media II: Point Sources and Bounded Beams. Wave Phenomena* (H. Lotsch) (Springer Verlag, Berlin), Vol. 10.
- Camus, E., Berger, G., and Laugier, P. (1998). "Cortical bone velocity mapping using leaky surface acoustic waves," presented at the IEEE International Ultrasonics Symposium, Sendai, Japan.
- Cervený, V., and Ravindra, R. (1971). *Theory of Seismic Head Waves* (University of Toronto Press, Toronto).
- Chan, K. H., and Bertoni, H. L. (1991). "Ray representation of longitudinal lateral waves in acoustic microscopy," IEEE Trans. Ultrason. Ferroelectr. Freq. Control **38**(1), 27–34.
- Chubachi, N., Asai, T., and Sannomiya, H. (1992). "A new method to measure bone properties by means of leaky surface acoustic waves," J. Acoust. Soc. Jpn. **13**(2), 121–125.
- Chubachi, N., Kanai, H., Sannomiya, T., and Asai, H. (1997). "Reflection-type ultrasonic equipment for bone diagnosis," presented at the World Congress on Ultrasonics, Yokohama Japan.
- Duboeuf, F., Hans, D., Schoot, A. M., Giraud, S., Delmas, P. D., and Meunier, P. J. (1996). "Ultrasound velocity measured at the proximal phalanges: Precision and age-related changes in normal females," Rev. Rhum. Engl. Ed. **63**(6), 427–434.
- Ensminger, D. (1973). *Ultrasonics—The Low- and High-intensity Applications* (Dekker, New York).
- Ewing, W. M., Jardetzky, W. S., and Press, F. (1957). *Elastic Waves in Layered Media* (McGraw-Hill, New York), Vol. 189.

- Foldes, A. J., Rimon, A., Keinan, D. D., and Popovtzer, M. M. (1995). "Quantitative ultrasound of the tibia: a novel approach for assessment of bone status," *Bone (N.Y.)* **17**(4), 363–367.
- Fredfeldt, K.-E. (1986). "Sound velocity in the middle phalanges of the human hand," *Acta Radiol.: Diagn.* **27**(1), 95–96.
- Galea, P. (1992). "Observations of very high P-velocities in the subducted slab, New Zealand, and their relation with the slab geometry," *Geophys. J. Int.* **110**, 238–250.
- Glüer, C. C. (1997). "Quantitative ultrasound techniques for the assessment of osteoporosis: Expert agreement on current status," *J. Bone Min. Res.* **12**(8), 1280–1288.
- Hans, D., Srivastav, S. K., Singal, C., Barkmann, R., Njeh, C. F., Kantorovitch, E., Glueer, C. C., and Genant, H. K. (1999). "Does combining the results from multiple bone sites measured by a new quantitative ultrasound device improve discrimination of hip fracture?," *J. Bone Min. Res.* **14**(4), 644–651.
- Heelan, P. A. (1953). "On the theory of head waves," *Geophysics* **18**(4), 871–893.
- Lee, S. C., Coan, B. S., and Bouxsein, M. L. (1997). "Tibial ultrasound velocity measured *in situ* predicts the material properties of tibial cortical bone," *Bone (N.Y.)* **21**(1), 119–125.
- Lowet, G., and Van der Perre, G. (1996). "Ultrasound velocity measurement in long bones: measurement method and simulation of ultrasound wave propagation," *J. Biomech.* **29**, 1255–1262.
- Lowet, G., and Van der Perre, G. (1992). "Monitoring of bone consolidation by ultrasound velocity measurement," presented at the 14th Annual International Conference of the IEEE Engineering in Medicine and Biology Society, Paris, France.
- Officer, C. B. (1958). *Introduction to the Theory of Sound Transmission with Application to the Ocean* (McGraw-Hill, New York).
- Siegel, I. M., Anast, G. T., and Fields, T. (1958). "The determination of fracture healing by measurement of sound velocity across the fracture site," *Surg. Gynec. Obstet.* **107**, 327–332.
- Wabia, M. (1992). "Lateral waves in anisotropic optical waveguides," *Acta Phys. Pol. A* **81**(4–5), 503–516.

Seismic properties of Asian elephant (*Elephas maximus*) vocalizations and locomotion

C. E. O'Connell-Rodwell^{a)}

Center for Conservation Biology, Department of Biological Sciences, Stanford University,
Stanford, California 94305-5020

B. T. Arnason

Tezar Inc., P.O. Box 26235, Austin, Texas 78755-0235

L. A. Hart^{b)}

Department of Population Health and Reproduction, University of California, Davis, California 95616

(Received 14 February 2000; accepted for publication 14 September 2000)

Seismic and acoustic data were recorded simultaneously from Asian elephants (*Elephas maximus*) during periods of vocalizations and locomotion. Acoustic and seismic signals from rumbles were highly correlated at near and far distances and were in phase near the elephant and were out of phase at an increased distance from the elephant. Data analyses indicated that elephant generated signals associated with rumbles and "foot stomps" propagated at different velocities in the two media, the acoustic signals traveling at 309 m/s and the seismic signals at 248–264 m/s. Both types of signals had predominant frequencies in the range of 20 Hz. Seismic signal amplitudes considerably above background noise were recorded at 40 m from the generating elephants for both the rumble and the stomp. Seismic propagation models suggest that seismic waveforms from vocalizations are potentially detectable by instruments at distances of up to 16 km, and up to 32 km for locomotion generated signals. Thus, if detectable by elephants, these seismic signals could be useful for long distance communication. © 2000 Acoustical Society of America. [S0001-4966(00)03612-2]

PACS numbers: 43.80.Ka, 43.80.Lb, 43.80.Nd [WA]

I. INTRODUCTION

Elephants transmit (Payne *et al.*, 1986; Poole *et al.*, 1988), detect (Heffner and Heffner, 1982), and respond to (Langbauer *et al.*, 1991) airborne low frequency (20 Hz) vocalizations. Elephants may coordinate their long distance movements with other herds using these vocalizations (Martin, 1978), as well as detect and move toward thunderstorms from great distances (Lindeque and Lindeque, 1991).

Elephants communicate acoustically in the 20-Hz frequency range, an effective frequency for long distance transmission of airborne sound waves (Waser and Waser, 1977; Marten and Marler, 1977). When an elephant transmits airborne low frequency (20 Hz) vocalizations, a corresponding seismic wave with similar characteristics is transmitted in the ground (O'Connell *et al.*, 1997; Arnason *et al.*, 1998). This 20-Hz vocalization is also generated within the ideal frequency range for the long distance transmission of seismic energy. Below 20 Hz, the ambient seismic noise increases sharply, reducing the signal-to-noise ratio (Franti *et al.*, 1962). The absorption of seismic energy increases monotonically (in relative proportion) with increasing frequency, strongly attenuating at higher frequencies (White, 1965). Thus, a "sweet zone" window of frequency, where there is a maximum efficiency of transmission of seismic energy, ranges from about 10 to 40 Hz.

Airborne signals vary in their effective transmission range over the surface of the earth, depending on such envi-

ronmental conditions as weather, vegetation structure (Waser and Waser, 1977; Marten and Marler, 1977), height of signal emitter above the ground (Morton, 1975), as well as the time of day, vertical temperature gradients, and wind shear velocity and direction (Garstang *et al.*, 1995; Larom *et al.*, 1997). Scatter and reflection by trees, rocks, and other animals further reduce the signal-to-noise ratio (Michelson and Larsen, 1983), as does the presence of shadow zones close to the ground (Piercy *et al.*, 1977) and signal degradation or distortion over long distances (Richards and Wiley, 1980). Seismic signals, however, are subject to such influences as the homogeneity of the substrate, pore space fluid saturation ratio, and differential pressures (Toksöz *et al.*, 1979), such that it may be beneficial to communicate through the air under certain conditions and through the ground under other conditions.

The major modes of energy transfer in solid media are body waves such as P waves, S waves, combinations of P and S waves, or surface waves such as Rayleigh waves and Love waves (Fig. 1). Rayleigh waves expand in shallow, almost two-dimensional, cylindrical concentric shells along the surface of the earth, constrained to shallow depths. In an idealized, nonabsorbing case, the amplitude of a Rayleigh wave during ground surface transmission is inversely proportional to the square root of R (R = distance from the emitter to the receiver) with a loss of 3 dB for every doubling of distance. In contrast, body waves (Fig. 1) and airborne waves (in the ideal case of homogeneous air) expand in spherical concentric shells, or in three dimensions. Thus, the amplitude of these waves would be inversely proportional to R , with a loss of 6 dB with every doubling of distance. Under strict

^{a)}Electronic mail: oconnell@bing.stanford.edu

^{b)}Electronic mail: lahart@ucdavis.edu

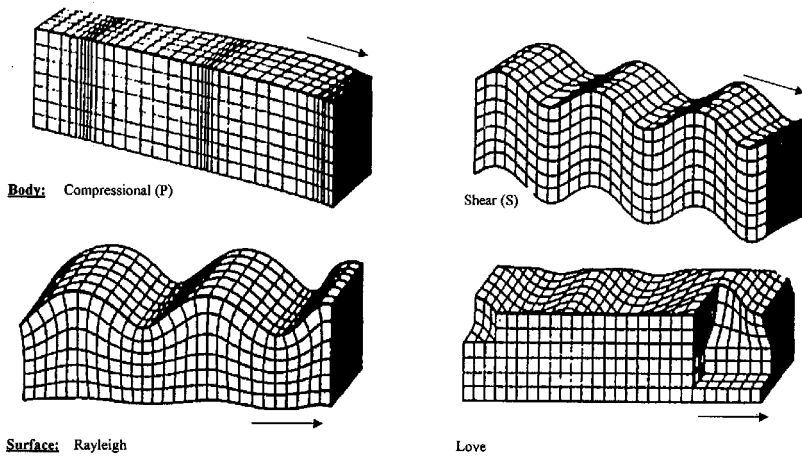


FIG. 1. Propagation of mechanical waves in the ground (adapted from Aicher and Tautz, 1990). Of all the wave types, only Rayleigh waves can travel as slow as 248–264 m/s in the ground. Other wave types exhibit a higher velocity and may suffer more attenuation with distance.

homogeneous, low absorption, isotropic conditions, a signal propagated as a Rayleigh wave attenuates less than airborne signals.

Among seismic signals, Rayleigh waves have been found in communication signals made by arthropods (Markl, 1983), crustaceans (Aicher and Tautz, 1990), amphibians (Narins, 1990), and elephant seals (Shipley *et al.*, 1992). Seismic signals can be a powerful component of an organism's communication system, serving as a tool for mate finding, prey detection, mutualism, intraspecific spacing, as well as inter- and intraspecific warnings. Organisms using seismic signals have a varied means of producing vibrations and use contact with a substrate for detecting the signals. Seismic signaling has been documented in a diverse range of arthropods (Cocroft, 1996; Sandeman *et al.*, 1996; Hoikkala *et al.*, 1994; Aicher and Tautz, 1990; DeVries, 1990; Brownell and Farley, 1979; Markl and Fuchs, 1972), as well as in amphibians (Narins 1990), fish (Dijkgraaf, 1967), and reptiles (Hetherington, 1992; Vleit, 1989; Herzog and Burghardt, 1977; Hartline, 1971). In mammals, seismic signaling has been found in a number of small rodent species (Narins *et al.*, 1997; Randall, 1993; Narins *et al.*, 1992; Rado *et al.*, 1987). The only large mammal known to detect seismic signals thus far is the elephant seal (Shipley *et al.*, 1992), where

detection was demonstrated up to 20 m. Human seismic energy generated by walking has been detected by instruments up to 50 m from the source (Department of Defense, 1965).

Although implied in many cases, the detection of seismic signals, or seismic components of signals, has been difficult to demonstrate behaviorally for many species. Some clear cases have been made, especially in arthropods (Cocroft, 1996, Aicher and Tautz, 1990), the blind mole rat (Heth *et al.*, 1991; Nevo *et al.*, 1991), and the golden mole (Narins *et al.*, 1997).

In this article, we describe the acoustic and seismic propagation of the vibrations associated with elephant vocalizations and movement, as measured in the air and ground, and measure signal levels within the ground media. We also discuss the implications that the presence of seismic components of vocalizations and locomotion might have for elephant long distance communication.

II. METHOD

We simultaneously recorded airborne and seismic signals during periods of vocalizations and locomotion by two female Asian elephants at a private training facility in Texas. Locomotion data were collected when the elephants moved

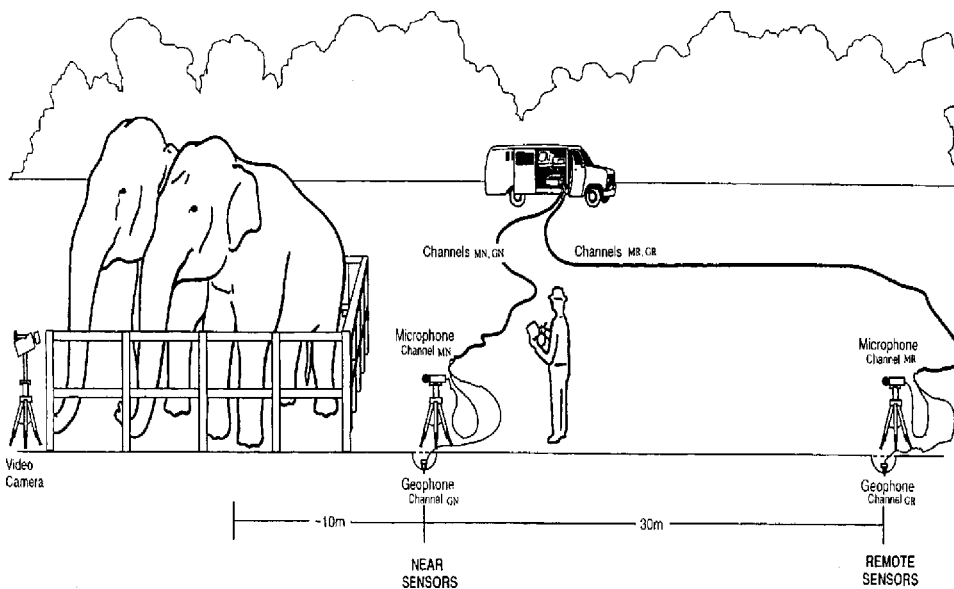


FIG. 2. Recording setup for seismic propagation experiments (artist: Steven Oerding).

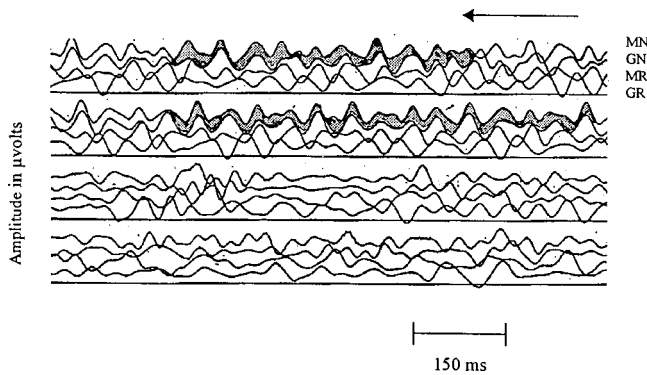


FIG. 3. The domain file of four channels illustrated during a rumble. Each channel was antialias filtered with a 16-bit analog-to-digital converter. The highlighted section of a rumble vocalization illustrates that channels MN and GN, the near microphone and geophone pair, record approximately the same waveform in phase, indicating that the signal is propagated from the same source, but then travels at different rates by the time the signal reaches channels MR and GR, the remote pair of sensors. Calculations for the velocity of the rumble signal moving between the near and far sensors, both acoustic and seismic, are summarized in Table II.

their feet during mock charges, a behavior we termed “foot stomping.” Data were acquired and processed by an integrated, computerized recording system housed in a van. Four channels of a data acquisition system acquired and processed signals simultaneously from two microphone/geophone pairs at near and remote points 10 and 40 m from the elephants (Fig. 2).

At the near and remote locations, the individual microphone and geophone were each connected to a junction box, which was wired to the data acquisition system through a two-twisted pair, shielded cable. Each of the two geophones was buried along with its loose cable to a depth of 14 cm directly beneath the corresponding microphone, which was mounted on a tripod at 0.5 m above the ground. At the near location, cable A carried channels microphone near (MN) and geophone near (GN) from the microphone and geophone to the data acquisition system, while cable B carried the remote channels microphone remote (MR) and geophone remote (GR) from the microphone and geophone.

Airborne signals were recorded on channels MN and MR, with a bandwidth of 1.0–250 Hz using a Neumann KM 131 omni-directional, free-field equalized pressure transducer microphone, with a flat response of 20–20 000 Hz, and

a Sony ECM-999PR 150-degree directional condenser microphone, with a frequency response of 20–20 000 Hz. Seismic signals were recorded on channels GN and GR using two Mandrel 10-Hz MD-79 vertically polarized geophones with a transduction coefficient of 0.230 V/cm/s.

The four channels of the data acquisition system were sequentially sampled at an aggregate rate of 8000 samples/second. After recordings were completed, a trapezoidal zero-phase filter of 3, 6, 40, and 100 Hz (cutoffs at 3 and 100 Hz; plateau at 6–40 Hz) was applied to all channels equally for the purposes of analysis. After filtering out the higher frequency events, a normalized cross correlation coefficient (CCC) function was calculated to determine the degree of similarity between signal waveforms and was computed between pairs of channels during rumbles and locomotion, comparing recordings from the near location, the far location, acoustic sensors, and seismic sensors. When normalized, a cross correlation of 1 indicates a perfect match, and values near zero indicate very little correlation (Sheriff, 1973). Automatic gain control was applied before plotting data so that small and large events could be viewed simultaneously.

The behavior of the elephants was continuously video and audio recorded using a Panasonic camcorder. Specific behaviors and the times of onset were noted: rumble vocalizations (evident from audible harmonics), movements, and social interactions. In the recording system, channels MN and GN carried the near microphone and near geophone signal, respectively, and channels MR and GR carried the remote microphone and remote geophone signals. Detailed analyses were conducted on rumbles and foot stomps drawn from three time domain files.

III. RESULTS

Rumbles and foot stomps were recorded on all four sensors (Fig. 3). Figure 4 shows a time domain file recorded during “foot stomping,” captured on the geophone records of channels GN and GR. “Foot stomps” had durations of 103–250 ms, whereas rumbles continued for 3–5 s.

We first analyzed the correlation between the acoustic and seismic signals of the rumble at the paired sets of near and far sensors. Table I reports the cross correlation coefficients (CCCs) and time lags of the maximum CCCs for the

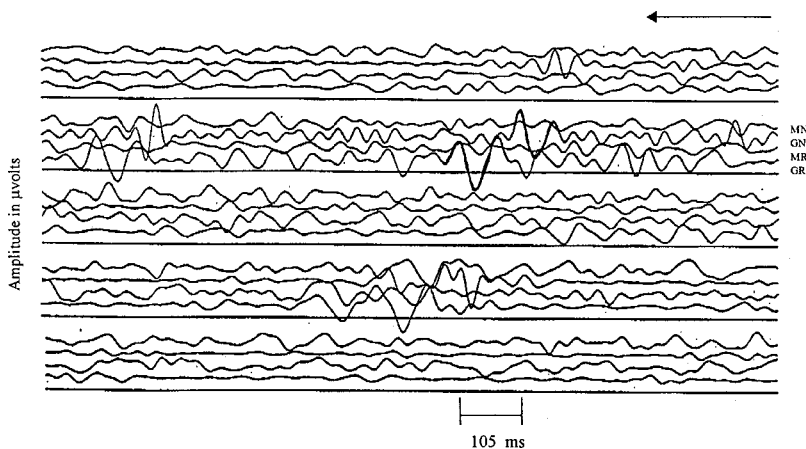


FIG. 4. Time domain file illustrating a foot stomp. The highlighted section illustrates that there is a substantial amount of seismic signal as measured in channels GN and GR. The signal is not distinguishable in the microphones (channels MN and MR).

TABLE I. Normalized cross correlation coefficient (CCC) functions and time lags computed for a rumble drawn from the microphone and geophone channels of the data acquisition system at the near and remote locations.

Sensors (channels)	Max CCC rumble	Lag (ms) rumble
Near: acoustic (MN), seismic (GN)	+0.820	1
Remote: acoustic (MR), seismic (GR)	+0.742	78.5

acoustic and seismic propagation of a single rumble at the near and then the far sensors. The duration of the CCC operator is 800 ms and the length of the CCC function output is 175 ms. For the rumble at the near recording site, signals on the record from the microphone and geophone (channels MN and GN) are highly correlated and have a brief time lag. The nearly instantaneous signal correlation between the two near sensors suggests that the elephant vocalizations were coupled to the air and ground in the elephant's immediate vicinity. The air pressure and ground motion near the elephant were in phase and highly correlated, indicating that both acoustic and seismic signals most likely originated from a source at or near the elephant. Upon reaching the far microphone and geophone, the signals were still well correlated, but now were temporally separate and no longer in phase as shown by the time lag, indicating that the acoustic and seismic signals were traveling at different velocities. Since the foot stomp was not evident on the acoustic record, only the rumble is presented in Table I.

We then analyzed the acoustic and seismic signal velocities of propagation from the recorded duration of time lapsed between the signal's arrival at the near and remote sensors, as represented in each case by the number of milliseconds of delay, as shown in Table II. The CCCs, time lags, and associated velocities of energy are presented for the near and far acoustic signals from the rumble. Comparable seismic signals are analyzed for both the rumble and the foot stomp, since the foot stomp is evident in the seismic but not acoustic record. For the rumble, acoustic signals from the near and far microphones (channels MN and MR) have a high maximum correlation across the distance with a lag time equivalent to the approximate velocity of air-borne sounds. The seismic signals in the near and far geophones (channels GN and GR) are also highly correlated with a time lag corresponding to a slower velocity of 248 m/s, suggestive of a Rayleigh wave type mode of propagation. Even though it was a stronger

signal, the CCC for the stomp was lower than that of the vocalization due to the broadband signal produced by the elephant foot. A broadband signal experiences greater dispersion, which has the tendency to lower the value of the CCC. The vocalizations have a narrower bandwidth, less dispersion, and thus a higher CCC value.

Thus, the acoustic and seismic signals from the rumble propagated separately at different velocities. Although the "foot stomp" signals were not perceptible in the microphones, the geophones detected substantial ground motion. The geophone records show a time lag equivalent to a seismic velocity of 264 m/s, similar to the seismic velocity recorded for the vocalizations.

The predominant frequency was estimated from the records as half the number of times that the computer trace (a time plot domain) crossed the axis per unit time. The mean frequency measured over four recorded rumbles was 20.66 Hz (± 2.07 s.d.), and 24.03 Hz (± 2.98 s.d.) for five "foot stomps." The duration of stomps was short and the frequency bandwidths of the stomps were broad, hence the higher frequency estimate and larger standard deviation. In contrast, the longer duration of rumbles was associated with a narrower frequency bandwidth, allowing calculation of a dominant frequency.

We noted a sharp drop-off of higher frequency acoustical energy over the 30 m from the near to the remote microphone. The acoustic recording from the microphone at 10 m shows significant rumble energy at the fundamental frequency (20 Hz); however, strong higher frequency harmonics, in the range of 40–100 Hz, predominated in the record. At the greater distance of 40 m, the 20-Hz rumble was clearly visible and the higher frequencies were attenuated and were nearly invisible. This attenuation in the acoustic transmission of the rumble vocalization occurred over a distance of only 30 m.

We then measured the vertical component of ground motion velocity at each geophone position by converting the output voltage of each geophone to units of velocity in $\mu\text{m/s}$. We used rms velocity for the rumble (due to the narrow bandwidth and extended duration of the signal) and peak-to-peak velocity for the stomp (due to the short duration, broadband nature of the signal), and present results from three rumbles and three stomps (Table III). An amplitude analysis from the geophone of one of the typical rumbles shows a rms voltage of 10.1 μV on the nearby geophone (estimated to be 3 to 12 m from the generating elephant), while one of the

TABLE II. Normalized cross correlation coefficient functions (CCC), time lags and velocities computed for a rumble and a stomp from acoustic and seismic sensors.

Sensors (channels)	Max CCC		Lag (ms)		Velocity (m/s)	
	Rumble	Stomp	Rumble	Stomp	Rumble	Stomp
Acoustic (MN, MR)	+0.806		98.5		309 ^a	
Seismic (GN, GR)	+0.762	+0.507	123	113	248	264

^aThe actual speed of sound in air is STP 340 m/s. Our measurement of 309 m/s was due to the difference in specifications between the two microphones causing an unequal phase shift at 20 Hz. We used a Sony and a Neumann microphone, each having a different delay between the time that the 20-Hz signal reaches the sensor and the time it outputs the corresponding voltage. We did not have this problem with our geophones as they were well matched.

TABLE III. Actual ground motion calculated from signal voltage as signal rms velocity for rumbles and as peak-to-peak (P-P) velocity for stomps. All measurements of velocity are presented in $\mu\text{m/s}$.

Rumble	Ground motion (rms velocity in $\mu\text{m/s}$)	
	Near	Far
1	0.212	0.121
2	0.178	0.086
3	0.437	0.264
Stomp	Ground motion (P-P velocity in $\mu\text{m/s}$)	
	Near	Far
1	12.5	4.2
2	15.3	3.6
3	48.7	17.0

“stomps” shows a peak-to-peak amplitude of 1124 μV . The measurements of the same rumble and stomp at a distance of 40 m were 6.1 and 392 μV , respectively. These measurements represented the relative ground motion velocities at the near geophone of 0.437 and 48.7 $\mu\text{m/s}$, and at the far geophone 0.264 and 17.0 $\mu\text{m/s}$ of velocity for the rumble and stomp, respectively.

In order to estimate the maximum detectable range of these signals, they must be compared to ambient seismic ground noise, figures we obtained from Frantti (1962). We calculated a minimum ground rms velocity noise at 20 Hz of 0.316 nm/s at a bandwidth of 1 Hz for the rumble. The minimum ground peak-to-peak velocity noise at 20 Hz was calculated as about 5 nm/s with a bandwidth of 10 Hz for the stomp. Using the model published for Rayleigh wave propagation in Solenhofen limestone (White, 1965) and our amplitude measurements at the near and far geophones, we are able to estimate the signal-to-noise ratios at extended distances from the generating elephant. We used these estimates to model signal-to-noise ratios as a function of distance from the generating elephant in the expression:

$$\text{SNR}(x) = K \left(\frac{e^{-\alpha x}}{\sqrt{x}} \right),$$

where K = a constant of proportionality, $\text{SNR}(x)$ = the SNR (signal to noise ratio) at distance x , e = the inverse of the natural (Napierian) logarithm, α_{Rayleigh} = the Rayleigh wave attenuation coefficient in units of (1/km) = 0.106/km for Solenhofen limestone (White, 1965) and x = the distance in km from the generating elephant to the point of SNR estimation. [A value for alpha (the absorption coefficient) must be chosen before an estimate of the SNR can be derived. Solenhofen limestone was used as a geological standard, which has a calculated Rayleigh wave coefficient of 0.106 per k @20 H (White, 1965). Solenhofen limestone is one of the least absorbing rock types.]

Table IV shows these values from the model. For example, at about 4 km from the generating elephant, the estimated signal-to-noise ratio of the stomp was about 222 and about 43.2 for the strongest rumble. Assuming five as a basic threshold of detection for the signal-to-noise ratio, the results of the model project that seismic signals from the elephant

TABLE IV. Signal-to-noise-ratio (SNR) estimated for the rumble and stomp energy as a function of distance from the generating elephant.

Distance (km)	Rumble						
	1		2		3		
	Near	Far	Near	Far	Near	Far	
1	57.7	68.8	48.5	48.9	119	150	
2	36.7	43.8	30.8	31.1	75.5	95.5	
4	21.0	25.0	17.6	17.8	43.2	54.6	
8	9.7	11.6	8.2	8.2	20.0	25.3	
16	2.9	3.5	2.5	2.5	6.1	17.7	
32	0.4	0.5	0.3	0.3	0.8	1.0	
Distance (km)	Stomp						
	1	838	611	214	152	263	129
	2	533	388	137	96.7	167	82.3
	4	305	222	78.2	55.3	95.8	47.1
	8	141	103	36.2	25.6	44.3	21.8
	16	43	31	11.0	7.8	13.4	6.6
	32	5.5	4.0	1.4	1.0	1.7	.9

rumbles (that we recorded) could be detected instrumentally above the ambient noise level at distances of up to 16 km and the “stomp” up to 32 km. Detection distances may be larger or smaller depending on the sensory abilities and specific signal processing algorithms that the elephant may employ to receive and decipher signals and the characteristics of the substrate.

IV. DISCUSSION

Our results show that elephant rumbles travel separately through the air and the ground. Both the rumble and the “stomp” have an apparent velocity of 248–264 m/s in the ground, a velocity substantially slower than the speed of sound in air. As air-to-ground coupling is minimal if the phase velocity of surface waves is significantly different than the speed of sound in air (Press and Ewing, 1951), the specific velocity for these signals demonstrates that they were not traveling through the air medium and coupling with the ground at the remote sensor.

The velocities of seismic waves vary depending on the substrate (White, 1965). In addition, Rayleigh waves vary in velocity (Press and Ewing, 1951), but among the various types of seismic waves, Rayleigh waves are the only ones with significant vertical components of motion capable of traveling as slow as the signals measured in this study (248–264 m/s) (White, 1965). Thus, both the seismic vocalization and “foot stomp” signals appear to be predominantly Rayleigh wave.

All airborne and seismic signals were produced with predominant frequencies centered around 20 Hz. A 20-Hz signal is within the ideal frequency range for the long distance transmission of sounds in the air (Waser and Waser, 1977) and ground (Frantti *et al.*, 1962).

As Rayleigh waves were slower than acoustic waves in the medium tested (248 m/s versus 340 m/s), a shorter wavelength was produced (248 m/s/20 Hz = 12.4 m versus 340 m/s/20 Hz = 17 m), making localization of sounds more feasible in the ground than in the air. We suggest that localization might be further facilitated in the ground due to the

fact that there is a greater phase difference between the front and back feet of an elephant relative to the phase difference between its two ears (approximately 2–2.5 m versus ± 0.5 m). The distance to a sound source could also be determined if elephants were able to use the difference in time of arrival between the seismic and acoustic signals to determine how far away a sound originated.

In comparison with acoustic signals, two physical properties that favor Rayleigh waves for long-distance communication are the lesser rate of attenuation associated with cylindrical rather than spherical spreading and the lesser effects of the environmental influences such as temperature, wind shear, and air pressure. Snell's law indicates that, due to temperature effects on sound velocity, sound waves are refracted upward into the atmosphere (Uman, 1984). Thus, thunder is seldom detected beyond 25 km, a type of "outer limit" due to refraction caused by temperature gradients and wind shear (Fleagle, 1949). Computer simulation models indicate that under temperature inversion conditions (which tend to increase audibility), low frequency airborne elephant vocalizations have the potential of traveling up to 10 km, and under noninversion conditions, up to 2 km (Larom *et al.*, 1997; Garstang *et al.*, 1995). If elephants were capable of detecting the seismic information we measured, the maximum range of their airborne communication would be enhanced considerably, according to distances modeled in this article for rumbles and foot "stomps."

Rayleigh waves are subject to the heterogeneous nature of the rock strata, however, implying that homogeneous hard substrates would have the best transmission quality. It is conceivable, then, that elephants would favor certain substrates when attempting to communicate over long distances, something akin to a whale using the SOFAR channel (Payne, 1995), or calling at a certain period of day to maximize signal transmission (Larom, 1997). Although seismic signals may not carry the specific spectral and intensity information that air-borne signals contain, they could, if elephants can perceive them, provide a general localizing mechanism based on time or phase differences (Aicher and Tautz, 1990), facilitating coordinated elephant movements beyond the range of air-borne signals.

Reuter *et al.* (1998) suggest that detection of seismic signals in elephants may be possible via bone conduction, due to the size of their middle ear ossicles. Somatosensory reception in the feet may also play a role in seismic reception and would be a more direct mechanism to detect vibrations without the problem of attenuation between the foot and the ear (O'Connell *et al.*, 1999). Such somatosensory receptors have been found in the trunk of the elephant (Rasmussen and Munger, 1996). Mole rats press their heads against the sides of their burrow (Rado *et al.*, 1987) and golden moles dip their heads in the sand (Narins *et al.*, 1997) presumably in order to make a more direct contact between the malleus and the vibrating substrate rather than suffering the attenuation problem of bone conduction via the feet.

If elephants could detect the seismic properties of low frequency vocalizations, movements of other herds, and weather patterns, seismic signals could expand the range of elephants' long distance communication capabilities, adding

a powerful component to their sensory perception. As long distance air-borne vocal communication is an important component of mate finding in elephants (Langbauer *et al.*, 1991), seismic properties of vocalizations may play a role in mate finding as well.

ACKNOWLEDGMENTS

We thank Peter Narins, Peter Marler, Don Owings, Bill Hamilton, Ben Hart, and Timothy Rodwell for their helpful comments on earlier drafts of the manuscript. John Fett Instruments provided geophones and some seismic bibliographic material. Constantin Popa and the Namibian Government loaned some communications equipment. Tezar, Inc. provided the customized data acquisition system. We would also like to thank the following facilities and their staffs for helping make the field work for this study possible: Pat Derby and Ed Stewart at the Performing Animal Welfare Society (PAWS), Dave Blasko and Steve Johnson at Marine World Africa, USA, Mike Tucker, Lisa Clay, and Scott Maddox at the Caldwell Zoo, and Mark Fox, Bob Steele, and Bucky Steele at Bucky Steele's private training facility in Texas.

- Aicher, B., and Tautz, J. (1990). "Vibrational communication in the fiddler crab, *Uca pugilator*: Signal transmission through the substratum," *J. Comp. Physiol.* **166**, 345–354.
- Arnason, B., O'Connell, C. E., and Hart, L. A. (1998). "Long range properties of seismic transmission of elephant vocalizations," *J. Acoust. Soc. Am.* **104**(3Pt.2), 1810.
- Brownell, P., and Farley, R. D. (1979). "Detection of vibrations in sand by tarsal sense organs of the nocturnal scorpion *Paruroctonus mesaensis*," *J. Comp. Physiol.* **131**, 23–30.
- Cocroft, R. B. (1996). "Insect vibrational defence signals," *Nature (London)* **382**, 679.
- Department of Defense. (1965). "Seismic intrusion detector for use in Republic of Vietnam," Department of Defense Dir 5200.10, Authority E. O. 11652 Sec. 5(A) and (D), LBJ Library PSM, p. 12.
- DeVries, P. J. (1990). "Enhancement of symbioses between butterfly caterpillars and ants by vibrational communication," *Science* **248**, 1104–1106.
- Dijkgraaf, S. (1967). *Lateral Line Detectors*, edited by P. H. Cahn (Indiana Univ. Press, Bloomington), pp. 83–95.
- Fleagle, R. G. (1949). "The audibility of thunder," *J. Acoust. Soc. Am.* **21**, 411–412.
- Frantti, G. F., Willis, D. E., and Wilson, J. T. (1962). "The spectrum of seismic noise," *Bull. Seismol. Soc. Am.* **52**, 113–121.
- Garstang, M., Larom, D., Raspet, R., and Lindeque, M. (1995). "Atmospheric controls on elephant communication," *J. Exp. Biol.* **198**, 939–951.
- Hartline, P. H. (1971). "Mid-brain responses of the auditory and somatic vibration systems in snakes," *J. Exp. Biol.* **54**, 373–389.
- Heffner, R., and Heffner, H. (1982). "Hearing in the elephant (*Elephas maximus*)," *J. Comp. Physiol. Psychol.* **96**, 926–944.
- Herzog, H. A., and Burghardt, G. M. (1977). "Vocalizations in juvenile crocodylians," *Z. Tierpsychol.* **44**, 294–304.
- Heth, G., Frankenberg, E., Pratt, H. and Nevo, E. (1991). "Seismic communication in the blind subterranean mole-rat: patterns of head thumping and of their detection in the *Spalax ehrenbergi* superspecies in Israel," *J. Zool. Lond.* **224**, 633–638.
- Hetherington, T. E. (1992). "Behavioural use of seismic cues by the sand-swimming lizard *Scincus-Scincus*," *Ethol. Ecol. Evol.* **4**, 5–14.
- Hoikkala, A., Kaneshiro, K. Y., and Hoy, R. R. (1994). "Courtship songs of the picture winged *Drosophila planitibia* subgroup species," *Anim. Behav.* **47**, 1363–1374.
- Langbauer, Jr., W. R., Payne, K. B., Charif, R. A., Rapaport, L., and Osborn, F. (1991). "African elephants respond to distant playbacks of low-frequency conspecific calls," *J. Exp. Biol.* **157**, 35–46.
- Larom, D., Garstang, M., Payne, K., Raspet, R., and Lindeque, M. (1997). "The influence of surface atmospheric conditions on the range and area reached by animal vocalizations," *J. Exp. Biol.* **200**, 421–431.

- Lindeque, M., and Lindeque, P. M. (1991). "Satellite tracking of elephants in northwestern Namibia," *Afr. J. Ecol.* **29**, 196–206.
- Markl, H. (1983). "Vibrational communication," in *Neuroethology and Behavioral Physiology*, edited by F. Huber and H. Markl (Springer-Verlag, Berlin), pp. 332–353.
- Markl, H., and Fuchs, S. (1972). "Alarm by rapping in carpenter ants," *Z. Vergl. Physiol.* **76**, 204–225.
- Marten, K., and Marler, P. (1977). "Sound transmission and its significance for animal vocalization," *Behav. Ecol. Sociobiol.* **2**, 271–290.
- Martin, R. (1978). "Aspects of elephant social organization," *Rhodesian Sci. News* **12**, 184–187.
- Michelson, A., and Larsen, O. N. (1983). "Strategies for acoustic communication in complex environments," in *Neuroethology and Behavioral Physiology*, edited by F. Huber and H. Markl (Springer-Verlag, Berlin), pp. 321–331.
- Morton, E. S. (1975). "Ecological sources of selection on avian sounds," *Am. Nat.* **109**, 17–34.
- Narins, P. M. (1990). "Seismic communication in Anuran amphibians White-Lipped Frogs thump the ground as they chirp," *BioScience* **40**, 268–274.
- Narins, P. M., Lewis, E. R., Jarvis, J. U. M., and O'Riain, J. (1997). "The use of seismic signals by fossorial southern African mammals: a neuroethological gold mine," *Brain Res. Bull.* **44**, 641–646.
- Narins, P. M., Reichman, O. J., Jarvis, J. U. M., and Lewis, E. R. (1992). "Seismic signal transmission between burrows of the cape mole-rat, *Georychus capensis*," *J. Comp. Physiol.* **170**, 13–22.
- Nevo, E., Heth, G., and Pratt, H. (1991). "Seismic communication in a blind subterranean mammal: A major somatosensory mechanism in adaptive evolution underground," *Proc. Natl. Acad. Sci. U.S.A.* **88**, 1256–1260.
- O'Connell, C. E., Hart, L. A., and Arnason, B. (1999). "Response to 'Elephant hearing,'" *J. Acoust. Soc. Am.* **105**, 2051–2052.
- O'Connell, C. E., Arnason, B., and Hart, L. A. (1997). "Seismic transmission of elephant vocalizations and movement," *J. Acoust. Soc. Am.* **102**(5Pt.2), 3124.
- Payne, K. B., Langbauer, Jr., W. R., and Thomas, E. M. (1986). "Infrasonic calls of the Asian elephant," *Behav. Ecol. Sociobiol.* **18**, 297–301.
- Payne, R. (1995). *Among Whales* (Scribner, New York), pp. 383–393.
- Piercy, J. E., Embleton, T. F. W., and Sutherland, L. C. (1977). "Review of noise propagation in the atmosphere," *J. Acoust. Soc. Am.* **61**, 1403–1418.
- Poole, J. H., Payne, K. B., Langbauer, Jr., W. R., and Moss, C. J. (1988). "The social context of some very low frequency calls of African elephants," *Behav. Ecol. Sociobiol.* **22**, 385–392.
- Press, F., and Ewing, M. (1951). "Ground roll coupling to atmospheric compressional waves," *Geophysics* **16**, 416–430.
- Rado, R., Levi, N., Hauser, H., Witcher, J., Adler, N., Intrator, N., Wollberg, Z., and Terkel, J. (1987). "Seismic signalling as a means of communication in a subterranean mammal," *Anim. Behav.* **35**, 1249–1251.
- Randall, J. A. (1993). "Behavioural adaptations of desert rodents Heteromyidae," *Anim. Behav.* **45**, 263–287.
- Rasmussen, L. E. L., and Munger, B. (1996). "The sensorineural specializations of the trunk tip (finger) of the Asian elephant, *Elephas maximus*," *Anat. Rec.* **246**, 127–134.
- Reuter, T., Nummela, S., and Hemila, S. (1998). "Elephant hearing," *J. Acoust. Soc. Am.* **104**, 1122–1123.
- Richards, D. G., and Wiley, R. H. (1980). "Reverberations and amplitude fluctuations in the propagation of sound in a forest: implications for animal communication," *Am. Nat.* **115**, 381–399.
- Sandeman, D. C., Tautz, J., and Lindauer, M. (1996). "Transmission of vibration across honeycombs and its detection by bee leg receptors," *J. Exp. Biol.* **199**, 2585–2594.
- Sheriff, R. E. (1973). *Encyclopedic Dictionary of Exploration Geophysics* (Society of Exploration Geophysicists, Tulsa, OK), p. 42.
- Shiple, C., Stewart, B. S., and Bass, J. (1992). "Seismic communication in northern Elephant seals," in *Marine Mammal Sensory Systems*, edited by J. A. Thomas, R. A. Kastelein, and A. Y. Supin (Plenum, New York), pp. 553–562.
- Toksöz, M. N., Johnston, D. H., and Timur, A. (1979). "Attenuation of seismic waves in dry and saturated rocks: I. Laboratory measurements," *Geophysics* **44**(4), 681–690.
- Uman, M. A. (1984). *Lightning* (Dover, New York), pp. 181–201.
- Vleit, K. A. (1989). "Social displays of the American alligator (*Alligator mississippiensis*)," *Am. Zool.* **29**, 1019–1031.
- Waser, P., and Waser, M. S. (1977). "Experimental studies of primate vocalizations: specializations for long-distance propagation," *Z. Tierpsychol.* **43**, 239–263.
- White, J. E. (1965). *Seismic Waves: Radiation, Transmission and Attenuation* (McGraw Hill, New York).

Japanese monkeys perceive sensory consonance of chords

Akihiro Izumi^{a)}

Department of Behavioral and Brain Sciences, Primate Research Institute, Kyoto University, Inuyama, 484-8506, Japan

(Received 12 April 2000; accepted for publication 14 September 2000)

Consonance/dissonance affects human perception of chords from early stages of development [e.g., Schellenberg and Trainor, *J. Acoust. Soc. Am.* **100**, 3321–3328 (1996)]. To examine whether consonance has some role in audition of nonhumans, three Japanese monkeys (*Macaca fuscata*) were trained to discriminate simultaneous two-tone complexes (chords). The task was serial discrimination (AX procedure) with repetitive presentation of background stimuli. Each tone in a chord was comprised of six harmonics, and chords with complex ratios of fundamental frequency (e.g., frequency ratio of 8:15 in major seventh) resulted in dissonance. The chords were transposed for each presentation to make monkeys attend to cues other than the absolute frequency of a component tone. Monkeys were initially trained to detect changes from consonant (octave) to dissonant (major seventh). Following the successful acquisition of the task, transfer tests with novel chords were conducted. In these transfer tests, the performances with detecting changes from consonant to dissonant chords (perfect fifth to major seventh; perfect fourth to major seventh) were better than those with detecting reverse changes. These results suggested that the consonance of chords affected the performances of monkeys. © 2000 Acoustical Society of America. [S0001-4966(00)03712-7]

PACS numbers: 43.80.Lb, 43.66.Gf, 43.75.Cd [WA]

I. INTRODUCTION

Humans perceive chords (simultaneous complexes of tones) with simple (i.e., small-integer) frequency ratios of tones as more consonant, or more pleasant, than chords with relatively complex ratios. For example, octave chords with simple frequency ratios of 1:2 are perceived consonant, whereas major seventh chords with frequency ratios of 8:15 are perceived relatively dissonant. This sense of consonance is referred to as sensory consonance, and it has been proposed to derive from amplitude fluctuation (Plomp and Lev-elt, 1965; Kameoka and Kuriyagawa, 1969a, b). Harmonic components of complex tones with complex frequency ratios tend to fall within an identical critical band, and the fluctuation resulting from the interaction between harmonics is perceived as a sense of dissonance. Practically, the degree of consonance/dissonance with a complex-tone chord is well predicted by the frequency ratio simplicity/complexity (for review, see Schellenberg and Trehub, 1994b). As well as adults, human infants also perceive sensory consonance (Schellenberg and Trainor, 1996). Furthermore, infants were shown to prefer consonance to dissonance (Zentner and Kagan, 1996, 1998; Trainor and Heinmiller, 1998). These studies have revealed that humans use the consonance property in perceiving chord structures from early stages of development, and suggested that such percept is independent of particular musical experience.

If the perception of consonance is independent of musical experience, there is a possibility that nonhuman animals naturally share similar perceptual characteristics. In studies investigating perceptual invariance of chord structure, Hulse *et al.* (1995) tentatively suggested that European starlings discriminated chords by the sensory consonance of stimuli.

To systematically examine whether the consonance property has some role in nonhuman audition, the present study investigated the perception of chords in Japanese monkeys. Monkeys were examined whether they discriminate two-tone chords by the sensory consonance dimension. Each tone in a stimulus was comprised of six harmonics, and chords with simple frequency ratios resulted in sensory consonant while chords with complex ratios resulted in sensory dissonant. In experiment 1, monkeys were initially trained to discriminate two types of chords. They were then tested with various novel chords to determine whether they perceived transposed chords (chords with the same interval but different in absolute frequency) as similar. Experiment 2 was designed to examine whether the discrimination of chords depended on sensory consonance.

II. EXPERIMENT 1

Monkeys were initially trained to discriminate two chords, including octaves and major sevenths (one-semitone difference). To test whether monkeys learned the chord structure, the discrimination was then transferred to other chords with novel frequencies.

A. Method

1. Subjects

Subjects were three Japanese macaques (*Macaca fuscata*) who previously participated in an experiment examining auditory gap duration discrimination (Izumi, 1999). Two of them were females (H, 7 years old; K, 6 years old) and the other one was a male (I, 6 years old). They were housed in individual cages with water freely available. Depending on their performance, they were deprived of food by having their body weights reduced to 90% of their free-feeding

^{a)}Electronic mail: aizumi@pri.kyoto-u.ac.jp

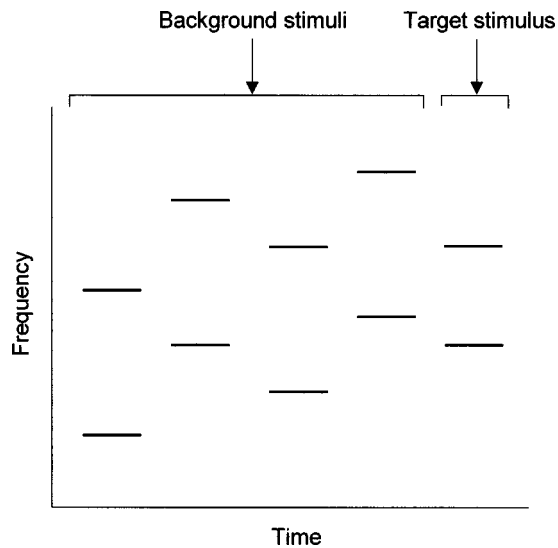


FIG. 1. Schematic representation of a trial. Each stimulus consisted of two simultaneous tones. Each tone was comprised of six harmonics; however, for simplicity, only the fundamental component is shown here. Background stimuli were repetitively presented with transposition: Frequencies of the two tones were randomly varied while the frequency ratio between them was fixed. A target stimulus followed backgrounds, and it differed in the frequency ratio (and therefore the frequency interval) of the two tones.

weights. The use of these subjects adhered to the Guide for the Care and Use of Laboratory Primates (1986) of the Primate Research Institute, Kyoto University.

2. Apparatus

The apparatus was similar to that described in a previous study (Izumi, 1999). Tests took place in a double-walled sound-attenuating chamber (Tracoustics, RE-246A). A speaker (Bose, 101VM), a lever, and a feeding box, connected to a universal feeder (Davis Scientific Instruments, UF-100), were on one side of the experimental box (50 cm wide \times 60 cm deep \times 70 cm high) within the chamber. Two cue lamps (miniature bulbs) were mounted above the lever and feeding box. The lamp above the feeding box was illuminated throughout a session, and the other lamp above the lever was turned on when a trial could be initiated. A personal computer generated auditory stimuli with a sound card (Digidesign, AudiomediaIII). The stimuli were prepared with 16-bit precision and 22.05-kHz sampling rate. Stimuli were band-pass filtered between 100 and 6000 Hz (NF Electronics, 3624), amplified (Audio-Technica, AT-MA55), and presented via the speaker. The auditory stimulus level was calibrated with a sound level meter (Rion, NA-80) and a microphone (Rion, UC-33P) placed at the position of the subject's head. The computer controlled the behavioral procedure and data collection with a customized program.

3. Procedure

a. Behavioral procedure. A go/no-go procedure was used with positive reinforcement operant conditioning. Figure 1 shows a schematic representation of a trial. When the cue lamp above the lever was turned on, a subject could initiate a trial by pressing the lever. After 0.5 s, background stimuli were presented two to five times at a rate of one per

2 s. These stimuli consisted of two simultaneous tones (lower tone and higher tone) comprised of six harmonics of equal intensity. The duration of the stimulus was 500 ms with 10-ms rise–fall time. Stimulus intensity was approximately 60 dB SPL.

The frequency relation of the two tones (i.e., frequency ratio) in background chords was fixed, though the absolute pitch changed randomly for each presentation. The frequency of the lower tone in each chord was selected from 12 frequencies in the equal temperament (A3–G4#; 220–415 Hz). This transposition reduced the possibility that the monkeys discriminated the stimuli on the basis of absolute pitch. The equal temperament divides an octave into 12 equal semitone intervals on the log scale of the frequency, and it provides great facility for transposition with small number of tones. Although consonant chords (except the octave) in the equal temperament do not correspond to exact simple frequency ratios of tones, the frequency deviations from chords in just intonation are very small and there is little effect on the relative consonance of chords (see Schellenberg and Trehub, 1994b).

Half of the trials were “change” trials, in which a target stimulus followed the presentation of the background stimuli. The target stimulus was different from background stimulus in the frequency ratio of the tones (i.e., consonance). The frequency of the lower tone component of a target stimulus was selected from the same frequency set as the background stimuli. In these trials, releasing the lever during 2 s from the onset of target stimulus was defined as a “hit.” To monitor the false alarm rate, the other half of the trials were “catch” trials. In these trials, an extra background stimulus (catch stimulus) was presented before the presentation of a target stimulus. In these trials, releasing the lever during 2 s from the onset of the catch stimulus was defined as a “false alarm.”

In both “change” and “catch” trials, subjects were rewarded immediately with a small piece of sweet potato when they released the lever within 2 s of the target stimulus. A reward was followed by an intertrial interval (ITI) of 3 s. Releasing the lever outside the reward period was mildly punished with a prolonged ITI (10 s). During an ITI, the cue lamp above the lever was turned off. Pressing the lever during the interval was punished with resetting the corresponding ITI of 3 or 10 s. A trial was repeated after the ITI if the subjects released the lever before the presentation of target or catch stimulus.

Each subject had two sessions in a day through the training and the transfer test. During training, a session was terminated when the subject completed 96 trials. Transfer tests were initiated after the subjects achieved 80% correct responses in two successive sessions. In transfer tests, a session consisted of 112 trials and each subject had a total of four transfer sessions.

b. Stimulus conditions. In the training phase, the subjects were required to detect the change of chords from octave to major seventh. This change reduced the interval size by one semitone (from 12 to 11 semitones), and decreased the consonance of chords. The reason why there was only one direction of changes was to avoid confusing the monkeys. Em-

TABLE I. Chords used experiment 1. Monkeys were initially trained to detect changes from octaves to major sevenths. In the transfer test, monkeys were required to detect changes from octaves to all chords presented in this table.

Chord name	Interval size (semitone)	Frequency ratio
Unison	0	1:1
Minor second	1	15:16
Major second	2	8:9
Minor third	3	5:6
Major third	4	4:5
Perfect fourth	5	3:4
Tritone	6	32:45
Perfect fifth	7	2:3
Minor sixth	8	5:8
Major sixth	9	3:5
Minor seventh	10	9:16
Major seventh	11	8:15
Octave	12	1:2
Minor ninth	13	15:32

pirically, performances of the monkeys usually deteriorate when bi-directional changes are required to be detected.

In the transfer test, chords of background stimuli were identical to those used in the training phase; the chord was an octave. As target stimuli, 14 new chords with various frequency relations, including octave, were introduced (Table I). These target stimuli consisted of a lower tone with fixed fundamental frequency (A4; 440 Hz) and a higher tone with various fundamental frequencies (A4–A5#; 440–932 Hz). Responses to these novel targets were rewarded as responses to targets in the training. If the discrimination depended on absolute frequency of the chords, performance of the monkeys would not be affected by the frequency interval of the new targets. If monkeys attended to chord structures including interval size or consonance of chords, discriminating the new octave chord from the background octave chords would be difficult.

c. Calculation of discrimination index. In transfer phase, the hit and false alarm (FA) rate for each stimulus condition, number of background repetitions, and subject were calculated, and these values were then transformed to d' values according to signal-detection theory. Practically, the discrimination seemed to be easy in some conditions and data usually contained a hit rate of 1. To avoid infinite d' (i.e., either 0 or 1 for hit or FA rate), each hit and FA rate was transformed as

$$R_t = (R_o - 0.5) \times 0.99 + 0.5, \quad (1)$$

where R_o and R_t are original and transformed rates, respectively. This process has little effect on d' scores; a chance performance (hit rate=FA rate) corresponds to d' of 0, and the possible score is 5.15 at maximum (hit rate=1, FA rate=0). For example, a hit rate of 0.9 and a FA rate of 0.1 roughly corresponds to d' of 2.5.

B. Results and discussion

All three monkeys successfully acquired the task of chord discrimination. Though monkeys H and I required only 4 sessions to achieve criterion performance, monkey K required 16 sessions. Figure 2 shows the mean d' values

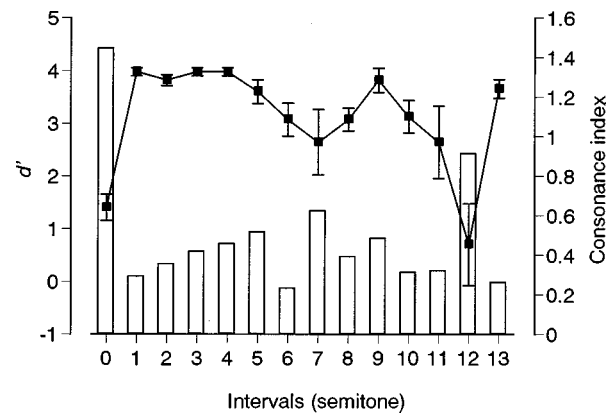


FIG. 2. Mean discrimination performances in experiment 1. Each symbol represents the mean discrimination index for each stimulus condition (left ordinate; e.g., 0 = no discrimination response). Error bars represent standard errors. Each bar represents the consonance index by Schellenberg and Treuh (1994b). Higher values of the index correspond to greater simplicity of the frequency ratio and more consonance.

based on the performance of the monkeys in the transfer test. A two-way analysis of variance with stimulus condition and number of background repetitions revealed that there were significant main effects of stimulus condition [$F(13,26) = 8.87, p < 0.001$]. The effect of background repetition and interaction was not significant. Tukey's HSD test revealed that the performance with a target of an octave chord (12-semitone interval) was significantly lower than the performance with other chords except unison (7- and 11-semitone intervals: $p < 0.05$; other intervals: $p < 0.01$). The performance with a unison chord target (0 semitone interval) was also lower than that with intervals of 1 to 5, 9, and 13 semitones ($p < 0.01$).

The results showed successful transfer of the discrimination to new target chords except unison and octave chords. The decrement of performance with the octave target suggested the cue for discrimination was not absolute frequency of a component or a combination of two frequencies in a chord. Rather, the structures of chords including sensory consonance seem important. The reason why unison was difficult to discriminate from octave may be that these chords are consonant and similar in the spectral patterns. The frequency of each component in both chords is an integer multiple of the frequency of the lowest component, and these chords can be easily regarded as a single complex tone.

It was not statistically significant, but monkeys showed lower performance around the perfect fifth interval (7 semitones). The perfect fifth is a consonant chord, and the reason for this dip in performance may be that the discrimination of monkeys depended on the consonance of chords to some extent.

III. EXPERIMENT 2

As a follow up to experiment 1, perception of sensory consonance in monkeys was again examined with novel stimuli. In the present experiment, two pairs of consonant and dissonant chords were used as stimuli (perfect fifth and major seventh; perfect fourth and minor second). The consonant and dissonant chords were reversed as background and

TABLE II. Chords used in experiment 2. The frequency ratio and interval size of each chord are shown in parentheses. There were four types of conditions in a session; consonant and dissonant chords in each pair were reversed in their role as background and target stimuli.

Chord pair	Consonant chord	Dissonant chord
Pair 1	Perfect fifth (2:3; 7 semitones)	Major seventh (8:15; 11 semitones)
Pair 2	Perfect fourth (3:4; 5 semitones)	Minor second (15:16; 1 semitone)

target stimuli in each session. Monkeys were required to discriminate a change from consonant to dissonant chords and vice versa. This test paradigm may show the effect of consonance in the discrimination independent of absolute interval sizes.

A. Method

After monkeys completed experiment 1, they proceeded to the new transfer test of experiment 2 without additional training. The method used in the present experiment was identical to that in experiment 1 except in stimulus conditions. Testing was conducted with two pairs of consonant and dissonant chords shown in Table II. The chords in each pair were reversed as background and target stimuli within each session. Monkeys were required to detect changes from perfect fifth to major seventh, from major seventh to perfect fifth, from perfect fourth to minor second, and from minor second to perfect fourth. All four conditions were presented randomly in each session. Responses to the changes with these novel stimuli were rewarded as in training. The lower tone in each background chord was selected from 12 frequencies as in experiment 1 (A3–G4♯; 220–415 Hz), and the lower tone in each target chord was selected from three frequencies (C4♯, D4, D4♯; 277, 294, 311 Hz). In this setting of frequencies, background stimuli included all tones of target stimuli. Though the size of interval difference between background and target stimuli was variable in experiment 1, the interval size always changed by three semitones in the present experiment. A session was concluded when the subject completed 96 trials, and each subject had a total of four sessions.

B. Results and discussion

Figure 3 shows the mean d' values based on the performance of the monkeys. A two-way analysis of variance with stimulus condition and number of background repetition revealed that there were significant main effects of stimulus condition [$F(3,6) = 8.81, p < 0.05$]. The effect of background repetition and the interaction was not significant. Tukey's WSD test revealed that the discrimination performance with the change from perfect fifth to major seventh and the change from major seventh to perfect fifth was significantly better than performance in the reverse conditions ($p < 0.05$). In other words, the discrimination performance for chord changes from consonant to dissonant was better than that for changes from dissonant to consonant. These results at least suggest the performances of the monkeys were affected by the consonance of chords.

The discrimination indices for changes from dissonant to consonant were below 0 (i.e., the performances were below

chance level). This indicated monkeys tended to respond to background stimuli (dissonant) more frequently than target stimuli (consonant). The strategies of monkeys might be to respond when dissonant chords were presented regardless of the stimulus conditions. Humans show similar tendencies: They detect changes from intervals with simple frequency ratios to those with relatively complex ratios more easily than changes from complex to simple ratios (Schellenberg and Trehub, 1994a; Trainor, 1997). In the present study monkeys were initially trained to discriminate changes from intervals of 12 semitones (consonant) to 11 semitones (dissonant). The training would result in the apparent asymmetry of perception, so it is not clear whether monkeys naturally possess such tendencies.

The discrimination indices in experiment 2 seem generally lower than those in experiment 1. It is impossible to say definitively, but one possible reason is monkeys were confused because they were required to detect bi-directional changes in a session. Monkeys may detect targets by fixed criterion (i.e., decrease of consonance), but such a criterion is not always appropriate when a stimulus is reversed as background and target stimuli in a session.

IV. GENERAL DISCUSSION

The present results suggested the monkeys discriminated chords based on the sensory consonance, and it was shown such percept is not unique in humans. This is in accord with

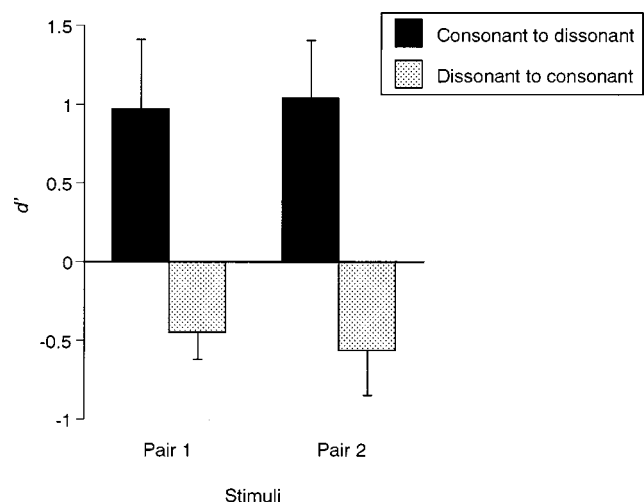


FIG. 3. Mean discrimination index for each stimulus condition in experiment 2. The ordinate represents the discrimination index, and the abscissa represents chords pairs. Pair 1 consisted of perfect fifth and major seventh chords, and pair 2 was perfect fourth and minor second chords. Error bars represent standard errors.

the idea that sensitivity to sensory consonance emerges independent of musical training (e.g., Schellenberg and Trainor, 1996).

It may be reasonable to think that sensory consonance has some significance in the monkeys' auditory world. Monkeys' audition is independent of music, and consonance perception may participate in a more general process of perceptual organization. Bregman and Doehring (1984) revealed that simple frequency ratios induce perceptual fusion of two simultaneous pure tones in humans. Common percept may have a role in nonhumans to perceive their auditory world. Sounds are mixed in the air, and animals may analyze such sounds into suitable groups. For example, European starlings can detect target songs from song complexes (Hulse *et al.*, 1997; Wisniewski and Hulse, 1997). Probably monkeys possess similar ability to perceive their auditory world. To detect harmonic components embedded in ambient noises and to perceive these components as a discrete call, consonance may have a role. Monkeys usually produce vocalizations with rich harmonic components (Green, 1975). If such vocalizations overlap each other, sensory dissonances could occur. For both humans and monkeys, the presence of dissonance, or possibly the complexity of frequency ratios, may raise the possibility that the sound emerged from more than two sources.

One remaining question is whether simplicity of frequency ratios without sensory consonance (i.e., amplitude fluctuation) affects auditory perception in monkeys as well as in humans (Schellenberg and Trehub, 1994a, 1996; Deutsch, 1973; Trainor, 1997; Cohen *et al.*, 1987; Demany and Armand, 1984). For example, Demany and Armand (1984) demonstrated that three-month-old infants perceive a melody and its octave transposition as similar. Although several studies with nonhumans have investigated the effect of frequency ratio simplicity, especially the perception of octave similarity, it is still far from a consensus. For example, Blackwell and Schlosberg (1943) reported rats perceive octave similarity, but this result is not generally accepted mainly because of the use of tones with high frequencies (e.g., 10 kHz): Such perceptual effects in humans are lost below these frequency ranges (see Demany and Armand, 1984). Further, perception of octave similarity was not demonstrated in starlings (Cynx, 1993). On the other hand, Richards *et al.* (1984) showed some examples of octave transposition in vocal mimicry by a dolphin. The dolphin sometimes transposed her mimic vocalizations by an octave when the model stimuli were outside her apparently preferred range of vocalizations. The octave transposition suggested dolphins perceive octave similarity.

In terms of the role of frequency ratio simplicity without sensory consonance, perception of harmonic intervals composed of pure tones or perception of melodic intervals may be examined in nonhumans with similar methods as in the present study. Demany and Semal (1990) showed that humans perceive melodic octaves more accurately than harmonic octaves at high frequency ranges (e.g., 2000 Hz), and it is interesting to investigate both harmonic and melodic intervals in monkeys. It has been proposed that perception of frequency ratio simplicity is learned through exposure to

overtone structures of natural harmonic sounds (e.g., vowels) in early stages of development (Terhardt, 1974, 1984), and the sensitivity to sensory consonance prompts the process of learning (Schellenberg and Trainor, 1996). Monkeys have vocalizations with rich harmonic structures (see Green, 1975), and they perceive sensory consonance as shown in the present study. These facts could promote monkeys to acquire sensitivities for frequency ratios. On the other hand, Sinnott and Brown (1993a, b) suggested that monkeys rely on temporal-coding mechanisms less than humans do in perceiving lower frequencies. If the perception of frequency ratio depends on such a temporal-coding system (see Ohgushi, 1978, 1983), frequency ratio simplicity could be difficult to perceive in monkeys.

V. CONCLUSION

In the present study, Japanese monkeys were revealed to perceive sensory consonance/dissonance of chords, and it was shown such percept is not unique in humans. However, it was still uncertain whether monkeys naturally show perceptual asymmetry between consonant and dissonant as humans do because of the possible influences of the training protocol.

ACKNOWLEDGMENTS

The author is grateful to Professor Shozo Kojima for his guidance and encouragement throughout this study. Thanks are also due to Sumiharu Nagumo for his technical support. This study was supported by Grants-in-Aid for JSPS Fellows (No. 3192), Ministry of Education, Science, and Culture, Japan.

- Blackwell, H. R., and Schlosberg, H. (1943). "Octave generalization, pitch discrimination, and loudness thresholds in the white rat," *J. Exp. Psychol.* **33**, 407–419.
- Bregman, A. S., and Doehring, P. (1984). "Fusion of simultaneous tonal glides: The role of parallelness and simple frequency relations," *Percept. Psychophys.* **36**, 251–256.
- Cohen, A. J., Thorpe, L. A., and Trehub, S. E. (1987). "Infants' perception of musical relations in short transposed tone sequences," *Can. J. Psychol.* **41**, 33–47.
- Cynx, J. (1993). "Auditory frequency generalization and a failure to find octave generalization in a songbird, the European starling (*Sturnus vulgaris*)," *J. Comp. Psych.* **107**, 140–146.
- Demany, L., and Armand, F. (1984). "The perceptual reality of tone chroma in early infancy," *J. Acoust. Soc. Am.* **76**, 57–66.
- Demany, L., and Semal, C. (1990). "Harmonic and melodic octave templates," *J. Acoust. Soc. Am.* **88**, 2126–2135.
- Deutsch, D. (1973). "Octave generalization of specific interference effects in memory for tonal pitch," *Percept. Psychophys.* **13**, 271–275.
- Green, S. (1975). "Variation of vocal pattern with social situation in the Japanese monkey (*Macaca fuscata*): A field study," in *Primate Behavior*, edited by L. A. Rosenblum (Academic, New York), Vol. 4, pp. 1–102.
- Hulse, S. H., Bernard, D. J., and Braaten, R. F. (1995). "Auditory discrimination of chord-based spectral structures by European starlings (*Sturnus vulgaris*)," *J. Exp. Psychol.* **124**, 409–423.
- Hulse, S. H., MacDougall-Shackleton, S. A., and Wisniewski, A. B. (1997). "Auditory scene analysis by songbirds: Stream segregation of birdsong by European starlings (*Sturnus vulgaris*)," *J. Comp. Psych.* **111**, 3–13.
- Izumi, A. (1999). "The effect of marker frequency disparity on the discrimination of gap duration in monkeys," *Perception* **28**, 437–444.
- Kameoka, A., and Kuriyagawa, M. (1969a). "Consonance theory: Part I. Consonance of dyads," *J. Acoust. Soc. Am.* **45**, 1451–1459.

- Kameoka, A., and Kuriyagawa, M. (1969b). "Consonance theory: Part II. Consonance of complex tones and its calculation method," *J. Acoust. Soc. Am.* **45**, 1460–1469.
- Ohgushi, K. (1978). "On the role of spatial and temporal cues in the perception of the pitch of complex tones," *J. Acoust. Soc. Am.* **64**, 764–771.
- Ohgushi, K. (1983). "The origin of tonality and a possible explanation of the octave enlargement phenomenon," *J. Acoust. Soc. Am.* **73**, 1694–1700.
- Plomp, R., and Levelt, J. M. (1965). "Tonal consonance and critical bandwidth," *J. Acoust. Soc. Am.* **38**, 548–560.
- Richards, D. G., Wolz, J. P., and Herman, L. M. (1984). "Vocal mimicry of computer-generated sounds and vocal labeling of objects by a bottlenosed dolphin, *Tursiops truncatus*," *J. Comp. Psych.* **98**, 10–28.
- Schellenberg, E. G., and Trainor, L. J. (1996). "Sensory consonance and the perceptual similarity of complex-tone harmonic intervals: Tests of adult and infant listeners," *J. Acoust. Soc. Am.* **100**, 3321–3328.
- Schellenberg, E. G., and Trehub, S. E. (1994a). "Frequency ratios and the discrimination of pure tone sequences," *Percept. Psychophys.* **56**, 472–478.
- Schellenberg, E. G., and Trehub, S. E. (1994b). "Frequency ratios and the perception of tone patterns," *Psychonom. Bull. Rev.* **1**, 191–201.
- Schellenberg, E. G., and Trehub, S. E. (1996). "Children's discrimination of melodic intervals," *Dev. Psychol.* **32**, 1039–1050.
- Sinnott, J. M., and Brown, C. H. (1993a). "Effects of varying signal and noise levels on pure-tone frequency discrimination in humans and monkeys," *J. Acoust. Soc. Am.* **93**, 1535–1540.
- Sinnott, J. M., and Brown, C. H. (1993b). "Effects of varying signal duration on pure-tone frequency discrimination in humans and monkeys," *J. Acoust. Soc. Am.* **93**, 1541–1546.
- Terhardt, E. (1974). "Pitch, consonance, and harmony," *J. Acoust. Soc. Am.* **55**, 1061–1069.
- Terhardt, E. (1984). "The concept of musical consonance: A link between music and psychoacoustics," *Music Percept.* **1**, 276–295.
- Trainor, L. J. (1997). "Effect of frequency ratio on infants' and adults' discrimination of simultaneous intervals," *J. Exp. Psychol.* **23**, 1427–1438.
- Trainor, L. J., and Heinmiller, B. M. (1998). "The development of evaluative responses to music: Infants prefer to listen to consonance over dissonance," *Infant Behav. Dev.* **21**, 77–88.
- Wisniewski, A. B., and Hulse, S. H. (1997). "Auditory scene analysis in European starlings (*Sturnus vulgaris*): Discrimination of song segments, their segmentation from multiple and reversed conspecific songs, and evidence for conspecific song categorization," *J. Comp. Psych.* **111**, 337–350.
- Zentner, M. R., and Kagan, J. (1996). "Perception of music by infants," *Nature (London)* **383**, 29.
- Zentner, M. R., and Kagan, J. (1998). "Infants' perception of consonance and dissonance in music," *Infant Behav. Dev.* **21**, 483–492.

LETTERS TO THE EDITOR

This Letters section is for publishing (a) brief acoustical research or applied acoustical reports, (b) comments on articles or letters previously published in this Journal, and (c) a reply by the article author to criticism by the Letter author in (b). Extensive reports should be submitted as articles, not in a letter series. Letters are peer-reviewed on the same basis as articles, but usually require less review time before acceptance. Letters cannot exceed four printed pages (approximately 3000–4000 words) including figures, tables, references, and a required abstract of about 100 words.

Conical radiating waves from immersed wedges

Anne-Christine Hladky-Hennion^{a)} and Philippe Langlet

IEMN (UMR 8520 CNRS), département ISEN, 41 Boulevard Vauban, 59046 Lille Cedex, France

Michel de Billy

Groupe de Physique des Solides, Universités Paris 6 et 7, Tour 23, 2 Place Jussieu, 75251 Paris cedex 05, France

(Received 29 December 1999; revised 20 June 2000; accepted 9 September 2000)

The finite-element approach has previously been used, with the help of the ATILA code, to model the subsonic and supersonic waves in immersed waveguides [A. C. Hladky-Hennion *et al.*, *J. Sound Vib.* **212**, 265–274 (1998)]. This method has given a precise account of the experimental results and has shown the major effects. In this paper, a new representation of radiating waves is presented, leading to a simple understanding of the physical phenomenon: radiating waves are propagating with the same phase velocity on the surface of a cone, the axis of which is the wedge direction.

© 2000 Acoustical Society of America. [S0001-4966(00)02512-1]

PACS numbers: 43.20.Hq [ANN]

I. INTRODUCTION

Different authors have experimentally¹ as well as theoretically² studied the effect of the water loading on the velocity of propagation of the flexural modes. With a view to describing subsonic and supersonic waves, the finite-element method^{3,4} has been used to solve the problem, using Lagasse's technique,⁵ and has shown the variations of the wedge wave velocity as a function of the apex angle. Even if this method has permitted a good knowledge of the wedge waves in water, it has shown that, when the wedge wave velocity is larger than the sound wave speed in water, the imaginary part of the radial wave number (the wave number in the plane perpendicular to the wedge) is negative. Thus, the amplitude of the radial wave increases with the distance from the tip of the wedge. The aim of this paper is to analyze the reemission in the fluid. Therefore, a new way to represent the radiating waves has been studied and is presented. Because the formalism has been extensively detailed in Refs. 3 and 4, only the main results are first reproduced. Then, brass and duraluminum wedges are studied and the finite-element results lead to a simple understanding of the physical phenomenon.

II. THEORETICAL FORMULATION

An acoustic wave, characterized by its wave number k_z , is propagating along a uniform, infinite, and immersed wave-

guide, in the z direction. Because the section of the waveguide is uniform in the z direction, it is possible to solve the problem with the help of a bidimensional mesh and to reconstitute the whole solution.^{3–5} The particular case of a wedge waveguide is considered (Fig. 1), but the formalism can be applied to any immersed waveguide, of any cross section. The time dependence ($e^{-j\omega t}$) is implicit in the equations.

With a view to finding the eigenfrequencies, a finite-element system of equations has to be solved.³ The matrices, appearing in the finite-element system of equations, are calculated by integrating over the x and y variables on the cross section. Thus, the displacement field is z dependent but a bidimensional mesh, depending on x and y , is sufficient to take into account the propagating wave in the z direction. On the external fluid boundary, k_r is the radial component of the wave vector, which is related to k_z by the following relation:⁶

$$k^2 = k_r^2 + k_z^2 = \frac{\omega^2}{V_f^2}, \quad (1)$$

where V_f is the sound speed in water ($V_f = 1489$ m/s). The acoustic wave in the fluid is written as

$$e^{j(k_z z + k_r r)}. \quad (2)$$

In Ref. 4, all the matrices appearing in the finite-element system of equations are written as a function of ω , the angular frequency. Thus, for a given real value of ω , solving the system gives k_z and k_r . Then, the propagation modes are characterized by their wave velocity, noted V_z , which is the

^{a)}Electronic mail: hladky@isen.fr

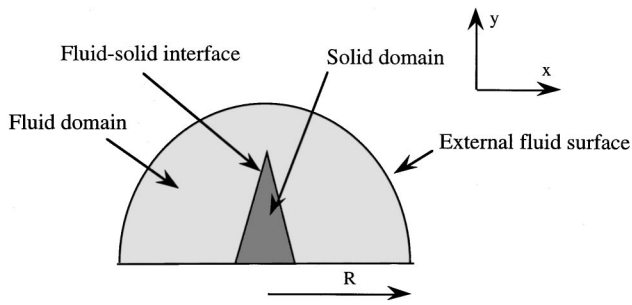


FIG. 1. Finite-element domains of the immersed wedge in the xy plane.

ratio between ω and the k_z wave number. It is a phase velocity.

Using this method, the subsonic modes ($V_z < V_f$) are well described: they propagate along the wedge without attenuation (k_z real) and the wave is exponentially decreasing in the plane perpendicular to the wedge (k_r imaginary).

On the contrary, it is more difficult to describe the supersonic modes using this method ($V_z > V_f$), because both k_r and k_z are complex: the wedge wave is propagating with attenuation in the z direction [$\text{Im}(k_z) > 0$] and the calculations exhibit the existence of a propagating radial component, the amplitude of which increases with the distance from the tip of the wedge [$\text{Im}(k_r) < 0$]. Even if a similar phenomenon was observed for the generalized Rayleigh wave,⁷⁻¹¹ the aim of this part is to give a physical meaning to this behavior.

Let us define by α the angle between the radiating waves and the wedge direction

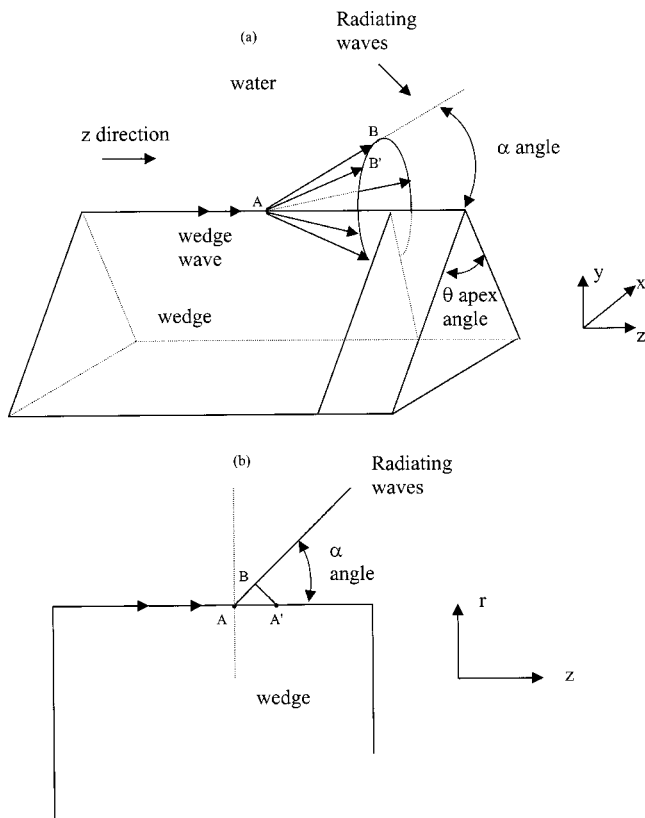


FIG. 2. Definition of the cone of radiating waves in the case of immersed wedges, when wedge wave velocity is supersonic.

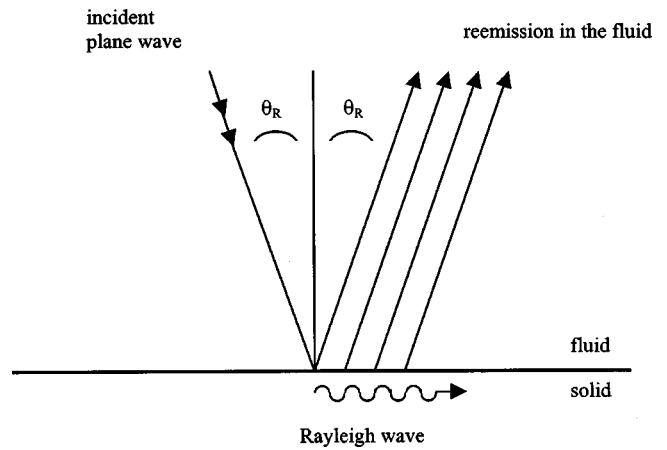


FIG. 3. Generalized Rayleigh wave propagating at the interface fluid–solid. Incident angle=Rayleigh angle.

$$\text{tg}(\alpha) = \frac{\text{Re}(k_r)}{\text{Re}(k_z)}. \quad (3)$$

Using Eq. (1) and simple trigonometric relations, the α angle can also be defined by

$$\cos(\alpha) = \frac{V_f}{V_z(\theta)}, \quad (4)$$

where θ is the apex angle. Then, the radiating wave in the α direction (i.e., $r = z \text{tg}(\alpha)$) is written as

$$e^{j(\text{Re}(k_z)z + \text{Re}(k_r)z \text{tg}(\alpha))} e^{-(\text{Im}(k_z)z + \text{Im}(k_r)z \text{tg}(\alpha))}. \quad (5)$$

Because the given value of ω is real [i.e., the imaginary part of Eq. (1) is equal to 0], the evanescent part of the acoustic wave radiating in the α direction is equal to zero [$\text{Im}(k_z)z + \text{Im}(k_r)z \text{tg}(\alpha) = 0$]. It means that radiating waves are propagating waves in the α direction, without attenuation, and are lying on the surface of a cone, having as axis the wedge direction, which is the z direction [Fig. 2(a)]. There is no attenuation in the AB way of Fig. 2(b). The half-angle of the cone is the α angle, defined in Eq. (4). On the cone, the acoustic waves have the same phase velocity.

Moreover, considering a propagating wave in a direction perpendicular to the cone [i.e., $r = -z/\text{tg}(\alpha)$], which corresponds to the BA' way of Fig. 2(b), the calculation, using relation (2), shows that the acoustic wave always has the same phase and is exponentially decreasing, when it comes nearer the wedge. This direction is an equiphase direction.¹²

Similar cones were previously obtained by Keller,¹³ in the case of diffraction of optical rays by an aperture of any shape in a thin screen. Moreover, Diachok *et al.*¹⁴ have shown that, in the case of ultrasonic waves incident on flat liquid–solid interfaces, for Rayleigh-angle incidence, reflection takes place into a cone rather than only into the forward direction.

There is a relation between these radiating cones and the generalized Rayleigh wave. Considering an incident plane wave, at the interface fluid–solid (Fig. 3), if the incident angle corresponds to the Rayleigh angle [$\theta_R = \arcsin(V_f/V_R)$, where V_R is the Rayleigh wave velocity], the incident wave also creates a Rayleigh wave, which propagates at the interface fluid–solid (Fig. 3). This surface

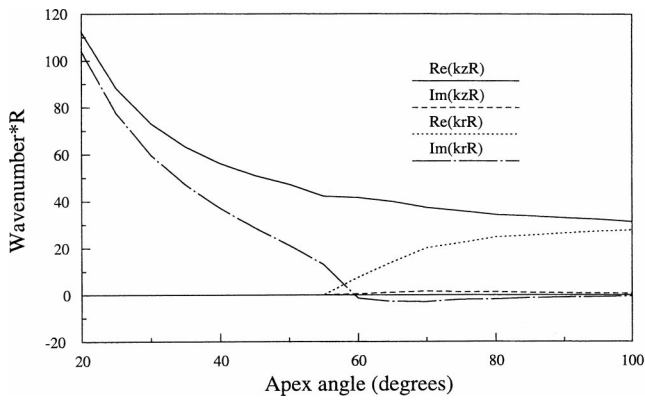


FIG. 4. Variations of the real and imaginary parts of k_r and k_z wave numbers, as a function of the apex angle of the immersed brass wedge. Full line: $\text{Re}(k_z R)$; dashed line: $\text{Im}(k_z R)$; dotted line: $\text{Re}(k_r R)$; dashed-dotted line: $\text{Im}(k_r R)$.

wave takes a part of the energy of the incident beam and reemits energy in the fluid. The reemission is in the direction of the reflected wave.¹⁵ The case of radiating wedge waves is close to the case of the generalized Rayleigh wave but the excitation is different: it is space limited. Therefore, we obtain conical radiating waves instead of plane waves.

III. IMMERSSED BRASS WEDGE

In this part, brass wedge samples, with different apex angles (5° step), are considered. The analysis of the wedge in air and in water has already been performed^{3,4} and has shown that the transition angle θ_t is equal to 60° : if the apex angle is lower than θ_t the wedge waves are subsonic, if the apex angle is greater or equal to θ_t the wedge waves are supersonic.

Figure 4 presents the variations of the real and imaginary parts of k_r and k_z wave numbers, multiplied by the radius R (see Fig. 1) of the external fluid boundary, as a function of the apex angle; thus k_r and k_z are dimensionless. R is large enough, thus, the nonreflection condition on the external fluid boundary is correct. Figure 5 presents the variations of the α angle defined in Eq. (4) as a function of the apex angle. The following remarks can be deduced from the curves presented in Figs. 4 and 5.

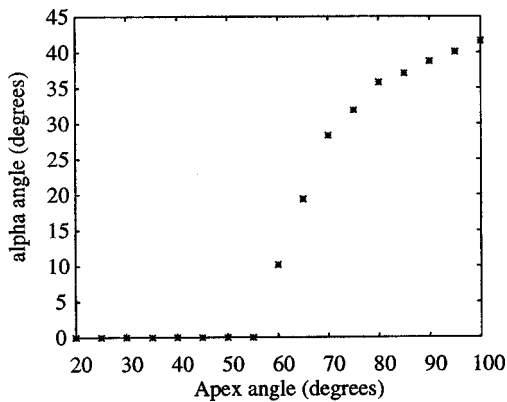


FIG. 5. Variations of the α angle (half-angle of the cone on which radiating waves are propagating), as a function of the apex angle of the immersed brass wedge.

Antisymmetrical plane

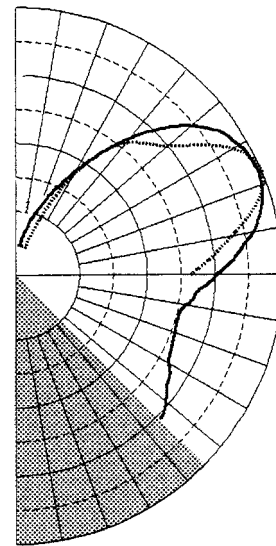


FIG. 6. Antisymmetrical wedge mode of a brass sample immersed in water. Half-apex angle= 45° . Normalized pressure field in a plane perpendicular to the wedge direction, with a linear scale. Full line: finite-element results, dashed line: experimental results.

(1) If the wedge wave velocity is subsonic, the wave is propagating in the z direction without attenuation (k_z is real) and there is no reemission in the fluid (k_r is imaginary). α is equal to zero; the acoustic wave is localized at the tip of the wedge.

(2) If the wedge wave velocity is supersonic, both k_z and k_r are complex. The imaginary part of k_r is negative. The radiating wave propagates without attenuation on the surface of a cone, the axis of which is the wedge direction and the half-angle of which is α . At the transition between subsonic and supersonic modes (60°), the half-angle of the cone is small: the radiating waves propagate near the tip. For high apex angles (100°), it has been shown⁴ that the wedge wave velocity is close to the Rayleigh wave velocity V_R . Thus, using Eq. (4) with $V_z = V_R$, it can be deduced that the half-angle of the cone is $90^\circ - \theta_R$, which is numerically

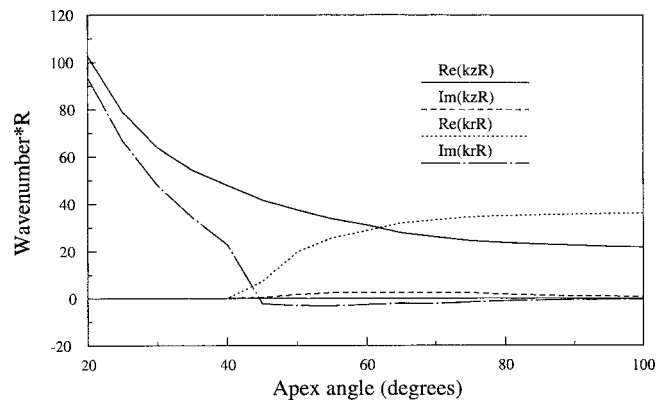


FIG. 7. Variations of the real and imaginary parts of k_r and k_z wave numbers, as a function of the apex angle of the immersed duraluminum wedge. Full line: $\text{Re}(k_z R)$; dashed line: $\text{Im}(k_z R)$; dotted line: $\text{Re}(k_r R)$; dashed-dotted line: $\text{Im}(k_r R)$.

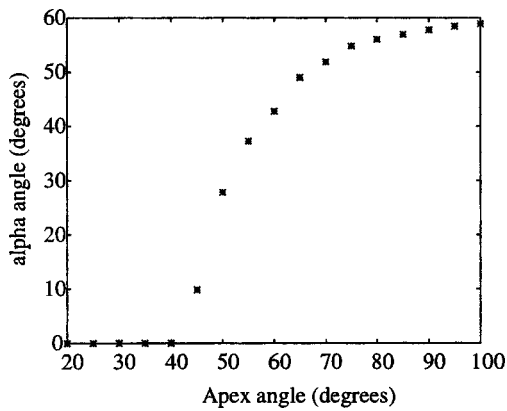


FIG. 8. Variations of the α angle (half-angle of the cone on which radiating waves are propagating), as a function of the apex angle of the immersed duraluminum wedge.

verified (in brass, $\theta_R=48^\circ$ and for a 100° apex angle $\alpha=41^\circ$).

For an apex angle equal to 90° , Fig. 6 presents the radiated normalized pressure in a plane perpendicular to the wedge direction, measured and calculated. The direction where the amplitude is maximum is equal to 67.5° with respect to the antisymmetrical plane. The pressure is equal to zero on the antisymmetrical plane: there is a minimum radiation at the tip and the waves are radiating from the two adjacent surfaces of the wedge. This figure shows that the amplitude of the radiated pressure is not the same on the circumference of the cone. Thus, the cone is an equivelocity cone but is not an equiamplitude cone. On the AB way and the AB' way of Fig. 2(a), the wave is propagating without attenuation but it does not have the same amplitude on the two ways.

IV. IMMERSSED DURALUMINUM WEDGE

Duraluminum wedges, with different apex angles, are studied (5° step).⁴ The transition angle θ_t , between subsonic and supersonic waves, is equal to 45° . Because the wave velocities are higher in duraluminum than in brass, the transition angle is smaller. In the same way, the variations of the real and imaginary parts of k_r and k_z wave numbers, multiplied by the radius R , and of the α angle, as a function of the apex angle, are presented in Figs. 7 and 8. Once again, the comments concerning these curves are the same as those concerning brass samples (Sec. III). The radiating waves are propagating without attenuation on the surface of a cone. For high-apex angles (100°), the half-angle of the cone is about 59° , which is equal to $90^\circ - \theta_R$ ($\theta_R=31^\circ$ in duraluminum). In the same way, Fig. 9 presents the radiated pressure in a plane perpendicular to the wedge direction. In that case, the direction where the amplitude is maximum is equal to 65° with respect to the antisymmetrical plane.

V. CONCLUSION

In this paper, the propagation of wedge waves along immersed wedges has been studied, with the help of the

Antisymmetrical plane

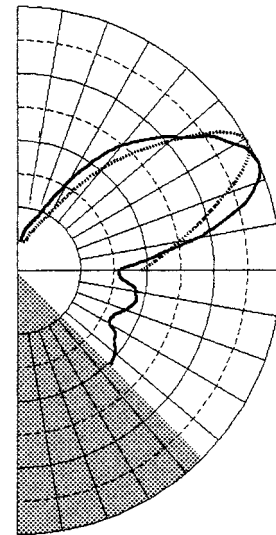


FIG. 9. Antisymmetrical wedge mode of a duraluminum sample immersed in water. Half-apex angle= 45° . Normalized pressure field in a plane perpendicular to the wedge direction, with a linear scale. Full line: finite-element results; dashed line: experimental results.

finite-element method. It has allowed a good description of the subsonic and supersonic waves and of the reemission in the fluid.

(1) If the mode is subsonic, the wave is propagating in the wedge direction and is attenuated in a perpendicular plane. There is no reemission in the fluid.

(2) If the mode is supersonic, the radiating waves are lying on the surface of a cone, having as an axis the wedge direction. They propagate along the cone without attenuation. The half-angle of the cone is small when the apex angle is just greater than θ_t , the angle which corresponds to the transition between subsonic and supersonic modes. Then, for higher apex angles, the half-angle of the cone is equal to $90^\circ - \theta_R$.

ACKNOWLEDGMENTS

The authors wish to thank B. Poirée from the Direction Générale de l'Armement (DGA), France, for his suggestions and comments.

¹J. R. Chamuel, "Edge waves along immersed elastic elliptical wedge with range dependent apex angle," IEEE Ultrasonics Symposium, pp. 313–318 (1993).

²V. V. Krylov, "On the velocities of localized vibration modes in immersed solid wedges," J. Acoust. Soc. Am. **103**, 767–770 (1998).

³A.-C. Hladky-Hennion, P. Langlet, and M. de Billy, "Finite element analysis of the propagation of acoustic waves along waveguides immersed in water," J. Sound Vib. **200**, 519–530 (1997).

⁴A.-C. Hladky-Hennion, P. Langlet, R. Bossut, and M. de Billy, "Finite element modelling of radiating waves in immersed wedges," J. Sound Vib. **212**, 265–274 (1998).

⁵P. E. Lagasse, "Higher-order finite element analysis of topographic guides supporting elastic surface waves," J. Acoust. Soc. Am. **53**, 1116–1122 (1973).

⁶P. M. Morse and H. Feshbach, *Methods of Theoretical Physics, Part II* (McGraw-Hill, New York, 1953).

- ⁷L. M. Brekhovskikh, *Waves in Layered Media* (Academic, New York, 1960).
- ⁸H. Überall, "Surface waves in acoustics," *Phys. Acoust.* **9**, 1–60 (1973).
- ⁹G. Quentin, A. Derem, and B. Poirée, "The formalism of evanescent plane waves and its importance in the study of the generalized Rayleigh wave," *J. Acoust.* **3**, 321–336 (1990).
- ¹⁰I. A. Viktorov, *Rayleigh and Lamb Waves—Physical Theory and Applications* (Plenum, New York, 1967).
- ¹¹I. A. Viktorov, "Types of acoustic surface waves in solids (review)," *Sov. Phys. Acoust.* **25**(1), 1–9 (1979).
- ¹²B. Poirée, "Les ondes planes évanescentes dans les fluides parfaits et les solides élastiques," *J. Acoust.* **2**, 205–216 (1989).
- ¹³J. B. Keller, "Diffraction by an aperture," *J. Appl. Phys.* **28**, 426–444 (1957).
- ¹⁴O. I. Diachok and W. G. Mayer, "Conical reflection of ultrasound from a liquid–solid interface," *J. Acoust. Soc. Am.* **47**, 155–157 (1970).
- ¹⁵J. L. Izbicki, G. Maze, and J. Ripoché, "Diffusion acoustique par un plan. Onde de Rayleigh," in *La Diffusion Acoustique par des Cibles Élastiques de Forme Géométrique Simple*, edited by N. Gespa (Cedocar, Paris, 1987).

Seismic-like scaling regime in impulse reflection from underwater sediment

Eric Smith

Applied Research Laboratories, The University of Texas, Austin, Texas 78713-8029

(Received 1 March 1999; accepted for publication 30 August 2000)

A universal scaling law is known empirically to characterize the high-frequency decay of bandpassed seismic coda. An explanation advanced for this universality, based on multiple-Rayleigh scatter of nonuniform strength, is generic enough to suggest that similar scaling may apply to decay of the impulse response in other random media. A submerged sand layer is probed experimentally as a candidate for such a medium, and its incoherent acoustic impulse reflection is found to have an exponential decay regime similar to that in seismology. © 2000 Acoustical Society of America. [S0001-4966(00)01612-X]

PACS numbers: 43.30.Ft, 43.30.Ma [SAC-B]

I. CONTEXT AND INTRODUCTION

A remarkable universal scaling law has been found to characterize the incoherent elastic sound field following the direct arrivals of main shocks from earthquakes or explosions, known as seismic coda. The decay of coda divided into passbands is found to be exponential, and its quality factor in each band, called coda- Q or Q_C , scales with the center frequency of the band as $Q_C \sim (f/f_0)^p$, with f_0 a normalization frequency and p between 0.5 and 1, values $p \sim 2/3$ being preferred.¹

By itself, exponential decay is not surprising, because repeated action of generic scattering and absorption mechanisms leads to this.² Scaling as a positive power of frequency is more surprising [single-Rayleigh scattering predicts $Q_C \sim (f/f_0)^{-3}$], but could possibly be modeled by distributing scatterer properties between small-feature (Rayleigh) and large-feature [geometric, for which coherent attenuation $\sim (f/f_0)^1$, and which might be imaged in coda by other backscattering mechanisms].³

The deeply surprising feature of seismic coda scaling is its universality: the above description characterizes earthquakes and explosions in all parts of the world, with diverse source/receiver placements and intervening propagation environments. Though the exponent is very different from that predicted for single-Rayleigh scattering, this universality suggests a scattering mechanism that is similar to Rayleigh in its simplicity, not relying on details of the scatterer properties or their distribution.

Universal exponential decay, with frequency scaling as above, has been predicted to result from random, multiple-Rayleigh scattering of nonuniform strength.⁴ Universality follows from the featurelessness of Rayleigh scatterers, and positive-power scaling of Q_C results from their progressively more effective retainment of energy by multiple scattering with increasing frequency. Exponential decay is the last subdiffusive behavior before acoustic localization, and results from the (statistical) nonuniformity of the scattering medium. Though much of the mathematical description resembles that for localization, only random multiple scattering and nonuniformity are input to the model; the severe prediction of proper localization is not required.

The genericity of the foregoing calculation suggests that

similar behavior may be found in any random, heterogeneous acoustic medium. While the calculations were performed for fluid media, to reduce complexity, similar calculations for localizing systems have been compared for fluids and elastic solids.⁵ Because the dimensionalities of scatterers are the same, and multiple scattering renders the incoherent sound field isotropic, scaling results for the two cases are identical. To the extent that Biot theory⁶ represents at least the dimensional analysis of two-component, random, fluid/solid media, scatterer dimensionalities again match those in fluid and elastic cases, so the scaling in the mixed system should also be the same.

A nonseismic system in which such decay may have been seen is ultrasound in randomly etched metal plates. Experiments on these were performed to identify localized waves (lower dimensions localize more strongly than higher dimensions), but an anomalous loss at late times was observed as well.⁷

An underwater sediment layer can also be viewed as a random scatterer of nonuniform strength. Even very carefully controlled sediments are random at the grain scale, and it is known that the heterogeneity of stress transmission through the sediment frame persists to much larger scales in the form of force chains, even for nominally homogeneous sediments like bead packs.⁸ Though the heterogeneity in a sediment bulk may be statistically uniform, the interface with the water represents a discontinuity in scattering strength, a singular limit of nonuniformity. Moreover (and relevant to the experiments of Ref. 7 as well), *any* single realization of a random medium, of finite size, is in a sense nonuniform, because a given scattered wavelet need not see all moments of the statistical distribution, even over all time.

Therefore it is of interest, whether acoustic impulses reflected from an underwater sediment layer qualitatively resemble seismic coda, or have similar universal scaling behaviors. This was investigated by reflecting broadband (25–350-kHz) signals from a graded sand layer in a laboratory tank, and analyzing the properties of the incoherent impulse reflection. A seismic-like scaling regime was observed, with power law $p \sim 0.75$, for 50-kHz bands at center frequencies from 75–275 kHz.

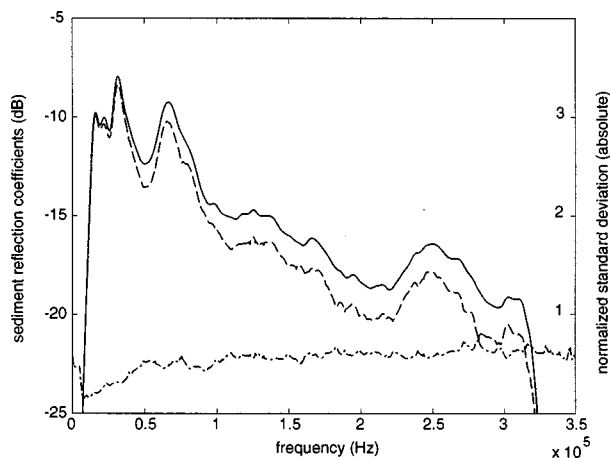


FIG. 1. Population means of frequency-domain reflection coefficients R . Solid is the level of the mean of $|R|$ in dB, dashed is the mean of the dB level of $|R|$, and dash-dot is the normalized standard deviation $\hat{\sigma}$, computed from their difference.

II. EXPERIMENTAL AND ANALYTIC METHOD

Experiments were carried out on unwashed river sand in an indoor calibration tank at the Applied Research Laboratories: The University of Texas (ARL:UT). This was done to minimize corruption by surface roughness and unknown bed formation, which can be difficult to control in natural sediments. The sediment was placed in August 1972. The positions of subsurface layers are known from a surface-wave survey,⁹ subsequent to which the sand has not been disturbed except by occasional temporary burial of small objects. Surface topography was flattened by grading with a straight, horizontal aluminum bar, suspended beneath a rolling rail-mounted cart, which was later used to carry the transducer. The level of the sediment was thus made parallel to the plane in which the transducer was moved.

A broadband, 1-3 composite transducer was used to transmit and receive 15-bit, pseudorandom (quasi-random shift-register sequence) signals clocked at 400 kHz, 1 m from the sand surface at normal incidence. The transducer and electronic system were calibrated by reflecting the same signal from the flat upper water surface (inverted orientation) at 1 m. Flatness of the water was verified by phase-stability of the return, to within ± 1 mm. Signals received from the sand were deconvolved by this near-ideal mirror return, to produce the impulse response from the sediment layer alone. Because the same geometry was used for all shots, no spreading corrections were needed.

A population of 101 independent impulse responses was generated in this way, by rastering the transducer laterally above a patch of flattened sand roughly 3×3 m in area. Typical displacement between shots was 5–10 cm, but no attempt was made to sample on a very uniform lattice. The transmitting face was leveled with a spirit level, and its flatness with respect to the transmitted beam pattern verified by test shots from a flat concrete wall.

Figure 1 shows two population means of the reflection coefficient, whose Fourier transform is the sediment's reflected-impulse response. The difference between the loga-

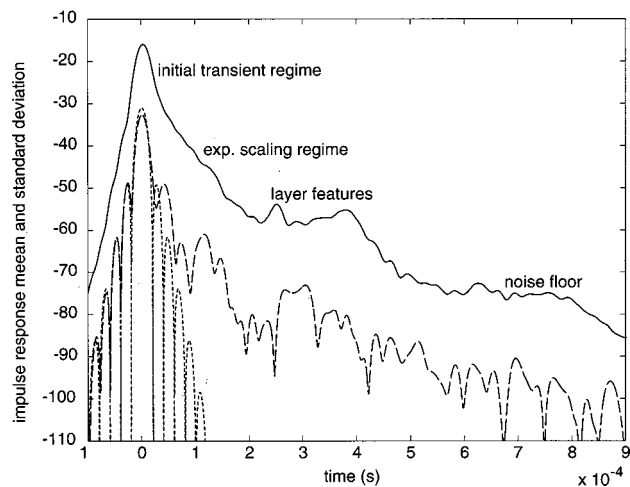


FIG. 2. General features of the time-domain impulse response. Band center frequency is 125 kHz. Solid is the standard deviation, dashed is the absolute value of the coherent mean, and dotted is the transform of the window function. Initial transient, exponential decay regime, layer-induced features, and system noise floor denoted in the figure.

rithm of the mean absolute reflection coefficient, and the mean logarithm, gives the normalized standard deviation

$$\hat{\sigma} \equiv \sqrt{\frac{\langle |R|^2 \rangle}{\langle |R| \rangle^2}}, \quad (1)$$

where R is the complex (nominally, Kirchhoff) reflection coefficient as a function of frequency, and angle brackets denote the population average. $\hat{\sigma}$ is found to be surprisingly large ~ 0.6 , but nearly frequency-independent, above 50 kHz. This provides an estimate of surface-profile flatness as $\sim \pm 0.8$ cm, which will be confirmed more explicitly in other data below.

Time-domain impulse responses were analyzed with quadrature completion. Real-valued measured responses were bandpassed in 50-kHz bands, and the positive-frequency band only was inverse-Fourier transformed (with a factor-2 magnitude correction), to produce the positive-frequency complex waveform with the same real part as the measured impulse response. The coherent population mean was subtracted from each signal, leaving a complex difference, whose absolute square was used to compute the point-by-point variance in the time domain, and hence also the standard deviation. This standard deviation treats magnitude and phase errors with equal weight, and defines the incoherent part of the reflection impulse response.

Figure 2 shows the mean and standard deviation for one passband, together with the time-domain representation of the passband window. The mean clearly shows the sand-water interface reflection, and little additional ‘‘coda’’-structure from secondary coherent reflections. The standard deviation shows an initial transient at the time of the top-surface specular reflection, followed by a good-quality exponential coda-decay regime, which is eventually lost in some complex structure, and finally the steady-state noise floor.

The arrival time of the complex structure in Fig. 2 coincides with the position of a surveyed sublayer interface.⁹ It was excluded by windowing in the time domain, to produce

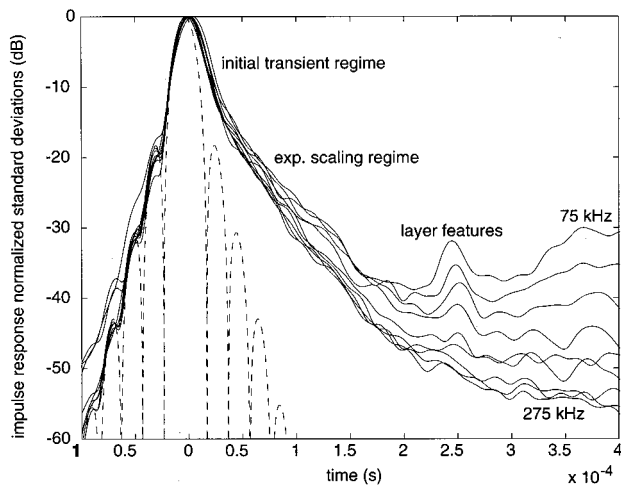


FIG. 3. Solid lines are band-limited, normalized standard deviations of the time-domain reflected impulse response. Center frequencies are from 75–275 kHz in 25-kHz increments. Limiting frequencies are marked in the figure. Alignment of advanced sidelobes with the window envelope (dashed) constrains flatness of surface. Nonoverlapping exponential decay regions show frequency-dependent decay time constant.

Fig. 1, which removed oscillations of the correct period and did not otherwise change the smooth background curve of the reflection coefficients. A similar very thin layer, identified in the survey but too close in time to be excluded by windowing, is believed to cause the 50-kHz-period oscillation remaining at low frequencies in Fig. 1. The statistical noise floor from environment and apparatus was identified separately, from a population of shots taken with the transducer stationary.

III. SCALING OF CODA DECAY

The largest set of standard deviations with frequency bands lying entirely within the usable range of apparatus/signal type/noise environment, normalized by their maximum magnitude, is shown in Fig. 3. Because there is no time information in the frequency window used, the aligned reproduction by all 50-kHz-bandpassed standard deviations, of the advanced sidelobes of the window function, verifies that surface height fluctuations do not dither the arrival time in this population by more than $\sim 20 \mu\text{s}$. Similar windowing into 100-kHz bands (not shown) completely obscures the window sidelobes, so the root-mean-square (rms) height fluctuation is constrained from above and below to be $\sim \pm 0.8 \text{ cm}$.

The asymmetry between advanced and retarded halves of the standard deviation clearly distinguishes sand-induced coda from band-related features. The inferred nonzero fluctuation in height is believed to account for the initial transient, as an addition with roughly the shape of the window, to an otherwise uniform exponential decay.

The normalized reflection levels (dB) were fitted linearly to time in a least-squares sense, in the region between 30 and 170 μs . Using the definition

$$|A(t + \delta t)| \equiv |A(t)| e^{-\pi f \delta t / Q_C}, \quad (2)$$

for the time-domain amplitude A , the resulting coda- Q values are plotted in Fig. 4, together with their power-law fit to

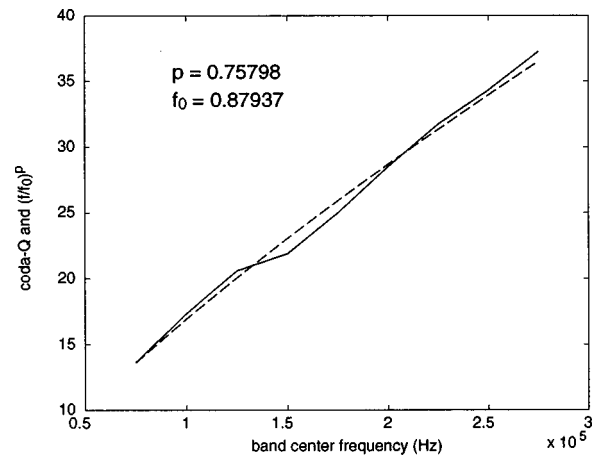


FIG. 4. Coda- Q vs band center frequency (solid), with power-law fit (dashed). Time interval determining Q_C from Fig. 3 is 30–170 μs , and values p and f_0 are denoted in the figure.

frequency f .

The individual fits to exponential decay are featureless and of good quality, confirming the ensemble randomness of the population used, over this time window. The power-law fit is credible, and there is a sufficient combination of bandwidth and statistics to establish clearly that coda- Q grows with frequency, more slowly than $(f/f_0)^1$.

Similar fits were done with 70- and 100-kHz bands, with no change in result. 20-kHz bands began to limit the effective number of shots per band, enough that fitted Q_C values became erratic, though the qualitative increase at high frequencies remained.

IV. COMMENTS AND CONCLUSION

The exponential decay regime covers 25–30 dB in level, and is observable for roughly the first 0.2 ms after the top-surface specular reflection. The fact that the sublayer interface feature is smeared in time indicates that the height of that interface varies, but the way its removal eliminates oscillations in the frequency-domain reflection coefficient shows that it is a well-defined repeat of the top-surface arrival. Therefore, this additional structure in the time-domain impulse response is interpreted as an unfortunate corruption that prematurely obscures the exponential decay, but not a bulk departure from it.

The time constant for decay is not frequency-independent, as in the prediction for smooth-fractal surface-roughness scattering.¹⁰ Since other beam characteristics decay with angle, and hence time, as power laws, and since the roughness was smoothed artificially, existence of an exponential decay regime seems most likely due to scattering in the bulk. (Other evidence from collocated reflection and transmission measurements made in natural sediments, where similar decay was observed in some cases, supports this interpretation.¹¹)

The observed scaling of the quality factor with frequency is not, alone, a sufficient parameter to determine the order of scattering or distribution of scatterer properties. It does, however, resemble the scaling seen in seismic coda, and the forces determining heterogeneity of human-placed

(but otherwise natural), unconsolidated sediments are surely very different from those in the earth's lithosphere. Therefore, if such scaling is observed repeatedly in different sediments, it will compel some explanation based on universality, such as the multiple-Rayleigh scattering hypothesis.

The power law obtained above, though within the range of seismic observations, is also not their most likely value,¹ or the one predicted in the simplest model of multiple scattering (2/3).⁴ That prediction was made for smooth statistical nonuniformity, though, and a sediment interface is the opposite limit of discontinuous scattering strength. The latter configuration has been treated only in one dimension, for a single wave species (compression) that properly localizes within the bulk.¹² Important directions for future work are to treat this configuration in general dimensions, and to consider multiple scattering in poro-elastic theories, which can couple different wave species with potentially different scattering behavior.

ACKNOWLEDGMENTS

I thank N. P. Chotiros for the use of his excellent experimental apparatus, R. Rostvold for experimental assistance during early stages of this investigation, and Chotiros and R. L. Weaver for discussion and suggestions.

¹H. Sato and M. C. Fehler, *Seismic Wave Propagation and Scattering in the Heterogeneous Earth* (Springer-Verlag, New York, 1998), Ch. 3.

²H. Sato and M. C. Fehler, *Seismic Wave Propagation and Scattering in the Heterogeneous Earth* (Springer-Verlag, New York, 1998), Ch. 5.

³D. R. Jackson, D. P. Winebrenner, and A. Ishimaru, "Application of the composite roughness model to high-frequency bottom backscattering," *J. Acoust. Soc. Am.* **79**, 1410–1422 (1986).

⁴E. Smith, "Localization in non-uniform media: Exponential decay of the late-time Ginzburg-Landau impulse response," *Phys. Rev. B* **58**, 5346–5366 (1998).

⁵S. John, H. Sompolinsky, and M. J. Stephen, "Localization in a disordered elastic medium near two dimensions," *Phys. Rev. B* **27**, 5592–5603 (1983).

⁶R. D. Stoll, *Sediment Acoustics* (Springer-Verlag, New York, 1989).

⁷R. L. Weaver, "Anderson localization of ultrasound," *Wave Motion* **12**, 129–142 (1990); "Anderson localization in the time domain: Numerical studies of waves in two-dimensional disordered media," *Phys. Rev. B* **49**, 5881–5895 (1994); this interpretation suggested by R. L. Weaver, private communication.

⁸C.-H. Liu and S. R. Nagel, "Sound in sand," *Phys. Rev. Lett.* **68**, 2301–2304 (1992); C.-H. Liu, "Spatial patterns of sound propagation in sand," *Phys. Rev. B* **50**, 782–794 (1994).

⁹B. A. Luke, "In situ measurement of stiffness profiles in the seafloor using the spectral-analysis-of-surface-waves (SASW) method," Ph.D. dissertation, The University of Texas at Austin, 1994, p. 175 (the discontinuities are more prominent, and therefore more easily identified in shear stiffness, but the bedding structure of the sand remains well-defined, without regard to how it is measured).

¹⁰M. V. Berry and T. M. Blackwell, "Diffractal echoes," *J. Phys. A* **14**, 3101–3110 (1981).

¹¹E. Smith, W. T. Wood, and W. Jans, "Scaling regimes in incoherent surface-reflected and in-sediment sound fields," *J. Acoust. Soc. Am.* **105**, 1265(A) (1999).

¹²P. Sheng, B. White, Z.-Q. Zhang, and G. Papanicolaou, in *Scattering and Localization of Classical Waves in Random Media*, edited by P. Sheng (World Scientific, Teaneck, NJ, 1990), pp. 563–619.

Psychophysical customization of directional transfer functions for virtual sound localization

John C. Middlebrooks,^{a)} Ewan A. Macpherson, and Zekiye A. Onsan
*Kresge Hearing Research Institute, Department of Otorhinolaryngology, University of Michigan,
1301 E. Ann Street, Ann Arbor, Michigan 48109-0506*

(Received 26 May 2000; revised 28 August 2000; accepted 7 September 2000)

The accuracy of virtual localization when using nonindividualized external-ear transfer functions can be improved by scaling the transfer functions in frequency [Middlebrooks, *J. Acoust. Soc. Am.* **106**, 1493–1510 (1999)]. The present letter describes a psychophysical procedure by which listeners identified appropriate scale factors. The procedure ran on nonspecialized equipment, took as little as 20 min, and could be used successfully by inexperienced listeners. Scale factors obtained from the psychophysical procedure approximated factors computed from acoustical measurements from individual listeners. Roughly equivalent virtual-localization accuracy was obtained using scale factors derived from acoustical measurements, from the psychophysical procedure, or from listeners' physical dimensions. © 2000 Acoustical Society of America. [S0001-4966(00)01912-3]

PACS numbers: 43.66.Pn, 43.66.Qp [DWG]

I. INTRODUCTION

In virtual sound location, listeners hear specially filtered sounds through headphones and localize virtual targets that appear to be located in the space surrounding the listener (e.g., Wightman and Kistler, 1989). The necessary filters are head-related transfer functions (HRTFs), which are measured by recording the signals that arrive in the ear canals when probe sounds are presented in a free sound field. When the HRTFs are those measured from a listener's own ears, virtual targets appear close to the locations of the original sound sources; we have called this the "own-ear" condition. In contrast, when HRTFs are measured from a different listener (the "other-ear" condition), localization can be markedly degraded, most noticeably showing an increase in the rate of front/back confusions (Wenzel *et al.*, 1993; Middlebrooks, 1999b).

We recently explored inter-subject differences in directional transfer functions (DTFs), which are the directional components of HRTFs. Among 45 listeners, DTFs varied systematically in the center frequencies of peaks and notches in magnitude spectra (Middlebrooks, 1999a). Inter-subject differences could be reduced substantially by scaling DTFs in frequency, and scaling improved virtual-localization performance in an other-ear condition (Middlebrooks, 1999b). Those observations raised the possibility of customizing one reference set of HRTFs by frequency scaling, thereby avoiding the inconvenience of making individual HRTF measurements. The previous study realized no practical benefit, however, since computation of the needed scale factors required individual DTFs. The present letter describes an alternative, psychophysical, procedure for estimating scale factors and demonstrates the effectiveness of such scale factors in improving virtual localization.

II. PSYCHOPHYSICAL ESTIMATION OF SCALE FACTORS

The psychophysical procedure ran on an Intel-based laptop computer, using the on-board 16-bit sound card (NeoMagic MagicWave 3DX Sound System) and Sennheiser HD265 headphones. The digital output sampling rate was 44.1 kHz. The software ran entirely in MATLAB (The Mathworks, Natick, MA). Listeners adjusted the volume control to a comfortable listening level. Tests were conducted in an anechoic chamber, although informal tests indicated that the procedure worked just as well in a quiet office.

The procedure was tested with DTFs that had been measured from listeners S16, S35, and S44 of a previous study (Middlebrooks, 1999a); that report provides details of measurement procedures. DTFs were measured by the same procedure for all the listeners in the present study for the purpose of validating psychophysical results. Each set of DTFs comprised a right- and left-ear pair of DTFs for each of 400 sound-source locations. The previous study demonstrated that spectral features of DTFs tend to correlate with the physical sizes of listeners. For convenience, we refer to the three sets of DTFs from the previous study as the Small (S35), Medium (S44), and Large (S16) DTF sets. The listeners from whom those DTFs were measured had demonstrated accurate virtual localization. The Small, Medium, and Large DTFs scaled at the 1st, 40th, and 95th percentiles, respectively, relative to the 45 sets of DTFs measured in the previous study.

Sound stimuli for the psychophysical procedure consisted of noise bursts that were convolved in the time domain with directional impulse responses. Directional impulse responses were computed as follows. A complex DTF was transformed to the time domain, interpolated by a factor of 32, then decimated in the time domain by a factor of i , where i was an integer between 15 and 42. The result was an impulse response scaled in frequency by a factor of 0.47 to 1.31. The scaled impulse response was truncated to 256 points.

^{a)}Address correspondence to: John C. Middlebrooks, Kresge Hearing Research Institute, Department of Otorhinolaryngology, University of Michigan, 1301 E. Ann St., Ann Arbor, MI 48109-0506, Phone: 734-763-7965, FAX: 734-764-0014, Email: jmidd@umich.edu

The psychophysical procedure assessed listeners' preferences for various scale factors. The listener viewed a computer graphic of a profile of a cartoon head. An arrow pointed from the ear of the cartoon to one of five elevations in the vertical midline. From trial to trial, the elevations varied sequentially among -30° , 0° , 30° , 180° , and 240° , measured relative to the frontal horizontal plane. High rear elevations were avoided because we have found that many subjects show relatively poor localization accuracy for targets in that region (Middlebrooks, 1999b; also Wightman and Kistler, 1989). On each trial, the listener heard virtual targets in two 725-ms intervals separated by a 400-ms silent gap. The target in each interval consisted of a 725-ms Gaussian noise sample that was filtered by the scaled right-ear and left-ear DTFs for the direction indicated by the arrow; the Gaussian sample was identical between the intervals of each trial but varied among trials. The DTF pair in each interval was scaled by one of two factors that differed by $5/32$, $7/32$, or $9/32$. Higher and lower scale factors were assigned randomly to first or second intervals. The listeners used computer keys to indicate the interval in which the target seemed more like a free-field source presented from the direction indicated by the arrow, i.e., to select the scale factor that resulted in the more veridical virtual target. Listeners were instructed to give priority to the front/back location over the vertical location. The preferred scale factor for one listener and one set of DTFs was estimated in one block of 240 trials. Each block was completed in two runs, each lasting about 10 min.

Scale factors were varied in steps of $1/32$ from $-7/32$ to $+7/32$ around a central factor. A central factor of 1.00 was used most often, but centers as low as 0.70 or as high as 1.10 were used to accommodate especially large or small listeners, respectively. In each block of trials, a listener heard DTFs for five locations scaled by each scale factor on six or eight trials (i.e., 30 to 40 tests of each scale factor). The *preference* for each scale factor was defined as the percentage of trials in which the interval containing that scale factor was selected. The following procedure was used to determine *preferred scale factors* from plots of preference versus scale factor. The highest point in the plot was selected along with all contiguous points showing $\geq 50\%$ preference and the two bordering points that showed $< 50\%$ preference. A parabola was fit to those points, and the preferred scale factor was given by the factor corresponding to the peak of the parabola.

The psychophysical scaling procedure was tested with two groups of listeners. The 15 *naïve* listeners (8 male, 7 female, ages 19–33 yr) were paid listeners recruited from the University students and staff. They had no prior experience in psychophysical tasks. The 5 *experienced* listeners (4 male, 1 female, ages 28–45 yr) were recruited from the laboratory staff; they are designated S04, S22, S41, plus authors JM (S27) and EM (S18). All had prior experience in virtual localization. The physical sizes of the listeners spanned nearly the entire range represented in the previous sample of 45 listeners (Middlebrooks, 1999a). All listeners were screened by conventional tests for hearing thresholds within 20 dB of audiometric zero. Each was given brief instruction and about

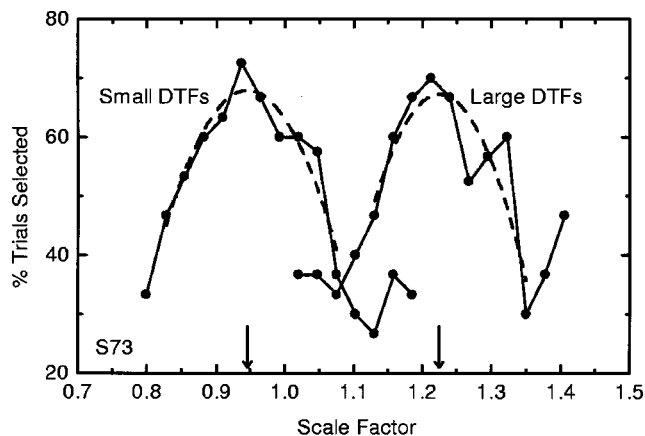


FIG. 1. Preference plot for listener S73 using the Small and Large DTFs. The dashed lines show parabolas fit to the points around the peak preference. The arrows indicate the “preferred scale factors” for the two conditions.

15 min of practice in the scaling procedure. Then, each was tested in the scaling procedure using the Medium DTFs. Each listener repeated blocks of trials with the Medium DTFs until he or she produced an acceptable preference plot, as defined below. A subset of the successful listeners was tested subsequently using their own DTFs and/or the Small or Large DTFs. The naïve listeners gradually gained experience as they ran more tests, although they received no feedback or additional training.

III. RESULTS OF SCALE-FACTOR ESTIMATION

Figure 1 shows preference plots obtained from one of the naïve listeners using the Small and Large DTFs. The preferred scale factors were 0.95 and 1.22, respectively. The preferred scale factor of 1.22, for example, indicates that the listener preferred to scale the larger subject's DTFs to higher frequencies; note that a higher range of tested scale factors was used for this relatively small listener using the Large DTFs. In the Large DTF example, preferences ranged from 70% to 30%, a range of 40%. Across all the preference plots that showed a single clear peak, maximum preferences ranged from 60% to 97% (median=70%) and the range from minimum to maximum preference ranged from 23% to 90% (median=43%).

Preference plots were judged as acceptable when they showed a well-defined peak that yielded an unambiguous preferred scale factor. Unacceptable preference plots showed multiple peaks or were too flat or irregular to indicate an unambiguous preference. One measure of the success of the psychophysical scaling procedure was the number of blocks of trials required for each listener to produce an acceptable preference plot. All listeners began with the Medium DTFs and required one block (five of the naïve listeners and all five experienced listeners), two to three blocks (six listeners) or five to eight blocks (four listeners). Across all 43 cases of 20 listeners and Medium, Small, and/or Large DTFs, 21 required only 1 block, 14 required 2–3 blocks, and 8 required 4–8 blocks.

The scaling procedure also was tested with 19 listeners using DTFs measured from their own ears. Twelve were suc-

cessful within the first test block, six required two to five blocks, and one naïve listener (S67, discussed below) was unsuccessful after ten blocks. The results supported our expectation that the preferred scale factor for listeners using their own DTFs would be near 1.0. Half of the preferred scale factors were within 0.02 of 1.00, and the root-mean-squared (rms) deviation from 1.00 was only 0.0375.

In our previous experiment (Middlebrooks, 1999a), a metric that was termed the “spectral difference” represented inter-subject differences between sets of DTFs. Plots of spectral differences versus scale factors showed an obvious minimum at what we will call the “acoustical scale factor.” In the present study, preferred scale factors estimated using the psychophysical procedure closely approximated the acoustical scale factors in most cases. Acoustical and preferred scale factors were compared for 43 cases (20 listeners and Medium, Small, and/or Large DTFs). The preferred scale factors correlated highly with the acoustical scale factors ($r = 0.89$), and the root-mean-squared (rms) difference between acoustical and preferred scale factors was only 0.069. We showed previously that the acoustical scale factor could be estimated with some accuracy from a term (the “physical scale factor”) based on the widths of listeners’ heads and the heights of their pinna cavities (Middlebrooks, 1999a). In the present study, the correlation of acoustical and physical scale factors was $r = 0.85$ and the rms difference was 0.077. The rms deviation of physical scale factors from acoustical scale factors was not significantly greater than the rms deviation of preferred scale factors from acoustical scale factors [paired $t(43) = 1.00$, $p > 0.2$].

Results from three of the listeners require individual comment. Listeners S67 and S79 tended to show preference plots that contained two peaks at scale factors differing by 0.1–0.2. For both of those listeners, it was possible to use the physical scale factor to select between the two peaks, and the acoustical scale factor confirmed that selection for both subjects. The third listener (S78) was physically large, and his preferred scale factors agreed with the physical scale factor computed from his physical dimensions. His DTFs, however, resembled those of a smaller subject and his acoustical scale factors were 0.10–0.19 lower than his physical and preferred scale factors. In tests of virtual localization like those described in Sec. III, S78’s performance using any scale factor was generally inaccurate compared to other listeners. We have no satisfactory explanation for the results from listener S78, although we suspect a difficulty in the measurement of DTFs from that listener.

IV. VALIDATION OF PREFERRED SCALE FACTORS

We tested in a subset of listeners the amount by which the scale factor that was preferred for five locations generalized to improved virtual localization at a larger number of locations. The localization procedure was similar to that used in a previous study (Middlebrooks, 1999b). Listeners stood in a darkened anechoic chamber and oriented toward virtual targets, 100 ms in duration, presented through headphones. Head orientation was monitored with an electromagnetic tracker (Polhemus). Each block of trials consisted of one trial at each of 131 virtual target locations, each synthesized with

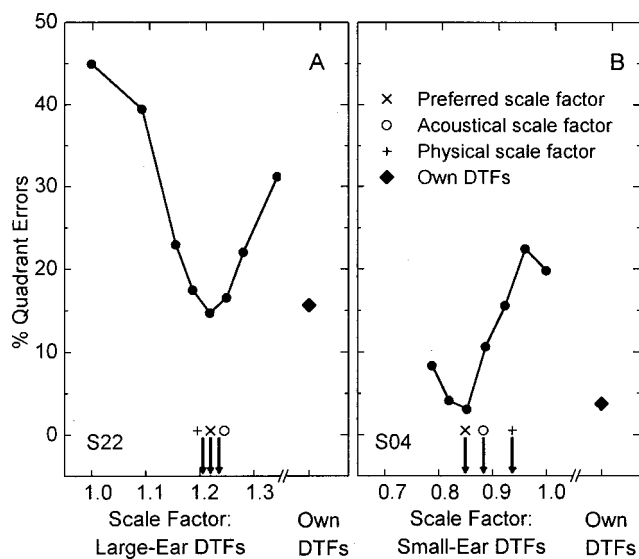


FIG. 2. Accuracy of virtual localization is represented by the percentage of quadrant errors, which are errors of $>90^\circ$ in the polar (i.e., vertical and front/back) dimension. Circles connected by lines represent error rates obtained when using nonindividualized DTFs scaled in frequency by the factor indicated on the horizontal axis. Filled diamonds indicate error rates obtained when listeners used DTFs measured from their own ears; DTFs were not scaled in that condition. Arrows along the abscissa indicate scale factors estimated from three procedures. (A) Listener S22 using the Large DTFs. (B) Listener S04 using the Small DTFs.

the listener’s own DTFs (not scaled) or with another listener’s DTFs scaled by one of 5–10 factors, a total of 655–1310 trials. The choice of target locations emphasized locations near the vertical midline, where errors in the use of spectral localization cues were likely to be most conspicuous: 80% of virtual targets were located within 20° of the vertical midline. Each block was completed in 7–12 runs of 112–131 trials. Locations, sets of DTFs, and scale factors were interleaved among trials. A listener heard his or her own DTFs on an average of no more than one of six trials.

Figure 2 shows for two listeners a measure of virtual localization accuracy: the percentage of quadrant errors. We have defined quadrant errors as errors larger than 90° in the vertical and/or front/back dimension (Middlebrooks, 1999b). Listener S22 [Fig. 2(A)] showed quadrant errors on 15.6% of trials in the own-ear condition and on 45% of trials when using the Large DTFs, unscaled (i.e., scale factor=1.0). Scaling the Large DTFs by a factor of 1.22 (i.e., moving spectral features to higher frequencies) reduced the quadrant-error rate to 14.7%. Acoustical, preferred, and physical scale factors all fell within 0.016 of 1.22. That is, any of those scale factors substantially improved localization accuracy compared to no scaling. Listener S04 [Fig. 2(B)] showed a 19.8% quadrant-error rate with the unscaled Small DTFs, but that rate was reduced to 3.1% by scaling by a factor near the acoustical or preferred scale factors. In this case, the physical scale factor resulted in less reduction in the quadrant-error rate, a rate of 15.5%.

Figure 3 summarizes the quadrant-error rates of five listeners, each using one or two sets of DTFs (a total of nine cases). The abscissa gives the quadrant-error rate obtained in the unscaled other-ear condition, and the ordinate shows the quadrant-error rates for the condition of the other-ear scaled

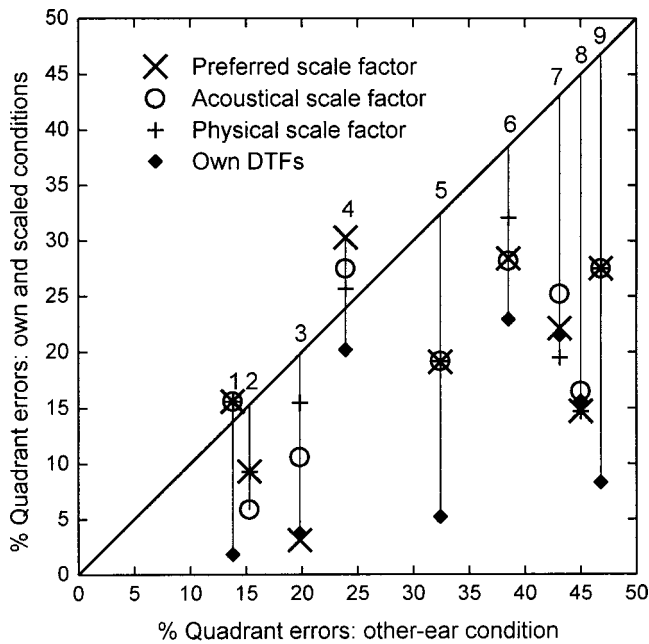


FIG. 3. Rates of quadrant errors using scale factors obtained by three procedures. Each numbered set of symbols connected by a vertical line represents rates of quadrant errors obtained by one listener using one set of DTFs scaled by various factors and using his or her own DTFs. The abscissa indicates the error rate in the unscaled other-ear DTFs condition, and the line with unity slope plots that rate.

by various factors and for the own-ear condition. In all but cases 1 and 4, scaling by the preferred scale factor reduced by half or more the difference between quadrant-error rates in the unscaled-other-ear and own-ear conditions; note that case 4 showed a high quadrant-error rate even in the own-ear condition. In all but case 3 [also shown in Fig. 2(B)], the quadrant-error rates obtained using acoustical, physical, and preferred scale factors differed by no more than 5.7%.

V. DISCUSSION AND CONCLUSIONS

In pilot experiments, we explored and rejected several psychophysical procedures for finding scale factors. For instance, procedures that required actual virtual-localization judgements were difficult for inexperienced listeners because the listener was forced to listen to a large percentage of targets synthesized with nonoptimal scale factors; the apparent locations of such targets often were poorly defined. Also, localization procedures were time consuming. Each of the cases in Fig. 3, for example, required two to four listener hours. Adaptive procedures that we tested were complicated by nonmonotonic relations between localization errors and scale factors, which resulted from the presence of quadrant errors. The two-interval preference procedure that we adopted best met our objectives. Most native listeners (and

all experienced listeners) found a preferred scale factor in one to three 20-min blocks of trials. The proportion of naïve listeners (4/15) who required more than three blocks with the Medium DTF set was comparable to the proportion of listeners who showed difficulty in our routine virtual-localization procedures, even when using DTFs measured from their own ears. The scale factors yielded by the psychophysical procedure agreed closely with the acoustical scale factors computed from DTFs measured from the individual listeners.

In validation experiments (Sec. IV), we obtained essentially equivalent localization performance with acoustical, physical, and preferred scale factors. Computation of the acoustical scale factors for scaling between two listeners requires acoustical measurements from both listeners, so acoustical scale factors offer no practical benefit toward the goal of customizing a reference set of DTFs. Physical scale factors offer the advantage that they require only simple instruments and negligible measurement time. One potential limitation is that one might not have the needed physical dimensions from the subject from the which the reference set of DTFs was measured. A psychophysical procedure for finding preferred scale factors, like that described here, has the disadvantage that it requires around one hour of training and measurement time and that some listeners have difficulty in finding a preferred scale factor. Advantages of a psychophysical procedure are that it is based on a perceptual measurement related to virtual localization, so it might serve to identify good or bad virtual localizers, and that, in principle, it could be used with any set of transfer functions. Practically, a hybrid approach might be best, in which one uses physical dimensions to define a narrow range of scale factors to be tested, then uses a psychophysical procedure to find the preferred scale factor within that range.

ACKNOWLEDGMENTS

This research was supported by ONR SBIR Contract No. N00014-99-M-0232 (to Planning Systems, Inc.) and NIH Grant No. RO1 DC000420. We thank Dr. Gary Gibian and Dr. Walter Koroljow for their contributions to the formulation of this project.

- Middlebrooks, J. C. (1999a). "Individual differences in external-ear transfer functions reduced by scaling in frequency," *J. Acoust. Soc. Am.* **106**, 1480–1492.
- Middlebrooks, J. C. (1999b). "Virtual localization improved by scaling nonindividualized external-ear transfer functions in frequency," *J. Acoust. Soc. Am.* **106**, 1493–1510.
- Wenzel, E. M., Arruda, M., Kistler, D. J., and Wightman, F. L. (1993). "Localization using nonindividualized heat-related transfer functions," *J. Acoust. Soc. Am.* **94**, 111–123.
- Wightman, F. L., and Kistler, D. J. (1989). "Headphone stimulation of free-fields listening. II: Psychophysical validation," *J. Acoust. Soc. Am.* **85**, 868–878.

Minimum audible angles in the horizontal and vertical planes: Effects of stimulus onset asynchrony and burst duration

Thomas Z. Strybel and Ken Fujimoto

Department of Psychology, California State University Long Beach, Long Beach, California 90840

(Received 21 March 2000; revised 24 July 2000; accepted 19 September 2000)

The effects of burst duration and stimulus onset asynchrony (SOA, the onset–onset time difference) on the minimum audible angle (MAA) were measured in the horizontal and vertical planes using high-pass noise bursts. Four listeners were tested with two burst durations (10 and 50 ms) and five SOAs (25, 50, 100, 200, and 400 ms), using an adaptive paradigm. In both planes, MAAs were lowest at burst duration = 50 ms, and the MAAs decreased exponentially with SOA. Although the effect of burst duration was generally larger in the vertical plane than in the horizontal plane, the plane of presentation did not affect the relationship between SOA and MAA. © 2000 Acoustical Society of America. [S0001-4966(00)04612-9]

PACS numbers: 43.66.Pn, 43.66.Qp, 43.66.Mk [DWG]

I. INTRODUCTION

The most widely used measure of auditory spatial resolution is the minimum audible angle (MAA), the minimum separation between two sources that can be reliably detected. Mills (1958) was the first to investigate the MAA in the horizontal plane, and many have researched it since. MAAs are related to localization performance (e.g., Middlebrooks and Green, 1992), although the width of the MAA psychometric function is a better predictor of localization errors than the MAA threshold (Recanzone, Makhama, and Guard, 1998). MAAs have been measured frequently in the horizontal plane but rarely in the vertical plane.

In the horizontal plane, the MAA depends on a combination of spatial and temporal factors (Grantham, 1995). The spatial factors that affect MAA are the same factors that affect localization (e.g., Mills, 1958; Saberi *et al.*, 1991; Chandler and Grantham, 1992). The MAA depends on temporal factors because the sources are normally presented sequentially (however, see Perrott, 1984). With sequential presentation, SOA (stimulus onset asynchrony or the onset–onset time difference) affects the MAA (Perrott and Pacheco, 1989; Grantham, 1985, 1997.) The MAA decreases with SOA up to 100–150 ms and is constant up to 500 ms (the largest SOA tested). An effect of burst duration on the horizontal MAA has not been obtained, however. Grantham (1985, 1997) found no differences between MAAs measured for burst durations of 10 and 50 ms, consistent with recent localization data at burst durations between 3 and 500 ms (e.g., Frens and Van Opstal, 1995; Hofman and Van Opstal, 1998).

These temporal effects are consistent with the notion of a minimum integration time (MIT) in the auditory system (e.g., Grantham, 1985, 1997; Chandler and Grantham, 1992). The MIT is the time required for spatial resolution performance to reach an optimal level (Chandler and Grantham, 1992). It is related to the binaural system's limited ability to process changes in interaural time and intensity differences (Grantham and Wightman, 1979; Blauert, 1983). Estimates of MIT vary considerably (70–700 ms). Many stimulus and contextual factors are known to affect MIT estimates, and

separating the contributions of the binaural processor from these effects is difficult (e.g., Chandler and Grantham, 1992; Saberi and Hafter, 1997).

We know less about vertical spatial resolution. The vertical MAA is higher (4°–5°) than the horizontal MAA (1°–2°) for sources at 0° azimuth and 0° elevation (Perrott and Saberi, 1990). Vertical resolution is reduced at higher elevations (Wettschurek, 1973) but improves at peripheral azimuth locations. In fact, the vertical and horizontal MAAs at 90° azimuth are equivalent (Saberi *et al.*, 1991). The effects of temporal variables on the vertical MAA have not been investigated, however. Temporal factors might affect vertical MAAs differently because different cues are involved: Horizontal localization is based on interaural time and intensity differences; vertical localization is accomplished with monaural spectral cues. Furthermore, Hofman and Van Opstal (1998) found that the auditory system required an 80-ms “look” for stable vertical localization. In the present experiment, we examined the effect of temporal factors (burst duration and SOA) on vertical and horizontal MAAs.

II. METHOD

A. Participants

Four adults (including coauthor KF) were tested, all having hearing within normal limits. Two participated in previous experiments on auditory motion perception, but none had any experience on MAA tasks. All participants were trained on the method and apparatus for at least 1 h before data collection.

B. Apparatus

The participant was seated in a large test room with Martek foam panels on all surfaces. Head position was maintained with a chinrest. A linear array of 33 loudspeakers (RadioShack 5.1-cm tweeters) was positioned 1.46 m in front of the participant, with the center loudspeaker (the standard) at 0° azimuth and elevation. The angular distance between each loudspeaker was 2°. The linear array could be rotated in the vertical plane around the center speaker, mak-

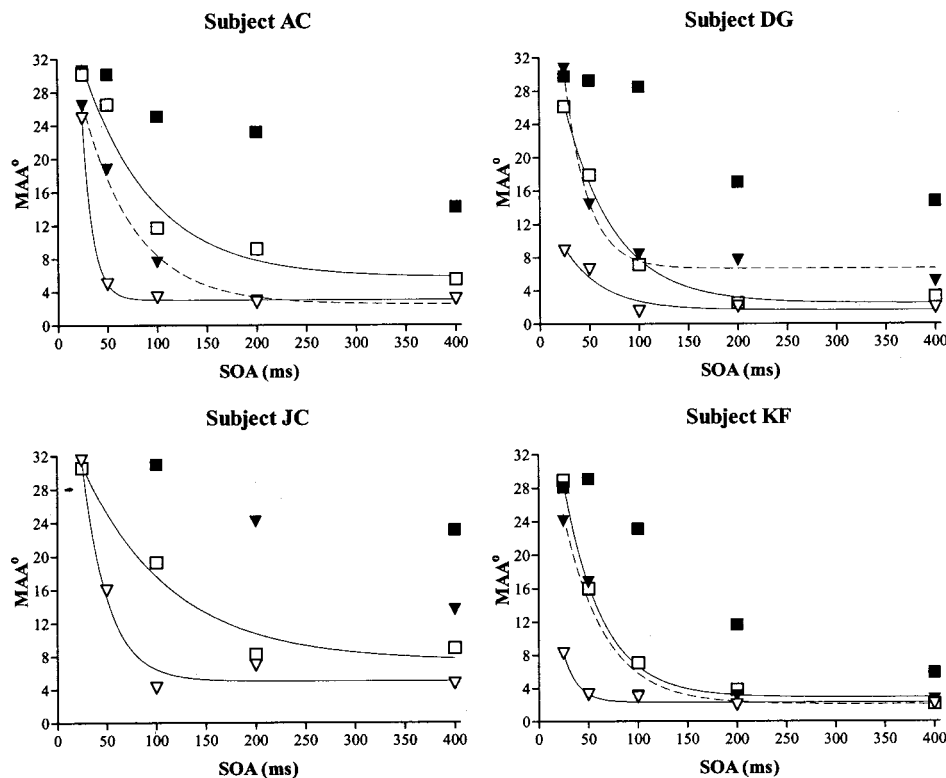


FIG. 1. Horizontal and vertical MAAs for each subject. Solid points are vertical MAAs, open points horizontal MAAs. Squares show burst durations of 10 ms; inverted triangles show burst durations of 50 ms. Solid lines are the best-fitting exponential decay functions in the horizontal plane at 10- and 50-ms burst durations. The dashed line is the best-fitting exponential decay function at 50-ms burst duration in the vertical plane.

ing the speakers extend $\pm 32^\circ$ in either the horizontal or vertical planes. The stimulus was high-pass noise with a lower frequency cutoff of approximately 4600 Hz, and amplitude of 55 dB A-weighted. The lower frequency cutoff was a function of the loudspeakers used. These loudspeakers provided adequate cues for horizontal and vertical localization, yet were small enough to allow a 2° minimum separation. Octave-band analysis determined loudspeaker characteristics. The average response of the loudspeakers was the same (within 1 dB) at 8 and 16 kHz, with the range of responses across loudspeakers within 3 dB. At 4 kHz, the average response decreased 7 dB relative to the average response at 8 kHz, with the range of responses across loudspeakers within 3 dB. Burst durations were either 10 or 50 ms, and rise/decay times were less than 1 ms. Tucker Davis Technologies' programmable modules controlled stimulus generation, timing, and speaker selection.

C. Procedure

A 2AFC adaptive method was used to measure vertical and horizontal MAAs. Both the order of the sequence (standard first or second) and the direction of the comparison stimulus (left/right or up/down) were randomly determined on each trial. A randomized standard-comparison sequence prevented participants from responding to the absolute position of the comparison source (Hartmann and Rakerd, 1989). On each trial the participant reported whether the second sound was to the left/right of the first sound in horizontal conditions, and above/below the first sound in the vertical conditions. A 3-down, 1-up rule was employed. At the beginning of each trial block, the separation was set to 32° , the maximum allowable separation. When the participants re-

sponded correctly on three consecutive trials, the separation was halved until either the step reached the minimum separation (2°) or the participant made an incorrect response. After a single incorrect response, the step size was fixed at 2° . For each block 15 reversals were obtained, and the mean of the last 10 reversals was computed as the MAA. The participant received a short rest period after each block before repeating the procedure. Three blocks were run at each condition and the final MAA was computed as the mean of the three threshold determinations. In some vertical conditions, the MAA either exceeded or was near the limits of our speaker array. Therefore, if the participant was unable to identify the position of the lag stimulus after eight trials at the maximum separation, we stopped the block. Each participant was tested at two burst durations (10 and 50 ms) and five SOAs (25, 50, 100, 200, and 400 ms) in both the horizontal and vertical planes in random order.

III. RESULTS

Figure 1 presents horizontal and vertical MAAs as a function of burst duration and SOA for each participant. In the horizontal plane, the MAAs of all participants decreased exponentially with SOA, and the MAAs at burst duration = 50 ms were lower than at burst duration = 10 ms. In the vertical plane, the MAAs of some participants exceeded the maximum separation of our speaker array. One participant (JC, lower-left panel) had MAAs that were larger than 32° at most SOAs and burst durations in the vertical plane. Participant JC also had a horizontal MAA greater than 32° at SOA = 50 ms, burst duration = 10 ms. The vertical MAAs of the remaining participants were within the limits of our array at burst duration = 50 ms but exceeded or were near the

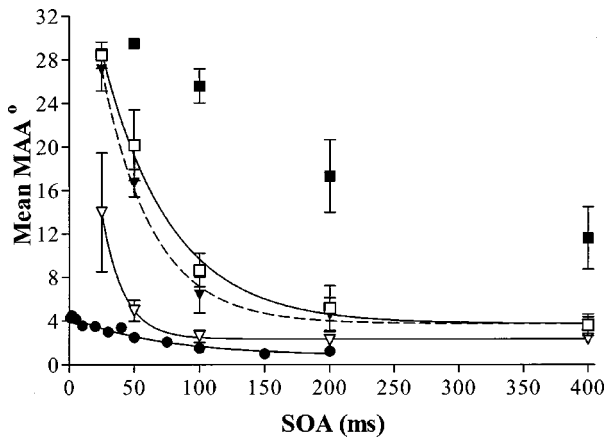


FIG. 2. Mean MAA in horizontal and vertical planes for three subjects who reliably discriminated sources in the vertical plane. Solid points are vertical MAAs and open points horizontal MAAs. Squares represent burst durations of 10 ms, and inverted triangles burst durations of 50 ms. Error bars represent ± 1 standard error of the mean over subjects. Circles are horizontal MAAs at 10-ms burst duration taken from Perrott and Pacheco (1989). Solid lines are the best-fitting exponential decay functions in the horizontal plane at 10- and 50-ms burst durations. The dashed line is the best-fitting exponential decay function at 50-ms burst duration in the vertical plane.

maximum separation at some 10-ms burst duration conditions. Nevertheless, at burst duration=50 ms, vertical MAAs decreased exponentially with SOA. At burst duration = 10 ms, only one participant (KF—lower right panel) completed the required number of reversals for all three blocks at SOA=25 ms. Participant AC (upper-left panel) completed the required number of reversals in two blocks at SOA = 25 ms and participant DG completed the required number of reversals in only one block at SOAs=25 and 50 ms.

A repeated measures analysis of variance was performed on the horizontal MAAs, with burst duration and SOA as factors. Figure 2 presents the MAAs averaged across three participants (JC was omitted). The effects of burst duration, SOA, and their interaction were significant [burst duration: $F(1,2)=296.51$; $p=0.0034$; SOA: $F(4,8)=49.88$; $p=0.0001$; burst duration \times SOA: $F(4,8)=4.61$; $p=0.03$]. The mean MAAs at burst duration=50 ms were consistently lower than MAAs at 10 ms. The differences in performance were greatest at short SOAs, but even at SOA=400 ms the MAA at 50 ms [2.3°, standard error of the mean (SEM)=0.4°] was lower than at 10 ms (3.6°, SEM=1.0°). The best-fitting lines at each duration in Fig. 2 show the significant interaction of burst duration and SOA. These solid lines represent the best-fitting negative exponential functions at

each burst duration. The parameters of the exponential decay functions are shown in Table I. In the horizontal plane, the slope at burst duration=50 ms was steeper than the slope at 10 ms. The steeper slope at 50 ms was caused in part by the relatively poor performance at SOA=25 ms. In this condition, the lead and lag stimuli overlap in time and this would increase the chances of hearing a single fused image. In fact, when exponential functions were fitted to the horizontal MAAs with SOA=25 ms omitted, the slope was lowered to -0.04 at 50 ms but was unchanged at 10 ms.

A significant interaction of burst duration and SOA suggests that total duration of the sequence did not determine the MAA, contrary to Grantham (1997). To confirm that total duration did not determine the MAA, the MAAs in the present experiment were regressed against the total duration (burst duration+SOA) of the sequence. The fit was poorer than the fit of MAAs to individual burst durations ($r^2=0.83$ for total duration vs $r^2=0.99$ and 0.99 for 10-ms and 50-ms burst durations, respectively.) Using Chandler and Grantham's (1992) manner of computation (the MAA 25% higher than the asymptote), the MIT at burst duration = 50 ms (133 ms) was lower than the MIT at burst duration = 10 ms (184 ms), as shown in Table I. Both values are within the range of previous estimates, however.

The MAAs and exponential parameters from Perrott and Pacheco (1989) are included in Fig. 2 and Table I. The burst duration in this experiment was 10 ms, and SOAs ranged between 1 and 200 ms. Perrott and Pacheco used broadband noise, and always presented the standard before the comparison stimulus. These differences may explain the lower MAAs shown in Fig. 2, compared with our results. Although the largest differences were found at the short SOAs, even at SOA=200 ms, Perrott and Pacheco's MAA (1.25°) was lower than the MAA obtained here (5.2°). However, the similarity between the slopes at 10 ms, shown in Table I, suggests that methodological differences may have improved acuity but did not affect the relationship between SOA and acuity.

Figure 2 and Table I also show the MAAs and exponential parameters in the vertical MAA task. MAAs at burst duration=50 ms were much lower than at 10 ms. Even at SOA=400 ms, the MAA at burst duration=10 ms (11.6° SEM=2.9°) was much higher than at burst duration = 50 ms (3.6° SEM=0.8°). At burst duration=10 ms, the MAAs decreased exponentially with SOA but the slope was very small. We provide no best-fitting line in Fig. 2 because

TABLE I. Parameters of exponential decay functions [$Y=(\text{span})e^{-kX} + \text{plateau}$], r squares, and MIT estimates for each burst duration and plane of separation.

Burst duration (ms)	Slope (k ; °/ms)	Span (°)	Plateau (°)	r^2	MIT (ms)
Horizontal plane					
10 (Perrott and Pacheco, 1989)	-0.01	3.6	0.8	.96	...
10	-0.02	40.5	3.7	.99	184
50	-0.06	51.9	2.4	.99	133
Vertical plane					
50	-0.03	44.8	3.8	.99	119

of the inability of subjects to complete the task at short SOAs. At burst duration=50 ms, the MAAs decreased with SOA at a much higher rate. At 50 ms the vertical MIT, shown in Table I, was 119 ms, similar to our horizontal estimates. Moreover, the slope of the vertical function is within the range of slopes obtained in the horizontal plane.

IV. DISCUSSION

Contrary to the findings of Grantham (1997) on spatial resolution, we obtained a reliable effect of burst duration on the horizontal MAA. In the present experiment, both the slope and the size of the MAAs were affected by burst duration. Even at the longest SOA the MAA at 10 ms was 1.5 times higher than at 50 ms. Methodological differences (e.g., differences in stimulus spectrum, psychophysical method, and stimulus presentation order) may have contributed to the discrepant outcomes. Although the effect of SOA in our experiment was similar to the effect obtained by Perrott and Pacheco (1989), our MAAs were larger, especially at short SOAs. Two major differences between our study and Perrott and Pacheco are stimulus spectrum (high-pass vs broadband noise) and stimulus order (constant vs random). Presumably, both factors contributed to the larger MAAs obtained here. These various effects of method on the MAA make an accurate estimate of the MIT difficult. Nevertheless, our estimates (133–184 ms) are within the range of previous estimates in the horizontal plane (e.g., Chandler and Grantham, 1992; Saberi and Hafter, 1997).

In the vertical plane, the effects of burst duration were generally larger. At the longest SOA, the vertical MAA at burst duration=10 ms was three times the MAA at 50 ms. Although no previous tests of timing on the vertical MAA have been reported, recent vertical localization data do predict an effect of burst duration. According to Hofman and Van Opstal (1998), reliable vertical localization requires that the burst duration exceed 80 ms. Although the effect of burst duration on the MAA was generally larger in the vertical plane, the effect of SOA does not depend on plane of presentation. Vertical MAAs at burst duration=50 ms decreased exponentially with SOA at a rate similar to that obtained for horizontal MAAs. Our estimate of the vertical MIT (119 ms) was lower than our horizontal estimates, but within the range of previous estimates obtained in the horizontal plane (e.g., Chandler and Grantham, 1992; Saberi and Hafter, 1997).

- Blauert, J. (1983). *Spatial Hearing* (MIT Press, Cambridge).
- Chandler, D. W., and Grantham, W. D. (1992). "Minimum audible movement angle in the horizontal plane as a function of stimulus frequency and bandwidth, source azimuth, and velocity," *J. Acoust. Soc. Am.* **91**, 1624–1636.
- Eddins, D. A., and Green, D. M. (1995). "Temporal integration and temporal resolution," in *Handbook of Perception and Cognition, 2nd ed.: Hearing*, edited by B. C. J. Moore (Academic, San Diego).
- Frens, M. A., and Van Opstal, A. J. (1995). "A quantitative study of auditory-evoked saccadic eye movements in two dimensions," *Exp. Brain Res.* **107**, 103–117.
- Grantham, D. W. (1985). "Auditory spatial resolution under static and dynamic conditions," *J. Acoust. Soc. Am. Suppl.* **1** **77**, S50.
- Grantham, D. W. (1995). "Spatial hearing and related phenomena," in *Handbook of Perception and Cognition 2nd ed.: Hearing*, edited by B. C. J. Moore (Academic, San Diego).
- Grantham, D. W. (1997). "Auditory motion perception: Snapshots revisited," in *Binaural Hearing in Real and Virtual Environments*, edited by R. H. Gilkey and T. R. Anderson (Erlbaum, Hillsdale, NJ).
- Grantham, D. W., and Wightman, F. L. (1979). "Auditory motion aftereffects," *Percept. Psychophys.* **26**, 403–408.
- Hartmann, W. M., and Rakerd, B. (1989). "On the minimum audible angle—A decision theory approach," *J. Acoust. Soc. Am.* **55**, 2031–2041.
- Hofman, P. M., and Van Opstal, A. J. (1998). "Spectro-temporal factors in two-dimensional human sound localization," *J. Acoust. Soc. Am.* **103**, 2634–2648.
- Middlebrooks, J. C., and Green, D. M. (1991). "Sound localization by human listeners," *Annu. Rev. Psychol.* **42**, 135–159.
- Mills, A. W. (1958). "On the minimum audible angle," *J. Acoust. Soc. Am.* **30**, 237–246.
- Perrott, D. R. (1984). "Concurrent minimum audible angle: A re-examination of the concept of auditory spatial acuity," *J. Acoust. Soc. Am.* **74**, 1201–1206.
- Perrott, D. R., and Pacheco, S. (1989). "Minimum audible angle thresholds for broadband noise as a function of the delay between the onset of the lead and lag signals," *J. Acoust. Soc. Am.* **85**, 2669–2672.
- Perrott, D. R., and Saberi, K. (1990). "Minimum audible angle thresholds for sources varying in both elevation and azimuth," *J. Acoust. Soc. Am.* **87**, 1728–1731.
- Recanzone, G. H., Makhama, S. D. D. R., and Guard, D. C. (1998). "Comparison of relative and absolute sound localization ability in humans," *J. Acoust. Soc. Am.* **103**, 1085–1097.
- Saberi, K., and Hafter, E. R. (1997). "Experiments on auditory motion discrimination," in *Binaural Hearing in Real and Virtual Environments*, edited by R. H. Gilkey and T. R. Anderson (Erlbaum, Hillsdale, NJ).
- Saberi, K., Dostal, L., Sadralodabai, T., and Perrott, D. R. (1991). "Minimum audible angles for horizontal, vertical and oblique orientations: Lateral and dorsal planes," *Acustica* **75**, 57–61.
- Wettschurek, R. G. (1973). "Die absoluten unterschiedsschwellen der richtungswahrnehmung in der medianebene beim naturlichen horen, sowie beim horen kunstkopf-ubertragungssystem," *Acustica* **28**, 197–208.